5TH FERMI SYMPOSIUM PROCEEDINGS

October 20-24 2014,
Nagoya, Japan

fermi
Gamma-ray
Space Telescope

- GRB

- AGN

- Analysis

- EPO

- Future

5th Fermi Symposium

October 20-24, 2014 ,Nagoya University, Japan

Symposium URL: http://fermi.gsfc.nasa.gov/science/mtgs/symposia/2014/
(Presentation files and proceeding files were uploaded.)

SOC: Markus Ackermann, Bill Atwood, Ronaldo Bellazzini, Roger Blandford, Elliott Bloom, Philippe Bruel, Fernando Camilo, Patrizia Caraveo, Dan Castro, Elisabetta Cavazzuti, Jan Conrad, Guillaume Dubus, Justin Finke, Yasushi Fukazawa, Isabelle Grenier, Jochen Greiner, Nobu Kawai, Julie McEnery, Peter Michelson, Nicola Omodei, Bill Paciesas, Judy Racusin, Steve Ritz, Chris Shrader, Hiro Tajima, Tad Takahashi, Yasunobu Uchiyama, Anna Watts, Colleen Wilson-Hodge

LOC: Lynn Cominsky, Yasushi Fukazawa, J.D. Myers, Tsunefumi Mizuno, Judy Racusin, Hiromitsu Takahashi, Hiro Tajima, Yasuyuki Tanaka, Toni Venters

Proceeding Editor: Yasushi Fukazawa, Yasuyuki Tanaka, Ryosuke Itoh

Satio Hayakawa and dawn of high-energy astrophysics in Japan

Jun Nishimura
ISAS/JAXA, Sagamihara, Kanagawa, Japan

(Abstract) Gamma ray astrophysics is now one of the most exciting fields in the space physics, in which the Fermi satellite has been playing an important role in exploring new phenomena and findings. Needless to say, great strides were also made recently in higher energy region by the ground based IACT (Imaging Air Cherenkov Telescopes) of Veritas, HESS and Magic. The closely related fields of the gamma-ray astrophysics, X-ray astrophysics as well as the direct observations of Cosmic-ray particles have given us exciting information on the violent phenomena occurring in the stars, our Galaxy, and other galaxies as well as Intergalactic space.
I am most pleased to talk in this 5th Fermi symposium at Nagoya University, where Hayakawa spent his most active time as a pioneer and an outstanding leader, promoting and organizing the young physicists in a wide range of physics topics, particularly in the field of high-energy astrophysics including Infrared astrophysics in the space.

1.

As in the case of other countries, in our country, cosmic-ray physicists first promoted high-energy astrophysics. Hayakawa started cosmic-ray studies under S.Tomonaga, in the field of the high-energy particle physics. Soon after, around 1950s, his interests move to the cosmic–ray studies as an approach to high-energy astrophysics. He anticipated that it would become a central topic in near future when not so many scientists had paid attentions to this field yet.

As early as 1948, Feinberg and Primakoff [1] discussed the energy loss of cosmic-ray electrons by the Inverse Compton process between cosmic-ray electrons and star lights. Some of the photons boosted by high-energy cosmic-ray electrons in this process are emitted as gamma rays in the space. However, the flux of gamma rays was estimated to be very small, and detecting them was thought to be difficult. This may be the first prediction of gamma rays from space, outside of gamma rays from the Sun.

Four years later, in 1952, Hayakawa pointed out the significance of the gamma-ray astrophysics predicting galactic diffuse gamma rays from the decay of π^o produced in the collisions of cosmic rays with interstellar matters [2]. Since his flux estimate was also small, most cosmic-ray physicists were reluctant to attempt experiments, because it would be extremely difficult to detect the gamma rays under the strong background of cosmic rays. In the same year, Hutchinson also estimated the relative intensity of bremsstrahlung gamma rays by the collisions of high-energy cosmic-ray electrons and interstellar matter [3].

Six years after Hayakawa's prediction, P. Morrison advocated the importance of the gamma rays in the high-energy astrophysics, and predicted the most optimistic estimates so far of gamma-ray flux from the space [4].

This prediction encouraged the cosmic-ray physicists, since it might be easier to detect the gamma rays with rather simple detectors. His prediction was so optimistic, and in some cases it was several orders of magnitude higher than what we observe in recent measurements.

Several balloon experiments tries to detect gamma rays from the space, but with a disappointing lack of success until the gamma-ray satellite OSO-3 first succeeded in observing significant indication of gamma from the Galactic disc [5]. The results of OSO-3 almost agreed with predictions by Hayakawa.

After OSO-3, Gamma-ray Satellites SAS-2, COS-B, CGRO (Compton Gamma ray Observatory), and Integral were launched, and today the Fermi Gamma-ray Satellite has been in operation since 2008. Now gamma-ray astrophysics is one of the most important ways to explore the violent phenomena in the Universe.

The prediction of fluxes in X-ray astrophysics came almost ten years after that of Gamma-ray astrophysics, but X-ray stars were successfully detected in 1962, almost five years before the first significant detection of gamma rays by OSO-3. X-ray astrophysics is closely related to gamma-ray astrophysics, and our understanding of the high-energy phenomena in the space are naturally performed in connection with the results of gamma-ray astrophysics.

Hayakawa also presented several important arguments in high energy astrophysics including:

- Super Nova origin of Cosmic rays
- Long lived Radio Isotope Be^{10} as a spallation fragment from primary cosmic rays in Galactic Space
- High Energy primary Electron, and others

Some details of these topics are in the following sections.

2. Birth of Cosmic-ray Studies in our country

Around 1930, several laboratories had started cosmic-ray research in our country. Among those the Nishina laboratory in Riken, was the largest scale efforts, and conducted most comprehensive researches in this field.

Y.Nishina returned to Japan in 1928, after spending several years studying the modern physics in Europe. Nishina is known as one of the authors of the paper of presenting the Klein-Nishina formula of Compton scattering. This work was performed in Bohr Institute before he left Copenhagen for Japan. He believed it was the most important to extend the Modern Physics in our country, and he asked to Riken to invite the distinguished scientists to introduce Modern Physics to Japan. Heisenberg and Dirac were invited in 1929, and they gave a series of lectures at the University of Tokyo. Nishina himself also lectured on the Modern Physics in a few universities. Yukawa and Tomonaga were graduate students in those days, and they were greatly stimulated to study this field by the lectures.

Nishina laboratory was founded in Riken in 1931. He created four groups in his laboratory; i.e.,

- Theory
- Cosmic rays
- Nuclear Physics by constructing Cyclotron on the same scale as the largest one in Berkley, US.
- Radio biology.

One of the achievements of cosmic ray research in this laboratory was the identification of mesons in cosmic rays, by constructing magnetic cloud chamber of 40 cm dia. with magnetic field of 1.7 T. In 1937, Y.Nishina, M.Takeuchi and T.Ichimiya succeeded to observed the Muon track in their chamber [6], at almost simultaneously with similar works by Neddermeyer–Anderson [7] and Street-Stevens [8].

Nishina-Takeuchi-Ichimiya identified the mass of a meson from the track in their magnetic Cloud Chamber as 223 ± 36me. This was the most accurate measurements in those days, and was within a range of the most recent values of 206.768…me. When they found this Muon track, Nishina immediately contacted Yukawa, informing him that the track is most likely the meson Yukawa has predicted. The arguments that who found the Muons first are presented in reference [9].

Parallel to the research of this magnetic Cloud Chamber, the Nishina laboratory observed the cosmic-ray intensity deep underground at 1400m.w.e. to 3000m.w.e. during 1939-1944 at Shimizu Tunnel, which is, locates almost 150km North-Northwest from Tokyo [10]. The observed intensity at 3000m.w.e. was the deepest point data before the observation by Bollinger in US was established in 1951 [11].

Plans were made for continuous observations of cosmic-ray flux at five different latitudes of Sakhalin, Hokkaido, Tokyo, Taiwan and Palau, and construction of five stable ionization chambers named as Nishina-Type was set in motion in 1935. However all of those chambers were kept in Tokyo because of the War II, but successful to observe the first Forbush increase from the Solar flare in 1942 [12]. Latitude effect surveys and balloon observations were also performed.

During the World War II, the experimental works were suppressed, however, significant progress were continued in the theoretical physics, with semi-regular meeting held relating to meson theory. It is to be noted that the two meson theory was proposed by Sakata, Inoue, Tanikawa already in 1942, in advance to Marshak and Bethe (1947) to resolved the conflicts between lifetime and interaction cross-sections observed in cosmic rays and those of theoretical prediction. In relation to this two-meson theory Taketani also proposed that the gamma rays from the decay of the neutral mesons are the main source of the soft components of cosmic rays in the atmosphere in 1942. Some details of those of the works in the Nishina laboratory are found in the reference [9].

Figure 1: Tomonaga with his Colleagues and Students Hayakawa is right behind Tomonaga. Around1950.
Left to right: Front: S.Sakata, S.Tomonaga, M.Taketani.
Middle: K.Baba, S. Hayakawa, T. Miyajima.
Back: O.Minakawa, T. Kinoista J. Koba.
(From: Tomonaga Memorial Room, University of Tsukuba)

After the War-II, Hayakawa studies cosmic rays under S.Tomonaga in relating to the works of the Nishina laboratory, as the field of the high-energy physics. He provided the analysis of depth and intensity relation observed deep underground in Shimizu Tunnel. He showed that the intensity depth curve bending from the power spectrum can be well explained as the effect of π-μ decay life time including energy losses by the processes of Radiation, Photo-nuclear reaction and Direct pair creations by muons in 1949 [13]. K. Greisen published the same concept on the effect of the π-μ decay to the depth intensity curve independently in US at almost the same time [14].

3. Gamma-Ray Astrophysics

3.1. Gamma-ray Astrophysics predicted by Hayakawa

Hayakawa first concentrated his effort on cosmic rays as an approach to the field of particle physics, but around the 1950s, his interests also extended to cosmic-ray research as high energy astrophysics. He found also it may be favourable given the situation in our country, since cosmic-ray research in high energy astrophysics does not quite require the most recent accelerator results as does cosmic-ray research as the particle physics. Our country is remote from where the work in high-energy accelerator physics was centered.

He made significant contributions himself, and stimulated the young scientists to work in this field. In his paper on:

> *"Propagation of the Cosmic Radiation through Interstellar Space,*
> *S. Hayakawa, 1952, Prog. Theor. Phys.8, p571",*

Figure 2: S. Hayakawa
He performed comprehensive works on Cosmic rays and high-energy Astrophysics, and predicted the importance of Gamma-ray astrophysics through π^o decay in 1952.

he discussed how much interstellar matter is traversed by cosmic rays during he transport from the sources to the Earth, referring to the observed data on heavy primaries in cosmic rays by two groups of the Bradt – Peters (1950), and Dainton-Fowler-Kent. (1951).

In his paper, he also mentioned that gamma-ray emission from the π^0 mesons produced in collisions of cosmic rays and the interstellar medium during the propagation of cosmic rays, is such that:

" *In this passage through this thickness secondary particles are scarcely produced except photons which are due to the decay of neutral pions. The intensity of the secondary photons are estimated as about 0.1% of the total intensity at the geomagnetic latitude 55°, but as nearly 1.5% at the equator".*

This means, Hayakawa predicted the gamma ray flux of

$$\sim 2x10^{-4}/cm^2 s.sr.$$

which almost agree with recently accepted data.

The concept was accepted that it is important for gamma rays from space to be observed, since the gamma-ray flux is proportional to the amount of matter in the line of sight that is,

(Cosmic rays density) times (Density of Interstellar medium).

Thus observation of the gamma ray flux bring us important information on the density of Cosmic rays and Interstellar medium in space, which would be difficult to obtain in otherwise.

However the flux was so faint, almost all cosmic ray scientists were reluctant to attempt experiments with the detector technologies of the time, since they thought that the extraction of the gamma ray flux is very difficult given the strong background of cosmic rays.

3.2. Gamma-ray Flux Predicted by P.Morrison [4]

Six year after the perdition by Hayakawa, P Morrison advocated the importance of Gamma ray astrophysics in 1958. His main argument is that the astrophysics was developed in the past by observing visible light and radio wave, but those photons were descendants of the gamma rays produced from the high-energy phenomena in the stars and Galaxies. In this respect, it is important to observe directly the gamma rays from the source to understand what are happening in the space. Instead of diffuse gamma rays estimated by Hayakawa, he focused to the point sources of gamma rays of the Active stars and Galaxies.

He first discussed on the processes of gamma-ray production:
Synchrotron, Bremsstrahlung, Nuclear gamma rays, πo-decay, Matter and Antimatter annihilations.

In the case of the Radio luminous colliding galaxies of Cyg-A, he estimated the gamma ray flux by assuming the energy source of galaxy is due to the matter – antimatter annihilation. His estimated flux of Gamma rays of Cyg-A was

$$0.1\text{-}1.0/cm^2 s$$

in the range of a few MeV to a few hundred MeV. This is several orders higher than Hayakawa's estimate for the flux of diffuse gamma rays.

Then Morrison proposed we could observe the gamma rays rather easily, if we point the detectors to the source.

Figure 3 : P. Morrison
He advocated the importance of the Gamma–ray Astrophysics particularly on the point sources in 1958**.**

In his paper [4]:
"<u>On Gamma-ray Astrophysics</u>
P. Morrison
1958, IL. Nuovo Cimento VII, No.6, 858",

he mentioned that *:*
"Flights of several hr.'s duration are adequate, and the altitude required are not extreme. Telemetering of data,

or even recovery of the apparatus with stored data. Reasonable angular discrimination can perhaps be obtained in the low energy region at least using lead collimation, should balloon loads permit. Otherwise, the use of scintillation counters, possibly taking advantage of coincidences with Compton scattered photons to help define angles, seems capable of adequate energy and angular discrimination below 1 or 2 MeV. The dominance of pair-production makes counting techniques even more satisfactory, and angular discrimination easier, in the energy range from 10MeV to a few hundred MeV. Here emulsion might be of value."

This statement encouraged many scientists to carry the balloon observations, but they were unsuccessful till the significant observation was made by OSO-3 [5] in late 1960s, almost ten years after the prediction by Morrison.

The importance of Gamma-ray astrophysics, however, has been well recognized by those papers of Hayakawa [2], Morrison [4], together with the as-yet unsuccessful experiments to detect the gamma rays.

In fact, I remember his speech at the dinner party of ICRR (International Conference of Cosmic-ray Conference), in Kyoto in 1961, C. F. Powell, the Nobel Laureate in 1950, said :

Figure 4. C.F. Powell
Nobel Laureate for identifying Pions and Muons using Nuclear Emulsions. He served as a Chairman of Cosmic Ray commission of IUPAP.

> *"In the near future, we cosmic ray physicists shall tell to the Astronomers !*
> *How much interstellar matter there is, and how it is distributed in our Galaxy !"*

3.3. Short Summary

Explore-XI was the first gamma-ray satellite and detected 31 gamma rays during 7month, but later they found it was suffered by heavily backgrounds [15]. The same group improved the detectors and put then on board the OSO-3. OSO-3 detected high-energy gamma rays (>50MeV) from the Galactic plane for the first time in 1967-68 fifteen years after Hayakawa's prediction [5].

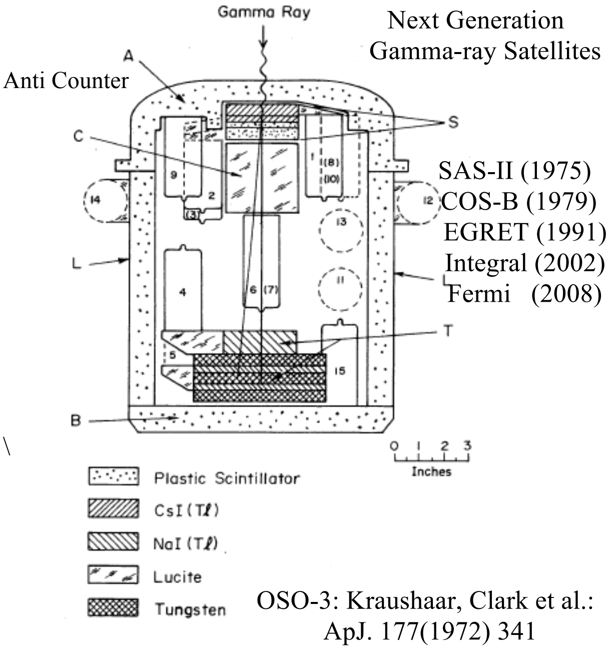

OSO-3: Kraushaar, Clark et al.: ApJ. 177(1972) 341

Figure 5: Gamma-ray satellite OSO-3 [5], and next generation satellites.

They equipped CsI and NaI scintillators arranged as a "phoswich" detector, combining Cerenkov counters inside shielding counters made of plastic scintillators. A total number of 621 gamma rays were observed by this satellite during 16 month in approximate agreement with Hayakawa's prediction.

Following to OSO-3, Satellite SAS-2 COS-B, EGRET, Integral were launched, and the Fermi Satellite are now in work since 2008. SAS-2, Cos-B and EGRET equipped the spark chamber as the imaging detectors to identify the pair electrons from gamma rays without ambiguity from the background tracks. These satellites with spark chambers may be called the second generation of the gamma ray satellites. Integral and Fermi are considered as the third generation of the gamma ray satellites equipped with sophisticated solid state detectors and electronics instead of spark chamber, and thus can analyse the large amounts of data with high statistical accuracy. In particular Fermi satellite can observe gamma rays of energy range extended up to several hundred GeV with high accuracies. Then the gamma-ray astrophysics developed to one of the most significant field to explore the violent phenomena in the Galaxy, and in the Active Galaxies.

When we recall the beginning of the gamma-ray astrophysics, we found:

Hayakawa's prediction was relatively accurate, predicting so faint flux. Then, cosmic-ray physicists reluctant to attempt the experiments.

On the other hand, Morrison's Prediction was optimistic, and encouraged the physicists to carry out gamma–ray detection experiment. His optimistic estimation surely opens the door of the gamma ray astrophysics.

We found the Irony what happed in this history that:

" Accurate expectations do not always help to open the door of new field,
but
Optimistic and even somewhat erroneous expectation promoted to start the Gamma–ray Astrophysics. "

4. X-ray Astrophysics

In contrast to gamma-ray Astronomy, X-rays from space got little attention in the 1950s.

B. Rossi at MIT, had discussions to see the possible observation of X rays from Celestial bodies except to the Sun early in 1960. Hayakawa also joined the meeting. No promising objects for X–ray emission sources were proposed, since the role of compact stars and the extremely high magnetic field of the neutron stars were not yet well understood at the time. The only possibility discussed was faint fluorescent X rays from the lunar surface produced by solar x-rays or cosmic rays.

However, Rossi commented:

"The Nature is more imaginative in many case than we suspect!! ,"

and requested a sounding rocket mission with three Geiger counters on board, an excellent decision.

Figure 6 : B. Rossi

Rossi is a pioneer of on Cosmic ray research since early 1930s, and also the originator of X-ray astrophysics with his MIT colleagues in 1962 [16].

He and his colleague found an extremely strong X-ray flux from the direction of Scorpio X-1 [16]. This is the beginning of X-ray astrophysics.

It is interesting to note that the prediction of X-ray astrophysics came 10 years later than Gamma-ray astrophysics, but the first successful observation was almost 5 years earlier than that of gamma rays.

As to the start of X-ray astrophysics in our country, it was important that M.Oda was asked to join to the MIT group by Rossi, for the early development of the X-ray astrophysics. The reason he was asked to join was that Oda was temporarily in the laboratory of Rossi early 1950's to work on the Extensive Air Showers.

Oda invented the modulation collimator (Fig. 7) during his stay at MIT, and successfully located the position of the optical counterpart of SCOX-1.

In 1965, when the Institute of Space and Aeronautical Science, the Collaborative Institute of Space Science in our country, was founded in the University of Tokyo, he came back to the Institute and spent much effort to develop the X-rays astronomy in our country.

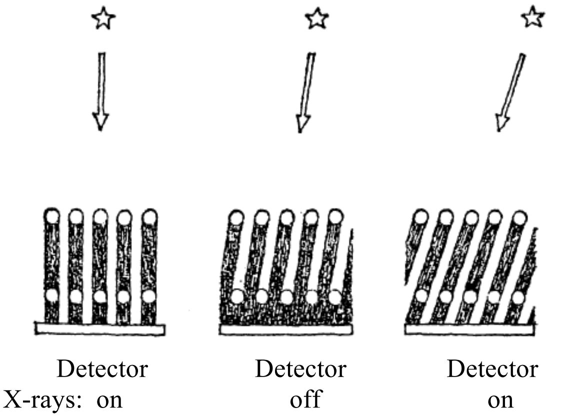

Figure 7 : Modulation Collimator invented by Oda .
By observing the time modulation of the point source, he could locate the X-ray sources with wide field view of detectors.

M. Oda and S. Miyamoto, staff of Oda's laboratory, S. Hayakawa himself and Y. Tanaka, staff of his laboratory had push forward this field in our country.

Unlike Gamma-ray astrophysics, X-rays were detectable by simple detectors, because of their high intensity. In this respect, X-ray astrophysics has been attractive to scientists in our country, where our space facilities had only small-payload launching capability until recently. One of the achievements with modulation collimators in early days by balloon observations are shown Fig. 8 and 9, which was to locate the precise position of CygX-1 [17].

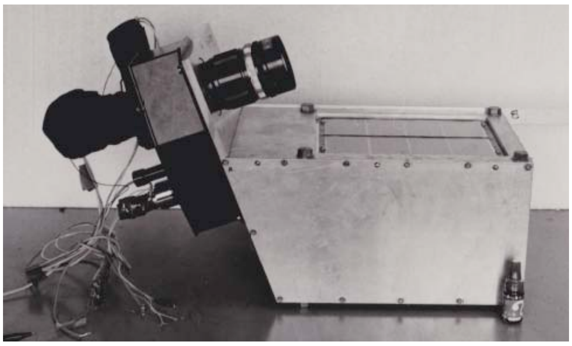

Figure 8. Balloon Borne Detector to locate the CygX-1 with Modulation Collimator.

The Right hand side in Figure 8 is the detector with Modulation collimators to observe the location of CygX-1. Optical Telescope on the left hand side observes the location of the known stars to identify the absolute direction of this detectors [17].

Figure 9: Location of CygX-1 observed by Uhuru Satellite in US and Balloon observations in Japan with the detector shown in Fig. 8.

The location predicted by each group agrees within an error box of each group of several arc min. Soon after Westerberg Radio Telescope find a radio source in these area and Pin-pointed the location.

At almost the same time, similar work with Uhuru, the first scientific satellite for X-rays, was performed in the US [18], and the results agree with each other as shown in Fig.9. The X-ray source location was examined by the radio telescope at Westerbork, and a variable radio source was found. Then the optical counterpart was identified, and it was found that the source is associated with a heavy non-visible star of almost 15 times of mass of the sun. Thus, CygX-1 was presumed to be the first candidate of Black hole.

The first Japanese X-ray satellite, Hakucho, was launched in 1979, and next X-ray satellites followed at intervals of a few years.

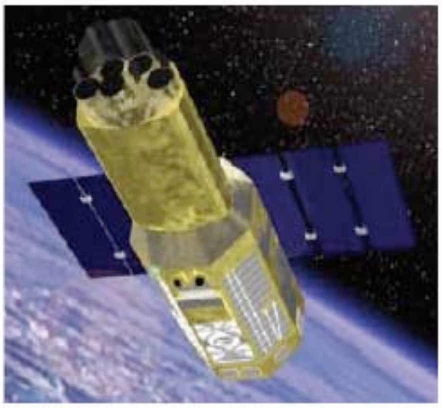

Figure 10: Suzaku
High sensitivity, Soft X-ray Imaging Spectroscopy and Wideband of soft to hard X-ray Spectroscopy.
About 1.7 tons weight, in orbit since 2005.

Although Japanese satellites were small compared to the satellites of other countries in those days, we provided the important advantage of quick response to new findings, to successfully develop X-ray astrophysics in our country. In recent years, however, observations are required more precise, and the satellite required becomes heavy. We now have Suzaku satellite in operation, and Astro-H is to be launched within a few years. The on board instruments are getting more sophisticated as shown in Fig. 10 and 11.

Figure 11. Astro-H
High Resolution Soft X-ray Spectroscopy, and High-sensitivity hard X-ray imaging spectroscopy.
About 2.7 tons weight to be launched in 2015 to early 2016.

4. Cosmic rays

Origin of Cosmic rays, transportations from source to the Earth and the composition of Cosmic rays are closely related to the high-energy phenomena occurring in the Galaxy. In this respect, Hayakawa made several significant contributions. Some of those are:

4.1 Supernova Origin of Cosmic Rays (1956)

W. Baade and F. Zwickey first proposed the model of “Super Nova Origin of Cosmic rays” based on the large energy release of Super Nova explosion (1934) [19]. Later I.S. Shcklovsky and V.L. Ginzburg extended this concept on the bases of the strong radio wave and visible lights from Crab nebula are assumed as the synchrotron radiation by the high energy electrons accelerated in the supernova, and predicted the light should be polarized in 1950s [20], [21]. This model was supported by the observations of polarized of light by J.H. Oort and T.H. Walraven in 1956 [22].

Hayakawa approached the problems in a different way by focusing the relative abundance of the composition of cosmic rays at the source after correcting the fragmentations of heavy elements during the transportation. He presented the model of “Supper-Nova Origin of Cosmic rays” based on the relative overabundance of heavy nuclei in cosmic rays. A super nova is the last stage in the evolution of a massive star, when the relative abundance of heavy elements is large. This argument was accepted to support the model of super nova origin of comic rays when it was published. [23].

Stimulated by his work, more detailed arguments have been developed later and discussions are now still continued to identify the sources taking account of the compositions of cosmic rays and the possible sources.

4.1. Be^{10} as to the measure of confinement time of Cosmic rays

During the transportation of cosmic rays from the source to the Earth in the Galaxy, he mentioned the importance of the long lived radioactive nuclei such as Be^{10} (τ~1.5*10^{6}yr) spallation products of the collisions between cosmic rays and interstellar gas. The fraction of survived Be^{10} gives us the information how long cosmic rays were confined in our Galaxy. Thus the fraction of Survived Be^{10} constrains the amount of cosmic rays required to be produced per unit time in our Galaxy [24]. i.e., the acceleration efficiency of cosmic rays.

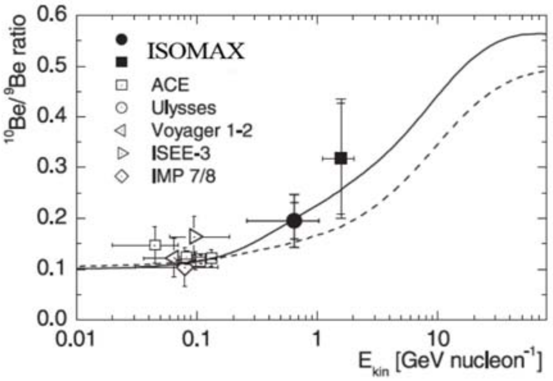

Figure 12: Be^{10}/Be^{9}, From [26] of ISOMAX. (2004). Most recent data published by Pamela group (2013) [27] around 1GeV/Nucleon are not included here, which are consistent with that of ISOMAX [26]

The small flux of Be^{10} is difficult to detect, and was first observed around 0.1GeV/nucleon by Garcia Munos et al. using the IMP 7 and 8 satellites, in 1977 [25]. Around 1GeV, ISOMAX and Pamela with magnet spectrometer succeeded in observing the Be^{10} [26], [27]. Those results are shown in Fig. 12, which indicate the confinement time of the cosmic rays is about 10^{7}years around 1GeV. More detailed observations will be made in the near future, which may allow a more precise estimate of the confinement time of cosmic rays in our Galaxy.

4.2. Cosmic-ray Electrons

Unlike other cosmic-ray components, primary cosmic-ray electrons loss their energy primarily by Synchrotron and Inverse Compton processes during transport from the source to the earth. Since these energy losses are approximately proportional to the square of the electron energy, the spectrum of the electrons adds an interesting feature, particularly at higher energies. Positrons in cosmic rays are naturally produced by the decay of muons produced in collisions between cosmic rays and interstellar medium, and in fact the observed positron intensity below 10GeV, is approximately consistent with the expectation values being entirely secondary. If additional sources other than secondary positrons existed, there is the attractive problem of the production and accelerations of cosmic rays. Ginzburg [28] and Hayakawa et al. first pointed out the importance of measuring the fraction of the flux of Positrons to Electrons in 1958 [28], [24].

The flux of electron is small, under 1% of the overall cosmic ray flux beyond a few GeV, and for precise measurements we need to identify the electrons by rejecting the much more abundant hadronic showers seen in detectors. That is the reason why the first measurements of primary electrons were delayed until 1961, compared to other components of cosmic rays.

The first successful observation was made by P.Meyer and R.Vogt (1961) with scintillation counters and by J. Earl (1961) with an imaging detector, a balloon borne cloud chamber. Many experiments were performed since the discovery of electrons in 1960s. Among the many works on the observation of electrons, I show an example of the observations made by Japan and US collaborations around 1980 [29].

The detector is the emulsion chamber, which is a sandwich of lead plates and nuclear emulsions coated on both sides of a thin plastic plate as shown in Fig. 13. Electrons are identified by tracing showers back to the primary electron track using a microscope. Electron showers begin with an associated electron pair created by the primary electrons within a top layer of a few radiation lengths of the detector. The rejection power to proton is estimated as 10^{4}-10^{5}. The detailed will be found in the original paper [29]. The energies of electrons are identified by counting the number of shower tracks within the 100mirons from then shower axis. As illustrated in the Fig.14, we see, no particular structure on the electron spectrum was observed beyond the statistical errors.

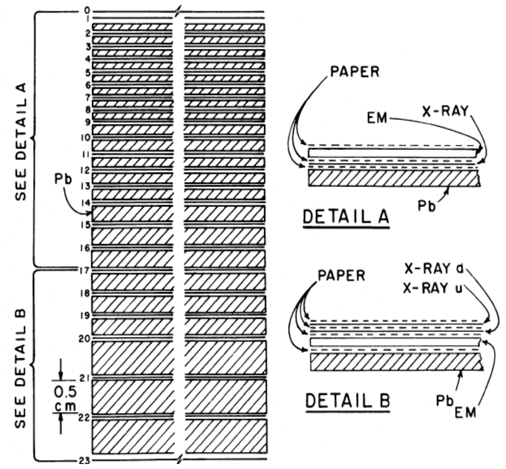

Figure 13 : Emulsion chamber configuration as a Detector of cosmic-ray electrons in 1976 flight [29].

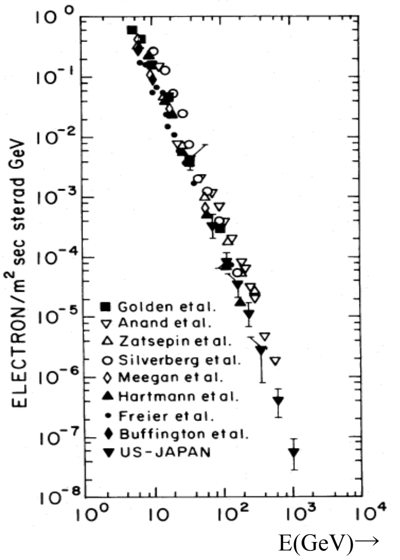

Figure 14. Observed Cosmic-Ray electron Spectrum around 1980 [28]

A large total exposure factor was accumulated by a series of balloon observations, by 2000 almost seven times of those of [28] of 1980 (finally ~8.2m^{2}sr day beyond 1TeV), and electrons up to a few TeV region were observed in these detectors [29].

4.2.1. Effects of nearby sources of Electrons

The theoretical argument on the possible deviation of the smooth power law of electron spectrum was first mentioned by C.S.Shen [30] based on the Pulsar and Supernova origin of cosmic rays in 1970.

The electrons lose energy almost proportional to the square of their energies, by the Synchrotron and Inverse Compton processes. Then if electrons of energy of E are observed at the Earth, they must be emitted from a source within the past T years, where T is inversely proportional to the energy of E. The value of T also depends on the energy densities of ambient photons and magnetic field. As an illustration, using the proper energy density of ambient photon and magnetic field, we estimate that for electrons with E>1TeV must have been produced within T<10^5 years.

During this lifetime of T, 1TeV electron can travel about 1kpc depending on the values of diffusion parameter. If the energy is smaller than 1TeV, the lifetime T is longer, and the travel distance increases. This means if we look the higher energy spectrum of electrons they must have been produced more recently than those of low energy electrons. Accordingly, the distance of their sources must be nearer. As the energy of electrons become higher, the location of the source must be nearer, and the number of available sources (SNR and Pulsars) is limited. In the higher energy region, we expect only a few sources for electrons, and we would expect large non-statistical fluctuations of the electron spectrum and anisotropy for nearby sources.

Each individual source might create a feature in the spectrum. We would therefore expect to observe humps and the anisotropies in the spectrum, corresponding to the identifiable sources.

These describe the concept by Shen, and more details will be found in his paper [31]. When Shen proposed this concept, he assumed sources were the observed SNR and pulsars, but the parameters of those objects were not clear at the time. Later, several authors, Cowsik-Lee (1979), Nishimura et al. (1979), Aharonian et al. (1995), Atoyan et al. (1995), Pohl-Espoid (1998), Erykin–Wolendale (1998) and Kobayashi et al. (2004), discussed these features more details using the most recent data of those objects [32], [33]. I presented some of the results in early days to the international Conference of Cosmic rays in Kyoto, 1979.

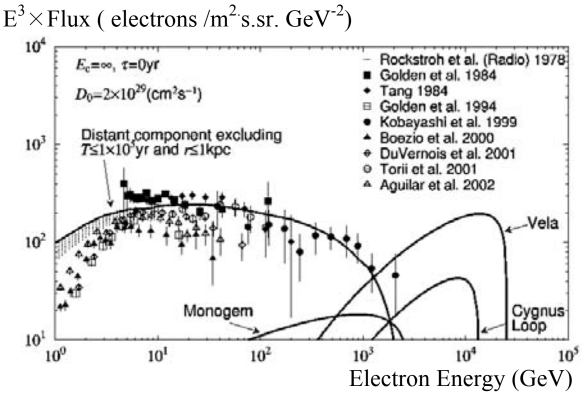

Figure 15: An example of the effect to Cosmic-ray electron spectrum by nearby sources [33]

However, the rapporteur of my friend, did not refer at all this work. He explained that such event might occur at extremely high-energy region where the flux is few, then it could not be observed and the argument is not realistic and he said to me why he discarded my report.

Such response is some times occur when the new concept were proposed. After 30 years from this episode, the hump of electron spectrum becomes one of the important phenomena relating to the origin of cosmic rays and even to the existence of the Dark Matters, which are now to be discussed in this meeting.

4.2.2. Observed hump in the Electron Spectrum

The hump of electron spectrum was first reported in the series of the observations of large balloon-borne ATIC detector program.

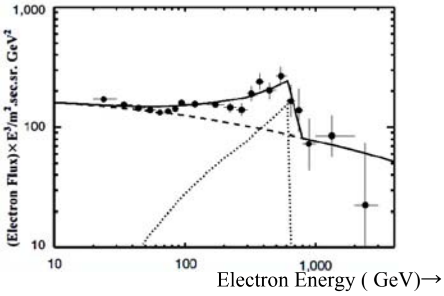

Figure 16: Observed hump in the electron spectrum between 300-800GeV by ATIC group [34].

J. Chang et al. of ATIC group claimed the excess of cosmic-ray electrons at energies of 300GeV – 800 GeV. which could be interpreted as due to the nearby source of electrons or due to the pair electrons from the annihilation of dark maters of mass of around 600GeV [33]. Their data are shown in Fig. 16.

Several observations followed to provide more details of the electron and positron spectrum relating to these indications.

HESS presented the spectrum of primary electrons observed through Cherenkov radiation from the extensive air showers of the primary electrons [35]. This indicates the decline of the spectrum beyond 1 TeV.

4.2.3. Positron Excess

The Pamela Satellite, a magnet spectrometer detector which was launched in 2006, found a definite increase of the positron fraction from 10 to 100GeV, which indicated the existence of positron sources other than secondary positrons from muon decay [36].

The Fermi satellite observed the primary electron spectrum and also estimate the positron fraction by exploiting the East and West Asymmetry of the electron components [37]. Most recent data are due to AMS (Alpha Magnet Spectrometer), which has almost ten times larger acceptance area of Magnetic spectrometer than Pamela. AMS was launched and installed on International Station in 2011, and observed more significant data than Pamela on the positron fraction as well as electron spectrums [38].

A summary of the data on Cosmic-ray electrons from these recent observations is shown in Fig. 19. The hump at several hundred GeV exists, but looks to be smeared in shape by combining those data compared to the hump seen by ATIC. The fraction of positron is definitely increased up to 500GeV, indicating the existence of sources other than secondary production from the decay of muons, but increasing rate ceases beyond 200GeV as shown in Figure 20

Then the problems are what are the sources of high-energy electrons and particularly the positrons.

PAMELA

Payload for **Anti**matter **E**xploration and **L**ight Nuclei **A**strophysics

S Ω ~21.5cm^2.sr

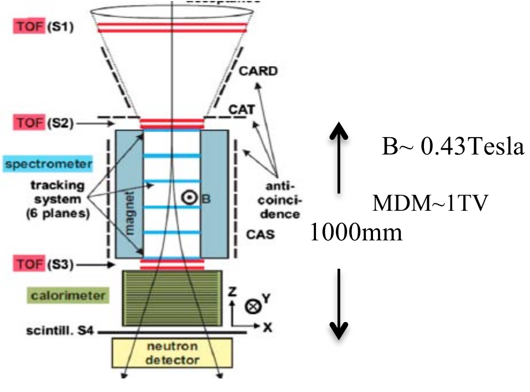

Figure 17: Configuration of Pamela,
Margent spectrometer for cosmic rays. In orbit 2008 [36].

AMS (Alpha Magnet Spectrometer):

S Ω ~300cm^2.sr

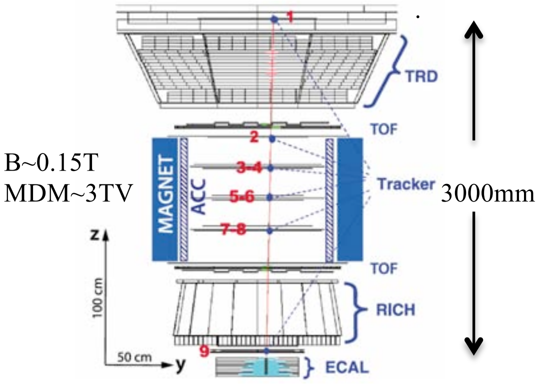

Figure.18: AMS (Alpha magnet Spectrometer)
Large size spectrometer to observe High Energy Cosmic Rays, installed on International station in 2011. [38]

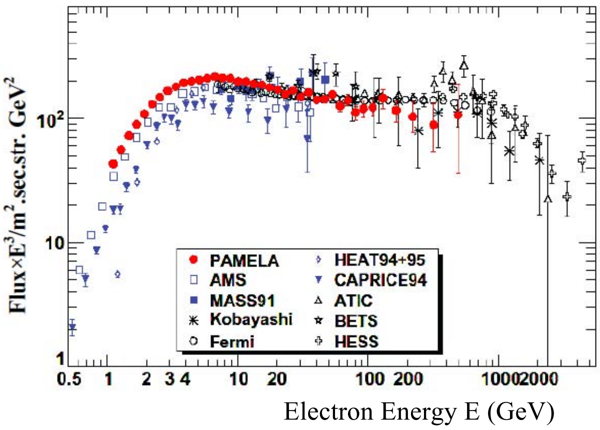

Figure. 19: Electron Spectrum; from [36]
Most recent data of AMS [38] are not included, but the AMS data is limited to ~500GeV. Below a few hundred GeV the data of AMS are consistent with those of Pamela [36].

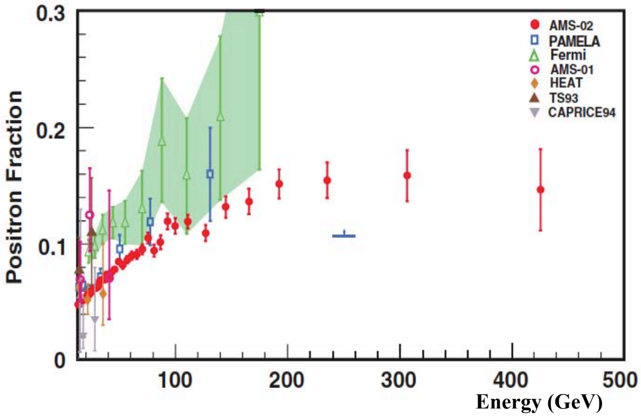

Figure.20: Positron Excess
The fraction of positron is definitely increasing with positron energy. This indicates the existence of sources other than secondary product of muon decays, but increasing rate ceases beyond 200GeV [38]. The fraction of the secondary positrons from muons is estimated under 0.02 beyond 100GeV [36].

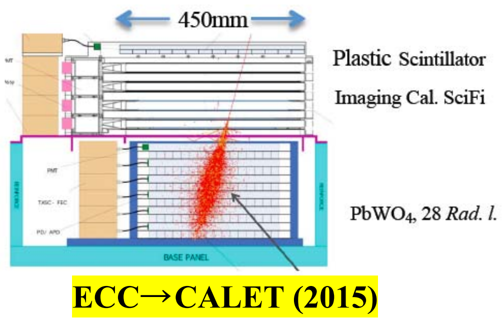

Figure 21: Calet detector layout (**Cal**orimetric **E**lectron **T**elescope) [39]
Inside bracket shows the expected launching yr.

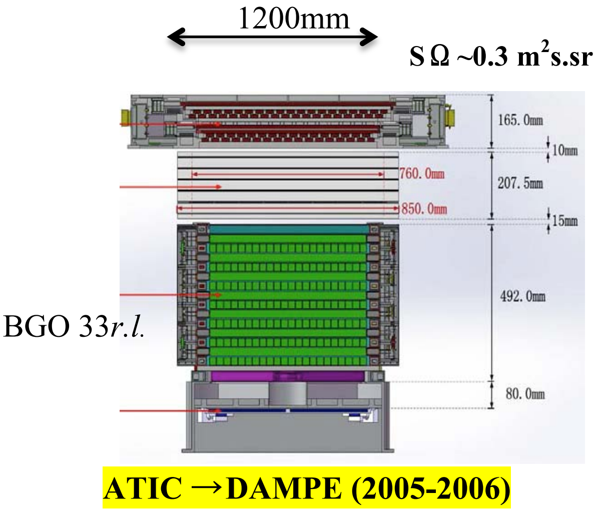

Figure 22: DAMP detector layout [40]
(**Da**rk **M**atter **P**article **E**xplore)
Inside bracket shows the expected launching yr.

Possibilities are discussed of nearby sources by pulsars and/or SNR surrounded by gas material and /or dark matter. In case of Dark matter annihilation, positron fractions increase with positron energies, but should drop abruptly beyond the rest energy of Dark matter. Similar but not so sharp feature would also be seen in case of nearby source. These ideas are to be discussed in this meeting. To obtain a more precise spectrum of electrons from the GeV to TeV region, several new programs are planned to be in operation within a few years. Those are shown in Fig. 21, 22, 23 and 24. The detectors have essentially large detection area with deep depth of calorimeter or to detect the Geo-Synchrotron X-rays together with the detection of the arrival direction of incoming particles to see the possible anisotropies of the particles. These are enable us to detect small flux of electrons and gamma rays with high rejection power against to the hadronic components. These experiments will bring us new findings relating the sources of high-energy electrons and /or related dark matter in near future.

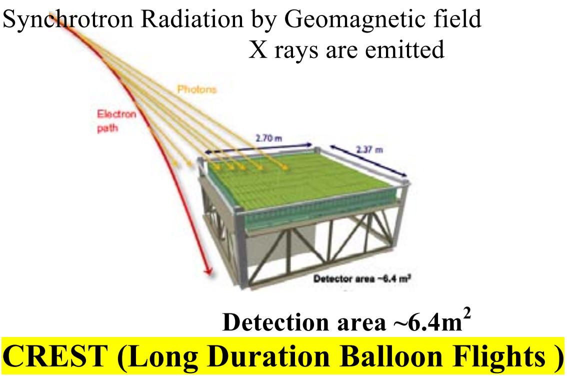

Figure 23: CREST detector Layout
(**C**osmic-**r**ay **E**lectron **S**ynchrotron **T**elescope) [41]

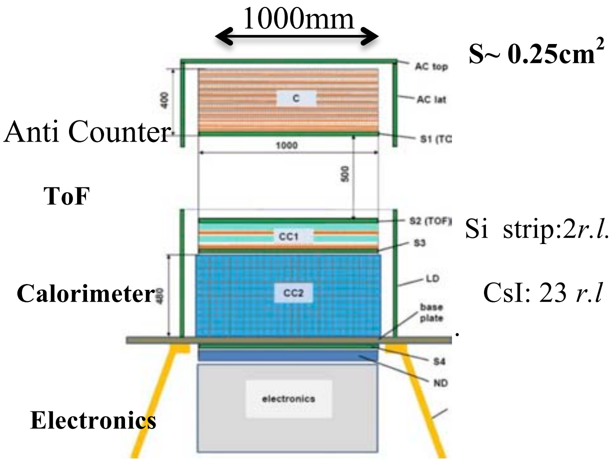

Gamma 400 (2020)

Figure 25: Gamma 400 detector layout [42]
Inside bracket shows the expected launching yr.

5. Summary and Acknowledgements

In describing the “Dawn of high energy Astrophysics Japan”, I found we owe very much to Hayakawa for his tremendous efforts to develop this field with his pioneering works and stimulation in our country. We deeply appreciate him for his outstanding leadership for many years from his young days in early 1950. I hope the success of this symposium in Nagoya through good discussions, explorations and new findings.

In closing my talk, I would like to acknowledge to the organizing committee for inviting me to talk this subject. I also wish to thank to my colleagues for their useful comments in preparation of this manuscript.

References

[1] E.Feinberg and H. Primakoff, 1948, Phys. Rev. **73**, 449

[2] S.Hayakawa, 1952, Prog. Theor. Phys. **8**, 571

[3] W. Hutchinson, 1952, Phil. Mag**. 43,** 847

[4] P.Morrison, 1958, Il Nuovo Ciment **7**, 858

[5] W.L. Kraushaar et al. , 1972, ApJ, **177**, 341
The first gamma ray satellite is Explore X1 (1961) by the same group of OSO-3, but they found the results of Explore-XI was greatly suffered by backgrounds.

[6] Y. Nishina, M. Takeuchi and T. Ichimiya 1937, Phys. Rev. 52, 1198

[7] S.H. Neddermeyer and C.D Anderson, 1937, Phys. Rev. **51**, 884

[8] J.C. Street and E.C. Stevenson, 1937, Phys. Rev. **52**, 1005

[9] Early studies on cosmic ray research in Japan are found in a Report by J. Nishimura, in
Proc. of Centurial symposium 2012 on “Cosmic ray Discovery” Denver, CO. USA, June 26-28, 2012
Edited by: Jonathan F. Ormes
AIP Conference Proceedings, **1516**, page 25
Melville, NY, USA, 2013[10]

[10] Y. Miyazaki, 1949, Phys. Rev. **76**, 1733

[11] M.Bollinger, 1951, Ph. D Thesis, Cornell University

[12] S.E.Forbush, 1946, Phys. Rev. 1946, **70**, 711

[13] S. Hayakawa, 1948, Prog. Theor. Phys. **3**,199

[14] K. I. Greisen, 1948,Phys. Rev. **71**, 521

[15] W.L. Kraushaar et al., 1965, ApJ. **141,** 84

[16] R. Giacconi et al., 1962, PRL. **9**, 439

[17] S. Miyamoto et al, 1971, ApJ, **168**, L11

[18] H. Tananbraum et al., 1971, ApJ, **165**, L37

[19] W. Baard, and F. Zwickey, 1934, Proc. National Acad. Science, 20, 254

[20] I.S.Sylovasky, 1953, Dokl. Akad. Nauk. USSR, **90**, 983

[21] V.L. Ginzburg and J. Evans, 1951, Dokl. Akad. Nauk. USSR, **76**, 377
V.L.Ginzburg, 1956, Izv. Akad. Nauk. USSR, **20**, 5

[22] J.H. Oort and Th. Walraven, 1956, Bull. Astr. Inst. Netherland, **12**, 285

[23] S. Hayakawa, Prog. Thor. Phys. 1956, **15**, 111

[24] S. Hayakawa, K. Ito, and Y Terashima, 1958, Prog. Theor. Phys. Supple **6**,1

[25] Garcia Munos et al., 1977, ApJ. **217**, 859

[26] T. Hams et al, 2004, ApJ.**611**, 892

[27] E.A.Bogomolov et al., 2013, Bull. Russian Academy of Science, Phys. , **77**, 609

[28] V.L. Ginzburg, 1958, Prog. In Elementary and Cosmic Ray Physics, Vol.4, Amsterdam, North Holland Publishing

[29] J. Nishimura et al., 1980, ApJ, **238**, 394

[30] T.Kobayashi et al., 2012, ApJ, **760**, 146

[31] C.S.Shen, 1970, ApJ, **162,** L181

[32] Nishimura, 1979, Proc. Int. Cosmic Ray Conf. Kyoto **1**, 478

[33] T. Kobayashi et al. 2004, ApJ, **601**, 3340
References of other works are found in this ref.

[34] J. Chang et al., 2008, Nature, **456**, 362

[35] F. Aharonian, et al., 2008, PRL, 101, 261104

[36] O. Adriani et al., 2008, Nature**, 458**, 607
W. Menn et al., 2013, Adv. Sp. Res. **51**, 2019

[37] M.Ackermann et al., 2010, Phys. Rev. D. **82**, 092004
C. Sgro on behalf of Fermi LTA Collaboration, Presented at Nagoya Fermi Meeting, 2014, Oct. 20, In this Proceedings

[38] L. Accardo et al., 2014, PRL. **113**, 221101
M. Aguilar et al., 2014, PRL. **113**, 221102

[39] S. Torii et al., 2011, NIM. Phys. Res. A., 630, 55

[40] Meng Su, 2014, “Debate on Nature of Dark matter”
http://www.cfa.harvard.edu/events/2014/sackler/

[41] S. Coutu et al., 2011, Nuclear Phys. B (Proc. Suppl.) **215,** 250

[42] A.M. Galpar et al., arXiv 1306_6175,
P. Cumani et al.in this Proc.

Detection of VHE Bridge emission from the Crab pulsar with the MAGIC Telescopes

T. Saito
Kyoto University, Kyoto, 606-8052 Japan
S. Bonnefoy
Universidad Complutense, Madrid, E-28040 Spain
K. Hirotani
Academia Sinica, Institute of Astronomy and Astrophysics (ASIAA), Taipei, P.O. Box: 23-141 Taiwan
R. Zanin on behalf of the MAGIC Collaboration
Universitat de Barcelona, ICC, IEEC-UB, Barcelona, E-08028 Spain

arXiv:1502.02757v1 [astro-ph.HE] 10 Feb 2015

The Crab pulsar is the only astronomical pulsed source detected above 100 GeV. The emission mechanism of very high energy gamma-ray pulsation is not yet fully understood, although several theoretical models have been proposed. In order to test the new models, we measured the light curve and the spectra of the Crab pulsar with high precision by means of deep observations. We analyzed 135 hours of selected MAGIC data taken between 2009 and 2013 in stereoscopic mode. In order to discuss the spectral shape in connection with lower energies, 4.6 years of Fermi-LAT data were also analyzed. The known two pulses per period were detected with a significance of 8.0 σ and 12.6 σ. In addition, significant bridge emission was found between the two pulses with 6.2 σ. This emission can not be explained with the existing theories. These data can be used for testing new theoretical models.

1. Introduction

The Crab pulsar and the surrounding Crab nebula are the remnant of the supernova of AD 1054. Both the pulsar and the nebula are well studied in a very wide energy range starting from radio (10^{-5} eV) to VHE energies (up to tens of TeV). It is one of the youngest pulsars known and its spin down luminosity (4.6×10^{38} erg/s) is the highest among Galactic neutron stars. To date, this pulsar is the only one for which pulsed emission has been detected above 100 GeV.

Gamma-ray pulsation from the Crab pulsar up to ~ 10 GeV had been known since the 1990s [Nolan et al. 1993]. In 2008, pulsations were detected by the MAGIC telescope at energies above 25 GeV [Aliu et al. 2008]. This result suggested that the emission originates in the outer magnetosphere. The simplest curvature radiation scenario in the outer magnetosphere predicts an exponential cutoff in the energy spectrum at GeV energies [e.g., Muslimov and Harding 2004, Takata et al. 2006, Tang et al. 2008]. *Fermi*-LAT observations from 100 MeV to a few tens of GeV, which started in August 2008, showed a clear break in the spectrum at ~ 6 GeV [Abdo et al. 2010] supporting this scenario. A few years later, however, MAGIC and VERITAS [Aleksić et al. 2011, 2012a, Aliu et al. 2011] found that the energy spectrum of the Crab pulsar extends up to 400 GeV following a power law. The emission above 100 GeV is difficult to explain only with the curvature radiation, and additional or different emission mechanisms are required. Several new models were recently proposed to explain the energy spectrum of the Crab pulsar [e.g., Aleksić et al. 2011, Aharonian et al. 2012].

Here we present new results from the continuing monitoring of the Crab pulsar with the MAGIC telescopes that will help to constrain any model for the emission. In order to discuss the Crab pulsar spectra at energies lower than those accessible to MAGIC, *Fermi*-LAT data were also analyzed.

2. Instruments, data sets, and analysis methods

2.1. The MAGIC Telescopes

The MAGIC telescopes are two Imaging Atmospheric Cherenkov Telescopes located on the island of La Palma (Spain) at 2200 m above sea level. Both telescopes consist of a 17 m diameter reflector and a fast imaging camera with a field of view of 3.5°. The trigger threshold for regular observations at zenith angles below 35° is around 50 GeV and the sensitivity above 290 GeV (in 50 h) is 0.8% of the Crab nebula flux with an angular resolution better than 0.07° [Aleksić et al. 2012b].

For this study we used 135 hours of data taken at zenith angles below 35° during optimal technical and weather conditions between September 2009 and April 2013. Standard MAGIC analysis, as described in Moralejo et al. [2009] and Aleksić et al. [2012b], was applied to the data. The conversion from event arrival times to pulsar rotational phases used Tempo2 software [Hobbs et al. 2006] and a dedicated package inside MARS [López 2006]. The spin parameters of the Crab pulsar were taken from the monthly reports of the Jodrell Bank Radio telescope[1] [Lyne et al. 1993].

2.2. *Fermi*-LAT

The Large Area Telescope (LAT) is a pair conversion gamma-ray detector on board the *Fermi* satellite [Atwood et al. 2009]. It can detect high-energy gamma rays from 20 MeV to more than 300 GeV. It has been operational since August 2008 and all the collected data are publicly available. In this work, we have used 5.5 years of Pass 7 reprocessed data[2] from 2008 August 4 to 2014 January 31. The region of interest was chosen to be 30° around the Crab pulsar.

Along with the public data, the LAT team provides the corresponding analysis software and instrument response functions (IRF) designed for the analysis of that particular dataset. We have used the version v9r32p5 of the *Fermi*-LAT ScienceTools[3] and the P7REP_SOURCE_V15 IRF. From the downloaded data we have discarded events taken at zenith angles above 100° to reduce the contamination of albedo gamma rays coming from the Earth's limb. To compute the pulse phase, we used the same spin parameters as for the MAGIC analysis. The obtained fluxes were computed by maximizing the likelihood of a given source model using the gtlike tools. The binned likelihood method was adopted and a 40° square area with 0.2° bin width was used for the likelihood maximization. Apart from the Galactic (gal_iem_v05.fits) and extragalactic (iso_source_v05.txt) diffuse emission, we considered as background sources for the likelihood fits all sources listed in the second LAT source catalogue [Nolan et al. 2012]. The data taken during the periods when the Crab nebula was flaring were not excluded from the analysis. These flares should not have any impact on the pulsed emission results because it is known that the pulsation component did not change during the flares [Buehler et al. 2012], and the average nebula flux including flare periods was subtracted when the pulsar signal was determined. Regarding the reported Fermi-LAT spectrum from the Crab nebula, the six Crab flares that lasted a few days might be responsible for a few percent of the photons below 1 GeV in the overall 5.5 year dataset. Given that the effect is expected to be small, and that this paper focusses on the emission from the pulsar, we did not correct for this effect.

3. Results

3.1. Light curve above 50 GeV

Figure 1 shows the light curves of the Crab pulsar measured by MAGIC. Two peaks are clearly visible. Following our previous study [Aleksić et al. 2012a], we define phase ranges for the two peaks as $\mathrm{P1_M}$ (phase -0.017 to 0.026) and $\mathrm{P2_M}$ (0.377 to 0.422). The background level (hadrons and continuum gamma rays) is estimated using the phase range between 0.52 and 0.87 and it is then subtracted from the histograms[4]. The number of excess events in $\mathrm{P1_M}$ between 50 GeV and 400 GeV is 930 ± 120 (8.0 σ) and in $\mathrm{P2_M}$ is 1510 ± 120 (12.6 σ).

In addition to the two main peaks, significant emission between them is also visible. The region between the peaks is generally called the Bridge. Defining the Bridge region as the gap between $\mathrm{P1_M}$ and $\mathrm{P2_M}$, namely, between 0.026 and 0.377 (hereafter $\mathrm{Bridge_M}$), we obtain an excess of 2720 ± 440 (6.2 σ) events in this region. Adopting the definition used at lower energies for the Bridge as the region $0.14 - 0.25$ from Fierro et al. [1998] (hereafter $\mathrm{Bridge_E}$), then the number of excess events is 880 ± 200 (4.4 σ). This excess increases to 1940 ± 370 (5.2 σ) if we extend $\mathrm{Bridge_E}$ with the so-called trailing wing of P1 and the leading wing of P2, namely to the interval of $0.04 - 0.32$ [see Fierro et al. 1998]. It should be noted that this detection confirms the hint of bridge emission already reported in [Aleksić et al. 2012a].

3.2. Comparison with lower energies

Figure 2 shows the light curves at optical, X-ray, and gamma-ray energies obtained with various instruments, together with the $50-400$ GeV light curve from the bottom panel of Fig. 1. The background was subtracted in the same way as the MAGIC light curves (see Sect. 3.1). The intensity and morphology of the bridge emission varies considerably with energy. It is very weak at optical wavelengths and in the $100-300$ MeV range, while there is an appreciable difference at X-rays and soft gamma rays. At the energies covered by MAGIC, the peaks become much sharper and a prominent bridge emission appears.

It is known that the flux ratio between the two peaks strongly depends on energy, as does the ratio between the first peak and the bridge [see, e.g., Kuiper et al. 2001]. Fig. 3 shows the flux ratio between $\mathrm{P2_M}$ and $\mathrm{P1_M}$ and that between $\mathrm{Bridge_E}$ and $\mathrm{P1_M}$ as a function of energy from optical ($\sim$ 2 eV)

---

[1] http://www.jb.man.ac.uk/~pulsar/crab.html

[2] http://fermi.gsfc.nasa.gov/ssc/data/analysis/documentation/Pass7REP_usage.html

[3] http://fermi.gsfc.nasa.gov/ssc/data/analysis/scitools/overview.html

[4] An estimation of the background using the off-peak interval from the LAT Second Pulsar Catalog, namely the phase range between 0.61 and 0.89, lead to very similar results.

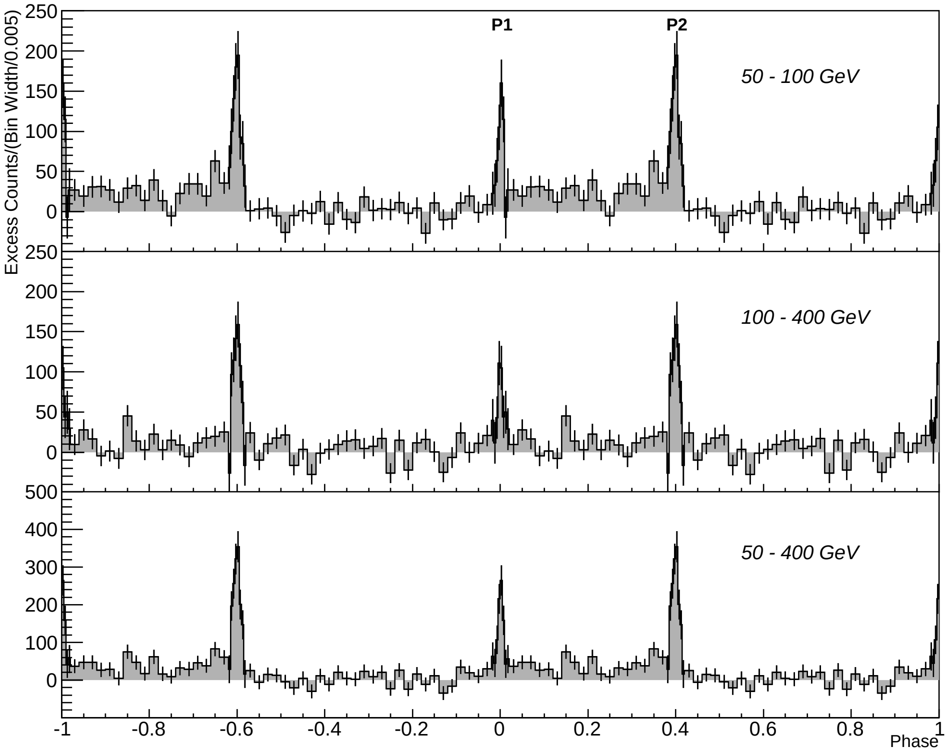

Figure 1: Light curves of the Crab pulsar obtained by MAGIC from 50 GeV to 100 GeV (top), from 100 GeV to 400 GeV (middle), and for the full analyzed energy range (bottom). The bin widths around the peaks are 4 times smaller (0.005) than the rest (0.02) in order to highlight the sharpness of the peaks.

to 400 GeV. Steady emission was subtracted before the ratios were computed. The ratios $\mathrm{P2_M/P1_M}$ and $\mathrm{Bridge_E/P1_M}$ behave similarly. These ratios increase with energy up to 1 MeV, decrease up to 100 MeV, and increase again from that energy on. At $50-400$ GeV, the ratios basically follow the trend seen at lower energies.

3.3. Spectral energy distribution

The spectral energy distributions (SEDs) of the $\mathrm{P1_M}$, $\mathrm{P2_M}$, $\mathrm{Bridge_M}$, and $\mathrm{Bridge_E}$ between 100 MeV and 400 GeV are shown in Fig. 4, together with the Crab nebula SED obtained with a subset of the data used for the pulsar analysis. The SEDs were calculated using *Fermi*-LAT data below 50 GeV (below 200 GeV for the nebula), and MAGIC data above 50 GeV. The nebula SED is connected smoothly between the two instruments. The *Fermi*-LAT data were fit with a power law with an exponential cutoff, while the MAGIC data were fit with a simple power-law function. The obtained fit parameters are summarized in Table I. The power-law indices between 50 GeV and 400 GeV are about 3 and no significant difference is seen between different pulse phases. The uncertainty in the absolute energy scale is estimated as 17%, whereas the systematic error of the flux normalization is estimated to be 18%. We estimate the overall systematic uncertainty uncertainty on the spectral slope to be 0.3.

4. Discussion

In summary, the Crab pulsar above 50 GeV exhibits a light curve with a significant bridge emission between two sharp peaks (Fig. 1). The flux ratios $\mathrm{P2_M/P1_M}$ and $\mathrm{Bridge_E/P1_M}$ increase with increasing photon energy between 100 MeV and 400 GeV (Figs. 2 and 3). Between 30 GeV and 400 GeV, the fluence in the bridge phase is comparable to that in the P1 phase (Fig. 4). The SEDs in the $50-400$ GeV range could be fit with power-law functions for the three phases.

There are several models which can explain the VHE emission of the Crab pulsar, such as Aleksić et al. [2011], Aharonian et al. [2012], Bednarek [2012], Arka and Dubus [2013], Chkheidze et al. [2013]. However, none of them can explain the VHE pulse profile and the spetrum consistently. Further theoreticaly studies and deeper observations of the Crab and other gamma-ray pulsars are needed to understand the VHE emission

Table I Spectral Parameters

phase	$F_1{}^a$ $[10^{-11}\mathrm{MeV}^{-1}\mathrm{cm}^{-2}\mathrm{s}^{-1}]$	$\Gamma_1{}^a$	$E_c{}^a$ [GeV]	$F_{100}{}^b$ $[10^{-11}\mathrm{TeV}^{-1}\mathrm{cm}^{-2}\mathrm{s}^{-1}]$	$\Gamma_2{}^b$
$\mathrm{P1_M}$	8.87 ± 0.14	1.88 ± 0.01	3.74 ± 0.15	4.18 ± 0.59	3.25 ± 0.39
$\mathrm{P2_M}$	3.14 ± 0.07	1.97 ± 0.01	7.24 ± 0.64	8.48 ± 0.62	3.27 ± 0.23
$\mathrm{Bridge_M}$	7.70 ± 0.11	1.74 ± 0.01	7.19 ± 0.39	12.2 ± 3.3	3.35 ± 0.79
$\mathrm{Bridge_E}$	0.95 ± 0.04	1.44 ± 0.04	6.94 ± 0.90	3.7 ± 1.1	3.51 ± 0.97

[a] Parameters obtained by fitting a function $F(E) = F_1(E/1\mathrm{GeV})^{-\Gamma_1}\exp(E/E_c)$ to *Fermi*-LAT data between 100 MeV and 300 GeV

[b] Parameters obtained by fitting a function $F(E) = F_{100}(E/100\mathrm{GeV})^{-\Gamma_2}$ to MAGIC data between 50 GeV and 400 GeV

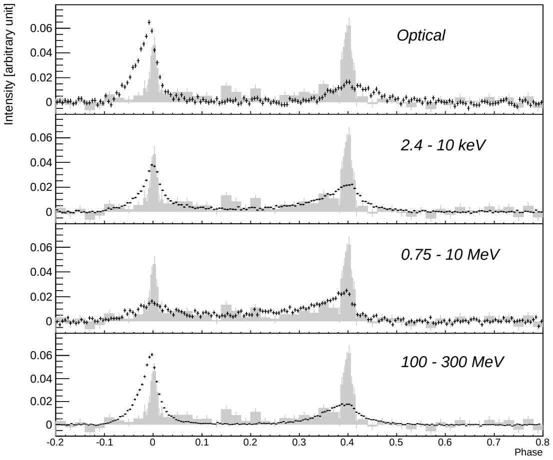

Figure 2: Light curve of the Crab pulsar at optical wavelength, 2.4 – 10 keV X-rays, 0.75 – 10 MeV, and 100 – 300 MeV gamma rays (from top to bottom). The light curve at 50 – 400 GeV is overlaid on each plot for comparison. The optical light curve was obtained with the MAGIC telescope using the central pixel of the camera [Lucarelli et al. 2008]. The keV and MeV light curves are from Kuiper et al. [2001]. The 100 – 300 MeV light curve was produced using the *Fermi*-LAT data. All light curves are zero-suppressed by estimating the background using the events in the phase range from 0.52 to 0.87.

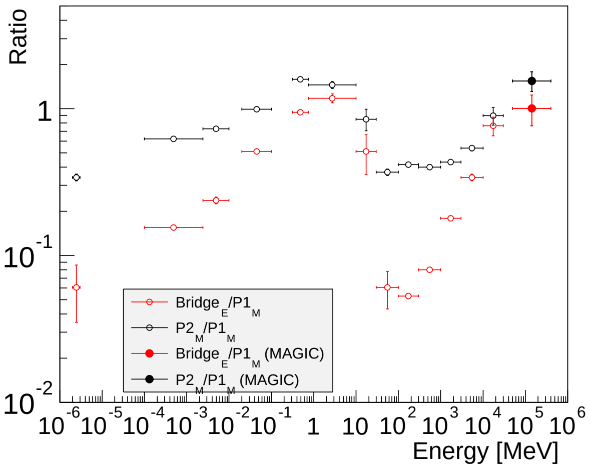

Figure 3: $\mathrm{P2_M/P1_M}$ ratio (black markers) and $\mathrm{Bridge_E/P1_M}$ ratio (red markers) as a function of energy. At optical energies (a few eV), the ratios are obtained using the central pixel of the MAGIC camera [Lucarelli et al. 2008]. From 100 eV to 100 MeV, ratios are computed based on the light curves shown in Kuiper et al. [2001]. From 100 MeV to 30 GeV, *Fermi*-LAT data were used.

mechanism of pulsars.

Acknowledgments

We would like to thank the Instituto de Astrofsica de Canarias for the excellent working conditions at the Observatorio del Roque de los Muchachos in La Palma. The support of the German BMBF and MPG, the Italian INFN, the Swiss National Fund SNF, and the Spanish MINECO is gratefully acknowledged. This work was also supported by the CPAN CSD2007-00042 and MultiDark CSD2009-00064 projects of the Spanish Consolider- Ingenio 2010 programme, by grant DO02-353 of the Bulgarian NSF, by grant 127740 of the Academy of Finland, by the DFG Cluster of Excellence Origin and Structure of the Universe, by the DFG Collaborative Research Centers SFB823/C4 and SFB876/C3, by the Polish MNiSzW grant 745/N-HESS-MAGIC/2010/0, by the Croatian Science Foundation (HrZZ) Project 09/186 and by the Formosa Program between National Science Council in Taiwan and Consejo Superior de Investigaciones Cientificas in Spain administered through grant number NSC100-2923-M-007-001-MY3.

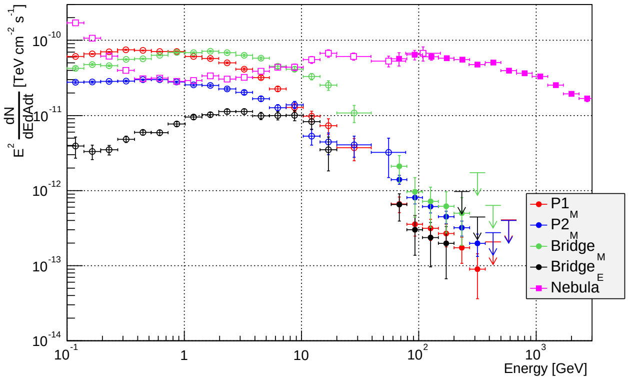

Figure 4: Spectral energy distributions of the Crab nebula, $P1_M$, $P2_M$, $Bridge_M$, and $Bridge_E$ measured with *Fermi*-LAT (below 50 GeV) and MAGIC (above 50 GeV). The flux values averaged over the rotation period are plotted.

References

P. L. Nolan, Z. Arzoumanian, D. L. Bertsch, J. Chiang, C. E. Fichtel, J. M. Fierro, R. C. Hartman, S. D. Hunter, G. Kanbach, D. A. Kniffen, et al., ApJ **409**, 697 (1993).

E. Aliu, H. Anderhub, L. A. Antonelli, P. Antoranz, M. Backes, C. Baixeras, J. A. Barrio, H. Bartko, D. Bastieri, J. K. Becker, et al., Science **322**, 1221 (2008), 0809.2998.

A. G. Muslimov and A. K. Harding, ApJ **606**, 1143 (2004), astro-ph/0402462.

J. Takata, S. Shibata, K. Hirotani, and H.-K. Chang, MNRAS **366**, 1310 (2006), astro-ph/0511690.

A. P. S. Tang, J. Takata, J. J. Jia, and K. S. Cheng, ApJ **676**, 562 (2008), 0711.2719.

A. A. Abdo, M. Ackermann, M. Ajello, W. B. Atwood, M. Axelsson, L. Baldini, J. Ballet, G. Barbiellini, M. G. Baring, D. Bastieri, et al., ApJ **708**, 1254 (2010), 0911.2412.

J. Aleksić, E. A. Alvarez, L. A. Antonelli, P. Antoranz, M. Asensio, M. Backes, J. A. Barrio, D. Bastieri, J. Becerra González, W. Bednarek, et al., ApJ **742**, 43 (2011), 1108.5391.

J. Aleksić, E. A. Alvarez, L. A. Antonelli, P. Antoranz, M. Asensio, M. Backes, J. A. Barrio, D. Bastieri, J. Becerra González, W. Bednarek, et al., A&A **540**, A69 (2012a), 1109.6124.

E. Aliu, T. Arlen, T. Aune, M. Beilicke, W. Benbow, A. Bouvier, S. M. Bradbury, J. H. Buckley, V. Bugaev, K. Byrum, et al., Science **334**, 69 (2011), 1108.3797.

F. A. Aharonian, S. V. Bogovalov, and D. Khangulyan, Nature **482**, 507 (2012).

J. Aleksić, E. A. Alvarez, L. A. Antonelli, P. Antoranz, M. Asensio, M. Backes, J. A. Barrio, D. Bastieri, J. Becerra González, W. Bednarek, et al., Astroparticle Physics **35**, 435 (2012b), 1108.1477.

A. Moralejo, M. Gaug, E. Carmona, P. Colin, C. Delgado, S. Lombardi, D. Mazin, V. Scalzotto, J. Sitarek, D. Tescaro, et al., ArXiv e-prints (2009), 0907.0943.

G. B. Hobbs, R. T. Edwards, and R. N. Manchester, MNRAS **369**, 655 (2006), arXiv:astro-ph/0603381.

M. López, Ph.D. thesis, Universidad Complutense de Madrid, https://magicold.mpp.mpg.de/publications/theses/MLopezMoya.pdf (2006).

A. G. Lyne, R. S. Pritchard, and F. Graham-Smith, MNRAS **265**, 1003 (1993).

W. B. Atwood, A. A. Abdo, M. Ackermann, W. Althouse, B. Anderson, M. Axelsson, L. Baldini, J. Ballet, D. L. Band, G. Barbiellini, et al., ApJ **697**, 1071 (2009), 0902.1089.

P. L. Nolan, A. A. Abdo, M. Ackermann, M. Ajello, A. Allafort, E. Antolini, W. B. Atwood, M. Axelsson, L. Baldini, J. Ballet, et al., ApJS **199**, 31 (2012), 1108.1435.

R. Buehler, J. D. Scargle, R. D. Blandford, L. Baldini, M. G. Baring, A. Belfiore, E. Charles, J. Chiang, F. D'Ammando, C. D. Dermer, et al., ApJ **749**, 26 (2012), 1112.1979.

J. M. Fierro, P. F. Michelson, P. L. Nolan, and D. J. Thompson, ApJ **494**, 734 (1998), arXiv:astro-ph/9709123.

F. Lucarelli, J. A. Barrio, P. Antoranz, M. Asensio, M. Camara, J. L. Contreras, M. V. Fonseca, M. Lopez, J. M. Miranda, I. Oya, et al., Nuclear Instruments and Methods in Physics Research A **589**, 415 (2008).

L. Kuiper, W. Hermsen, G. Cusumano, R. Diehl, V. Schönfelder, A. Strong, K. Bennett, and M. L. McConnell, A&A **378**, 918 (2001), arXiv:astro-ph/0109200.

W. Bednarek, MNRAS **424**, 2079 (2012), 1205.4855.

I. Arka and G. Dubus, A&A **550**, A101 (2013), 1208.2819.

N. Chkheidze, G. Machabeli, and Z. Osmanov, ApJ **773**, 143 (2013).

Fermi/LAT Study of the Cygnus Loop Supernova Remnant: Discovery of a Point-like Source and of Spectral Differences in its gamma-ray emission

I. Reichardt* and R. Terrier
Astroparticule et Cosmologie (APC), Université Paris 7 Denis Diderot, 75205 Paris Cedex 13, France
J. West and S. Safi-Harb
Department of Physics and Astronomy, University of Manitoba, Winnipeg, MB R3T 2N2, Canada
E. de Oña-Wilhelmi
Institut de Ciències de l'Espai (IEEC-CSIC), 08193 Bellaterra, Spain
J. Rico
Institut de Física d'Altes Energies (IFAE), 08193 Bellaterra, Spain

arXiv:1502.03053v2 [astro-ph.HE] 3 Mar 2015

The Cygnus Loop is a nearby supernova remnant (SNR) observed across the electromagnetic spectrum. With the analysis of 6 years of Fermi/LAT data we find that, what previous studies had considered a single source, consists of an extended source plus a point-like source south-east of the SNR. The extended gamma-ray emission is well correlated with the thermal X-ray emission of the SNR, and the energy spectrum displays a pronounced maximum at $\sim 0.6\,\mathrm{GeV}$. However, in a region where the radio emission is strongly and distinctly polarized, the gamma-ray spectrum shows no sign of a break. Therefore, the spatially resolved gamma-ray emission permits the study of different interaction conditions of the SNR and the surrounding medium.

1. INTRODUCTION

The Cygnus Loop is the remnant of a core-collapse supernova explosion that occurred about 14000 year ago [Levenson et al. 1998] at a distance of 540^{+100}_{-80} pc [Blair et al. 2005]. The Cygnus Loop is among the closest supernova remnants (SNRs) to Earth, which implies that it could act as a local accelerator. Due to its proximity, the Cygnus Loop is seen on the sky with an angular size of about 3 degrees. In general, the blast wave of the SNR is not breaking out of a dense cloud, but running into a wall of atomic gas related to the cavity in which the supernova occurred. The wall slows down the shock, which becomes bright in optical emission lines. The reflected shock propagates through the hot interior, which enhances the X-ray emission in correlation with the optical emission [Graham et al. 1995, Levenson et al. 1996]. However, some portions of the shock proceed unimpeded through low-density inter-cloud medium.

X-ray emission from reflection-shocked gas is particularly bright in the east. In contrast, the south of the SNR (the so-called *breakout*) is very dim in X-rays. This is often regarded as caused by the expansion of the blast wave into a low-density medium. However, Uyanıker et al. [2002] found that the polarization of the 2695 MHz emission was much higher there with respect to the north of the shell. A possible interpretation of this feature is that a second SNR is present in that region, and interacts with the Cygnus Loop.

No compact object is firmly associated with the collapsed progenitor of the Cygnus Loop. A few candidates lie within the breakout, where the *ASCA* survey revealed a point-like source, but it is not firmly established as a neutron star [Miyata et al. 2001]. There is yet another compact object with a candidate pulsar wind nebula nearby, revealed by *Suzaku* and *XMM-Newton* observations [Katsuda et al. 2012]. No pulsations have been detected from any of these objects. In addition, a very high transverse proper motion of $\sim 1300\,\mathrm{km\ s^{-1}}$ is needed if it is assumed that one of these candidate neutron stars departed from the geometric center of the Cygnus Loop some 14000 years ago. Such a supersonic movement would produce a cometary shape in the X-ray emission that has not been observed so far. However, this could be explained if the neutron star was related to the second SNR suggested by Uyanıker et al. [2002].

The detection of GeV gamma-ray emission from the Cygnus Loop was published in Katagiri et al. [2011], who analyzed two years of *Fermi*/LAT data comprised between August 2008 and August 2010. In this analysis, the shape of the Cygnus Loop was modeled as a ring, somewhat more extended than the shell seen at other wavelengths. The spectrum is curved (modeled as a log-parabola), and the fit to a one-zone hadronic model returns plausible values for the parameters.

In this work we analyze six years of *Fermi*/LAT data using the latest software. The factor 3 increase in statistics with respect to the previous study provides unprecedented sensitivity to study both spatial and spectral features of the gamma-ray emission from the Cygnus Loop.

---

*now at INFN Padova, Italy (`ignasi.reichardt@pd.infn.it`).

2. DATA ANALYSIS

We analyzed *Fermi*/LAT `Pass 7` Reprocessed data corresponding to the period between August 4^{th} 2008 (start of science operations) and September 7^{th} 2014. We defined the ROI as a circle of 10° radius centered at the position (RA, DEC) = $(20^h58^m11^s, 29°23'56'')$, J2000, which is 2° displaced towards negative Galactic latitudes with respect to the catalog position of the Cygnus Loop. This is done in order to be less affected by the diffuse emission from the Galactic plane. Data were processed with the version v9r32p5 of the *ScienceTools*. We selected class 3 events in the energy range between 58.5 MeV and 300 GeV, with the recommended quality cuts (including the requirement for the spacecraft to be in normal operation mode, LAT_CONFIG=1, data to be flagged as good quality, DATA_QUAL=1, and a cut on the rocking angle of the spacecraft, ABS(ROCK_ANGLE)< 52°). In addition, we applied a zenith angle cut of 100° in order to prevent event contamination from the Earth limb. Data were binned in sky coordinates with the `gtbin` tool, using square bins of 0.125° side. This tool produces a *counts map*, with the number of events recorded by the detector.

We performed a binned likelihood analysis with a model containing the standard Galactic and extra-galactic diffuse emission models provided in the *ScienceTools*, plus the sources in the 2FGL catalog lying up to 15° away of the ROI center. We call the model with the point-like sources plus the Galactic and extra-galactic backgrounds the *null hypothesis*, which has a maximum likelihood $\mathcal{L}_0$. Then, we generate alternative models by adding spatial templates and by changing the functions describing spectral shape. By varying the parameters of each models, we compute the corresponding maximum likelihood $\mathcal{L}_{model}$. We choose the best representation of the Cygnus Loop as the model which obtains the highest value of the likelihood ratio $\mathrm{LR}=2\log(\mathcal{L}_0/\mathcal{L}_{model})$.

For any of the tested models, we can use the tool `gtmodel` to produce an *expected counts map* given the exposure associated to the data set. For visualization purposes, we produce what we call the *S/N map* by subtracting the expected counts map from the actual counts maps, and then dividing by the square root of the expected counts map.

Complementary to the *Fermi*/LAT data analysis, we have re-analyzed the 11 cm radio emission observed by the 100 m Effelsberg telescope. Uyanıker et al. [2002] proposed the Cygnus Loop be divided in two regions for the two-SNR interpretation. Based on our re-analysis, which considers the presence of extended Stokes I radio emission in addition to the distinct and intensely polarized radio emission, we have re-defined the regions to be more equal in size and both having a circular shape. We consider that the southwest (SW) feature is the circular region of 1.07° radius centered at (RA, DEC) = $(20^h49^m, 29°47')$ as shown in Figure 1.

3. RESULTS

3.1. Morphology

The S/N maps at different energy ranges, produced with the null hypothesis are shown in Figure 1. While an extended source is clearly seen at energies below 10 GeV, in the last panel only residual, localized emission is present south of the SNR.

As a first step we reproduced the analysis from Katagiri et al. [2011]. For this purpose we modeled the Cygnus Loop as a ring of 1.6/0.7 degree outer/inner diameter, centered at (RA, DEC) = $(20^h51^m, 30°50')$. The ring is divided in four quadrants, and the spectral parameters of all of them are varied simultaneously. We note that the hard spot remaining above 10 GeV is included in the southeast (SE) quadrant of the ring used in Katagiri et al. [2011]. By substituting the SE quadrant by a point-like source, we find that LR improves by 124. The position of this point-like source optimized by the tool `gtfindsrc` is (RA, DEC) = $(20^h53^m55^s, 29°24'45'')$ with an uncertainty of 0.02°. We call this source J2053.9+2924. Its position is coincident with the X-ray and radio source 2E 2051.7+2911, which is likely an AGN [Brinkmann et al. 1997]. Therefore, we consider that J2053.9+2924 is a source in the background of the Cygnus Loop, and should not intervene in the modeling of the diffuse emission[1].

Having included J2053.9+2924 in the list of point-like sources, we maximize the likelihood of a template generated from the X-ray counts map observed by ROSAT [Aschenbach and Leahy 1999], re-binned to match the pixel size of maps of the present analysis. The likelihood ratios for the spatial models mentioned above are shown in Table I. It is clear that the thermal X-ray emission correlates very well with the observed gamma-ray emission, and requires less degrees of freedom than the ring to describe it.

The X-ray emission is very faint in the region of highly polarized radio emission, but we divide the spatial template in order to study this particular region. The templates for the main (NE) emission is cropped to avoid having pixels accounted for twice in the overlapping region (Figure 2). We verify that both regions

---

[1] The point-like source found in this analysis is called 3FGL J2053.9+2922 in the recently published Third *Fermi*/LAT Source Catalog [The Fermi-LAT Collaboration 2015]. We note that the source overlaps with the template for the Cygnus Loop, which in 3FGL is still modeled as the ring defined in Katagiri et al. [2011].

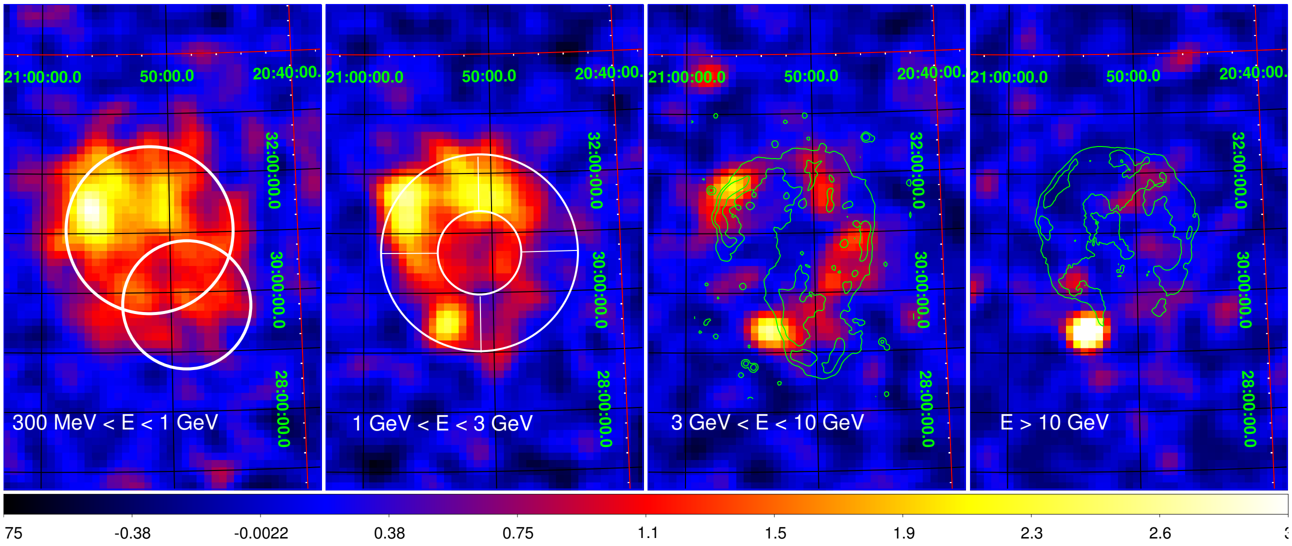

Figure 1: S/N maps of the null hypothesis in different energy ranges. From left to right, the panels include: the two regions discussed in section 3.2; the ring used for modeling in Katagiri et al. [2011]; the radio intensity contours from Uyanıker et al. [2002]; and the X-ray contours from Aschenbach and Leahy [1999].

Table I Likelihood ratio (LR) of the tested templates, with the number of degrees of freedom (d.o.f) added to the null hypothesis after selecting the best spectral model (Section 3.2). Three of the additional d.o.f. always correspond to the spectral parameters of J2053.9+2924, except for (1), where original template by Katagiri et al. [2011] is tested.

Model	**LR**	**d.o.f**
0) Null hypothesis	0	0
1) Ring Divided in four quadrants	2069	12
2) 3/4 Ring SE quadrant substituted by J2053.9+2924	2193	12
3) ROSAT template	2204	6
4) ROSAT template Divided in NE and SW	2238	8

contribute significantly to the overall emission. Next, we proceed to test different the spectral models.

3.2. Spectrum

The energy spectrum of the source is shown in Figure 3. The global emission, as well as the emission of the NE region are well described by a log-parabolic shape. To infer the spectral shape of the SW region, we test a power-law shape, a log-parabolic shape, and a power law with exponential cutoff. Because of the proximity of J2053+2923 to this region, we also test all three possible models for the point-like source. Then, we evaluate the likelihood ratio of each combination with respect to the initial assumption of both components having power-law shaped spectrum. We observe that models where J2053+2923 has an additional degree of freedom in the spectrum have a likelihood ratio with respect to the power-law/power-law hypothesis of $\sim$ 10, whereas models where the additional degree of freedom is added to the SW region only improve the likelihood ratio by $\sim$ 1. Therefore, we conclude that there is $\sim 3\,\sigma$ evidence that the spectrum of J2053+2923 is curved, whereas the spectrum of the SW region is compatible with being a simple power law. The best fit spectral parameters of the global emission and the studied regions are shown in Table II.

Table II Spectral parameters of the Cygnus Loop and its NE and SW regions under the assumption of a log-parabolic spectral shape, $dN/dE = N_0(E/1\,\mathrm{GeV})^{-\alpha-\beta\log(E/1\,\mathrm{GeV})}$. The photon flux at energies above 58.5 MeV is shown in the last column.

Region	α	β	**Flux** $10^{-8}\mathrm{ph\,cm^{-2}s^{-1}}$
Cygnus Loop	2.26 ± 0.03	0.25 ± 0.03	13.5 ± 0.9
NE	2.24 ± 0.04	0.32 ± 0.04	9.0 ± 0.9
SW	2.27 ± 0.06	0	7.2 ± 1.1

3.3. The point-like source J2053+2923

The point-like source South of the Cygnus Loop is detected with high significance (TS=214). As mentioned in Section 3.2, the spectrum is described ei-

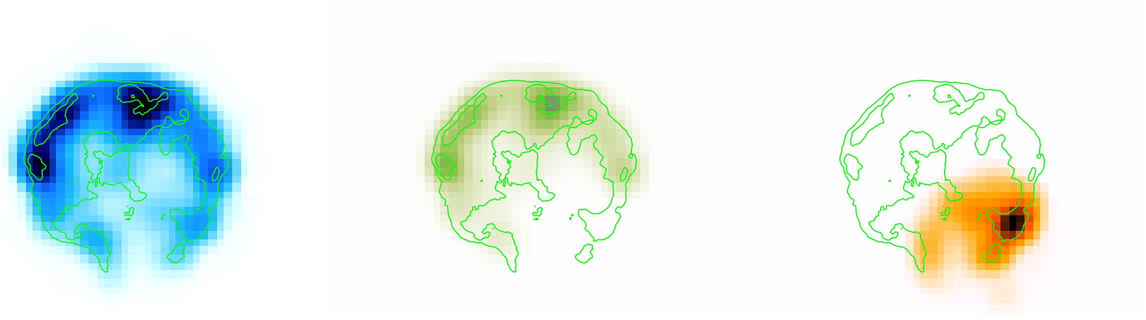

Figure 2: Sketch of the templates used in the *Fermi*/LAT analysis. From left to right: the total emission, the NE region, and the SW region. Color code matches that from Figure 3. Green contours are the same X-ray contours as in Figure 1 [Aschenbach and Leahy 1999].

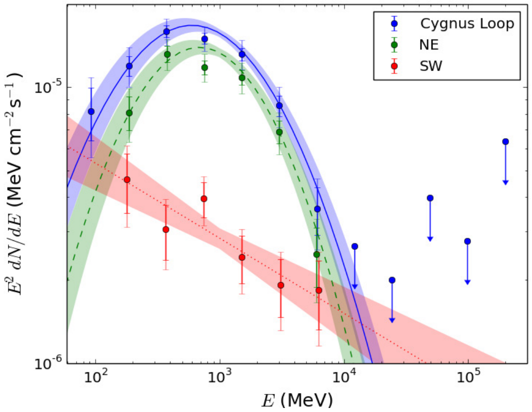

Figure 3: Energy spectrum of the Cygnus Loop (blue). The emission from the NE region is shown in green, while the SW region is represented in red. The statistical uncertainty range of the best model is shown as a shaded area. Spectral points include statistical uncertainties (solid bars) and systematic uncertainties (shaded bars).

ther by a power law with exponential cutoff or by a log-parabolic shape, but the power law with exponential cutoff hypothesis is slightly preferred. The cutoff energy is $(22 \pm 10_{stat})$ GeV, while the spectral index below the cutoff is $1.46 \pm 0.18_{stat}$. The source is not significantly detected at low energies. Using the same spectral binning as for the Cygnus Loop, the flux is measurable ($\mathrm{TS}_{bin} > 10$) between 1 GeV and 72 GeV, making this source a candidate very-high-energy emitter. We also performed an unbinned likelihood analysis in time intervals of 60 days. The source is detected with $\mathrm{TS}_{2month} > 10$ in 13 out of 37 such intervals. This hint of variability supports the association with the background AGN, 2E 2051.7+2911.

4. CONCLUSIONS

Due to its proximity and angular size, the Cygnus Loop permits spatially resolved studies of different parts of the SNR, that interact with different components of surrounding medium. Particularly, it is known that the NE of the shell interacts with relatively dense medium and is thus bright in X-rays and optical emission lines compared to other parts of the shell. These inhomogeneities are likely to happen in other remnants from core-collapse supernovae, while remaining unnoticed due to lack of resolution of the instruments. Understanding the physical mechanisms that power the gamma-ray emission of the Cygnus Loop, and the differences between different regions of the shell, may help understand the variety of spectral shapes that SNRs display at gamma-ray energies.

The fact that most of the gamma-ray emission from the Cygnus Loop follows closely the thermal X-ray emission from shocked matter supports the idea that most of its gamma-ray emission is emitted by interactions of accelerated hadrons with the dense medium. In this case, a low-energy break is expected in the spectrum due to the production threshold of neutral pions [Ackermann et al. 2013].This is the case for the energy spectrum measured in this analysis, which has a maximum around 0.6 GeV. However, the SW portion of shell (which is brighter in radio and fainter in X-rays), has a different gamma-ray spectrum without indication of a spectral break. The explanation for the different gamma-ray properties, and the related radiative processes of the two regions, including the two-SNR scenario, is under investigation.

Acknowledgments

This work was supported by the interdisciplinary project `Labex UnivEarthS` from Sorbonne Paris cité (ANR-10-LABX-0023 and ANR- 11-IDEX-0005-02). We also acknowledge support by NSERC through the

Canada Research Chairs and Discovery Grants programs.

References

N. A. Levenson, J. R. Graham, L. D. Keller, and M. J. Richter, ApJS **118**, 541 (1998), arXiv:astro-ph/9805008.

W. P. Blair, R. Sankrit, and J. C. Raymond, AJ **129**, 2268 (2005).

J. R. Graham, N. A. Levenson, J. J. Hester, J. C. Raymond, and R. Petre, ApJ **444**, 787 (1995).

N. A. Levenson, J. R. Graham, J. J. Hester, and R. Petre, ApJ **468**, 323 (1996).

B. Uyanıker, W. Reich, A. Yar, R. Kothes, and E. Fürst, A&A **389**, L61 (2002), arXiv:astro-ph/0205443.

E. Miyata, K. Ohta, K. Torii, T. Takeshima, H. Tsunemi, T. Hasegawa, and Y. Hashimoto, ApJ **550**, 1023 (2001), arXiv:astro-ph/0011535.

S. Katsuda, H. Tsunemi, K. Mori, H. Uchida, R. Petre, S. Yamada, and T. Tamagawa, ApJ **754**, L7 (2012), 1206.4367.

H. Katagiri, L. Tibaldo, J. Ballet, F. Giordano, I. A. Grenier, T. A. Porter, M. Roth, O. Tibolla, Y. Uchiyama, and R. Yamazaki, ApJ **741**, 44 (2011), 1108.1833.

B. Aschenbach and D. A. Leahy, A&A **341**, 602 (1999).

W. Brinkmann, J. Siebert, E. D. Feigelson, R. I. Kollgaard, S. A. Laurent-Muehleisen, W. Reich, E. Fuerst, P. Reich, W. Voges, J. Truemper, et al., A&A **323**, 739 (1997).

The Fermi-LAT Collaboration, ArXiv e-prints (2015), 1501.02003.

M. Ackermann, M. Ajello, A. Allafort, L. Baldini, J. Ballet, G. Barbiellini, M. G. Baring, D. Bastieri, K. Bechtol, R. Bellazzini, et al., Science **339**, 807 (2013), 1302.3307.

The apparent discontinuity in the periodicity of the GeV emission from LS I +61°303

F. Jaron, M. Massi
Max-Planck-Institute for Radio Astronomie, Auf dem Hügel 69, D-53121 Bonn, Germany

The γ-ray binary LS I +61°303 shows a discontinuity of the periodicity in its GeV emission. In this paper, we show that during the epochs when the timing analysis fails to determine the orbital periodicity, the periodicity is in fact present in the two orbital phase intervals $\Phi = 0.0 - 0.5$ and $\Phi = 0.5 - 1.0$. That is, there are two periodic signals, one towards periastron (i.e., $\Phi = 0.0 - 0.5$) and another one towards apastron ($\Phi = 0.5 - 1.0$). The apastron peak shows the same orbital shift as the radio outburst and, in addition, reveals the same two periods P_1 and P_2 that are present in the radio data. The γ-ray emission of the apastron peak normally just broadens the emission of the peak around periastron. Only when it appears at $\Phi = 0.8 - 1.0$ because of the orbital shift, it is detached enough from the first peak to become recognizable as a second orbital peak, which is the reason why the timing analysis fails. Two γ-ray peaks along the orbit are predicted by the two-peak accretion model for an eccentric orbit that was proposed by several authors for LS I +61°303.

1. Introduction

The stellar system LS I +61°303 is a member of the small class of γ-ray binaries, which are defined as binary stars with a peak in the spectral energy distribution above 1 MeV [1]. A sketch of the system is shown in Fig. 1. LS I +61°303 consists of a Be star and a compact object in an eccentric orbit, $e = 0.72 \pm 0.15$ [5], with orbital period $P_1 = 26.4960 \pm 0.0028\,\mathrm{d}$ [6]. The Be star is rapidly rotating and losing mass in form of an equatorial disk [5]. The nature of the compact object could not yet be established, because the masses are poorly constrained due to the large uncertainty in the inclination angle [5]. The orbital phase of the binary system is defined as

$$\Phi = \frac{t - t_0}{P_1} - \mathrm{int}\left(\frac{t - t_0}{P_1}\right), \qquad (1)$$

where $t_0 = \mathrm{MJD}\ 43366.275$ [6]. Periastron occurs at orbital phase $\Phi = 0.23$ [5].

Radio outbursts are observed at orbital phases $\Phi = 0.5 - 0.9$, i.e., around apastron. Their peak flux densities are modulated in amplitude and orbital phase occurrence by a long-term period $P_{\mathrm{long}} = 1667 \pm 8\,\mathrm{d}$ [6]. The long-term phase Θ is defined analogous to the orbital phase Φ by replacing P_1 by P_{long}.

The source LS I +61°303 is highly variable and periodic all over the electromagnetic spectrum from radio to very high energy γ-rays [2, 5, 6, 7]. The GeV γ-ray light curve, as obtained using *Fermi* LAT data, has so far been reported to peak at orbital phases around periastron [2, 9] (see Fig. 1). Timing analysis shows that the orbital period is present in the *Fermi* LAT light curve from this source, however not with equal power all of the time [9, 10]. There are times (Θ-phases) when the period is outstanding and there are times when the period is completely absent from the power spectrum, as shown well in Fig. 4 of [10]. Moreover, Fig. 3 of [10] shows that GeV data also show the long-term periodical variation affecting the radio data, but only at a specific orbital phase interval, $\Phi = 0.5 - 1.0$, that is around apoastron.

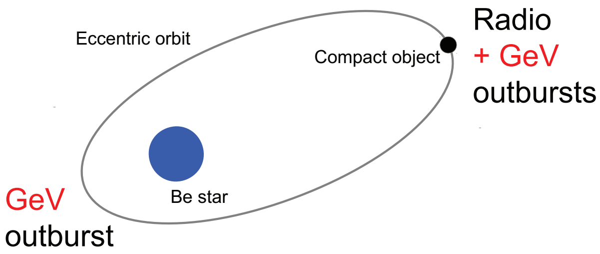

Figure 1: Sketch of LS I +61°303. The periodic GeV outburst at periastron was first reported by [2]. In Sect. 3 a newly discovered periodic apastron GeV peak is discussed [3]. The radio outburst occurs only at apastron, whereas at periastron, only a low level of emission is present [see Fig. 1-Right in 4].

We are aimed here to investigate the discontinuity in the periodicity of the GeV γ-ray emission at periastron, the possible relationship of its disappearance with the variation of the emission around apastron, and finally the possible relationship between GeV and radio emission.

2. Data analysis

For the present analysis [3] we use *Fermi* LAT data from LS I +61°303 spanning the time range August 5, 2008 (MJD 54683) until June 30, 2014 with an energy range of 100 MeV to 300 GeV. For the computation of the light curves we used the script like_lc.pl written by Robin Corbet. [1] Only source-event-class photons were selected for the analysis. Photons with a zenith angle greater than 100° were excluded to reduce contamination from the Earth's limb. For the diffuse emission we used the model gll_iem_v05_rev1.fit and the template iso_source_v05_rev1.txt. We used the instrument response function (IRF) P7REP/background_rev1, and the model file was generated from the 2FGL catalogue [11], all sources within 10° of LS I +61°303 were included in the model. LS I +61°303 was fitted with a log-parabola spectral shape and with all parameters left free for the fit, performing an unbinned maximum likelihood analysis. The other sources were fixed to their catalogue values. We produced light curves with a time bin size of one day and of five days.

We investigated [for details see 3] the temporal evolution of the orbital periodicity by means of a wavelet analysis [12] and Lomb-Scargle timing analysis [13, 14].

3. Results: A periodic signal around apastron

3.1. Wavelet analysis

Our results are shown Fig. 2. The first plot of Fig. 2 presents the examined data set. The wavelet analysis was applied to the γ-ray data vs time, however, for a straightforward comparison with radio data, we express in the other plots of Fig. 2 the x-axis as the long-term phase Θ. The second plot of Fig. 2 shows the wavelet plot for the whole data set, i.e., the whole orbital period $\Phi = 0.0-1.0$. The absence of the orbital period around $\Theta \approx 7.2$ is consistent with the previous finding shown in Fig. 4 of [10]. When wavelet analysis is performed only on data from the orbital phase intervals $\Phi = 0.0-0.5$ (middle) and $\Phi = 0.5-1.0$ (bottom), it is revealed that *there is always a periodic signal at* $\Phi = 0.0-0.5$ *(periastron). Moreover, there is a periodic signal at* $\Phi = 0.5-1.0$ *(apastron).* The latter becomes particularly strong during the time when the orbital period is absent from the power spectra of $\Phi = 0.0-1.0$ [3].

3.2. Lomb-Scargle timing analysis

Figure 3 shows Lomb-Scargle periodograms of the γ-ray flux from LS I +61°303. The data have been selected from orbit phase intervals like in the previous section. In the periodogram for the entire orbit (Fig. 3 a) the strongest feature is a peak which agrees well with the orbital period P_1 found by [17]. Figures 3 d, e, and f, refer to only data from $\Phi = 0.5-1.0$. In this orbital phase interval the peak at $P_{\rm long}$ is a very strong feature, in agreement with the findings of [10]. Moreover, the zoom of Fig. 3 d, i.e., Fig. 3 e, shows a second peak, $P_2 = 26.99 \pm 0.08$ d. This second peak becomes stronger and is almost as strong as the peak at $P_1 = 26.48 \pm 0.08$ d in the 5 day integrated data in Fig. 3 f. The periods P_1, P_2 (see Fig. 4), and $P_{\rm long}$ here present are typical periodicities in radio data as shown in [15].

3.3. Folded *Fermi* LAT data: The apastron GeV peak and its orbital shift

Figure 5 a and b show *Fermi* LAT data from the time ($\Theta \approx 7.2$) of the disappearance of the orbital period from the power spectra folded with the orbital period. A second peak is evident at orbital phases $\Phi = 0.8-1.0$. Figure 5 c shows *Fermi* LAT data for another Θ. It is now interesting to compare these plots with radio data. Because of the long-term periodicity we can compare γ-ray and radio data having the same fractional part of Θ. Figure 5 d shows GBI radio data at 8 GHz [for details see 3].

4. Conclusions

During the intervals where the orbital periodicity is absent from the power spectra, wavelet and the folded light curves show two periodic signals, one at periastron and a second at apastron. The presence of the second periodic outburst disturbs the timing analysis and prevents it from finding the orbital periodicity. Comparison with the folded radio data (Fig. 4 d) suggests that the apastron GeV peak follows the same orbital shift as the radio outbursts [3]. It is well-known the phenomenon of the orbital shift of the radio outburst in LS I +61°303: The largest outbursts occur at orbital phase 0.6, afterwards, with the long-term periodicity, the orbital phase of the peak of the outburst changes, as analysed by [16] in terms of orbital phase shift, by [17] in terms of timing residuals, and reproduced recently by the precessing jet model in [18], here shown in Fig. 5.

Our result of two GeV peaks along the orbit corroborates the two-peak accretion model for LS I +61°303. The hypothesis that a compact object that accretes material along an eccentric orbit undergoes two accretion peaks along the orbit was suggested and developed by several authors for the system LS I +61°303 [19, 20, 21, 22]. The first accretion peak is predicted to occur close to the Be star and to give rise to a major high-energy outburst. The second accretion peak is predicted to occur much farther away from the Be star, where the radio outburst occurs, and a minor

---

[1] `http://fermi.gsfc.nasa.gov/ssc/data/analysis/user/`

high-energy outburst is predicted there [21]. The predicted periastron event corresponds well to the observed GeV peak towards periastron, the second predicted high-energy outburst, corresponds well to the here discussed apoastron peak.

Acknowledgments

We thank Bindu Rani for carefully reading the manuscript and for useful comments. We thank Robin Corbet for answering our questions concerning the computation of light curves. We thank Walter Alef and Alessandra Bertarini for their assistance with computation power. Wavelet software was provided by C. Torrence and G. Compo, and is available at URL: `http://atoc.colorado.edu/research/wavelets/`. The Green Bank Interferometer was operated by the National Radio Astronomy Observatory for the U.S. Naval Observatory and the Naval Research laboratory during the time period of these observations. This work has made use of public *Fermi* LAT data obtained from the High Energy Astrophysics Science Archive Research Center (HEASARC), provided by NASA Goddard Space Flight Center.

References

[1] Dubus, G. 2013, A&A Rev., 21, 64
[2] Abdo, A. A., Ackermann, M., Ajello, M., et al. 2009, ApJ, 701, L123
[3] Jaron, F., & Massi, M. 2014, A&A, 572, AA105
[4] Massi, M., Jaron, F., & Hovatta, T. 2015, arXiv:1502.00934
[5] Casares, J., Ribas, I., Paredes, J. M., Martí, J., & Allende Prieto, C. 2005, MNRAS, 360, 1105
[6] Gregory, P. C. 2002, ApJ, 575, 427
[7] Albert, J., Aliu, E., Anderhub, H., et al. 2009, ApJ, 693, 303
[8] Massi, M., Ros, E., & Zimmermann, L. 2012, A&A, 540, AA142
[9] Hadasch, D., Torres, D. F., Tanaka, T., et al. 2012, ApJ, 749, 54
[10] Ackermann, M., Ajello, M., Ballet, J., et al. 2013, ApJ, 773, LL35
[11] Nolan, P. L., Abdo, A. A., Ackermann, M., et al. 2012,
[12] Torrence, C. & Compo, G. P. "A Practical Guide to Wavelet Analysis", Bulletin of the American Meteorological Society, 1998, 61-78
[13] Lomb, N. R. 1976, Ap&SS, 39, 447
[14] Scargle, J. D. 1982, ApJ, 263, 835
[15] Massi, M., & Jaron, F. 2013, A&A, 554, AA105 ApJS, 199, 31
[16] Paredes, J. M., Estalella, R., & Rius, A. 1990, A&A, 232, 377
[17] Gregory, P. C., Peracaula, M., & Taylor, A. R. 1999, ApJ, 520, 376
[18] Massi, M., & Torricelli-Ciamponi, G. 2014, A&A, 564, AA23
[19] Taylor, A. R., Kenny, H. T., Spencer, R. E., & Tzioumis, A. 1992, ApJ, 395, 268
[20] Marti, J., & Paredes, J. M. 1995, A&A, 298, 151
[21] Bosch-Ramon, V., Paredes, J. M., Romero, G. E., & Ribó, M. 2006, A&A, 459, L25
[22] Romero, G. E., Okazaki, A. T., Orellana, M., & Owocki, S. P. 2007, A&A, 474, 15

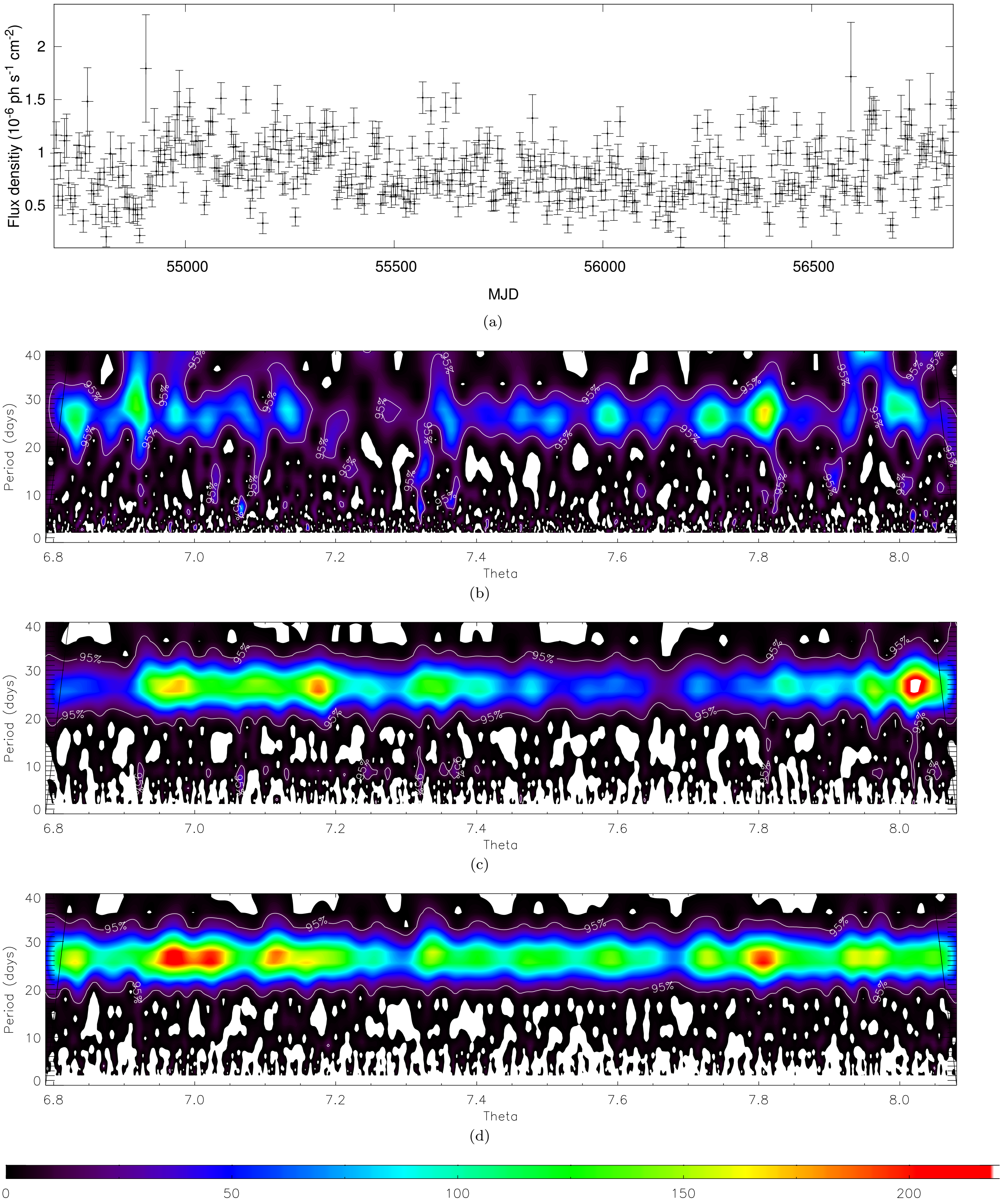

(a)

(b)

(c)

(d)

Figure 2: Wavelet analysis of *Fermi*-LAT data. The strength of periodicity is colour coded as indicated in the bottom bar. (a) *Fermi*-LAT data with a time bin of 1 d. (b) Wavelet analysis for the whole orbital interval $0.0 - 1.0$ (b–d use a time bin of one day). (c) Wavelet analysis for the orbital interval $\Phi = 0.5 - 1.0$, i.e., around apoastron. (d) Wavelet for the orbital interval $\Phi = 0.0 - 0.5$, i.e., around periastron.

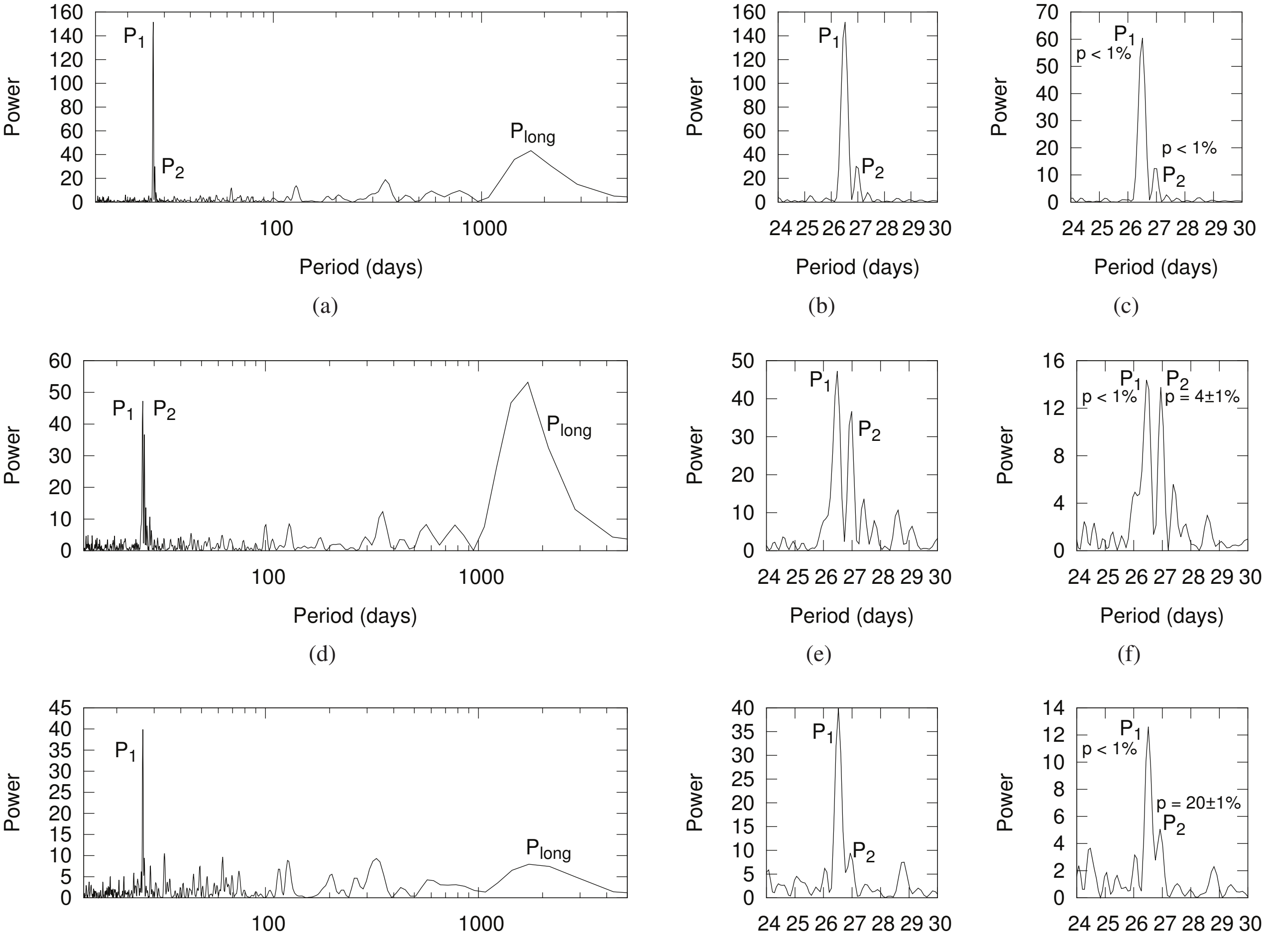

(a) (b) (c)

(d) (e) (f)

(g) (h) (i)

Figure 3: Lomb-Scargle periodogram of the *Fermi* LAT data (with a time bin of one day). Figure 3 in [3]. (a) Data in the orbital phase $\Phi = 0.0 - 1.0$. (b) Zoom of Fig. 3 a. (c) Same as 3 b for data with a time bin of 5 d. (d) Data in the orbital phase $\Phi = 0.5 - 1.0$. The periods P_2 and $P_{\rm long}$ here present are typical periodicities in radio data [15]. (e) Zoom of Fig. 3 d. (f) Same as 3 e for data with a time bin of 5 d. (g) Data in the orbital phase $\Phi = 0.0 - 0.5$. (h) Zoom of Fig. 3 g. (i) Same as 3 h for data with a time bin of 5 d.

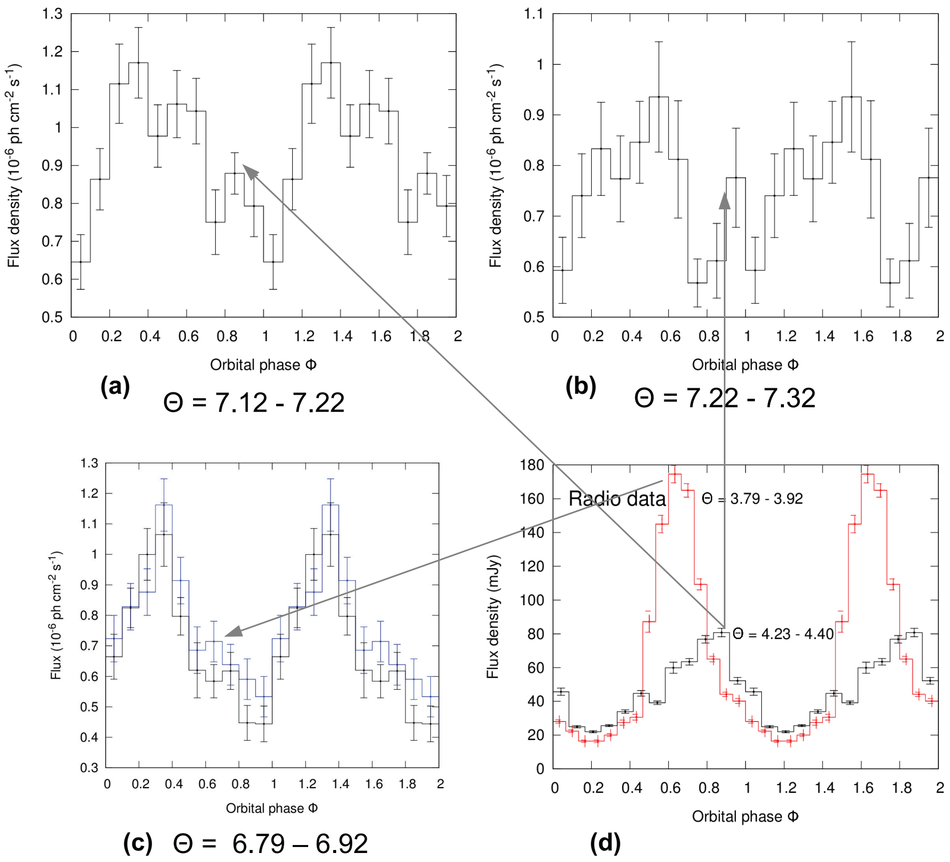

Figure 4: (a)-(c) Folded *Fermi* LAT γ-ray data (100 MeV – 300 GeV). The blue curve in (c) is that of [9]. (d) Folded GBI 8 GHz radio data. The here discovered periodic apastron GeV peak follows the same timing characteristic (i.e., P_1 and P_2 are both present) as the periodic radio peak, which also occurs around apastron. During the time when the orbital period disappears from the power spectra of the γ-ray light curve (see Fig. 2 b, $\Theta \approx 7.2$) the apastron GeV peak becomes well visible in the folded light curve, because it is more displaced from the periastron peak (see [3] and here Sect. 4).

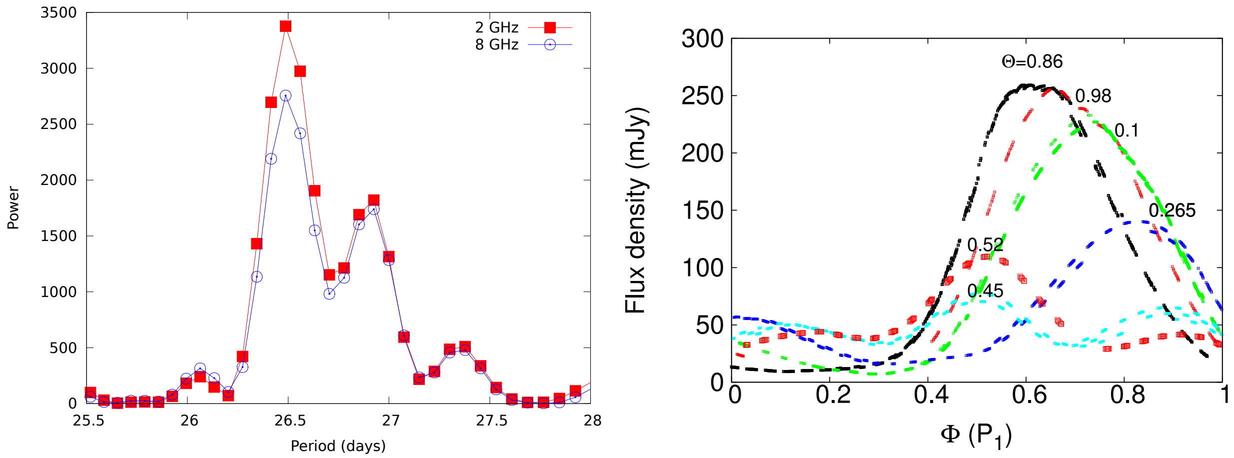

Figure 5: Left: Timing analysis of 6.7 years of GBI radio data at 2 and 8 GHz results in two periods, $P_1 = 26.49 \pm 0.07$ d, $P_2 = 26.92 \pm 0.07$ d. The long-term period $P_{\rm long} = 1667 \pm 8$ d is consistent with the period $P_{\rm beat} = 1/(\nu_1 - \nu_2) = 1667 \pm 393$ d resulting from the beating between the two close periodicities P_1 and P_2 [15]. Right: Orbital shift of the radio outburst of LS I +61°303 in the precessing jet model of [18]. At $\Theta = 0.86$ the outbursts peak at $\Phi \approx 0.6$. At $\Theta = 0.265$ the outbursts peak at $\Phi \approx 0.85$.

New pulsars detected in gamma-rays with the *Fermi*-LAT

H. Laffon, D. A. Smith
Centre d'Etudes Nucléaires de Bordeaux-Gradigan, IN2P3/CNRS, Université de Bordeaux, BP 120 F-33175 Gradignan cedex
L. Guillemot
Laboratoire de Physique et Chimie de l'Environnement et de l'Espace, Université d'Orléans/CNRS and Station de Radioastronomie de Nançay, Observatoire de Paris, CNRS/INSU
on behalf of the *Fermi*-LAT Collaboration

arXiv:1502.03251v2 [astro-ph.HE] 25 Feb 2015

The *Fermi* Large Area Telescope (LAT) is a powerful pulsar detector, as demonstrated by the over one hundred objects in its second catalog of pulsars. Pass 8 is a new reconstruction and event selection strategy developed by the *Fermi*-LAT collaboration. Due to the increased acceptance at low energy, Pass 8 improves the pulsation detection sensitivity. Ten new pulsars rise above the 5 sigma threshold and are presented in this work, as well as one previously seen with the former Pass 7 reconstruction.

More than 60% of the known pulsars with spin-down power ($\dot{E}$) greater than 10^{36} erg/s show pulsations in gamma-rays, as seen with the *Fermi* Large Area Telescope. Many non-detections of these energetic pulsars are thought to be a consequence of a high background level, or a large distance leading to a flux below the sensitivity limit of the instrument. The gamma-ray beams of the others probably miss the Earth. The new Pass 8 data now allows the detection of gamma ray pulsations from three of these high spin-down pulsars, PSRs J1828−1101, J1831−0952 and J1837−0604, as well as three others with $\dot{E} \geq 10^{35}$ erg/s. We report on their properties and we discuss the reasons for their detection with Pass 8.

1. Introduction

Since its launch in June 2008, the *Fermi* satellite has accumulated thousands of hours of observations of the sky. Events recorded by the LAT have very accurate ($\leq 1\mu s$) timestamps derived from GPS clocks onboard the satellite. This precise timing associated with the well-known position of the spacecraft allowed the detection of 132 pulsars listed in the second pulsar catalog (2PC) of gamma-ray pulsars [1]. These objects can be classified in different categories, allowing population studies, as shown in Section 2.

Pass 8 is a new reconstruction and event selection strategy developed by the *Fermi*-LAT collaboration. It allows better acceptance and sensitivity at low energies compared to Pass 7 data (P7REP), as described in Section 3. Most pulsars have spectra that cut off around a few GeV and therefore have most of their flux at these low energies. As a consequence, we expect more pulsar detections in the future thanks to the new Pass 8 reconstruction. Of the eleven new pulsars presented in Section 3 (see Figs. 1, 2 and Table I), ten were not seen with Pass 7. These new detections bring the total number of gamma-ray pulsars known at present to 163 (see Fig. 4). If we also count radio millisecond pulsars discovered at the position of unidentified gamma-ray sources but for which an ephemeris reliable enough to phase-fold the LAT data is not yet available, over 200 gamma-ray pulsars are now known.

The fraction of pulsars detected in gamma-rays increases with spin-down power ($\dot{E}$), as shown in Fig. 3. However, different factors such as distance or low signal-to-background ratio can complicate their detection. This is the case for the six energetic pulsars ($\dot{E} \geq 10^{35}$ erg s^{-1}) presented here, which are located in the central regions of our Galaxy. We focus on these high spin-down power pulsars in Section 4.

2. General properties of gamma-ray pulsars

Gamma-ray pulsars can be divided in two main categories. "Young" ones are produced after a supernova explosion of a massive star and "recycled" ones are old pulsars re-accelerated after the accretion of matter from a binary companion. The latter objects rotate much faster than the young ones with a period of the order of 1 to 30 ms, and are called "millisecond pulsars" (MSPs). The two main categories are well separated in the $P - \dot{P}$ diagram represented in Fig. 4. The fraction of MSPs among the *Fermi*-LAT pulsars currently amounts to 43% while the fraction of MSPs among the total number of known pulsars is only of the order of 10%.

When a pulsar is already known from radio or X-ray observations, the corresponding ephemeris is used to search for pulsations in the LAT data. This technique allowed the detection of more than a hundred of young and recycled pulsars.

"Blind period searches" of unidentified LAT sources, in LAT data and with radiotelescopes, led to dozens of new pulsars. Deep radio follow-ups of the gamma-ray pulsars discovered in the LAT blind searches determined that nearly all are "radio-quiet" ($S_{1400} \leq 30$ μJy, see Fig. 3 in [1]).

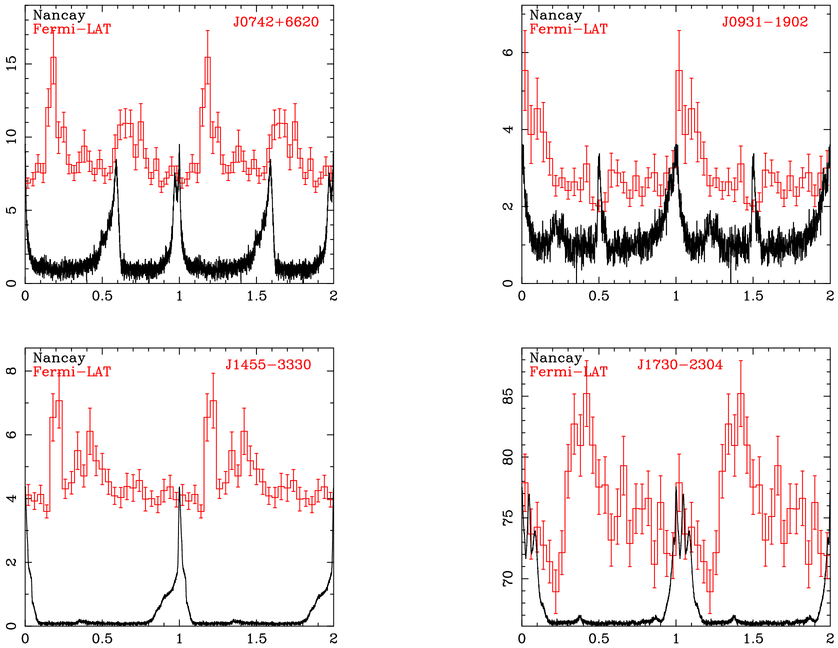

Figure 1: Gamma-ray (red) and radio (black) phase-folded light-curve of each new millisecond pulsar. The x-axis is the phase rotation of the pulsar and the y-axis corresponds to the weighted gamma-ray counts as obtained with the probability-weighting method described in the text. The radio data come from the Nançay radiotelescope [4] but PSR J0931−1902 was first detected with the Green Bank Telescope [5].

Geometry determines the radio and gamma-ray beam shapes. It depends on the angles of the magnetic and rotation axes relative to each other and to the line-of-sight from the Earth. It also depends on how the "light cylinder" (radius $r = cP/2\pi$, where an object in co-rotation with a neutron star turning with period P would reach the speed of light) crosses the not-quite-dipole shaped magnetic field. Therefore, beam shapes are observables that can constrain emission models. *Fermi*-LAT's 40 radio-quiet pulsars are precious in this regard: nearly all other known pulsars are seen with radio telescopes ("radio-loud"), meaning that they all have geometries such that the radio beam sweeps the Earth. The radio-quiet pulsars have the radio beams tilted elsewhere. The gamma-ray beams are very narrow in neutron star longitude (due to concentration of the gamma-radiating electrons and positrons along "caustically" focussed magnetic field lines), but are very broad in latitude, being brightest near the neutron star equator, and fading towards the poles. Romani & Watters [2, 11] use these arguments to generate an "Atlas" of gamma-ray beam profiles, including tallies of the numbers of radio-loud versus quiet pulsars. The *Fermi*-LAT pulsars also differ from those often chosen for geometry studies by their large spin-down powers indicative of strong magnetic fields and relatively short periods, resulting in different magnetospheric configurations.

3. New detections with Pass 8

In the beginning of the mission, event reconstruction was based on pre-launch instrument simulations. This reconstruction was close to reality but after analysing the first data, the *Fermi*-LAT collaboration realized that due to residual signals induced by background cosmic-rays the selection efficiency was not optimal, in particular at lower energies. Therefore the simulations were improved in order to take into account this effect and to better characterize the instrument performance. A completely new reconstruction was developed to limit the loss of data due to parasite signals. The event selection is now optimized and the systematic errors are significantly reduced. Together with this new reconstruction called "Pass 8" [3], the collaboration produced corresponding diffuse models to describe the extragalactic diffuse emission as well as gamma-ray emission due to cosmic-ray interaction with the Earth's atmosphere. The Galactic diffuse model from the previous reconstruction P7REP was scaled to take into account the enhancement of the emission expected from Pass 8 acceptance improvement. This new reconstruction shows a gain in effective area of 30% above 1 GeV and a factor 2 at 100 MeV compared to the previous reconstruction P7REP. The angular resolution is also improved, leading to a sensitivity gain of 40% for point-like sources.

So far ten new pulsars have indeed been detected

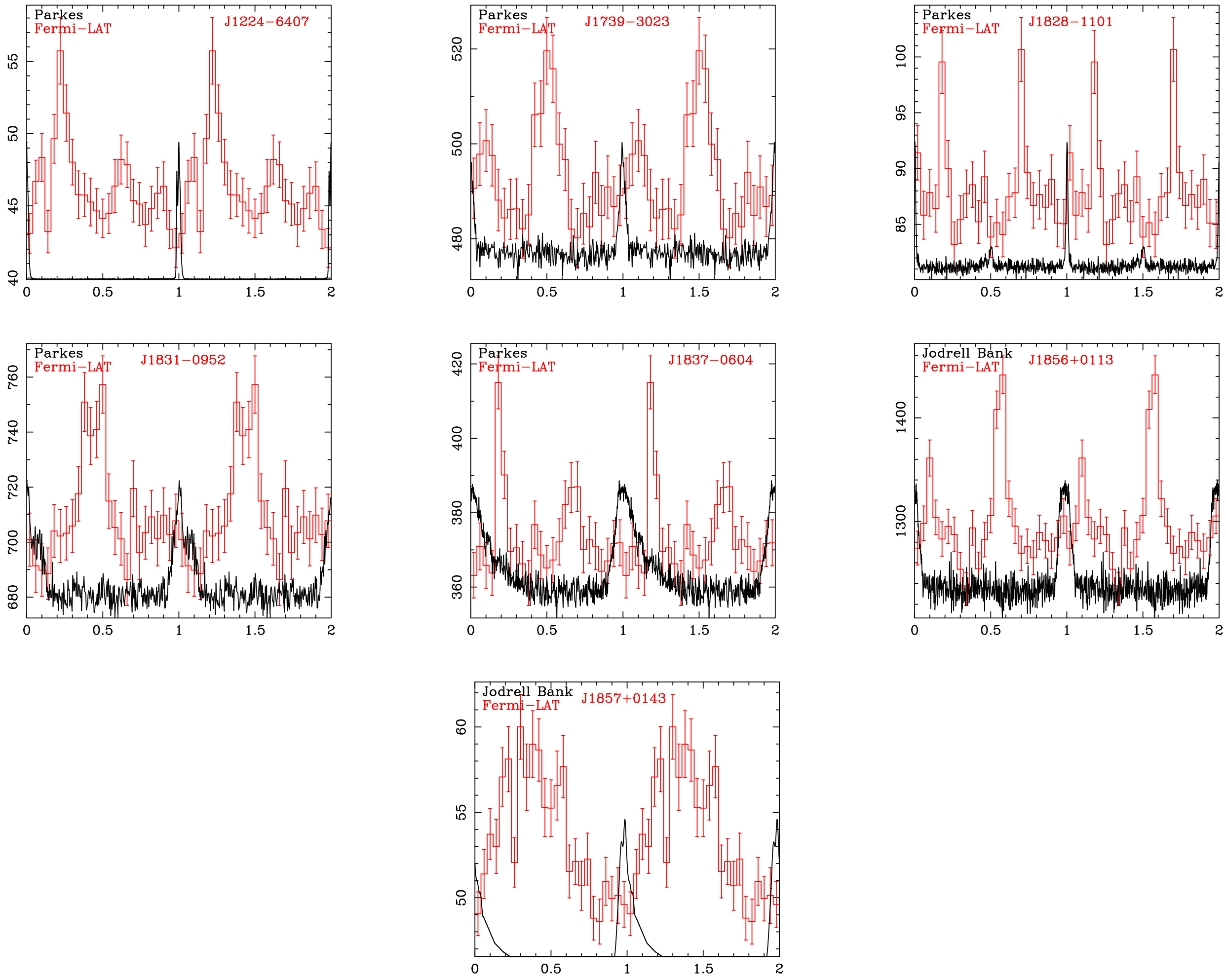

Figure 2: Gamma-ray (red) and radio (black) phase-folded light-curve of the newly detected young pulsars. The radio data come from the Parkes telescope [6] for PSRs J1224−6407, J1739−3023, J1828−1101, J1831−0952 and J1837−0604 and from Jodrell Bank Observatory [7] for PSRs J1856+0113 and J1857+0143.

exclusively with Pass 8. We also analysed one more pulsar, PSR J1856+0113, that was already seen with P7REP data (just above the 5σ threshold) but for which Pass 8 improved the pulsation detection to over 8σ. Hence we present here 11 new pulsars analysed with the Pass 8. Their gamma-ray and radio light-curves are presented in Fig. 1 (MSPs) and Fig. 2 (young) and their properties are listed in Table I.

To detect pulsations, regions of 3° around the radio position of the pulsars were selected. The data were phase-folded using radio ephemerides from different radiotelescopes: Nançay [4], Parkes [6] and Jodrell Bank [7]. A probability-based event selection was then applied, using the shape of the point-spread function to estimate the events' probability of originating from the pulsar. The lowest H-test value obtained for this sample of pulsars is ∼40 for PSR J1828−1101.

The spectral analysis was performed using the *Fermi ScienceTools* and after selecting a region of 15° around each pulsar. We restricted to the energy range between 100 MeV and 300 GeV and we used the *Source* class events. Sources from the third *Fermi*-LAT catalog (3FGL) [8] were included in the model of the regions and a point-like source with a power-law spectral shape was added at the center of each ROI, corresponding to the position of each pulsar. PSRs J0742+6620, J0931−1902 and J1837−0604 were coincident with unidentified 3FGL sources, which we assumed to stem from the pulsars, therefore the position of the corresponding source was shifted to the radio position of the pulsar. When performing the fit of the region with *gtlike*, the spectral parameters of sources within a radius of 5° were let free as well as the ones within 10° and with a TS value above 1000 (taken arbitrarily) in the 3FGL. No phase selection was applied to the data for this analysis.

Although all pulsars presented here are significantly detected with their pulsations in gamma-rays, their spectral analysis was not successful in many cases. For all but two of the pulsars (J1730−2304 and J1857+0143), the light-curves show very narrow peaks (see Figs. 1 and 2) easily detected by phase-folding. However when considering the full phase-band for the spectral analysis, the faint signal fades behind the background level and the source is not detected, as can be seen by the TS value column in Table I. An analysis selecting only the on-phase intervals for each pulsar will be made for future publication.

Among the 11 new objects, 4 are MSPs and two of them have a period of ∼ 8 ms. These two new detections start to fill the bridge between MSPs and young populations in Fig. 4. All the new MSPs but one (J1730−2304) are located far from dense background regions (with a latitude $|b| > 20°$) where we can detect very faint objects such as J0931−1902 which is the pulsar with the lowest energy flux measured with the LAT at present (see Table I as well as [1, 12]).

4. Focus on high spin-down power pulsars

More than 60% of pulsars with $\dot{E} \geq 10^{36}$erg/s are detected in gamma-rays, and more than 50% for $\dot{E} \geq 10^{35}$erg/s, as can be seen in Fig. 3. Six of the new gamma-ray pulsars presented here belong to the energetic pulsar category, $\dot{E} \geq 10^{35}$erg/s.

The pulsar timing campaign for *Fermi* [9] focused on pulsars with $\dot{E} \geq 10^{34}$ erg/s. In Figure 3 (top) nearly 90% of the young high $\dot{E}$ pulsars have indeed been monitored. The lower rate for MSPs is due to those discovered after the campaign list was established. The fraction is lower for low $\dot{E}$ pulsars, but they are abundant, resulting in a large sample nevertheless. The choice of which low $\dot{E}$ pulsars are monitored by radio telescopes could conceivably lead to bias in the fraction of gamma-detected pulsars shown here. Pass 8 makes the LAT more efficient at finding pulsars and thus reduces the biases in determining these fractions.

A very large fraction of high $\dot{E}$ MSPs are gamma-ray pulsars: the small light-cylinder leads to very broad beams. See [10] for a discussion of those not seen in gamma-rays. The gamma-ray deathline is at lower $\dot{E}$ for MSPs compared to slower pulsars. For the young pulsars, the fraction increases with $\dot{E}$, passing the 50% mark around 10^{35} erg/s. Luminosity increases with $\dot{E}$, but sensitivity and background levels account for only part of the undetected pulsars. Beam geometry is surely the dominant factor: the "Atlas" of gamma-ray profiles provided by [11], and similar studies since then, show that models do indeed predict roughly that fraction of pulsars where the gamma-ray beam either misses the Earth, or is so broad as to give unpulsed detection. Hou et al. [12] discuss this is more detail.

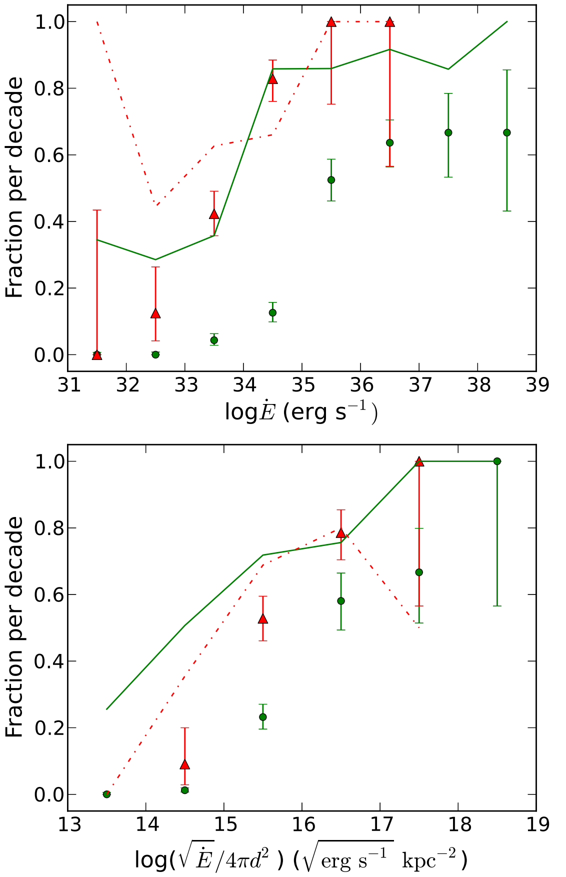

Figure 3: For each decade in spin-down power (top) or in heuristic gamma-ray flux (bottom, see text), the solid green line shows the fraction of known "young" pulsars ($P_0 \geq 30$ ms) for which we have rotation ephemerides, and the dashed red line shows the same for MSPs ($P_0 \leq 30$ ms). We consider only pulsars outside of globular clusters. We have gamma-ray phase-folded all pulsars for which we have ephemerides. The green dots (red triangles) show the fraction of these gamma-ray phase-folded young (millisecond) pulsars for which the LAT sees pulsations. The error bars are the 68% confidence level statistical uncertainties on the fraction, using the Bayesian calculation of [15].

The "heuristic" gamma-ray flux, $\sqrt{\dot{E}}/d^2$ (see 2PC equation 18) uses the idea that gamma-ray luminosity L_γ scales with the open field line voltage $\propto \sqrt{\dot{E}}$, loosely born out by the correlation between L_γ and $\dot{E}$ seen in 2PC Figure 9. The solid line in Figure 3, bottom, differs from that in the top frame because of the radio-quiet pulsars for which we have no distance estimate. Figure 3 shows (as does 2PC Figure 15)

Table I : Temporal and spectral properties of the new pulsars detected with Pass 8. The first four lines are the new MSPs. The period and spin-down power are taken from [13]. The distance in Column 4 is estimated from the dispersion measurement using the NE2001 model [14], and the uncertainties come from re-running NE2001 for ±20% of the DM. Column 5 corresponds to the test statistic value obtained after the spectral analysis described in the text (*), or after a study with the *pointlike* tool(†). G_{100} is the integrated energy flux between 0.1 and 300 GeV assuming a power-law spectrum with the corresponding index value $-\Gamma$. Columns 8 and 9 give the total gamma-ray luminosity in the 0.1 to 300 GeV energy band and the gamma-ray conversion efficiency $\eta = L_\gamma/\dot{E}$. The first uncertainty in L_γ and η comes from the statistical uncertainties in the spectral fit while the second is due to the distance uncertainty. When the pulsar is too weak or lying in background-contaminated regions, we could not derive a spectrum, therefore we do not give any spectral information.

PSR Name	Period (ms)	$\dot{E}$ (erg s^{-1})	Distance (kpc)	TS	Γ	G_{100} (10^{-11} erg cm^{-2} s^{-1})	L_γ (10^{33} erg s^{-1})	Efficiency (%)
J0742+6620	2.89	2.0×10^{34}	0.68 ±0.10	$143^\star$	2.4±0.1	0.49 ± 0.06	$0.27 \pm 0.03 \pm 0.07$	$1.3 \pm 0.2 \pm 0.4$
J0931−1902	4.64	1.4×10^{33}	1.88 ±0.51	$23^\star$	2.0±0.2	0.22 ± 0.06	$0.9 \pm 0.2^{+0.6}_{-0.4}$	$65 \pm 18^{+40}_{-30}$
J1455−3330	7.99	1.9×10^{33}	0.53±0.07	$0.5^\dagger$	-	-	-	-
J1730−2304	8.12	1.5×10^{33}	0.53±0.05	$65^\star$	2.6±0.05	1.16 ± 0.09	$0.39 \pm 0.03 \pm 0.07$	$26 \pm 2 \pm 5$
J1224−6407	216.50	1.9×10^{34}	3.15 ± 0.41	$0.04^\dagger$	-	-	-	-
J1739−3023	114.37	3.0×10^{35}	2.91 ±0.38	$29^\star$	2.33±0.005	1.61 ± 0.02	$16.2 \pm 0.2 \pm 4$	$5.27 \pm 0.07 \pm 1$
J1828−1101	72.05	1.6×10^{36}	6.63±1.05	$73^\star$	2.5±0.1	2.7 ± 0.4	$140 \pm 20 \pm 40$	$9 \pm 1 \pm 3$
J1831−0952	67.27	1.1×10^{36}	4.05±0.37	$2.3^\dagger$	-	-	-	-
J1837−0604	96.29	2.0×10^{36}	6.41±0.67	$439^\star$	2.50±0.05	7.6 ± 0.5	$370 \pm 30 \pm 80$	$19 \pm 1 \pm 4$
J1856+0113	267.44	4.3×10^{35}	3.07±0.32	$0.4^\dagger$	-	-	-	-
J1857+0143	139.76	4.5×10^{35}	5.75±0.44	$0.0^\dagger$	-	-	-	-

that for $\sqrt{\dot{E}}/d^2$ below $10^{15}\sqrt{\text{erg s}^{-1}}$ kpc^{-2} the number of detected pulsars falls to zero. This is due both to the LAT's flux sensitivity and to the $\dot{E}$ deathline near 10^{33}erg s^{-1} seen in both Figure 4 and the top of Fig. 3.

We note that all of the newly detected energetic pulsars lie in very crowded regions close to the galactic center and are therefore subject to a high diffuse emission level. Three of them are also quite far away with a distance estimate above 5 kpc. Pass 8 demonstrates here its ability to detect faint sources above the background, with its sensitivity gain of 40% for point-like sources.

Finally, an important factor for pulsation detection is also the quality and completeness of the radio timing which can be achieved thanks to the precious collaboration of radiotelescopes teams.

Conclusion

We presented 4 new MSPs and 7 new young pulsars detected in gamma-rays with the *Fermi*-LAT. Two of the MSPs are among the faintest gamma-ray pulsars detected at present with an energy flux below 5×10^{-12} erg cm^{-2} s^{-1}. Six of the new young pulsars are very energetic objects, with $\dot{E} > 10^{35}$ erg s^{-1}, and located in the central regions of the Galaxy. Among the undetected energetic pulsars, different limitations prevent the detection such as a large distance inducing a flux below the sensitivity limit of the instrument; a high background level leading to a low signal-to-noise ratio; or intrinsic pulsar features (low cutoff, wide peaks, beam sampling...). There is no hope to detect pulsars whose gamma-ray beam do not sweep Earth, but the other limitations can be overtaken with the increased acceptance of Pass 8 data which will certainly help detecting more new objects, as it was demonstrated in this work.

Acknowledgments

We thank Gregory Desvignes of the Max Planck Institut für Radioastronomie, Auf dem Hügel, Bonn, Germany, for his work on Nançay data reduction. We also thank our radio collaborators Matthew Kerr, Simon Johnston, Cristobal Espinoza and Ismaël Cognard for providing up-to-date ephemerides of pulsars presented in this work.

The *Fermi*-LAT Collaboration acknowledges support for LAT development, operation and data analysis from NASA and DOE (United States), CEA/Irfu and IN2P3/CNRS (France), ASI and INFN (Italy), MEXT, KEK, and JAXA (Japan), and the K.A. Wallenberg Foundation, the Swedish Research Council and the National Space Board (Sweden). Science analysis support in the operations phase from INAF (Italy) and CNES (France) is also gratefully acknowledged.

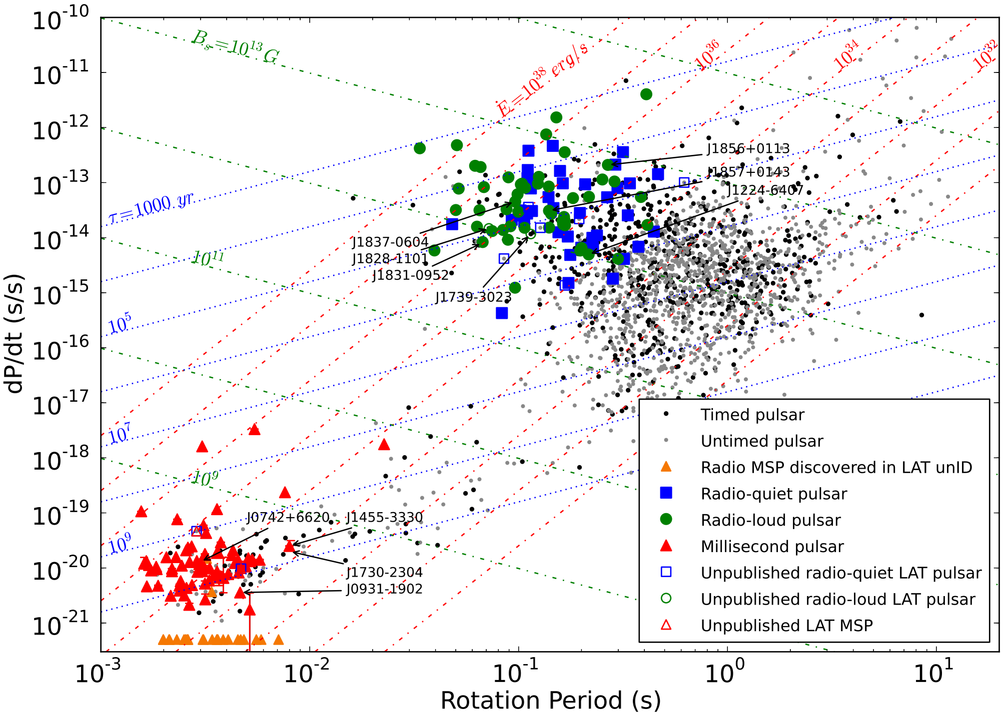

Figure 4: P-$\dot{P}$ diagram with red triangles representing the gamma-ray MSPs, blue squares are the radio-quiet gamma-ray young pulsars and green dots are radio-loud gamma-ray young ones. We emphasized the newly detected objects. Black dots are timed but undetected pulsars in gamma-rays and grey ones are pulsars we have not phase-folded.

References

[1] Abdo, A. A. et al., “The Second *Fermi* Large Area Telescope Catalog of Gamma-Ray Pulsars”, ApJS, 208, 17 (2013)

[2] Romani, R. W. and Watters, K. P, “Constraining Pulsar Magnetosphere Geometry with gamma-ray Light Curves”, ApJ, 714, 810 (2010)

[3] Atwood, W. et al., “Pass 8: Toward the Full Realization of the Fermi-LAT Scientific Potential”,arXiv:1303.3514 (2013)

[4] Cognard, I. et al., “Discovery of Two Millisecond Pulsars in Fermi Sources with the Nançay Radio Telescope”, ApJ, 732, 47 (2011)

[5] Lynch et al., in preparation

[6] Weltevrede, P. et al., “Pulsar Timing with the Parkes Radio Telescope for the Fermi Mission”, PASA, 27, 64 (2010)

[7] Hobbs, G. et al., “Long-term timing observations of 374 pulsars”, MNRAS, 353, 1311 (2004)

[8] Acero, F. et al., “*Fermi* Large Area Telescope Third Source Catalog”, arXiv:1501.02003 (2015)

[9] Smith, D. A. et al., “Pulsar timing for the *Fermi* gamma-ray space telescope”, AAP, 492, 923 (2008)

[10] Guillemot, L. and Tauris, T. M., “On the non-detection of gamma-rays from energetic millisecond pulsars - dependence on viewing geometry”, MNRAS, 439, 2033 (2014)

[11] Watters, K. P. et al., “An Atlas for Interpreting gamma-ray Pulsar Light Curves”, ApJ, 695, 1289 (2009)

[12] Hou X., et al., “Six faint gamma-ray pulsars seen with the *Fermi* Large Area Telescope. Towards a sample blending into the background”, AAP, 570, A44 (2014)

[13] http://www.atnf.csiro.au/people/pulsar/psrcat/

[14] Cordes, J. M. and Lazio, T. J. W., “NE2001.I. A New Model for the Galactic Distribution of Free Electrons and its Fluctuations”, astro-ph/0207156 (2002)

[15] Paterno, M., “Calculating Efficiencies and Their Uncertainties” , FERMILAB-TM-2286-CD, May 22, 2004.

Very high energy gamma-ray follow-up observations of novae and dwarf novae with the MAGIC telescopes.

J. Sitarek
University of Łódź, PL-90236 Lodz, Poland,
IFAE, Campus UAB, E-08193 Bellaterra, Spain

W. Bednarek
University of Łódź, PL-90236 Lodz, Poland

R. López-Coto
IFAE, Campus UAB, E-08193 Bellaterra, Spain

E. de Oña Wilhelmi for the MAGIC Collaboration
Institute of Space Sciences, E-08193 Barcelona, Spain

R. Desiante
Università di Udine, and INFN Trieste, I-33100 Udine, Italy

F. Longo
Università di Trieste and INFN Trieste, Italy

E. Hays for the *Fermi*-LAT Collaboration
NASA Goddard Space Flight Center, Greenbelt, MD 20771, USA

In the last few years the *Fermi*-LAT instrument has detected GeV gamma-ray emission from a few novae. Such GeV emission can be interpreted in terms of an inverse Compton process of electrons accelerated in a shock. It is expected that hadrons can be accelerated in the same conditions, but reaching much higher energies. They can produce a second component in the gamma-ray spectrum at TeV energies. We performed follow-up observations of selected novae and dwarf novae in a search of the second component in the gamma-ray spectrum. This can shed light on the acceleration process of leptons and hadrons in nova explosions. We have performed observations with the MAGIC telescopes of 3 sources, a symbiotic nova YY Her, a dwarf nova ASASSN-13ax and a classical nova V339 Del shortly after their outbursts.

I. INTRODUCTION

A classical nova is a thermonuclear runaway leading to the explosive ejection of the envelope accreted onto a white dwarf (WD) in a binary system in which the companion is either filling or nearly filling its Roche surface [1–3]. They are a type of cataclysmic variables, i.e. optically variable binary systems with a mass transfer from a companion star to WD. Novae are typically detected first in optical observations when the brightness of the object increases by 7-16 magnitudes. The energy spectra of novae often contain a thermal X-ray continuum. The symbiotic novae, like the classical novae, are also initiated by a thermonuclear explosion on the surface of the WD. However in the case of symbiotic novae, the WD is deep immersed in the wind of a late-type companion star (see e.g. [4, 5]).

The diffusive shock acceleration at the blast wave of symbiotic novae was expected to accelerate particles up to energies of a few TeVs [6]. In 2010 the first GeV gamma-ray emission was detected by the *Fermi*-LAT from the symbiotic nova V407 Cyg [7]. Such gamma-ray emission can be explained in terms of either leptonic or hadronic models [7, 8]. In the former case, the local radiation fields create a target for the inverse Compton (IC) scattering of the electrons. On the other hand, protons accelerated in the same conditions can interact with the matter producing gamma-rays via proton-proton interactions. Several models have been put forward to explain the GeV radiation. For instance, the GeV gamma-ray emission can be attributed to the IC process on the strong radiation field of the red giant [9]. The same model predicts a second component in the TeV range due to proton-proton interactions with the wind of the red giant. Also [10] consider acceleration of leptons and hadrons in the nova shock. In that model the magnetic field, which determines the acceleration efficiency, is obtained assuming an equipartition with the thermal energy density upstream of the shock. The GeV γ-ray emission is then a product of IC scattering of the nova light by the electrons.

In the last few years the *Fermi*-LAT has discovered GeV gamma-ray emission from a few more novae: V1324 Sco, V959 Mon, V339 Del, and V1369

Cen [8, 11]. Most of these sources are classical novae. Contrary to the symbiotic ones, they do not exhibit a strong wind of the companion star. Interestingly, symbiotic and classical novae all exhibit similar spectral properties of the GeV emission. In classical novae the particles acceleration can occur e.g. on a bow shock between the nova ejecta and the interstellar medium or in weaker internal shocks due to inhomogenuity of the nova ejecta [8]. In particular orbital motion of the system can lead to shaping the nova ejecta into a combination of a faster polar wind of the WD ejecta, and a denser material drifted along the equatorial plane [12].

So far no very-high-energy (VHE; E>100 GeV) gamma-ray emission has been detected from any nova event. VERITAS observations of V407 Cyg which started 10 days after the nova explosion yielded a differential upper limit on the flux at 1.6 TeV of $2.3 \times 10^{-12}\,\mathrm{erg\,cm^{-2}\,s^{-1}}$[13]

Beginning in Fall 2012 the MAGIC telescopes conducted a nova follow-up program in order to detect a possible VHE gamma-ray component. The program was first aimed on symbiotic novae. After the reports of detection of GeV emission from classical novae by the *Fermi*-LAT, the program was extended also to bright classical novae and opened up to additional outbursts from cataclysmic variables.

In here we report on MAGIC and *Fermi*-LAT (see Section II for description of the used instruments and analysis methods) observations of the 3 sources observed within this program: a symbiotic nova YY Her (Section III A), a dwarf nova ASASSN-13ax (Section III B) and a classical nova V339 Del (Section III C).

II. INSTRUMENTS

The three sources were first detected and observed by optical instruments. The results of the MAGIC observations were supported by the analysis of quasi-simultaneous *Fermi*-LAT observations.

A. MAGIC telescopes

The VHE gamma-ray observations were performed with the MAGIC telescopes. MAGIC is a system of two 17 m Cherenkov telescopes located on the Canary Island of La Palma at a height of 2200 m a.s.l. The telescopes can perform observations of gamma rays with energies as low as ∼50 GeV and up to tens of TeV. During Summer 2011 and 2012 MAGIC underwent a major upgrade [14]. After the upgrade the sensitivity of the MAGIC telescopes in the best energy range ($\gtrsim 300$ GeV) is $\sim 0.6\%$ of Crab Nebula flux in 50 h of observations [15]. All the data used for this paper were taken after the upgrade. The data were analyzed using the standard analysis chain [15, 16]. The significance of a gamma-ray excess was computed according to Eq. 17 of [17]. The upper limits on the flux were calculated following the approach of [18] using 95% C.L. and accounting for a possible 30% systematic uncertainty on the effective area of the instrument.

B. *Fermi*-LAT

The *Fermi*-LAT, launched in 2008, is a pair-conversion telescope that detects photons with energies from 20 MeV to > 300 GeV [19]. Thanks to a large field of view (∼ 2.4 sr), the *Fermi*-LAT observatory, operated in scanning mode, provides coverage of the full sky every three hours enabling searches for transient sources and overlap with ground-based observatories. We analyzed the LAT data in the energy range 100 MeV − 300 GeV using an unbinned maximum likelihood method [20] as implemented in the *Fermi* Science Tools v9r32p5, the P7REP_SOURCE_V15 LAT Instrument Response Functions (IRFs), and associated standard Galactic and isotropic diffuse emission models[27]. We selected events within a region of interest (ROI) of 15° centered on the LAT best position (following [8]) for V339 Del and required a maximum zenith angle of 100° in order to avoid contamination from Earth limb photons. Additionally, we applied a gtmktime filter (no.3) recommended for combined survey and pointed mode observations[28], selecting good quality data at times when either the rocking angle was less than 52° or the edge of the analysis region did not exceed the maximum zenith angle at 100°. Sources from the 2FGL catalogue [21] located within the ROI were included in the model used to perform the fitting procedure.

III. SOURCES OBSERVED

We report here results of the MAGIC and *Fermi*-LAT observations of YY Her, ASASSN-13ax and V339 Del.

A. YY Her

YY Her is a symbiotic nova system that undergoes a recurrent pattern of outbursts. MAGIC observations of YY Her occurred on the night of 2013 Apr $22^{\mathrm{nd}}/23^{\mathrm{rd}}$, 7 days after the optical maximum. No significant VHE gamma-ray emission was detected. We computed flux upper limits at 95% confidence level obtaining $< 5.0\times10^{-12}\mathrm{ph\,cm^{-2}\,s^{-1}}$ above 300 GeV. Also in *Fermi*-LAT no emission was detected over a longer interval 2013 Apr 10^{th} to Apr 30^{th} (MJD 56392.5 to 56412.5). Upper limits at 95% confidence level were

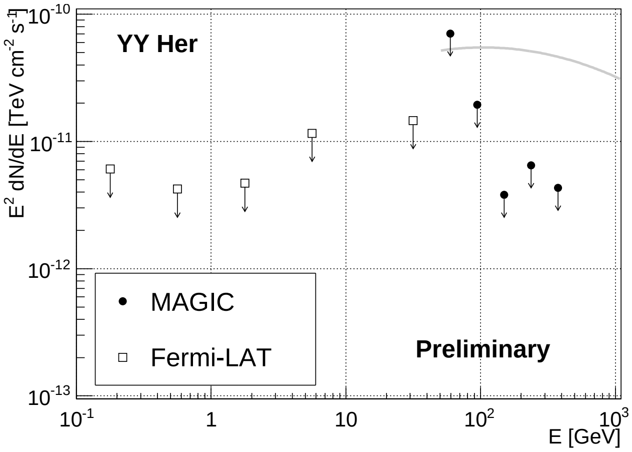

FIG. 1: Differential upper limits on the flux from YY Her as measured by the *Fermi*-LAT (empty squares) and MAGIC (full circles). See text for details of the time ranges covered by the points. For comparison a spectrum of Crab Nebula is shown with a gray curve.

set as $2.8 \times 10^{-8}\mathrm{ph\,cm^{-2}\,s^{-1}}$ above 100 MeV. Differential upper limits obtained from the *Fermi*-LAT and MAGIC observations of YY Her are shown in Fig. 1.

B. ASASSN-13ax

ASASSN-13ax is a member of a different class of cataclysmic variables, the dwarf novae, which are known for significantly weaker optical outbursts (2-6 magnitudes) than classical novae. Instead of undergoing a thermonuclear explosion on the surface of the WD, these outbursts are caused by the gravitational energy release from a partial collapse of the accretion disk surrounding the WD. The MAGIC observations were performed on two consecutive nights starting on 2013 Jul 4th, soon after the optical outburst seen on 2013 Jul 1st. In the absence of detectable VHE emission, upper limits at 95% confidence level were set as $< 1.5 \times 10^{-12}\mathrm{ph\,cm^{-2}\,s^{-1}}$ above 300 GeV. Emission was not detected in the LAT over the interval 2013 Jun 25th to Jul 15th (MJD 56468.5 to 56488.5). Upper limits at 95% confidence level were set as $1.6 \times 10^{-8}\mathrm{ph\,cm^{-2}\,s^{-1}}$ above 100 MeV. Differential upper limits obtained from the *Fermi*-LAT and MAGIC observations of ASASSN-13ax are shown in Fig. 2

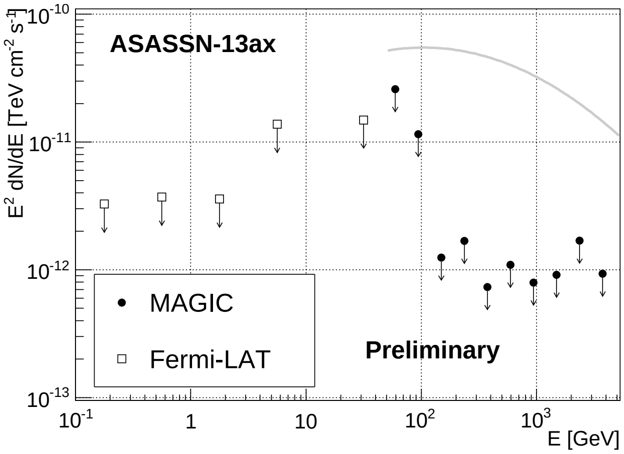

FIG. 2: Differential upper limits on the flux from ASASSN-13ax as measured by the *Fermi*-LAT (empty squares) and MAGIC (full circles). See text for details of the time ranges covered by the points. For comparison a spectrum of Crab Nebula is shown with a gray curve.

C. V339 Del

V339 Del was a fast, classical nova detected by optical observations on 2013 Aug 16th (CBET #3628). The nova was exceptionally bright reaching a magnitude of V$\sim$ 5 mag (see top panel of Fig. 3), and it triggered follow-up observations at frequencies ranging from radio to VHE gamma-rays. Photometric measurements suggest a distance for V339 Del of 4.5 ± 0.6 kpc [22]. The spectroscopic observations performed on MJD 56522.1 revealed emission wings extending to about ± 2000 km/s and a Balmer absorption component at a velocity of 600 ± 50 km/s [23]. The pre-outburst optical images revealed the progenitor of nova V339 Del to be a blue star [24].

Originally MAGIC observations of V339 Del were motivated by its extreme optical outburst. Soon after MAGIC started observations they were additionally supported by the detection of GeV emission by the *Fermi*-LAT from the direction of V339 Del. The MAGIC observations started already on the night of 2013 Aug 16/17th, however they were marred by bad weather conditions. The good quality data used for most of the analysis spanned 8 nights between 2013 Aug 25th and Sep 4th. The total effective time was 11.6 h. In addition to the nightly upper limits we performed a dedicated analysis of the poor quality (affected by calima, a dust layer originating from Sahara) night of 2013 Aug 16/17th. We applied an estimated energy and collection area corrections based on LIDAR measurements [25]. No VHE gamma-ray signal was found from the direction of V339 Del. We computed a night by night integral upper limit above 300 GeV (see bottom panel of Fig. 3. The differential upper limits for the whole good quality data set computed in bins of energy are shown in Fig. 4.

Nova V339 Del was the subject of a *Fermi* Target of Opportunity (ToO) observation [26] triggered by the optical discovery (CBET #3628); the ToO started on 2013 Aug 16th and lasted for six days. The gamma-ray emission from V339 Del was first detected by *Fermi*-LAT in 1-day bins on Aug 18th [8]. The

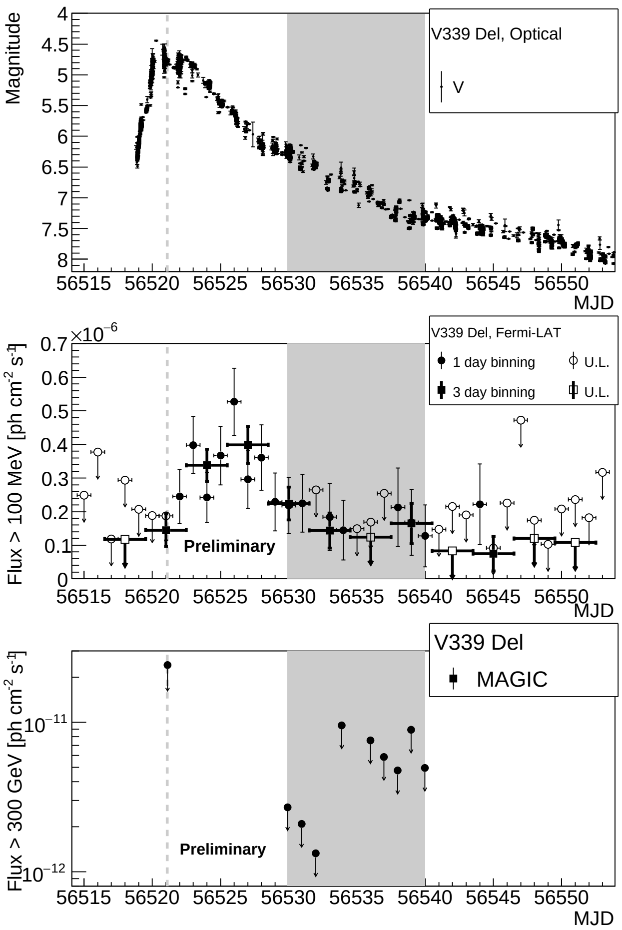

FIG. 3: Multi-wavelength light curve of V339 Del during the outburst in August 2013. Top panel: optical observations in the V band obtained from AAVSO-LCG[a] service. Middle panel: the *Fermi*-LAT flux (filled symbols) and upper limits (empty symbols) above 100 MeV in 1-day (circles, thin lines) or 3-day (squares, thick lines). A 95% C.L. flux upper limit is shown for time bins with TS<4. Bottom panel: Upper limit on the flux above 300 GeV observed with MAGIC telescopes. The gray band shows the observation nights with MAGIC. The dashed gray line shows a MAGIC observation night affected by bad weather.

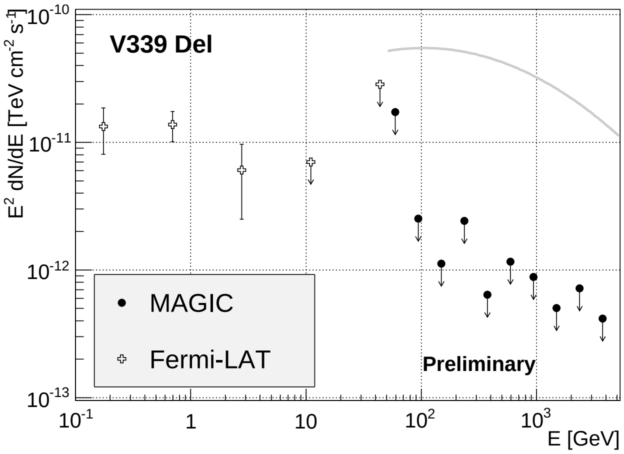

FIG. 4: Differential upper limits on the flux from V339 Del as measured by MAGIC (filled circles) and the flux measured by *Fermi*-LAT (empty crosses) in the same time period, 25th of August and 4th of September. For comparison a spectrum of Crab Nebula is shown with a gray curve.

emission peaked on Aug 22nd and entered a slow decay phase afterwards (see middle panel in Fig. 3). For the light-curves, the data were fit using a power law spectral model initially leaving the photon index and the normalization free to vary. We then fixed the photon index at the average value of 2.3 calculated over the most significant detections (Test Statistic values TS>9)[29]. The LAT Spectral Energy Distribution (SED) of V339 Del shown in Fig. 4 was extracted in five logarithmically spaced energy bins from 100 MeV to 100 GeV. Similarly to the light-curves, energy binned data shown in Fig. 4 were fit using a simple power law and showing a 95% C.L. upper limit for bins with TS<9. In the period coincident with the MAGIC observations (2013 Aug 25th to Sep 4th) the *Fermi*-LAT spectrum can be described by an effective power law with an index of 2.37 ± 0.17 and flux above 100 MeV of $(0.15 \pm 0.04) \times 10^{-6}\mathrm{ph\,cm^{-2}\,s^{-1}}$. The rather low statistical significance (TS=49) does not constrain the value of an exponential cut-off of the emission in this period. Note, however, that the most energetic photon, with $E = 5.9\,\mathrm{GeV}$ was recorded on Aug 30th, i.e. within the time period covered by the MAGIC observations. The *Fermi*-LAT analysis for a broader time range, 2013 Aug 22nd to Sep 12th (MJD 56526-56547), covering the whole decay phase of the Fermi-LAT light curve allowed us to obtain a more significant signal with a TS of 121. Nevertheless we obtain a similar value of flux above 100 MeV, $(0.13 \pm 0.03) \times 10^{-6}\mathrm{ph\,cm^{-2}\,s^{-1}}$, for this broader period. The spectrum in this case can be described, with improved significance of 3.3σ with respect to the simple power law, by an exponentially cut-off power law with an index of 1.44 ± 0.29 and a cut-off energy of $1.6 \pm 0.8\,\mathrm{GeV}$.

IV. CONCLUSIONS

The MAGIC telescopes performed observations of 3 objects: the symbiotic nova YY Her, the dwarf nova ASASSN-13ax and the classical nova V339 Del. No significant VHE gamma-ray emission was found from the direction of any of them. Out of these three objects, V339 Del is the only one detected at GeV energies. It has also extensive optical observations which shed some light on both the companion star and the photosphere of the nova. Therefore it has the highest

---

[a] http://www.aavso.org/lcg

potential for constraining the leptonic and hadronic processes in novae. MAGIC will continue follow-up observations of the promising novae candidates in the following years.

Acknowledgments

We would like to thank the Instituto de Astrofísica de Canarias for the excellent working conditions at the Observatorio del Roque de los Muchachos in La Palma. The support of the German BMBF and MPG, the Italian INFN, the Swiss National Fund SNF, and the ERDF funds under the Spanish MINECO is gratefully acknowledged. This work was also supported by the CPAN CSD2007-00042 and MultiDark CSD2009-00064 projects of the Spanish Consolider-Ingenio 2010 programme, by grant 127740 of the Academy of Finland, by the Croatian Science Foundation (HrZZ) Project 09/176 and the University of Rijeka Project 13.12.1.3.02, by the DFG Collaborative Research Centers SFB823/C4 and SFB876/C3, and by the Polish MNiSzW grants 745/N-HESS-MAGIC/2010/0 and NCN 2011/01/B/ST9/00411.

The *Fermi* LAT Collaboration acknowledges generous ongoing support from a number of agencies and institutes that have supported both the development and the operation of the LAT as well as scientific data analysis. These include the National Aeronautics and Space Administration and the Department of Energy in the United States, the Commissariat à l'Energie Atomique and the Centre National de la Recherche Scientifique / Institut National de Physique Nucléaire et de Physique des Particules in France, the Agenzia Spaziale Italiana and the Istituto Nazionale di Fisica Nucleare in Italy, the Ministry of Education, Culture, Sports, Science and Technology (MEXT), High Energy Accelerator Research Organization (KEK) and Japan Aerospace Exploration Agency (JAXA) in Japan, and the K. A. Wallenberg Foundation, the Swedish Research Council and the Swedish National Space Board in Sweden. Additional support for science analysis during the operations phase is gratefully acknowledged from the Istituto Nazionale di Astrofisica in Italy and the Centre National d'Études Spatiales in France.

---

[1] Bode, M. F., & Evans, A. 2008, Classical Novae, 2nd Edition. Edited by M.F. Bode and A. Evans. Cambridge Astrophysics Series, No. 43, Cambridge: Cambridge University Press, 2008.
[2] Starrfield, S., Iliadis, C., Timmes, F. X., Hix, W. R., Arnett, W. D., Meakin, C., Sparks, W. M. 2012, Bulletin of the Astronomical Society of India, 40, 419
[3] Stella Novae: Past and Future Decades. ASP Conference Series, Vol. 490, Edited by P. A. Woudt and V. A. R. M. Ribeiro, 2014
[4] Shore, S. N., et al., 2011, A&A, 527, AA98
[5] Shore, S. N., et al., 2012, A&A, 540, AA55
[6] Tatischeff, V., & Hernanz, M. 2007, ApJL, 663, L101
[7] Abdo, A. A., et al. 2010, Science, 329, 817
[8] Ackermann, M., et al. 2014, Science, 345, 554-558
[9] Sitarek, J., & Bednarek, W. 2012, Phys. Rev. D , 86, 063011
[10] Martin, P., & Dubus, G. 2013, A&A, 551, A37
[11] Cheung, C. C., Jean, P., & Shore, S. N. 2013, The Astronomer's Telegram, # 5653
[12] Chomiuk, L., Linford, J. D., Yang, J., et al. 2014, Nature (London) , 514, 339
[13] Aliu, E., et al. 2012, Astrophys. J. , 754, 77
[14] Aleksić, et al. 2014, arXiv:1409.6073
[15] Aleksić, et al. 2014, arXiv:1409.5594
[16] Zanin R. et al., 2013, Proc of 33rd ICRC, Rio de Janeiro, Brazil, Id. 773
[17] Li, T.-P., & Ma, Y.-Q. 1983, Astrophys. J. , 272, 317
[18] Rolke, W. A., López, A. M., & Conrad, J. 2005, NIM A, 551, 493
[19] Atwood, W. B., et al. 2009, Astrophys. J. , 697, 1071
[20] Mattox, J. R., et al. 1996, Astrophys. J. , 461, 396
[21] Nolan, P. L., et al. 2012, Astrophys. J. Supp. 199, 31
[22] Schaefer, G. H., Brummelaar, T. T., Gies, D. R., et al. 2014, Nature (London) , 515, 234
[23] Shore, S. N., et al. 2013, The Astronomer's Telegram, # 5312
[24] Denisenko, D., Jacques, C., Pimentel, E., et al. 2013, IAU Circ., 9258, 2
[25] Fruck, C., Gaug, M., Zanin, R., et al. 2014, Proc of 33rd ICRC, Rio de Janeiro, Brazil, arXiv:1403.3591
[26] Hays, E., Cheung, T., Ciprini, S., The Fermi LAT Collaboration 2013, The Astronomer's Telegram # 5302
[27] The P7REP data, IRFs, and diffuse models (gll_iem_v05.fit and iso_source_v05.txt) are available at http://fermi.gsfc.nasa.gov/ssc.
[28] http://fermi.gsfc.nasa.gov/ssc/data/analysis/documentation/Cicerone/Cicerone_Likelihood/Exposure.html
[29] The source significance is ∼ sqrt(TS) assuming one degree of freedom

Pulsar Emission above the Spectral Break - A Stacked Approach

A. McCann
EFI & KICP at The University of Chicago, Chicago, IL, 60637, USA

NASA's *Fermi* space telescope has provided us with a bountiful new population of gamma-ray sources following its discovery of over 150 new gamma-ray pulsars. One common feature exhibited by all of these pulsars is the form of their spectral energy distribution, which can be described by a power law followed by a spectral break occurring between ∼1 and ∼8 GeV. The common wisdom is that the break is followed by an exponential cutoff driven by radiation-reaction-limited curvature emission. The discovery of pulsed gamma rays from the Crab pulsar, the only pulsar so far detected at very high energies (E>100 GeV), contradicts this "cutoff" picture. Here we present a new stacked analysis with an average of 4.2 years of data on 115 pulsars published in the 2nd *Fermi*-LAT catalog of pulsars. This analysis is sensitive to low-level ∼100 GeV emission which cannot be resolved in individual pulsars but can be detected from an ensemble.

arXiv:1503.01670v1 [astro-ph.HE] 5 Mar 2015

1. Introduction

One common feature exhibited by all known gamma-ray pulsars is the form of their spectral energy distribution (SED) which can be described by a power-law followed by a spectral break occurring between 1 and 8 GeV [Abdo et al. 2013]. The unanimity of the break energy across the entire *Fermi*-LAT pulsar sample is suggestive that the sites of acceleration and processes of gamma-ray emission are common across different pulsar types and that they are not strongly dependent on the pulsar spin or energetics. Further, it has been shown that across the *Fermi*-LAT pulsar sample the spectral-break energy is weakly correlated with the magnetic-field strength at the light cylinder [Abdo et al. 2010b, 2013]. Such behavior is expected in models where emission is produced by curvature radiation (CR) occurring at the radiation-reaction limit in the outer magnetosphere [Abdo et al. 2010b, Harding et al. 2008]. This has become the most favored general description of gamma-ray emission from pulsars in the *Fermi*-LAT era. In these models one expects that the SED will fall off exponentially above the break energy. There is, however, compelling evidence suggesting that CR occurring in the outer magnetosphere is not a complete description of pulsar emission at, and above, the GeV SED break:

1. The discovery of power-law-type emission from the Crab pulsar at energies exceeding 100 GeV[1] cannot be easily explained by curvature emission from the outer magnetosphere [Aliu et al. 2011, Lyutikov et al. 2012] unless the radius of curvature of the magnetic field line is larger than the radius of the light cylinder [Bednarek 2012]. Some recent models attribute the pulsed very-high-energy (VHE; $E >$100 GeV) emission from the Crab pulsar to inverse-Compton (IC) scattering originating in the outer magnetosphere [Du et al. 2012, Lyutikov et al. 2012, Lyutikov 2012] or to IC scattering from beyond the light cylinder [Aharonian et al. 2012, Pétri 2012].
2. The radiation-reaction limit of CR occurs when the acceleration gains achieved by an electron are equaled by radiation losses. The photon energy at which this occurs in the outer magnetosphere can be expressed in terms of the pulsar period, the surface magnetic field strength, the radius of curvature of the accelerated particle and an efficiency factor. Lyutikov et al. [2012] has shown that the break-energy values for several pulsars reported in the first *Fermi*-LAT pulsar catalog are so high that they require the efficiency factor and radius of curvature to approach or even reach their maximal allowable values[2].
3. Recent studies of the Geminga pulsar with *Fermi*-LAT and VERITAS (see Figure 1) show that the SED above the GeV break is compatible with a steep power law [Aliu et al. 2015, Lyutikov 2012], but no emission has been seen above 100 GeV. Similar conclusions can be drawn from an analysis of the Vela pulsar with *Fermi*-LAT data from Leung et al. [2014], who show that multi-zone or time-dependent emission models are needed to fit the slower-than-exponential fall of the SED above 10 GeV.

The question of whether the Crab pulsar is unique, or whether non-exponentially-suppressed gamma-ray spectra are common in gamma-ray pulsars is of great importance. Beyond the modeling of pulsar emission,

---

[1] At this symposium the MAGIC collaboration presented evidence indicating that the power-law spectrum of the Crab pulsar may extend to TeV energies. See `http://fermi.gsfc.nasa.gov/science/mtgs/symposia/2014/abstracts/185`

[2] In more realistic models the acceleration efficiency is expected to be a few percent to a few tens of percent [Lyutikov et al. 2012].

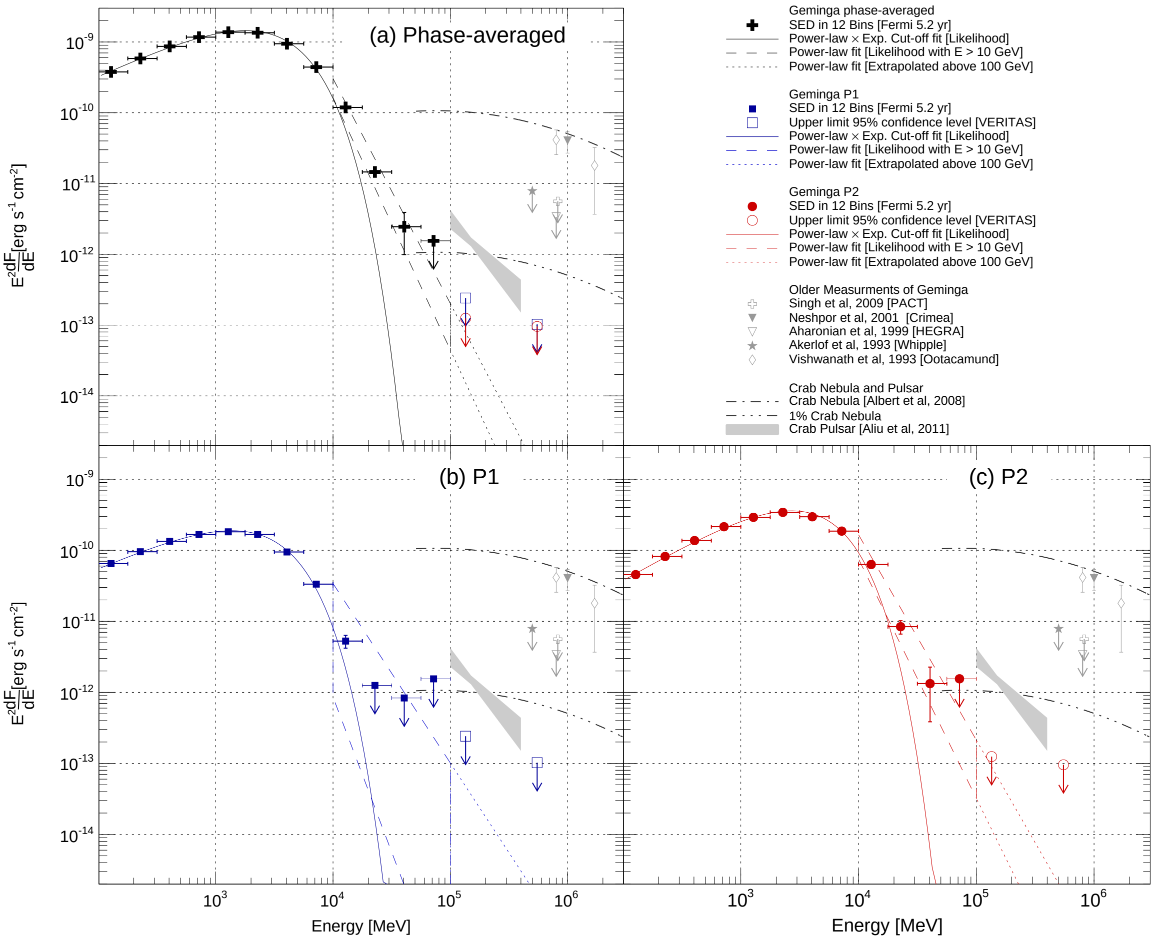

[ht]

Figure 1: SEDs data points and flux upper limits for the Geminga pulsar. Measurements of the Crab Nebula and pulsar are plotted for comparison. It is clear, even in the phase-resolved analysis, that the SED falls slower than an exponential and appears more consistent with a simple power-law. Figure taken from Aliu et al. [2015].

questions concerning the emission spectra of pulsars have significant implications for galactic dark matter searches, where unassociated gamma-ray excesses can be interpreted as the remnants of dark matter annihilation (e.g., Abazajian & Kaplinghat 2012). Since pulsars are likely the main background for these searches, categorizing the shape of pulsar spectra is a critical step towards validating any indirect dark matter signal in the gamma-ray domain. To search for non-exponentially-suppressed emission above 50 GeV, we have performed a stacked analysis of gamma-ray pulsars which is sensitive to emission which cannot be resolved in the *Fermi*-LAT analysis of individual objects, but can be detected if aggregated from an ensemble. A stacked analysis which yields evidence of cumulative emission above 50 GeV would prove that some population of gamma-ray pulsars clearly exhibits non-exponentially-suppressed emission. This would indicate that inverse-Compton or wind-zone emission is common in gamma-ray pulsars and that pulsars contribute to the sub-TeV diffuse emission of the galaxy.

2. Analysis

2.1. The Aperture Photometry Method

A maximum likelihood fitting procedure is typically employed when performing spectral analysis of *Fermi*-LAT data. The *Fermi*-LAT data can also be analyzed with an *Aperture Photometry* (AP) method where the raw event counts from a region of interest (ROI) are combined with a measure of the instrument exposure (cm^2 s) to the region to determine the flux. This AP method is less sensitive and less accurate than the likelihood fitting procedure but it "provides a model independent measure of the flux" and it "is less computationally demanding"[3]. We demonstrate here that the AP method can be used to produce accurate SEDs

---

[3] `http://fermi.gsfc.nasa.gov/ssc/data/analysis/scitools/aperture_photometry.html`

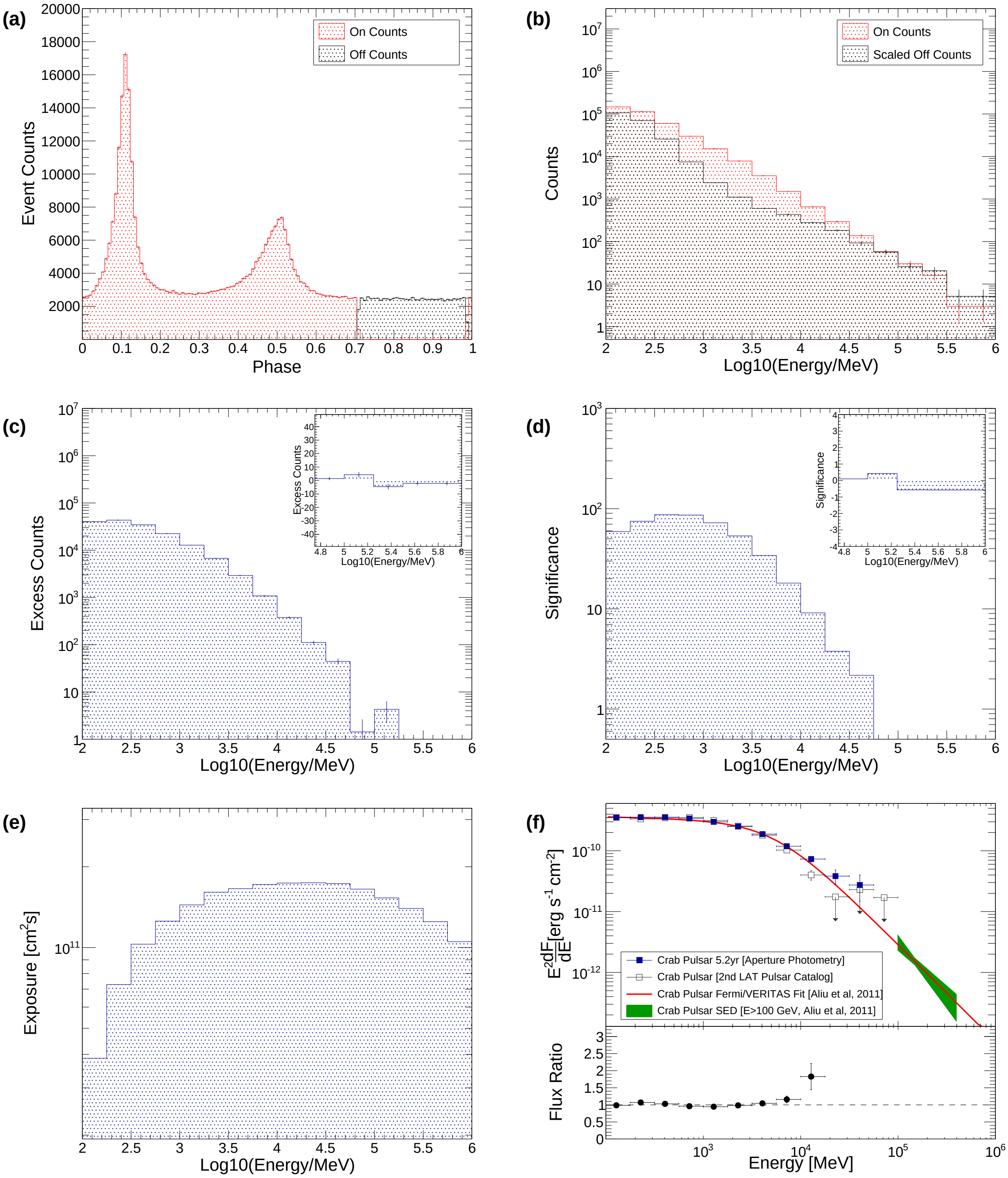

Figure 2: Aperture photometry analysis steps for the Crab pulsar. Panel (a) plots the phase distribution (light curve) of the Crab pulsar from 5.2 years of *Fermi*-LAT observations. The *Off* phase range, [0.71 − 0.99], is defined in the 2nd *Fermi*-LAT catalog of gamma-ray pulsars (2PC). Panel (b) plots the distribution of photon energies for events which fell in the *On* and *Off* phase ranges. The *Off* events have been scaled by α which is the ratio of the *On* phase gate(s) size to the *Off* gate(s) size . Panel (c) shows the energy distribution of the excess events and panel (d) shows the significance of the excess in each energy bin. Panel (e) shows the *Fermi*-LAT exposure for the ROI used in each energy bin determined from `gtexposure`. In panel (f) the Crab pulsar AP SED is plotted alongside the Crab pulsar SED determined from a likelihood fit done in the 2PC. A broken power-law fit to *Fermi*-LAT and VERITAS data from Aliu et al. [2011] is plotted, as well as the VERITAS >100 GeV bow-tie. Below the SED plotted in panel (f) is the ratio of the AP flux to the 2PC flux in each bin, showing the level of agreement between the AP method and the likelihood method. This figure is taken from McCann [2014].

from multi-year pulsar data sets since an accurate determination of the background rate can be measured from the "*Off*-pulse" phase range. The analysis presented here proceeds as follows:

1. Over the 100 MeV to 1 TeV energy range, logarithmically-spaced energy binning with 4 bins per decade is chosen.
2. An ROI is chosen around each pulsar with an energy-dependent radius. The radius chosen is three times the 68% point-spread-function (PSF) containment radius determined from a "front-conversion" Vela analysis by Ackermann et al. [2013]. In order to maintain sufficient statistics at high energies, the radius of the ROI was fixed to 0.45° above 10 GeV.
3. The *Fermi*-LAT analysis tools `gtselect`, `gtmktime`, `gtbin` and `gtexposure` are then run over each pulsar ROI for all observations performed within the period of validity of the pulsar timing solution.
4. The photon event list is barycentered and phase-folded using the `Tempo2` package [Hobbs et al. 2006] with the *Fermi* `Tempo2` plugin and the corresponding timing solution.
5. Within each energy bin, a cut on phase is applied and events which fall within the *Off* phase region and those which fall outside this region - the *On* phase region - are selected. The ratio of the size of the *On* phase range to the size of the *Off* phase range, defined as α, is then used to scale the number of event counts in the *Off* phase region ($\mathrm{N_{off}}$) to the number in the *On* region ($\mathrm{N_{on}}$).
6. The number of excess pulsed events is then defined as $\mathrm{N_{ex}}=\mathrm{N_{on}}-\alpha\mathrm{N_{off}}$ and the flux is $\mathrm{N_{ex}}$ divided by the exposure ($\mathcal{T}$) calculated in step 3 using `gtexposure`. The significance of the excess is calculated using Equation 17 from Li & Ma [1983].

Following this procedure one can derive the energy distributions for the *On* and *Off* phase regions, and the instrument exposure, for any pulsar. These distributions and the derived AP SED are shown for the Crab pulsar in Figure 2.

2.2. Stacking The Pulsar Data Sets

Fermi-LAT has detected over 150 new gamma-ray pulsars[4] and the stacking performed in this work uses 115 pulsars listed in the Second *Fermi*-LAT Catalog of Gamma-ray Pulsars [Abdo et al. 2013], which shall be referred to as 2PC throughout[5]. The 115 pulsar sample is composed of 39 millisecond pulsars and 76 "young" non-recycled pulsars with an average data set spanning 4.2 yr[6]. The six AP analysis steps listed in Section 2.1 were followed for each pulsar and using the resulting values of $\mathrm{N_{on}}$, $\mathrm{N_{off}}$ and $\mathcal{T}$, it is quite simple to determine the total excess,

$$\mathrm{Ex}^{i}_{\mathrm{tot}} = \sum_{j=1}^{\mathrm{N}} (\mathrm{N}^{j,i}_{\mathrm{on}} - \alpha^{j}\mathrm{N}^{j,i}_{\mathrm{off}}) \qquad (1)$$

the total exposure,

$$\mathcal{T}^{i}_{\mathrm{tot}} = \sum_{j=1}^{\mathrm{N}} \mathcal{T}^{j,i} \qquad (2)$$

and thus, the average flux,

$$\mathrm{Flux}^{i}_{\mathrm{av}} = \frac{\mathrm{Ex}^{i}_{\mathrm{tot}}}{\mathcal{T}^{i}_{\mathrm{tot}}} \qquad (3)$$

for N pulsars in a given energy bin, i. The significance of the total excess is determined by the generalized version of Equation 17 from Li & Ma [1983] (see Aharonian et al. 2004). In cases where the significance is less than 2σ, the method of Helene [1983] is used to derive the 95% confidence-level upper limit on the total excess, which is in turn used to compute a flux upper limit.

3. Results

The stacking analysis results for the young pulsar and millisecond pulsar ensembles are shown in Figure 3. No significant excesses are seen in these analyses at energies above 50 GeV. Upper limits on the average flux, determined at the 95% confidence-level, are listed in Table I for three energy bins above 50 GeV. Limits are also presented in units of the Crab pulsar where the broken power-law fit to the *Fermi*-LAT and VERITAS data presented in Aliu et al. [2011] defines a Crab pulsar unit. In addition to these analyses, we stacked sub-samples of the

---

[4] `https://confluence.slac.stanford.edu/display/GLAMCOG/Public+List+of+LAT-Detected+Gamma-Ray+Pulsars`

[5] A total of 117 pulsars are listed in the 2PC, however, the Crab pulsar was excluded from this analysis since we are investigating whether high-energy Crab-pulsar-like emission is seen in other pulsars. Further, PSRJ2215+5135 was also excluded from the study since no *Off* phase region was listed for this source in the 2PC.

[6] The amount of data analyzed here depends entirely on the availability and validity of pulsar spin-down timing solutions used for phase-folding.

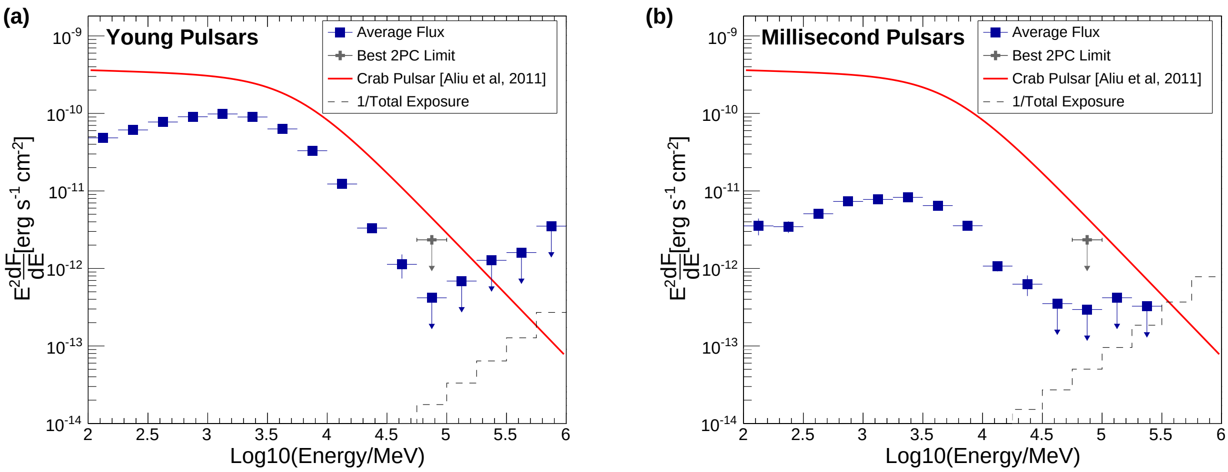

Figure 3: Panel (a) shows the average flux (square markers) from 76 young pulsars determined by dividing the total excess by the total exposure (see Equations 1−3). The dashed-line histogram shows one over the total exposure, indicating the flux which would correspond to a single excess photon. This is the minimum possible flux which could be measured given the total exposure. The gray cross shows the most constraining limit on emission from a single pulsar in the 56.2−100 GeV range presented in the 2PC. The 2PC presented no limits at higher energies. The broken power-law fit to the Crab pulsar data from Aliu et al. [2011] is plotted for scale. Panel (b) plots the same quantities for the stacked analysis of 39 millisecond pulsars. This figure is adapted from figures presented in McCann [2014].

data where each sub-sample was composed of the 10 pulsars with the largest value of a given parameter. Sub-sample selections based on gamma-ray luminosity, spin-down power, spin-down power over distance squared, gamma-ray photon flux and non-thermal X-ray energy flux were investigated[7]. No significant excesses were observed above 50 GeV in any of these sub-sample stacking analyses.

The shape of the average young pulsar and average millisecond pulsar SEDs were categorized by fitting a power law times a super-exponential cutoff function

$$E^2\frac{dF}{dE} = A\left(\frac{E}{1\ \mathrm{GeV}}\right)^{\Gamma} e^{-\left(\frac{E}{E_{\mathrm{cut}}}\right)^{b}} \quad (4)$$

to the SED data. These fits are presented in Figure 4. Fixing $b = 1$ reduces Equation 4 to a power law times an exponential cutoff function and, as expected, this functional form does not reproduce the sub-exponential fall of the SED above the break. However it can be used to measure the average flux-weighted value of the spectral index (Γ) and cutoff (E_{cut}) parameters [Abdo et al. 2013]. It is clear from Figure 4 that the average SEDs have qualitatively the same shape, with the average flux from the 39 millisecond pulsars about an order of magnitude lower than the average flux from the 76 young pulsars. The spectral parameters derived from fitting the two ensembles are remarkably similar and are presented in the caption of Figure 4.

4. Discussion and Conclusion

Following a stacked analysis of 115 gamma-ray pulsars, with an average exposure of ∼4.2 yr per pulsar, we find no evidence of cumulative emission above 50 GeV. Stacked searches exclusive to the young pulsars, the millisecond pulsars, and several other promising sub-samples also return no significant excesses above 50 GeV. Any average emission present in the entire pulsar sample is limited to be below ∼7% of the Crab pulsar in the 56-100 GeV band. The average flux limits presented in Table I are roughly 3 times lower than the best flux limits achieved in dedicated individual pulsar analyses done in the 2PC in the 56-100 GeV band.

One should note that a limit on the average flux from 115 pulsars at 7% of the Crab pulsar level is consistent with, for example, a scenario in which all 115 pulsars emit at 7% of the Crab pulsar level. It is also consistent with a scenario in which 8 pulsars emit at 100% the level of the Crab pulsar and the remaining 107 pulsars have zero emission. Therefore this analysis does not exclude the possibility of finding several pulsars which are as bright as the Crab pulsar above 50 GeV, or several dozen which are ten times dimmer. It does, however, constrain the average flux from the ensemble, and therefore for every individual pulsar detected above this flux limit, the average emission from the remaining pulsars is constrained to

---

[7] The Crab pulsar was excluded from all of these sub-sample stacking analyses. The parameter values listed in the 2PC catalog were used in all cases.

	All		Young Pulsars		Millisecond Pulsars	
Energy Range [GeV]	Flux Limit [$\times 10^{-12}$ cm^{-2}s^{-1}]	Flux Limit [Crab pulsar units]	Flux Limit [$\times 10^{-12}$ cm^{-2}s^{-1}]	Flux Limit [Crab pulsar units]	Flux Limit [$\times 10^{-12}$ cm^{-2}s^{-1}]	Flux Limit [Crab pulsar units]
56.2 — 100	1.57	0.07	2.03	0.09	1.44	0.07
100 — 177	1.52	0.31	1.88	0.38	1.14	0.23
177 — 316	1.34	1.21	1.96	1.76	0.50	0.45

Table I Limits at the 95% confidence level on the average flux from stacked ensembles of gamma-ray pulsars. The limit values presented in Crab pulsar units assume the broken power-law fit to the Crab pulsar data from Aliu et al. [2011] is a Crab pulsar flux unit.

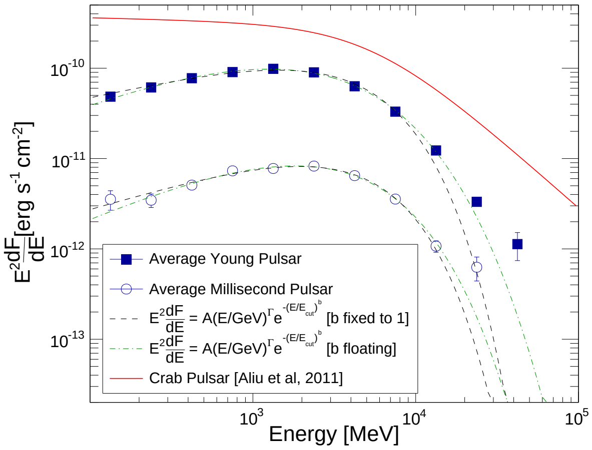

Figure 4: The average SEDs derived from the stacking of the 76 young pulsars and 39 millisecond pulsars. The SEDs are each fit with a power law times a super-exponential cutoff keeping b both fixed to unity and allowing it to float. For the pure exponential cutoff case ($b = 1$) the best fit Γ value is 0.54±0.05 for the millisecond pulsars and 0.41±0.01 for the young pulsars while the best fit E_{cut} values are 3.60±0.21 GeV and 3.54±0.04 GeV, respectively. Allowing b to float we find that sub-exponential forms ($b < 1$) are preferred, with the best-fit b value of 0.59±0.02 for the young pulsars and 0.7±0.15 for the millisecond pulsars. The broken power-law fit to the Crab pulsar data from Aliu et al. [2011] is plotted for scale. Note that only statistical uncertainties on the SED data points were used during the fitting and thus the uncertainty on the best-fit parameter values are likely underestimated. This figure is taken from McCann [2014].

be further below the limit.

In the 100 MeV to ∼50 GeV energy range we find that the average SEDs returned from the young pulsar and millisecond pulsar stacking analyses are very similar in shape and are generally compatible with a power law times a sub-exponential cutoff. Abdo et al. [2010] and Celik & Johnson [2011] have shown that a sub-exponential cutoff function approximates a superposition of exponential cutoffs, thus the appearance of a sub-exponential cutoff in the ensemble SED is to be expected within a curvature radiation model. We note, however, that the highest energy spectral point is higher than the best fit sub-exponential cutoff function at the $\sim 2.4\sigma$ level in both the young pulsar and millisecond pulsar cases. This cannot be taken as strong evidence for a non-exponentially-suppressed pulsar emission component aggregating in the stacked analysis, however, the available data cannot rule it out beyond the level of the limits shown in Figure 3 and Table I.

Beyond this work, improvements can be made using the forthcoming *Fermi*-LAT pass-8 data release which will improve the *Fermi*-LAT acceptance by ∼25% at 100 GeV [Atwood et al. 2013]. Improvements to this stacking analysis can also be made by employing a likelihood framework to stack the sources (see Ackermann et al. 2011 for example), rather than the simple *On* minus *Off* procedure described here. The flux sensitivity of any stacking analysis will, however, ultimately be bounded by the exposure of the *Fermi*-LAT. A future stacking analysis which doubles both the number of pulsars and the duration of observation used will increase the exposure by a factor of 4, indicating that future stacking analyses which do not yield detections may improve on the limits presented here by perhaps one or two orders of magnitude.

A more detailed account of the stacking analysis methods and results of this study can be found in McCann [2014].

Acknowledgments

This research is supported in part by the Kavli Institute for Cosmological Physics at the University of Chicago through grant NSF PHY-1125897 and an endowment from the Kavli Foundation and its founder Fred Kavli. I am grateful to the VERITAS collaboration for their support. In particular, I am very grateful to Pat Moriarty, David Hanna, Nepomuk Otte, Benjamin Zitzer, Jeremy Perkins, Scott Wakely, Nahee Park, Jeffery Grube and Christopher Bochenek for very helpful discussions on aspects of the analysis presented here.

References

Abazajian, K. N., & Kaplinghat, M. 2012, Phys. Rev. D , 86, 083511

Abdo, A. A., Ackermann, M., Ajello, M., et al. 2010, ApJ , 713, 154

Abdo, A. A., Ackermann, M., Ajello, M., et al. 2010b, ApJS , 187, 460

Abdo, A. A., Ajello, M., Allafort, A., et al. 2013, ApJS , 208, 17

Ackermann, M., Ajello, M., Albert, A., et al. 2011, Physical Review Letters, 107, 241302

Ackermann, M., Ajello, M., Allafort, A., et al. 2013, ApJ , 765, 54

Aharonian, F., Akhperjanian, A. G., Barrio, J. A., et al. 1999, A&A , 346, 913

Aharonian, F., Akhperjanian, A., Beilicke, M., et al. 2004, A&A , 421, 529

Aharonian, F. A., Bogovalov, S. V., & Khangulyan, D. 2012, Nature , 482, 507

Akerlof, C. W., Breslin, A. C., Cawley, M. F., et al. 1993, A&A , 274, L17

Albert, J., Aliu, E., Anderhub, H., et al. 2008, ApJ , 674, 1037

Aliu, E., The VERITAS Collaboration et al. 2011, Science, 334, 69

Aliu, E., Archambault, S., Archer, A., et al. 2015, ApJ , 800, 61

Atwood, W., Albert, A., Baldini, L., et al. 2013, arXiv:1303.3514

Bednarek, W. 2012, MNRAS, 424, 2079

Celik, O., & Johnson, T. J. 2011, American Institute of Physics Conference Series, 1357, 225 utoffs

Du, Y. J., Qiao, G. J., & Wang, W. 2012, ApJ , 748, 84

Harding, A. K., Stern, J. V., Dyks, J., & Frackowiak, M. 2008, ApJ , 680, 1378

Helene, O. 1983, Nuclear Instruments and Methods in Physics Research, 212, 319

Hirotani, K. 2001, ApJ , 549, 495

Hobbs, G. B., Edwards, R. T., & Manchester, R. N. 2006, MNRAS, 369, 655

Leung, G. C. K., Takata, J., Ng, C. W., et al. 2014, ApJ , 797, LL13

Li, T.-P., & Ma, Y.-Q. 1983, ApJ , 272, 317

Lyutikov, M., Otte, N., & McCann, A. 2012, ApJ , 754, 33

Lyutikov, M. 2012, ApJ , 757, 88

McCann, A. 2014, arXiv:1412.2422

Neshpor, Y. I., Stepanyan, A. A., Zyskin, Y. L., et al. 2001, Astronomy Letters, 27, 228

Pétri, J. 2012, MNRAS, 424, 2023

Singh, B. B., Chitnis, V. R., Bose, D., et al. 2009, Astroparticle Physics, 32, 120

Vishwanath, P. R., Sathyanarayana, G. P., Ramanamurthy, P. V., & Bhat, P. N. 1993, A&A , 267, L5

Discovery of TeV gamma-ray emission from the Pulsar Wind Nebula 3C 58 by MAGIC

O. Blanch Bigas, R. Lopez
IFAE, Campus UAB, Bellaterra, E-08193 Spain
and E. Carmona
Centro de Investigaciones Energéticas, Medioambientales y Tecnológicas, Madrid, E-28040 Spain
on behalf of the MAGIC collaboration

M.A. Pérez-Torres
Inst. de Astrofísica de Andalucía (CSIC), Granada, E-18080 Spain

The Pulsar Wind Nebula (PWN) 3C 58 is energized by one of the highest spin-down power pulsars known (5% of Crab pulsar) and it has been compared to the Crab Nebula due to their morphological similarities. This object was detected by Fermi-LAT with a spectrum extending beyond 100 GeV. We analyzed 81 hours of 3C 58 data taken with the MAGIC telescopes and we detected VHE gamma-ray emission for the first time at TeV energies with a significance of 5.7 sigma and an integral flux of 0.65% C.U. above 1 TeV. The differential energy spectrum between 400 GeV and 10 TeV is well described by a power-law function $d\Phi/dE = f_o(E/1TeV)^{-\Gamma}$ with $f_o = (2.0 \pm 0.4stat \pm 0.6sys)10^{-13}cm^{-2}s^{-1}TeV^{-1}$ and $\Gamma = 2.4 \pm 0.2sta \pm 0.2sys$. This leads 3C 58 to be the least luminous PWN ever detected at VHE and the one with the lowest flux at VHE to date. According to time-dependent models in which electrons up-scatter photon fields, the best representation favors a distance to the PWN of 2 kpc and FIR comparable to CMB photon fields. If we consider an unexpectedly high FIR density, the data can also be reproduced by models assuming a 3.2 kpc distance. A low magnetic field, far from equipartition, is required to explain the VHE data. Hadronic contribution from the hosting supernova remnant (SNR) requires unrealistic energy budget given the density of the medium, disfavoring cosmic ray acceleration in the SNR as origin of the VHE gamma-ray emission.

1. General description

The supernova remnant 3C 58 (SNR G130.7+3.1) has a flat radio spectrum and is brightest near the center, therefore it was classified as a pulsar wind nebula [PWN; 1]. It is centered on PSR J0205+6449, a pulsar discovered in 2002 with the *Chandra* X-ray observatory [2]. It is widely assumed that 3C 58 is located at a distance of 3.2 kpc [3], but recent H I measurements suggest a distance of 2 kpc [4]. The age of the system is estimated to be $\sim$ 2.5 kyr [5] from the PWN evolution and energetics, however this is a matter of debate. The pulsar has one of the highest spin-down powers known ($\dot{E} = 2.7\times10^{37}$erg s^{-1}). The PWN has a size of $9'\times6'$ in radio, infrared (IR), and X-rays [6, 7, 8, 9]. Its luminosity is $L_{\ 0.5\ -\ 10\ \mathrm{keV}} = 2.4 \times 10^{34}$ erg s^{-1} in the X-ray band, which is more than 3 orders of magnitude lower than that of the Crab nebula [10]. 3C 58 has been compared with the Crab because the jet-torus structure is similar [8]. Because of these morphological similarities with the Crab nebula and its high spin-down power (5% of Crab), 3C 58 has historically been considered one of the PWNe most likely to emit γ rays.

The pulsar J0205+6449 has a period P=65.68 ms, a spin-down rate $\dot{P} = 1.93 \times 10^{-13}$s s^{-1}, and a characteristic age of 5.38 kyr [2]. It was discovered by the *Fermi*-LAT in pulsed γ rays. The measured energy flux is $F_{\gamma>0.1\mathrm{GeV}}$=(5.4±0.2)$\times10^{-11}$ erg cm^{-2}s^{-1} with a luminosity of $L_{\gamma>0.1\mathrm{GeV}}$=(2.4±0.1)$\times10^{34}$ erg s^{-1}, assuming a distance for the pulsar of 1.95 kpc [11]. The spectrum is well described by a power-law with an exponential cutoff at E$_{\mathrm{cutoff}}$=1.6 GeV [12]. No pulsed emission was detected at energies above 10 GeV [13]. In the off-peak region, defined as the region between the two γ-ray pulsed peaks (off-peak phase interval ϕ=0.64–0.99), the Fermi Collaboration reported the detection of emission from 3C 58 [12]. The reported energy flux is (1.75±0.68)$\times10^{-11}$erg cm^{-2}s^{-1} and the differential energy spectrum between 100 MeV and 316 GeV is well described by a power-law with photon index $\gamma = 1.61 \pm 0.21$. No hint of spatial extension was reported at those energies. The association of the high-energy unpulsed steady emission with the PWN is favored, although an hadronic origin related to the associated SNR can not be ruled out. 3C 58 was tagged as a potential TeV γ-ray source by the Fermi Collaboration [13].

The PWN 3C 58 was previously observed in the VHE γ-ray range by several IACTs. The Whipple telescope reported an integral flux upper limit of 1.31$\times10^{-11}$ cm^{-2}s^{-1} $\sim$ 19 % C.U. at an energy threshold of 500 GeV [14], and VERITAS established upper limits at the level of 2.3 % C.U. above an energy of 300 GeV [15]. MAGIC-I observed the source in 2005 and established integral upper limits above 110 GeV at the level of 7.7$\times10^{-12}$ cm^{-2}s^{-1} ($\sim$4 % C.U.)[16]. The improved sensitivity of the MAGIC telescopes with respect to previous observations and the *Fermi*-LAT results motivated us to perform deep VHE observations of the source.

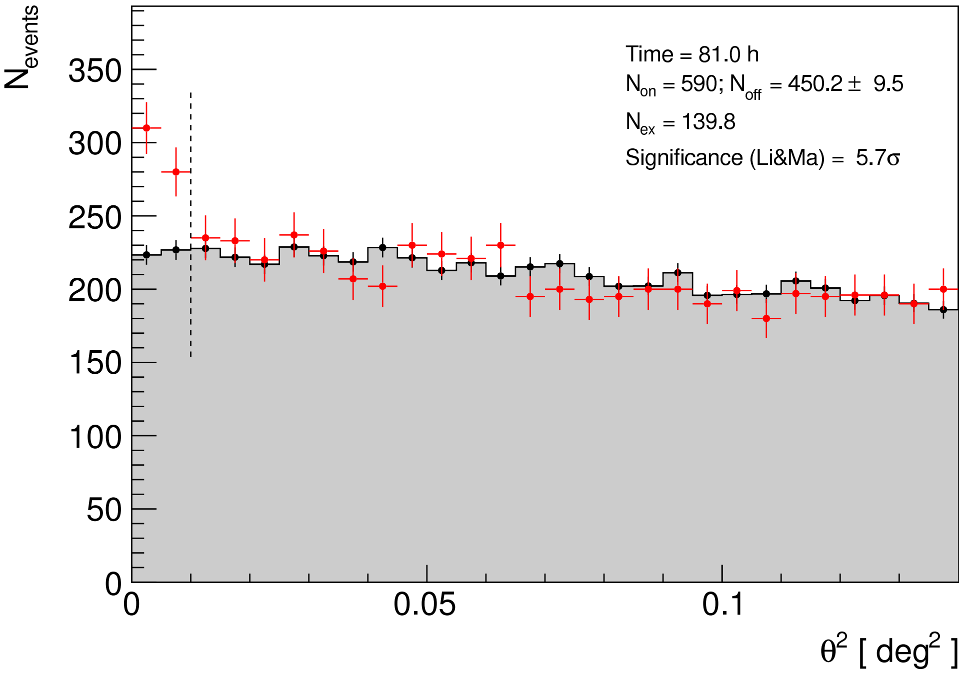

Figure 1: Distribution of squared angular distance, θ^2, between the reconstructed arrival directions of gamma-ray candidate events and the position of PSR J0205+6449 (*red points*).

2. MAGIC observations and results

MAGIC observed 3C 58 in the period between 4 August 2013 to 5 January 2014 for 99 hours, and after quality cuts, 81 hours of the data were used for the analysis. The data were analyzed using the MARS analysis framework [17]. The source was observed at zenith angles between 36° and 52°. The data were taken in *wobble-mode* [18] pointing at four different positions situated 0.4° away from the source to evaluate the background simultaneously with 3C 58 observations.

The applied cuts yield an energy threshold of 420 GeV. The significance of the signal, calculated with the LiMa formula, is 5.7σ, which establishes 3C 58 as a γ-ray source. The θ^2 distribution is shown in Figure 1. As the five OFF positions were taken for each of the wobble positions, the OFF histograms were reweighted depending on the time taken on each wobble position.

We show in Figure 2 the relative flux (excess/background) skymap, produced using the same cuts as for the θ^2 calculation. The TS significance, which is the LiMa significance applied on a smoothed and modeled background estimate, is higher than 6 at the position of the pulsar PSR J0205+6449. The excess of the VHE skymap was fit with a Gaussian function. The best-fit position is RA(J2000)=2h 05m $31(09)_{stat}(11)_{sys}$s ; DEC(J2000)=64° $51'(1)_{stat}(1)_{sys}$. This position is statistically deviant by 2σ from the position of the pulsar, but is compatible with it at 1σ if systematic errors are taken into account. In the bottom left of the image we show the point spread function (PSF) of the smeared map at the corresponding energies, which is the result of the sum in quadrature of the instrumental angular resolution and the applied smearing ($4.7'$ radius, at the analysis energy threshold). The extension of the signal is compatible with the instrument PSF. The VLA contours are coincident with the detected γ-ray excess.

Figure 3 shows the energy spectrum for the MAGIC data, together with published predictions for the gamma-ray emission from several authors, and two spectra obtained with three years of *Fermi*-LAT data, which were retrieved from the *Fermi*-LAT second pulsar-catalog [2PC, 12] and the *Fermi* high-energy LAT catalog [1FHL, 13]. The 1FHL catalog used events from the *Pass 7 Clean class*, which provides a substantial reduction of residual cosmic-ray background above 10 GeV, at the expense of a slightly smaller collection area, compared with the *Pass 7 Source class* that was adopted for 2PC [20]. The two γ-ray spectra from 3C58 reported in the 2PC and 1FHL catalogs agree within statistical uncertainties. The differential energy spectrum of the source is well fit by a single power-law function $d\phi/dE = f_0(E/1\ \mathrm{TeV})^{-\Gamma}$ with $f_0 = (2.0 \pm 0.4_{\mathrm{stat}} \pm 0.6_{\mathrm{sys}})10^{-13}\mathrm{cm}^{-2}\mathrm{s}^{-1}\mathrm{TeV}^{-1}$, $\Gamma = 2.4 \pm 0.2_{\mathrm{stat}} \pm 0.2_{\mathrm{sys}}$ and χ^2=0.04/2. The systematic errors were estimated from the MAGIC performance paper [21] including

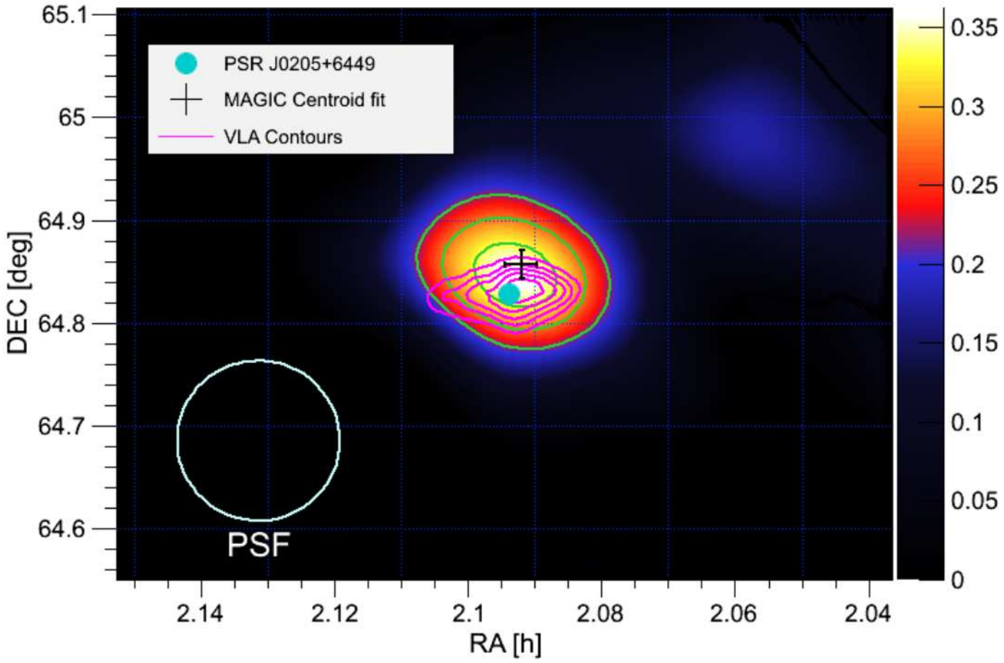

Figure 2: Relative flux (excess/background) map for MAGIC observations. The cyan circle indicates the position of PSR J0205+6449 and the black cross shows the fitted centroid of the MAGIC image with its statistical uncertainty. In green we plot the contour levels for the TS starting at 4 and increasing in steps of 1. The magenta contours represent the VLA flux at 1.4 GHz [19], starting at 0.25 Jy and increasing in steps of 0.25 Jy.

the upgraded telescope performances. The integral flux above 1 TeV is $F_{E>1\ \mathrm{TeV}} = 1.4 \times 10^{-13}\mathrm{cm}^{-2}\mathrm{s}^{-1}$. Taking into account a distance of 2 kpc, the luminosity of the source above 1 TeV is $L_{\gamma,E>1\ \mathrm{TeV}} = (3.0 \pm 1.1){\times}10^{32} d_2^2$ erg s^{-1}, where d_2 is the distance normalized to 2 kpc.

3. Discussion

Several models have been proposed that predict the VHE γ-ray emission of PWN 3C 58.

[25] presented a one zone model of the spectral evolution of PWNe and applied it to 3C 58 using a distance of 3.2 kpc. The VHE emission from this model consists of IC scattering of CMB photons and optical-to-IR photons, and also of pion decay. The flux of γ rays above 400 GeV predicted by this model is about an order of magnitude lower than the observation.

[22] proposed a time-dependent model in which positrons gain energy in the process of resonant scattering by heavy nuclei. The VHE emission is produced by IC scattering of leptons off CMB, IR, and synchrotron photons and by the decay of pions due to the interaction of nuclei with the matter of the nebula. The age of 3C 58 is assumed to be 5 kyr, using a distance of 3.2 kpc and an expansion velocity of 1000 km s^{-1}. According to this model, the predicted integral flux above 400 GeV is $\sim$10^{-13} cm^{-2}s^{-1}, while the integral flux above 420 GeV measured here is 5$\times$10^{-13}cm^{-2}s^{-1}. Calculations by [26], using the same model with an initial expansion velocity of 2000 km s^{-1} and considering IC scattering only from the CMB, are consistent with the observed spectrum. However, the magnetic field derived in this case is $B \sim 14\mu$G and it underestimates the radio emission of the nebula, although a more complex spectral shape might account for the radio nebula emission.

[27] developed a time-dependent model of the spectral evolution of PWN including synchrotron emission, synchrotron self-Compton, and IC. They evolved the electron energy distribution using an advective differential equation. To calculate the observability of 3C 58 at TeV energies they assumed a distance of 2 kpc and two different ages: 2.5 kyr and 1 kyr [23]. For the 2.5 kyr age, they obtained a magnetic field $B \sim 17\ \mu$G, while for an age of 1 kyr, the magnetic field obtained is B=40 μG. The emission predicted by this model is closer to the *Fermi* result for an age of 2.5 kyr.

[28] presented a different time-dependent leptonic diffusion-loss equation model without approximations, including synchrotron emission, synchrotron self-Compton, IC, and bremsstrahlung. They assumed a distance of 3.2 kpc and an age of 2.5 kyr

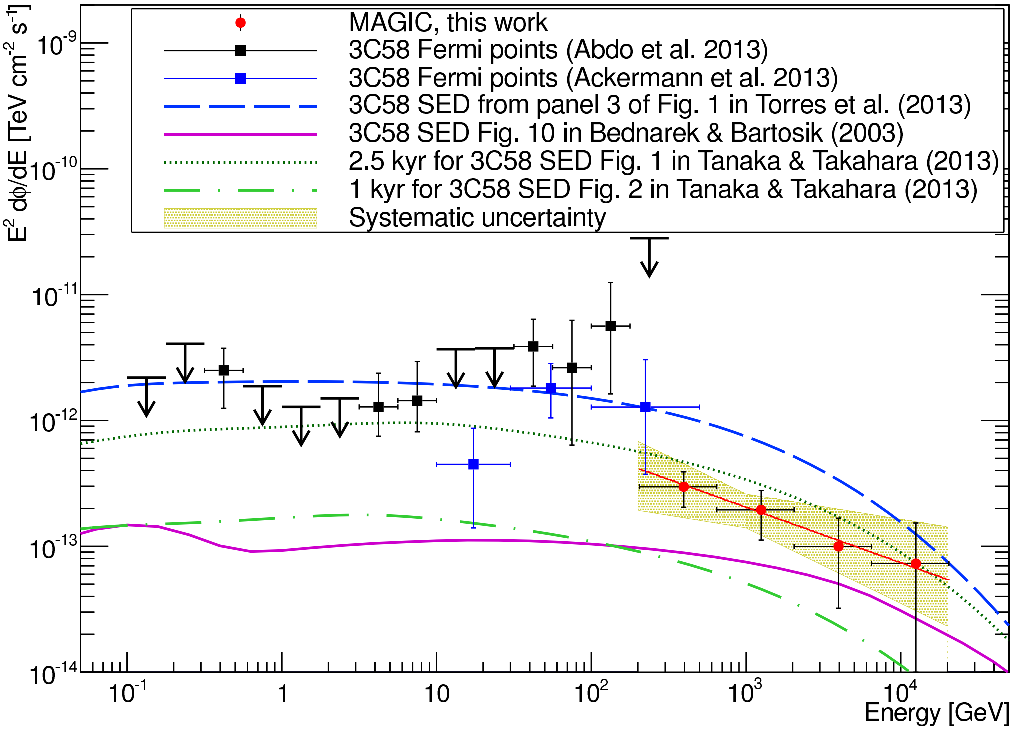

Figure 3: 3C 58 spectral energy distribution in the range between 0.1 GeV and 20 TeV. Red circles are the VHE points reported in this work. The best-fit function is drawn in red and the systematic uncertainty is represented by the yellow shaded area. Black squares and black arrows are taken from the *Fermi*-LAT second pulsar-catalog results [12]. Blue squares are taken from the *Fermi* high-energy LAT catalog [13]. The magenta line is the SED prediction for 3C 58 taken from Figure 10 of [22]. The clear green dashed-dotted line is the SED predicted by [23], assuming an age of 1 kyr, and the dark green dotted line is the prediction from the same paper, assuming an age of 2.5 kyr. The blue dashed line represents the SED predicted by [24] assuming that the Galactic FIR background is high enough to reach a flux detectable by the MAGIC sensitivity in 50h.

to calculate the observability of 3C 58 at high energies [24]. The predicted emission, without considering any additional photon source other than the CMB, is more than an order of magnitude lower than the flux reported here. It predicts VHE emission detectable by MAGIC in 50 hours for an FIR-dominated photon background with an energy density of 5 eV/cm^3. This would be more than one order of magnitude higher than the local IR density in the Galactic background radiation model used in GALPROP [$\sim$0.2 eV cm^{-3}; 29]. The magnetic field derived from this model is 35 μG. To reproduce the observations, a large FIR background or a revised distance to the PWN of 2 kpc are required. In the first case, a nearby star or the SNR itself might provide the necessary FIR targets, although no detection of an enhancement has been found in the direction of the PWN. As we mentioned in Sec. 1, a distance of 2 kpc has recently been proposed by [4] based on the recent H I measurements of the Canadian Galactic Plane Survey. At this distance, a lower photon density is required to fit the VHE data.

We have shown different time-dependent models in this section that predict the VHE emission of 3C 58. The SED predicted by them are shown in Figure 3. They use different assumptions for the evolution of the PWN and its emission. [25] divided the evolution of the SNR into phases and modeled the PWN evolution inside it. In [22] model, nuclei play an important role in accelerating particles inside the PWN. [24] and [27] modeled the evolution of the particle distribution by solving the diffusion-loss equation. [24] fully solved the diffusion-loss equation, while [27] neglected an escape term in the equation as an approximation. Another difference between these latter two models is that [27] took synchrotron emission, synchrotron self-Compton and IC into account, while [24] also consider the bremsstrahlung. The models that fit the γ-ray data derived a low magnetic field, far from equipartition, very low for a young PWN, but comparable with the value derived by [9] using other data.

4. Conclusions

We have for the first time detected VHE γ rays up to TeV energies from the PWN 3C 58. Following the assumptions in [30], it is highly unlikely that the measured flux comes from hadronic emission of the SNR.

The measured luminosity and flux make 3C 58 into an exceptional object. It is the weakest VHE PWN detected to date, a fact that attests to the sensitivity of MAGIC. On the other hand, it is also the least luminous VHE PWN, far less luminous than the original expectations. Its ration $L_{VHE}/\dot{E} \simeq 10^{-5}$ is the lowest measured, similar to Crab, which makes into a very inefficient γ-ray emitter. Only a closer distance of 2 kpc or a high local FIR photon density can qualitatively reproduce the multiwavelength data of this object in the published models. Since the high FIR density is unexpected, the closer distance with FIR photon density comparable with the averaged value in the Galaxy is favored. The models that fit the γ-ray data derived magnetic fields which are very far from equipartition.

Acknowledgments

We would like to thank the Instituto de Astrofsica de Canarias for the excellent working conditions at the Observatorio del Roque de los Muchachos in La Palma. The support of the German BMBF and MPG, the Italian INFN, the Swiss National Fund SNF, and the Spanish MINECO is gratefully acknowledged. This work was also supported by the CPAN CSD2007-00042 and MultiDark CSD2009-00064 projects of the Spanish Consolider-Ingenio 2010 programme, by grant 127740 of the Academy of Finland, by the DFG Cluster of Excellence Origin and Structure of the Universe, by the Croatian Science Foundation (HrZZ) Project 09/176, by the DFG Collaborative Research Centers SFB823/C4 and SFB876/C3, and by the Polish MNiSzW grant 745/N-HESSMAGIC /2010/0. We would like to thank S. J. Tanaka for providing us useful information about his model.

References

[1] K.W. Weiler and N. Panagia, “Are Crab-type Supernova Remnants (Plerions) Short-lived?”, A&A 70, 1978.
[2] S.S Murray et al, ”Discovery of X-Ray Pulsations from the Compact Central Source in the Supernova Remnant 3C 58”, ApJ 568, 2002.
[3] D.A. Roberts et al, ”High Resolution HI Observations of 3C58”, A&A 274, 1993.
[4] R. Kothes, ”Distance and age of the pulsar wind nebula 3C 58”, A&A 560, 2013.
[5] R.A. Chevalier, ”Young Core-Collapse Supernova Remnants and Their Supernovae”, ApJ 619, 2005.
[6] M.F. Bietenholz et al, ”The Radio Spectral Index and Expansion of 3C 58”, ApJ 560, 2001.
[7] F. Bocchino et al, ”The X-ray nebula of the filled center supernova remnant 3C 58 and its interaction with the environment”, A&A 369, 2001.
[8] P. Slane et al, ”New Constraints on the Structure and Evolution of the Pulsar Wind Nebula 3C 58”, ApJ 616, 2004.
[9] P. Slane et al,”The Infrared Detection of the Pulsar Wind Nebula in the Galactic Supernova Remnant 3C 58”, ApJ 676, 2008.
[10] K. Torii et al, ”ASCA Observations of the Crab-Like Supernova Remnant 3C 58”, PASJ 52, 2000.
[11] Y. Xu et al, ”The Distance to the Perseus Spiral Arm in the Milky Way”, Science 311, 2006.
[12] A.A. Abdo et al, ”The Second Fermi Large Area Telescope Catalog of Gamma-Ray Pulsars”, ApJS 208, 2013.
[13] The Fermi-LAT Collaboration, ”The First Fermi-LAT Catalog of Sources Above 10 GeV”, arXiv:1306.6772, 2013.
[14] T.A. Hall and S.P. Wakely, VERITAS Collaboration, ”Observations of Galactic Pulsars and Shell-Type SNRs with the Whipple 10 m Imaging Atmospheric Cherenkov Telescope”, ICRC, Hamburg, 2001.
[15] E. Aliu, ”Search for VHE γ-ray emission in the vicinity of selected pulsars of the Northern Sky with VERITAS”, American Institute of Physics Conference Series, 2008.
[16] H. Anderhub et al, ”Search for Very High Energy Gamma-ray Emission from Pulsar-Pulsar Wind Nebula Systems with the MAGIC Telescope”, ApJ 710, 2010.
[17] R. Zanin et al, ”MARS, the MAGIC analysis and reconstruction software”, ICRC, Rio Janeiro, 2013.
[18] V.P. Fomin et al, ”New methods of atmospheric Cherenkov imaging for gamma-ray astronomy. I. The false source method”, Astroparticle Physics 2, 1994.
[19] J.J. Condon et al, ”The NRAO VLA Sky Survey”, Astron. J. 115, 1998.
[20] M. Ackermann et al, ”The Fermi Large Area Telescope on Orbit: Event Classification, Instrument Response Functions, and Calibration”, ApJS 203, 2012.
[21] Aleksić et al, ”The major upgrade of the MAGIC telescopes, Part II: The achieved physics performance using the Crab Nebula observations”, arXiv:1409.5594, 2014.
[22] W. Bednarek and M. Bartosik, ”Gamma-rays from the pulsar wind nebulae”, A&A 405, 2003.
[23] S.J. Tanaka and F. Takahara, ”Properties of young pulsar wind nebulae: TeV detectability and pulsar properties”, MNRAS 429, 2013.
[24] D.F. Torres et al, ”An Energy-conserving, Particle-dominated, Time-dependent Model of 3C 58 and Its Observability at High Energies”, ApJ 763, 2013.

[25] Bucciantini et al, "Modelling spectral evolution of pulsar wind nebulae inside supernova remnants", MNRAS 410, 2011.

[26] W. Bednarek and M. Bartosik, "TeV gamma-rays from the Northern sky pulsar wind nebulae", Journal of Physics G Nuclear Physics, 2005.

[27] S.J. Tanaka and F. Takahara, "A Model of the Spectral Evolution of Pulsar Wind Nebulae", ApJ 715, 2010.

[28] J. Martín et al, "Time-dependent modelling of pulsar wind nebulae: study on the impact of the diffusion-loss approximations", MNRAS 427, 2012.

[29] T.A. Porter et al, "Inverse Compton Emission from Galactic Supernova Remnants: Effect of the Interstellar Radiation Field", , ApJ 648, 2006.

[30] L.O. Drury et al, "The gamma-ray visibility of supernova remnants. A test of cosmic ray origin", A&A 287, 1994.

Study of luminosity and spin-up relation in X-ray binary pulsars with long-term monitoring by MAXI/GSC and Fermi/GBM

Mutsumi Sugizaki, Tatehiro Mihara
Institute of Physical and Chemical Research (RIKEN), 2-1 Hirosawa, Wako, Saitama 351-0198, Japan
Motoki Nakajima
Nihon University, 2-870-1 Sakaecho-nishi, Matsudo, Chiba 101-830, Japan
Kazutaka Yamaoka
Nagoya University, Furo-cho, Chikusa-ku, Nagoya 464-8601, Japan

We study the relation between luminosity and spin-period change in X-ray binary pulsars using long-term light curve obtained by the MAXI/GSC all-sky survey and pulse period data from the Fermi/GBM pulsar project. X-ray binaries, consisting of a highly magnetized neutron star and a stellar companion, originate X-ray emission according to the energy of the accretion matter onto the neutron star. The accretion matter also transfers the angular momentum at the Alfven radius, and then spin up the neutron star. Therefore, the X-ray luminosity and the spin-up rate are supposed to be well correlated. We analyzed the luminosity and period-change relation using the data taken by continuous monitoring of MAXI/GSC and Fermi/GBM for Be/X-ray binaries, GX 304−1, A 0535+26, GRO J1008−57, KS 1947+300, and 2S 1417−624, which occurred large outbursts in the last four years. We discuss the results comparing the obtained observed relation with that of the theoretical model by Ghosh & Lamb (1979).

1. Introduction

X-ray binary pulsars (XBPs) are systems consisting of magnetized neutron stars and mass-donating stellar companions. Since the neutron stars are strongly magnetized, the matter flows from the companion are dominated by the magnetic pressure inside the Alfven radius, and then funneled onto the magnetic poles along the magnetic field lines. The accretion matter also transfers its angular momentum at the Alfven radius. Therefore, the pulsar spin-up rate and the mass accretion rate, i.e. the X-ray luminosity, are thought to be closely correlated (e.g. Ghosh & Lamb 1979, hereafter GL79 [1]). The issue is relevant to the fundamental parameters of the neutron stars such as mass, radius, and magnetic field, as well as the XBP evolution scenarios.

Be XBPs, which include Be stars extending circumstellar disk around the equator, are one of the major XBP subgroups [2]. They often exhibit large outbursts lasting for about a few weeks to a few months mostly at around the orbital phase of the neutron-star periastron passage. During these outbursts, simultaneous spin-up episodes are often observed (e.g. [3]). This is naturally explained by an increase in the accretion rate induced by the interaction with Be-star disk, and the associated transfer of the angular momentum to the neutron star via disc-magnetosphare coupling. These events give us an opportunity to study the relation between the luminosity and the spin-up rate quantitatively.

In this paper, we present the study on the relation using the long-term light curve obtained by the MAXI/GSC all-sky survey and the period change obtained from the archived results of Fermi/GBM pulsar project. These data, taken by the continuous monitor for over four years, enable us to investigate their time variations over the entire outburst activities in Be XBPs. We describe the observation in § 2, the analysis procedure in § 3, and then discuss about the obtained results in § 4.

2. Observation Data

Since the MAXI (Monitor of All-sky X-ray Image; [4]) experiment onboard the International Space Station started in 2009 August, the GSC (Gas Slit Camera; [5]), one of the two MAXI detectors, has been scanning almost the whole sky every 92-minute orbital cycle in the 2–30 keV band. To obtain the long-term luminosity variation of Be XBPs covering the outbursts as well as the intermission/quiescence, we use archived GSC light-curve data in 2–20 keV band, which are processed with a standard procedure [6] by the MAXI team and archived at MAXI web site[7].

The GBM (Gamma-ray Burst Monitor; [8]) onboard the Fermi Gamma-Ray Space Telescope, is an all-sky instrument sensitive to X-rays and gamma-rays with energies between 8 keV and 40 MeV. The Fermi GBM pulsar project [9, 10] provides results of timing analysis of a number of positively detected X-ray pulsars, including their pulsation periods and pulsed fluxes via the web site [11] since the in-orbit operation started in 2008 July. We utilized the archived pulse period data of Be XBPs.

We selected five Be XBPs, GX 304−1, A 0535+26, GRO J1008−57, KS 1947+300 and 2S 1417−624 from targets listed in the MAXI/GSC and the Fermi/GBM archive for this study, because they exhibited large outburst activities in the last four years and their surface magnetic fields are well determined by the cycloton resonance feature in the X-ray spectrum (execpt for 2S 1417−624). Table I summarized characteristic parameters of these Be XBPs and figure 1 shows the time variation of the bolometric luminosity calculated from MAXI/GSC 2–20 keV light curve data and that of the pulse period obtained from the Fermi/GBM pulsar data during outbursts for each source.

3. Analysis

Observed pulse-period variations of XBPs include two distinct effects, the intrinsic pulsar spin-period change and the orbital Doppler effect. In Be XBPs, both of them are supposed to correlate with the orbital phase. Therefore, it is not straightforward to resolve each component from the observed data. Although the pulse period data of XBPs in the Fermi/GBM archive are corrected for the orbital Doppler effect if their orbital elements are determined, the orbital elements have not been known in all of the Be XBPs with our interests. Hence, we construct a semi-empirical model implementing both these effects and then fit it to the data, in an attempt to simultaneously determine the intrinsic pulse period change and the orbital elements.

3.1. Modeling of period change in XBPs

We here employ the simple theoretical model of the pulsar spin-up by the mass accretion via disk, proposed by GL79 [1]. The model has been examined with X-ray data, and its validity and limits are well studied (e.g. [3, 13]). In this model, the pulsar spin-up rate $-\dot{P}_{\rm spin}$ (s yr^{-1}) is given by

$$-\dot{P}_{\rm spin} = 5.0 \times 10^{-5} \mu_{30}^{2/7} n(\omega_{\rm s}) S_1(M) P_{\rm spin}^2 L_{37}^{6/7} \quad (1)$$

$$S_1(M) = R_6^{6/7} (M/M_\odot)^{-3/7} I_{45}^{-1}$$

where μ_{30}, $R_{\rm NS6}$, $M_{\rm NS\odot}$, I_{45}, $P_{\rm spin}$, L_{37} are the magnetic dipole moment of the neutron star in units of 10^{30} G cm^3, radius in 10^6 cm, mass in $M_\odot$, moment of inertia in 10^{45} g cm^2, spin perid in s, luminosity in 10^{37} erg s^{-1}, $n(\omega_{\rm s})$ is a dimensionless torque that depends on the fastness parameter $\omega_{\rm s}$ and approximately constant at ~ 1.4 in slow rotating pulsars satisfying $(P_{\rm spin} L_{37}^{3/7}) \gg 1$.

The equation 1 implies that the spin-up rate $-\dot{P}_{\rm spin}$ follows the luminosity L as $-\dot{P}_{\rm spin} \propto L^{6/7}$. The power-law index γ in a model of $-\dot{P}_{\rm spin} \propto L^\gamma$ obtained from the fit to the observed data sometimes disagreed with the theoretical value of 6/7 and favor the rather higher value of ~ 1.2 [3, 13]. Besides this, the comparison of absolute spin-up rate with equation 1 has been hampered by a large uncertainty in the bolometric luminosity correction, which is in turn due to beaming effects (e.g. [3, 12]). We hence employ the spin-up model expressed by

$$-\dot{P}_{\rm spin} = \alpha L_{37}^\gamma \quad (2)$$

in which the power-law index $\gamma = 6/7$ and a correlation factor, $\alpha = 1.7 \times 10^{-7} \mu_{30}^{2/7} P_{\rm spin}^2$ s d^{-1} $(= \alpha_0)$ reduced from the equation 1 and typical neutron-star parameters of $R_6 = 1$, $M = 1.4 M_\odot$, $I_{45} = 1$, are treated as free parameters.

XBPs are also known to spin down during the quiescence due to the propeller effects. The rate is much smaller than the spin-up during the outburst bright phases, but may not be negligible. We accounted its effect with a constant spin-down parameter, β, added to $\dot{P}_{\rm spin}$ as an offset.

By combining the spin-up and spin-down models above, the intrinsic pulsar-spin period $P_{\rm spin}(t)$ is expressed by

$$\begin{aligned} P_{\rm spin}(t) &= P_0 + \int_{\tau_0}^{t} \dot{P}_{\rm spin}(\tau) d\tau \\ &= P_0 + \int_{\tau_0}^{t} \left\{ -\alpha L_{37}^\gamma(\tau) + \beta \right\} d\tau \quad (3) \end{aligned}$$

where we set the time basis τ_0 at the first periastron passage in the period under analysis and define the pulsation period at the time τ_0 as $P_0 = P_{\rm spin}(\tau_0)$. The model equation 3 includes four free parameters, P_0, α, β, γ and requires the luminosity data $L_{37}(t)$ as a function of time. We calculated the luminosity from data of the MAXI/GSC 2–20 keV light curve in 1-d time bin assuming the source distance, the typical energy spectrum of a cutoff power law from the past results, and the source emission to be isotopic.

The period modulation due to the binary orbital motion is calculated by using the binary elements, which consists of orbital period $P_{\rm B}$, eccentricity e, projected semi-major axis $a_{\rm x} \sin i$, epoch τ_0 and argument ω_0 of the periastron. The pulsar orbital velocity $v_{\rm l}(t)$ along the line of sight is

$$v_{\rm l}(t) = \frac{2\pi a_{\rm x} \sin i}{P_{\rm B}\sqrt{1-e^2}} \left\{ \cos\left(\nu(t) + \omega_0\right) + e \cos\omega_0 \right\} \quad (4)$$

where $\nu(t)$ is a parameter called 'true anomaly' describing the motion on the elliptical orbit and calculated from the Kepler's equation. The observed pulse period, $P_{\rm obs}(t)$, is then expressed by

$$P_{\rm obs}(t) \simeq P_{\rm spin}(t) \left(1 + \frac{v_{\rm l}(t)}{c} \right). \quad (5)$$

3.2. Period-change model fit

We applied the spin-period-change model, $P_{\rm spin}(t)$ in equation 3, to the Fermi/GBM archived period data

Table I Characteristic parameters of selected Be X-ray binary pulsars and the best-fit parameters (α, β) used in the period change model.

Target name	P_{pulse}	P_{orbit}	$a_{\mathrm{X}} \sin i$	e	B	D	α/α_0	β	Ref.
	(s)	(d)	(lt-s)		(10^{12} G)	(kpc)		(10^{-9} s s^{-1})	
GX 304−1	275	132.19	500	0.5	4.7	2.0	0.28	2.0	[15, 16]
A 0535+26	103	111.10	267	0.47	4.3	2.4	1.3	3.6	[17, 18]
GRO J1008−57	93	249.48	530	0.68	6.6	5.8	0.49	2.5	[19, 20]
KS 1947+300	18	40.42	137	0.034	1.1	10	3.2	0.69	[21, 22]
2S 1417−624	17	42.18	188	0.44	–*	11	(6.8)*	0.0:fix	[23, 24]

*: The surface magnetic field B has not been measured. It is assumed to be 2×10^{12} G.

for A 0535+26, KS 1947+300, and 2S 1417−624, in which the binary orbital effects were corrected with the known orbital elements. About GRO J1008−57, the orbital effects are not corrected in the archived data, but the orbital elements have been estimated by [19]. We thus fit the data to the period model, $P_{\mathrm{obs}}(t)$ in equation 5, which includes the orbital effect, employing the orbital elements given in [19]. About GX 304−1, its orbital elements have not been measured. We fit the period data with the model $P_{\mathrm{obs}}(t)$ in which the orbital elements are floated.

As results of many model-fit attempts, we found that the model is able to reproduce the data approximately with $\gamma \sim 1$ in all of the five targets. We thus fix the parameter γ at 6/7, predicted by GL79 [1], in order to concentrate on the correlation factor α, hereafter. In figure 1 bottom panels, the obtained best-fit models with $\gamma = 6/7$ are superposed on the period data. The best-fit parameters are shown in table I, where the values of α are given by the ratio to that ($= \alpha_0$) predicted by GL79 [1].

4. Discussion

We fitted pulse period variation of five Be XBPs observed with Fermi/GBM to the model implementing the spin-up due to the mass accretion via disk, expressed by $\dot{P}_{\mathrm{spin}} = \alpha L^{6/7}$ based on GL79 [1] and the luminosity estimated from the MAXI/GSC light curve. The results show that the model successfully reproduce the data in all of the five samples. The obtained best-fit parameters imply that the correlation factor α from the luminosity $L^{6/7}$ to the spin-up rate $\dot{P}$ largely agree with α_0 predicted by GL79 [1]. The dispersion of the ratio, $\alpha/\alpha_0 \sim 0.3$ to 3, is naturally expected from the uncertainty in the bolometric luminosity correction due to the beaming effect.

However, the values of α/α_0 seems to have some tendency against the pulse period, the orbital period, and the eccentricity, which are suggested to have a relation with Be-XBP subgroups [14]. This will become clearer with increasing data in the near future.

Acknowledgments

The authors thank all of the MAXI team members for enabling the data analysis for the science study as well as the Fermi/GBM pulsar project for providing the useful analysis results to the public.

References

[1] Ghosh, P., & Lamb, F. K. 1979, ApJ, 234, 296
[2] Reig, P. 2011, Ap&SS, 332, 1
[3] Bildsten, L., et al. 1997, ApJS, 113, 367
[4] Matsuoka, M., et al. 2009, PASJ, 61, 999
[5] Mihara, T., et al. 2011, PASJ, 63, 623
[6] Sugizaki, M. et al. 2011, PASJ, 63, 635
[7] http://maxi.riken.jp/
[8] Meegan, C., et al. 2009, ApJ, 702, 791
[9] Finger, M. H., et al. 2009, arXiv:0912.3847
[10] Camero-Arranz, A., et al. 2010, ApJ, 708, 1500
[11] http://gammaray.nsstc.nasa.gov/gbm/science/pulsars/
[12] Wilson, C. A., et al. 2002, ApJ, 570, 287
[13] Reynolds, A. P., et al. 1996, A&A, 312, 872
[14] Knigge, C., et al. 2011, Nature, 479, 372
[15] Yamamoto, T., et al. 2011, PASJ, 63, 751
[16] Sugizaki, M., Yamamoto, T., Mihara, T., & Nakajima, M. 2014, Suzaku-MAXI 2014: Expanding the Frontiers of the X-ray Universe, 226
[17] Caballero, I., et al. 2013, ApJL, 764, LL23
[18] Müller, D., at al. 2013, A&A, 552, AA81
[19] Kühnel, M., et al. 2013, A&A, 555, A95
[20] Yamamoto, T., et al. 2014, PASJ, 66, 59
[21] Galloway, D. K., at al. 2004, ApJ, 613, 1164
[22] Fürst, F., et al. 2014, ApJL, 784, LL40
[23] Finger, M. H., et al. 1996, A&AS, 120, 209
[24] İnam, S. Ç., et al. 2004, MNRAS, 349, 173

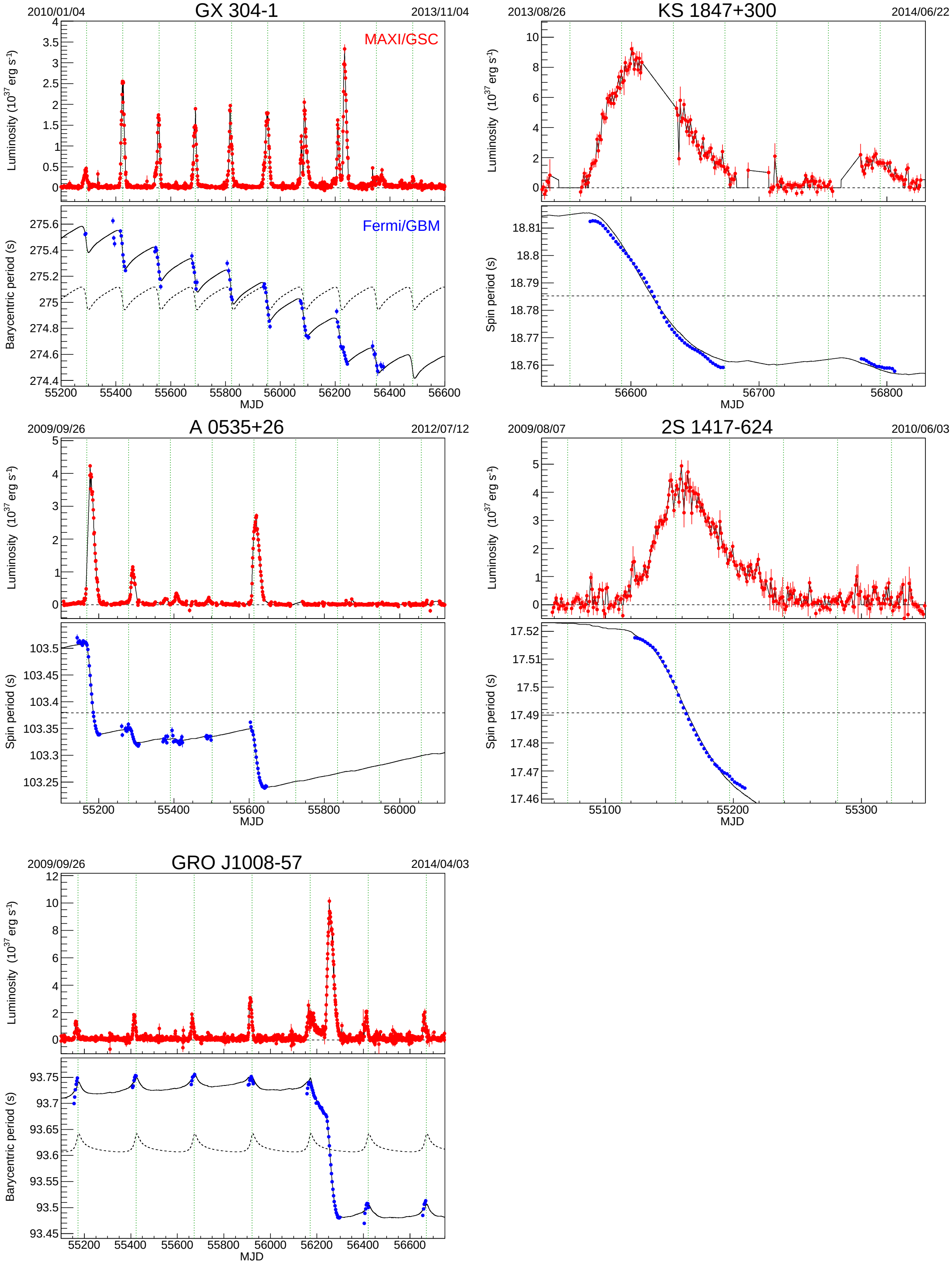

Figure 1: For each target of GX 304−1, A 0535+26, GRO J1008−57, KS 1947+300, and 2S 1417−624, time variation of luminosity estimated from MAXI/GSC 2–20 keV light curve data in 1-d time bin (top) and and that of pulse period during the outbursts obtained from Fermi/GBM pulsar data (bottom) are plotted. In the top panels, solid lines represent the luminosity data $L_{37}(t)$ used for the period-change model fit. In the bottom panel, solid and dash lines represent the best-fit period model and the inclusive orbital Doppler effects which have been corrected in A 0535+26, KS 1947+300, and 2S 1417−624.

MAXI monitoring of blazars and blackhole binaries

Juri Sugimoto, Mutsumi Sugizaki, Tatehiro Mihara, and Masaru Matsuoka
MAXI team, Institute of Physical and Chemical Research (RIKEN),
2-1 Hirosawa, Wako, Saitama 351-0198, Japan

Hitoshi Negoro
Department of Physics, Nihon University, 1-8-14,
Kanda-Surugadai, Chiyoda-ku, Tokyo 101-8308

Satoshi Nakahira
ISS Science Project Office, Institute of Space and Astronautical Science (ISAS),
Japan Aerospace Exploration Agency (JAXA),
2-1-1 Sengen, Tsukuba, Ibaraki 305-8505, Japan

Yoshihiro Ueda
Department of Astronomy, Kyoto University, Kitashirakawa-Oiwake-cho, Sakyo-ku, Kyoto 606-8502, Japan

Naoki Isobe
Institute of Space and Astronautical Science (ISAS),
Japan Aerospace Exploration Agency (JAXA), 3-1-1 Yoshinodai,
Chuo-ku, Sagamihara, Kanagawa 252-5210, Japan

Since August 2009, MAXI experiment on the ISS has been performing all-sky X-ray monitoring. With MAXI, we detected flaring activities of some blezars, including Mrk 421, Mrk 501, and 3C 273. Recently, new X-ray flaring activities were detected from two blazers, MAXI J1930+093 = 2FGL J1931.1+0938 [7] and 2MAXI J0243-582 = BZB J0244-5819 [5]. The MAXI monitoring also covers black hole binaries, including Cyg X–1 and Cyg X–3 which emit GeV gamma-rays. Their gamma-ray emission was found to coincide with their X-ray state transitions. We present light curves and outstanding events of these sources.

I. MAXI

We use the observations of Monitor of All sky X-ray Image (MAXI) [3]. MAXI was launched in 2009 July and attached to the International Space Station (ISS). The ISS with MAXI orbits the earth in 92 minutes, and MAXI scans the objects in the all sky once in an orbit. MAXI has already reported more than one hundred transients[14]. The observed results are immediately released through the internet, promoting rapid follow-up observations with telescopes around the world. MAXI has two kinds of X-ray cameras: the Gas Slit Camera (GSC: [4]) covering the energy band of 2–20 keV. and the Solid-state Slit Camera (SSC: [12, 13]) covering 0.7–7 keV. We can downloaded one-day bin and 90 min bin archival data for making light curves from the MAXI home page[15]. The energy spectra, images and also light curves of both the GSC and the SSC can be processed by the MAXI on-demand data web page[16] [6].

II. OBSERVATION OF BLAZARS FOR 5 YEARS

MAXI is monitoring 21 BL Lacs and 3 quasars. We show the light curves for 5 years by MAXI/GSC of Mrk 421, Mrk 501 and 3C 273 in Figure 1. We reported their X-ray flares and brightenings to the Astronomer's Telegram (Atel, showed as grey lines in Figure 1).

III. NEW DETECTION OF TWO BLAZARS

A. 2FGL J1931.1+0938

At 05:31:55 UT on March 2, 2014, MAXI nova alert system detected a new faint X–ray source which was ∼10 mCrab in Figure 2. We named it MAXI J1930+093 and reported to the Atel#5943 [7]. After that, Swift/XRT observed the error region of MAXI. Swift found an X-ray source which was the same intensity as MAXI observation, and identified it to the BL Lac object 2FGL J1931.1+0938.

B. BZB J0244–5819

At 19:24:10 UT on March 24, 2014, MAXI nova alert system detected transient object which was 6.6 mCrab in Figure 3. It had been identified as 2MAXI J0243–582 in the MAXI/GSC 37-Month catalog [2]. We proposed a Swift ToO observation with 4-point

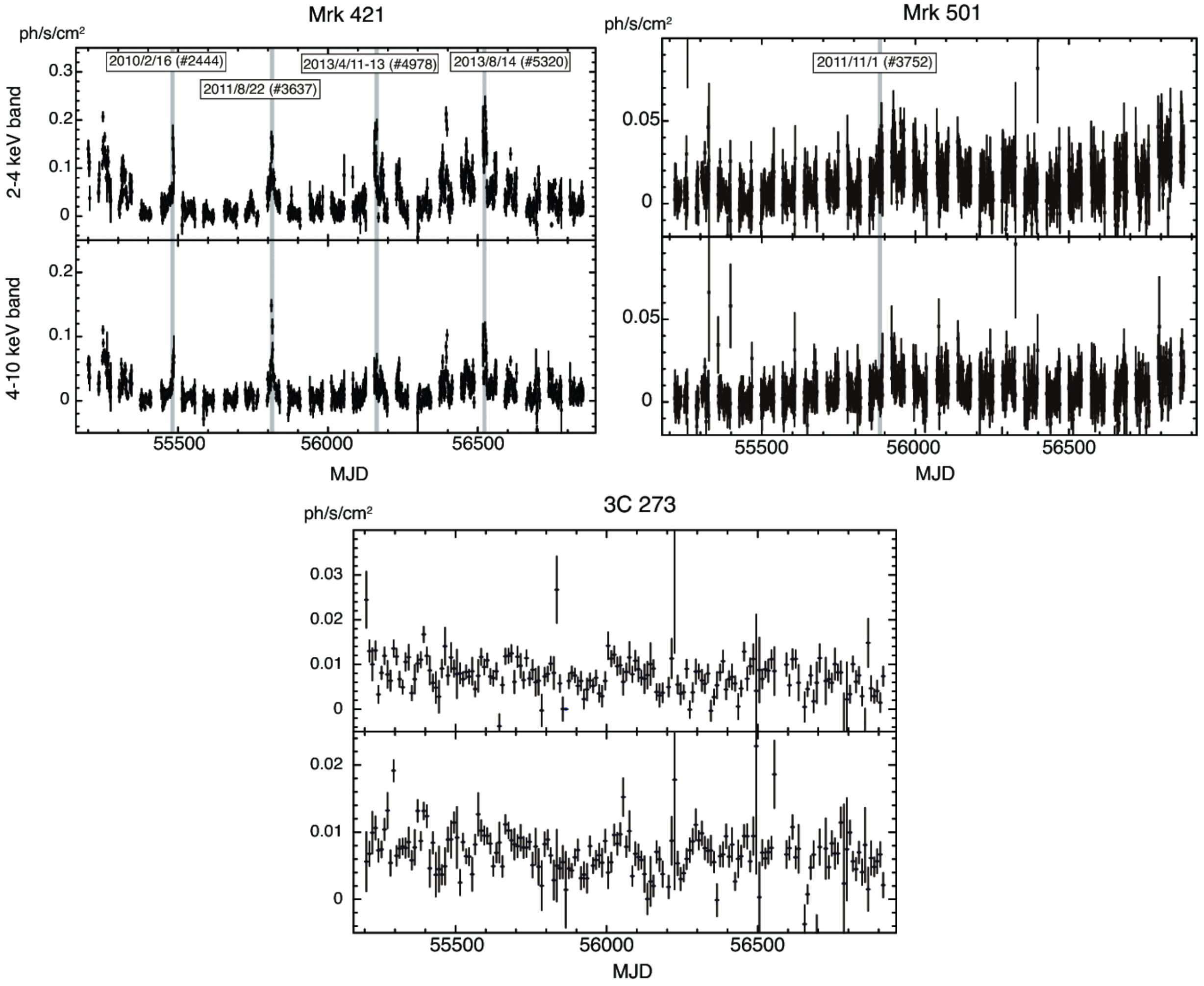

FIG. 1: MAXI/GSC light curves of blazars, Mrk 421, Mrk 501 and 3C 273. Binning is 1 day for Mrk 421 and Mrk 501 and 10 days for 3C 273. The dates in the figure are MAXI notifications to Atel.

tiling to cover the MAXI error circle with the Swift XRT. In the Swift XRT image, we find a bright point source at (RA, Dec)= (2h 44m 40.10s, −58d 19m 54.8s) with an estimated error of 2.3 arcseconds radius (90% c.l.). This position lies 1.54 arc-seconds from the NED position of the BL Lac object BZB J0244–5819. We therefore suggest that the trigger source is an X-ray flare of BZB J0244–5819 (=MAXI J0243–582) (ATel#6012 [5]).

IV. BLACK HOLE BINARY CYG X-1

Cygnus X-1 (Cyg X–1) is one of the most famous high mass X-ray binaries (HMXBs), and is composed of a black hole (BH) and a massive giant companion star. X–ray from Cyg X–1 is highly variable,the binary period is 5.6 d, and the distance is $1.86^{+0.12}_{-0.11}$ kpc [9]. The galactic BH binaries have two spectral states, a low/hard state that is dominated by a power-law spectrum, corresponding to the radiatively inefficient accretion flow (RIAF), and a high/soft state that is dominated by a thermal emission from the standard optically thick accretion disk [1, 10].

A. Light curve

MAXI obtained a long-term light curve for more than 5 years of Cyg X–1 [11]. Cyg X–1 had been in the low/hard state until June 2010, and after that it stayed in the high/soft state for about ten months [8].

Figure 4 shows light curves with one-day bin of Cyg X–1 obtained with GSC from 15 August 2009 (55058 MJD) to 9 November 2014 (56970 MJD), in three energy bands (2–4 keV, 4–10 keV and 10–20 keV). The two kinds of hardness ratios, $I(4\text{–}10\ \text{keV})/I(2\text{–}4\ \text{keV})$ and $I(10\text{–}20\ \text{keV})/I(4\text{–}10\ \text{keV})$, are also plotted. The state of Cyg X–1 can be recognized by the values of the hardness ratios.

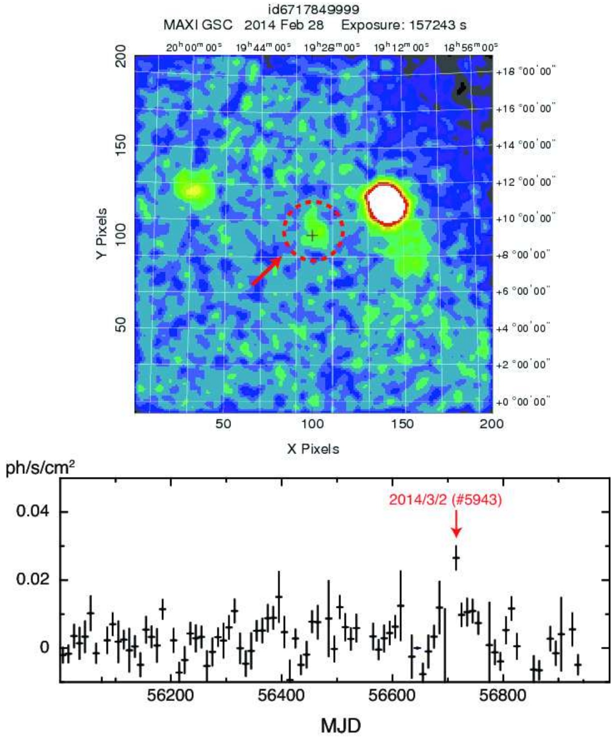

FIG. 2: The upper panel is a trigger image of 2FGL J1931.1+0938 by MAXI/GSC in 4–10 keV band, shown with a red arrow. The lower panel shows the light curve in 2–10 keV energy band. 1 bin is 10 days.

The low/hard state continued for about ten months since the start of the MAXI observation. A transition to the high/soft state occurred around 55378 MJD and then continued for another ten-month. After several state transitions, it has stayed in the high/soft state since 56107 MJD.

B. Hardness-intensity diagram

The upper panel of Figure 5 shows a hardness-intensity diagram. The vertical axis shows count rates in the 2–10 keV band, and the horizontal axis indicates the hardness ratios of the count rates in the 4–10 keV band to those in the 2–4 keV band. The lower panel in Figure 5 shows a histogram of the number of data points in certain bins of the hardness ratio. We can see clear two peaks, which correspond to the high/soft state and the low/hard state. To separate the period into those two states, we fit the histogram with two gaussian functions, and determined the mean values and standard deviations of the gaussian functions. Then we defined the state of each data point, by checking whether the hardness ratio of the data point is in $\pm 3\sigma$ of the distributions. Blue and red data points in Figure 5 are thus defined the low/hard state and the high/soft state, respectively. Black points are between then and considered as the transition. The determined terms of the states are summarized in Table I.

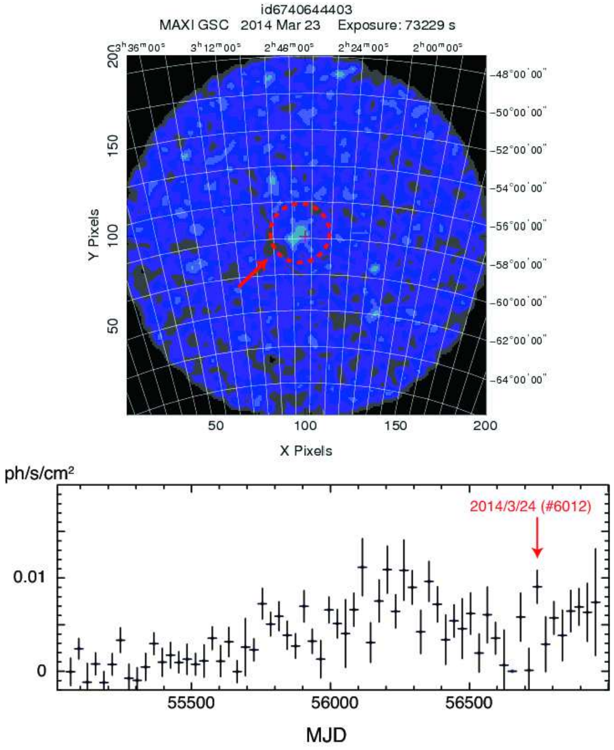

FIG. 3: The upper panel is a trigger image of BZB J0244-5819 by MAXI/GSC in 4–10 keV band, shown with a red arrow. The lower panel shows the light curve in 2–10 keV energy band. 1 bin is 30 days.

TABLE I: The terms of spectrum states

spectrum state	start MJD	end MJD
hard	55058	55376
soft	55378	55673
hard	55680	55788
soft	55789	55887
hard	55912	55941
soft	55943	56068
hard	56069	56076
soft	56078	56733
hard	56735	56741
soft	56742	56757
hard	56781	56824
soft	56854	∼

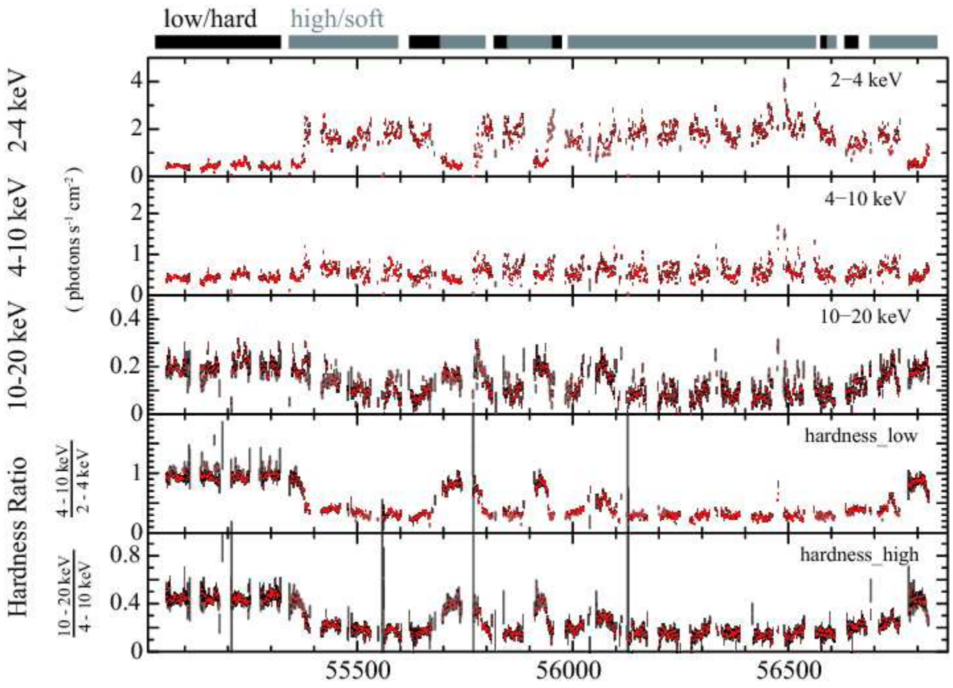

FIG. 4: One-day bin light curves and hardness ratios of Cyg X–1 obtained with MAXI/GSC. From top to bottom panel, light curves in the energy bands: 2–4 keV, 4–10 keV and 10–20 keV, and the hardness ratios of I(4–10 keV)/I(2–4 keV) and I(10–20 keV)/I(4–10 keV) are shown. The black and grey regions show the terms in the low/hard state, and in the high/soft state, respectively.

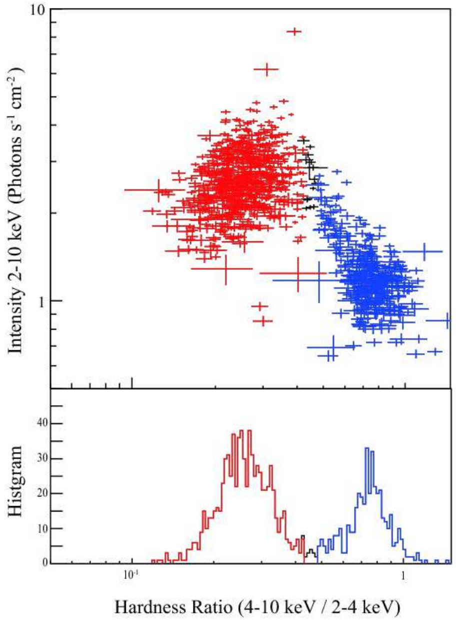

FIG. 5: Upper: the hardness-intensity diagram of Cyg X–1. Lower: the histogram of the hardness ratio distribution. The hardness ratio is calculated by dividing 4–10 keV band count rate by 2–4 keV one. The blue data points are in the low/hard state and the red ones are in the high/soft state. We treat the black ones to be during the transition.

Acknowledgments

This work was supported by RIKEN Junior Research Associate Program.

---

[1] Done, C., Gierliński, M., & Kubota, A. 2007, A&A Rev., 15, 1

[2] Hiroi, K., Ueda, Y., Hayashida, M., et al. 2013, ApJS, 207, 36

[3] Matsuoka, M., Kawasaki, K., Ueno, S., et al. 2009, PASJ, 61, 999

[4] Mihara, T., Nakajima, M., Sugizaki, M., et al. 2011, PASJ, 63, 623

[5] Nakahira, S., Ueno, S., Tomida, H., et al. 2014, The Astronomer's Telegram, 6012, 1

[6] Nakahira, S., et al., 2013, Journal of Space Science Informatics Japan, 2, 29

[7] Negoro, H., Serino, M., Nakahira, S., et al. 2014, The Astronomer's Telegram, 5943, 1

[8] Negoro, H., Kawai, N., Kawasaki, Y. U. K., et al. 2010, The Astronomer's Telegram, 2711, 1

[9] Orosz, J. A., McClintock, J. E., Aufdenberg, J. P., et al. 2011, ApJ, 742, 84

[10] Remillard, R. A., & McClintock, J. E. 2006, ARA&A, 44, 49

[11] Sugimoto, J., Mihara, T., Matsuoka, M., et al. 2014, Suzaku-MAXI 2014: Expanding the Frontiers of the X-ray Universe, 222

[12] Tomida, H., Tsunemi, H., Kimura, M., et al. 2011, PASJ, 63, 397

[13] Tsunemi, H., Tomida, H., Katayama, H., et al. 2010, PASJ, 62, 1371

[14] `http://maxi.riken.jp/top/doc/maxi_atel.html`

[15] `http://maxi.riken.jp/`

[16] `http://maxi.riken.jp/mxondem/`

X-Ray Studies of Redbacks

Mallory S.E. Roberts
New York University Abu Dhabi, Abu Dhabi, UAE / Eureka Scientific, Oakland, CA. USA
Maura A. McLaughlin, Peter A. Gentile
West Virginia University, Morgantown WV, USA
Paul S. Ray
Naval Research Laboratory, Washington DC, USA
Scott M. Ransom
National Radio Astronomy Observatory, Charlottesville VA, USA
Jason W.T. Hessels
ASTRON, Dwingeloo, Netherlands

arXiv:1502.07208v1 [astro-ph.HE] 25 Feb 2015

We consider the X-ray properties of the redback class of eclipsing millisecond pulsars. These are transitional systems between accreting low-mass X-ray binaries and binary millisecond pulsars orbiting white dwarfs, and hence their companions are non-degenerate and nearly Roche-lobe filling. The X-ray luminosity seems to scale with the fraction of the pulsar sky subtended by the companion, suggesting the shock region is not much larger than the companion, which is supported by modeling of the orbital light curves. The typical X-ray photon spectral index is ~ 1 and the typical 0.3-8 keV X-ray efficiency, assuming a shock size on the order of the companion's Roche lobe cross-section, is on the order of 10%. We present an overview of previous investigations, and present new observations of two redbacks, a Chandra observation of PSR J1628−3205 and a XMM-Newton observation of PSR J2129−0429. The latter shows a clearly double peaked orbital light curve with variation of the non-thermal flux by a factor of ~ 11, with peaks around orbital phases 0.6 and 0.9. We suggest the magnetic field of the companion plays a significant role in the X-ray emission from intrabinary shocks in redbacks.

1. The Redback Population

Millisecond pulsars are thought to be formed in binary systems where an old neutron star is spun-up via long term accretion from an evolved companion. In recent years, the MSP recycling scenario has been dramatically confirmed through observations of so-called “redback” millisecond pulsar systems [Roberts 2011] which have non-degenerate companions and in some cases transition between states with no visible radio pulsations but with optical and X-ray evidence of an accretion disk, and a state where radio pulsations are observed that regularly eclipse near superior conjunction. The first of these transition objects, PSR J1023+0038, showed optical evidence for an accretion disk in 2001 which had disappeared by 2004 [Thorstensen & Armstrong 2005] . In 2007, radio pulsations were discovered [Archibald et al. 2009], and in 2013 the MSP returned to an accreting state [Stappers et al. 2014].

Millisecond pulsars in compact binary systems have the potential of providing unique insights into pulsar winds. The companion forces a shock to occur at a distance d_s only $\sim 10^4$ times the light cylinder radius of the pulsar $R_{lc} = P_s c/2\pi$ (where P_s is the spin period, and c the speed of light), as compared to the more typical $d_s \sim 10^8 - 10^9 R_{lc}$ of the termination shock of pulsar wind nebulae around young, isolated pulsars. This means that the shock probes the wind in a region which might be significant in determining how the magnetization parameter σ, the ratio of magnetic energy to kinetic energy, goes from a presumably high value at the light cylinder to an apparently low value at the termination shock in typical pulsar wind nebulae [cf. Kennel & Coroniti 1984]. The basic shock emission theory for such intrabinary shocks has generally followed the outline of Arons & Tavani [1993] first developed for the original black widow system. In this model, the pulsar wind shocks with material ablated from the companion's surface, which is presumably swept back around the companion and ejected from the system. In these models, it is generally assumed that the only significant source of magnetic field is the magnetization of the wind, and that the X-ray emission is synchrotron which can be somewhat beamed either through a partially ordered magnetic field or doppler boosting.

A *Chandra* observation of PSR J1023+0038 in its radio pulsar state revealed significant orbital variability over five consecutive orbits [Bogdanov et al. 2011], with a pronounced dip in the X-ray flux at superior conjunction, when the companion is between the pulsar and observer and the intrabinary shock produced through the interaction of stellar outflows is obscured. The X-ray spectrum consists of a dominant non-thermal component from the shock and at least one thermal component, likely originating from heated pulsar polar caps. The eclipse depth and duration imply that the shock is localized near or at the companion surface. However, the companion only subtends $\sim 1\%$ of the pulsar's sky, so that if the wind is isotropic, only $\sim 1\%$ of the pulsar's wind is intercepted by the companion, and only $\sim 7\%$ would be intercepted if the wind is confined to an equatorial sheet. Bogdanov et al. [2011] inferred a high σ from the estimated magnetic field of $\sim$ 40G required to account for the soft X-ray luminosity.

An observation with *NuSTAR* of PSR J1023+0038 just before it returned to the accreting state [Tendulkar et al. 2014] showed that the spectrum of the intrabinary shock is a very hard power law (photon index $\Gamma = 1.17$) with no apparent cutoff out to $\sim$ 50keV, for a remarkable X-ray efficiency of $\sim$ 2% of the total spin down power, or around all of the nominal spin down power in the wind that would be intercepted by the companion. Such a hard spectrum is not easily obtained from a pulsar wind nebula shock, and such efficiency is unprecedented. This might be an indication of a significant equatorial enhancement in the wind or a significantly higher moment of inertia than the canonical $10^{45}\mathrm{gm\,cm}^2$, but it is still a remarkably high efficiency under any circumstances.

Systematic studies of X-ray emission from redbacks show some commonalities. Linares [2014] examined the *Swift* XRT data on redbacks and noted that, while in the pulsar state, their 0.5-10 keV luminosities tend to be in the range of $L_x \sim 10^{32}\mathrm{erg\,s}^{-1}$ divided into relatively high luminosity ($L_X \gtrsim 10^{32}$ergs s^{-1}) and relatively low ($L_X \lesssim 10^{32}$ergs s^{-1}). Studies of individual systems show that, on average, there is orbital modulation with an overall increase of about a factor of 2 centered around inferior conjunction, often with a hint of a double peaked structure [Bogdanov et al. 2014,?, Gentile et al. 2014, Kong et al. 2012]. However, in most cases the overall count rate is too low to clearly distinguish fine structure to the orbital light curve. Black widows, on the other hand, show a much greater variety in their orbital light curves, with some, like the original black widow PSR B1957+20 [Huang et al. 2012], having peaks centered around superior conjunction and others around inferior conjunction [Gentile et al. 2014]. On average, the redbacks are more luminous than the black widows in X-rays.

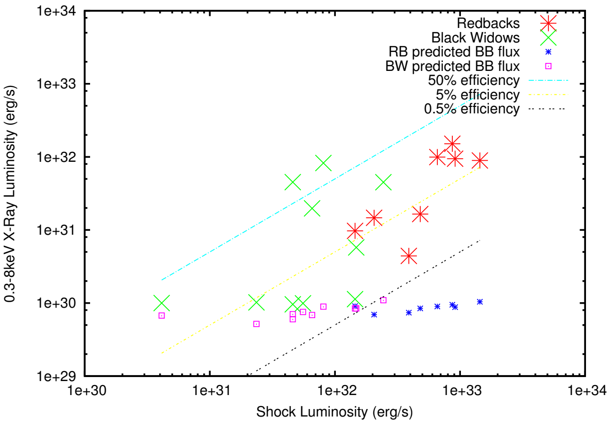

Figure 1: Comparison of the X-Ray luminosity from the redback population to that of the black widow population. We define the shock luminosity as $\dot{E}\Omega_c$ where Ω_c is the fraction of the pulsar sky subtended by the companion. We also plot the expected blackbody luminosity for each pulsar, assuming the relationship of Bognar et al. [2015] $L_{bb} = 10^{21.28}\dot{E}^{0.25}$

Table I Redbacks

Pulsar	$\log \dot{E}^a$	d^b	Γ	$\log L_X^c$	Ω_c^d	refs
J1023+0038	34.7	1.3	$1.00^{+0.05}_{-0.08}$	32.0	1.3%	(1)
J1227−4859	35.0	1.4	$1.16^{+0.07}_{-0.08}$	31.9	1.6%	(2)
J1628−3205	34.2	1.2	$1.2^{+0.8}_{-0.7}$	31.3	1.1%	
J1723−2837	34.7	0.75	$1.12^{+0.02}_{-0.02}$	32.1	2.0%	(3)
J1816+4510	34.7	4.5	–	31.0	0.28%	(4) (5)
J2129−0429	34.6	0.9	$1.04^{+0.11}_{-0.12}$	31.3	1.2%	
J2215+5135	34.7	3.0	$1.2^{+0.4}_{-0.3}$	31.9	1.4%	(6)
J2339−0533	34.4	0.4	$1.09^{+0.40}_{-0.13}$	30.6	1.6%	(7) (8)

a. erg/s b. kpc, from dispersion measure except for J1023+0038 from parallax [Deller et al. 2012] and J1816+4510 from optical Kaplan et al. [2013] c. erg/s 0.3-8 keV d. estimated percentage of pulsar sky subtended by companion, (1) Bogdanov et al. [2011] (2) Bogdanov et al. [2014] (3) Bogdanov et al. [2014] (4) Stovall et al. [2014] (5) Kaplan et al. [2013] (6) [Gentile et al. 2014] (7) Romani & Shaw [2011] (8) Ray et al. [2014]

The light curve modeling of Bogdanov et al. [2011] suggests that the X-ray emission happens very close to the surface of the companion, which suggests that little of the wind that is not directly intercepted by the companion takes part in the X-ray emitting shock. The fraction of the pulsar's sky subtended by the companion, Ω_c, can be calculated from knowledge of the relative masses (requiring knowledge of the orbital inclination angle), the fraction of the Roche lobe the companion fills, and the orbital separation. The inclination angle and Roche lobe filling fraction can be estimated from optical photometric light curves (eg. [Breton et al. 2013]), and when combined with optical radial velocity measurements and the pulsar orbit solution can be used to estimate the masses of the individual components. In the table, we calculate Ω_c from our "best guess" estimates of neutron star mass, Roche lobe filling factor, and inclination angle using optical fits where available. On average, we estimate $\Omega_c \sim 1.3\%$ for redbacks and $\Omega_c \sim 0.3\%$ for black widows, accounting for much of the relative brightness of the shock emission of redbacks compared to black widows.

We define a "shock luminosity" as $\dot{E}\Omega_c$ and plot that vs. the observed 0.3-8 keV X-ray luminosity of redbacks and black widows (Fig.1). We also plot the "expected" 0.3-8 keV blackbody emission from each pulsar based on a correlation determined from MSPs with good parallax measurements $\log L_{bb} = (0.25\pm0.16)\log\dot{E} + (21.28\pm5.36)$ [Bognar et al. 2015]. We see that the shock luminosity and X-ray luminosity are correlated, with a typical soft X-ray efficiency relative to the shock luminosity of $\sim$ 12%, albeit with large scatter. We make no estimate of errors in the shock luminosity, being as they are dominated by the very uncertain distances in most cases and a lack of strong constraints from the optical data on inclination and the masses from the optical data in many cases. The redback with the smallest estimated Ω_c and hence has one of the lowest luminosities is PSR J1816+4510. Optical studies of its companion suggest that it may be a proto-white dwarf which is significantly underfilling its Roche lobe [Kaplan et al. 2013].

Spectrally, the X-ray emission tends to have a constant thermal component, presumably from heated polar caps and consistent with the typical thermal emission from MSPs, and an orbitally variable power-law component. The fit power-law tends to be very hard with photon spectral index $\Gamma \sim 1$, harder than the typical spectra of pulsar wind nebulae around isolated young pulsars which have $\Gamma \sim 1.5$ in their inner, uncooled regions [Kargaltsev & Pavlov 2010]. Below we report on new X-ray observations of two redbacks discovered by the Green Bank Telescope.

2. PSR J1628−3205

Discovered in a survey of *Fermi* sources with the GBT at 820 MHz (Sanpa-Arsa et al. in prep), PSR J1628−3205 is a 3.21 ms pulsar in a 5.0 hr orbit around a companion with minimum mass $M_c > 0.16M_\odot$(assuming $M_{ns} = 1.4M_\odot$) (Hessels et al. in prep). The pulsar is eclipsed for about 20% of the orbit. It is modestly energetic with a standard spin-down energy of $\dot{E} = 1.8 \times 10^{34}$ ergs and an estimated distance from the pulse dispersion measure $d \sim 1.2$ kpc. Optical observations suggest it is Roche lobe filling with minimal heating of the companion [Li et al. 2014].

We observed PSR J1628−3205 for 20 ks (slightly more than one orbit) on 05 May 2012 with the *Chandra* ACIS-S and detected $\sim$ 180 counts. The counts as a function of orbital phase and energy, plotted in Figure 2, suggest that there may be a dip in the above 2 keV flux near superior conjunction. The spectrum seems to have a significant power law component, with a purely blackbody spectrum not giving an acceptable fit. Using the CSTAT statistic of XSPEC (appropriate given the low number of counts per bin) suggests a pure power law fit provides a somewhat reasonable fit (C-Statistic 24.97 with 22 degrees of freedom), with best fit absorption $nH = 1.3(0.2 - 2.5) \times 10^{21}\mathrm{cm}^{-2}$ and power-law index $\Gamma = 1.60(1.23 - 2.00)$. Using the KS test statistic to determine goodness of fit results in 20% of realizations having a lower test statistic, suggesting improvements can be made. Since most MSPs have a significant thermal component to their X-ray emission, we next tried an absorbed blackbody plus power-law fit. This resulted in a C-statistic of 21.08 with 20 degrees of freedom, with less than 1% of KS realizations having a smaller test statistic. The best fit values were $nH = 2.2 \times 10^{21}\mathrm{cm}^{-2}$, $kT = 0.20$ keV and $\Gamma = 1.14$. The covariance between the blackbody temperature and the power-law index made it difficult to derive reasonable error bars if all parameters were allowed to vary freely, but by constraining the blackbody temperature to vary only between $kT = 0.1 - 0.25$ keV, within which range are the vast majority of MSPs, we find 90% confidence regions of $nH = (0.3 - 8.4) \times 10^{21}\mathrm{cm}^{-2}$ and $\Gamma = (0.5 - 2.0)$. The 0.3-8 keV model flux is $F_x = 8.8 \times 10^{-14}\mathrm{erg\,cm^{-2}\,s^{-1}}$ with an unabsorbed flux of $F_x = 1.2 \times 10^{-13}\mathrm{erg\,cm^{-2}\,s^{-1}}$, with roughly 70% in the power law and 30% in the blackbody. The fit nH is consistent with the Drimmel et al. [2003] Galactic extinction model for a distance of 1.2 kpc.

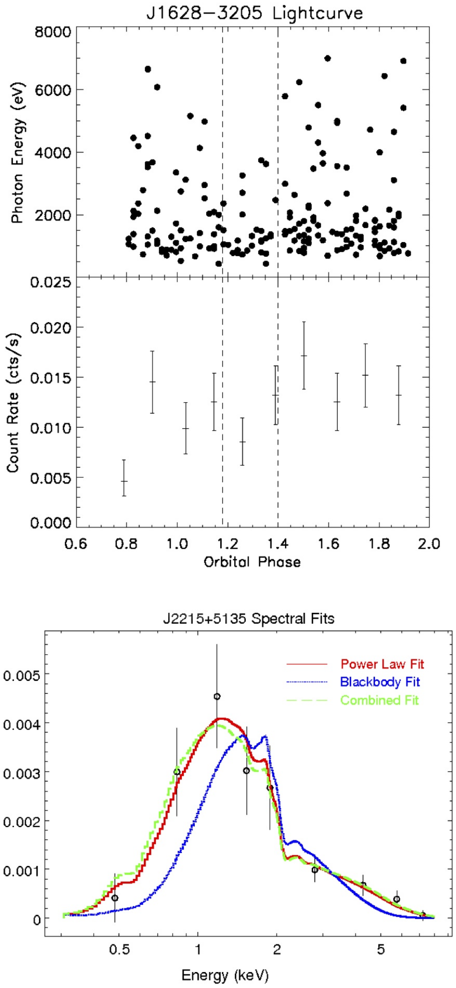

Figure 2: 20 ks Chandra ACIS-S observation of PSR J1628−3205. *Top:* Individual photon energies and average count rates as a function of orbital phase. The pulsar superior conjunction is defined as phase 1.25. The dashed lines show roughly the phase range of the radio eclipse. *Bottom:* 0.3-8keV spectrum showing absorbed power-law, blackbody, and blackbody+ power-law fits.

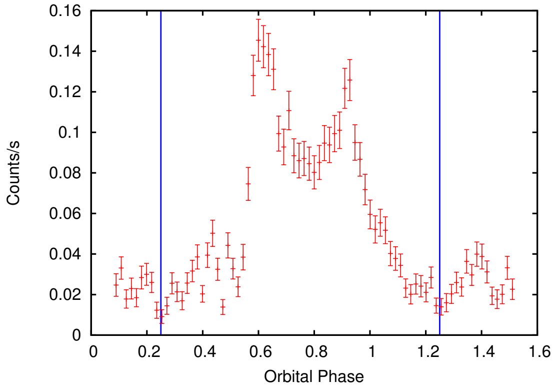

Figure 3: $XMM-Newton$ 0.1-10 keV light curve of PSR J2129−0429 as a function of orbital phase. The pulsar superior conjunction is indicated by vertical blue lines.

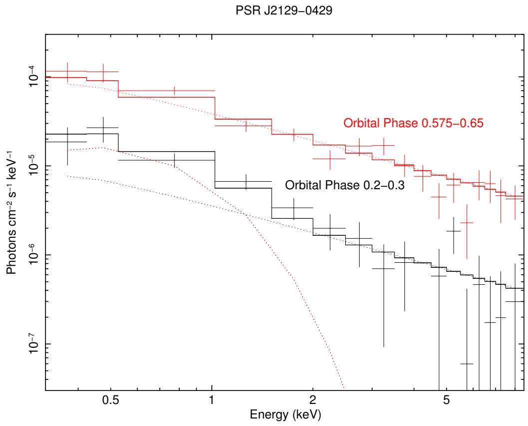

Figure 4: Unfolded $XMM-Newton$ PN spectrum of PSR J2129−0429 at two orbital phases, keeping the blackbody component fixed.

3. PSR J2129−0429

Discovered in a survey of *Fermi* sources using the GBT at 350 MHz [Hessels et al. 2011], PSR J2129−0429 is a 7.61 ms pulsar in a 15.2 hr orbit around a $M_c > 0.37 M_\odot$companion which shows extensive radio eclipses, as much as half the orbit at low frequencies (Hessels et al. in prep). The pulsar has a very high magnetic field for a MSP ($B \sim 1.6 \times 10^9$ G), and so still has a high spin down energy $\dot{E} \sim 3.9 \times 10^{34}$ despite its relatively long spin period. The dispersion measure distance is $d \sim 0.9$ kpc. A variable, bright UV counterpart was evident in the *Swift* UVOT, as was significant X-ray variability from the *Swift* XRT data. Further optical observations suggest the companion is minimally heated and mostly Roche lobe filling and radial velocity measurements suggest a pulsar mass $M_{ns} > 1.7 M_\odot$and a companion mass $M_c \sim 0.5 M_\odot$[Bellm et al. 2013]. These system properties suggest that PSRJ2129−0429 is in a relatively early stage in its evolution compared to other redbacks which are more fully spun-up and have typical magnetic fields of a few 10^8 G. Very large orbital variations are observed through radio timing, and pulsations are dominant in the γ-ray emission.

We observed PSR J2129−0429 for 70 ks with $XMM-Newton$. There were no background flares during the observation, meaning we got continuous coverage over slightly more than a complete orbit. The X-ray light curve has very large amplitude variations, with two clear peaks centered on the pulsar's inferior conjunction (Fig.3). We first fit the spectrum with an absorbed blackbody plus power-law, which gave an adequate fit. The flux is dominated by the power-law component, with an average 0.3-8 keV flux $F_x = 2.25 \pm 0.05 \mathrm{erg\,cm^{-2}\,s^{-1}}$. There is very little absorption ($nH = 1.8(0-4.6) \times 10^{20} \mathrm{cm}^{-2}$) and the thermal component ($kT = 0.21(0.16{-}0.26)$ keV) has a 0.3-8 keV flux $F_{bb} \sim 1.2 \times 10^{-14} \mathrm{erg\,cm^{-2}\,s^{-1}}$, or about 1/4 of the flux near superior conjunction. The power-law component is very hard ($\Gamma = 1.04(0.92-1.15)$), similar to other redbacks. Presuming a constant thermal component throughout the orbit, the difference in the non-thermal flux between the peak at orbital phases 0.575-0.65 and the minimum at phases 0.2-0.3 is about a factor of 11 (Fig. 4). There is no evidence of significantly increased absorption. Complete spectral results will be presented in an upcoming paper (Roberts et al. in prep).

This very remarkable variability suggests that a large fraction of the shock region is blocked by the companion around superior conjunction, suggesting a quite small emission region and a large inclination angle. The two distinct peaks may be a result of doppler boosting and/or relativistic beaming of the synchrotron radiation. The latter would require a strong, well ordered magnetic field. The orbital phases of the peaks, ~ 0.6 and ~ 0.9, are quite curious. If the shock was wrapped around the companion, then you would expect there to be peaks between phases 0.0-0.5. The qualities may suggest a significant role for the magnetic field of the companion. If the companion is tidally locked, like one would expect, then the orbital period of 15.2 hr is the spin period of the companion, which is very rapid. Low mass, rapidly spinning stars can have surface magnetic fields of several hundred to a few thousand Gauss [Morin 2012]. Such potentially large companion fields should not be ignored when investigating the shock emission from redbacks.

In summary, X-ray emission from the intrabinary shock in redbacks is orbitally dependent, with the increased emission centered on inferior conjunction with potentially a fairly ubiquitous double peaked structure. The emission seems to come from a region that is not much larger than the companion, is very hard and very efficient, which needs explanation. The previously ignored potential role of the companion's magnetic field in the shock dynamics needs to be considered.

Acknowledgments

Support for this work was provided by the National Aeronautics and Space Administration through Chandra Award Number GO2-13056X issued by the Chandra X-ray Observatory Center, which is operated by the Smithsonian Astrophysical Observatory for and on behalf of the National Aeronautics Space Administration under contract NAS8-03060. This work is based on observations obtained with XMM-Newton, an ESA science mission with instruments and contributions directly funded by ESA Member States and the USA (NASA).

References

Archibald, A. M., Stairs, I. H., Ransom, S. M., et al. 2009, Science, 324, 1411

Arons, J., & Tavani, M. 1993, Astrophys. J., 403, 249

Bellm, E., Djorgovski, S. G., Drake, A. J., et al. 2013, American Astronomical Society Meeting Abstracts #221, 221, #154.10

Bogdanov, S., Archibald, A. M., Hessels, J. W. T., et al. 2011, Astrophys. J., 742, 97

Bogdanov, S., Patruno, A., Archibald, A. M., et al. 2014, Astrophys. J., 789, 40

Bogdanov, S., Esposito, P., Crawford, F., III, et al. 2014, Astrophys. J., 781, 6

Bognar, K., Roberts, M., & Chatterjee, S. 2015, American Astronomical Society Meeting Abstracts, 225, #346.11

Breton, R. P., van Kerkwijk, M. H., Roberts, M. S. E., et al. 2013, Astrophys. J., 769, 108

Deller, A. T., Archibald, A. M., Brisken, W. F., et al. 2012, ApJL, 756, L25

Drimmel, R., Cabrera-Lavers, A., & López-Corredoira, M. 2003, A& A, 409, 205

Gentile, P. A., Roberts, M. S. E., McLaughlin, M. A., et al. 2014, Astrophys. J., 783, 69

Hessels, J. W. T., Roberts, M. S. E., McLaughlin, M. A., et al. 2011, American Institute of Physics Conference Series, 1357, 40

Huang, R. H. H., Kong, A. K. H., Takata, J., et al. 2012, Astrophys. J., 760, 92

Kaplan, D. L., Bhalerao, V. B., van Kerkwijk, M. H., et al. 2013, Astrophys. J., 765, 158

Kargaltsev, O., & Pavlov, G. G. 2010, X-ray Astronomy 2009; Present Status, Multi-Wavelength Approach and Future Perspectives, 1248, 25

Kennel, C. F., & Coroniti, F. V. 1984, Astrophys. J., 283, 694

Kong, A. K. H., Huang, R. H. H., Cheng, K. S., et al. 2012, ApJL, 747, L3

Li, M., Halpern, J. P., & Thorstensen, J. R. 2014, Astrophys. J., 795, 115

Linares, M. 2014, Astrophys. J., 795, 72

Morin, J. 2012, EAS Publications Series, 57, 165

Ray, P. S., Belfiore, A. M., Saz Parkinson, P., et al. 2014, American Astronomical Society Meeting Abstracts #223, 223, #140.07

Roberts, M. S. E. 2011, American Institute of Physics Conference Series, 1357, 127

Romani, R. W., & Shaw, M. S. 2011, ApJL, 743, L26

Roy, J., Ray, P. S., Bhattacharyya, B., et al. 2014, arXiv:1412.4735

Stappers, B. W., Archibald, A. M., Hessels, J. W. T., et al. 2014, Astrophys. J., 790, 39

Stovall, K., Lynch, R. S., Ransom, S. M., et al. 2014, Astrophys. J., 791, 67

Tendulkar, S. P., Yang, C., An, H., et al. 2014, Astrophys. J., 791, 77

Thorstensen, J. R., & Armstrong, E. 2005, AJ, 130, 759

X-ray Emission from Middle-Aged Gamma-Ray Pulsars

S. Kisaka
Institute of Particle and Nuclear Studies, KEK, Tsukuba, Ibaraki, 305-0801 Japan

S. J. Tanaka
Institute for Cosmic Ray Research, University of Tokyo, Kashiwa, Chiba, 277-8582 Japan

Electrons/positrons produced in a pulsar magnetosphere emit synchrotron radiation, which is widely believed as the origin of the non-thermal X-ray emission detected from pulsars. Particles are produced by curvature photons emitted from accelerated particles in the magnetosphere. These curvature photons are detected as pulsed γ-ray emissions from pulsars with age $\lesssim 10^6$ yr. Using γ-ray observations and analytical model, we impose severe constraints on the synchrotron radiation as a mechanism of the non-thermal X-ray emission. In most middle-aged pulsars ($\sim 10^5 - 10^6$ yr) which photon-photon pair production is less efficient in their magnetosphere, we find that the synchrotron radiation model is difficult to explain the observed non-thermal X-ray emission.

I. INTRODUCTION

Pulsed non-thermal X-ray emissions are detected from rotation-powered pulsars. Synchrotron radiation is widely believed as the emission mechanism [20]. Electrons and/or positrons produced in the magnetosphere initially have non-zero value of the pitch angle, so that they emit the synchrotron radiation. Thus, the non-thermal X-ray emission is important to clarify the particle production in the pulsar magnetosphere.

Observed non-thermal X-ray luminosity $L_{\rm nth}$ is typically $\sim 10^{-3} - 10^{-5}$ times smaller than the spin-down luminosity [e.g., 8]. Non-thermal emission is detected at $\nu_{\rm obs} \gtrsim 1$ keV. At soft X-ray band ($\lesssim 1$ keV), thermal component significantly contributes to the total luminosity. The origin of this thermal luminosity is considered as the bombardment of particles moving to the polar cap surface [e.g., 6]. The luminosity ratio between the non-thermal and the thermal components is typically $\xi \equiv L_{\rm nth}/L_{\rm th} \sim 10^{-1} - 10$ [e.g., 12].

In the magnetosphere of older pulsars, the pair production through the photon-photon collision is less effective. As a pulsar gets old, the spin period P increases as well as the radius of the light cylinder $R_{\rm lc} = Pc/2\pi$ increases, where c is the speed of light. For the pulsars with age $\gtrsim 10^5$ yr, the luminosity of the whole surface thermal emission significantly decreases [e.g., 23]. Then, the number density of the X-ray photons at the outer magnetosphere of pulsars with $\gtrsim 10^5$ yr is too small to produce the significant number of pairs through photon-photon collision [e.g., 7, 19].

Magnetic pair production is considered as one of the main pair-production process in the magnetosphere [e.g., 18]. Some authors [e.g., 2, 4, 25] propose that the synchrotron radiation from pairs produced through the magnetic pair-production explains the non-thermal X-ray emission from pulsars including middle-aged one. These pairs are produced from curvature photons emitted by accelerated particles with inward direction.

Recently, Kisaka & Tanaka [10] argue that the synchrotron radiation model with ingoing accelerated particles and magnetic pair production does not explain the observed non-thermal emission for pulsars with $\gtrsim 10^6$ yr (Figure 4 in [10]). Middle-aged pulsars locate the allowed region on $P - \dot{P}$ diagram in their results.

In the analysis of Kisaka & Tanaka [10], one of the most important parameter is the Lorentz factor of the accelerated particles. Since there is no observational constraint on the Lorentz factor in old pulsars, Kisaka & Tanaka [10] adopt the maximum value (equation 2 in [10]). This value is much larger than the realistic one, which is determined by the force balance between the electric field acceleration and the radiation reaction force [e.g., 3]. In the model of [10], smaller Lorentz factor of acceleration particles always more stringent limits on synchrotron radiation model for the non-thermal X-ray emission.

Fermi detects the pulsed γ-ray emission from more than 100 pulsars including middle-aged ones [1]. The cutoff energies of detected pulsars are typically ~ 1 GeV. Observed γ-ray emission is considered as the curvature radiation from accelerated particles. Then, we can evaluate the Lorentz factor of the accelerated particles from the characteristic energy of the curvature radiation. Therefore, γ-ray observations could impose more realistic and stringent constraints on the synchrotron radiation model.

In this proceeding, we give the constraints on the synchrotron radiation as the mechanism of the non-thermal X-ray emission from middle-aged gamma-ray pulsars. In particular, we impose the upper limit on the Lorentz factor of accelerated particles from γ-ray observations. In Sec. 2, we introduce some assumptions and two constraints for the location of the X-ray emission region. Results and discussion are presented in Sec. 3.

II. CONSTRAINTS

We investigate the case that produced particles in the magnetosphere emit synchrotron radiation in X-ray band. We only focus on the magnetic pair-production as the production mechanism of synchrotron emitting particles. The magnetic pair-production is efficient within $\lesssim 3{-}5R_{\rm NS}$ for GeV γ-ray photons, where $R_{\rm NS}$ is the radius of the neutron star. Since no attenuation feature due to the magnetic pair-production is detected in the observed γ-ray spectra [1] in γ-ray pulsars, the particle acceleration occurs at the relatively outer magnetosphere ($\gtrsim 10R_{\rm NS}$) considered by such as outer gap model [e.g., 3]. Therefore, we only consider that the accelerated particles move to the direction of the neutron star. For the structure of the magnetic field, we assume dipole field.

In our definitions, "primary particles" means the electrons and positrons that are accelerated and emit curvature photons that can convert pairs. "Secondary particles" means those produced outside the acceleration region of primary particles $r_{\rm pri}$, including the second and higher generation particles. The production and emission locations of second and higher generation particles $r_{\rm sec}$ are almost the same, and then we do not separately treat second and higher generation particles.

The difference from previous model [10] is that an observed characteristic energy of the γ-ray emission $E_{\rm cur}$ imposes a constraint on the Lorentz factor of the primary particles $\gamma_{\rm p}$. The observed γ-ray emission at ~ 1 GeV is considered as the curvature radiation from the primary particles [e.g., 3, 5]. The characteristic energy of curvature radiation is described by

$$E_{\rm cur} = 0.29\frac{3}{4\pi}\frac{h\gamma_{\rm p}^3 c}{R_{\rm cur}(r_{\rm pri})}, \tag{1}$$

where h is Planck constant. From the assumption of the dipole magnetic field, we use the approximation $R_{\rm cur}(r_{\rm pri}) \sim (r_{\rm pri}R_{\rm lc})^{1/2}$ as a curvature radius of a field line. Hereafter, we use $Q_x \equiv Q/10^x$ in cgs units, except for a frequency $h\nu_{\rm keV} \equiv h\nu/1{\rm keV}$ and an energy $E_{\rm cut,GeV} \equiv E_{\rm cur}/1$ GeV.

Note that observed γ-ray photons are emitted from outgoing particles. The Lorentz factor of the outgoing particles tends to be larger than that of ingoing one as following reason. Because the magnetic field and ambient photon density is larger for smaller radial distance from a neutron star, the location of the particle production is near the inner boundary of the particle acceleration region [e.g., 7, 21, 22]. Then, the outgoing particles obtain larger energy due to the electric field acceleration [20]. Therefore, we consider that the Lorentz factor estimated from equation (1) is the upper limit on the ingoing accelerated particles.

The observed frequency of non-thermal component $\nu_{\rm obs,keV} \gtrsim 1$ keV and the luminosity ratio $\xi \sim 0.1 - 10$ impose the lower and upper limits on the emission location of synchrotron radiation [10]. Following Kisaka & Tanaka [10] we consider two conditions, the characteristic frequency (Sec. II A) and the luminosity of synchrotron radiation (Sec. II B).

A. Characteristic frequency

To emit the synchrotron radiation, particle momentum perpendicular to the magnetic field has to satisfy the condition $\gamma \sin\alpha \sim \gamma\alpha > 1$, where γ is the particle Lorentz factor and $\alpha \leq 1$ is the pitch angle which is typically much smaller than 1. This condition gives a lower limit on the frequency of the synchrotron radiation,

$$\nu_{\rm obs} \gtrsim \frac{eB(r_{\rm sec})}{2\pi m_{\rm e}c\alpha}, \tag{2}$$

where e and $m_{\rm e}$ are the charge and the mass of a electron. Using the assumption of a dipole magnetic field, the strength of the magnetic field is $B(r_{\rm sec}) \sim B_{\rm s}(r_{\rm sec}/R_{\rm NS})^{-3}$, where $B_{\rm s}$ is the magnetic field at the surface. Then, the condition (2) gives the lower limit for the emission location [e.g., 13, 16],

$$r_{\rm ct,6} \sim 2.9\alpha^{-1/3}\nu_{\rm obs,keV}^{-1/3}B_{\rm s,12}^{1/3}. \tag{3}$$

B. Non-thermal luminosity

Observed luminosity of the non-thermal component $L_{\rm nth}$ imposes the limit on the emission location. The luminosity of the synchrotron radiation is described as $P_{\rm syn}N_{\rm s}$, where $P_{\rm syn}$ is the power of the synchrotron radiation emitted by a single electron and $N_{\rm s}$ is the number of the secondary particles. In our model, secondary particles are produced by the curvature photons of the primary particles. Then, the number of the secondary particles are described by $N_{\rm s} \sim N_\gamma \tau N_{\rm p}$, where N_γ is the effective number of curvature photons emitted by a single primary electron, τ is the optical depth for the pair production and $N_{\rm p}$ is the number of the primary particles. Considering the higher generation pairs, the number of produced particles is maximally increased by a factor of $\gamma_{\rm s,pair}(r_{\rm pri})/\gamma_{\rm s,lt}(r_{\rm sec})$, where $\gamma_{\rm s,pair}$ is the Lorentz factor of the particle produced by a curvature photon and $\gamma_{\rm lt}$ is the lower threshold value of the Lorentz factor for the magnetic pair production. Therefore, the required condition to explain the observed luminosity is described by

$$P_{\rm syn}(r_{\rm sec})N_\gamma(r_{\rm pri}, r_{\rm sec})\tau N_{\rm p}(r_{\rm sec}) \times \frac{\gamma_{\rm s,pair}(r_{\rm pri})}{\gamma_{\rm s,lt}(r_{\rm sec})} > L_{\rm nth}. \tag{4}$$

We evaluate the number of the secondary particles $N_{\rm s} \sim N_\gamma \tau N_{\rm p}$. The effective number of the curvature photons $N_\gamma(r_{\rm pri}, r_{\rm sec})$ is

$$\begin{aligned} N_\gamma(r_{\rm pri}, r_{\rm sec}) &\sim \dot{N}_\gamma(r_{\rm pri}) t_{\rm ad}(r_{\rm sec}) \\ &\sim \frac{P_{\rm cur}(r_{\rm pri})}{E_{\rm cur}} t_{\rm ad}(r_{\rm sec}), \end{aligned} \tag{5}$$

where $P_{\rm cur}(r_{\rm pri})$ is the power of curvature radiation by a single electron,

$$P_{\rm cur}(r_{\rm pri}) = \frac{2e^2c}{3R^2_{\rm cur}(r_{\rm pri})}\gamma_{\rm p}^4. \tag{6}$$

The Lorentz factor of the primary particle $\gamma_{\rm p}$ is obtained by the observed energy $E_{\rm cur}$ (equation 1). In the derivation of equation (5), we assume that the primary particles continuously emit the curvature radiation during the advection timescale of the secondary particles,

$$t_{\rm ad}(r_{\rm sec}) \sim \frac{r_{\rm sec}}{c}. \tag{7}$$

For the optical depth of magnetic pair production, we use

$$\tau \sim 1 \tag{8}$$

as long as the curvature photon energy exceeds the pair-production threshold for the magnetic pair-production [17]

$$\frac{E_{\rm cur}}{2m_{\rm e}c^2}\frac{B_\perp(r_{\rm sec})}{B_{\rm q}} > \frac{1}{15}, \tag{9}$$

where $B_{\rm q} = m_{\rm e}^2c^3/e\hbar \sim 4.4\times10^{13}$G and $B_\perp(r_{\rm sec}) \sim B(r_{\rm sec})\alpha$. In our model, we consider the ingoing primary particles as the origin of pair cascade process. The kinetic energy flux of them $\dot{N}_{\rm p}\gamma_{\rm p}m_{\rm e}c^2$ is constrained by the observed thermal luminosity $L_{\rm th}$,

$$\dot{N}_{\rm p} = \frac{L_{\rm th}}{\gamma_{\rm p}m_{\rm e}c^2}. \tag{10}$$

The number of the primary particles is described by

$$N_{\rm p} \sim \dot{N}_{\rm p}t_{\rm cool}, \tag{11}$$

because the cooling timescale of the secondary particle $t_{\rm cool}$ is always shorter than the advection timescale at the region where magnetic pair production occurs. This cooling timescale is described by

$$t_{\rm cool}(r_{\rm sec}) \sim \frac{\gamma_{\rm s,syn}(r_{\rm sec})\alpha m_{\rm e}c^2}{P_{\rm syn}(r_{\rm sec})}, \tag{12}$$

where the Lorentz factor of the secondary particles $\gamma_{\rm s,syn}$ is determined by the observed frequency,

$$\nu_{\rm obs} = 0.29\frac{3}{4\pi}\gamma^2_{\rm s,syn}(r_{\rm sec})\frac{eB(r_{\rm sec})\alpha}{m_{\rm e}c}. \tag{13}$$

The Lorentz factor $\gamma_{\rm s,pair}(r_{\rm pri})$ of secondary particles is

$$\gamma_{\rm s,pair}(r_{\rm pri}) = \frac{E_{\rm cur}}{2m_{\rm e}c^2}. \tag{14}$$

From equation (9), we take the threshold th eLorentz factor as

$$\gamma_{\rm s,lt}(r_{\rm sec}) = \frac{1}{15}\frac{B_{\rm q}}{B_\perp(r_{\rm sec})}. \tag{15}$$

The relation between two point $r_{\rm pri}$ and $r_{\rm sec}$ is geometrically given by (Appendix in [10])

$$r_{\rm pri,6} \sim 27r_{\rm sec,6}^{2/3}R_{\rm open,lc}^{1/3}P_0^{1/3}, \tag{16}$$

where $R_{\rm open,lc} \equiv R_{\rm open}/R_{\rm lc}$ and $R_{\rm open}(\geq R_{\rm lc})$ is the maximum distance from the centre of the neutron star to the top of the magnetic loop on a given field line .

Using equations (4), (5), (8), (11), (14) and (15), we obtain the upper limit on the emission location,

$$\begin{aligned} r_{\rm LBsyn,6} &\sim 2.5\times10^{-3}\alpha^{4/5}\xi_{-1}^{-6/5}\nu_{\rm obs,keV}^{3/5} \\ &\quad\times R_{\rm open,lc}^{-1/5}E_{\rm cut,GeV}^{6/5}P_0^{-4/5}B_{\rm s,12}^{3/5}. \end{aligned} \tag{17}$$

III. RESULTS AND DISCUSSION

To explain the observed non-thermal X-ray emission, the emission location $r_{\rm sec}$ has to satisfy the condition,

$$r_{\rm ct} < r_{\rm sec} < r_{\rm LBsyn}. \tag{18}$$

Using the condition $r_{\rm ct} < r_{\rm LBsyn}$, we obtain the death lines for the synchrotron radiation on the P–$\dot{P}$ plane as

$$\begin{aligned} \dot{P} &> 0.66\alpha^{-16}\xi_{-1}^{9}\nu_{\rm obs,keV}^{-7} \\ &\quad\times R_{\rm open,lc}^{3/2}E_{\rm cur,GeV}^{-9}P_0^{5}\ {\rm s\ s^{-1}}, \end{aligned} \tag{19}$$

where we use $B_{\rm s,12} \sim 6.4P_0^{1/2}\dot{P}_{-14}^{1/2}$.

We show the results (equation 19) in figure 1. Large symbols (squares and crosses) show the γ-ray pulsars from Fermi 2nd pulsar catalog [1]. Red squares denote pulsars whose non-thermal X-ray emission is detected. This figure show that even if the luminosity ratio $\xi = 0.1$ and pitch angle $\alpha = 1$, the characteristic energy of the curvature radiation $E_{\rm cur} \gtrsim 5$ GeV is required to explain the observed non-thermal X-ray emission in our model. However, observed characteristic energy for most γ-ray pulsars typically $E_{\rm cur} \lesssim 5$ GeV [1]. Therefore, the proposed model of the synchrotron emission [e.g., 2, 4, 25] is difficult to explain the observed non-thermal component.

We briefly discuss other models. In the synchrotron models with the photon-photon pair-production, the

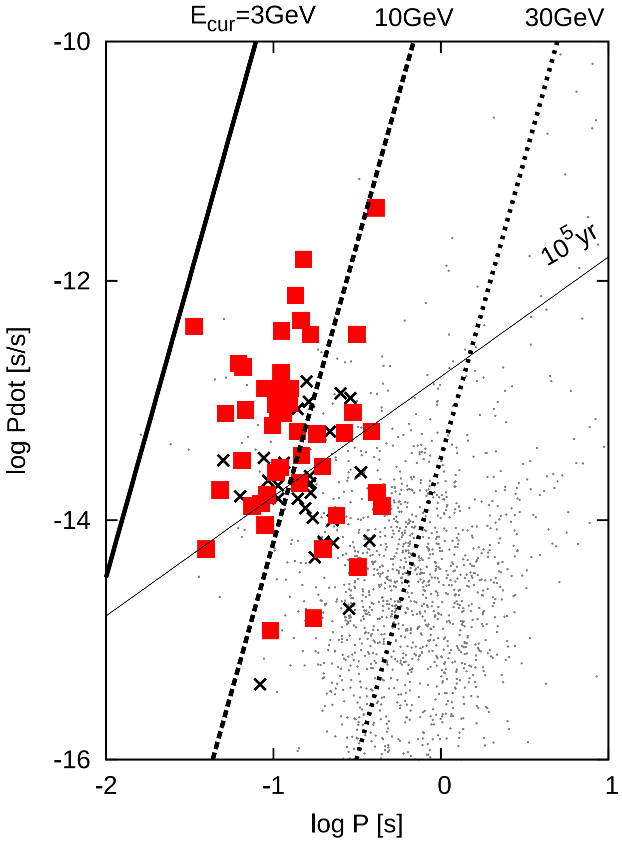

FIG. 1: Synchrotron radiation death lines on the $P - \dot{P}$ diagram. Thick lines are obtained from inequality (19) for the characteristic energy of the curvature radiation $E_{\rm cur} = 3$ GeV (solid line), 10 GeV (dashed line) and 30 GeV (dotted line). For other parameters, we set $\alpha = 1$, $\xi = 0.1$, $R_{\rm open} = R_{\rm lc}$ and $h\nu_{\rm obs} = 1$ keV. Thin solid line denote the characteristic age 10^5 yr. Large points denote the gamma-ray pulsars with non-thermal X-ray detected (red squares) and non-detected (black crosses) from 2nd Fermi Pulsar Catalog [1]. Small dots denote other pulsars taken from ATNF Pulsar Catalog [11]. The characteristic energies of the curvature radiation are $\lesssim 5$ GeV for middle-aged gamma-ray pulsars, so that the model does not explain their non-thermal X-ray emissions.

number density of seed photons is too small to produce the number of pairs [10]. The model of the synchrotron radiation with outgoing primary particles and magnetic pair-production may be possible to explain the observed non-thermal X-ray emission (Figure 1 in [10]). In this case, γ-ray photons have to be produced near the surface as the same as polar cap model [5]. However, the observed γ-ray pulse profile and spectral cutoff shape favor that γ-ray emission region is far from NS [e.g., 1, 15]. A possible idea to resolve this inconsistency is that more than two particle acceleration regions exist in the magnetosphere [e.g., 14, 24]. This model should be constrained by geometrical analysis using observed pulse profiles at both γ-ray and X-ray [e.g., 9]. Due to poor photon statistics, pulse profiles of non-thermal component have been detected for only small number of middle-aged pulsars. If pulse profiles will be detected for large samples in future observations such as NuSTAR and ASTRO-H, we can impose more significant constraint on the particle production in the magnetosphere.

Acknowledgments

This work is supported by KAKENHI 24103006 (S.K.) and 2510447 (S.J.T.).

---

[1] Abdo, A. A., et al. 2013, ApJS, 208, 17
[2] Cheng, K. S., & Zhang, L. 1999, ApJ, 515, 337
[3] Cheng, K. S., Ho, C., & Ruderman, M. 1986, ApJ, 300, 522
[4] Cheng, K. S., Gil, J., & Zhang, L. 1998, ApJ, 493, L35
[5] Daugherty, J. K., & Harding, A. K. 1996, ApJ, 458, 278
[6] Halpern, J. P., & Ruderman, M. 1993, ApJ, 157, 869
[7] Hirotani, K. 2013, ApJ, 766, 98
[8] Kargaltsev, O., Durant, M., Pavlov, G. G., & Garmire, G. P. 2012, ApJS, 201, 37
[9] Kisaka, S., & Kojima, Y. 2011, ApJ, 739, 14
[10] Kisaka, S., & Tanaka, S. J. 2014, MNRAS, 443, 2063
[11] Manchester, R. N., Hobbs, G. B., Teoh, A., & Hobbs, M. 2005, AJ, 129, 1993
[12] Marelli, M., De Luca, A., & Caraveo, P. A. 2011, ApJ, 733, 82
[13] O'Dell, S. L., & Sartori, L. 1970, ApJ, 161, L63
[14] Petrova, S. A. 2013, ApJ, 764, 129
[15] Pierbattista, M., Harding, A. K., Grenier, I. A., Johnson, T. J., Caraveo, P. A., Kerr, M., & Gonthier, P. L. 2015, A&A, 575, A3
[16] Rudak, B., & Dyks, J. 1999, MNRAS, 303, 477
[17] Ruderman, M. A., & Sutherland, P. G. 1975, ApJ, 196, 51
[18] Sturrock, P. A. 1971, ApJ, 164, 529
[19] Takata, J., & Chang, H.-K. 2009, MNRAS, 392, 400

[20] Takata, J., Chang, H.-K., & Shibata, S. 2008, MNRAS, 386, 748
[21] Takata, J., Shibata, S., Hirotani, K., & Chang, H.-K. 2006, MNRAS, 366, 1310
[22] Timokhin, A. N. 2010, MNRAS, 408, 2092
[23] Yakovlev, D. G., & Pethick, C. J. 2004, ARA&A, 42, 169
[24] Yuki, S., & Shibata, S. 2012, PASJ, 64, 43
[25] Zhang, L., & Cheng, K. S. 1997, ApJ, 487, 370

2FHL: The second Catalog of hard *Fermi*-LAT sources

M. Ajello, A. Domínguez
Department of Physics and Astronomy, Clemson University, Kinard Lab of Physics, Clemson, SC 29634-0978, USA
S. Cutini, D. Gasparrini
Agenzia Spaziale Italiana (ASI) Science Data Center, I-00133 Roma, Italy and INFN, Sezione di Perugia, I-06123 Perugia, Italy and
on behalf of the Fermi-LAT Collaboration

The *Fermi* Large Area Telescope (LAT) has been routinely gathering science data since August 2008, surveying the full sky every three hours. The first Fermi-LAT catalog of sources detected above 10 GeV (1FHL) relied on three years of data to characterize the >10 GeV sky. The improved acceptance and point-spread function of the new Pass 8 event reconstruction and classification together with six years of observations now available allow the detection and characterization of sources directly above 50 GeV. This closes the gap between ground-based Cherenkov telescopes, which have excellent sensitivity but small fields of view and short duty cycles, and all-sky observations at GeV energies from orbit. In this contribution we present the second catalog of hard Fermi-LAT sources detected at >50 GeV.

1. Introduction

The Large Area Telescope (LAT) on board the *Fermi* satellite has been efficiently surveying the GeV sky detecting over 3000 sources in just four years of exposure (see the 3FGL catalog, [1]). These sources are detected in the 0.1–300 GeV band and given *Fermi*'s peak sensitivity at ∼1 GeV are representative of the GeV sky. On the other hand, Cherenkov telescopes, with their good angular resolution and excellent point-source sensitivity have been exploring, due to their limited field of views, small patches of the > 50 GeV sky[1]. In the effort to fill the gap, the LAT-collaboration released a catalog of sources detected, in 3 years, at > 10 GeV (so called 1FHL catalog, [2]).

Recently a new event reconstruction and characterization analysis (known as Pass 8, [3]) has been developed by the *Fermi*-LAT collaboration. Pass 8 significantly improves the background rejection, point-spread function (PSF), effective area of the LAT and helps understanding its systematic uncertainties. All these impressive improvements lead to a significant increase of the LAT sensitivity (Atwood et al., 2013a,b). Furthermore, these improvements are specially significant at $E > 50$ GeV with an increase in the acceptance of $\gtrsim 25\,\%$ and an improvement in the PSF by a factor between 20 % at 50 GeV and 50 % at 500 GeV. At these high energies, because of the almost lack of background, the sensitivity of *Fermi*-LAT improves almost linearly with time as it should in a photon-limited regime (as opposed to a background-limited regime where the sensitivity improves with the square root of exposure time).

Taking advantage of the improvements delivered by Pass 8, we are preparing an all-sky catalog of sources detected at $E > 50$ GeV in ∼6 years of data. These sources will constitute the second catalog of hard *Fermi*-LAT sources (2FHL). This proceeding shows that the 2FHL catalog provides a view of the high-energy sky that is complementary to that of the 3FGL catalog and has the potential to allow for unprecedented broad band studies of the SED of old and newly discovered sources and to increase the efficiency of the searches of current Cherenkov telescopes.

2. The 2FHL Catalog

In about 6 years of exposure, *Fermi*-LAT has detected approximately 55000 photons (belonging to the P8 source class) all-sky at >50 GeV. The preliminary all-sky map in Fig. 1 shows that *Fermi*-LAT observes large scale diffuse emission in the direction of our Galaxy and coincident with the so-called *Fermi* bubbles [4, 5] as well as many point-like sources.

The analysis to detect sources is performed similarly to the other *Fermi*-LAT catalogs. The first step comprises the detection of source candidates (so called seeds) as fluctuations above the background. The sky is then divided into region of interests (ROIs), for which a sky model is built including all point sources in the ROI and also the Galactic and isotropic diffuse models [6]. This model is fitted to the data via a standard maximum-likelihood unbinned algorithm. The fit is typically repeated twice and in between the two fits the source position is optimized using standard *Fermi* tools[2].

---

[1] VERITAS, H.E.S.S and MAGIC have successfully lowered, in recent years, their low energy threshold and have started exploring the sub-100 GeV band.

[2] In this case gtfindsrc was used, see http://fermi.gsfc.nasa.gov/ssc/data/analysis/software.

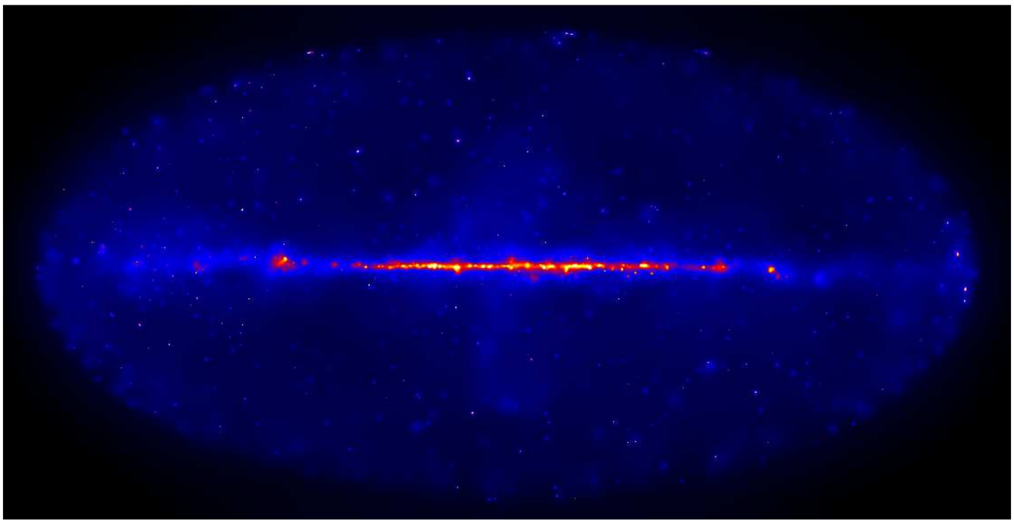

Figure 1: Adaptively smoothed count map, in Galactic coordinates, at >50 GeV.

Once a best fit has been found for a given ROI, the spectra of all sources are generated in three logarithmic energy bins from 50 GeV to 2 TeV.

The 2FHL catalog comprises (preliminarily) ~350 sources detected and characterized exclusively at >50 GeV. For comparison, ~145 are the known Very High-energy (VHE) sources reported in the TeVCat[3]. The 2FHL thus represents a leap forward for the study and characterization of the VHE sky. It is interesting to note that 2FHL sources are selected on the basis of their average flux and thus the 2FHL catalog may be considered an unbiased census of the VHE sky. A preliminary association shows that ~70 2FHL sources are detected in TeVCat as well and that the 2FHL comprises ~100 sources that were not detected in either the 1FHL or TeVCat.

Of all sources detected in the 2FHL, blazars (or blazar-like objects) represent ~75 %, while unassociated sources and Galactic sources make up the rest.

2.1. Angular and Position Resolution

Pass 8 improves the PSF of the LAT at all energies. Above 50 GeV the PSF has a 68 % containment radius of ~0.1° and remains constant with energy. Such PSF, not dissimilar from the one of Cherenkov telescopes, allows *Fermi*-LAT to localize sources with an average precision of 4′ at 95 % confidence. Fig. 2 shows that *Fermi*-LAT can easily separate nearby sources like it is the case for NGC 1275 and IC 310. However, such resolution is most useful in the plane of the Galaxy, where it helps to solve crowded regions and resolve extended sources.

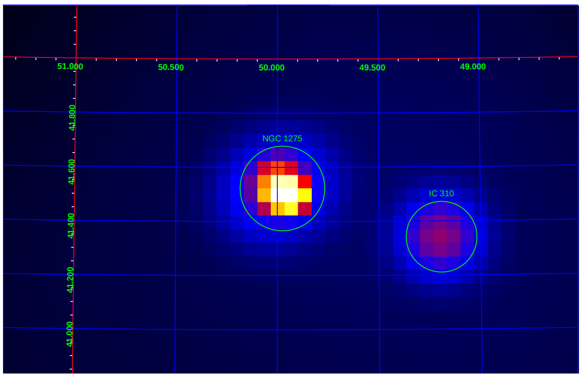

Figure 2: Adaptively smoothed count map of the region around NGC 1275 and IC 310 separated by roughly 0.6 deg.

2.2. Spectra

The 2FHL catalog will report, for every source, 3 energy-bin spectra in the energy range 50 GeV – 2 TeV. An example is reported, for Mrk 421, in Fig. 3. High synchrotron peaked (HSP) blazars, like Mkn 421, are detected by *Fermi*-LAT, typically, as power-law sources with a photon index of ~1.8 (when integrated over the full energy range as in the 3FGL). It is clear that above 50 GeV (e.g. the 2FHL) *Fermi*-LAT samples already the descending part of the high-energy peak of the spectral energy distribution (SED) of such sources and that the data from the 3FGL, 1FHL and 2FHL catalogs allow us to characterize the emission at the peak of such sources rather well. While Mkn 421

---

[3] http://tevcat.uchicago.edu

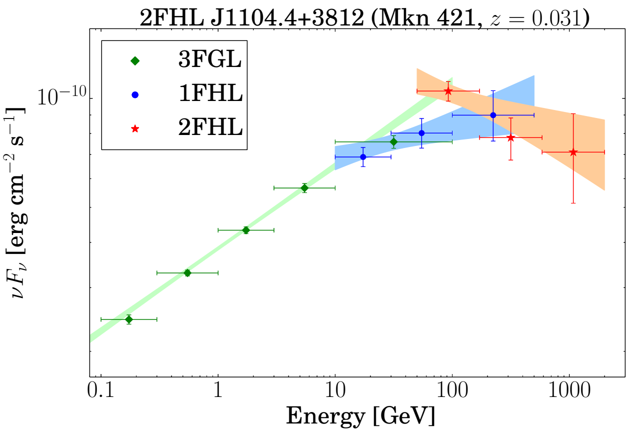

Figure 3: Preliminary spectrum of Mkn 421 in 2FHL together with data from 1FHL and 3FGL. The three catalogs rely on different exposure times.

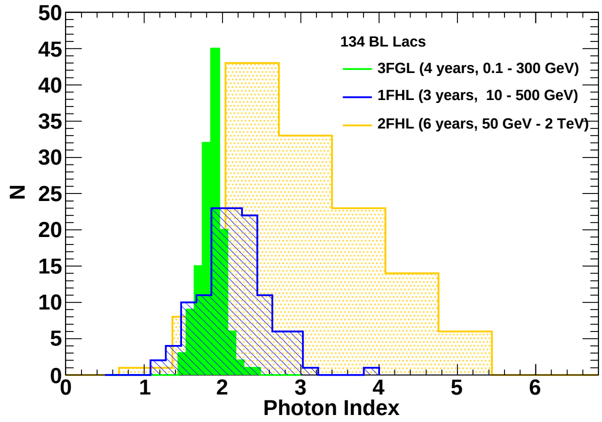

Figure 4: Distribution of the power-law photon indices for 134 BL Lacs detected in the 3FGL, 1FHL and 2FHL catalogs. Note the softening of the photon index when moving from lower energies (3FGL) to higher energies (1FHL and 2FHL).

represents probably the best example, Fig. 4 shows that such conclusion holds, on statistical grounds, for most BL Lacs detected by *Fermi*-LAT.

The 2FHL catalog comprises BL Lacs detected up to redshift ∼1.5. The improved reconstruction and increased acceptance allow *Fermi*-LAT to detect photons up to ∼2 TeV (see e.g. Fig. 3). Both these aspects enable studies of the extragalactic background light (EBL) which can absorb high-energy photons emitted from sources at cosmological distances (EBL,[7, 8, 9]). BL Lacs with substantial high-energy emission at e.g. >100 GeV are excellent probes of the EBL and have already been used with success to constrain the γ-ray opacity of the Universe [10, 11, 12]. We expect that the 2FHL, thanks to improved acceptance of high-energy photons yielded by Pass 8, will enable accurate studies of the EBL.

3. Conclusions and Outlook

The 2FHL catalog of *Fermi*-LAT sources detected at >50 GeV represents an unbiased census of the VHE sky. This work probes larger energies than any previous *Fermi*-LAT catalogs thanks to the improved Pass 8 dataset. The view of the γ-ray sky delivered by the 2FHL is complementary and different than that of the (e.g.) 3FGL catalog. Indeed, we find that most extragalactic sources are softer in the 2FHL than in the 3FGL, implying a peak of their spectral energy distribution somewhere in the *Fermi* band.

The 2FHL catalog will comprise sources detected on the basis on their average flux. Since 75 % of the detected sources are blazars, the 2FHL will yield important information for the generation of the high-energy part of the γ-ray background [13, 14]. It will also allow a first estimate of the source count distribution of VHE sources acting as a pathfinder for the surveys performed by the upcoming Cherenkov Telescope Array [15].

Finally, the good angular resolution achieved, thanks to Pass 8, by *Fermi*-LAT at >50 GeV will allow unprecedented studies of the Galaxy allowing to resolve crowded regions as well as new extended sources. We envision that this aspect of 2FHL will act as a lower energy counterpart of the H.E.S.S. Galactic plane survey [16] and the survey carried out by HAWC [17].

Acknowledgments

The Fermi LAT Collaboration acknowledges generous ongoing support from a number of agencies and institutes that have supported both the development and the operation of the LAT as well as scientific data analysis. These include the National Aeronautics and Space Administration and the Department of Energy in the United States, the Commissariat l'Energie Atomique and the Centre National de la Recherche Scientifique / Institut National de Physique Nuclaire et de Physique des Particules in France, the Agenzia Spaziale Italiana and the Istituto Nazionale di Fisica Nucleare in Italy, the Ministry of Education, Culture, Sports, Science and Technology (MEXT), High Energy Accelerator Research Organization (KEK) and Japan Aerospace Exploration Agency (JAXA) in Japan, and the K. A. Wallenberg Foundation, the Swedish Research Council and the Swedish National Space Board in Sweden. Additional support for science analysis during the operations phase is gratefully acknowledged from the Istituto Nazionale di Astrofisica in Italy and the Centre National d'Etudes Spatiales in France.

References

[1] The Fermi-LAT Collaboration. Fermi Large Area Telescope Third Source Catalog. *ArXiv:1501.02003*, January 2015.

[2] M. Ackermann, M. Ajello, A. Allafort, W. B. Atwood, L. Baldini, et al., The First Fermi-LAT Catalog of Sources above 10 GeV. *ApJS*, 209:34, December 2013.

[3] W. B. Atwood, L. Baldini, J. Bregeon, P. Bruel, A. Chekhtman, et al., New Fermi-LAT Event Reconstruction Reveals More High-energy Gamma Rays from Gamma-Ray Bursts. *ApJ*, 774:76, September 2013.

[4] M. Su, T. R. Slatyer, and D. P. Finkbeiner. Giant Gamma-ray Bubbles from Fermi-LAT: Active Galactic Nucleus Activity or Bipolar Galactic Wind? *ApJ*, 724:1044–1082, December 2010.

[5] M. Ackermann, A. Albert, W. B. Atwood, L. Baldini, J. Ballet, et al., The Spectrum and Morphology of the Fermi Bubbles. *ApJ*, 793:64, September 2014.

[6] J.-M. Casandjian. The Fermi-LAT model of interstellar emission for standard point source analysis. *ArXiv:1502.07210*, February 2015.

[7] R. J. Gould and G. Schréder. Opacity of the Universe to High-Energy Photons. *PRL*, 16:252–254, February 1966.

[8] G. G. Fazio and F. W. Stecker. Predicted High Energy Break in the Isotropic Gamma Ray Spectrum: a Test of Cosmological Origin. *Nature*, 226:135–136, April 1970.

[9] F. W. Stecker, O. C. de Jager, and M. H. Salamon. TeV gamma rays from 3C 279 - A possible probe of origin and intergalactic infrared radiation fields. *ApJL*, 390:L49–L52, May 1992.

[10] M. Ackermann, M. Ajello, A. Allafort, P. Schady, L. Baldini, et al., The imprint of the extragalactic background light in the gamma-ray spectra of blazars. *Science*, 338:1190–1192, November 2012.

[11] A. Abramowski, F. Acero, F. Aharonian, A. G. Akhperjanian, G. Anton, et al., Measurement of the extragalactic background light imprint on the spectra of the brightest blazars observed with H.E.S.S. *ArXiv:1212.3409*, December 2012.

[12] A. Domínguez, J. D. Finke, F. Prada, J. R. Primack, F. S. Kitaura, B. Siana, and D. Paneque. Detection of the Cosmic γ-Ray Horizon from Multiwavelength Observations of Blazars. *ApJ*, 770:77, June 2013.

[13] M. Ackermann, M. Ajello, A. Albert, W. B. Atwood, L. Baldini, et al., The spectrum of isotropic diffuse gamma-ray emission between 100 MeV and 820 GeV. *arXiv:1410.3696*, October 2014.

[14] M. Ajello, D. Gasparrini, M. Sánchez-Conde, G. Zaharijas, M. Gustafsson, et al., The Origin of the Extragalactic Gamma-Ray Background and Implications for Dark Matter Annihilation. *ApJL*, 800:L27, February 2015.

[15] G. Dubus, J. L. Contreras, S. Funk, Y. Gallant, T. Hassan, et al., Surveys with the Cherenkov Telescope Array. *Astroparticle Physics*, 43:317–330, March 2013.

[16] S. Carrigan, F. Brun, R. C. G. Chaves, C. Deil, A. Donath, et al., and for the H. E. S. S. collaboration. The H.E.S.S. Galactic Plane Survey - maps, source catalog and source population. *ArXiv:1307.4690*, July 2013.

[17] S. Westerhoff. HAWC: A next-generation all-sky gamma-ray telescope. *Advances in Space Research*, 53:1492–1498, May 2014.

TANAMI counterparts to IceCube high-energy neutrino events

F. Krauß[1,2], B. Wang[1,2,3], C. Baxter[1,2,4], M. Kadler[2], K. Mannheim[2], R. Ojha[5,6,7], C. Gräfe[1,2], C. Müller[2,1], J. Wilms[1], B. Carpenter[5,6], R. Schulz[1,2]
on behalf of the TANAMI and the *Fermi*-LAT Collaborations

[1] *Dr. Remeis Observatory/ECAP, FAU, Sternwartstr.7, 96049 Bamberg, Germany*
[2] *Institut für Theoretische Physik und Astrophysik,*
Universität Würzburg, Emil-Fischer-Str. 31, 97074 Würzburg, Germany
[3] *Department of Physics and Astronomy, University of Pittsburgh, Pittsburgh, PA 15260 USA*
[4] *School of Physics and Astronomy, University of Edinburgh,*
Old College, South Bridge, Edinburgh, EH8 9YL, Scotland
[5] *NASA, Goddard Space Flight Center, Greenbelt, MD 20771, USA*
[6] *Catholic University of America, Washington, DC 20064, USA and*
[7] *University of Maryland, Baltimore County, Baltimore, MD 21250, USA*

Since the discovery of a neutrino flux in excess of the atmospheric background by the IceCube Collaboration, searches for the astrophysical sources have been ongoing. Due to the steeply falling background towards higher energies, the PeV events detected in three years of IceCube data are the most likely ones to be of extraterrestrial origin. Even excluding the PeV events detected so far, the neutrino flux is well above the atmospheric background, so it is likely that a number of sub-PeV events originate from the same astrophysical sources that produce the PeV events. We study the high-energy properties of AGN that are positionally coincident with the neutrino events from three years of IceCube data and show the results for event number 4. IC 4 is a event with a low angular error ($7^{\circ}\!.1$) and a large deposited energy of 165 TeV. We use multiwavelength data, including *Fermi*-LAT and X-ray data, to construct broadband spectra and present parametrizations of the broadband spectral energy distributions with logarithmic parabolas. Assuming the X-ray to γ-ray emission in blazars originates in the photoproduction of pions by accelerated protons, their predicted neutrino luminosity can be estimated. The measurements of the diffuse extragalactic background by *Fermi*-LAT gives us an estimate of the flux contributions from faint unresolved blazars. Their contribution increases the number of expected events by a factor of $\sim$2. We conclude that the detection of the IceCube neutrinos IC4, IC14, and IC20 can be explained by the integral emission of blazars, even though no individual source yields a sufficient energy output.

I. INTRODUCTION

The IceCube Collaboration's announcement of the discovery of a neutrino flux in excess of the atmospheric background is an inflection point in multimessenger astronomy [11]. Due to the steeply falling atmospheric background spectrum, events at the highest energies most likely have an extraterrestrial origin [1].

Neutrino emission from the jets of active galactic nuclei (AGN) [17] and cores [23] has been predicted, but alternative possibilities are gamma-ray bursts [25] and pevatrons in the Galactic center region [5]. All IceCube events are consistent with an isotropic distribution, and therefore extragalactic sources are the prime candidates. Only the predicted flux of $\sim 10^{-8}\,\mathrm{GeV/cm^2/s/sr}$ at energies from 100 TeV to a few PeV from AGN jets matches the observed excess flux well [15].

AGN with jets that are observed at small angles to the line of sight are called 'blazars'. Their non-thermal emission becomes relativistically boosted. The low energy emission is generally attributed to synchrotron emission. Emission at higher energies can be explained by hadronic and leptonic models. In hadronic models, protons (as well as electrons) are accelerated in the jet. The protons interact with seed photons at lower energies (e.g., from the accretion disk or external radiation fields) and produce pions [pion photoproduction; 16]. Subsequent pion decays produce neutrinos and γ-rays. Currently, the observed spectral energy distributions (SEDs) of AGN can be described equally well with hadronic and leptonic emission processes due to a large number of free parameters [e.g, 7]. Unambiguous evidence of hadronic processes could be provided by an association of neutrino events with an individual blazar. In pion photoproduction, the neutrino flux can be directly calculated from the observed flux of the high-energy bump in the SED $F_\nu = F_\gamma$. This estimate has been confirmed by Monte-Carlo simulations [19]. The neutrino fluence can therefore be estimated directly from the integrated X-ray to γ-ray flux of the broadband SED.

Due to the large angular uncertainties, several possible candidate blazars can be identified for each of the IceCube shower events. We have previously shown [14] that the 2 events at PeV energies from the first two years of IceCube (IC20, dubbed 'Ernie' and IC 14, 'Bert') can be explained calorimetrically by the six candidate blazars from the TANAMI sample. Here,we study the multiwavelength properties of AGN from the TANAMI sample, as well as *Fermi* blazars that are positionally coincident with the neutrino events

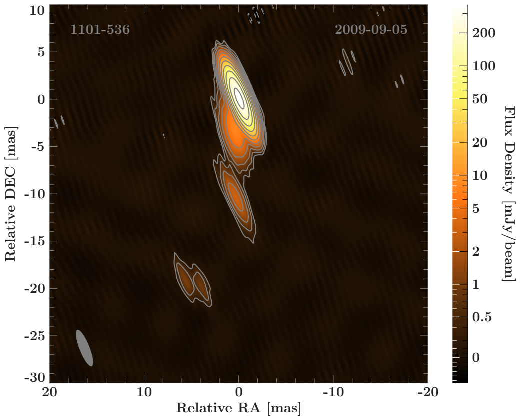

FIG. 1: First-epoch TANAMI VLBI image of 2FGL J1103.9−5356 at 8.4 GHz. The color scale indicates the flux density distribution, the white contours are scaled logarithmically and increase by factors of 2, with the lowest contour set to the 3σ-noise-level. The gray ellipse in the lower left corner shows the beam with (4.1×1) mas at 22°. This blazar shows a bright radio core with a brightness temperature of $T_{\mathrm{B}} = 5.43 \times 10^{10}$ K (for $S_{\mathrm{core}} \sim 0.39$ Jy) and a single-sided jet in southern direction.

from three years IceCube data. We address the question whether the sub-PeV neutrino events can be explained by blazars in the error field. In particular, we calculate the expected neutrino fluence of the the four blazars in the field of IceCube event 4 (IC4). IceCube event number 4 has a lower median angular error of $7\overset{\circ}{.}1$ compared to the PeV events with error radii of up to 13° and a higher energy than most of the other IC events (165 TeV), i.e., has a low probability of being of atmospheric origin. Inside the IC4 error field, there are four γ-ray bright AGN listed in the 2LAC catalog [2]. We report on the multiwavelength properties of these four sources below.

II. MULTIWAVELENGTH DATA

Tracking Active Galactic Nuclei with Austral Milliarcsecond Interferometry (TANAMI)[27] [21] is a multiwavelength program that monitors extragalactic jets of the Southern Sky.

Figure 1 shows the first-epoch high-resolution image of 2FGL J1103.9−5356 (PKS 1101−536) obtained with Very Long Baseline Interferometry (VLBI) at 8.4 GHz. An 8.4 GHz VLBI image of PKS 1104−445 has been shown by [21]. Both sources show core-dominated radio structures typical for blazars with a single-sided jet, indicating relativistically beamed emission. The two other IC 4 candidate sources have not been observed in the TANAMI VLBI program as of 2015.

X-ray data taken during the IceCube period are from the TANAMI program and the public archives of Swift [8] and *Chandra*. *Swift*/XRT and *Chandra*/ACIS data were reduced with standard methods, using the most recent software packages (HEASOFT 6.15.1, CIAO 4.6) and calibration databases. Spectra were grouped to a minimum signal-to-noise ratio of 5 to ensure the validity of χ^2 statistics. For a low SNR, the spectra were grouped to a minimum signal-to-noise ratio of 2 and the use of Cash statistics [9]. Spectral fitting was performed with ISIS 1.6.2 [10]. The X-ray data were deabsorbed using the Galactic N_{H} value [13], abundances from [26], and cross sections from [24]. We have used the γ-ray spectra from the 2FGL catalog [20].

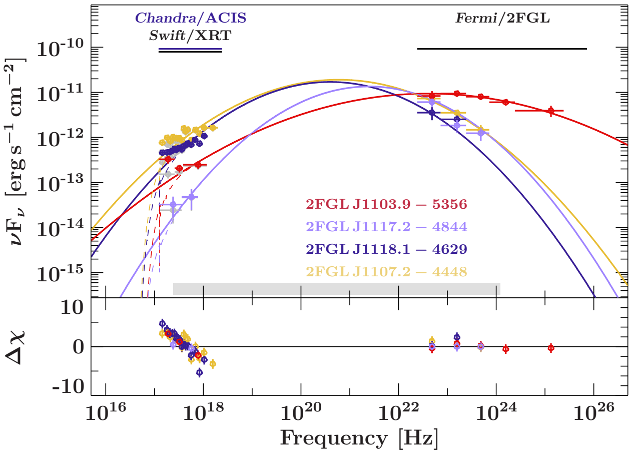

FIG. 2: X-ray to γ-ray SED of all four 2LAC sources including a log parabola fit to the data. The gray area shows the energy range used for the calculation of the neutrino events

III. RESULTS

Electromagnetic cascades in pion photoproduction emit at X-ray and γ-ray energies, and we approximate the non-thermal photon flux F_γ by the integrated flux between 1 keV and 5 GeV [14]. The broadband spectra were fit with a logarithmic parabola [18] including X-ray absorption.

The X-ray to γ-ray SEDs of all four sources are shown in Fig. 2. As shown by [14], this allows us to model the high-energy hump with logarithmic parabolas in order to estimate the integrated flux and the fluence in the IceCube integration period. This fluence can be used to directly estimate the number of neutrinos. Using the IceCube integration period of $\Delta t = 998$ days, and an effective area of $A_{\mathrm{eff}} = 10^5\,\mathrm{cm}^2$ for contained events, we obtain the values listed in Table I. The numbers would be lower for a realistic spectrum of the emitted neutrinos or if some fraction of the emission is produced in a leptonic, proton-synchrotron, or Bethe-Heitler process. The steepness of the blazar γ-

TABLE I: Integrated electromagnetic energy flux from 1 keV to 5 GeV and expected electron neutrino events in 998 days of IceCube data for the 4 candidate blazars of IceCube event 4. Uncertainties are statistical only.

Source 2FGL	Assoc. source	F_γ [10^{-11}] [erg/s/cm^2]	events
J1103.9−5356	PKS 1101−536	$7.6^{+1.7}_{-1.4}$	0.22 ± 0.05
J1107.2−4448	PKS 1104−445	$14.0^{+1.7}_{-1.8}$	$0.40^{+0.05}_{-0.06}$
J1117.2−4844	PMN J1117−4838	8^{+6}_{-5}	$0.23^{+0.18}_{-0.15}$
J1118.1−4629	PKS 1116−46	11.3 ± 0.6	0.33 ± 0.02
Sum			$\mathbf{1.18 \pm 0.18}$

ray luminosity function [22] further implies that in a large field, the neutrino fluence will have significant contributions from the brightest sources in the field, as well as from fainter, unresolved sources.

A. Contributions from unresolved blazars

At the sensitivity of current catalogs, a large number of faint blazars are not resolved into individual point sources by *Fermi*-LAT, but do contribute to the diffuse extragalactic gamma-ray background (EGB). In order to calculate the number of expected neutrinos, one should also consider the substantial contribution of this most numerous part of the blazar population. The fraction of blazars in the EGB has been estimate to lie between 50% and 80% [12]. At 100 GeV, half of the EGB has been resolved into individual blazars (mainly BL Lac type objects) by *Fermi*-LAT [4].

We compare the values of the EGB flux to the total flux of resolved blazars, in order to estimate the contributions from unresolved blazars, assuming pion photoproduction. We find a total integrated flux for all four 2LAC sources of $F_{100\,\mathrm{MeV}-820\,\mathrm{GeV}} = 1.71 \times 10^{-7}\,\mathrm{ph/s/cm^2}$, which corresponds to $3.54 \times 10^{-6}\,\mathrm{ph/s/cm^2/sr}$ for a 7.1° error field. The extragalactic background is $F_{100\,\mathrm{MeV}-820\,\mathrm{GeV}} = 7.2 \pm 0.6 \times 10^{-6}\,\mathrm{ph/cm^2/s/sr}$ [4], a factor of ~ 2 higher than the value for the resolved blazars. This suggest that a substantial fraction of the extragalactic neutrino flux in this field originates from faint, unresolved blazars, instead of the bright, low-redshift sources.

IV. CONCLUSION

Assuming that the high-energy emission originates in pion photoproduction, the maximum expected number of electron neutrino events from all four 2LAC sources for IC4 is 1.18±0.18 for 998 days. This is close to the number of detected events, but given the different factors that might reduce the neutrino output below the rate predicted by our basic model (leptonic contributions, neutrino spectra, etc.; see [14]) it seems unlikely that any of the individual brightest blazars in the field of IC4 can explain the observed neutrino flux. This situation is similar to the fields of the two PeV neutrinos IC14 and IC21 [14], where the predicted neutrino flux of the six brightest blazars matched the IceCube observed flux, but the individual sources fell short of yielding sufficient fluence. The integral flux of bright individual blazars and faint remote sources, however, rises a factor of 2 above the observed flux in this field, consistent with the hypothesis that the population of blazars as a whole can explain the IceCube results.

Acknowledgments

We acknowledge support and partial funding by the Deutsche Forschungsgemeinschaft grant WI 1860-10/1 (TANAMI) and GRK 1147, Deutsches Zentrum für Luft- und Raumfahrt grants 50 OR 1311/50 OR 1103, and the Helmholtz Alliance for Astroparticle Physics (HAP). We thank J.E. Davis and T. Johnson for the development of the slxfig module and the SED scripts that have been used to prepare the figures in this work. This research has made use of a collection of ISIS scripts provided by the Dr. Karl Remeis-Observatory, Bamberg, Germany at `http://www.sternwarte.uni-erlangen.de/isis/`. The Long Baseline Array and Australia Telescope Compact Array are part of the Australia Telescope National Facility, which is funded by the Commonwealth of Australia for operation as a National Facility managed by CSIRO. The *Fermi*-LAT Collaboration acknowledges support for LAT development, operation and data analysis from NASA and DOE (United States), CEA/Irfu and IN2P3/CNRS (France), ASI and INFN (Italy), MEXT, KEK, and JAXA (Japan), and the K.A. Wallenberg Foundation, the Swedish Research Council, and the National Space Board (Sweden). Science analysis support in the operations phase from INAF (Italy) and CNES (France) is also gratefully acknowledged.

[1] Aartsen M.G., Ackermann M., Adams J., et al., 2014b, Physical Review Letters 113, 101101.

[2] Ackermann M., Ajello M., Allafort A., et al., 2011, Astrophys. J. 743, 171.

[3] Ackermann M., Ajello M., Albert A., et al., 2012, ApJS 203, 4.

[4] Ackermann M., Ajello M., Albert A., et al., 2015, Astrophys. J. 799, 86.

[5] Aharonian F.A., Atoyan A.M., 1996, A&A 309, 917.

[6] Atwood W.B., Abdo A.A., Ackermann M., et al., 2009, ApJ 697, 1071.

[7] Böttcher M., Reimer A., Sweeney K., Prakash A., 2013, Astrophys. J. 768, 54

[8] Gehrels N., Chincarini G., Giommi P., et al., 2004, ApJ 611, 1005.

[9] Cash W., 1979, ApJ 228, 939.

[10] Houck J.C., Denicola L.A., 2000, In: Manset N., Veillet C., Crabtree D. (eds.) Astronomical Data Analysis Software and Systems IX, 216. Astronomical Society of the Pacific Conference Series, p. 591.

[11] IceCube Collaboration 2013, Science 342, 6161, 1242856.

[12] Inoue Y., Totani T., 2009, Astrophys. J. 702, 523.

[13] Kalberla P.M.W., Burton W.B., Hartmann D., et al., 2005, A&A 440, 775.

[14] Krauß F., Kadler M., Mannheim K., et al., 2014, Astron. Astrophys. 566, L7.

[15] Learned J.G., Mannheim K., 2000, Annual Review of Nuclear and Particle Science 50, 679.

[16] Mannheim K., Biermann P.L., 1989, A&A 221, 211.

[17] Mannheim K., 1995, Astroparticle Physics 3, 295.

[18] Massaro E., Perri M., Giommi P., Nesci R., 2004, A&A 413, 489.
Mannheim K., 1995, Astroparticle Physics 3, 295.

[19] Mücke A., Rachen J.P., Engel R., et al., 2000, Nuclear Physics B Proceedings Supplements 80, C810.

[20] Nolan P.L., Abdo A.A., Ackermann M., et al., 2012, ApJS 199, 31.

[21] Ojha R., Kadler M., Böck M., et al., 2010, A&A 519, A45.

[22] Singal J., Petrosian V., Ajello M., 2012, ApJ 753, 45.

[23] Stecker F.W., 2013, Phys. Rev. D 88, 047301.

[24] Verner D.A., Ferland G.J., Korista K.T., Yakovlev D.G., 1996, Astrophys. J. 465, 487.

[25] Waxman E., Bahcall J., 1997, Physical Review Letters 78, 2292.

[26] Wilms J., Allen A., McCray R., 2000, ApJ 542, 914.

[27] `http://pulsar.sternwarte.uni-erlangen.de/tanami`

The GeV Excess Shining Through: Background Systematics for the Inner Galaxy Analysis

F. Calore[*], C. Weniger
GRAPPA Institute, University of Amsterdam, Science Park 904, 1090 GL Amsterdam, The Netherlands
I. Cholis
Center for Particle Astrophysics, Fermi National Accelerator Laboratory, Batavia, IL, 60510, USA

arXiv:1502.02805v1 [astro-ph.HE] 10 Feb 2015

Recently, a spatially extended excess of gamma rays collected by the *Fermi*-LAT from the inner region of the Milky Way has been detected by different groups and with increasingly sophisticated techniques. Yet, any final conclusion about the morphology and spectral properties of such an extended diffuse emission are subject to a number of potentially critical uncertainties, related to the high density of cosmic rays, gas, magnetic fields and abundance of point sources. We will present a thorough study of the systematic uncertainties related to the modelling of diffuse background and to the propagation of cosmic rays in the inner part of our Galaxy. We will test a large set of models for the Galactic diffuse emission, generated by varying the propagation parameters within extreme conditions. By using those models in the fit of *Fermi*-LAT data as Galactic foreground, we will show that the gamma-ray excess survives and we will quantify the uncertainties on the excess emission morphology and energy spectrum.

1. Introduction

One of the most challenging results for indirect dark matter searches in recent years is the discovery of an excess emission in the gamma-ray flux from the center of our Galaxy. The first indications of such an excess date back to 2009 [Goodenough and Hooper 2009, Vitale et al. 2009]. Since then, several analyses of gamma-ray data from the Large Area Telescope aboard the *Fermi* satellite [Gehrels and Michelson 1999], hereafter *Fermi*-LAT, claimed the existence of the excess above the standard astrophysical background at GeV energies [Goodenough and Hooper 2009, Hooper and Goodenough 2011, Boyarsky et al. 2011, Hooper and Linden 2011, Abazajian and Kaplinghat 2012, Macias and Gordon 2014, Abazajian et al. 2014, Daylan et al. 2014, Zhou et al. 2014]. The excess emission results from analyses of both the inner few degrees of the Galaxy [Abazajian and Kaplinghat 2012, Macias and Gordon 2014, Abazajian et al. 2014, Daylan et al. 2014, Zhou et al. 2014, Gordon and Macias 2013] and *higher* latitudes [Daylan et al. 2014, Hooper and Slatyer 2013, Huang et al. 2013], extending up to tens of degrees. Intriguingly, the observed spectral energy distribution and the spatial properties of the *Fermi* GeV excess match the expectation for a signal from dark matter particles annihilating in the halo of the Milky Way. Nevertheless, some discussion about astrophysical explanations were put forward, as, for example, about the emission from a population of point-like sources below the telescope's detection threshold [Hooper et al. 2013, Calore et al. 2014a, Cholis et al. 2014, Petrovic et al. 2014a], or violent burst events at the Galactic center with injection of leptons and/or protons some kilo-/mega-years ago [Carlson and Profumo 2014, Petrovic et al. 2014b].

Regardless of the possible interpretations, all analyses agree on the fact that an extra-emission over the *standard* astrophysical background is present in the inner region of the Galaxy. We stress here that the Galactic center is one of the most promising targets for dark matter searches since there the typically predicted profiles for the dark matter distribution lead to the largest photon flux from dark matter origin. However, the Galactic center is maybe the most challenging target for dark matter searches: our knowledge of the conditions at the Galactic center is indeed very poor and the astrophysical background (from point sources as well as from diffuse emission processes) is affected by large uncertainties.

A critical point is to answer the question "An excess above what?". The excess emission is defined with respect to specific astrophysical foregrounds and backgrounds, like the Galactic diffuse emission (which originates from the interactions of cosmic rays with gas and photons in the Galaxy), point-like and extended sources. Those components should be modelled independently. Therefore, it is crucial to explore different foreground and background models in order to robustly identify and characterise the excess emission.

We will present here part of the analysis performed in Calore et al. [2014b], where we showed for the first time that the excess is statistically robust against theoretical model systematics, bracketed by exploring previously neglected uncertainties on the Galactic diffuse emission, and that the proper treatment of background modelling uncertainties allows more freedom for models fitting the excess [Calore et al. 2014c].

---

[*] Speaker. E-mail: f.calore@uva.nl

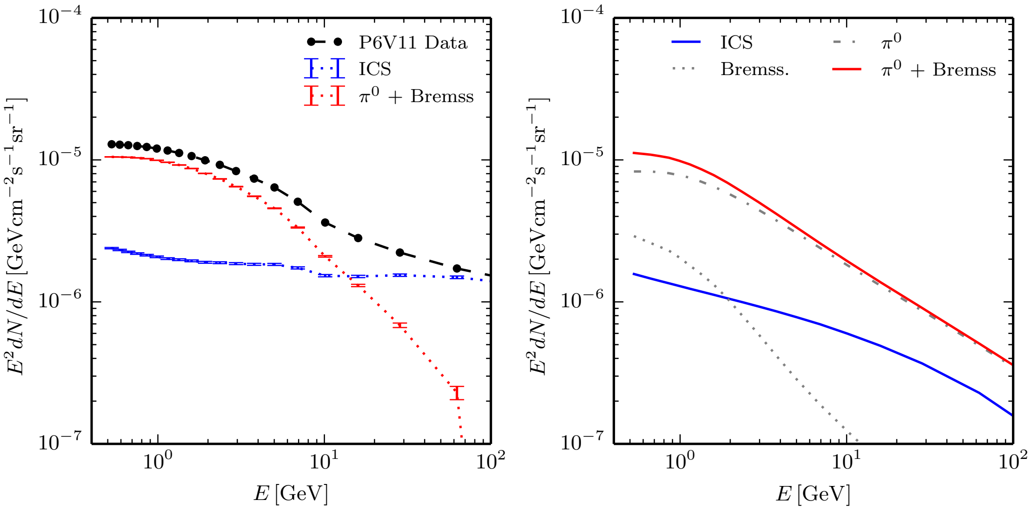

Figure 1: *Left panel:* ICS and π^0+Bremss contributions to the `P6V11` background model. *Right panel:* Spectra predicted by a typical Galactic diffuse model for ICS, π^0 and bremsstrahlung emission. Fluxes in the $40^\circ \times 40^\circ$ ROI, $|b| > 2^\circ$.

2. On the importance of foreground modelling

The dominant source of background for the Galactic center analysis is the emission originating from the interaction of cosmic rays with dust and gas in the Galaxy. The three main production mechanisms of Galactic diffuse gamma rays are: the Inverse Compton scattering (ICS) of electrons on low-energy ambient photons, the decay of abundantly produced neutral pions and the bremsstrahlung of electrons in the interstellar medium. Most of previous analyses adopted the same background model to describe the Galactic diffuse emission, namely the `P6V11` background model, provided by the *Fermi*-LAT Collaboration for the *sole* purpose of point source analysis.[1] Using this model for analysis of extended sources introduces systematic effects that might lead to biased statements about the spectrum and morphology of the *Fermi* GeV excess emission.

To visualise this effect, we decomposed the `P6V11` model in the main contributions to the Galactic diffuse emission. The spectra for ICS, π^0 and bremsstrahlung (that we consider as a unique component "π^0+Bremss") are predicted by a standard model for cosmic-ray propagation in the Galaxy (see Calore et al. [2014b] for more details). We fitted simultaneously the ICS and π^0+Bremss components to `P6V11` mock-data. From Figure 1, left panel, the reader can see that an extremely hard ICS emission at energies $\geq$ 10 GeV is an intrinsic property of the `P6V11` background model. The effect on any analysis that employs it as Galactic diffuse emission model is to over-subtract the ICS component at high energies, forcing the GeV excess spectrum to fall-off at $\geq$ 10 GeV.

This exercise demonstrates the relevance of modelling *separately* the different contributions to the Galactic diffuse emission. Indeed, ICS, π^0 and bremsstrahlung possess intrinsically different morphologies because of the different targets that originate these components: the gas for the π^0 and bremsstrahlung, and the interstellar radiation field for the ICS. Moreover, given the different cosmic-ray species responsible of the gamma-ray emission (protons for π^0 and electrons for ICS and bremsstrahlung), also the way in which the morphology changes with energy is different for the three contributions.

Such arguments strongly motivated the study of the variation of the spectral and morphological properties of the excess due to the modelling of the Galactic diffuse emission.

3. Home-brew Galactic diffuse emission

In order to robustly identify the excess despite of large variations in the foreground emission, we built a set of Galactic diffuse models by varying cosmic-ray propagation parameters within a given set of assumptions. We note that the observed emission results from a line of sight integral and, as such, it receives contributions from all distances. In particular,

---

[1] `http://fermi.gsfc.nasa.gov/ssc/data/p6v11/access/lat/ring_for_FSSC_final4.pdf`

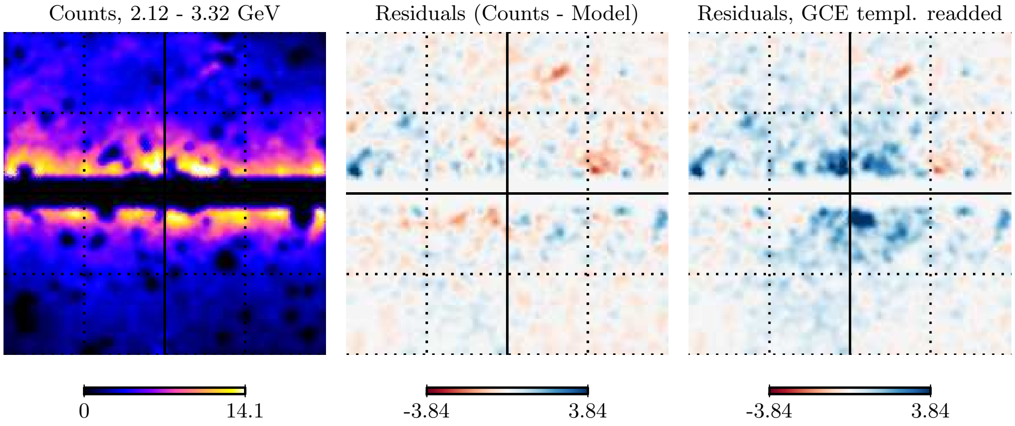

Figure 2: *Left panels:* Count maps (the $|b| > 2°$ cut and the point-source mask are clearly visible). *Central panels:* Residuals when subtracting all emission model templates. *Right panels:* Residuals when re-adding the GeV excess template absorbed emission.

the emission that comes from the Galactic center is – in the models we are adopting – relatively subdominant (about 10%) and the Galactic diffuse emission is dominated by local processes. Therefore, our work should read as the characterisation of the uncertainties due to the Galactic gamma-ray emissivity along the line of sight. We worked in the framework of steady state solutions to the transport equation of cosmic-ray propagation in the Galaxy. Homogeneous diffusion, re-acceleration and convection were considered. We adopted models from the set of Ackermann et al. [2012] to test variations of the diffusion zone geometry, the source distribution, the spin temperature and the magnitude cut (for an explanation of cosmic-ray propagation parameters and their range of variation see Calore et al. [2014b]). Additionally, we generated our own Galactic diffuse models using `Galprop v54` (webrun version). With those models, we explored the remaining uncertainties related to the diffusion coefficient, re-acceleration, convection, interstellar radiation field, and Galactic center magnetic field distributions. In total, we built a set of about 60 models for the Galactic diffuse emission that test "extreme" variations in the parameter space. We here quote the explored parameter ranges:

- geometry of the diffusion zone: $4 \leq z_D \leq 10$ kpc and $r_D = 20$ or 30 kpc;
- source distributions: SNR, pulsars, OB stars;
- diffusion coefficient at 4 GV: $D_0 = 2 - 60 \times 10^{28}$ $\mathrm{cm}^2\,\mathrm{s}^{-1}$;
- Alfvén speed: $v_\mathrm{A} = 0 - 100\ \mathrm{km\,s^{-1}}$;
- gradient of convection velocity: $dv/dz = 0 - 500$ $\mathrm{km\,s^{-1}\,kpc^{-1}}$;
- interstellar radiation field model factors (for optical and infrared emission): 0.5 – 1.5;
- magnetic field parameters: $5 \leq r_c \leq 10$ kpc, $1 \leq z_c \leq 2$ kpc, and $5.8 \leq B(r = 0, z = 0) \leq 117$ μG.

We note that we did not test those models against local cosmic-ray data and large scale diffuse gamma-ray data (or even microwave data).

As already mentioned, we made a few simplifying assumptions that we summarise below and that will become relevant for future refined analyses of the GeV excess : (i) homogeneity and isotropy of cosmic-ray diffusion, re-acceleration, and convection; (ii) radial symmetry of cosmic-ray source distribution in the Galactic disk (i.e. no modelling of the spiral arms), and same source distribution for different cosmic-ray-species sources; (iii) steady state regime, excluding transient phenomena as, for example, burst events.

4. The data analysis

In order to analyse gamma rays collected by the *Fermi*-LAT from the inner Galaxy, we adopt a template-based multi-linear regression technique, see, for example, Dobler et al. [2010], Su et al. [2010]. The data sample corresponds to 284 weeks of reprocessed *Fermi*-LAT data (from 4 August 2008 on) in the energy range 300 MeV – 500 GeV. The Region-Of-Interest (ROI), i.e. the *inner Galaxy*, is defined as

$$|\ell| \leq 20° \quad \text{and} \quad 2° \leq |b| \leq 20° \,, \tag{1}$$

The choice of the latitude cut is such to avoid the large contamination of point sources in the innermost few degrees, where the source confusion is very high. We prepare the data according to standard prescriptions provided by the *Fermi*-Science-Support-Center. We binned the data on an `healpix` grid with resolution parameter $n_{\text{size}} = 256$, for each energy bin (24 in total) defined in a way such to guarantee good statistics also at the highest energies.

We compare the data maps with the model maps, obtained by the superposition of the different templates adopted in the analysis (see below). The best-fit normalisation of each model template is derived through a maximum likelihood method, based on the Poisson likelihood function (cf. Eq. (2.3) in Calore et al. [2014b]).

The spatial model templates adopted in the analysis are:

- Point-like sources template as derived from the 2FGL Abdo et al. [2011], with fixed spectra and flux normalisations.
- *Fermi* bubbles modelled by a uniform-brightness spatial template with bubbles' edges as in Su et al. [2010].
- Isotropic gamma-ray diffuse background with uniform-brightness emission template.
- Galactic diffuse emission ICS and π_0+Bremss *independent* templates as modelled from Sec. 3.
- GeV excess template whose volume emissivity is parametrised by the spherically symmetric generalized NFW profile,

  $$\rho(r) = \rho_s \frac{(r/r_s)^{-\gamma}}{(1 + r/r_s)^{3-\gamma}} \,, \qquad (2)$$

  squared, and with (best-fit) spectral index $\gamma = 1.2$. This choice is clearly motivated by the dark matter annihilation interpretation of the GeV excess, although we tested a large range of variation for the profile parameters.

The fitted spectra of the *Fermi* bubbles and isotropic diffuse background templates are constrained to vary within the measured spectra from Franckowiak [2013] and Ackermann [2012], respectively.

In the analysis, we introduced the following technical improvements: a non-logarithmic energy binning such to counterbalance the reduced photon statistics above 10 GeV, a weighted adaptive masking of point sources, and the full treatment of the *Fermi*-LAT point spread function.

5. Selection of main results

In this section, we present a selection of the results of the analysis, and we refer the reader to Calore et al. [2014b] for a thorough explanation of our findings. Figure 2 represents the residual (i.e. data - model counts) emission obtained when subtracting from the raw data the emission associated with the model templates (central panel). The residuals are at the level of 20% in the whole ROI, but, when the GeV excess template associated to the model is re-added (right panel), the residuals in the central region of the ROI increase significantly, attesting the presence of the excess, which is, after the other components are subtracted, the most pronounced large-scale excess in our ROI.

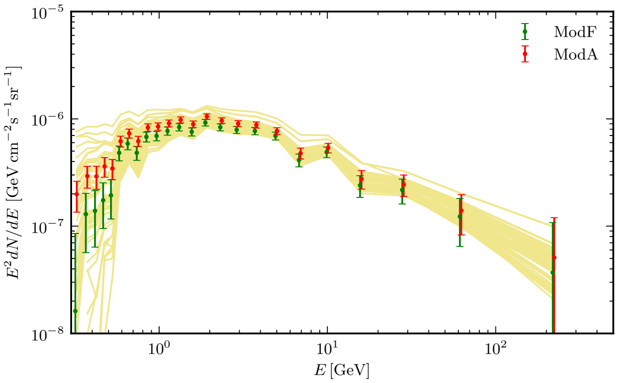

Figure 3: Spectral energy distribution of the GeV excess template, for a generalised NFW profile with an inner slope $\gamma = 1.2$. The *yellow band* corresponds to all of the 60 GDE models. Two models are highlighted: the model that provides the best fit to the data (model F, *green points*) and a reference model (*red points*).

Figure 3 represents the spectral energy distribution of the excess emission, i.e. the emission absorbed by the GeV excess template during the fitting procedure. The yellow band results from *all* the adopted Galactic diffuse models. Such a band brackets the uncertainty due to the theoretical modelling of the Galactic diffuse emission and affecting the extraction of the GeV excess spectrum. The GeV excess emission is found to be remarkably stable against the tested variations of the Galactic foreground. The typical GeV excess spectrum shows a rising below 1 GeV (with a spectral index harder than $\sim$ 2 for all Galactic diffuse models) and features a peak at energies around 1–3 GeV. Despite previous analyses, at higher energies, the spectrum is described by a power-law with slope $\sim$ -2.6. The coloured data points indicate the spectrum (with statistical errors) that corresponds to the best-fit Galactic diffuse model (model F) and another exemplary model discussed in Calore et al. [2014b] (model A).

The envelope of the yellow lines corresponds to the *theoretical model uncertainty*, which is due to the variation induced by the Galactic diffuse modelling. Such uncertainty is, at all energies, larger than the statistical errors, indicating the importance of the proper treatment of background model systematics.

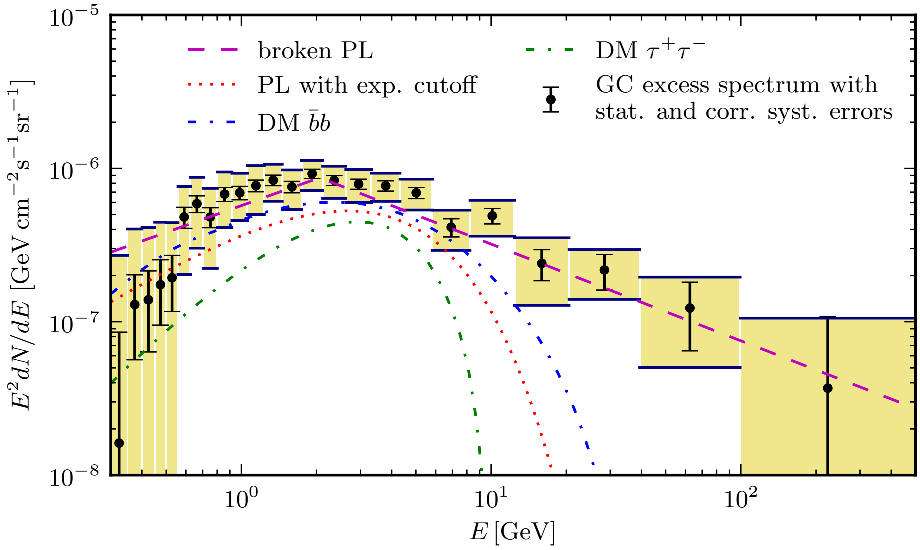

Figure 4: GeV excess emission spectrum, together with statistical and systematical errors, for model F (i.e. best-fit model). Several spectral models have been fitted to the data. All the spectra (except the $\tau^+\tau^-$) provide a quite reasonable fit to the data. This is due to the correlation of the systematic errors (see text).

Spectrum	Parameters	χ^2/dof	p-value
broken PL	$\alpha_1 = 1.42^{+0.22}_{-0.31}$, $\alpha_2 = 2.63^{+0.13}_{-0.095}$, $E_{\rm break} = 2.06^{+0.23}_{-0.17}$ GeV	1.06	0.39
DM $\chi\chi \to \bar{b}b$	$\langle\sigma v\rangle = 1.76^{+0.28}_{-0.27} \times 10^{-26}$ cm^3 s^{-1}, $m_\chi = 49^{+6.4}_{-5.4}$ GeV	1.08	0.36
DM $\chi\chi \to \bar{c}c$	$\langle\sigma v\rangle = 1.25^{+0.2}_{-0.18} \times 10^{-26}$ cm^3 s^{-1}, $m_\chi = 38.2^{+4.6}_{-3.9}$ GeV	1.07	0.37
PL with exp. cutoff	$E_{\rm cut} = 2.53^{+1.1}_{-0.77}$ GeV, $\alpha = 0.945^{+0.36}_{-0.5}$	1.37	0.12
DM $\chi\chi \to \tau^+\tau^-$	$\langle\sigma v\rangle = 0.337^{+0.047}_{-0.048} \times 10^{-26}$ cm^3 s^{-1}, $m_\chi = 9.96^{+1.1}_{-0.91}$ GeV	1.52	0.06

Table I Spectral fits to the GeV excess spectrum, with $\pm 1\sigma$ errors. We show best-ft parameters, reduced χ^2, and corresponding p-value.

As it can be already deduced from the residual plots, the Galactic diffuse models tested in the present analysis do not describe the data at the statistical level, but, still, they show large residuals in the ROI. Indeed, although the reduced χ^2 for the best-fit Galactic diffuse model (model F) in the energy range from 500 MeV to 3.31 GeV is close to one ($\simeq 1.10$) because of the large number of free parameters, the corresponding p-value is ridiculously small, $\simeq 10^{-300}$.

On the base of this argument, it is important to find an alternative way of assessing the systematics uncertainties affecting the excess. In Calore et al. [2014b], we relied on an empirical method to derive model systematics due to how well the different Galactic diffuse models describe the data along the disk, away from the Galactic center. The derivation and definition of the *empirical model systematics* were presented during this conference in a complementary talk, "Robust Identification of the GeV Galactic Center Excess at Higher Latitudes".[2] Quantifying the background empirical model systematics turned out to be crucial for making statistics based claims on the possible interpretations of the excess.

6. Interpretations

As explained in Sec. 1, several interpretations have been proposed, ranging from purely astrophysical to dark matter explanations. As a first constraint, the predicted model spectrum must provide a good fit to the GeV excess spectrum. We performed parametric fits to the GeV excess observed spectrum fully taking into account the systematic uncertainties.

---

[2] C. Weniger et al., proceedings RICAP-14 (to appear soon).

To do so, we made use of a χ^2 function with a non-diagonal covariance matrix, which models the correlated empirical model systematics. The χ^2 function used writes as:

$$\chi^2 = \sum_{ij} \left(\frac{d\bar{N}}{dE_i}(\vec{\theta}) - \frac{dN}{dE_i} \right) \Sigma_{ij}^{-1} \left(\frac{d\bar{N}}{dE_j}(\vec{\theta}) - \frac{dN}{dE_j} \right) , \tag{3}$$

with Σ_{ij}^{-1} the covariance matrix. The covariance contains model uncertainties that were derived from the size of typical residuals along the Galactic disk. They amount to variations in the excess template that are similar to the ones shown in Figure 3, and are illustrated in Figure 4 by the yellow boxes. For details we refer the reader to Calore et al. [2014b].

We tested several spectra that are related to the GeV excess viable interpretations. Table I summarises our findings. In particular, parametric fits with correlated errors show equal preference for a broken power-law spectrum and for the spectrum from dark matter annihilation into b-quarks. Remarkably, the p-value for a spectrum due to dark matter annihilation into τ-leptons is higher the 0.05. The reason for which dark matter annihilation spectra provide good fit to the GeV excess is due to the fact that systematics errors are correlated in energy and can be understood in terms of the covariance matrix (we refer the interested reader to Calore et al. [2014c]).

7. Conclusion

The analysis of the *Fermi*-LAT data performed in Calore et al. [2014b] confirmed the presence of an excess emission in the *inner Galaxy* and some of its, previously found, specific properties, such as the 2–3 GeV peaked spectral energy distribution, the extension to high latitudes and the compatibility with a spherically symmetric spatial distribution. Those properties were demonstrated to be remarkably stable against theoretical model systematics, due to the variations in the modelling of the Galactic diffuse emission.

We assess empirical model systematics from a scan of the gamma-ray flux along the disk and we used those uncertainties as a proxy for the systematics affecting the GeV excess at the Galactic center.

Contrary to previous results, we do *not* confirm the fall-off of the GeV excess spectrum at $E \gtrsim 10$ GeV, but we do find a high energy tail of the spectrum extending up to 100 GeV. However, when we properly treat model systematics and include them in the spectral fits as correlated errors, we demonstrated that it is possible to equally well fit the excess spectrum with both a broken power-law and a gamma-ray spectrum typically expected from dark matter particles annihilation into $\bar{b}b$ final states. This implies a large, previously neglected, freedom for models fitting the GeV excess.

Acknowledgments

We are grateful to the organisation of the V *Fermi* Symposium for the possibility to present this work during the Conference. F.C. acknowledges support from the European Research Council through the ERC starting grant WIMPs Kairos, P.I. G. Bertone. This work has been supported by the US Department of Energy (FERMILAB-CONF-15-037-A) The authors wish to thank JACoW for their guidance in preparing this template.

References

L. Goodenough and D. Hooper (2009), 0910.2998.

V. Vitale, A. Morselli, and for the Fermi/LAT Collaboration, ArXiv e-prints (2009), 0912.3828.

N. Gehrels and P. Michelson, Astroparticle Physics **11**, 277 (1999).

D. Hooper and L. Goodenough, Phys.Lett. **B697**, 412 (2011), 1010.2752.

A. Boyarsky, D. Malyshev, and O. Ruchayskiy, Phys.Lett. **B705**, 165 (2011), 1012.5839.

D. Hooper and T. Linden, Phys.Rev. **D84**, 123005 (2011), 1110.0006.

K. N. Abazajian and M. Kaplinghat, Phys.Rev. **D86**, 083511 (2012), 1207.6047.

O. Macias and C. Gordon, Phys.Rev. **D89**, 063515 (2014), 1312.6671.

K. N. Abazajian, N. Canac, S. Horiuchi, and M. Kaplinghat (2014), 1402.4090.

T. Daylan, D. P. Finkbeiner, D. Hooper, T. Linden, S. K. N. Portillo, et al. (2014), 1402.6703.

B. Zhou, Y.-F. Liang, X. Huang, X. Li, Y.-Z. Fan, et al. (2014), 1406.6948.

C. Gordon and O. Macias, Phys.Rev. **D88**, 083521 (2013), 1306.5725.

D. Hooper and T. R. Slatyer, Phys.Dark Univ. **2**, 118 (2013), 1302.6589.

W.-C. Huang, A. Urbano, and W. Xue (2013), 1307.6862.

D. Hooper, I. Cholis, T. Linden, J. Siegal-Gaskins, and T. Slatyer, Phys.Rev. **D88**, 083009 (2013), 1305.0830.

F. Calore, M. Di Mauro, and F. Donato (2014a), 1406.2706.

I. Cholis, D. Hooper, and T. Linden (2014), 1407.5625.

J. Petrovic, P. D. Serpico, and G. Zaharijas (2014a), 1411.2980.

E. Carlson and S. Profumo (2014), 1405.7685.

J. Petrovic, P. D. Serpico, and G. Zaharijas (2014b), 1405.7928.

F. Calore, I. Cholis, and C. Weniger (2014b), 1409.0042.

F. Calore, I. Cholis, C. McCabe, and C. Weniger (2014c), 1411.4647.

M. Ackermann et al. (Fermi-LAT Collaboration), Astrophys.J. **750**, 3 (2012), 1202.4039.

G. Dobler, D. P. Finkbeiner, I. Cholis, T. R. Slatyer, and N. Weiner, Astrophys.J. **717**, 825 (2010), 0910.4583.

M. Su, T. R. Slatyer, and D. P. Finkbeiner, Astrophys. J. **724**, 1044 (2010), 1005.5480.

A. A. Abdo et al. (Fermi LAT) (2011), 1108.1435.

A. Franckowiak, *Spectrum of the fermi bubbles* (2013).

M. Ackermann, *Intensity and origin of the extragalactic gamma-ray background* (2012).

VERITAS Observations of the Galactic Center Ridge

A. W. Smith for the VERITAS Collaboration*
University of Maryland, College Park, College Park, MD, 20742 USA
NASA Goddard Space Flight Center, Greenbelt, MD, 20771, USA
**veritas.sao.arizona.edu*

Due to its extraordinarily high concentration of known relativistic particle accelerators such as pulsar wind nebula, supernova remnants, dense molecular cloud regions, and the supermassive black hole (Sgr A*); the center of the Milky Way galaxy has long been an ideal target for high energy (HE, 0.1-100 GeV) and very high energy (VHE, 50 GeV-50 TeV) gamma-ray emission. Indeed, detections of Sgr A* and other nearby regions of gamma-ray emission have been reported by EGRET and Fermi-LAT in the HE band, as well as CANGAROO, Whipple, HESS, VERITAS, and MAGIC in the VHE band (see [1] for a summary). Here we report on the results of extended observations of the region with VERITAS between 2010-2014. Due to the visibility of the source for VERITAS in the Northern Hemisphere, these observations provide the most sensitive probe of gamma-ray emission above 2 TeV in one of the most complicated and interesting regions of our home galaxy.

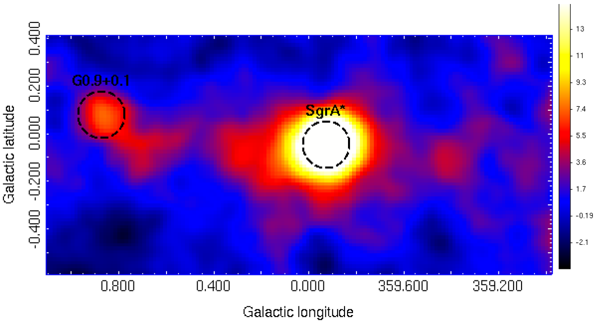

Figure 1: The VERITAS 2D significance map of the Galactic Center Ridge, smoothed with the 0.12^0 PSF of the instrument for these observations. The central source is saturated due to high significance. Also shown in black dashed circles is the VERITAS PSF for the observations.

1. THE GALACTIC CENTER RIDGE

The Galactic Center region is perhaps one of the most interesting local regions for study in the very high energy (>100 GeV) gamma-ray band. This is primarily due to its high concentration of star forming regions, pulsar wind nebulae, supernova remnants, and of course the central accelerator Sgr A*; all of which are known sources of VHE gamma rays. The region has been studied extensively in both the TeV band, as well as the GeV band with Fermi-LAT [refs]. Due to its high density of possible gamma-ray sources, the confirmed number of individual sources (point or extended) is relatively low (<5), with a very large proportion of gamma-ray emission in the region coming from either unresolved point sources, or a diffuse, extended component. Observations of this region with HESS [refs] reveal a distinct band of emission stretching along the central region of the plane; this emission seemingly correlated with dense molecular cloud regions. As this diffuse component is assumed to be generated from cosmic ray interactions with the molecular clouds, the study of this region in the TeV band also allows for a characterization of the cosmic ray flux near the Galactic Center.

In addition to the conventional gamma-ray sources in the Galactic Center, this region is also believed to be the closest, densest concentration of particle dark matter in our local universe. If the lightest supersymmetric particle (χ, or the neutralino) is indeed the correct explanation for particle dark matter, the Galactic Center should present a flux of GeV-TeV gamma rays due to $\chi\chi$ self-annihilations. While this flux is model dependent, some dark matter models place it within the sensitivity of current detectors, while many more will be probed by the upcoming CTA observatory. Regardless, the principal limiting factor in the use of observations of the Galactic Center for constraining dark matter is the poorly understood nature of the conventional gamma-ray sources in the region. Therefore, a better understanding of the gamma-ray source population in the Galactic Center can also provide insight into indirect searches for particle dark matter.

In this proceeding we present preliminary results from the VERITAS observations of the Galactic Center region in the >2 TeV regime. These results confirm many of the previous HESS results in the >300 GeV region, but due to the higher energy range of the VERITAS observations, also provide a unique window on the highest energy gamma-ray emission in the Galactic Center region.

2. VERITAS OBSERVATIONS

The Very Energetic Radiation Imaging Telescope Array System (VERITAS), located in Southern Arizona (USA) is an array of four 12-meter imaging atmospheric Cherenkov telescopes (IACTs) providing excellent angular resolution and sensitivity to cosmic TeV sources. In normal operations (i.e. high elevation observations), VERITAS is sensitive in the energy range of 80

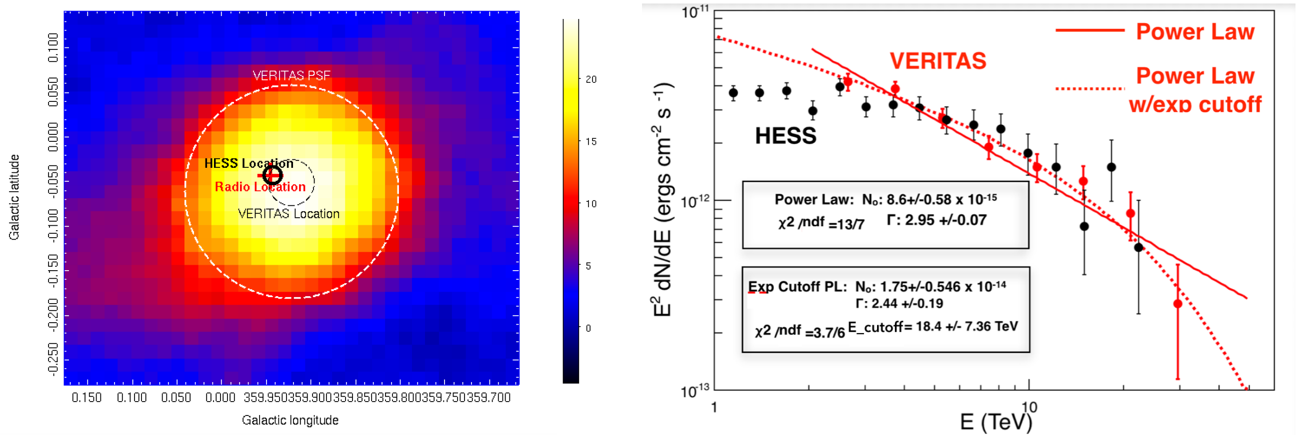

Figure 2: The smoothed VERITAS 2D significance map of the Sgr A* (left). The right panel shows the VERITAS (red) and HESS (black) spectral points derived from the Sgr A* observations along with the fits described in the text. Note, the fits were made to VERITAS points only.

GeV to 50 TeV and has the capability to detect a 1% Crab Nebula flux in approximately 25 hours of observations. VERITAS has an energy resolution of 15% at 1 TeV and a typical angular resolution of <0.1^0.

Between 2010-2014, VERITAS accrued ~85 hours of quality selected, livetime observations of the Sgr A* region. Due to the Northern Hemisphere location of VERITAS, the Sgr A* region never transits above 30^0 elevation. This large zenith angle to the source results in a higher energy threshold (>2 TeV) for VERITAS observations. Normally, such observations would result in very poor angular resolution for ground based gamma-ray telescopes. However, using a specialized analysis technique (see [2][3][4]) in which the displacement between the center of gravity of a parameterized Hillas ellipse and the location of the shower position within the camera plane is utilized. This displacement or “DISP” method results in enhanced angular resolution at large zenith angle observations where small parallactic displacements between shower images would normally degrade angular resolution significantly (see [1] for a description).

3. RESULTS

3.1. Sgr A*

In the 85 hours of observations taken between 2010-2014, VERITAS strongly detected gamma-ray emission above 2 TeV from Sgr A*. A total of 735 excess gamma-ray events were detected by VERITAS, resulting in a detection significance of >25σ). The resulting 2 dimensional significance map, as well as the derived energy spectrum are shown in Figure 2.

The VERITAS position of the Sgr A* is in agreement with both the radio and HESS source locations [5]. The differential energy spectrum is fit by both a simple power law of the form $N_0 \times (E/10\ \mathrm{TeV}^{-\Gamma})$ as well as a power law with an exponential cutoff of the form $N_0 \times e^{(-E/E_{cutoff})} \times (E/10\ \mathrm{TeV})^{-\Gamma}$ We find that the exponential cutoff power law model provides a better fit (reduced $\chi2$ of 0.6 vs 1.8). The cutoff energy of 18 (+/-7.4) TeV is higher than that reported in [6]. Since VERITAS will continue observing the Sgr A* region at energies above 2 TeV, VERITAS will be able to more accurately constrain the cutoff energy of the Sgr A* spectrum a crucial parameter to physical models of emission from the source in both hadronic/leptonic as well as plerionic/accretion scenarios.

3.2. G0.9+0.1

The composite SNR (X-ray plerionic core + radio shell) has previously been detected by the HESS collaboration [7] as a relatively weak source (2% of the Crab Nebula flux above 300 GeV). The current VERITAS observations also detect G0.9+0.1 as a significant TeV source above 2 TeV with a total of 134 excess counts, corresponding to a >7σ source detection. The VERITAS source position for G0.9+0.1 is consistent with both the plerionic core as well as the HESS location. The derived energy spectrum of the source is well fit by pure power law with an index of Γ= 2.3+/-0.1, with no indications of an energy cutoff up to >25 TeV.

3.3 Ridge Emission

In [5], the HESS collaboration presented the residual maps (i.e. after subtracting known point sources within the field of view) of the >300 GeV

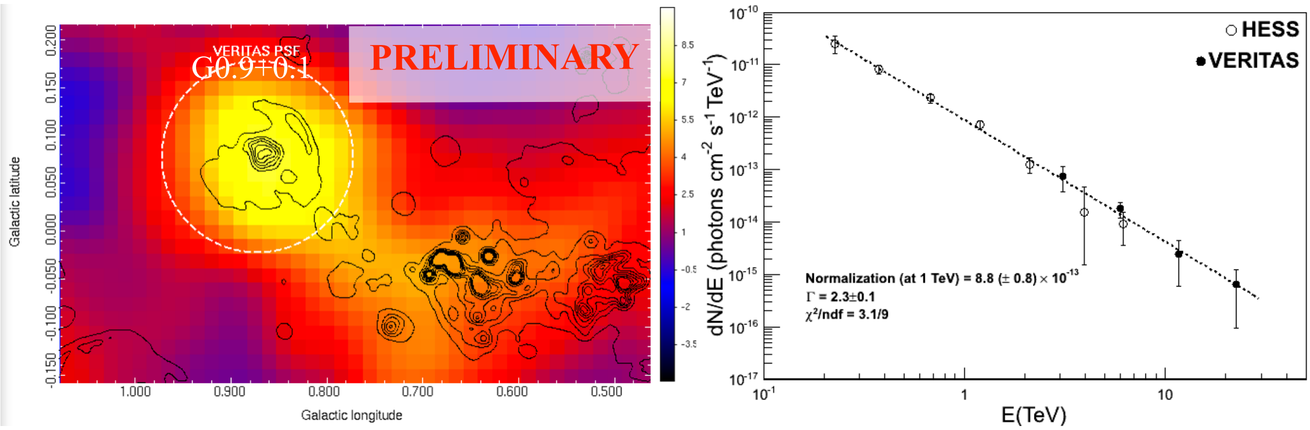

Figure 3: The smoothed VERITAS 2D significance map of the G0.9+0.1 region along with ARCO 20cm radio contours (left). Also shown (right) is the VERITAS differential energy spectrum of G0.9+0.1 along with the HESS spectral points from [7].

emission from the Galactic Plane. These residual maps revealed a complicated network of diffuse gamma-ray emission within the central 3^0 of the Galactic Plane. When plotted along with the CO emission contours (see [5]), the HESS emission appears correlated with dense molecular cloud regions (bright in CO line emission). However, given the complicated nature of the region, this measurement was unable to rule out the possibility of a significant contribution to the TeV flux coming from unresolved point sources.

In Figure 4 is shown the VERITAS >2 TeV residual significance maps of the inner Galactic Center region after the point source emission from Sgr A* and G0.9+0.1 has been removed. It is clear from these maps that a diffuse component of TeV emission is present above 2 TeV both directly adjacent to Sgr A*, as well as extending ~0.80 to the left of Sgr A* along the Galactic plane.

Figure 4 also shows the HESS 300, 325, and 350 excess event contours (green), the ARCO 20cm radio emission contours (black), and the point sources from the 3FGL catalog (blue). As can be these maps that a diffuse component of TeV emission is present above 2 TeV both directly adjacent to, and extending $\sim 0.8^0$ in Galactic longitude to the left of Sgr A*. seen there are direct correlations with both the HESS >300 GeV emission, as well as co-locations of 3FGL sources [8]. While there appears to be a good correspondence between the 20cm emission at the

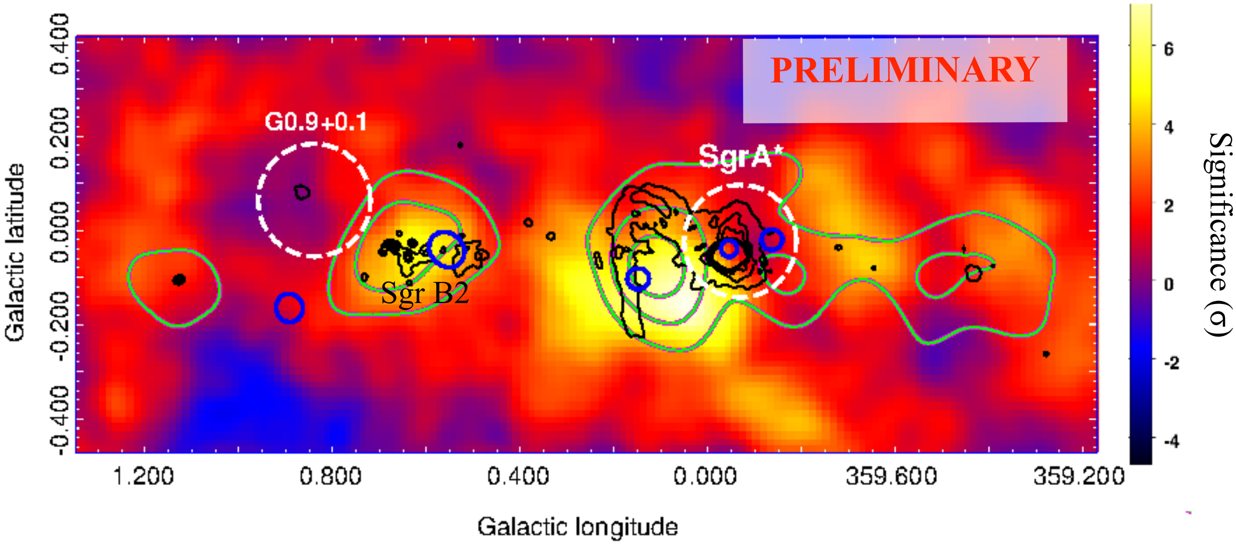

Figure 4: The smoothed VERITAS 2D residual significance map after emission from both Sgr A* and G0.9+0.1 have been removed (white dashed circles). Blue circles represent Fermi-LAT point sources from the 3FGL catalog, 20cm radio contours (ARCO) are shown in black, and the HESS >300 GeV excess event contours are shown in green.

location of the Sgr B2 star forming region, the correlation between radio emission and > 2 TeV emission directly adjacent to the location of Sgr A* is less obvious. An upcoming publication will provide further examination of these residual maps.

References

[1] A. Archer et al. , 2014 *ApJ* 790 149
[2] Kosack, K.P., Badran, H.M., Bond, I.H., et al. 2004, ApJ, 608, 97
[3] Domingo-Santamaria, E., Flix, J., Rico, J., Scalzotto, V., Wittek, W. 2005,
Proc. of the ICRC, 5, 363
[4]_Buckley, J.H., Akerlof, C.W., Carter-Lewis, D.A., et al. 1998, A&A, 329, 639
[5] Aharonian, F.A., et al. 2006a, Nature, 439, 695
[6] Viana, A., & Moulin, E. 2013, Proceedings of the 33rd ICRC.
[7] F. Aharonian et al., Astron. Astrophys. 432 (2005) L25-L29
[8] F. Acero et al., Submitted to ApJ Supplements, arxiv/1501.02003

The *Fermi*-LAT model of interstellar emission for standard point source analysis

Jean-Marc Casandjian for the *Fermi* Large Area Telescope Collaboration
Laboratoire AIM, CEA-IRFU/CNRS/Université Paris Diderot,
Service d'Astrophysique, CEA Saclay, 91191 Gif sur Yvette, France[*]

(Dated: February 26, 2015)
(Rsion 2)

We describe the development of the model for interstellar γ-ray emission that is the standard adopted by the LAT team and is publicly available. The model is based on a linear combination of templates for interstellar gas column density and for the inverse Compton emission. The spectral energy distributions of the γ-ray emission associated with each template are determined from a fit to 4 years of *Fermi*-LAT data in 14 independent energy bins from 50 MeV to 50 GeV. We fit those distributions with a realistic model for the emission processes to extrapolate to higher energies. We also include large-scale structures like Loop I and the *Fermi* bubbles following an iterative procedure that re-injects filtered LAT counts residual maps into the model. We confirm that the cosmic-ray proton density varies with the distance from the Galactic center and find a continuous softening of the proton spectrum with this distance. We observe that the *Fermi* bubbles have a shape similar to a catenary at their bases.

I. PRINCIPLE

This paper describes the model of interstellar emission recommended for point source analyses of the *Fermi*-LAT Pass 7 reprocessed data (P7REP) [1]. The high-energy interstellar γ-ray emission is produced by the interaction of energetic cosmic rays (CRs) with interstellar nucleons and photons. The decay of secondary particles produced in hadron collisions, the inverse Compton scattering of the interstellar radiation field (ISRF) by electrons and their bremsstrahlung radiation emission in the interstellar medium (ISM) are the main contributors to the Galactic diffuse emission. The interstellar emission model is based on a template method: we assumed that the diffuse γ-ray intensity at any energy can be modeled as a linear combination of maps or templates of hydrogen column-density (I_H) and a predicted inverse Compton (IC$_p$) intensity map (I_{IC_p}) calculated by GALPROP [26]. The intensity of each template in each energy bin is determined from a fit to the P7REP Clean class events from the first 4 years of the mission binned into 14 equal logarithmic intervals from 50 MeV to 50 GeV.

In addition to the interstellar emission, the LAT detects γ rays from other sources that need to be taken into account in the analysis. We do this by adding dedicated components to account for a residual intensity of the Earth limb (I_{limb}), for point and extended γ-ray sources (I_{ext}), and for the emission from the Sun and the Moon (I_{sun_moon}). Finally we add an uniform intensity template (I_{iso}) to account for unresolved γ-ray sources and CR contamination in the data. For a given counts map pixel and energy band we calculated the predicted number of counts (N_{pred}) detected by *Fermi*-LAT as:

$$\begin{aligned} N_{pred}(E) = & \sum_{i=H\ templates} q_i(E)\widetilde{I}_{H_i} + N_{IC}(E)\widetilde{I}_{IC_p}(E) \\ & + N_{iso}(E)\widetilde{I}_{iso} + N_{LoopI}(E)\widetilde{I}_{LoopI} + \sum_{i=patch} N_{patch_i}(E)\widetilde{I}_{patch_i} \\ & + N_{limb}(E)\widetilde{I}_{limb} + \sum_{i=point\ src} N_{pt_i}(E)\widetilde{\delta}(i) \\ & + \sum_{i=extend\ src} N_{ext_i}(E)\widetilde{I}_{ext_i} + \widetilde{I}_{sun\_moon}(E) \end{aligned} \tag{1}$$

where E is the energy. We use the notation $\widetilde{I}$ to denote predicted counts maps resulting from the convolution by the LAT PSF of the product of an intensity map I and the instrument exposure and pixel solid angle. In Equation 1 each template of hydrogen column density I_H is multiplied by its associated hydrogen γ-ray emissivity q. The factors N_{IC}, N_{limb}, and N_{iso} represent the renormalization factors associated to I_{IC_p}, I_{limb}, and I_{iso}. I_{sun_moon} is kept fixed in the analysis. Equation 1 also incorporates coefficients associated to extended sources (N_{ext}) and to point sources (N_{pt}) represented by the Dirac δ function. I_{LoopI} and N_{LoopI} account for local IC emission from Loop I. For unmodeled excesses, we also introduced in Equation 1 patches of uniform intensity (I_{patch}) with normalization factors N_{patch}. The procedure behind the construction of our interstellar emission model was to find templates for the gas column density and IC$_p$, fit Equation 1 to *Fermi*-LAT counts maps with q, N_{IC}, N_{iso}, N_{LoopI}, N_{patch}, N_{limb}, N_{pt} and N_{ext} left free to vary in each energy bin and to extrapolate the coefficients related to the hydrogen templates and IC_p outside the energy range of the fit.

---

[*] Electronic address: casandjian@cea.fr

II. TEMPLATE DESCRIPTION

About 99% of the ISM mass is gas and about 70% of this mass is hydrogen. The hydrogen gas exists in the form of neutral atoms in cold and warm phases, in the form of neutral molecules (H_2), and in an ionized state. Helium and heavier-elements are assumed to be uniformly mixed with the hydrogen.

H I is traced by its radio 21-cm line radiation; we derived its column density NH I from the 21-cm line radiation temperatures under the assumption of a uniform spin (excitation) temperature (T_S). The 21-cm all-sky Leiden-Argentine-Bonn (LAB) composite survey of Galactic H I [2] is used to determine the all-sky distribution of NH I. We derived NH I from the observed brightness temperature using a T_S of 140 K which provided the best fit to the *Fermi*-LAT data in regions with $90° \leq l \leq 270°$ and $|b| < 70°$. Because the CR flux varies with Galactocentric distance and Equation 1 is valid only if the CR flux is uniform in each template, we partitioned the Galaxy into Galactocentric annuli and assign to each annulus the corresponding H I column density.

The molecular hydrogen which does not have a permanent dipole moment, generally can not be observed directly in its dominantly cold phase. The observation of molecular gas relies on other molecules and especially on the 2.6-mm J=1→0 line of carbon 12 monoxide (CO). It is common to assume that the H_2 column density is proportional to the velocity-integrated CO brightness temperature $W(\mathrm{CO})$. The molecular hydrogen-to-CO conversion factor is expressed as $X_{CO}=N(\mathrm{H_2})/W(\mathrm{CO})$. We obtained the $W(\mathrm{CO})$ spatial distribution from the Center for Astrophysics composite survey [3]. We derived Galactocentric annuli from radial CO velocities in a similar way as for H I.

Unfortunately CO is not a perfect tracer of H_2. Moreover NH I derived under the hypothesis of a uniform T_S=140 K is likely to be biased in lines of sight crossing regions of different T_S. Those approximations lead to large underestimates of the quantities of gas called dark neutral medium (DNM) in our Galaxy [4–6]. Since dust is well mixed with gas, we accounted for this gas by including in our model a template related to the total dust column density. We derived a DNM template as the residual map obtained after subtracting from the dust optical depth map of the [7] parts linearly correlated with the NH I and $W(\mathrm{CO})$ annuli. Subtracting the correlated parts from the dust optical depth map revealed coherent structures across the sky both in the positive and in the negative residuals. The negative residuals are likely related to regions in which an average T_S of 140 K is too low, and thus NH I is overestimated. In this paper we call this map the “NH I correction map”. The positive residuals reveal gas in addition to that traced by NH I and $W(\mathrm{CO})$. Here we associated this excess map to the DNM distribution even if it also includes regions in which an average T_S of 140 K is too high and potentially incorporates also ionized hydrogen that might be mixed with dust.

Due to their proximity, CR protons and electrons interacting with the Earth limb make the Earth by far the brightest γ-ray source in the sky [8]. The *Fermi* standard observational strategy is such that the Earth is not directly in the field of view of the LAT. However a large number of limb photons entering the LAT at large zenith angles are still detected. We constructed a simple template based on the subtraction of the counts map derived with a zenith angle cut at 100° to a counts map restricted to angles above 80°.

In fitting the model for interstellar diffuse emission we included templates for 21 extended sources and 2179 point sources at positions listed in a first iteration of the third *Fermi*-LAT catalog (3FGL) [9] derived with a preliminary iteration of the Galactic diffuse emission model. We also incorporated in the fit the γ-ray emission from the Sun and the Moon. Their intensities were not allowed to vary during the γ-ray template fit procedure.

While the different gas column-density maps offer templates for photons originating mainly from π^0-decay and Bremsstrahlung emission, there is no direct observational template for the IC emission. Instead it must be calculated. For that we used the prediction from the GALPROP code with GALDEF identification $^{S}Y^{Z}6^{R}30^{T}150^{C}2$, a representative diffusive reacceleration model described in [10].

Excesses originating for example from Loop I [10, 11] or the *Fermi* Bubbles [12, 13] are observed when we compared a preliminary template model derived only from the templates mentioned above to the *Fermi*-LAT observations. There is no accurate a priori template for the γ-ray emission of those large structures. Not including them in Equation 1, as well as other structures that we observed in the residuals at lower latitudes, will strongly bias the fit. To reduce this bias we roughly modeled the strongest emitting region of Loop I with a selected region of the 408 MHz radio continuum intensity from the survey of [14]. To account for excesses not correlated with radio templates we introduced ad hoc patches in Equation 1. The patches are regions of spatially uniform intensity whose shapes encompass regions with an excess of photons of at least about 20% compared to the preliminary model. We added 4 patches including a large rounded shape filling Loop I and three smaller patches closer to the Galactic plane. Additionally, we have created two patches for the *Fermi* bubbles. We also made a disk-shaped patch around the Cygnus region. We used the patches to derive the γ-ray emissivities of the hydrogen that we deduced from the fit of Equation 1 to the *Fermi*-LAT data. But the patches do not provide an accurate enough description of the interstellar emission to be added to the final interstellar model. Instead we have incorporated a filtered γ-ray residuals map obtained with the patches removed as described below.

III. GAMMA-RAY FIT AND EMISSIVITY INTERPRETATION

We did not fit Equation 1 to the *Fermi*-LAT all-sky at once, we applied latitude and longitude cuts to define subsets corresponding to regions where some templates are prominent. We fitted the local atomic hydrogen in the whole longitude range but away from the Galactic plane at latitudes $|b| > 10^\circ$. We lowered this latitude cut for local CO annulus to 4° and to 3° for the NH I correction maps and DNM template obtained from the negative and positive dust residual. For the annuli with Galactocentric radii larger than 10 kpc (H I and CO outer Galaxy annuli) we applied only a longitude cut corresponding to $90^\circ < l < 270^\circ$. For those 4 independent fits we left all the template normalization coefficients of Equation 1 free to vary in each of the 14 energy bins except for the Sun and the Moon templates.

The inner Galactic region is particularly difficult to model. The gas column densities are affected by optical depth correction, self-absorption of H I and limited kinematic distance resolution at low longitudes. Additionally γ-ray point and extended sources are numerous, a DNM template is lacking, and the IC$_p$ morphology is uncertain. Possibly for one of those reasons, or because of an excess of CR or an incorrect modeling of a foreground emission, we observed a broad unmodeled emission (referred to as "extra emission" in the rest of the text) in the direction of the inner Galaxy with a maximum in the first Galactic quadrant at a longitude of ∼30°. Up to this stage this emission was approximately accounted for by patches of uniform intensity. At this point we removed the patches in Equation 1 and we modeled the extra emission with a two-step iterative procedure:

In the first step we fitted Equation 1 to the *Fermi*-LAT observations excluding $5^\circ < l < 90^\circ$ and $|b| < 20^\circ$. We obtained a residual map with some emission not accounted for, we selected the positive residuals, we smoothed them with a 2-dimensional Gaussian symmetric kernel of 3° FWHM and re-injected them in Equation 1 as a template for another iteration. We iterated three times up to the point where the positive residual intensities approximately equalled the intensities of negative ones. We obtained a first set of γ-ray emissivities in the inner H I and CO annuli. Due to the difficulty of modeling the extra emission we reduced the number of free templates and continued the procedure with a single hydrogen template for each annulus: NH=NH I+2X_{CO}W(CO). We deduced the X_{CO} conversion factor as half the ratio between the emissivity associated to the H I template and the one associated to the CO one. We repeated the fitting procedure with the single NH for inner templates iteratively adding the positive residuals of the fit to the extra emission template. In this way we obtained a first version of the inner template emissivity and a template for the extra emission and large scale structures.

For the second step we fitted the whole Galaxy including the first quadrant with all the templates parameters free to vary. We added to Equation 1 the template for the extra emission obtained in step one. We repeated the iteration and derived the final emissivities per hydrogen atom in the inner annuli. We also obtained a template corresponding to the extra emission and large scale structures.

Figure 1 shows the differential γ-ray emissivity per hydrogen atom $\frac{dq}{dE} = q/\Delta E$, where ΔE is the energy bin width, for the 9 Galactocentric annuli and the central molecular zone (CMZ) region scaled to emissivity per hydrogen atom assuming X_{CO}=0.5×10^{20} cm^2 (K km s^{-1})$^{-1}$. To derive an interstellar diffuse emission model at energies up to 600 GeV we fitted the emissivities with a γ-ray production model of bremsstrahlung emission and hadronic decay and used this model for the extrapolation. We fitted the differential emissivity of each annulus between 200 MeV and 30 GeV with a parametrized proton flux and a γ-ray production cross-section based on [15]. We adopted a spectral model for CR protons of the form: $A\beta^{P_1}R^{-P_2}$ where $\beta = v/c$, R is the rigidity of the proton and (A, P_1, P_2) are free parameters [16] and folded this proton functional with the γ-ray production cross-section. *Fermi*-LAT detects γ rays resulting not only from proton-proton collisions but also from the interaction of heavier CR or ISM nuclei. We used the results of [17] to scale the proton-proton cross-section to the nucleus-nucleus cross-section taking into account the ISM and CR composition. The γ rays detected by $Fermi$ at energies relevant for this work are also produced by bremsstrahlung of electrons and positrons. We accounted for this contribution using an electron spectral form with free parameters and the cross section of [18]. We fitted the bremsstrahlung emission together with the hadron decay component first to the local emissivities. We derived a proton functional parameter P_1 and a bremsstrahlung contribution that we assumed constant for the other annuli. We then fitted the other annuli with only two parameters: the proton spectrum normalization A and proton spectral index P_2. In Figure 1 the emissivity resulting from this fit is represented by a dotted line.

To check the validity of the γ-ray template fitting procedure we studied the coherence of the resulting proton spectral parameters between the different annuli. In Figure 2 we plotted the proton spectral index P_2 versus the Galactocentric distance of the annulus. We observe a continuous softening of the proton spectra with the distance from the center of the

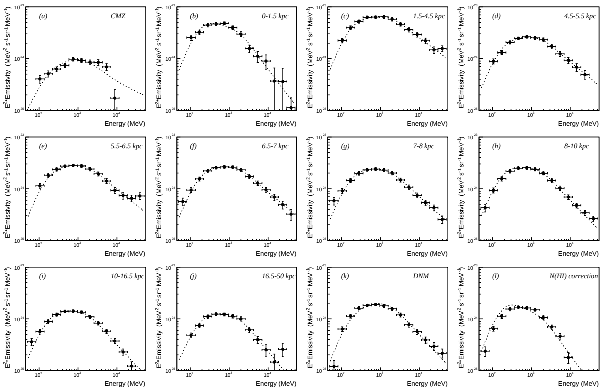

FIG. 1: (a)-(j): The γ-ray emissivity per hydrogen atom in H I and H_2 phases for the CMZ and the 9 Galactocentric annuli. In order to extrapolate to higher energies we fitted a model based on proton density and production cross-section (dashed line). We applied the same procedure for the DNM (k) and the NH I correction (l) maps. We did not display in the graph points with emissivities lower than $10^{-25} MeV^2 s^{-1} sr^{-1} MeV^{-1}$ nor points corresponding to the lowest energy bin that were also not used in the analysis.

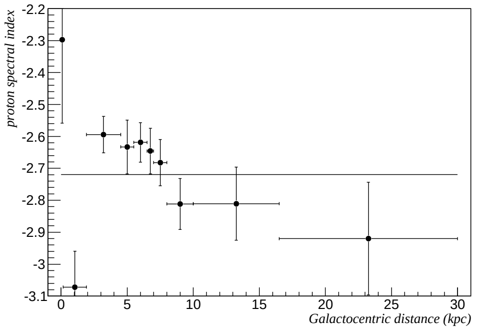

FIG. 2: Proton spectrum spectral index P_2 versus the distance from the Galaxy center. The spectral indexes are extracted from the fit of the γ-ray emissivities for various hydrogen Galactocentric annuli. We did not include any systematic uncertainty in the spectral index error bar. The Galactocentric distance error bar represents the radial width of the annuli. For comparison we draw in solid line the spectral index for proton energies above 100 GeV extracted from the GALPROP model $^SY^Z6^R30^T150^C2$ [10].

Galaxy. The spectral indices of protons extracted from the emissivities measured in the first annulus and the CMZ correspond to a region extending ±10° from the Galactic center where confusion with other templates or point sources is possible. It might also be contaminated by the soft extra emission not totally suppressed by the iterative fit procedure.

Figure 3 shows the radial distribution of proton density integrated above 10 GeV evaluated from the present work. We observe a steep CR density increase around 3 kpc. Again, part of this increase can be due to a contamination by the extra emission of the emissivity for the annulus extending to ±30° in longitude. We also observe that the inferred CR proton density in the CMZ is about 4 times lower than the local one (about 8 times lower if we assume the same X_{CO} as for the local annuli). [19] suggested a lower X_{CO} to explain the anomalously low γ-ray production compared to the CO column density in COS-B. Again, caution should be used to interpret the proton density in the CMZ given possible confusion with point sources or with the extra emission, especially at low energies. In Figure 3 we also show the CR proton density predicted by GALPROP $^SY^Z6^R30^T150^C2$. We note a reasonable agreement with the ones derived from γ-ray observations, however beyond 5 kpc the predicted proton density gradient is steeper than the observed one [20–23]. GALPROP also predicts a broader distribution around 3 kpc.

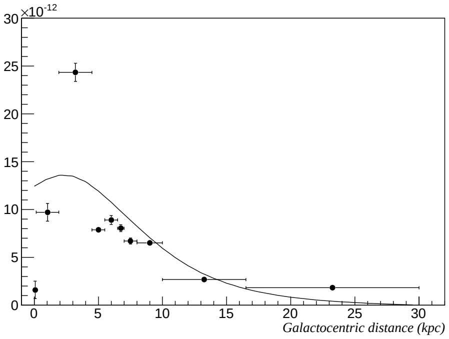

FIG. 3: Integrated proton flux above 10 GeV versus Galactocentric distance. For comparison we included the integrated proton flux from the GALPROP $^SY^Z6^R30^T150^C2$ model (solid line). We did not include any systematic uncertainty in the integrated proton flux error bar. Those systematic uncertainties could be significant for example close to the GC where the integrated proton flux depends on the X_{CO} ratio used in the analysis.

We applied the same fit method for the coefficients associated with the DNM and NH I correction templates obtained from the positive and negative dust residual. In the case of the NH I correction template we left all the spectral parameters for electrons and protons free to obtain a better fit to the data. Figure 1 (k) and (l) show the emissivities associated with the DNM and the NH I correction templates together with the fit. To display in this graph the emissivities inferred from the optical depth map in the same units as those from the column density maps, we divided the measured and fitted emissivities by an arbitrary gas-to-dust ratio of 4×10^{21} cm^{-2} mag^{-1}.

From the fit of Equation 1 we obtained a normalization factor N_{IC} continuously increasing from ~1 at 50 MeV to ∼2 at 2 GeV and then continuously decreasing back to ∼1 at 50 GeV. Above 50 GeV the LAT γ-ray statistics is low causing a correlation of the IC template with the isotropic emission in the fit. We decided to rely on GALPROP predictions for the extrapolation to high energies and did not apply any scaling to I_{IC_p} for energies above 50 GeV.

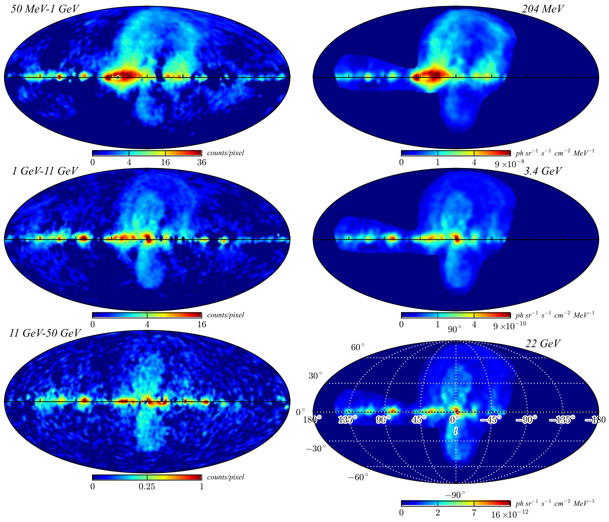

FIG. 4: Left column: Mollweide projection in Galactic coordinates of the *Fermi*-LAT counts map after subtracting point and extended sources, the limb and isotropic emission, and a conventional interstellar model based on fitted gas emissivities and scaled IC$_p$ only. The residual map is shown for three energy bands: 50 MeV–1 GeV (top), 1–11 GeV (middle), 11–50 GeV (bottom). We smoothed those three maps with a 2-dimensional symmetric Gaussian of 3° FWHM. Right: intensity of the modeled large scale emission RES_{IC} at energies: 204 MeV (top), 3.4 GeV (middle), 22 GeV (bottom). All the maps are displayed with a square root scaling and a pixel size of 0.25°.

IV. MODELING THE LARGE SCALE STRUCTURE AND THE EXTRA EMISSION

To include in our interstellar emission model the γ rays produced by phenomena that lack templates like the large scale structures, we first created a conventional interstellar emission model based on gas emissivities and IC obtained as described above. We added the sources from a preliminary version of the 3FGL catalog, the predicted Sun and Moon intensities and used an isotropic and limb normalization derived from the local H I annuli fit. Figure 4 (left column) shows the positive difference between the *Fermi*-LAT counts map and the counts map expected from this model integrated in three energy bands: 50 MeV-1 GeV, 1-11 GeV, and 11-50 GeV. As expected, since we did not include in the model any large structures nor patches, we observe positive counts residuals including the regions around Loop I and the *Fermi* Bubbles. We also observe the extra emission broadly distributed along the plane at longitudes less than 50° and to a lesser extent at longitudes around 315°. We also observe an extended excess of counts toward the Galactic center at the base of the *Fermi* bubbles. Figure 5 shows a closeup of the Galactic center region representing the difference between the *Fermi*-LAT counts integrated between 1.7 GeV and 50 GeV and those expected from the conventional model using only the determined gas emissivities and IC emission. To reduce the contrast due to the bright γ-ray emission of the Galactic plane, we divided this difference by the conventional model counts (Figure 5a) and by the square root of this number (Figure 5b,c,d). The fluxes of some preliminary 3FGL sources located in the Galactic ridge depend to some extent on the interstellar emission model, so a fraction of the interstellar emission can be incorrectly assigned to point sources. To avoid any bias we did not subtract them from the counts map in Figure 5a and 5b. They were subtracted in Figure 5c and 5d. We deduce from those plots that the bases of the *Fermi* bubbles have the form of a catenary in which the γ-ray emission is enhanced. We observe hints that this enhancement is perpendicular to the Galactic plane and originates from the γ-ray source located in the direction of the Galactic center. As pointed out by [12] the ROSAT all-sky survey [24] shows structures similar to the one of the *Fermi* bubbles. Figure 6 shows that the *Fermi* bubbles have a similar shape within 20° from the Galactic center in X and γ rays. We note that the X-ray detected by ROSAT are strongly absorbed at absolute latitudes of less that 2° which can produce the same artifacts as the use of an overestimated hydrogen emissivities for the inner annuli in the *Fermi*-LAT residual maps. Other extended excesses are present along the Galactic plane including in the Cygnus region. We did not observe strong negative residuals except in the direction of the Carina arm tangent where the model largely over-predicts the observations.

We chose to model those large scale and extra γ-ray emissions by assuming they all originate from IC interactions of a population of CR electrons with the cosmic microwave background radiation. The physical motivation behind the production of those γ rays in the energy range between 50 MeV and 50 GeV is not relevant if the resulting model is consistent with the data. For simplicity we favored a unique ISRF and γ-ray production process. We fitted in each pixel an electron spectral form so that the conventional model added to this IC emission reproduces the total counts of the pixel. In order to reduce in the modeled IC map the number of undetected point sources and small extended structures coming from the counts map, we transformed the spatial distribution of the electron spectral parameters into wavelets and filtered

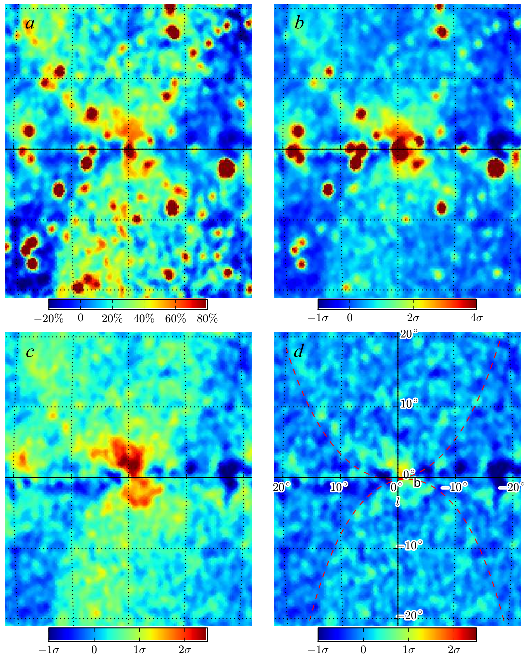

FIG. 5: Closeup of a region within 20° of the Galactic center showing the *Fermi*-LAT counts map integrated between 1.7 GeV and 50 GeV after subtracting a conventional model of interstellar emission made only of emission correlated with the gas and the IC_p. To reduce the contrast between the Galactic plane emission and higher latitudes, we display the residual in fractional units, dividing the residuals by the model (a), and in units of standard deviation, dividing the residuals by the square root of the model (b). In (c) we additionally subtracted the point and extended sources from a preliminary 3FGL list. In (d) we show the residual map with the large-scale emission modeled by RES_{IC} subtracted, it contains features smaller than the angular scale included in RES_IC. The red dashed lines correspond to the catenary function $10.5 \times (cosh((l-1)/10.5)-1)$ (north) and $-8.7 \times (cosh((l+1.7)/8.7)-1)$ (south) that reproduce approximately the edge of the bubbles for latitude below 20°. We smoothed the 4 maps with a Gaussian of 1° FWHM.

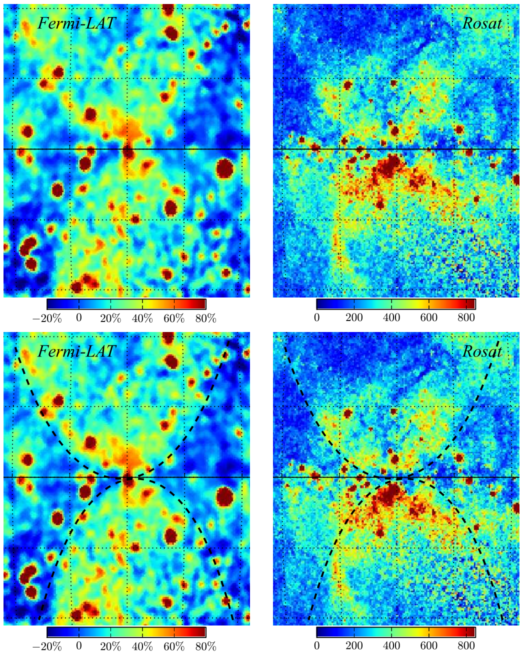

FIG. 6: Comparison between the *Fermi*-LAT residuals shown in Figure 5a and the ROSAT all-sky survey [24] for energies 0.73–2.04 keV. The ROSAT observations are displayed in 10^{-6} counts s^{-1} $arcmin^{-2}$. The second row shows the same plots as in the first row together with the catenary curves given in Figure 5.

out scales smaller than 2°. We created a spatial mask drawn by hand that encompasses only regions where the large-scale structures and extra emission is the largest. We call this masked and filtered emission RES_{IC} and show it in the right column of Figure 4 at energies approximately corresponding to the geometric average of the energy interval used to display the counts map of the left column. We observe a good agreement between the large-scale structures observed in the counts map and the one we have modeled. In Figure 5d we show the residual map integrated between 1.7 GeV and 50 GeV in the direction of the Galactic center when RES_{IC} is included in the model. The residual map is flat apart from some emission toward the Galactic center and the *Fermi* bubbles. This emission corresponds to the small scales filtered out in the wavelet decomposition.

V. RESULTING MODEL OF GALACTIC INTERSTELLAR EMISSION

We derived a final model for the interstellar emission from the sum of the modeled differential gas γ-ray emissivities ($\frac{dq_{fit}}{dE}$), the renormalized I_{IC_p}, and from the large-scale and extra emission RES_{IC} (Equation 2).

$$\begin{aligned} I(E,l,b) = & \sum_{i=HI,H_2,DNM} \frac{dq_{fit_i}}{dE}(E) I_{H_i}(l,b) \\ & + N_{IC}(E) I_{IC_p}(E,l,b) + RES_{IC}(E,l,b) \end{aligned} \tag{2}$$

We compared the *Fermi*-LAT counts map integrated between 360 MeV and 50 GeV (Figure 7, top) to the one predicted by the interstellar emission model given by Equation 2 combined with the ones originating from non-Galactic interstellar origin (Figure 7, middle) . We derived the residual map (Figure 7, bottom) by subtracting the model from the data and normalizing by the square root of the model to enhance

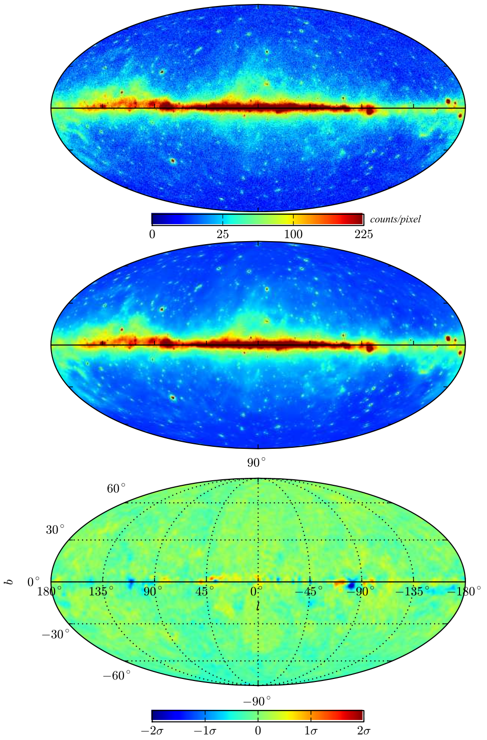

FIG. 7: Top: All-sky Mollweide projection for 4 years of *Fermi*-LAT γ-ray counts in the 0.36–50 GeV energy band. Middle: counts prediction in the same energy range based on the interstellar emission model combined with modeled point and extended sources (including the Sun and the Moon), the Earth limb emission and the isotropic emission. Both maps are displayed with square root scaling to enhance emission away from the plane. Bottom: residual map in units of standard deviations after smoothing with a Gaussian of 2° FWHM. The pixel size for the three maps is 0.25°.

deviations above statistical fluctuations. The overall agreement between observations and model is very good, partly because some excesses we observed were modeled and re-injected into the interstellar model.

We derived from Equation 2 a model of the interstellar emission available at the *Fermi* Science Support Center (FSSC) website as a FITS file named *gll_iem_v06.fit*. We resampled all the maps to a 0.125° grid. The FITS file comprises 30 logarithmically-spaced energy bins between 50 MeV and 600 GeV. It gives the differential intensity of the Galactic diffuse emission model in photons sr^{-1} s^{-1} cm^{-2} MeV^{-1}. This model tuned to LAT data is not corrected for the energy dispersion, it can then be used directly with LAT data. The Pass 7_V15 IRFs (P7REP_CLEAN_V15) are the recommended set for Pass 7 reprocessed data and this model. The difference with the Pass 7_V10 used for this fitting mainly resides in an improved Monte Carlo PSF and in an updated fitting procedures to determine the parameters for the LAT effective area representation. Those minor differences modify the exposure but not the reconstructed LAT events. The minimum ratio of exposure maps (V15/V10) is 0.98 at 50 MeV and the maximum 1.05 at 1 GeV. In order to use the model with the final IRFs we rescaled the intensity by the ratio of the exposure maps evaluated for each of the 30 energy bins of the Galactic diffuse emission model. The model is then intended for use with the instrument response functions versions P7REP_SOURCE_V15, P7REP_CLEAN_V15, and P7REP_ULTRACLEAN_V15.

Acknowledgments

The *Fermi* LAT Collaboration acknowledges generous ongoing support from a number of agencies and institutes that have supported both the development and the operation of the LAT as well as scientific data analysis. These include the National Aeronautics and Space Administration and the Department of Energy in the United States, the Commissariat à l'Energie Atomique and the Centre National de la Recherche Scientifique / Institut National de Physique Nucléaire et de Physique des Particules in France, the Agenzia Spaziale Italiana and the Istituto Nazionale di Fisica Nucleare in Italy, the Ministry of Education, Culture, Sports, Science and Technology (MEXT), High Energy Accelerator Research Organization (KEK) and Japan Aerospace Exploration Agency (JAXA) in Japan, and the K. A. Wallenberg Foundation, the Swedish Research Council and the Swedish National Space Board in Sweden.

Additional support for science analysis during the operations phase is gratefully acknowledged from the Istituto Nazionale di Astrofisica in Italy and the Centre National d'Études Spatiales in France.

Some of the results in this paper have been derived using the HEALPix [25] package.

---

[1] J. Bregeon, E. Charles, and M. W. for the Fermi-LAT collaboration, arXiv **1304**, 5456 (2013)

[2] P. M. W. Kalberla, W. B. Burton, D. Hartmann, E. M. Arnal, E. Bajaja, R. Morras, and W. G. L. Pöppel, A&A **440**, 775 (2005)

[3] T. M. Dame, D. Hartmann, and P. Thaddeus, ApJ **547**, 792 (2001)

[4] I. A. Grenier, J.-M. Casandjian, and R. Terrier, Science **307**, 1292 (2005)

[5] P. A. R. Ade, N. Aghanim, M. Arnaud, M. Ashdown,

J. Aumont, C. Baccigalupi, A. Balbi, A. J. Banday, R. B. Barreiro, J. G. Bartlett, et al., A&A **536**, 19 (2011)

[6] D. Paradis, K. Dobashi, T. Shimoikura, A. Kawamura, T. Onishi, Y. Fukui, and J.-P. Bernard, A&A **543**, 103 (2012)

[7] D. J. Schlegel, D. P. Finkbeiner, and M. Davis, ApJ **500**, 525 (1998)

[8] A. A. Abdo, M. Ackermann, M. Ajello, W. B. Atwood, L. Baldini, J. Ballet, G. Barbiellini, D. Bastieri, B. M. Baughman, K. Bechtol, et al., Phys. Rev. D **80**, 122004 (2009)

[9] J. Ballet and T. H. Burnett, 33rd ICRC, RIO DE JANEIRO 2013 (2013)

[10] M. Ackermann, M. Ajello, W. B. Atwood, L. Baldini, J. Ballet, G. Barbiellini, D. Bastieri, K. Bechtol, R. Bellazzini, B. Berenji, et al., ApJ **750**, 3 (2012)

[11] J.-M. Casandjian, I. Grenier, and for the Fermi Large Area Telescope Collaboration, arXiv **0912**, 3478 (2009)

[12] M. Su, T. R. Slatyer, and D. P. Finkbeiner, ApJ **724**, 1044 (2010)

[13] M. Ackermann, A. Albert, W. B. Atwood, L. Baldini, J. Ballet, G. Barbiellini, D. Bastieri, R. Bellazzini, E. Bissaldi, R. D. Blandford, et al., ApJ **793**, 64 (2014)

[14] C. G. T. Haslam, C. J. Salter, H. Stoffel, and W. E. Wilson, Astronomy and Astrophysics Supplement Series **47**, 1 (1982)

[15] T. Kamae, N. Karlsson, T. Mizuno, T. Abe, and T. Koi, ApJ **647**, 692 (2006)

[16] Y. Shikaze, S. Haino, K. Abe, H. Fuke, T. Hams, K. C. Kim, Y. Makida, S. Matsuda, J. W. Mitchell, A. A. Moiseev, et al., APh **28**, 154 (2007)

[17] M. Mori, APh **31**, 341 (2009)

[18] R. J. Gould, Physical Review **185**, 72 (1969)

[19] L. Blitz, J. B. G. M. Bloemen, W. Hermsen, and T. M. Bania, A&A **143**, 267 (1985)

[20] J. B. G. M. Bloemen, A. W. Strong, H. A. Mayer-Hasselwander, L. Blitz, R. S. Cohen, T. M. Dame, D. A. Grabelsky, P. Thaddeus, W. Hermsen, and F. Lebrun, A&A **154**, 25 (1986)

[21] A. W. Strong and J. R. Mattox, A&A **308**, L21 (1996)

[22] A. A. Abdo, M. Ackermann, M. Ajello, L. Baldini, J. Ballet, G. Barbiellini, D. Bastieri, B. M. Baughman, K. Bechtol, R. Bellazzini, et al., ApJ **710**, 133 (2010)

[23] M. Ackermann, M. Ajello, L. Baldini, J. Ballet, G. Barbiellini, D. Bastieri, K. Bechtol, R. Bellazzini, B. Berenji, E. D. Bloom, et al., ApJ **726**, 81 (2011)

[24] S. L. Snowden, R. Egger, M. J. Freyberg, D. McCammon, P. P. Plucinsky, W. T. Sanders, J. H. M. M. Schmitt, J. Truemper, and W. Voges, ApJ **485**, 125 (1997)

[25] K. M. Górski, E. Hivon, A. J. Banday, B. D. Wandelt, F. K. Hansen, M. Reinecke, and M. Bartelmann, ApJ **622**, 759 (2005)

[26] http://galprop.stanford.edu

High-Energy Neutrinos in Light of Fermi-LAT

Markus Ahlers
WIPAC & Department of Physics, University of Wisconsin–Madison, Madison, WI 53706, USA

The production of high-energy astrophysical neutrinos is tightly linked to the emission of hadronic γ-rays. I will discuss the recent observation of TeV to PeV neutrinos by the IceCube Cherenkov telescope in the context of γ-ray astronomy. The corresponding energy range of hadronic γ-rays is not directly accessible by extragalactic γ-ray astronomy due to interactions with cosmic radiation backgrounds. Nevertheless, the isotropic sub-TeV γ-ray background observed by the *Fermi* Large Area Telescope (LAT) contains indirect information from secondary emission produced in electromagnetic cascades and constrains hadronic emission scenarios. On the other hand, observation of PeV γ-rays would provide a smoking-gun signal for Galactic emission. In general, the cross-correlation of neutrino emission with (extended) Galactic and extragalactic γ-ray sources will serve as the most sensitive probe for a future identification of neutrino sources.

1. Introduction

The recent observation of a flux of high-energy astrophysical neutrinos [1, 2, 3, 4] has added an important new pillar to multi-messenger astronomy. Neutrinos are tracers of hadronic interactions of cosmic rays (CRs) via the production and decay of charged mesons. Unlike the observation of γ-rays, which can also be produced by leptonic emission, *i.e.* synchrotron emission, bremsstrahlung or inverse-Compton scattering of high-energy electrons, the detection of neutrinos is direct evidence of the presence of high-energy CRs. Due to their weak interaction with matter neutrinos at all energies can arrive from very distant sources and probe the Universe as far as the Hubble horizon. In contrast, γ-rays at energies beyond a few TeV scatter strongly in cosmic radiation backgrounds and initiate electromagnetic cascades shifting the γ-ray emission into the sub-TeV region. Cosmic rays are deflected via Galactic and extragalactic magnetic fields and can only correlate with their sources at energies approaching the *Greisen-Zatspin-Kuz'min* (GZK) cutoff [5, 6], $E_{\rm GZK} \simeq 50\,{\rm EeV}$. Thus, astronomical observations of non-thermal point sources emitting in the energy band between 10 TeV and 10 EeV are only possible via astrophysical neutrinos.

On the other hand, the weak interaction of neutrinos with matter is a challenge for their detection requiring enormously large instruments. One possibility consist of the detection of Cherenkov light emitted by high-energy secondary charged particles produced in neutrino interactions in optically transparent media. This is the concept of the IceCube detector which consists of a cubic kilometer of deep glacial ice at the geographic South Pole that is instrumented by an array of digital optical modules (DOMs). The small number of signal events have to compete against large backgrounds from CR activity in the atmosphere producing high-energy muons and atmospheric neutrinos.

Only recently, the IceCube Collaboration was able to identify a flux of high-energy astrophysical neutrinos [1, 2, 3, 4]. The flux of neutrinos observed in the so-called *high-energy starting event* (HESE) analysis consists of 37 events with deposited energies between 30 TeV and 2 PeV observed within a period of three years [3]. To extract an astrophysical signal the analysis identifies events with bright Cherenkov light emission of secondary charged particles that passed a virtual outer veto layer of DOMs [7]. This does not only veto most of the atmospheric muons, but also a large portion of atmospheric neutrino in the Southern Hemisphere which are vetoed by co-produced shower muons [8]. The topologies of the HESE events are classified in terms of *tracks* and *cascades*, depending on whether the neutrino interaction produced a muon track inside the detector or just a nearly spherical emission pattern at its interaction vertex, respectively. The expected number of background events are about 15 atmospheric muons and neutrinos. The total significance of the flux is at 5.7σ [3].

Figure 1 shows the distribution of the HESE events in Galactic coordinates. The different event topologies of tracks and cascades are shown as diamonds and filled circles, respectively. The area of the symbols indicate the relative increase of deposited energy. The most energetic events consist of three PeV cascades (#14, #20 & #35). Due to the spherical emission of the cascades the uncertainty in the reconstruction of their initial neutrino arrival direction is typically larger than 10° and is indicated as thin circles in the sky map. For tracks the reconstruction has a resolution of better than 1°. The red shaded area shows 10% steps of the minimal Earth absorption of neutrinos in the sample assuming 30 TeV as their minimum energy. Accounting for the zenith angle dependence of signal and background the emission is consistent with an isotropic and equal-flavor flux at a level of

$$E^2_\nu J^{\rm IC}_{\nu_\alpha} \simeq (0.95 \pm 0.3) \times 10^{-8}{\rm GeV s^{-1} cm^2 sr^{-1}}\,, \quad (1)$$

per neutrino flavor assuming an E^{-2} power-law emission. Track events can only be produced by charged current interactions of muon neutrinos and hence the track-to-cascade ratio contains information of the fla-

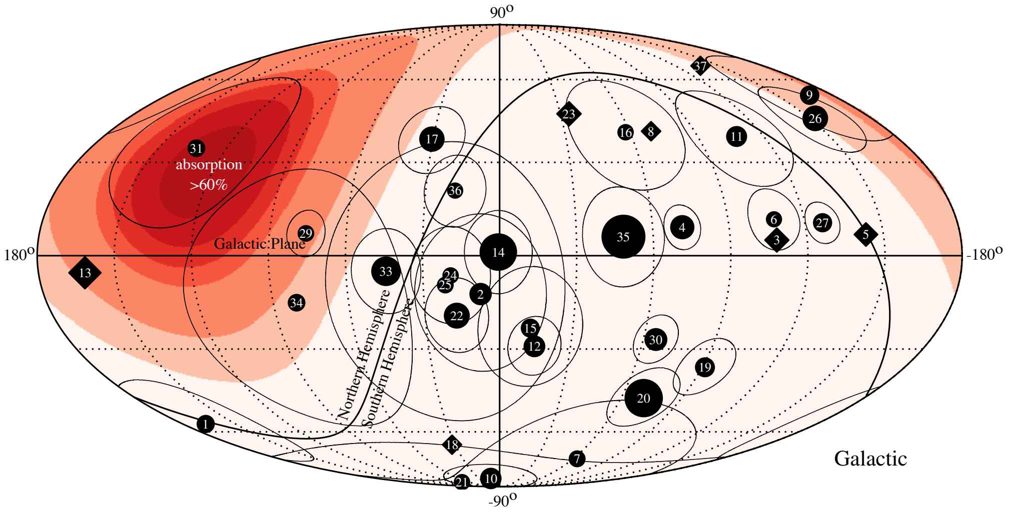

Figure 1: The arrival directions of IceCube events from Ref. [3]. The events are classified as tracks (diamonds) and cascades (filled circles). The relative detected energy of the events is indicated by the area of the symbols. The thin lines around the arrival direction of the cascade events indicate the systematic uncertainty of the reconstruction. Two likely background events (#28 and #35) from the 37 events are omitted from the plot. The red shaded region shows the minimal ($E_\nu = 30$ TeV) absorption of the neutrino flux due to scattering in the Earth in 10% steps.

vor composition [9, 10, 11, 12, 13]. A recent analysis of IceCube shows that the observation is consistent with an equal flavor composition expected from astrophysical sources [14]. The best-fit spectral index of the HESE analysis is at 2.3 with an total uncertainty of ± 0.3 [3]. Note, that a recent IceCube analysis extending the veto idea to neutrinos at (1-10) TeV favors a softer spectrum of 2.46 ± 0.12 [4].

Various astrophysical scenarios have been suggested that might be (partially) responsible for the observed flux of neutrinos. The absence of significant signs of anisotropy in the data is consistent with an extragalactic population of sources. Source candidates include galaxies with intense star formation [15, 16, 17, 18, 19, 20], cores of active galactic nuclei (AGN) [21, 22, 23], low-luminosity AGN [24, 25], blazars [26, 27, 28], low-power GRBs [29, 30, 31], cannonball GRBs [32], intergalactic shocks [33], and active galaxies embedded in structured regions [16, 34, 35]. Galactic contributions are in general identifiable by anisotropies in the arrival direction of neutrinos. The data shows no evidence for this, but this might be hidden by the limited event statistics and angular resolution of cascades. Possible contributions to super-TeV neutrinos are the diffuse neutrino emission of galactic CRs [36, 37, 38], the joint emission of galactic PeV sources [39, 40] or microquasars [41], and extended galactic structures like the *Fermi Bubbles* [36, 42, 43] or the galactic halo [44]. A possible association with the sub-TeV diffuse galactic γ-ray emission [45] and constraints from the non-observation from diffuse galactic PeV γ-rays [36, 46], have also been investigated. More exotic scenarios have suggested a contribution of neutrino emission from decaying heavy dark matter [47, 48, 49, 50].

Constraining the origin of the IceCube observation by neutrino data itself is challenging due to low event statistics, large backgrounds and systematic effects. Progress can be made by the fact the neutrino emission is intimately related to the production of hadronic γ-rays. Observation of γ-ray astronomy can hence help to constrain or identify the neutrino emission. In particular, the wealth of data coming from the *Fermi* telescope which allows for a cross-correlation with neutrino events in IceCube's field of view can help to identify possible sources, as we will discuss in the following.

2. Pinpointing Neutrino Sources

As mentioned in the introduction the neutrino observation is consistent with an isotropic flux. This would naturally arise from a superposition of faint point-sources of an extra-galactic source population. For simplicity, let's consider a distribution of continuously emitting sources with the same emission rate $Q_\nu(E) \propto E^{-\gamma}$ and red-shift dependent density $\mathcal{H}(z)$. The individual point-source spectrum J (in units of

GeV^{-1}s^{-1}cm^{-2}) at red-shift z is then given as

$$J(z,E) = \frac{(1+z)^2 Q_\nu((1+z)E)}{4\pi d_L^2(z)}\,, \tag{2}$$

for a luminosity distance $d_L(z) = (1+z)\int \mathrm{d}z'/H(z')$ defined by the red-shift Hubble expansion rate $H(z)$. In the following we assume a flat universe dominated by vacuum energy with $\Omega_\Lambda \simeq 0.7$ and cold dark matter with $\Omega_\mathrm{m} \simeq 0.3$ [51]. The Hubble parameter at earlier times is then given by its value today of $H_0 \simeq 70$ km s^{-1} Mpc^{-1} and the relation $H^2(z) = H_0^2\,(\Omega_\Lambda + \Omega_\mathrm{m}(1+z)^3)$. On the other hand, the average diffuse flux of neutrinos originating in multiple cosmic sources is simply given by

$$J_\mathrm{tot}(E_\nu) = \frac{1}{4\pi}\int_0^\infty \mathrm{d}z\frac{\mathrm{d}\mathcal{V}}{\mathrm{d}z}\mathcal{H}(z)J_\nu(z,E)\,, \tag{3}$$

where $\mathcal{V}(z) = (4\pi/3)d_c^3(z)$ is the co-moving volume with co-moving distance $d_c(z) = d_L(z)/(1+z)$. This quantity is normalized by the diffuse flux of Eq. (1). The contribution of an (average) source at co-moving distance r can then be expressed via the local density $\mathcal{H}_0 = \mathcal{H}(0)$ and an evolution factor

$$\xi_z(E) = \int_0^\infty \mathrm{d}z \frac{(1+z)^{-\gamma}}{\sqrt{\Omega_\Lambda + (1+z)^3\Omega_\mathrm{m}}}\frac{\mathcal{H}(z)}{\mathcal{H}(0)}\,. \tag{4}$$

Based on the diffuse flux (1) we can then estimate the contribution of individual point sources. For a continuously emitting source at a distance $d = d_1 10$ Mpc the mean neutrino flux is given as

$$E_\nu^2 J_\nu \simeq \frac{(0.9\pm0.3)\times 10^{-12}}{\xi_{z,2.4}\mathcal{H}_{0,-5}d_1^2}\,\frac{\mathrm{TeV}}{\mathrm{cm}^2\,\mathrm{s}}\,, \tag{5}$$

where $\mathcal{H}_0 = \mathcal{H}_{0,-5}10^{-5}\mathrm{Mpc}^{-3}$ is the local source density. An analogous argument can be made for transient sources [52]. In this case the time-integrated neutrino flux F (in units of GeV^{-1}cm^{-2}) from an individual transient can be expressed as

$$E_\nu^2 F_\nu \simeq \frac{0.3\pm0.1}{\xi_{z,2.4}\dot{\mathcal{H}}_{0,-6}d_1^2}\,\frac{\mathrm{GeV}}{\mathrm{cm}^2}\,, \tag{6}$$

where $\dot{\mathcal{H}}_0 = \dot{\mathcal{H}}_{0,-6}10^{-6}\mathrm{Mpc}^{-3}\mathrm{yr}^{-1}$ is the local flaring/burst density rate.

In Eqs. (5) and (6) the distance d and density $\mathcal{H}$ are kept as independent parameters. However, the first identified neutrino point-source will be the brightest one in the field of view (FoV), *i.e.* the closest one for equal-luminosity sources. The position of the closest source of an ensemble follows a statistical distribution [52]. Figure 2 shows the expected flux range of the closest continuous (top) or transient (bottom) neutrino source assuming a homogeneous local distribution with density $\mathcal{H}_0$ or density rate $\dot{\mathcal{H}}_0$, respectively. The different shaded bands indicate the 10% percentiles around the mean (solid line). The calculation assumes a source distribution following that of star-formation rate, $\xi_z \simeq 2.4$, using the estimates of Refs. [53, 54]. The plots in Fig. 2 also indicates the point-source sensitivity of IceCube in the Northern Hemisphere after 5 years of observation. IceCube is presently only sensitive to sparse sources with densities of $\mathcal{H}_0 \lesssim 10^{-7}\,\mathrm{Mpc}^{-3}$ like flat-spectrum radio quasars or very rare $\dot{\mathcal{H}}_0 \lesssim 10^{-8}\,\mathrm{Mpc}^{-3}\,\mathrm{yr}^{-1}$ transient source classes like gamma-ray bursts.

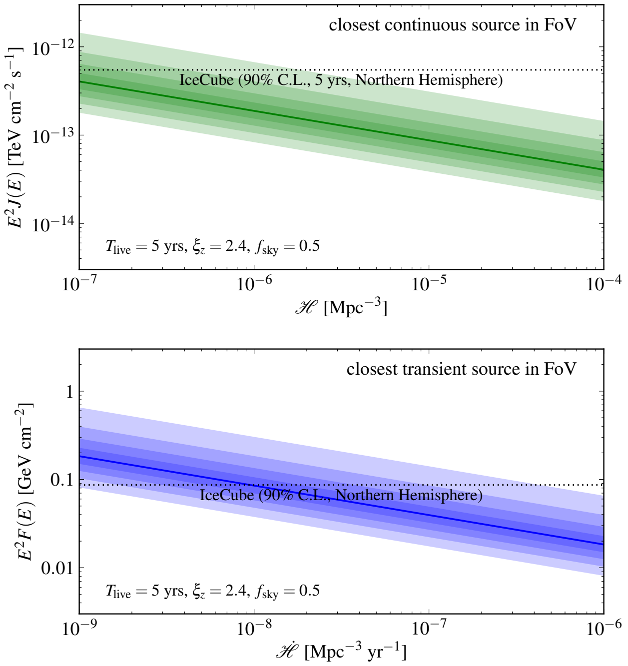

Figure 2: Expected emission of the closest neutrino source in terms of the average source density. The shaded regions show the 10% percentiles around the mean (solid line) expected from a random distribution of sources (from Ref. [52]).

Significant progress can be made by cross-correlating neutrino events with source catalogues [55, 56]. In particular, *Fermi* observations of extra-galactic γ-ray sources with an un-biased FoV provide an excellent catalogue for stacking searches, *e.g.* blazar sources [57]. In particular, the large background of atmospheric events can be significantly reduced by searching for neutrino events in coincidence with the position and time of transient sources [56]. For instance, IceCube has been looking for neutrino emission in coincidence with gamma-ray bursts (GRBs). The present limit on the combined ("stacked") emission from GRBs reported via the GRB Coordinates Network [58] and the *Fermi* GBM catalogs over a period of five years places an upper limit on their diffuse muon-neutrino flux which is about 1% of the observed diffuse emission (1), constraining the GRB origin of the emission [59].

3. Diffuse Neutrinos

The overall energy density of the observed neutrino flux is close to a theoretical limit for neutrino production in the sources of ultra-high energy (UHE) CRs [60]. This might just be a coincidence, but it can also indicate a multi-messenger relation. The neutrino and CR nucleon (N) emission rates Q (in units of $\mathrm{GeV}^{-1}\mathrm{s}^{-1}$) are related via

$$\frac{1}{3}\sum_\alpha E_\nu^2 Q_{\nu_\alpha}(E_\nu) \simeq \frac{1}{4}\frac{f_\pi K_\pi}{1+K_\pi} E_N^2 Q_N(E_N) \tag{7}$$

where $f_\pi < 1$ is the pion production efficiency, K_π the ratio of charged to neutral pions and $E_\nu \simeq 0.05 E_N$. The emission rate density of UHE CRs depend on spectrum and composition. For an E^{-2} flux of protons it can be estimated as $E_p^2 Q_p(E_p) \simeq (1-2) \times 10^{44}\,\mathrm{erg\,Mpc^{-3}\,yr^{-1}}$ [61]. Hence, using Eq. (3) the diffuse neutrino flux can be estimated as

$$E_\nu^2 J_\nu(E_\nu) \simeq \frac{\xi_z f_\pi K_\pi}{1+K_\pi}(2-4)\times 10^{-8}\,\mathrm{GeV\,cm^{-2}\,s^{-1}\,sr}\,, \tag{8}$$

were ξ_z is again given by Eq. (4). Since $f_\pi < 1$ this provides a theoretical upper limit on neutrino production, the *Waxman-Bahcall* (WB) bound [60].

Neutrino fluxes close to this limit would require very efficient CR production with optical thickness $\tau_{p\gamma/pp} \gg 1$, such that $f_\pi \simeq 1$, *i.e.* CR reservoirs [62] such as starburst galaxies [15, 63] or clusters of galaxies [34, 35, 64]. Interestingly, the energy density of Galactic CRs require a similar energy density. Assuming that 1% of the kinetic energy of 10^{51} erg of a supernova (SN) explosion is converted to CRs and assuming normal galaxies with densities $\mathcal{H}_0 \simeq 10^{-3}\mathrm{Mpc}^{-3}$ and a SN rate of 10^{-2} yr^{-1} we arrive at $E_p^2 Q_p(E_p) \simeq 10^{44}\,\mathrm{erg\,Mpc^{-3}\,yr^{-1}}$. This coincidence together with the saturation of the WB bound has let to speculations that Galactic and extragalactic CRs might be produced in the same transient sources [62].

Hadronic interactions of CRs will not only produce neutrinos, but also hadronic γ-rays. The production rates are related by

$$\frac{1}{3}\sum_\alpha E_\nu^2 Q_{\nu_\alpha}(E_\nu) \simeq \frac{K_\pi}{4} E_\gamma^2 Q_\gamma(E_\gamma)\,. \tag{9}$$

Note, that this relation does not depend on the pion production efficiency, but only on the relative charged-to-neutral pion rate K_π. However, the production rate described by Eq. (9) is not necessarily the emission rate of the sources. For instance, in hadronic sources that efficiently produce neutrinos via $p\gamma$ interactions the target photon field can also efficiently reduce the hadronic γ-rays via pair production. Inverse-Compton scattering and synchrotron emission in magnetic fields will then shift the emitted γ-ray spectrum to lower energies. This is a calorimetric process that will conserve the total energy of hadronic γ-rays.

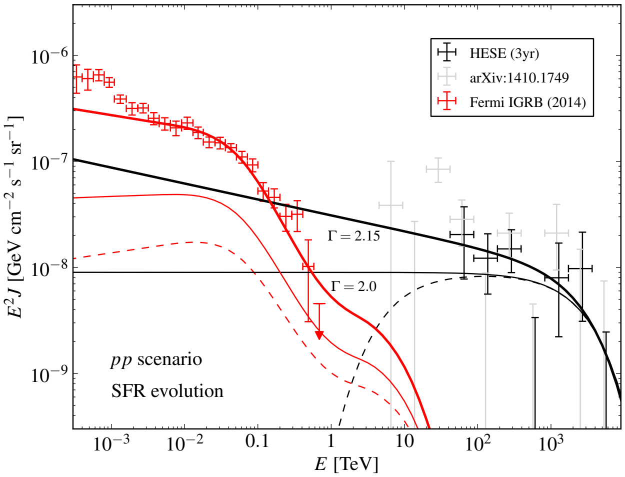

Figure 3: Isotropic γ-ray background (IGRB) inferred by *Fermi* [70] compared to the diffuse per-flavor neutrino flux observed by IceCube[1, 4] (updated plot of Ref. [36]). The black lines show possible neutrino models consistent with the IceCube data. The red lines are the corresponding γ-rays of *pp* scenarios reprocessed in the cosmic radiation background. The thick and thin solid lines show a power-law emission with $\Gamma = 2.15$ and $\Gamma = 2$, respectively, with an exponential cutoff around PeV. The dashed lines show an emission that is peaked in the 10TeV-PeV and only contributes in the γ-ray emission via cascades photons.

On the other hand, optically thin sources where the hadronic production is dominated by CR-gas interactions (*pp* sources) are expected to release the hadronic γ-rays described by Eq. (9). For this production mechanism the pion production efficiency is only weakly depend on the initial CR energy. The emitted neutrino and γ-ray spectra essentially follow the initial power-law spectrum of CRs, *cf.* Eq. (7). Nevertheless, the high-energy γ-rays of extragalactic sources will interact with cosmic radiation backgrounds, in particular the cosmic microwave background. Here again, the pair production and subsequent inverse-Compton scattering of the high energy electrons will lead to electromagnetic cascades. As a result, the initial energy density of hadronic γ-ray will be shifted into the sub-TeV γ-ray band, where they supplement the direct emission of the source. The observed γ-ray background in this energy region provides hence a general upper limit on the diffuse hadronic emission [65], which also applies to the production of cosmogenic neutrinos produced via the GZK interaction [66, 67, 68, 69].

Figure 3 shows three *pp* emission scenarios that follow the diffuse neutrino observation in the TeV-PeV energy range. The black and red lines show the neutrino and γ-ray spectra after accounting for cosmic evolution and cascading in cosmic radiation backgrounds. The thick solid line shows the case of an emission following $E^{-2.15}$ with an exponential cutoff around PeV. This scenario is marginally consistent with the inferred isotropic diffuse γ-ray background (IGRB) by *Fermi* [70]. The emission at sub-TeV energies is dominated by the direct photons of the sources.

For harder emission ($\Gamma = 2.0$, thin lines) the cascaded spectrum is still a significant contribution to the IGRB. The effect of cascades γ-rays is clearly visible as a bump in the GeV-TeV energy range. For illustration we also show the effect of a low energy cutoff in the intrinsic γ-ray and neutrino spectra (dashed lines). As we already emphasized, this emission spectrum is not expected for a *pp* scenario. However, the observed γ-ray spectrum is in this case dominated by secondary cascaded photons. The contribution to the *Fermi* IGRB between 100 GeV to 1 TeV is still at the level of 10%.

In general, this shows that the diffuse γ-ray contribution to the *Fermi* IGRB is large for *pp* scenarios soft emission spectra ($\Gamma \gtrsim 2.2$) are inconsistent with the data [16]. On the other hand, $p\gamma$ scenarios will most likely contribute to the *leptonic* emission of sources via reprocessed γ-rays. In this case, the hadronic counterparts of the IceCube observation can be identified in the source emission itself, but the energy range will depend on the particular source type.

4. Galactic TeV-PeV γ-rays

In the previous section we focused on the relation between CRs, γ-rays and neutrinos of extragalactic sources, which seem consistent with the absence of strong anisotropies in the observed neutrino spectrum. However, with the limited angular resolution and statistics of the observation it is possible that Galactic sources which are sufficiently extended contribute to the data. These extended emission regions are also observed by *Fermi* via the diffuse γ-ay emission of the Galactic Plane (GP) [71] or the extended *Fermi Bubbles* (FB) [72, 73]. In fact, as indicated in the sky map of Fig. 1 two of the PeV cascades (#14 & #35) are within angular uncertainties consistent with an emission along the Galactic Plane and the weak cluster of cascades in an extended region around the Galactic Center might also indicate the presence of Galactic neutrino emission.

Over Galactic distances the corresponding emission of hadronic TeV-PeV γ-rays are not completely attenuated by radiation backgrounds. In particular the observation of PeV γ-rays with an attenuation length of about 10 kpc via pair production in the cosmic microwave background (CMB) would be a *smoking gun* for Galactic production [36, 46]. Figure 4 shows the interaction length of photons for pair production and inverse-Compton scattering of photons with the CMB and the extragalactic background light (EBL) [74]. Extra-galactic candidate sources for PeV neutrino production, like Centaurus A at a distance of 4 Mpc shown in the plot, are only visible by hadronic γ-ray emission below 100 TeV. The diffuse flux of γ-rays from cosmic sources is only visible below 1 TeV due to EBL absorption.

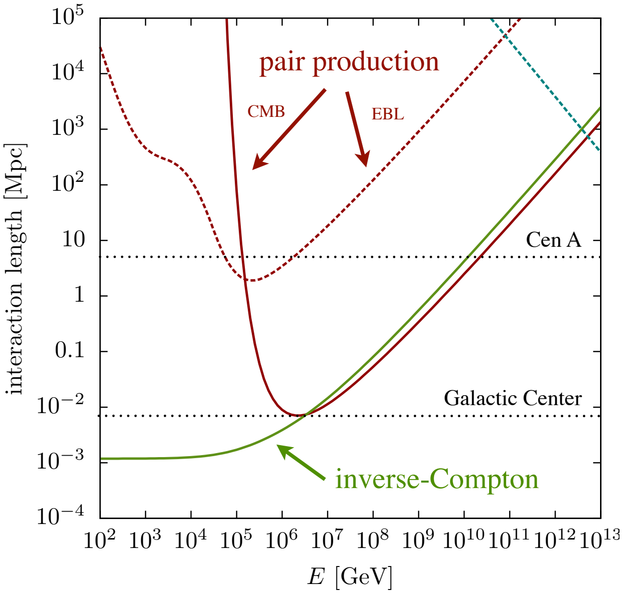

Figure 4: The interaction length of pair production and inverse-Compton scattering of photons with the CMB and EBL. Typical distance scales like the Galactic Center and the close-by radio galaxy Cen A are indicated.

The origin of the extended Galactic γ-ray emission known as the *Fermi Bubbles* [72] is unclear, but leptonic [75] as well as hadronic [76, 77] scenarios have been proposed, which can be distinguished via their corresponding neutrino emission [78]. Figure 5 shows the recent *Fermi* result of the emission spectrum of the FB region [73]. The red lines shows possible hadronic emissions from a power-law CR spectrum with different spectral indices and exponential cutoffs assuming a *pp* origin [79]. The black lines show the corresponding diffuse neutrino flux in comparison with the IceCube data. The models indicate that the extrapolated neutrino emission is probably irrelevant for PeV neutrino emission, but can have a noticeable contribution at energies of $(1-10)$ TeV [4]. Note, that the extension of the *Fermi Bubbles* is only about 10% of the full sky.

A guaranteed contribution to the diffuse emission of the Galactic Plane is the hadronic emission produced by interactions of diffuse CRs with gas [36, 37, 38]. In general, this emission is expected to follow the local diffuse CR spectrum. Usually it is assumed that the average spectrum in our Galaxy is close to the observed one with a power-law $E^{-2.75}$ up to the *knee* at $(3-4)$ PeV where the spectrum softens. In this case the contribution to the diffuse neutrino flux at PeV is not expected to be significant. Nevertheless, some authors have argued that the average spectrum in our

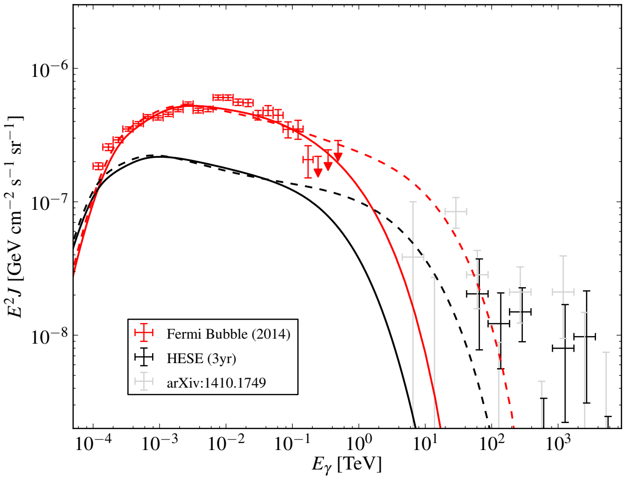

Figure 5: The diffuse flux from the *Fermi Bubbles* [73] compared to the diffuse per-flavor neutrino flux observed by IceCube[1, 4]. We show hadronic models of γ-ray (red lines) and per-flavor neutrino (black lines) emission. The lines show power-law emission of CR protons following the model in Ref. [73] (Eq. (16)) with $n = 2.1$ and $E_{\rm cut} = 13.7$ TeV (solid) or $n = 2.15$ and $E_{\rm cut} = 200$ TeV (dashed), respectively. In the case of a large cutoff the neutrino emission extends into the energy region studied in [4].

Milky Way might be harder and the locally observed spectrum might be softer due to a local and recent CR injection [80]. Again, this would not only produce an anisotropy of the neutrino emission along the GP, but also PeV γ-rays.

Exotic contributions like decaying heavy dark matter will also produce an extended emission [47, 48, 49, 50]. About 50% of the Galactic signal will be within 60° around the Galactic Center. It can be expected that these decaying dark matter scenarios leading to strong neutrino emission will also produce γ-rays up to an energy set by the mass scale. Interestingly, the neutrino emission of extragalactic dark matter decay will be at a similar flux level as the Galactic contribution. Hence, the high-energy neutrino events far off the Galactic Center can also be accounted for in this scenario without fine-tuning.

5. Summary and Outlook

The first observation of high-energy astrophysical neutrinos have added an important new observable of multi-messenger astronomy. Their energy density is comparable to the power density of Galactic or extragalactic cosmic rays integrated over the Hubble timescale. It also similar to the energy density of the isotropic γ-ray background. These similarity might be the result of calorimetric processes and suggest that a large contribution of high-energy messengers have a hadronic origin.

The absence of strong anisotropies in the data can be a natural consequence of neutrino emission in extragalactic sources. The identification of individual sources via clusters in neutrino arrival directions is challenging due to the limited angular reconstruction, low signal statistics and large atmospheric backgrounds. Cross-correlation of neutrino events with catalogues of transient and continuous γ-rays sources will provide the best chance to identify the neutrino sources.

Interestingly, the isotropic diffuse γ-ray background observed by *Fermi*-LAT already constrains extragalactic hadronic emission scenarios. Neutrino production via cosmic ray interactions with gas (*pp* scenario) predict neutrino and hadronic γ-ray spectra that follow the cosmic ray power-law spectrum. The tail of sub-TeV γ-rays for soft spectral indices $\Gamma \gtrsim 2.2$ are inconsistent with the observed γ-ray background level. Harder emission scenarios can also be constrained by the identification of known diffuse γ-ray contributions, such as unresolved blazars.

Needless to say that neutrino astronomy would benefit from a larger instrument with an increased sensitivity for neutrino point sources. The proposed *IceCube–Gen2* extension [81] plans to increase the effective volume of IceCube by about a factor of 10. For transient sources which are not dominated by atmospheric backgrounds this would increase the sensitivity by about a factor of $10^{2/3} \simeq 5$.

Acknowledgments

The author would like to thank the organizers of the *5th Fermi Symposium* 2014 for a very pleasant and stimulating conference. This work is supported by the National Science Foundation under grants OPP-0236449 and PHY-0236449.

References

[1] IceCube Collaboration, M. Aartsen *et al.*, Phys.Rev.Lett. **111**, 021103 (2013), 1304.5356.
[2] IceCube, M. Aartsen *et al.*, Science **342**, 1242856 (2013), 1311.5238.
[3] IceCube Collaboration, M. Aartsen *et al.*, Phys.Rev.Lett. **113**, 101101 (2014), 1405.5303.
[4] IceCube Collaboration, M. Aartsen *et al.*, (2014), 1410.1749.
[5] K. Greisen, Phys.Rev.Lett. **16**, 748 (1966).
[6] G. Zatsepin and V. Kuzmin, JETP Lett. **4**, 78 (1966).

[7] S. Schonert, T. K. Gaisser, E. Resconi, and O. Schulz, Phys.Rev. **D79**, 043009 (2009), 0812.4308.

[8] T. K. Gaisser, K. Jero, A. Karle, and J. van Santen, Phys.Rev. **D90**, 023009 (2014), 1405.0525.

[9] L. A. Anchordoqui, H. Goldberg, F. Halzen, and T. J. Weiler, Phys.Lett. **B621**, 18 (2005), hep-ph/0410003.

[10] O. Mena, S. Palomares-Ruiz, and A. C. Vincent, Phys.Rev.Lett. **113**, 091103 (2014), 1404.0017.

[11] A. Bhattacharya, R. Gandhi, W. Rodejohann, and A. Watanabe, JCAP **1110**, 017 (2011), 1108.3163.

[12] V. Barger *et al.*, (2014), 1407.3255.

[13] W. Winter, Phys.Rev. **D90**, 103003 (2014), 1407.7536.

[14] IceCube Collaboration, M. Aartsen *et al.*, (2015), 1502.03376.

[15] A. Loeb and E. Waxman, JCAP **0605**, 003 (2006), astro-ph/0601695.

[16] K. Murase, M. Ahlers, and B. C. Lacki, Phys.Rev. **D88**, 121301 (2013), 1306.3417.

[17] H.-N. He, T. Wang, Y.-Z. Fan, S.-M. Liu, and D.-M. Wei, Phys.Rev. **D87**, 063011 (2013), 1303.1253.

[18] L. A. Anchordoqui, T. C. Paul, L. H. M. da Silva, D. F. Torres, and B. J. Vlcek, Phys.Rev. **D89**, 127304 (2014), 1405.7648.

[19] X.-C. Chang and X.-Y. Wang, Astrophys.J. **793**, 131 (2014), 1406.1099.

[20] N. Senno, P. Mszros, K. Murase, P. Baerwald, and M. J. Rees, (2015), 1501.04934.

[21] F. Stecker, C. Done, M. Salamon, and P. Sommers, Phys.Rev.Lett. **66**, 2697 (1991).

[22] F. W. Stecker, Phys.Rev. **D88**, 047301 (2013), 1305.7404.

[23] O. Kalashev, D. Semikoz, and I. Tkachev, (2014), 1410.8124.

[24] Y. Bai *et al.*, Phys.Rev. **D90**, 063012 (2014), 1407.2243.

[25] S. S. Kimura, K. Murase, and K. Toma, (2014), 1411.3588.

[26] F. Tavecchio and G. Ghisellini, (2014), 1411.2783.

[27] P. Padovani and E. Resconi, Mon.Not.Roy.Astron.Soc. **443**, 474 (2014), 1406.0376.

[28] C. D. Dermer, K. Murase, and Y. Inoue, JHEAp **3-4**, 29 (2014), 1406.2633.

[29] E. Waxman and J. N. Bahcall, Phys.Rev.Lett. **78**, 2292 (1997), astro-ph/9701231.

[30] K. Murase and K. Ioka, Phys.Rev.Lett. **111**, 121102 (2013), 1306.2274.

[31] S. Ando and J. F. Beacom, Phys.Rev.Lett. **95**, 061103 (2005), astro-ph/0502521.

[32] S. Dado and A. Dar, Phys.Rev.Lett. **113**, 191102 (2014), 1405.5487.

[33] K. Kashiyama and P. Meszaros, Astrophys.J. **790**, L14 (2014), 1405.3262.

[34] V. Berezinsky, P. Blasi, and V. Ptuskin, Astrophys J. **487**, 529 (1997), astro-ph/9609048.

[35] K. Murase, S. Inoue, and S. Nagataki, Astrophys.J. **689**, L105 (2008), 0805.0104.

[36] M. Ahlers and K. Murase, Phys.Rev. **D90**, 023010 (2014), 1309.4077.

[37] M. Kachelriess and S. Ostapchenko, Phys.Rev. **D90**, 083002 (2014), 1405.3797.

[38] J. C. Joshi, W. Winter, and N. Gupta, **3414**, 3419 (2013), 1310.5123.

[39] D. Fox, K. Kashiyama, and P. Meszaros, Astrophys.J. **774**, 74 (2013), 1305.6606.

[40] M. Gonzalez-Garcia, F. Halzen, and V. Niro, Astropart.Phys. **57-58**, 39 (2014), 1310.7194.

[41] L. A. Anchordoqui, H. Goldberg, T. C. Paul, L. H. M. da Silva, and B. J. Vlcek, (2014), 1410.0348.

[42] S. Razzaque, Phys.Rev. **D88**, 081302 (2013), 1309.2756.

[43] C. Lunardini, S. Razzaque, K. T. Theodoseau, and L. Yang, Phys.Rev. **D90**, 023016 (2014), 1311.7188.

[44] A. M. Taylor, S. Gabici, and F. Aharonian, Phys.Rev. **D89**, 103003 (2014), 1403.3206.

[45] A. Neronov, D. Semikoz, and C. Tchernin, Phys.Rev. **D89**, 103002 (2014), 1307.2158.

[46] N. Gupta, Astropart.Phys. **48**, 75 (2013), 1305.4123.

[47] B. Feldstein, A. Kusenko, S. Matsumoto, and T. T. Yanagida, Phys.Rev. **D88**, 015004 (2013), 1303.7320.

[48] A. Esmaili and P. D. Serpico, JCAP **1311**, 054 (2013), 1308.1105.

[49] Y. Bai, R. Lu, and J. Salvado, (2013), 1311.5864.

[50] J. F. Cherry, A. Friedland, and I. M. Shoemaker, (2014), 1411.1071.

[51] Particle Data Group, K. Olive *et al.*, Chin.Phys. **C38**, 090001 (2014).

[52] M. Ahlers and F. Halzen, (2014), 1406.2160.

[53] A. M. Hopkins and J. F. Beacom, Astrophys.J. **651**, 142 (2006), astro-ph/0601463.

[54] H. Yuksel, M. D. Kistler, J. F. Beacom, and A. M. Hopkins, Astrophys.J. **683**, L5 (2008), 0804.4008.

[55] IceCube Collaboration, M. Aartsen *et al.*, (2014), 1406.6757.

[56] IceCube Collaboration, M. Aartsen *et al.*, Astrophys.J. **779**, 132 (2013), 1307.6669.

[57] IceCube Collaboration, T. Gluesenkamp, Proceedings of RICAP 2014 (2014).

[58] `http://gcn.gsfc.nasa.gov`.

[59] IceCube Collaboration, M. Aartsen *et al.*, (2014), 1412.6510.

[60] E. Waxman and J. N. Bahcall, Phys.Rev. **D59**, 023002 (1999), hep-ph/9807282.

[61] M. Ahlers and F. Halzen, Phys.Rev. **D86**, 083010 (2012), 1208.4181.

[62] B. Katz, E. Waxman, T. Thompson, and A. Loeb, (2013), 1311.0287.

[63] I. Tamborra, S. Ando, and K. Murase, JCAP **1409**, 043 (2014), 1404.1189.

[64] F. Zandanel, I. Tamborra, S. Gabici, and S. Ando, (2014), 1410.8697.

[65] V. Berezinsky and A. Y. Smirnov, Phys.Lett. **B48**, 269 (1974).

[66] V. Berezinsky and G. Zatsepin, Phys.Lett. **B28**, 423 (1969).

[67] V. Berezinsky, A. Gazizov, M. Kachelriess, and S. Ostapchenko, Phys.Lett. **B695**, 13 (2011), 1003.1496.

[68] M. Ahlers, L. Anchordoqui, M. Gonzalez-Garcia, F. Halzen, and S. Sarkar, Astropart.Phys. **34**, 106 (2010), 1005.2620.

[69] G. Decerprit and D. Allard, Astron.Astrophys. **535**, A66 (2011), 1107.3722.

[70] The Fermi LAT collaboration, M. Ackermann *et al.*, (2014), 1410.3696.

[71] Fermi-LAT Collaboration, M. Ackermann *et al.*, Astrophys.J. **750**, 3 (2012), 1202.4039.

[72] M. Su, T. R. Slatyer, and D. P. Finkbeiner, Astrophys.J. **724**, 1044 (2010), 1005.5480.

[73] Fermi-LAT Collaboration, M. Ackermann *et al.*, Astrophys.J. (2014), 1407.7905.

[74] A. Franceschini, G. Rodighiero, and M. Vaccari, Astron.Astrophys. **487**, 837 (2008), 0805.1841.

[75] P. Mertsch and S. Sarkar, Phys.Rev.Lett. **107**, 091101 (2011), 1104.3585.

[76] R. M. Crocker and F. Aharonian, Phys.Rev.Lett. **106**, 101102 (2011), 1008.2658.

[77] R.-z. Yang, F. Aharonian, and R. Crocker, (2014), 1402.0403.

[78] C. Lunardini and S. Razzaque, Phys.Rev.Lett. **108**, 221102 (2012), 1112.4799.

[79] T. Kamae, N. Karlsson, T. Mizuno, T. Abe, and T. Koi, Astrophys.J. **647**, 692 (2006), astro-ph/0605581.

[80] A. Neronov and D. Semikoz, (2014), 1412.1690.

[81] IceCube Collaboration, M. Aartsen *et al.*, (2014), 1412.5106.

Shedding new light on the Sun with the *Fermi* LAT

N. Omodei, V. Petrosian, W. Liu, F. Rubio da Costa, Q. Chen
Stanford University/KIPAC, Stanford, CA, USA 94305
M. Pesce-Rollins
INFN-Pisa, Pisa, Italy 56100
E. Grove
U.S. Naval Research Lab, SW Washington, DC, USA 20375
F. Longo
INFN-Trieste, Trieste, Italy 34127
on behalf of the *Fermi*-LAT collaboration

During its first six years of operation, the *Fermi* Large Area Telescope (LAT) has detected >30 MeV gamma-ray emission from more than 40 solar flares, nearly a factor of 10 more than those detected by EGRET. These include detections of impulsive and sustained emissions, extending up to ∼20 hours in the case of the 2012 March 7 X-class flares. We will present an overview of solar flare detections with LAT, highlighting recent results and surprising features, including the detection of >100 MeV emission associated with flares located behind the limb. Such flares may shed new light on the relationship between the sites of particle acceleration and gamma-ray emission.

1. Introduction

Understanding the processes of particle acceleration and impulsive energy release which occur in numerous sites throughout the Universe is one of the major goals of space physics and astrophysics. The Sun is the most powerful particle accelerator in the solar system and its proximity permits investigating the entire electromagnetic spectrum of these acceleration phenomena. During solar flares, the Sun is capable of accelerating electrons and ions to relativistic energies on time scales as short as a few seconds, as indicated by observations of X-rays, microwaves, γ-rays, and neutrons produced when the flare-accelerated particles interact with the solar atmosphere [Forrest and Chupp 1983, Kane et al. 1986]. In general, the γ-ray emission light curve is similar to that of the HXRs (possibly with some delay), lasting for 10–100 seconds. This is referred to as the “impulsive” phase of the flare. However, the *Energetic Gamma Ray Experiment Telescope* (EGRET) on-board CGRO [Kanbach et al. 1988, Esposito et al. 1999] also detected a sustained emission in gamma rays for more than an hour after the impulsive phases of 3 flares [Ryan 2000a]. The expected increase of solar activity during the current solar maximum is producing a large number of solar flares, including bright GOES X-class and moderate M-class flares.

2. Fermi observations of the Sun

Launched in 2008, the *Fermi* observatory is comprised of two instruments; the Large Area Telescope (LAT) designed to detect gamma-rays from 20 MeV up to more than 300 MeV [Atwood et al. 2009a] and the Gamma-ray Burst Monitor (GBM) which is sensitive from ∼ 8 keV up to 40 MeV [Meegan et al. 2009]. During the first 18 months of operation coinciding with the solar cycle minimum, the *Fermi* LAT detected >100 MeV gamma-ray emission from the quiescent Sun [Abdo et al. 2011a]. As the solar cycle approaches it maximum, the LAT has detected several solar flares above 30 MeV during both the impulsive and the temporally extended phases [Ohno et al. 2011, Omodei et al. 2011, Tanaka et al. 2012, Petrosian et al. 2012, Omodei et al. 2012]. The first *Fermi* GBM and LAT detection of the impulsive GOES M2.0 flare of 2010 June 12 is presented in Ackermann et al. [2012a]. The analysis of this flare was performed using the LAT Low-Energy (LLE) technique [Pelassa et al. 2010] because the soft X-rays emitted during the prompt emission of a flare penetrate the anti-coincidence detector (ACD) of the LAT causing a pile-up effect which can result in a significant decrease in gamma-ray detection efficiency in the standard on-ground photon analysis [Atwood et al. 2009a]. The pile-up effect has been addressed in detail in Ackermann et al. [2012a] and Abdo et al. [2009]. The list of all LAT detected flares, and the analysis of the first two flares with long lasting high-energy emission (2011 March 7–8 and 2011 June 7) is presented in Ackermann et al. [2014], Ajello et al. [2014].

2.1. June 2010: An impulsive event

On 2010 June 12 00:30 UT a moderate *GOES* M2.0 class X-ray flare erupted from the active region (AR) 11081 located approximately N23°W43°. At the time of the flare the *Fermi* spacecraft was in sunlight and during a relatively low-background portion of its orbit[1]. The GBM triggered on the flare at 00:55:05.64 UT and detected keV emission for ≈10 m. The 11 − 26 keV emission recorded by the GBM NaI detectors rose precipitously for about 40 s and is shown in Figure 1a. For comparison we include the GOES 0.5 – 4 Åprofile and note that this emission is dominated by 3 keV thermal photons as is reflected in its slower rise and extended tail. The 100 − 300 keV time profile observed by the GBM's solar facing NaI detector is also plotted in Figure 1a. It is clear that the emission peaks more sharply and ends sooner at higher X-ray energies.

The accompanying hard X-ray emission from the flare was detected in the LAT's ACD and is reflected in the shape of the average number of ACD tile hits as a function of time (shown in Figure 1b). The broad peak with a maximum near 00:57 UT of the hit distribution has a shape similar to the 11 – 26 keV emission and the impulsive peak is similar to the 100 to 300 keV flux observed by the GBM NaI detector. As shown by the red curve in Figure 1c there is no evidence for the flare in the well-screened standard LAT data products. [What is shown here are the events belonging to the `P6TRANSIENT` event class, Atwood et al. 2009b]. This is the direct consequence of the pulse pile-up effect. The black curve in Figure 1c is the LAT LLE >30 MeV event rate for the time of the flare.

White light emission observed by the Helioseismic and Magnetic Imager (HMI) on the *Solar Dynamics Observatory* (*SDO*) [Martínez Oliveros et al. 2011] in a single 45 s exposure during the hard X-ray emission revealed two compact *footpoints* about 10^4 km apart.

The >30 MeV LLE spectrum of this flare revealed flare emission up to an energy of ∼400 MeV. The nuclear line emission observed with the GBM implies the presence of accelerated ions up to at least 50 MeV nucleon^{-1}. It is possible that the flare-accelerated proton spectrum extended up to the ∼300 MeV threshold for pion production. Alternatively, it is also possible that the LAT emission is from electron bremsstrahlung, either from an extension to high energies of the electron spectrum producing the X-ray bremsstrahlung observed in the GBM or from an additional hard electron component. One possible way to resolve this ambiguity is to jointly fit the GBM and LAT spectra assuming different origins for the LAT emission.

In Figure 2 we plot the background-subtracted photon spectrum from 0.3 to 400 MeV including both the GBM and LAT data. We made two fits, using *rmfit 3.4*[1], customized for the specific solar flare, and the *OSPEX*[2] analysis packages, to the joint data sets. In the first fit we assume that the observed LAT emission was from pion-decay radiation (top panel of Figure 2) and the other assuming that it was from a hard power-law spectrum of electron bremsstrahlung (bottom panel). Based on the statistical quality of the fits to the LAT spectrum we cannot distinguish between the two emission models but, if the LAT emission is from electron bremsstrahlung, we have found that it cannot be a simple extension of the low-energy bremsstrahlung components that we determined from fits to the GBM data; it must be from a distinct population of electrons extending to energies of several hundred MeV. However, this high energy electron component would produce a spectrum that steepens beyond tens of MeV due to synchrotron energy losses that increase with energy [see Park et al. 1997], and must have a quite different origin. Consequently we believe that this is a less likely scenario than the hadronic model.

Assuming that the LAT emission is from hadronic interactions, we have fit the LAT spectrum with calculated pion-decay templates [Murphy et al. 1987], which depends on the ambient density, composition and magnetic field, on the accelerated-particle composition, pitch angle distribution and energy spectrum. The templates represent a particle population with an isotropic pitch angle distribution and a power-law energy spectrum ($dN/dE \propto E^{-s}$, with E the kinetic energy of the protons) interacting in a thick target with a coronal composition [Reames 1995] taking ^{4}He/H = 0.1. With 67% confidence (based on χ^2) we conclude that the spectrum of accelerated ions responsible for the pion-decay emission must be steeper than a power-law with index −4.5. We note that there is no change in the quality of the fits for indices steeper than −5 due to limited statistics >400 MeV. We can use the results of our GBM and LAT spectral analyses to obtain information on ions accelerated in the impulsive phase of the June 12 flare. Murphy et al. [1997] have described how parameters derived from integrated spectroscopic fits and temporal studies can be used to obtain this information. We first use the nuclear de-excitation line, neutron-capture line, and pion-decay fluences to estimate the overall shape of the accelerated ion spectrum. These three emissions are produced by accelerated ions within distinct energy ranges: ∼5-20 MeV for the de-excitation lines, ∼10-50 MeV for the neutron capture line, and >300 MeV for the pion-decay emission. Ratios of these emissions therefore determine the relative numbers of accelerated ions in the associated energy ranges. We then obtain spectral indices across these energy ranges

---

[1] The *Fermi* observatory is in a nearly circular orbit with an inclination of 25.6° at 565 km.

[1] R.S. Mallozzi, R.D. Preece, & M.S. Briggs, "RMFIT, A Lightcurve and Spectral Analysis Tool", Robert D. Preece, University of Alabama in Huntsville, (2008): http://fermi.gsfc.nasa.gov/ssc/data/analysis/user/

[2] SolarSoft: http://www.lmsal.com/solarsoft/

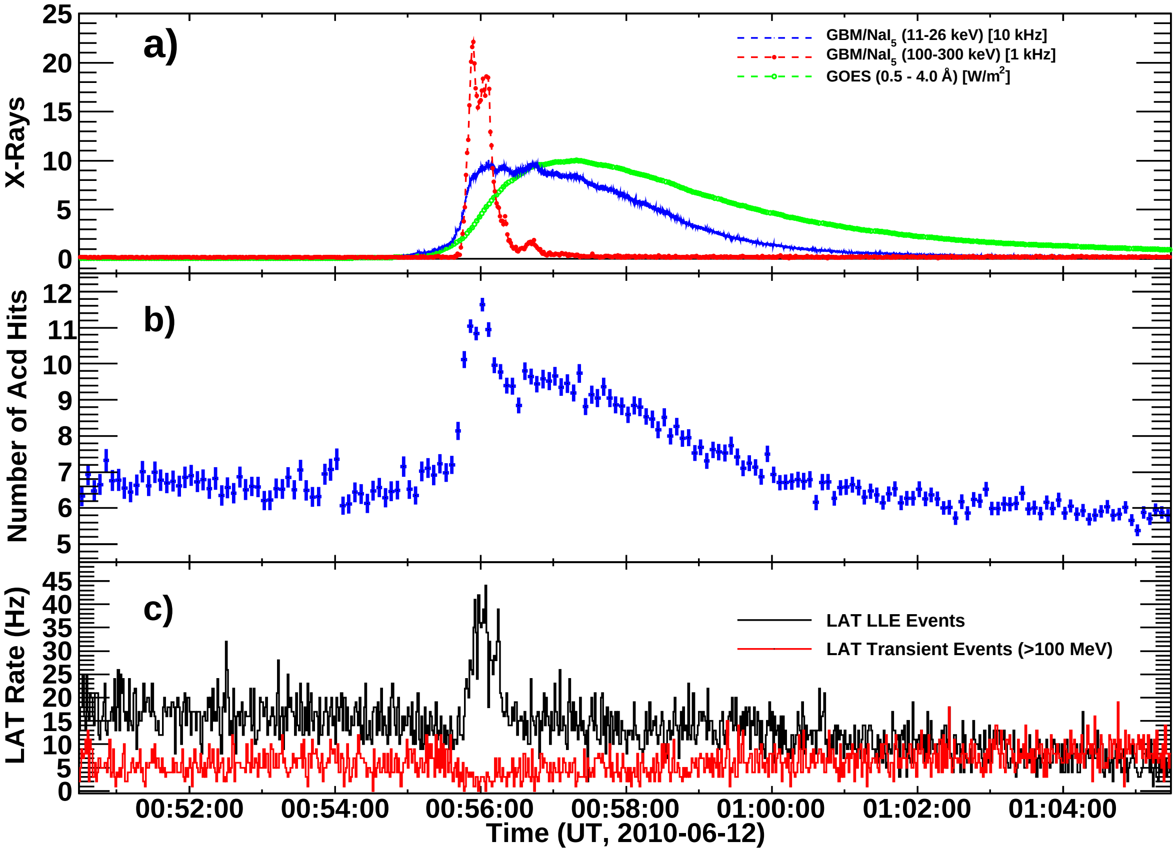

Figure 1: Time histories related to the 2010 June 12 solar flare. a) *GOES* 0.5 – 4 Årates, and GBM NaI 11 – 26 keV and 100 – 300 keV relative rates; b) LAT ACD hit rate >100 keV containing contributions from background, >100 keV solar flare X rays (impulsive peak) and pulse pile up from 10's of keV solar X rays following the NaI 11 – 26 keV profile in 1a); and c) LLE and LAT Transient Class event rates.

by comparing measured ratios with ratios from theoretical calculations [Murphy et al. 1987, 2005, 2007] based on updated nuclear cross sections.

If we assume that the LAT emission >30 MeV was entirely due to pion-decay emission, then we estimate that the flare-accelerated ion spectrum was consistent with a series of power laws, softening with energy, with indices of ∼−3.2 between ∼ 5 − 50 MeV, ∼−4.3 between ∼50–300 MeV, and softer than ∼−4.5 above 300 MeV. In Table I we summarize our findings, reporting the processes responsible for the detected emission, energy range of emitted gamma-rays, as well as the energy and spectral index of the accelerated ions/electron distribution.

Component	γ-rays (MeV)	electrons/ions (MeV)	Spectral Index acc. particles
Brem.	0.1–1	0.1–1	-3.2
Brem.	2–10	2–10	<-1.2
HE Brem.	10–200	10–200	≈-2.0
Neutron Capt.	2.2	5-50	~ -3.2
Nuclear lines	5-20	50-300	~ -4.3
Pions	>30	$\gtrsim 300$	$\lesssim -4.5$

Table I Derived quantities for accelerated particle distributions (with a cut-off at 2.4 MeV)

2.2. March 2012: Impulsive and sustained emission of a bright flare

On 2012 March 7 two bright X-class flares originating from the AR NOAA AR#:11429 (located at N16°E30°) erupted within an hour of each other, marking one of the most active days of Solar Cycle 24. The first flare started at 00:02:00 UT and reached its maximum intensity (X5.4) at 00:24:00 UT while the second X1.3 class flare occurred at 01:05:00 UT, reaching its maximum 9 minutes later.

The GOES satellite observed intense X-ray emission beginning at about 00:05:00 UT and lasting for several hours. Moreover, it detected Solar Energetic Particles (SEP) protons in three energy bands origi-

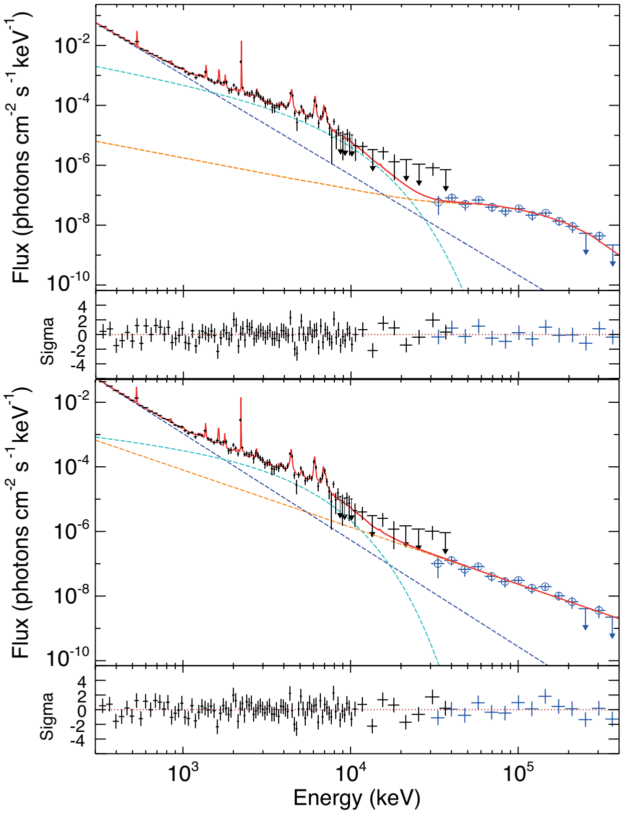

Figure 2: Combined GBM/LAT photon spectrum accumulated between 00:55:40 and 00:56:30 showing the best total fit using the same components as in Figure 3 plus an additional component for the LAT emission. The upper panel shows a pion-decay fit to the LAT spectrum; alternatively the lower panel shows a power-law fit, presumedly representing a third electron bremsstrahlung component. Note that because this is a photon representation the lines are plotted at their intrinsic resolution and appear to be more significant than they really are.

nating these flares. The Reuven Ramaty High-Energy Solar Spectroscopic Imager [RHESSI, Lin et al. 2002] was not observing the Sun during this period. On the top panel of Figure 3 we plot the X-ray data from GOES 15 satellite measured in both 3–25 keV and 1.5–12 keV, as well as the detected proton flux.

The *Fermi* LAT >100 MeV count rate was dominated by the gamma-ray emission from the Sun[2], which was nearly 100 times brighter than the Vela Pulsar in the same energy range. During the impulsive phase (the first eighty minutes) the X5.4 flare was so intense that the LAT observation suffered from the pile-up effect so we used the LLE technique to analyze the impulsive phase of this bright flare.

We fit the data using `XSPEC`[3] to test three models. The first two are simple phenomenological functions, to describe bremsstrahlung emission from accelerated electrons, namely a pure power law (PL) and a power law with an exponential cut-off (EXP):

$$\frac{dN(E)}{dE} = N_0\,\epsilon^{-\Gamma}\exp\left(-\frac{E}{E_{co}}\right); \tag{1}$$

where Γ is the photon index and E_{co} is the cut-off energy. We found that the data clearly diverge from a pure power law spectrum and that the EXP provides a better fit in all time intervals considered. The third model used the same pion decay templates [Murphy et al. 1987] used for the 2010 June 2 flare. When using the pion-decay templates to obtain the gamma-ray flux value we fit the data varying the proton spectral index from 2 to 6, in steps of 0.1. In this way, we fit the LAT data with a model with two free parameters, the normalization and the proton index s.

To study the temporally-extended emission, we perform time-resolved spectral analysis in Sun-centered coordinates by transforming the reference system from celestial coordinates to ecliptic Sun-centered coordinates. This is necessary in order to compensate for the effect of the apparent motion of the Sun during the long duration of the flare. We select intervals when the Sun was in the FOV (angular distance from the LAT boresight $< 70°$) and use the unbinned maximum likelihood algorithm implemented in `gtlike`[4].

We include the isotropic template model that is used to describe the extragalactic gamma-ray emission and the residual cosmic ray (CR) contamination[5], leaving its normalization as the free parameter. Over short time scales, the diffuse Galactic emissions produced by CR interacting with the interstellar medium are not spatially resolved and are hence included in the isotropic template. We also add the gamma-ray emission from the quiescent Sun modeled as a point source located at the center of the disk, with a spectrum described by a simple power law with a spectral index of 2.11 and an integrated energy flux ($>$ 100 MeV) of 4.7×10^{-10} erg cm^{-2} s^{-1} [corresponding to a flux of 4.6×10^{-7} ph cm^{-2} s^{-1} as reported in Abdo et al. 2011b]. We did not include the extended Inverse Compton (IC) component described in Abdo et al. [2011b] because it is too faint to be detected during these time intervals. We fit the data with the same two phenomenological functions used

---

[2] http://apod.nasa.gov/apod/ap120315.html

[3] http://heasarc.gsfc.nasa.gov/docs/xanadu/xspec/index.html

[4] We used `ScienceTools` version 09-28-00 available from the *Fermi* Science Support Center `http://fermi.gsfc.nasa.gov/ssc/`

[5] We used `iso_p7v6source.txt` available from the *Fermi* Science Support Center

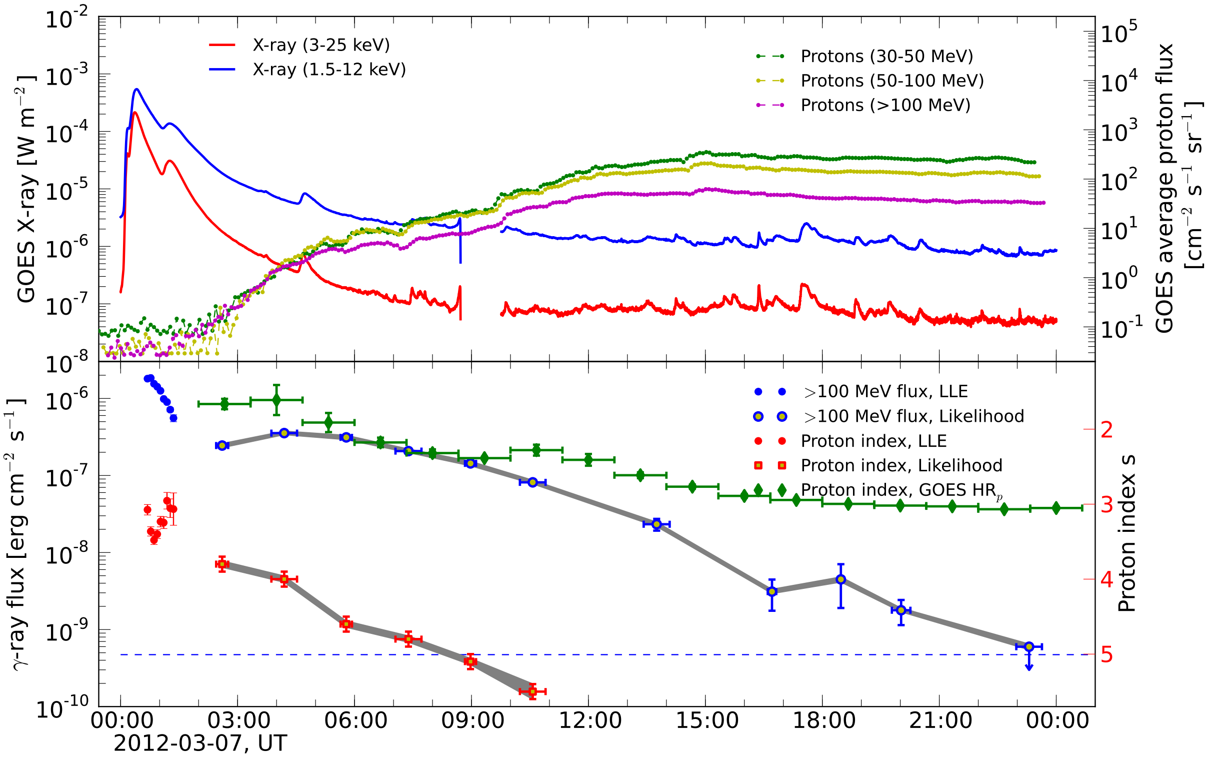

Figure 3: Long lasting emission. **Top panel**: soft X-rays (red: 1.5–12 keV, blue: 3–25 keV) from the *GOES* 15 satellite. On the right axis, 5-minute averaged proton flux (green: 30–50 MeV, yellow: 50–100 MeV, magenta: >100 MeV). We display the average of detectors A and B. **Bottom panel**: high-energy gamma-ray flux above 100 MeV measured by the *Fermi* LAT. The Blue/red circles represent the flux and the derived proton spectral index obtained with the LLE analysis (covering the initial period, when the instrumental performance was affected by pileup of hard-X-rays in the ACD tiles). The blue circles and red squares represent the flux and derived proton spectral index, respectively, obtained by standard likelihood analysis. Green diamonds are the *GOES* proton spectral indexes derived from the hardness ratio, as described in the text. The gray bands correspond to the systematic uncertainty associated with flux measurements and of the estimated proton index due to uncertainties on the effective area of the instrument. The horizontal dashed line corresponds to the value of the gamma-ray flux from the quiescent Sun, from Abdo et al. [2011b].

for the impulsive phase of the flare and use the likelihood ratio test to estimate whether the addition of the exponential cut-off is statistically significant. The Test Statistic (TS) Mattox et al. [1996] is defined as twice the increment of the logarithm of the likelihood $\mathcal{L}$ obtained by fitting the data with the source and background model components simultaneously. Because the null hypothesis (i.e. the model without an additional source) is the same for the two models, the increment of the TS (ΔTS=TS$_{\rm PLEXP}$-TS$_{\rm PL}$) is equivalent to the corresponding difference of maximum likelihoods computed between the two models.

For each interval, if ΔTS ≥ 30 (roughly corresponding to 5σ) then the PLEXP model provides a significantly better fit than the simple power-law and we retain the additional spectral component. In these time intervals, we also used the pion decay model to fit the data and estimated the corresponding proton spectral index. We performed a series of fits with the pion decay template models calculated for a range of proton spectral indices. We then fit the resulting profile of the log-likelihood function with a parabola and determine its minimum ($\mathcal{L}_{\rm min}$) and the corresponding value s_0 as the maximum likelihood value of the proton index.

In the lower panel of Figure 3 we combine the LLE and likelihood analysis results, showing the evolution of both the gamma-ray flux and the derived spectral index of the protons[6]. In the last five time intervals the power-law representation is adequate to describe

---

[6] After approximately 11:00:00 UTC the flux of the Sun diminished to the point that the spectral index of the proton distribution cannot be significantly constrained.

the data; in the last bin, the flare is only marginally significant (TS=7); the flux and the photon index are compatible with the values of the quiescent Sun. For this reason we have indicated the last point as an upper limit (computing the 95% C.L.). Unlike during the impulsive phase, the spectrum during the temporally extended phase becomes softer monotonically (s increases).

We also compare our results with the *GOES* proton spectral data. For this, we selected two energy bands (>30 MeV and >100 MeV) and corrected the light curve by the proton time-of-flight (TOF) to 1 AU by considering the TOF for 30 MeV and 100 MeV protons (i.e. the maximum delay in each energy band). As a measure of the spectral index of the SEP protons ($s_{\rm SEP}$), we compute the Hardness Ratio HR_p defined as:

$$\mathrm{HR}_p = \ln \frac{\mathrm{P}_{>100\mathrm{MeV}}}{\mathrm{P}_{>30\mathrm{MeV}}} \tag{2}$$

where P is the integral of the proton flux (assuming that the proton flux is proportional to a power law). The HR_p is related to the value of the spectral index, $s_{\rm SEP}$, of the SEP protons observed at 1 AU, roughly as:

$$s_{\rm SEP} \sim 1 - 0.83\,\mathrm{HR}_p \tag{3}$$

To estimate the uncertainty associated with this procedure we repeat the calculation neglecting the TOF correction. In this way we obtain two values for the SEP spectral index for each time bin, corresponding to the actual and zero delay due to the time of flight. In Figure 3 we report the estimated proton spectral index as the average of these two values and its uncertainty as half the difference of these two values. However we note that the $s_{\rm SEP}$ is for protons with energy less than a few hundred MeV while s is for protons with energies greater than 300 MeV. Diffusion is expected to play an important role in the transport of these SEPs but an in-depth transport analysis is beyond the scope of this paper. From our comparison we find that the proton spectral index inferred from the gamma-ray data is systematically softer than the value of the index derived directly from SEP observations but that the temporal evolution (hard-to-soft) is similar.

Uncertainties in the calibration of the LAT introduce systematic errors on the measurements. The uncertainty of the effective area is dominant, and for the `P7SOURCE_V6` event class it is estimated to be ∼10% at 100 MeV, decreasing to ∼5% at 560 MeV, and increasing to ∼10% at 10 GeV and above. We studied the effect of the systematic uncertainties on our final results via the bracketing technique described in detail in Ackermann et al. [2012b]. We find that the uncertainties on the flux are <10% and on the inferred proton index are <0.10. The results are represented by the gray bands in Figure 3.

3. New observations: the behind-the-limb synopsis

On 2013 October 11 at 07:01 UT a GOES M1.5 class flare occurred with soft X-ray emission lasting 44 min and peaking at 07:25:00 UT. Figure 4 shows the GOES, *STEREO*-B, *RHESSI*, *Fermi* GBM and LAT lightcurves of this flare. LAT detected >100 MeV emission for ∼30 min with a peak flux between 07:20:00–07:25:00 UT. *RHESSI* coverage was from 07:08:00 − 07:16:40 UT, overlapping with *Fermi* for 9 min.

Images in Figure 5 from the *STEREO*-B Extreme-UltraViolet Imager [EUVI; Wuelser et al. 2004] and the *SDO* Atmospheric Imaging Assembly [AIA; Lemen et al. 2012] of the photosphere indicate that the AR was ∼9.9° behind the limb at the time of the flare. LASCO onboard the *Solar and Heliospheric Observatory* (*SOHO*) observed a backside asymmetric halo CME associated with this flare beginning at 07:24:10 UT with a linear speed of 1200 km/s [SOHO LASCO CME CATALOG 2013] and a bright front over the Northeast. Both *STEREO* spacecrafts detected energetic electrons, protons, and heavier ions including helium, as well as type-II radio bursts indicating the presence of a coronal–heliospheric shock. *SDO* observed a global EUV wave (Liu et al. 2015, in prep.), possibly the coronal counterpart of the shock. *STEREO*-B had an unblocked view of the entire flare and detected a maximum rate of 3.5×10^6 photons/sec in its 195 Å channel, corresponding to a GOES M4.9 class [Nitta et al. 2013] if it had not been occulted.

The LAT data were analyzed using the unbinned maximum likelihood algorithm `gtlike` implemented in the *Fermi* `ScienceTools`[7] with `P7REP_SOURCE_V15` instrument response functions. We selected gamma-rays from a 12° region centered on the Sun and within 100° of the zenith to reduce contamination from the Earth's limb. For *RHESSI* data, we implemented the CLEAN imaging algorithm [Hurford et al. 2002] using the detectors 3−9 to reconstruct the X-ray images. We used the FITS World Coordinate System software package [Thompson and Wei 2010] to co-register the flare location between *STEREO* and *SDO* images. The *STEREO* light curves are pre-flare background subtracted, full-Sun integrated photon rates.

We measure the direction of the LAT > 100 MeV gamma-ray emission [as described in Ajello et al. 2014] and find a best fit position for the emission centroid at heliocentric coordinates of $(-855'', 75'')$ with a 68% error radius of $251''$, as shown in Figure 5(b). *RHESSI* X-ray sources integrated over

---

[7] We used version 09-30-01 available from the *Fermi* Science Support Center `http://fermi.gsfc.nasa.gov/ssc/`

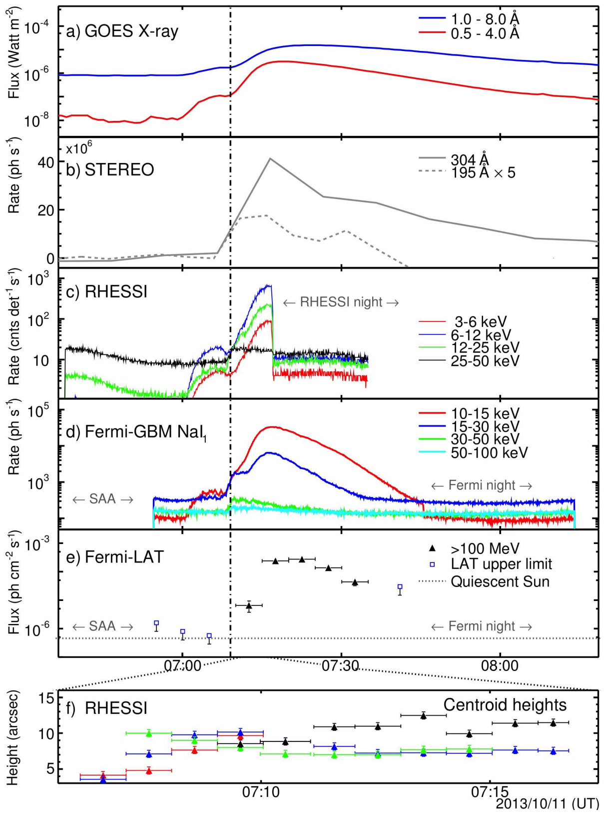

Figure 4: **PRELIMINARY:** Light curves of the 2013 October 11 flare as detected by a) *GOES*, b) *STEREO*, c) *RHESSI*, d) GBM, e) LAT and e) *RHESSI* emission centroid heights, with the same color coding as in c). *Fermi* exited the South Atlantic Anomaly (SAA) at 06:57:00 UT.

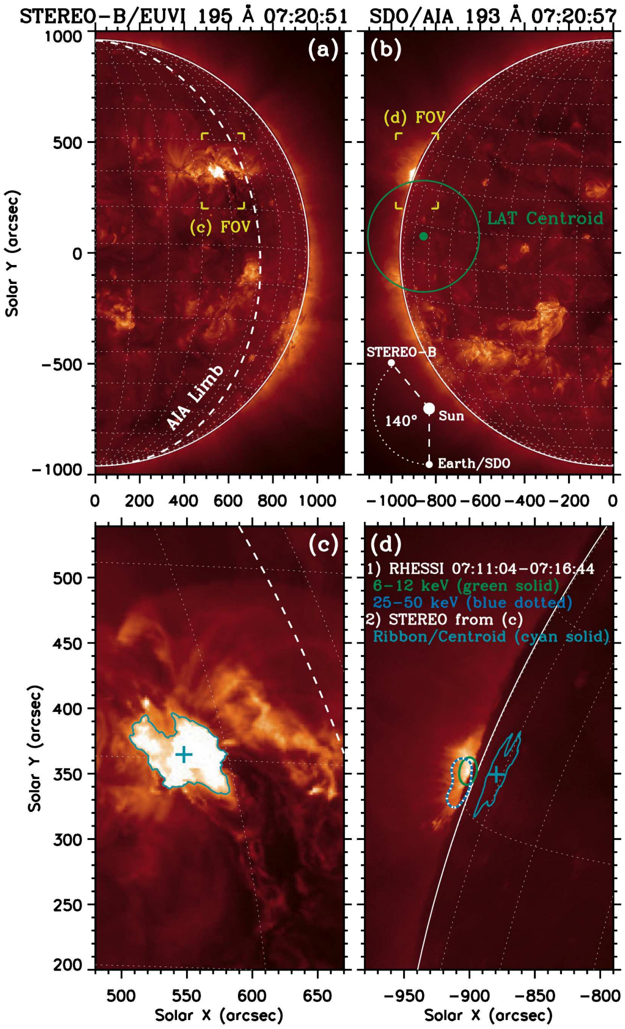

Figure 5: **PRELIMINARY:** *STEREO*-B (left) and *SDO* (right) images near the flare peak. The white-dashed line in (a) and (c) represents the solar limb as seen by *SDO*. The green line in (b) shows the 68% error circle for the LAT source centroid. The cyan contour and plus sign in (c) mark the *STEREO* flare ribbon and its centroid, respectively. Their projected view as seen from the AIA perspective is shown in (d), in which the centroid is located at 9.9° behind-the-limb. The green and blue-dotted contours in (d) show *RHESSI* sources. The rectangular brackets in (a) and (b) mark the field of view (FOV) for (c) and (d), respectively.

07:11:04–07:16:44 UT are shown as 80%-level, off-limb contours in Figure 5(d).

The temporal evolution of the projected *RHESSI* source heights above the solar limb are shown in Figure 4(f). The higher-energy emission generally comes from greater heights, consistent with expectations for a loop-top source [e.g., Masuda et al. 1994, Sui and Holman 2003, Liu et al. 2004]. If this were a footpoint source, we would expect an opposite trend since larger column depths are required for stopping higher-energy electrons [e.g., Liu et al. 2006, Kontar, E. P. et al. 2008]. Moreover, from *SDO*/AIA movies we find no signature of EUV ribbons, even in the late phase during the *RHESSI* night. Together, these observations provide convincing evidence that the footpoints were indeed occulted.

4. Discussion

We have presented the analysis of three solar flares detected by the *Fermi* LAT at high energy, and we highlight some of the similarities and differences of these flares. The high-energy emission of the 2012 June solar flare seems to be correlated with HXR emission, suggesting that acceleration of particles and gamma-ray emission take place close in space. Specifically, particles accelerated at the loop top could propagate along the loop field lines interacting and emitting gamma-rays at the footprint. For this flare, there is no evidence for precipitation of trapped flare particles, particles accelerated in magnetic loops after the impulsive phase, particles accelerated in CME-associated reconnecting current sheets [Ryan 2000b], or particles sharing the same origin as the Solar Energetic Particles (SEPs) observed in space [Ramaty et al. 1987, Cliver et al. 1993]. On the other hand, flares with long (or sustained) gamma-ray emission have also been observed by the *Fermi* LAT. Temporal and spectral analysis suggests that, even if the short impulsive phase is clearly visible at > 100 MeV energies, the sustained long lasting emission is more correlated with SEP properties, suggesting that, for this class of flares, either long trapping, continuous acceleration, or acceleration at the CME shock could be a better explanation. The behind-the-limb flare detection at high-energy adds additional considerations that are extremely useful for understanding the physics of particle acceleration and gamma-ray production during solar flares. We have presented preliminary results from the 2013 October 11 solar flare from *Fermi*, *RHESSI*, *SDO* and *STEREO*. *STEREO*-B images indicate that the flare occurred in an AR 9.9° behind-the-limb. *RHESSI* and GBM NaI_1 detected HXRs up to 50 keV from the flaring loop-top. The most unusual aspect of this flare is the LAT detection of photons of energies ϵ >100 MeV for about 30 minutes with some photons having energies up to several GeV.

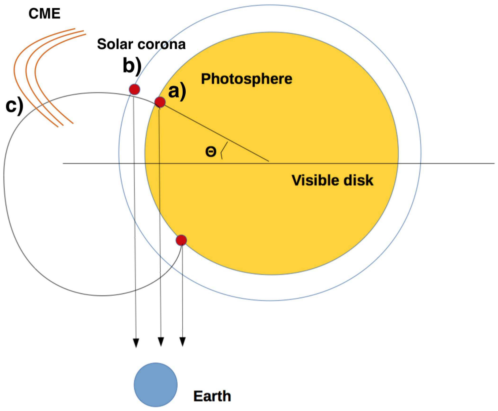

Figure 6: Model a): acceleration at the flare, gamma-ray emission site below the photosphere; b) acceleration at the flare, gamma-ray emission in the corona above the limb; c) acceleration (or re-acceleration) at the CME-shock, gamma-ray emission at the Sun.

We consider three scenarios for the emission site of the gamma-rays, outlined in Figure 6. Electrons or protons with energies $E > \epsilon$ can produce these photons after traversing a column depth of matter which is much larger than the depth penetrated by HXR producing electrons (model a). For occulted flares the emitted photons must traverse even larger depths than particles and they may be scattered and absorbed. Alternatively, acceleration and gamma-ray emission can take place in the corona above the limb (model b), suggesting trapping of particles, e.g., by strongly converging magnetic fields. In the third model (model c) CME-shock accelerated particles can travel back to the Sun along magnetic fields connecting the acceleration site with the visible side of the Sun. *Fermi* LAT observation of the 2013 October 11 flare (paper in preparation) shows that model a) can be ruled out. The LAT detection of gamma-ray emission from a flare with $\theta > 20°$ also poses some complications to the second scenario (model b), as particles will have to be accelerated even further away in the corona, where densities are very low. Acceleration (or re-acceleration) at the CME shock (model c) remains possible. *Fermi* LAT observations are becoming very important to disentangle models of particles acceleration and gamma-ray production in solar flares. Future LAT observations, combined with a systematic study of the solar flares detected at high energy, will very likely help to understand this fascinating problem, as well as to improve our knowledge of particle acceleration in astrophysical sources in general.

Acknowledgments

The *Fermi* LAT Collaboration acknowledges support from a number of agencies and institutes for both development and the operation of the LAT as well as scientific data analysis. These include NASA and DOE in the United States, CEA/Irfu and IN2P3/CNRS in France, ASI and INFN in Italy, MEXT, KEK, and JAXA in Japan, and the K. A. Wallenberg Foundation, the Swedish Research Council and the National Space Board in Sweden. Additional support from INAF in Italy and CNES in France for science analysis during the operations phase is also gratefully acknowledged.

References

D. J. Forrest and E. L. Chupp, *Nature* **305**, 291 (1983).

S. R. Kane, E. L. Chupp, D. J. Forrest, G. H. Share, and E. Rieger, *Astrophys. J. Lett.* **300**, L95 (1986).

G. Kanbach, D. L. Bertsch, C. E. Fichtel, R. C. Hartman, S. D. Hunter, D. A. Kniffen, B. W. Hughlock, A. Favale, R. Hofstadter, and E. B. Hughes, *Space Sci. Rev.* **49**, 69 (1988).

J. A. Esposito, D. L. Bertsch, A. W. Chen, B. L. Dingus, C. E. Fichtel, R. C. Hartman, S. D. Hunter, G. Kanbach, D. A. Kniffen, Y. C. Lin, et al., *Astrophys. J. Supp.* **123**, 203 (1999).

J. M. Ryan, *Space Sci. Rev.* **93**, 581 (2000a).

A. A. Atwood, W. B.Abdo, M. Ackermann, M. Ajello, L. Baldini, J. Ballet, G. Barbiellini, M. G. Baring, D. Bastieri, K. Bechtol, R. Bellazzini, et al., *Astrophys. J.* **697**, 1071 (2009a), 0902.1089.

C. Meegan, G. Lichti, P. N. Bhat, E. Bissaldi, M. S. Briggs, V. Connaughton, R. Diehl, G. Fishman, J. Greiner, A. S. Hoover, et al., *Astrophys. J.* **702**, 791 (2009), 0908.0450.

A. A. Abdo, M. Ackermann, M. Ajello, L. Baldini, J. Ballet, G. Barbiellini, D. Bastieri, K. Bechtol, R. Bellazzini, B. Berenji, et al., *Astrophys. J.* **734**, 116 (2011a), 1104.2093.

M. Ohno, H. Takahashi, Y. T. Tanaka, V. Vasileiou, N. Omodei, D. Gruber, and A. Goldstein, The Astronomer's Telegram **3635**, 1 (2011).

N. Omodei, G. Vianello, M. Pesce-Rollins, A. Allafort, and D. Gruber, The Astronomer's Telegram **3552**, 1 (2011).

Y. T. Tanaka, N. Omodei, N. Giglietto, H. Takahashi, D. J. Thompson, S. Ciprini, and P. R. Den Hartog, The Astronomer's Telegram **3886**, 1 (2012).

V. Petrosian, Q. Chen, N. Giglietto, N. Omodei, G. Share, Y. Tanaka, and Fermi Collaboration, in *American Astronomical Society Meeting Abstracts 220* (2012), vol. 220 of *American Astronomical Society Meeting Abstracts*, p. 424.04.

N. Omodei, F. Longo, G. Share, M. Briggs, D. Gruber, F. LAT, and GBM Collaborations, in *American Astronomical Society Meeting Abstracts 220* (2012), vol. 220 of *American Astronomical Society Meeting Abstracts*, p. 424.03.

M. Ackermann, M. Ajello, A. Allafort, W. B. Atwood, L. Baldini, G. Barbiellini, D. Bastieri, K. Bechtol, R. Bellazzini, P. N. Bhat, et al., *Astrophys. J.* **745**, 144 (2012a).

V. Pelassa, R. Preece, F. Piron, N. Omodei, S. Guiriec, and Fermi LAT & GBM collaborations, ArXiv e-prints (2010), 1002.2617.

A. A. Abdo et al., Astroparticle Physics **32**, 193 (2009).

M. Ackermann, M. Ajello, A. Albert, A. Allafort, L. Baldini, G. Barbiellini, D. Bastieri, K. Bechtol, R. Bellazzini, E. Bissaldi, et al., The Astrophysical Journal **787**, 15 (2014), URL `http://stacks.iop.org/0004-637X/787/i=1/a=15`.

M. A. A. Ajello, A. Allafort, L. Baldini, G. Barbiellini, D. Bastieri, R. Bellazzini, E. Bissaldi, E. Bonamente, T. J. Brandt, J. Bregeon, et al., The Astrophysical Journal **789**, 20 (2014), URL `http://stacks.iop.org/0004-637X/789/i=1/a=20`.

W. B. Atwood, A. A. Abdo, M. Ackermann, W. Althouse, B. Anderson, M. Axelsson, L. Baldini, J. Ballet, D. L. Band, G. Barbiellini, et al., *Astrophys. J.* **697**, 1071 (2009b), 0902.1089.

J. C. Martínez Oliveros, S. Couvidat, J. Schou, S. Krucker, C. Lindsey, H. S. Hudson, and P. Scherrer, *Sol. Phys.* **269**, 269 (2011), 1012.0344.

B. T. Park, V. Petrosian, and R. A. Schwartz, *Astrophys. J.* **489**, 358 (1997).

R. J. Murphy, C. D. Dermer, and R. Ramaty, *Astrophys. J. Supp.* **63**, 721 (1987).

D. V. Reames, Advances in Space Research **15**, 41 (1995).

R. J. Murphy, G. H. Share, J. E. Grove, W. N. Johnson, R. L. Kinzer, J. D. Kurfess, M. S. Strickman, and G. V. Jung, *Astrophys. J.* **490**, 883 (1997).

R. J. Murphy, G. H. Share, J. G. Skibo, and B. Kozlovsky, *Astrophys. J. Supp.* **161**, 495 (2005).

R. J. Murphy, B. Kozlovsky, G. H. Share, X. Hua, and R. E. Lingenfelter, *Astrophys. J. Supp.* **168**, 167 (2007).

A. A. Abdo, M. Ackermann, M. Ajello, L. Baldini, J. Ballet, G. Barbiellini, D. Bastieri, K. Bechtol, R. Bellazzini, B. Berenji, et al., *Astrophys. J.* **734**, 116 (2011b).

R. P. Lin, B. R. Dennis, G. J. Hurford, D. M. Smith, A. Zehnder, P. R. Harvey, D. W. Curtis, D. Pankow, P. Turin, M. Bester, et al., *Sol. Phys.* **210**, 3 (2002).

J. R. Mattox, D. L. Bertsch, J. Chiang, B. L. Dingus, S. W. Digel, J. A. Esposito, J. M. Fierro, R. C. Hartman, S. D. Hunter, G. Kanbach, et al., *Astrophys. J.*v.461 **461**, 396 (1996).

M. Ackermann, M. Ajello, A. Albert, A. Allafort, W. B. Atwood, M. Axelsson, L. Baldini, J. Ballet, G. Barbiellini, D. Bastieri, et al., *Astrophys. J. Supp.* **203**, 4 (2012b).

J. Wuelser, J. R. Lemen, T. D. Tarbell, C. J. Wolfson, J. C. Cannon, B. A. Carpenter, and et al., Society of Photo-Optical Instrumentation Engineers (SPIE) Conference Series (2004).

J. Lemen, A. Title, D. Akin, P. Boerner, C. Chou, J. Drake, D. Duncan, C. Edwards, F. Friedlaender, G. Heyman, et al., Solar Physics **275**, 17 (2012), ISSN 0038-0938, URL `http://dx.doi.org/10.1007/s11207-011-9776-8`.

SOHO LASCO CME CATALOG, `http://cdaw.gsfc.nasa.gov/CME_list/` (2013).

N. V. Nitta, M. J. Aschwanden, P. F. Boerner, S. L. Freeland, J. R. Lemen, and J.-P. Wuelser, *Sol. Phys.* **288**, 241 (2013), 1304.4163.

G. J. Hurford, E. J. Schmahl, R. A. Schwartz, A. J. Conway, M. J. Aschwanden, A. Csillaghy, B. Dennis, C. Johns-Krull, S. Krucker, R. P. Lin, et al., Solar Physics **210**, 61 (2002), ISSN 0038-0938, URL `http://dx.doi.org/10.1023/A3A1022436213688`.

W. T. Thompson and K. Wei, *Sol. Phys.* **261**, 215 (2010).

S. Masuda, T. Kosugi, H. Hara, S. Tsuneta, and Y. Ogawara, *Nature* **371**, 495 (1994).

L. Sui and G. D. Holman, *Astrophys. J. Lett.* **596**, L251 (2003).

W. Liu, Y. W. Jiang, S. Liu, and V. Petrosian, *Astrophys. J. Lett.* **611**, L53 (2004), astro-ph/0401381.

W. Liu, S. Liu, Y. W. Jiang, and V. Petrosian, *Astrophys. J.* **649**, 1124 (2006), astro-ph/0603510.

Kontar, E. P., Hannah, I. G., and MacKinnon, A. L., *A&A* **489**, L57 (2008), URL `http://dx.doi.org/10.1051/0004-6361:200810719`.

J. M. Ryan, *Space Sci. Rev.* **93**, 581 (2000b).

R. Ramaty, R. J. Murphy, and C. D. Dermer, *Astrophys. J. Lett.* **316**, L41 (1987).

E. W. Cliver, S. W. Kahler, and et al., in *International Cosmic Ray Conference* (1993), vol. 3 of *International Cosmic Ray Conference*, pp. 91–+.

Analysis of the Impulsive Phase of Solar Flares with Pass 8 LAT data

R. Desiante
Udine University, INFN-Trieste & C.I.F.S., Italy
F. Longo
Trieste University & INFN-Trieste, Italy
N. Omodei
Stanford University/KIPAC, Stanford, CA, USA
M. Pesce-Rollins
INFN-Pisa, Italy
V. Pelassa
University of Alabama in Huntsville/CSPAR, Huntsville, AL, USA
on behalf of the *Fermi*-LAT Collaboration

We show the results of analyses performed on high-energy gamma-ray emission during the impulsive phase of solar flares detected by the LAT using Pass 8 data. We compare results obtained with Pass 7 and Pass 8 data sets, using both LAT Low Energy and standard data classes. With a dedicated event selection, Pass 8 allows standard analysis during the impulsive phase: it has been designed to be less susceptible to pile-up in the LAT Anti-Coincidence Detector caused by the intense hard X-ray emission at early times.

1. INTRODUCTION

A solar flare is an intense and rapid energy release in the solar corona driven by stored magnetic energy liberated by coronal magnetic reconnection processes. This energy release results in acceleration of particles, including electrons, protons and heavy nuclei, to a wide range of energies and in heating of coronal and chromospheric plasma.

Looking at the X and gamma-ray light curves we can distinguish four different temporal phases of solar flares emission [1] [2]:

- precursor, observed as a gradual raise of emission mainly visible in soft X-rays;
- impulsive, characterized by a rapid raise of hard X and gamma-ray flux;
- gradual, slow decaying of X and gamma-ray flux;
- extended, mainly observed as a sustained gamma-ray emission that can lasts for several hours.

Coronal Mass Ejections (CMEs) are also often observed in close association with gamma-ray detected solar flares.

1.1. The impulsive phase of Solar Flares as seen by the LAT

The Gamma-ray Burst Monitor (GBM) and the Large Area Telescope (LAT), the two instruments onboard to the *Fermi* Observatory, can detect photons with energies from 8 keV up to 300 GeV. Both instruments also have very large fields of view (FOV) achieving together an unprecedented coverage of the X and gamma-ray sky: the GBM FOV consists of the whole not-occulted sky and the LAT scans about the 20% of the sky at any instant. These characteristics make the *Fermi* Spacecraft a perfect observatory to study and monitor both the quiescent phase and the eruptive phases of solar activity at high energies [3] [4] [5] [6] [7].

The first impulsive solar flare detected by *Fermi* occurred on 2010 June 12 00:30 UT: together the *Fermi* LAT and the GBM observed X and gamma-ray emission, from few keV up to $\sim$ 400 MeV, in coincidence with a moderate GOES M2.0 class solar flare. As fully explained in [4], the observed spectrum has been interpreted as:

- electron bremsstrahlung, nuclear lines and pion decay components for energies < 10 MeV;
- high-energy electron bremsstrahlung or pion decay component above 30 MeV.

The analysis of LAT data was performed using only the LAT Low Energy Events Technique (LLE) [8] because the intense X-ray flux occurring during the prompt phase of a solar flare causes pile-up in the anti-coincidence detector (ACD) of the LAT [4] [9] resulting in a strong suppression of the rate of standard LAT Pass 6 / Pass 7 on-ground photon classification [10]. We show that these issues have been carefully addressed in new Pass 8 photon classification.

LLE event selection, that does not suffer of ACD pile-up, uses less discriminating criteria then the standard on-ground processing, resulting in a larger effective area but a lower signal-to-noise ratio: LLE data are background dominated and not suitable for localization studies.

2. PASS 8 DATA: IMPROVEMENTS FOR SOLAR FLARES SCIENCE

The event selection developed for the LAT has been periodically updated. While Pass 7 REP is the current event analysis distributed to the community, the new Pass 8 data, that will be available in next few months, represent a radical revision of the entire event-level analysis that includes every aspect of the data reduction process. The improvements include a significant reduction in background contamination, an increased effective area, a better point-spread function, a better control on the systematic uncertainties and an extension of the energy range below 100 MeV and above a few hundred GeV [11] [12]. This means to improve the solar flares detection capabilities of the LAT, in particular at low energies; the increase in photon statistics will also allow to better constrain the spectral features and to reduce the uncertainties in localization studies. As already mentioned in Sec.1.1, a solar-flare dedicated event class selection has been also developed: this will alleviate the ACD pile-up effect often present during impulsive solar flares [13].

2.1. Data analysis: Light-curves and Spectra

Light-curves in Fig.1 show a comparison of different LAT TRANSIENT data collected in the energy range 35 MeV - 10 GeV:

- P7 TR and P8 R100 are the loosest event classes for the the two different response functions Pass 7 REP and Pass 8;
- P8 SFR is the solar flare optimized event class newly developed in Pass 8.

We consider LAT observations of three different solar flares:

- SOL2010-06-12, M2.0 GOES class, already mentioned in Sec.1.1;
- SOL2011-09-06, X2.1 GOES class, detected on 2011 September 06 22:17 UT;
- SOL2012-06-03, M3.3 GOES class, occurred on 2012 June 03 17:53 UT.

While impulsive and sustained gamma-ray emission from SOL2012-06-03 has been significantly detected using Pass 7 standard event classes, SOL2010-06-12 and SOL2011-09-06 were detected in Pass 7 only through LLE technique [6].

If we focus on standard event selections, Fig.1 shows that Pass 8 performs better both on previously detected and not-detected flares. Moreover, the P8 SFR event class, developed with a better treatment of ACD variables, produces a less noisy light-curve for all flares. In the case of SOL2011-09-06 (the highest GOES class flare of our sample), this results also in a greater number of total counts detected; the Pass 7 signal is instead completely suppressed because of ACD pile-up caused by the intense X-ray flux.

We also tested the improvements of Pass 8 event selection on LLE technique. In Fig.2 there is a comparison of light-curves obtained using Pass 8 LLE data versus Pass 7 LLE data for SOL2010-06-12 (left panel) and SOL2011-09-06 (right panel). The number of detected counts (upper plots) is higher for P7 LLE since Pass 8 event selection is less affected by background contamination but, as shown by the normalized number of detected counts (bottom plots), the P8 LLE light-curves provide a better signal-to-noise ratio.

To test the benefit of using Pass 8 data for spectral analysis we produced LAT (40 MeV - 1 GeV) and GBM-BGO (0.3 - 40 MeV) spectra accumulated during the LLE-detection time range for SOL2011-09-06 and SOL2012-06-03. Using the tool XSPEC [1] we fit the data with the usual components (Fig.3 and Fig.4): a power-law for electron bremsstrahlung in the BGO energy range, a nuclear lines template, Gaussian lines at 0.511 MeV and 2.223 MeV (related respectively to positron-electron annihilation and neutron capture) and a pion template in the high-energy part of the spectrum [4]. While a rigorous spectral analysis is beyond the scope of this presentation, we want to stress that:

- spectral analysis is now possible using P8 standard event classes also during the impulsive phase of solar flares;
- for both flares analyzed, R100 data cover a slightly wider energy range compared with P7 LLE data.

3. PROSPECTS AND CONCLUSIONS

Pass 8 data allow to study the Impulsive Phase of solar flares with standard LAT selections. Moreover Pass 8 event reconstruction improvements also impact the LLE selection technique. A dedicated Pass 8 solar flare events class, less susceptible to ACD pile-up, is in development.

Preliminary results using Pass 8 data are in agreement with Pass 7 and but show greater signal-to-noise ratios and promising improvements for spectral analysis. Validation of Pass 8 data at low energy (< 100 MeV) is on-going in order to address energy dispersion issues. We plan a systematic study of GBM-BGO

---

[1] `http://heasarc.gsfc.nasa.gov/xanadu/xspec/`

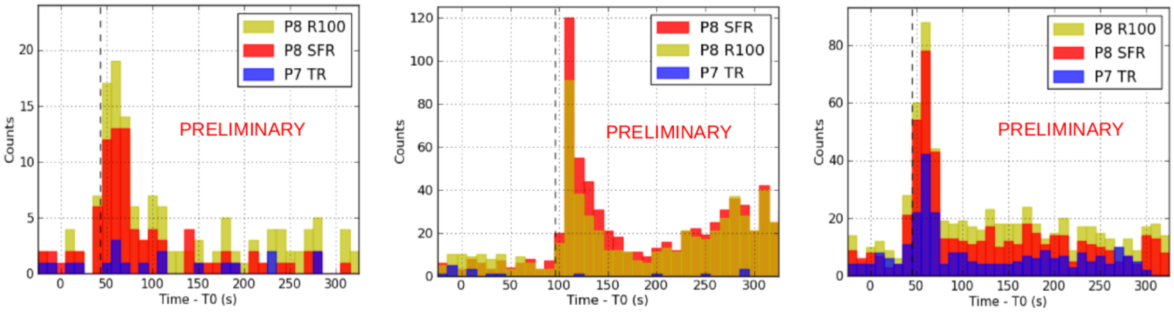

Figure 1: SOL2010-06-12 (left panel), SOL2011-09-06 (middle panel), SOL2012-06-03 (right panel). For each solar flare we compare the light-curves obtained using different event selections. Data are extracted in the energy range 35 MeV - 10 GeV. T0 is the GBM trigger time; the dashed line marks the LLE detection time.

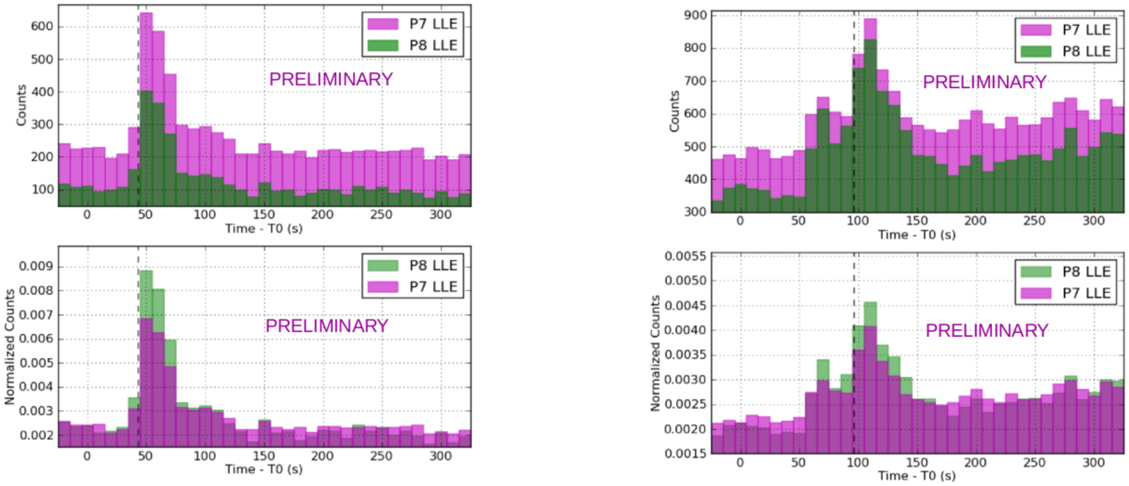

Figure 2: Light-curves obtaind using Pass 8 LLE data VS P7 LLE data for SOL2010-06-12 (left panel) and SOL2011-09-06 (right panel). For each flare, the upper plot shows the number of detected counts while the bottom plot shows the number of detected counts normalized to the total.

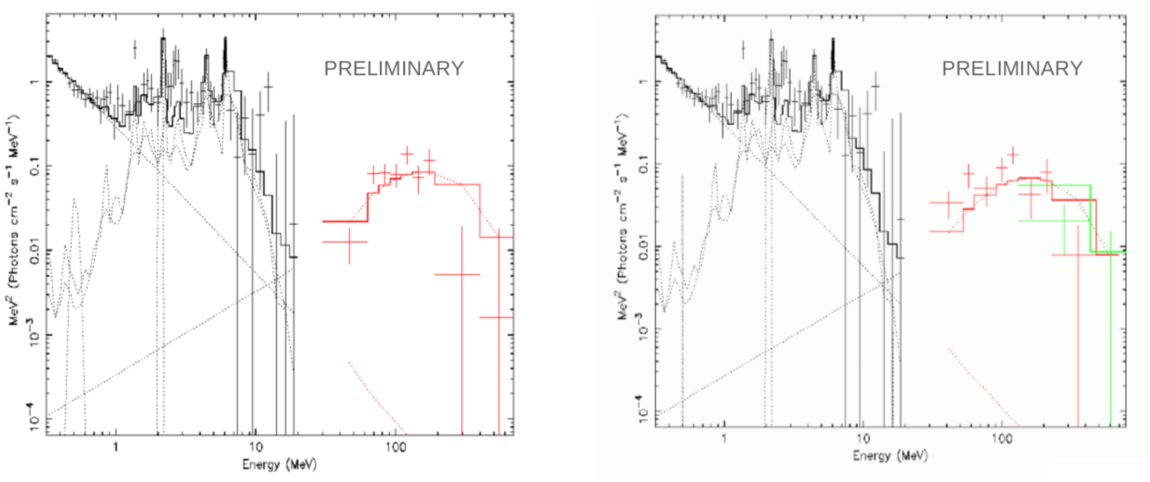

Figure 3: SOL2011-09-06: background subctracted count spectra obtaind using GBM-BGO (black), P7 LLE (red, left panel), P8 LLE (red, right panel) and P8 R100 data (green, right panel).

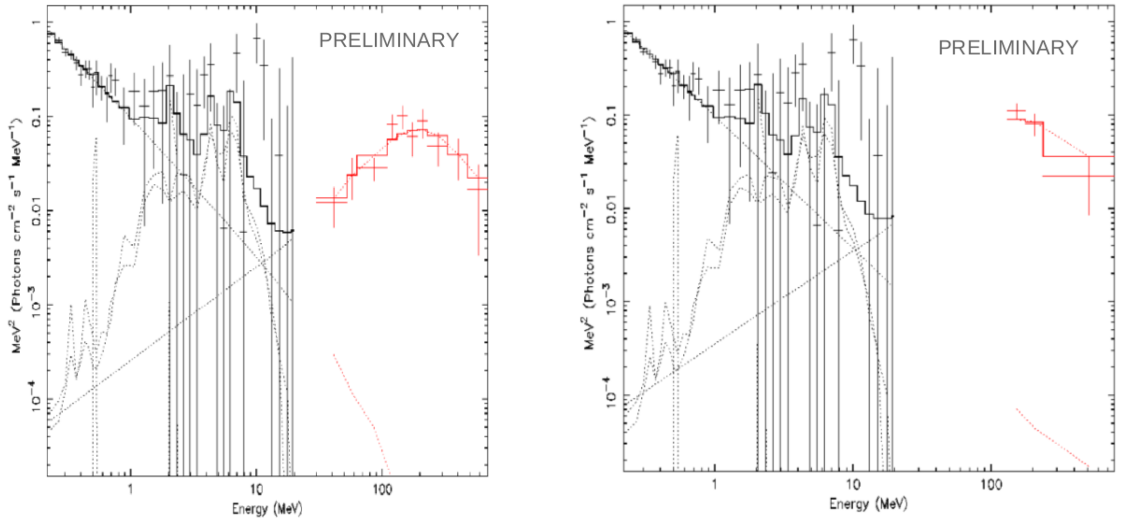

Figure 4: SOL2012-06-03: background subctracted count spectra obtaind using GBM-BGO (black), P7 LLE (red, left panel) and P8 R100 data (red, right panel).

bright solar flares, useful to better understand the high-energy emission processes occuring in the solar corona.

Pass 8 improvements will allow to better study the low energy gamma-ray part of the spectrum and discriminate between hadronic and leptonic origin. Temporal studies on the onset of high-energy emission are also on-going.

Acknowledgments

The *Fermi*-LAT Collaboration acknowledges support for LAT development, operation and data analysis from NASA and DOE (United States), CEA/Irfu and IN2P3/CNRS (France), ASI and INFN (Italy), MEXT, KEK, and JAXA (Japan), and the K.A. Wallenberg Foundation, the Swedish Research Council and the National Space Board (Sweden). Science analysis support in the operations phase from INAF (Italy) and CNES (France) is also gratefully acknowledged.

References

[1] H.S. Hudson, Space Science Reviews, Volume 158, Issue 1, pp.5-41, 2011
[2] E.R. Priest, Science, Vol.214, P. 356, 1981
[3] A.A. Abdo et al., ApJ, 734, 116, 2011
[4] M. Ackermann et al., ApJ, 745, 144, 2012
[5] M. Ajello et al., ApJ, 789, 20, 2014
[6] M. Ackermann et al., ApJ, 787, 15, 2014
[7] N. Omodei et al., ArXiv e-prints: 1502.03895, 2015
[8] V. Pelassa et al., ArXiv e-prints: 1002.2617, 2010
[9] A. A. Abdo et al., Astropart. Phys., 32, 193, 2009
[10] W. B. Atwood et al., ApJ, 697, 1071, 2009
[11] W. B. Atwood et al., ArXiv e-prints: 1303.3514, 2012
[12] L. Baldini et al., "Astroparticle Physics 2014, A Joint TeVPA/ IDM Conference", `http://indico.cern.ch/event/278032/session/6/contribution/24/material/slides/0.pdf`
[13] M. Pesce-Rollins et al, "Astroparticle Physics 2014, A Joint TeVPA/ IDM Conference", `http://indico.cern.ch/event/278032/session/9/contribution/201/material/slides/0.pdf`

Galaxy Clusters with the Fermi-LAT: Status and Implications for Cosmic Rays and Dark Matter Physics

S. Zimmer
Oskar Klein Center for Cosmoparticle Physics and Department of Physics, Stockholm University, Stockholm, SE 10691, Sweden
for the *Fermi*-LAT Collaboration

Galaxy clusters are the most massive systems in the known universe. They host relativistic cosmic ray populations and are thought to be gravitationally bound by large amounts of Dark Matter, which under the right conditions could yield a detectable γ-ray flux. Prior to the launch of the Fermi satellite, predictions were optimistic that Galaxy clusters would be established as γ-ray-bright objects by observations through its prime instrument, the Large Area Telescope (LAT). Yet, despite numerous efforts, even a single cluster detection is still pending.

1. Introduction

Galaxy clusters (GC) represent the largest virialized objects that are believed to have formed through a hierarchical build up of structures over the evolution of the universe. In this picture, baryonic matter accretes towards the gravitational well caused by large amounts of Dark Matter (DM) which make up 26% of the energy density of the Universe [Ade *et al.* 2014]. Through gravitational interaction, smaller structures merge with one another, forming groups of galaxies and eventually clusters. Determining the exact nature of DM is one of the greatest challenges of modern physics and weakly interactive massive particles (WIMPs) prove to be strong candidates fulfilling the role as DM particle [Bergstrom 1999, 2009]. The neutralino, which in several extensions of the standard model of particle physics is predicted to be the lightest stable supersymmetric particle, provides a natural WIMP candidate. In many of these models the neutralino can self-decay or annihilate into lighter standard model particles, among others high energy γ rays which, if observed, can be used to trace back the origin of the interaction and indirectly detect DM [Baltz *et al.* 2008].

While clusters are promising targets due to their large DM content, predicted γ-ray emission on top of that of individual cluster member galaxies constitutes an irreducible foreground. This foreground emission arises from cosmic ray (CR) interactions with the intra-cluster medium (ICM) and is motivated by conventional astrophysics [see, e.g. Petrosian *et al.* 2008, for a review], while the observation of DM-induced γ rays may be regarded as a somewhat more exotic signature [Pinzke *et al.* 2011].

In this contribution I will review the most recent studies of GCs with the Fermi Large Area Telescope (LAT) undertaken by the instrument team. I will start by summarizing recent efforts aiming at the astrophysical emission scenario of CR interactions resulting in a detectable γ-ray flux (Section 2) and briefly report on work in progress in regards to DM constraints that can be obtained from GCs (Section 3). Finally, I will discuss one of the challenges involved when searching for large extended sources such as GCs (Section 4) and conclude by commenting on the implications for future searches with the LAT.

2. Cosmic Ray Induced γ rays

The majority of the baryonic mass in GCs is present in the form of hot ionized gas, the ICM, which has been detected via thermal X-ray emission observed by contemporary space telescopes such as ROSAT or XMM-Newton [see, e.g. Kaastra *et al.* 2008, for a review]. In addition, large scale radio synchrotron emission has been detected in a number of the most nearby clusters which can be classified into halos and relics [Ferrari *et al.* 2008]. The latter appear polarized, while the former are not, suggesting a different emission mechanism to be at play. The observation of radio-synchrotron emission indicates the presence of a pool of relativistic electrons (CRe). Together with magnetic fields this provides a favorable environment for high energy particle interactions between the CRes and the ICM which may be observable through the detection of γ rays or hard X-rays [see, e.g. the excellent review by Brunetti and Jones 2014]. However, due to the short diffusion times, CRes must be constantly replenished, e.g. through injection by active galactic nuclei (AGN) or be created through secondary processes.

Another intriguing possibility are hadronically-induced γ rays. Here CR protons (CRp) may be accelerated within the ICM through means of diffusive shock acceleration (DSA) and due to their large diffusion time remain within the cluster volume. CRp then interact with the ICM and produce γ rays via decay of neutral pions. The latter has received particular attention as Pinzke and Pfrommer [2010] have shown the emergence of a universal model describing the CR interactions in a cosmological framework based on smooth-particle hydrodynamics simulations. In their model, the resultant γ-ray spectrum is dominated by the aforementioned π^0 decay and IC emission is essentially negligible. The spectrum shows the characteristic π^0 bump at ~ 130 MeV and for energies > 500 MeV follows a powerlaw with index 2.3.[1] The resulting spatial distribution is close to that of the thermal X-rays as it is expected that the CRs are following the gas. One key assumption when creating the model is that the maximum injection efficiency, $\zeta_{p,\max}$ at which protons can be accelerated via DSA is similar to that what has previously been observed in SNRs [Helder *et al.* 2009].[2] Together with the claimed universality of the spectrum, this allowed us to employ the joint likelihood technique, a statistical method in which each target is optimized according to its individual nuisance parameters and then the information from each individual likelihood is combined into a global likelihood by multiplying them [see Anderson 2014, this conference, for a technical discussion and applications].

The starting point for the study in Ackermann *et al.* [2014a] has been the extended HIFLUGCS catalog, a X-ray flux-limited complete sample of nearby GCs. Selecting a set of 50 clusters, we found a global excess at the level of $\sim 2.7\sigma$ which however could be entirely attributed to previously non-detected individual cluster member galaxies (with known counterparts in the radio band). Thus, with four years of LAT data, no cluster was detected and flux upper limits were set. The most constraining cluster in the sample is the Coma cluster with a reported integral flux limit of $4.0 \times 10^{-10}\mathrm{ph/cm^2/s}$ assuming an extended emission characteristic according to the benchmark model by Pinzke and Pfrommer [2010] and $2.5\times10^{-10}\mathrm{ph/cm^2/s}$ when considering a pointlike emission.[3] Based on the joint likelihood approach, we also find that in order to account for the non-observation, DSA must be either substantially less efficient ($\zeta_{p,\max} \lesssim 21\%$) or conversely, the CR-to-thermal pressure ratio must be lower than 1%, making the contribution of CRp's to the ambient γ-ray flux negligible [see also the discussion in Vazza and Brüggen 2014].

3. Dark Matter constraints from Cluster Observations

Given its non-detection, ongoing searches for γ rays from GC can thus be used to constrain the available parameter space of WIMP DM. Generically, the induced γ-ray flux from WIMP pair annihilation can be expressed as

$$\phi_s(\Delta\Omega) = \underbrace{\frac{1}{4\pi}\frac{\langle\sigma v\rangle}{m_{DM}^2}}_{\Phi_{PP}} \times \underbrace{\int_{\Delta\Omega}\int_{l.o.s.}\rho^2(r)dl\, d\Omega'}_{J-factor} . \quad (1)$$

In the above equation Φ_{PP} refers to the particle physics term containing both the mass of the WIMP and its velocity-averaged pair annihilation cross section $\langle\sigma v\rangle$. The second term is referred to as astrophysical, or J-factor and is the line of sight integral of the DM column density. N-body simulations suggest that DM clusters (clumps) across all mass scales, forming sub haloes in addition to the smooth main halo. The amount of substructure as well as the properties are largely unknown and current N-body simulations do not have the capabilities yet to resolve the smallest substructures. Hence, extrapolations over several orders of magnitude are necessary. For this (abbreviated) discussion it is sufficient to address the amount of substructure by the introduction of a dimensionless boost factor b, which relates the J-factor obtained by assuming a universal NFW halo [Navarro *et al.* 1997] to that obtained when considering different amounts of substructure. Depending on the extrapolation scheme, boost factors for clusters may vary between O(30) to O(1000) [see e.g. the discussion in Sánchez-Conde *et al.* 2011]. While the predicted annihilation flux profile is similar for both model predictions, the overall predicted flux may vary by orders of magnitude. This fact makes DM constraints from clusters (at least as far as annihilation is considered) more model dependent than e.g. those obtained from the observation of nearby dwarf spheroidal galaxies [Ackermann *et al.* 2014b].[4]

Ongoing work (based on a five year dataset) is focusing yet again on a subsample of the most massive nearby clusters, selected from the X-ray flux limited HIFLUCGS sample. We demand there to be no appreciable overlap by requiring a distance between each cluster of the sum of the virial radius of each cluster along with a 2° buffer accounting for the tails in the LAT point spread function (PSF). For the resulting 34 clusters we construct spatial templates according to substructure models considering both a *conservative* boost factor of O(30) [Sánchez-Conde and Prada 2014] and contrast this with a more *optimistic* choice of O(1000) [Gao *et al.* 2012]. For both configurations we perform a binned likelihood analysis. After having found the best fit parameters of our background fit, we construct a bin-by-bin likelihood function by assuming a simple powerlaw with index 2.0 in each energy bin which would account for the cluster emission. The advantage is that the resulting flux limits can be used to directly test spectrally different models without the need of repeating the entire likelihood procedure [see Ackermann *et al.* 2014b, for details regarding the bin-by-bin method]. In Fig. 1 we show both the J-factor distribution from our chosen sample as well as the estimated sensitivity by selecting high-latitude regions in the sky which are selected such that the center a) does not contain a 3FGL source [The Fermi-LAT Col-

---

[1] The interested reader is referred to Pinzke and Pfrommer [2010]. The true spectrum is concavely shaped but for the considered LAT energies, it can approximated with a powerlaw as discussed in the main text.

[2] In their works, the authors adopt $\zeta_{p,\max} = 50\%$ as benchmark when calculating their γ-ray predictions [Pinzke *et al.* 2011].

[3] These limits were calculated over the entire energy range of 500 MeV to 200 GeV.

[4] Note that the question of substructure is typically less important in the case of decay as the associated J-factor scales linearly with the DM density.

laboration 2015] and b) does not coincide with a cluster center or a circular region with a radius corresponding to the virial radius of the cluster.[5]

4. Challenging individual targets: very extended emission from the Virgo cluster

While the discussed emission mechanisms vary appreciably with regards to the spectral form of the predicted emission, the studies that I discussed here have in common that the targets are large extended sources.[6] However, even among these extended sources, there are extreme cases. The largest target is the Virgo cluster, our closest neighbor which appears as a structure in the Northern part of the sky that extends up to 14° in diameter. The cluster itself is undergoing a complex merger in which the main clumps centered around the giant ellipticals M87 and M49 are moving towards each other.

The poor PSF at low energy together with the large surface area require special care when searching for an extended emission contribution, as recently claimed [Han *et al.* 2012, Macías-Ramírez *et al.* 2012]. It is important to emphasize that the model for the Galactic foreground emission that is usually employed when analyzing Fermi-LAT data is optimized for point source searches. Indeed, when confronting a dataset comprising three years of collected photons between 100 MeV and 100 GeV, we find an extended excess if we employ the standard diffuse model [Ackermann *et al.* 2015].[7] However, when systematically performing a scan over the entire ROI by using a uniform disk of 3° radius, we find two distinct maxima which are spread out and appear away from both sub clump centers as shown in Fig. 2. Moreover, when using a set of alternatively derived diffuse foreground models [Ackermann *et al.* 2012, de Palma *et al.* 2013], the significance of this extended excess varies appreciably, implying that the source of the excess may be due to an incomplete modeling of the Galactic foreground emission.

5. Outlook

Despite intense efforts no γ-ray emission has been detected from clusters to date. In the meantime radio observations have revealed more and more systems containing extended, yet faint radio sources. This radio emission will remain the driving force when searching for non-thermal emission from galaxy clusters. The LAT with its continuous sky survey capabilities will remain instrumental in probing the important $\sim \mathrm{MeV} - \mathrm{GeV}$ domain which is much too low for air Cherenkov telescopes to be sensitive to. In particular the extension towards lower energies, enabled by the latest reconstruction algorithms, collectively dubbed *Pass 8* will help in achieving this goal [Atwood *et al.* 2013], as it provides a better PSF and an increased acceptance towards lower energies.

As for DM constraints, clusters will remain challenging targets - due to their large extension and the intrinsic uncertainties in their J-factors. However, they are also complementary targets to probe in case evidence arises from more promising targets such as dwarf galaxies or the Galactic center.

Acknowledgments

The *Fermi*-LAT Collaboration acknowledges support for LAT development, operation and data analysis from NASA and DOE (United States), CEA/Irfu and IN2P3/CNRS (France), ASI and INFN (Italy), MEXT, KEK, and JAXA (Japan), and the K.A. Wallenberg Foundation, the Swedish Research Council and the National Space Board (Sweden). Science analysis support in the operations phase from INAF (Italy) and CNES (France) is also gratefully acknowledged.

I wish to acknowledge the financial travel support of the W. Kobbs and Grundströms foundation and thank the organizers for a stimulating meeting.

References

Ackermann, M., M. Ajello, A. Albert, *et al.*, 2014a, ApJ **787**, 18.

Ackermann, M., M. Ajello, A. Allafort, *et al.*, 2010, J. Cosmology Astropart. Phys. **5**, 025.

Ackermann, M., M. Ajello, W. B. Atwood, *et al.*, 2012, ApJ **750**, 3.

Ackermann, M., A. Albert, B. Anderson, *et al.*, 2014b, Phys. Rev. D **89**(4), 042001.

Ackermann, M., *et al.*, 2015, in preparation .

Ade, P. A. R., N. Aghanim, C. Armitage-Caplan, *et al.*, 2014, A&A **571**, A16.

Anderson, B., 2014, this conference, in *eConf C141020.1.*

Atwood, W., A. Albert, L. Baldini, *et al.*, 2013, ArXiv e-prints 1303.3514.

Baltz, E., B. Berenji, G. Bertone, *et al.*, 2008, JCAP **0807**, 013.

---

[5] For this analysis we select the subset of P7REP photons that pass the CLEAN class and apply the recommended instrument response function `P7REP_CLEAN_V15`.

[6] With large we refer to an emission radius of $\sim 2 - 3^\circ$ (as in the case of the Fornax and Coma cluster, respectively).

[7] For this analysis we select `Pass 7` (P7V6) photons passing the `SOURCE` selection together and apply the recommended models for modeling the Galactic diffuse and isotropic emission. The reader is referred to the web pages of the Fermi Science Support Center for details: `http://fermi.gsfc.nasa.gov/ssc/data/access/lat/BackgroundModels.html`

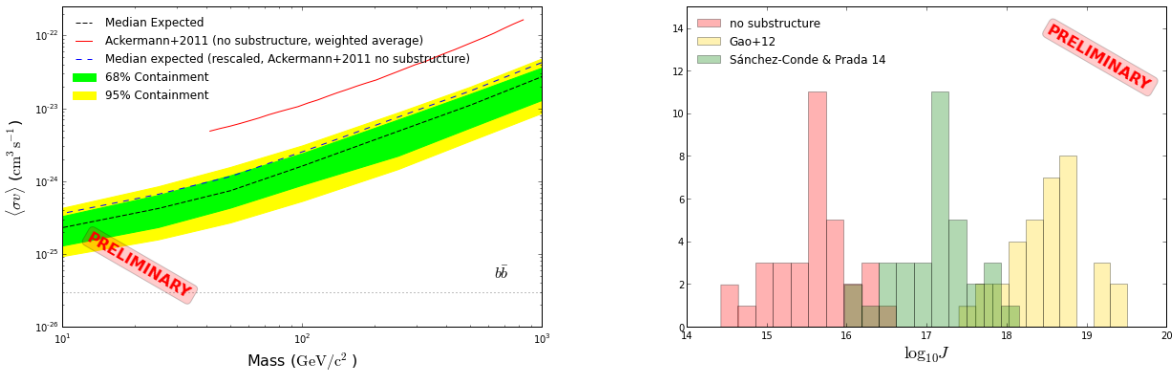

Figure 1: *Left:* Expected sensitivity (evaluated by calculating the combined one-sided 95% C.L. upper limit) for annihilating WIMP DM into $b\bar{b}$ from a combined analysis of 34 galaxy clusters in 5 years of LAT data using photons from 500 MeV-500 GeV. Each cluster model contains a conservative amount of substructure. The red solid line corresponds to the first LAT team publication based on 11 months of data [Ackermann *et al.* 2010] in which each individual limit has been weighted with the assumed J-factor (NFW only). *Right:* Distribution of J-factors for our chosen cluster sample. In the main text we refer to the setup by Sánchez-Conde and Prada [2014] as *conservative* setup. The *optimistic* configuration refers to the distribution labeled with Gao *et al.* [2012].

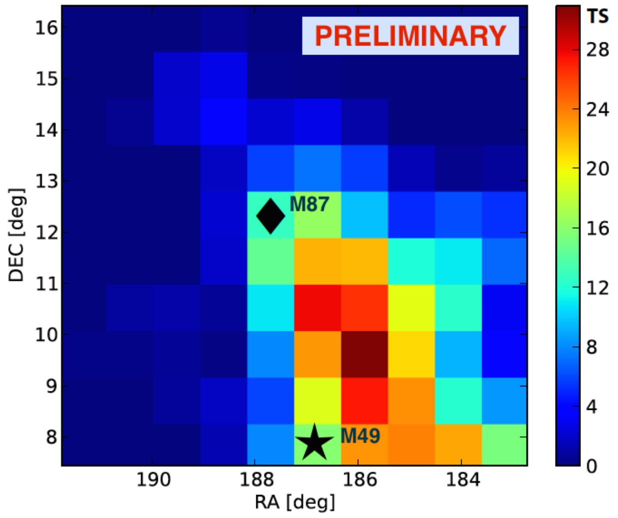

Figure 2: Grid scan of TS values when placing a uniform disk emission template with a powerlaw and $\gamma = 2.0$ on various positions in the map. This representation allows to map the observed excess when the foreground Galactic diffuse emission is modeled using the standard template for point source analysis. For reference we add the reported NED positions for the central galaxies M87 and M49 as diamond and star-shaped markers, respectively.

Bergstrom, L., 1999, Nucl. Phys. Proc. Suppl. **70**, 31.
Bergstrom, L., 2009, New J. Phys. **11**, 105006.
Brunetti, G., and T. W. Jones, 2014, International Journal of Modern Physics D **23**, 1430007.
de Palma, F., T. J. Brandt, G. Johannesson, L. Tibaldo, and for the Fermi LAT collaboration, 2013, ArXiv e-prints 1304.1395.
Ferrari, C., F. Govoni, S. Schindler, *et al.*, 2008, Space Sci. Rev. **134**, 93.
Gao, L., J. F. Navarro, C. S. Frenk, *et al.*, 2012, MNRAS **425**, 2169.
Han, J., C. S. Frenk, V. R. Eke, *et al.*, 2012, MNRAS **427**, 1651.
Helder, E. A., J. Vink, C. G. Bassa, *et al.*, 2009, Science **325**, 719.
Kaastra, J. S., F. B. S. Paerels, F. Durret, *et al.*, 2008, Space Sci. Rev. **134**, 155.
Macías-Ramírez, O., C. Gordon, A. M. Brown, *et al.*, 2012, Phys. Rev. D **86**(7), 076004.
Navarro, J. F., C. S. Frenk, and S. D. M. White, 1997, ApJ **490**, 493.
Petrosian, V., A. Bykov, and Y. Rephaeli, 2008, Space Sci. Rev. **134**, 191.
Pinzke, A., and C. Pfrommer, 2010, MNRAS **409**, 449.
Pinzke, A., C. Pfrommer, and L. Bergström, 2011, Phys. Rev. D **84**(12), 123509.
Sánchez-Conde, M. A., M. Cannoni, F. Zandanel, *et al.*, 2011, J. Cosmology Astropart. Phys. **12**, 011.
Sánchez-Conde, M. A., and F. Prada, 2014, MNRAS **442**, 2271.
The Fermi-LAT Collaboration, 2015, ArXiv e-prints 1501.02003.
Vazza, F., and M. Brüggen, 2014, MNRAS **437**, 2291.

arXiv:1502.02566v2 [astro-ph.HE] 10 Feb 2015

Isotropic diffuse γ-ray background: unveiling Dark Matter components beyond the contribution of astrophysical sources.

Mattia Di Mauro,*
Dipartimento di Fisica, Università di Torino, via P. Giuria 1, 10125 Torino, Italy
Istituto Nazionale di Fisica Nucleare, Sezione di Torino, Via P. Giuria 1, 10125 Torino, Italy and
LAPTh, Université de Savoie, CNRS, 9 Chemin de Bellevue, B.P. 110, F-74941 Annecy-le-Vieux, France

We present the first interpretation of the new isotropic diffuse γ-ray background (IGRB), measured by the *Fermi* Large Area Telescope (LAT), based on a statistical analysis. We demonstrate that the γ-ray emission from unresolved active galactic nuclei and star forming galaxies is consistent with the *Fermi*-LAT IGRB data within the uncertainties both on the choice of the Galactic diffuse emission model and on the γ-ray emission mechanism of these sources. Furthermore, adding to the extragalactic sources the contribution from a smooth Galactic halo of annihilating weakly interacting dark matter (DM) particles, we are able to set stringent limits on the DM annihilation cross section. Finally, we demonstrate that the addition of DM can significantly improve the fit to IGRB data.

1. Introduction

Recently, the Large Area Telescope (LAT) on board the *Fermi Gamma-ray Space Telescope (Fermi)* has published a new measurement of the isotropic diffuse γ-ray background (IGRB) and the extragalactic γ-ray background (EGB) in the energy range 100 MeV-820 GeV [1]. The origin of this γ-ray residual represents one of the most mysterious open problems in astrophysics. The IGRB is usually associated to the γ-ray emission from unresolved, namely not detected by the *Fermi*-LAT, blazars, misaligned active galactic nuclei (MAGN) and star forming (SF) galaxies [2, 3, 4]. The most powerful Galactic contributors of the IGRB are expected to be pulsars, due to the large sample of detected sources. However, very recently in Ref. [5] the γ-ray emission from high-latitude ($|b| > 20°$) unresolved pulsars has been derived to account for, at most, the 1% of the IGRB.

The annihilation of dark matter (DM) particles, in the halo of the Milky Way (MW) and in external galaxies, constitutes a possible exotic mechanism for the production of γ rays. Indeed, one of the most promising strategies for the search of DM, in the scenario of weakly interacting massive particles (WIMPs), is the indirect detection through γ rays produced from the annihilation of WIMPs.

We first explore in Sec. 2 at which extent the astrophysical populations may explain the EGB and IGRB data and then in Sec. 3 we add the contribution from a DM Galactic halo to constrain the DM annihilation cross section. We use a statistical fitting procedure which includes both the *Fermi*-LAT data errors and the theoretical uncertainties on the γ-ray emission from astrophysical sources. For the first time we show the effect of the choice of the Galactic diffuse emission (GDE) model, used to derive the IGRB and EGB data, and how this affects the results on DM.

2. *Fermi*-LAT IGRB data explained with astrophysical sources

At least the 10% of the γ-ray photons, detected at latitude $|b| > 20°$ by the *Fermi*-LAT, are emitted from Galactic and extragalactic resolved sources. Indeed, the *Fermi*-LAT catalogs contain thousands of point sources. One of the most natural explanation for the origin of the IGRB, is that it arises from the superposition of a numerous population of unresolved sources with a flux lower than the point source sensitivity threshold of the LAT [2, 6].

A diffuse γ-ray flux has been predicted for various source populations. A large fraction of the IGRB is expected to come from active galactic nuclei (AGN) which are divided, according to the orientation of the jets with respect to the line of sight, into blazars and MAGN. Blazars are the most numerous population in the *Fermi*-LAT catalogs and are divided into BL Lacertae (BL Lac) objects and flat-spectrum radio quasars (FSRQs) according to the absence or presence of strong broad emission lines in their optical/UV spectrum, respectively. The γ-ray emission from unresolved blazars has been estimated to be around 20-30% of the integrated IGRB above 100 MeV (see e.g. [2, 7, 8]. MAGN are only a dozen in the γ-ray catalogs but the unresolved counterparts are expected to be much more numerous than blazars. The diffuse γ-ray emission from MAGN is expected to be aroud 20-30% of the integrated IGRB above 100 MeV [3, 9]. Finally, SF galaxies are predicted to have a numerous unresolved population and their contribution has been derived to be from a few % up to almost the totality of the IGRB (see e.g. [4, 10]). In particular the *Fermi*-

---

*Electronic address: mattia.dimauro@to.infn.it

LAT Collaboration [4] has deduced that the contribution of unresolved SF galaxies is among 4% and 24% of the integrated IGRB above 100 MeV and they have considered two different Spectral Energy Distribution (SED): a power law (PL) and a Milky Way (MW) function.

Truly diffuse processes, like ultra-high energy cosmic-ray interactions with the extragalactic background light or intergalactic shocks, are other possible γ-ray emission mechanisms (see Ref. [11] and references therein). However, there are still quite large uncertainties associated to these processes and a subdominant contribution to the IGRB is theoretically possible (see e.g. Refs. [12, 13, 14]). Therefore, we do not take into account these contributions in the rest of the paper.

We consider in our analysis the γ-ray emission from unresolved SF galaxy, MAGN, BL Lac, and FSRQ populations as derived in [2, 3, 4, 8]. In Fig. 1 we display the *Fermi*-LAT IGRB and EGB data derived with the Model A of GDE [1], together with the γ-ray fluxes predicted for AGN and SF galaxies. It is evident that both the IGRB and EGB data are consistent with the emission from these extragalactic populations.

We now determine with a chi-square statistical method at which extent AGN and SF galaxies can explain the IGRB and EGB data. We perform a fit to the IGRB and EGB measurements with a χ^2 function including both the errors of the *Fermi*-LAT data and the theoretical uncertainties of the γ-ray emission from astrophysical sources (see for all the details [15]). The theoretical uncertainties on AGN mainly produce a renormalization of their average unresolved γ-ray flux while the SF galaxy contribution contains also a large uncertainty due to the SED. We thus consider, at the first order, the 1-σ error on the AGN and SF galaxy unresolved emission as the width of the bands shown in Fig. 1 while the average fluxes are represented by the curves in Fig. 1. Both the SF galaxy SED, namely the MW and the PL models, are taken into account to include also our ignorance on the spectral shape of these sources.

We explore the possibility that the theoretical predictions adopted may be affected by an additional uncertainty on the spectral shape. This possibility is included by varying the power-law index of AGN taking into account the relevant 1-σ error on this parameter (see for further details [15]). The uncertainties on the SF galaxies SED is already considered by performing all our analysis with both the MW and PL models.

The results are shown in Tab. I, where we display the reduced chi-square ($\tilde{\chi}^2 = \chi^2/\text{d.o.f.}$) for the fit on the IGRB and EGB data. The analysis is performed on the *Fermi*-LAT data derived with each of the benchmark GDE models considered in [1] and labelled with A, B and C. The γ-ray emissions from unresolved BL Lacs, FSRQs, MAGN and SF galaxies are able to explain the high-latitude IGRB and EGB data with no need for significant adjustments of the average parameters. A better agreement is provided by the MW modeling of the SF galaxy emission and with the Model C of the GDE [1]. Indeed, the PL model of SF galaxies is in some tension with the data sets obtained with GDE Model A and B (see Tab. I). The choice of the Galactic foreground model has a large relevance on the goodness of the fit. We display in Fig. 2 the fluxes corresponding to the best fit configuration with the IGRB and the EGB data obtained with Model A of the GDE. It is remarkable that each contribution has a very different shape but they add in a way that their sum is consistent with a power-law with an exponential cutoff.

$\tilde{\chi}^2$	IGRB (MW)	EGB (MW)	IGRB (PL)	EGB (PL)
MODEL A	1.72; 1.56	0.95; 1.02	3.20; 2.54	1.41; 1.36
MODEL B	1.33; 1.32	1.57; 1.72	2.30; 1.96	1.83; 2.06
MODEL C	0.82; 0.84	0.60; 0.60	1.67; 0.95	0.77; 0.84

Table I The reduced chi-square value $\tilde{\chi}^2 = \chi^2/\text{d.o.f.}$ for the fits performed using only the normalizations as free parameters (left numbers in each column) or varying also the slope of the spectra (right numbers in each column). The analysis is performed with both the MW and PL SF galaxy models and for the three Galactic foreground models of the IGRB and EGB data [1].

3. Constraints on a DM contribution to the *Fermi*-LAT IGRB data

A possible contribution to the high latitude γ-ray IGRB could arise from annihilating DM particles present both in the halo of the MW and in external halos [16]. DM can produce γ rays both directly (the so-called *prompt* emission), or indirectly via the inverse Compton scattering of the electrons and positrons, produced by the DM annihilation, off the ambient light of the interstellar radiation field. In order to simplify the discussion we consider only the DM distributed in a halo of the MW. Moreover, we do not consider any specific particle physics model and we fix the branching ratio equal to 1 for any of the discussed annihilation channels. The photon and electron spectra have been calculated using the Pythia Montecarlo code for DM annihilations into e^+e^-, $\mu^+\mu^-$, $\tau^+\tau^-$, $b\bar{b}$, $t\bar{t}$ and W^+W^- channels. We have assumed an Einasto DM profile with a local DM density of $\rho_\odot = 0.4$ GeV/cm^3. For all the details about the γ-ray flux due to DM annihilation in the halo of the MW we refer to [15, 17].

As a first analysis, we derive upper limits for the DM annihilation cross section $\langle\sigma v\rangle$, fitting the IGRB and EGB data with the astrophysical sources discussed in Sect. 2 and the addition of a Galactic DM halo. The results are shown in Fig. 3 for the DM anni-

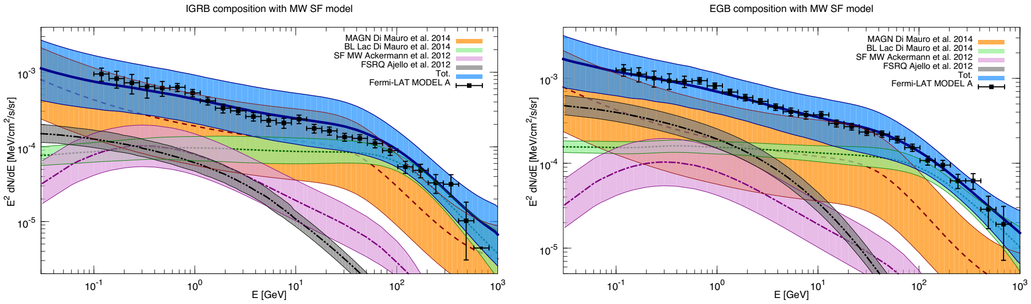

Figure 1: Left (right) panels show the γ-ray emission from unresolved (unresolved+resolved) sources, together with the IGRB (EGB) data [1]. Lines and relevant uncertainty bands represent the contribution from the following source populations: MAGN (orange dashed), BL Lacs (green dotted), FSRQs (grey double dot-dashed), MW model of SF galaxies (purple dot-dashed), and the sum of all the contributions (blue solid). IGRB and EGB data have been derived with Galactic foreground Model A.

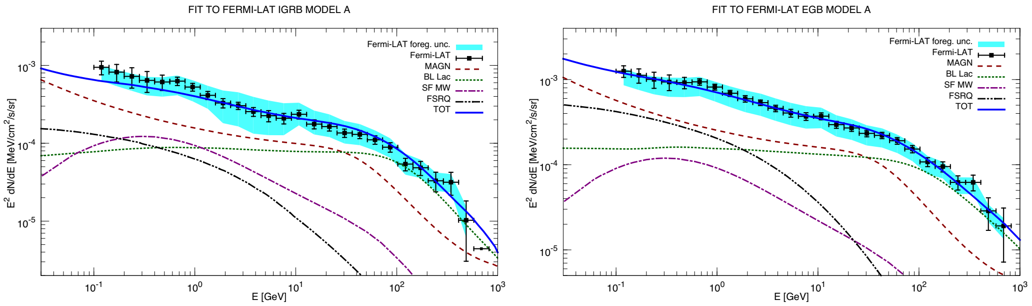

Figure 2: The γ-ray flux best fit on Model A of IGRB (left panels) and EGB (right panels) data is shown for: BL Lac (dotted green), MAGN (dashed brown), SF (dot-dashed purple), FSRQ population (dot-dot-dashed black), the sum of AGN and SF (solid blue). We display with a cyan band also the uncertainty associated to the *Fermi*-LAT GDE model [1].

hilation channels listed above, different confidence levels (C.L.s) and considering the Model A of the Galactic foreground. In the case of the $b\bar{b}$ DM annihilation channel and for masses lighter than 30 GeV, the upper bounds on $\langle\sigma v\rangle$ are below the thermal relic value while at 10 TeV our analysis excludes $\langle\sigma v\rangle \gtrsim 10^{-24}\text{cm}^3/\text{s}$. Moreover, the limits obtained for the DM annihilation into $\tau^+\tau^-$ are quite stringent: the thermal relic cross section is excluded at 3-σ C.L. up to a DM mass of about 330 GeV, while at $m_\chi \simeq 1$ TeV the bound is around $10^{-25}\text{cm}^3/\text{s}$. As expected, the upper bounds obtained with a fit to the EGB data are very similar to the ones obtained with the IGRB data and in general are only slightly looser.

For the first time we explore the impact of the GDE model in the estimation of upper limits on the DM annihilation cross section. The results are illustrated, for a 2-σ C.L and for the annihilation channels e^+e^- and $b\bar{b}$, in Fig. 4. The choice of the GDE model turns out to have a significant role in the values of the upper limits on $\langle\sigma v\rangle$. The results vary on average within a factor of two but the differences can reach a factor of 10 in the case of $b\bar{b}$ at about $m_\chi \simeq 200$ GeV. The bounds obtained on the IGRB with Model B of the GDE are always looser with respect to the ones derived with Model A or C.

As a second analysis, we attempt to identify DM configurations which can significantly improve the fit to the IGRB data. In this part we perform a fit to the *Fermi*-LAT data with extragalactic sources and a DM component as done before, but letting the WIMP DM mass m_χ and $\langle\sigma v\rangle$ varying simultaneously. Our results are displayed in Fig. 5, for the $b\bar{b}$ DM annihilation channel and for the IGRB data associated to the three Galactic foreground models. In the case of Model A and B, we obtain closed regions up to 3-σ C.L. with the best fits located around $m_\chi \simeq$ 5-20 GeV and $\langle\sigma v\rangle \simeq$ 1-3 $\cdot\, 10^{-26}\text{cm}^3/\text{s}$ while for Model C the 1-σ C.L. closed region opens up at already 2-σ C.L., translating the results into upper limits. The addition of a DM component is almost irrelevant for IGRB Model C while, in the case of leptonic or $b\bar{b}$ channels, improves the IGRB fit, for models A and B, with $\Delta\chi^2 = \chi^2_{\text{astro}} - \chi^2_{\text{astro+DM}} \geq 6.5$, where χ^2_{astro} and $\chi^2_{\text{astro+DM}}$ are the best fit χ^2 with only astrophysical sources or with the addition of a DM component. In the case of e^+e^-, $\tau^+\tau^-$ and $b\bar{b}$ channels, the best fit

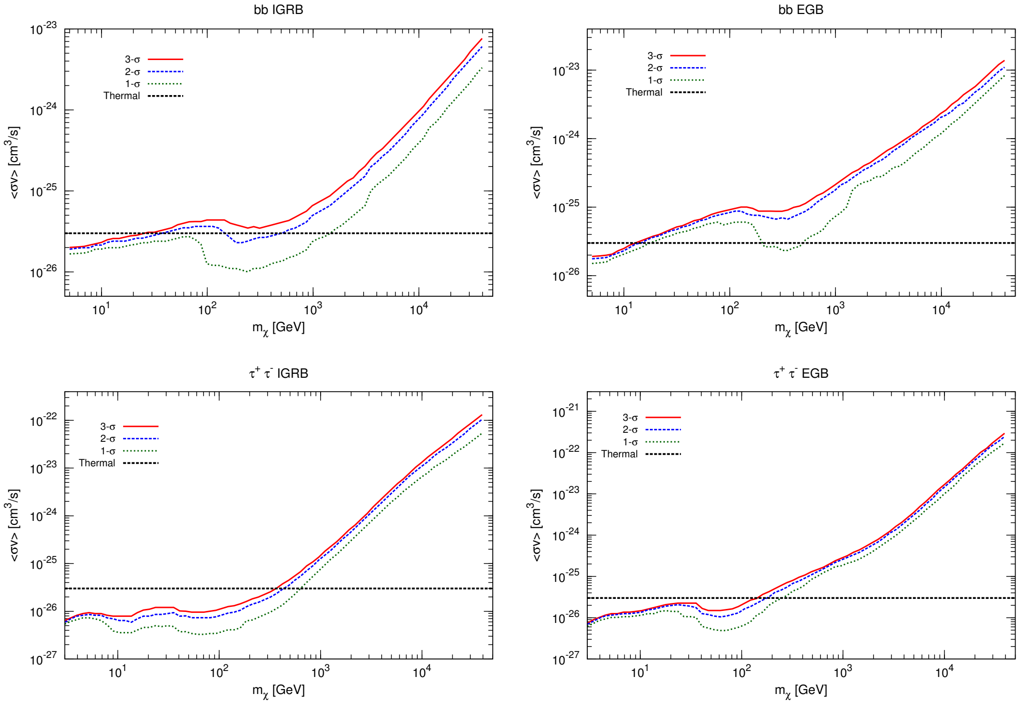

Figure 3: Upper limits on $\langle\sigma v\rangle$ as a function of the DM mass m_χ for $b\bar{b}$ (top panels) and $\tau^+\tau^-$ (botton panels) channels. The upper limits are derived with a fit to the IGRB (left panels) and EGB (right panels) data, within GDE Model A. The 3-σ, 2-σ and 1-σ C.L.s are shown with solid, dashed and dotted curves, respectively. The horizontal dotted line specifies the thermal relic annihilation cross section value.

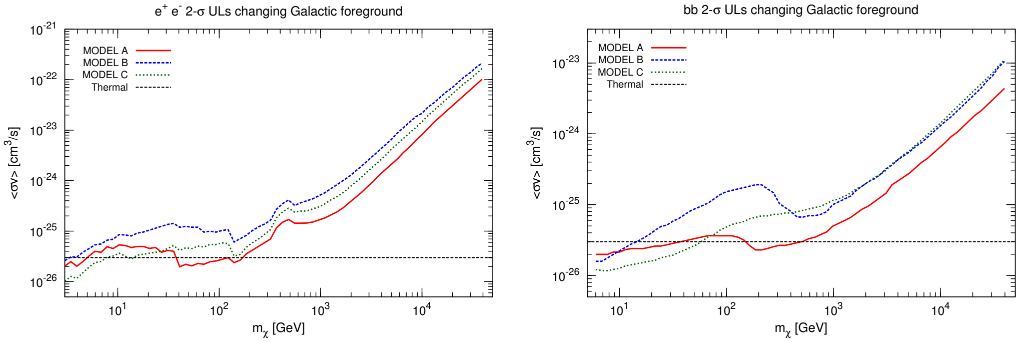

Figure 4: 2-σ C.L. upper limits on the annihilation cross section for the e^+e^- (left panels) and $b\bar{b}$ (right panels) channels obtained with the IGRB data derived with three different GDE models [1].

values of the DM mass range from few GeV up to 20 GeV and the annihilation cross section values are close to the thermal one while the $\mu^+\mu^-$ channel requires $\langle\sigma v\rangle \simeq$ 1-3 $\cdot\, 10^{-25}\mathrm{cm}^3/\mathrm{s}$. It is remarkable that including a DM component does not require the standard astrophysical contributions to differ significantly from the average emission [15]. Therefore, a DM component can very well fit the IGRB data with a realistic unresolved emission from extragalactic sources.

The results illustrated in Fig. 5 demonstrate that a DM contribution to IGRB may significantly improve the fit to the IGRB with respect to the interpretation with only astrophysical source populations. However, the significance of this potential exotic signal strongly depends on the choice of the Galactic foreground model considered to derive the IGRB spectrum. It is evident in Fig. 5 that for Model A and B of the GDE we may have an hint of DM up to 3-σ C.L. while for Model C for 2 and 3-σ C.L. we can only set upper limits on the annihilation cross section. These results confirm how a deep knowledge of the GDE is mandatory to unveil a DM contribution in the IGRB

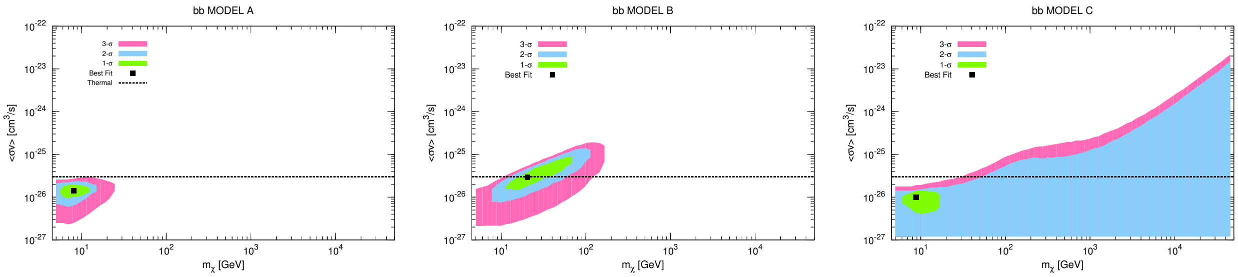

Figure 5: Contour plots in the $\langle\sigma v\rangle$-m_χ plane for $b\bar{b}$ channel calculated with a fit of the astrophysical sources and a DM component on the IGRB data. The black dots refer to the values of the best fit, and the (closed or open) green, blue and pink regions indicate the 1, 2 and 3-σ C.L. Left, center and right panels correspond to the case of Model A, B and C of the IGRB.

data. In Fig. 6 we illustrate the best fit configuration for the $b\bar{b}$ DM annihilation channel and Moled A of the GDE. This is the case with the largest significance of DM with respect to the best fit with only astrophysical populations with $\Delta\chi^2 = 18.9$. In this specific best fit, the DM mass is m_χ=8.2 GeV, and the annihilation cross section is $\langle\sigma v\rangle = 1.4 \cdot 10^{-26}$cm^3/s. It is clear in Fig. 6 that this configuration of extragalactic sources and DM reproduce very well the IGRB and EGB data.

The upper bounds reported in Figs. 3 and 4 improve the results derived in [17], in the so-called 'best-fit' scenario, by a factor of $\sim$3 at $m_\chi \sim 10$ GeV and a factor of 30 at $m_\chi \sim 10$ TeV. Our limits also improve significantly the upper limits on $\langle\sigma v\rangle$ derived by the *Fermi*-LAT analysis for a Galactic halo of DM [18] and with the analysis of 25 dwarf Spheroidal galaxies [19]. We notice that for $m_\chi \simeq 10$ TeV the upper bounds found in [20] by the H.E.S.S. Collaboration, which are optimized at energies larger than about 1 TeV, are of the same entity as ours for the leptonic channels, while for hadronic channels they are about one order of magnitude weaker. In addition, we derive similar results with respect to the very recent analysis performed by the *Fermi*-LAT Collaboration in Refs. [21, 22].

4. Conclusions

We have performed the first detailed statistical analysis for the interpretation of the recent IGRB data, measured by the *Fermi*-LAT Collaboration [1]. We first test the hypothesis that a numerous sample of unresolved extragalactic sources may explain the *Fermi*-LAT IGRB data. For the first time a χ^2 function which includes the data errors and the theoretical uncertainties on the γ-ray emission from BL Lacs, FSRQs, MAGN and SF galaxies has been considered. The theoretical uncertainty from each of this extragalactic population has been first parametrized only with a renormalization factor and then generalized adding also a possible change in the photon index of the γ-ray SED. Since the spectral shape of SF galaxies is not well constrained we have considered both the MW and the PL models. In our results the IGRB and the EGB data are well fitted by the unresolved emission from AGN and SF galaxies with best fit parameters close to the average theoretical values. We also demonstrate how the choice of the Galactic foreground model, used to derive the IGRB and EGB data, affects the results.

We explore also a possible contribution from the annihilation of WIMP DM particles distributed in the halo of our Galaxy. As a first analysis, we derive upper limits on the DM annihilation cross section, combining the γ-ray emission from astrophysical sources and DM in order to fit the IGRB and EGB data. The upper bounds calculated with this method are stringent and rule out the thermal relic cross section for a wide range of DM mass values for the $b\bar{b}$ and $\tau^+\tau^-$ annihilation channels.

We finally derive DM configurations which improve the fit to the IGRB data with respect to the case with only astrophysical sources. The best fit DM mass ranges from few GeV up to 20 GeV and the annihilation cross section $\langle\sigma v\rangle$ values are close to the thermal one. A DM component may fit, together with AGN and SF galaxies, very well the IGRB and EGB data with best fit parameters for the astrophysical populations close to the average theoretical values. However depending on the Galactic foreground model and the value of the C.L., we obtain a possible hint of DM or we set only upper limits.

Our results show how crucial is the IGRB in the study of the extragalactic source populations and for DM searches. It is today a powerful tool to constrain the DM properties and with a future improvement in the knowledge of the GDE and of the unresolved emission from AGN and SF galaxies, may probe a DM contribution to the γ-ray sky.

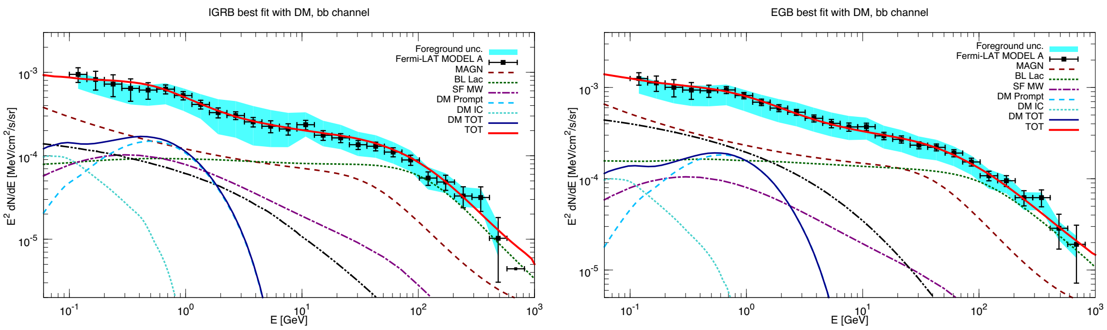

Figure 6: The differential γ-ray flux for the unresolved (left panels) and entire (right panels) BL Lac, FSRQ, MAGN, SF galaxy populations and the DM contribution with $b\bar{b}$ channel (splitted into the prompt and the ICS emission) as fixed by the best fit to the Model A of the IGRB and EGB data.

References

[1] M. Ackermann *et al.*, “The spectrum of isotropic diffuse gamma-ray emission between 100 MeV and 820 GeV,” *ApJ*, vol. 799, p. 86, 2015.

[2] M. Di Mauro *et al.*, “Diffuse γ-ray emission from unresolved BL Lac objects,” *ApJ*, vol. 786, p. 129, 2014.

[3] M. Di Mauro *et al.*, “Diffuse γ-ray emission from misaligned active galactic nuclei,” *ApJ*, vol. 780, p. 161, 2014.

[4] M. Ackermann *et al.*, “GeV Observations of Star-forming Galaxies with *Fermi* LAT,” *ApJ*, vol. 755, p. 164, 2012.

[5] F. Calore *et al.*, “Diffuse gamma-ray emission from galactic pulsars,” *ApJ*, vol. 796, p. 1, 2014.

[6] M. Di Mauro *et al.*, “Fermi-LAT γ-ray anisotropy and intensity explained by unresolved Radio-Loud Active Galactic Nuclei,” *JCAP*, vol. 1411, no. 11, p. 021, 2014.

[7] M. Ajello *et al.*, “The Cosmic Evolution of Fermi BL Lacertae Objects,” *ApJ*, vol. 780, p. 73, 2014.

[8] M. Ajello *et al.*, “The Luminosity Function of Fermi-detected Flat-Spectrum Radio Quasars,” *ApJ*, vol. 751, p. 108, 2012.

[9] Y. Inoue, “Contribution of Gamma-Ray-loud Radio Galaxies' Core Emissions to the Cosmic MeV and GeV Gamma-Ray Background Radiation,” *ApJ*, vol. 733, p. 66, May 2011.

[10] I. Tamborra *et al.*, “Star-forming galaxies as the origin of diffuse high-energy backgrounds: Gamma-ray and neutrino connections, and implications for starburst history,” *JCAP*, vol. 1409, no. 09, p. 043, 2014.

[11] F. Calore, V. de Romeri, and F. Donato, “Conservative upper limits on WIMP annihilation cross section from Fermi-LAT γ rays,” *Phy. Rev. D*, vol. 85, p. 023004, Jan. 2012.

[12] V. Berezinsky *et al.*, “Restricting UHECRs and cosmogenic neutrinos with Fermi-LAT,” *Physics Letters B*, vol. 695, pp. 13–18, Jan. 2011.

[13] S. Gabici and P. Blasi, “On the detectability of gamma rays from clusters of galaxies: mergers versus secondary infall,” *Astropart.Phys.*, vol. 20, pp. 579–590, Feb. 2004.

[14] F. Zandanel *et al.*, “High-energy gamma-ray and neutrino backgrounds from clusters of galaxies and radio constraints,” *ArXiv:1410.8697*, Oct. 2014.

[15] M. Di Mauro and F. Donato, “The composition of the Fermi-LAT IGRB intensity: emission from extragalactic point sources and dark matter annihilations,” *ArXiv:1501.05316*, Jan. 2015.

[16] F. Calore *et al.*, “Gamma-ray anisotropies from dark matter in the Milky Way: the role of the radial distribution,” *MNRAS*, vol. 442, pp. 1151–1156, 2014.

[17] T. Bringmann *et al.*, “Constraining dark matter annihilation with the isotropic γ-ray background: updated limits and future potential,” *Phy. Rev. D*, vol. 89, p. 023012, 2014.

[18] M. Ackermann *et al.*, “Constraints on the Galactic Halo Dark Matter from Fermi-LAT Diffuse Measurements,” *ApJ*, vol. 761, p. 91, 2012.

[19] M. Ackermann *et al.*, “Dark matter constraints from observations of 25 Milky Way satellite galaxies with the Fermi Large Area Telescope,” *Phy. Rev. D*, vol. 89, no. 4, p. 042001, 2014.

[20] A. Abramowski *et al.*, “Search for dark matter annihilation signatures in H.E.S.S. observations of Dwarf Spheroidal Galaxies,” *Phy. Rev. D*, vol. D90, no. 11, p. 112012, 2014.

[21] M. Ajello *et al.*, “The Origin of the Extragalactic Gamma-Ray Background and Implications for Dark-Matter Annihilation,” 2015.

[22] M. Ackermann *et al.*, “Limits on Dark Matter Annihilation Signals from the Fermi LAT 4-year Measurement of the Isotropic Gamma-Ray Background,” 2015.

Improved limits on sterile neutrino dark matter from full-sky observations by the Fermi-GBM

Shunsaku Horiuchi[1], Kenny C. Y. Ng[2], Jennifer M. Gaskins[3], Miles Smith[4], Robert Preece[5]
[1]*Center for Neutrino Physics, Department of Physics, Virginia Tech, Blacksburg, VA 24061*
[2]*Center for Cosmology and AstroParticle Physics (CCAPP), Ohio State University, Columbus, OH 43210*
[3]*GRAPPA Institute, University of Amsterdam, 1098 XH Amsterdam, The Netherlands*
[4]*Jet Propulsion Laboratory, Caltech, 4800 Oak Grove Drive, Pasadena, 91109 CA and*
[5]*Dept. of Space Science, University of Alabama Huntsville, Huntsville, AL 35805*

For the first time, we use the Gamma-ray Burst Monitor (GBM) on-board the *Fermi* satellite to search for sterile neutrino decay lines in the energy range 10–25 keV corresponding to sterile neutrino mass range 20–50 keV. This energy range has been out of reach of traditional X-ray satellites such as *Chandra*, *Suzaku*, *XMM-Newton*, and gamma-ray satellites such as *INTEGRAL*. Furthermore, the extremely wide field of view of the GBM opens a large fraction of the Milky Way dark matter halo to be probed. We start with 1601 days worth of GBM data, implement stringent data cuts, and perform two simple line search analyses on the reduced data: in the first, the line flux is limited without background modeling, and in the second, the background is modeled as a power-law. We find no significant excess lines in both our searches. We set new limits on sterile neutrino mixing angles, improving on previous limits by approximately an order of magnitude. Better understanding of detector and astrophysical backgrounds, as well as detector response, can further improve the limit.

I. INTRODUCTION

Right-handed neutral fermions (henceforth sterile neutrinos) arise in most implementations of the seesaw mechanism to generate neutrino masses, and yield extremely rich phenomenology (for recent reviews, see, e.g., [1, 2]). In particular, in the mass range of 1–100 keV, sterile neutrinos can be produced in sufficient quantities in the Early Universe to be a viable dark matter candidate. If the production proceeds via oscillations with active neutrinos, the momentum distribution of the sterile neutrino results in a warm dark matter candidate [3]. However, other production mechanisms have been shown to result in sterile neutrino dark matter that act very similarly to cold dark matter [4–8]. Astrophysically, a dark matter sterile neutrino lies in the parameter space to be produced in core-collapse supernova cores [9], providing a new mechanism for explosion [10], as well as explaining the origin of strong neutron star kicks [11–13].

As a viable dark matter candidate, sterile neutrinos are stable on cosmological time scales, but nevertheless they have decay channels that become interesting indirect detection targets for large concentrations of dark matter. The primary decay we target is the radiatively decay channel into an active neutrino and a photon. As the photon carries half of the sterile neutrino mass energy, the photon lies in the X-ray range. The signal is spectrally distinct from most expected astrophysical backgrounds, since the signal line is broadened by the velocity dispersion of the dark matter particles. Coupled with the expected spatial morphology – spherical and centrally concentrated at the Galactic center – searches with X-rays can be a very powerful probe [14].

Many searches have been performed in the past, using X-ray satellites such as *Chandra*, *Suzaku*, and *XMM-Newton*; observing a wide range of targets, from galaxy clusters, nearby galaxies, and dwarf satellites of the Milky Way, to the cosmic X-ray background. Most recently, an unexplained X-ray line was detected from a stack of galaxy clusters as well as the Andromeda galaxy [15, 16] (see also followup studies supporting and refuting these initial claims, e.g., [17–23]), which can be interpreted as the decay of 7 keV sterile neutrinos [24].

In this proceedings, we report initial results of using the Gamma-ray Burst Monitor (GBM) onboard the *Fermi* satellite to search for X-ray lines arising from sterile neutrino decay. Among the advantages of using the GBM for this purpose include: (i) its all-sky coverage, which allows the entire Milky Way dark matter halo to be studied, and (ii) the energy range of the GBM, which fills a gap in energy coverage between X-ray satellites and gamma-ray satellites. We therefore focus on the energy range $E_\gamma = 10$–25 keV corresponding to sterile neutrino mass $m_s = 20$–50 keV, and explore the Milky Way because of its proximity and well-studied dark matter distribution.

II. EXPECTED SIGNAL

A. Intensity calculation

The radiative decay of sterile neutrino has a decay rate of [14, 25],

$$\Gamma_s \simeq 1.36 \times 10^{-32}\,\mathrm{s}^{-1} \left(\frac{\sin^2 2\theta}{10^{-10}}\right)\left(\frac{m_s}{1\,\mathrm{keV}}\right)^5 , \qquad (1)$$

where we have assumed a Majorana sterile neutrino.

The photon intensity (number flux per solid angle) arising from sterile neutrino dark matter decay, from the direction of angle ψ away from the Galactic Center, is

$$
\begin{aligned}
\mathcal{I}(\psi, E) &\equiv \frac{dN}{dA dT d\Omega dE} \qquad (2)\\
&= \frac{\rho_\odot R_\odot}{4\pi m_s \tau_s}\left(\mathcal{J}(\psi)\frac{dN}{dE} + R_{\rm EG}\int \frac{dz}{h(z)}\frac{dN}{dE'}\right),
\end{aligned}
$$

where the first term in the brackets is the contribution from the Galactic halo and the second term is the contribution from extragalactic halos. Here, $\tau_s = 1/\Gamma_s$ is the sterile neutrino lifetime, $\rho_\odot = 0.4\,{\rm GeV\,cm^{-3}}$ is the local dark matter mass density, $R_\odot = 8.5\,{\rm kpc}$ is the Sun's distance to the galactic center, and $dN/dE = \delta(E - m_s/2)$ is the photon spectrum. $\mathcal{J}(\psi)$ is the so-called J-factor or boost factor, and is the integral of the dark matter mass density ρ in the Milky Way halo along the line-of-sight,

$$
\mathcal{J}(\psi) = \frac{1}{\rho_\odot R_\odot}\int_0^{\ell_{max}} d\ell\ \rho(\psi, \ell)\,, \qquad (3)
$$

where ℓ_{max} is the outer limit of the dark matter halo. We assume the dark matter distribution is spherically symmetric about the Galactic Center, hence

$$
\begin{aligned}
\rho(\psi, \ell) &= \rho(r_{\rm GC}(\psi, \ell)) \qquad (4)\\
&= \rho\left(\sqrt{R_\odot^2 - 2\,\ell\,R_\odot\cos\psi + \ell^2}\right). \qquad (5)
\end{aligned}
$$

We adopt $\ell_{max} = 250\,{\rm kpc}$ in this work. Although the value of ℓ_{max} differs depending on the adopted halo model, the contribution to $\mathcal{J}(\psi)$ from beyond $\sim 30\,{\rm kpc}$ are negligible.

For the dark matter density profile ρ we adopt a NFW profile as our canonical profile. Although the Milky Way dark matter density profile at small radii remains uncertain, it is known well enough for robust predictions of sterile neutrino decay signals on the scales of interest for the GBM. We adopt the following generic dark matter halo profile, motivated by numerical simulations,

$$
\rho^{\alpha\beta\gamma}(r) = \rho_\odot\left(\frac{r}{R_\odot}\right)^{-\gamma}\left[\frac{1 + (R_\odot/R_s)^\alpha}{1 + (r/R_s)^\alpha}\right]^{(\beta-\gamma)/\alpha}, \qquad (6)
$$

where parameters for commonly used profiles are summarized in Table I. Another profile favored by recent simulations is the Einasto profile,

$$
\rho^{\rm Ein}(r) = \rho_\odot \exp\left(-\frac{2}{\alpha_E}\frac{r^{\alpha_E} - R_\odot^{\alpha_E}}{R_s^{\alpha_E}}\right), \qquad (7)
$$

with $\alpha_E = 0.17$ and scale radius $R_s = 20$ kpc. The difference in the J-factor between these profiles are shown in Figure 1. Here, the J-factors are shown as functions of the angle ψ away from the Galactic Center. When the J-factor are convolved by the GBM field of view, which is energy dependent but typically ~ 40 degrees (see Figure 2), the differences between dark matter profiles is dramatically reduced.

TABLE I: Dark matter profile parameters for widely adopted dark matter profiles in the literature. Our canonical profile is the NFW profile.

Profile	α	β	γ	R_s [pc]
NFW	1	3	1	20
cNFW	1	3	1.15	23.7
Isothermal	2	2	0	3.5

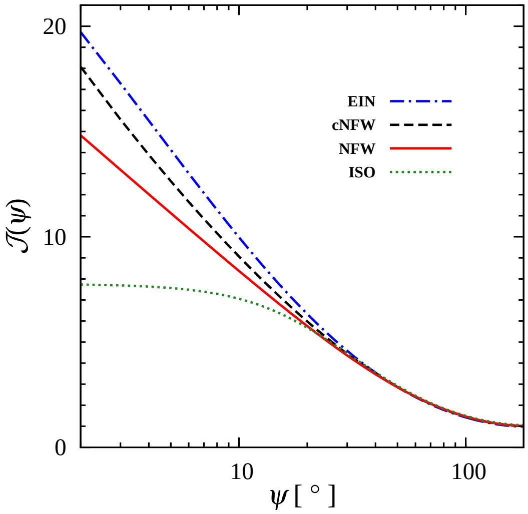

FIG. 1: The J-factor, $\mathcal{J}(\psi)$, as a function of half opening angle ψ relative to the Galactic Center, for four Milky Way dark matter halo profiles. Note the J-factor will be convolved by the GBM field of view, which is energy dependent but 40 degrees or more (see Figure 2), which dramatically reduces the difference between the dark matter profiles for the analysis.

B. Signal modeling for the GBM

The Fermi-GBM consists of 12 NaI detectors and 2 BGO detectors, the former covering energies 8 keV to 1 MeV, and the latter covering 200 keV to 40 MeV. The NaI detectors are physically placed on the corners and sides of the satellite. At any given time, 3 – 4 NaI detectors view an Earth occultation, i.e., when the earth is within 60 degrees of the detector zenith. In the following, we perform a search using data from a single NaI detector, det-0. Det-0 is conveniently placed closest to the Fermi-LAT zenith (offset angle 20.6°). Thus, as the LAT engages in survey mode, which are designed to maximize sky coverage, so does det-0. Analyses on additional detectors are forthcoming.

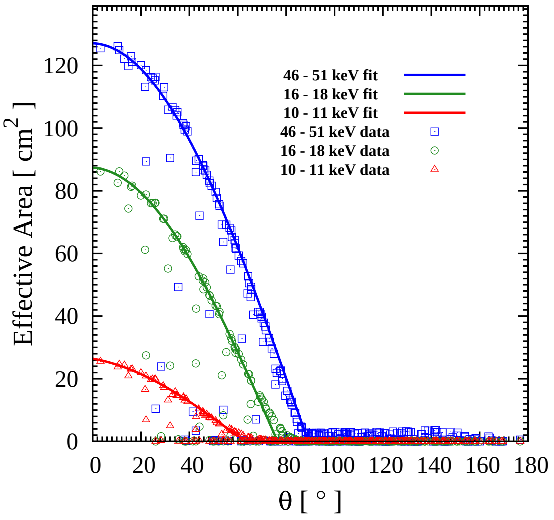

FIG. 2: The effective area for det-0 NaI detector versus photon arrival angle with respect to the detector normal. Three energy ranges utilized in the sterile neutrino search are shown. The occasional dips in the effective area are due to blockages from the satellite components.

The response of det-0 are shown in Figures 2 and 3, where the effective area is shown as functions of the angle away from the detector normal, θ, and the photon energy. The angular dependence can be well-fitted with a Cosine function (shown by the solid line). The occasional dips are due to blockage from satellite components.

One important consideration for the GBM is that it lacks photon-tracking capabilities, i.e., the photon count as a function of incident angle cannot be simply obtained. Earth occultation techniques can be effectively used to obtain directionality for point sources [26], but remains difficult for diffuse sources. Fortunately, the lack of photon tracking ability is not very problematic for our sterile neutrino search, since the decay signal has a very large angular extent. However, it does mean it is difficult to accurately re-construct an intensity sky map (Eq. 2). We opt to simulate the instrument observable by properly modeling the signal taking into account detector response. In this case, the instrumental observable is the photon count rate as a function of the NaI detector pointing direction.

The photon counts is energy dependent and direction dependent, i.e., $\nu_{i,j}$, where i labels the energy bin and j labels the detector pointing direction. The expected number of photons per observing time, T_j, from a particular detector pointing direction, is then

$$\begin{aligned}\frac{d\nu_{i,j}}{dT_j} &= \int_{E_i^{\rm min}}^{E_i^{\rm max}} dE \int_{2\pi} d\Omega(\theta) \int d\tilde{E} \\ &\quad \times \left\{ \mathcal{I}(\psi, \tilde{E})\, G\left(E, \tilde{E}\right)\, A_{\rm eff}(\tilde{E}, \theta) \right\},\end{aligned} \tag{8}$$

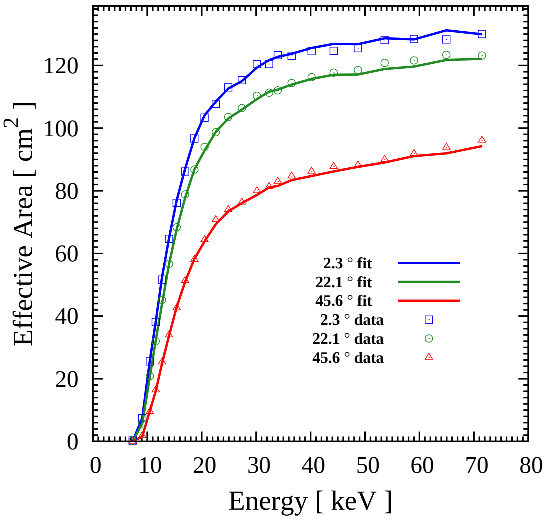

FIG. 3: The same as Fig. 2 but plotted against energy, for three incident angles. The fits come from the angular fits for various energies.

where $E_i^{\rm max}$ and $E_i^{\rm min}$ are the boundaries of the i-th energy bin. We have integrated over the hemisphere the NaI detector points, i.e., over the detector zenith angle θ, and attribute all the photons to the pixel defined by pointing j. A position on the sky with an angle relative to the GC, ψ, is thus related to the detector zenith angle and the pixel that the detector points at through $\psi \rightarrow \psi(\theta, j)$. The pointing direction of the detector is therefore defined by $\psi(0, j)$. The factor $G(E, \tilde{E})$ takes into account the energy resolution of the NaI detector, which we model as a Gaussian with width given by the pre-launch calibrations [27, 28]. Lastly, $A_{\rm eff}(E, \theta)$ is the NaI detector effective area, which depends on energy and the detector zenith angle, as in Figures 2, 3.

III. DATA REDUCTION

We use a total of 1601 days worth of data, from 12-AUG-2008 to 31-DEC-2012. We use the CSPEC data with nominal 4.096 s time resolution and 128 channels in energy from 5 to 1402 keV. We then implement a wide range of data cuts to minimize a wide range of background contributions, which are summarized below.

- LAT cuts: we use the Fermi-LAT cuts “LAT_CONFIG=1”, “LAT_MODE=5”, “DATA_QUAL=1”, “ROCK_ANGLE<50”, and “SAA=F”, where the first three conditions ensure the detector configurations and data qualities are suitable for scientific analysis, and the fourth condition ensures the Earth is not in the LAT’s field of view, which is approximately, although not exactly, the field of view of det-0

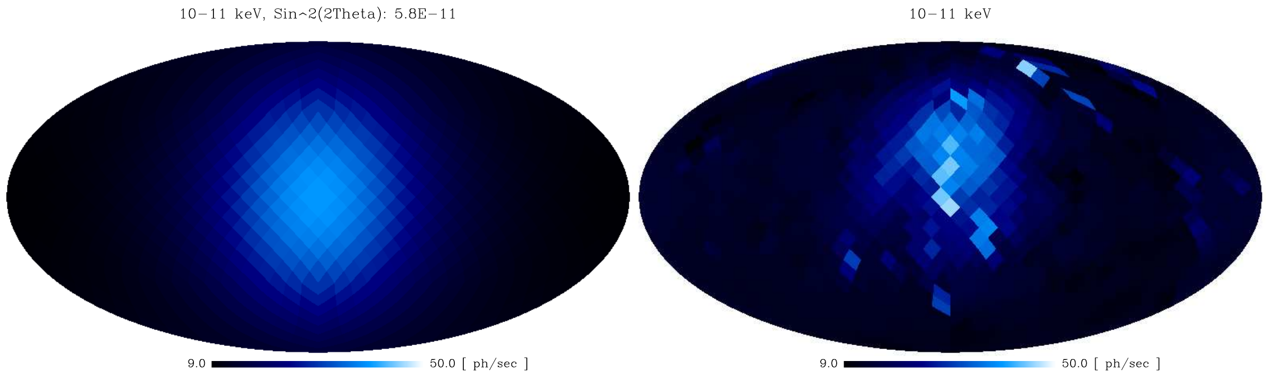

FIG. 4: All-sky counts maps in 10 – 11 keV energy range, showing the simulate dark matter map assuming the NFW profile (left) and the reduced data (right). The dark matter simulation assumes a sterile neutrino of mass 20 keV and mixing angle $\sin^2 2\theta = 5.8 \times 10^{-11}$. For det-0 only.

(this is addressed later). The cuts also exclude epochs where the satellite is passing through the South Atlantic Anomaly (SAA), which has high cosmic-ray activity that significantly increases the radioactivity of the satellite.

- Additional transient source cut: this removes epochs when the GBM detects transient sources, including gamma-ray bursts, direct cosmic-ray hits, solar flares, Galactic x-ray transients, and magnetospheric events.
- Extended SAA cut: the LAT cuts do not completely remove the effects of the SAA on the NaI detectors. The reason is that the satellite remains significantly radioactive even after leading the SAA. We therefore remove the data collected in orbits that pass through the SAA successively.
- Additional Earth cuts: we apply two additional cuts to remove backgrounds related to the Earth. The first requires the angle between the NaI detector normal and the vector from the Earth center to be less than 50°, which reduces emissions from the Earth limb. The second requires the geomagnetic latitude to be less than $|20|^\circ$, which reduces cosmic-ray induced vents.

The reduced data product contains observed counts in 128 energy bins and 768 equal area sky pixels in healpix projection. The total live time after reduction equals $\sim 4.6 \times 10^6$ seconds ($\sim$ 53 days). Despite the dramatic reduction in live time, the analysis is still systematic limited. In the energy range and region of interest, the total counts is more than $\sim 10^7$ photons for each energy bin.

Figure 4 shows the simulated dark matter photon count rate (left) and the reduced data count rate (right) for det-0. Both are shown with the same dynamical range. Shown is the energy range 10–11 keV, which is our lower energy range. We observe a clear excess of photons towards the Galactic Center direction in the reduced data, which we interpret to be from astrophysical emissions from the Milky Way. Spectral analysis indicates the excess peaks at low energies, and is dramatically reduced by 30–40 keV, when the data is dominated by cosmic-ray induced backgrounds. This is confirmed by the high-energy sky map showing small variations that trace the Earth magnetic field structure.

IV. LINE SEARCH ANALYSIS

Two line search strategies are implemented on the reduced data. The first is a conservative analysis based only on flux comparison, the second makes use of the spectral difference between signal (line) and background (dominated by a power-law within a small enough search energy window).

A. Flux analysis

The most conservative constraint on a sterile neutrino decay amplitude is to require the decay signal counts do not exceed the total measured photon counts. Thus, we do not make any assumptions of the detector background and astrophysical background.

The comparison is made bin by bin, and consists of comparing the predicted signal

$$\nu_i \; = \; \sum_j^{ROI} T_j \frac{d\nu_{i,j}}{dT_j} \,, \tag{9}$$

to the observed photon counts,

$$d_i = \sum_j^{ROI} N_{i,j} \,, \tag{10}$$

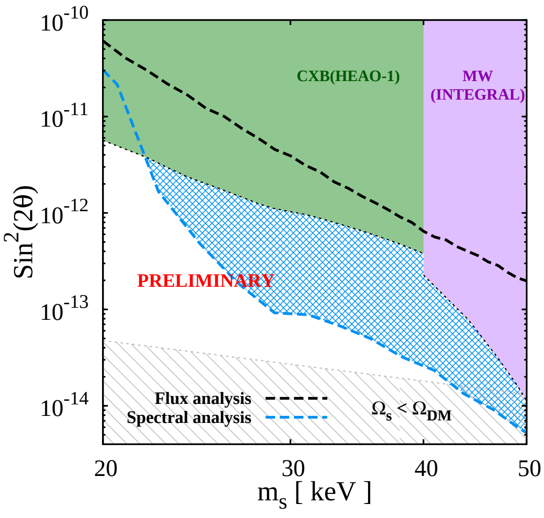

FIG. 5: Constraints on the sterile neutrino mixing angle $\sin^2(2\theta)$ as a function of the sterile neutrino mass m_s. Our new limits are shown by the dashed lines: the upper (black) line is from our conservative flux limit analysis, while the stronger lower (blue) line is from modeling the background as a power-law. The latter limit improves by preceding ones, obtained by observations of cosmic X-ray background (CXB) by HEAO-1 [30], by about an order of magnitude.

where $N_{i,j}$ is the number of counts in energy bin i and pixel j measured by the det-0.

B. Spectral analysis

The flux analysis can be improved by modeling the background. We perform a spectral analysis which captures the different spectral shapes of the sterile neutrino decay signal and the backgrounds.

The background is modeled as a power-law,

$$\frac{db}{dE} = \beta\left(\frac{E}{E_0}\right)^{-\gamma}\mathcal{N}(E)\,, \tag{11}$$

where the normalization β and index γ are left as free parameters. This assumption is made in a small energy window defined by

$$\mathrm{Max}\,(i_{\min}, i-\Delta w) < i < i+\Delta w, \tag{12}$$

using a fixed window of $\Delta w = 5$. This choice results in each energy width side being about $3-4\,\sigma$ of the energy resolution. The energy window is truncated at $i_{\min} = 6$, which corresponds to a central bin energy of 9.4 keV. For line energies near the low energy cutoff, the energy window is thus asymmetric.

We first perform a χ^2 test to assess whether the assumption of a power-law is a good local background model. By way of minimizing the negative logarithm of the likelihood function, we find the best-fit β_0 and γ_0 for all energy windows defined by Eq. (12). We assume a Gaussian probability distribution function for each energy bin, giving the likelihood function as

$$\mathcal{L}(\beta,\gamma|d) = \prod_i \frac{1}{\sqrt{2\pi}\sigma_{\mathrm{Aeff}}} e^{-\frac{(b_i-d_i)^2}{2\sigma_{\mathrm{Aeff}}{}^2}}\,, \tag{13}$$

where the product is taken over the energy bins, and σ_{Aeff} is the systematic uncertainty of the effective area,

$$\sigma_{\mathrm{Aeff}} = 0.05(\nu_i + b_i)\,. \tag{14}$$

The present analysis is not limited by statistical uncertainty; rather, it is dominated by systematic uncertainties. We adopt a constant 5% uncertainty on the effective area as a conservative choice. The χ^2 per degree of freedom for most energy windows is found to cluster between 1.1 and 1.4, although in some higher energy cases they can be as low as 0.5. We conclude that these findings justify the use of the local power-law assumption, as well as the 5% uncertainty in the effective area.

Finally, the sterile neutrino decay line is added to the central energy bin for each energy window. The line signal has one free parameter, f_s, the normalization, which scales linearly with the mixing angle $\sin^2 2\theta$. Thus, the search has three free parameters, β, γ, and f_s. The former two are treated as nuisance parameters, and f_s is the parameter of interest. The likelihood is

$$\mathcal{L}(f_s,\kappa|d) = \prod_i \frac{1}{\sqrt{2\pi}\sigma_{\mathrm{Aeff}}} e^{-\frac{(\nu_i+b_i-d_i)^2}{2\sigma_{\mathrm{Aeff}}{}^2}}\,, \tag{15}$$

where κ are the nuisance parameters. Finally, we use the profile likelihood analysis [29] for treating nuisance parameters. In practice, this involves calculating the profile likelihood $-\ln\mathcal{L}_p(f_s)$ for several fixed values of m_s, where for each f_s the $-\ln\mathcal{L}$ is minimized with respect to all other parameters κ.

V. STERILE NEUTRINO LIMITS

We find no significant detections of lines in both our analyses. We determine the 95% C.L. one-sided upper limits on the amplitude, f_s^{95}, by requiring a $2\Delta\ln\mathcal{L} = 2.71$. The limits are shown in Figure 5. While the limits from the conservative flux analysis is weaker than previous limits, our spectral analysis limit results in an improvement of about a factor of ~ 10 compared to those based on observations of cosmic X-ray background (CXB) by HEAO-1 [30]. The spectral analysis limit deteriorates at low energy, because the number of energy bins decreases, and also because the energy window is increasingly asymmetric. The latter in particular results in reduced ability to distinguish between the power-law background model and the line signal.

VI. CONCLUSIONS AND DISCUSSIONS

We have used a GBM NaI detector (det-0) to set upper limits on sterile neutrino dark matter decays into mono-energetic photons. Two line analyses were implemented: the first is a conservative flux search, and the second is a spectral search assuming the background can be modeled as a power-law over small energy windows. In the energy range of 10–25 keV, corresponding to sterile neutrino mass of 20–50 keV, our new upper limit is an improvement of about an order of magnitude compared to previous limits using the CXB with *HEAO-1* data.

The current analyses are dominated by systematic uncertainties primarily in the effective area. A better understanding of the GBM detector will therefore improve the limits presented in this proceeding. Work is currently underway to investigate other NaI detectors onboard the GBM.

Acknowledgments

We thank John Beacom for useful discussions. We also thank the Fermi-GBM team for providing the transient event time intervals. K.C.Y.N. was supported by a Fermi Guest Investigator award (Cycle 4), and NSF Grant PHY-1101216 (to John Beacom).

[1] A. Kusenko, Phys. Rept. **481**, 1 (2009) [arXiv:0906.2968 [hep-ph]].

[2] A. Boyarsky, O. Ruchayskiy and M. Shaposhnikov, Ann. Rev. Nucl. Part. Sci. **59**, 191 (2009) [arXiv:0901.0011 [hep-ph]].

[3] S. Dodelson and L. M. Widrow, Phys. Rev. Lett. **72**, 17 (1994) [hep-ph/9303287].

[4] X. D. Shi and G. M. Fuller, Phys. Rev. Lett. **82**, 2832 (1999) [astro-ph/9810076].

[5] K. Abazajian, G. M. Fuller and M. Patel, Phys. Rev. D **64**, 023501 (2001) [astro-ph/0101524].

[6] T. Asaka, M. Laine and M. Shaposhnikov, JHEP **0701**, 091 (2007) [hep-ph/0612182].

[7] A. Boyarsky, J. Lesgourgues, O. Ruchayskiy and M. Viel, JCAP **0905**, 012 (2009) [arXiv:0812.0010 [astro-ph]].

[8] D. Boyanovsky and J. Wu, Phys. Rev. D **83**, 043524 (2011) [arXiv:1008.0992 [astro-ph.CO]].

[9] A. Kusenko and G. Segre, Phys. Lett. B **396**, 197 (1997) [hep-ph/9701311].

[10] J. Hidaka and G. M. Fuller, Phys. Rev. D **74**, 125015 (2006) [astro-ph/0609425].

[11] G. M. Fuller, A. Kusenko, I. Mocioiu and S. Pascoli, Phys. Rev. D **68**, 103002 (2003) [astro-ph/0307267].

[12] M. Barkovich, J. C. D'Olivo and R. Montemayor, Phys. Rev. D **70**, 043005 (2004) [hep-ph/0402259].

[13] C. L. Fryer and A. Kusenko, Astrophys. J. Suppl. **163**, 335 (2006) [astro-ph/0512033].

[14] K. Abazajian, G. M. Fuller and W. H. Tucker, Astrophys. J. **562**, 593 (2001) [astro-ph/0106002].

[15] E. Bulbul, M. Markevitch, A. Foster, R. K. Smith, M. Loewenstein and S. W. Randall, Astrophys. J. **789**, 13 (2014) [arXiv:1402.2301 [astro-ph.CO]].

[16] A. Boyarsky, O. Ruchayskiy, D. Iakubovskyi and J. Franse, Phys. Rev. Lett. **113**, no. 25, 251301 (2014) [arXiv:1402.4119 [astro-ph.CO]].

[17] S. Riemer-Sorensen, arXiv:1405.7943 [astro-ph.CO].

[18] T. E. Jeltema and S. Profumo, arXiv:1408.1699 [astro-ph.HE].

[19] A. Boyarsky, J. Franse, D. Iakubovskyi and O. Ruchayskiy, arXiv:1408.2503 [astro-ph.CO].

[20] D. Malyshev, A. Neronov and D. Eckert, Phys. Rev. D **90**, no. 10, 103506 (2014) [arXiv:1408.3531 [astro-ph.HE]].

[21] M. E. Anderson, E. Churazov and J. N. Bregman, arXiv:1408.4115 [astro-ph.HE].

[22] T. Tamura, R. Iizuka, Y. Maeda, K. Mitsuda and N. Y. Yamasaki, arXiv:1412.1869 [astro-ph.HE].

[23] O. Urban, N. Werner, S. W. Allen, A. Simionescu, J. S. Kaastra and L. E. Strigari, arXiv:1411.0050 [astro-ph.CO].

[24] K. N. Abazajian, Phys. Rev. Lett. **112**, no. 16, 161303 (2014) [arXiv:1403.0954 [astro-ph.CO]].

[25] P. B. Pal and L. Wolfenstein, Phys. Rev. D **25**, 766 (1982).

[26] C. A. Wilson-Hodge, G. L. Case, M. L. Cherry, J. Rodi, A. Camero-Arranz, P. Jenke, V. Chaplin and E. Beklen *et al.*, Astrophys. J. Suppl. **201**, 33 (2012) [arXiv:1201.3585 [astro-ph.HE]].

[27] E. Bissaldi, A. von Kienlin, G. Lichti, H. Steinle, P. N. Bhat, M. S. Briggs, G. J. Fishman and A. S. Hoover *et al.*, Exper. Astron. **24**, 47 (2009) [arXiv:0812.2908 [astro-ph]].

[28] C. Meegan, G. Lichti, P. N. Bhat, E. Bissaldi, M. S. Briggs, V. Connaughton, R. Diehl and G. Fishman *et al.*, Astrophys. J. **702**, 791 (2009) [arXiv:0908.0450 [astro-ph.IM]].

[29] W. A. Rolke, A. M. Lopez and J. Conrad, Nucl. Instrum. Meth. A **551**, 493 (2005) [physics/0403059].

[30] A. Boyarsky, A. Neronov, O. Ruchayskiy, M. Shaposhnikov and I. Tkachev, Phys. Rev. Lett. **97**, 261302 (2006) [astro-ph/0603660].

The VERITAS Dark Matter Program

B. Zitzer
Argonne National Laboratory, Argonne, IL, 60439 USA
for the VERITAS Collaboration
veritas.sao.arizona.edu

In the cosmological paradigm, cold dark matter (DM) dominates the mass content of the Universe and is present at every scale. Candidates for DM include many extensions of the standard model, with a weakly interacting massive particle (WIMP) in the mass range from ∼10 GeV to greater than 10 TeV. The self-annihilation or decay of WIMPs in astrophysical regions of high DM density can produce secondary particles including very high energy (VHE) gamma rays with energy up to the DM particle mass. VERITAS, an array of atmospheric Cherenkov telescopes, sensitive to VHE gamma rays in the 85 GeV - 30 TeV energy range, has been utilized for DM searches. The possible astrophysical objects considered to be candidates for indirect DM detection are VERITAS dwarf spheroidal galaxies (dSphs) of the Local Group and the Galactic Center, among others. This presentation reports on our extensive observations of these targets and constraints of the dark matter physics from these objects, including the methodology and preliminary results of a combined DM search of five dSphs.

1. INTRODUCTION

The search for Standard Model (SM) particles resulting from the annihilation of Dark Matter particles provides an important complement to that of direct searches for DM interactions and accelerator production experiments. Among the theoretical candidates for the DM particle [1], weakly interacting massive particles are well motivated since they naturally provide the measured present day cold DM density [2]. Candidates for WIMP dark matter are present in many extensions of the SM of particle physics, such as supersymmetry (SUSY) [3] or theories with extra dimensions [4]. In such models, the WIMPs either decay or self-annihilate into standard model particles, most of which produce either a continuum of gamma rays with energies up to the DM particle mass, or mono-energetic gamma-ray lines.

Attractive targets for indirect DM searches are nearby massive objects with high inferred DM density which are not expected to be sources of VHE gamma rays. The Galactic Center is likely the brightest source of gamma rays resulting from DM annihilations, however the detected VHE gamma-ray emission is coincident with the supermassive black hole Sgr A* and a nearby pulsar wind nebula [5], motivating searches for DM annihilation in the Galactic Center halo where the VHE gamma-ray background is expected to be significantly lower [6]. Galaxy Clusters have a large DM content. However, they are extended for VERITAS, and the possibility exists of a VHE background from conventional processes [7] [8], although not yet detected. Galactic DM sub-halos would appear as unidentified objects (UNIDs) without multi-wavelength counterparts in Fermi-LAT data. If a Fermi UNID were detected in VHE, it could potentially be from DM. Dwarf spheroidal galaxies (dSphs) are additional attractive targets for DM searches. Dwarf spheroidal galaxies are relatively close (∼50 kpc), and have a low rate of active or recent star formation, which suggests a low background from conventional astrophysical VHE processes [9].

The following sections describe the status of observations and data analysis of each of the DM targets described above as of fall 2014, followed by conclusions and a discussion of the future of the VERITAS DM program.

2. SUB-HALOS

Recent cosmological N-body, high-resolution simulations [10] indicate that DM halos are populated with a wealth of substructures [11]. Because of tidal disruption near the Galactic disk, most of the sub-halos are thought to survive at high Galactic latitude. The lack of material in these regions prevents the DM overdensities from attracting enough baryonic matter and trigger star formation. DM clumps would therefore be invisible to most astronomical observations from radio to X-rays. DM structures residing in the the Milky Way halo can be nearby the Sun and therefore have a bright gamma-ray annihilation signal [12]. These clumps would likely be only visible at gamma-ray energies and therefore may not have shown up in astronomical catalogs yet. Since gamma-ray emission from DM annihilation is expected to be constant, DM clumps could then appear in all-sky monitoring programs [14] done at gamma-ray energies. These can be best provided by the Fermi-LAT instrument. Very likely, the distinct spectral cut-off at the DM particle mass is located at energies too high to be measurable by Fermi within a reasonable timescale (see, e.g. the WIMP mass lower limits in [15]) and can only be detected by ground-based telescopes, such as VERITAS. Furthermore, detection of this spectral cut-off at the same energy in multiple objects would stand as a visible signature of DM. The Second Fermi-LAT Catalog (2FGL) contains 1873 high energy gamma-

Table I Preliminary DM Sub-halo Results. Flux upper limits are given in units of Crab Nebula flux.

2FGL Name	**Exposure (hrs)**	**Significance (σ)**	**Excess Counts**	E_{tr} **(GeV)**	$F_{\gamma}^{99\%CL}(C.U.)$
J0312.8+2013	9.7	-1.5	-26 ± 17	220	< 0.9%
J0746.0−0222	9.1	-0.9	-15 ± 16	320	< 1.1%

ray sources detected by the LAT instrument after the first 24 months of observations. For each source, positional and spectral information are provided as well as identification or possible associations with cataloged sources at other wavelengths. Although Fermi-LAT has a good angular resolution, a firm identification based on positional coincidence alone is not always feasible. Thus, 576 sources in the 2FGL lack any clear association. These are the so-called unassociated Fermi objects (UFOs), a population among which DM clumps might be represented [16]. In order to extract possible DM clump candidates out of the 2FGL UNIDs, we adapt the selection criteria from [17], selecting sources by requesting them:

- to lie outside the Galactic Plane,
- to be non-variable,
- to exhibit a power law spectra, and
- to not have possible counterparts.

The original list obtained from the 2FGL catalog is then filtered to select only sources observable with VERITAS with a maximum zenith angle at culmination of 40°, in order to pursue the lowest energy threshold. Additionally, an estimate of required observation time for a 5σ detection, dubbed *detectability*, is computed based on a 2FGL Catalog flux extrapolation to the VERITAS energy range.

The preliminary results of the VERITAS observations shown in Table 1 are in tension with the extrapolation of the gamma-ray spectra from the Fermi-LAT to very high energies. Additional data from these UNIDs and others by VERITAS and other Cherenkov telescopes may completely completely rule out a direct extrapolation of the Fermi-LAT which would give strong DM model constraints or potentially detect a DM signature, provided that they are truly without counterparts at other wavelengths.

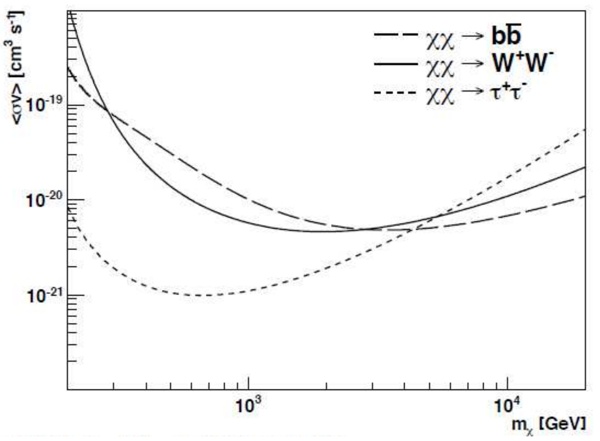

Figure 1: Dark Matter velocity-averaged cross-section limits from the Coma galaxy cluster. Figure taken from [19].

3. GALAXY CLUSTERS

Clusters of galaxies are the largest viralized objects in the Universe, with typical sizes of a few Mpc and masses on the order of 10^{14} to 10^{15} $M_{\odot}$. Most of the mass ($\sim$ 80%) is dark matter, as indicated by galaxy dynamics and gravitational lensing [18]. Aside from DM annihilation, it is possible to have gamma-ray emission from cosmic-ray interactions, producing neutral pions [7], or inverse Compton of ambient photons [8].

VERITAS has taken 18.6 hours of dedicated observations of the Coma cluster between March and May 2008. The Coma cluster is a close (z=0.023) and massive (M$\sim$ $10^{15}M_{\odot}$) cluster which has been thoroughly studied across all wavelengths. The standard analysis of the Coma cluster data using point-source cuts for the core of the cluster yielded 17 excess counts, with a significance of 0.84σ, indicating a non-detection. Upper limits of 0.83% of the Crab Nebula flux were placed for the core of the Coma cluster with 95% confidence, assuming a powerlaw spectral index of -2.3. With the absence of a signal from the Coma cluster, limits of the velocity-averaged cross-section for DM annihilation were placed at $\mathcal{O}(10^{-21})$, as shown in Figure 1 [19].

An archival VERITAS galaxy cluster search is also in the works, looking for galaxy clusters that have happened to overlap in the same FOV as other targeted observations. ROSAT and SDSS galaxy cluster catalogs are being used to cross-check with other VERITAS observations, Most notably M87 in the Virgo cluster of galaxies [20] and NGC 1275 in the Perseus cluster [21].

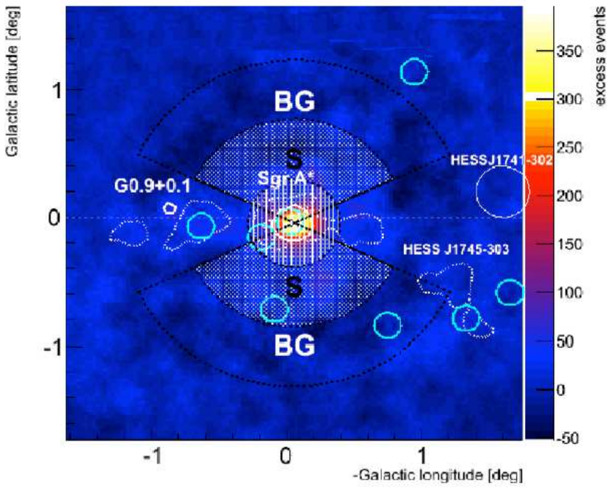

Figure 2: Skymap of the galactic center region using a subset of the VERITAS data. DM signal and background regions are indicated north and south of SgrA*.

4. GALACTIC CENTER

The center of our galaxy, SgrA*, is a strong VHE source, along with several other VHE sources nearby [22] and possible diffuse emission [23], making Dark Matter detection in that region a complicated, but not impossible, prospect.

The Galactic center was observed by VERITAS in 2010-2014 for $\sim$ 80 hrs (good quality data) at zenith angles of $z = 60 - 66$ deg (average threshold of $E_{\rm thr} \simeq 2.5$ TeV). The higher effective areas due to the large zenith angle observations make the VERITAS observations now the most sensitive instrument for the Galactic Center region above 2 TeV. The detection of SgrA* by VERITAS and VHE emission in the region through conventional processes are discussed in greater detail elsewhere in these proceedings [24].

The DM signal and background regions for the Galactic center region will use arc-shaped regions north and south of the Galactic plane to avoid diffuse emission and VHE sources, as shown in Figure 2. The VERITAS observations were accompanied by off-source observations of a field located in the vicinity of the Galactic center region (with similar zenith angles and sky brightness) without a known TeV γ-ray source. These observations are used to study the background acceptance throughout the field of view and will assist in the identification of a diffuse γ-ray component surrounding the position of the Galactic center.

The DM search for the Galactic center region is still in the preliminary stages. Work is currently underway for computing J factors for the signal and background regions for the arc-shaped regions described above.

5. DWARF GALAXIES

Dwarf spheroidal galaxies (dSphs) best meet the criteria for a clear and unambiguous detection of dark matter. They are gravitationally-bound objects and contain up to $\mathcal{O}(10^3)$ times more mass in DM than in visible matter [1]. As opposed to the Galactic center, globular clusters and clusters of galaxies, dSphs present the clear advantage of being free of any significant astrophysical emission. Their high Galactic latitude and relative proximity to Earth ($\sim$ 50 kpc) make them very good targets for high signal-to-noise detection.

Between the start of full VERITAS array operations and Summer 2013, five dSphs have been observed with VERITAS: Segue 1, Ursa Minor (UMi), Draco, Boötes 1, and Willman 1. The VERITAS collaboration has previously published a 48 hour exposure on Segue 1 [26] and ~15 hour exposures on the other four mentioned here [25]. Deeper exposures on Segue, UMi and Draco have been taken after these publications. To obtain the lowest possible energy threshold for DM searches, looser cuts optimized *apirori* on soft spectral VHE sources were used for the collective data set. The combination of looser cuts and deeper exposures revealed certain systematic effects in the cosmic-ray (CR) background data. The first is a gradient in the VERITAS cameras dependent on the zenith angle of observations across the FOV. The second systematic effect results from bright stars in the VERITAS FOV that cause the high voltage to pixels in the cameras to be suppressed. Both of these systematic effects have been corrected for and the results are summarized in Table 2. The 'crescent' background method which also developed for dSph analysis [27] was also used for the Table 2 results.

The first background systematic effect, relating to the zenith gradient, was corrected using a zenith-dependent acceptance map. The standard VERITAS analysis uses only a radially-dependent acceptance, i.e. the angle between the reconstructed event direction and the array pointing direction. Measuring the gradient utilized a map that is the ratio of the number of all reconstructed events in a sky map within a given search radius (defined as 0.17 degree in this work) to the (radial only) acceptance in that same bin, a parameter we will refer to as *flatness* in the rest of this work. If the acceptance adequately describes the CR background, then excluding any stars or known VHE sources, it should not correlate with any external parameters. However, a strong correlation was seen with the mean zenith angle of each reconstructed event position in the skymap bin. This correlation in the skymap bins is shown in Figure 3. This gradient is corrected in the data by fitting the correlation with a fourth-degree polynomial and using that to reweight the acceptance map. The α parameter from Li & Ma equation 17 is then re-calculated [28], [29].

Table II Preliminary DM DSph Results

DSph Name	**Exposure (hrs)**	**Significance (σ)**	**Excess Counts**	E_{tr} **(GeV)**	$F_\gamma^{99\%CL}(C.U.)$
Segue 1	92.0	0.7	94.4 ± 134.1	150	$< 0.4\%$
Ursa Minor	59.7	-0.1	-7.2 ± 68.5	290	$< 0.3\%$
Draco	49.9	-1.0	-73.2 ± 69.1	220	$< 0.3\%$
Boötes 1	14.0	-1.0	-38.5 ± 36.7	170	$< 0.3\%$
Willman 1	13.7	-0.6	-28.7 ± 46.2	180	$< 1.0\%$

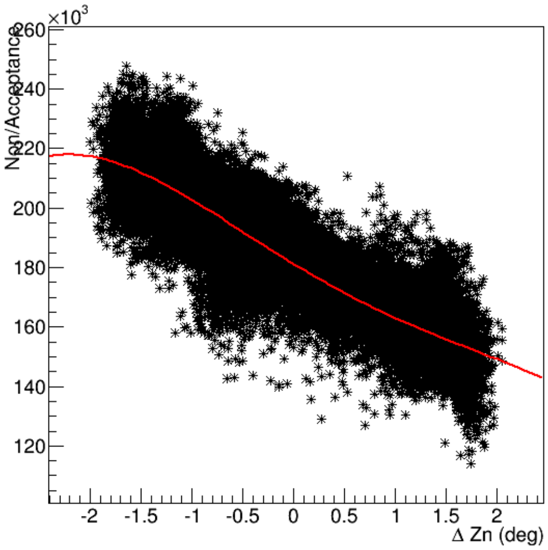

Figure 3: Scatter plot of the flatness parameter on the y-axis, and the mean zenith difference between the array tracking direction and event reconstruction direction on the x-axis for the Segue 1 data summarized in Table 2. A fit of this scatter to a fourth-degree polynomial is shown in red.

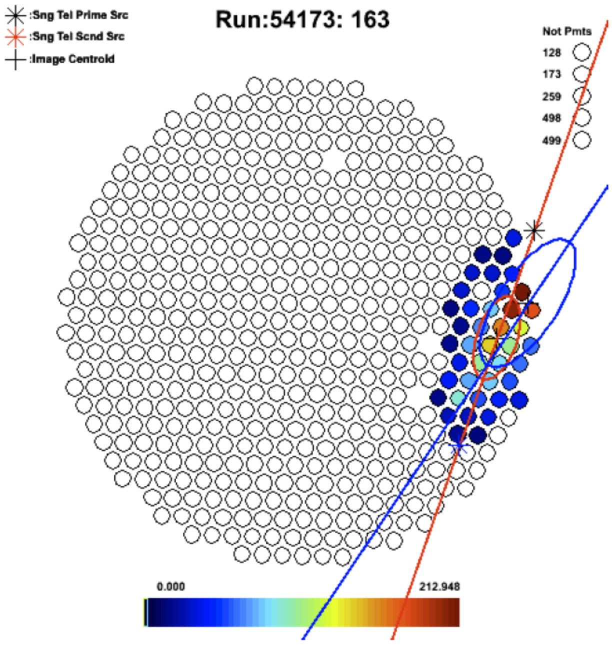

Figure 4: Example of the HFit and standard Hillas event characterization. The HFit shower image is the blue ellipse outline, while the standard Hillas moment analysis is the red ellipse outline. Figure from [30].

It should be noted that the difference of the adjusted value of α to the non-adjusted value is typically less than 1%. However, the difference to the γ-ray excess and significance becomes larger over time as statistics accumulate.

The second background systematic effect is due to "holes" that are seen in the data relating to bright stars in the FOV that would trip the high voltage of camera pixels or raise cleaning thresholds due to higher night-sky background levels. Missing pixels would in turn effect both energy and gamma-ray position reconstruction. A method of using a 2D Gaussian likelihood fit to each shower image is utilized here, called *HFit* [30]. Standard VERITAS analysis uses the moments of the shower images, commonly referred to as Hillas parameters. By using the 2D elliptical fitting to each image, missing data from disabled or broken PMTs are effectively interpolated around, as are images truncated by the edge of the cameras, as shown in Figure 4. This has been shown to reduce both the size and the depth of the holes due to bright stars seen in the data, including but not limited to the B magnitude 3.4 star Eta Leonis which is located 0.68° away from the center of the Segue 1 dSph. The effectiveness of HFit on a independent data sample is shown in Figure 5, which shows the apparent surface brightness in the CR background (which is in reality a deficit for reasons described above) at a star location in the FOV of the blazar RGB J1058+564 (Merak, 2.4 B magnitude).

Work is currently underway to utilize the data for the previously published papers plus additional data for a combined DM physics result. This result will use the methodology developed by Geringer-Sameth et al. [31] to utilize both the individual energy and event reconstruction information as well as astrophysical "J factors" from a generalized NFW profile by Geringer-Sameth and Walker [32].

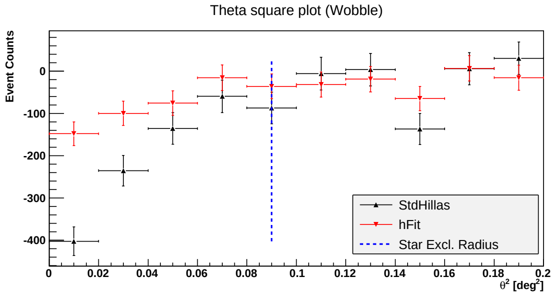

Figure 5: Apparent surface brightness of background cosmic ray events as a function of angle θ from the bright star, Merak, in the FOV of RGB J1058+564 using both the HFit algorithm and the standard Hillas shower image characterization. The VERITAS data analysis typically excludes regions around bright stars or known VHE sources from cosmic-ray background characterization. The default radius for background exclusion region for Merak is also shown as the dashed blue line.

6. CONCLUSIONS

New DM publications from the VERITAS collaboration are forthcoming: the combined analysis of the dSphs should be publically available within the next six months, which promises to be the most robust result of any DM result in VHE gamma rays so far, while DM results for the Galactic Center, Fermi UNIDs and the archival galaxy cluster search should be ready on longer timescales. New analysis techniques are being developed by the VERITAS collaboration which promise large gains to our DM sensitivity, as an example an extended analysis of the dSphs which would incorporate longer tails of the DM density profile, which would in turn give a boost to the J factors by as much as a factor of $\sim$2. A combined analysis with Fermi-LAT, or other γ-ray instruments could potentially provide a boost to DM sensitivity.

The VERITAS collaboration has a historical commitment to substantial DM observations and plans to do so in the foreseeable future. Recently, a new long-term plan for VERITAS has gone into effect, which has a significant fraction (15-20%) of the total dark observation time dedicated to DM observations. The focus of this long-term plan is dSphs; however the galactic center, Fermi UNIDs and galaxy clusters will not be completely ignored. If executed consistently over the expected lifetime of VERITAS, these observations will form the basis of an important and unique contribution to the field of indirect DM detection.

Acknowledgments

This research is supported by grants from the U.S. Department of Energy Office of Science, the U.S. National Science Foundation and the Smithsonian Institution, by NSERC in Canada, by Science Foundation Ireland (SFI 10/RFP/ AST2748) and by STFC in the U.K. We acknowledge the excellent work of the technical support staff at the Fred Lawrence Whipple Observatory and at the collaborating institutions in the construction and operation of the instrument. The VERITAS Collaboration is grateful to Trevor Weekes for his seminal contributions and leadership in the field of VHE gamma-ray astrophysics, which made this study possible.

References

[1] Bertone, G., et al. 2005, PhR, 405, 279
[2] Komatsu, et al. 2011, ApJS, 192, 18
[3] Jungman, G., et al. 1996, PhR, 267, 195
[4] Servant, G., et al. 2003, Nuclear Physics B, 650, 391
[5] Aharonian, F., et al. 2006, PhRvL, 97, 221102
[6] Abramowski, A., et al. 2011, PhRvL, 106, 161301
[7] Pfrommer, C., & Enßlin, T. A. 2004, A&A, 413, 17
[8] Schlickeiser, R., et al. 1987, A&A, 182, 21
[9] Mateo, M. L. 1998, ARA&A, 36, 435
[10] Springel, V., et al. 2008, MNRAS, 391, 1685
[11] Diemand, J., et al. 2008, Nature, 454, 735
[12]
[13] Pieri, L., et al., 2008, MNRAS, 384, 1627
[14] Kamionkowski, et al., 2010, PRD, 81, 043532
[15] Nakamura, K., et al., 2010, J.Phys.G G37, 075021.
[16] Buckley, M. R., & Hooper, D., 2010, PRD, 82, 063501
[17] Nieto, D., et al., 2011, 32nd ICRC, arXiv:1109.5935
[18] Diaferio, A., et al., 2008, SSRv, 134, 7
[19] Arlen, T., et al., 2012, ApJ, 757, 123
[20] Abramowski, A., et al., 2012, ApJ, 746, 151
[21] V. A. Acciari et al., 2009, ApJ 706, L275
[22] F. A. Aharonian, et al., 2004, A&A 425, L13.
[23] F. A. Aharonian, et al., 2006, Nature, 439 695.
[24] A. W. Smith, et al., These proceedings.
[25] Acciari, V. A., et al., 2010, ApJ, 720, 1174
[26] Aliu, E., et al., 2012, PRD, 85, 062001
[27] Zitzer, B., et al., arXiv:1307.8367
[28] Li, T.-P., & Ma, Y.-Q. 1983, ApJ, 272, 317
[29] Berge, D., Funk, et al., J. 2007, A&A, 466, 1219
[30] Christiansen, J., et al., American Institute of Physics Conference Series, 1505, 709
[31] Geringer-Sameth, A., et al., 2014, arXiv:1410.2242
[32] Geringer-Sameth, A., et al., 2014, arXiv:1408.0002

arXiv:1502.02390v1 [astro-ph.HE] 9 Feb 2015

The gamma-ray spectrum from annihilation of Kaluza-Klein dark matter and its observability

Satoshi Tsuchida and Masaki Mori
Department of Physical Sciences, Ritsumeikan University, Kusatsu 525-8577, Shiga, Japan

The lightest Kaluza-Klein particle (LKP), which appears in the theory of universal extra dimensions, is one of the good candidates for cold dark matter. The gamma-ray spectrum from annihilation of LKP dark matter shows a characteristic peak structure around the LKP mass. We investigate the detectability of this peak structure by considering energy resolution of near-future detectors, and calculate the expected count spectrum of the gamma-ray signal. In order to judge whether the count spectrum contains the LKP signal, the χ squared test is employed. If the signal is not detected, we set some constraints on the boost factor that is an uncertain factor dependent on the substructure of the LKP distribution in the galactic halo. Detecting such peak structure would be conclusive evidence that dark matter is made of LKP.

1. Introduction

At present, most of the matter in the Universe is believed to be dark. The existence of non-luminous matter, so-called dark matter, was suggested by F. Zwicky in 1930s [1]. The dark matter problem is one of the most important mysteries in cosmology and particle physics [2]. One feasible candidate for dark matter is the weakly interacting massive particle (WIMP), which appears in the theory of beyond standard model. WIMPs are good candidates for cold dark matter (CDM), where *cold* implies a non-relativistic velocity at the decoupling time in the early Universe. CDM comprises a large percentage of the matter density in the Universe [3], and is necessary to form the present structure of the Universe.

The theory of universal extra dimensions (UED) is a popular theory beyond the standard model [4], where *universal* means that all fields of the standard model can propagate into extra dimensions. New particles predicted by this theory are called Kaluza-Klein (KK) particles. Here, we consider the theory of UED containing only one extra dimension. The extra dimension is compactified with radius R. At tree level, the KK particle mass is given by [5]

$$m^{(n)} = \sqrt{\left(\frac{n}{R}\right)^2 + m_{\rm EW}^2} \tag{1}$$

where n is a mode of the KK tower, and $m_{\rm EW}$ is a zero mode mass of an electroweak particle.

We assume that the lightest KK particle (LKP) is a feasible candidate for dark matter, and we denote it $B^{(1)}$. Then, $B^{(1)}$ is the first KK mode of the hypercharge gauge boson. Dark matter should be electrically neutral and stable particles. Hence, LKP either does not interact with the standard model particles or only weakly interacts with them. In addition, LKP should have a small decay rate to survive for a cosmological time. In the extra dimension, the four-dimensional remnant of momentum conservation is to be conserved as KK parity, and so LKP is stable. This hypothesis corresponds to the LKP mass $m_{B^{(1)}}$ being in the range 0.5 TeV $\lesssim m_{B^{(1)}} \lesssim$ 1 TeV using the above condition for CDM density [6]. In this paper, we assume the $m_{B^{(1)}}$ is 800 GeV firstly, then we consider the change of result in the mass range of 500 GeV to 1000 GeV.

There are many LKP annihilation modes which contain gamma-rays as final products. These include gamma-ray "lines" from two-body decays, and "continuum" emission. Branching ratios into these modes can be calculated for $B^{(1)}$ pair annihilation [4, 5, 6] and are not dependent on parameters other than $m_{B^{(1)}}$. This paper considers three patterns for the continuum: $B^{(1)}$ pairs annihilate into (i) quark pairs, (ii) lepton pairs which cascade or produce gamma-rays, or (iii) two leptons and one photon ($l^+l^-\gamma$). The gamma-ray spectrum of the continuum component is reproduced in Fig.1 as per Ref.[5]. In this figure, the solid line shows the total number of photons per $B^{(1)}$ pair annihilations, the dotted line shows the number of photons via quark fragmentation, the dashed line shows the number of photons via lepton fragmentation, and the dot-dashed line shows the number of photons from the $l^+l^-\gamma$ mode as a function of $x = E_\gamma/m_{B^{(1)}}$.

When $B^{(1)}$ pairs annihilate into photon pairs, they appear as a "line" at the $m_{B^{(1)}}$ in the gamma-ray spectrum. This is the most prominent signal of KK dark matter, while in most theories line models are loop-suppressed and thus usually subdominant [7]. Thus, this study focuses on the detectability of this "line" structure by near-future detectors accounting for their finite energy resolution.

The distribution of dark matter is expected to be non-uniform in the Universe, and to be concentrated in massive astronomical bodies due to gravity. The gamma-ray flux from annihilation of dark matter particles in the galactic halo can be written as [8, 9]

$$\begin{aligned} \Phi_\gamma &= (\text{Astrophys}) \times (\text{Particle phys}) \\ &= J(\psi) \times \Phi^{\rm PP} \end{aligned} \tag{2}$$

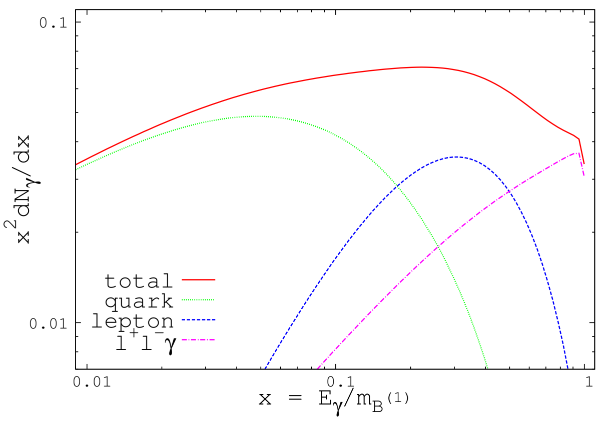

Figure 1: (Color online) Gamma-ray spectra of continuum components. The lines show the number of photons multiplied by $x^2 = (E_\gamma/m_{B^{(1)}})^2$ as follows: the solid line shows the total number of photons per $B^{(1)}B^{(1)}$ annihilation, the dotted line shows the number via quark fragmentation, the dashed line shows the number via lepton fragmentation, and the dot-dashed line shows the number from the $l^+l^-\gamma$ component. We have assumed $m_{B^{(1)}} = 800$ GeV and mass splitting is 5% at the first KK level.

where the astrophysics factor, represented by a dimensionless function $J(\psi)$, is calculated as follows:

$$J(\psi) = \frac{1}{8.5\text{kpc}}\left(\frac{1}{0.3\ \text{GeV cm}^{-3}}\right)^2 \times \int_{\text{l.o.s}} \rho^2(l)dl(\psi) \tag{3}$$

The function $\rho(l)$ is the dark matter density along the line-of-sight $l(\psi)$, where ψ is the angle with respect to the galactic center. The particle physics factor is written as

$$\Phi^{\text{PP}} = \text{Const} \times N_\gamma \langle\sigma v\rangle \tag{4}$$

where N_γ is the number of photons created per annihilation, and $\langle\sigma v\rangle$ is the total averaged thermal cross section multiplied by the relative velocity of particles. The value of $\langle\sigma v\rangle$ is accurately computed for a given dark matter candidate, so its uncertainty is small in terms of considering the cross section containing only an s-wave. However, this is not always the case, because some models have velocity-dependent cross sections [10, 11]. In addition, the astrophysics factor is highly dependent on the substructure of the dark matter distribution in the galactic halo along the line-of-sight. Thus, we should consider the so-called "boost factor" which indicates the relative concentration of the dark matter in astronomical bodies compared with some benchmark distributions. The boost factor is affected by $\langle\sigma v\rangle$ and $\rho^2(l)$, and is defined by

$$\begin{aligned} B_{\text{tot}} &= B_\rho \times B_{\sigma v} \\ &= \left(\frac{\langle\rho^2(l)\rangle_{\Delta V}}{\langle\rho_0^2(l)\rangle_{\Delta V}}\right)\left(\frac{\langle\sigma v\rangle_{v\simeq v_{\text{disp}}}}{\langle\sigma v\rangle_{v\simeq v_{\text{F}}}}\right)_{\Delta V} \end{aligned} \tag{5}$$

where v_{disp} is the velocity dispersion, v_{F} is the typical velocity at freeze-out, a volume ΔV is a diffusion scale, and $\rho_0(l)$ is a typical dark matter density profile, such as Navarro-Frenk-White (NFW) [12]. B_ρ could be as high as 1000 when accounting for the expected effects of adiabatic compression [13].

In the case of gamma-ray flux from LKP annihilation, the particle physics factor is almost fixed for a given model, and the boost factor mostly depends on the astrophysical contribution. In this paper, we vary only B_{tot} as a parameter which describes our limited knowledge regarding the astrophysical contribution, and consider constraints on its value from observation.

Recent progress in gamma-ray observation has revealed new findings in the galactic center region. The high energy gamma-rays from the galactic center have been observed by the High Energy Stereoscopic System (HESS) [14], the Large Area Telescope on board the Fermi Gamma-Ray Space Telescope (Fermi-LAT) [15] and other experiments. However, the observed gamma-ray spectrum is represented as a power-law plus an exponential cut-off, and is hardly compatible with a dark matter signal [16]. Recently, some evidence regarding the enhancement of the continuum component of the gamma-ray emission from the galactic center region detected by the Fermi-LAT has been reported and argued as a possible signal from the decay of dark matter particles [17, 18, 19]. Further, an enhancement of around 130 GeV in the energy spectrum of gamma-rays from the galactic center region has been reported which may indicate a possible dark matter signal [20, 21, 22, 23]. Discussion relating to unifying the continuum and the line has also been presented [24]. However, the analysis by the Fermi-LAT collaboration did not confirm the significance of the line detection [25, 26]. Thus, the situation is still unclear and more sensitive observation is necessary to resolve the issue.

In the following, we focus on gamma-ray observation with near-future missions, such as the Calorimetric Electron Telescope (CALET) [27]. CALET is a fine resolution calorimeter for cosmic-ray observation to be installed on the International Space Station. CALET will detect gamma-rays in the energy range of 4 GeV to 1 TeV with about 1000 cm^2 effective area, and a few percent energy resolution, suitable for gamma-ray line detection [28].

In this paper, we analyze the gamma-ray spectra from $B^{(1)}$ pair annihilation accounting for the finite energy resolution of gamma-ray detectors and purposefully discuss the observability of the "line" at the $m_{B^{(1)}}$. We then give possible constraints on the boost factor by near-future detectors.

2. The effect of energy resolution

The gamma-ray spectrum $d\Phi_\gamma(\Delta\Omega)/dE_\gamma$ reaching a detector can be expressed as [5]

$$E_\gamma^2 \frac{d\Phi_\gamma(\Delta\Omega)}{dE_\gamma} \simeq \text{Const} \times B_{\text{tot}} \times x^2 \frac{dN_\gamma}{dx}, \qquad (6)$$

where $\Delta\Omega$ is the angular acceptance of the detector,

$$\text{Const} \simeq 3.5 \times 10^{-8} \left(\frac{\langle \sigma v \rangle}{3 \times 10^{-26} \text{cm}^3 \text{s}^{-1}} \right) \times \left(\frac{0.8\text{TeV}}{m_{B^{(1)}}} \right) \langle J_{\text{GC}} \rangle_{\Delta\Omega} \Delta\Omega, \qquad (7)$$

and $\langle J_{\text{GC}} \rangle_{\Delta\Omega}$ is a dimensionless line-of-sight integral averaged over $\Delta\Omega$. If we assume an NFW profile, $\langle J_{\text{GC}} \rangle_{\Delta\Omega} \Delta\Omega$ equals to 0.13 for a $\Delta\Omega = 10^{-5}$ [29]. In this case dN_γ/dx includes both the continuum and line components.

Now, we discuss the effect of energy resolution. If the measured energies of detected gamma-rays behave like a Gaussian distribution and the energy resolution is 1%, the measured "continuum" gamma-ray spectrum is blurred and should appear as shown in Fig.2. Here we draw the curve assuming the following equation

$$g(E) \propto \int f(E') \times \exp\left[-\frac{(E-E')^2}{2\sigma_E^2} \right] dE', \qquad (8)$$

where $f(E')$ corresponds to a function shown by the solid line in Fig.1, and σ_E is the energy resolution.

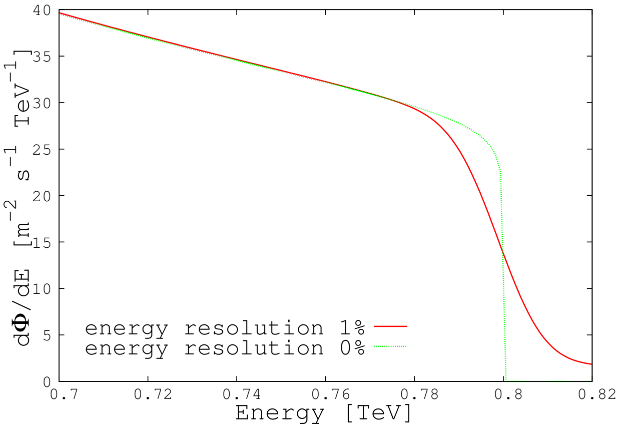

Figure 2: (Color online) Gamma-ray spectra of the continuum accounting for energy resolution assuming $m_{B^{(1)}} = 800$ GeV. The solid line assumes an energy resolution of 1% with a Gaussian distribution, and the dotted line does not include the effect of energy resolution, as per the solid line in Fig.1. The assumed boost factor is 1000.

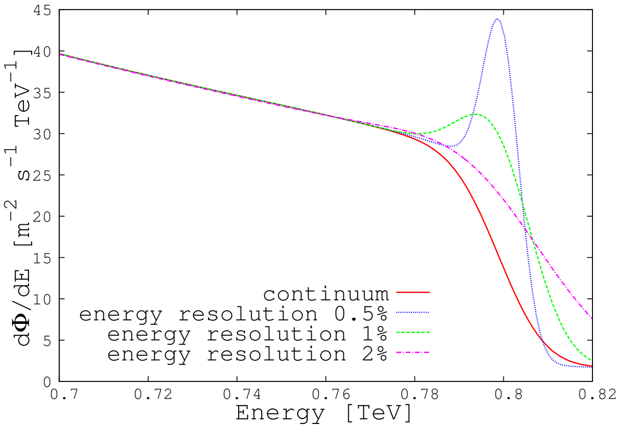

Figure 3: (Color online) Gamma-ray spectra of continuum plus line diffused by the energy resolution assuming $m_{B^{(1)}} = 800$ GeV. The solid line shows the continuum component only, assuming the energy resolution of 1%, while the dotted, dashed and dot-dashed lines show the continuum plus line components assuming energy resolution values of 0.5%, 1%, 2% respectively. The assumed boost factor is 1000.

Next, we analyze how the "line" from the $B^{(1)}$ pair annihilation into photon pairs looks above the "continuum". The three patterned lines shown in Fig.3 assume different energy resolutions which we take as 0.5%, 1% and 2% with the Gaussian distribution. In Fig.3, the solid line shows the continuum component only with an energy resolution of 1%, and the patterned lines show "line" plus "continuum" spectra for different energy resolutions: the dotted line, dashed line and dot-dashed line show the spectra when the energy resolution is 0.5%, 1%, 2% respectively, assuming the boost factor $B_{\text{tot}} = 1000$.

We can transform the spectra into counts to be observed by gamma-ray detectors. This is accomplished through multiplying by a factor of 0.03 for an assumed observation time of 1 yr and an assumed effective area of 1000 cm^2. These values arise from the typical aforementioned CALET sensitivity [28]. When analyzing observational data, the energy bin width must be specified. A bin width of 1% of $m_{B^{(1)}}$ (about one standard deviation of energy reconstruction) was used in order to avoid energy information loss. The resulting histograms are shown in Fig.4, where plots of the three cases corresponding to energy resolutions of 0.5%, 1% and 2% are shown. The figure shows that if the energy resolution of the detectors becomes 2% or worse, the characteristic peak indicating the $m_{B^{(1)}}$ will be diffused, making it hard to resolve into the line and continuum components. Thus, the energy resolution for gamma-ray detectors should be better than 2%, in order to "resolve the line" without the need for detailed analysis.

Thus far, we have taken the LKP mass to be $m_{B^{(1)}} = 800$ GeV, and calculated count spectrum for its mass. Now, we vary the mass from 500 GeV to 1000 GeV in 100 GeV intervals, and calculate the

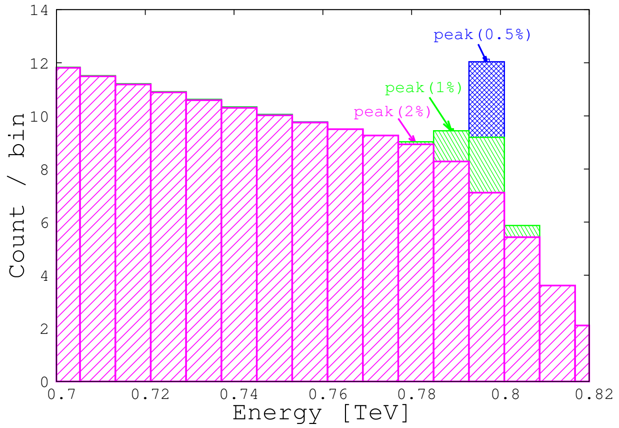

Figure 4: (Color online) Expected count spectra near the peak assuming energy resolutions of 0.5%, 1% and 2% assuming $m_{B^{(1)}} = 800$ GeV. The bin width of histograms is 8 GeV, equaling 1% of the $m_{B^{(1)}}$. The assumed boost factor is 1000.

count spectrum for each mass. The results are shown in Fig.5. This figure shows that the characteristic peak structure is visually clearer when $m_{B^{(1)}}$ is heavier. That is, the line component becomes relatively larger since the continuum component decreases for heavier $m_{B^{(1)}}$.

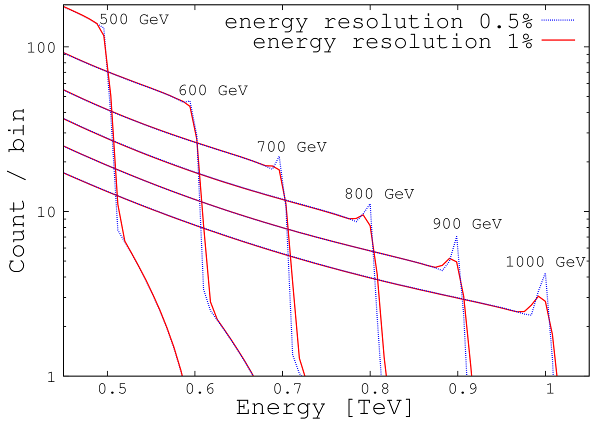

Figure 5: (Color online) Expected count spectra, assuming energy resolutions of 0.5% and 1%. The data space is 8 GeV, which is 1% of for the $m_{B^{(1)}} = 800$ GeV. The assumed boost factor is 1000.

3. Discussion

We now discuss the observability of the LKP signal in near-future detectors, taking account of the observed background spectrum. That is, we give estimates for the accessible range of the boost factor when the observed counts are significantly different from the background spectrum. Here, we assume the gamma-ray spectrum from HESS J1745-290 located near the center of the Galaxy is the source of the background. Its spectrum is given by [14]

$$\frac{d\Phi}{dE} = (2.55 \pm 0.06 \pm 0.40)\left(\frac{E}{\text{TeV}}\right)^{-2.10\pm0.04\pm0.10} \times \exp\left[-\frac{E}{(15.7 \pm 3.4 \pm 2.5)\text{TeV}}\right] \times 10^{-8}\ \text{TeV}^{-1}\ \text{m}^{-2}\ \text{s}^{-1}. \qquad (9)$$

Note that with the energy resolution of HESS (15%), the LKP "line" signal is broadened and hard to detect.

To investigate the detectability quantitatively, we employ a χ-squared test method to judge whether the excess counts are statistically meaningful.

First, we define χ^2 as

$$\chi^2 = \sum^{N} \frac{([\text{count} + \text{background}] - \text{background})^2}{\text{background}} \qquad (10)$$

where N is the number of energy bins, corresponding to degrees of freedom for the χ-squared test. We then specify the energy range:

$$\text{Energy range} = [100\ \text{GeV}, 1\ \text{TeV}] \qquad (11)$$

with bin width of 0.8 GeV (= 0.1% for $m_{B^{(1)}} = 800$ GeV). Thus, N is about 1000 in this case. The upper bound of the energy range under analysis is fixed as $m_{B^{(1)}} + 3\sigma_E$ to allow finite energy resolution. Hence, at this energy, the degree of freedom is one ($N = 1$). Then, we vary the lower bound of the energy range to lower energies. Thus, N gradually increases as we expand the energy range to lower energies. For example, N at the peak for 1% energy resolution is

$$N\left[E_{\text{peak}}, m_{B^{(1)}} + 3\sigma_E\right] = 40. \qquad (12)$$

We investigate the value of boost factor when χ^2 is bigger than some critical value for each N. The relation between N and the upper bound of the boost factor is shown in Fig.6, where the "peak" on each line corresponds to the value when N equals to Eq.(12). Then, $3\sigma^{\pm}$ are the energy width limits within 3σ from the peak. Thus, they are given as

$$N \text{ at } 3\sigma^{\pm} = N\left[E_{\text{peak}} \pm 3\sigma_E, m_{B^{(1)}} + 3\sigma_E\right] \qquad (13)$$

One can see from this figure that the limit on the boost factor does not change rapidly when we include energy bins well below the peak. An accessible boost factor would be smaller than 500 when N is in the range 30 - 200. These values of N correspond to being near the peak energy for annihilation of LKP.

We applied similar analyses for other LKP masses. The results shown in Fig.7 indicate that the constraint for the boost factor is tighter for lighter $m_{B^{(1)}}$. In

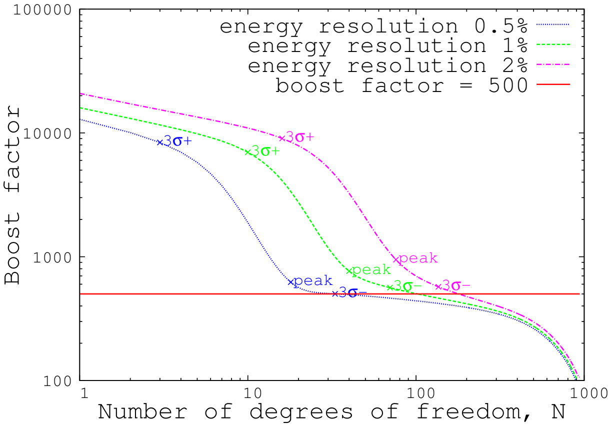

Figure 6: (Color online) Expected limits on the boost factor for the $m_{B^{(1)}} = 800$ GeV as a function of the number of degrees of freedom of the observed energy range. The horizontal solid line shows a boost factor of 500. The dotted, dashed and dot-dashed lines show the boost factor when χ^2 values are bigger than critical values for energy resolution 0.5%, 1.0%, and 2% respectively.

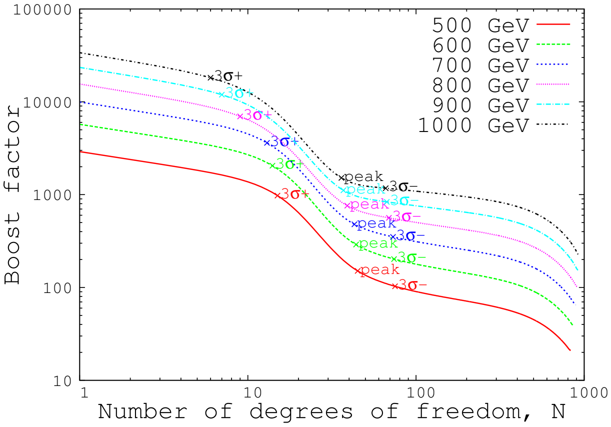

Figure 7: (Color online) Expected limits on the boost factor for each mass, assuming an energy resolution of 1%, as a function of the number of degrees of freedom of the observed energy range.

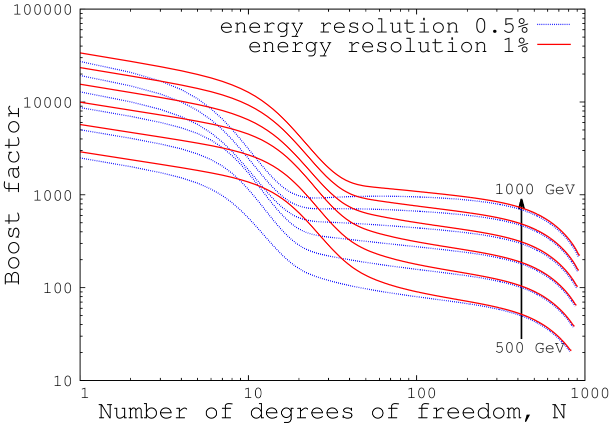

Figure 8: (Color online) Comparison of the expected limits of boost factors with 1% and 0.5% energy resolution. The individual lines refer to the scenarios with masses set from 500 GeV to 1000 GeV in 100 GeV intervals.

addition, we compared the results when using energy resolution of 1% and 0.5%, as shown in Fig.8. The number of events near the peak increases with better energy resolution, and the resulting constraint near the peak is tighter.

Some constraints from observations on the KK dark matter models have been reported. The Fermi-LAT team searched for gamma-ray emission from dwarf spheroidal galaxies around the Milky Way galaxy and set constraints on dark matter models with non-detection results [30]. The HESS array of imaging air Cherenkov telescopes observed the Sagittarius dwarf spheroidal galaxy in the sub-TeV energy region and derived lower limits on the $m_{B^{(1)}}$ of 500 GeV [31]. These results put constraints on $\langle \sigma v \rangle$ of dark matter halo KK particles. The present limits allow the maximum value of boost factors of several to 1.5×10^4 depending on $m_{B^{(1)}}$. Our analysis on future high energy resolution observation improves the limits on the boost factor or the chance to detect the signal. If such signals are detected, we will be able to say that dark matter is made of LKP, which will be evidence of the existence of extra dimensions.

4. Conclusion

Energy resolution plays a key role in detecting the line structure of the gamma-ray spectrum expected from annihilation of LKP dark matter as predicted by UED theories. This paper investigated the effects of energy resolution of gamma-ray detectors and calculated the expected count spectrum. The predicted gamma-ray spectrum is the sum of the continuum and a line corresponding to $m_{B^{(1)}}$, but this characteristic spectrum is diluted when we account for the finite energy resolution of detectors as shown in Fig.2 and Fig.3. Further, if we assume the exposure (area multiplied by observation time) of near-future detectors, count statistics will be the final limiting factor. The characteristic peak indicating the $m_{B^{(1)}}$ would be diffused if the energy resolution is 2% or worse. However, with qualitative statistical analysis, we may be able to detect a peak statistically by subtracting a background from the observed spectrum. In addition, if $m_{B^{(1)}}$ is heavy, the observed gamma-ray spectrum will show the characteristic peak clearly because the continuum component decreases relative to the line component.

This paper also estimated the accessible range of the boost factor using a χ-squared test assuming the HESS J1745-290 spectrum as a background. If the observed energy range for gamma-rays extends to lower energies, the accessible range of the boost factor will be lowered since a higher amount of continuum events will be detected. If the signal is not detected, the upper limit of the boost factor is about 500 if only taking data near the peak, and about 100 if the whole energy range is covered. Furthermore, if $m_{B^{(1)}}$ is light or the energy resolution of the detector is good (say the order of 0.5%), we may tightly constrain the boost factor.

If the gamma-ray line structure is observed in the future, we may identify LKP dark matter, which will provide strong evidence for the existence of extra dimensions.

Acknowledgments

We would like to thank Y. Sugawara, and K. Sakai for useful discussions. We also thank F. Matsui for helpful comments.

References

[1] F. Zwicky, Helv. Phys. Acta. **6**, 110 (1933).
[2] For a review, See, e.g., G. Bertone, D. Hooper, and J. Silk, Phys. Rep. **405**, 279 (2005).
[3] D. N. Spergel *et al.* (WMAP Collaboration), Astrophys. J. Suppl. Ser. **148**, 175 (2003).
[4] H. C. Cheng, K. T. Matchev, and M. Schmaltz, Phys. Rev. D **66**, 036005 (2002).
[5] L. Bergström, T. Bringmann, M. Eriksson, and M. Gustafsson, Phys. Rev. Lett. **94**, 131301 (2005).
[6] G. Servant and T.M.P. Tait, Nucl. Phys. B **650**, 391 (2003).
[7] T. Bringmann and C. Weniger Physics of Dark Universe **1**, 194 (2012)
[8] L. Bergström, New J. Phys. **11**, 105006 (2009).
[9] E. Aliu *et al.*, Astrophys. J. **697**, 1299 (2009).
[10] N. Arkani-Hamed, D. P. Finkbeiner, T. R. Slatyer, and N. Weiner, Phys. Rev. D **79**, 015014 (2009).
[11] M. Ibe, H. Murayama, and T. T. Yanagida, Phys. Rev. D **79**, 095009 (2009).
[12] J. F. Navarro, C.S. Frenk, and S. D. White, Astrophys. J. **462**, 563 (1996).
[13] F. Prada, A. Klypin, J. Flix, M. Martinez, and E. Simonneau, Phys. Rev. Lett. **93**, 241301 (2004).
[14] F. Ahanronian *et al.*, Astron. Astrophys. **503**, 817 (2009).
[15] P. L. Nolan *et al.*, Astrophys. J. Suppl. Ser. **199**, 31 (2012).
[16] F. Aharonian *et al.* (HESS Collaboration), Phys. Rev. Lett. **97**, 221102 (2006).
[17] D. Hooper and L. Goodenough, Phys. Lett. B **697**, 412 (2011).
[18] D. Hooper and T. Linden, Phys. Rev. D **84**, 123005 (2011).
[19] K. N. Abazajian and M. Kaplinghat, Phys. Rev. D **86**, 083511 (2012).
[20] T. Bringmann, X. Huang, A. Ibarra, S. Vogl, and C. Weniger, J. Cosmol. Astropart. Phys. 07 (2012) 054.
[21] C. Weniger, J. Cosmol. Astropart. Phys. 08 (2012) 007.
[22] M. Su and D. P. Finkbeiner, arXiv:1206.1616v2.
[23] D. P. Finkbeiner, M. Su, and C. Weniger, J. Cosmol. Astropart. Phys. 01 (2013) 029.
[24] M. Asano, T. Bringmann, G. Sigl, and M. Vollmann, Phys. Rev. D **87**, 103509 (2013).
[25] M. Ackermann *et al.* (Fermi-LAT collaboration), Phys. Rev. D **86**, 022002 (2012).
[26] M. Ackermann *et al.* (Fermi-LAT collaboration), Phys. Rev. D **88**, 082002 (2013).
[27] S. Torii, Nucl. Instrum. Methods. A **630**, 55 (2011).
[28] M. Mori *et al.*, Proc. 33rd ICRC (Rio de Janeiro), Paper 0248 (2013).
[29] A. Cesarini, F. Fucito, A. Lionetto, A. Morselli, and P. Ullio, Astropart. Phys. **21**, 267 (2004).
[30] A. A. Abdo *et al.* (Fermi-LAT collaboration), Astrophys. J. **712**, 147 (2010).
[31] F. Aharonian *et al.*, Astropart. Phys. **29**, 55 (2008).

Primordial Black Holes

Jane H. MacGibbon
Dept of Physics, University of North Florida, Jacksonville, FL, 32224 USA
Tilan N. Ukwatta
Space and Remote Sensing (ISR-2) and Physics Division (P-23), Los Alamos National Laboratory, Los Alamos, NM, 87544, USA
J.T. Linnemann, S.S. Marinelli, D. Stump, K. Tollefson
Dept of Physics and Astronomy, Michigan State University, East Lansing, MI, 48824 USA

Primordial Black Holes (PBHs) are of interest in many cosmological contexts. PBHs lighter than about 10^{12} kg are predicted to be directly detectable by their Hawking radiation. This radiation should produce both a diffuse extragalactic gamma-ray background from the cosmologically-averaged distribution of PBHs and gamma-ray burst signals from individual light black holes. The Fermi, Milagro, Veritas, HESS and HAWC observatories, in combination with new burst recognition methodologies, offer the greatest sensitivity for the detection of such black holes or placing limits on their existence.

1. INTRODUCTION

A black hole (BH) is an object of classical gravity [1] whose mass M_{BH} is contained within its Schwarzschild volume which has radius

$$r_{BH} = \frac{2GM_{BH}}{c^2} \qquad (1)$$

[2]. Here G is the universal gravitational constant, c is the speed of light and we have assumed that the BH has negligible rotation and/or electric charge. (Extension in General Relativity to include rotation and/or electric charge is straightforward.) Because Eq (1) implies that the average density inside a black hole goes as $\rho_{BH} \propto M_{BH}/{r_s}^3 \propto {M_{BH}}^{-2}$, large mass black holes may be more easily produced than small mass black holes, at least in the present universe. In fact a $10^8 M_\odot$ black hole has the density of water. Today there is strong evidence for the existence of stellar mass black holes (formed as supernova remnants) and $10^6 M_\odot$-$10^{10} M_\odot$ supermassive black holes in most galactic centers. There is also mounting evidence for black holes with masses intermediate between stellar mass black holes and supermassive black holes.

'Primordial Black Hole' (PBH) refers to a black hole of any size formed in the early universe (where by 'early universe' we mean before the formation of the first stars). Possible PBH formation mechanisms include the collapse of overdense regions arising from primordial density inhomogeneities (such as occur in many Inflation models, in particular those with a blue, peaked or 'running index' spectrum), an epoch of low pressure (soft equation of state), or cosmological phase transitions; and mechanisms involving topological defects, such as cosmic strings oscillating into their Schwarzschild volume or the collapse of domain walls. (For a recent review of PBH formation mechanisms and limits see [3] and references therein.) In almost all scenarios, the PBH mass at the time of formation is roughly equal to, or smaller than, the cosmic horizon (or Hubble) mass $M_H \approx 10^{15}(t/10^{-23}\text{s})$g. Thus the range of possible PBH initial masses is enormous – from the Planck mass for PBHs forming around the Planck time, to $10^5 M_\odot$ for PBHs forming around 1 s, or larger if forming later. Within a particular formation scenario, usually the PBHs are produced over a narrow initial mass range. An exception is scale-invariant cosmological primordial density perturbations which could produce PBHs over an extensive initial mass range with an initial mass spectrum of the form $dn/dM_i \propto M_i^{-\alpha}$ where $\alpha = 5/2$ for formation in the radiation era. Although scale-invariant density perturbations are not as well motivated in present cosmological models as they were a couple of decades ago, gamma-ray limits on the present cosmologically-averaged number density of PBHs were earlier derived assuming an $M_i^{-5/2}$ initial mass function.

The formation constraints on PBHs inform us about cosmology. The PBHs themselves may also produce effects on cosmological scales. PBHs surviving today should behave as cold dark matter (CDM). (In fact, present limits allow $10^{17} - 10^{26}$g PBHs to contribute all of Ω_{CDM} [3].) Like other CDM, PBHs should cluster in galactic haloes. They may also enhance the clustering of other dark matter, for example in WIMP and Ultra Compact Massive Halo scenarios. If a stable state such as a Planck mass relic remains after low mass PBHs have expired, the relics themselves are CDM candidates. PBHs may have played a role in the development of cosmological entropy, baryogenesis, the reionization of Universe in earlier epochs and producing observable annihilation lines. Very large PBHs may influence large scale structure development, seed SMBHs, or generate observable cosmic x-rays in their accretion disks.

The number of PBHs formed with initial masses of $10^9 - 10^{43}$g have been constrained primarily by primordial nucleosynthesis, cosmic microwave background (CMB) anisotropies, MACHO searches and, in the case of $M_{BH} \lesssim 10^{17}$g BHs, the search for Hawking radiation. Hawking radiation constraints derived from the 100 MeV extragalactic gamma-ray background and Galactic gamma-ray, e^+, e^- and anti-proton backgrounds place an upper limit on the background distribution of $M_{BH} \approx 5 \times 10^{14}$g PBHs of roughly $\Omega_{PBH} \lesssim 10^{-9}$. Direct searches for the final gamma-ray burst of Hawking radiation from an expiring PBH allow us to directly constrain the local number density of $M_{BH} \approx 5 \times 10^{14}$g PBHs and much lighter BHs.

2. BLACK HOLE BURSTS

2.1. Black Hole Thermodynamics

The work by Hawking and Beckenstein in the 1970's on extending the Laws of Classical Thermodynamics to include black holes (i.e. Classical Gravitation) resulted in the recognition of the Hawking (Gravitational) temperature T_{BH}

$$kT_{BH} = \frac{\hbar c^3}{8\pi G M_{BH}} = 1.06 \left(\frac{M_{BH}}{10^{13}\mathrm{g}}\right)^{-1} \mathrm{GeV} \qquad (2)$$

where k and $\hbar$ are the Boltzmann and reduced Planck constants, respectively [4]. An $M_{\odot}$ black hole has a temperature of 10^{-7} K; a 10^{25} g black hole has the same temperature as the present CMB; and a 10^{11} g black hole has a temperature of ~ 100 GeV. Hawking also derived the thermal flux radiating from a black hole of temperature T_{BH} to be

$$\frac{d^2N_s}{dtdQ} = \frac{\Gamma_s}{2\pi\hbar}\left[\exp\left[\frac{Q}{kT_{BH}}\right] - (-1)^{2s}\right]^{-1} \qquad (3)$$

per particle degree of freedom where Q is the energy of the Hawking-radiated particle, s is the particle spin and Γ_s is the absorption probability [5]. In the geometric optics (short-wavelength) limit, $\Gamma_s \approx 27G^2{M_{BH}}^2Q^2/\hbar^2c^6$. Strictly Eqs (2) and (3) apply for a non-rotating, non-electrically charged black hole. Extension to a black hole with angular momentum and/or electric field is straightforward but because a small black hole emits its angular momentum and electric charge quickly [5] compared to cosmological timescales we will assume PBHs surviving today have negligible angular momentum and electric field.

In the standard (MacGibbon-Webber) emission picture, a black hole should directly Hawking-radiate those particles which appear non-composite compared to the wavelength of the radiated energy (or equivalently the black hole size) at a given T_{BH} [6]. In order of increasing T_{BH} , as T_{BH} surpasses successive particle rest mass thresholds, the black hole initially directly emits photons (and gravitons), then neutrinos, electrons, muons and eventually direct pions. Once $T_{BH} \gtrsim \Lambda_{QCD} \approx 200 - 300\,\mathrm{MeV}$, the QCD confinement scale, the black hole should directly Hawking-radiate, not pions which are now composite at such temperatures, but quarks and gluons. Analogous to QCD jet behaviour in accelerators, the quarks and gluons will subsequently shower and hadronize into the astrophysically stable species γ, ν, p, $\bar{p}$, e^- and e^+ as they stream away from the black hole. Because of the large number of degrees of freedom for the fundamental QCD particles, the instantaneous emission spectra from $T_{BH} > \Lambda_{QCD}$ black holes are dominated by the component produced by the decay of the Hawking-radiated QCD particles. The instantaneous photon flux from a $T_{BH} > \Lambda_{QCD}$ black hole is dominated by this secondary QCD photon component while the directly Hawking-radiated photons contribute, at a given T_{BH}, significantly only at the highest energies. For $T_{BH} = 0.3 - 100\,\mathrm{GeV}$ black holes, the total instantaneous fluxes of the final-state stable particles are

$$\dot{N}_{p\bar{p}} \approx 2.1(\pm 0.4) \times 10^{23} \left[\frac{T_{BH}}{\mathrm{GeV}}\right]^{1.6\pm0.1} \mathrm{s}^{-1}$$

$$\dot{N}_{e^\pm} \approx 2.0(\pm 0.6) \times 10^{24} \left[\frac{T_{BH}}{\mathrm{GeV}}\right]^{1.6\pm0.1} \mathrm{s}^{-1}$$

$$\dot{N}_{\gamma} \approx 2.2(\pm 0.7) \times 10^{24} \left[\frac{T_{BH}}{\mathrm{GeV}}\right]^{1.6\pm0.1} \mathrm{s}^{-1}$$

$$\dot{N}_{\nu\bar{\nu}} \approx 5.6(\pm 1.7) \times 10^{24} \left[\frac{T_{BH}}{\mathrm{GeV}}\right]^{1.6\pm0.1} \mathrm{s}^{-1}$$

And the average energies of the fluxes scale as roughly ${T_{BH}}^{0.5}$, not as T_{BH} (as for the directly Hawking-radiated components) [6]. Thus, even very high temperature black holes will produce significant fluxes of final state particles which have energies around 100 MeV – 1 TeV.

As the black hole Hawking-radiates, its mass is carried off by the mass-energy of the emitted particles. The black holes mass loss rate is thus

$$\dot{M}_{BH} \approx -5.34 \times 10^{25} f(M_{BH})(M_{BH}/\mathrm{g})^{-2}\mathrm{g\,s}^{-1} \quad (4)$$

where the weight $f(M_{BH})$ accounts for the total number of directly emitted states and is normalized to unity for $M_{BH} \gg 10^{17}$g black holes which emit only photons and the three neutrino species. The relativistic contributions to $f(M_{BH})$ per particle degree of freedom are $f_{s=0} = 0.267$, $f_{s=1/2} = 0.147$ (uncharged), $f_{s=1/2} = 0.142$ (charge $e^{\pm}$), $f_{s=1} = 0.060$, $f_{s=3/2} = 0.020$, and $f_{s=2} = 0.007$ [7]. For a $T_{BH} \approx 50\,\mathrm{GeV}$ black hole emitting all experimentally-confirmed Standard Model degrees of freedom including the 125 GeV Higgs boson, $f(M_{BH}) \approx 15$.

Integrating Eq (4), the remaining evaporation lifetime of an M_i black hole is then

$$\tau_{evap} \approx 6.24 \times 10^{-27} f(M_i)^{-1}(M_i/\mathrm{g})^3\mathrm{s}. \qquad (5)$$

The mass of a PBH whose evaporation lifetime equals the age of the universe is $M_* \approx 5.00(\pm 0.04) \times 10^{14}$g [8].

Comparison of the observed diffuse extragalactic gamma-ray background around 100 MeV with the gamma-ray background that would be produced by a cosmological distribution of $M_* \approx 5 \times 10^{14}$g PBHs places the strictest limit on an cosmologically-averaged distribution of M_* PBHs. The limit, updated in 2010 using the Fermi LAT data, is $\Omega_{PBH}(M_*) \lesssim 5 \times 10^{-10}$ [3]. (This M_* limit is stricter and more robust

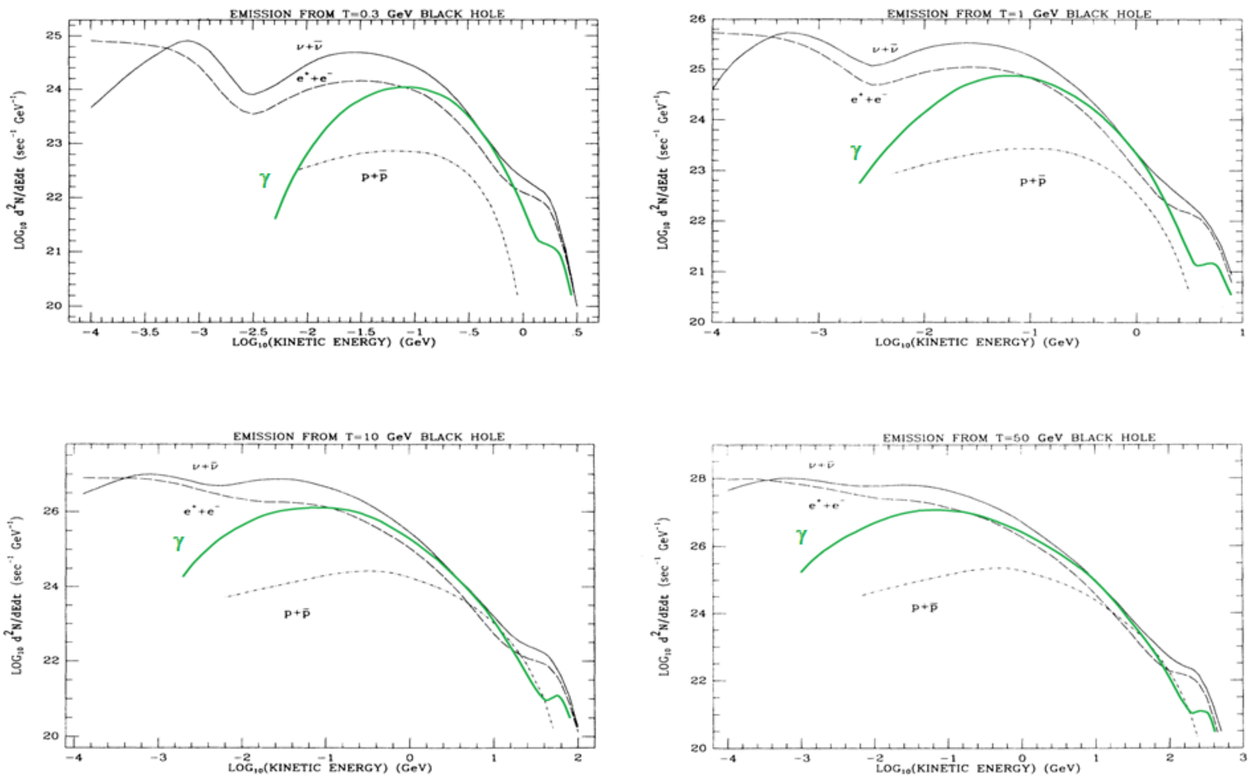

Figure 1: The instantaneous gamma-ray flux $d^2N/dtdE$ detectable by Fermi-LAT from $T_{BH} = 0.1 - 50$ GeV black holes [6]. For T_{BH} in this range, the flux should remain approximately constant over the lifetime of the Fermi Observatory.

than the limits on the cosmological distribution of PBHs of any other mass derived by this or any other method.) Because PBHs should behave as CDM, however, they should not be uniformly distributed throughout the universe but should cluster in galactic halos (and possibly also on smaller scales). Assuming PBH clustering in the Galactic halo, the local number density of PBHs should be enhanced by a factor of $\eta_{local} \sim 2 \times 10^5 (\Omega_{halo}/0.1)^{-1}$ where Ω_{halo} is the cosmological density parameter associated with galactic halos [9]. Clustering in the Galaxy leads to the possibility that PBHs are contributing to the Galactic halo gamma-ray background (as investigated by Wright using EGRET observations [10]), matter-antimatter interactions and microlensing events. Comparisons of the spectra from a Galactic distribution of PBHs with the observed Galactic antiproton and positron backgrounds around 100 MeV lead to limits on a Galactic distribution of $M_* \approx 5 \times 10^{14}$g PBHs which are similar or somewhat weaker than the extragalactic gamma-ray limit. These antiproton- and positron-derived limits, however, depend on the modeling of the propagation and leakage times of charged particles in the Galaxy and on the Galactic distribution of PBHs, and so are not as robust as the extragalactic 100 MeV gamma-ray limit on the cosmologically-averaged distribution of PBHs.

We note that the extragalactic and Galactic limits are derived using the black hole emission spectra integrated over both a distribution of PBHs and Galactic or cosmological timescales.

2.2 Signatures of Black Hole Bursts

Independently we can derive limits by directly searching for the present emission from an individual black hole. Equally importantly, we can predict the light curve that would be produced in a detector by an individual black hole and devise methodologies to distinguish the BH burst signal from other known gamma-ray source types. Burst searches are the direct method for detecting black hole Hawking radiation and do not depend on assumptions concerning the formation mechanism of the black hole. In fact, burst searches are equally searches for any local small black holes created in the present universe, as well as primordially-produced PBHs. Although there are no currently-fashionable theories predicting the production of such small black holes in the present Galaxy, we should not bias ourselves observationally against their possible existence, given the widespread acceptance of the existence in the Galaxy and beyond of stellar mass and higher mass black holes. We should investigate the black hole burst signature template so that we can recognize BH/PBH bursts if they are seen in a detector.

Let us now predict the black hole burst signature. Re-writing Eq (5), a black hole with temperature T_{BH} has a remaining evaporation lifetime of

$$\tau_{evap} \approx 5.0 \times 10^{11} \left(\frac{f(T_{BH})}{15}\right)^{-1} \left(\frac{T_{BH}}{\mathrm{GeV}}\right)^{-3} \mathrm{s}. \quad (6)$$

A $T_{BH} \approx 1$ GeV black hole has a remaining lifetime of ~ 16,000 yr; a $T_{BH} \approx 10$ GeV black hole has a remaining lifetime of ~ 20 yr; a $T_{BH} \approx 25$ GeV black hole has a remaining lifetime of ~ 1 yr; a $T_{BH} \approx 300$ GeV black hole has a remaining lifetime of ~ 1 hr; a $T_{BH} \approx 2$ TeV black hole has a remaining lifetime of ~ 100 s; and a $T_{BH} \approx 20$ TeV black hole has a remaining lifetime of ~ 100 ms.

As can be seen from Eqs (2) and (4), the $M_{BH} \ll M_*$ black hole's mass quickly decreases as it radiates and its temperature increases at an accelerating pace. Recall that the photons produced from the decays of the directly Hawking-radiated QCD particles dominate the net instantaneous photon flux from a $T_{BH} > \Lambda_{QCD}$ black hole and have an average energy that scales as roughly ${T_{BH}}^{0.5}$, not as T_{BH}. Thus substantial numbers of 100 MeV – 10 TeV photons will be produced even during the final explosive stage of the black hole's evaporative lifetime.

With respect to detecting gamma-ray black hole bursts with the Fermi Observatory, there are 3 cases of BH signals that we need to consider:

Case (i) The gamma-ray spectrum from a $3\ \mathrm{MeV} < T_{BH} < 12\ \mathrm{GeV}$ black hole will appear to be almost constant as a function of time over the lifetime of the Fermi Observatory. (Recall that the remaining evaporation lifetime of a $T_{BH} = 10$ GeV black hole is ~ 20 yrs.)

Case (ii) The gamma-ray spectrum from a $12\ \mathrm{GeV} < T_{BH} < 50\ \mathrm{GeV}$ black hole will evolve significantly as a function of time over the lifetime of the Fermi Observatory but almost all its gamma-ray flux arriving over that time will lie within the LAT detector's energy range, 20 MeV - 300 GeV. (Recall that the remaining evaporation lifetime of a $T_{BH} = 50$ GeV black hole is ~ 50 days.)

Case (iii) The gamma-ray spectrum from a $T_{BH} >$ 50 GeV black hole will be a quickly evolving burst with part of its flux arriving in the LAT energy range and significant flux at energies above the LAT range. In the final stages of burst evolution, the incoming flux will not be resolvable as a function of time and the time-integrated flux will be deposited in one time interval in the detector. (Recall that the remaining evaporation lifetime of a $T_{BH} = 170$ TeV black hole is ~ 100 μs.)

In Figure 1, we show the instantaneous gamma-ray flux $d^2N/dtdE$ which would be seen by the LAT from $T_{BH} = 0.1 - 50$ GeV black holes [6], relevant to Cases (i) and (ii). For black holes with these temperatures the flux is dominated by the photons resulting from the Hawking-radiated QCD particles. The gamma-ray flux from a $T_{BH} = 20$ MeV black hole, which is below the threshold to emit a QCD component and whose photons are all directly Hawking-radiated, is shown in Figure 2 [6].

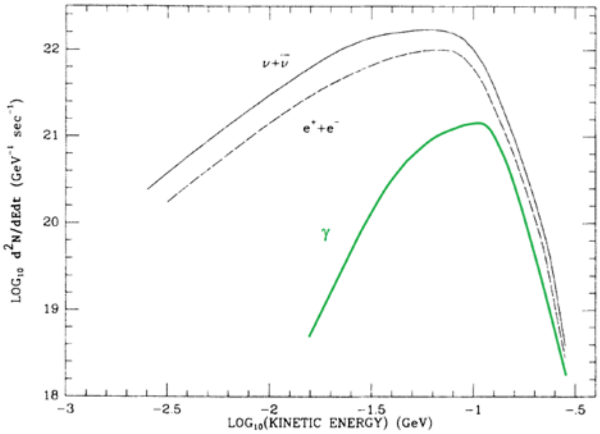

Figure 2: The instantaneous gamma-ray flux from a $T_{BH} = 20$ MeV black hole, which is below the threshold to emit a QCD component [6].

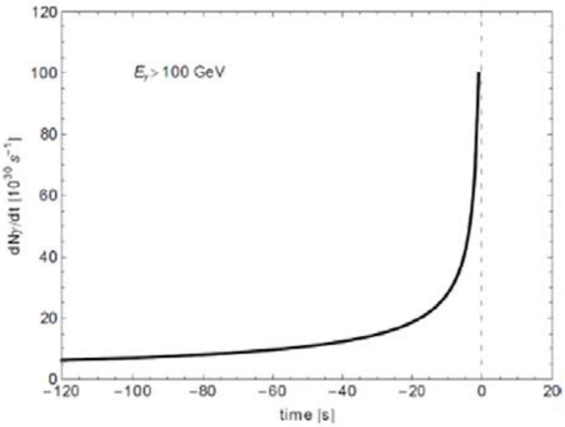

Figure 3: Preliminary calculation for the PBH burst light curve dN/dt arriving in the detector with energy above a given threshold, here $E_\gamma = 100$ GeV.

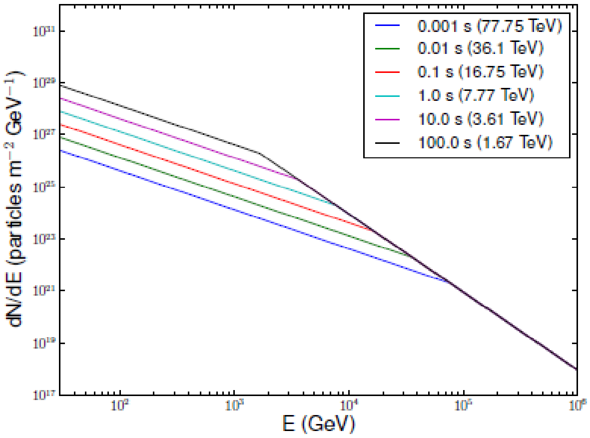

Figure 4: The gamma-ray spectrum dN/dE time-integrated over various remaining black hole evaporation lifetimes [11].

For Case (iii), we show in Figure 3 our preliminary calculation for the PBH burst light curve, i.e. the number of photons arriving per unit time with energy above a given threshold. (In Figure 3, the energy threshold is taken to be $E_\gamma = 100\,\text{GeV}$). In Figure 4, we plot the gamma-ray spectrum time-integrated over various BH remaining evaporation lifetimes [11].

In Table 1, we list a number of distinguishing characteristics to discern a black hole burst from other known GRB source types. In particular, the BH burst will show a soft-to-hard (that is, low average energy to high average energy) time evolution and will be non-repeating. If it is bursting in free space, it should not be accompanied by an afterglow, but generation of an afterglow may be possible if the black hole is bursting in an ambient high density plasma or ambient high magnetic field.

Table 1: Differences between black hole burst signals and GRBs of known source types.

Gamma-Ray Bursts (known GRB types)	BH Bursts
Detected at cosmological distances	Local, unlikely to be detected from beyond Galaxy
Most GRBs show hard-to-soft evolution	Hard-to-soft evolution expected
Hadrons not expected from GRBs	Accompanied by hadronic bursts which may be detectable if local
Gravitational wave signal expected	No accompanying gravitational wave signal
Time duration ranges from fractions of second to hours	Time duration of burst most likely 1-100 seconds
Fast Rise Exponential Decay (FRED) light curve	Exponential Rise Fast Fall (ERFF) light curve
X-ray, optical, radio afterglows expected	No multi-wavelength photon afterglows unless in exotic ambient environment
TeV emission unknown	TeV spectra predicted
Multi-peak time profile	Single-peak time profile
May be repeating	No burst repetition

If no black hole bursts are observed by a detector, the null detection implies an upper limit on the local number density of small black holes. An amalgamation of recent limits and limits which would be set by null detection with HAWC are shown in Figure 5. As a general statement, the strongest limits have been set by searching for bursts of about $1 - 100\,\text{s}$ duration because the detector signal weakens for bursts of shorter duration and the background dampens signal recognition at longer duration. The advantages [12] of the Fermi Observatory, are that it is not background-limited, it has good angular and time resolution, a wide field of view and a low energy threshold, and it is anticipated to have a very long operational lifetime. Preliminary limits derived from a search of Fermi LAT data to date for pairs of photons with an arrival interval shorter than the time expected for a Poisson-distributed photon background give an upper limit of $2 \times 10^3\,\text{pc}^{-3}\text{yr}^{-1}$ on BH bursts of $10^5\,\text{s}$ duration (corresponding to $T_{BH} \gtrsim 200\,\text{GeV}$ and $M_{BH} \lesssim 6 \times 10^{10}\,\text{g}$) [13].

The $\dot{M}_{BH} \propto {M_{BH}}^{-2}$ dependence of Eq (4) means that, for any population of black holes that have masses today around some $M_{BH} \ll M_*$ (i.e. that have remaining lifetimes much less than the age of the universe), the number of black holes per mass interval around M_{BH} today is

$$\frac{dn}{dM_{BH}} \propto {M_{BH}}^2 \tag{7}$$

independent of the BH formation time, formation mechanism or spatial distribution [9]. For black holes recently created with mass $M_i \ll M_*$, the distribution (7) applies around the evolved mass M_{BH} even if the initial mass distribution had initially been almost a delta function at M_i (because in reality there is always some smearing of such a delta function).

In the case of PBHs with initial masses of $M_i \sim M_*$ created in the early universe, the distribution (7) applies today up to $M_{BH} \sim M_*$ but the mass distribution with which the PBHs were initially created would still apply above M_* today because $M_i > M_*$ PBHs have lost little mass over the history of the universe. Therefore, using Eq (7), we can extrapolate the burst search limits to derive a limit on the number of $M_i \sim M_*$ PBHs created in the early universe. All of the BH burst search limits to date when extrapolated up to $M_i \sim M_*$ correspond to limits on the cosmologically-averaged number density of M_* PBHs which are weaker than the limit derived from the 100 MeV extragalactic gamma-ray background. For reasonable values of the enhancement due to CDM clustering in the Galaxy, the 100 MeV extragalactic limit on the cosmologically-averaged number density of M_* PBHs corresponds to a local BH burst limit of $\sim 10\,\text{pc}^{-3}\text{yr}^{-1}$.

It should be noted, however, that the BH burst search limits are robust limits on the number density of small black holes close to Earth, regardless of their formation epoch or formation mechanism. Such black holes, if they are observed, are not necessarily the evolved state of $M_i \sim M_*$ PBHs formed in the early universe. Also, the assumptions concerning the clustering or spatial distribution of local BHs/PBHs used in the analysis may be incorrect, making detection in a given scenario more or less likely.

2.3 Further Comments on the Black Hole Burst Spectra

In the above analysis, the black hole is assumed to Hawking-radiate only the experimentally-confirmed fundamental particle species of the Standard Model of particle physics. If further fundamental modes beyond the Standard Model exist, the extra modes may enhance

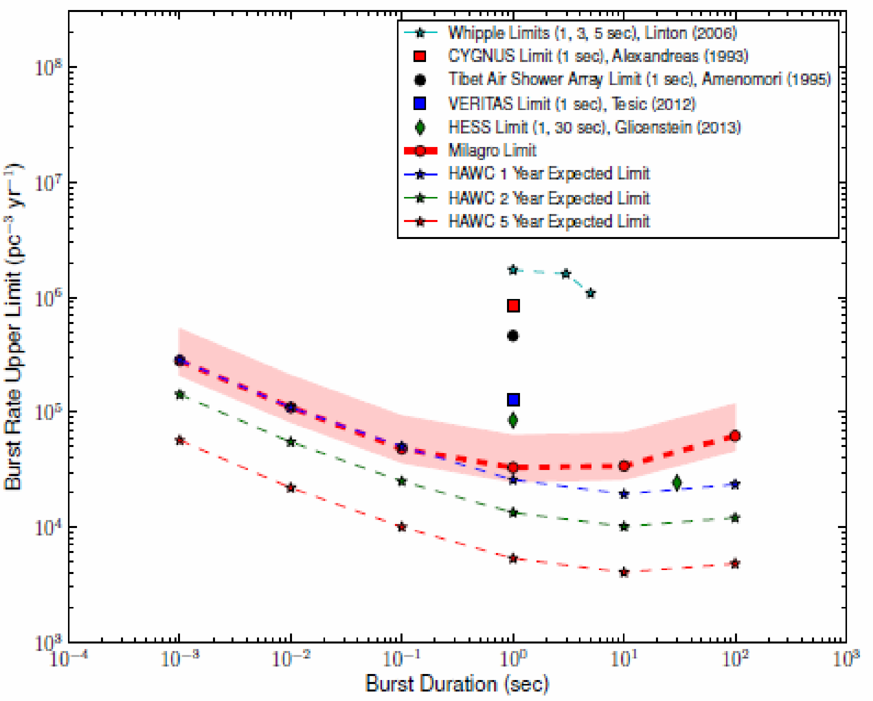

Figure 5: Limits on the local number density of black hole bursts in $\mathrm{pc}^{-3}\mathrm{yr}^{-1}$ set by null-detection in previous burst searches, together with projected limits which would be set by null-detection at the HAWC Observatory [11].

both the instantaneous flux from the black hole and the rate at which M_{BH} decreases and T_{BH} increase. This will shorten the black hole's remaining evaporation lifetime and the duration of the final burst. If new fundamental modes appear only at temperatures well above 100 TeV, the overall effect on the predicted observable spectra is, most likely, negligible. A significant number of new fundamental modes at lower energies are postulated, though, in some extensions to the Standard Model but it is expected that the weighting factor in Eqs [4] – [6] remains of order $f(M_{BH}) \lesssim 100$ [7]. For example in Supersymmetry models, each $s = 1/2$ fundamental particle has an $s = 0$ superpartner and each $s = 1$ fundamental particle has an $s = 1/2$ superpartner, giving $f(M_{BH}) \lesssim 45$. The accompanying enhancement to the instantaneous flux and dN/dE spectra at a particular energy would depend on the actual decay processes of the new modes.

A number of PBH burst scenarios invoking significant self-interaction of the Hawking-radiated particles in the vicinity of the black hole after emission have been proposed. If such self-interaction did occur after emission, it would not change the remaining evaporation lifetime but would decrease the average energy of the photons arriving at the detector, i.e. decrease the expected observable spectra at high energies and increase the spectra at low energies [14]. Such photosphere models have recently been re-analyzed in detail and it has been strongly argued that the conditions for photosphere or quark-gluon plasma development are not met in the vicinity of the evaporating black hole [8]. Specifically, the time interval between successive Hawking emissions, the damping of Hawking emission and the limited amount of energy per emission near a species' rest mass threshold, and the Lorentz-transformed distance over which a scattered particle becomes 'on-shell' are such as to prevent the Hawking-radiated particles undergoing a significant number of QED or QCD interactions in the neighbourhood of the black hole. Hagedorn models [15] which invoke an exponential increase in fundamental hadronic states around a limiting temperature of $T_{BH} \sim m_{\pi}$, and which would produce a more detectable BH burst signal peaking at lower photon energy, are inconsistent both with accelerator experiments at these and higher energies (which confirm the quark model interpretation) and with the gravitational definition of T_{BH} whose evolution is determined by the BH mass-energy loss rate. Hagedorn-type behaviour which may occur at extremely high energies in string theories would have negligible effect on the BH burst signal.

Although photospheres produced by intrinsic self-interaction of the radiated particles in the vicinity of a stand-alone BH appear to be ruled out, it may be possible to produce a non-intrinsic photosphere or distortion of the burst signal if the BH is embedded in an ambient high density plasma or strong magnetic field. Such scenarios have not yet been modeled in detail. The standard emission model BH gamma-ray spectra also do not yet incorporate the recently-recognized inner bremsstrahlung (single-vertex bremsstrahlung) component which is expected to dominate the directly Hawking-radiated photon component below about 50 MeV [16].

3. SUMMARY

There is strong motivation for investigating the possibility of detecting black hole burst signals. Detection of an evaporating black hole burst would be definitive experimental proof of the amalgamation of classical gravity with classical and quantum thermodynamics, pioneered by Hawking and Bekenstein. Equally importantly, the final stages of the evaporation process would open a direct observational window into particle physics at energies higher than can ever be achieved with terrestrial accelerators. For example, the black hole evaporation rate will be significantly increased if the supersymmetry modes exist. Details of the final stage of the BH burst may give insight into a quantum aspect of gravitation. Deviations of the BH burst signature from the predicted standard emission model spectra could also be used a probe of ambient extreme astrophysical environments. Detection or non-detection of PBHs give important constraints on the conditions in the early universe, in particular the amplitude and spectral index of initial density perturbations on smaller scales than are probed by the cosmic microwave background measurements. Thus, even if there is null-detection of BH bursts, there is strong motivation for improving the search limits and the implied upper limits on the number density of PBHs.

Updated detailed modeling of the BH burst signal that could be observed by the Fermi Observatory and exploration of new search methodologies is currently ongoing.

Acknowledgments

JHM wishes to thank the organizers of the 5th Fermi Symposium for their hospitality.

References

[1] A. Einstein, “Die Feldgleichungen der Gravitation”, Sitzungsberichte der Preussischen Akademie der Wissenschaften zu Berlin, 844 (1915); A. Einstein “Die Grundlage der allgemeinen Relativitätstheorie”, Annalen der Physik 49, 769 (1916)

[2] K. Schwarzschild, “Über das Gravitationsfeld eines Massenpunktes nach der Einsteinschen Theorie”, Sitzungsberichte der Deutschen Akademie der Wissenschaften zu Berlin, Klasse fur Mathematik, Physik, und Technik, 189 (1916); K. Schwarzschild, “Über das Gravitationsfeld einer Kugel aus inkompressibler Flussigkeit nach der Einsteinschen Theorie”, Sitzungsberichte der Deutschen Akademie der Wissenschaften zu Berlin, Klasse fur Mathematik, Physik, und Technik, 189 (1916)

[3] B.J. Carr et al., “New cosmological constraints on primordial black holes”, Phys.Rev.D 81, 104019 (May 2010)

[4] S.W. Hawking, “Black hole explosions?”, Nature 248, 30 (Mar 1974); S.W. Hawking, “Particle creation by black holes”, Commun.math.Phys. 43, 199 (Apr 1975)

[5] D.N. Page, “Particle emission rates from a black hole: Massless particles from an uncharged , nonrotating hole”, Phys.Rev.D 13, 198 (Jan 1976); D.N. Page, “Particle emission rates from a black hole. II - Massless particles from a rotating hole”, Phys.Rev.D 14, 3260 (Dec 1976); D.N. Page, “Particle emission rates from a black hole. III – Charged leptons from a nonrotating hole”, Phys.Rev.D 16, 2402 (Oct 1977)

[6] J.H. MacGibbon and B.R. Webber, “Quark- and gluon-jet emission from primordial black holes: The instantaneous spectra” Phys.Rev.D 41, 3052 (May 1990)

[7] J.H. MacGibbon, “Quark- and gluon-jet emission from primordial black holes. II. The emission over the black-hole lifetime” Phys.Rev.D 44, 376 (July 1991)

[8] J.H. MacGibbon, B.J. Carr and D.N. Page, “Do evaporating black holes form photospheres?” Phys.Rev.D 78, 064043 (Sept 2008)

[9] J.H. MacGibbon and B.J. Carr, “Cosmic ray from primordial black holes” Ap.J. 371, 447 (Apr 1991)

[10] E.L. Wright, “On the density of primordial black holes in the Galactic halo” Ap.J. 459, 487 (Mar 1996)

[11] A.A. Abdo et al., “Milagro limits and HAWC sensitivity for the rate-density of evaporating primordial black holes”, Astropart.Phys. 64, 4 (Feb 2015)

[12] T.N. Ukwatta et al., “Sensitivity of the Fermi detectors to gamma-ray bursts from evaporating primordial black holes (PBHs)” Proc.12th Marcel Grossmann Meeting, Paris, Jul 2009

[13] D. Malyshev et al., “Expected *Fermi*-LAT limits on primordial black hole evaporation”, 5th Fermi Symposium, Nagoya, Oct 2014

[14] A.F. Heckler, “Formation of a Hawking-radiation photosphere around microscopic black holes”, Phys.Rev.D 55, 480 (Jan 1997); A.F. Heckler, “Calculation of the emergent spectrum and observation of primordial black holes”, Phys.Rev.Lett. 78, 3430 (May 1997);

[15] R. Hagedorn, “Statistical thermodynamics of strong interactions at high-energies”, Nuovo Cim.Suppl. 3, 147 (1965)

[16] D.N. Page, B.J. Carr and J.H. MacGibbon, “Bremsstrahlung effects around evaporating black holes” Phys.Rev.D 78, 064044 (Sept 2008)

The First 100 LAT Gamma-Ray Bursts: A New Detection Algorithm and Pass 8

G.Vianello, N.Omodei
Stanford University, Stanford, CA, United States
on behalf of the Fermi/LAT collaboration

Observations of Gamma-Ray Bursts with the *Fermi* Large Area Telescope have prompted theoretical advances and posed big challenges in the understanding of such extreme sources, despite the fact that GRB emission above 100 MeV is a fairly rare event. The first *Fermi*/LAT GRB catalog, published a year ago, presented 28 detections out of 300 bursts detected by the Fermi Gamma-Ray Burst Monitor (GBM) within the LAT field of view. Building on the results from that work and on recent development in the understanding of the systematic errors on GBM localizations, we developed a new detection algorithm which increased the number of detections by 40%. Even more recently the development of the new event analysis for the LAT ("Pass 8") has increased the number of detections within the first 3 years of the mission to 45, up 50% with respect to the published catalog. The second LAT GRB catalog, in preparation, will cover more than 6 years of the mission and will break the barrier of 100 detected GRBs, a more than 20-fold improvement with respect to observations before the *Fermi* era in the same energy range. We will review the main features of the new algorithm, as well as preliminary results from this investigation.

1. High-energy emission from Gamma-Ray Bursts

Fermi/LAT observations are uncovering new and unexpected properties of the high-energy emission from Gamma-Ray Bursts (GRBs) shedding light on physics mechanisms, such as particle acceleration and emission processes, in ultra-relativistic regime. The first LAT GRB catalog [Ackermann et al. 2013] contained 35 bursts, with 28 detected above 100 MeV with the standard likelihood analysis and 7 with the LAT Low-Energy technique (LLE). It established new high-energy features of GRBs, namely:

- Additional power-law component during prompt emission: the prompt emission of most GRBs have been successfully described in the past with the Band function [Band et al. 1993]. In many bright GRBs observed by the LAT an additional power-law component is required to account for high-energy data.
- Delayed onset: the emission above 100 MeV is systematically delayed with respect to the low-energy emission seen in the keV–MeV energy range.
- Extended duration: the emission above 100 MeV is also systematically longer than the prompt emission, and decays smoothly as a power law with typical decay index of -1, pointing to a different physical origin with respect to the spiky prompt emission.

Early afterglow models [Kumar and Barniol Duran 2009, Ghisellini et al. 2010] could explain the observed time decay, the delayed onset as the outflow deceleration time scale, and the lack of variability. Hadronic models could explain these features as well: the onset delay could be the time to produce electromagnetic cascades [e.g., Dermer and Atoyan 2006, Gupta and Zhang 2007, Asano and Inoue 2007] or the time required to accelerate, accumulate, and cool down relativistic protons via proton-synchrotron emission in a very strong magnetic field [Razzaque et al. 2009]. Furthermore, energy-dependent delays would be expected in proton-synchrotron models where the cooling break shifts to lower energies at later times. On the other hand, we have analyzed the record-breaking GRB 130427A finding that, while several features of the "prompt" emission are in agreement with some internal-shocks models, other key details such as the estimated Lorentz factors for the colliding shells contradict expectations, possibly calling for different scenarios [Preece et al. 2014]. Also, the maximum energy of the photons in conjunction with a featureless high-energy light curve rules out both synchrotron and Synchrotron Self Compton from Fermi-accelerated particles as emission mechanism, a radical departure from the standard external-shock model for the LAT emission [Ackermann et al. 2014]. New observations and insights are hence needed to foster further theoretical developments and overcome these difficulties.

Our new specialized analysis described in Sect. 3 allows the detection of faint high-energy GRB counterparts, increasing the efficiency of detection by more than 50% and, when used in conjuction with the new "Pass 8" event selection, yielding more than 100 bursts over the time span of the *Fermi* mission. The analysis and characterization of this new sample is in progress. When completed, it will provide the needed new insights. In particular, we will be able to settle some open questions which we could not firmly establish in the first catalog due to the limited statistics:

- The existence of a separate population of hyper-energetic events, characterized by a ratio between high- and low-energy fluence much larger than the others.

- The high-energy emission for all but 2 GRBs in the sample decays as t^{-1} at late times, which in the context of the fireball model favors an adiabatic expansion. The other two GRBs instead decay as expected from a radiative regime ($t^{-1.5}$) [Blandford and McKee 1976, Katz and Piran 1997], but they suffered from less-than-optimal observing conditions. Is there a class of truly radiative fireballs?
- One of the GRBs in the sample presented a high-energy cutoff in the extra power-law component, while another one in the low-energy Band component. How common are spectral cutoffs? Do bursts with a cutoff have any other peculiar feature?

Analyzing the new enlarged sample will answer these questions, and will uncover new features.

2. Pass 8 and GRBs

The newly-developed "Pass 8" analysis is an event analysis rebuilt from the ground up with respect to previous versions ("Pass 6" and "Pass 7"). We refer the reader to other contributions in this Symposium for an introduction and for all the details about such analysis. Here we show how it will improve the number of GRB detections. We started by performing a large number of simulations of GRBs. In particular, we fixed 10 flux values logarithmically spaced between 10^{-8} and 2×10^{-7} erg cm^{-2} s^{-1}. Since the LAT effective area is a function of the cosine of the off-axis angle θ of the GRB, we also fixed a grid of 10 values uniformly distributed in $\cos\theta$. For each pair (flux, $\cos\theta$) we performed 200 simulations. These simulations were performed with the tool *gtobssim*, which accounts for the Poisson nature of the observation. For all simulations we used a fixed power-law spectrum with index -2, which is what is typically observed by the LAT [Ackermann et al. 2013]. We then overimposed these simulated GRBs on a background taken from a real observation, and performed a likelihood analysis for each realization, recording the results. We repeated this procedure using "Pass 7" data at first (*P7REP_SOURCE_V15* class), and then a preliminary version of "Pass 8" data (*P8_SOURCE_V1* class). We then compared the results. In order to determine the relative sensitivity between the two datasets, we computed the median significance for each point in the (flux, $\cos\theta$) grid, computed as the square root of the TS value. The results are shown in Fig. 1. It is clear that Pass 8 can detect GRBs at much lower fluxes. We stress that the actual value for a particular detection threshold (for example the 5σ one) depends on many factors (background level, duration of the GRBs, Zenith angle...) which are kept fixed in our simulations. Therefore, this is a comparative study, it is not a determination of the absolute sensitivity of Pass 8.

3. New triggered search for Gamma-Ray Bursts

Before the launch of *Fermi* it was estimated that the LAT would have observed 10-12 GRBs/year above 100 MeV and 6-8 above 1 GeV [Band et al. 2009]. During the first 3 years, however, observations were slightly below such expectations [Ackermann et al. 2013, Guetta et al. 2011]. Recently we developed a new search algorithm for GRBs, which is now up and running 24/7. As shown in Fig. 2, it provides 45% more detections than the algorithm used for the catalog when using Pass 7 data, and 60% more when using the newly-developed Pass 8 data. This improvement was achieved exploiting the results of the first LAT GRB catalog, presented in Sect. 1. The new algorithm consists of 10 searches running in parallel over time intervals logarithmically spaced from the trigger time to 10 ks after that. For each of these time intervals, these are the steps of the new algorithm:

1. A trigger is received either in real-time through the GCN system[1] or during an off-line analysis. In real-time most of the triggers are from the GBM, although also triggers from *Swift*, *INTEGRAL* and other observatories are received and processed.
2. If the trigger comes from the GBM, a "finding map" is produced to account for the position uncertainty. It has been recently reported that the GBM localizes GRBs with a systematic error of up to 15° [Connaughton et al. 2014]. Since this systematic error dominates over the statistical one, we always use finding maps of 30 × 30 deg. The finding map is essentially a TS map like the one produced by the tool *gttsmap*. Indeed, a grid in equatorial coordinates and with a spacing of 0.7 deg is created covering the finding map. For each point of the grid, a likelihood analysis is performed including a new source at that position. However, points in the grid having less than 3 photons within 10 deg are not considered. This avoids running a likelihood analysis, which is computer-intensive, in regions of the finding

---

[1] Gamma-Ray Coordinate Network, http://gcn.gsfc.nasa.gov/

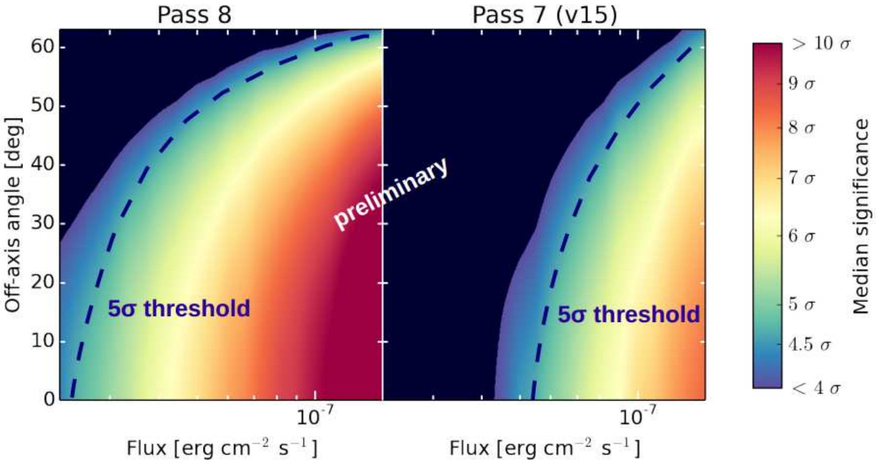

Figure 1: Median significance as a function of flux and off-axis angle for Pass 8 (left) and Pass 7 (right). The dashed line is the 5σ threshold. Pass 8 goes to much lower fluxes than Pass 7.

map where there is no possibility of detecting a new point source. At the end of each likelihood a TS value is computed, and associated with the point in the grid. When all points have been processed, the maximum of the TS in the map is considered the best guess for the position of the new transient, and marked for further analysis. Note that if the trigger comes from *Swift* or *INTEGRAL*, this step is not executed, since their localization errors are much smaller than the typical size of the LAT PSF.

3. The position of the candidate transient is optimized with the tool *gtfindsrc*

4. A new likelihood analysis is performed on the best position found. If the TS from this final analysis is above a certain threshold, we consider it a new detection

5. If running in real time, the results from the analysis are used by Burst Advocates to disseminate alerts to the community through GCNs.

In all likelihood analyses involved in the sequence the likelihood model consist of the Galactic template and the Isotropic template provided by the Fermi collaboration, plus all point sources from the 2FGL source catalog. While the normalization of the two templates are left free to vary, all parameters for the 2FGL sources are kept fixed. If the algorithm finds a new candidate source with a position compatible with one of the 2FGL sources, further analysis are performed manually to distinguish between a real transients, and other phenomena such as AGN flares. The algorithm does indeed trigger on flaring sources, which are also found by other real-time algorithms such as ASP [Band et al. 2009] and FAVA [Ackermann et al. 2013].

The procedure involves a certain number of trials, which might appear large. However, all the time windows are overlapping and involve the same region on the sky, therefore these trials are not independent at all, with many photons present in many of the time windows. Thus, the effective number of trials is rather small. While the full characterization is still in progress, preliminary simulations indicates that a 5σ detection corresponds to $TS \sim 28$.

A first run of the new algorithm on $\sim$ 5 years of preliminary Pass 8 data returned 86 detections. Adding the $\sim$ 20 LLE-only detections, we have already reached the milestone of 100 LAT-detected GRBs. Given the current rate of detections we also expect to exceed 100 likelihood detections within the year, an impressive milestone significantly exceeding pre-launch expectations. As expected, the new detections populate the lower part of the fluence distribution, demonstrating that the new algorithm and “Pass 8” improve the sensitivity of the search. This is shown in Fig. 3.

We also note that this preliminary study is using the “Pass 8” Source class for all time scales. It has been shown in the past that for short time scales ($< 200s$) using classes with larger acceptance at the expense of a larger background is beneficial. We will be using such classes in the final study, further increasing the number of detections.

Acknowledgments

The *Fermi* LAT Collaboration acknowledges generous ongoing support from a number of agencies and institutes that have supported both the development and the operation of the LAT as well as scientific data analysis. These include the National Aero-

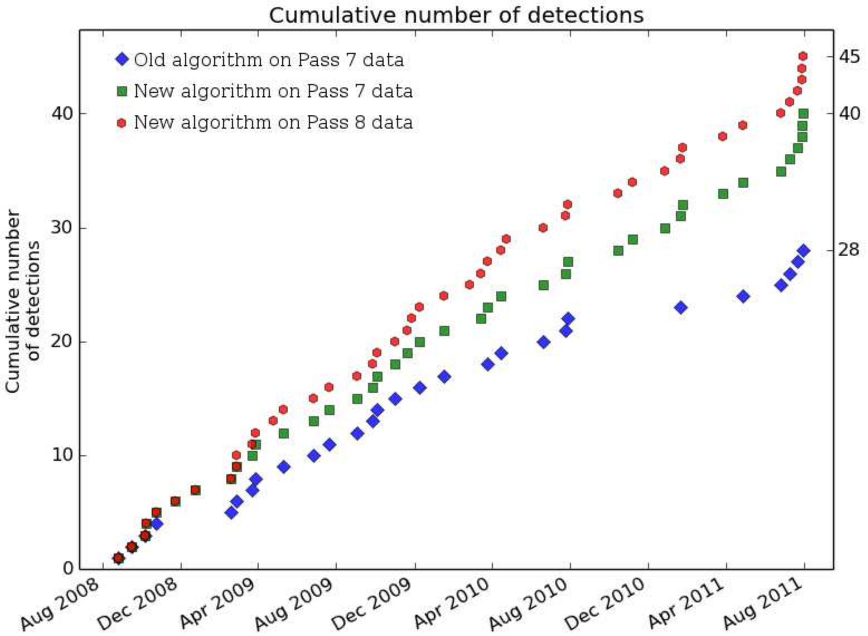

Figure 2: Cumulative detections for the time span covered by the LAT GRB catalog [Ackermann et al. 2013]. The new analysis yields 45% more detections than the one used in the catalog when run on the same data (blue and green), and 60% more with Pass 8 data.

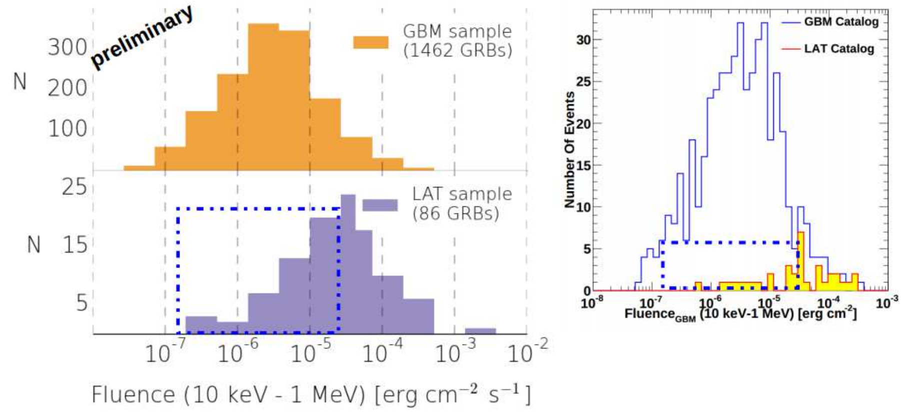

Figure 3: Left panel: low-energy fluence distribution for the whole GBM sample (upper panel) and for the sample detected with the new algorithm in LAT data (lower panel). Right panel: similar plot from the first LAT GRB catalog [Ackermann et al. 2013]. The blue dashed line marks the region where most of the new detections lie, showing the increased sensitivity of the new algorithm with respect to the old one.

nautics and Space Administration and the Department of Energy in the United States, the Commissariat à l'Energie Atomique and the Centre National de la Recherche Scientifique / Institut National de Physique Nucléaire et de Physique des Particules in France, the Agenzia Spaziale Italiana and the Istituto Nazionale di Fisica Nucleare in Italy, the Ministry of Education, Culture, Sports, Science and Technology (MEXT), High Energy Accelerator Research Organization (KEK) and Japan Aerospace Exploration Agency (JAXA) in Japan, and the K. A. Wallenberg Foundation, the Swedish Research Council and the Swedish National Space Board in Sweden.

Additional support for science analysis during the operations phase is gratefully acknowledged from the Istituto Nazionale di Astrofisica in Italy and the Centre National d'Études Spatiales in France.

References

M. Ackermann, M. Ajello, K. Asano, M. Axelsson, L. Baldini, J. Ballet, G. Barbiellini, D. Bastieri, K. Bechtol, R. Bellazzini, et al., ApJS **209**, 11 (2013), 1309.4899.

D. Band, J. Matteson, L. Ford, B. Schaefer, D. Palmer, B. Teegarden, T. Cline, M. Briggs, W. Paciesas, G. Pendleton, et al., ApJ **413**, 281 (1993).

P. Kumar and R. Barniol Duran, ArXiv e-prints (2009).

G. Ghisellini, G. Ghirlanda, L. Nava, and A. Celotti, MNRAS **403**, 926 (2010), 0910.2459.

C. D. Dermer and A. Atoyan, New Journal of Physics **8**, 122 (2006), arXiv:astro-ph/0606629.

N. Gupta and B. Zhang, MNRAS **380**, 78 (2007), arXiv:0704.1329.

K. Asano and S. Inoue, ApJ **671**, 645 (2007), 0705.2910.

S. Razzaque, C. D. Dermer, and J. D. Finke, ArXiv e-prints **0908.0513** (2009).

R. Preece, J. M. Burgess, A. von Kienlin, P. N. Bhat, M. S. Briggs, D. Byrne, V. Chaplin, W. Cleveland, A. C. Collazzi, V. Connaughton, et al., Science **343**, 51 (2014), http://www.sciencemag.org/content/343/6166/51.full.pdf, URL `http://www.sciencemag.org/content/343/6166/51.abstrac`

M. Ackermann, M. Ajello, K. Asano, W. B. Atwood, and M. Axelsson, Science **343**, 42 (2014), http://www.sciencemag.org/content/343/6166/42.full.pdf, URL `http://www.sciencemag.org/content/343/6166/42.abstrac`

R. D. Blandford and C. F. McKee, Physics of Fluids **19**, 1130 (1976).

J. I. Katz and T. Piran, ApJ **490**, 772 (1997).

D. L. Band, M. Axelsson, L. Baldini, G. Barbiellini, M. G. Baring, D. Bastieri, M. Battelino, R. Bellazzini, E. Bissaldi, G. Bogaert, et al., ApJ **701**, 1673 (2009), 0906.0991.

D. Guetta, E. Pian, and E. Waxman, A&A **525**, A53 (2011), 1003.0566.

V. Connaughton, M. S. Briggs, A. Goldstein, C. A. Meegan, W. S. Paciesas, R. D. Preece, C. A. Wilson-Hodge, M. H. Gibby, J. Greiner, D. Gruber, et al., ArXiv e-prints (2014), 1411.2685.

M. Ackermann, M. Ajello, A. Albert, A. Allafort, E. Antolini, L. Baldini, J. Ballet, G. Barbiellini, D. Bastieri, K. Bechtol, et al., ApJ **771**, 57 (2013), 1304.6082.

Varying Faces of Photospheric Emission in Gamma-ray Bursts

Magnus Axelsson
KTH Royal Institute of Technology, Oskar Klein Center, 106 91 Stockholm, Sweden
on behalf of the *Fermi*-LAT Collaboration

Among the more than 1000 gamma-ray bursts observed by the *Fermi Gamma-ray Space Telescope*, a large fraction show narrow and hard spectra inconsistent with non-thermal emission, signifying optically thick emission from the photosphere. However, only a few of these bursts have spectra consistent with a pure Planck function. We will discuss the observational features of photospheric emission in these GRBs as well as in the ones showing multi-component spectra. We interpret the observations in light of models of subphotospheric dissipation, geometrical broadening and multi-zone emission, and show what we can learn about the dissipation mechanism and properties of GRB jets.

1. INTRODUCTION

Despite having been studied for well over 20 years, the emission mechanisms active during the prompt phase in gamma-ray bursts (GRBs) remain unclear. A robust prediction of the fireball model for GRBs [1, 2] is that the relativistic jet is initially opaque and therefore photospheric emission is inevitable. Yet its strength is uncertain and it is therefore not necessarily detectable. In 1986, both Paczynski [3] and Goodman [4] suggested a strong contribution of photospheric emission in GRB spectra; however, the observed spectra generally appear nonthermal and these models were therefore not considered viable.

Interest in the photospheric component resumed with observations of GRBs using *Compton Gamma-Ray Observatory*/BATSE (20–2000 keV). Ryde [5] found that in many individual emission pulses an equally good or better fit could be found by using a model comprising a Planck function and a power-law, as compared to the traditional Band function. Additionally, it was found that the evolution of the Planck function component during the prompt phase followed well defined and consistent characteristics. The Planck component was interpreted as the photosphere of the GRB. At present there is again mounting evidence from theoretical considerations that the photosphere of the relativistic outflow (jet) plays an important role [6, 7, 8, 9].

In this paper the observational signs so far attributed to photospheric emission will be discussed and interpreted in light of models of subphotospheric dissipation, geometrical broadening and multi-zone emission. Photospheric emission can give rise to many different spectral shapes, and pure blackbody emission is rarely expected.

2. OBSERVATIONS

As noted above, predictions of photospheric emission came early in the study of GRBs. Yet it was not until the detailed spectral studies made possible by *CGRO*/BATSE that the first clear observational signs were seen. In part this may be due to the ambiguity in attributing spectral components to distinct physical processes. This has to some extent meant that the search for photospheric emission has become a search for blackbody (or Planckian) components in the spectrum: while the photosphere can in principle give rise to many different shapes, a blackbody can only come from the photosphere.

2.1. Blackbody-like spectra

Ghirlanda et al. [10] first reported the presence of a blackbody component in the initial phase of some GRBs detected with *CGRO*/BATSE. Ryde [5] also showed that some GRBs could be well fit with single Planck functions throughout the prompt phase. However, such cases are extremely rare. In the entire BATSE catalogue, only 6 out of $\sim$ 2200 GRBs are well described by a pure blackbody. The situation is similar for the *Fermi* catalogue: only 2 such bursts in over 1400 have reported [11, 12].

Although these numbers may seem low, what is perhaps more surprising is that there are such cases at all. Already from the start, it was shown that purely geometrical considerations meant that photospheric emission should be somewhat broader than a single temperature Planck function. The fact that there are such narrow spectra is thus very constraining for theoretical models.

An interesting case for the study of photospheric emission is GRB090902B, one of the brightest bursts seen by *Fermi*. During the first part of the emission episode, the main spectral peak is very narrow and well-fit by a multicolor blackbody [13]. However, during later times in the pulse the spectrum broadens considerably. As the spectral evolution can be followed, it is clear that the same component is seen throughout the prompt phase. The blackbody-like spectrum at early times ties it to the photosphere, and GRB090902B thus shows that photospheric emission

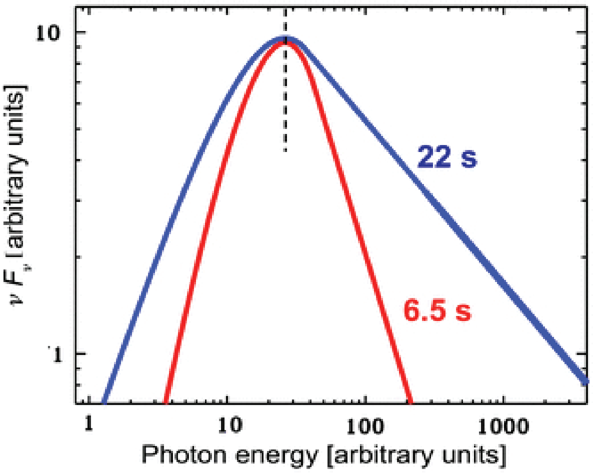

Figure 1: Peak-aligned spectra from GRB090902B at two different times, showing the change in width of the spectral peak. At early times in the pulse (red), the spectrum is very narrow and well described by a multicolor blackbody. Later in time (blue), the spectrum has significantly broadened, and is well fit by a Band component with typical parameters.

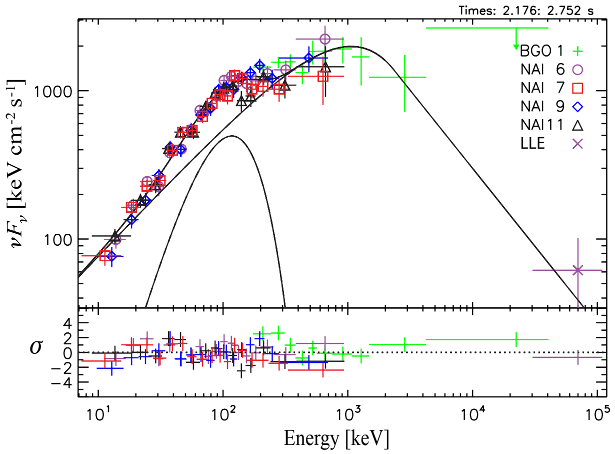

Figure 2: Spectrum from GRB110721A, showing the clear detection of an extra component in addition to the Band function. This component was fit using a blackbody and interpreted as photospheric emission in Axelsson et al. [15].

is not necessarily Planckian.

In summary:

- Observations of "blackbody-like spectra" indicate that the photosphere is detected, and thereby also plays a role in GRB prompt emission and the formation of spectra.
- The fact that some spectra are well fit by single-temperature blackbodies has strong theoretical implications on the physical conditions of the emission region.
- The slightly wider spectra allow us to probe the broadening mechanisms active in the outflow. This is particularly true for bursts such as GRB090902B where width changes strongly during the pulse.

However, most spectra are not well described by a single narrow component. Nevertheless, evidence of photospheric emission in some GRBs motivates us to search for its presence also in other bursts.

3. MULTI-COMPONENT SPECTRA

One of the most striking results of the *Fermi* satellite is the discovery of multiple components in the spectrum of GRBs. Bright bursts, where the signal-to-noise ratio is highest, show statistically significant deviations from a simple Band function [14]. One component commonly found is a power-law extending to high energies (e.g., GRB 080916C). However, a few bursts also show features at lower energies (≤ 100 keV), which are well-fit by a Planck function. Perhaps the strongest such example is GRB110721A, where the significance of the extra component was greater than 5σ [15].

The results found with *Fermi* match those previously seen in BATSE data. Ryde [5] found that a model comprising a blackbody and a power-law provided a good fit to several GRB spectra observed by BATSE. The power-law index was greater than -2, so it was clear that there had to be a turn-over at higher energies. With the much broader energy range afforded by *Fermi*, the power-law seen in the BATSE data is revealed as the low-energy slope of the Band component. It should be noted that also *Fermi* has detected a power-law component in the spectra; however, this feature is seen in addition the the Band component, and the temporal behavior is very different. Its origin is not yet understood, but may be related to the mechanism producing the temporally extended GeV emission [14].

Another feature which strengthens the common origin of the blackbody components in BATSE and *Fermi* spectra is their temporal evolution. The BATSE components showed a typical behavior where the temperature decayed with time as a broken power-law. This distinctive feature is also seen in the *Fermi* data.

3.1. Effects of multiple components

The additional blackbody component detected is typically subdominant, in general contributing only 5-10% of the total flux. For this reason, its presence

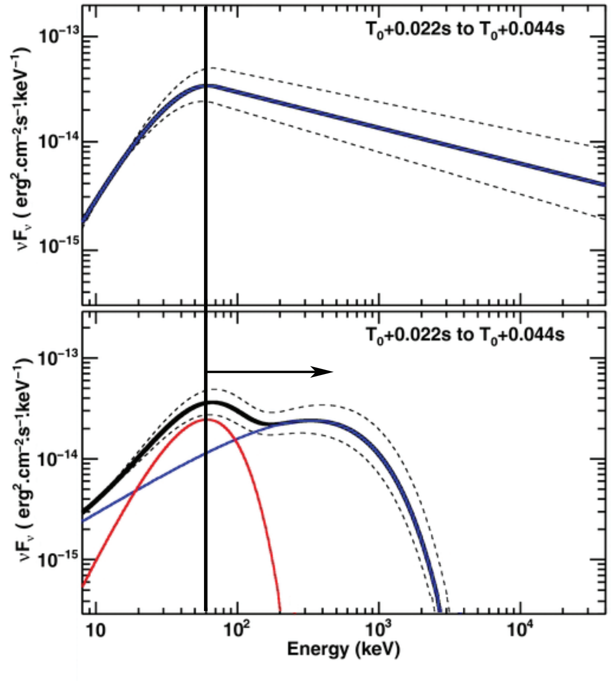

Figure 3: Resulting fits when the spectrum from GRB120323 is fit with a pure Band component (top) and an additional blackbody component (bottom). Adding the blackbody component does not give a statistically sufficient improvement to claim its presence. However, the parameters of the Band component are changed when the blackbody component is present, and therefore different interpretations may be allowed. Adapted from Guiriec et al. [16].

can only be firmly seen in very bright GRBs. However, it may still be present in many more GRBs, and this can have important consequences. When spectra are fit with models comprising a blackbody in addition to the main Band component, the parameters of the Band component change. This means that although a photospheric component may not be statistically detected, its presence can have a large impact on the interpretation of the bulk of the emission. For instance, the peak of the Band component will shift to higher energies, and the measured value of the low-energy slope, α, will soften [16]. An example of this is shown in Figure 3, where the spectrum of GRB120323 is fit with and without an additional blackbody component. The changed parameters may lead to the Band component being more compatible with synchrotron emission, and thus change the theoretical interpretation also of the main emission component.

As thermal emission is a well-known physical process, identifying such a component allows physical parameters of the outflow to be derived [17]. These include the bulk Lorentz factor, jet-launching radius and saturation radius. For instance, studies of GRB110721A have found that the Lorentz factor was initially around 1000, then decreased throughout the pulse to values $\sim$ 200 [15]. The jet launching radius was instead found to increase from 3×10^6 cm to 2×10^9 cm [18].

4. INTERPRETATIONS

In the case of "typical" single-component GRB spectra, it is generally assumed that a single process is giving rise to the emission. For spectra well-fit by a single or multi-temperature blackbody, the most likely candidate is photospheric emission.

For the multi-component GRBs, the interpretation is less straight-forward. A natural first assumption is to connect the two components to different emission regions. The blackbody component is then attributed to thermal emission arising from the photosphere, and the Band component related with non-thermal radiation further out in the jet. There are many different possible realizations of the scenario. For instance, the location of the photospheric radius in relation to the saturation radius will affect the strength of the blackbody and different magnetizations of the outflow will change the ratio between the two components [19].

As mentioned above, identifying a blackbody component in the spectrum can alleviate some of the difficulties facing interpretations suggesting a synchrotron origin for the Band component. Many observed GRBs have hard spectra below their νF_ν peaks. Those with indices $\alpha > -1.5$ below this peak cannot possess electrons that radiate synchrotron emission in the expected fast cooling regime, within this spectral window; this is the so-called fast-cooling α index limit [20]. Models including a low-energy blackbody component allow for softer slopes of the Band component, thereby making the interpretation more compatible with synchrotron.

Spectra with hard α slopes are however not the only issue facing synchrotron interpretations. Studying the widths of spectra, it can be seen that most are too narrow to accommodate synchrotron emission from realistic electron distributions [21]. This is shown in Fig. 4. In these cases adding a blackbody component will not help, but rather worsen the issue; the width of the Band function component in a composite spectrum is if anything more narrow than the entire spectrum.

An alternative to multiple emission zones is that the entire spectrum arises from the photosphere. This of course requires a radical departure from the framework where photospheric emission is described by a (single or multicolor) blackbody. One suggested way of altering the spectrum is subphotospheric emission. In brief, in this scenario energy is dissipated below the photosphere, modifying the emergent spectrum. Different models propose different origins, such as magnetic reconnection [22], internal shocks [23] or collisional dissipation [24]. By varying the amount of dis-

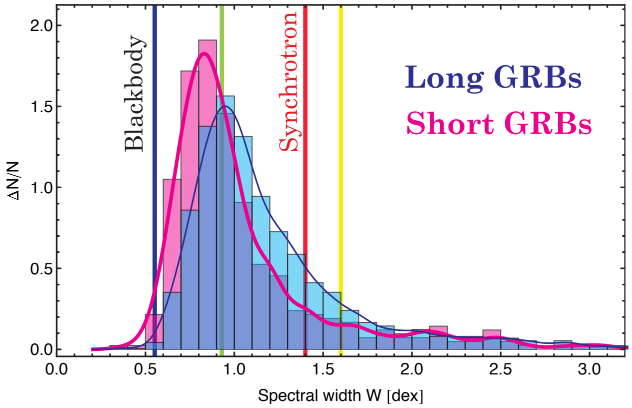

Figure 4: Distribution of widths of GRB spectra measured by *CGRO*/BATSE and *Fermi*/GBM. The solid lines indicate the width of a blackbody, and synchrotron from three electron distributions: monoenergetic (green), Maxwellian (red) and power-law with index -2 (yellow). Adapted from Axelsson & Borgonovo [21].

sipation and parameters of the outflow, it is possible to produce a wide range of spectral shapes by such subphotospheric energy release [25, 26].

As described by Paczyński [3], geometrical effects will broaden the spectrum. Considering relativistic limb darkening, Lundman et al. [27] used a combination of analytical model and Monte Carlo simulation to study the emergent spectrum from a jet. It was found that for a narrow jet, with opening angle is of the order of the relativistic beaming angle, a broadening of the photospheric spectrum is expected for any viewing angle. For a broader jet, the broadening effect is strong only if the viewing angle lies along the edge of the outflow, i.e., is close to the jet angle.

Apart from increasing signal to noise in spectra, is there any way to distinguish between these scenarios? Recently, polarimetry has become the focus of attention, and does provide valuable extra information. In the case of non-thermal emission, synchrotron radiation is expected to have high degrees of polarization. Yet also photospheric emission can be polarized, though polarization degrees $\leq 40\%$ are expected [28]. Predictions of correlations between spectra and polarization may thus allow us to determine the physics behind the prompt phase emission. Unfortunately, there are at present very few reliable measurements of polarization in GRBs.

5. CONCLUSIONS

Photospheric emission has been detected in a growing number of GRBs, with Planckian components appearing together with other components, or dominating the spectrum. This shows that the photosphere plays a part in the formation of the spectra.

Most GRB spectra do not look thermal, and many instead having multiple components. This can be interpreted as radiation from two separate emission regions, or as pure photospheric emission. Understanding the role of the photosphere is thus important to probe the physics of the outflow itself.

Polarimetry provides a possible way to determine the contribution of the photosphere. There are today several proposed missions capable of measuring polarization in GRBs, which promises new insight into the physics of the relativistic jet.

Acknowledgments

The *Fermi*-LAT Collaboration acknowledges support for LAT development, operation and data analysis from NASA and DOE (United States); CEA/Irfu and IN2P3/CNRS (France); ASI and INFN (Italy); MEXT, KEK, and JAXA (Japan); and the K.A. Wallenberg Foundation, the Swedish Research Council and the Swedish National Space Board (Sweden). Science analysis support in the operations phase from INAF (Italy) and CNES (France) is also gratefully acknowledged.

References

[1] G. Cavallo & M. J. Rees 1978, MNRAS,183, 359
[2] M. J. Rees & P. Mészáros 1994, ApJ, 430, L93
[3] B. Paczyński 1986, ApJ, 308, L43
[4] J. Goodman 1986, ApJ, 308, L47
[5] F. Ryde 2004, ApJ, 614, 827
[6] D. Lazzati et al. 2010, ApJ, 725, 1137
[7] I. Vurm et al. 2011, ApJ, 738, 77
[8] D. Giannios 2011, arXiv:1111.4258
[9] B.-B. Zhang et al. 2011, ApJ, 730, 141
[10] G. Ghirlanda et al. 2003, A&A, 406, 879
[11] G. Ghirlanda et al. 2013, MNRAS, 432, 3237
[12] J. Larsson et al. 2015, ApJ, submitted.
[13] F. Ryde et al. 2010, ApJ, 709, L172
[14] M. Ackermann et al. 2013, ApJS, 209, 1
[15] M. Axelsson et al. 2012, ApJ, 757, L31
[16] S. Guiriec et al. 2013, ApJ, 770, 32
[17] F. Ryde & A. Pe'er 2009, ApJ, 702, 1211
[18] S. Iyyani et al. 2013, MNRAS, 433, 2739
[19] R. Hascoët et al. 2013, A&A, 551, 124
[20] R. Preece et al. 1998, ApJ, 506, 23
[21] M. Axelsson & L. Borgonovo 2015, MNRAS, 447, 3150
[22] D. Giannios 2008, A&A, 480, 305
[23] K. Ioka 2010, Progr. Theoret. Phys., 124, 667
[24] A. Beloborodov 2010, MNRAS, 407, 1033
[25] A. Pe'er et al. 2006, ApJ, 642, 995
[26] T. Nymark et al. 2011, arXiv:1111.0308
[27] C. Lundman et al. 2013, MNRAS, 428, 2430
[28] C. Lundman et al. 2014, MNRAS, 440, 3292

Temporal properties of bright BGO GRBs detected by Fermi

E. Bissaldi[1,2,3], E. Peretti[2], F. Longo[2,3]
[1] *INFN – Sez. di Bari, Via E. Orabona 4, 70125 Bari, Italy*
[2] *Physics Dep., University of Trieste, Via Valerio 2, 34127 Trieste, Italy*
[3] *INFN – Sez. di Trieste, Via Valerio 2, 34127 Trieste, Italy*

On behalf of the Fermi LAT Collaboration

We present results of an analysis of a sample of bright Gamma-Ray Bursts (GRBs) detected by Fermi-GBM up to more than 1 MeV, which were collected during six years of Fermi operations. In particular, we focus on the GRB durations over several energy bands of the prompt emission of a subsample of bright GRBs detected up to 10 MeV by GBM and, when possible, up to 1 GeV by Fermi-LAT, thus expanding the Duration–Energy relationship in GRB light curves to high energies for the first time. We find that the relationship for these energetic GRBs is flatter than reported for other samples, suggesting that the high– and low–energy emission mechanisms are closely related.

I. FERMI GBM AND LAT INSTRUMENTS

The Fermi satellite has been observing the gamma–ray sky since its launch in June 2008. It carries on–board two instruments: the Gamma-ray Burst Monitor (GBM) and the Large Area Telescope (LAT). GBM consists of 12 Sodium Iodide (NaI, 8–900 keV) and 2 Bismuth Germanate (BGO, 200 keV–40 MeV) scintillation detectors [1]. Figure 1 shows the placement and orientation of the detectors on the spacecraft, which allow GBM to have a Field-of-View (FoV) as large as the full unocculted sky. GBM detects ∼250 GRBs per year [2].

The LAT instruments include a Tracker-Converter, a Calorimeter and an Anti–Coincidence Detector [3]. The LAT standard analysis covers an energy range of 100 MeV–300 GeV. Thanks to the LAT Low Energy (LLE) technique [4], this coverage is extended down to 10 MeV. 35 GRBs were observed by LAT during the first 3 years of operation [5], but many more are expected to be found thanks to a new analysis algorithm [6] and to the newly implemented LAT event reconstruction *Pass 8* [7].

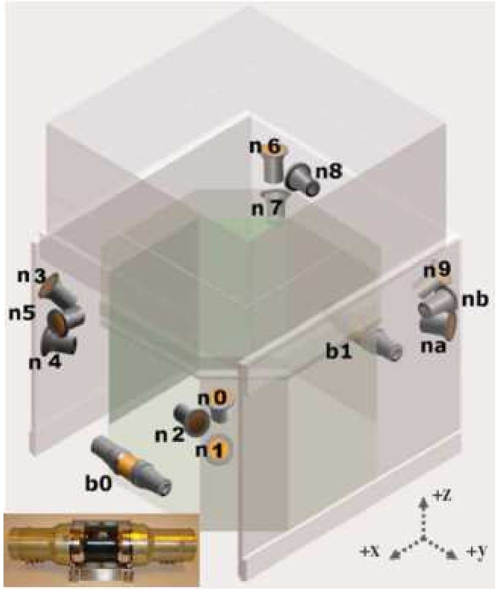

FIG. 1: Schematic view of the Fermi GBM detectors. The insert in the bottom left corner shows one of the two BGO detectors.

II. SAMPLE SELECTION CRITERIA

We follow the same approach as in [8] for the BATSE bright GRBs and in [9] for the GBM BGO bright GRBs collected over the first year of operation. Here we extend the previous analysis to six years of GBM data (from August 2008 to July 2014).

The first coarser selection is based on the analysis of the GBM telemetry packets. Bursts showing an increase of more than 80 counts/s over background in at least one BGO detector over the full BGO energy range are selected. The second finer selection is based on the analysis of the count rate excess above background measured by the BGO detector(s) in the 500 keV–1 MeV range during the main burst emission episode. We analyse the GBM TTE files (see [1] for GBM data type description) over four different timescales (64, 128, 256, and 512 ms). Bursts with a 4σ detection are selected.

The final sample of *bright BGO GRBs* includes 311 bursts, of which 68 are short and 243 are long ones. We repeat the same procedure on three other BGO energy ranges, namely 1–2 MeV, 2–5 MeV, and 5–10 MeV, and check for the detection significance.

In Figure 4 we plot these significances calculated in the four BGO energy bands as a function of the LAT boresight angle θ. The dashed vertical line indicates the LAT FoV at $\theta = 65^o$. GBM-only detections are marked as gray circles. Filled and empty circles represent long and short GRBs. 69 bursts from our sample

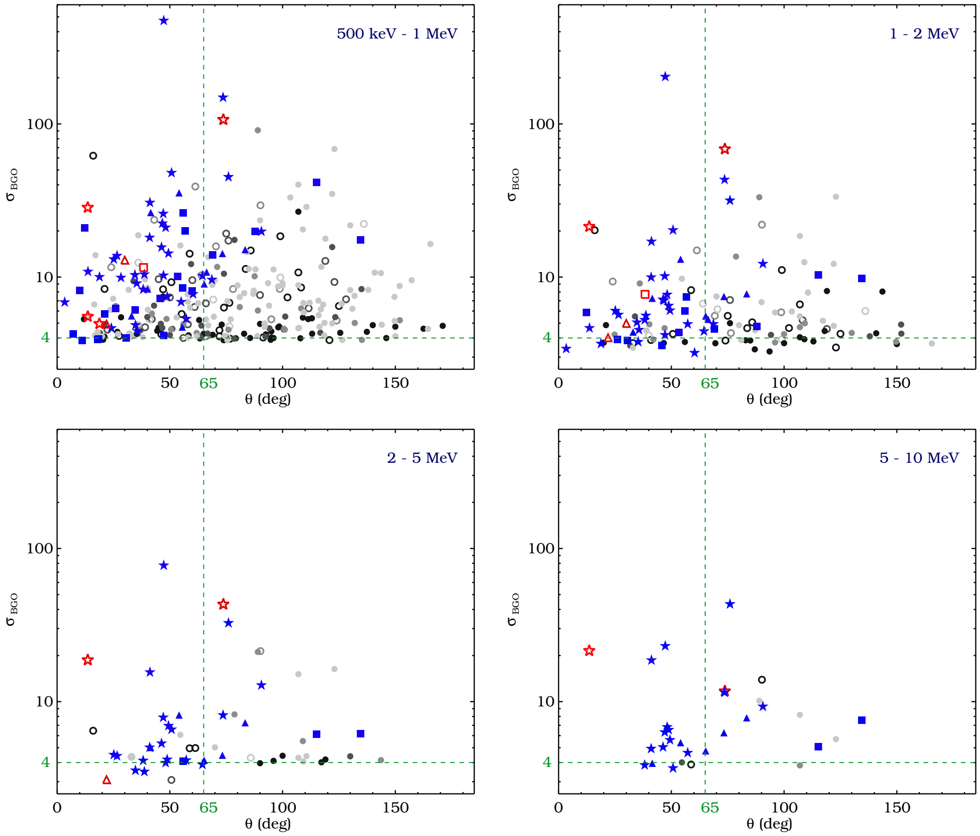

FIG. 2: BGO detection significance versus LAT boresight angle θ, calculated in four BGO energy ranges (see top right corner of each plot).

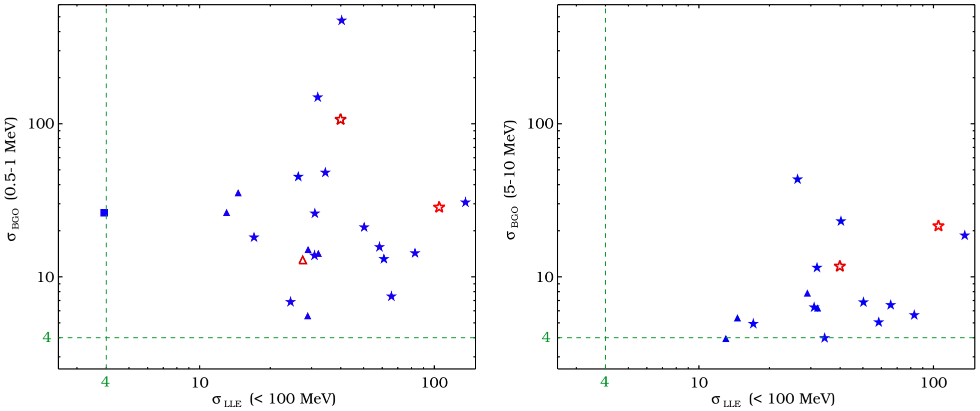

FIG. 3: BGO versus LLE detection significances for two different BGO energy ranges: 0.5–1 MeV (*left panel* and 5–10 MeV (*right panel*).

are also detected by the LAT [11]: 58 GRBs are detected with the standard likelihood analysis above 100 MeV (*stars*). Out of those, 33 are detected also below 100 MeV with the LLE technique (*squares*). Moreover, there are 11 bursts which are detected only with LLE analysis (*triangles*). Long-duration GRBs are plotted with *blue* symbols and short GRBs are plotted in *red*.

In these proceedings we want to focus only on the brightest events of our sample according to two criteria: (a) the BGO detection significance in the 500–1000 keV energy band, combined with the significance in the 5–10 MeV energy; and (b) the LLE detection significance in the 10 MeV – 1 GeV energy range. The latter is calculated by means of an algorithm presented in Section 3.3.1 of [5] and specifically designed for LLE source detection. The LLE data presented in this analysis are produced from *Pass 8* data.

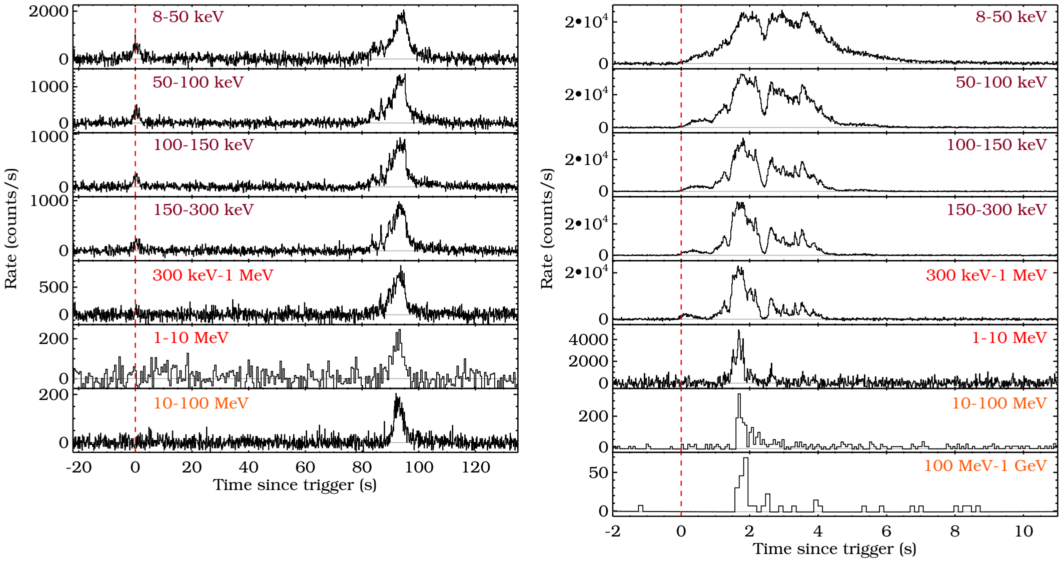

FIG. 4: Light curves over several energy bands of two GRBs from our subsample: GRB 100116A (*left panel*) and GRB 131014A (*right panel*)

If we independently select the 20 brightest events with both criteria, we end up with a subsample of 27 GRBs, which are listed in Table II. There are 21 long and 6 short GRBs in this new subsample. In the table we specify the GRB name (column 1), the GBM trigger number and trigger time in Mission Elapsed Time (MET, columns 2 and 3), the angle to the LAT boresight θ (column 4), the GBM duration (T_{90}) calculated in the 50–300 keV energy band and reported by [2] (column 5), the BGO and NaI detectors used for the temporal analysis (columns 6 and 7), and the detection significances in two BGO (columns 8 and 9) and in the LLE energy range (column 10).

A. Energy dispersion analysis

In order to select the best energy bands for the temporal analysis, we first want to study the effect of energy dispersion (ΔE) in NaI and BGO data by means of simulations. We randomly choose 15 GRBs from the latest GBM spectral catalog [12] and use the best model to simulate their spectra with XSPEC[13]. Finally, we compare the model predicted rates with the measured and simulated rates overs several NaI and BGO energy ranges.

We find that BGO data show an excess count rate in most energy bands ($\sim$30%), worsening towards high energies ($\sim$60%). NaI data show a smaller excess in count rates with respect to what is seen in BGOs ($\sim$20%), but in narrow energy bands below 40 keV we see that ΔE $\sim$ 30%. In order to keep ΔE $<$ 10% in NaI detectors and ΔE $<$ 20% in BGO detectors, we decide to selected the energy bands shown in the Table I. There are four energy bands covered by NaI detectors, two covered by BGO detectors and two covered by the LLE technique, for a total of eight valid spectral bands for the Duration–Energy relationship analysis.

TABLE I: Energy bands of each detector selected for the Duration–Energy analysis

Detector	Energy bands
NaI	8 –50 keV
	50–100 keV
	100–150 keV
	150–300 keV
BGO	0.3 – 1 MeV
	1 – 10 MeV
LLE	10–100 MeV
	100–1000 MeV

III. TEMPORAL ANALYSIS

We select GBM and LLE TTE data usually binned at 8 ms in case of short GRBs and enhance the binning up to 64 ms in case of long GRBs. GBM NaI and BGO detectors are checked for orientation to the trigger ($< 60^{\circ}$) and blockages from the spacecraft. We then select the three most illuminated NaI detectors and one or both BGO detectors (see columns 8 and 9 of Table II). The GBM energy ranges for the duration analysis are chosen after the careful check for the detector's energy dispersion presented in Section

TABLE II: Sample of 27 bright BGO and LLE GRBs

GRB Name	**GBM Trigger #**	**GBM Trigger Time (MET)**	θ **(Deg.)**	**GBM** T_{90}^{a} **(s)**	**BGO det.**	**NaI det.**	$\sigma_{\rm BGO}$ **0.5–1 Mev**	$\sigma_{\rm BGO}$ **5–10 MeV**	$\sigma_{\rm LLE}$ **<100 MeV**
080916C	080916009	243216766.614	52.0	63.0 ± 0.8	0	3+4+6	7.4	6.5	65.7
090227B	090227772	257452263.407	72.0	1.3 ± 1.0	0	2+1+0	106.6	11.7	39.9
090228	090228204	257489602.911	16.0	0.45 ± 0.14	0	0+3+1	62.0	0.0	0.0
090510	090510016	263607781.971	13.0	0.96 ± 0.14	1	6+7+9	28.5	21.5	105.0
090902B	090902462	273582310.313	51.0	19.33 ± 0.29	0+1	1+0+9	48.0	4.0	34.3
090926A	090926181	275631628.987	48.0	13.76 ± 0.29	1+0	7+6+3	21.1	6.8	50.3
100116A	100116897	285370262.242	29.0	102.5 ± 1.5	0	0+3+1	13.8	0.0	30.9
100724B	100724029	301624927.992	52.0	114.7 ± 3.2	0	1+0+2	14.3	5.6	82.8
100826A	100826957	304556304.898	71.0	85.0 ± 0.7	1	7+8+6	14.2	6.3	32.1
101014A	101014175	308722314.622	54.0	449.4 ± 1.4	1	7+6+8	35.5	5.4	14.6
101123A	101123952	312245496.973	86.0	103.9 ± 0.7	1	10+9+11	15.1	7.8	29.0
110328B	110328520	323008161.194	31.0	141.3 ± 29.8	1	9+6+0	5.6	0.0	28.9
110529A	110529034	328322924.872	30.0	0.51 ± 0.09	1	9+7+6	12.9	0.0	27.5
110721A	110721200	332916465.760	43.0	21.8 ± 0.6	1	9+6+7	30.6	18.6	135.9
110731A	110731465	333803371.954	6.0	7.5 ± 0.6	0+1	0+3	6.9	0.0	24.4
120817B	120817168	366868952.723	58.8	0.11 ± 0.05	1	7+6+8	14.2	4.0	0.0
130305A	130305486	384176354.369	41.4	25.6 ± 1.6	1	9+6+0	26.4	4.0	13.0
130310A	130310840	384638984.503	75.9	16.0 ± 2.6	1	10+9+11	45.1	43.4	26.3
130427A	130427324	388741629.420	47.1	138.2 ± 3.2	1	9+10+0	472.8	23.1	40.3
130504B	130504314	389345526.386	61.3	0.38 ± 0.18	0	3+4	39.0	0.0	0.0
130504C	130504978	389402940.518	47.5	73.2 ± 2.1	1+0	9+0+1	25.9	6.3	31.0
130518A	130518580	390578080.525	40.9	48.6 ± 0.9	0+1	3+6+7	18.1	4.9	17.1
131014A	131014215	403420143.202	73.2	3.20 ± 0.09	1	9+10+11	148.9	11.5	31.9
131108A	131108862	405636118.759	24.1	18.5 ± 0.4	1+0	6+3+7	13.1	0.0	61.0
140206B	140206275	413361375.843	46.3	116.7 ± 4.2	0	1+0+3	15.7	5.0	58.4
140306A	140306146	415769387.951	54.7	67.3 ± 2.6	0	3+4+0	16.1	4.0	0.0
140523A	140523129	422507160.625	55.8	19.2 ± 0.4	0	3+4+5	26.3	0.0	4.0

(a) Calculated in the 50–300 keV energy band and reported by [2].

II A. The LLE energy range is split into two intervals, namely 10–100 Mev and 100 MeV–1 GeV. Errors on the various durations are computed following the prescriptions by [10]. Moreover, systematic errors were computed through an analysis of three random samples of bursts, weak, medium, and bright ones: in each energy band, we changed the various analysis parameters (i.e. burst background and light curve binning selections) and obtained errors of the order of 10–15% in NaI and 20–30% in BGO data. Finally, systematic errors were add to the statistical ones.

Figure 4 shows two example light curves from GRB 100116A and GRB 131014A. The trigger time is marked with a vertical dashed red line and the energy ranges are labeled in every panel. From the top: the first four panels represent NaI data (*dark red labels*), the subsequent two panels represent BGO data (*red labels*) while the last panel(s) represent LLE data (*orange labels*).

GRB 100116A (*left panel*) is a rather long GRB, with a two–episode emission, separated by an 80 s long quiescient period. The peak at trigger time disappears at higher energies. GRB 131014A (*right panel*) is much shorter than GRB 100116A and a delayed start of the high–energy emission is evident. This feature is quite common in LAT-detected bursts (see [5]).

IV. DURATION–ENERGY RELATION

The burst duration (T_{90}) is calculated by means of IDL–based routines and is defined as 90% of the accumulation time in count space in each energy band. We also calculate T_{05}, which we define as the beginning of T_{90} at 5% of counts. Burst durations and T_{05} values are computed in each energy band previously defined in Table I.

Results for GRB 100116A and GRB 131010A are plotted in Figure 2. The *top panels* show the Energy–Duration relation, while the *bottom panels* show the

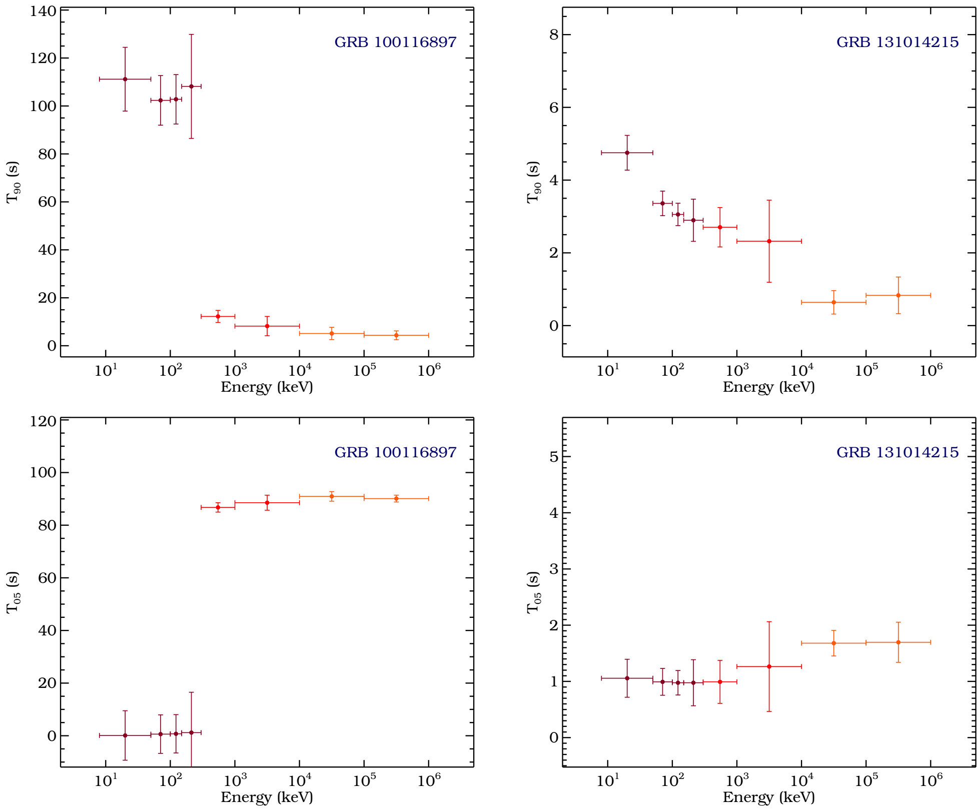

FIG. 5: Duration–Energy relation (*top panels*) and T_{05}–energy relation (*bottom panels*) calculated for GRB 100116A (*left*) and GRB 131010A (*right*). Different colors represent different data used for the analysis in each energy band as shown in the labels of Figure 3.

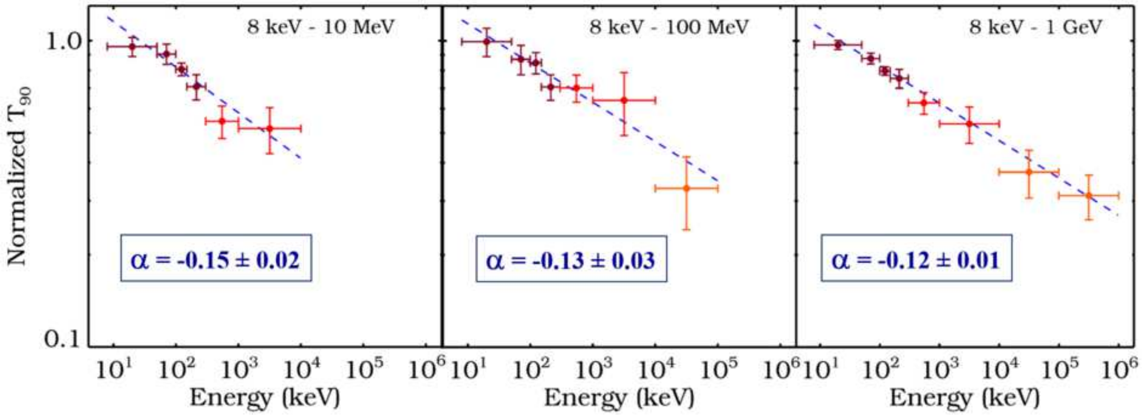

FIG. 6: Normalized Duration–Energy relation calculated for the 27 bright bursts of our subsample. Different colors represent different data used for the analysis in each energy band as shown in the labels of Figure 3.

T_{05}–Energy relation. We adopt different colors for the data points in order to represent the data from different detectors (*dark-red:* NaI, *medium-red*: BGO; *light-red*: LLE) which were used for the analysis in each energy band (as indicated in the labels of Figure 3). In the case of GRB 100116A, the duration drops from $T_{90} \sim 110$ s to just few seconds, while GRB 131014A's duration smoothly decreases from one energy band to the next. This effect is visible also in the T_{05} vs. Energy plots, where the delayed start of the higher–energy emission in GRB 131014A is clearly visible.

In order to compare and evaluate the whole subsample of 27 bursts, we normalize all T_{90} measurements and plot them as a function of energy in Figure 6. Again, different colors indicate different detectors used for the temporal analysis. Since not all bursts in the submsample are seen over all energy bands, we plot our results in three panels: 7 GRBs in our subsample are detected only up to 10 MeV, so no LLE duration could be computed (*left panel*). Other 7 GRBs are detected in LLE but only up to 100 MeV (*middle panel*), while 13 GRBs are detected all the way up to 1 GeV (*right panel*).

We fit the data with a simple power law (PL) model (*blue dashed lines*) in order to compare the slopes of the Duration–Energy relations to what is previously reported in the literature. Results for the PL slope α are reported in box in the middle of each panel. [8], using BATSE data from 25 to > 300 keV, and more recently [9], using GBM BGO data from 300 keV to 10 MeV, reported values of the PL slope α between -0.4 and -0.3. Such values are much steeper then what we find in this analysis. Particularly energetic GRBs showing prompt high–energy emission, i.e. > 10 MeV, have a much flatter behavior of the Duration–Energy relation. This possibly indicates that the prompt high–energy emission is closely related to the low–energy one.

V. OUTLOOK

Our future analysis steps include (a) The comparison of the PL slope α of the Duration–Energy relation deduced from the 27 bright GRBs subsample with the one deduced from the full sample of 311 bright BGO GRBs; The correlation of the Duration–Energy relation parameters with the burst spectral properties; and (c) The study of the temporal properties of pulses using temporally–resolved spectral analysis for the brightest peak of each GRB in the subsample; and (d) The study of the Duration–Energy relation at energies > 1 GeV, using the LAT standard analysis. This last step could help determining if the highest–energy emission is in fact afterglow emission shortly following the start of the prompt phase emission as seen at smaller frequencies.

---

[1] Meegan C., et al., "The Fermi Gamma-Ray Burst Monitor", ApJ 702, 791M, 2009

[2] von Kienlin A., et al., "The Second Fermi GBM Gamma-Ray Burst Catalog: The First Four Years", ApJS 211, 13V, 2014

[3] Atwood W. B., et al., "The Large Area Telescope on the Fermi Gamma-Ray Space Telescope Mission", ApJ 697, 1071A, 2009

[4] Pelassa V., et al., "The LAT Low-Energy technique for Fermi Gamma-Ray Bursts spectral analysis", Proceedings for the 2009 Fermi Symposium, eConf Proceedings C091122

[5] Ackermann M., et al., "The First Fermi-LAT Gamma-Ray Burst Catalog", ApJ 778, 82A, 2013

[6] Vianello G., Omodei, N., "The First 100 LAT Gamma-Ray Bursts: A New Detection Algorithm and Pass 8", These Proceedings, eConf C141020.1

[7] Atwood W. B., et al., "New Fermi-LAT Event Reconstruction Reveals More High-energy Gamma Rays from Gamma-Ray Bursts", ApJ 774, 76A, 2013

[8] Richardson G., "Intrinsic dependence of gamma-ray burst durations on energy", AIPC 384, 87R, 1996

[9] Bissaldi E., et al., "First-year Results of Broadband Spectroscopy of the Brightest Fermi-GBM Gamma-Ray Bursts", ApJ 733, 97B, 2011

[10] Koshut T., et al., "Systematic Effects on Duration Measurements of Gamma-Ray Bursts", ApJ 463, 570K, 1996

[11] *Fermi LAT GRB Table.*

[12] Gruber D., et al., "The Fermi GBM Gamma-Ray Burst Spectral Catalog: Four Years of Data", ApJS 211, 12G, 2014

[13] Arnaud, K. A., 1996, "XSPEC: The First Ten Years", ASPC 101, 99, 1996

Hints of the jet composition in gamma-ray bursts from dissipative photosphere models

P. Veres
The George Washington University, Department of Physics,
725 21st St, NW, Washington, DC 20052, USA
Center for Space Plasma and Aeronomic Research (CSPAR),
University of Alabama in Huntsville, Huntsville, AL 35899, USA

We present a model for gamma-ray bursts where a dissipative photosphere provides the usual spectral peak around MeV energies accompanied by a subdominant thermal component. We treat the initial acceleration of the jet in a general way, allowing for magnetic field- and baryon dominated outflows. In this model, the GeV emission associated with GRBs observed by Fermi LAT, arises as the interaction of photospheric radiation and the shocked electrons at the deceleration radius. Through recently discovered correlations between the thermal and nonthermal peaks within individual bursts, we are able to infer whether the jet was Poynting flux or baryon dominated.

I. INTRODUCTION

Gamma-ray bursts (GRBs) are one of the most extreme phenomena in the universe. They involve relativistic, jetted emission emanating either from a compact binary merger or form the core collapse of a massive star. The prompt MeV range emission component is usually followed by a longer lasting afterglow at lower energies but sometimes also in the GeV range.

The afterglow can be modeled by shocks propagating in the circumstellar material [6, 8]. It is possible to derive physical parameters of the late outflow and its surroundings (e.g. [7]).

The properties, such as the composition of the relativistic outflow, however, are difficult find. Dissipative photosphere models [1, 4] are among the best suited to describe the observed properties of GRB prompt emission. In these scenarios, energy is dissipated below the photosphere through some mechanism and released as the optical depth decreases below unity to produce the prompt MeV range radiation.

In Section 2, we will present the theoretical model for a particular dissipative photosphere scenario. In Section 3 we will apply this model to the observations of correlations between thermal and non-thermal components in bright bursts. Finally we present our conclusions regarding the inferences we can make for the GRB jet composition.

II. MODEL

We model the Lorentz factor of the initial outflow as $\Gamma \propto R^{\mu}$. If the energy density of the outflow is dominated by baryons, one expects $\mu \approx 1$ [5]. In case the magnetic fields dominate the energy budget, one can have an increase as slow as $\mu = 1/3$. We introduced the model in [10], then generalized for arbitrary values of μ in [9]. The acceleration stops at the saturation radius and the Lorentz factor becomes constant, then decelerates. The start of deceleration is roughly the start of the afterglow phase (see Figure 1).

The main point of such a generalized approach is that the jet can become optically thin while it is still accelerating. This will happen for μ close to 1/3. The $\mu \lesssim 1$ cases involve photospheres occurring in the coasting phase.

The photospheric radius, where the outflow becomes optically thin will be at:

$$\frac{r_{\rm ph}}{r_0} = \left(\frac{L\sigma_{\rm T}}{8\pi m_{\rm p} c^3 r_0}\right)\frac{1}{\eta\Gamma_{\rm ph}^2} \qquad (1)$$

which can be expressed more conveniently by:

$$\frac{r_{\rm ph}}{r_0} = \eta_{\rm T}^{1/\mu}\begin{cases} (\eta_{\rm T}/\eta)^{1/(1+2\mu)} & \text{if } \eta > \eta_{\rm T} \\ (\eta_{\rm T}/\eta)^3 & \text{if } \eta < \eta_{\rm T} \end{cases} . \qquad (2)$$

Here r_0 is the jet launching radius, L denotes luminosity, η is the coasting Lorentz factor and $\Gamma_{\rm ph}$ is the Lorentz factor at the photosphere. η_T is a critical Lorentz factor, which discriminates between the ”photosphere in the accelerating phase” and ”photosphere in the coasting phase” cases and can be calculated by equating the saturation radius to the radius of the photosphere:

$$\eta_T = \left(\frac{L\sigma_T}{8\pi m_p c^3 r_0}\right)^{\frac{\mu}{1+3\mu}} \approx \begin{cases} 120\ L_{53}^{1/6} r_{0,7}^{-1/6} & \text{if } \mu = 1/3 \\ 1300\ L_{53}^{1/4} r_{0,7}^{-1/4} & \text{if } \mu = 1 \end{cases} \qquad (3)$$

The main MeV peak will develop close to the photosphere. We model it as synchrotron radiation from weakly relativistic shocks (involving Lorentz factors $\Gamma_r \gtrsim 1$). A sub-dominant thermal component will accompany the synchrotron peak with characteristic temperature in the range of 1 keV-100 keV in accordance with observations.

The synchrotron peak will have the following dependence on the intrinsic physical parameters:

$$E_{\rm peak} \propto \begin{cases} L^{\frac{3\mu-1}{4\mu+2}}\ \eta^{-\frac{3\mu-1}{4\mu+2}}\ r_0^{\frac{-5\mu}{4\mu+2}}\ \Gamma_r^3 & \text{if } \eta > \eta_T \\ L^{-1/2}\ \eta^3\ \Gamma_r^3 & \text{if } \eta < \eta_T, \end{cases} \qquad (4)$$

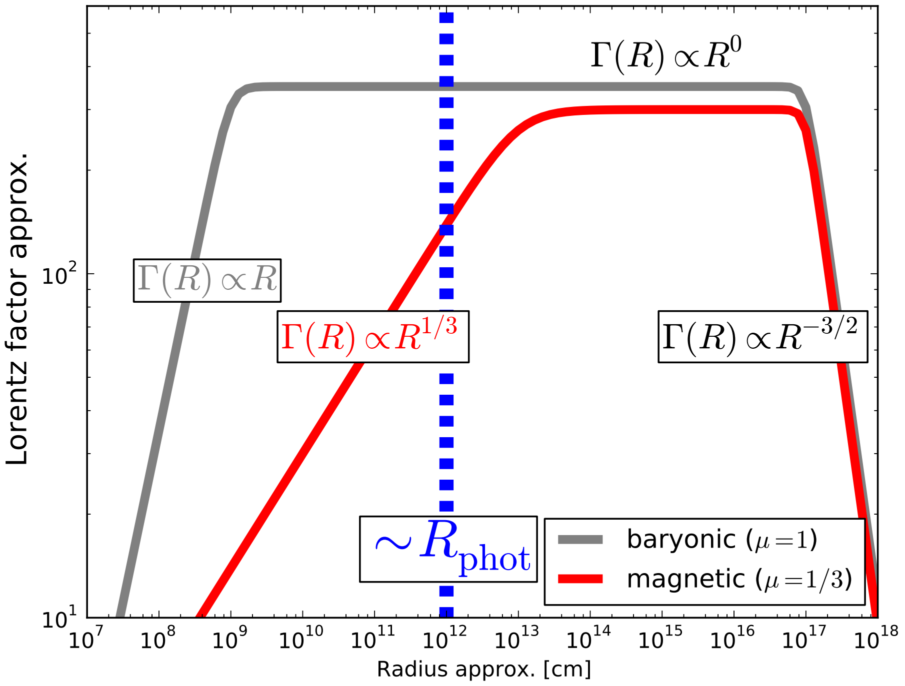

FIG. 1: Illustration of the Lorentz factor evolution with radius for two extremal μ values. Note that the photosphere occurs in the acceleration phase for $\mu = 1/3$ and in the coasting phase for $\mu = 1$.

while the thermal component will have the following dependence:

$$T_{\rm obs} \propto \begin{cases} L^{\frac{14\mu-5}{12(2\mu+1)}}\ \eta^{\frac{2-2\mu}{6\mu+3}}\ r_0^{-\frac{10\mu-1}{6(2\mu+1)}} & \text{if } \eta > \eta_T \\ L^{-5/12}\ \eta^{8/3}\ r_0^{1/6} & \text{if } \eta < \eta_T . \end{cases} \quad (5)$$

The above scenario is able to fit bright LAT detected bursts [9], but cannot discriminate between the magnetic and baryonic cases.

III. APPLICATION OF THE MODEL TO OBSERVATIONS

[2] developed a model that includes a synchrotron and a thermal component. This model can successfully fit the spectra of GRBs. By fitting this model to bright GRBs, [3] found a correlation between the peak energy of the synchrotron and the peak of the thermal component, $E_{\rm peak} \propto T^{\alpha}$. Every burst in the sample has characteristic α index (see Figure 2 and Table I).

Using the model described in the previous section, we can link the theoretically derived peak energy with the temperature of the thermal component (Equations 4 and 5). We can carry out this exercise either through the luminosity (L) or the coasting Lorentz factor(η)

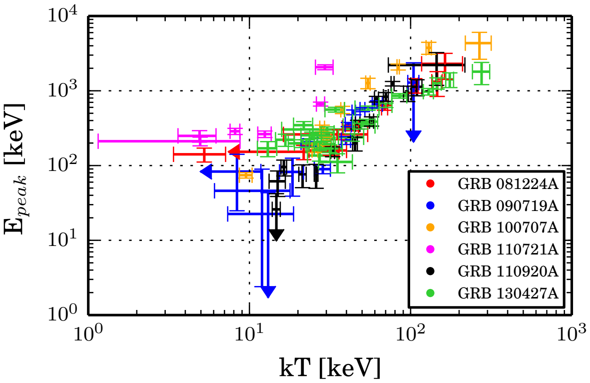

FIG. 2: The correlation between the synchrotron peak energy and the thermal peak for six bursts with time-resolved spectra (Figure from [3]).

and get similar expressions. For the "photosphere in the acceleration phase" we have:

$$E_{\rm peak} \propto T^{\frac{6(3\mu-1)}{14\mu-5}}, \quad (6)$$

while if the "photosphere is in the coasting phase", we have:

$$E_{\rm peak} \propto T^{1.2}. \quad (7)$$

TABLE I: Results for determining jet composition

GRB Name	α	Jet Type	μ
GRB 081224A	1.01 ± 0.14	baryonic	–
GRB 090719A	2.33 ± 0.27	magnetic	0.39 ± 0.01
GRB 100707A	1.77 ± 0.07	magnetic	0.42 ± 0.01
GRB 110721A	1.24 ± 0.11	baryonic	–
GRB 110920A	1.97 ± 0.11	magnetic	0.4 ± 0.01
GRB 130427A	1.02 ± 0.05	baryonic	–

Now, it is a simple task to identify the observed α indices with the indices in the above equations.

We compile the results in table I for our sample of six bursts. For bursts with higher values of α we derive a μ, which points towards a magnetic origin in the cases of GRBs 090719A, 100707A and 110920A respectively. In the remaining cases, the α index does not depend on μ. Nonetheless, the values of α for GRBs 081224A, 110721A and 130427A are very close to the theoretically derived 1.2. This points to the "photosphere in coasting phase" scenario, which in turn is easiest to realize in the baryon dominated case (because for reasonable parameters the critical Lorentz factor is $\eta_T \gtrsim 1000$).

IV. CONCLUSION

We presented a model where the initial acceleration of the gamma-ray burst outflow is written as a function of a parameter (μ). This parameter characterizes the composition of the outflow. By deriving a relation between the synchrotron peak energy and the temperature of the thermal component from the model, we were able to explain the observed relation between the two quantities and infer the composition of the gamma-ray burst outflow.

Half of the sample appears magnetically dominated while the other baryon dominated. Thus, there are no obvious trends among bright bursts regarding their composition.

Acknowledgments

The author thanks P. Mészáros, K. Dhuga, W. Briscoe, J. M. Burgess, B.-B. Zhang for their help and collaboration. This work was partially supported by the OTKA NN 111016 grant. The author further thanks the kind support of the Physics Department and the Astro Group at the George Washington University.

---

[1] Beloborodov, A. M. 2010, MNRAS, 407, 1033
[2] Burgess, J. M. et al. 2014, ApJ, 784, 17
[3] Burgess, J. M. et al. 2014, ApJ, 784, 43
[4] Giannios, D. 2012, MNRAS, 422, 3092
[5] Mészáros, P., Laguna, P., & Rees, M. J. 1993, ApJ, 415, 181
[6] Mészáros, P. & Rees, M. J., 1997, ApJ, 476, 232
[7] Panaitescu, A, & Kumar, P., ApJL, 560, 49
[8] Sari, R., Piran, T. & Narayan, R., 1998, ApJL, 497, 17
[9] Veres, P., Zhang, B. B., & Mészáros, P. 2013, ApJ, 764, 94
[10] Veres, P. and Mészáros, P. 2012, ApJ, 755, 12

Cosmic Gamma-ray Background Radiation

Yoshiyuki Inoue
JAXA International Top Young Fellow, Institute of Space and Astronautical Science JAXA, 3-1-1 Yoshinodai, Chuo-ku, Sagamihara, Kanagawa 252-5210, Japan[*]

The cosmic gamma-ray background radiation is one of the most fundamental observables in the gamma-ray band. Although the origin of the cosmic gamma-ray background radiation has been a mystery for a long time, the *Fermi* gamma-ray space telescope has recently measured it at 0.1–820 GeV and revealed that the cosmic GeV gamma-ray background is composed of blazars, radio galaxies, and star-forming galaxies. However, *Fermi* still leaves the following questions. Those are dark matter contribution, origins of the cosmic MeV gamma-ray background, and the connection to the IceCube TeV–PeV neutrino events. In this proceeding, I will review the current understandings of the cosmic gamma-ray background and discuss future prospects of cosmic gamma-ray background radiation studies. I also briefly review the current status of cosmic infrared/optical background radiation studies.

1. Introduction

The cosmic background radiation is one of the most fundamental observables from the sky. It is the result of integrated emission from its origins over the cosmic history. Figure. 1 shows the measured cosmic background radiation spectrum from microwave to gamma rays.

The origins of cosmic background radiation from microwave to X-ray are well understood. For example, the cosmic X-ray background (CXB) has been conclusively shown to be the integrated light produced via the accretion process of active galactic nuclei (AGNs), in particular Seyferts, hosting supermassive black holes [e.g. 1]. By contrast, the origin of the cosmic gamma-ray background (CGB)[1] has been an intriguing mystery for these forty years since its discovery by the *SAS*-2 satellite [2, 3]. Moreover, gamma-ray signatures from dark matter particles are expected to be buried in the CGB. The CGB has drawn a lot of attention from the community for a long time.

Before the *Fermi* gamma-ray space telescope (hereinafter *Fermi*) era, neither spectrum nor origins of the cosmic GeV gamma-ray background were not well understood. Although EGRET onboard the *CGRO* satellite reported the spectrum at 0.03–50 GeV [4, 5], an anomaly was known to exist at GeV energies, the so-called EGRET GeV anomaly [6]. Regarding the origins of the background, blazars were expected to explain it. However, due to small EGRET samples, it was predicted that blazars' contribution is at the level of 20-100% depending on models [see e.g. 7, and references therein]. More accurate determination of the CGB spectrum and more extragalactic source samples were required to understand the nature of the CGB. *Fermi* has recently reported a broadband CGB spectrum and the large *Fermi* source catalog has enabled us to unveil the origins of the CGB at the GeV gamma-ray band. At the same time, the current *Fermi* measurement still leaves the following unanswered problems. First, the signature of dark matter annihilation/decay has not yet observed in the CGB. Second, the origins of the cosmic MeV gamma-ray background are not understood at all. Lastly, the cosmic TeV gamma-ray background has not been explored yet. Especially understanding of its connection to the recent IceCube neutrino events will be an important key in this multi-messenger astronomy era.

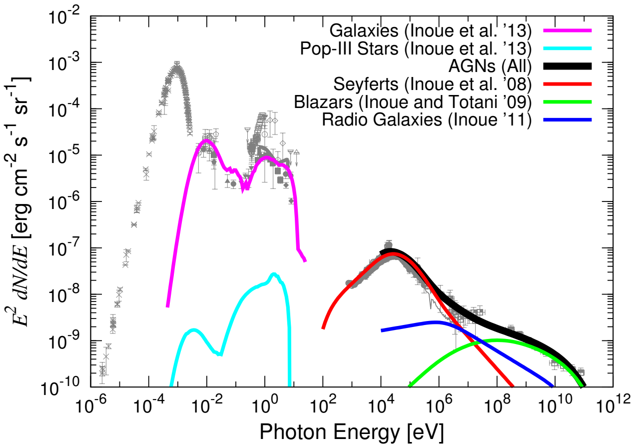

Figure 1: The cosmic background radiation spectrum from microwave to gamma-ray energies. Contribution from galaxies [8], Pop-III stars [8], Seyferts [9], blazars [7], radio galaxies [10], and all AGNs is shown by purple, cyan, red, green, blue, and black curve, respectively. The references for the measurements are in [8, 11].

In this paper, I review our current understandings of the cosmic GeV gamma-ray background radiation in §.2. Then, future prospects of the cosmic gamma-ray background studies will be discussed in §.3. I also briefly review the current status of cosmic infrared/optical background radiation studies in §.4.

---

[*] Electronic address: yinoue@astro.isas.jaxa.jp

[1] The cosmic gamma-ray background (CGB) is also called as the extragalactic gamma-ray background (EGRB or EGB) or the isotropic gamma-ray background (IGRB).

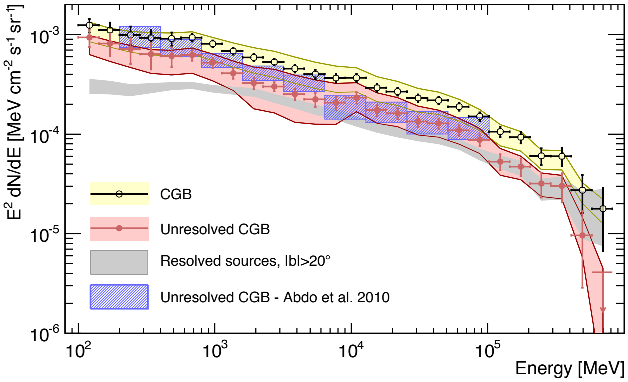

Figure 2: The CGB intensities measured by *Fermi*. The error bars include the statistical uncertainty and systematic uncertainties. The shaded bands indicate the systematic uncertainty arising from uncertainties in the Galactic foreground. The CGB intensity is the sum of the unresolved CGB and the resolved LAT sources (resolved CGB) at high Galactic latitudes, $|b| > 20$ deg. Taken from Ackermann et al. 2014 [12], but the legends in the plot are modified.

Summary is given in §.5.

2. Cosmic GeV Gamma-ray Background Radiation

2.1. Measurements

Fermi has recently allowed a broadband and accurate measurement of the CGB spectrum between 0.1–820 GeV [12], which is updated from the previous report [13]. The anomaly seen in the EGRET CGB spectrum disappeared. *Fermi* has resolved $\sim$ 30% of the cosmic GeV gamma-ray background to point sources at $\sim$ 1 GeV and resolved more at higher energies. This implies that current and future Cherenkov gamma-ray telescopes will be able to reveal a great portion of the CGB at $\gtrsim$ 100 GeV with their better sensitivities at these energies [14]. The resulting unresolved background spectrum is found to be compatible with a power law with a photon index of 2.32 that is exponentially cut off at 279 GeV. The total intensity of the unresolved CGB is 7.2×10^{-6} cm^{-2}s^{-1}sr^{-1} above 0.1 GeV. The measured cutoff signature may reflect gamma-ray attenuation by the cosmic infrared/optical background. However, further studies will be required to conclude it as the result of the gamma-ray attenuation, since it also depends on intrinsic spectra and evolution of source populations.

2.2. Compositions

Various gamma-ray emitting sources have been discussed as the origins of the cosmic GeV gamma-ray background in the literature. Those are blazars [e.g. 7, 15, 16], star-forming galaxies [e.g. 17, 18], radio galaxies [e.g. 10, 15, 17], gamma-ray bursts (GRBs) [e.g. 19], high Galactic-latitude pulsars [e.g. 20], intergalactic shocks [e.g. 21, 22], Seyferts [e.g. 9], cascade from ultra-high-energy cosmic rays [e.g. 23, 24], large galactic electron halo [25], cosmic-ray interaction in the solar system [26], and dark matter annihilation/decay [e.g. 27]. Among these possible candidates, *Fermi* has observed gamma rays from blazars, star-forming galaxies, radio galaxies, GRBs, and high-latitude pulsars [39]. These are guaranteed populations contributing to the CGB. Since gamma-ray bursts and high-latitude pulsars are known to make little contribution [19, 28], I focus on blazars, radio galaxies, and star-forming galaxies below.

2.2.1. Blazars

Blazars emit gamma rays via the inverse Compton scattering processes (e.g. [30, 31, 32, 33], but see also hadronic processes [34, 35]). Observationally, blazars are known to be divided into two population, flat spectrum radio quasars (FSRQs) and BL Lacs, and it has been suggested that the spectral energy distributions (SEDs) of blazars evolve with luminosity, as described by the so-called blazar sequence [36, 37]. They are dominant extragalactic gamma-ray sources [38, 39]. Therefore, it is naturally expected that blazars explain the cosmic GeV gamma-ray background [see e.g. 7]. However, its fraction was very uncertain in the EGRET era due to its small samples.

With the large sample of gamma-ray blazars, *Fermi* has enabled us to accurately evaluate the cosmological evolution of blazars. Ajello et al. (2012) [40] constructed the gamma-ray luminosity function (GLF) of FSRQs with the *Fermi* FSRQ samples. Regarding BL Lacs, redshifts of about half of BL Lacs are not determined, which makes difficult to construct GLFs of BL Lacs. Recently Ajello et al. (2014) [29] have successfully constructed the GLF of BL Lacs by using redshift constraints on individual BL Lacs. These studies confirmed that FSRQs and BL Lacs, i.e. blazars, show the luminosity-dependent density evolution like X-ray AGNs [1], which was suggested since the EGRET era [7, 41]. Base on these efforts, blazars are known to explain $\sim$50% of the CGB flux above 0.1 GeV [e.g. 51]. At higher energies ($\gtrsim$ 100 GeV), blazars explain $\sim$100% of the cosmic gamma-ray background flux.

Interestingly, HBLs (low-luminosity BL Lacs) show strong negative cosmological evolution, while FSRQs and luminous BL Lacs (so-called LBLs and IBLs) show positive evolution like Seyferts and the cosmic star formation history [1, 42]. From other wavelength studies, BL Lacs were known to show no or negative

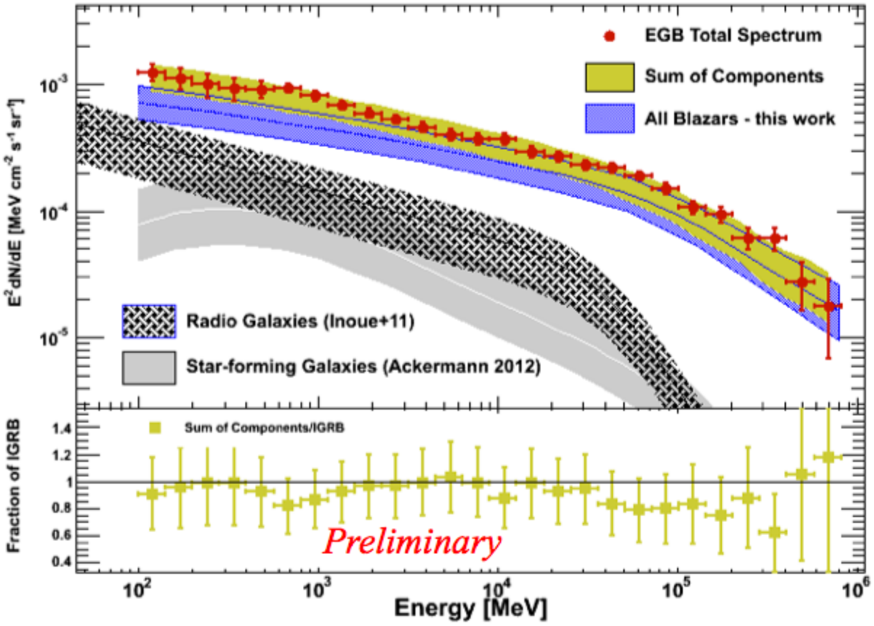

Figure 3: Top Panel: The cosmic gamma-ray background spectrum of blazars (bule [29]), radio-galaxies (black striped, [10]), star-forming galaxies, and summation of these three populations (yellow). The CGB measurement is shown by red points. Bottom Panel: the residual emission, computed as the ratio of the summed contribution to the CGB spectrum. Taken from Ajello et al. 2014 presented at the workshop "High Energy Messengers: Connecting the Non-Thermal Extragalactic Backgrounds" [51].

evolution (e.g. [43, 44] but see also [45] reporting positive evolution). Such negative evolution is different from the evolution of other AGN populations. The understanding of the physical cause of this negative evolution may be an important key to understand the AGN evolutionary history.

2.2.2. Radio Galaxies

Fermi has detected gamma rays from ∼10 misaligned AGNs (i.e., radio galaxies) [46]. Although they are fainter than blazars, radio galaxies in the entire sky are more numerous than blazars. It is naturally expected that they will make a significant contribution to the CGB. To study the contribution of gamma-ray-loud radio galaxies to the CGB, their GLF is required. However, it is not straightforward to construct it because of the limited *Fermi* radio galaxy samples. On the contrary, the radio luminosity function (RLF) of radio galaxies is well established [e.g. 47], since they are mainly detected in the radio band. Therefore, by using the correlation between radio and gamma-ray luminosities of radio galaxies, we are able to convert the RLF to the GLF. Base on this method, radio galaxies are expected to explain ∼ 20 % of the CGB at > 0.1 GeV [10, 48].

2.2.3. Star-forming Galaxies

Fermi has also detected gamma rays from 7 star-forming galaxies [46]. Those gamma rays are produced interactions of cosmic rays with gas or interstellar radiation fields. Since there are numerous galaxies in the sky, they are also expected to contribute to the CGB. However, similar to radio galaxies, GLF of star-forming galaxies can not be constructed solely with the *Fermi* samples. Therefore, using the correlation between infrared and gamma-ray luminosities, both of which trace the star formation activity, the contribution of star-forming galaxies to the background can be estimated with the well-established infrared luminosity functions [e.g. 18, 49]. The expected contribution is 10–30% of the CGB at > 0.1 GeV [49].

Figure. 3 show the contribution of these three populations to the cosmic gamma-ray background spectrum. Summing blazars, radio galaxies, and star-forming galaxies, we can explain ∼ 90% of the CGB radiation at > 0.1 GeV. By considering the measurement and model uncertainties, *Fermi* has enabled us to unveil that the cosmic GeV gamma-ray background is composed of blazars, radio galaxies, and star-forming galaxies. However, I note that radio galaxies and star-forming galaxies still rely on the luminosity correlation due to the small samples. This situation is very similar to blazar studies in the early EGRET era [15, 16, 50]. Therefore, further data will be required to precisely evaluate the fraction of these two populations.

3. Prospects for future Cosmic Gamma-ray Background Radiation Studies

Fermi has unveiled the origins of the cosmic GeV gamma-ray background. However, there are still three unsolved questions. First, we do not see the signature of dark matter particles in the CGB spectrum, although they are expected to contribute to the CGB. How can we probe dark matters with future cosmic gamma-ray background studies? Second, although the cosmic X-ray and GeV gamma-ray backgrounds are well understood, the cosmic MeV background has not been fully explored yet due to the observational difficulties. What are the origins of the cosmic MeV gamma-ray background? Lastly, the cosmic TeV gamma-ray background has never been observed yet, although *Fermi* has revealed the CGB up to 820 GeV. Recently, IceCube detected a few tens of TeV–PeV neutrino events. Although their origins are still debated, those neutrino events should be associated with gamma rays at those energies. How are the cosmic gamma-ray background and the cosmic TeV–PeV neutrino background connected? I briefly summarize future prospects of these three issues.

3.1. *Anisotropy* of the Cosmic GeV Gamma-ray Background Radiation

Fermi has accurately measured the cosmic GeV gamma-ray background spectrum [12]. *Fermi* has also measured the anisotropy, i.e. the angular power spectrum, of the CGB at 1–50 GeV [52]. Ando & Komatsu (2006) [53] proposed that anisotropy in the CGB is a smoking-gun signature of annihilation of dark matter particles. Since dark matter traces the large-scale structure of the universe, the emission from dark matter is anisotropic and its spatial pattern is unique and predictable [e.g. 54]. The measured angular power spectrum was consistent with the constant value at all multipoles, which means the Poisson term, so-called the shot-noise, dominates the signals. By comparing the expected CGB angular power spectrum from dark matter annihilation with the measured power spectrum, upper limits on the annihilation crosse section are placed [55]. The current data exclude $< \sigma v > \gtrsim 10^{-25}$ cm^{3}s^{-1} for annihilation into bb^- at the dark matter mass of 10 GeV. Since the analysis was based on the first 22-month data, the limits can be improved further with current and future *Fermi* data.

Sirasaki et al. (2014) [56] have recently reported the first measurement of the cross correlation of weak gravitational lensing and the CGB emission (see Figure. 4). The cross correlation is also a powerful probe of signatures of dark matter annihilation [57], because both cosmic shear and gamma-ray emission originate directly from the same dark matter distribution in the Universe. Using the cosmic shear data from the CFHTLenS (154 deg^2), they exclude dark matter annihilation cross sections of $< \sigma v >= 10^{-24}$–10^{-25} cm^{3}s^{-1} for 100 GeV dark matter. There are several wider optical survey projects in near future such as the Subaru Hyper Suprime-Cam (HSC), the Dark Energy Survey, and the Large Synoptic Survey Telescope (LSST). HSC and LSST will cover 1400 deg^2 and 20000 deg^2, respectively. These future surveys will increase the sensitivity to probe the dark matter annihilation cross sections.

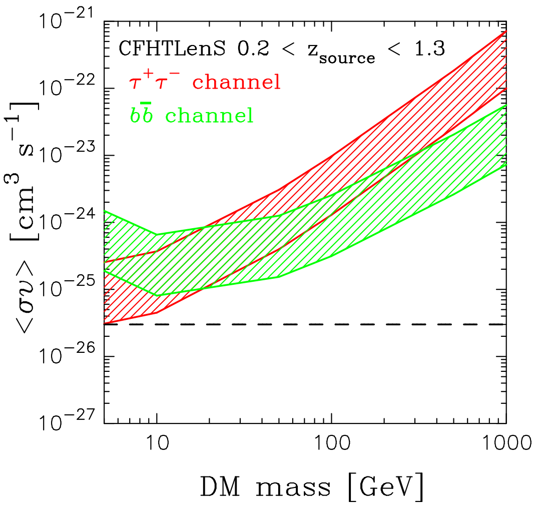

Figure 4: The 68 % confidence level upper limits on $\langle \sigma v \rangle$ as a function of DM mass using the cross correlation of cosmic shear and the CGB emission. The cosmic shear data from the CFHTLenS (154 deg^2) is used here. The red shaded region shows the upper bound for the $\tau^+\tau^-$ channel and the green region is for the $b\bar{b}$ channel. Note that the widths of the shaded regions indicate the model uncertainty. Taken from Shirasaki et al. 2014 [56].

The anisotropy is also useful to constrain the cosmological evolution of sources. Since the number density of blazars are smaller than radio galaxies and star-forming galaxies, blazars contribute to the anisotropy more significantly than the other two do. Therefore, the anisotropy measurement enabled us to put constraints on the blazar evolution models [58, 59, 60].

3.2. Cosmic *MeV* Gamma-ray Background Radiation

By contrast to the cosmic X-ray/GeV gamma-ray backgrounds, the origin of the cosmic MeV gamma-ray background at $\sim 1 - 10$ MeV is still an intriguing mystery. The background spectrum from several hundreds keV to several tens MeV is smoothly connected to the CXB spectrum and shows much softer than the GeV component [61, 62, 63], indicating a different origin from that above 100 MeV. The Seyfert spectra

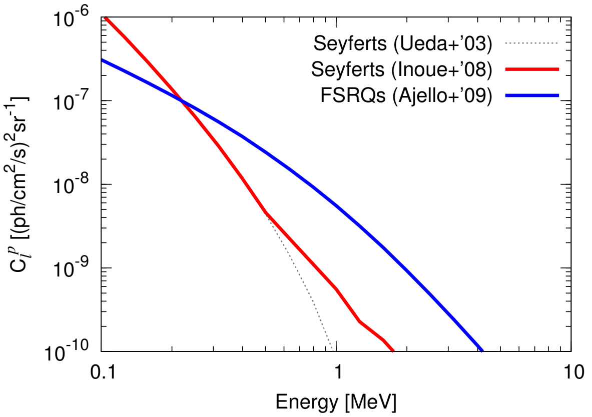

Figure 5: Expected Poisson term of the angular power spectrum of the cosmic MeV gamma-ray background at 200 keV– 10 MeV. Red and blue curve corresponds to Seyferts with non-thermal electrons in coronae [9] and FSRQs [68], respectively, assuming the MeV background is explained by them. For reference, we also plot the model of Seyferts with thermal cutoff [73] by dotted curve which does not explain the MeV background radiation. Taken from Inoue et al. 2013 [11]

adopted in population synthesis models of the CXB cannot explain this component because of the assumed exponential cutoff at a few hundred keV, where thermal hot corona above the accretion disk is assumed.

Several candidates have been proposed to explain the MeV background. One was the nuclear-decay gamma-rays from Type Ia supernovae [SNe Ia; 64]. However, recent measurements of the cosmic SN Ia rates show that the expected background flux is about an order of magnitude lower than observed [65, 66]. Seyferts can naturally explain the MeV background including the smooth connection to the CXB [9, 67]. Comptonized photons produced by non-thermal electrons in coronae surrounding accretion disks can produce the MeV power-law tail [9]. There is also a class of blazars, called MeV blazars which are FSRQs, whose spectra peak at MeV energies. These MeV blazars could potentially contribute to the MeV background as well [68]. Radio galaxies have been also discussed as the origin of the MeV background [17]. However, recent studies show that the expected background flux from radio galaxies is $\sim 10\%$ of the total MeV background flux [10, 69]. Annihilation of the dark matter particles has also been discussed [70, 71, 72], but those are less "natural" dark matter candidates, with a mass scale of MeV energies, rather than GeV-TeV dark matter candidates. In either cases, there is little observational evidence of MeV emission from these candidates and a quantitative estimate is not easy due to the sensitivity of the MeV measurements.

It is not easy to resolve the MeV sky as in the soft X-ray or the GeV gamma-ray bands. However, anisotropy in the background radiation will shed new light on this problem as in the GeV gamma-ray background [53]. Fig. 5 shows the Poisson term of the angular power spectra of Seyferts with non-thermal components in coronae [9] and FSRQs [68]. For reference, we also plot Seyferts with simple thermal cutoff spectra [73], but note that those do not explain the MeV background. Since the contribution of the correlation term is negligible in this energy region and the assumed flux limits, the angular power spectrum is dominated by the Poisson term. This Poisson term measurement is useful enough to distinguish the origin of the MeV background. The difference of the C_l^p of Seyferts [9] and FSRQs [68] is more than an order of magnitude. The reason why we can clearly distinguish the origin is as follows. Seyferts are fainter but more numerous than blazars. These two differences are able to make future MeV instruments such as the SGD on board *Astro-H* [74] clearly detect the origin of the MeV gamma-ray sky through the angular power spectrum of the sky.

If the origin of the MeV background is non-thermal emission from Seyfert [9], this implies that magnetic reconnection heats the corona above the disk and accelerate non-thermal electrons in the corona. As discussed in [9, 75], this scenario will be also tested by future X-ray and sub-mm observations of individual sources. If it is FSRQs [68], this implies that there are two distinct FSRQ populations in MeV and GeV because of the spectral difference between the MeV and GeV background. This will suggest that there are two different populations in FSRQs between MeV and GeV. This may pose a problem to the AGN unification scheme.

3.3. Cosmic *TeV* Gamma-ray Background Radiation

The cosmic TeV gamma-ray background has not been observed yet, although *Fermi* has measured the CGB up to 820 GeV. Here, very high energy (VHE; $\gtrsim$ 100GeV) gamma-rays propagating through the universe experience absorption by the interaction with the cosmic optical/infrared background (COB and CIB) via electron–positron pair production [e.g. 8]. Those generated electron–positron pairs scatter the cosmic microwave background (CMB) radiation via the inverse Compton scattering and generate secondary gamma-ray emission component (the so-called cascade emission) in addition to the absorbed primary emission [2]. At redshift z, the scattered photon energy $E_{\gamma,c}$ appears at lower energy than the in-

---

[2] The pairs may loose their energy through the plasma beam instabilities ([78, 79], but see also [80]).

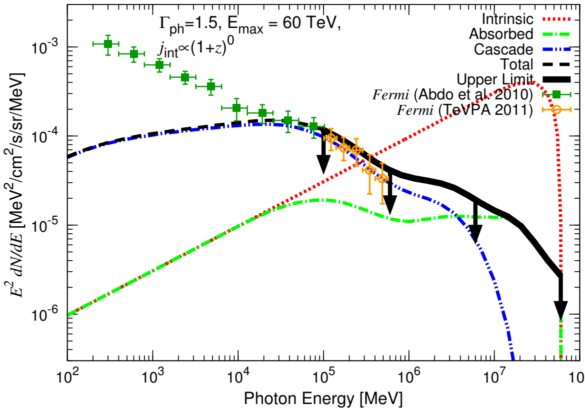

Figure 6: Upper limit on the CGB by requiring the cascade emission not to exceed the CGB data below 100 GeV in the model-independent way. We set the photon index $\Gamma = 1.5$ and the maximum energy $E_{\max} = 60$ TeV with no redshift evolution. Dotted, dot–dashed, double dot–dashed and dashed curves show the intrinsic spectrum (no absorption), absorbed, cascade, and total (absorbed+cascade) CGB spectrum, respectively. Thick solid curve with arrows show the upper limit. The filled square points show the observed CGB data with the 11-months *Fermi* data [13]. The circle points show the observed CGB data with the 24-months *Fermi* data [77]. Error bars represent 1-σ uncertainty of the data. Taken from Inoue & Ioka 2012 [76]

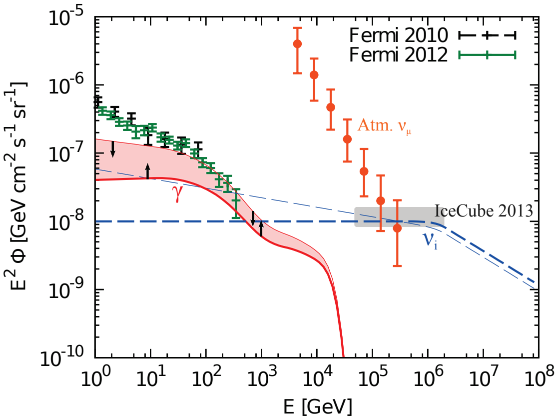

Figure 7: The allowed range in *pp* scenarios explaining the measured IceCube neutrino flux, which is indicated by the shaded area with arrows. The integrated neutrino background (dashed) and corresponding CGB (solid) are shown for $\Gamma = 2.0$ (thick) and $\Gamma = 2.14$ (thin). No redshift evolution is assumed here. The shaded rectangle indicates the IceCube data [83]. Taken from Murase et al. 2013 [84].

trinsic photon energy $E_{\gamma,i}$, typically $E_{\gamma,c} \approx 0.8\,(1+z)\,(E_{\gamma,i}/1\,\mathrm{TeV})^2$ GeV. This cascade component is also expected to contribute to the CGB [76, 81, 82]. Therefore, the current CGB measurement below 100 GeV sets an upper limit on the CGB itself at the TeV gamma-ray band. The limit is conservative for the electromagnetic cascade emission from the VHE CGB interacting with the cosmic microwave-to-optical background radiation *not* to exceed the current CGB measurement [76] (See Figure 6).

Measurements of the cosmic TeV gamma-ray background spectrum is also important from the multi-messenger point of view. The IceCube Collaboration has recently reported the detection of TeV–PeV neutrinos for the first time [83, 85]. This detection opens up a multi-messenger connection among photons, neutrinos, and cosmic rays. The origin of the IceCube neutrinos are still under debate [see 86, for reviews]. Conventionally, those high energy neutrinos are produced by cosmic rays via hadronuclear (*pp*) and/or photohadronic ($p\gamma$) interactions. In either cases, gamma rays must be produced. If the IceCube events originate in the extragalactic sky, the origins of these neutrino events are also responsible for the cosmic TeV gamma-ray background radiation. Importantly, the measured cosmic gamma-ray background flux around 0.7 TeV is $E_\gamma^2 dN_\gamma/dE_\gamma \sim 2\times10^{-8}$ GeV cm^{-2} s^{-1} sr^{-1}, while the measured neutrino background flux in the 100 TeV–PeV range is $E_\nu^2 dN_\nu/dE_\nu \sim 10^{-8}$ GeV cm^{-2} s^{-1} sr^{-1} per flavor [83, 85].

In $p\gamma$ scenarios, secondary spectra have a strong dependence on target photon field energy distribution [87, 88], while *pp* scenarios give power-law secondary spectra following the initial cosmic-ray spectrum. Therefore, the current *Fermi* and IceCube measurements put powerful constraints on *pp* scenarios [84]. The allowed range in *pp* scenarios explaining the neutrino events is shown in Figure. 7, taken from Murase, Ahlers, and Lacki (2013) [84], in which the gamma-ray attenuation by the CIB/COB is taken into account. The IceCube data indicate that these sources contribute at least 30–40% of the cosmic very high energy gamma-ray background and even ∼ 100% for softer spectra. As discussed above, blazars, which are not *pp* sources, are responsible for ∼ 100% of that background flux, which is inconsistent with the discussion here. Therefore, further studies in these fields including evolution and SED of blazars are required to ease this tension.

4. Cosmic Optical and Infrared Background Radiation

The determination of the cosmic optical and infrared background radiation, sometimes called the extragalactic background light (EBL), is important to the CGB science. The COB/CIB, the diffuse, isotropic background radiation from far-infrared (FIR) to ultraviolet (UV) wavelengths, is believed to be predominantly composed of the light from stars and dust integrated over the entire history of the universe [see 89, for reviews]. The observed spectrum of the local COB/CIB at $z = 0$ has two peaks of comparable energy density. The first peak in the optical to the near-infrared (NIR) is attributed to direct starlight, while the second peak in the FIR is attributed to emission from dust that absorbs and reprocesses the starlight [8, 90]. The energy density of the local COB/CIB has been constrained to be < 24 nW m^{-2} sr^{-1} at optical wavelengths, and < 5 nW m^{-2} sr^{-1} between 8 μm and 31 μm [104]. Combined with the lower limits from galaxy counts, the total EBL intensity at $z = 0$ from 0.1 μm to 1000 μm is inferred to lie in the range 52–99 nW m^{-2} sr^{-1} [105].

Integration over galaxy number counts provides a firm lower bound on the COB, and the observed trend of the counts with magnitude indicates that the COB at $z = 0$ has been largely resolved into discrete sources in the optical/NIR bands [see e.g. 91, 92]. However, the precise determination of the COB/CIB has been a difficult task. Direct measurements of the COB/CIB in the optical and NIR bands have been hampered by bright foreground emission caused by interplanetary dust, the so-called zodiacal light. An excess from galaxy counts in the NIR background has been reported by several experiments [see e.g. 93, 94]. Although this excess can be explained by redshifted light from first stars [93], reionization observations disfavor such scenario which leads overproduction of ionizing photons at high redshifts [95, 96]. Later it was also found that this excess would be inconsistent with TeV observations of nearby blazars (e.g. [97], but see also [98]). Recently, Matsuoka et al. (2011) [99] reported measurements of the COB at 0.44 μm and 0.65 μm from outside the zodiacal region using observational data from Pioneer 10/11, which are consistent with the galaxy counts.

The COB/CIB can also be probed indirectly through observations of high-energy gamma rays from extragalactic objects [e.g. 100, 101, 102]. Gamma rays propagating through the intergalactic space are attenuated by the pair production interactions with low-energy photons of the COB/CIB. For gamma-rays of given energy E_γ, the pair production cross section peaks for low-energy photons with energy $\epsilon_{\rm peak} \simeq 2m_e^2c^4/E_\gamma \simeq 0.5\,(1~{\rm TeV}/E_\gamma)$ eV, where m_e is the electron mass and c is the speed of light. In terms of wavelength, $\lambda_{\rm peak} \simeq 2.5(E_\gamma[{\rm TeV}])~\mu$m. Measuring the attenuation features in the spectra of extragalactic GeV-TeV sources offers a valuable probe of the COB/CIB that is indirect. Although this method can be limited by incomplete knowledge of the intrinsic spectra of the source before attenuation, by assuming a plausible range for such spectra, observations of blazars by current ground-based telescopes have been able to place relatively robust upper limits to the COB/CIB [e.g. 97]. This has been complemented by *Fermi* observations of blazars and GRBs that placed upper limits on the $\gamma\gamma$ opacity up to $z = 4.35$ [103]. Very recently, H.E.S.S. has successfully measured the imprint of the local COB/CIB in the spectra of bright blazars, assuming only that their intrinsic spectra have smooth shapes [106]. *Fermi* has also positively detected the redshift-dependent signature of the COB attenuation up to $z = 1.5$, utilizing the collective spectra of a large number of blazars [107]. However, recently it has also known that there is a class of extreme HBLs which shows very hard spectra at the TeV gamma-ray band [see e.g. 8]. As their emission mechanism is still under debate [98, 108], further careful analysis on the COB/CIB determination from gamma-ray observations would be required.

Interestingly, very recently the CIBER collaboration has reported an excess in the CIB fluctuation from galaxies' contribution at 1.1 and 1.6 μm [109], which has previously reported at 3–5 μm by *Spitzer* and *AKARI* [110, 111, 112]. This discovery may suggest a new population in the CIB other than galaxies. Further studies such as the CIB spectrum measurements will be important to unveil the origin of this excess.

5. Summary

Fermi has very recently allowed a broadband measurement of the cosmic GeV gamma-ray background spectrum between 0.1–820 GeV. *Fermi* has resolved ~30% of it to point sources at ~1 GeV and more fraction at higher energies. The unresolved background spectrum is compatible with a power law with a photon index of 2.32 that is exponentially cut off at 279 GeV. Moreover, theoretical works based on the *Fermi* measurements have unveiled the origin of the cosmic GeV gamma-ray background which has been a long standing problem in astrophysics. It is composed of blazars, radio galaxies, and star-forming galaxies. At > 100 GeV, blazars dominate the background flux. It should be noted that estimation of contributions of radio galaxies and star-forming galaxies relies on limited samples. This situation is similar to blazar studies in the early EGRET era. Moreover, SEDs at the TeV gamma-ray band of these three populations are not fully understood. Future observational data will give deeper understanding on the cosmic GeV gamma-ray background.

Although *Fermi* has unveiled the origins of the cosmic GeV gamma-ray background, there are still unsolved questions. Those can be categorized to the following three theme; dark matter contribution, the cosmic MeV gamma-ray background, and the cosmic TeV gamma-ray background. These problems can be probed as follows. First, anisotropy of the cosmic GeV gamma-ray background will be useful to constrain the dark matter properties. Furthermore, cross correlation between the cosmic shear and the gamma-ray sky will be also a powerful probe of signatures of dark matter annihilation. Especially, cross correlation studies with coming optical wide field surveys will put tight constraints on dark matter properties. Second, anisotropy will also the key to understanding the origin of the cosmic MeV gamma-ray background, since it reflects the source distribution in the sky. Lastly, the cosmic TeV gamma-ray background has been already constrained by itself at the GeV gamma-ray band because the secondary gamma rays can not overproduce the measured gamma-ray background flux. More interestingly, if extragalactic *pp* scenario is responsible for the recent IceCube neutrino events, they will contribute 30–100% of the cosmic gamma-ray background at $\gtrsim 100$ GeV, which is inconsistent with the expected blazars' contribution ($\sim$100%) at this energy band. Further detailed comparison between *Fermi* and IceCube would be important to understand the origin of the cosmic TeV gamma-ray and the TeV–PeV neutrino background.

Acknowledgments

The author acknowledges support by the Research Fellowship of the Japan Society for the Promotion of Science and the JAXA international top young fellowship. The author wish to thank JACoW for their guidance in preparing this template. This work supported by Department of Energy contract DE-AC03-76SF00515.

References

[1] Y. Ueda, M. Akiyama, G. Hasinger, T. Miyaji, and M. G. Watson, *ApJ* **786**, 104 (2014).
[2] C. E. Fichtel et al. *ApJL* , 217, L9 (1977)
[3] C. E. Fichtel, G. A. Simpson, & D. J. Thompson, *ApJ* , 222, 833 (1978).
[4] P. Sreekumar et al., *ApJ* **494**, 523 (1998).
[5] A. W. Strong, I. V. Moskalenko, and O. Reimer, *ApJ* **613**, 956 (2004).
[6] F. W. Stecker, S. D. Hunter, and D. A. Kniffen, Astroparticle Physics **29**, 25 (2008).
[7] Y. Inoue and T. Totani, *ApJ* **702**, 523 (2009).
[8] Y. Inoue, S. Inoue, M. A. R. Kobayashi, R. Makiya, Y. Niino, and T. Totani, *ApJ* **768**, 197 (2013).
[9] Y. Inoue, T. Totani, and Y. Ueda, *ApJL* **672**, L5 (2008), 0709.3877.
[10] Y. Inoue, *ApJ* **733**, 66 (2011), 1103.3946.
[11] Y. Inoue, K. Murase, G. M. Madejski, and Y. Uchiyama, *ApJ* **776**, 33 (2013).
[12] M. Ackermann et al., arXiv:1410.3696 (2014), 1410.3696.
[13] A. A. Abdo et al., Physical Review Letters **104**, 101101 (2010).
[14] S. Funk, J. A. Hinton, for the CTA Consortium, Astroparticle Physics **43**, 348 (2013).
[15] P. Padovani, G. Ghisellini, A. C. Fabian, and A. Celotti, *MNRAS* **260**, L21 (1993).
[16] F. W. Stecker, M. H. Salamon, and M. A. Malkan, *ApJL* **410**, L71 (1993).
[17] A. W. Strong, A. W. Wolfendale, and D. M. Worrall, *MNRAS* **175**, 23P (1976).
[18] V. Pavlidou and B. D. Fields, *ApJL* **575**, L5 (2002).
[19] S. Casanova, B. L. Dingus, and B. Zhang, *ApJ* **656**, 306 (2007).
[20] C.-A. Faucher-Giguère and A. Loeb, *JCAP* **1**, 005 (2010).
[21] A. Loeb and E. Waxman, *Nature* **405**, 156 (2000).
[22] T. Totani and T. Kitayama, *ApJ* **545**, 572 (2000).
[23] A. Dar and N. J. Shaviv, Physical Review Letters **75**, 3052 (1995).
[24] O. E. Kalashev, D. V. Semikoz, and G. Sigl, *PRD* **79**, 063005 (2009).
[25] U. Keshet, E. Waxman, and A. Loeb, *JCAP* **4**, 006 (2004).
[26] I. V. Moskalenko and T. A. Porter, *ApJL* **692**, L54 (2009).
[27] Bergström, L., Edsjö, J., & Ullio, P., *PRL* **87**, 251301 (2001).
[28] J. M. Siegal-Gaskins, R. Reesman, V. Pavlidou, S. Profumo, and T. P. Walker, *MNRAS* **415**, 1074 (2011).
[29] M. Ajello et al., *ApJ* **780**, 73 (2014).
[30] M. J. Rees, *MNRAS* **137**, 429 (1967).
[31] L. Maraschi, G. Ghisellini, and A. Celotti, *ApJL* **397**, L5 (1992).
[32] C. D. Dermer and R. Schlickeiser, *ApJ* **416**, 458 (1993).
[33] M. Sikora, M. C. Begelman, and M. J. Rees, *ApJ* **421**, 153 (1994).
[34] K. Mannheim and P. L. Biermann, *A&A* **221**, 211 (1989).
[35] A. Mücke, R. J. Protheroe, R. Engel, J. P. Rachen, and T. Stanev, Astroparticle Physics **18**, 593 (2003).
[36] G. Fossati, L. Maraschi, A. Celotti, A. Comastri, and G. Ghisellini, *MNRAS* **299**, 433 (1998).
[37] H. Kubo, T. Takahashi, G. Madejski, M. Tashiro, F. Makino, S. Inoue, and F. Takahara, *ApJ* **504**, 693 (1998).
[38] R. C. Hartman et al., *ApJS* **123**, 79 (1999).
[39] P. L. Nolan et al., *ApJS* **199**, 31 (2012).
[40] M. Ajello et al., *ApJ* **751**, 108 (2012).
[41] T. Narumoto and T. Totani, *ApJ* **643**, 81 (2006).

[42] A. M. Hopkins and J. F. Beacom, *ApJ* **651**, 142 (2006).
[43] P. Giommi, M. T. Menna, and P. Padovani, *MNRAS* **310**, 465 (1999).
[44] P. Padovani, P. Giommi, H. Landt, and E. S. Perlman, *ApJ* **662**, 182 (2007).
[45] M. J. M. Marchã and A. Caccianiga, *MNRAS* **430**, 2464 (2013).
[46] A. A. Abdo et al., *ApJ* **720**, 912 (2010).
[47] C. J. Willott, S. Rawlings, K. M. Blundell, M. Lacy, and S. A. Eales, *MNRAS* **322**, 536 (2001).
[48] M. Di Mauro, F. Calore, F. Donato, M. Ajello, and L. Latronico, *ApJ* **780**, 161 (2014), 1304.0908.
[49] M. Ackermann et al., *ApJ* **755**, 164 (2012).
[50] F. W. Stecker and M. H. Salamon, *ApJ* **464**, 600 (1996).
[51] M. Ajello et al., High Energy Messengers: Connecting the Non-Thermal Extragalactic Backgrounds (2014) `https://kicp-workshops.uchicago.edu/hem2014/`.
[52] M. Ackermann et al., *PRD* **85**, 083007 (2012).
[53] S. Ando and E. Komatsu, *PRD* **73**, 023521 (2006).
[54] S. Ando, E. Komatsu, T. Narumoto, and T. Totani, *PRD* **75**, 063519 (2007).
[55] S. Ando and E. Komatsu, *PRD* **87**, 123539 (2013).
[56] M. Shirasaki, S. Horiuchi, and N. Yoshida, *PRD* **90**, 063502 (2014).
[57] S. Camera, M. Fornasa, N. Fornengo, and M. Regis, *ApJL* **771**, L5 (2013).
[58] A. Cuoco, E. Komatsu, and J. M. Siegal-Gaskins, *PRD* **86**, 063004 (2012).
[59] J. P. Harding and K. N. Abazajian, *JCAP* **11**, 026 (2012).
[60] M. Di Mauro, A. Cuoco, F. Donato, and J. M. Siegal-Gaskins, ArXiv e-prints (2014), 1407.3275.
[61] Y. Fukada et al., *Nature* **254**, 398 (1975).
[62] K. Watanabe et al., in *Proceedings of the Fourth Compton Symposium*, edited by C. D. Dermer, M. S. Strickman, and J. D. Kurfess (1997), vol. 410 of *American Institute of Physics Conference Series*, pp. 1223–1227.
[63] G. Weidenspointner et al., in *American Institute of Physics Conference Series*, edited by M. L. McConnell and J. M. Ryan (2000), vol. 510 of *American Institute of Physics Conference Series*, pp. 467–470.
[64] D. D. Clayton and R. A. Ward, *ApJ* **198**, 241 (1975).
[65] K. Ahn, E. Komatsu, and P. Höflich, *PRD* **71**, 121301 (2005).
[66] S. Horiuchi and J. F. Beacom, *ApJ* **723**, 329 (2010).
[67] V. Schoenfelder, *Nature* **274**, 344 (1978).
[68] M. Ajello et al., *ApJ* **699**, 603 (2009).
[69] F. Massaro and M. Ajello, *ApJL* **729**, L12 (2011).
[70] K. A. Olive and J. Silk, Physical Review Letters **55**, 2362 (1985).
[71] K. Ahn and E. Komatsu, *PRD* **71**, 021303 (2005).
[72] K. Ahn and E. Komatsu, *PRD* **72**, 061301 (2005).
[73] Y. Ueda, M. Akiyama, K. Ohta, and T. Miyaji, *ApJ* **598**, 886 (2003).
[74] T. Takahashi et al., in *Society of Photo-Optical Instrumentation Engineers (SPIE) Conference Series* (2012), vol. 8443 of *Society of Photo-Optical Instrumentation Engineers (SPIE) Conference Series*, p. 1.
[75] Y. Inoue and A. Doi, *PASJ* (2014), 1411.2334.
[76] Y. Inoue and K. Ioka, *PRD* **86**, 023003 (2012).
[77] M. Ackermann et al., TeV Particle Astrophysics 2011 (2011) `http://agenda.albanova.se/conferenceDisplay.py?confId=2600`.
[78] P. Chang, A. E. Broderick, C. Pfrommer, E. Puchwein, A. Lamberts, and M. Shalaby, ArXiv e-prints (2014), 1410.3797.
[79] A. E. Broderick, P. Chang, and C. Pfrommer, *ApJ* **752**, 22 (2012).
[80] L. Sironi and D. Giannios, *ApJ* **787**, 49 (2014).
[81] P. S. Coppi and F. A. Aharonian, *ApJL* **487**, L9 (1997), astro-ph/9610176.
[82] K. Murase, J. F. Beacom, and H. Takami, *JCAP* **8**, 030 (2012).
[83] M. G. Aartsen et al., Physical Review Letters **111**, 021103 (2013).
[84] K. Murase, M. Ahlers, and B. C. Lacki, *PRD* **88**, 121301 (2013).
[85] M. G. Aartsen et al., Physical Review Letters **113**, 101101 (2014).
[86] K. Murase, ArXiv e-prints (2014), 1410.3680.
[87] K. Murase, Y. Inoue, and C. D. Dermer, *PRD* **90**, 023007 (2014).
[88] C. D. Dermer, K. Murase, and Y. Inoue, Journal of High Energy Astrophysics **3**, 29 (2014).
[89] E. Dwek and F. Krennrich, Astroparticle Physics **43**, 112 (2013).
[90] A. Domínguez et al., *MNRAS* **410**, 2556 (2011).
[91] P. Madau and L. Pozzetti, *MNRAS* **312**, L9 (2000).
[92] T. Totani, Y. Yoshii, F. Iwamuro, T. Maihara, and K. Motohara, *ApJL* **550**, L137 (2001).
[93] T. Matsumoto et al., *ApJ* **626**, 31 (2005).
[94] K. Tsumura, T. Matsumoto, S. Matsuura, I. Sakon, and T. Wada, *PASJ* **65**, 121 (2013).
[95] P. Madau and J. Silk, *MNRAS* **359**, L37 (2005).
[96] Y. Inoue, Y. T. Tanaka, G. M. Madejski, and A. Domínguez, *ApJL* **781**, L35 (2014), 1312.6462.
[97] F. Aharonian et al., *Nature* **440**, 1018 (2006).
[98] W. Essey and A. Kusenko, Astroparticle Physics

33, 81 (2010).

[99] Y. Matsuoka, N. Ienaka, K. Kawara, and S. Oyabu, *ApJ* **736**, 119 (2011).

[100] R. J. Gould and G. Schréder, Physical Review Letters **16**, 252 (1966).

[101] J. V. Jelley, Physical Review Letters **16**, 479 (1966).

[102] F. W. Stecker, O. C. de Jager, and M. H. Salamon, *ApJL* **390**, L49 (1992).

[103] A. A. Abdo et al., Science **323**, 1688 (2009).

[104] M. Meyer, M. Raue, D. Mazin, and D. Horns, *A&A* **542**, A59 (2012).

[105] S. Horiuchi, J. F. Beacom, and E. Dwek, *PRD* **79**, 083013 (2009).

[106] A. Abramowski et al., *A&A* **550**, A4 (2013).

[107] M. Ackermann et al., Science **338**, 1190 (2012).

[108] E. Lefa, F. M. Rieger, and F. Aharonian, *ApJ* **740**, 64 (2011).

[109] M. Zemcov et al., Science **346**, 732 (2014).

[110] A. Kashlinsky, R. G. Arendt, J. Mather, and S. H. Moseley, *Nature* **438**, 45 (2005).

[111] A. Cooray et al., *ApJL* **659**, L91 (2007).

[112] T. Matsumoto et al., *ApJ* **742**, 124 (2011).

Radiation from Particles Accelerated in Relativistic Jet Shocks and Shear-flows

K.-I. Nishikawa
Department of Physics, University of Alabama in Huntsville, ZP12, Huntsville, AL 35899, USA

P. Hardee
Department of Physics and Astronomy, The University of Alabama, Tuscaloosa, AL 35487, USA

I. Dutan
Institute of Space Science, Atomistilor 409, Bucharest-Magurele RO-077125, Romania

B. Zhang
Department of Physics, University of Nevada, Las Vegas, NV 89154, USA

A. Meli
Department of Physics and Astronomy, University of Gent, Proeftuinstraat 86 B-9000, Gent, Belgium

E. J. Choi, and K. Min
Korea Advanced Institute of Science and Technology, Daejeon 305-701, South Korea

J. Niemiec
Institute of Nuclear Physics PAN, ul. Radzikowskiego 152, 31-342 Kraków, Poland

Y. Mizuno
Institute for Theoretical Physics, University of Frankfurt am Main, 60438, Germany

M. Medvedev
Department of Physics and Astronomy, University of Kansas, KS 66045, USA

Å Nordlund, and J. T. Frederiksen
Niels Bohr Institute, University of Copenhagen,
Juliane Maries Vej 30, 2100 Copenhagen , Denmark

H. Sol
LUTH, Observatore de Paris-Meudon, 5 place Jules Jansen, F-92195 Meudon Cedex, France

M. Pohl
Institut fur Physik und Astronomie, Universitäat Potsdam, D-14476 Potsdam-Golm,
Germany; DESY, Platanenallee 6, D-15738 Zeuthen, Germany

D. Hartmann
Department of Physics and Astronomy, Clemson University, Clemson, SC 29634, USA

We have investigated particle acceleration and emission from shocks and shear flows associated with an unmagnetized relativistic jet plasma propagating into an unmagnetized ambient plasma. Strong electro-magnetic fields are generated in the jet shock via the filamentation (Weibel) instability. Shock field strength and structure depend on plasma composition (($e^{\pm}$ or e^{-}- p^{+} plasmas) and Lorentz factor. In the velocity shear between jet and ambient plasmas, strong AC ($e^{\pm}$ plasmas) or DC (e^{-}- p^{+} plasmas) magnetic fields are generated via the kinetic Kelvin-Helmholtz instability (kKHI), and the magnetic field structure also depends on the jet Lorentz factor. We have calculated, self-consistently, the radiation from electrons accelerated in shock generated magnetic fields. The spectra depend on the jet's initial Lorentz factor and temperature via the resulting particle acceleration and magnetic field generation. Our ongoing "Global" jet simulations containing shocks and velocity shears will provide us with the ability to calculate and model the complex time evolution and/or spectral structure observed from gamma-ray bursts, AGN jets, and supernova remnants.

I. INTRODUCTION

Blazars and Gamma-Ray Bursts (GRBs) are the most luminous phenomena in the universe. Despite extensive observational and theoretical programs, our understanding of the physics remains quite limited. There is broad consensus that both are powered by relativistic jets, which are directly imaged by interferometry in the case of blazars, and that the jets are launched and collimated mainly by magnetic forces e.g., [1–4]. However, there is uncertainty regarding details such as (1) magnetic versus kinetic domination, (2) rapid acceleration of particles to GeV and TeV energies, (3) location of highly variable gamma-ray emission and (4) source of seed photons if inverse Compton, (5) the scale of magnetic field turbulence in the radiation zone(s), and (6) the role of large and small scale instabilities in jet structure, dynamics, magnetization, particle energization and radiation.

For blazars, the observational data are now quite rich, with dense time sampling of flux at many frequencies from radio to GeV and TeV γ-ray, linear polarization at radio to optical, and images with subparsec linear resolution at mm wavelengths e.g., [5, 6]. For GRBs, the basic measurements of γ-ray and X-ray flux vs. time during the burst have been supplemented by observations of the afterglow at soft X-ray, optical, IR, and radio frequencies. What is missing is a comprehensive theoretical framework for interpreting this wealth of observational data. There are numerous studies that consider only radiative processes, instabilities, or particle acceleration (see [7]), and a smaller number that pair the first with one of the latter two e.g., [8]. While separating analyses into soluble parts is a valuable technique, in GRB and AGN jets the dynamics, instabilities, and energy gains and losses are coupled processes. Here we present recent progress in shock and velocity shear simulations using a relativistic particle-in-cell (**RPIC**) code.

II. SHOCK SIMULATIONS

.pdf

A. Particle Acceleration and Magnetic Field Generation

RPIC simulations have been used to study particle acceleration, magnetic field generation, and emission from collisionless shocks. Simulations reveal that the filamentation (**Weibel**) instability, which generates magnetically wrapped current filaments, dominates relativistic shock processes [9]. There are significant differences between electron-positron pair and electron-ion shocks as the ion filamentation instability enhances shock magnetic field generation and thermal energy density relative to pair plasmas e.g., [10–20].

Our 3-D MPI parallelized RPIC code has been used to simulate relativistic electron-ion jet propagation into an unmagnetized ambient electron-ion plasma ($m_i/m_e = 16$) with equal jet and ambient electron number density, and jet thermal velocity $v^{e}_{j,th} = 0.2c$ where c is the speed of light, and the jet Lorentz factor is $\gamma = 15$. The simulation used a system with dimension $(L_x, L_y, L_z) = (8192\Delta,\ 64\Delta, 64\Delta)$, where Δ is the cell size, and a total of ~ 1 billion particles (16 particles/cell/species for the ambient plasma) [21]. This computational domain is twelve times longer than in our previous simulations ([12, 18]).

Figure 1 shows the averaged (in the $y - z$ plane) ion density and electromagnetic field energy along the electron-ion jet at simulation time $t = 7372\omega_{pe}^{-1}$. The resulting profiles of jet (red), ambient (blue), and total (black) ion density are shown in Figure 1a. Warm jet ions are thermalized and ambient electrons are accelerated in the resulting leading (bow) and trailing (jet) shock system. Ambient ions are accelerated and pile up towards the jet front. The ambient plasma density increases behind the jet front, with additional increase to a higher plateau farther behind the jet front indicating the leading shock. The jet ion density remains approximately constant. The **strongest electromagnetic fields** are located at $x/\Delta = 4,500$ as shown in Figure 1b and are associated with the trailing shock. These strong fields may lead to the observed time dependent GRB afterglow emission. The longer simulation system has allowed significant nonlinear shock Weibel instability and associated particle acceleration development.

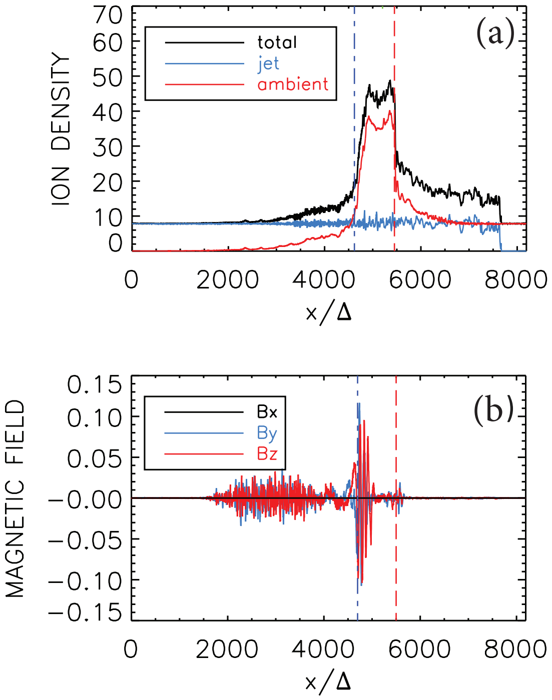

FIG. 1: Panel (a) shows the ion density (black: total, red: ambient, and blue: jet), and panel (b) shows the magnetic field components at the end of the simulation ($T = 7372/\omega_{pe}$). Electromagnetic field energy densities are normalized by the jet kinetic energy density, and quantities are averaged over the $yz-$plane.

B. Self-Consistent Synthetic Spectra

We have calculated the radiation spectra directly from our simulations by integrating the expression for the retarded power, derived from Liénard-Wiechert potentials, for a large number of representative particles in the PIC representation of the plasma [22–32].

The synthetic spectra shown in Figure 2a are obtained for emission from electrons in jets with **Lorentz factors** of $\gamma = 10$, 20, 50, 100, and 300. Spectra are obtained from an ensemble of electrons selected from the region where the Weibel instability, particle acceleration, and magnetic field generation are strongest. For each jet Lorentz factor we computed spectra for cold, $v_{\rm jet,th} = 0.01c$, (thin lower lines) and warm, $v_{\rm jet,th} = 0.1c$, (thick upper lines) jet electrons [34–37]. Here the spectra are calculated for radiation beamed along the jet axis. We note that radiation losses are not included [38, 39].

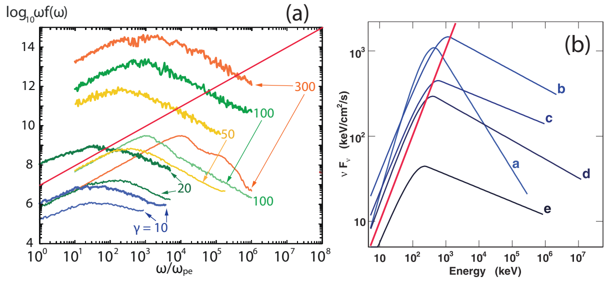

FIG. 2: Panel (a) shows synthetic spectra for jets with Lorentz factors of $\gamma = 10$, 20, 50, 100, and 300 and cold (thin lines) or warm (thick lines) jet electrons. Panel (b) shows modeled Fermi spectra in νF_ν units at early (a) to late (e) times [33]. Straight red lines indicate a slope of $\nu F_\nu = 1$.

Synthetic spectra are Bremsstrahlung-like at low frequencies ([23]) because the magnetic fields generated by the Weibel instability are weak and electron acceleration is modest. Synthetic spectra low frequency slopes are very similar to those of the spectra shown in Fig. 2b from [33]. Comparison between our synthetic spectra and the spectra from Abdo et al.[33] suggest that the spectral evolution observed from early to late times is mimicked by our synthetic spectra evolution from higher to lower jet Lorentz factor. However, further investigation is necessary and this is one of our future research efforts.

III. VELOCITY SHEAR SIMULATIONS

A. Slab Jet Velocity Shear

In this simulation study we used a core-sheath plasma jet structure instead of the counter-streaming plasma setups used in previous simulations by [40–46]. The basic setup and illustrative results are shown in Figure 3. In our setup, a jet core with velocity $v_{\rm core}$ in the positive x direction resides in the middle of the computational box (see Figure 3a). The upper and lower quarters of the box contain a sheath plasma that can be stationary or moving with velocity $v_{\rm sheath}$ [47–50]. This setup is similar to that in our RMHD simulations ([51]) that used a cylindrical jet core. Overall, this structure is similar in spirit, although not in scale to that proposed for AGN relativistic jet cores surrounded by a slower moving sheath, and is also relevant to GRB jets. However, here we represent the jet core and sheath as plasma slabs. Initially, the system is charge and current neutral.

The simulations were performed using a numerical grid with dimension $(L_{\rm x}, L_{\rm y}, L_{\rm z}) = (1005\Delta, 205\Delta, 205\Delta)$, where Δ is the cell size, and periodic boundary conditions in all directions. The jet and sheath (electron) plasma number density measured in the simulation frame is $n_{\rm jt} = n_{\rm am} = 8$. The electron skin depth, $\lambda_{\rm s} = c/\omega_{\rm pe} = 12.2\Delta$, where $\omega_{\rm pe} = (e^2 n_{\rm am}/\epsilon_0 m_{\rm e})^{1/2}$ is the electron plasma frequency and the electron Debye length for the ambient electrons $\lambda_{\rm D}$ is 1.2Δ. The jet-electron thermal velocity is $v_{\rm jt,th,e} = 0.014c$ in the jet reference frame, where c is the speed of light. The electron thermal velocity in the ambient plasma is $v_{\rm am,th,e} = 0.03c$, and ion thermal velocities are smaller by $(m_{\rm i}/m_{\rm e})^{1/2}$. Simulations were performed using an electron-positron ($e^{\pm}$) plasma or an electron-proton (e^-- p^+ with $m_{\rm p}/m_{\rm e} = 1836$) plasma for jet Lorentz factors of 1.5, 5.0, and 15.0 with the sheath plasma at rest ($v_{\rm sheath} = 0$) [49].

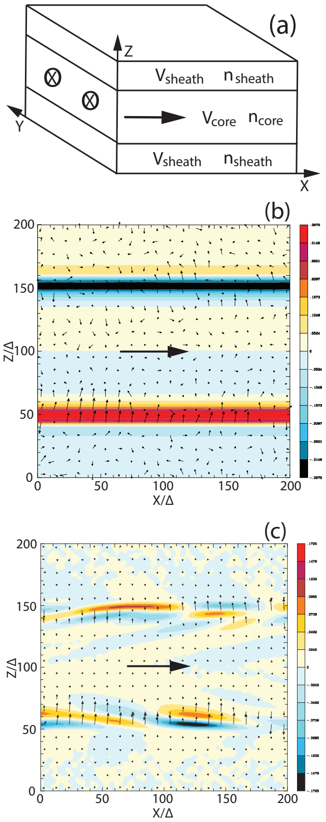

FIG. 3: Panel (a) shows our three-dimensional simulation setup. Panels (b) & (c) show the magnetic field component $B_{\rm y} > 0$ (red) and $B_{\rm y} < 0$ (blue) plotted in the $x - z$ plane (jet flow indicated by large arrows) at the center of the simulation box, $y = 100\Delta$ at $t = 300\,\omega_{\rm pe}^{-1}$, (b) for the e^-- p^+ case and (c) for the $e^{\pm}$ case, both with $\gamma_{\rm jt} = 15$. The smaller arrows indicate the magnetic field direction in the plane. Panels (b) & (c) cover one fifth of the simulation system length in the x direction.

The development of the velocity shear surfaces is shown in Figure 3b for e^-- p^+ and Figure 3c for $e^{\pm}$ plasmas with $v_{\rm core} = 0.9978c$ ($\gamma_{\rm jt} = 15$). For the e^-- p^+ case, a nearly DC magnetic field is generated at the shear-surfaces with negative (blue) $B_{\rm y}$ at $z = 150\Delta$ and positive (red) $B_{\rm y}$ at $z = 50\Delta$. Additionally, a

B_z (and B_x) magnetic field component, shown by the small arrows in Figure 3b, is generated at the shear surfaces by current filaments. On the other hand, for the $e^{\pm}$ case a relatively long wavelength ($\sim 100\Delta$) AC magnetic field is generated at the shear surfaces. Note the alternating $B_y > 0$ (red) and $B_y < 0$ (blue) along the flow direction. While our results are similar to those found by [45, 46], there are significant important structural differences because their simulations were two-dimensional and used a counter-streaming setup.

B. Cylindrical Jet Velocity Shear

Since relativistic jets and internal filamentary structures are more suitably modeled as intrinsically cylindrical, we have investigated velocity shear in cylindrical geometry for a pair ($e^{\pm}$) and an electron-proton (e^{-}- p^{+}) jet. Figure 4 shows isocontour images of the x component of the current along with magnetic field lines generated by the kKHI for $e^{\pm}$ and e^{-}- p^{+} jets. The isocontour images show that in the e^{-}- p^{+} jet case currents are generated in sheet like layers and the magnetic fields are wrapped around the jet. On the other hand, in the $e^{\pm}$ jet case many distinct current filaments are generated near the velocity shear and the individual current filaments are wrapped by the magnetic field. The clear difference in the magnetic field structure between these two cases may make it possible to distinguish different jet compositions via differences in circular and linear polarization.

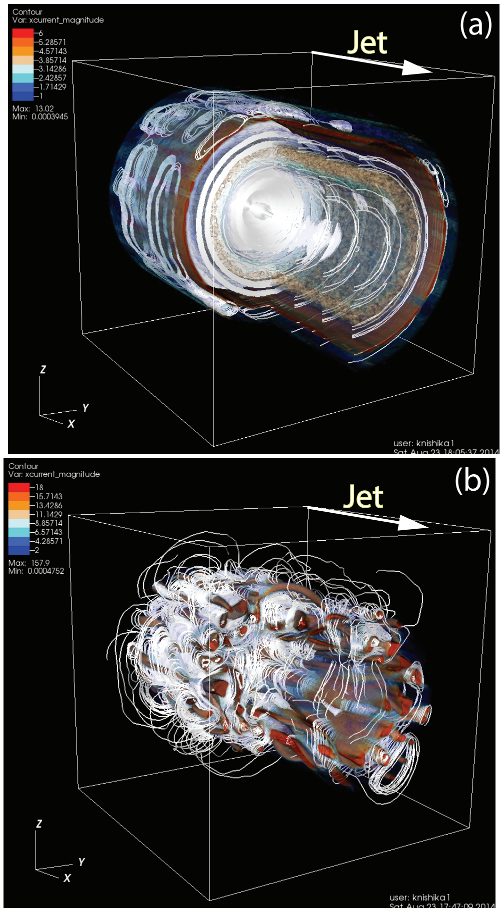

FIG. 4: Isocontour plots of the J_x magnitude with magnetic filed lines (one fifth of the jet size) for (a) an e^{-}- p^{+} and (b) an $e^{\pm}$ jet at simulation time $t = 300\Omega_{pe}^{-1}$. The 3D displays are clipped along the jet and perpendicular to the jet in order to view the interior.

IV. A COMBINED SHOCK AND VELOCITY SHEAR SIMULATION

We have begun "global" simulations involving injection of a cylindrical jet into an ambient plasma in order to investigate shock (Weibel instability) and velocity shear (kKHI) simultaneously. Previously these two processes have been investigated separately. In reality a jet or internal filament is injected into an ambient plasma resulting in velocity shear and shocks in a potentially complicated shock/shear system.

In order to begin investigation of the combined processes we have performed a simulation where a relativistic cylincrical jet is injected into an ambient plasma. We used a small system size of $(L_x, L_y, L_z) = (1005\Delta, 131\Delta, 131\Delta)$ with jet radius $r_j = 20\Delta$ and Lorentz factor $\gamma_{jt} = 5$ to examine the fundamental differences between $e^{\pm}$ and e^{-}- p^{+} jet cases and to test synthetic spectra computations. Previous synthetic spectra computations can be found in [28, 35–37, 47, 48].

A. 2D Density, Current and Magnetic Field Structure

Figure 5 shows 2D mid-plane slices of the electron density and the transverse magnetic field. Current filaments at the jet front are excited by fast current-driven instability in the shock precursor [52, 53].

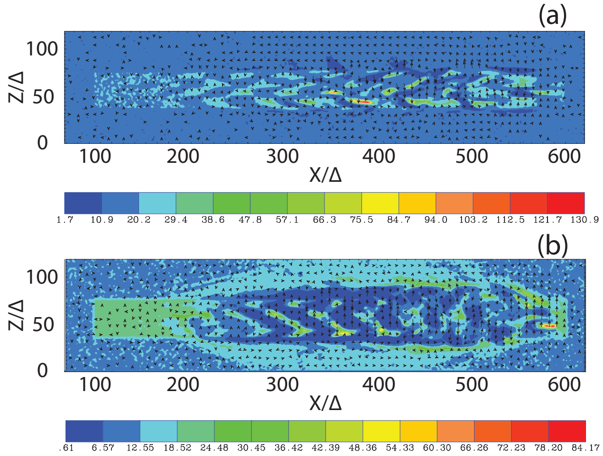

FIG. 5: Mid-plane slices of the electron density for jet Lorentz factor $\gamma_{jt} = 5$ at simulation time $t = 500\,\omega_{pe}^{-1}$. The jet is injected at $x/\Delta = 100$, propagates to the right, and the jet front is located at $x/\Delta = 600$. The upper panel (a) shows the electron density structure for the mass ratio $m_i/m_e = 1836$, and the lower panel (b) for the electron-positron case. Associated current structures are shown in Figure 6.

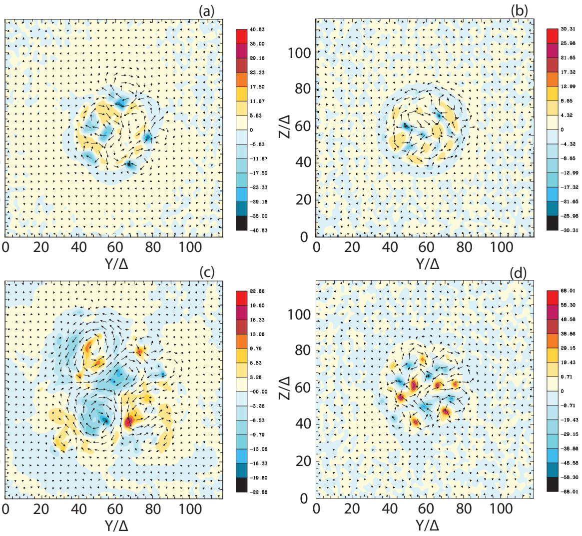

FIG. 6: Slices at $x/\Delta = 480$ (left column) and at $x/\Delta = 580$ (right column) at simulation time $t = 500\,\omega_{\rm pe}^{-1}$ showing currents and magnetic fields for ((a) and (b)) mass ratio $m_{\rm i}/m_{\rm e} = 1836$ and for ((c) and (d)) the electron-positron case. Jets come out of the page at plane center.

Comparing the electron-proton and electron-positron cases reveals significant electron density structure differences. Jet electrons and protons remain within the jet in the electron-proton case, but are found outside the jet in the electron-positron case due to mixing with ambient electrons and positrons as the positrons have more mobility than heavy protons.

Our previous simulations of the Weibel instability (e.g., [14]), showed current filaments associated with the growing instability and Figure 6 shows the structure of current filaments in cross sections of the jet at two locations. For the electron-proton case the current filaments lie within the jet and a negative current is dominant outside the jet (as in a previous simulation shown in Fig. 7a and 7b in Nishikawa et al.[49]. However, for the electron-positron case, current filaments are found both inside and outside the jet. In particular, large current filaments can be seen at $x/\Delta = 480$ outside the jet, similar to what was observed in the slab model (Nishikawa et al.[47–50]).

B. 3D Current and Magnetic Field Structure

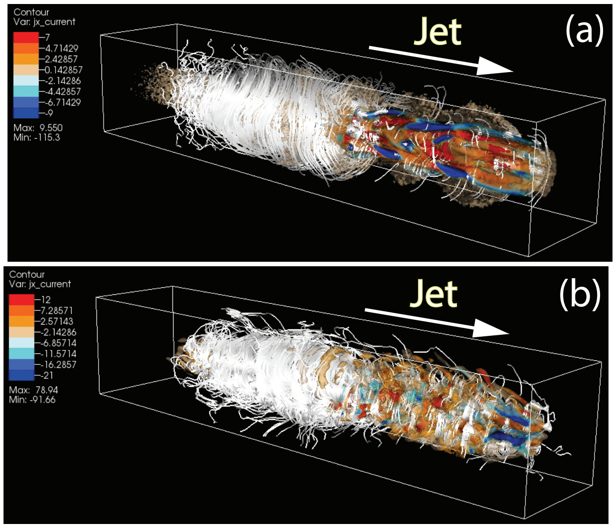

FIG. 7: Global jet simulations for e^-- p^+ and $e^\pm$ jets at time $t = 500\Omega_{\rm pe}^{-1}$. Panel (a) shows the e^-- p^+ jet where long and continuous current filaments are confined within the jet. Panel (b) shows the $e^\pm$ jet where short current filaments are found within and outside the jet.

Figure 7 shows 3D current filament isosurfaces along with magnetic field lines that are generated by the Weibel instability and by the kKHI. Only the front part of the jet is displayed ($120 < x/\Delta < 520$) and the jet is propagating from back left to forward right. The cube is clipped at $x/\Delta = 320$ and $y/\Delta = 66$ in order to view cross sections parallel and perpendicular to the jet axis. For both cases, compact current filaments are confined mostly within the jet at the jet front (see also Figure 6b and 6d). The magnetic fields wrap around the current filaments. Since the simulation system is small, current structures are at an early stage of development, and a fully developed shock system is not yet formed at the jet front. In the e^-- p^+ case long and continuous current filaments remain confined within the jet along the velocity shear surface behind the jet front(Fig. 7a). For the $e^\pm$ case short current filaments are found within and outside the jet along the velocity shear surface behind the jet front (Fig. 7b). This presence of current filaments inside and outside the jet in the $e^\pm$ case is also observed in slab geometry (see Fig. 3a and Nishikawa et al.[49]), where current filaments were found farther outside the jet at smaller jet Lorentz factors.

Small system simulations cannot fully distinguish between current filaments generated by the Weibel instability and those generated by the kKHI, and velocity shear effects are insufficiently resolved. Larger simulations need to be performed to clearly reveal the differences between the two cases, e.g., Nishikawa et al.[14] and Choi et al.[21], and allow proper evaluation of emission from the jet boundary.

V. FUTURE WORK: HELICAL MAGNETIC FIELDS AND RECONNECTION

Our preliminary 3D global structure simulations indicate the importance of using global simulations to investigate the combined evolution of collisionless shocks and velocity shears. In order to resolve collisionless shock and velocity shear structures we will perfume global jet simulations using much larger systems with $(L_{\rm x}, L_{\rm y}, L_{\rm z}) = (8005\Delta, 405\Delta, 405\Delta)$. Additionally, a very large system is needed in order to scale kinetic processes to larger scale jet structures. A larger system will allow us to obtain a much more reasonable picture of the evolution of the magnetic field and subsequently the dependence of spectra and polarization on jet composition through synthetic emission computations.

Recently, Markidis et al.[54] performed three-dimensional PIC simulations of a flux rope instability using a single flux rope with a simple screwpinch configuration [55], i.e., the helical magnetic field has a constant pitch (e.g., [56]). An artificial ion to electron mass ratio equal to 25 was chosen to reduce the simulation execution time, and the initial current was carried by the electrons (ions were initially stationary). The simulation revealed magnetic reconnection during the kink instability of the flux rope. Secondary signatures of magnetic reconnection included a quadrupolar structure in the density, a bipolar structure in the Hall field, and a reconnection associated electric field in proximity to the reconnection region.

In our future work we will inject jets like those shown in Figure 7 but containing a helical magnetic field like that implemented in Markidis et al. [54] and using a setup like that used in Wieland et al. [57]. This setup avoids transient phenomena due to an infinitely sharp contact discontinuity at the colliding front and avoids an artificial magnetic field pileup. In our setup we will generate a helical magnetic field via faster jet ions (protons or positrons) instead of electrons. This configuration will allow investigation of (1) the effect of helical magnetic field on growth of the Weibel instability and the kKHI, (2) the possible development of MHD-like kink and/or global KHI, and (3) the development of magnetic reconnection.

VI. CONCLUSIONS

We have presented 3D PIC simulations of collisionless shock and velocity shear development mediated by the Weibel instability and the kKHI for both electron-positron and electron-ion plasmas. The processes studied here are important in AGN and GRB jets that are expected to have shocks and velocity shears between faster and slower moving plasmas both within the jet and at the jet external medium interface.

We have shown via shock simulations that shock structure depends on the composition of the plasma, e.g., Choi et al.[21] and Nishikawa et al.[14]. The collisionless electron-ion ($m_{\rm i}/m_{\rm e} = 16$) shock shows a sharper rise in the electron density at the forward shock than the electron-positron case (see Fig.1a and compare to Fig. 1a in Nishikawa et al.[14]). This sharper rise occurs because in the electron-positron case jet electrons propagate through the forward shock to the jet front but in the electron-ion case the jet electron density declines in front of the forward shock. This decline in the electron-ion case is due to the ambipolar electric fields created at the jet front by the heavier ions.

We have shown via velocity shear simulations that velocity shear structure depends on the composition of the plasma and the jet Lorentz factor, e.g., Nishikawa et al.[48–50]. The growth rate for the kKHI for the mildly relativistic jet case ($\gamma_{\rm j} = 1.5$) is larger than the relativistic jet case ($\gamma_{\rm j} = 15$). In particular, the different magnetic field velocity shear structure associated with electron-positron composition versus electron-proton composition should have consequences for the polarization of jets in very high-resolution radio imaging. For a simple cylindrical geometry velocity shear case an electron-proton jet primarily builds magnetic field in the toroidal direction at the velocity shear surface. In contrast, a pair-plasma jet generates sizable radial field components that are only about a factor of two weaker than the toroidal field. In either case, strong electric and magnetic fields in the velocity shear zone will also be conducive to particle acceleration.

When global jet injection simulations are performed the combination of shock and velocity shear structures makes the situation more complicated but our preliminary simulations show clear differences between electron-positron and electron-proton plasmas. Our preliminary simulations are too short for definitive statements on the efficacy of the process and the resulting spectra. However, it is clear that the magnetic field structure along with particle acceleration and transport in compact regions will be necessary for a realistic assessment and interpretation of observed emission spectra and polarization.

Acknowledgments

K.-I. Nishikawa and/or P. Hardee have been supported by NSF awards AST-0908010 and AST-0908040, and by NASA awards NNG05GK73G, NNX07AJ88G, NNX08AG83G, NNX08AL39G, NNX09AD16G, NNX12AH06G, NNX13A P-21G, and NNX13AP14G. J. Niemiec has been supported by the Polish National Science Centre via awards DEC-2011/01/B/ST9/03183 and DEC-2012/04/A/ST9/00083. Y. Mizuno has been supported by the Ministry of Science and Technology of Taiwan via awards NSC 100-2112-M-007-022-MY3 and MOST 103-2112-M-007-023-MY3. M. Pohl is supported via award PO 1508/1-2 from the Deutsche Forschungsgemeinschaft. Simulations were performed on Columbia and Pleiades at the NASA Advanced Supercomputing (NAS), Kraken and Nautilus at The National Institute for Computational Sciences (NICS), and Stampede at The Texas Advanced Computing Center. This research was begun during the program "Chirps, Mergers and Explosions: The Final Moments of Coalescing Compact Binaries" at the Kavli Institute for Theoretical Physics, which is supported by the NSF via grant PHY05-51164. Initial kKHI work began at the Aspen Center for Physics workshop "Astrophysical Mechanisms of Particle Acceleration and Escape from the Accelerators" (September 1-15, 2013).

---

[1] Vlahakis, N. & Knigl, A., ApJ, 596, 1080, 2003

[2] McKinney, J. C., MNRAS, 368, 1561, 2006

[3] Komissarov, S. S., Barkov, M. V., Vlahakis, N., Königl, A., MNRAS, 380, 51, 2007

[4] Tchekhovskoy, A., McKinney, J.C., & Narayan, R., MNRAS, 388, 551, 2008

[5] Krawcznski, H., ApJ, 659, 1063, 2007

[6] Narayan, R., & Piran, T., MNRAS, 420, 604, 2012

[7] Hardee, P., Fermi meets Jansky – AGN in Radio and Gamma-Rays Savolainen, T., Ros, E., Porcas, R.W., & Zensus, J.A. (eds.) June 21-23, 2010, Bonn, Germany arXiv:1007.0426, 2010

[8] Dexter, J., McKinney, J. C., & Agol, E., MNRAS, 421, 1517, 2012

[9] Dieckmann, M. E., Frederiksen, J. T., Bret, A., & Shukla, P.K., Phys. Plasmas, 13, 112110, 2006

[10] Nishikawa, K.-I., Hardee, P., Richardson, G., Preece, R., Sol, H., & Fishman, G.J., ApJ, 595, 555, 2003

[11] Nishikawa, K.-I., Hardee, P., Richardson, G., Preece, R., Sol, H., & Fishman, G.J., ApJ, 622, 927, 2005

[12] Nishikawa, K.-I., Hardee, P., Hededal, C. B., & Fishman, G.J., ApJ, 642, 1267, 2006

[13] Nishikawa, K.-I., Hededal, C.B., Hardee, P., Fishman, G.J., Kouveliotou, C., & Mizuno, Y., Ap&SS, 307, 319, 2007

[14] Nishikawa, K. -I., J. Niemiec, M. Medvedev, H. Sol, P. Hardee,Y. Mizuno, B. Zhang, M. Pohl, M. Oka, D. H. Hartmann, ApJ, 698, L10, 2009

[15] Frederiksen, J. T., Hededal, C. B., Haugbølle, T., & Nordlund, Å., held at NBIfAFG/NORDITA, Copenhagen, Denmark, August, 2002, 2003 (arXiv:astro-ph/0303360)

[16] Frederiksen, J. T., Hededal, C. B., Haugbølle, T., & Nordlund, Å., ApJ, 608, L13, 2004

[17] Hededal, C. B. and Nishikawa, K.-I., ApJ, 623, L89, 2005

[18] Ramirez-Ruiz, E., Nishikawa, K.-I., & Hededal, C. B., ApJ, 671, 1877, 2007

[19] Spitkovsky, A., in Proceeding of Astrophysical Sources of High Energy Particles and Radiation, eds. T. Bulik, B. Rudak, G. Madejski, AIP Conf. Proc., v. 801, p. 345, 2005

[20] Spitkovsky, A., ApJ, 673, L39, 2008

[21] Choi, E.J., Min, K., Nishkawa, K.-I., & Choi, C. R., PhPl, 21, 072905

[22] Jackson, J. D., *Classical Electrodynamics*, Interscience, 1999

[23] Hededal, C.B., Gamma-Ray Bursts, Collisionless Shocks and Synthetic Spectra, Ph.D. thesis, 2005 (arXiv:astro-ph/0506559)

[24] Nishikawa, K.-I., Medvedov, M., Zhang, B., Hardee, P., Niemiec, J., Nordlund, A., Frederiksen, J., Mizuno, Y., Sol, H., & Fishman, G.J., AIP Conference Proceedings, Vol.1113, pp.235-237, 2009

[25] Nishikawa, K.-I., Niemiec, J., Medvedev, M., Zhang, B., Hardee, P., Mizuno, Y., Nordlund, Å. Frederiksen, J., Sol, H., Pohl, M., Hartmann, D. H., Oka, M., & Fishman, J. F., Intern. J. of Mod. Phys. D, 19, 715, 2010

[26] Nishikawa, K.-I. Niemiec, J., Medvedev, M., Zhang, B., Hardee, P., Mizuno, Y., Nordlund, Å., Frederiksen, J., Sol, H., Pohl, M., Hartmann, D. H., & Fishman, J. F., Proceedings of Deciphering the Ancient Universe with Gamma-Ray Bursts, AIP Conference Proceedings, vol. 1279, pp. 261-264, 2010

[27] Nishikawa, K.-I. Niemiec, J., Medvedev, M., Zhang, B., Hardee, P., Mizuno, Y., Nordlund, A., Frederiksen, J., Sol, H., Pohl, M., Hartmann, D. H., Fishman, G. J., relativistic shocks and associated radiation from turbulent magnetic fields, in the proceeding of 5th International Conference on Numerical Modeling of Space Plasma Flows, June 13 - 18, 2010, San Diego, CA, ASP Conference Series, v. 429, pp. 127 - 135, 2010

[28] Nishikawa, K.-I., Niemiec, J., Medvedev, M., Zhang, B., Hardee, P., Nordlund, A., Frederiksen, J., Mizuno, Y., Sol, H., Pohl, M., Hartmann, D. H., Oka, M., & Fishman, G. J., Advances in Space Research, 47, pp. 1434 - 1440, 2011

[29] Martins, J.L., Martins, S.F., Fonseca R.A., & Silva, L.O., Proc. of SPIE, 7359, 73590V-1–8, 2009

[30] Sironi, L., & Spitkovsky, A., ApJ, 707, L92, 2009

[31] Frederiksen, J. T., Haugbølle, T., Medvedev, M. V., & Nordlund, Å., ApJ, 722 L114, 2010

[32] Medevedv, M. V., Frederiksen, J. T., Haugbølle, T., Medvedev, M. V., & Nordlund, Å., ApJ, 737:55(10pp), 2011

[33] Abdo, A. A., Ackermann, M., Ajello, M., Axelsson, M., Baldini, L., Ballet, J., Barbiellini, G., Bastieri, D., Baughman, B. M., and 167 coauthors, Science, 323 1688, 2009

[34] Nishikawa, K.-I., Niemiec, J., Medvedev, M., Zhang, B., Hardee, P., Nordlund, A., Frederiksen, J., Mizuno, Y., Sol, H., Pohl, M., Hartmann, D. H., Oka, M., & Fishman, G. J., Proceeding of Gamma Ray Bursts 2010 Conference, IAU Conference Proceeding Series, v. 1358, pp. 87 - 90, 2011b

[35] Nishikawa, K.-I., Niemiec, J., Medvedev, M., Zhang, B., Hardee, P., Nordlund, A., Frederiksen, J., Mizuno, Y., Sol, H., Pohl, M., Hartmann, D. H., Oka, M., & Fishman, G. J., Proceeding of High Energy Phenomena in Relativistic Outflows III Barcelona, June 27 - July 1, 2011 , I. J. Mod. Phys, Conf. Ser., 8, 259, 2012a

[36] Nishikawa, K.-I., Choi, E.-J., Min, K., Hardee, P., Mizuno, Y., Zhang, B., Niemiec, J., Medvedev, M., Nordlund, Å., Frederiksen, J., Sol, H., Pohl, M., Hartmann, D. H., & Fishman, J. F., in the proceeding of 6th International Conference on Numerical Modeling of Space Plasma Flows, June 13 - 17, 2011, Valencia, Spain, ASP Conference Series, v. 459, 143, 2012b

[37] Nishikawa, K.-I., Zhang, B., Choi, E.-J., Min, K., Hardee, P., Mizuno, Y., Niemiec, J., Medvedev, M., Nordlund, Å., Frederiksen, J., Sol, H., Pohl, M., Hartmann, D. H., & Fishman, J. F., IAU Symposium 279: Death of Massive Stars: Supernovae & Gamma-Ray Bursts, 371, 2012c

[38] Jaroschek, C. H., & Hoshino, M., PRL, 103, 075002, 2009

[39] Medvedev, M.V. & Spitkovsky, A., ApJ, 700, 956,

2009

[40] Alves, E. P. Magnetic field generation via the Kelvin-Helmholtz instability, Master thesis, Universidate Témica de Lisbon, 2010

[41] Alves, E. P., Grismayer, T., Martins, S. F., Fiúza, F., Fonseca, R. A., Silva, L. O., ApJL, 746, L14, 2012

[42] Alves, E. P., Grismayer, T., Fonseca, R. A., Silva, L. O., New Journal of Physics 16, 035007, 2014

[43] Grismayer, T., Alves, E. P., Fonseca, L. O. Silva, L. PRL, 111, 015005, 2013a

[44] Grismayer, T., Alves, E. P., Fonseca, L. O. Silva, L. PPCF, 55, 124031, 2013b

[45] Liang, E., Boettcher, M., & Smith, I, ApJL, 766, L19, 2013

[46] Liang, E., Boettcher, M., & Smith, I, ApJL, 779, L27, 2013

[47] Nishikawa, K.-I., Hardee, P., Mizuno, Y., Dutan, I., Zhang, B., Medvedev, M., Choi, E. J., Min, K. W., Niemiec, J., Nordlund, Å., Frederiksen, J. T., Sol, H., Pohl, M., Hartmann, D. H. Gómez, J., & Marscher, A., EPJ Web of Conferences, v. 61, 02003, 2013a (http://www.epj-conferences.org/)

[48] Nishikawa, K.-I., Zhang, B., Dutan, I., Medvedev, M., Hardee, P., Choi, E.-J. Min, K., Niemiec, J., Mizuno, M., Nordlund, Å., Frederiksen, J., Sol, H., Pohl, M., & Hartmann, D. H., Ann. Geophys., 31, 1535, 2013b

[49] Nishikawa, K.-I., Hardee, P., Dutan, I., Niemiec, J., Medvedev, M., Mizuno, Y., Meli, A., Sol, H., Zhang, B., Pohl, M.,& Hartmann, D. H., ApJ, 793, 60, 2014a (arXiv:1405.5247)

[50] Nishikawa, K.-I., Hardee, P., Mizuno, Y., Dutan, I., Zhang, B., Medvedev, M., Meli, A., Choi, E. J., Min, K. W., Niemiec, J., Nordlund, Å., Frederiksen, J. T., Sol, H., Pohl, M., Hartmann, D. H. Gómez, J., & Marscher, A., International Journal of Modern Physics: Conference Series, 28, 1460195, 2014b

[51] Mizuno, Y., Hardee, P., & Nishikawa, K.-I., ApJ, 662, 835, 2007

[52] Lemoine, M., Pelletier, G.,, Gremillet, L., & Plotnikov, L., MNRAS, 440, 1365, 2014

[53] Lemoine, M., Pelletier, G.,, Gremillet, L., & Plotnikov, L., EPL, 106, 55001, 2014

[54] Markidis, S. , Lapenta, G., Delzanno, G. L., Henri, P., Goldman, M. V., Newman, D. L., Intrator, T. & Laure, E. Plasma Phys. Control. Fusion 56, 064010, 2014

[55] Freidberg, J. P., MHD – macroscopic equilibrium Plasma Physics and Fusion Energy (Cambridge: Cambridge University Press), 2007

[56] Mizuno, Y., Lyubarsky, Y., Nishikawa, K.-I., & Hardee, P. E., ApJ, 757, 16, 2012

[57] Wieland, V., Pohl1, M., Niemiec, J., Rafighi, I., & Nishikawa, K.-I., ApJ, to be submitted, 2014

Insights into the particle acceleration of a peculiar gamma-ray radio galaxy IC 310

J. Sitarek
University of Łódź, PL-90236 Lodz, Poland,
IFAE, Campus UAB, E-08193 Bellaterra, Spain

D. Eisenacher Glawion, K. Mannheim
Universität Würzburg, D-97074 Würzburg, Germany

P. Colin for the MAGIC Collaboration
Max-Planck-Institut für Physik, München, Germany

M. Kadler
Universität Würzburg, D-97074 Würzburg, Germany

R. Schultz, F. Krauß
Universität Würzburg, D-97074 Würzburg, Germany,
Dr. Remeis-Sternwarte Bamberg, Astronomisches Institut der
Universität Erlangen-Nürnberg, ECAP, D-96049 Bamberg, Germany

E. Ros
Max-Planck-Institut für Radioastronomie, D-53121 Bonn, German,
Observatori Astronòmic, Universitat de València, E-46980 Paterna, València, Spain,
Departament d'Astronomia i Astrofísica, Universitat de València, E-46100 Burjassot, València, Spain

U. Bach
Max-Planck-Institut für Radioastronomie, D-53121 Bonn, German

J. Wilms
Dr. Remeis-Sternwarte Bamberg, Astronomisches Institut der
Universität Erlangen-Nürnberg, ECAP, D-96049 Bamberg, Germany

IC 310 has recently been identified as a gamma-ray emitter based on observations at GeV energies with Fermi-LAT and at very high energies (VHE, $E > 100$ GeV) with the MAGIC telescopes. Despite IC 310 having been classified as a radio galaxy with the jet observed at an angle > 10 degrees, it exhibits a mixture of multiwavelength properties of a radio galaxy and a blazar, possibly making it a transitional object. On the night of 12/13$^{\text{th}}$ of November 2012 the MAGIC telescopes observed a series of violent outbursts from the direction of IC 310 with flux-doubling time scales faster than 5 min and a peculiar spectrum spreading over 2 orders of magnitude. Such fast variability constrains the size of the emission region to be smaller than 20% of the gravitational radius of its central black hole, challenging the shock acceleration models, commonly used in explanation of gamma-ray radiation from active galaxies. Here we will show that this emission can be associated with pulsar-like particle acceleration by the electric field across a magnetospheric gap at the base of the jet.

I. INTRODUCTION

The nearby lenticular (S0, $z = 0.0189$) galaxy IC 310 located in the Perseus cluster exhibits an active galactic nucleus (AGN). This object has been detected at high energies (above 30 GeV) with *Fermi*/LAT [23] as well as at TeV energies [3, 5]. The jet of IC310, extending in the outward direction from the center of the cluster led to early assignment of this object as a head-tail radio galaxy [19, 27, 29]. However, using the Very-Long-Baseline Interferometry (VLBI) technique, a parsec-scale one-sided jet was found to follow the large-scale jet within about 10° [16]. The alignment of the jet at different scales, without any hints of bending put in doubt the above classification. Instead, the inner jet appears to be blazar-like with a missing counter jet due to relativistically boosted emission. Further indications for transitional behavior between a radio galaxy and a blazar were found in IC 310 in various energy ranges [25]. The mass, M, of the black hole of IC 310 can be inferred from its relation with the velocity dispersion, σ, of the host galaxy [6, 15], namely $M = (3^{+4}_{-2}) \times 10^8 M_\odot$.

MAGIC (Major Atmospheric Gamma Imaging Cherenkov) is a system of two 17-m diameter Imaging Atmospheric Cherenkov telescopes located on La Palma, Canary Islands. It allows observations of gamma-ray sources with energies above 50 GeV. During the observations of the Perseus cluster performed in the end of 2012 MAGIC telescopes revealed an extreme gamma-ray flare from IC 310 on the night of 12/13$^{\text{th}}$ of November [6]. In addition, the source was observed in radio band by European VLBI Network (EVN) during October/November 2012.

In Section II we report the data analysis and results of the MAGIC observations during the flare and the radio observations. In Section III we discuss possible interpretation of the ultrafast variability of the gamma-ray emission observed from IC 310.

II. RESULTS

A. MAGIC

MAGIC telescopes were observing the Perseus cluster on the night of 12/13$^{\text{th}}$ of November for 3.7 h. The observations consisted of 4 pointings, two of the them with a standard offset of 0.4° with respect to IC 310 and the remaining ones are at a distance 0.94° away from the object. The signal extraction and calibration of the data, the image parametrization, the direction and energy reconstruction as well as the gamma-hadron separation were applied with the standard analysis software MARS as described in [30].

In the night of the flare a strong signal of 507 gamma-like events above 300 GeV in the region around IC 310 in excess of the background estimated as 47 events was observed. Due to still limited statistics of events and a very rapid variability behavior, the classical approach for the calculation of light curves in gamma-ray astronomy which is based on the fixed width of the time bins is not optimal in this case. We used instead a method similar to the one commonly used for data of X-ray observatories for the computing of energy spectra. We first identify all periods in the data during which the telescopes were not operational (in particular $\lesssim 1$ min gaps every 20 min when the telescope is slewing and reconfiguring for the next data run). Afterwards, we bin the remaining time periods based on a fixed number (in this case 9) of ON events per bin. We estimate the number of background events in each time bin from four off-source regions at the same distance from the camera center. Using toy MC simulations we validated that this method limits the bias in flux value and its error [6]. As the signal to background ratio above 300 GeV is much larger than 1 this assures that the precision of individual points in the light curve is close to 3σ.

The resulting light curve is presented in Fig. 1. The mean flux above 300 GeV during this period is $\Phi_{\text{mean}} = (6.1 \pm 0.3) \times 10^{-11}\,\text{cm}^{-2}\text{s}^{-1}$. This is four times higher than the high state flux of $(1.60 \pm 0.17) \times 10^{-11}\,\text{cm}^{-2}\text{s}^{-1}$ reported in [5]. The emission is highly variable, fitting the light curve in the full time range with a constant reveals a χ^2/N.d.o.f of 199/58 corresponding to a probability of 2.6×10^{-17}.

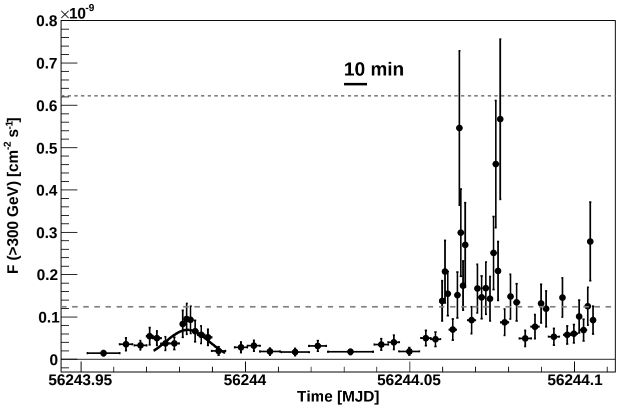

FIG. 1: Light curve of IC 310 observed with the MAGIC telescopes in the night of November 12/13$^{\text{th}}$, 2012, above 300 GeV. As a flux reference, the two gray lines indicate levels of 1 and 5 times the flux level of the Crab Nebula, respectively. The precursor flare (MJD 56243.972–56243.994) has been fitted with a Gaussian distribution. The figure is reprinted from [6].

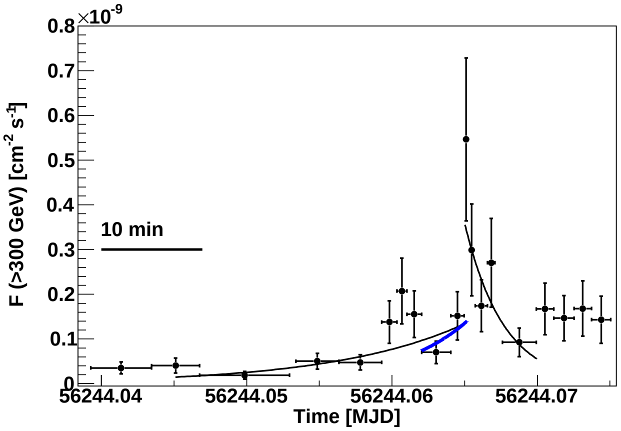

FIG. 2: Zoom of the first big flare seen in the light curve of IC 310 above 300 GeV. Black lines show exponential fits to the rising and decay edges to the substructures in the light curve. The blue line shows the slowest doubling time necessary to explain the raising part of the flare at C.L. of 95%. The figure is reprinted from [6].

We use the rapidly rising part of the 1$^{\text{st}}$ big flare (MJD 56244.0620–56244.0652) in order to compute the conservative, slowest doubling time, τ_{D}, which is still consistent with the MAGIC data. We fit the light curve with a set of exponential functions, each time assuming a given τ_{D} value and computing the corresponding fit probability. We obtain that 4.9 min is the largest value of τ_{D}, which can still marginally fit the data with probability > 5% (see the blue line in Fig. 2). Note that the corresponding time scale in the frame of reference of IC 310 will be slightly shorter:

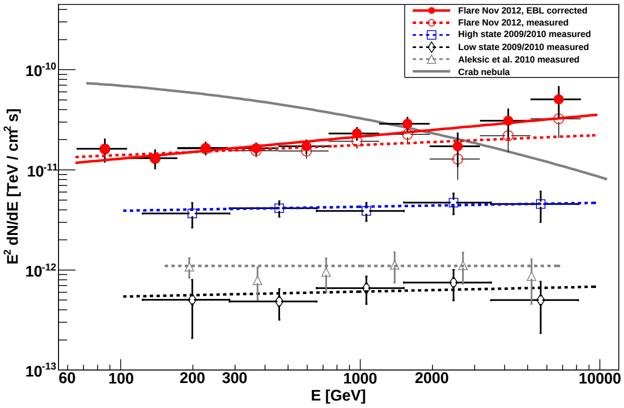

FIG. 3: MAGIC measurement of average spectral energy distributions of IC 310 during the flare (red) . For comparison we show the results from the high (blue, open squares) and low (black, open markers) states reported in [5] and the average results (gray triangles) reported in [3]. The dashed lines show power-law fits to the measured spectra, and the solid line with filled circles depicts the spectrum corrected for absorption in the extragalactic background light according to [12]. As a reference, the spectral power-law fit of the Crab Nebula observations from [4] is shown (gray, solid line). The figure is reprinted from [6].

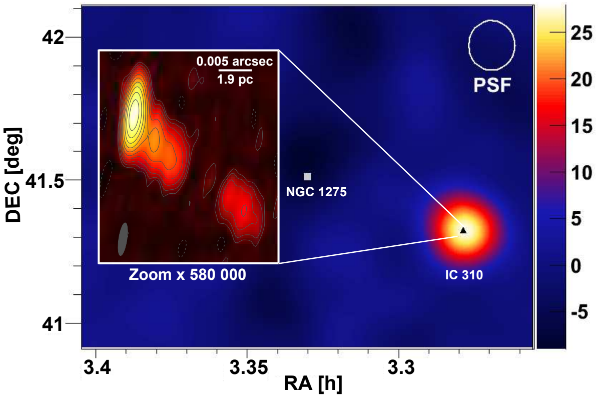

FIG. 4: Significance map (color scale) of the Perseus cluster in gamma rays observed in the night of November 12/13th, 2012, with the MAGIC telescopes. The inset shows the radio jet image of IC 310 at 5.0 GHz obtained with the European VLBI Network (EVN) on October 29, 2012. Contour lines (and associated to them color scale) increase logarithmically by factors of 2 starting at three times the noise level. The ratio of the angular resolution between MAGIC and the EVN is 1:580 000. The figure is reprinted from [6].

$4.9/(1+z)\,\mathrm{min} = 4.8\,\mathrm{min}$.

The observed spectrum can be described by a simple power law (see Fig. 3):

$$\frac{\mathrm{d}F}{\mathrm{d}E} = f_0 \times \left(\frac{E}{1\mathrm{TeV}}\right)^{-\Gamma}. \tag{1}$$

The flux normalization at 1 TeV obtained from the fit is $f_0 = (17.7{\pm}0.9_{\mathrm{stat}}{\pm}2.1_{\mathrm{syst}})\times10^{-12}\mathrm{TeV}^{-1}\,\mathrm{cm}^{-2}\,\mathrm{s}^{-1}$ Even while the mean flux during the flaring night is $4-30$ larger than previous measurements, the spectral index, $\Gamma = 1.90 \pm 0.04_{\mathrm{stat}} \pm 0.15_{\mathrm{syst}}$ is consistent with them within the statistical and systematic errors. No significant bend or cut-off is seen in the spectrum up to TeV energies. As part of the observation was carried out with a higher then usual offset angle from the camera center the systematic error on the flux normalization is slightly larger (12%) then reported in [7]. The error of the energy scale is 15%.

B. EVN

IC 310 has been observed with the EVN at 1.7, 5.0, 8.4 and 22.2 GHz between 2012-10-21 and 2012-11-07. The data were amplitude and phase calibrated using standard procedures with the Astronomical Image Processing System (AIPS, [14]) and imaged and self-calibrated using DIFMAP [28].

In inset panel of Fig. 4 we present the image with the highest dynamic range obtained from the observation at 5.0 GHz from 2012-10-29. The image has a peak flux density of 77 mJy/beam and a 1σ noise level of 0.027 mJy/beam. The restoring beam has a major and minor axis of $4.97\times1.24\,\mathrm{mas}^2$ with the major axis at a position angle of $-8.5°$. It contains a total flux density of $S_{\mathrm{total}} = 109\,\mathrm{mJy}$, which we conservatively assume to be accurate to 10%. The dynamic range DR of the image, defined as the ratio of the peak flux density to tripled noise level in the image is ≈ 950.

The angle θ of the radio jet to the line-of-sight can be determined from Doppler boosting arguments for a given jet speed β and spectral index α by considering the ratio R of the flux density in the jet and counter-jet:

$$R = \left(\frac{1+\beta\cos\theta}{1-\beta\cos\theta}\right)^{2-\alpha}. \tag{2}$$

Following [16] we use the DR as an upper limit for the detection of a counter-jet. This gives us an upper limit of θ:

$$\theta < \arccos\left(\frac{DR^{1/(2-\alpha)}-1}{DR^{1/(2-\alpha)}+1}\right). \tag{3}$$

Substituting DR in Eq. 2, assuming a flat spectral index of $\alpha = 0$ and $\beta \to 1$, we obtain an upper limit for the angle between the jet and the line-of-sight of $\lesssim 20°$.

Additionally, the extension of the projected one-sided kpc radio jet of $\sim 350\,\mathrm{kpc}$ measured at a wavelength of 49 cm [29] yields an estimate of a lower limit for the angle. De-projecting the jet using the upper limit quoted above would results in a lower limit of the jet length of ∼1 Mpc. Radio galaxies typically show jets extending up to 150 kpc-300 kpc [24]. The maximal length of radio jets has been measured to be a few Mpcs which corresponds to an angle of $\sim 5-10^\circ$ in the case of IC 310. Smaller angles would rapidly increase the de-projected length of the jet to values far above the maximum of the distribution of the jet lengths.

III. INTERPRETATION

GeV and TeV gamma-ray emission from blazars and radio galaxies is often explained in terms of shock-in-jet models. Charged particles are accelerated in an active region moving along the jet. Causality condition provides that the variability time scale of the observed emission can be used to constrain the size of the emission region.

A conservative estimate of the shortest variability time scale in the frame of reference of IC 310 yields $\Delta t/(1+z) = 4.8$ min. Using the best mass estimate of IC 310 black hole this measurement corresponds to 20% of the light travel time across the event horizon. Even allowing for the factor 3 uncertainty in the mass the fraction, 60%, is still below one. The ultrafast variability casts a shadow of doubt on the current shock-in-jet paradigm. The moving shock plasma leads to a shortening of the observed variability time scale Δt compared with the variability time scale $\Delta t'$ in a frame comoving with the shock given by $\Delta t = (1+z)\delta^{-1}\Delta t'$. This effect is often used to explain ultrafast variability from blazars [1, 2] in which δ can be nearly arbitrarily large providing that the jet moving with large Lorentz factor is observed at a very small angle. In the case of IC 310 however the estimation of the observation angle $10^\circ - 20^\circ$ obtained from the radio observations constrain the maximum Doppler factor to be $\lesssim 6$.

All of these attempts to explain the sub-horizon scale variability with relativistic projection effects alone encounter a fundamental problem [20]. If the perturbations giving rise to the blazar variability are injected at the jet base, the time scale of the flux variations in the frame comoving with the jet is affected by time dilation with Lorentz factor Γ_j. In blazars where $\delta \sim \Gamma_\mathrm{j}$, the Lorentz factor cancels out, and the observed variability time scale is ultimately bounded below by Δt_BH.

Additionally, a very high value of the Doppler factor is required to avoid the absorption of the TeV gamma rays due to interactions with low-energy synchrotron photons. Such synchrotron photons are inevitably produced together with the gamma rays in the shock-in-jet scenario. The optical depth to pair creation by the gamma rays can be approximated by $\tau_{\gamma\gamma}(10 \text{ TeV}) \sim 300\,(\delta/4)^{-6}\,(\Delta\mathrm{t}/1 \text{ min})^{-1}\left(\mathrm{L_{syn}}/10^{42} \text{ erg s}^{-1}\right)$. Adopting, conservatively, a non-thermal infrared luminosity of ∼ 1% of the gamma-ray luminosity during the flare, the emission region would be transparent to the emission of 10 TeV gamma rays only if $\delta \gtrsim 10$.

In summary, trying to interpret the IC 310 flare in the framework of the shock-in-jet model meets difficulties. Alternative models can involve stars falling into the jet [8, 9], mini-jet structures within the jets [13] or magnetospheric models [10, 17, 21, 26]. In the case of IC 310 star-in-jet model cannot provide sufficient luminosity to explain the TeV flare [6]. Also jets-in-jet models suffer from rapidly dropping luminosity at larger observation angles [6]. Moreover the magnetic reconnection which can led to production of such mini-jets is expected to occur in the main jet rather at larger distances from the black hole.

In magnetospheric models, particle acceleration is assumed occur in electric fields parallel to the magnetic fields. This mechanism is common to the particle-starved magnetospheres of pulsars, but it could also operate in the magnetospheres anchored to the ergospheres of accreting black holes (see Fig. 5). Electric fields can exist in vacuum gaps when the density of charge carriers is too low to cause their shortcut, i.e. below the so-called Goldreich-Julian charge density. Electron-positron pairs in excess of the Goldreich-Julian charge density can be produced thermally by photon-photon collisions in a hot accretion torus or corona surrounding the black hole. It has also been suggested, that particles can be injected by the reconnection of twisted magnetic loops in the accretion flow [22]. A depletion of charges from thermal pair production is expected to happen when the accretion rate becomes very low. In this late phase of their accretion history, supermassive black holes are expected to have spun up to maximal rotation. Black holes can sustain a Poynting flux jet by virtue of the Blandford-Znajek mechanism [11]. Jet collimation takes place rather far away from the black hole, i.e. at the scale of the light cylinder beyond $\sim 10 r_\mathrm{g}$. Gaps could be located at various angles with the jet axis corresponding to the polar and outer gaps in pulsar magnetospheres leading to fan beams at rather large angles with the jet axis. As the gap height and seed particle content depend sensitively on plasma turbulence and accretion rate, the gap emission is expected to be highly variable. For an accretion rate of $\sim 10^{-4}$ of the Eddington accretion rate and maximal black hole rotation, the gap height in IC 310 is expected to be $h \sim 0.2 r_\mathrm{g}$ [17] which is in line with the variability times seen in the observations. Depending on the electron temperature and geometry of the radiatively inefficient accretion flow, its thermal cyclotron luminosity can be low enough to warrant the absence of pair creation attenuation in the spectrum of gamma rays. In this picture, the intermittent variability witnessed in IC 310 is due to a runaway effect. As particles accelerate to ultrahigh energies, electromagnetic cascades

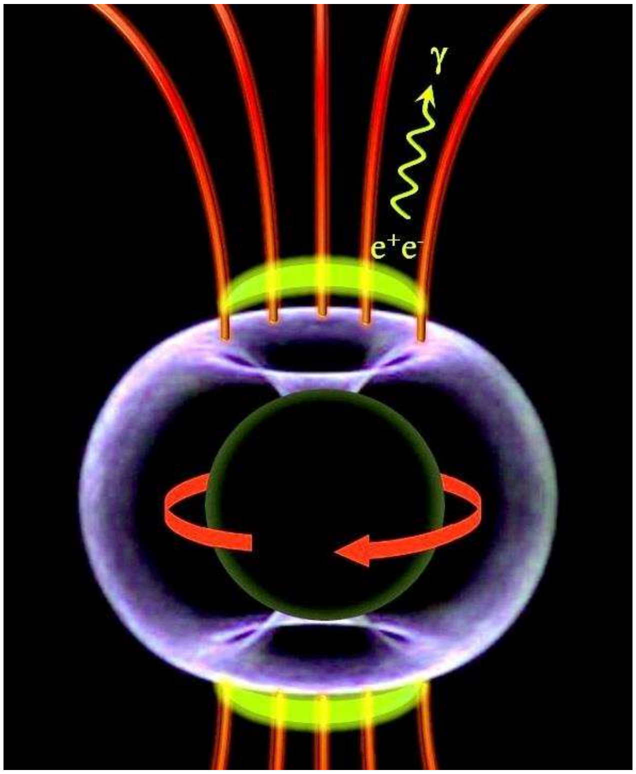

FIG. 5: Scenario for the magnetospheric origin of the gamma-rays: A maximally rotating black hole with event horizon r_{g} (black sphere) accretes plasma from the center of the galaxy IC 310. In the apple-shaped ergosphere (blue) extending to $2r_{\mathrm{g}}$ in the equatorial plane, Poynting flux is generated by the frame-dragging effect. The rotation of the black hole induces a charge-separated magnetosphere (red) with polar vacuum gap regions (yellow). In the gaps, the electric field of the magnetosphere has a component parallel to the magnetic field accelerating particles to ultra-relativistic energies. Inverse-Compton scattering and intense pair production due to interactions with low-energy thermal photons from the plasma accreted by the black hole leads to the observed gamma rays. The figure is reprinted from [6].

develop multiplying the number of charge carriers until their current shortcuts the gap. The excess particles are then swept away with the jet flow, until the gap reappears.

IV. CONCLUSIONS

Radio galaxies and blazars with very low accretion rates allow us to obtain a glimpse of the jet formation process near supermassive black holes. Observations of IC 310 performed with the MAGIC telescopes showed variability with time scale below 5 min, shorter than the light crossing time of the event horizon of its black hole. The commonly used in AGNs shock-in-jet models have troubles to explain such emission. A plausible explanation involves emission from vacuum gaps in the magnetosphere of IC 310. Interestingly, such explanation invite to explore analogies with pulsars where particle acceleration takes place in two stages. In the first stage, particle acceleration occurs in the gaps of a charge-separated magnetosphere anchored in the ergosphere of a rotating black hole, and in a second stage at shock waves in the force-free wind beyond the outer light cylinder.

Acknowledgments

We would like to thank the Instituto de Astrofísica de Canarias for the excellent working conditions at the Observatorio del Roque de los Muchachos in La Palma. The support of the German BMBF and MPG, the Italian INFN, the Swiss National Fund SNF, and the Spanish MICINN is gratefully acknowledged. This work was also supported by the CPAN CSD2007-00042 and MultiDark CSD2009-00064 projects of the Spanish Consolider-Ingenio 2010 programme, by grant 127740 of the Academy of Finland, by the DFG Cluster of Excellence "Origin and Structure of the Universe", by the Croatian Science Foundation (HrZZ) Projects 09/176, by the University of Rijeka Project 13.12.1.3.02, by the DFG Collaborative Research Centers SFB823/C4 and SFB876/C3, and by the Polish MNiSzW grant 745/N-HESS-MAGIC/2010/0. We thank also the support by DFG WI 1860/10-1. J. S. was supported by ERDF and the Spanish MINECO through FPA2012-39502 and JCI-2011-10019 grants. E. R. was partially supported by the Spanish MINECO projects AYA2009-13036-C02-02 and AYA2012-38491-C02-01 and by the Generalitat Valenciana project PROMETEO/2009/104, as well as by the COST MP0905 action 'Black Holes in a Violent Universe'. The European VLBI Network is a joint facility of European, Chinese, South African and other radio astronomy institutes funded by their national research councils. The research leading to these results has received funding from the European Commission Seventh Framework Programme (FP/2007-2013) under grant agreement No. 283393 (RadioNet3).

---

[1] F. Aharonian, *et al.*, *ApJ* **664**, L71 (2007).

[2] J. Albert, *et al.*, *ApJ* **669**, 862 (2007).

[3] J. Aleksić, *et al.*, *ApJ* **723**, L207 (2010).
[4] J. Aleksić, *et al.*, *Astroparticle Physics* **35**, 435 (2012).
[5] J. Aleksić, *et al.*, *A&A* **563**, A91 (2014a).
[6] J. Aleksić, *et al.*, *Science*, **346**, 1080 (2014b).
[7] J. Aleksić, *et al.*, arXiv:1409.5594 (2014)
[8] M. V. Barkov, F. A. Aharonian, V. Bosch-Ramon, *ApJ* **724**, 1517 (2010).
[9] W. Bednarek, R. J. Protheroe, *MNRAS* **287**, L9 (1997).
[10] V. S. Beskin, Y. N. Istomin, V. I. Parev, *SOVAST* **36**, 642 (1992).
[11] R. D. Blandford, R.L. Znajek, *MNRAS* **179**, 433 (1977).
[12] A. Domínguez, *et al.*, *MNRAS* **410**, 2556 (2011).
[13] D. Giannios, D. A. Uzdensky, M. C. Begelman, *MNRAS* **402**, 1649 (2010).
[14] E. W. Greisen, *Information Handling in Astronomy - Historical Vistas* **285**, 109 (2003).
[15] K. Gültekin, *et al.*, *ApJ* **698**, 198 (2009).
[16] M. Kadler, *et al.*, *A&A* **538**, L1 (2012).
[17] A. Levinson, F. Rieger, *ApJ* **730**, 123 (2011).
[18] M. L. Lister, *et al.*, *AJ* **146**, 120 (2013).
[19] G. K. Miley, *Annu. Rev. Astron. Astrophys.* **18**, 165 (1980).
[20] R. Narayan, & T. Piran, *MNRAS*, **420**, 604 (2012).
[21] A. Neronov, F. A. Aharonian, *ApJ* **671**, 85 (2007).
[22] A. Y. Neronov, D. V. Semikoz, I. I. Tkachev, *New Journal of Physics* **11**, 065015 (2009).
[23] A. Neronov, D. Semikov, I. Vovk, *A&A* **519**, L6 (2010).
[24] M. J.Neeser, S. A. Eales, J. D. Law-Green, *ApJ* **451**, 76 (1995).
[25] T. A. Rector, J. T. Stocke, E. S. Perlman, *ApJ* **516**, 145 (1999).
[26] F. M. Rieger, K. Mannheim, *A&A* **353**, 473 (2000).
[27] M. Ryle, M. D. Windram, *MNRAS* **138**, 1 (1968).
[28] M. C. Shepherd, T. J. Pearson, G. B. Taylor (1994), vol. 26, pp. 987-989.
[29] D. Sijbring, A. G. de Bruyn, *A&A* **331**, 901 (1998)
[30] R. Zanin, *et al.*, *Proc. to the 33rd ICRC, Id. 0773, Rio de Janerio, Brazil* (2013).

The Extreme Gamma-Ray Blazar S5 0716+714: Jet Conditions from Radio-Band Variability and Radiative Transfer Modeling

M.F. Aller, P.A. Hughes, H.D. Aller,
University of Michigan, Ann Arbor, MI 48109 USA
S.G. Jorstad, A.P. Marscher, V. Bala
Institute for Astrophysical Research, Boston University, Boston, MA 02215 USA
T. Hovatta
Aalto University Metsähovi Radio Observatory, Metsähovintie 114, 02540 Kylmälä, Finland

As part of a program to identify the physical conditions in the jets of γ-ray-flaring blazars detected by *Fermi*, including the role of shocks in the production of high-energy flaring, we obtained 4 years of 3-frequency, centimeter-band total flux density and linear polarization monitoring observations of the radio-bright blazar S5 0716+714 with the University of Michigan 26-m paraboloid. Light curves constructed from these data exhibit a series of rapid, high-amplitude, centimeter-band total flux density outbursts, and changes in the linear polarization consistent with the passage of shocks during the γ-ray flaring. The observed spectral evolution of the radio-band flares, in combination with radiative transfer simulations incorporating propagating shocks, was used to constrain the shock and jet flow conditions in the parsec-scale regions of the jet. Eight forward-moving, transverse shocks with unusually-strong shock compression factors, a very fast Lorentz factor of the shocks of 77, a bulk Lorentz factor of the flow of 20, a viewing angle of 12°, and an intrinsic opening angle of the radio jet of 5.2° were identified.

1. Overview

Recent work to localize the site of the GeV emission from blazars using radio-band imaging data has identified a close temporal correlation between activity in the 43 GHz core, a physical region associated with a standing shock [1], and flaring in the γ-ray band [2], while evidence for enhanced centimeter-band activity during γ-ray flaring has been found for large source samples [3]. Such results support the notion of a common disturbance for the production of both the radio-band and γ-ray activity and the localization of the γ-ray flaring in the parsec-scale region of the jet during at least some flares, e.g. [4]. Hence radio-band linear polarization and total flux density data can be used to probe the physical conditions at or near to the γ-ray emission site under the assumption that γ-ray flaring originates in the parsec-scale jet.

The role of shocks in the production of optical-to-radio-band flaring has been widely accepted since the 1980s, and it has been a commonly-cited mechanism for particle acceleration to γ-ray energies in recent work [5]. However, few detailed studies have been carried out to identify the presence of shocks during γ-ray flares and to determine their role in the production of γ-ray flaring. Comparison of simulated light curves based on radiative transfer calculations incorporating the shock paradigm with radio-band total flux density and linear polarization variability observations can be used to identify the properties of shocks (strength, orientation, and sense) and to constrain jet flow conditions. The latter include the bulk motion of the flow, the viewing angle of the jet, the intrinsic jet opening angle, and the degree of order of the magnetic field. While time-intensive, modeling has the advantage of disentangling complex effects, including relativistic aberration and Doppler boosts, and is preferable to indirect methods based on simple assumptions and the combining of unmatched properties. While useful in obtaining statistical results to delineate parameter space, such procedures can lead to erroneous results for individual sources, in particular where the flow conditions are extreme (fast) and the shocks are strong.

The intermediate-spectral-peaked (ISP) object S5 0716+714 is both radio and γ-ray bright, and it has exhibited a history of intense variability across the spectrum, including detection in the TeV band, making it well-suited for application of the shock paradigm. To attain this goal, we carried out intensive monitoring of the linear polarization and total flux density with the University of Michigan 26-m telescope (hereafter UMRAO) at three frequencies (14.5, 8, and 4.8 GHz) during 2008.5 through 2012.5. These data, complemented by millimeter VLBA imaging data at 43 GHz, which probes structural changes in the inner jet of this highly core-dominated source, are modeled here.

2. The Data

2.1. Historical Variability at Radio Band and at GeV Energies

Centimeter-band total flux density (S) and linear polarization (LP) observations of the γ-ray-bright BL Lacertae object 0716+714 were obtained from the early 1980s through 2012.5 as part of the University of Michigan (UMRAO) variability program. Such

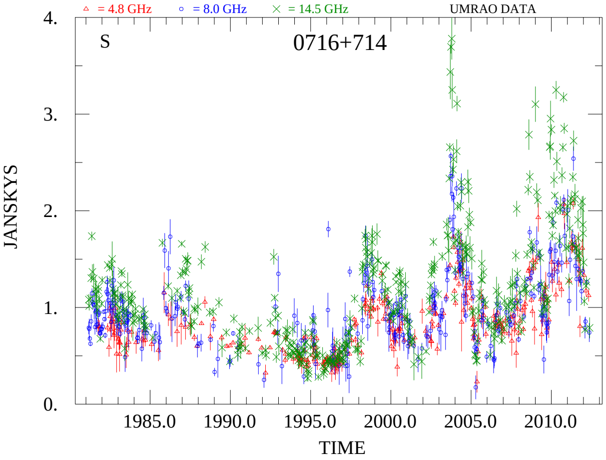

Figure 1: Multi-decade total flux density light curve for 0716+714. The data at 14.5, 8, and 4.8 GHz are denoted by crosses, circles, and triangles respectively.

long-term data are useful for placing the observations during the *Fermi* era in context. Two-week-averaged long-term total flux density measurements, shown in Figure 1, illustrate nearly continuous activity over 3.5 decades of monitoring. The amplitude of the total flux density exhibited a minimum near 0.3 Jy in the mid 1990s during the operation of EGRET aboard the Compton Gamma Ray Observatory (CGRO). The source was within the EGRET field of view several times in the 1990s, and 5 detections with $\sqrt{TS} \geq 3.5$ ($\geq 3\sigma$ determinations) are listed in the Third EGRET Catalog [6]. These occurred at Viewing Periods with midpoints 1992.05, 1992.19, 1992.46, 1993.55, & 1995.14. The peak centimeter-band total flux density amplitudes were considerably lower than those in the *Fermi* era, and these EGRET detections occurred during centimeter-band outburst phases which ranged from onset to radio-peak. The characteristic behavior of the centimeter-band variability is notably different after 2002. Thereafter high-amplitude, rapid flaring commenced which has been particularly intense and sustained since the launch of *Fermi*.

2.2. Variability Since the Launch of Fermi

A blow-up of the UMRAO total flux density and linear polarization data since mid-2008 and the weekly-binned γ-ray photon flux light curve in the 0.1–200 GeV band is shown in Figure 2. The photon fluxes (panel 1) were obtained using **ScienceTools**–v9r27p1 and P7SOURCE_V6 event selection. The LAT data were extracted within a 10° region of interest (ROI) centered upon the position of the target. These used an unbinned likelihood analysis (tool gtlike) to determine the photon fluxes by including in the model all of the sources within 15° of the target and by freezing the spectral index of all sources to the value in the 2FGL catalogue. Daily-averaged UMRAO centimeter-band data are shown in panels 2-4. With the higher sampling attained since the launch of *Fermi*, the individual radio-band flares comprising an outburst are resolved during each activity phase; sufficient resolution in the data is an important requirement for identifying the number of individual flares within an outburst envelope and is used to set the number of shocks. The linear polarization is shown in panels 3 and 4 in the form of fractional linear polarization and electric-vector position angle (EVPA). There is a 180° ambiguity in the determination of the UMRAO EVPAs, and our convention is to restrict the UMRAO EVPA values to lie in the range of 0° - 180°. In this plot, however, we have allowed the range to be slightly larger to minimize the occurrence of apparent jumps.

VLBA imaging data provide important additional constraints in the analysis of the variability in this source. Source-integrated 15 GHz data from the MOJAVE website (http://www.physics.purdue.edu: orange squares) and core fluxes obtained from the BU blazar program, VLBA-BU-BLAZAR, (http://www.bu.edu/blazars/VLBAproject.html) providing monthly data at 43 GHz are included in this figure. The agreement between the 15 GHz MOJAVE imaging data and the 14.5 GHz source-integrated UMRAO measurements confirms that there is no significant contribution from extended VLA-scale structure to either the total or polarized flux. The redshift for this source is not known directly from spectroscopic measurements. However, adopting a value of 0.3 has led to a maximum apparent component speed of ≥40c based on the analysis of 5 moving MOJAVE components, and a change in the 15 GHz projected inner jet position angle in late 2009-early 2010 is identified from the structural changes with time [7]. A preliminary analysis of the 43 GHz VLBA monitoring data obtained in the Boston University Blazar program identified complex structural changes in the inner jet region and both stationary and moving jet components; 3 of the component ejections (times at which the feature separated from the core) were temporally-associated with γ-ray flares during the time window presented [8]. Comparison of the amplitudes and variations in the millimeter and centimeter band gives a measure of the opacity between the respective emission sites and a fiducial location in the jet flow since the 43 GHz 'core' is associated with a physical feature in the flow. The fact that both the linear polarization and the total flux density measurements characteristically track at 15 and 43 GHz suggests that either the 43-15 GHz emission region is optically thin during this time window, or that the emission sites are spatially close to each other.

Cross-correlations of the fluxes from ground-based

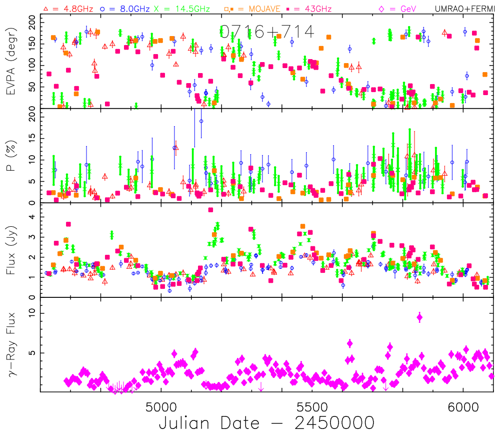

Figure 2: The γ-ray and centimeter-band total flux density and linear polarization light curves: May 13, 2008 through June 12, 2012. From bottom to top: (panel 1) the weekly-binned γ-ray light curve in units of photons/s/cm^2 x 10^{-7}, and (panels 2-4) radio-band total flux density, fractional linear polarization (P%), and electric vector position angle (EVPA) shown as daily-averaged data. Core fluxes at 43 GHz from the Boston University program (magenta squares) and source-integrated 15 GHz MOJAVE VLBA data (orange squares) are included.

and satellite instruments at a variety of wavebands have been carried out for segments of the data sets in a number of recent papers, e.g. [9], and characteristic time scales identified using structure functions and periodograms [10]. This work identifies complex relationships which are overall consistent with the production of flaring by a common disturbance which propagates outward in the jet with time. The matching of individual total flux density flares in the radio and γ-ray light curves, however, is complicated by the presence of nearly continuous activity in the radio-band in the post-launch time-period, intrinsic difference in the doubling time for flaring in the two bands, and by geometric effects, e.g. [11], including changes in jet orientation with time and jet curvature.

3. Radiative Transfer Modeling

The framework and assumptions adopted in the radiative transfer modeling are detailed in [12]. We adopt a scenario in which propagating shocks pass through a region of the jet containing a predominantly-turbulent, passive magnetic field; the support for the presence of a turbulent magnetic field comes from the UMRAO result for hundreds of sources showing low levels of fractional polarization (typically a few percent) on timescales of decades, and no evidence for the high values (P>20%) of the fractional linear polarization in the parsec-scale domain predicted by some models. Such high fractional linear polarizations might be expected for isolated regions of highly-ordered magnetic field, e.g. as found in some jet components from VLBI polarimetry observations, but not in the underlying quiescent flow. While the magnetic field is predominantly turbulent in our model, an additional ordered axial magnetic field component was initially included in the modeling to reproduce the stable EVPAs observed in UMRAO sources during the relatively-rare time windows of quiescence, but early modeling revealed that this axial magnetic field can have a significant effect on the simulated light curves and that higher values than the initially-adopted value of 2% in magnetic energy were required to match the data. The value of the axial magnetic field is one of the parameters determined by the modeling. The shocks compress the plasma in the emission region, increasing the emissivity and producing an increase in the degree of order of the magnetic field. The signature of the passage of a shock in the light curves is an outburst in total flux density, an increase in the fractional linear polarization, and an ordered swing in the EVPAs, and it is the spectral evolution with time in both the linear polarization and the total flux density which constrains our models. The number of shocks used in the simulation is established from the structure apparent in the total flux density and linear polarization light curves, combined with the expected burst profile for a single shock [12]. The shocks are allowed to be oriented at an arbitrary direction relative to the jet flow and are specified by two angles. The angle η, the shock obliquity, specifies the angle relative to the direction of the upstream flow. A second angle specifies the azimuthal direction of the shock normal, but as discussed in [12], the simulation is relatively insensitive to the choice of the value for this free parameter. For simplification it is assumed that the shock occupies the cross section of the flow and propagates at a constant rate.The attributes which specify a shock are its onset time, length, compression factor, sense (forward or reverse), and orientation.

Table I Shock Parameters

Shock	1	2	3	4	5	6	7	8
T_o-2000	0.85	08.9	09.8	10.15	10.6	11.2	11.4	11.8
κ	0.18	0.18	0.18	0.2	0.17	0.2	0.27	0.25

4. Modeling Results for 0716+714: Shock and Flow Parameters

The iterative procedure used for the analysis is illustrated in [13] which presents details and results for events modeled in three additional γ-ray-bright blazars, and the sensitivity of the model to changes in the values for the key model parameters is examined in [14]. An initial shock obliquity was chosen based on the changes in the UMRAO EVPA light curves. In this source swings through approximately 90° occurred, consistent with the passage of a shock whose front is transverse to the jet axis. By assumption all of the shocks during the activity modeled have the same orientation. The length of each shock (defined as the evolved extent of the shocked flow) was set at 0.005 times the length of the flow. The shock sense was found to be forward moving; we explored the possibility of reverse shocks, but these led to inconsistencies with results based on VLBI measurements. The individual start times and compression factors (κ) required to reproduce the spectral and temporal variability are listed in Table I for each shock. Typical compressions for other γ-ray-flaring sources are 0.5 - 0.8, and the shocks in 0716+714 require unusually strong compressions as suggested by the very rapid rises in the light curves.

Parameters specifying the jet are given in Table II. The value of the optically-thin spectral index α ($S \propto \nu^{-\alpha}$) was set to 0.25 based on the rather flat total flux density spectra in general in the UMRAO sources, and the fiducial 'thermal' Lorentz factor of the energy spectrum was arbitrarily set to 1000 at 8 GHz. The model assumes a power law distribution of the radiating particles with cutoff γ_i. The low energy cutoff, determined to be 50 in this source, was constrained primarily by the EVPAs. The bulk Lorentz factor was determined from the observed P%; the derived value of 20 is high compared to the values in the range 5-10 determined for our other modeled sources, but is consistent with the high values of β_{app} determined from VLBI measurements for the fastest components. The flow viewing angle is determined primarily by the observed fractional linear polarization but uses the observed EVPA and the range of its change as a secondary constraint. For comparison, typical values found from our modeling of other sources are in the range 1.5° to 4°, and our derived value of this parameter is unusually high for a blazar. The apparent component speed, β_{app}, is computed from the shock Lorentz factor and the viewing angle. The shock Lorentz factor, in turn, comes from the bulk Lorentz factor of the quiescent flow and the shock strength (compression factor).

The simulated light curves based on the shock and jet parameters given in the tables are shown in Figure 3 right and the UMRAO data used as constraints are shown in Figure 3 left. The scaling of time in the model light curves is set by the duration of the activity modeled, while the total flux density is scaled to match the peak amplitude of the total flux density at the highest UMRAO frequency, 14.5 GHz. Recall that there are 180° ambiguities in the determination of the EVPAs. Hence in the comparison of the data and the model only the range of the swings should be considered and not the values. The shock onsets are marked along the abscissa of the lower panel of the left plot. These mark the times at which the leading edge of the shock enters the flow, and they do not correspond to times at which the brightness centroids of new VLBI components cross those of the stationary 'core'. Those times, based on the 43 GHz data, are also indicated in the figure.

4.1. Deviations between the Model and the Data

While the model is able to reproduce the general character of the variability, including the spectral behavior as a function of time, the amplitude range of the total flux density flares, and the global event shape and the position of features, there are some important differences between the observed and simulated light curves which indicate that refinements to the model are required. Geometric effects have been cited in a number of papers, and an association between changes in the inner jet PA at 43 GHz and with γ-ray activity is proposed in [15]. These would be expected to affect the character of the total flux density light curves which are successfully reproduced in terms of the amplitude range and the spectral behavior with time. More difficult to account for are the differences between the observed and simulated fractional linear polarization. Refinements to the model are required to reproduce the spectral character of the 8 GHz polarimetry data, especially during shocks 2 through 5. Further, in the early part of the simulation, the values of P% are too high at all three frequencies (e.g. at 4.8 GHz 10 versus 5). Modifications which we hope to explore in future work in an effort to improve the fit of the model include allowing for a range of shock obliquities in the simulation and including a modest contribution from an additional ordered (possibly helical) magnetic field component.

5. Discussion and Conclusions

Radiative transfer modeling of the UMRAO data incorporating 8 forward-moving shocks is able to reproduce the primary features of the spectral variability in both total flux density and linear polarization in 0716+714. The modeling identifies a high bulk Lorentz factor of the flow, consistent with prior results, a wide intrinsic jet opening angle compared with other blazars [13] and unusually strong shock compressions. The apparent speeds of the emission pattern are high, but less than the Lorentz factor since the observer lies outside of the critical cone of the fast flow. The viewing angle, a parameter which is very well constrained by both the linear polarization and the total flux density measurements, is higher than

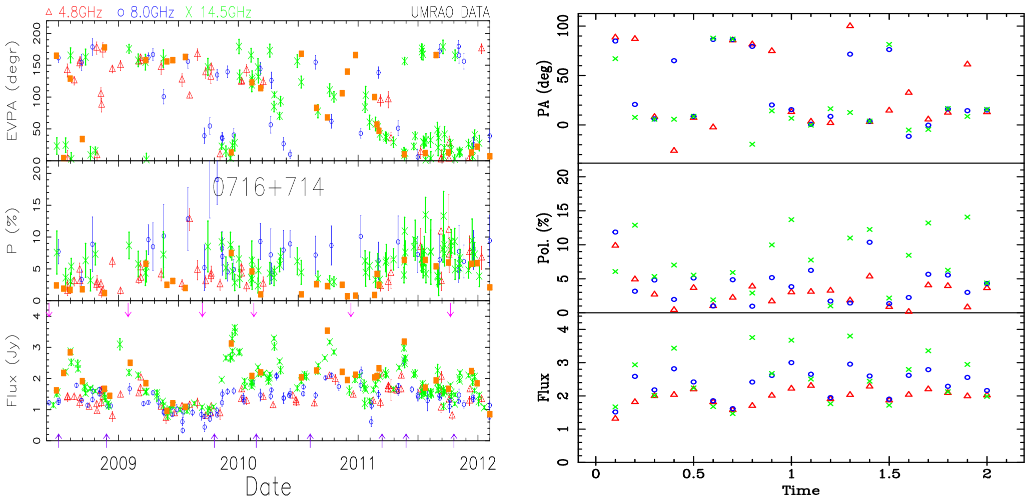

Figure 3: Left: Observed total flux density and linear polarization for the time segment modeled. The symbol convention follows Figure 1. The MOJAVE source integrated values are included for comparison. In panel 2 the error bars are omitted for clarity. The upward arrows along the abscissa of the lower panel (Flux) mark the shock start times. The downward arrows along the top of this panel mark the component separation times from new model-fitting of the 43 GHz VLBA data. Right: Simulated total flux density and linear polarization light curves based on the shock and jet parameters given in the text. Time is expressed in arbitrary units using 20 time steps over the time window modeled. The three frequencies are color and symbol coded to match the convention adopted for displaying the data.

found for the outbursts which we modeled in other γ-ray-bright sources. These results are consistent with the impression from the light curves alone that the jet conditions in this source are extreme.

The fact that the 43 GHz VLBA and 14.5 GHz monitoring data in *both* the linear polarization and the total flux density track so well during the γ-ray flaring is unusual compared to other blazars. The modeling identifies that the radio-band emission originates in a partially optically-thick part of the jet, and this result rules out the optically thin scenario suggested as a possible explanation to explain the tracking of the millimeter and centimeter-band flux and linear polarization data. The millimeter and centimeter-band data, combined with the modeling, support an interpretation of spatially-close centimeter and millimeter-band emission sites. The localization of the γ-ray site relative to the 43 GHz core region remains a controversial issue. The variability in this source is complex, and the broadband data exhibit time-dependent behavior which complicates attempts to establish significant correlations. These may arise from a complex mix of changing physical conditions within the jet, geometric effects, and more than one γ-ray emission site. The correlations identified are consistent with the production of at least some γ-ray flares within the parsec-scale radio jet, and the modeling provides relevant source parameters for those γ-ray flare events.

This work illustrates the importance of multifrequency linear polarization monitoring data. They have the power to directly probe the magnetic field direction and degree of order in blazars and to provide relativistic jet flow and shock properties which cannot be obtained directly from observations.

Table II Jet Parameters

PARAMETER	**VALUE**
Spectral Index	0.25
Fiducial Lorentz Factor	1000
Cutoff Lorentz Factor	50
Bulk Lorentz Factor	20
Jet Opening Angle	5.2°
Viewing Angle	12.0°
Shock Lorentz Factor	77
Shock β_{app}	9.5c
Energy in the Axial **B** Field	36%

Acknowledgments

Funding was provided by NSF grant AST-0607523 and NASA *Fermi* GI grants NNX09AU16G, NNX10AP16G, and NNX11AO13G (U. Michigan); NSF grant AST-0907893 and NASA *Fermi* GI grants NNX08AV65G and NNX11AQ03G (Boston U.); and Academy of Finland project number 267324 (T.H). Computational resources and services were provided by Advanced Research Computing at the University of Michigan, Ann Arbor. This project has made use of data from the MOJAVE website which is maintained by the MOJAVE team.

References

[1] A.P. Marscher, S.J. Jorstad, F.D. D'Arcangelo, et al., "The inner jet of an active galactic nucleus as revealed by a radio-to-γ-ray outburst", Nature, 452, 966, 2008.

[2] S.G. Jorstad, A.P. Marscher, I. Agudo, N. MacDonald, T. Scott, & K. Williamson, "Relation Between Events in the Millimeter-wave Core and Gamma-ray Outbursts in Blazars", AAS Meeting 219, 154.29, 2012.

[3] Y.Y. Kovalev, H.D. Aller, M.F. Aller, et al., "The Relation Between AGN Gamma-Ray Emission and Parsec-Scale Radio Jets", ApJ, 696, L17, 2009.

[4] I. Augudo, et al., "On the Location of the γ-Ray Outburst Emission in the BL Lacertae Object AO 0235+164 Through Observations Across the Electromagnetic Spectrum", ApJ, 735, L10, 2011.

[5] A. Meli & P.I. Biermann, "Active galactic nuclei jets and multiple oblique shock acceleration: starved jets", A&A, 556, 88, 2013.

[6] R.C. Hartman, D.L. Bertsch, S.D. Bloom, et al., "The Third EGRET Catalogue of High-Energy Gamma-Ray Sources", ApJS, 123, 79, 1999.

[7] M.L. Lister, M.F. Aller, H.D. Aller, et al., "MOJAVE. X. Parsec-Scale Jet Orientation Variations and Superluminal Motion in Active Galactic Nuclei", AJ, 146, 120, 2013.

[8] D.A. Morozova, S.G. Jorstad, A.P. Marscher, et al. "Multiwavelength Observations of 6 BL Lac Objects in 2008-2012", EPJ Web of Conferences, 61, 04018, 2013.

[9] B. Rani, T.P. Krichbaum, L. Fuhrmann, et al., "Radio to gamma-ray study of blazar S5 0716+714", A&A, 552, A11, 2013.

[10] N.H. Liao, J.M. Bai, H.T. Liu, et al., "Multiwavelength Variability Properties of Fermi Blazar S5 0716+714", ApJ, 783, 83, 2014.

[11] U. Bach, T.P. Krichbaum, E. Ros, et al., "Kinematic study of the blazar S5 0716+714", A&A, 433, 815, 2005.

[12] P.A. Hughes, M. F. Aller, & H.D. Aller, "Oblique Shocks as the origin of Radio to Gamma-Ray Variability in Active Galactic Nuclei", ApJ, 735, 81, 2011.

[13] M.F. Aller, P.A. Hughes, & H.D. Aller, "Constraining the Physical Conditions in the Jets of γ-Ray Flaring Blazars using Centimeter-band Polarimetry and Radiative Transfer Simulations. I. Data and Models for 0420-014, OJ 287, and 1156+295", ApJ, 791, 53, 2014.

[14] P.A. Hughes, M. F. Aller, & H.D. Aller, "Constraining the Physical Conditions in the Jets of γ-Ray Flaring Blazars using Centimeter-band Polarimetry and Radiative Transfer Simulations. II. Exploring Parameter Space and Implications", ApJ, 799, 207, 2015.

[15] B. Rani, T.P. Krichbaum, A.P. Marscher, S.G. Jorstad, J.A. Hodgson, L. Fuhrmann, & J.A. Zensus, "Jet outflow and gamma-ray emission correlations in S5 0716+714", A&A, 571, L2, 2014.

Shot Analysis of Kepler Blazar W2R 1926+42

M. Sasada, S. Mineshige
Department of Astronomy, Graduate School of Science,
Kyoto University, Kitashirakawa-Oiwake-cho, Sakyo-ku,
Kyoto 606-8502, Japan; sasada@kusastro.kyoto-u.ac.jp

S. Yamada
Department of Physics, Tokyo Metropolitan University,
Minami-Osawa 1-1 Hachioji, Tokyo 192-0397, Japan

H. Negoro
Department of Physics, Nihon University, 1-8 Kanda-Surugadai, Chiyoda-ku, Tokyo 101-8308, Japan

Blazars show rapid and violent variabilities, which timescale are often less than a day. We studied intraday variations by applying a "shot analysis" technique to *Kepler* monitoring of blazar W2R 1926+42 in Quarter 14. We obtained a mean profile calculated from 195 rapid variations. The mean profile shows three components; one is a sharp structure distributed within ±0.1 day of the peak, and two slow-varying components. This spiky-peak component reflects features of rapid variations directly. The profile of peak component shows an exponential rise and decay of which timescales are different, 0.0416 and 0.0588 day respectively. This component is too sharp to represent a standard function which is often used to express blazar variations. This asymmetric profile at the peak is difficult to be explained by a simple variation of the Doppler factor by changing a geometry of the emitting region. This result indicates that intraday variations arise from a production of high-energy accelerated particles in the jet.

I. INTRODUCTION

Blazars have relativistic jets whose axes are closely directed along their line of sight [4, 5]. Timescales of brightness variations in blazars are related to sizes of emitting regions and these speeds in relativistic jets. Variations, however, have a variety of timescales from minutes to decades. A power spectrum density (PSD) of blazar shows a power-law distribution, which means that variations of blazars show noise-like behaviors [14]. These various brightness variations in blazars can be happened by a variety of physical situations in relativistic jets. The shorter-timescale variations should be reflected to the physics of inner-emitting regions of a jet. Thus, the study of short-timescale variations is important to investigate the origin of variation in blazar jets.

Blazars show rapid variations having a timescale of less than 1 day. These rapid variations have been reported in wide wavelengths from radio to gamma-ray bands; in the radio [19], optical [7], X-ray [14], and TeV gamma-ray bands [3]. The *Fermi* space telescope has scanned the entire gamma-ray sky every hours, and detected a lot of large-amplitude variations as flares [2, 17, 22]. Detected flares in the gamma-ray band often continued for less than 1 day, and had a variety of shapes, not only a simple rise and decay. We need higher time-resolution and photon-statistics observations to study the detailed feature of rapid variations.

An optical continuous monitoring of blazar W2R 1926+42 with a high time-sampling rate by *Kepler* spacecraft [6] detected a lot of rapid variations. Its light curve revealed detailed shapes of numerous variations with large signal-to-noise ratio. We report general features of rapid variations having a timescale less than 1 day by stacking these detected variations, and producing a mean profile of rapid variations, so-called shot analysis. This paper is organized as follows. Details of *Kepler* observation and the way of shot analysis are described in section 2. Observational results and features of the mean profile of rapid variations are reported in section 3. We discuss an origin of rapid variations of the object in section 4, and section 5 gives several concluding remarks.

II. OBSERVATION AND ANALYSIS

A. *Kepler* data

Kepler monitored over a hundred thousand objects in Cygnus regions, and obtained continuous light curves with two timing settings, long (thirty-minute) or short (one-minute) cadences. Blazar W2R 1926+42 is listed in *Kepler* target list. It has been obtained a continuous light curve with the long cadence since Quarter 11. In Quarter 14, the object had been monitored in the short cadence mode for 100 days. We produced the calibrated "SAP_FLUX" light curve with one-minute time resolution by the automated *Kepler* data processing pipeline [13].

W2R 1926+42 is classified as a low-frequency peaked BL Lac object at $z = 0.154$ estimated from two absorption lines [9]. Edelson et al. reported that there were numerous flares with timescales as short as a day in the *Kepler* light curve of Quarter 11 and 12 [10]. The PSD calculated from the light curve showed approximately a power-law distribution, but not simple. It showed a flattening at frequencies below $7{\times}10^{-5}$ Hz.

B. Shot analysis

Frequency-domain analyses (e.g. PSD) are not easy to relate with physical mechanisms directly. On the other hand, time-domain analyses keeping phase information of variations can be useful for studying physical mechanisms of variation. We need, however, large photon statistics to study variations with these time-domain analyses, because it is difficult to study detailed features of variations by using only partial data with observational uncertainty. Additionally, observed variations in blazars usually have a variety of shapes. Thus, it is difficult to understand general features of variations in blazars by studing only individual variations.

We apply the light curve of W2R 1926+42 obtained by *Kepler* to a shot analysis proposed by Negoro et al. to study the general features of rapid variations without local features of individual variations, because a mean profile of rapid variations calculated by the shot analysis can be cancelled the local features of individual variations [18]. We analyzed following procedures to make a mean profile; First, we select rapid variations as candidates of shots. Second, we estimate the observational uncertainty in the light curve. Then, we select the rapid variations with four times larger amplitudes than the standard deviation of the observational uncertainty after subtracting the baseline components. We define these variations as shots.

There are two possibilities for varying the observed brightness, intrinsic variation of the object and variation by the observational uncertainty. It is natural that the variation by the observational uncertainty is dominant rather than the intrinsic variation in shorter period, especially in the period between two observing points which lie next to each other. We estimate the standard deviation σ of differences between two neighboring points, and define σ as the observational uncertainty, $\sigma = 17.15$ count s^{-1}.

Rapid variations are often superposed on long-term variations in light curves of blazars [20]. We approximate a baseline component of rapid variation by a second-order local polynomial fitting to the light curve without the period of the rapid variation. We subtract the calculated baseline component from the light curve, and extract the rapid variation. We detect a shot when the estimated amplitude of extracted rapid variation without the contribution of the baseline component is larger than our threshold, $>4\sigma$. Additionally, the peak time of the shot is defined at the time of the maximum flux among the period of rapid variation after subtracting the baseline component. We calculate a mean profile of detected shots by stacking with reference to each peak.

III. RESULTS

Figure 1 shows an optical light curve of the object obtained by *Kepler*. The object showed a violent variability with various timescales ranging from several tens of minutes to over ten days, limiting for the observational uncertainty. In the light curve, there are not only a large-amplitude long-term variation like from JD 2456150 to 2456160, but also a lot of flare-like variations with timescale of hours. These rapid variations existed throughout the entire period of this monitoring. Figure 2 shows examples of rapid variations. We range these rapid variations with reference to the peak times of individual extrema. Figure 2 clearly shows that these variations had a variety of shapes.

We detect 195 shots from the obtained light curve, in pursuance of the definition of shot described in section 2.2. We calculate a mean profile of these detected shots by appling the shot analysis. Upper panel of figure 3 shows the mean profile of shots without the data at peak time, because positive fluctuations of the counts at $t = 0$ are summed up systematically [18]. There are mainly three components at the mean profile of shots shown in figure 3; a sharp component distributed in ± 0.1 day of the peak time (component 1), and slow-variable components ranging from -0.50 to -0.15 day and from 0.10 to 0.45 day (component 2 and 3), respectively. An increase and decrease of flux in component 1 are approximately exponential rise and decay. Additionally, the profile at the peak is changing from rising to decaying phases for approximately ten minutes.

If shot profiles change depending on selected amplitudes of shots, the calculated mean profile does not reflect to general features of shot. We verify whether there is an amplitude dependence to the profile or not. We separate detected shots in three terms based on these amplitudes, 4–6σ, 6–8σ, and over 8σ, and calculate mean profiles using selected shots. Although calculated profiles show small differences caused by the limited number of shot samples, the mean profile of shots has no clear trend associated with these amplitudes.

We estimate the systematic uncertainty of the obtained mean profile of shots associated with limited sampling by a non-parametric bootstrap approach. First, we resample 195 shots with replacement from detected shots, and calculate a mean profile from the resampled 195 shots. We produce 10000 pseudo mean profiles of shots following this procedure with different resamplings. We normalize an average of each

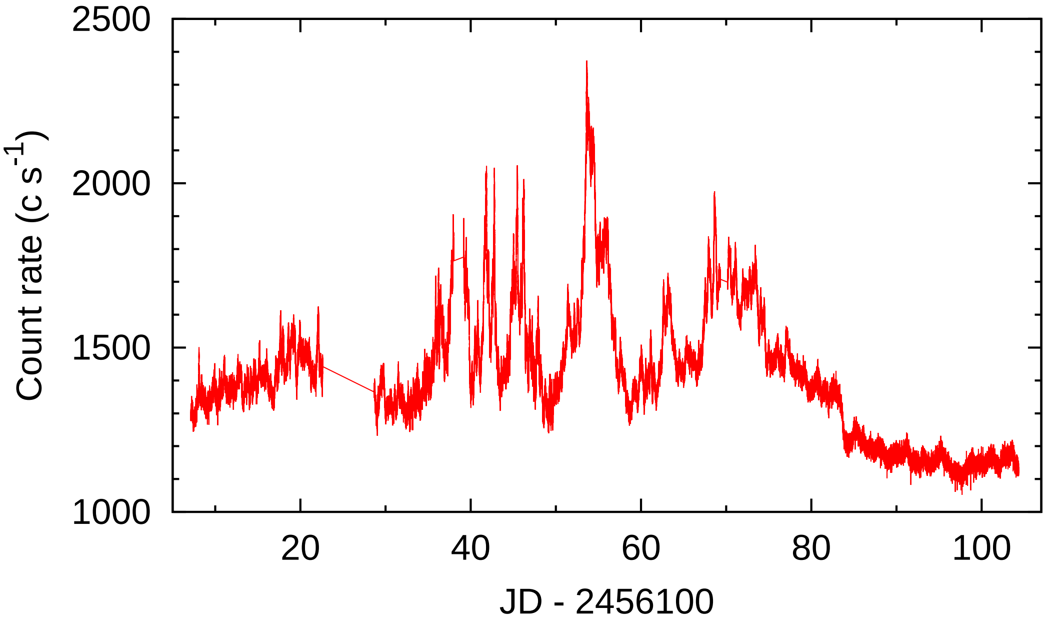

FIG. 1: Light curves obtained by *Kepler* spacecraft in Quarter 14. The object monitored for 100 d with one-minute time resolution.

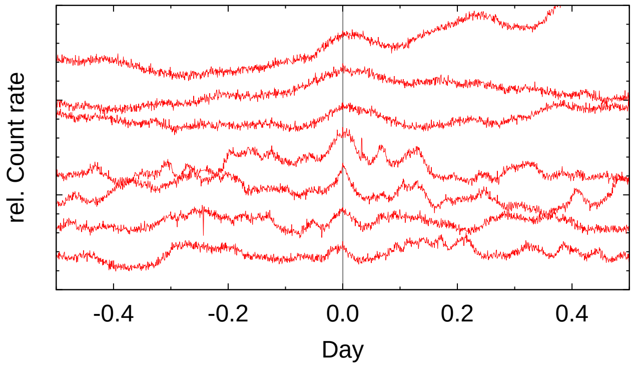

FIG. 2: Examples of rapid variations. These variations are ranged with reference to peak times of individual extrema during the period of rapid variations. From bottom to top, the peak times of rapid variations are JD 2456134.84, 2456147.23, 2456147.91, 2456151.40, 2456152.15, and 2456153.04, respectively.

mean profile within ±1 day, and calculate standard deviations in each time bin. The standard deviations of normalized mean profiles can be regarded as the systematic uncertainties associated with the sampling of shots. The bottom panel of figure 3 shows calculated standard deviations. These deviations are ranging from 6 to 10 count s^{-1}. Detected components from 1 to 3 in the mean profile of shots can be regarded as the real phenomena, not the artificial ones caused by the systematic uncertainty of the sampling of shots.

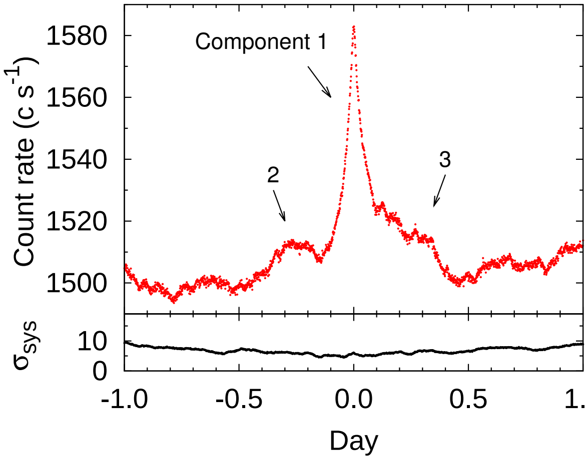

FIG. 3: A mean profile of detected shots. Upper panel shows the mean profile of shots and bottom panel shows the standard deviation estimated from a non-parametric bootstrap method. See text for detail.

Component 1 reflects general features of shots directly, because this component is distributed around the peak time. First, we apply this exponential shape of component 1 to a function proposed by Abdo et al.;

$$F(t) = F_0 \, [e^{-t/T_r'} + e^{t/T_d'}]^{-1} + F_c, \qquad (1)$$

where T_r' and T_d' are variation timescales of rise and decay phases, F_c represents a constant level underlying the component 1, and F_0 measures the amplitude of the shot [1]. We evaluate its goodness of fit by χ^2 test, $\chi^2 = \sum \{F_{\rm data}(t_i) - F_{\rm model}(t_i)\}^2$. The χ^2 of the best fitted function is 2278 within ±0.1 day of the mean profile to except contaminations of other components. On the other hand, we apply an another function;

$$F(t) = \begin{cases} F_0 \; e^{-t/T_r} + F_c, & t < 0 \\ F_0 \; e^{t/T_d} + F_c, & t > 0, \end{cases} \qquad (2)$$

where T_r and T_d are e-folding times of rise and decay, and F_c and F_0 are the same in the case of function (1). We also calculated the χ^2 of this function, χ^2=469. Figure 4 shows the applied functions with the best fitted parameters superposed on the mean profile and its residuals. Although the function (1) shows obvious residuals during the peak time in panels "a" and "b" of figure 4, the residuals in the case of function (2) are suppressed shown in panels "c" and "d". This indicates that the mean profile is more spiky than the expected profile from function (1). Therefore, the goodness of fit of the function (2) is more plausible than that of function (1) to represent the component 1 of the mean profile.

We estimated the best-fitted parameters with a chi-squared test. The mean profile, however, has a systematic uncertainty caused by the sampling of shots as mentioned above. We applied the non-parametric bootstrap approach to calculate the confidence level with the same way to estimate the errors of calculated parameters. First, we calculated 10000 pseudo mean profiles estimated from resamples with replacement from detected shots. We calculated the best-fitted parameters against individual pseudo profiles, and estimated the confidence levels in these parameters. In table 1, we show the best-fitted parameters of function (2) to the mean profile and the ranges of 95 % confidence levels. We applied the Wilcoxon rank-sum test which was a non-parametric significance test (also referred to as the Mann-Whitney U-test) to the distributions of T_r and T_d calculated by the bootstrap approach [15, 25]. We confirmed the difference between the T_r and T_d, because the p-value was less than 10^{-15}. Therefore, the component 1 in the mean profile of shots has an asymmetric profile.

TABLE I: Parameters of best-fitted function (2) to component 1 of the mean profile of shots

	Best value	**95% confidence level**
T_r (day)	0.0416	[0.0320, 0.0543]
T_d (day)	0.0588	[0.0399, 0.0919]
F_0 (count s^{-1})	76	[65, 88]
F_c (count s^{-1})	1508	[1484, 1537]

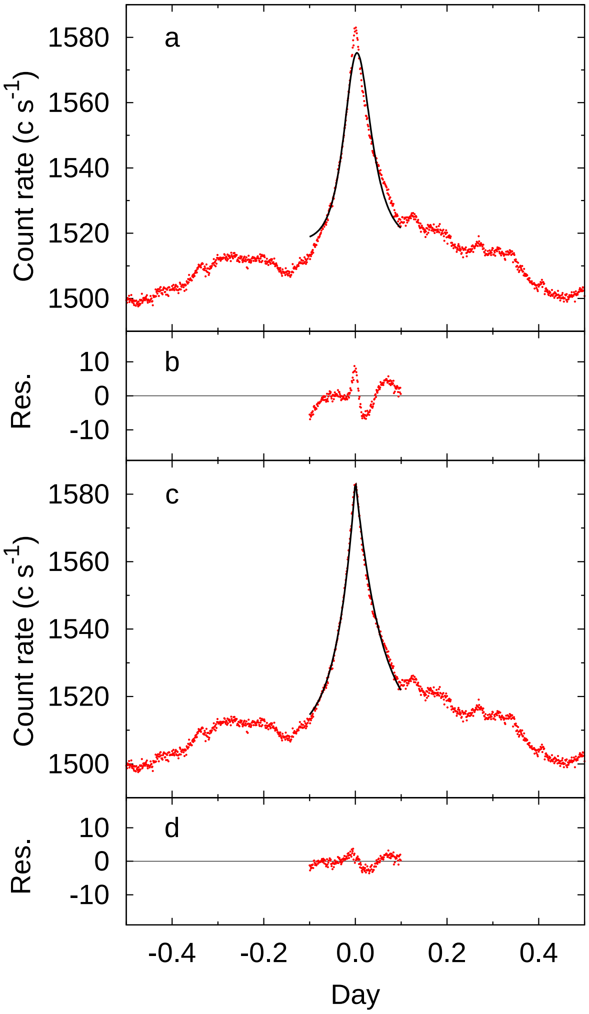

FIG. 4: Best-fitted functions superposed on mean profiles of shots. Panels "a" and "c" show a mean profile of shots and the best-fitted functions (1) and (2). Panels "b" and "d" show residuals between the mean profiles and the estimated best-fitted functions.

IV. DISCUSSION

We obtained the optical continuous light curve of blazar W2R 19426+42 with one-minute time resolution by *Kepler* spacecraft. The object showed violent variability and a lot of rapid variations with timescales less than a day. We detected 195 rapid variations as shots of which amplitude were larger than 4σ after subtracting these baseline components, and applied to the shot analysis. The mean profile produced from detected shots shows three components, one fast-spiky (component 1) and two slow-varying components. Component 1 shows an asymmetric profile, faster-rise and slower-decay features with the spiky but smooth-connected peak.

It is poorly understood whether rapid variations are intrinsic phenomena or apparent one caused by a geometrical changing in the jet. There are several models that flux variations are explained as apparent brightness variations, for example varying the Doppler factor for changing the viewing angle [24] or gravitational lensing effect [8]. These models, however, expect that the averaged variation profile is almost symmetric in a simple situation, because the Doppler factor should be changed symmetrically in the averaged variation. In other words, the rise and decay timescales should be equal. Estimated rise and decay timescales of rapid variations, however, are different described in section 3. Thus, these models can be ruled out in the case of rapid variations. Thus, rapid variations may come from authentic phenomena. It is plausible that there is a particle acceleration during the rapid variation, and then, higher-energy particles increase in the emitting region of the variation.

The synchrotron cooling timescale $\tau_{\rm syn}$ is represented as, $\tau_{\rm syn}{\sim}3.2{\times}10^4 B^{-3/2}E^{-1/2}\delta^{-1/2}$ sec, where B is a strength of magnetic field, E is an observed energy band, and δ is the Doppler factor [21, 23]. If the dissipation of high-energy particles in rapid variations is caused by the synchrotron cooling, $\tau_{\rm syn}$ in the rest frame can be represented using the decaying timescale T_d, $\tau_{\rm syn} = \delta\ T_d/(1+z)$. We estimate δ of 5.8 from observed T_d of the mean profile of shots, where E is 2.25 eV and assuming B as 0.5 G which is typical value among the gamma-ray detected BL Lac objects [11]. The mean profile reflects common features of rapid variations. Thus, the estimated δ should be a typical value of inner regions where rapid variations happen.

V. CONCLUSION

The optical continuous light curve with one-minute time sampling obtained by *Kepler* revealed that the mean profile of rapid variations almost showed exponential rise and decay. Rise and decay timescales of shot profile, however, are different, and the profile shows asymmetric profile. A particle acceleration process can produce this asymmetric variations. There are several scenarios which can explain the particle-acceleration mechanism causing the rapid variations; shock-in-jet scenario [16], magnetic reconnection scenario [12]. The shot analysis is also feasible to study the spectral feature of variations, because of large signal-to-noise ratio. Unfortunately, *Kepler* performed only one-band monitoring. Spectral and further observational studies are needed to completely understand the mechanism of rapid variations.

Acknowledgments

This work was supported by a Grant-in-Aid for JSPS Fellows.

---

[1] Abdo, A. A., et al. 2010, ApJ, 722, 520
[2] Abdo, A. A., et al. 2011, ApJ, 733, L26
[3] Aharonian, F., et al. 2007, ApJ, 664, L71
[4] Antonucci, R. 1993, ARA&A, 31, 473
[5] Blandford, R. D. & Königl, A. 1979, ApJ, 232, 34
[6] Borucki, W., et al. 2010, Sci, 327, 977
[7] Carini, M., Miller, H. R., & Goodrich, B. D. 1990, AJ, 100, 347
[8] Chang, K., & Refsdal, S. 1979, Nature, 282, 561
[9] Edelson, R., & Malkan, M. 2012, ApJ, 751, 52
[10] Edelson, R., et al. 2013, ApJ, 766, 16
[11] Ghisellini, G., et al. 2010, MNRAS, 402, 497
[12] Giannios, D., Uzdensky, D. A., & Begelman, M. C. 2009, MNRAS, 395, L29
[13] Jenkins, J., et al. 2010, ApJ, 713, L87
[14] Kataoka, J., et al. 2001, ApJ, 560, 659
[15] Mann, H. B., & Whitney, D. R. 1947, Annals of Mathematical Statistics, 18, 50
[16] Marscher, A. P., & Gear, W. K. 1985, ApJ, 298, 114
[17] Nalewajko, K. 2013, MNRAS, 430, 1324
[18] Negoro, H., Miyamoto, S., & Kitamoto, S. 1994, ApJ, 423, L127
[19] Quirrenbach, A., et al. 1992, A&A, 258, 279
[20] Sasada, M., et al. 2008, PASJ, 60, 37
[21] Sasada, M., et al. 2010, PASJ, 62, 645
[22] Saito, S., Stawarz, Ł., Tanaka, Y. T., Takahashi, T., Madejski, G., & D'Ammando, F. 2013, ApJ, 766, L11
[23] Tashiro, M., et al. 1995, PASJ, 47, 131
[24] Villata, M., & Raiteri, C., M. 1999, A&A, 347, 30
[25] Wilcoxon, F. 1945, Biometrics Bulletin, 1, 80

Fermi LAT detection of two high Galactic latitude gamma-ray sources, Fermi J1049.7+0435 and J1103.2+1145

Masaki Nishimichi, Takeshi Okuda and Masaki Mori
Department of Physical Sciences, Ritsumeikan University, Kusatsu, Shiga 525-8577, Japan

Philip G. Edwards
CSIRO Astronomy and Space Science, PO Box 76, Epping NSW 1710, Australia

Jamie Stevens
CSIRO Astronomy and Space Science, Locked Bag 194, Narrabri NSW 2390, Australia

During a search for gamma-ray emission from NGC 3628 (Arp 317), two new unidentified gamma-ray sources, Fermi J1049.7+0435 and J1103.2+1145 have been discovered [15]. The detections are made in data from the Large Area Telescope (LAT), on board the Fermi Gamma-ray Space Telescope, in the 100 MeV to 300 GeV band during the period between 2008 August 5 and 2012 October 27. Neither is coincident with any source listed in the 2FGL catalogue [17]. Fermi J1049.7+0435 is at Galactic coordinates $(l, b) = (245.34°, 53.27°)$, $(\alpha_{J2000}, \delta_{J2000}) = (162.43°, 4.60°)$. Fermi J1103.2+1145 is at Galactic coordinates $(l, b) = (238.85°, 60.33°)$, $(\alpha_{J2000}, \delta_{J2000}) = (165.81°, 11.75°)$. Possible radio counterparts are found for both sources, which show flat radio spectra similar to other Fermi LAT detected AGN, and their identifications are discussed. These identification have been supoorted by snap-shot observations with the Australia Telescope Compact Array at several epochs in 2013 and 2014,

I. INTRODUCTION

The Second Fermi LAT source catalog [17] includes as many as 1,873 sources, but initial attempts to identify counterparts at other wavelengths resulted in 575 sources remaining unidentified. The 2FGL catalog is based on the first 24 months of LAT observation since its launch in 2008, but the LAT has now accumulated more than 5 years of high-energy gamma-ray data almost flawlessly, presenting the possibility of finding new sources which were too faint to be detected in the first two years of data or showed flaring activity after the catalog was created.

In this paper we report on two new gamma-ray sources serendipitously discovered in the constellation Leo and discuss possible conterparts based on radio observations including recent snap-shots with the Australia Telescope Compact Array[23].

II. ANALYSIS

Our original aim was to search for gamma-ray emission from NGC 3628 (Arp 317), one of the three galaxies called the ‘Leo Triplet’, for which possible starburst activity has been reported based on XMM observations [22]. Five years of archival data of Fermi LAT has been analyzed using the Fermi Science Tools supplied by Fermi Science Support Center ([8], Fermi Science Tools v9r23p1). The energy range used in the present analysis was from 100 MeV to 300 GeV. ‘Source’ class events detected at zenith angles smaller than 100° were used for analysis, assuming ‘P7SOURCE_V6’ instrument response function along with the standard analysis pipeline suggested by FSSC. The significance of gamma-ray signal has been estimated by maximum likelihood method with a help of the `gtlike` program (which we used in the binned mode) included in the tools. The data periods for this studies span from 2008 August 4 to 2012 October 27.

For NGC 3628 (Arp 317), the test statistic, TS, returned by `gtlike` is consistent with zero, indicating there is no evidence of gamma-ray emission. Thus we calculated upper limits to gamma-ray flux from NGC 3628 of $1.4\,(1.3) \times 10^{-9}$ cm^{-2}s^{-1}, at 95% C.L., above 100 MeV for the period 2008 August 4 to 2010 July 31 (2010 July 31 to 2012 October 27). This is translated to gamma-ray luminosity upper limit of $2.5\,(2.3) \times 10^{43}$ erg s^{-1} assuming the distance of 12 Mpc which is derived as the median of 8 measurements, which range from 6.7 to 14.2 Mpc [14].

During the study of NGC 3628, we noticed two rather bright gamma-ray sources in the field of view centered on NGC 3628 and within a radius of 15° [15]. They are not coincident with any source listed in the 2FGL catalogue [17] nor in the 3EG catalogue [11]. Figure 1 shows a gamma-ray countmap of this area. The positions for these sources were estimated using the `gttsmap` program which calculates the TS value assuming an unknown source at various positions in the field-of-view of interest, and the maximum TS values were obtained for positions shown in the Table I. The errors of the positions are conservatively estimated as the radius at which the TS value drops to the half value.

Figures 2 and 3 show the time variation of gamma-ray fluxes of the newly detected sources in half-year

TABLE I: Best positions of new sources

Name	α_{J2000} (deg)	δ_{J2000} (deg)	$\ell^{\rm II}$ (deg)	$b^{\rm II}$ (deg)	error radius (arcmin)
J1049.7+0435	162.43	4.60	245.34	53.27	51
J1103.2+1145	165.81	11.75	238.85	60.33	66

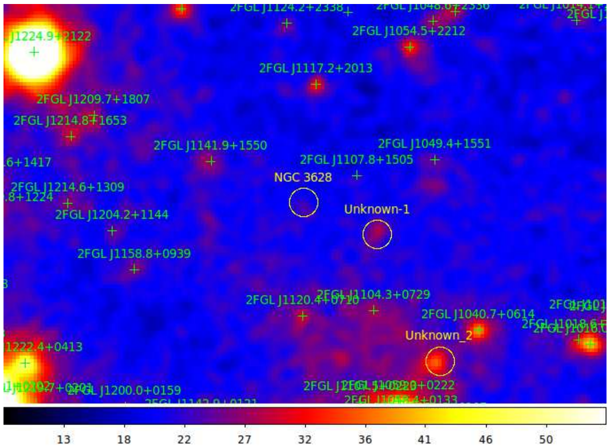

FIG. 1: Gamma-ray countmap around the NGC 3628 region. The map is created in 0.1° grid and smoothed for the data during 2008 August 05 to 2013 July 03. 2FGL sources are annotated, and two new gamma-ray sources are marked as 'Unknown_1' (J1103.2+1145) and 'Unknown_2' (J1049.7+0435).

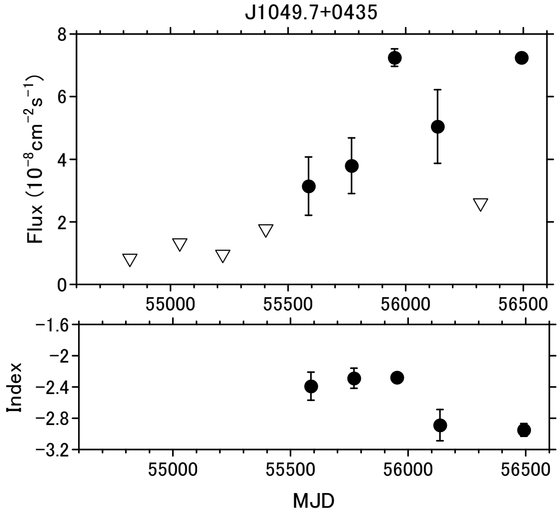

FIG. 2: Time variation of gamma-ray flux of J1049.7+0435 in half-year bins for the period from 2008 August 5 to 2013 October 10. Triangles are upper limits (95% C.L.).

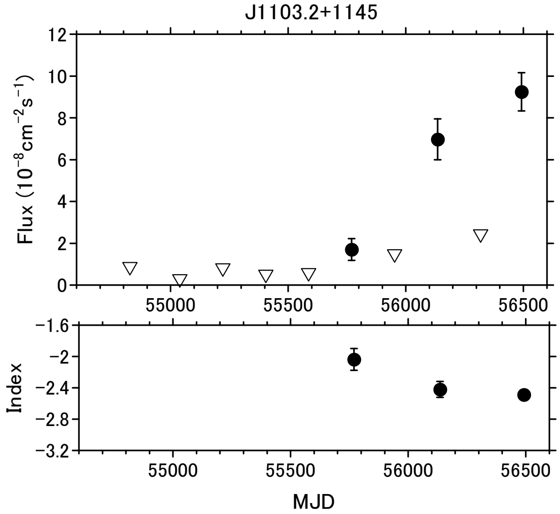

FIG. 3: Time variation of gamma-ray flux of J1103.2+1145 in half-year bins for the period from 2008 August 5 to 2013 October 10. Triangles are upper limits (95% C.L.).

bins. For these plots we added data until 2013 October 10. One can see in the first two years their fluxes are below the detection threshold ($TS < 25$), which is why they are not listed in the 2FGL catalog based on data over the similar period [17]. The first of our two sources has subsequently been detected in the Fermi All-sky Variability Analysis [4] and catalogued as 1FAV J1051+04.

III. DISCUSSION

The variability of both sources display at gamma-ray energies suggests they are more likely to be AGN than members of other populations of identified gamma-ray sources [16]. The gamma-ray spectral indices are more consistent with those of flat spectrum radio quasars (FSRQs) than of BL Lac objects [2]: FSRQs are on average found to be more variable than BL Lac objects [2, 16].

Mattox et al. [12, 13] showed that (extragalactic) gamma-ray sources were more likely to be associated with brighter radio sources, and in particular those sufficiently compact to be detectable in VLBI observations. Radio compactness is generally associated with a flatter radio spectrum, resulting from synchtrotron self-absorption at lower frequencies, which is also a characteristic of Fermi-detected AGN [1]. (Although, as noted by, e.g., Ref. [7], radio spectral indices determined from single dish observations are affected by steeper-spectrum radio lobes in some sources, which disguise the presence of a flat-spectrum radio core.)

We have, therefore, searched for potential counterparts in the Green Bank 6-cm (GB6 [9]) catalog and determined spectral indices between 20 cm and 6cm using the NRAO VLA Sky Survey (NVSS [6]) catalog.

The closest GB6 radio source to J1049.7+0435 is GB6 J1050+0432, with an angular separation of 7 arcmin. The source has a flux density of 99±10 mJy at 4.8 GHz, and the corresponding 20 cm source, NVSS J105010+043251, has a flux density of 101.2 mJy, yielding a spectral index α (where $S \propto \nu^{+\alpha}$) of 0.0. Two fractionally brighter GB6 sources have both larger angular offsets and signficantly flatter spectra: GB6 J1049+0505, 113 mJy, 30 arcmin separation, α=−0.8; GB6 J1051+0449, 101 mJy, 29 arcmin separation, α=−0.9. We note that the GB6 and NVSS flux densities were made some years apart, and so these spectral indices should be taken as representative values rather than absolute measurements. As this declination range is also covered by the Parkes-MIT-NRAO equatorial survey [10], we can compare the GB6 value with that PMN J1050+0432, which has a 4.8 GHz flux density of 98±12 mJy.

For J1105.2+1145, the closest GB6 source is GB6 J1103+1158, with an angular separation of 14 arcmin. The source has a 4.8 GHz flux density of 306±27 mJy, with the corresponding 20cm source, NVSS J110303+115816, having a flux density of 262.6 mJy, resulting in a spectral index of 0.1. Other relatively bright GB6 sources in the area are further away and with steeper spectral indices: GB6 J1103+1114, 116 mJy, 31 arcmin, α=−0.7; GB6 J1104+1103, 277 mJy, 46 arcmin, α=−0.8. A Seyfert 1 galaxy, Mrk 728, is 0.89 deg from J1103.2+1145 and is not likely the counterpart. GB6 J1103+1158 corresponds to the quasar SDSS 110303.52+115816.5, which lies at a redshift of 0.912 [20]. Furthermore, the quasar has been detected in the VLBA Calibrator Survey VLBI observations [18], confirming the presence of a compact core in this radio-loud AGN.

Catalogued radio positions and flux densities for the two sources are tabulated in Table II.

We have additionally made snap-shot observations of J1049.7+0435 and J1103.2+1145 (at their NVSS positions) with the Australia Telescope Compact Array at several epochs in 2013 and 2014, as part of an on-going program to monitor gamma-ray sources [21] with the measured flux densities are listed in Table III. The observations at 17 GHz and 38 GHz were preceded by a pointing scan on a nearby bright compact source to refine the global pointing model. Data were processed in Miriad in the standard manner. Flux density calibration was bootstrapped to the standard ATCA flux density calibrator, PKS 1934−638. Errors are conservatively estimated as 5% at lower frequencies and 10% at highest frequencies, where these include statistical and systematic errors, with the latter dominating.

GB6 J1050+0432 has brightened considerably, by a factor of 2.7, since the GB6 and PMN observations (which date back to the late 1980s and early 1990s), and has an inverted spectrum with $\alpha \sim 0.25$, strengthening the case for an association with J1049.7+0435. Note also the increased gamma-ray flux in the latest half year (Fig.2).

GB6 J1103+1158 is a little fainter than the catalogued GB6 value, however the ATCA observations confirm that the spectral index remains flat, at $\alpha \sim -0.1$, up to 38 GHz. There is no evidence of significant variability over the 4 months spanned by these observations, however comparison with the GB6 flux density indicates the presence of longer timescale variability.

We have also examined the ASDC Sky Explorer (ASDC [5]) and NASA/IPAC Extragalactic Database (NED [14]) for other possible counterparts, but we did not find any good candidates nearer than radio sources mentioned above.

In the light of the above facts, we tentatively identify both gamma-ray sources with the radio sources mentioned above. Petrov et al. [19] make a detailed consideration of the utility of radio observations in finding counterparts to unidentified Fermi sources. The associations proposed here would be strengthened by improved gamma-ray localisations, and/or evidence of contemporaneous multi-wavelength flaring, and, in the case of GB6 J1050+0432, with VLBI observations to determine whether the source contains a compact, parsec-scale, radio core.

IV. CONCLUSIONS

A search for gamma-rays from NGC 3628 (Arp 317), for which possible starburst activity has been reported, found no evidence for >100 MeV emission. However, two new GeV sources, Fermi J1049.7+0435 and J1103.2+1145, have been found near the Leo Triplet region using Fermi-LAT archival data spanning 5 years. The fluxes for both sources increase over the 5 yr period: thus they are not included in 2FGL catalog. Their flux variability and spectral indices are compatible with those of gamma-ray detected AGN. Based on angular separation, radio flux density and spectral index, we associate J1049.7+0435 with GB6 J1050+0432, and J1103.2+1145 with the quasar GB6 J1103+1158. Further multiwavelength studies are required to confirm these identifications.

TABLE II: Possible radio counterparts,

Gamma-ray source	catalog (frequency)	RA (J2000)	Dec (J2000)	Radio flux density (mJy)
J1049.7+0435	NVSS (1.4 GHz)	10 50 10.06	+04 32 51.3	101.2
	GB6 (4.8 GHz)	10 50 08.6	+04 32 37	99
J1103.2+1145	NVSS (1.4 GHz)	11 03 03.55	+11 58 16.6	262
	GB6 (4.8 GHz)	11 03 03.7	+11 58 20	306

TABLE III: ATCA radio observations (unit: mJy). See text for details.

Gamma-ray source	Epoch	5.5 GHz	9.0 GHz	17 GHz	38 GHz
GB6 J1050+0432	2013 Oct 20	276	311	371	
	2014 Apr 7			430	
	2014 Sep 14	274	341	275	265
GB6 J1103+1158	2013 May 10	254	238	216	230
	2013 Aug 20	254	245		
	2013 Sep 8	246	230		
	2014 Apr 7	237	265	173	147
	2014 Sep 14	210	210	209	225

Acknowledgments

This work is supported in part by the Grant-in-Aid from the Ministry of Education, Culture, Sports, Science and Technology (MEXT) of Japan, No. 22540315. The Australia Telescope Compact Array is part of the Australia Telescope National Facility which is funded by the Commonwealth of Australia for operation as a National Facility managed by CSIRO. Leonid Petrov is acknowledged for his independent suggestion of GB6 J1103+1158 as the possible counterpart to J1103.2+1145.

[1] Abdo, A.A. et al., Astrophys. J., 2010, 715, 429
[2] Ackermann, M. et al. 2011, Astrophys. J., 743, 171
[3] Ackermann, M. et al. 2012, Astrophys. J., 753, 83
[4] Ackermann, M. et al. 2013, Astrophys. J., 771, 57
[5] ASI Science Data Center (ASDC), http://www.asdc.asi.it/
[6] Condon, J. J., Cotton, W. D., Greisen, E. W., et al. 1998, Astron. J., 115, 1693
[7] Edwards, P. G. 2005, Astrophys. Sp. Sci, 297, 31
[8] Fermi Science Support Center (FSSC), http://fermi.gsfc.nasa.gov/ssc/
[9] Gregory, P. C., Scott, W. K., Douglas, K., & Condon, J. J. 1996, Astrophys. J. Suppl., 103, 427
[10] Griffith, M. R., Wright, A. E., Burke, B. F., & Ekers, R. D. 1995, Astrophys. J. Suppl., 97, 347
[11] Hartman, R. C., Bertsch, D. L., Bloom, S. D., et al. 1999, Astrophys. J. Suppl., 123, 79
[12] Mattox, J. R., Schachter, J., Molnar, L., Hartman, R. C., & Patnaik, A. R. 1997, Astrophys. J., 481, 95
[13] Mattox, J. R., Hartman, R. C., & Reimer, O. 2001, Astrophys. J. Suppl., 135, 155
[14] NASA/IPAC Extragalactic Database (NED), http://ned.ipac.caltech.edu/
[15] Nishimichi, M. & Mori, M., 2013, Astronomer's Telegram, #4949
[16] Nolan, P. L., Tompkins, W. F., Grenier, I. A., & Michelson, P. F. 2003, Astrophys. J., 597, 615
[17] Nolan, P.L., Abdo, A.A., Ackermann, M. et al., Astrophys. J. Suppl., 2012, 199, 31
[18] Petrov, L., Kovalev, Y. Y., Fomalont, E., & Gordon, D. 2005, Astron. J., 129, 1163
[19] Petrov, L., Mahony, E. K., Edwards, P. G., et al. 2013, Mon. Not. R. Astron. Soc., 432, 1294
[20] Schneider, D. P., Hall, P. B., Richards, G. T., et al. 2007, Astron. J., 134, 102
[21] Stevens, J., Edwards, P. G., Ojha, R., et al. 2012, Fermi & Jansky Proceedings — eConf C1111101, arXiv:1205.2403
[22] Tüllman, R., Pietsch, W., Rossa, J. et al., Astron. Astrophys., 2006, 448, 43
[23] The essential content of this paper has been published in Astrophys. J. 784, 94 (4pp) , 2014.

Star-Jet Interactions and Gamma-Ray Outbursts from 3c454.3

M.V. Barkov[1,2,3], D.V. Khangulyan[4], V. Bosch-Ramon[5], F.A. Aharonian[6,2], A.V. Dorodnitsyn[7,8]
[1] *Astrophysical Big Bang Laboratory, RIKEN, 2-1 Hirosawa, Wako, Saitama 351-0198, Japan*
[2] *Max-Planck-Institut für Kernphysik, Saupfercheckweg 1, D-69117 Heidelberg, Germany*
[3] *Space Research Institute RAS, 84/32 Profsoyuznaya Street, Moscow, 117997, Russia*
[4] *Institute of Space and Astronautical Science/JAXA,*
3-1-1 Yoshinodai, Chuo-ku, Sagamihara, Kanagawa 252-5210, Japan
[5] *Departament d'Astronomia i Meteorologia, Institut de Ciències del Cosmos (ICC),*
Universitat de Barcelona (IEEC-UB), Martí i Franquès, 1, E08028, Barcelona, Spain
[6] *Dublin Institute for Advanced Studies, 31 Fitzwilliam Place, Dublin 2, Ireland*
[7] *Laboratory for High Energy Astrophysics, NASA Goddard*
Space Flight Center, Code 662, Greenbelt, MD, 20771, USA and
[8] *Department of Astronomy/CRESST, University of Maryland, College Park, MD 20742, USA*

We propose a model to explain the ultra-bright GeV gamma-ray flares observed from the blazar 3C454.3. The model is based on the concept of a relativistic jet interacting with compact gas condensations produced when a star (red giant) crosses the jet close to the central black hole. The study includes an analytical treatment of the evolution of the envelop lost by the star within the jet, and calculations of the related high-energy radiation [16]. The model readily explains the day-long, variable on timescales of hours, GeV gamma-ray flare from 3C454.3, observed during November 2010 on top of a weeks-long plateau. In the proposed scenario, the plateau state is caused by a strong wind generated by the heating of the star atmosphere by nonthermal particles accelerated at the jet-star interaction region. The flare itself could be produced by a few clouds of matter lost by the red giant after the initial impact of the jet. In the framework of the proposed scenario, the observations constrain the key model parameters of the source, including the mass of the central black hole: $M_{\rm BH} \simeq 10^9 M_\odot$, the total jet power: $L_{\rm j} \simeq 10^{48}\,{\rm erg\,s^{-1}}$, and the Doppler factor of the gamma-ray emitting clouds, $\delta \simeq 20$. Whereas we do not specify the particle acceleration mechanisms, the potential gamma-ray production processes are discussed and compared in the context of the proposed model. We argue that synchrotron radiation of protons has certain advantages compared to other radiation channels of directly accelerated electrons.

I. INTRODUCTION

3C454.3 is a powerful flat-spectrum radio quasar located at a redshift $z_{\rm rs} = 0.859$. This source is very bright in the GeV energy range; during strong flares, its apparent (isotropic) luminosity can reach $L_\gamma \gtrsim 10^{50}$ erg s^{-1} [e.g. 1, 2, 22, 23]. The mass of the central black hole (BH) in 3C454.3 is estimated in the range $M_{\rm BH} \approx (0.5-4)\times 10^9\,M_\odot$ [9, 12]. This implies an Eddington luminosity $L_{\rm Edd} \approx (0.6-5)\times 10^{47}$erg s^{-1}, which is several orders of magnitude below L_γ. Although the large gap within $L_{\rm Edd}$ and L_γ is naturally explained by relativistic Doppler boosting, the estimates of the jet power during these flares appear, in any realistic scenario, close to or even larger than the Eddington luminosity [9].

The GeV emission from 3C454.3 is highly erratic, with variability timescales as short as 3 hr, as reported, in particular, for the December 2009 flare [2]. The most spectacular flare regarding both variability and gamma-ray luminosity was observed in November 2010 by *AGILE*and *Fermi*/LAT[1, 23] telescopes. During this high state, with the most active phase lasting for 5 days, the apparent luminosity in GeV achieved $L_\gamma \approx 2\times 10^{50}$ erg s^{-1}. Around the flare maximum, the rising time was $t_{\rm r} \approx 4.5$ hr, and the decay time, $t_{\rm f} \approx 15$ hr. The detection of photons with energies up to ≈ 30 GeV, the short variability, and the contemporaneous X-ray flux constrain the Doppler boosting of the emitter to $\delta_{\rm min} \gtrsim 16$ to avoid severe internal $\gamma\gamma$ absorption in the X-ray radiation field [1].

A remarkable feature of the gamma-ray emission from 3C454.3 is the so-called plateau phase revealed during the bright flare in 2010. It is characterized by a long-term brightening of the source, a few weeks before the appearance of the main flare. Such plateau states have been observed by *Fermi*/LATfor three flares [e.g. 1, 2], with the plateau emission being about an order of magnitude fainter than that of the main flare.

Remarkably, the rapid gamma-ray variability of 3C454.3 is accompanied by an activity at lower energies. The simultaneous multiwavelength observations of the source during flares have revealed a strong correlation with optical and X-rays. It has been interpreted as evidence that the gamma-ray source is located upstream from the core of the 43 GHz radio source, which is at a distance $z <$ few pc from the central BH [see, e.g., 13, 14, 24].

Over the recent years, several works have attempted to explain the flaring gamma-ray activity of 3C454.3 within the framework of the standard synchrotron self-Compton (SSC) or external inverse-Compton (EIC) models [9, 11, 15, 21]. In the SSC scenario, it is possible to reproduce the spectral energy distribution (SED) from optical wavelengths to gamma-rays. In these models most of the jet power is (unavoidably) carried by protons, and only a small fraction is contained in relativistic electrons and the magnetic field. The required proton-to-Poynting flux ratio of $L_{\rm p}/L_{\rm B} \sim 100$ is quite large. Such a configuration would be hard to reconcile, at least in the gamma-ray emitting region close to the central BH, with an undisturbed jet which is launched by the Blandford-Znajek [8] type (BZ) process, in which the luminosity of the jet is dominated by Poynting flux and the jet consists of $e^{\pm}$-pairs. In this regard we should mention that recent relativistic magnetohydrodynamical (MHD) simulations of jet acceleration yield much less efficiency of conversion of the magnetic energy into bulk motion kinetic energy; these calculations [17, 18] predict a quite modest ratio $(L_{\rm p} + L_{e^{\pm}})/L_{\rm B} \lesssim 4$.

The jet-RG interaction (JRGI) scenario has been invoked to explain the day-scale flares in the nearby non-blazar type AGN M87 [6, 10], It has been applied also to the TeV blazar PKS 2155−304 [5] to demonstrate that the jet-driven acceleration of debris from the RG atmosphere can explain ultra-fast variability of very high-energy gamma-ray emission on timescales as short as $\tau \sim 200$ s. A distinct feature of the JRGI scenario is the high magnetization ($L_{\rm B}/L_{\rm p,e} \gg 1$) of the relativistic flows located at sub-parsec distances, where the gamma-ray production supposedly takes place. Although the strong magnetic field, $B \geq 10$ G, dramatically reduces the efficiency of the inverse Compton scattering of electrons, it opens an alternative channel of gamma-ray production through synchrotron radiation of protons [3, 20]. The latter can be effectively realized only in the case of acceleration of protons to the highest possible energies, up to 10^{20}eV. Thus the second (somewhat "hidden") requirement of this model is a very effective acceleration of protons with a rate close to the theoretical limit dictated by the classical electrodynamics [4].

It is interesting to note that also inverse Compton models can be accommodated, at least in principle, in the JRGI scenario. Moreover, unlike most of the leptonic models of powerful blazars, in which the requirement of a very low magnetic field, implying a deviation from the equipartition condition by orders of magnitude, generally is not addressed and explained, the JRGI scenario can offer a natural way for leptonic models to be effective assuming that the gamma-ray emission is produced through the inverse Compton scattering in shocked clouds originally weakly magnetized [see 7].

In this work, we show that the JRGI scenario gives a viable mechanism for the explanation of the flares seen in 3C454.3. We also argue that within this model the plateau state can form due to the interaction of the jet with a stellar wind excited by nonthermal (accelerated) particles that penetrate into the red giant atmosphere.

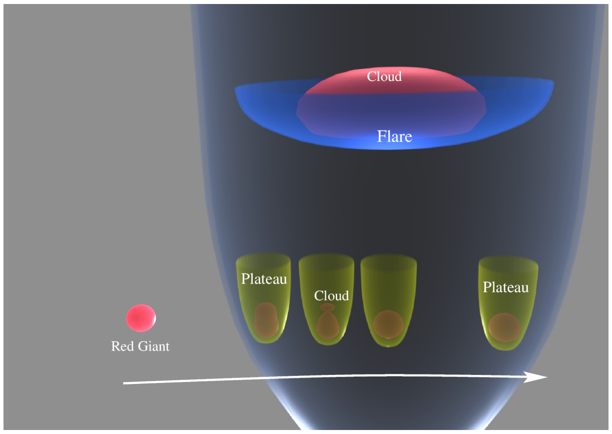

FIG. 1: Sketch for the JRGI scenario, in which a star moving from left to right penetrates into the jet. The star external layers are shocked and carried away, and a cometary tail, origin of the plateu emission, forms. The acceleration and expansion of the bigger clouds from the initially blown-up external layers of the star would lead to the main flare.

II. STAR-JET INTERACTION SCENARIO

In the *fast cooling regime*, the proper intensity of the nonthermal emission, i.e. the intensity in the blob co-moving reference frame, is proportional to the energy released at the jet-blob interface. This energy release can be characterized by a simple dynamical model, which describes the acceleration of the blob by the jet ram pressure. In this model there are just a few relevant parameters that describe the basic properties of the jet and the blob: the jet ram pressure ($P_{\rm j}$) and bulk Lorentz factor ($\Gamma_{\rm j}$), and the blob mass ($M_{\rm b}$) and radius ($r_{\rm b}$; or, equivalently, its cross-section: $S_{\rm b} = \pi r_{\rm b}^2$) [for details, see 5]. The time dependence of the intensity of the jet/blob interaction corrected for the Doppler boosting can be treated as a first-order approximation for the radiation lightcurve.

The mass of the cloud ΔM formed at the initial stage can be estimated by comparing the jet ram pressure,

$$P_0 \simeq \frac{L_{\rm j}}{c\pi\omega_0^2} \qquad (1)$$

with the gravitational force. Here, ω_0 is the jet cross-section at the star crossing height. This gives the following estimate:

$$\Delta M = \frac{\pi P_0 R_*^4}{G M_*} \qquad (2)$$

where M_* and R_* are the RG mass and radius, respectively.

Since the initial size of the expelled cloud should be comparable to the size of the star, it is possible to estimate the cloud expansion time as $t_{\rm exp} \propto 2R_*/c_{\rm s}$, where $c_{\rm s}$ is the sound speed of the shocked material: $c_{\rm s} \approx \left[(4\pi R_*^3/3)\gamma_{\rm g}P_0/M_{\rm c}\right]^{1/2}$. The cloud expansion time is

$$t_{\rm exp} \approx A_{\rm exp}\left(\frac{M_{\rm c}}{\gamma_{\rm g}R_* P_0}\right)^{1/2}, \qquad (3)$$

where $\gamma_{\rm g} = 4/3$ is the plasma adiabatic coefficient, and according to the RHD simulation by [10], a value of 1.5 can be adopted for $A_{\rm exp}$.

The blob acceleration occurs on a timescale of [5]

$$t_{\rm acc} \approx \begin{cases} \frac{z_0}{c} & \text{if} \quad D<1 \\ \frac{z_0}{c}\frac{1}{D} & \text{if} \quad D>1\,. \end{cases} \qquad (4)$$

The D–parameter that will be often used in the paper has a simple meaning. It is a dimensionless inverse mass of the blob:

$$D \equiv \frac{P_0 \pi r_{\rm b}^2 z_0}{4c^2 M_{\rm b}\Gamma_0^3}\,. \qquad (5)$$

The above timescale corresponds to the blob acceleration in the laboratory reference frame. However, since the blob gets accelerated towards the observer, the emission delay, as seen by the observer, should be approximately corrected by a factor of $1/(2\Gamma_0^2)$. Thus, the observed peak of the emission should be delayed by a time interval of

$$\Delta t = t_{\rm exp} + t_{\rm acc}/(2\Gamma_0^2)\,. \qquad (6)$$

The emission produced by lighter clouds allows an estimation of the time required for the star to cross the jet. Once the star enters into the jet, the process of jet-star interaction should proceed steadily, with the production of these lighter clouds being roughly constant on average. Thus, the whole duration of the light cloud-associated emission, if observed, can be taken as a direct measurement of the jet crossing time $t_0 \approx 2\omega_0/V_{\rm orb}$, where $V_{\rm orb} \lesssim \sqrt{2GM_{\rm BH}/z_0}$ is the star velocity. Adopting the paradigm of magnetically-accelerated jets, it is possible to derive a very simple expression for this timescale:

$$t_0 \gtrsim 2^{3/2} z_0/c\,. \qquad (7)$$

In this way, the duration of the jet-star interaction is determined by the interaction distance from the central BH.

Assuming a fixed efficiency ξ in the blob reference frame for the transfer of jet power to nonthermal gamma rays (where $\xi \ll 1$), and correcting for Doppler boosting, one can estimate the luminosity of a blob:

$$L_\gamma = 4\xi c F_{\rm e} P_0 \Gamma_0^2 \pi r_{\rm b}^2\,, \qquad (8)$$

where the correction function $F_{\rm e}$ depends on time; or, equivalently, on the blob location in the jet. We note that the structure of the jet, i.e., the dependence of the jet Lorentz factor on z, determines the actual dependence of $F_{\rm e}$ on z.

The maximum value of $F_{\rm e}$ monotonically depends on the D parameter, approaching a value of 0.4 if $D \gtrsim 1$ and being ~ 0.1 for $D = 0.1$. This relatively weak dependence allows us to derive the maximum blob luminosity. Also it is possible to obtain an estimate of the total energy emitted by a blob or an ensemble of sub-blobs as a result of the fragmentation of the original cloud ($M_{\rm c} = \sum M_{\rm b}$),

$$E_\gamma \simeq 8\xi \bar{F}_{\rm e} M_{\rm b/c} c^2 \Gamma_0^3\,, \qquad (9)$$

which accounts for the total energy transferred by the jet to a blob during the acceleration process, $M_{\rm b}c^2\Gamma_0$, and for the anisotropy of the emission due to relativistic effects represented by the factor Γ_0^2.

III. THE NOVEMBER 2010 FLARE

A. General structure of the active phase

The total apparent energy of the GeV gamma-ray radiation detected during the flare observed from 3C454.3 in November 2010 was about $E_{\rm tot} \approx L_\gamma \Delta t/(1+z_{\rm rs}) \approx 2.3 \times 10^{55}$ erg. The exceptionally high flux during this period allows the derivation of a very detailed lightcurve, as seen from Figure 1 in [1]. The nonthermal activity lasted for $t_{\rm full} \sim 80$ days. The onset of the activity period was characterized by a plateau stage. During the first $t_{\rm pl} \sim 13$ days, a rather steady flux was detected, with an apparent luminosity $L_{\rm pl} \approx 10^{49}$ erg s^{-1}. The plateau stage was followed by an exceptionally bright flare, the total duration which was $t_{\rm fl} \sim 5$ days, with a rise time of $t_{\rm r} \sim 4.5$ h. The maximum flux reached was 7×10^{-5} ph cm^{2}s^{-1}, which corresponds to a luminosity of $L_\gamma \simeq 2\times10^{50}$erg s^{-1}. The final stage of the flare phase was characterized by variable emission with a flux approximately a factor of ~ 5 weaker than the main flare, but still a factor of ~ 2 above the plateau level.

The observed luminosity of the plateau phase allow us to determine a lower limit on the star mass-loss rate, which can be derived by differentiating equation (9):

$$\dot{M}_* \approx 10^{23} L_{\rm pl,49}\xi^{-1}\Gamma_{0,1.5}^{-3}\,{\rm g\ s^{-1}}\,, \qquad (10)$$

where $L_{\rm pl,49} = L_{\rm pl}/10^{49}\,{\rm erg\ s^{-1}}$.

To evaluate the feasibility of the JRGI scenario for the 3C454.3 main flare, it is necessary to check whether the flux, the total energy release, and the flare delay with respect to the onset of the plateau, are well described by equations 6, 8, and 9 for a reasonable choice of jet/star properties.

A total energy budget of the flare of $\sim 2 \times 10^{55}$erg is feasible, according to equation (9), if

$$M_{\rm c,30}\Gamma_{0,1.5}^3 \approx \frac{0.04 E_{\gamma,55}}{\xi \bar{F}_{\rm e}} \approx \frac{0.1}{\xi \bar{F}_{\rm e}}\,, \qquad (11)$$

where $M_{\rm c,30} = M_{\rm c}/10^{30}$ g is the mass of the blown up RG envelop (i.e. the initially formed cloud). This requirement appears to be very close to the one provided by equation 2:

$$M_{\rm c,max} \approx \frac{5\times 10^{29}}{F_{\rm e,max}} R_{*,2}^4 M_{*,0}^{-1} L_{\gamma,50} \Gamma_{0,1.5}^{-2} S_{\rm b,32}^{-1}\,{\rm g}\,, \qquad (12)$$

where $R_{*,2} = R_*/10^2 R_\odot$ and $M_{*,0} = M_*/M_\odot$, respectively.

The second term in equation 6 is expected to be short compared to the duration of the plateau phase, even for $D \sim 0.1$, and thus the duration of the initial plateau phase constrains the expansion time (see equation (3)):

$$t_{\rm exp} \approx 5.4 \times 10^6 F_{\rm e,max}^{1/2} \xi^{1/2} \times$$

$$M_{\rm c,30}^{1/2} R_{*,2}^{-1/2} L_{\gamma,50}^{-1/2} \Gamma_{0,1.5} S_{\rm b,32}^{1/2}\,{\rm s}\,. \qquad (13)$$

[1] found that the emission of the main flare consisted of 5 components (see Figure 2 in that work): a nearly steady contribution, like a smooth continuation of the plateau emission, and 4 sub-flares of similar duration and energetics. In the framework of the JRGI scenario, such a description is very natural. The steady component would be attributed to light clouds, continuously ejected by the star, and the four subflares would correspond to much heavier blobs formed out of the blown-up stellar envelop during the initial stage. On the other hand, the decomposition of the main flare in four sub-flares implies a strict limitation on the variability timescale. The flare rise/decay timescales should be longer than the blob light crossing time corrected for the Doppler boosting. Since the shortest variability scale was $\sim 5{\rm h}/(1+z_{\rm rs}) \sim 10^4$ s, the maximum possible size of the emitting blobs can be estimated as:

$$r_{\rm b} \approx 10^{16} \Gamma_{0,1.5}\,{\rm cm}\,. \qquad (14)$$

If the jet is magnetically driven, this size constraint can be expressed through the mass of the central BH:

$$\frac{r_{\rm b}}{\omega} < 0.5\, M_{\rm BH,9}^{-1}\,, \qquad (15)$$

which is restrictive only in the case of $M_{\rm BH,9} \gg 1$. For $M_{\rm BH,9} \lesssim 1$, the blobs can cover the entire jet without violating the causality constraint.

In summary, if the flare detected with *Fermi*/LATwas produced by an RG entering into the jet, the jet properties should satisfy to the restrictions imposed by the flux level, total energy release, and the duration of the plateau stage, respectively. Interestingly, this set of equations allows the derivation of a *unique* solution, which can constrain all the key parameters through the value of the D parameter:

$$P_0 = 3 \times 10^6 \frac{F_{\rm e,max}^{1.5} D^{1.5}}{\bar{F}_{\rm e}^{2.5} \xi z_{0,17}^{1.5}}\,{\rm erg\,cm^{-3}}\,, \qquad (16)$$

$$M_{\rm c} = 4 M_{\rm b} = 5 \times 10^{30} \frac{F_{\rm e,max}^{1.5} D^{1.5}}{\bar{F}_{\rm e}^{2.5} \xi z_{0,17}^{1.5}}\,{\rm g}\,, \qquad (17)$$

$$\Gamma_0 = 8 \left(\frac{\bar{F}_{\rm e} z_{0,17}}{F_{\rm e,max} D}\right)^{0.5}\,, \qquad (18)$$

and

$$S_{\rm b} = 8 \times 10^{30} \frac{z_{0,17}^{0.5} \bar{F}_{\rm e}^{1.5}}{F_{\rm e,max}^{1.5} D^{0.5}}\,{\rm cm}^2. \qquad (19)$$

The lower limit on the jet luminosity is

$$L_{\rm j} > c S_{\rm b} P_0 = 8 \times 10^{47} z_{0,17}^{-1} \xi^{-1} \frac{D}{\bar{F}_{\rm e}}\,{\rm erg\,s^{-1}}\,, \qquad (20)$$

which exceeds the Eddington limit for the mass of the central BH $M_{\rm BH} \sim 5 \times 10^8 M_\odot$. To assess the feasibility of such a strongly super-Eddington jet remains out of the scope of this paper, although we note that [19] have presented observational evidence indicating that such jets may not be uncommon.

The coherent picture emanating from the jet properties derived above suggests that the JRGI scenario can be responsible for the flare detected from 3C454.3 for a solution of the problem with a reasonable set of model parameters. This solution is designed to satisfy the requirements for (i) the total energy; (ii) the peak luminosity; and (iii) the duration of the plateau phase. Therefore, some additional observational tests are required to prove the feasibility of the suggested scenario.

Finally, the flare raise time, which is related to the blob acceleration timescale (see equation 4), can be calculated for the obtained solution. Interestingly, in the limit of small D-values, this timescale appears to be independent on D, the only remaining free parameter, and matches closely the detected raise time of $t_{\rm r} \sim 4.5$h:

$$t_{\rm acc}/\left(2\Gamma_{\rm b}^2\right) \simeq 5{\rm h}\,. \qquad (21)$$

This agreement can be treated as a cross-check that shows the feasibility of the proposed scenario.

IV. MODELING THE LIGHTCURVE AND THE SPECTRUM

To check whether JRGI plus synchrotron radiation can explain the observations in the case of magnetically dominated jets (i.e., $k = 1$), we have computed the lightcurve of the November 2010 flare and the SED for one of its subflares. The radiation output was assumed to be dominated by proton synchrotron, being external or synchrotron self-Compton neglected due to the strong magnetic field.

To derive the lightcurve, equation 8 has been used. In Figure 2, a computed lightcurve that approximately mimics the November 2010 flare is presented. The lightcurve has been obtained assuming four subflares of total (apparent) energy of 10^{55} erg each, plus a plateau component with luminosity of 2×10^{49} erg s^{-1}. For each subflare, we have adopted $D = 0.1$. The normalization of the lightcurve has been determined adopting the following values: the Lorentz factor $\Gamma_0 = 28$, the ram pressure $P_{\rm j} = 3 \times 10^6$ erg cm^{-3}, blob radius $r_{\rm b} = 2.7 \times 10^{15}$ cm and $\xi = 0.3$. These parameters imply a minimum jet luminosity of $L_{\rm j} = 2.3 \times 10^{48}$ erg s^{-1}. The remaining parameters for the emitter are $z_0 = 1.3\times10^{17}$ cm and $M_{\rm b} = 1.3\times10^{30}$ g. The corresponding mass of the matter lost by the RG to explain the four subflares is 5×10^{30} g, not far from the upper-limit given in equation 2.

To calculate the SED, we have adopted a spectrum for the injected protons $Q \propto E^{-p} \exp(-E/E_{\rm cut})$, and an homogeneous (one-zone) emitter moving towards the observer with Lorentz factor $\Gamma_{\rm b} = 12$. The minimum proton Lorentz factor has been taken equal to the shock Lorentz factor in the blob frame, i.e. $E_{\rm min} = \Gamma_0/\Gamma_{\rm b} m_{\rm p}c^2$. The cutoff energy, $E_{\rm cut}$, has been obtained fixing $\eta = 4 \times 10^3$, i.e., a relatively modest acceleration efficiency. For the maximum proton energy, i.e. how far beyond the cutoff the proton energy is considered, we adopted two values: $E_{\rm max} = \infty$ and $E_{\rm max} = 3E_{\rm cut}$. Regarding the latter case, we note that assuming a sharp high-energy cut is very natural. The injection spectrum was selected to be hard, $p = 1$, to optimize the required energetics.

In Figure 3, the SED of a subflare is shown. The impact of the internal absorption on the gamma-ray spectrum is negligible, although the emission of the secondary pairs appears in the energy band constrained by optical measurements [14]. For the chosen model parameters, the synchrotron secondary component goes right through the optical observational constraints, and for slightly higher z_0-values, the secondary emission will be well below the optical points. Also, we note that the obtained spectrum does not violate the X-ray upper-limits obtained by *Swift*.

To illustrate the impact of external $\gamma\gamma$ absorption, we have introduced a photon field peaking at 40 eV with a luminosity 4×10^{46} erg s^{-1}, produced in a ring with radius 10^{18} cm at $z = 0$ around the jet base. Two photon fields have been adopted, a black body and one represented by a δ-function, to simulate the impact of a dominant spectroscopic line. As seen in Figure 3, the impact of such an external field can be important. The treatment of the secondary emission of the produced pairs is beyond the scope of this work.

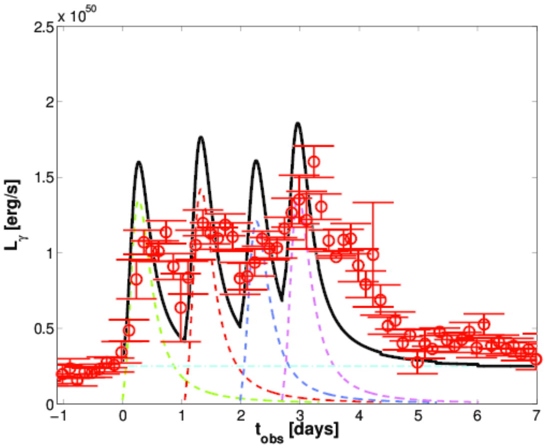

FIG. 2: Lightcurve computed adopting the parameters $L_{\rm j} = 2.3 \times 10^{48}$ erg s^{-1}, $z = 1.33 \times 10^{17}$ cm $\Gamma_{\rm j} = 28$, $M_{\rm c} = 1.3 \times 10^{30}$ g, $r_{\rm c} = 2.7 \times 10^{15}$ cm, and $\xi = 0.3$. We show 4 subflares (dashed lines), plateau background (dot-dashed line), and the sum of all of them (solid line). The observational data points and error bars are obtained from the *Fermi*/LAT3h binned count rates and photon index using luminosity distance of $D_{\rm L} = 5.5$Gpc and assuming a pure powerlaw spectrum between 0.1 and 5 GeV.

In addition to optical photons, radio emission was also detected at the flare epoch and thought to be linked to the gamma-ray activity [14]. This radiation is strongly sensitive to the details of the flow dynamics, and at this stage we will not try to interpret radio observations. However, we note that the energetics involved in gamma-ray production is very large, and JRGI comprehends complex magnetohydrodynamical and radiative processes, so it could easily accommodate the presence of a population of radio-emitting electrons at $z \geq z_{\rm flare}$.

Swift X-rays could be also linked to the JRGI activity. X-rays may come from secondary pairs produced via pair creation, or from a primary population of electrons(/positrons). However, as with radio data, given the complexity of the problem we have not tried at this stage to explain the X-ray emission contemporaneous to the GeV flare.

V. DISCUSSION

The observations of 3C454.3 with *Fermi* revealed several quite puzzling features, in particular the peculiar lightcurve, with a nearly steady plateau phase that was interrupted by an exceptionally bright flare.

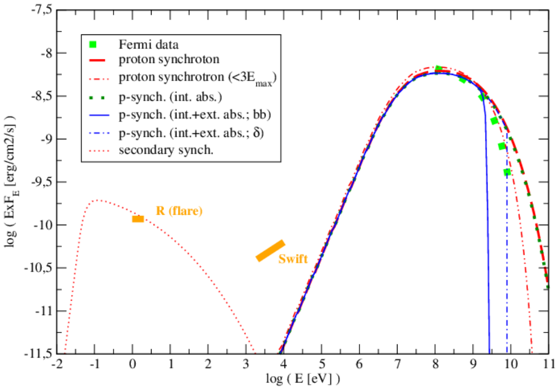

FIG. 3: Computed SED of the synchrotron emission for a subflare of the 2010 November. The thick dashed line shows intrinsic gamma-ray emission for the case of $E_{\rm max} = \infty$. Dotted and dot-dot-dashed line shows gamma-ray spectra corrected for internal absorption only for $E_{\rm max} = \infty$ and $E_{\rm max} = 3E_{\rm cut}$, respectively. The thin solid and the dot-dashed lines correspond to the cases when absorption is dominated by a black body and a monoenergetic photon field, respectively. The computed synchrotron SED of the secondary pairs produced via internal pair creation is also shown (dotted line). The parameters of the flare are the same as in Figure 2. The shown observational data are from *Fermi*/LAT, Swift [1], and the flux in the R band [14].

The detected flux corresponds to an apparent luminosity of $2 \times 10^{50}\,{\rm erg s^{-1}}$, which almost unavoidably implies a presence of a very powerful jet [see e.g. 9, 16]. In the case of powerful jets, the JRGI scenario should proceed in a quite specific way as compared to other cases already considered in the literature [5]. In particular, the mass of the material initially removed from the star might be very large, resulting in rather long cloud expansion and acceleration timescales, the main flare being significantly delayed with respect to the moment of the star entrance into the jet. The plateau emission would otherwise start just after the jet penetration, and come from the jet crushing of lighter clouds ejected from the stellar surface while the star travels through the jet. The duration of the plateau phase would be determined by the time required by the main cloud to expand and accelerate.

We have studied the lightcurve obtained with *Fermi* in the context of the JRGI scenario aiming to satisfy three main properties of the flare: total energy, maximum luminosity and duration of the plateau stage. It was shown that the key properties of the jet, i.e. the jet ram pressure (linked to its luminosity) and Lorentz factor, as well as the cloud/blob characteristics, i.e. mass and cross section, can be reconstructed as functions of the dimensionless parameter D. It was also shown that in the limit of small D-values, the parameter space is less demanding concerning the jet luminosity, and the key characteristics of the model saturate at values independent of D, which allows conclusive cross-checks of the scenario. In particular, the flare raise time appeared to be an independent parameter, with its value of 5 h closely matching the rising time of of 4.5 h obtained observationally. Furthermore, it was shown (see [16]) that for the inferred jet properties the jet-induced stellar wind can provide a mass-loss rate large enough to generate a steady emission component with a luminosity comparable to that of the plateau.

Although the analysis of different radiation channels involves additional assumptions regarding the spectrum of the nonthermal particles and density of the target fields, it was possible to show that for magnetic fields not far below equipartition (as expected in a magnetically launched jet) all the conventional radiation channels can be discarded, and the emission detected with *Fermi* can be produced through proton synchrotron emission (unless $\eta \to 1$, making electron synchrotron also feasible). We note that in this case the emission from pairs created within the blob may also explain the reported optical enhancement at the flare epoch.

Since the duration of the expansion phase determines the delay between the onset of the plateau phase and the flare itself, it is important to check whether the suggested scenario is consistent with other flares registered with *Fermi* from the source, e.g., in December 2009 and April 2010 [2, 22]. This issue can be addressed through a simple scaling that relates the duration of the plateau phase to the total energy released during the active phase: $t_{\rm pl} \propto E_{\rm tot}^{1/2}$. Therefore, for the previous events, with energy releases 1-2 orders of magnitude smaller than that of the November 2010 flare, a rough estimation of the plateau duration gives plateau durations between 1.3 and 4 days, consistent with observations.

Acknowledgments

The authors are thankful to S. Kelner for useful discussions and Benoit Lott for kindly provided observational data. BMV acknowledge partial support by JSPS (Japan Society for the Promotion of Science): No.2503786, 25610056, 26287056, 26800159. BMV also MEXT (Ministry of Education, Culture, Sports, Science and Technology): No.26105521 and RFBR grant 12-02-01336-a. V.B.-R. acknowledges support by the Spanish Ministerio de Ciencia e Innovación (MICINN) under grants AYA2010-21782-C03-01 and FPA2010-22056-C06-02. V.B.-R. acknowledges financial support from MINECO through a Ramón y Cajal fellowship. This research has been supported by the Marie Curie Career Integration Grant 321520.

---

[1] A. A. Abdo and et al. Fermi Gamma-ray Space Telescope Observations of the Gamma-ray Outburst from 3C454.3 in November 2010. *ApJ*, 733:L26, June 2011.

[2] M. Ackermann and et al. Fermi Gamma-ray Space Telescope Observations of Gamma-ray Outbursts from 3C 454.3 in 2009 December and 2010 April. *Astrophys. J.* , 721:1383–1396, Oct. 2010.

[3] F. A. Aharonian. TeV gamma rays from BL Lac objects due to synchrotron radiation of extremely high energy protons. *New Astronomy*, 5:377–395, Nov. 2000.

[4] F. A. Aharonian. Proton-synchrotron radiation of large-scale jets in active galactic nuclei. *MNRAS*, 332:215–230, May 2002.

[5] M. V. Barkov, F. A. Aharonian, S. V. Bogovalov, S. R. Kelner, and D. Khangulyan. Rapid TeV Variability in Blazars as a Result of Jet-Star Interaction. *Astrophys. J.* , 749:119, Apr. 2012.

[6] M. V. Barkov, F. A. Aharonian, and V. Bosch-Ramon. Gamma-ray Flares from Red Giant/Jet Interactions in Active Galactic Nuclei. *Astrophys. J.* , 724:1517–1523, Dec. 2010.

[7] M. V. Barkov, V. Bosch-Ramon, and F. A. Aharonian. Interpretation of the Flares of M87 at TeV Energies in the Cloud-Jet Interaction Scenario. *Astrophys. J.* , 755:170, Aug. 2012.

[8] R. D. Blandford and R. L. Znajek. Electromagnetic extraction of energy from Kerr black holes. *MNRAS*, 179:433–456, May 1977.

[9] G. Bonnoli, G. Ghisellini, L. Foschini, F. Tavecchio, and G. Ghirlanda. The γ-ray brightest days of the blazar 3C 454.3. *MNRAS*, 410:368–380, Jan. 2011.

[10] V. Bosch-Ramon, M. Perucho, and M. V. Barkov. Clouds and red giants interacting with the base of AGN jets. *A&A*, 539:A69, Mar. 2012.

[11] G. Ghisellini, L. Foschini, F. Tavecchio, and E. Pian. On the 2007 July flare of the blazar 3C 454.3. *MNRAS*, 382:L82–L86, Nov. 2007.

[12] M. Gu, X. Cao, and D. R. Jiang. On the masses of black holes in radio-loud quasars. *MNRAS*, 327:1111–1115, Nov. 2001.

[13] S. G. Jorstad and et al. Flaring Behavior of the Quasar 3C 454.3 Across the Electromagnetic Spectrum. *Astrophys. J.* , 715:362–384, May 2010.

[14] S. G. Jorstad, A. P. Marscher, M. Joshi, N. R. MacDonald, T. L. Scott, K. E. Williamson, P. S. Smith, V. M. Larionov, I. Agudo, and M. Gurwell. Parsec-Scale Jet Behavior of the Quasar 3C 454.3 during the High Gamma-Ray States in 2009 and 2010. *arXiv:1205.0520*, May 2012.

[15] K. Katarzyński and G. Ghisellini. Dissipation of jet bulk kinetic energy in powerful blazars. *A&A*, 463:529–537, Feb. 2007.

[16] D. V. Khangulyan, M. V. Barkov, V. Bosch-Ramon, F. A. Aharonian, and A. V. Dorodnitsyn. Star-Jet Interactions and Gamma-Ray Outbursts from 3C454.3. *Astrophys. J.* , 774:113, Sept. 2013.

[17] S. S. Komissarov, M. V. Barkov, N. Vlahakis, and A. Königl. Magnetic acceleration of relativistic active galactic nucleus jets. *MNRAS*, 380:51–70, Sept. 2007.

[18] S. S. Komissarov, N. Vlahakis, A. Königl, and M. V. Barkov. Magnetic acceleration of ultrarelativistic jets in gamma-ray burst sources. *MNRAS*, 394:1182–1212, Apr. 2009.

[19] M. López-Corredoira and M. Perucho. Kinetic power of quasars and statistical excess of MOJAVE superluminal motions. *A&A*, 544:A56, Aug. 2012.

[20] A. Mücke and R. J. Protheroe. A proton synchrotron blazar model for flaring in Markarian 501. *Astroparticle Physics*, 15:121–136, Mar. 2001.

[21] M. Sikora, R. Moderski, and G. M. Madejski. 3C 454.3 Reveals the Structure and Physics of Its "Blazar Zone". *Astrophys. J.* , 675:71–78, Mar. 2008.

[22] E. Striani and et al. The Extraordinary Gamma-ray Flare of the Blazar 3C 454.3. *Astrophys. J.* , 718:455–459, July 2010.

[23] S. Vercellone and et al. The Brightest Gamma-Ray Flaring Blazar in the Sky: AGILE and Multi-wavelength Observations of 3C 454.3 During 2010 November. *ApJ*, 736:L38, Aug. 2011.

[24] A. E. Wehrle, A. P. Marscher, S. G. Jorstad, M. A. Gurwell, M. Joshi, N. R. MacDonald, K. E. Williamson, I. Agudo, and D. Grupe. Multiwavelength Variations of 3C 454.3 during the 2010 November to 2011 January Outburst. *Astrophys. J.* , 758:72, Oct. 2012.

The Extragalactic sky with the High Energy Stereoscopic System.

D. A. Sanchez
Laboratoire d'Annecy-le-Vieux de Physique des Particules, Université de Savoie, CNRS/IN2P3
On behalf of the H.E.S.S. collaboration

The number of extragalactic sources detected at very hight energy (VHE, E>100GeV) has dramatically increased during the past years to reach more than fifty. The High Energy Stereoscopic System (H.E.S.S.) had observed the sky for more than 10 years now and discovered about twenty objects. With the advent of the fifth 28 meters telescope, the H.E.S.S. energy range extends down to 30 GeV. When H.E.S.S. data are combined with the data of the Fermi Large area Telescope, the covered energy range is of several decades allowing an unprecedented description of the spectrum of extragalactic objects. In this talk, a review of the extragalactic sources studied with H.E.S.S. will be given together with first H.E.S.S. phase II results on extragalactic sources.

1. The H.E.S.S. array

The High Energy Stereoscopic System (H.E.S.S.) is located near the Gamsberg mountain in Namibia at an altitude of 1800 meters. H.E.S.S. detects γ-ray photons by recording the Cherenkov light produced by the electromagnetic shower resulting from the interaction of the photons with the atmosphere.

The Phase I of the project was completed in December 2003. At this time the array was made of four 12-meters telescopes. Each telescope has a camera composed of 960 Photo-multipliers (PMTs) and works in stereoscopic mode.

The H.E.S.S. Phase I array has a field of view of 5 degrees, an angular resolution of 0.1 degree for an energy threshold down to 100 GeV. The array is taking data for more than 10 years now and has increased the catalogue of sources detected in the very high energy range (VHE, E >100 GeV) and our knowledge of the field. H.E.S.S. has discovered more than 80 objects (galactic or extragalactic, Fig. 1), performed a deep Galactic plane survey, dark matter searches, multiwavelength campaigns with other instruments and studies of the extragalactic background light with blazars.

One of the aims of H.E.S.S. is the detection of gamma-ray bursts (GRBs). While no GRB has been detected so far in the VHE range, more than 20 follow-up have been performed [3]. H.E.S.S. also monitors variable and bright objects and responds to target of opportunity in order to better know the mechanisms that produce the variability of blazars.

The experiment entered into its Phase II with the addition of a fifth telescope (named CT5) placed in the middle of the array. The dish is 32.6 meters by 24.3 meters, equivalent to 28-meters circular dish for a focal length of 36 meters. The telescope is equipped with a Alt-Az mount [11]. The camera composed of 2048 PMTs for a total weight of ≈ 3 tons, can record 3600 images per second [9] and is mounted on an autofocus system. A picture of this telescope is show on figure 2. The field of view of this telescope is 3.5 degrees for an angular resolution from ≈ 0.4 degree to less than 0.1. The energy coverage of the H.E.S.S. experiment is then extended down to energies of a few tens of GeV. Characteristics of the CT5 telescope are summarized in Table I.

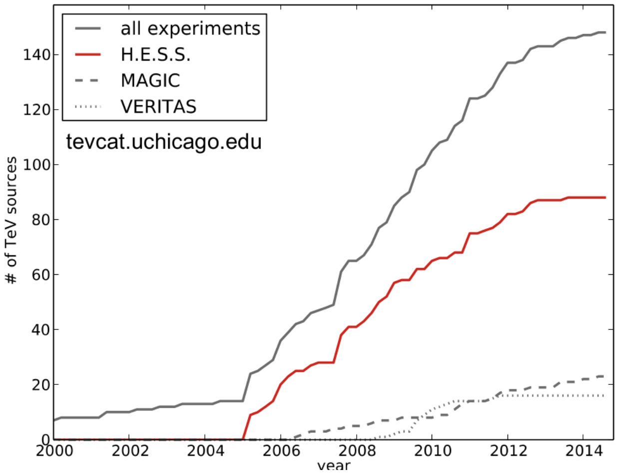

Figure 1: Extragalactic and Galactic sources detected in the VHE range. The gray line is the total of discovered object while the red one is the contribution of the H.E.S.S. experiment.

H.E.S.S. Phase II is the first hybrid array of Cherenkov telescopes and is designed to work in different configurations. Data can be taken by CT5 only in the so-called *Mono mode*. The *hybrid mode* involves all five telescopes for a better sensitivity in the entire energy range. Stereoscopic observations with only the four 12-meters telescopes are still possible. The ability to split the array in 2 (CT5 Mono mode + the four 12 meters telescopes) allows to increase the observation time which is rather low for such an experiment (≈ 1000 hours per year).

In this work, the last results of the H.E.S.S. Phase I array are presented and new preliminary results of observations carry in CT5 Mono mode on extragalactic targets are given.

Figure 2: The fifth H.E.S.S. telescope.

Table I Characteristics of the CT5 telescope.

Mount type Height of elevation axis	Alt-Az mount 24 m
Dish Dimensions Focal length Total mirror area	32.6 m by 24.3 m equivalent to 28 m circular dish 36 m 614 m^2
Photo sensors Pixel size FoV Camera weight	2048 42 mm 3.5 degrees 3.0 tons

2. Recent H.E.S.S. phase I results

2.1. Long term monitoring of PKS 2155-304

The high frequency peaked BL Lac (HBL) object PKS 2155-304 is the brightest object of the southern sky in VHE. This source has been the target of several campaigns in the past involving H.E.S.S. [1, 4] and other instruments. This HBL is also famous for the flare that happened in June 2006 with variation at the minute time scale [6].

Due to its brightness, the source has been monitored by the H.E.S.S. telescopes since 2004. Data taken between 2004 and 2012, except the June/July exposures where the sources underwent a flare, were analysed using a Hillas-type analysis [7]. The nightly binned light curve above 300 GeV has been used for the analysis and the corresponding mean flux is $2.02 \times 10^{-11}\mathrm{cm}^{-2}\,\mathrm{s}^{-1}$.

The power spectral density (PSD) has been calculated (Fig 3) and fitted with a power law of index β. A forward folding method together with a likelihood estimator described in [12] were used to fit the model to the data. The best fit value is $\beta = 0.9 \pm 0.2$ for the data set presented here which corresponds to the source being at a low flux state. This has to be compared with the value found during the 2006 flare $\beta = 2$ but on short time-scales. This may be a sign of a break in the PSD with a change of β from 2 to 1 or a change in the PSD between the two flux states.

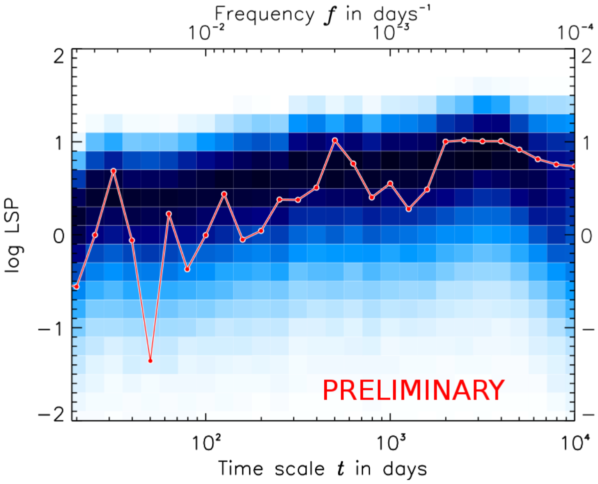

Figure 3: Power Spectral density of PKS 2155-304 (red line and dots) obtained with the H.E.S.S. data. The color area gives the results of the simulations used to fit the data.

2.2. The 2012 Flare of PG 1553+113

In March 2012, the HBL PG 1553+113 underwent a flare observed by H.E.S.S. during 2 nights. This data set have been used to determine the source redshift and possible Lorentz invariance violation (LIV) effects. The redshift has been constrained to be $z = 0.49 \pm 0.04$ and an lower limit on the energy scale at which LIV effects take place has been set to $E_{QG,1} > 4.10{\times}10^{17}$ GeV and $E_{QG,2} > 2.10{\times}10^{10}$ GeV for linear and quadratic LIV effects. More details can be found in [14] and [8]

3. H.E.S.S. II first results on extragalactic objects

Since the inauguration on September 2012, CT5 has been in a commissioning phase. The HBLs PKS 2155-304 and PG 1553+113 serve as calibration targets. The analysis of the data was performed using the Model analysis [10] with cuts adapted for the Mono observations with CT5.

A. PG 1553+113

This source has a soft spectrum in the VHE energy range, H.E.S.S. measured a spectral index of

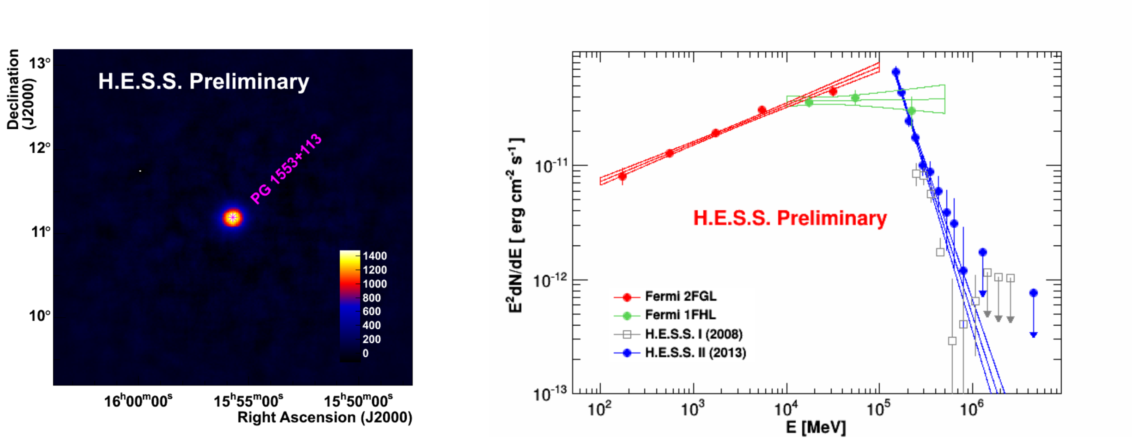

Figure 4: Excess map (left) and spectral energy distribution (right) of PG 1553+113 obtained with CT5 in Mono mode. The CT5 SED is given by the blue points and contour. *Fermi* 2FLG (red) and 1FHL (blue) results are also presented. The gray points are archival data from [2].

Table II Preliminary results on PG 1553+113 obtained with CT5 in 2014.

Live Time	15.1 h
Excess	2508 γ
Significance	26.6 σ
Zenith	$\approx 35°$
Rate	$2.77 \pm 0.11\gamma$/min

Table III Preliminary results on PKS 2155-304 obtained with CT5 in 2014.

Live Time	42.9 h
Excess	4442 γ
Significance	29.7 σ
Zenith	$\approx 21°$
Rate	$1.72 \pm 0.06\gamma$/min

$\gamma = 4.6 \pm 0.6$ [2]. This makes it well suited for observations with CT5. A total of 15.1 hours of live time has been analysed and an excess of more than 2500 events has been found. This corresponds to $2.77 \pm 0.11\gamma$ per minutes for a significance of 26.6 sigma (Table II).

An excess map around the coordinates of the object and the resulting spectral energy distribution of the source are given on figure 4. The spectrum measured with CT5 is compared with the non contemporaneous data from the *Fermi* second source catalogue (2FGL) [13] and first high energy catalogue (1FHL) [16].

B. PKS 2155-304

PKS 2155-304 is naturally a good target for calibration purposes and has been observed for a total live time of 42.9 hours in 2013. The analysis yields an excess of more the 4400 events for a detection at a 29.7 σ level (Table III). Excess map of the field of view and SED are shown on figure 5. The 2FGL and 1FHL are also used for comparison.

A large part of the data were taken during a multiwavelength campaign with NuSTAR and *Fermi*. These data were used to build the most precise SED of this object to date: NuSTAR extended the X-ray spectrum up to 79 keV and *Fermi* PASS 8 data were used. More details and results are given in [15] and in a forthcoming publication.

4. CT5 as a transients machine

One of the main goals of the H.E.S.S. Phase II is to study the variability on short time-scales. Figure 6 presents the differential sensitivity of CT5 and *Fermi* as a function of time. Below 10^7 seconds, CT5 is clearly much more sensitive that the LAT above 25 GeV. This opens a new window for the detection of GRBs in this energy range. An alert system has been developed to reply to GCN alerts and an automatic re-pointing procedure is in place in case of such an alert. CT5 can, in such case, be on target within a minute [11] allowing prompt observations.

5. Conclusions

The H.E.S.S. array is taking data now since more than 10 years and has allowed many discoveries. With the advent of the Phase II of the experiment, a new window has been opened in the 30 GeV-100 GeV energy range. After a commissioning phase, CT5 is now running running in a normal operation mode.

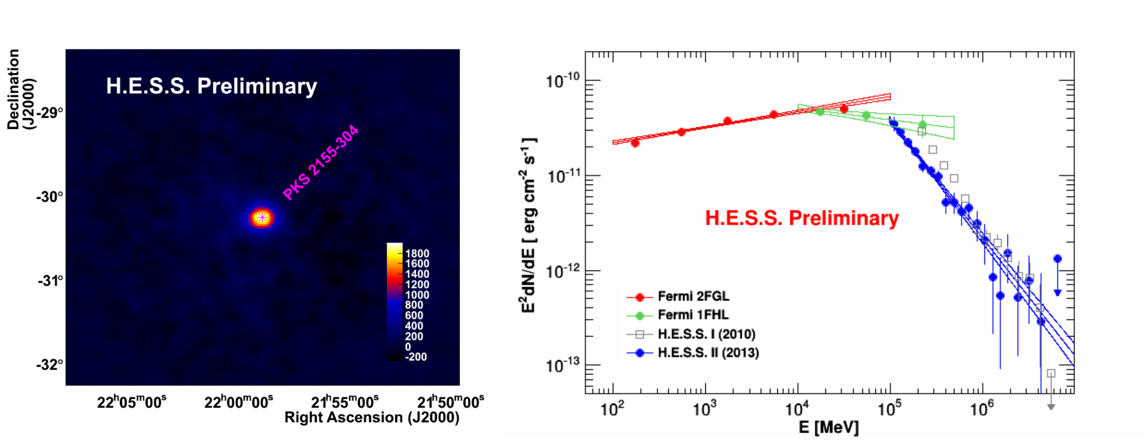

Figure 5: Excess Map (left) and spectral energy distribution (right) of PKS 2155-304 obtained with CT5 in Mono mode. The CT5 SED is given by the blue points and contour. *Fermi* 2FLG (red) and 1FHL (blue) results are also presented. The gray points are archival data from [5].

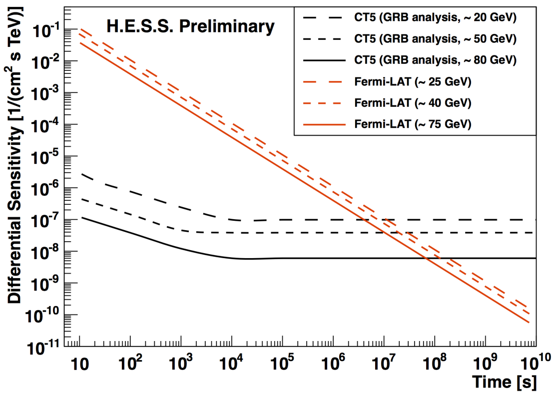

Figure 6: Comparison of the differential sensitivity of the *Fermi*-LAT and CT5 as a function of time and for different energy thresholds.

Acknowledgments

The support of the Namibian authorities and of the University of Namibia in facilitating the construction and operation of H.E.S.S. is gratefully acknowledged, as is the support by the German Ministry for Education and Research (BMBF), the Max Planck Society, the French Ministry for Research, the CNRS-IN2P3 and the Astroparticle Interdisciplinary Programme of the CNRS, the U.K. Science and Technology Facilities Council (STFC), the IPNP of the Charles University, the Polish Ministry of Science and Higher Education, the South African Department of Science and Technology and National Research Foundation, and by the University of Namibia. We appreciate the excellent work of the technical support staff in Berlin, Durham, Hamburg, Heidelberg, Palaiseau, Paris, Saclay, and in Namibia in the construction and operation of the equipment.

The *Fermi*-LAT Collaboration acknowledges support for LAT development, operation and data analysis from NASA and DOE (United States), CEA/Irfu and IN2P3/CNRS (France), ASI and INFN (Italy), MEXT, KEK, and JAXA (Japan), and the K.A. Wallenberg Foundation, the Swedish Research Council and the National Space Board (Sweden). Science analysis support in the operations phase from INAF (Italy) and CNES (France) is also gratefully acknowledged.

The work of DS has been supported by the Investissements d'avenir, Labex ENIGMASS.

References

[1] Aharonian, F., Akhperjanian, A. G., Bazer-Bachi, A. R., et al. 2005, A&A, 442, 895
[2] Aharonian, F., Akhperjanian, A. G., Barres de Almeida, U., et al. 2008, A&A, 477, 481
[3] Aharonian, F., Akhperjanian, A. G., Barres de Almeida, U., et al. 2009, A&A, 495, 505
[4] Aharonian, F., Akhperjanian, A. G., Anton, G., et al. 2009, ApJL, 696, L150
[5] Abramowski, A., Acero, F., et al. 2010, A&A, 520, AA83
[6] Aharonian, F., et al. 2007, ApJL, 664, L71
[7] Aharonian, F., et al. 2006, A&A, 457, 899
[8] Abramowski, A., Aharonian, F., Ait Benkhali, F., et al. 2015, arXiv:1501.05087
[9] Bolmont, J., Corona, P., Gauron, P., et al. 2014, Nuclear Instruments and Methods in Physics Research A, 761, 46
[10] de Naurois, M. & Rolland, L. 2009, Astroparticle Physics, 32, 231

[11] Hofverberg, P., Kankanyan, R., Panter, M., et al. 2013, arXiv:1307.4550
[12] Kastendieck, M. A., Ashley, M. C. B., & Horns, D. 2011, A&A, 531, AA123
[13] Nolan, P. L., Abdo, A. A., Ackermann, M., et al. 2012, ApJS, 199, 31
[14] Sanchez D.A. et al, Probe of Lorentz Invariance Violation effects and determination of the distance of PG 1553+113, these proceedings.
[15] Sanchez D.A. et al, Multiwavelength campaign on the HBL PKS 2155-304: A new insight on its spectral energy distribution, these proceedings.
[16] The Fermi-LAT Collaboration 2013, arXiv:1306.6772

Multiwavelength campaign on the HBL PKS 2155-304 : A new insight on its spectral energy distribution

D. A. Sanchez
Laboratoire d'Annecy-le-Vieux de Physique des Particules, Université de Savoie, CNRS/IN2P3
B. Giebels, D. Zaborov
Laboratoire Leprince-Ringuet/École Polytechnique/IN2P3/CNRS
R. D. Parsons
Max-Planck-Institut fur Kernphysik
G. M. Madejski, A. Furniss
Kavli Institute for Particle Astrophysics and Cosmology,Department of Physics and SLAC National Accelerator Laboratory
On behalf of the NuSTAR, *Fermi* and H.E.S.S. collaborations

arXiv:1502.02915v2 [astro-ph.HE] 17 Feb 2015

The blazar PKS 2155-304 was the target of a multiwavelength campaign from June to October 2013 which widely improves our knowledge of its spectral energy distribution. This campaign involved the NuSTAR satellite (3-79 keV), the *Fermi* Large Area Telescope (LAT, 100 MeV-300 GeV) and the High Energy Stereoscopic System (H.E.S.S.) array phase II (with an energy threshold of few tens of GeV). While the observations with NuSTAR extend the X-ray spectrum to higher energies than before, H.E.S.S. phase II, together with the use of the LAT `PASS 8`, enhance the coverage of the γ-ray regime with an unprecedented precision. In this work, preliminary results from the multi-wavelength analysis are presented.

1. Introduction

Several new and upgraded instruments have come online in the last few years. In the X-ray regime, NuSTAR, using true focusing optics, is providing an unprecedented view of the hard-X-ray sky with its wide energy range (3-79 keV). In the very-high-energy γ-ray regime, H.E.S.S. is now operating with five telescopes including the largest Cherenkov telescope ever constructed. Additionally, a major upgrade to the *Fermi*-LAT instrumental response functions (IRFs), `PASS 8` [5], is now being implemented, increasing the sensitivity on the high-energy γ-ray sky.

The high frequency peaked BL Lac (HBL) object PKS 2155-304 was the target of a new multi-wavelength campaign from April to October 2013 involving these three instruments. This campaign provides a more complete coverage of the X-ray and γ-ray range than the previous campaign held in 2008, which involved *Fermi*, H.E.S.S. and also ATOM, *Swift* and *RXTE* and lasted for 11 days [1].

NuSTAR observed PKS 2155-304 multiple times, starting with a $\approx$40 ks observation in April 2013 designed for cross-calibration purposes of various high energy astrophysical instruments. Seven subsequent observations (lasting $\approx$10 ks each), in July, August, and September 2013, were scheduled to be strictly simultaneous with H.E.S.S., during local moonless night-time periods at the H.E.S.S. location. Furthermore, some independent observations of PKS 2155-304 were conducted with H.E.S.S. for calibration and monitoring purposes. In its normal operation mode, the *Fermi*-LAT is observing the full sky and each source is seen 30 minutes every 3 hours.

2. Observations

2.1. H.E.S.S. Mono-mode

The H.E.S.S. experiment consists of an array of 5 telescopes: four $12m$ diameter dish telescopes in operation since 2004 and and a fifth, CT5, a $28m$ diameter dish, in operation since 2012. This yields an energy threshold of the instrument to be of the order of a few tens of GeV. The results of the first observations conducted with the fifth H.E.S.S. telescope standalone (in the so-called Mono-mode) are here presented in this work.

The data have been analysed with the `Model` analysis [6] with cuts adapted for this telescope. PKS 2155-304 is detected at a level of 26.4σ in 35 hours of live time. The spectrum is well described by a simple power-law with an energy threshold of 98 GeV:

$$F(E) = (26.1 \pm 1.2) \times 10^{-10} \mathrm{cm}^{-2}\,\mathrm{s}^{-1} E_*^{-(3.25\pm0.08)}$$

with $E_* = E/(196\ \mathrm{GeV})$ the decorrelation energy. This spectrum is consistent with the source being at a low flux state, lower than the flux measured in 2008. Figure 1 presents the spectral energy distribution (SED) measured with CT5.

Variability has been found on the night-by-night light curve with a fractional excess variance $F_{\mathrm{var}} = 67 \pm 10\%$, higher than what has been found in 2008.

2.2. *Fermi*-LAT data

The *Fermi*-LAT [2] data have been analysed using the ScienceTools `v9R34P1` and the new `PASS 8` IRFs

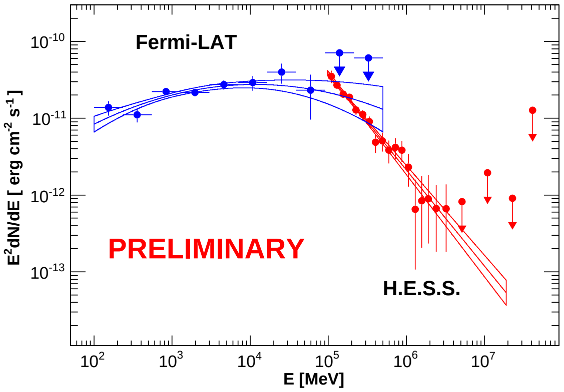

Figure 1: Spectral energy distribution of PKS 2155-304 obtained with *Fermi*-LAT in blue and H.E.S.S. in red. Contours give the 1 σ error band.

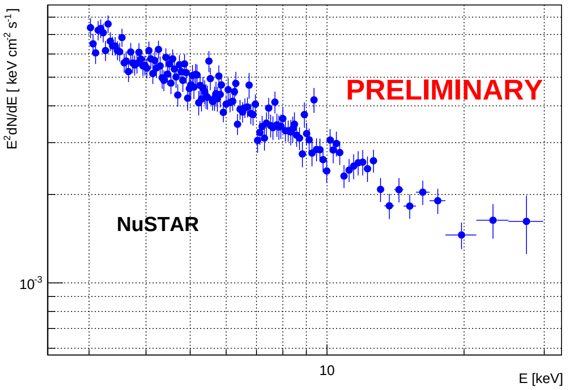

Figure 2: Spectral energy distribution measured by NuSTAR.

yielding an extended energy range with respect to previous analysis and an increased effective area, better PSF and background rejection with respect to the `PASS 7` IRFs.

Photons with an energy from 100 MeV to 500 GeV region of interest within 15 degrees of the source coordinates were used. Data have been analysed using a binned maximum likelihood analysis implemented in `gtlike`. The sky model has been built using the 4 years catalogue of point sources [10] and the spectrum is found to be best fitted by a log-parabola model of the form:

$$F(E) \propto E_*^{-(1.73\pm0.07)-(0.05\pm0.02)\ log_{10}E_*}$$

where $E_* = E/(904\ \mathrm{MeV})$, for an integrated flux above 100 MeV $I = (8.15 \pm 0.89) \times 10^{-8}\mathrm{cm}^{-2}\,\mathrm{s}^{-1}$ (see Fig. 1).

The spectrum is found to be consistent with results obtained with `PASS 7` IRFs but with increased statistic. No variability has been found in the *Fermi* light curve, nevertheless the flux is lower than the one measured in 2008 during the first *Fermi*-H.E.S.S. campaign on this object.

2.3. NuSTAR observations and results

NuSTAR [8] consists of two co-aligned telescopes, and the data from both telescopes were fitted simultaneously to a spectral model using XSPEC. For all observations, the source was detected at high significance from the lower end of NuSTAR bandpass (≈3 keV) up to (typically) 40 keV. The data were reduced using the standard NuSTAR pipeline (NuSTARDAS) with the source extracted from a region 80″ in radius around the centroid of the source, and the background subtracted from a similarly sized source-free region. Each pointing was analyzed independently. We found that in all cases, the source was adequately fitted with a power law model.

Flux variability have been found from one observation to another and the NuSTAR spectrum seems to be steeper when the source is fainter (ranging roughly from $\Gamma = 2.5$ to 3) - a trend also seen in other HBL objects studied by NuSTAR.

We also searched for the onset of the inverse Compton component, expected to appear at some point in the hard X-ray/soft gamma-ray spectrum. Here, we searched for statistically significant improvement of the quality of fit with the addition of a hard (assumed $\Gamma_{\mathrm{hard}} = 2$) spectral component. There is no clear indication for a presence of such component (primarily because the cosmic X-ray background and instrumental background become more significant at higher energies), and we can limit the flux of this component in the 20–40 keV band to be less than $\sim 10^{-12}$ erg cm^{-2} s^{-1} (Fig. 2).

3. Spectral energy distribution

The time-averaged SED of the source measured from April to October 2013 is presented on Fig 3. In the optical wavelengths, data from the SMARTs [4] and Steward Observatory [11] programs have been used (light blue points). Nine exposures of *Swift*-XRT data have been analysed to extend the X-ray spectrum at lower energies. The archival data from [1] are also shown for comparison. The source was at a lower flux state in all wavebands during the 2013 campaign.

A one zone synchrotron self-Compton model [3] has been used to reproduce the observed data. The emitting population of electrons $N_e(\gamma)$ is described by a broken power law with an index $p_1 = 1.8$ below $\gamma = 4000$ and $p_2 = 4.3$ above for a total number of electrons of 4.1×10^{52}. The spherical zone of radius $R = 7.1 \times 10^{16}$cm is filled with a constant magnetic

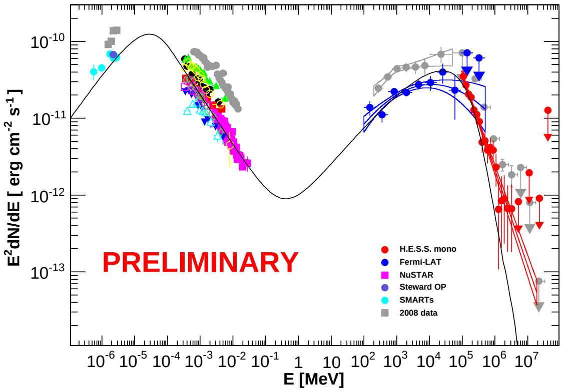

Figure 3: Optical to TeV SED of the object. Optical data come from SMARTs and Steward Observatory programs.*Swift* data have been also analysed. The gray points are the archival data from [1]. The black line is the results of the SSC calculation described in the text.

field $B = 0.05$ Gauss. The emission zone has a bulk Lorentz factor $\delta = 20$. The extragalactic background light absorption is taken into account using the model of [7].

The ratio of the escape time over the synchrotron cooling time is 0.3, between 0.3 and 3 as recommended by [9]. The particle energy density dominates the magnetic energy with an equipartition factor of $U_e/U_b \approx 7.3$. The broken power law shape used for the electrons distrubtion can be fitted in a restricted energy range by a curve model since the photon spectra is not strictly a broken power law. A more detailed SSC modelisation will be presented in a forecoming paper.

4. Conclusion

The HBL PKS 2155-304 has been observed in 2013 with NuSTAR, *Fermi*-LAT and H.E.S.S. (CT5) allowing the SED to be measured with an unprecedented precision. The source is found to be at a lower flux state in the γ-ray regime with respect to the campaign led in 2008.

No contamination of the X-ray flux by the inverse Compton component has been found in the NuSTAR data. The SED is well described be an one zone SSC model which is self-consistent and with a jet that is particle dominated.

Acknowledgments

The support of the Namibian authorities and of the University of Namibia in facilitating the construction and operation of H.E.S.S. is gratefully acknowledged, as is the support by the German Ministry for Education and Research (BMBF), the Max Planck Society, the French Ministry for Research, the CNRS-IN2P3 and the Astroparticle Interdisciplinary Programme of the CNRS, the U.K. Science and Technology Facilities Council (STFC), the IPNP of the Charles University, the Polish Ministry of Science and Higher Education, the South African Department of Science and Technology and National Research Foundation, and by the University of Namibia. We appreciate the excellent work of the technical support staff in Berlin, Durham, Hamburg, Heidelberg, Palaiseau, Paris, Saclay, and in Namibia in the construction and operation of the equipment.

The *Fermi*-LAT Collaboration acknowledges support for LAT development, operation and data analysis from NASA and DOE (United States), CEA/Irfu and IN2P3/CNRS (France), ASI and INFN (Italy), MEXT, KEK, and JAXA (Japan), and the K.A. Wallenberg Foundation, the Swedish Research Council and the National Space Board (Sweden). Science analysis support in the operations phase from INAF (Italy) and CNES (France) is also gratefully acknowledged.

The work of DS has been supported by the Investissements d'avenir, Labex ENIGMASS.

References

[1] Aharonian, F.,et al. 2009, ApJl, 696, L150
[2] Atwood, W. B., et al. 2009, ApJ, 697, 1071
[3] Band, D. L. & Grindlay, J. E. 1985, ApJ, 298, 128
[4] Bonning, E. et al. 2012, ApJ, 756, 13
[5] Bruel, P. these proceedings
[6] de Naurois, M. & Rolland, L. 2009, Astroparticle Physics, 32, 231
[7] Franceschini, A., Rodighiero, G., & Vaccari, M. 2008, A&A, 487, 837
[8] Harrison, F. A. al. 2013, ApJ, 770, 103
[9] Tavecchio, F. et al. 1998, ApJ, 509, 608
[10] The Fermi-LAT Collaboration 2015, submited to ApJ, arXiv:1501.02003
[11] `http://james.as.arizona.edu/~psmith/Fermi/`

Probe of Lorentz Invariance Violation effects and determination of the distance of PG 1553+113.

D. A. Sanchez
Laboratoire d'Annecy-le-Vieux de Physique des Particules, Université de Savoie, CNRS/IN2P3
F. Brun
DSM/Irfu, CEA Saclay
C Couturier, A Jacholkowska, J.-P. Lenain
LPNHE, Université Pierre et Marie Curie Paris 6, Université Denis Diderot Paris 7, CNRS/IN2P3
On behalf of the *Fermi* and H.E.S.S. collaborations

arXiv:1502.02920v1 [astro-ph.HE] 10 Feb 2015

The high frequency peaked BL Lac object PG 1553+113 underwent a flaring event in 2012. The High Energy Stereoscopic System (H.E.S.S.) observed this source for two consecutive nights at very high energies (VHE, E >100 GeV). The data show an increase of a factor of three of the flux with respect to archival measurements with the same instrument and hints of intra-night variability. The data set has been used to put constraints on possible Lorentz invariance violation (LIV), manifesting itself as an energy dependence of the velocity of light in vacuum, and to set limits on the energy scale at which Quantum Gravity effects causing LIV may arise. With a new method to combine H.E.S.S. and *Fermi* large area telescope data, the previously poorly known redshift of PG 1555+113 has been determined to be close to the value derived from optical measurements.

1. Introduction

PG 1553+113 is a high frequency peaked BL Lac object located in the Serpens Caput constellation. The object has been detected in VHE by H.E.S.S. [2] in 2006 and in high energies (HE, 100 MeV<E<300 GeV) by *Fermi* [1]. The γ-ray spectrum presents the largest HE-VHE spectral break measured to date [1, 8]. The source has an unknown redshift despite several attempts to measure it. The best estimate to-date, made by spectroscopy [4], is 0.43< z <0.58.

In April 2012, the source underwent a flare reported by the MAGIC collaboration [3]. Subsequently, the source has been observed by the H.E.S.S. telescopes. The data are used in this work to constrain its redshift and to probe a possible Lorentz invariance violation.

2. Data Analysis

2.1. H.E.S.S. data analysis

The H.E.S.S. telescopes have observed PG 1553+113 in April 2012 for two nights. Data were analysed using the `Model` analysis [5] with `Loose` cuts. The object has been detected with a significance of 21.5σ in 3.5 hours of live time. The source spectrum is well fitted by a power-law model of the form:

$$F(E) \propto E_*^{-(4.85\pm0.25)}$$

where $E_* = E/(327\ \mathrm{GeV})$ and the flux is found to be 3.5 times higher than the measurements made in 2005-2006 [2].

Indications of intra-night variability have been found with the fit to a constant of the light-curve yielding a χ^2 of 21.34 for 7 d.o.f. ($P_{\chi^2} = 3.3 \times 10^{-3}$).

Data taken in 2005-2006 were re-analysed and the spectrum is, in this case, well fitted by a log-parabola model:

$$F(E) \propto E_*^{-(5.39\pm0.43)-(3.95\pm1.40)\ log_{10} E_*}$$

where $E_* = E/(360\ \mathrm{GeV})$. Both spectra (archival and flare) are presented on figure 1.

2.2. *Fermi*-LAT data analysis

The *Fermi*-LAT data, from 300 MeV to 300 GeV, have been analysed with the ScienceTools `V9R32P5` and instrumental response functions `P7REP_SOURCE_V15`. A region of interest of 15 degrees has been used and the sky model has been built using the third *Fermi* catalog [10].

Data contemporaneous to the H.E.S.S. exposures taken in 2012 are well fitted by a power-law of index $\Gamma = 1.72 \pm 0.26$. The pre-flare data are defined by the data taken from August 8, 2008 up to March 1st 2012. The measured spectrum is described by a log-parabola model (Fig. 1).

Variability has been probed before, during and after the flare using a bayesian blocks analysis [9]. No counterpart to the VHE flare was found in the HE light curve.

3. Determination of the redshift

The extragalactic background light (EBL) is a field of infrared photons that interacts with the VHE γ-rays

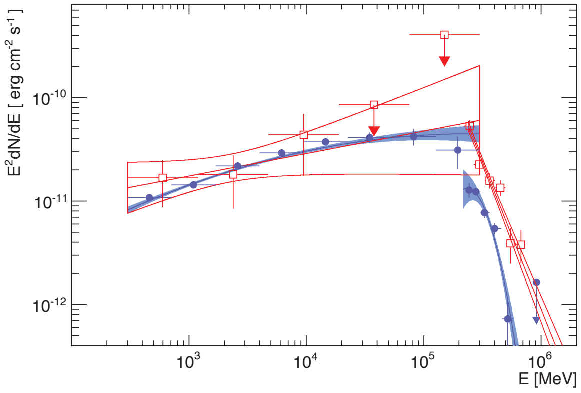

Figure 1: Spectral energy distribution in *gamma*-ray measured with *Fermi*-LAT and H.E.S.S. during the flare (red) and in the pre-flare state (see text) in blue.

on their way to Earth. This absorption leaves a footprint on the source spectrum that is used in this work to constrain its distance using a new bayesian model. The Bayes theorem reads $P(\Theta|Y) \propto P(\Theta)P(Y|\Theta)$ where Y stands for the data and Θ the parameters. The likelihood, $P(Y|\Theta)$, is minimized during the spectrum determination. The model used here is a power-law corrected for EBL absorption i.e $\phi = N \times (E/E_0)^{-\Gamma} \times e^{-\tau(E,z)}$. and then Θ is N, Γ and z.

To construct the prior $P(\Theta)$, the following assumptions have been made:

- EBL-corrected power-law cannot be harder than the *Fermi* measurement, the prior being then a truncated Gaussian of mean Γ_{Fermi} and width σ that accounts for statistical and systematic uncertainties of both instruments.
- Softening of this power-law, that arises from emission effects, is permitted with a constant probability.
- It is also assumed that distant sources are harder to detect and that $P(z) \propto exp(-\tau(z))$.

The EBL absorption is computed using the model of [6]. Marginalising over the parameters gives a redshift $z = 0.49 \pm 0.04$ (Fig. 2) in agreement with other measurement [4] or constraints derived using GeV-TeV data [8].

4. Lorentz invariance violation (LIV)

Tests for a possible LIV effect were performed by searching for a non-zero dispersion parameter $\tau_n(\sim \frac{\Delta t}{(\Delta E)^n})$ in the H.E.S.S. data of the flare. This is done by testing a correlation between arrival times of the photons and their energies.

A maximum likelihood analysis based on [7], has been modified to tackle the non-negligible background present in the data.

For $n_{\rm ON}$ events recorded in the ON-source region with arrival times t_i and energies E_i, the likelihood reads:

$L(\tau_n) = \prod_{i=1}^{n_{\rm ON}} P(E_i, t_i|\tau_n)$ with:

$$P(E_i, t_i|\tau_n) = w_s \cdot P_{\rm Sig}(E_i, t_i|\tau_n) + (1 - w_s) \cdot P_{\rm Bkg}(E_i, t_i)$$

The probability $P_{\rm Sig}$ was mainly determined from a parametrization of the light curve at low energies parametrization while $P_{\rm Bkg}$ was built assuming a constant background. The factor w_s accounts for the relative weight of signal events with respect to background events.

Constraints on τ_n led to lower limits on the Quantum Gravity energy scale $E_{\rm QG}$. The 95% 1-sided lower limits for the subluminal case are: $\mathrm{E}_{\rm QG,1} > 4.32 \times 10^{17}$ GeV and $\mathrm{E}_{\rm QG,2} > 2.11 \times 10^{10}$ GeV for linear and quadratic LIV effects, respectively. Figure 3 compares these results with other limits from less distant AGN flares. While the statistics is more limited here, the distance of the source makes the sensitivity to possible LIV effects comparable to previous results.

5. Conclusions

The VHE emitter PG 1553+113 underwent a flaring event in VHE with an increase of its flux by a factor of 3.5. No counterpart of this flare was found in the HE regime by *Fermi*.

This data set has been used to constrain the redshift of the source to be $z = 0.49 \pm 0.04$ using a novel method based on γ-ray data. The flare is also used to put lower limits on the LIV effect with $\mathrm{E}_{\rm QG,1} > 4.32 \times 10^{17}$ GeV and $\mathrm{E}_{\rm QG,2} > 2.11 \times 10^{10}$ GeV for linear and quadratic effects.

Acknowledgments

The support of the Namibian authorities and of the University of Namibia in facilitating the construction and operation of H.E.S.S. is gratefully acknowledged, as is the support by the German Ministry for Education and Research (BMBF), the Max Planck Society, the French Ministry for Research, the CNRS-IN2P3 and the Astroparticle Interdisciplinary Programme of the CNRS, the U.K. Science and Technology Facilities Council (STFC), the IPNP of the Charles University, the Polish Ministry of Science and Higher Education, the South African Department of Science and Technology and National Research Foundation, and by the University of Namibia. We appreciate the excellent

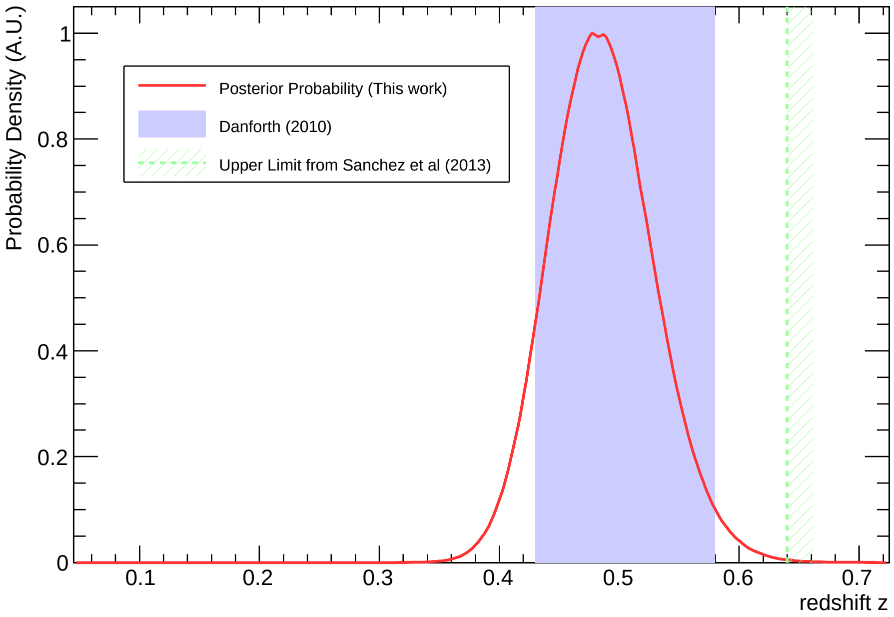

Figure 2: Posterior probability for the redshift determination and comparaison with other measurements.

work of the technical support staff in Berlin, Durham, Hamburg, Heidelberg, Palaiseau, Paris, Saclay, and in Namibia in the construction and operation of the equipment.

The *Fermi*-LAT Collaboration acknowledges support for LAT development, operation and data analysis from NASA and DOE (United States), CEA/Irfu and IN2P3/CNRS (France), ASI and INFN (Italy), MEXT, KEK, and JAXA (Japan), and the K.A. Wallenberg Foundation, the Swedish Research Council and the National Space Board (Sweden). Science analysis support in the operations phase from INAF (Italy) and CNES (France) is also gratefully acknowledged.

The work of DS has been supported by the Investissements d'avenir, Labex ENIGMASS.

References

[1] Abdo, A. A., et al. 2009 ApJ, 707, 1310

[2] Aharonian F. et al. 2008, A&A, 477, 481

[3] Cortina, J. 2012, The Astronomer's Telegram, 3977

[4] Danforth, C. W. et al. 2010, The Astrophysical Journal, 720, 976

[5] de Naurois, M. & Rolland, L. 2009, Astroparticle Physics, 32, 231

[6] Franceschini, A., Rodighiero, G., & Vaccari, M. 2008, A&A, 487, 837

[7] Martinez, M., & Errando, M. 2009, Astroparticle Physics, 31, 226

[8] Sanchez, D. A., Fegan, S., & Giebels, B. 2013, A&A, 554, A75

[9] Scargle, J. D. 1998, ApJ, 504, 405

[10] The Fermi-LAT Collaboration 2015, submited to ApJ, arXiv:1501.02003

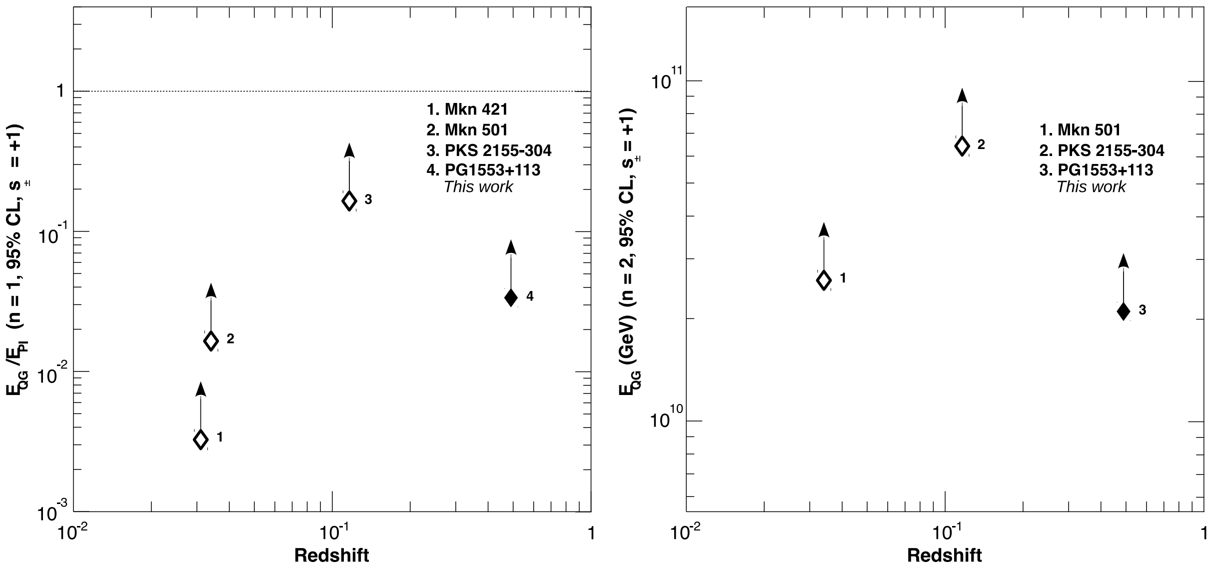

Figure 3: Lower limits on $E_{QG,1}$ from linear dispersion (left) and on $E_{QG,2}$ from quadratic dispersion (right) for the subluminal case obtained with AGN as a function of redshift.

FACT - Monitoring Blazars at Very High Energies

D. Dorner[1], M. L. Ahnen[2], M. Bergmann[1], A. Biland[2], M. Balbo[3], T. Bretz[2], J. Buß[5], S. Einecke[5],
J. Freiwald[5], C. Hempfling[1], D. Hildebrand[2], G. Hughes[2], W. Lustermann[2], K. Mannheim[1],
K. Meier[1], S. Mueller[2], D. Neise[2], A. Neronov[3], A.-K. Overkemping[5], A. Paravac[1], F. Pauss[2],
W. Rhode[5], T. Steinbring[1], F. Temme[5], J. Thaele[5], S. Toscano[3], P. Vogler[2], R. Walter[3], A. Wilbert[1]
[1] *Universität Würzburg, Institute for Theoretical Physics and Astrophysics,*
Emil-Fischer-Str. 31, 97074 Würzburg, Germany
[2] *ETH Zurich, Institute for Particle Physics, Otto-Stern-Weg 5, 8093 Zurich, Switzerland*
[3] *University of Geneva, ISDC Data Center for Astrophysics,*
Chemin d'Ecogia 16, 1290 Versoix, Switzerland and
[5] *TU Dortmund, Experimental Physics 5, Otto-Hahn-Str. 4, 44221 Dortmund, Germany*

The First G-APD Cherenkov Telescope (FACT) was built on the Canary Island of La Palma in October 2011 as a proof of principle for silicon based photosensors in Cherenkov Astronomy. The scientific goal of the project is to study the variability of active galatic nuclei (AGN) at TeV energies. Observing a small sample of TeV blazars whenever possible, an unbiased data sample is collected. This allows to study the variability of the selected objects on timescales from hours to years. Results from the first three years of monitoring will be presented.

To provide quick flare alerts to the community and trigger multi-wavelength observations, a quick look analysis has been installed on-site providing results publicly online within the same night. In summer 2014, several flare alerts were issued. Results of the quick look analysis are summarized.

I. FIRST G-APD CHERENKOV TELESCOPE

The First G-APD Cherenkov Telescope (FACT) has been operational since October 2011 on the Canary Island of La Palma. It is located at 2200 meter a.s.l. at the Observatorio del Roque de los Muchachos next to the MAGIC Telescopes. Like its two neighbouring telescopes, FACT is a ground-based gamma-ray telescope using the Imaging Air Cherenkov Technique (IACT). The project uses the refurbished mount of HEGRA CT3 and the recoated mirrors of HEGRA CT1, providing a mirror area of $9.5\,m^2$. Figure 1 shows the telescope during the observations of the full moon in June 2013. In addition, FACT was equipped with a new drive system and a novel camera using silicon based photosensors (SiPMs, a.k.a. Geigermode Avalanche Photo Diodes (G-APDs)). The camera consists of 1440 pixels and has a total field of view of 4.5 degree. Details on the design and construction of the telescope and the camera can be found in [1].

A. Major Goals

The technological challenge of the project was the proof of principle of SiPMs in Cherenkov astronomy. So far, only photo-multiplier tubes (PMTs) have been used in Cherenkov telescopes. To overcome the limitations for observations during strong moonlight due to the aging of the PMTs, different photosensors were considered. SiPMs were selected, as they are very robust and do not show aging when exposed to bright light. FACT is the first project which built a Cherenkov camera equipped with SiPMs and tested it in regular operation. The camera has now been operational since October 2011, and no SiPM has failed or showed any problem or aging.


FIG. 1: First G-APD Cherenkov Telescope during the observations of the full moon in June 2013. Credit: Daniela Dorner

The scientific goal of the FACT operations is the long-term monitoring of bright TeV blazars. At very high energies (VHE), the available observation time is limited, as IACTs run in pointing mode and have a limited field of view. Active galactic nuclei (AGN), however, are highly variable objects. As the measured variablity time scales of blazars range from minutes to years, long-term monitoring is mandatory. Although the shock-in-jet scenario can explain some features of the variability, the picture is still inconclusive lacking continuous data sets sampling a wide range of time scales. The observation schedule of FACT focusses on a small sample of bright blazars with the goal to obtain an unbiased and even sampling over the entire visibility period for the sources.

B. Profiting from SiPMs

Several aspects of SiPMs make them the ideal photosensors for a monitoring instrument. First of all, the robustness towards bright ambient light allows to extend the observations into the full moon period. It has been shown that even when observing the full moon, showers can still be recorded [3]. Observing during strong moonlight makes it possible to reduce the gaps in the light curves.

It is known that the gain of SiPMs depends on the temperature and the applied voltage and with the latter on the ambient light. As both the temperature and the ambient light are changing, a feedback system was introduced to keep the gain of the SiPMs stable. Details on the studies of the gain stablity and on the feedback system can be found in [2].

Keeping the gain stable and homogeneous over the camera, no calibration of the photosensors is needed. For an independent crosscheck of the calibration, FACT is equipped with an external light pulser.

Studying the dependence of the trigger threshold on the ambient light, it is possible to set the trigger threshold directly according to the measured currents [2]. Knowing the position of the moon and the observed sources, it is also possible to predict the threshold for each observation [4]. In this way, a constistent performance of the system is achieved which facilitates the analysis of the data. Furthermore, the stable performance allows to use the rate of background events or other parameters for data quality checks as shown in [5] and [2].

C. Towards Robotic Operation

The stable performance of the detector also allows for remote and automatic operation of the telescope. While in the first few months, there was a shift crew on-site, very soon remote operations started. In addition, the operation was automatized step by step. In the meantime, the system can be operated via a web interface which has been optimized for smartphone-usage. In Figure 2, a screenshot of the web interface can be seen. It allows not only to monitor the instrument and all its subsystems, but after authentication also to control the system. The control has been automatized such that in the meantime the shifter just needs to start a script at the beginning of the night, monitor the system and the weather during the night and stop the script at the end of the night. Known issues like communication problems are automatically taken care off by the script. The shifter only needs to interfere in case of bad weather or when an unknown problem appears. In case of emergencies that need immediate intervention at the system, an agreement ensures support from the MAGIC shift crew.

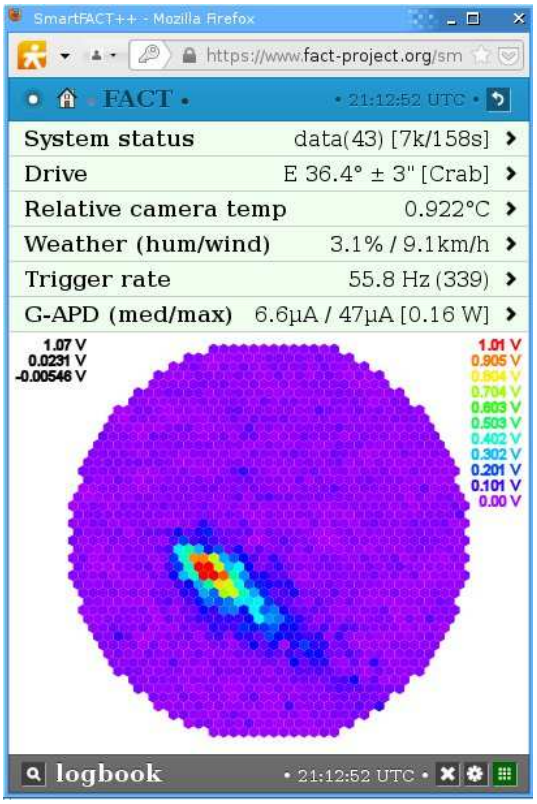

System status	data(43) [7k/158s]
Drive	E 36.4° ± 3" [Crab]
Relative camera temp	0.922°C
Weather (hum/wind)	3.1% / 9.1km/h
Trigger rate	55.8 Hz (339)
G-APD (med/max)	6.6µA / 47µA [0.16 W]

FIG. 2: Smartfact: a web interface to monitor the system and operate the telescope.

II. LONG-TERM MONITORING

A. Scientific Motivation

As blazars show variability on time scales from minutes to years, long-term monitoring is mandatory to uncover the mechanisms driving the variability due to the propagation of perturbations down the jet. Short snapshots with more sensitive larger telescopes such as MAGIC are necessary to understand the underlying physics of the central engine encoded in the shortest variability time scales. Multi-wavelength observations are very important to study the spectral aging of the emission regions during their propagation down the jet and to reveal the underlying radiation mechanisms. The spectral energy distribution (SED) of these objects exhibits two bumps where the position of the peaks depends on the type of the object. For high-frequency peaked blazars, the high energy peak is located at GeV to TeV energies making them the most interesting targets for FACT.

B. Source Sample

Being most sensitive at TeV energies, there is a limited number of sources which are good candidates for the long-term monitoring program of FACT. The two AGN most observed by FACT are Mrk 421 and Mrk 501 which were detected in 1992 and 1996 by Whipple [6, 7] and have been observed since then in several multi-wavelength (MWL) campaigns. However, in these MWL campaigns the observations are still rather sparse, e.g. one observation every three to ten days. The two sources were also part of the Whipple monitoring program where from Mrk 421 878.4 hours in 783 nights were collected in 14 years [8].

In the first three years of operation, FACT has observed Mrk 421 for 537 hours during 291 nights and Mrk 501 for 924 hours during 372 nights. Also, the sources 1ES 2344+51.4, 1ES 1959+650, 1ES 1218+304, IC 310, 1H0323+342, RGB J0521.8+2112 and PKS 0736+01 have been observed. While the first two belong to the regular monitoring sample, the other sources have been observed only for 10 to 60 hours. For performance studies, also a lot of observations of the Crab Nebula have been carried out.

Including observations during strong moonlight, each year about 3000 hours of observations are available. Taking into account bad weather and technical problems, about 1800 hours per year remain of which about 1500 hours are physics data.

C. MWL Observations

To draw conclusions on the underlying physics processes, it is necessary to study both peaks of the SED. Because of the variability of the sources, the observations must be carried out simultaneously. As continuous monitoring is not available in most wavelength ranges, MWL campaigns and Target of Opportunity (ToO) observations are appropriate means to obtain reasonable temporal overlap. Due to its blazar monitoring program and fast data pipeline, FACT can readily provide suitable triggers for ToO observations.

III. QUICK LOOK ANALYSIS

To provide quick alerts for ToO observations, it is important to analyse the data quickly. For this, a quick look analysis (QLA) was set up on La Palma in December 2012.

A. Setup

Once the data are written on disk, they are immediately processed by the QLA. To avoid any interference with the data taking, the data are transfered to another computer, where they are then analysed. The data are typically recorded and processed in bunches of five minutes. For technical reasons, also shorter durations of runs may occur. For the QLA, the data are binned consequently in five minutes or multiples of it. The data are processed with an automatic pipeline where each step automatically starts the next one once it is finished. As a last step, the results are inserted into a mysql database from where the plots for a web interface are produced.

B. Open Access

The results from the QLA are publicly available at `http://www.fact-project.org/monitoring` since September 2013. The data are available in 20-minute and nightly binning. The results provided on the website are excess rates. Details on the analysis and how the excess rates are calculated follow in the next section. The results shown on the website do not include any data quality check and also no correction for the dependence of the threshold on the zenith distance and ambient light. Therefore, the values are lower limits in case of larger zenith distance or moonlight. Nevertheless, they are sufficient to trigger other observations. Starting from March 2014, official flare alerts to other instruments have been issued regularly.

C. Analysis

As the offline analysis in the data center, the QLA is also performed with the Modular Analysis and Reconstruction Software (MARS) [9]. Compared to the final analysis, the pipeline is optimized to process the data as quickly as possible.

In case a new analysis version is available, the old data are not reprocessed with this new version. For example on May 26th 2014, a new software version was introduced. For different software versions, the results can differ slightly.

The steps performed in the QLA, are shortly discussed in the following paragraphs. For a quick estimate of the flux, it is not necessary to calculate a spectrum using Monte Carlo simulations. Instead, the excess-rate is used.

a. Calibration As mentioned before, calibrating the data is not necessary in case the feeback system keeps the gain stable and homogeneous. When the QLA was set up, the feedback system was not yet available in its final version. Therefore, in the first version of the QLA the data were calibrated using data from the external light pulsar. Starting from May 26th 2014, this calibration is no longer used.

In the step of the calibration, also the signal is extracted and bad pixels are interpolated.

b. Image Cleaning Based on the extracted signal and extracted timing information, the images are cleaned, i.e. pixels only containing noise are removed. For this, two thresholds are applied for the signal and a time coincidence window for the arrival time. First, all pixels with a signal higher than threshold 1 are kept (core pixels). In addition, all neigbouring pixels are kept in case their signal is higher than threshold 2. Furthermore, pixels are only kept when their difference in arrival time to the neighbouring pixel is smaller than 17.5 ns. The thresholds for the signal were first 4.0 and 2.5. For the new calibration, the levels had to be increased to 5.2 and 3.3 to keep the excess rates roughly the same.

Next, a statistical analysis of the shower images is done, calculating various image parameters which can be used to reconstruct the type, the origin and the energy of the primary particle.

c. Background Suppression In a first step, events that cannot be reconstructed are removed, i.e. events which

- consist of only five pixels or less
- have more than three islands
- have $Leakage > 0.1$ where $Leakage$ is defined by the ratio of signal in the outermost ring of pixels in the camera to the total signal

Next, the background suppression cuts are applied where the following cuts are used:

- $0.18 < SlopeSpreadWeighted < 0.68$
- $log10(Area) > (log10(Size) - 2) \cdot 1.1 - 1.55$
- $Conc_{core} < 0.13$
- $Conc_{COG} < 0.15$

where $Size$ and $Area$ the total amount of light in and the area [10] of the shower image. $Conc_{core}$ and $Conc_{COG}$ are the ratio of the the signal in the core pixel and three pixels next to the center of gravity to the total signal of the shower image, representing the concentration of the light in the image. While $Slope$ is development of the arrival time along a shower axis, $SlopeSpreadWeighted$ is the spread of the slope along the main shower axis weighted with the $Size$.

For the reconstruction of the shower origin, the disp is calculated [11]. The disp is parametrized as follows: $disp = \xi \cdot (1 - Width/Length)$ where $Width$ and $Length$ are the standard deviations of the signal along the two shower axes. ξ is the sum of the following correction terms:

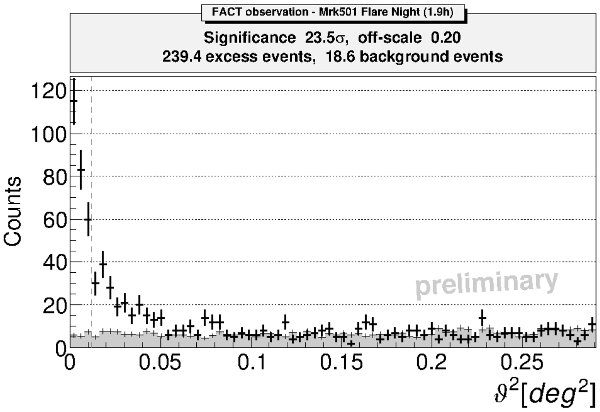

FIG. 3: θ^2-plot of Mrk 501 from 1.9 hours of data from the night of 8th to 9th June 2012.

- constant term: 1.14136
- slope term: $0.0681437 \cdot Slope$
- leakage term: $2.62932 \cdot log10(Leakage + 1)$
- size term: $0.0507821 \cdot (log10(Size) - 1.51279)^2$ if $(log10(Size) > 1.51279)$

d. Excess-Rate Curves Next, θ^2 is calculated as the distance between $Dist$ and $disp$ where $Dist$ is the distance of the center of gravity to the nominal source position. Plotting the θ^2 distribution, one can determine whether the source is detected. An example can be seen in Figure 3. The on-measurement is shown as black crosses, the off measurement as gray area. The vertical dashed line represents the cut in θ^2 which determines the signal region. To calculate the excess, the off-measurement is subtracted from the on-measurement in the signal region. Deviding this by the ontime of the observation, the excess rate is obtained which is a measure of the flux. As the trigger threshold and therefore the energy threshold depend on the amount of ambient light and the zenith distance, the same applies for the excess rate.

To study the variability of the sources in detail, either the excess rate needs to be corrected for the effect of zenith distance and ambient light or the flux needs to be calculated reconstructing the energy with the help of simulated data. For sending alerts, the excess rates are sufficient. Knowing the excess rates of the Crab Nebula, a rough correction of the excess rates can be made. As a larger zenith distance or more ambient light decrease the excess rate, the measured excess rate can be considered as lower limit.

IV. RESULTS

The excess rates calculated in the QLA are used to get a rough idea of the variability of the sources and to trigger ToO observations. Apart from Mrk 421 and Mrk 501, the other sources did not show any significant flares or activity in the last three years. In the following, the excess rate curves of the former are discussed. To get an overview of the activity, the excess rate curves are shown in a nightly binning. As directly the results of the QLA are shown, no data quality check or correction of the excess rate is included here.

A. Mrk 421

Although Mrk 421 was first observed in January 2012, here only the QLA results starting from December 12th 2012 are shown. The excess rate curve shown in Figure 4 in the top panel includes roughly 500 hours of data. A big flare was observed in April 2013, and in winter 2014/15 the source showed several times a flux higher than the flux of the Crab Nebula.

B. Mrk 501

Mrk 501 was first observed in May 2012. In June 2012, a flare was observed [5, 12]. In Figure 4, only the QLA results starting from December 12th 2012 are shown. The excess rate curve shown here (lower panel) includes roughly 740 hours of data. After a short flare in February 2013, Mrk 501 showed some moderate activity (around the flux of the Crab Nebula) in summer 2013. In summer 2014, the source got more active with two flares and an enhanced flux around 2-3 times the flux of the Crab Nebula.

C. Flare Alerts

In March 2013, FACT officially started sending alerts to other instruments. Since then, seven flare alerts have been issued. Between June and August 2014, six times an alert was sent as Mrk 501 met the trigger criteria of three Crab units. In Figure 5, a zoom in the excess rate curve to the time range of the flare alerts is shown. As two alerts on 19th and 21st of June triggered observations of other instruments, the big flare on June 24th was also observed by HESS [13].

V. SUMMARY AND OUTLOOK

FACT using SiPMs has proven to be an ideal setup for the long-term monitoring of blazars: The robustness of these photosensors allows to extend the observations into times with strong moonlight closing the gaps in light curves. Furthermore, the stable performance allows for a high data taking efficiency and facilitates the analysis.

To foster ToO observations, a quick look analysis was set up allowing to send flare alerts within a short time. In 2014, seven flare alerts have been issued. From Mrk 501 and Mrk 421, several flares and periods with enhanced flux level have been observed.

The next steps are to include in the quick look analysis an automatic data quality check and a correction of the excess rates for the effect that the trigger threshold changes with zenith distance and ambient light.

Acknowledgments

The important contributions from ETH Zurich grants ETH-10.08-2 and ETH-27.12-1 as well as the funding from the Swiss SNF, the German BMBF (Verbundforschung Astro- und Astroteilchenphysik) and the DFG (collaborative research center SFB 876/C3) are gratefully acknowledged. We are thankful for the very valuable contributions from E. Lorenz, D. Renker and G. Viertel during the early phase of the project. We also thank the Instituto de Astrofisica de Canarias for allowing us to operate the telescope at the Observatorio Roque de los Muchachos in La Palma, the Max-Planck- Institut fr Physik for providing us with the mount of the former HEGRA CT 3 telescope, and the MAGIC Collaboration for their support. We further thank the group of M. Tose from the College of Engineering and Technology at Western Mindanao State University, Philippines, for providing us with the scheduling web interface.

---

[1] H. Anderhub et al., 'Design and operation of FACT - the first G-APD Cherenkov telescope', JINST 8, 2013, P6008

[2] A. Biland et al., 'Calibration and performance of the photon sensor response of FACT - The first G-APD Cherenkov telescope', JINST 9, 2014, P0012

[3] M.-L. Knoetig for the FACT Collaboration, 'FACT - Long-term stability and observations during strong Moon light', ICRC 2013

[4] T. Bretz for the FACT Collaboration, 'FACT - Threshold prediction for higher duty cycle and improved scheduling', ICRC 2013

[5] D. Dorner for the FACT Collaboration, 'FACT - Long-term Monitoring of Bright TeV-Blazars', ICRC 2013

[6] M. Punch et al., 'Detection of TeV photons from the active galaxy Markarian 421', Nature 358, 1992

[7] J. Quinn et al., 'Detection of Gamma Rays with E >

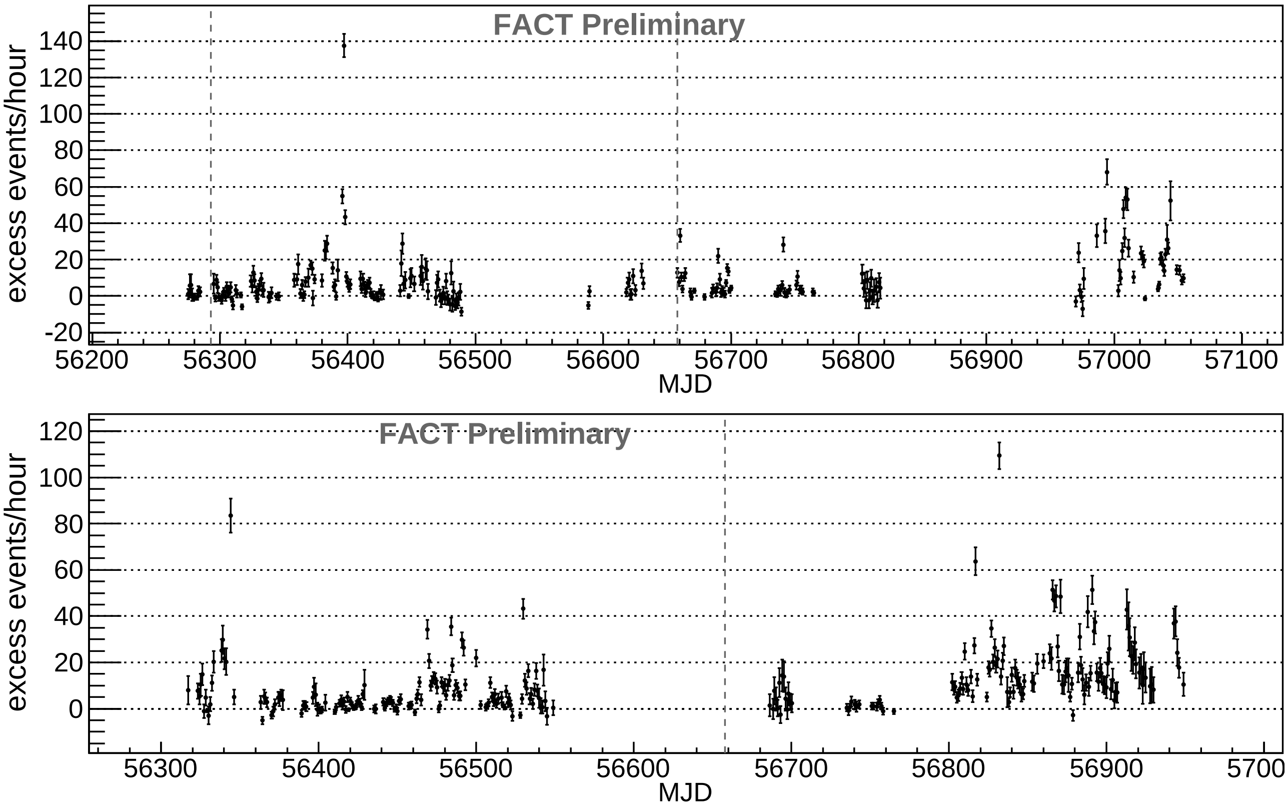

FIG. 4: Excess rate curves for Mrk 421 (top panel) and Mrk 501 (bottom panel) starting from December 12th 2012. The start of a new year is marked with a gray, dashed, vertical line.

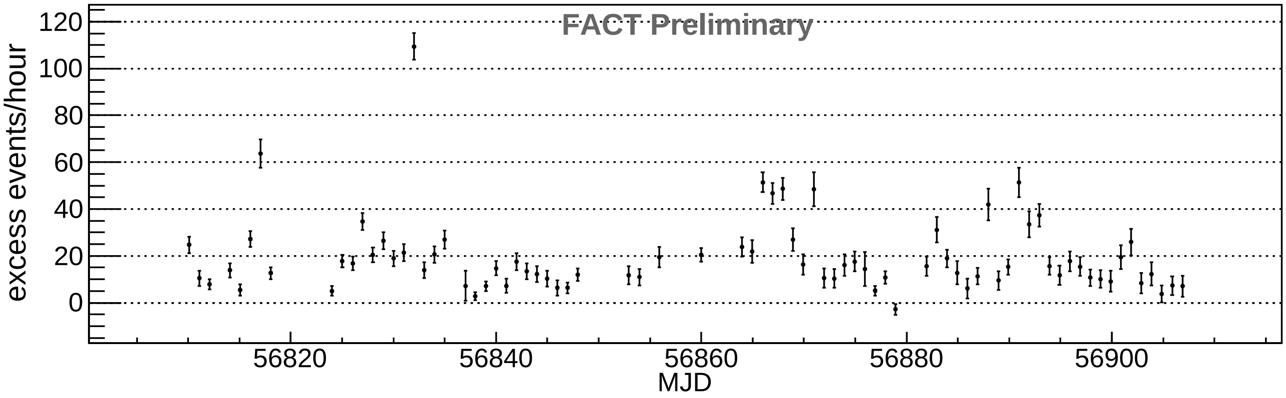

FIG. 5: Excess rate curve of Mrk 501 from June to September 2014.

300 GeV from Markarian 501', ApJL 456, 1996

[8] V.A. Acciari et al., 'Observation of Markarian 421 in TeV gamma rays over a 14-year time span', APh 54, 2014

[9] T. Bretz and D. Dorner, 'MARS - CheObs ed. – A flexible Software Framework for future Cherenkov Telescopes', Astroparticle, Particle and Space Physics, Detectors and Medical Physics Applications, 2010

[10] B. Riegel et al.,'A systematic study of the interdependence of IACT image parameters', ICRC 2005

[11] R.W. Lessard et al., 'A new analysis method for reconstructing the arrival direction of TeV gamma rays using a single imaging atmospheric Cherenkov telscope', APh 15, 2001

[12] T. Bretz et al., 'FACT - The first G-APD Cherenkov telscope (first results)', AIP, 2012

[13] C. Stegmann for the H.E.S.S. collaboration, 'Increased VHE activity from Mrk 501 detected with H.E.S.S.', Atel #6268, 2014

Blazar Variability and Evolution in the GeV Regime

S. Tsujimoto, J. Kushida, K. Nishijima, and K. Kodani
Tokai university, Hadano city, Japan, 259-1292

One of the most important problem of the blazar astrophysics is to understand the physical origin of the blazar sequence. In this study, we focus on the GeV gamma-ray variability of blazars and evolution perspective we search the relation between the redshift and the variability amplitude of blazars for each blazar subclass. We analyzed the Fermi-LAT data of the TeV blazars and the bright AGNs (flux $\geq 4\times10^{-9}$ cm^{-2}s^{-1}) selected from the 2LAC (the 2nd LAT AGN catalog) data base. As a result, we found a hint of the correlation between the redshift and the variability amplitude in the FSRQs. Furthermore the BL Lacs which have relatively lower peak frequency of the synchrotron radiation and relatively lower redshift, have a tendency to have a smaller variability amplitude.

I. INTRODUCTION

The blazar is the class of the active galactic nuclei (AGN) which has the most number of extragalactic source in the very-high-energy gamma-ray regime ($E > 100$ GeV)[12]. They are characterized by double-peaked nonthermal emission with spectral energy distribution (SED) in radio to gamma-ray regime. Blazars include BL Lacertae objects (BL Lacs) and flat spectrum radio quasars (FSRQs). In addition BL Lacs include high-frequency peaked BL Lac objects (HBLs), intermediate-frequency peaked BL Lac objects (IBLs) and low-frequency peaked BL Lac objects (LBLs). In the leptonic model, the low and high bump of SED is explained by the synchrotron and the Synchrotron Self Compton (SSC) and/or External Compton (EC) radiations. The estimation of EC in the second hump is a matter of great importance in estimating external photons.

One of the characteristic of the blazar spectra is blazar sequence. In 1998, Fossati et al. combined three complete blazar samples[4]; The 2 Jy samples of FSRQs[8], the radio selected 1 Jy samples of BL Lacs[6] and the X-ray selected sample(Einstein Slew Survey) of BL Lacs [2]. The thirty-third sources of selected sample were detected in high-energy gamma-ray regime ($E > 100$ MeV) by the EGRET instrument on-board the compton gamma ray observatory (CGRO). These sources were devided 5 bins based on the 5 GHz radio luminosity and averaged the SED of the each type of the blazars. The made SED suggested some relationship; first, the synchrotron peak frequency and the bolometric luminosity have the anti-correlation. second, the synchrotron peak frequency and the compton peak frequency have the positive-correlation. finally, the compton dominance (the ratio of the inverse Compton to synchrotron luminosity) and the bolometric luminosity have positive-correlation. These correlations are known as “the blazar sequence” in considering the blazar physics. We aim to reveal the relation between the evolution process of AGNs and the blazar sequence based on the systematical study for many blazars .

In this study, we calculated ~ 100 AGNs (blazars) to find the difference of the variability amplitude in blazar types and evolution of the variability amplitude (activity). We applied the fractional variability amplitude ($F_{\rm var}$) to calculate the variability amplitude considering the error. The $F_{\rm var}$ is defined as Eq.(1) which was given by Vaughan et al. (2003).

$$F_{\rm var} = \sqrt{\frac{S^2 - \overline{\sigma^2_{err}}}{\overline{F}^2}} \tag{1}$$

Note that S^2 is the total variance of the light curve, $\overline{\sigma^2_{err}}$ is the mean square of flux error and $\overline{F}^2$ is the square of mean flux. Fvar error (uncertainty) is defined as Eq.(2) by Poutanen et al. (2008).

$$\Delta F_{\rm var} = \sqrt{F^2_{\rm var} + err(\sigma^2_{\rm NXS})} - F_{\rm var} \tag{2}$$

Where $err(\sigma^2_{\rm NXS})$ is defined as Eq.(3) by Vaughan et al. (2003)

$$err(\sigma^2_{\rm NXS}) = \sqrt{\left(\sqrt{\frac{2}{N}}\frac{\overline{\sigma^2_{err}}}{F^2}\right)^2 + \left(\sqrt{\frac{\overline{\sigma^2_{err}}}{N}}\frac{2F_{\rm var}}{F}\right)^2} \tag{3}$$

$F_{\rm var}$ is often used in computation variability amplitude for each spectral band[7].

In this study, we studied the flux variation of AGNs with the $F_{\rm var}$ on the high-energy gamma-ray regime to get the variation charactor of each class (type).

II. DATA SELECTION

We selected AGNs from the second LAT AGN catalog (2LAC)[3] and TeVCat[12]. Selection criteria were as follows,

I : It was decided which subclass was belonged to (HBL or IBL or LBL or FSRQ).

II : It had known redshift.

III : flux $\geq 4 \times 10^{-9}$ cm^{-2} s^{-1} in 2LAC.

TABLE I: Analyzed AGN list [3, 12]

Source name	**Redshift z**	**Class (type)**	**Source name**	**Redshift z**	**Class (type)**	**Source name**	**Redshift z**	**Class (type)**
Messier 87	0.0044	FRI	MS 1221.8+2452	0.218	HBL	4C +55.17	0.899298	FSRQ
NGC 1275	0.017559	FRI	PKS 0301-243	0.26	HBL	PKS 0823-223	0.91	IBL
Mrk 421	0.031	HBL	S2 0109+22	0.265	IBL	PKS 0420-01	0.916	FSRQ
Mrk 501	0.034	HBL	1ES 0414+009	0.287	HBL	AO 0235+164	0.94	LBL
1ES 2344+514	0.044	HBL	S5 0716+714	0.31	IBL	S3 0218+357	0.944	Blazar
Mrk 180	0.045	HBL	OT 081	0.322	LBL	OP 313	0.997249	FSRQ
1ES 1959+650	0.048	HBL	1ES 0502+675	0.341	HBL	PKS 0454-234	1.003	FSRQ
AP Lib	0.049	LBL	PKS 1510-089	0.361	FSRQ	4C +14.23	1.038	FSRQ
1ES 1727+502	0.055	HBL	3C 66A	0.41	IBL	PKS 2201+171	1.076	FSRQ
BL Lacertae	0.069	IBL	PKS 0735+17	0.424	LBL	PKS 0426-380	1.111	LBL
PKS 2005-489	0.071	HBL	4C +21.35	0.432	FSRQ	PKS B1908-201	1.119	FSRQ
RGB J0152+017	0.08	HBL	1ES 0647+250	0.45	HBL	OG 050	1.254	FSRQ
1ES 1741+196	0.083	HBL	PG 1553+113	0.5	HBL	PKS 1551+130	1.30814	FSRQ
W Comae	0.102	IBL	GB 1310+487	0.501	FSRQ	PKS 0244-470	1.385	FSRQ
1ES 1312-423	0.105	HBL	PKS 2326-502	0.518	FSRQ	PKS 2023-07	1.388	FSRQ
VER J0521+211	0.108	IBL	3C 279	0.536	FSRQ	S4 1030+61	1.40095	FSRQ
PKS 2155-304	0.116	HBL	MG2 J071354+1934	0.54	FSRQ	PKS 0402-362	1.417	FSRQ
B3 2247+381	0.1187	HBL	BZQ J0850-1213	0.566	FSRQ	PKS 0250-225	1.419	FSRQ
RGB J0710+591	0.125	HBL	PKS 1424+240	0.6035	IBL	PKS 1454-354	1.424	FSRQ
H 1426+428	0.129	HBL	4C 31.03	0.603	FSRQ	B2 1520+31	1.484	FSRQ
1ES 1215+303	0.13	HBL	PMN J2345-1555	0.621	FSRQ	PKS 2052-47	1.489	FSRQ
PKS 1717+177	0.137	LBL	PKS 1244-255	0.633	FSRQ	PKS 2227-08	1.55999	FSRQ
1ES 0806+524	0.138	HBL	S4 1849+67	0.657	FSRQ	TXS 1013+054	1.7137	FSRQ
1ES 0229+200	0.14	HBL	4C +56.27	0.664	LBL	PKS 0215+015	1.721	FSRQ
1RXS J101015.9-311909	0.142639	HBL	S5 1803+784	0.68	LBL	MG1 J123931+0443	1.76095	FSRQ
TXS 1055+567	0.14333	IBL	Ton 599	0.724565	FSRQ	MG2 J101241+2439	1.805	FSRQ
3C 273	0.158	FSRQ	B2 0716+33	0.779	FSRQ	4C +38.41	1.81313	FSRQ
H 2356-309	0.165	HBL	TXS 0106+612	0.785	FSRQ	PKS 0805-07	1.837	FSRQ
PKS 0829+046	0.173777	LBL	PKS 1622-253	0.786	FSRQ	PKS 1502+106	1.83928	FSRQ
1ES 1218+304	0.182	HBL	B2 2234+28A	0.795	LBL	4C 01+02	2.099	FSRQ
1ES 1101-232	0.186	HBL	PKS 0440-00	0.844	FSRQ	PKS 1329-049	2.15	FSRQ
1ES 0347-121	0.188	HBL	OC 457	0.859	FSRQ	S4 0917+44	2.18879	FSRQ
RBS 0413	0.19	HBL	3C 454.3	0.859	FSRQ	PMN J1344-1723	2.506	FSRQ
OX 169	0.211	FSRQ	TXS 1920-211	0.874	FSRQ			
1ES 1011+496	0.212	HBL	PKS 0537-441	0.892	LBL			

Table I shows the analyzed AGN list which 102 sources are included in. Source name, redshift, and class(type) are cited from 2LAC and TeVCat.

The redshift of PKS 1424+240 was referred to Furniss(2013)[5]. According to the TeVCat[12], the blazar class of S3 0218+357 (z=0.944) was not determined but we used it as high redshift VHE gamma-ray emitter.

III. DATA ANALYSIS

We analysed the Fermi reprocessed pass 7 data between 2008 August 04 and 2014 June 09, using the unbinned likelihood analysis with the Fermi Science Tools package version v9r33p0 available from the Fermi Science Support Center (FSSC)[13]. The likelihood analysis was selected that the events with photon energies in the range of 0.1-300 GeV and a Region Of Interest (ROI) of 10 degrees cen-

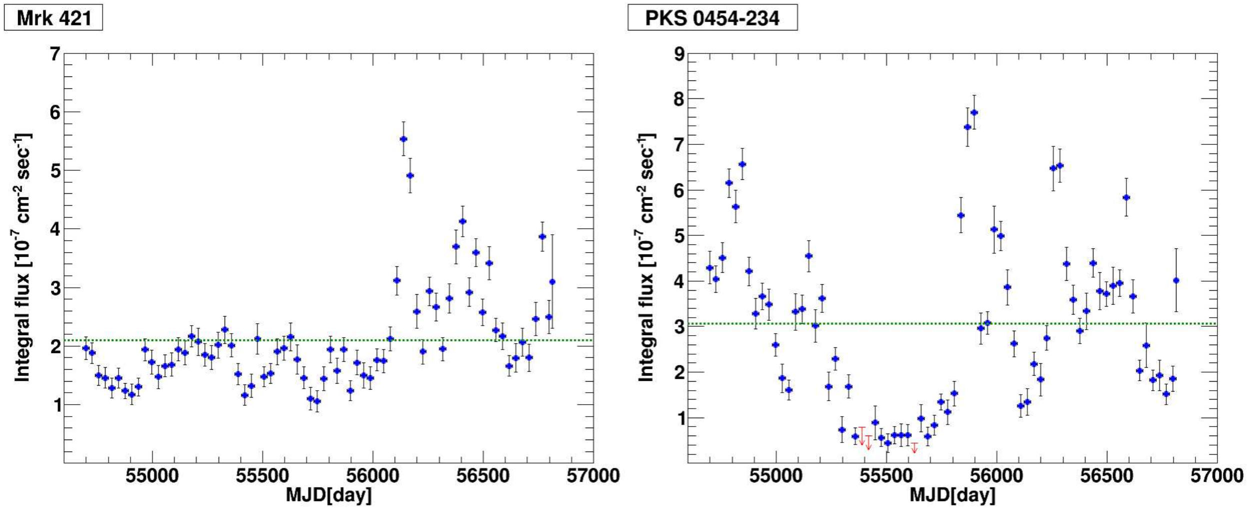

FIG. 1: Examples of the gamma-ray light curve about 6 years in 0.1–300 GeV. Blue plots: data points with a bin size of 30 days (bin size of last it is only about 4.4 days). Red allows: 95% C.L. upper limits. Green dotted lines: average flux of whole period. Left panel: Mrk 421(HBL). Right panel: PKS 0454-234(FSRQ).

tered at the position of Table I sources. We used "SOURCE" class ("evclass = 2") including both front and back events, because the "SOURCE" class is recommended for off-plane point source analysis by the likelihood analysis [15]. We excluded events with zenith angles larger than 100 degrees and time intervals when the rocking angle was larger than 52 degrees. The set of the instrument response functions of "P7REP_SOURCE_V15" was applied. Models which were used in this study include the isotropic diffuse background (iso_source_v05.txt[14]), galactic diffuse background (gll_iem_v05_rev1.fit[14]) and the Second Fermi LAT Catalog (2FGL) sources in ROI of 10 degrees centered at the position of Table I sources. The spectrum model was according to the 2FGL. Target blazars (Table I) were fitted with a Log-Parabola (LP):

$$\frac{dN}{dE} = N_0 \left(\frac{\mathrm{E}}{\mathrm{E}_0}\right)^{-(\alpha+\beta\log(\mathrm{E}/\mathrm{E}_0))} \tag{4}$$

because LP is typically used for modeling blazar spectra[16]. Where N_0[cm^{-2} s^{-1} MeV^{-1}] is normalization parameter, E_0 [MeV] is scale parameter, $-(\alpha+\beta\log(\mathrm{E}/\mathrm{E}_0))$ is spectrum index. If the parameter β is zero, LP is equal to Powar-Law spectrum. In this paper we fixed E_0 parameter of targets to E_0 = 100 MeV.

We judged the flux variation of target sources by some steps.
Step I: gamma-ray light curves, which width of the time bins was fixed on 30 days (shortest bin in this study), was made.
Step II: if calculated F_{var} was not required "Selection Criteria", we adopted more large bin size (60 days, 90 days, 150 days, and 300 days).
"Selection Criteria" were as follows, *I.* More than 40 % of the calculated integral flux of each bin were detected. *II.* Significant (over 2σ) variation was detected by the χ^2 test in the analyzed period. If the selection criteria *I.* and *II.* cleared, F_{var} of the target could be calculated.

IV. RESULTS AND DISCUSSION

Figure 1 shows the light curves of Mrk 421 and PKS 0454-234 as the light curve samples, which are the typical HBL and FSRQ sources, respectively. The green dashed lines represent the average flux of whole period. Each F_{var} and averaged flux were culculated as Mrk421: F_{var} = 39.3 ± 1.3 % averaged flux = $(2.10 \pm 0.22) \times 10^{-7}$ cm^{-1} s^{-1}, PKS0454: $F_{\mathrm{var}} = 58.7$ ± 1.3 % averaged flux = $(3.07 \pm 0.32) \times 10^{-7}$ cm^{-1} s^{-1}. Note, the F_{var} calculation was performed only over the 9 TS bins.

Another F_{var}s were obtained in the same method and the F_{var} as a function of the redshift is shown in Fig.2. Square and circle marks indicate TeVCat and not TeVCat sources, respectively. Each subclass of blazars are plotted in different colors (Blue:FSRQ, Red: HBL, Magenta: IBL, Green: LBL, Yellow: FRI, Black: uncertain type.). In Figure 2, Fvar indicates the variability amplitude of the GeV gamma-ray light curve. GeV gamma ray from FSRQs could be detected at high redshift(z > 0.5) and have the large Fvar. In addition, HBL and IBL assemble in z < 0.5. From these features, blazar subclass seems to change along the increasing redshift.
Peculiar features were as follows;
AO 0235+164 (z = 0.94, LBL) has particularly high

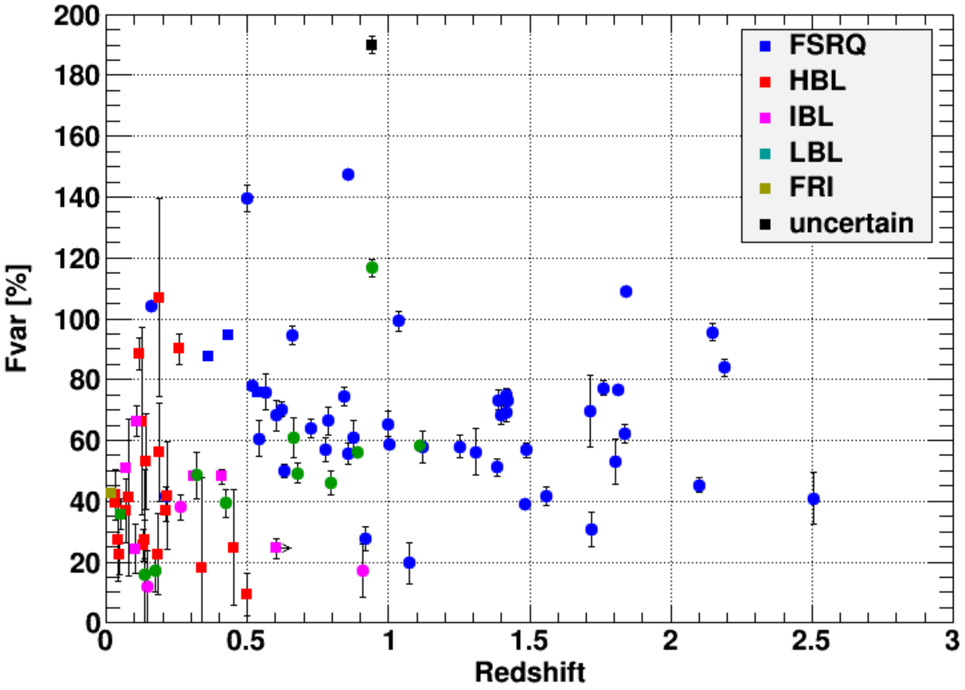

FIG. 2: The $F_{\rm var}$ as a function of the redshift. Square and circle marks indicate TeVCat and not TeVCat sources, respectively. Each subclass of blazars are plotted in different colors (Blue:FSRQ, Red: HBL, Magenta: IBL, Green: LBL, Yellow: FRI, Black: uncertain type.).

$F_{\rm var}$ (117 ± 2.8) in LBLs. This source was discussed that it might be FSRQ type blazar [1, 10]; therefore, high $F_{\rm var}$ value of this source might be caused by the FSRQ like characters. S3 0218+357 (z = 0.944, Uncertain type) which has the highest $F_{\rm var}$ (190 ± 2.8) in this analyzed sources is a gravitationally lensed blazar[17], hence the very high $F_{\rm var}$ value might be enhanced by the gravitationally lensed effect.

From Fig. 2, the $F_{\rm var}$ as a function of the redshift seems connection with FSRQs → LBLs → HBLs (IBLs). This trend shows possibility of the activity evolution and blazar class evolution.

Figure 3 shows the $F_{\rm var}$ histogram which is projected in the vertical axis of Fig. 2. The different colors show each subclass of blazars (Blue: FSRQ, Red: HBL, Magenta: IBL, Green: LBL, Yellow: FRI, Black: uncertain type).

However, there are some problems in this study. First, the middle-high redshift ($z > 0.2$) low $F_{\rm var}$ sources were not sufficient for discussions without selection effects. Second, this study could not considered the short time scale variability (< 30days). Thus, it is necessary to analyze the low $F_{\rm var}$ sources and short time scale.

V. CONCLUSIONS

We selected 102 AGNs (blazars) to reveal the relation between the evolution process of AGNs and the blazar sequence. We applied the fractional variability amplitude ($F_{\rm var}$) to calculate the variability amplitude considering the error.

The analyzed AGNs were selected from the second LAT AGN catalog (2LAC)[3] and TeVCat[12]. The analyzed data was Fermi reprocessed pass 7 data between 2008 August 04 and 2014 June 09, using the unbinned likelihood analysis with the Fermi Science Tools.

From these features, blazar subclass seems to change along the increasing redshift (connection with FSRQs → LBLs → HBLs (IBLs)). This trend shows possibility of the activity evolution and blazar class evolution. Peculiar features were as follows; AO 0235+164 (z = 0.94, LBL) has particularly high $F_{\rm var}$ (117 ± 2.8) in LBLs. This source was discussed that it might be FSRQ type blazar [1, 10]; therefore, high $F_{\rm var}$ value of this source might be caused by the FSRQ like characters. S3 0218+357 (z = 0.944, Uncertain type) which has the highest $F_{\rm var}$ (190 ± 2.8) in this analyzed sources is a gravitationally lensed blazar[17], hence the very high $F_{\rm var}$ value might be enhanced by the gravitationally lensed effect.

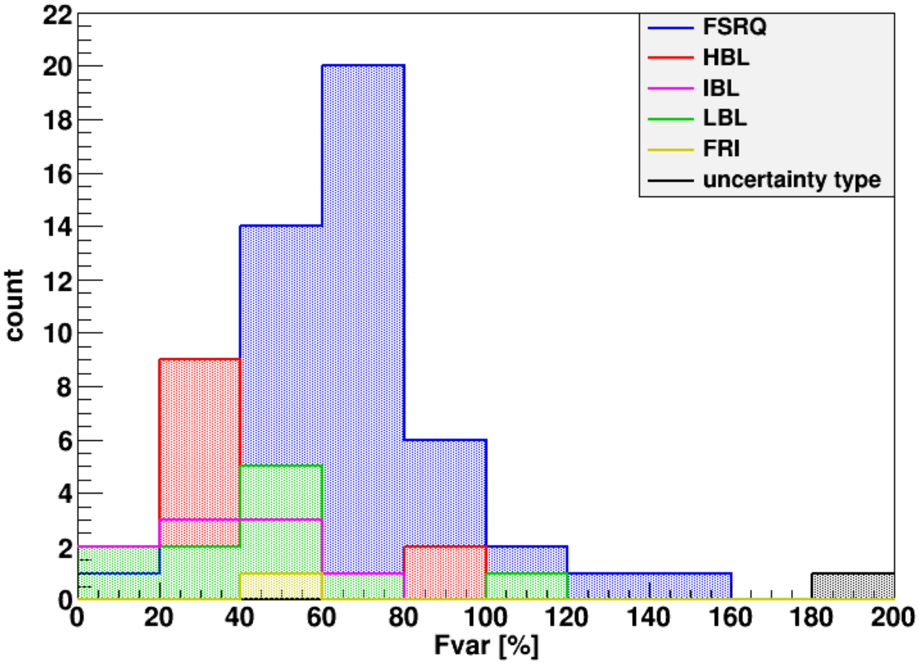

FIG. 3: The F_{var} distribution. The width of F_{var} bin is 20%. The different colors show each subclass of blazars (Blue: FSRQ, Red: HBL, Magenta: IBL, Green: LBL, Yellow: FRI, Black: uncertain type.).

However, there are some problems in this study. First, the middle-high redshift ($z > 0.2$) low F_{var} sources were not sufficient for discussions without selection effects. Second, this study could not considered the short time scale variability (< 30days). Thus, It is necessary to analyze the low F_{var} sources and short time scale.

---

[1] M. Ackermann et al., ApJ, 751, (2012) 159
[2] M. Elvis, et al., ApJS, 80, (1992) 257
[3] Fermi-LAT Collaboration, ApJ, 743,(2011) 171
[4] G. Fossati, et al., MNRAS, 299, (1998) 433
[5] A. Furniss, ApJ, 768, (2013) 6
[6] H. Kür, et. al, A&A, 45, (1981) 367
[7] MAGIC Collaboration, arXiv:1409.3389 (2014)
[8] P. Padovani and C.M. Urry, ApJ, 387, (1992) 449
[9] J. Poutanen, et. al, MNRAS, 1427, (2008) 389
[10] M. Stickel, et al., A&A Suppl. Ser., 105, (2014) 211
[11] S. Vaughan, et. al, MNRAS, 345, (2003) 1271
[12] http://tevcat.uchicago.edu/
[13] http://fermi.gsfc.nasa.gov/ssc/
[14] http://fermi.gsfc.nasa.gov/ssc/data/access/lat/BackgroundModels.html
[15] http://fermi.gsfc.nasa.gov/ssc/data/analysis/documentation/Cicerone/Cicerone_Data_Exploration/Data_preparation.html
[16] http://fermi.gsfc.nasa.gov/ssc/data/analysis/scitools/source_models.html
[17] http://www.astronomerstelegram.org/?read=6349

Fermi-LAT Detection of a Hard Spectrum Flare from the Gravitationally Lensed Blazar B0218+357

S. Buson
Università di Padova, Dipartimento di Fisica e Astronomia "G. Galilei", I-35131 Padova, Italy
INFN, Sezione di Padova, I-35131 Padova, Italy
C. C. Cheung
Space Science Division, Naval Research Laboratory, Washington, DC 20375-5352, USA
S. Larsson
Department of Physics, Stockholm University, AlbaNova, SE-106 91 Stockholm, Sweden
The Oskar Klein Centre for Cosmoparticle Physics, AlbaNova, SE-106 91 Stockholm, Sweden
Department of Astronomy, Stockholm University, SE-106 91 Stockholm, Sweden
J. D. Scargle
Space Sciences Division, NASA Ames Research Center, Moffett Field, CA 94035-1000, USA
on behalf of the *Fermi*-LAT Collaboration

arXiv:1502.03134v1 [astro-ph.HE] 10 Feb 2015

The *Fermi*-LAT has observed new γ-ray flares from the blazar B0218+357 during July 2014. While no significant change in the γ-ray spectrum has been previously observed through the flaring phase in late-2012, during this recent high activity the source displayed an exceptionally hard spectrum. The latter led to the detection of very high energy (VHE, $E > 100$ GeV) γ-rays from B0218+357 by the MAGIC telescopes, establishing this source as the most distant TeV emitter known to date. In addition to the detection of VHE emission, this blazar is of particular interest since it is known to be a double-image gravitationally lensed system with a lens delay of 11.46 ± 0.16 days measured in γ-rays. We present the *Fermi*-LAT study of the July 2014 flares and discuss them in the context of previous measurements.

1. Introduction

B0218+357 is a blazar at $z = 0.944 \pm 0.002$ [7] lensed by a galaxy at redshift $z = 0.6847$ [3]. The system appears as a double image in radio separated by 335 milli-arcseconds with a brighter western A and fainter eastern B images and an Einstein ring [12, 13]. The delay between the two images has been measured in radio as $\Delta t_{\rm r} = 10.5 \pm 0.2$ [2] and 10.1 ± 0.8 days [6]. Further timing analysis of the radio light curve from [6] using two independent methods resulted in two other possible delay values, $\Delta t_{\rm r} = 9.9^{+4.0}_{-0.9}$ or 11.8 ± 2.3 days [8]. B0218+357 was detected for the first time in γ-rays by the *Fermi* Large Area Telescope [LAT; 1]. Over the initial 4-years of LAT observations, B0218+357 displayed a γ-ray flux of $F_{E>100\rm MeV} = (2.4 \pm 0.9) \times 10^{-8}$ photons cm^{-2} s^{-1} and a photon index of $\Gamma = 2.28 \pm 0.03$ [3FGL J0221.0+3556; third *Fermi*-LAT Catalog, 3FGL, 14].

2. Gamma-ray flares from B0218+357

During the first six years of *Fermi*-LAT operations B0218+357 has displayed two major phases of enhanced activity. The first was a long-lasting one that developed between 2012 June and 2013 March. It was characterized by a series of prominent γ-ray flares that persisted over four months. A detailed study of this period led to the measurements of the first robust γ-ray lensing delay. Applying an auto-correlation function (ACF) to the evenly sampled light curve focused on the 2012-2013 enhanced γ-ray activity, a single dominant correlation peak was apparent. Its significance was evaluated to be 9σ. The delay in the γ-ray data was inferred to be 11.46 ± 0.16 days (1σ). With the same dataset it was possible to estimate the flux ratios (A/B), which were found to be consistent with unity, and similarly, infer a magnification ratio of about unity [5]. Importantly, during this period no indication for spectral variability was found. The γ-ray photon index $\Gamma = 2.30 \pm 0.03$ was consistent with the value derived before the start of the flaring; also, cf. the 3FGL value.

B0218+357 underwent a second enhanced phase during 2014 July. The flares were between 2014 July 11 and 27 (MJD 56849–56865) remarkably characterized by a distinctive hard spectrum [4]. Based on a preliminary analysis, on 2014 July 13 and 14 (MJD 56851 and MJD 56852) the source was observed with respective daily averaged fluxes ($E >$ 100 MeV) of $(6.5 \pm 1.4) \times 10^{-7}$ photons cm^{-2} s^{-1} with $\Gamma = 1.4 \pm 0.1$ and $(6.7 \pm 1.5) \times 10^{-7}$ photons cm^{-2} s^{-1} with $\Gamma = 1.6 \pm 0.1$. Because the gamma-ray delay was previously measured, LAT Target of Opportunity observations were triggered to trace the expected delayed emission, about 11 days after. Noteworthy, emission at VHE was subsequently reported by the MAGIC telescopes at the time of the expected delayed γ-ray flare [10, 11]. In the following we present the preliminary analysis of the 2014 LAT dataset.

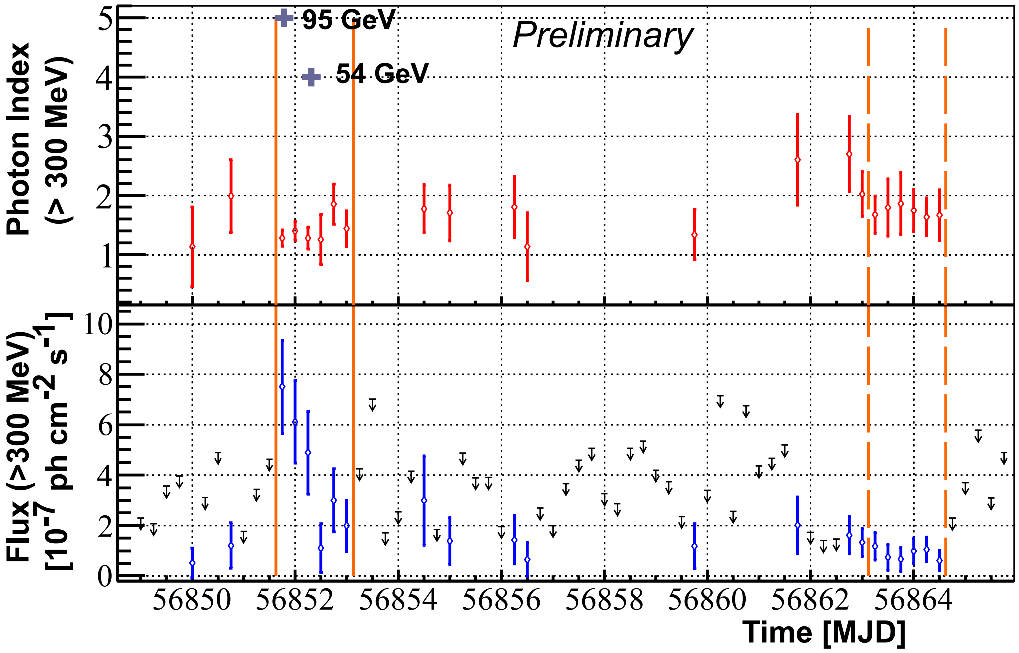

Figure 1: *Fermi*-LAT light curve computed in 6-hr bins at energies $E > 300$ MeV (lower panel) and the corresponding photon indices (upper panel). Vertical lines indicate the intervals of the flare (solid) and corresponding delayed emission (dashed). The two crosses indicate the arrival time of the two >50 GeV events (see Section 3.1 for more details).

3. Hard spectral phase during 2014

3.1. *Fermi*-LAT analysis

Fermi-LAT data have been analyzed as described in [5] but restricted to the energy range 300 MeV – 300 GeV to better characterize the hard-spectrum flaring behavior reported by [4] (ATel #6313). The source was modeled with a single power law with photon index free to vary. In the analysis, 95% confidence level upper limits were computed when the test statistic[1] (TS) [9] for the source was TS < 8. A preliminary study of data between MJD 56849–56865 confirms the detection of B0218+357. During this interval the photon index is found to be on average exceptionally smaller (below 2) with respect to the value of 2.3 reported in previous LAT studies [5]. Noteworthy, two high energy photons are positionally consistent with the source: a 95 GeV and a 54 GeV event, detected at ~MJD 56852, i.e. at the time of the initial flare.

3.2. Light Curve

Figure 1 presents the 6-hr light curve (>300 MeV) and the corresponding photon index versus time variations covering the time interval MJD 56849–56865. A first flaring phase, corresponding to flare of image A, is well defined by a fast flux increase accompanied by an exceptional hard spectrum and lasted 1.5 days. This phase is identified by six consecutive 6-hr source detections, as denoted in Figure 1 by the two continuous vertical lines between MJD 56851.625–56853.125. Immediately after this short flare the source returned to quiescence, displaying only sporadic activity for the subsequent ~11 days.

Then, at the time of the expected delayed emission, the source is observed again as denoted by the series of bins between the two dashed vertical lines, at MJD 56863.125–56864.625. These detections happen ~11.5 days later. The six consecutive 6-hr intervals with TS > 8 are distinguished again by a small photon index ($\Gamma < 2$). This second flaring phase corresponds to the flare of image B, based on the hard-spectrum signature. Formally, the ACF computed on the LAT light curve of 1-day binning between MJD 56849-56865 shows a peak around 11 days (not shown). Though its statistical significance has not yet been estimated it is notable that the peak is broadly consistent with the previous γ-ray delay of 11.46 ± 0.16 days.

We compare the flux measured during the first 1.5-day flaring episode, beginning at MJD 56851.625, with the observation shifted by 11.5 days. We derive the resultant average flux ratio A/B ~ 4.

---

[1] The TS corresponds roughly to the square of the significance assuming one degree of freedom.

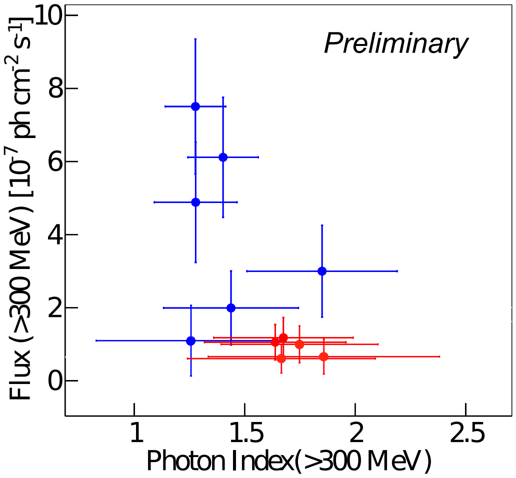

Figure 2: Scatter plot of the 6-hr binned fluxes and photon indices $E > 300$ MeV for the 1.5-day interval beginning at MJD 56851.625 (blue) and beginning at MJD 56863.125 (red), the same intervals reported in Figure 1 between solid and vertical lines, respectively.

4. Summary

Previous analysis of LAT data for the 2012 flares of the gravitationally lensed blazar B0218+357 found a γ-ray delay measurement of 11.46 ± 0.16 days and a flux ratio estimate between images (A/B) consistent with $\sim$1. From a preliminary analysis of the 2014 July LAT data, we found:

- Flares are characterized by peculiar hard spectra, with photon index $\Gamma < 2$;
- Based on the hard spectral signature of the flaring emission, the delay is compatible with the previous γ-ray delay measurement of 11.5 days;
- The average flux ratio (A/B) over this flaring episode is ~ 4: while this factor is different with respect to the previous γ-ray measurement, it is interestingly closer to the radio observations ($\sim$3 or 4) [2, 6];
- A 95 GeV and a 54 GeV photon were detected by the LAT during the first flare (A image) but were not observed during the second flare of image B. Nevertheless, the MAGIC detection ensures that in the second phase the source emission extends up to $\sim$100–200 GeV.

Acknowledgments

Work by C.C.C. was supported at NRL by NASA DPR S-15633-Y and Guest Investigator program 13-FERMI13-0009. S.L. acknowledges support by a grant from the Royal Swedish Academy Crafoord Foundation. The *Fermi*-LAT Collaboration acknowledges support for LAT development, operation and data analysis from NASA and DOE (United States), CEA/Irfu and IN2P3/CNRS (France), ASI and INFN (Italy), MEXT, KEK, and JAXA (Japan), and the K.A. Wallenberg Foundation, the Swedish Research Council and the National Space Board (Sweden). Science analysis support in the operations phase from INAF (Italy) and CNES (France) is also gratefully acknowledged.

References

1 Atwood, W. B., Abdo, A. A., Ackermann, M., et al. 2009, Astrophys. J., 697, 1071
2 Biggs, A. D., Browne, I. W. A., Helbig, P., et al. 1999, Mon. Not. R. Astron. Soc., 304, 349
3 Browne, I. W. A., Patnaik, A. R., Walsh, D., & Wilkinson, P. N. 1993, Mon. Not. R. Astron. Soc., 263, L32
4 Buson, S. & Cheung, C. C. 2014, The Astronomer's Telegram, 6316, 1
5 Cheung, C. C., Larsson, S., Scargle, J. D., et al. 2014, Astrophys. J. Lett., 782, L14
6 Cohen, A. S., Hewitt, J. N., Moore, C. B., & Haarsma, D. B. 2000, Astrophys. J., 545, 578
7 Cohen, J. G., Lawrence, C. R., & Blandford, R. D. 2003, Astrophys. J., 583, 67
8 Eulaers, E. & Magain, P. 2011, Astron. Astrophys., 536, A44
9 Mattox, J. R., Bertsch, D. L., Chiang, J., et al. 1996, Astrophys. J., 461, 396
10 Mazin D. et al.,. 2015, in this proceedings
11 Mirzoyan, R. 2014, The Astronomer's Telegram, 6349, 1
12 O'Dea, C. P., Baum, S. A., Stanghellini, C., et al. 1992, Astron. J., 104, 1320
13 Patnaik, A. R., Browne, I. W. A., King, L. J., et al. 1993, Mon. Not. R. Astron. Soc., 261, 435
14 The *Fermi*-LAT Collaboration. 2015, submitted to Astrophys. J. Suppl. Ser., arXiv:1501.02003

Time and Space Dependent Stochastic Acceleration Model for the Fermi Bubbles

K. Sasaki, K. Asano, T. Terasawa
University of Tokyo/Institute for the Cosmic Ray Research, Kashiwa, Chiba, Japan

Fermi-LAT reveals two huge gamma-ray bubbles existing in the Galactic Center, called 'Fermi Bubbles'. The existence of two microwave bubbles at the same region are also reported by the observation by WMAP, dubbed 'WMAP haze'. In order to explain these components, It has been argued that the gamma-rays arise from Inverse-Compton scattering of relativistic electrons accelerated by plasma turbulence, and the microwaves are radiated by synchrotron radiation. But no previous research reproduces both the Fermi Bubbles and WMAP haze under typical magnetic fields in the galaxy. We assume that shocks present in the bubbles and the efficiency of the acceleration by plasma turbulence, 'stochastic acceleration', changes with the distance from the shock front. The distance from the shock front increases with time, accordingly the efficiency of the acceleration changes with time. We also consider the time development of the electrons escape from the turbulence by diffusive loss. Our model succeed to reproduce both the observed characteristics of the Fermi Bubbles and WMAP haze under typical magnetic fields.

I. INTRODUCTION

Gamma ray data from the Fermi-LAT reveal two giant bubbles extending up to $\sim 50^\circ$ above and below the Galactic disk, called 'the Fermi Bubbles(FBs)'[1][2]. The spectra of the FBs are harder than ambient radiation fields, and they have 'sharp edge', which means sudden change of the brightness at the boundary. The surface brightness is almost constant in the FBs, though it doesn't mean the FBs have constant volume emissivities. There also exists the microwave bubbles in the same region, dubbed 'the WMAP haze'[3]. These huge structures may suggest past large-scaled activities in the Galactic Center(GC), near the massive black hole Sgr A^*.

Two representative models have been argued in order to explain both the FBs and the WMAP haze. 'Hadronic model' reproduces the FBs by the gamma ray from the π^0-decay process, and the WMAP haze by the radiation from the secondary electrons[4][5]. In the Hadronic model, protons are accelerated by the Diffusive Shock Acceleration(DSA) or other process, and they make π^0 after collision with cosmic-ray protons. $\pi^\pm$ are also made in this process, and they decay to $e^\pm$. These secondary particles radiate microwave in the magnetic field by the synchrotron radiation.

In contrast, 'Leptonic model' explains the FBs by the gamma ray from the Inverse Compton scattering(IC) process, and the WMAP haze by the synchrotron radiation from the relativistic electrons[6][7]. In the Leptonic model, it is assumed that electrons are accelerated by the second order Fermi acceleration(stochastic acceleration) by plasma turbulence or molecular clouds, in order to explain hard spectra of the FBs. These relativistic electrons give their energy to the ambient photons by the IC process, and they are observed as gamma ray. Some electrons radiate microwaves by the synchrotron radiation, and the WMAP haze are made.

However, both Hadronic and Leptonic model have problems. Hadronic models require so much energy $\sim 10^{57}$ erg, and estimated microwave spectrum conflicts with the WMAP data[5]. In the leptonic models, it is difficult to explain the WMAP haze under typical galactic magnetic field($B \sim 4\,\mu$G), so it is required strong magnetic field in the large scale[7].

So we construct the extended model based on the stochastic acceleration model by Mertsch & Sarkar[7]. Their model assumes that electrons are accelerated by the turbulence whose acceleration efficiency decreases with the distance from the shock front. But they don't consider the time development of the electron spectrum, and presume that electrons are at steady states. They also neglect the contribution of the electrons escape from the turbulence. So we extend their model by considering both time development and electrons out of the turbulence. In the sec.II, we explain our acceleration model. And in the sec.III, we show the results of our numerical calculation.

II. MODELS

We assume thet there is the shock front near the edge of the FBs and the plasma turbulences are drifted from the shock front with time by the advection at $V = v_{\rm pro}$.

In order to calculate the electron spectrum, we solve the Fokker-Planck equation,

$$\frac{\partial n}{\partial t} - \frac{\partial}{\partial p}\left(p^2 D_{pp}\frac{\partial}{\partial p}\frac{n}{p^2}\right) + \frac{n}{t_{esc}} + \frac{\partial}{\partial p}\left(\frac{dp}{dt}n\right) - Q_{inj} = 0 \quad (1)$$

where the momentum diffusion coefficient D_{pp} in the second term is described[7]

$$D_{pp}(\xi) = p^2 \frac{8\pi D_{xx}(\xi)}{9}\int_{1/L}^{k_d(\xi)} dk \frac{k^4 W(k,\xi)}{v_{\rm F}^2(\xi) + D_{xx}^2(\xi)k^2} \quad (2)$$

which represents the farther from the shock, the weaker the acceleration efficiency becomes.

In (2) p is energy, k is wavenumber, $v_{\rm F}(\xi)$ is the velocity of the fast-mode wave, and $W(k,\xi) = (u^2/4\pi)L^{-2/3}k^{-11/3}$ is the energy density of the Kolmogorov turbulence. $D_{xx}(\xi)$ is the spatial diffusion coefficient. The dimensionless parameter $\xi \equiv x/L$(x is the distance from the shock front, and L is the turbulence size) represents how far from the shock front.

The third term describes the diffusive loss from the turbulence, and then t_{esc} is accounted for $t_{esc} = L^2/D_{xx}$.

The forth term of (2) corresponds to the energy loss of the synchrotron radiation and the IC scatering,

$$\left(\frac{dp}{dt}\right)_{\rm cool} = P_{\rm syn} + P_{\rm IC} \tag{3}$$

$$P_{\rm syn} = \frac{4}{3}c\sigma_{\rm T}\gamma^2\beta^2 U_B \tag{4}$$

$$P_{\rm IC} = \frac{4}{3}c\sigma_{\rm T}\gamma^2\beta^2 U_{ph} \times f_{\rm KN} \tag{5}$$

$U_B = B^2/8\pi$ where $B = 4\,\mu G$, and U_{ph} is shown in Figure 1. $f_{\rm KN} \le 1$ is the factor due to the Klein–Nishina effect,which is numerically evaluated. In our models, $v_{\rm pro}$ is fixed $v_{\rm pro} = 250\,{\rm km\,sec^{-1}}$, which corresponds to sound speed at $kT \sim$ keV.

We presume that injection rate is constant,

$$Q_{inj}(p) \equiv Q_0\,\delta(p - p_0) \tag{6}$$

where the spectrum shape of injected electron is assumed to be δ-function, $n_{inj}(p) \propto \delta(p - p_0)$. In this paper,we use $cp_0 = 10^8$ eV.

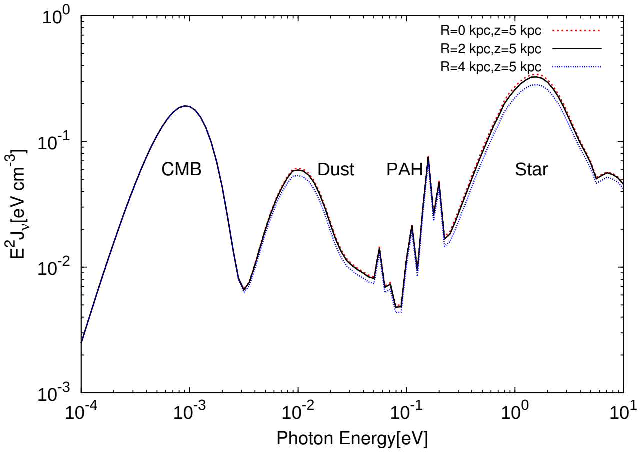

FIG. 1: Background Photon Fields[8].We use the black solid line($R = 2$ kpc,$z = 5$ kpc) as U_{ph}.

We consider the effect of time development, so we assume that the distance from the shock front changes with time like $\xi = x/L = v_{\rm pro}t/L$, and then D_{pp} becomes the function of the time t. We also consider the contribution of the electrons out of the turbulence, so we solve the equation of these electrons

$$\frac{\partial n_{esc}}{\partial t} + \frac{\partial}{\partial p}\left(\frac{dp}{dt}n_{esc}\right) - Q_{inj}^{esc} = 0 \tag{7}$$

where Q_{inj}^{esc} is equal to the escape rate from the turbulence $Q_{inj}^{esc} = n/t_{esc}$.

To verify the effect of the escape, we calculate the spectrum of electrons under three cases. 'No escape model' is the model in which we neglect the escape term n/t_{esc}(the limit $t_{esc} \to \infty$). In the 'Cut escape model', we consider the effect of escape but we don't deal with electron out of the turbulence(like[7]). So in the Cut escape model, we solve only (1), and don't solve (7). We consider the electrons out of the turbulence in the 'With escape model', then we solve both (1) and (7), and finally calculate sum of them $n_e = n + n_{esc}$.

After the calculation of the spectrum of the electrons, we estimate the Intensity from those electrons and compare with the data of the Fermi-LAT and the WMAP. In the next section sec.III, we show the results of our calculation.

III. RESULTS

Our results are shown in the Figure 2. We calculate equation (1) under the three cases at variable parameters L and Q_0 for $t = 2{\rm kpc}/v_{\rm pro} \simeq 8$ Myr. $v_{\rm pro} = 250{\rm kmsec^{-1}}$ and $B = 4\mu$G are fixed. The result of 'No escape model' is shown in blue solid line, 'Cut escape model' is shown in red solid line, and 'With escape model' is shown in black solid line. The data points in [9] are adopted.

Gamma ray data of the Fermi-LAT are nicely reproduced in all cases. But the microwave data of the WMAP are reproduced only by 'With escape model'(Figure 2). This is because of increasing of low energy particles due to escape from the turbulence. In this case the turbulence size $L = 10$ pc, smaller than that of in [7] $L = 2$ kpc. If we reproduce the WMAP data in other cases, stronger magnetic field is required at large scale.

IV. SUMMARY

We reproduce both the Fermi Bubble and the WMAP haze under typical galactic magnetic field $B = 4\mu$G by considering the effect of time dependence and electrons which escape from the turbulence. 'Cut escape model' which is similar to the model of previous research Mertsch & Sarkar [7] reproduce gamma ray data well, but predicted microwave emission is not

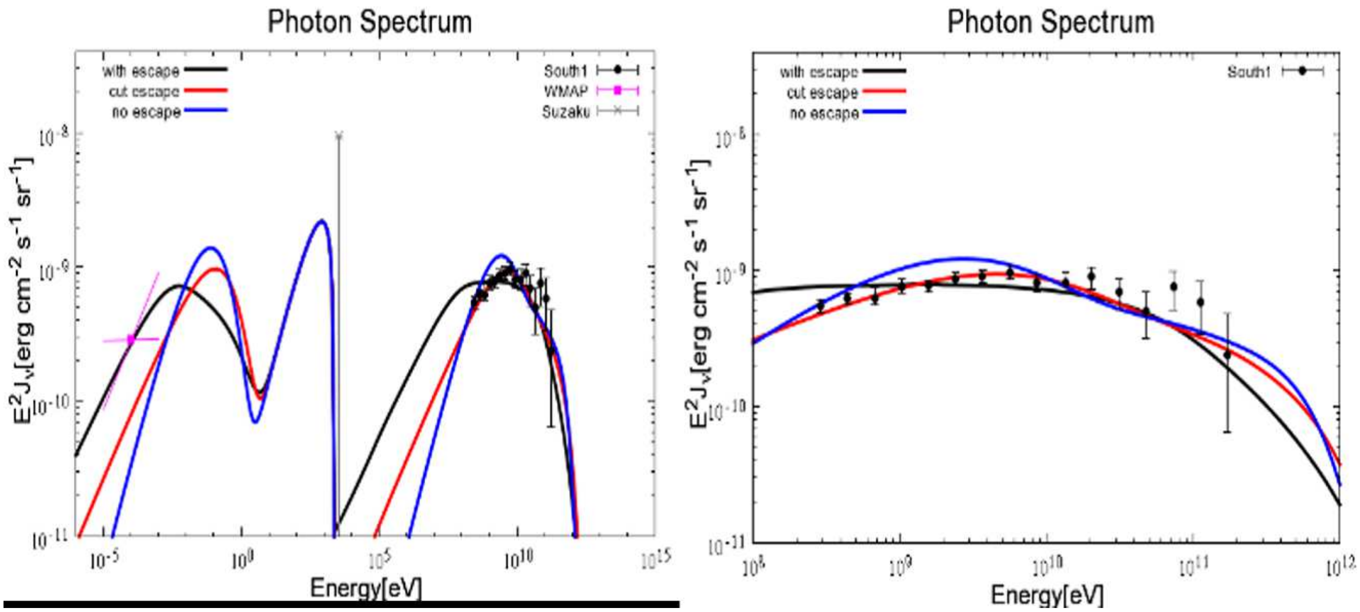

FIG. 2: **l**eft: Photon spectrum under three cases. **r**ight: Photon spectrum at gamma ray region. 'No escape model'(blue solid), 'Cut escape model'(red solid), 'With escape model'(black solid) are all shown.The data points are from [9].

enough at $B = 4\mu$G. Our results suggest that smaller turbulence size is better for reproducing microwave observation, because of more easily escaping from the turbulence.

Acknowledgments

We appreciate JaCOW for helpful discussion.

---

[1] Su, M., Slatyer, T. R., & Finkbeiner, D. P. 2010, ApJ, 724, 1044
[2] Ackermann, M., et al. 2014, ApJ, 793, 64
[3] Dobler, G., & Finkbeiner, D. P. 2008, ApJ, 680, 1222
[4] Crocker, R. M., & Aharonian, F. 2011, Phys. Rev. Lett., 106, 101102
[5] Fujita, Y., Ohira, Y., & Yamazaki, R. 2013, ApJ, 775, L20
[6] Cheng, K. S., Chernyshov, D. O., Dogiel, V. A., Ko, C. M., & Ip, W. H. 2011, ApJ, 731, L17
[7] Mertsch, P., & Sarkar, S. 2011, Phys. Rev. Lett., 107, 091101
[8] Vladimirov, A. E., Digel, S. W., Jóhannesson, G., et al. 2011, Computer Physics Communications, 263 182, 1156
[9] Yang, R., Aharonian, F., & Crocker, R. M. 2014, A&A, 567, A19

VERITAS Observations of the Unidentified Point Source HESS J1943+213

K. Shahinyan for the VERITAS Collaboration
University of Minnesota, Minnesota Institute for Astrophysics, Minneapolis, MN, 55455

The H.E.S.S. Galactic plane scan has revealed a large population of Galactic very high energy (VHE; E > 100 GeV) emitters. The majority of the galactic sources are extended and can typically be associated with pulsar wind nebulae (35%) and supernova remnants (21%), while some of the sources remain unidentified (31%) [1]. A much smaller fraction of point-like sources (5 in total, corresponding to 4%) are identified as gamma-ray binaries. Active galactic nuclei located behind the Galactic plane are also a potential source class. An active galaxy could be identified in the VHE regime by a point-like appearance, a high variability amplitude (up to a factor of 100) and a typically soft spectrum (due to absorption by the extra-galactic background light). Here we report on VERITAS observations of HESS J1943+213, an unidentified point source discovered to emit above 470 GeV during the extended H.E.S.S. Galactic plane scan [2]. This source is thought to be a distant BL Lac object behind the Galactic plane and, though it exhibits a steep spectrum it is a weak GeV source, only recently detected using 5 years of Fermi-LAT data [3]. Deep VERITAS observations at high elevations result in the most significant VHE detection of this object so far, with an excess above 200 GeV of more than 18σ. We use variability and spectral analyses of VERITAS data on HESS J1943+213 in a multi-wavelength context to address the source classification.

1. Identity of HESS J1943+213

HESS J1943+213 was first discovered in very-high-energy (VHE; E > 100 GeV) gamma rays during the H.E.S.S. Galactic plane scan [2]. Due to its point-like appearance in VHE gamma rays, three possible source classes were suggested: gamma-ray binary, pulsar wind nebula (PWN), and BL Lac object (blazar).

Assuming the source is a gamma-ray binary, ref. [2] used the lack of detection of a massive (O- or B-type) companion star to estimate a distance limit of greater than ∼25 kpc. This distance would place the binary well beyond the extent of the Galactic disk and would imply an X-ray luminosity 100-1000 times higher than known gamma-ray binaries. Such a distance limit is therefore problematic, and this scenario is disfavored. In addition, the point-like appearance in the X-rays and the soft VHE spectrum with a power-law index of Γ=3.1 ± 0.3 (in contrast to the softest known PWN index of 2.7) motivated ref. [2] to argue against the PWN scenario, leaving the blazar hypothesis. The authors found all observations to be consistent with the blazar scenario. The point-like nature in both X-rays and VHE, the soft VHE spectral index, and a preliminary IR spectrum showing lack of emission lines are expected for a blazar. Moreover, the hard X-rays observed with INTEGRAL IBIS and Swift BAT instruments show no evidence of a cutoff up to an energy of ∼195 keV. If the source is a blazar, it would be categorized as an extreme high-synchrotron-peak BL Lac object (extreme HBL), a class of blazars with the synchrotron peak located at energies >1 keV [4].

Since the discovery publication, the identity of HESS J1943+213 has been the topic of an ongoing debate. 1.6-GHz VLBI observations of the HESS J1943+213 counterpart with the European VLBI Network produced a detection that was claimed to show extension, with FWHM angular size of 15.7 mas (the expected size for a point source is 3.5 mas) [5]. Based on this measurement, the brightness temperature of the counterpart was estimated to be 7.7×10^7 K and was used to argue against the blazar scenario, as the expected brightness temperature of HBLs is in the 10^8–10^9 K range. In addition, ref. [5] employed a $1'$ feature observed in the 1.4-GHz VLA C-array configuration image to support the PWN hypothesis, with the assertion that the angular size of the feature is consistent with a Crab-like PWN placed at a distance of 17 kpc. On the other hand, ref. [6] argued in favor of an extreme HBL by constructing a spectral energy distribution and drawing comparisons to a known extreme HBL, 1ES 0347-121. More recently, ref. [3] bolstered the extreme HBL case by observing the near-infrared (K-band) counterpart of HESS J1943+213, claiming potential detection of an elliptical host galaxy with 10% probability the object is a star. Using 5 years of data, they also obtain the first significant detection of the source with Fermi LAT (within 2σ positional uncertainty) in the 1–300 GeV energy regime. Nonetheless, there is yet to be a definitive identification of the HESS J1943+213 source class.

Here we present results from VERITAS observations of HESS J1943+213 and discuss implications for the debate regarding the source identity.

2. VERITAS Observations

Very Energetic Radiation Telescope Array System (VERITAS) is an array of four 12-m imaging atmospheric Cherenkov telescopes, located in Arizona, USA at an elevation of ∼1270 m. The camera for each telescope is composed from 499 photo-multiplier

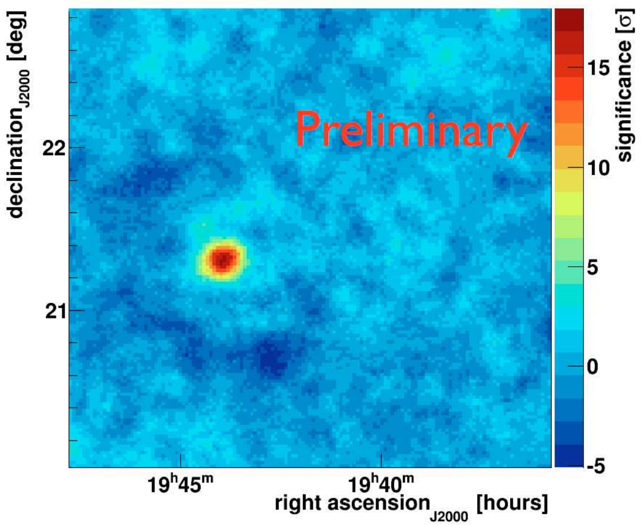

Figure 1: Significance sky map of VERITAS observations of HESS J1943+213.

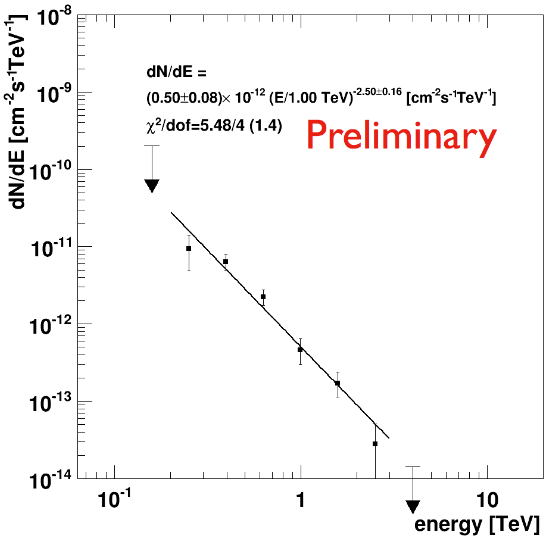

Figure 2: Differential energy spectrum of HESS J1943+213 with VERITAS, between 200 GeV and 2 TeV, with results from a fit to a power-law function.

tubes, with a field of view of approximately 3.5°. VERITAS is able to reliably reconstruct VHE gamma rays with energies between 100 GeV and 30 TeV [7], with the sensitivity to detect a 1% Crab Nebula flux source at 5σ in 25 hours. The systematic uncertainty in the energy determination is within the 15–20% range.

VERITAS observed HESS J1943+213 between May 27, 2014 (MJD 56804) and July 2, 2014 (MJD 56840) with 27.8 hours of total live time. Observations took place at elevations between 63° and 80°, leading to $\sim 18\sigma$ source detection above 200 GeV.

3. Results

Figure 1 shows the significance sky map near HESS J1943+213, including the detected source. The source location is consistent with the catalog position of HESS J1943+213. A preliminary VERITAS differential energy spectrum of the source is shows in Figure 2. The high elevation observations allow for a lower energy threshold and lead to a spectrum that extends down to 200 GeV, compared with 470 GeV from H.E.S.S. observations. The source spectrum is fit by a power-law function with an index of Γ=2.5 ± 0.16 in the energy range 200 GeV–2 TeV. The VERITAS spectrum of HESS J1943+213 appears harder than the spectrum from H.E.S.S. (Γ=3.1 ± 0.3), though a more rigorous comparison is necessary, as the energy ranges differ between the two detections.

The flux of $(1.30 \pm 0.20) \times 10^{-12}$ cm^{-2} s^{-1} measured with VERITAS above 470 GeV is consistent with a flux of $(1.25 \pm 0.20) \times 10^{-12}$ cm^{-2} s^{-1} from the H.E.S.S. detection. Additionally, no flux variability is seen within VERITAS observations.

As VERITAS is able to observe HESS J1943+213 at a much higher elevation than H.E.S.S., the detection rate of the source with VERITAS is $3.4\sigma/\sqrt{\text{hour}}$, compared with $1.8\sigma/\sqrt{\text{hour}}$ with H.E.S.S., allowing VERITAS to test for variability on a factor of four shorter timescales.

4. Discussion and Outlook

The agreement between fluxes measured approximately five years apart with VERITAS and H.E.S.S. and a lack of a variability detection in other energy bands is surprising if HESS J1943+213 is a blazar. Blazars are known to vary at all energies and at a wide range of timescales [8]. Although the stable flux of the source observed to date does not rule out the blazar hypothesis, continued non-detections of variability are becoming a growing challenge for this scenario.

VERITAS can probe timescales that are a factor of four shorter than those available to H.E.S.S and therefore represents the best VHE dataset available for searches of flux and spectral variability from this source. Advanced analysis techniques will provide an even higher sensitivity and allow for an additional factor of two improvement in the minimum variability timescale that can be tested.

The VERITAS-measured spectrum of HESS J1943+213, albeit preliminary, exhibits a harder index than the H.E.S.S. spectrum. The soft spectral index from H.E.S.S. constitutes one of the key pieces of evidence against the PWN hypothesis. Thus, in conjunction with the lack of detectible variability in the VHE regime, the harder VERITAS spectrum may be counted in favor of the PWN hypothesis.

VERITAS will continue observations of HESS J1943+213 and will monitor the source for potential variability. In addition, the upcoming PASS 8 Fermi-LAT data will allow for an improved detection and a spectrum of the source in GeV gamma rays, providing a significantly better handle on the gamma-ray peak of the HESS J1943+213 spectral energy distribution. Multi-wavelength studies of the source, including studies of its spectral energy distribution will be essential for definitively identifying the source class.

References

[1] Carrigan, S., Brun, F., Chaves, R. C. G., et al. 2013, arXiv:1307.4868

[2] H.E.S.S. Collaboration, Abramowski, A., Acero, F., et al. 2011, A&A, 529, AA49

[3] Peter, D., Domainko, W., Sanchez, D. A., van der Wel, A., Gässler, W. 2014, A&A, 571, AA41

[4] Costamante, L., Ghisellini, G., Giommi, P., et al. 2001, A&A, 371, 512

[5] Gabányi, K. É., Dubner, G., Giacani, E., et al. 2013, ApJ, 762, 63

[6] Tanaka, Y. T., Stawarz, Ł., Finke, J., et al. 2014, ApJ, 787, 155

[7] Holder, J., Atkins, R. W., Badran, H. M., et al. 2006, Astroparticle Physics, 25, 391

[8] Boettcher, M. 2012, arXiv:1205.0539

VERITAS Observations of Very High Energy Blazars and Potential for Cosmological Insight

A. Furniss for the VERITAS Collaboration
Stanford University, Stanford, CA, 94305 USA

Gamma-ray blazars are among the most extreme astrophysical sources, harboring phenomena far more energetic than those attainable by terrestrial accelerators. These galaxies are understood to be active galactic nuclei that are powered by accretion onto supermassive black holes and have relativistic jets pointed along the Earth line of sight. The emission displayed is variable at all wavelengths and timescales probed thus far, necessitating contemporaneous broadband observations to disentangle the details of the emission processes within the relativistic jets. The very high energy (VHE; $E \geq 100$ GeV) photons emitted by these sources are detectable with ground-based imaging atmospheric Cherenkov telescopes such as VERITAS. As these photons propagate extragalactic distances, the interaction with the diffuse starlight that pervades the entire Universe results in a distance and energy dependent gamma-ray opacity, offering a unique method for probing photon densities on cosmological scales. These galaxies have also been postulated to be potential sources of ultra-high-energy cosmic rays, a theory which can be examined through deep gamma-ray observations of sources which probe moderate gamma-ray opacities. Within this work, I will highlight ongoing research regarding the broadband emission from VERITAS-observed VHE blazars, as well as the potential to use them for cosmological insight.

I. VERITAS

VERITAS is an array of four imaging atmospheric Cherenkov telescopes in southern Arizona, each with a 3.5° field of view. The array is sensitive to very-high-energy (VHE) gamma-ray photons with energies from ~70 GeV to more than 10 TeV and can detect a 1% Crab-Nebula-flux source at 5 standard deviations (σ) in less than 28 hours. The telescope array uses 12-meter reflectors to focus dim, blue/UV Cherenkov light from gamma-ray and cosmic-ray interactions in the atmosphere onto cameras composed of 499 photomultiplier tubes (PMTs). More details on the VERITAS instrument can be found in [1] and [2].

II. STUDYING COSMOLOGY WITH VHE BLAZARS

Blazars are a type of active galaxy with a relativistic jet pointed toward the observer. These sources are perplexing objects which contain some of the most energetic particle processes in the Universe. These extreme sources produce non-thermal spectral energy distributions (SEDs), characterized by two broad peaks. The origin of the lower-energy peak is relatively well understood, resulting from the synchrotron radiation of relativistic leptons in the presence of a tangled magnetic field. The higher-energy SED peak is commonly attributed to inverse-Compton upscattering by the relativistic leptons within the jet of either the synchrotron photons themselves, namely synchrotron self-Compton (SSC) emission, or a photon field external to the jet, namely external Compton (EC) emission. Alternative models attribute the higher-energy peak of blazar emission to hadronic pion production and the resulting cascade emission, which can provide convincing evidence that sufficient hadronic acceleration is at work within VHE blazars to make them reasonable source of UHECRs.

VHE gamma rays that propagate through the intergalactic medium are absorbed by low energy extragalactic background light (EBL) photons via pair production, $\gamma + \gamma \rightarrow e^+ + e^-$[3]. The absorption modifies the intrinsic VHE gamma-ray spectra of extragalactic objects and limits the distance out to which these sources should be detectable by VHE instruments. The modification of the emitted spectrum is energy and redshift-dependent, making the distance to extragalactic VHE sources a vital parameter for the accurate interpretation of the observed VHE spectra.

The absorption of VHE gamma rays by the EBL is estimated using the model-specific (e.g. [4–6] gamma-ray opacity, $\tau(E, z)$, and the intrinsically emitted flux, F_{int}, is estimated from the observed flux, F_{obs}, using the relation $F_{int} = F_{obs} \times e^{\tau(E,z)}$. Although the EBL cannot be directly measured due to strong foreground sources, alterations to intrinsically emitted VHE blazar spectra by absorption by the EBL have been used to estimate the spectral properties of the EBL [7, 8], providing upper limits on the IR photon density which are consistent with the strict observational lower limits set by galaxy counts.

Recent work has indicated that the EBL density is closer to the observational lower limits than the indirectly set upper limits [9, 10]. Interestingly, there are VHE observations which, when corrected for absorption by even the lowest density EBL models, show indications of spectral hardening at the highest energies, but are strictly in agreement with the $\Gamma = 1.5$ spectral limitation (where $dN/dE \propto E^{-\Gamma}$) described in, e.g., [7].

The onset of spectral hardening at the highest energies in sources which probe moderate opacities is clearly predicted by theories which include secondary emission from UHECR extragalactic propagation and interaction with intervening diffuse photon fields such as the EBL and CMB. If VHE blazars eject sufficiently accelerated protons, photo-pion production with these photon fields can initiate cascades along the line of sight, producing a hard spectral feature at the highest energies from secondary gamma rays, as described in [11]. Detected gamma-ray emission can be definitively associated with these secondary emission processes using the spectral shape and variability characteristics that are observed in the gamma-ray band. For distant sources, it is expected that the secondary component would contribute a significant portion of the observed gamma-ray signal, particularly at the highest energies, where intrinsic gamma rays are attenuated over the long path length through the EBL, as explored in [12]. Any hard component displayed by extragalactic VHE sources should lack variability due to intrinsic variations in flux being washed out over a variety of path lengths - a useful observable for checking the feasibility of the secondary line-of-sight UHECR emission scenario.

Studying VHE blazars also enables the investigation of the magnitude of the intergalactic magnetic field (IGMF) through the study of the cascade emission along the source line of sight. The large scale magnetic fields that may exist in the regions between galaxies is known as the IGMF. Although the origin of this magnetic field is still unknown, and could have been generated at several points in the evolution of the early universe [13], the current IGMF has been proposed as the seed field for strong (10^{-6} G) fields observed in galaxies and galaxy clusters. Recent studies indirectly place upper (10^{-9} G) and lower (10^{-20} G) limits on the strength of the IGMF [14, 15]. Tighter constraints, and possible insight on any large scale structure (e.g. correlation length) on the field strength are necessary to constrain models explaining the IGMFs origin. The inclusion of this affect in emission models can enable an indirect probe to the IGMF through the inspection of extragalactic gamma-ray point source diffusion beyond the instrumental PSF. There have also been studies on the possibility that for bright blazars the pair cascade energy is dissipated in heating of the intergalactic medium [16, 17], a process that may need to be taken into account when using VHE blazars to study the IGMF and a topic where observations of bright VHE blazars which are significantly attenuated by EBL absorption can provide insight.

Notably, there is an additional, more exotic, mechanism potentially affecting gamma-ray propagation over extragalactic distances. A hard high-energy gamma-ray tail similar to that produced from UHECR interactions (or over-estimated absorption by the EBL) would result if VHE photons oscillate into axion-like particles (ALPs), allowing propagation through the EBL without interaction [18]. Evidence for an effect of just this sort has recently been claimed [19].

Motivated by the potential studies of extragalactic gamma-ray photon propogation and the interacting cosmological fields, VERITAS has collected deep observations of three distant VHE blazars (PKS 1424+240 at $z > 0.6035$, PG 1553+113 at $z > 0.395$ and 3C 66A at $0.3341 < z < 0.41$). We discuss the VERITAS observations, source characteristics and the flux correction for absorption by the EBL here.

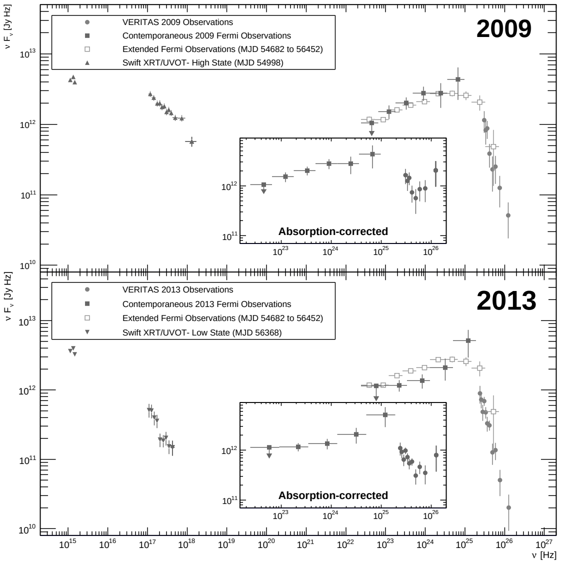

FIG. 1: Two broadband SEDs of PKS 1424+240, corresponding to a relatively high (upper panel) and a low (lower panel) state. Within the inset, the VHE data are corrected for absorption using the low-opacity Gilmore et al. 2012 EBL model for $z = 0.6$. The LAT data above 100 MeV, contemporaneous with the VERITAS observations in each year are shown along with the spectral results from full LAT observations. The *Swift* XRT and UVOT observations of a relatively low and high state are also shown.

III. VERITAS OBSERVATIONS OF DISTANT VHE BLAZARS

A. PKS 1424+240

PKS 1424+240 (VER J1427+237) is a distant very high energy (VHE; $E \geq 100$ GeV) blazar at $z \geq 0.6035$ [20]. At this *minimum* distance, the intrinsic VHE emission is significantly absorbed by the EBL. VERITAS observations of PKS 1424+240 were performed over three seasons and are reported in [21]. The first season (MJD 54881-55003) provides 28 hours of quality-selected livetime and is reanalyzed here, showing results consistent with those reported in [22].

The second season encompasses 14 quality-selected hours of observation between MJD 55598 and 55711, while the third season includes data spanning MJD 56334 to 56447, and provide 67 hours of quality-selected livetime with a threshold of 100 GeV, enabled by a camera upgrade in 2012.

The contemporaneous broadband SEDs of PKS 1424+240 for the relatively high state observed in 2009 and the relatively low state of 2013 are shown in Figure 1. When the observed VHE spectrum of PKS 1424+240 is corrected for the minimal absorption by the EBL, it appears that the source displays a complex spectral structure (insets of Figure 1). With the marginal ($\sim 2\sigma$) hardening at the highest energies, it is challenging to model the source emission with a standard SSC emission scenario.

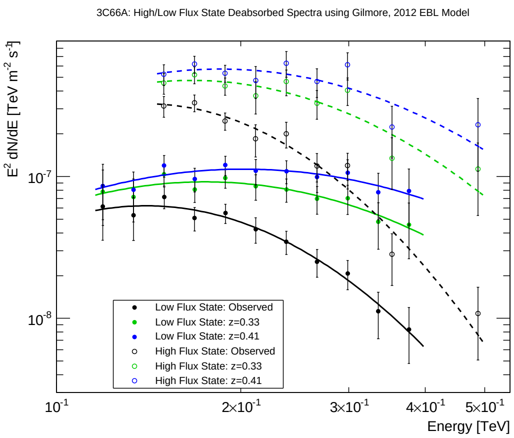

FIG. 2: VHE spectra of 3C 66A in both the low (solid black) and high (dotted black) flux state. The elevated state was observed over three days in October of 2008 (6 hours of livetime; MJD 54747-54749), while the low state is results from integrated observations between 2008 and 2014 (52 hours of livetime; MJDs 54361-54746 & 54750-56604). The observations are corrected for the expected absorption by the [4] EBL model, assuming the upper (blue) and lower (green) redshift limits of $z = 0.41$ and $z = 0.33$, respectively.

B. 3C 66A

As a bright gamma-ray source which was for a long time purported to be at a redshift of 0.44 from a erroneous spectroscopy measurements [23–25], 3C 66A is of great interest to the high-energy astrophysics community. Motivated by the featureless optical spectra displayed by the source, far-ultraviolet spectra were collected with COS onboard HST. Intergalactic medium absorption features within the spectra were used to place a firm lower limit on the blazar redshift of $z \geq 0.3347$. Additionally, an upper limit is set by statistically treating the non-detection of additional absorbers beyond $z = 0.3347$, indicating a redshift of less than 0.41 at 99% confidence and ruling out $z \geq$0.444 at 99.9% confidence [26].

This BL Lac object was first detected at VHE by VERITAS in 2008 [27, 28]. VERITAS observations in October of 2008 showed the source to be in an elevated state, displaying VHE emission at the level of 6% of the Crab (6 hours of livetime between MJD 54747-54749; dashed black line in Figure 2). Continued observation of the source were completed between 2008 and 2014, resulting in 52 hours of exposure while the source displayed a lower flux state of ~2% of the Crab Nebular (MJDs 54361-54746 & 54750-56604; solid black line Figure 2). The high and low states displayed by 3C 66A can both be fit with a curved log parabola of the form $E^2 dN/dE = N_0(E/E_0)^{-\Gamma-\beta\log(E/E_0)}$ (with E_0= 270 GeV) where $N_0 = (11.8 \pm 1.3) \times 10^{-8}$ and $(2.82 \pm 0.28) \times 10^{-8}$ TeV m^{-2} s^{-1} , $\Gamma = 3.07 \pm 0.4$ and 2.30 ± 0.43 and $\beta = 5.2 \pm 2.1$ and 4.8 ± 1.8 for the high and low states, respectively. The log-parabolic fit is preferred over a simple power-law fit at the $\sim 3\sigma$ level for both the low and high states.

With detection of 3C 66A out to 400 GeV in the low state, and 500 GeV in the high state, the gamma-ray opacity being probed by the source can be estimated for the redshift lower and upper limits according to the low density EBL model from [4]. For the low state, $\tau(z = 0.33, 400$ GeV$)$=1.4 and $\tau(z = 0.41, 400$ GeV$)$=1.8. For the high state, $\tau(z = 0.33, 500$ GeV$)$=1.8 and $\tau(z = 0.41, 500$ GeV$)$=2.5.

C. PG 1553+113

PG 1553+113 is readily detected in the high-energy (100 MeV to 100 GeV) and VHE gamma-ray regimes. VERITAS is capable of detecting PG 1553+113 above 100 GeV with a significance of 5σ after ~43 minutes of exposure, given its average flux of 6.9 % Crab. Without a firm spectroscopic redshift due to a featureless optical spectrum, recent UV measurements using the COS on HST have yielded the strictest redshift constraint on the source to date, setting a firm lower limit of $z \geq 0.395$ [29].

The observed VHE spectrum displayed in Figure 3 (left panel) results from 95 hours of observation, and is shown along with contemporaneous *Fermi* observations. These observations are detailed in [30]. The VERITAS spectrum is measured between 160 and 560 GeV, and is well defined by a differential power law with index 4.33 ± 0.09. The combined contemporaneous *Fermi* LAT and VERITAS data between 100 MeV and 560 GeV are well fit with a power-law with an exponential cutoff at 101.9±3.2 GeV. Part of the cutoff at this energy may be instrinsic, but it is expected that a significant fraction of the cutoff is due to absorption by the EBL. Through EBL absorption-

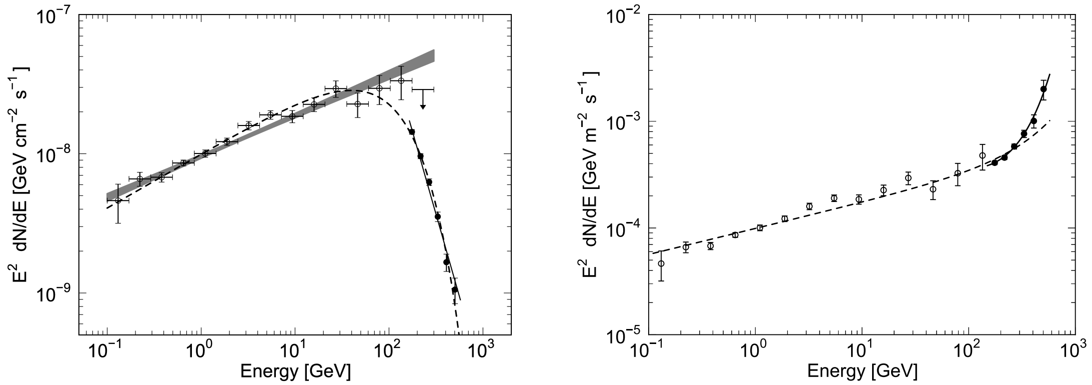

FIG. 3: **Left:** *Fermi*-LAT spectrum of PG 1553+113 (grey shaded area and open data points) plotted along with the VERITAS-observed spectrum (solid black data points and line). The highest-energy Fermi-LAT spectral bin is shown with a 95% confidence level upper limit. The best fit to the combined spectrum using a power law with an exponential cutoff are shown with a dashed line. **Right:** The absorption-corrected VHE spectrum (filled circle data points) a redshift of $z = 0.53$ and the EBL model from [4]. The solid curve represents the best fit to the intrinsic VHE spectrum using a power law with an exponential rise and was the fit used to set the upper limit on the source redshift. The dashed curve shows the best fit to the absorption-corrected gamma-ray spectrum.

correction using the model from [4], and the physically motivated requirement that the gamma-ray spectrum does not display an intrinsic exponential rise, the VHE spectrum measured by VERITAS allows a robust upper limit on the distance to the source of $z \leq 0.62$ (Figure 3, right panel).

IV. CONCLUSIONS

PKS 1424+240, 3C 66A and PG 1553+113 are all relatively bright VHE emitting blazars at significant redshifts. The bright VHE emission and significant distances have motivated deep VERITAS observations over multiple years . The steady emission allows spectral reconstruction up to hundreds of GeV, making the sources good targets for the study of VHE photon interaction with EBL photons along the line of sight. Improvement of our understanding of VHE blazar emission, VHE photon propagation across extragalactic distances and the cosmoligical fields which VHE photons interact with will continue to motivate VERITAS observations of these unique sources.

Acknowledgments

This research is supported by grants from the U.S. Department of Energy Office of Science, the U.S. National Science Foundation and the Smithsonian Institution, by NSERC in Canada, by Science Foundation Ireland (SFI 10/RFP/AST2748) and by STFC in the U.K. We acknowledge the excellent work of the technical support staff at the Fred Lawrence Whipple Observatory and at the collaborating institutions in the construction and operation of the instrument.

[1] Holder, J., Atkins, R., Badran, H. et al. 2006, Astropart. Phys., 25, 391
[2] Weekes, T. C. Badran, H., Biller, S. et al. 2002, Astropart. Phys., 17, 221
[3] Nikishov, A. I. 1962, JETP, 14, 393
[4] Gilmore, R., Somerville, R., Primack, J. & Dominguez, A. 2012, MNRAS, 422, 3189
[5] Domínguez, A., Primack, J., Rosario, D. J. et al. 2011, MNRAS, 410, 2556
[6] Franceschini, A., Rodighiero, G. & Vaccari, M. 2008, A&A, 487, 837
[7] Aharonian, F., Akhperjanian, A. G., Bazer-Bachi, A. R. et al. 2006, Nature, 440, 1018
[8] Albert, J., Aliu, E., Anderhub, H. et al. 2008, Science, 320, 1752
[9] Abramowski, A., Acero, F. Aharonian, F. et al., 2013, A&A, 550, 4
[10] Ackermann, M., Ajello, M., Allafort, A. et al. 2012, Science, 338, 1190
[11] Essey, W. & Kusenko, A. 2010, Astropart. Phys. 33, 81
[12] Essey,W. & Kusenko, A. 2014, Astropart. Phys. 57, 30
[13] Kulsrud et al. 2008, RPP., 71, 046901

[14] Neronov & Vovk. 2010, Science, 328, 73
[15] Taylor et al., 2011, A&A, 529, A144
[16] Broderick, A. et al. 2012, ApJ, 752, 22
[17] Schlickeiser, R. et al. ApJ, 758, 101
[18] de Angelis et al. 2011, PRD, 84: 105030
[19] Horns, D. & Meyer, M. 2012, JCAPP, 2: 33
[20] Furniss, A., Williams, D. A., Danforth, C. et al. 2013, ApJL, 768, 31
[21] Archambault, S. et al. 2014, ApJL, 726, 43
[22] Acciari, V. A., Aliu, E., Arlen, T. et al. 2010, ApJL, 708, 100
[23] Miller, J. S., French, H. B., & Hawley, S. A. 1978, in Pittsburgh Conf. BL Lac
[24] Kinney, A. L., Bohlin, R. C., Blades, J.C. & York, D. G. 1991, ApJS, 75, 645
[25] Bramel, D. A., Carson, J., Covault, C. E. et al. 2005, ApJ, 629, 108
[26] Furniss, A., Fumagalli, M., Danforth, C., Williams, D. A. & Prochaska, X. 2013, ApJ, 766, 35
[27] Acciari, V. A., Aliu, E., Arlen, T. et al. 2009, ApJ, 693, 104
[28] Abdo, A. A. et al. 2011, ApJ, 726,43
[29] Danforth, C. W. et al. 2010, ApJ, 720, 976
[30] Aliu, E. et al. 2015, ApJ, 799, 7

A Correlation Between Optical, X-ray, and Gamma-ray Variations in Blazar 3C 454.3

Yutaro Tachibana, Nobuyuki Kawai
Department of Physics, Tokyo Institute of Technology, 2-12-1, Ohokayama, Tokyo, Japan, 152-8550
Sean Pike
Depertment of Physics, Brown University, Providence, Rhode Island 02912, USA
on behalf of the MAXI Team and MITSuME Team

We present the light curve data of a remarkable blazer 3C 454.3 (z=0.859) in optical, X-ray, and gamma-ray bands. Since January 2008, we have been monitoring this object using the 50 cm MITSuME, a optical telescope, and detected several flares including extraordinary and simultaneous flares in the γ-ray and optical bands in November 2010. Additionally, the Monitor of All-sky Image (MAXI) has been observing 3C 454.3 continuously since August 2009. Using these data and gamma-ray flux observed with Fermi-LAT, we discuss features and correlations of flux variations between the energy bands.

1. INTRODUCTION

The flat-spectrum radio-loud quasar 3C 454.3 (z=0.859; Jackson and Brown, 1991) is a well known object as one of the most active and brightest sources in the gamma-ray sky. Optical and radio observations revealed that they are ascribed to strongly Doppler-boosted emission from relativistic electrons in a jet of plasma. The jet is oriented within ∼2° to the line of sight (Jorstad et al. 2005). The "small and big blue bump" has been detected by Raiteri et al. (2007) in the optical to ultraviolet band. The small blue bump is probably a mixture of a iron lines, Mg II lines, and Balmer continuum from the broad line region [Ogle et al. 2011]. On the other hand, the big blue bump is interpreted as a signature of the thermal accretion disk (eg. Pian et al. 1999). The X-to-γ-ray radiation from 3C 454.3 is commonly understood to be produced in the plasma jet through an Inverse-Compton (IC) scattering process off the same electrons that yield the radio to optical synchrotron emission. whereas, the origin of the seed photons for the IC scattering is not clear yet. Namely, (i) same synchrotron photons (SSC), (ii) photons coming from outside the jet (EC), or (iii) both of these would be possible to being seed photons. The X-ray range is most complicated because it might contain the high-energy tail of the synchrotron emission besides IC scattering component (Abdo et al. 2010). One example of the SED of 3C 454.3 is shown in Figure 1 (quoted from Vercellone et al. 2010).

Perhaps one of the most powerful tool to uncover the emission mechanism of the jet is time variability. Observing the with multi-wavelength for long period, and investigating correlations between different energy bands, we can build up a physical picture of the jet and its surroundings.

In this paper, we firstly show the light curve data in three energy bands, optical, X-ray, and γ-ray obtained by MITSuME and SMARTS[1], MAXI/GSC[2], and Fermi/LAT[3] respectively, secondly present some results of time domain analysis, and finally discuss about correlations of flux variations between these energy bands briefly.

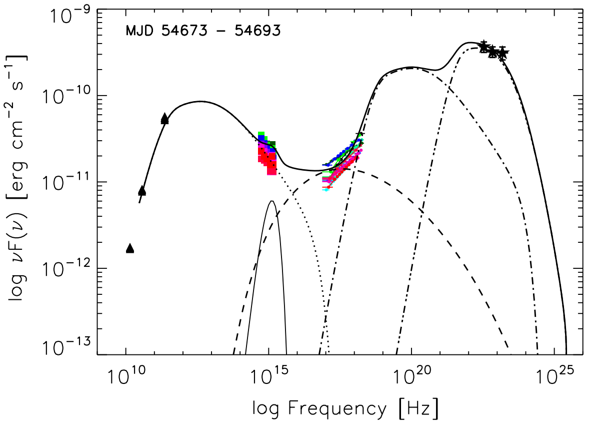

Figure 1: The SED of 3C 454.3 during the period MJD = 54673-54693. The thin sold, dotted, dashed, dot-dashed, and the triple-dot-dashed lines represent the accretion disk component, the SSC component, EC on the accretion disk, and EC on the broad line region (BLR), respectively (Vercellone et al. 2010). The sum of those the individual components is drawn by the thick solid line.

---

[1] http://www.astro.yale.edu/smarts/glast/home.php#
[2] http://maxi.riken.jp/top/
[3] http://fermi.gsfc.nasa.gov/ssc/data/access/lat/

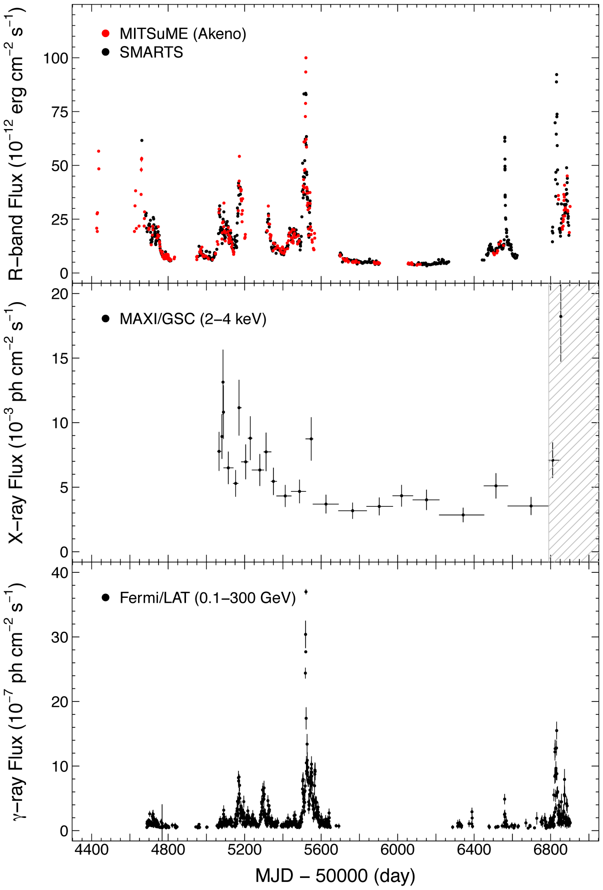

Figure 2: The 7-years light curves of 3C 454.3 from MITSuME and SMARTS (R-band), X-ray (2-4 keV) flux from MAXI/GSC, γ-ray (0.1-300 GeV) flux from Fermi/LAT. In the shadowed area on the X-ray light curve, contaminating by a nearby X-ray source is suspected.

2. THE DATA AND ANALYSIS

2.1. Light Curves in Multi Wavelength

Figure 2 shows the variation of R-band flux from MITSuME (Akeno Observatory, red points) and SMARTS (Bonning et al. 2012, black points), X-ray (2-4 keV) flux from MAXI/GSC, and γ-ray (0.1-300 GeV) daily averaged flux from Fermi/LAT. For converting the R-band magnitude to the flux, we assume that the 0 mag in R-band correspond to a flux of 1.42×10^{-5}ergcm^{-2}s^{-1} (Sasada et al. 2011). In the middle panel, the gray shaded region indicates the interval which may be contaminated by the nearby X-ray source IM Peg (see the ATel #6296). To see the X-ray flux variations easily, we summed the daily flux data points until satisfying the following condition at each data points: Flux/Error $\geq$ 5.

Variations, especially activities like flares, are seen to be completely correlated across the three energy bands. On the other hand, looking closely to variations in the light curves in the point of view of flare amplitudes, the X-ray band seems to show lower variabilities than the optical band and γ-ray bands. While it is certainly affected by a binning size, it was also noticed in Vercellone et al. (2010). Additionally, in the optical band and γ-ray band, flux responses originated from same events (same times) can be different from a flare to another. We will present a detailed analysis on this point in section 2.4.

2.2. Color-Magnitude Variation in Optical bands

Color-magnitude analysis is useful for investigating the property of spectral behavior of the optical variation. We show the R-I color indices as a function of I-band magnitude in Figure 3. 3C 454.3 shows flux fluctuation on a very short time scales (a few hours), so we used the R and I data taken simultaneously using the MITSuME tri-color camera for constructing the color magnitude diagram. As pointed out by Villata et al. (2006), this diagram shows the redder-when-brighter behavior which is interpreted as the contribution of a stable "blue" component, *i.e.* the thermal radiation from the accretion disk (big blue bump) lying under the variable "red" component *i.e.* the synchrotron radiation from the relativistic electrons in the jet. When

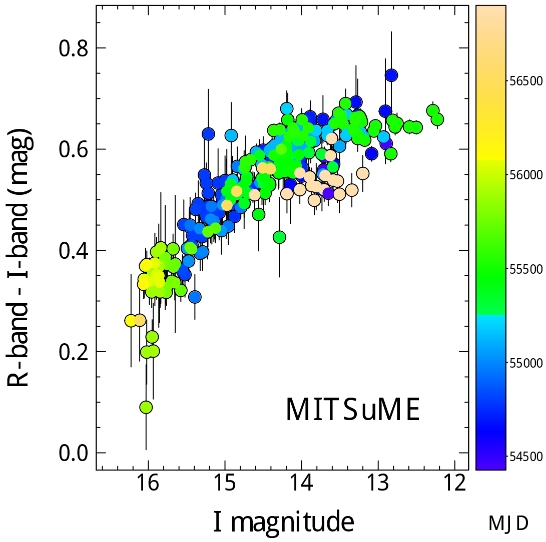

Figure 3: R-I color vs. I-band magnitude for 3C 454.3. Colors indicate the date of the observation in units of MJD as shown in the right bar. The redder-when-brighter trend and the plateau are shown in this digram.

the jet emission dominates that of the accretion disk, a plateau from R-magnitude ∼14 towards the brightest end will emerge in the color-magnitude diagram. It should be note that the magnitude of plateau have changed from ∼0.65 mag to ∼0.5 mag in a time between MJD ∼55500 and MJD ∼56800. This may indicate that some physical parameter of the accretion disk or the synchrotron emitting electrons (or both of these) are dramatically changed within this term.

2.3. The Ratio of The Optical and The Gamma-ray Flux

Studies about 3C 454.3 have revealed a close connection between the optical and γ-ray flux behavior not only in high activity states but also in non-flaring state (e.g. Bonning et al. 2008; Abdo et al. 2010a). Assuming photons in optical bands are produced by the synchrotron radiation of the relativistic electrons in the jet and γ-ray photons are produced through the IC scattering process by the same electrons, we can represent observed flux variations in these energy bands as

$$F_{\rm opt} \sim N_e \delta^{3+\alpha_0} B^{1+\alpha_0} \quad (1)$$

$$F_\gamma \sim N_e \delta^{4+2\alpha_g} U_{\rm ext}, \quad (2)$$

t thus the flux ratio of the optical band and the γ-ray is predicted as following:

$$\frac{F_{\rm opt}}{F_\gamma} \sim B^{1+\alpha_0} U_{\rm ext}^{-1} \delta^{\alpha_0-2\alpha_g-1}, \quad (3)$$

where N_e is total number of emitting electron, δ is Doppler factor of an synchrotron emitting plasma, α_0 and α_g are the spectral indices in the optical and γ-ray bands, respectively, B is magnetic field in the emitting region, and $U_{\rm ext}$ is the external seed photon field (Chatterjee et al. 2012).

Flux ratios calculated using the R-band flux and γ-ray flux pairs observed on same days are shown in Figure 4. From this figure,we can notice a trend that the flux ratio $F_{\rm opt}/F_\gamma$ becomes small as the source becomes bright. There seems to be some time lag in this tendency (the decrease of the ratio lags the increase of the brightness), and this point will be investigated in section 2.3.1. If the variation is only due to a change in N_e, the ratio $F_{\rm opt}/F_\gamma$ will be constant because the ratio does not depend on N_e, as shown in Eq.(3) . In addition, as can be appreciated from Eq.(1) and Eq.(2), if the variation arose from a change in B or $U_{\rm ext}$, the optical and the γ-ray variations will not be correlated. Therefore, this supposition is inconsistent with the previous research results, except the so called "γ-ray orphan" optical-UV flare (eg. Vercellone et al. 2011). For these reason, this trend may indicates that the Doppler factor δ plays a big role in the flux fluctuation in the optical and γ-ray bands. The origin of flux variation will also be discussed in section 2.5.

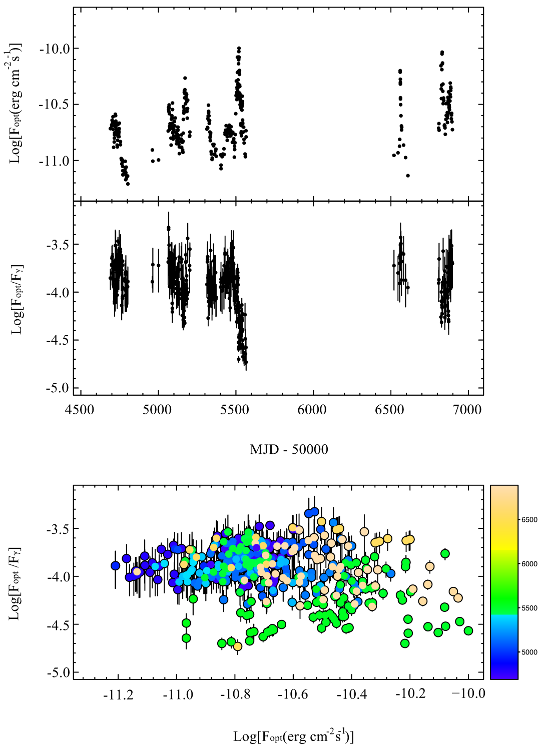

Figure 4: The R-band light curve in the last 6 years observation with the corresponding ratio $F_{\rm opt}/F_\gamma$ as a function of time is shown in top and middle panel. In this analysis, we selected only the combination data of the R-band and the γ-ray to calculate the ratio between these energy bands, hence the number of data point is less than the original data (shown in Figure 2). Note that the unit of $F_{\rm opt}$ and F_γ is [erg/cm^2/s] and [photons/cm^2/s], respectively, thus the ratio $F_{\rm opt}/F_\gamma$ is not a dimensionless quantity. The bottom panel is the ratio as a function of brightness level of the R-band and color indicates the date of the observation in units of MJD - 50000 as shown in the right bar.

2.3.1. Z-transformed Discrete Cross Correlation Function analysis

To investigate the time lag between the flux ratio $F_{\rm opt}/F_\gamma$ and the brightness of the optical band, we employed the Z-transformed Discrete Cross Correlation Function (ZDCF) introduced by Alexander (1997). This method can correct several biases of the discrete correlation function of Edelson & Krolik (1988) by using Fisher's z-transform and equal population binning (see the original paper for more detail). The calculated ZDCF between the flux ratio $F_{\rm opt}/F_\gamma$ versus the optical band flux $F_{\rm opt}$ during MJD = 55400 – 55550 is shown in Figure 5. In this period the most prominent change of the ratio and brightness was seen as shown in Figure 4. A positive time lag indicate that the variation of the flux ratio is delayed with respect

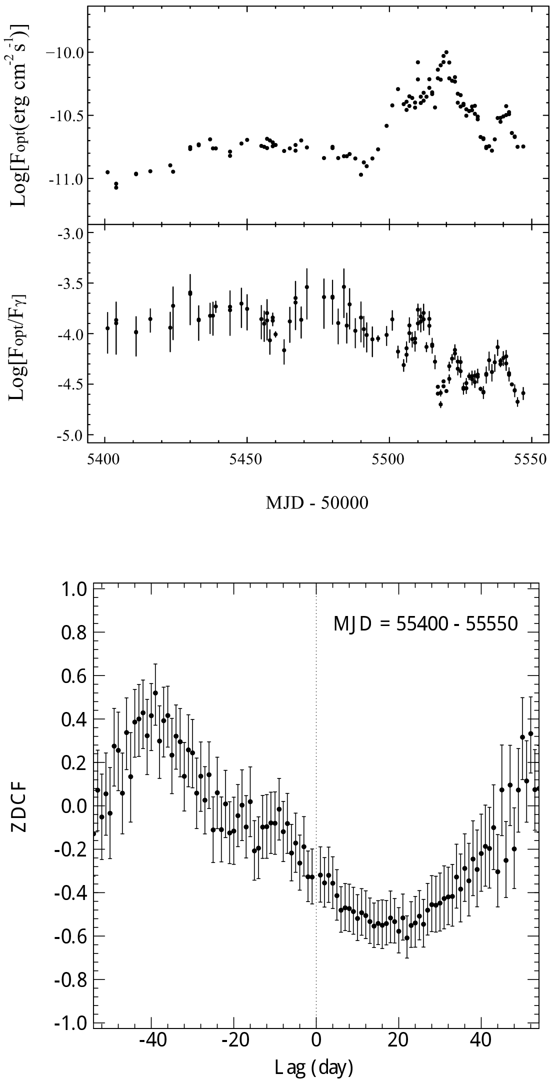

Figure 5: The R-band light curve in MJD = 55400-55550 with the corresponding ratio $F_{\rm opt}/F_\gamma$ as a function of time is shown in top and middle panel. The bottom panel is the ZDCF of the flux ratio $F_{\rm opt}/F_\gamma$ and R-band light curve during that interval. The time delay is defined as positive if the flux ratio variations lead that at R-band flux.

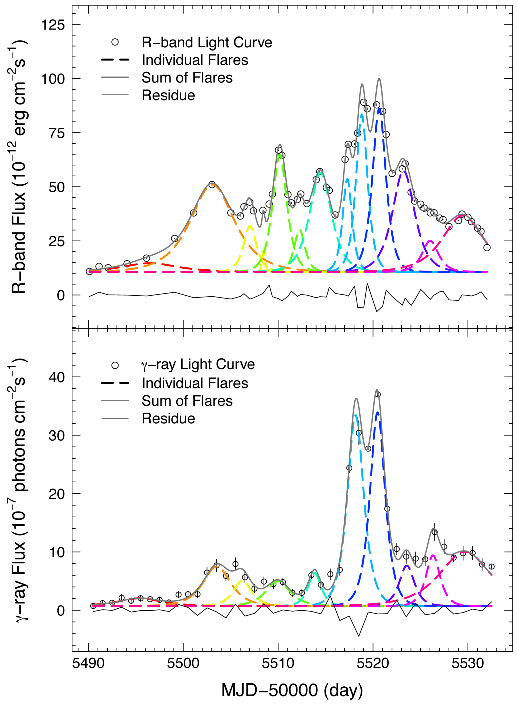

Figure 6: The decomposed light curves of R-band and γ-ray into individual flares are drawn by the dotted curve. The gray solid curve corresponds to summed flux of the modeling light curves, black open circles dente the observed light curve, the gray dotted line shows a residual flux, and same colors indicate that these flares were yielded by a same event in each panel.

to that of the brightness, thus the decrease of the flux ratio lags by typically about 20 day with respect to the increase of the flux in the optical band. The maximum likelihood 1σ error estimate calculated for the points between time-lags = -40 to 40 days is 22.00 $^{+4.12}_{-7.49}$ days. The physical meaning of this value is not clear at present. In a qualitative manner, however, we find the behavior of the flux ratio has the following two features: (i) fluctuations on relatively short time-scales (a few days) coincides with flare like activities, and (ii) a relatively long time-scale decreasing trend in active phase (MJD $\gtrsim$ 55490) in the middle panel of Figure 4. The 22.00 day lag found above is probably related to the latter feature, the long-term decreasing trend of the flux ratio associated with the large swings of the optical flux.

For the behavior of the flux ratio, described above as (i) and (ii), we can interpret this by a existence of parameters which change on long time scales (>50 days) besides the Doppler factor δ. Namely, if the external seed photon field $U_{\rm ext}$ increase or if magnetic field in a emitting region decreases gradually, the flux ratio will turn downward as shown in Figure 4 according the changes in these parameters. In addition, it is also possible that the baseline of the Doppler factor progressively increases as an angle between the line of sight and the direction of the jet progressively decreases.

2.4. flare analysis

The fluctuations in the optical and γ-ray light curves of blazars can be interpreted as a superposition of individual flares caused by same kind of events lying on a steady baseline flux (e.g. Abdo et al 2010c, Chattergee et al. 2012). For the optical band, for example, the steady component and the flaring component can be interpreted as thermal radiation from the accretion disk and synchrotron radiation in the jet, respectively. In order to investigate properties of the variable component, we decompose the light curves into individual flares represented by the following function:

$$F(t) = F_c + F_0 \left(e^{\frac{t_0 - t}{T_r}} + e^{-\frac{t_0 - t}{T_d}} \right)^{-1}, \qquad (4)$$

where F_c is an assumed constant flux level underlying the flare, F_0 is the amplitude of the flare, t_0 is the epoch of the peak of the flare, and T_r and T_d are the rise and decay time of the flare. F_0 was constrained to be equal to the lowest value of the flux during the focusing interval. In our analysis, we assume $T_r = T_d$ because the acceleration and cooling time scales of the relativistic electrons are expected to be substantially shorter than the light-crossing timescale of the synchrotron emitting region. Figure 6 shows the optical and γ-ray light curves for the period containing the brightest γ-ray flare in the Fermi observation from 3C 454.3. The individual flares presented by dashed lines of same colors in the R-band and the γ-ray light curves indicate that these variations were produced by the same origin. One can see that almost all flares are correlated in this period but flux responses in these energy bands originated from same events may be very different. On the other hand, the duration times of these flares are roughly equal. These aspects might be representing the origin of the observed flares. Assuming that the sub-equal duration time of the optical and γ-ray flares is caused by a light-travel time in a same emitting region and the difference of flux response is made by a variance of physical parameters in the emitting region such as δ or B, each flare observed might be yielded by different blobs of denser plasma possessing almost same size with substantially different parameters.

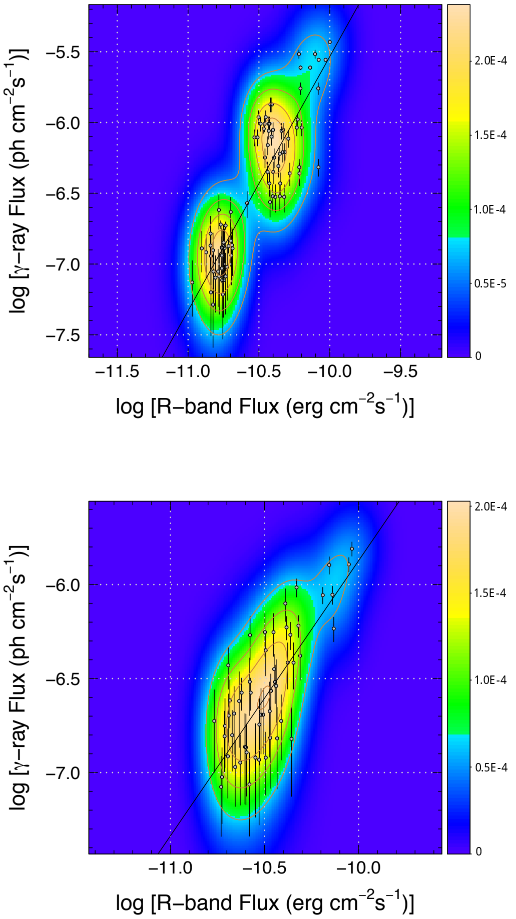

Figure 7: Log(F_{opt}) - Log(F_γ) dependences durring MJD = 55434-55532 and MJD = 56800-56910. Color contours indicate the density of data points and the solid line denote the numerical relation between the fluxes in those two energy bands.

2.5. Gamma-ray/Optical Correlation

As shown in Eq.(1) and (2), the optical flux F_{opt} and the γ-ray flux F_γ are related to each other through several parameters. For example, if the flux variation is due to a change in total number of emitting electron N_e, $F_\gamma \propto F_{\mathrm{opt}}$, and if it is due to a change in the Doppler factor δ, $F_\gamma \propto F_{\mathrm{opt}}^{(4+2\alpha_g)/(3+\alpha_0)}$. To investigate this relationship, we calculate the slope of the distribution in the Log(F_{opt}) vs. Log(F_γ) space. Data points in the Figure 7 show the observed γ-ray and the optical fluxes for the two substantially bright periods: MJD = 55434 - 55532 (upper panel), and 55680 - 56910 (bottom panel). Color contours indicate the density of data points and the lines denote the regression relation between the fluxes in those two bands, e.g., $F_\gamma \propto F_{\mathrm{opt}}^X$, where X is the slope of Log(F_{opt}) vs. Log(F_γ). In MJD = 55434 - 55532 and MJD = 56800 - 56910, parameter X is calculated as 1.79 and 1.46, respectively. According to Ackermann et al. (2010), in MJD = 55060 - 55160, OIR spectral index from SMARTS light curve is 1.55 ± 0.05, and the γ-ray spectral index is 1.5 ± 0.1. For $\alpha_0 = 1.55$ and $\alpha_g = 1.5$, we can obtain the relation $F_\gamma \propto F_{\mathrm{opt}}^{1.54}$. Thus, if we assume that the spectral index was largely unchanged and the γ-rays are produced by EC processes, this result seems to imply that the variation is mainly due to a change in δ and support the suggestion in section 2.3.

3. SUMMARY AND CONCLUSIONS

In this paper, we present the long-term light curve data of 3C 454.3 in three energy bands *i.e.* optical (R-band), X-ray (2-4 keV), and γ-ray (0.1-300 GeV) provided by MITSuME and SMARTS, MAXI/GSC, and Fermi/LAT, and reveal several time variability properties using the optical and the γ-ray flux data. Our main conclusions are as follows.

1. Using R-band and I-band data from MITSuME, the redder-when-brighter behavior and the "saturation" effect from R-magnitude ∼14 towards the brightest end are confirmed by the color-magnitude diagram. These results were pointed out by some previous research (*e.g.* Raiteri et al. 2008, Zhai et al. 2011). The remarkable result in this research is the finding of a sign of change in the plateau magnitude. The physical parameter of the accretion disk or the relativistic electron in the jet might have changed gradually and significantly.

2. We investigate a relation between the optical-band flux $F_{\rm opt}$ and the flux ratio of it to the γ-ray flux $F_{\rm opt}/F_\gamma$. The flux ratio becomes decreasing as the source becomes brightening, and this might indicate that the Doppler factor of an synchrotron emitting plasma is playing the most important role in the variations in the optical and γ-ray flux from 3C 454.3. More detailed analysis is performed for the period of MJD = 55400 to 55550. During this period, the flux ratio shows the interesting behaviors, namely, (i) steep dropping corresponding with the flares of the optical and the γ-ray, and (ii) slow declining during the highly active phase (MJD $\gtrsim$ 55490). It might be interpreted by an existence of a change of physical parameters in the jet besides the Doppler factor δ or increasing of baseline of the Doppler factor gradually for some reasons. In addition, the ∼ 20 days time-lag between the flux ratio and the optical flux variation is detected. A Interpretation of this phenomenon will be addressed in a future paper.

3. We performed a decomposition of the optical and γ-ray light curves of 3C 454.3 during its large flaring activity (MJD = 55490-55540). Almost all flares are correlated in this period, though flux responses vary significantly from one event to the other. This might indicate that the size of plasma blobs which radiate the optical and the γ-ray photons are almost same while those parameters besides its size are diverse.

4. For the two bright periods of 3C 454.3, we investigate the numerical relationship between $F_{\rm opt}$ and F_γ, and $F_\gamma \propto F_{\rm opt}^{1.79}$ and $F_\gamma \propto F_{\rm opt}^{1.46}$ are obtained in MJD = 55434 - 55532 and MJD = 56800 - 56910, respectively. These are roughly consistent with $F_\gamma \propto F_{\rm opt}^{1.54}$ which is expected if the variation is due to a change in the Doppler factor δ.

References

[1] Abdo et al., ApJ716 (2010) 835-849.
[2] Ackermann et al., ApJ721 (2010) 1383-1396.
[3] Alexander, MNRAS285 (1997) 891-897.
[4] Bonning et al., ApJ756 (2012) 13-28.
[6] Chatterjee et al., ApJ749 (2012) 191-203.
[6] Jackson and Brown, MNRAS250 (1991) 422-431.
[7] Jorstad et al., AJ130 (2005) 1418-1465.
[8] Matsuoka et al., PASJ61 (20059) 999-1010.
[9] Marshall et al., ApJS156 (2005) 13-33.
[10] Miniutti et al., PASJ59 (2007) 315-325.
[11] Nandra et al., ApJ476 (1997) 70-82.
[12] Noda et al., ApJ771 (2013) 100-112.
[13] Ogle et al., ApJS195 (2011) 19-38.
[14] Pian et al., ApJ521 (1999) 112-120.
[15] Raiteri et al., A&A473 (2007) 819-827.
[16] Raiteri et al., A&A534 (2011) 87-102.
[17] SaSada et al., PASJ63 (2011) 489-497.
[18] Vercellone et al., ApJ712 (2010) 405-420.
[19] Vercellone et al., ApJ736 (2011) L38-L45.
[20] Villata et al. A&A453 (2006) 817822
[21] Zhou et al., NewA36 (2015) 19-25.
[22] http://fermi.gsfc.nasa.gov/ssc/data/access/lat/
[23] http://maxi.riken.jp/top/
[24] http://www.astro.yale.edu/smarts/glast/home.php#

A strong radio brightening at the jet base of M87 in the period of the elevated TeV γ-ray state in 2012

K. Hada[a,b], M. Giroletti[a], M. Kino[c,d], G. Giovannini[a,e], F. D'Ammando[a], C. C. Cheung[f], M. Beilicke[g], H. Nagai[h], A. Doi[d], K. Akiyama[b,i], M. Honma[b,j], K. Niinuma[k], C. Casadio[l], M. Orienti[a], H. Krawczynski[7], J. L. Gómez[l], S. Sawada-Satoh[b], S. Koyama[b,d,i], A. Cesarini[m], S. Nakahara[n] and M. A. Gurwell[o]

[a]*INAF Istituto di Radioastronomia, via Gobetti 101, I-40129 Bologna, Italy*
[b]*Mizusawa VLBI Observatory, National Astronomical Observatory of Japan, Osawa, Mitaka, Tokyo 181-8588, Japan*
[c]*Korea Astronomy and Space Science Institute, 776 Daedukdae-ro, Yusong, Daejon 305-348, Korea*
[d]*Institute of Space and Astronautical Science, Japan Aerospace Exploration Agency, 3-1-1 Yoshinodai, Chuo, Sagamihara 252-5210, Japan*
[e]*Dipartimento di Fisica e Astronomia, Università di Bologna, via Ranzani 1, I-40127 Bologna, Italy*
[f]*Space Science Division, Naval Research Laboratory, Washington, DC 20375, USA*
[g]*Physics Department and McDonnell Center for the Space Sciences, Washington University, St. Louis, MO 63130, USA*
[h]*National Astronomical Observatory of Japan, Osawa, Mitaka, Tokyo 181-8588, Japan*
[i]*Department of Astronomy, Graduate School of Science, The University of Tokyo, 7-3-1 Hongo, Bunkyo-ku, Tokyo 113-0033, Japan*
[j]*Department of Astronomical Science, The Graduate University for Advanced Studies (SOKENDAI), 2-21-1 Osawa, Mitaka, Tokyo 181-8588, Japan*
[k]*Graduate School of Science and Engineering, Yamaguchi University, 1677-1 Yoshida, Yamaguchi, 753-8512, Japan*
[l]*Instituto de Astrofisica de Andalucia, CSIC, Apartado 3004, 18080 Granada, Spain*
[m]*Department of Physics, University of Trento, I38050, Povo, Trento, Italy*
[n]*Faculty of Science, Kagoshima University, 1-21-35 Korimoto, Kagoshima, Kagoshima 890-0065, Japan*
[o]*Harvard-Smithsonian Center for Astrophysics, Cambridge MA 02138 USA*

The nearby radio galaxy M87 offers a unique opportunity for exploring the connection between γ-ray production and jet formation at an unprecedented linear resolution. However, the origin and location of the γ-rays in this source is still elusive. Based on previous radio/TeV correlation events, the unresolved jet base (radio core) and the peculiar knot HST-1 at >120 pc from the nucleus are proposed as candidate site(s) of γ-ray production. Here we report our intensive, high-resolution radio monitoring observations of the M87 jet with the VLBI Exploration of Radio Astrometry (VERA) and the European VLBI Network (EVN) from February 2011 to October 2012, together with contemporaneous high-energy γ-ray light curves obtained by the Fermi Large Area Telescope. During this period, an elevated level of the M87 flux is reported at TeV with VERITAS. We detected a remarkable flux increase in the radio core with VERA at 22/43 GHz coincident with the VHE activity. Meanwhile, HST-1 remained quiescent in terms of its flux density and structure in the radio band. These results strongly suggest that the TeV γ-ray activity in 2012 originates in the jet base within 0.03 pc (projected) from the central supermassive black hole.

1. Introduction

The nearby radio galaxy M87 accompanies one of the best studied AGN jets. Its proximity (16.7 Mpc) and brightness have enabled detailed studies of this jet over decades through radio, optical and to X-ray at tens of parsec scale resolutions. Furthermore, the inferred very massive black hole ($M_{\rm BH} \simeq (3-6)\times 10^9\ M_\odot$) yields a linear resolution down to 1 milliarcsecond (mas) = 0.08 pc = 140 Schwarzschild radii ($R_{\rm s}$) (for $M_{\rm BH} = 6\times 10^9\ M_\odot$), making this source an ideal case to probe the relativistic-jet formation at an unprecedented compact scale with Very-Long-Baseline-Interferometer (VLBI) observations (e.g., Ly et al. 2007; Kovalev et al. 2007; Hada et al. 2011; Asada & Nakamura 2012; Doeleman et al. 2012; Hada et al. 2013). M87 is now widely known to show γ-ray emission up to the very-high-energy (VHE; $E > 100$ GeV) regime, where this source often exhibits active flaring episodes. The location and the physical processes of such emission have been a matter of debate over the past years, and there are two candidate sites which can be responsible for the VHE γ-ray production. One is a very active knot HST-1 which is located at more than 100 pc from the nucleus (Stawarz et al. 2006; Cheung et al. 2007; Harris et al. 2009). This argument is based on the famous VHE flare event in 2005, where HST-1 underwent a large radio-to-X-ray outburst jointly with a VHE flare. In contrast, the other candidate is the core/jet base, which is very close to the central black hole. This argument is based on the VHE event in 2008, where the core/VHE showed a remarkable correlation in the light curves. There was another VHE event in 2010, but this is rather elusive. Coincident with the VHE event, Chandra detected an enhanced flux from the X-ray core (Harris et al. 2011; Abramowski et al. 2012), and VLBA observations also suggested a possible increase of the radio core flux (Hada et al. 2012). However, Giroletti et al. (2012) found the emergence of a superluminal component in the HST-1 complex near the epoch of this event, which is reminiscent of the 2005 case.

Recently, the VERITAS Collaboration has reported new VHE γ-ray activity from M87 in early 2012 (Beilicke et al. 2012). While there were no remarkable flares like those in the previous episodes, the VHE flux in 2012 clearly exhibits an elevated state at a level of $\sim 9\sigma$ ($\Phi_{>0.35\,\mathrm{TeV}} \sim (0.2\text{–}0.3) \times 10^{-11}$ photons cm^{-2} s^{-1}) over the consecutive two months from February to March 2012. The observed flux is a factor of ~ 2 brighter than that in the neighboring quiescent periods. Therefore, this event provides another good opportunity for exploring the location of the VHE emission site by jointly using high-resolution instruments.

2. Observations

Here we report a multi-wavelength radio and MeV/GeV study of the M87 jet during this period using the VLBI Exploration Radio Astrometry (VERA, Fegure 1), the European VLBI Network (EVN), the Submillimeter Array (SMA) and the Fermi-LAT. We especially focus on the VLBI data in the radio bands; with VERA, we obtained the high-angular-resolution, dense-sampling-interval, phase-referencing data set at 22 and 43 GHz during the VHE activity in 2012: with the supportive EVN monitoring, we obtained a complementary data set at 5 GHz, which enables a high-sensitivity imaging of the M87 jet. A collective set of these radio data allows us to probe the detailed physical status and structural evolutions of M87 by pinpointing the candidate sites of the γ-ray emission i.e., the core and HST-1. For more details regarding the radio data analysis, see Hada et al. (2014).

The LAT data reported here were collected from 2011 February 1 (MJD 55593) to 2012 September 30 (MJD 56200). During this time, the Fermi observatory operated almost entirely in survey mode. The analysis was performed with the `ScienceTools` software package version v9r32p5. The LAT data were extracted within a 10° region of interest centred at the radio location of M87. Only events belonging to the 'Source' class were used. The time intervals when the rocking angle of the LAT was greater than 52° were rejected. In addition, a cut on the zenith angle ($< 100°$) was applied to reduce contamination from the Earth limb γ rays, which are produced by cosmic rays interacting with the upper atmosphere. The spectral analysis was performed with the instrument response functions `P7REP_SOURCE_V15` using an unbinned maximum-likelihood method implemented in the Science tool `gtlike`. A Galactic diffuse emission model and isotropic component, which is the sum of an extragalactic and residual cosmic ray background, were used to model the background. The normalizations of both components in the background model were allowed to vary freely during the spectral fitting.

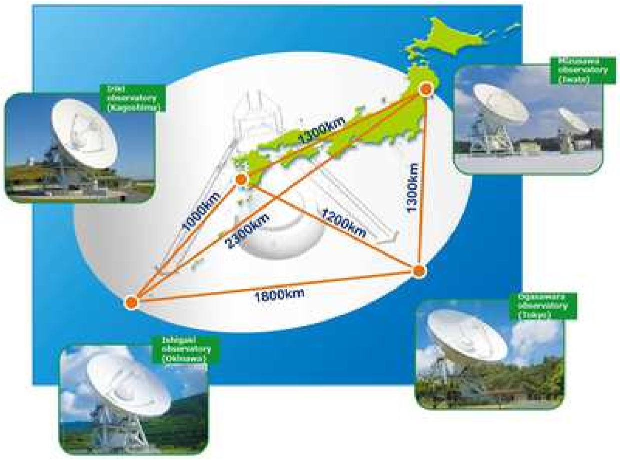

Figure 1: Layout of the VLBI Exploration of Radio Astrometry (VERA).

We evaluated the significance of the γ-ray signal from the sources by means of the maximum-likelihood test statistic TS $= 2\Delta\log(\text{likelihood})$ between models with and without a point source at the position of M87 (Mattox et al. 1996). The source model used in `gtlike` includes all of the point sources from the second Fermi-LAT catalog (2FGL; Nolan et al. 2012) that fall within 15° of the source. The spectra of these sources were parametrized by power-law functions, except for 2FGL J1224.9+2122 (4C 21.35) and 2FGL J1229.1+0202 (3C 273), for which we used a log-parabola as in the 2FGL catalogue. A first maximum-likelihood analysis was performed to remove from the model the sources having TS < 25 and/or the predicted number of counts based on the fitted model $N_{pred} < 3$. A second maximum-likelihood analysis was performed on the updated source model. In the fitting procedure, the normalization factors and the photon indices of the sources lying within 10° of M87 were left as free parameters. For the sources located between 10° and 15°, we kept the normalization and the photon index fixed to the values from the 2FGL catalogue.

Integrating over the period from 2011 February 1 to 2012 September 30 (MJD 55593–56200), the fit with a power-law model in the 0.1–100 GeV energy range results in a TS $= 134$, with an integrated average flux of $(2.22 \pm 0.43) \times 10^{-8}$ ph cm^{-2} s^{-1} and a photon index of $\Gamma = 2.25 \pm 0.10$. Taking into account the detection significance over the whole analysed period,

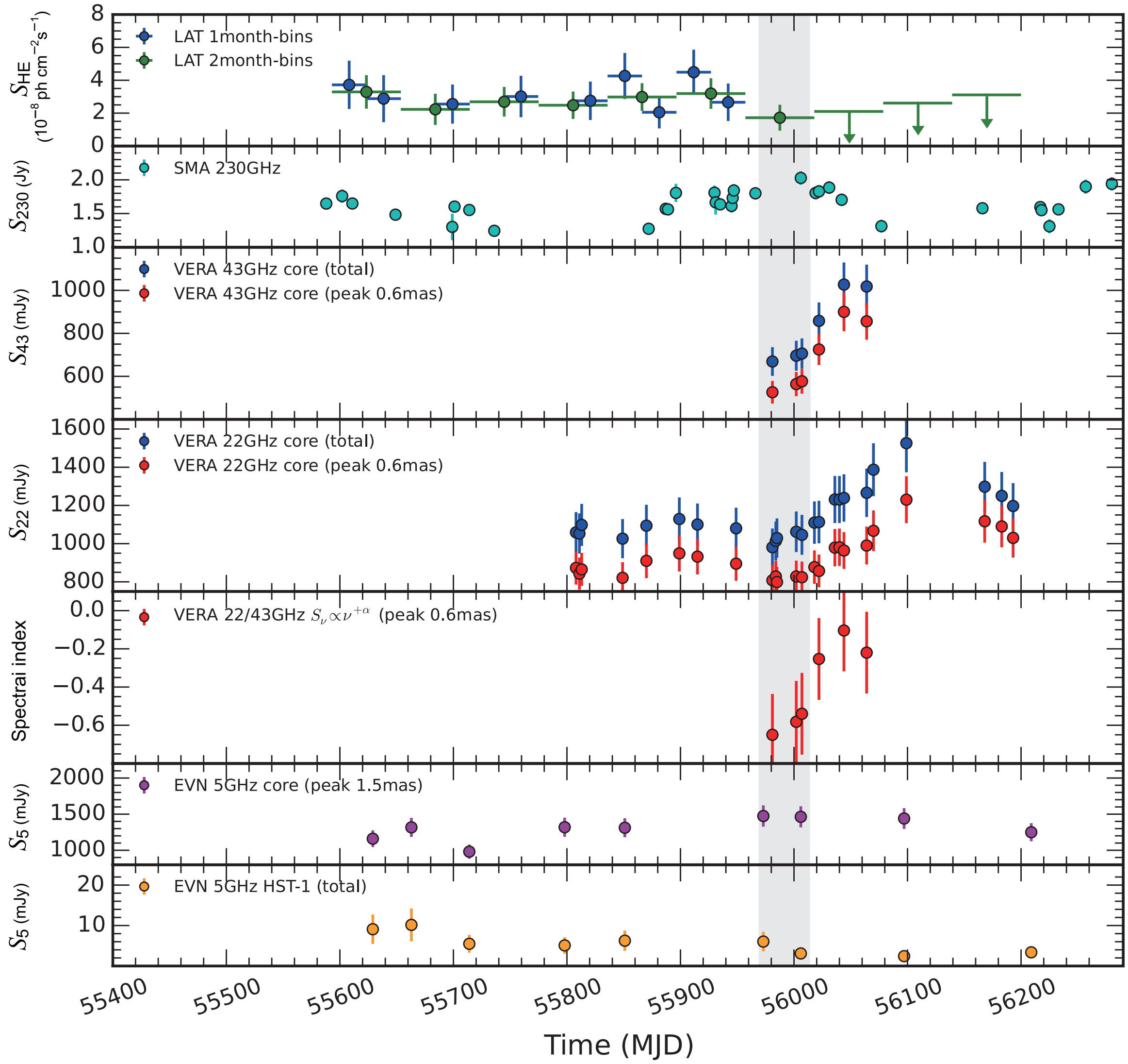

Figure 2: Multi-wavelength light curves of M87 between 2011 February and 2012 December. The vertical shaded area over the plots indicates a period of elevated VHE emission reported by Beilicke et al. (2012).

we produced the γ-ray light curves with 1-month and 2-month time bins. This choice of binning is compatible with those adopted in the previous M87 studies with LAT data (Abdo et al. 2009; Abramowski et al. 2012), and also reasonable for a comparison with the observed month-scale VHE activity in 2012. For each time bin, the spectral parameters for M87 and for all the sources within 10° from it were frozen to the value resulting from the likelihood analysis over the entire period. In the light curve with the 2-month time bins, if TS < 10, 2σ upper limits were evaluated, while only bins with TS > 10 are selected in the light curve with the 1-month time bins. We describe the results of the LAT light curves in Section 4.2.

Dividing the 1-month bins with higher flux in 5-day sub-bins, the highest flux of $(10.4\pm4.8)\times10^{-8}$ and $(8.6\pm3.4)\times10^{-8}$ ph cm^{-2} s^{-1} was detected on 2011 October 12-16 and 2012 January 16-20, respectively (these sub-bin data also show TS>10). By means of the `gtsrcprob` tool, we estimated that the highest energy photon emitted from M87 (with probability $>$ 90% of being associated with the source) was observed by LAT on 2011 April 7, at a distance of 0.09° from the source and with an energy of 254.0 GeV, extending into the VHE range.

2.1. Results

In Figure 2 we show a combined set of light curves of M87 from radio to MeV/GeV γ-ray between MJD 55400 and MJD 56280. Thanks to the dense, complementary coverages of VERA and EVN, we revealed the detailed evolutions of the radio light curves for both the core and HST-1. The most remarkable finding in these plots is a strong enhancement of the

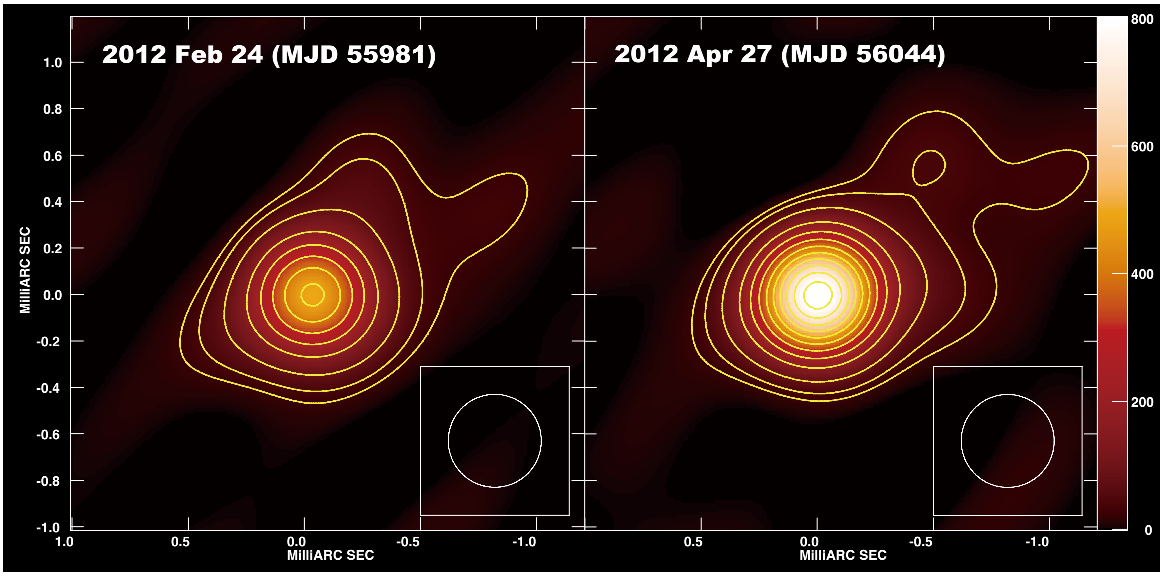

Figure 3: VERA 43 GHz images of the M87 jet during the elevated VHE state in 2012.

radio core flux at VERA 22 and 43 GHz, which occurred coincidentally with the elevated VHE state. At 22 GHz, we further detected a subsequent decay stage of the brightness at the last three epochs. Also at 43 GHz, we detected possible saturation of the flux increase near the last epoch. Meanwhile, the EVN monitoring confirmed a constant decrease of the HST-1 luminosity. Figure 3 describes VERA 43-GHz images during the VHE active period, which indicate the flux enhancement within the central resolution element of 0.4 mas, corresponding to a linear scale of 0.03 pc or 56 $R_{\rm s}$. We also note that the SMA data at 230 GHz also appear to show a local maximum in its light curve during the period of the elevated VHE state.

Another notable finding is a frequency-dependent evolution of the radio core flare. The VERA light curves clearly indicate that the radio core brightens more rapidly with a larger amplitude as frequency increases. At 43 GHz, the flux increased up to ~70% for the subsequent 2 months at an averaged rate of ~35%/month, and afterward the growth seems to be saturated. On the other hand, the core flux at 22-GHz progressively increased up to ~50% for the subsequent 4 months at a slower rate of ~12%/month. At 5 GHz, by contrast, the core remained virtually stable within the adopted error of 10%. This is the first time that such a frequency-dependent nature of the radio flare is clearly confirmed in the M87 jet. We also detected a core-shift between 22 and 43 GHz by using the VERA dual-beam astrometry technique (see Hada et al. 2014), where the amount of the shift was similar to the value obtained in the previous core-shift measurement (Hada et al. 2011).

Regarding the MeV/GeV regime, the LAT light curves were stable up to February 2012, and we did not find any significant flux enhancement during the period of the VHE activity. After March 2012, however, no significant emission was detected for the subsequent 6 months in the 1- and 2-month binned data, suggesting a change in the HE state after the VHE event. This indicates a decrease in the HE flux (by a factor of ~ 2) after the VHE event, in agreement with the level of decrease observed at VHE in 2012 April-May (Beilicke et al. 2012).

3. Discussion and summary

Following the 2008 episode this is the second time where a VHE event accompanied a remarkable radio flare from the core. Meanwhile, the radio luminosity of the HST-1 region was continuously decreasing, and we did not find any hints of the emergence of new components from HST-1 as seen in 2005 and 2010. These results strongly suggest that the VHE activity in 2012 is associated with the core at the jet base, while HST-1 is an unlikely source. We note that these remarkable flares are very rare also in radio bands (Acciari et al. 2009), so it is unlikely that an observed joint radio/VHE correlation is a chance coincidence, while the low statistics of the LAT light curves still do not allow conclusive results on the HE/VHE connection.

What kinds of mechanisms are responsible for the VHE production in the M87 core? Some of the existing models ascribe the VHE production to extremely compact regions near the central black hole (e.g., Neronov & Aharonian 2007; Lenain et al. 2008; Giannios et al. 2010; Barkov et al. 2012). These models well explain the rapid (a few days) variability observed in the previous VHE flares in 2005, 2008 and 2010. However as far as we consider the case in 2012, the size of the associated region expected from these models seems to be smaller than that suggested by VLBI and the observed longer timescale of the VHE variability. Indeed, a contemporaneous mm-VLBI observation at 230 GHz during the 2012 event also suggests the possible extended nature for the flaring region ($\gtrsim$0.3 mas; Akiyama et al. submitted).

Another popular scenario for the M87 VHE production comes from a blazar-type, two-zone emission model where the VHE emission originates in the upstream part of a decelerating jet (Georganopoulos et al. 2005) or in the layer part of the spine-sheath structure (Tavecchio & Ghisellini 2008). However in their steady state models, whether the models can explain the observed simultaneous radio/VHE correlation or not has not been well investigated yet because the emission regions associated with radio and VHE are spatially separated from each other. In this respect, a simple, homogeneous one-zone synchrotron self-Compton jet model examined by Abdo et al. (2009) would be interesting to note since one can in principle accept coincident radio/VHE correlations.

Our multi-frequency radio monitoring additionally revealed a frequency-dependent evolution of the radio light curves for the M87 core. Such a behavior is often explained by the creation of a plasma condensation, which subsequently expands and propagates down the jet under the effect of synchrotron-self-absorption (SSA). The stronger SSA opacity at the jet base causes a delayed brightening at lower frequencies, and the light curve at each frequency reaches its maximum when the newborn component passes through the $\tau_{\rm ssa}(\nu) \sim 1$ surface (i.e., the radio core at the corresponding frequency). In this context, by jointly using the observed time-lag (Δt_{43-22}) and core-shift ($\Delta r_{\rm proj,43-22}$), we can estimate an apparent speed of the propagating component such that $\beta_{\rm app,43\rightarrow 22} = \frac{\Delta r_{\rm proj,43-22}}{c\Delta t_{43-22}}$. This results in a speed about $\sim$0.04c–0.22c, suggesting that the newborn component is sub-relativistic. This is significantly smaller than the super-luminal features appeared from the core during the previous VHE event in 2008 (1.1c; Acciari et al. 2009), where the peak VHE flux is $\gtrsim$5 times higher than that in 2012. If we assume that propagating shocks or component motions seen in radio observations reflect the bulk velocity flow, this may suggest that the stronger VHE activity is associated with the production of the higher Lorentz factor jet.

We are currently upgrading our M87 monitoring project by using the KVN and VERA Array (KaVA; Niinuma et al. 2014), which dramatically improves jet imaging capability thanks to the increase of the number of telescopes/baselines plus the addition of shorter baselines. This will enable us to constrain the jet kinematics and radio/VHE connection more precisely.

Acknowledgments

The VERA is operated by Mizusawa VLBI Observatory, a branch of National Astronomical Observatory of Japan. e-VLBI research infrastructure in Europe is supported by the European Union's Seventh Framework Programme (FP7/2007-2013) under grant agreement no. RI-261525 NEXPReS. The European VLBI Network is a joint facility of European, Chinese, South African and other radio astronomy institutes funded by their national research councils. The Submillimeter Array is a joint project between the Smithsonian Astrophysical Observatory and the Academia Sinica Institute of Astronomy and Astrophysics and is funded by the Smithsonian Institution and the Academia Sinica.

The Fermi LAT Collaboration acknowledges generous ongoing support from a number of agencies and institutes that have supported both the development and the operation of the LAT as well as scientific data analysis. These include the National Aeronautics and Space Administration and the Department of Energy in the United States, the Commissariata l'Energie Atomique and the Centre National de la Recherche Scientifique Institut National de Physique Nucléaire et de Physique des Particules in France, the Agenzia Spaziale Italiana and the Istituto Nazionale di Fisica Nucleare in Italy, the Ministry of Education, Culture, Sports, Science and Technology (MEXT), High Energy Accelerator Research Organization (KEK) and Japan Aerospace Exploration Agency (JAXA) in Japan, and the K. A.Wallenberg Foundation, the Swedish Research Council and the Swedish National Space Board in Sweden. Additional support for science analysis during the operations phase is gratefully acknowledged from the Istituto Nazionale di Astrofisica in Italy and the Centre National dEtudes Spatiales in France.

References

Abdo, A. A., Ackermann, M., Ajello, M., et al. 2009, ApJ, 707, 55

Abramowski, A., Acero, F., Aharonian, F., et al. 2012, ApJ, 746, 151

Acciari, V. A., Aliu, E., Arlen, T., et al. 2009, Science, 325, 444

Aharonian, F., Akhperjanian, A. G., Bazer-Bachi, A. R., et al. 2006, Science, 314, 1424

Asada, K. & Nakamura, M. 2012, ApJ, 745, L28

Barkov, M. V., Bosch-Ramon, V., & Aharonian, F, A. 2012, ApJ, 755, 170

Beilicke, M., & VERITAS Collaboration 2012, arXiv:1210.7830

Cheung, C. C., Harris, D. E., & Stawarz, Ł. 2007, ApJ, 663, L65

Doeleman, S. S., Fish, V. L., Schenck, D. E., et al. 2012, Science, 338, 355

Georganopoulos, M., Perlman, E. S., & Kazanas, D. 2005, ApJ, 634, L33

Giannios, D., Uzdensky, D. A., & Begelman, M. C. 2010, MNRAS, 402, 1649

Giroletti, M., Hada, K., Giovannini, G., et al. 2012, A&A, 538, L10

Hada, K., Doi, A., Kino, M., et al. 2011, Nature, 477, 185

Hada, K., Kino, M., Nagai, H., et al. 2012, ApJ, 760, 52

Hada, K., Kino, M., Doi, A., et al. 2013, ApJ, 775, 70

Hada, K., Giroletti, M., Kino, M., et al. 2014, ApJ, 788, 165

Harris, D. E., Cheung, C. C., Stawarz, Ł., et al. 2009, ApJ, 699, 305

Harris, D. E., Massaro, F., Cheung, C. C., et al. 2011, ApJ, 743, 177

Kovalev, Y. Y., Lister, M. L., Homan, D. C, & Kellermann, K. I. 2007, ApJ, 668, L27

Lenain, J.-P., Boisson, C., Sol, H., & Katarzyński, K. 2008, A&A, 478, 111

Ly, C., Walker, R. C., & Junor, W. 2007, ApJ, 660, 200

Mattox, J. R., Bertsch, D. L., Chiang, J., et al. 1996, ApJ, 461, 396

Neronov, A., & Aharonian, F. A. 2007, ApJ, 671, 85

Niinuma, K., Lee, S.-S., Kino, M., et al. 2014, PASJ, 66, 103

Nolan, P., Abdo, A. A., Ackermann, M., et al. 2012, ApJS, 199, 31

Stawarz, Ł., Aharonian, F., Kataoka, J., et al. 2006, MNRAS, 370, 981

Tavecchio, F., & Ghisellini, G. 2008, MNRAS, 385, L98

Study for relation between direction of relativistic jet and optical polarization angle with multi-wavelength observation

R. Itoh, Y. Fukazawa, K. Kawaguchi, Y. Kanda
Department of Physical Science, Hiroshima University, Higashi-Hiroshima, Hiroshima 739-8526, Japan
Y. T. Tanaka, M. Uemura, K. S. Kawabata, H. Akitaya
Hiroshima Astrophysical Science Center, Hiroshima University, Higashi-Hiroshima, Hiroshima 739-8526, Japan
for the Kanata and OISTER team

Blazars are thought to possess a relativistic jet that is pointing toward the direction of the Earth and the elect of relativistic beaming enhances its apparent brightness. They radiate in all wavebands from the radio to the gamma-ray bands via the synchrotron and the inverse Compton scattering process. Numerous observations are performed but the mechanism of variability, creation and composition of jets are still controversial.

We performed multi-wavelength monitoring with optical polarization for 3C 66A, Mrk 421, CTA 102 and PMN J0948+0022 to investigate the mechanisms of variability and research the emission region in the relativistic jets. Consequently, an emergence of new emission component in flaring state is suggested in each object. The most significant aspect of these results is its wide range of sizes of emission regions from $10^{14} - 10^{16}$ cm, which implies the model with a number of independent emission regions with variety sizes and randomly orientation. The "shock-in-jet" scenario can explain high PD and direction of PA in each objects. It might reflect the common mechanism of flares in the relativistic jets.

1. INTRODUCTION

Blazars are highly variable active galactic nuclei (AGN) which emit radiation at all wavelengths from radio to gamma-rays. They have strong relativistic jets aligned with the observer's line of sight and are apparently bright due to relativistic beaming. Outstanding characteristics of blazars are their rapid and high-amplitude intensity variations or flares. Blazar consists of several sub-classes. BL Lac objects are detected to have weak emission line of equivalent width < 5 Å in the observer's optical band definition. In contrast, flat spectrum radio quasars (FSRQs) shows relatively strong emission lines. Blazars also can be classified into three types, based on their peak frequency of synchrotron radiation $\nu^S_{\rm peak}$ [3]; low-synchrotron-peaked blazars (LSP; for sources with $\nu^S_{\rm peak} < 10^{14}$ Hz), intermediate-synchrotron-peaked blazars (ISP; for 10^{14} Hz $< \nu^S_{\rm peak} < 10^{15}$ Hz) and high-synchrotron-peaked blazars (HSP; for 10^{15} Hz $< \nu^S_{\rm peak}$). Due to relativistic effect, radiation from jets dominates the overall spectral energy distribution and hence, their spectra in the optical band are featureless compared with other AGNs. From this reason, blazar is one of most suitable objects to study the jets.

Polarized radiation from blazars is one of the evidence of synchrotron radiation in low energies and it also varies drastically. The polarization of blazars is of interest for understanding the origin, confinement, and propagation of jets [4, 21]. Mead et al. (1990)[18] performed a large-sample study of blazars in the optical band and showed that high polarization degree (PD) and variability of polarization are common phenomena in blazars. Ikejiri et al. (2011)[10] reported statistical photopolarimetric observations of blazars with a daily timescale, and suggested that lower luminosity and higher peak frequency of synchrotron radiation objects (such as HSP blazar) had smaller amplitudes in their variations both in the flux, color, and PD. The author also reported the about 30% of blazars showed correlation between the optical flux and PD. Numerous observations are performed but the mechanism of variability, creation and composition of jets are still controversial.

In efforts to find a common mechanism of jets, we performed observations on various types of AGNs. Simultaneous multi-wavelength and optical polarimetric observations are powerful tools to probe the emission region in jets, thus we performed wide-band multi-wavelength (from radio to TeV gamma-ray) observations of relativistic jets in several types of AGNs with various timescales (from minute to year) to study of structures and emission regions of relativistic jets.

2. Observations

We constructed the framework of multi-wavelength and optical polarimetric observations of relativistic jets in AGNs with the *Fermi* Gamma-ray Space Telescope, Monitor of All-sky X-ray Image [MAXI; 17], the *Swift* Gamma-Ray-Burst Explorer [8], the Kanata optical and near infrared telescope, Optical and Infrared Synergetic Telescopes for Education and Research (*OISTER*), and Mizusawa VLBI Observatory.

We performed four objects observation with optical flux and polarization to see the relations between polarization angle (PA) and the direction of radio jets in the flaring state. In efforts to find a common mechanism of jets, we selected the different types of AGNs to see the difference between them. This study focused on four AGNs; ISP blazar 3C 66A, HSP blazar Mrk 421, FSRQ CTA 102 and radio-loud narrow-line Seyfert 1 galaxy (RL-NLSy1) PMN J0948+0022. Note that RL-NLSy1 is not the class of blazar but it thought to possess relativistic jet [2]. Some radio galaxies also known as GeV gamma-ray emitter and those class of AGNs might play an important role to probe the emission region in the relativistic jets (e.g., [20]). Individual results are reported in Itoh et al. (2013a)[12], Itoh et al. (2015, submitted to the PASJ)[15], Itoh et al. (2013b)[13] and Itoh et al. (2013c)[14] respectively. We selected the flare with good correlation between polarized flux and total flux in optical band.

3. Summary of case studies

In this section, we summarize our studies of individual blazar, Temporal variability in optical flux, polarization flux and PA are shown in figure 1. Table I shows a summary of differential angle (ΔDA) between position angle of radio jet measured by VLBI or VLBA ([5], [19], [7] and [6])

A. 3C 66A

We studied the long-term variations of 3C 66A over 2 years in the GeV band with *Fermi* and in the optical (flux and polarization) and near infrared band with the Kanata telescope. In 2008, we find a correlation between the gamma-ray flux and the optical properties. This is in contrast to the later behaviours during 2009–2010, a weak correlation along with a gradual increase of the optical flux. We conclude that the different behaviors observed between the first year and the later years might be explained by postulating two different emission components. ΔDA shown in Table I indicates that the position angle of radio jet is close to the average PA. It should be noted that a correlation between PD and total flux is significant in 2009.

B. Mrk 421

We observed the long-term variability of Mrk 421 from optical to X-ray band using the *Swift*, MAXI, and Kanata telescope from 2010 to 2011. In 2010, the variability in the X-ray band is clearly large, while the optical and UV flux shows gradual decreasing. Polarization properties also show the unique variability in 2010. The variation on the Stokes parameter QU plane suggested the presence of the proper polarization. On the other hand, the variability in the X-ray band is small in 2011, although the variability in the optical and UV band is relativistically large compared with that in 2010. We speculated that Mrk 421 has different variability mechanisms between 2010 and 2011 and emergence of a new emission component which have systematic difference of polarization at different periods. ΔDA indicates that PA is aligned to the parsec scale jet in 2010. We also found a good correlation between optical flux and polarized flux in 2010. These behaviours are similar to that in 3C 66A.

C. CTA 102

We densely monitored CTA 102 in the optical and near-infrared bands for the subsequent ten nights using *OISTER*, following *Fermi*-LAT detection of the enhanced gamma-ray activity. On MJD 56197 (2012 September 27, 4-5 days after the peak of bright gamma-ray flare), a polarized flux showed a transient increase, while a total flux and PA remained almost constant during the “orphan polarized-flux flare”. We also detected an intra-night and prominent flare on MJD 56202. Emergence of a new emission component with high PD up to 40% would be responsible for the observed two flares, and such a high PD indicates a presence of highly ordered magnetic field at the emission site. The observed directions of PA is perpendicular to the jet. The total and polarized fluxes showed quite similar temporal variations, but PA again remained constant during the flare.

D. PMN J0948+0022

We performed optical photopolarimetric monitoring of the RL-NLSy1 galaxy PMN J0948+0022 on 2012 December to 2013 February triggered by the flux enhancement in near infrared and γ-ray bands. Thanks to one-shot polarimetry of the HOWPol installed to the Kanata telescope, we have detected very rapid variability in the polarized-flux light curve on MJD 56281 (2012 December 20). The rise and decay times were about 140 sec and 180 sec, respectively. The PD reached $36 \pm 3\%$ at the peak of the short-duration pulse, while PA remained almost constant. The high PD provides a clear evidence of synchrotron emission within a highly ordered magnetic field at the emission site. These results provide new observational evidence that highly ordered magnetic field is present inside a very compact emission region of the order of $\sim 10^{14}$ cm and imposes severe constraint on theoretical studies unless central black hole mass is much smaller than currently considered. we found that PA in MJD 56202 is aligned to the parsec scale jet. Temporal profiles of the total flux and PD showed highly variable but well correlated behavior and discrete correlation function analysis revealed that no significant time lag of more than 10 min was present.

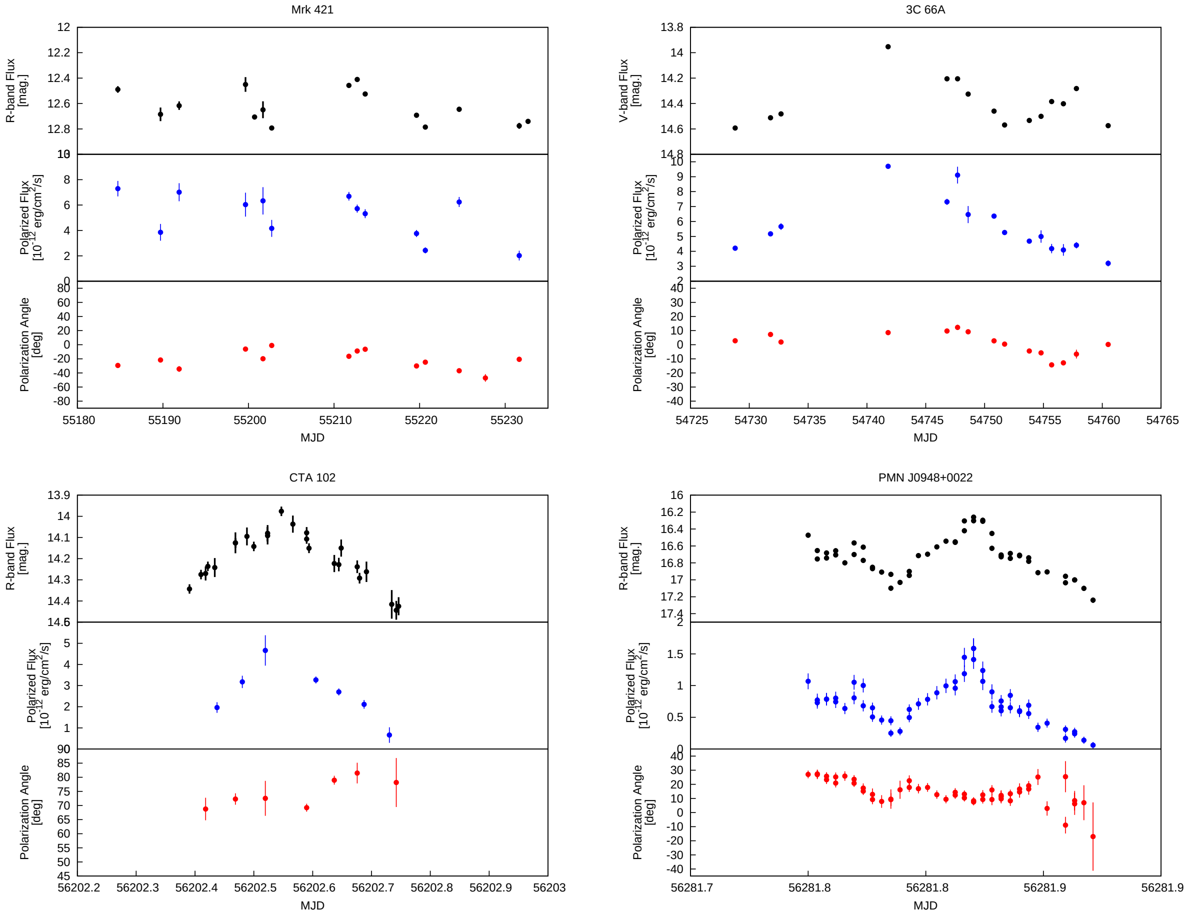

Figure 1: Light curves for each source. From top to bottom, the histories of the total flux in the R_C band, the polarized flux, and the polarization angle (PA) are shown. Note that the time scale of CTA 102 and PMN J0948+0022 (bottom two sources) are different from that in 3C 66A and Mrk 421. Details of each light curve are reported in [12], [13], [14] and [15]

Table I Summary of differential angle for each object.

Object name	**AGN type**	ΔDA[1] [deg]
3C 66A	BL Lac (ISP)	0 ± 5
Mrk 421	BL Lac (HSP)	10 ± 10
CTA 102	FSRQ	80 ± 10
PMN J0948+0022	RL-NLSy1	5 ± 5

[1]: Differential angle between the position angle of radio jet and optical polarization angle.

4. Discussion

A common characteristic among BL lac objects and RL-NLSy1 is that PA aligned with a direction parallel to the jet (see TableI). This phenomenon is well explained with the framework of “shock-in-jet” scenario, in which high PD and direction of PA are well explained with compressed emission region by the internal shocks. This phenomena is explained with below mechanism; a compressed shock that is perpendicular to the jet flow results that the electric polarization vector to be perpendicular to the emission blob and aligned with the jet axis. Impey et al. (2011)[11] reported that about 60% quasars shows alignment of the position angle of jet and polarization angle. Especially, author found that in 10 out of 11 BL Lac objects shows good alignment. It should be noted that these measurements of PA were collected without considering the flux state. Similar tendencies in hourly-scale variability were reported in other BL Lac objects [e.g., AO 0235+164, 9]. On the other hand, CTA 102 which is classified as FSRQ shows a different tendency. The difference of relation between PA and direction of the jet might be reflecting a difference of jets between BL lac objects and FSRQs. In general, FSRQs thought to have weaker shocks and/or a stronger underlying magnetic fields such as large-scale helical magnetic fields. Given this complicated situation, the measured PAs significantly different from the jet direction can still be accounted for by the "shock-in-jet" scenario. Therefore, it is suggested that the "shock-in-jet" is a common phenomena in relativistic jets, which independent on the synchrotron peaks, types of AGNs and timescale. Similar relations between PA and direction of the radio jet are reported in measurements of radio polarization [16]. It might reflect the common mechanism of flares in the relativistic jets but we need more sample to confirm this trend.

5. Acknowledgments

This work is supported by Optical & Near-infrared Astronomy Inter-University Cooperation Program and Grants-in-Aid for Scientific Research (23340048, 24000004, 24244014, and 24840031) by the Ministry of Education, Culture, Sports, Science and Technology of Japan.

References

[1] A. A. Abdo, et al. The Spectral Energy Distribution of Fermi Bright Blazars. *ApJ*, 716:30–70, June 2010.

[2] A. A. Abdo, et al. Radio-Loud Narrow-Line Seyfert 1 as a New Class of Gamma-Ray Active Galactic Nuclei. *ApJL*, 707:L142–L147, December 2009.

[3] M. Ackermann, et al. The Second Catalog of Active Galactic Nuclei Detected by the Fermi Large Area Telescope. *ApJ*, 743:171, December 2011.

[4] P. W. J. L. Brand. *Infrared and optical photopolarimetry of blazars*, pages 215–219. 1985.

[5] H.-B. Cai, et al. Multi-epoch VLBA observations of 3C 66A. *AAP*, 468:963–971, June 2007.

[6] A. Doi, et al. VLBI Observations of the Most Radio-Loud, Narrow-Line Quasar SDSS J094857.3+002225. *PASJ*, 58:829–834, October 2006.

[7] C. M. Fromm, et al. Catching the radio flare in CTA 102. II. VLBI kinematic analysis. *AAP*, 551:A32, March 2013.

[8] N. Gehrels, et al. The Swift Gamma-Ray Burst Mission. *ApJ*, 611:1005–1020, August 2004.

[9] V. A. Hagen-Thorn, et al. The Outburst of the Blazar AO 0235+164 in 2006 December: Shock-in-Jet Interpretation. *ApJ*, 672:40–47, January 2008.

[10] Y. Ikejiri, et al. Photopolarimetric Monitoring of Blazars in the Optical and Near-Infrared Bands with the Kanata Telescope. I. Correlations between Flux, Color, and Polarization. *PASJ*, 63:639–, June 2011.

[11] C. D. Impey, C. R. Lawrence, and S. Tapia. Optical polarization of a complete sample of radio sources. *ApJ*, 375:46–68, July 1991.

[12] R. Itoh, et al. A Study of the Long-Term Spectral Variations of 3C 66A Observed with the Fermi and Kanata Telescopes. *PASJ*, 65:18, February 2013.

[13] R. Itoh, et al. Dense Optical and Near-infrared Monitoring of CTA 102 during High State in 2012 with OISTER: Detection of Intra-night "Orphan Polarized Flux Flare". *ApJL*, 768:L24, May 2013.

[14] R. Itoh, et al. Minute-scale Rapid Variability of the Optical Polarization in the Narrow-line Seyfert 1 Galaxy PMN J0948+0022. *ApJL*, 775:L26, September 2013.

[15] R. Itoh, et al. An emergence of new polarized emission region in blazar Mrk 421 associated with X-ray flare *PASJ*, submitted.

[16] M. L. Lister, A. P. Marscher, and W. K. Gear. Submilliarcsecond Polarimetric Imaging of Blazar Jets at 43 GHz. *ApJ*, 504:702, September 1998.

[17] M. Matsuoka, et al. The MAXI Mission on the ISS: Science and Instruments for Monitoring All-Sky X-Ray Images. *PASJ*, 61:999–, October 2009.

[18] A. R. G. Mead, et al. Optical and infrared polarimetry and photometry of blazars. *AAPS*, 83:183–204, April 1990.

[19] B. G. Piner and P. G. Edwards. VLBA Polarization Observations of Markarian 421 after a Gamma-Ray High State. *ApJ*, 622:168–177, March 2005.

[20] Y. T. Tanaka et al. Six Years of Fermi-LAT and Multi-Wavelength Monitoring of the Broad-Line Radio Galaxy 3c 120: Jet Dissipation At Sub-Parsec Scales from the Central Engine. *ApJL*, 799:L18, January 2015.

[21] N. Visvanathan and B. J. Wills. Optical Polarization of 52 Radio-loud QSOS and BL Lacertae Objects. *AJ*, 116:2119–2122, November 1998.

Spectral Studies of Flaring FSRQs at GeV Energies Using Pass 8 *Fermi*-LAT Data

R. J. Britto, S. Razzaque
Department of Physics, University of Johannesburg, Auckland Park 2006, South Africa
B. Lott
Centre d'Études Nucléaires de Bordeaux-Gradignan, Université Bordeaux 1, UMR 5797/IN2P3, 33175 Gradignan, France
on behalf of the *Fermi*-LAT Collaboration

Flat spectrum radio quasars (FSRQs) are bright active galactic nuclei surrounded by gas clouds within a UV-visible intense radiation field that form the so-called broad line region (BLR). These objects emit relativistic jets from a region close to the central supermassive black hole and through the BLR. The *Fermi*-Large Area Telescope (*Fermi*-LAT) is sensitive to gamma-ray photons from ∼30 MeV to more than 300 GeV. We have performed spectral analysis of bright FSRQs in a 5.5 year (2008-2014) data sample collected by *Fermi*-LAT, using the new Pass 8 event selection and instrument response function. Also, our study of flaring episodes in a limited time range brings interesting results while compared to the full 5.5 year data samples.

1. Modelling the BLR radiation field

FSRQs constitute a class of active galactic nuclei (AGNs) with a dense BLR in which gamma rays with energy $\gtrsim 10$ GeV are absorbed due to electron-positron pair creation, if produced deep inside the BLR. Indeed, BLR is expected to be denser in FSRQs compared to the BL Lac class.

Operating since 2008, the *Fermi* satellite has amassed more than 6 years of data, continuously surveying the whole sky [3]. The sensitivity of *Fermi*-LAT is ideal for the study of the gamma-ray absorption inside FSRQs in the 100 MeV-300 GeV range. From constraints on gamma-ray absorption we may infer limits on the location of the gamma-ray emission region in the FSRQ jets.

We expect > 10 GeV photons of FSRQs to undergo absorption in the BLR, where the target photon with energy ϵ is a UV photon from the BLR radiation field. As most of these photons are expected to come from the emission lines, we use a model that includes the 6 strongest lines (NV, Lyα, OVI Lyβ, CIII NIII, NeVIII OIV, HeII Lyα) between ∼10 to 41 eV [13].

We model these lines using a Breit-Wigner distribution, given by:

$$BW(\epsilon) = \frac{n_i\ \omega_i}{2\ \pi[(\epsilon - \epsilon_i)^2 + (\omega_i/2)^2]}, \qquad (1)$$

where n_i and ω_i are the number density and width, respectively, for a given line i.

Under the commonly used relations $L_{BLR} = 0.1\ L_{disc}$ and $R_{BLR} = \sqrt{L_{disc}}$ [4, 7], where L_{BLR} is the luminosity of the BLR, R_{BLR} its radius, and L_{disc} the luminosity of the accretion disc. The photon density n_i of the radiation field for each line i can be written:

$$n_i[cm^{-3}] \simeq 1.66{\times}10^{11} \left(\frac{L_i}{10^{45} erg\ s^{-1}}\right) \left(\frac{10^{17} cm}{\epsilon_{i,eV} R_{BLR}^2}\right). \qquad (2)$$

The opacity is derived from [5, 8] and is expressed as a function of E and z:

$$\frac{d\tau_{\gamma\gamma}}{dx}(E,z) = \frac{r_0^2}{2}\left[\frac{m^2c^4}{E(1+z)}\right]^2$$

$$\times \sum_{i=1}^{6} \left(n_i\omega_i \int_{\frac{m^2c^4}{E(1+z)}}^{\infty} \frac{\bar{\varphi}\left[\frac{\epsilon E(1+z)}{m^2c^4}\right] d\epsilon}{[(\epsilon - \epsilon_i)^2 + (\omega_i/2)^2]\epsilon^2} \right), \qquad (3)$$

where r_0 is the classical electron radius, m the electron mass.

The $\tau_{\gamma\gamma}$ opacity in the BLR is then calculated as following:

$$\tau_{\gamma\gamma}(E,z) = a \times R_{BLR} \times \frac{d\tau_{\gamma\gamma}}{dx}(E,z), \qquad (4)$$

assuming the gamma rays are produced within $a \times R_{BLR}$, where R_{BLR} is the outer radius of BLR, and $a < 1$. Since this absorption happens at some distance from the supermassive black hole, this corrective factor that we called "a" represents the fraction of the BLR responsible for the absorption.

In Table I are displayed the line properties of the average spectrum of quasars we used in our model, as they were given in [13]. Since the He II Lyα line has quite large uncertainties, we arbitrary fixed its EW and relative flux to be equal to the ones of N V (uncertainty represented by (*)).

Very high energy gamma rays travelling from far distances undergo absorption in the extragalactic background light ("EBL", mainly composed of infrared-UV radiation). This absorption is to be considered above 10 GeV and has been implemented in our studies, from the model presented in [6].

Evidence of absorption in the BLR for some FSRQs have been reported in [11, 12].

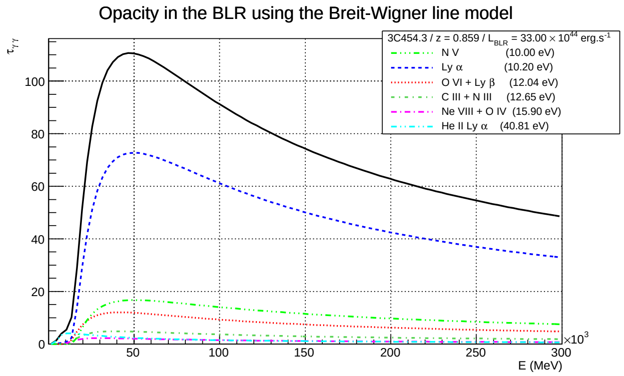

Figure 1: Opacity $\tau_{\gamma\gamma}(E, z)$ *versus* Energy, for 3C 454.3. The opacity sum on the 6 lines is drawn in plain black.

Table I Properties of 5 main lines of the average spectrum of quasars as compiled in [13], and He II Lyα as we defined it for this study.

Line	ϵ (eV)	EW (eV)	Relative flux
NV	10.0	0.16	0.22
Lyα	10.2	0.71	1.00
OVI Lyβ	12.04	0.19	0.191
CIII NIII	12.65	0.09	0.081
NeVIII OIV	15.90	0.08	0.047
HeII Lyα	40.81	0.16*	0.22*

2. Data processing and model fitting

We have analysed data of 7 bright gamma-ray FSRQs. Plots of the spectral energy distributions (SEDs) under the label “5.5 years” have been processed from 4 August 2008 till 30 April 2014. The sources we present in this paper are listed in Table II, *LII* and *BII* being respectively the Galactic latitude and longitude in decimal degrees.

Data were processed using the Pass 8 data representation (P8_SOURCE_V4), and the Science Tools version v9-34-01. Signal is reconstructed from each source using the unbinned likelihood tool[1], applied to LAT data in the 0.1-300 GeV energy range, within a region of interest (ROI) of 10° radius. A source region extended to an additional 10° annulus accounted for all the point sources of the *Second Fermi-LAT source catalog* [9], and for the Galactic diffuse emission (template_4years_P8_V2_scaled) and the isotropic diffuse emission (isotropic_source_4years_P8V3).

We computed the SEDs for all the sources of the selected sample with the Pass 8 data representation. Additionally, for the two brightest objects of our FSRQ sample, *i.e.* 3C 454.3 and PKS 1510-089, we also computed the SEDs with the PASS 7 reprocessed dataset (P7REP_SOURCE_V15) and verified the consistency of the results with respect to the PASS 8 ones. Although some bin-to-bin fluctuations appear due to energy wise event migrations, the two SEDs (Pass 7 and Pass 8) for both the sources are compatible (as shown in Figure 2 for 3C 454.3).

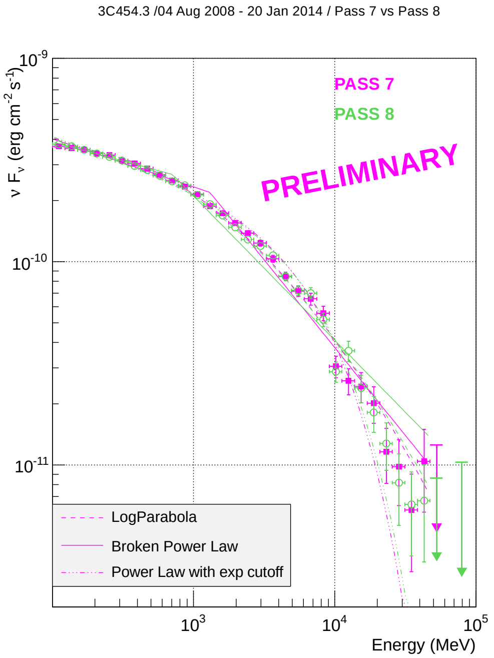

Figure 2: Comparison of the SED of 3C 454.3, produced with the Pass 7 (magenta) and Pass 8 (green) data sets.

A first set of fits was performed from 100 MeV till the highest energy data point (excluding upper limits), using a log-parabola (LP: $dN(E)/dE = N_0\ (E/E_0)^{-\alpha-\beta\ log(E/E_0))}$, with E_0 kept fixed at 297.6 MeV, and where “log” is the natural logarithm), a broken power law (BPL: $dN(E)/dE = N_0\ (E/E_b)^{-\Gamma_i}$, with $i = 1$ if $E < E_b$ and $i = 2$ if $E > E_b$), and a power law with an exponential cutoff (PLEC: $dN(E)/dE = N_0\ (E/E_p)^{-\Gamma_{PLEC}}\ exp(-E/E_c)$, with E_p kept fixed at 412.7 MeV). Other sets of fits were performed by adding exponential factors to model the EBL absorption [6] and the opacity of the BLR.

As the fits presented in the Sections 3 and 4 are binning dependant, the values of the fit parameters vary from one choice of binning to another. Narrow data binning could held spurious fluctuations, while wide data-binning could hide features. In order to estimate this systematic effect, we do the following: a first LP fit is performed on the SED, while keeping all parameters fixed to the values obtained by the unbinned likelihood analysis, and a χ^2/ndf is returned. A second LP fit is performed with N_0, α and β kept free,

---

[1] http://fermi.gsfc.nasa.gov/ssc/data/analysis/

Table II Characteristics of the 7 FSRQs used in this paper. Sources are ordered by decreasing flux in the 1-100 GeV energy range. Values of the luminosity in the broad line region (L_{BLR}) are taken or derived from [10, 14].

Name	RA (J2000.0)	Dec (J2000.0)	LII (deg.)	BII (deg.)	Redshift z	Flux 2FGL 1-100 GeV	Flux 1FHL 10-100 GeV	Photon index 1FGL	L_{BLR} ($10^{44} erg.s^{-1}$)
3C 454.3	22 53 57.7	+16 08 53.1	86.11	-38.19	0.859	9.65e-8	1.35e-9	2.46619	33.00
PKS 1510-08	15 12 50.5	-09 06 00.9	351.28	40.13	0.360	4.06e-8	7.35e-10	2.40756	5.62
4C +21.35	12 24 54.5	+21 22 46.9	255.08	81.65	0.434	3.54e-8	7.43e-10	2.54717	15.80
3C 279	12 56 11.0	-05 47 20.1	305.1	57.06	0.536	2.56e-8	5.37e-10	2.32061	3.10
PKS 0454-234	04 57 03.1	-23 24 52.0	223.7	-34.9	1.003	2.27e-8	2.99e-10	2.20649	3.70
B2 1520+31	15 22 09.8	+31 44 14.3	50.16	57.02	1.484	1.76e-8	4.27e-10	2.42125	8.00
PKS (B)1424-418	14 27 56.2	-42 06 18.6	321.44	17.26	1.522	1.47e-8	2.9e-10	2.31004	8.91

E_b kept fixed to the value returned by the unbinned likelihood analysis. We compare the fits to validate that the binned fit is compatible with the unbinned fit, though results differ. These systematics could be overcome by implementing an unbinned analysis for all fitted models in future.

Our modelling study is then done by fitting the SEDs using the LP, BPL and PLEC function that all now include EBL. These fits will be reported in the Sections 3 and 4, and compared to the fits that include both EBL and BLR absorption. The latter fits are written as $LP\tau$, $BPL\tau$, and $PLEC\tau$.

The observed spectrum $F_{obs}(E)$ will then be ultimately written:

$$F_{obs}(E) = e^{-\tau_{EBL}(E,z)} \; e^{-a \; \tau_{\gamma\gamma}(E,z)} \; F_{int}(E), \qquad (5)$$

where $F_{int}(E)$ is the LP, BPL or PLEC fitting function. Parameter a is kept free in the $[10^{-5}, 1]$ range to account for the fraction of radius of the BLR in which gamma rays may be absorbed.

The fitting procedure using the absorption models is implemented by interpolation of both the τ_{EBL} and $\tau_{\gamma\gamma}$ graphs. While comparing each "EBL + BLR absorption" fit (LPτ, BPLτ or PLECτ) with the "EBL + no BLR absorption" fit (LP, BPL or PLEC), and if both fits have a $\chi^2/ndf \lesssim 1$, we obtain a p-value which indicates the discrepancy between the fit with model and the fit without model, for a given function.

3. Results on the 5.5 years of data

We present now the results on the 7 bright FSRQs during the 5.5 years period previously defined in Section 2. Data under the label "5.5 years" are processed from 4 August 2008 till 30 April 2014. In Figure 3 are presented the SEDs of 3C 454.3, PKS 1510-089, TXS 1520+31 and PKS 1424-41. Some of the fits are not visible, mainly the BPL and PLEC. The reason is that they are overwritten by the BPLτ and PLECτ functions, for which the parameter a is very small.

We would consider having evidence for absorption in the BLR if we get all of the following:

- at least one good quality fit among one of the fits with EBL+BLR absorption (LPτ, BPLτ and PLECτ);
- parameter "a" with a relatively small error bar;
- a small p-value or a bad fit of the corresponding function with only EBL absorption (LP, BPL or PLEC).

In Table III are displayed the fit parameters of the 7 sources, along with the p-values used to compare the models (with *versus* without absorption). In blue bold face are the parameters that suggest a possible BLR absorption, as some of the above conditions are partially met for 3C 454.3 (with a p-value of 6.2×10^{-4} / 3.9 σ C.L.), and for TXS 1520+31 (with a p-value of 9.3×10^{-3} / 2.6 σ C.L.). We have no hint of absorption for the other sources we studied.

4. Results on high state/flaring episodes

Data were analysed during flaring/high state periods for the following sources:

- 3C 454.3 (high state and giant flare) during 02 Nov-05 Dec 2010 (MJD 55502.5-55535.5)[1];
- PKS 1510-089 during 19 Feb-04 Apr 2012 (MJD 55976.0-56021.0), along with MAGIC data from the same period (MAGIC data points taken from [2]);
- PKS 1424-41 during 30 Sep 2012-27 Jul 2013 (MJD 56200.0-56500.0), as a combined series of 4 successive radio flares).

During these outburst episodes, the gamma-ray emission region can have a different location compared

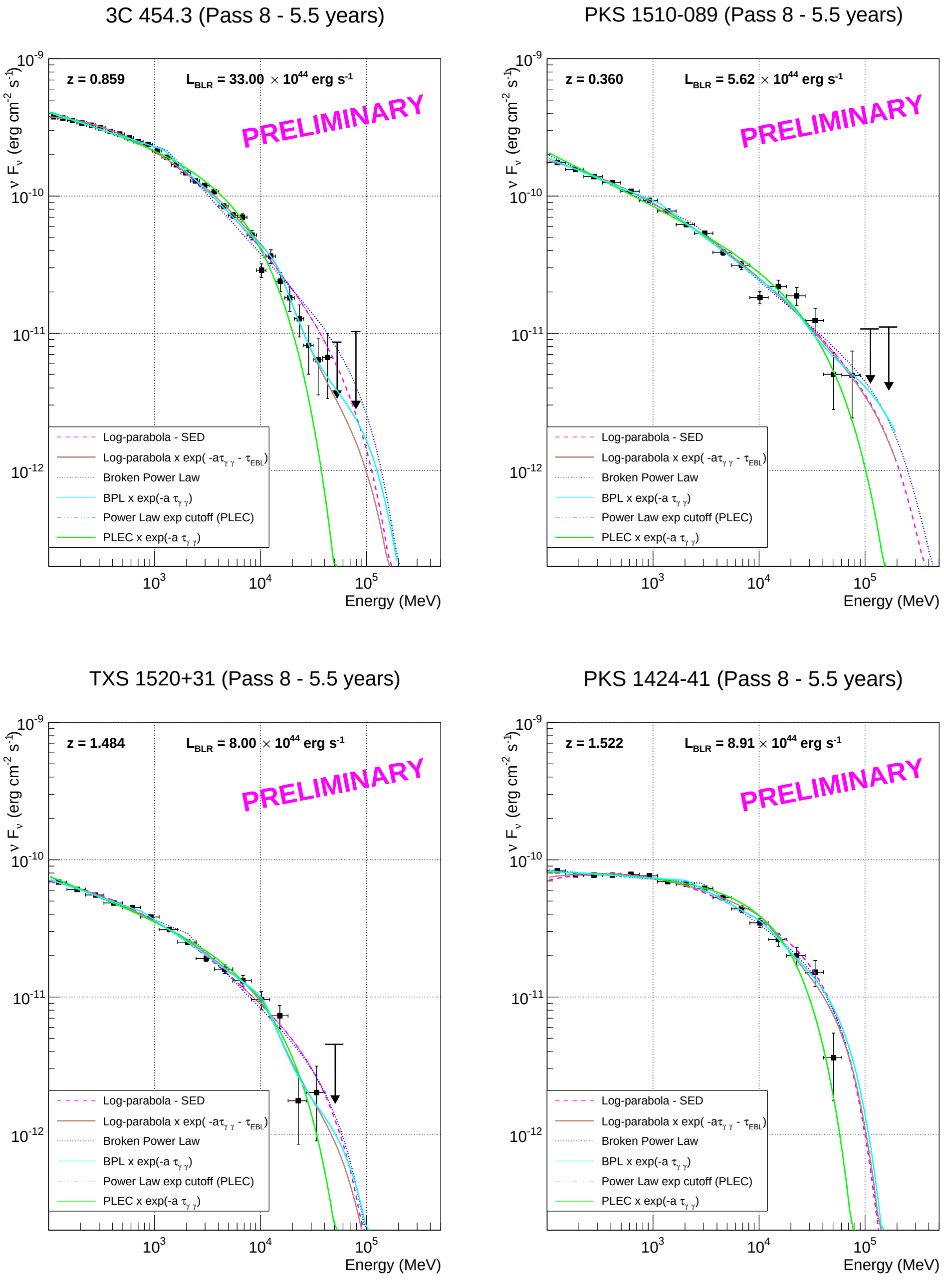
3C 454.3 (Pass 8 - 5.5 years)

PKS 1510-089 (Pass 8 - 5.5 years)

TXS 1520+31 (Pass 8 - 5.5 years)

PKS 1424-41 (Pass 8 - 5.5 years)

Figure 3: SEDs of 3C 454.3, PKS 1510-089, TXS 1520+31 and PKS 1424-41. *BPL* and *PLEC* fits are often hidden beneath *BPL*τ and *PLEC*τ.

to the quiescent state. In this section we present the results obtained on these three high states (Figure 4 and Table IV). Under the same criteria than the ones used in Section 3, we still find no evidence of BLR absorption, though we still have a hint of it for 3C 454.3 with a p-value of around 2.2×10^{-3} for the discrepancy between the BPL and BPLτ fits (significance of about 3 σ). Due to the unusual shape of the SED of PKS 1424-41 during this series of 4 flares, all fits have a large χ^2 value.

Though we dispose of less photons in the data analysis of flaring episodes, during strong and long flares, it could be possible to constrain the location of the gamma-ray production region if it is deep enough inside the BLR.

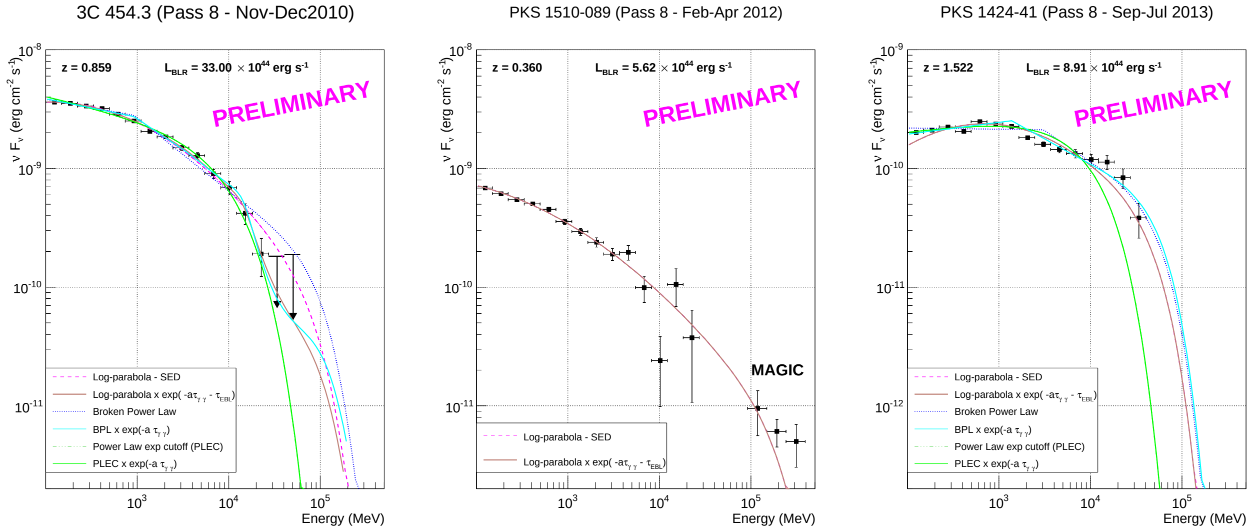

Figure 4: SEDs of 3C 454.3, PKS 1510-089 and PKS 1424-41 during the outburst periods. *PLEC* fits are hidden beneath $PLEC\tau$ for 3C 454.3 and PKS 1424-41. The flare of PKS 1510-089 was studied along with MAGIC data above ∼90 GeV and the combined LAT-MAGIC SED was fitted only with LP and LPτ function (LP hidden beneath LPτ).

5. Conclusions and perspectives

We find that the gamma-gamma absorption in the BLR is not significant enough to claim discovery for the models of BLR and spectral functions we have investigated. There are hints of absorption in case of 3C 454.3 and TXS 1520+31 with significance of the order of 3σ. An implication of our results could be that the gamma-ray emission zone in FSRQs might be located outside or at the outer edge of the BLR. However, further investigation on binning effects on the SED fits are required. Future work is also expected to improve the modelling of the BLR.

Acknowledgments

The *Fermi*-LAT Collaboration acknowledges support for LAT development, operation and data analysis from NASA and DOE (United States), CEA/Irfu and IN2P3/CNRS (France), ASI and INFN (Italy), MEXT, KEK, and JAXA (Japan), and the K.A. Wallenberg Foundation, the Swedish Research Council and the National Space Board (Sweden). Science analysis support in the operations phase from INAF (Italy) and CNES (France) is also gratefully acknowledged.

Thanks to Pfesesani Van Zyl for providing the PKS 1424-41 dates during radio flares and to Julian Sitarek and the MAGIC Collaboration for providing the MAGIC data points.

References

[1] A. A. Abdo et al, 2011, ApJL, 733:L26
[2] J. Aleksic et al, 2014, A&A, 569, A46
[3] W. B. Atwood et al, 2009, ApJ, 697, 1071
[4] J. A. Baldwin & H. Netzer, 1978, ApJ, 226, 1-20
[5] R. W. Brown, K. O. Mikaelian and R. J. Gould, 1973, ApJ L, 14, L203-L205
[6] J. D. Finke, S. Razzaque & C. D. Dermer, 2010, ApJ, 712, 238
[7] G. Ghisellini & F. Tavecchio, 2009, MNRAS, 397, 985
[8] R. G. Gould & G. P. Schréder, 1967, Physical Review, 155, 5
[9] P. L. Nolan, et al, 2012, ApJ S, 199, 31)
[10] L. Pacciani et al, 2014, ApJ, 790, 45
[11] J. Poutanen & B. Stern, 2010, ApJ L, 717:L118
[12] B. Stern & J. Poutanen, 2014, ApJ, 794, 8
[13] R. C. Telfer, W. Zheng, G. A. Kriss and A. F. Davidsen, 2002, ApJ, 565:773-785
[14] D. R. Xiong & X. Zhang, 2014, MNRAS, 441, 4, p.3375-3395

Table III Fitting parameters and derived significances for the 7 bright FSRQs of our sample. We mention (*) when *a* reached the lower edge of the fitting interval.

Parameter	Model		3C 454.3	PKS 1510-089	4C +21.35	3C 279	PKS 0454-234	TXS 1520+31	PKS1424-24
function *(without BLR absorption model)*	LP_*unbinned*	α	2.248 ± 0.005	2.294 ± 0.008	2.240 ± 0.009	2.254 ± 0.010	2.067 ± 0.013	2.273 ± 0.013	2.090 ± 0.008
	LP_*unbinned*	β	0.0897 ± 0.0024	0.0513 ± 0.0036	0.0445 ± 0.0044	0.0588 ± 0.0053	0.0793 ± 0.0053	0.0689 ± 0.0059	0.0753 ± 0.0039
	PL	E_b	298 ± 4.4	258 ± 6.4	317 ± 10.8	284 ± 10.2	358 ± 16.9	281 ± 11.2	620 ± 23.8
	LP	α	2.240 ± 0.008	2.292 ± 0.030	2.274 ± 0.025	2.266 ± 0.027	2.070 ± 0.019	2.274 ± 0.026	2.077 ± 0.015
	LP	β	0.0980 ± 0.0039	0.0511 ± 0.0093	0.0404 ± 0.0092	0.0539 ± 0.0099	0.0761 ± 0.0087	0.0687 ± 0.0110	0.0713 ± 0.0088
	BPL	Γ_1	2.242 ± 0.345	2.363 ± 0.030	2.280 ± 0.028	2.332 ± 0.029	2.138 ± 0.016	2.317 ± 0.033	2.066 ± 0.010
	BPL	Γ_2	2.856 ± 2.108	2.673 ± 0.075	2.521 ± 0.057	2.690 ± 0.098	2.681 ± 0.064	2.791 ± 0.121	2.564 ± 0.087
	BPL	E_b	1307 ± 5211.8	2387 ± 971.5	1439 ± 573.3	2738 ± 979.1	3062 ± 0.3	2036 ± 674.1	2947 ± 573.6
	PLEC	Γ_{PLEC}	2.241 ± 0.016	2.386 ± 0.034	2.340 ± 0.035	2.324 ± 0.032	2.088 ± 0.024	2.308 ± 0.038	2.028 ± 0.013
	PLEC	E_c	8250 ± 721.2	40228 ± 13971.0	52905 ± 28547.3	26932 ± 8335.2	14581 ± 2929.5	14378 ± 3950.2	16459 ± 2097.1
function *(with BLR absorption model)*	LPτ	α	2.243 ± 0.008	2.294 ± 0.033	2.274 ± 0.025	2.268 ± 0.029	2.082 ± 0.017	2.289 ± 0.033	2.079 ± 0.013
	LPτ	β	0.0876 ± 0.0051	0.0498 ± 0.0117	0.0404 ± 0.0092	0.0526 ± 0.0130	0.0590 ± 0.0103	0.0506 ± 0.0162	0.0542 ± 0.0142
	BPLτ	Γ_1	2.250 ± 0.012	2.312 ± 0.037	2.251 ± 0.031	2.301 ± 0.031	2.006 ± 0.025	2.272 ± 0.045	2.052 ± 0.011
	BPLτ	Γ_2	2.738 ± 0.049	2.583 ± 0.056	2.507 ± 0.048	2.590 ± 0.109	2.283 ± 0.034	2.518 ± 0.069	2.403 ± 0.066
	BPLτ	E_b	1225 ± 142.9	1152 ± 372.0	1062 ± 379.5	1616 ± 743.9	544 ± 101.1	769 ± 315.1	2052 ± 1.2
	PLECτ	Γ_{PLEC}	2.241 ± 0.016	2.386 ± 0.034	2.341 ± 0.035	2.324 ± 0.032	2.088 ± 0.024	2.308 ± 0.038	2.028 ± 0.013
	PLECτ	E_c	8251 ± 721.4	40239 ± 13864.7	52946 ± 27502.4	26936 ± 8309.2	14582 ± 2917.7	14381 ± 3982.3	16463 ± 2088.6
a	LPτ		**0.00516 ± 0.00185**	0.00147 ± 0.01118	0.00001 ± 0.00139	0.00232 ± 0.02143	0.02140 ± 0.01007	0.01500 ± 0.00943	0.00745 ± 0.00515
	BPLτ		0.00666 ± 0.00195	0.00785 ± 0.00735	0.00001 ± 0.00167	0.00919 ± 0.01496	0.03641 ± 0.00891	**0.02002 ± 0.00881**	0.00558 ± 0.00488
	PLECτ		0.00001 ± 0.00055	0.00001 ± 0.00529	0.00001 ± 0.00151	0.00001 ± 0.00682	0.00001 ± 0.00606	0.00001 ± 0.01584	0.00001 ± 0.00248
$\chi^2(ndf)$ *without abs. model*	LP_*unbinned*		36.419 (30)	7.454 (17)	18.821 (16)	5.288 (16)	14.783 (16)	8.988 (15)	36.173 (16)
	LP		**29.316 (27)**	7.278 (14)	13.009 (13)	4.609 (13)	11.516 (13)	**6.448 (12)**	22.826 (13)
	BPL		45.647 (26)	9.963 (13)	11.269 (12)	7.290 (12)	28.960 (12)	8.826 (11)	19.366 (12)
	PLEC		42.999 (26)	13.115 (13)	21.817 (12)	7.422 (12)	17.094 (12)	5.158 (11)	17.037 (12)
$\chi^2(ndf)$ *with abs. model*	LPτ		**17.591 (26)**	7.245 (13)	13.017 (12)	4.582 (12)	6.526 (12)	3.181 (11)	20.495 (12)
	BPLτ		25.071 (25)	7.242 (12)	9.870 (11)	5.694 (11)	4.282 (11)	**2.069 (10)**	17.474 (11)
	PLECτ		43.017 (26)	13.117 (13)	21.823 (12)	7.424 (12)	17.095 (12)	5.159 (11)	17.042 (12)
$\Delta\chi^2$ (ndf)	LP/PLτ		**1.173e+01**	3.360e-02	7.208e-03	2.747e-02	4.989e+00	3.267e+00	2.331e+00
	BPL/BPLτ		2.058e+01	2.720e+00	1.399e+00	1.596e+00	2.468e+01	**6.757e+00**	1.892e+00
	PLEC/PLECτ		1.812e-02	1.888e-03	6.614e-03	1.464e-03	1.646e-03	6.277e-04	4.025e-03
p-value	LP/LPτ		**6.166e-04**	8.546e-01	9.323e-01	8.684e-01	2.551e-02	7.070e-02	-
	BPL/BPLτ		-	9.908e-02	2.369e-01	2.064e-01	-	**9.337e-03**	-
	PLEC/PLECτ		-	-	-	-	-	-	-

Table IV Fitting parameters and derived significances for the 3 flares we studied in our FSRQ sample. We mention (*) when a reached the lower edge of the fitting interval.

Parameter	Model		3C 454.3	PKS 1510-089	PKS1424-24
			(Nov-Dec 2010)	(Feb-Apr 2012)	(Sep 2012-Jul 2013)
function *(without BLR absorption model)*	LP_*unbinned*	α	2.152 ± 0.008	¡ 2.268 0.027	2.022 ± 0.010
	LP_*unbinned*	β	0.0895 ± 0.0036	0.0451 0.0108	0.0766 ± 0.0052
	PL	E_b	286 ± 8.9	260 6.0	940 ± 35.4
	LP	α	2.153 ± 0.016	2.299 0.040	2.069 ± 0.014
	LP	β	0.0879 ± 0.0088	0.0569 0.0117	0.1134 ± 0.0120
	BPL	Γ_1	2.140 ± 0.022	2.367 0.038	2.010 ± 0.003
	BPL	Γ_2	2.617 ± 0.036	2.867 0.076	2.530 ± 0.055
	BPL	E_b	921 ± 0.4	2603 912.7	3062 ± 1.6
	PLEC	Γ_{PLEC}	2.183 ± 0.034	2.269 0.049	1.903 ± 0.021
	PLEC	E_c	9981 ± 2111.4	7921 2586.5	8361 ± 1117.7
function *(with BLR absorption model)*	LP$\mathcal{T}$	α	2.157 ± 0.018	2.299 0.022	2.069 ± 0.014
	LP$\mathcal{T}$	β	0.0764 ± 0.0116	0.0569 0.0065	0.1134 ± 0.0120
	BPL$\mathcal{T}$	Γ_1	2.156 ± 0.029	-	1.900 ± 0.019
	BPL$\mathcal{T}$	Γ_2	2.518 ± 0.050	-	2.426 ± 0.036
	BPL$\mathcal{T}$	E_b	921 ± 0.2	-	1375 ± 0.2
	PLEC$\mathcal{T}$	Γ_{PLEC}	2.183 ± 0.034	-	1.903 ± 0.021
	PLEC$\mathcal{T}$	E_c	9983 ± 2113.2	-	8361 ± 1135.7
a	LP$\mathcal{T}$		0.00703 ± 0.00551	0.04667 0.04550	0.00001 ± 0.00132
	BPL$\mathcal{T}$		**0.01059 ± 0.00591**	-	0.00001 ± 0.00320
	PLEC$\mathcal{T}$		0.00001 ± 0.00629	-	0.00001 ± 0.00108
χ^2(*ndf*) *without abs. model*	LP_*unbinned*		4.553 (14)	67.828 (17)	79.634 (15)
	LP		4.041 (11)	20.807 (14)	37.481 (12)
	BPL		**13.158 (10)**	15.137 (13)	101.358 (11)
	PLEC		6.912 (10)	37.461 (13)	77.643 (11)
χ^2(*ndf*) *with abs. model*	LP$\mathcal{T}$		0.928 (10)	20.807 (13)	37.489 (11)
	BPL$\mathcal{T}$		**3.780 (9)**	-	24.648 (10)
	PLEC$\mathcal{T}$		6.914 (10)	-	77.652 (11)
$\Delta\chi^2$ (ndf)	LP/PL$\mathcal{T}$		3.113e+00	6.395e-11	7.583e-03
	BPL/BPL$\mathcal{T}$		**9.378e+00**	-	7.671e+01
	PLEC/PLEC$\mathcal{T}$		1.586e-03	-	9.270e-03
p-value	LP/LP$\mathcal{T}$		7.769e-02	-	-
	BPL/BPL$\mathcal{T}$		**2.195e-03**	-	-
	PLEC/PLEC$\mathcal{T}$		0.000e+00	-	-

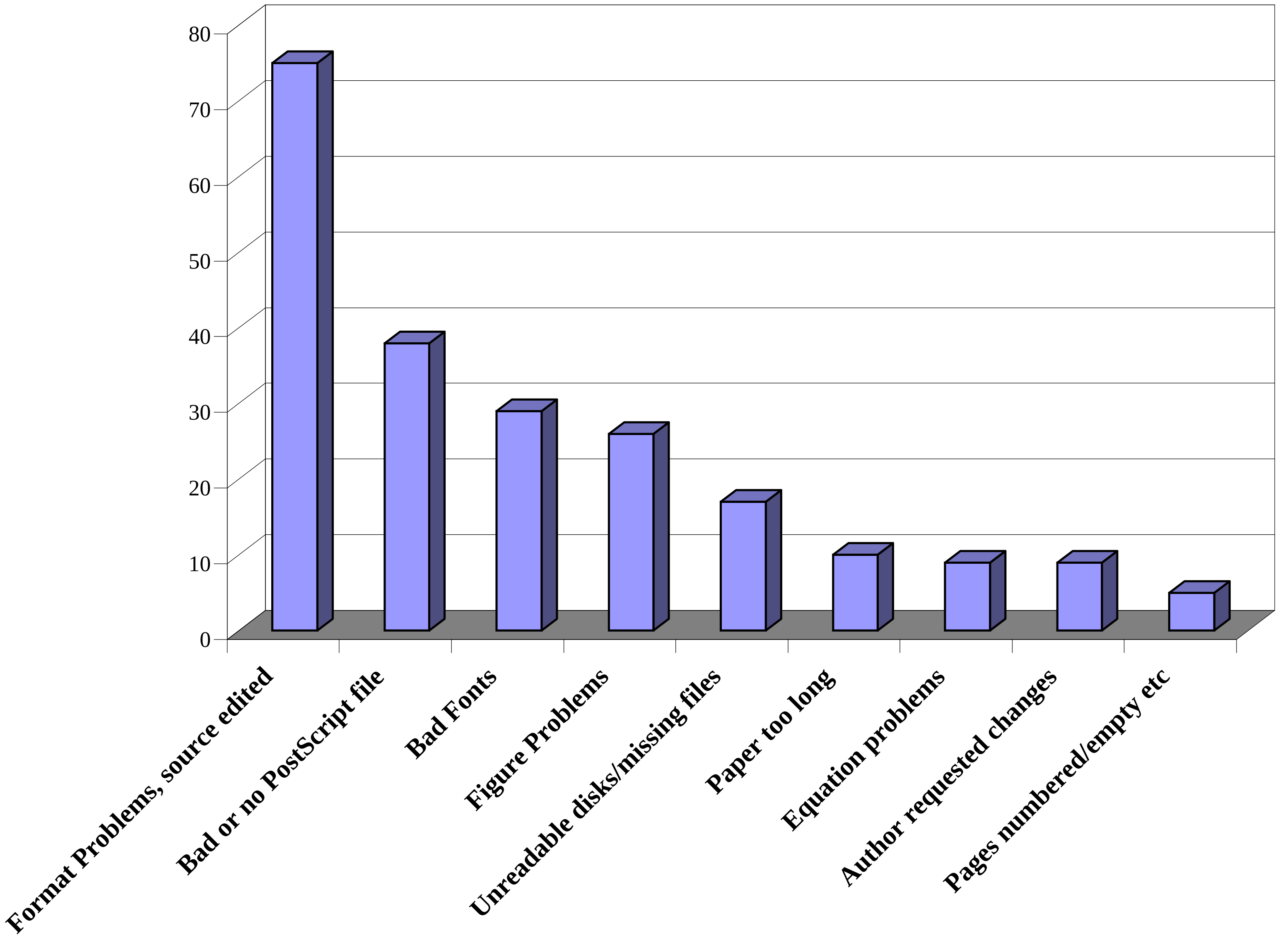

80
70
60
50
40
30
20
10
0
Format Problems, source edited
Bad or no PostScript file
Bad Fonts
Figure Problems
Unreadable disks/missing files
Paper too long
Equation problems
Author requested changes
Pages numbered/empty etc

Missing Gamma-Rays from kpc-scale AGN Jets: A Test of the IC/CMB Model

Eileen T. Meyer
Space Telescope Science Institute, Baltimore, MD 21218, USA and
University of Maryland Baltimore County, Baltimore, MD 21250, USA
Markos Georganopoulos
University of Maryland Baltimore County, Baltimore, MD 21250, USA
W. B. Sparks
Space Telescope Science Institute, Baltimore, MD 21218, USA
Leith Godfrey
ASTRON Netherlands Institute for Radio Astronomy, The Netherlands
Eric Perlman
Florida Institute of Technology, Melbourne, FL 32901, USA

The physical origin of the X-ray emission in powerful quasar jets has been a long-standing mystery. Though these jets start out on the sub-pc scale as highly relativistic flows, we do not have any direct measurement of their speeds on the kpc scale, where the vast distances from the core necessitate in situ particle acceleration. If the jets remain highly relativistic on kpc scales, then the X-rays could be due to inverse-Compton upscattering of CMB photons. However, the IC/CMB explanation predicts a high level of gamma-ray emission, which should be detectible by the *Fermi*/LAT. We have searched for and ruled out this emission at a high level of significance for the well-known sources 3C 273 and PKS 0637-752, suggesting the X-rays are synchrotron, though of unknown origin. These recent results with Fermi also suggest that the kpc-scale jets in powerful quasars are significantly slower than have been presumed under the IC/CMB model. I will discuss the surprising implications of these findings for the energetics and radiative output of powerful quasars as well as their impact on their environment.

In August 1999, the *Chandra* X-ray Observatory observed its first celestial target, quasar PKS 0637-752, during the initial focusing of the telescope [Schwartz et al. 2000, Chartas et al. 2000]. Along with the bright quasar core, *Chandra* unexpectedly detected X-rays from the kilo-parsec scale relativistic jet (previously known from radio imaging, Figure). Unlike the synchrotron spectrum of lower-power FR I jets like M87 which easily extend up to X-ray energies [e.g. Wilson and Yang 2002], the synchrotron spectrum of powerful quasar jets (including PKS 0637-752) generally peak at or below the IR/Optical band. The X-rays detected in the kpc-scale jet of PKS 0637-752 were orders of magnitude brighter than expected from the radio-optical synchrotron spectrum, or indeed from either synchrotron self-Compton (SSC) or inverse Compton upscattering of ambient CMB photons (IC/CMB) under equipartition conditions [Chartas et al. 2000]. Further, the X-ray spectrum of the jet was remarkably hard, with a photon index of 1.76 ± 0.1.

Proper motions measurements of sub-parsec scale jets of powerful quasars with Very Long Baseline Interferometry (VLBI) have detected superluminal proper motions which imply that these jets start out highly relativistic, with Lorentz factors (Γ) of 10-50 [Jorstad et al. 2005, Lister et al. 2009]. Though it had long been supposed based on population studies that jets decelerate and are at most mildly relativistic by the time they reach the kpc scale [e.g. Arshakian and Longair 2004, Mullin and Hardcastle 2009], no direct measurements have confirmed this. Tavecchio et al. [2000] and Celotti et al. [2001] thus suggested that the X-rays from the jet in PKS 0637-752 could be explained by IC/CMB emission if the jet *remained* highly relativistic (Γ ∼10), and was pointed at a fairly small angle to our line of sight (6°). This produces a much larger Doppler boosting factor (δ ∼10) and enables the IC/CMB X-rays to match the observations.

Over the past decade and a half since the launch of *Chandra*, dozens more kpc-scale quasar jets with anomalously hard and/or high X-rays have been detected [e.g. Sambruna et al. 2001, 2002, Siemiginowska et al. 2003, Sambruna et al. 2004, Marshall et al. 2005, Harris and Krawczynski 2006, Siemiginowska et al. 2007, Marshall et al. 2011, Kharb et al. 2012, Godfrey et al. 2012]. The IC/CMB model has been by far the most popular explanation of these X-rays, though problems have been noted [Hardcastle 2006]. Besides the unconfirmed fast speeds required on the kpc scale, IC/CMB often requires the jet to be pointed very close along our line-of-sight, leading to a deprojected jet length longer than 1 Mpc, the upper limit for jets observed in the plane of the sky. Further, the electrons responsible for upscattering the CMB into the *Chandra* band are at much lower energies than are traced by radio observations. This extension of the electron energy distribution is energetically costly, in some cases leading to 'super-Eddington' jet power requirements [Dermer and Atoyan 2004, Uchiyama et al. 2006]. These problems lead to the suggestion that the X-rays could alternatively be synchrotron emission from a second electron population in the jet, albeit of unknown origin [Hardcastle 2006, Uchiyama et al. 2006, Jester et al. 2006, Harris et al. 2004, Kataoka and Stawarz 2005]. he fundamental problem up to now has been that fitting the radio-to-X-ray spectral energy distribution (SED) alone cannot distinguish between the IC/CMB and synchrotron explanations for the X-rays [Cara et al. 2013]. The difference in power requirements between the two mechanisms is great, as is the extremely different idea of jet structure that they imply. Discriminating between these models is essential to make progress on the actual impact of jets on their environment.

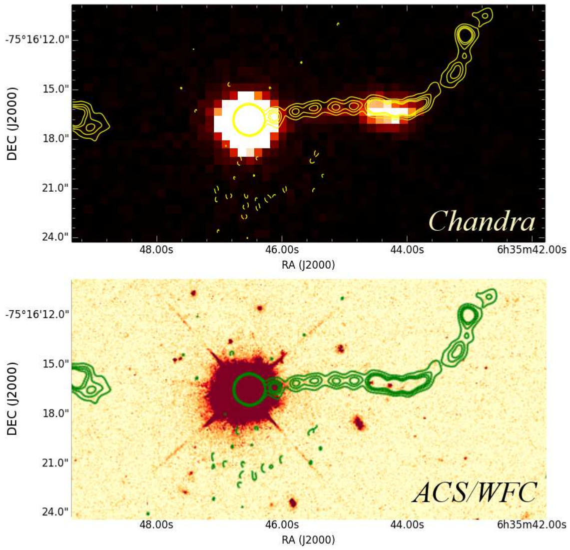

Figure 1: *Upper Panel: Chandra* X-ray image of PKS 0637-752, with ATCA 17 GHz radio contours overlaid. *Lower Panel:* Optical image of PKS 0637-752, taken with ACS/WFC on HST (F475W filter) with ATCA 17 GHz radio contours overlaid.

Georganopoulos et al. [2006], hereafter **G06**, suggested that *Fermi* Large Area Telescope (LAT) observations could confirm or rule out the IC/CMB mechanism for the X-rays, by detecting (or not) the high level of gamma-ray emission this mechanism requires. We have previously looked for this gamma-ray emission from the jet of 3C 273, and ruled out IC/CMB gamma-rays from (the brightest) knot A alone at the >95% level, and from knots A through D1 combined at the >99.9% level [Meyer and Georganopoulos 2014, hereafter **M14**].

At this meeting, we reported new *Fermi* observations of PKS 0637-752 which show that the expected steady gamma-ray emission from the IC/CMB mechanism is also ruled out by deep upper limits at the 99.9% level. We also present updated limits for 3C 273, showing that the expected gamma-rays from IC/CMB are now ruled out at the 99.99% level in more than one *Fermi* energy band. We will briefly discuss the implications of these measurements on two fronts. First, we show that a second synchrotron component is the only likely scenario left to explain the X-rays in these jets. Secondly, we find that irrespective of the X-ray emission mechanism, the deep upper limits at GeV energies place interesting constraints on the Doppler beaming factors which implies that these jets are not highly relativistic on the kpc scale. We will discuss the surprising implications of slow, synchrotron X-ray jets on our understanding of the total radiative output of quasars, especially at TeV energies.

1. methods

1.1. The *Fermi* Test of IC/CMB

As first noted by G06, the shape of the IC/CMB spectrum is constrained to match the synchrotron spectrum, with a shift in frequency and luminosity solely determined by the factor B/δ where δ is the Doppler beaming factor and B the magnetic field strength. From G06, we have:

$$\frac{\nu_c}{\nu_s} = \frac{\nu_{\rm CMB}\delta^2\gamma^2}{eB\delta\gamma^2/[2\pi m_e c(1+z)]} \qquad (1)$$

$$\frac{L_c}{L_s} = \frac{32\pi U_{\rm CMB}(1+z)^4\delta^4}{3(B\delta)^2}, \qquad (2)$$

where ν_c and ν_s (L_c, L_s) are the observed Compton and synchrotron frequencies (luminosities) emitted by electrons of Lorentz factor γ, e and m_e are the electron charge and mass, and $\nu_{\rm CMB} = 1.6\times10^{11}$ Hz is the CMB peak frequency at z = 0. However, if the observed X-ray fluxes are to be produced by the IC/CMB mechanism, then the value of B/δ is already uniquely determined by the requirement to match the X-ray flux level, at which point there is no freedom at all in the rest of the spectrum. The peak of the IC/CMB spectrum will fall in the GeV band. Note that this prediction is not predicated on any particular (e.g., equipartition) magnetic field strength.

The *Fermi*/LAT lacks the spatial resolution to detect the jet separately from the gamma-ray bright quasar core, which is only 10$''$ away – the *Fermi*/LAT 68% containment radius is on the order of tenths of a degree to degrees. However, in powerful quasars the inverse Compton core emission generally peaks at a few MeV, producing a soft, and extremely variable spectrum in the *Fermi* band, with long periods of relative quiescence. Indeed, PKS 0637-752 was detected in the 2nd *Fermi* source catalog [2FGL, Nolan et al. 2012] as both a very soft (photon index of Γ_p=2.71) and highly variabile source (variability index = 347). In contrast, the IC/CMB emission from the large scale jet is expected to be harder and completely non-variable. The latter property allows us to combine the *Fermi* data taken only when the quasar core is in a low state to try to detect or place limits on the IC/CMB emission.

1.2. Fermi Analysis of PKS 0637-752

We first combined the all-sky weekly LAT event and spacecraft files for weeks 9 through 325 of the *Fermi* mission, corresponding to Fermi Mission Elapsed Time (MET) from 239557417 to 430608212 and calendar dates 4 August 2008 to 24 August 2014. In order to analyze the region around PKS 0637-752, we used the publicly available 'quickAnalysis' script. The public scripts mentioned here are available at http://fermi.gsfc.nasa.gov/ssc/data/analysis/user/. to run the *Fermi* analysis tools and generate the filtered event file, livetime cube, and exposure map, using a region of interest (ROI) of 10° and an otherwise default configuration. The starting source list was generated from the publicly available make2FGLxml script, which generates the xml file pre-populated with 2FGL catalog sources. We used a binned maximum Likelihood to get an initial fit for all the catalog sources in our ROI. We also included sources a further 5° out from our ROI, but always fixed to the catalog values. PKS 0637-752 was detected with a very high test-statistic (TS, roughly significance squared) value of 289, a 100 MeV to 100 GeV photon flux of 3.16×10^{-8} s^{-1} cm^{-2}, and a photon index $\Gamma_p = 2.64$, similar to the value reported in the 2FGL catalog.

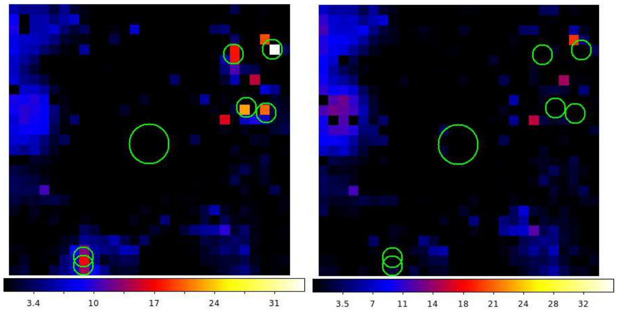

Figure 2: *Left:* An initial TS map of the region around PKS 0637-752, showing the excess TS present in 0.5° pixels over the best-fit likelihood model using 2FGL catalog sources. The large circle marks the position of PKS 0637−752. The smaller circles mark the positions of the six new sources not present in the 2FGL catalog (corresponding to regions of excess TS with pixel values >20). *Right:* The updated TS map (same FOV and binning) after the six sources were localized and fit with a binned likelihood.

Table I New sources in ROI of Targets

0637-752			3C 273		
RA_{2k} (deg)	Dec_{2k} (deg)	TS	RA (deg)	Dec (deg)	TS
82.43046	-72.74572	57.5	192.82676	-2.00263	70.7
81.13040	-69.60575	60.5	190.96827	-2.29561	82.3
78.98804	-72.72570	28.6	187.15935	-3.29476	60.2
86.33797	-70.34640	39.6	184.47577	-0.48239	92.5
119.70430	-80.70430	9.9	193.43690	3.47391	224.6
118.83300	-80.32970	16.1	192.63313	2.25116	65.7

We checked for additional significant sources within 7° of PKS 0637-752 but not in the 2-year LAT catalog by making a TS residual map. Rough starting positions of apparent new significant sources were measured from the TS map by hand, only considering as candidates those with a central pixel value (TS) > 20. Each new source was added to the XML model file as a powerlaw, and an initial spectral parameter fit derived via binned likelihood. We then refined the position of each source one at a time while the spectral parameters were held fixed. The existing tool, `gtfindsrc`, only works for unbinned likelihood analysis, so we built our own binned version of the tool which works in the same way. Using the frozen model, we used the python `minimize` function in the `scipy` package (L-BFGS-B method) to optimize the log-likelihood value versus the RA and Dec position, given a reasonable range of about 1 degree around the starting positions noted by hand. For the 7° ROI around PKS 0637-752, six new sources were added to the model, and an updated TS map run from this larger source list shows that the excess TS previously seen is now gone (right panel of Figure 2). A list of the new sources with their location and TS value is given at left in Table I.

PKS 0637-752 is a significant *Fermi* source, and was detected in the 2nd *Fermi* catalog, as 2FGL J0635.5-7516. Our approach to detecting and/or setting limits on the IC/CMB gamma-ray emission exploits the variability of the blazar core which cannot be spatially resolved separately from the large-scale jet due to the poor angular resolution of *Fermi.* During times when the blazar is quiescent, the hard, steady emission from IC/CMB will either appear as a steady plateau, or else the upper limits generated will place constraints on the level of the IC/CMB emission. In order to build a lightcurve of the core, the full 6-year dataset is divided into bins of equal good time interval (GTI) time, totalling 10.5 days. We then used our updated (2FGL + 6 new) model described above and ran a binned likelihood to fit PKS 0637-752 as a power-law source, with sources more than 5° away fixed. The resulting lightcurve for the core over the full time range is shown in Figure 3, with the 100 MeV - 100 GeV photon flux shown on top and the corresponding TS shown below. The clear variability in the light curve indicates that the total *Fermi* flux is dominated by the core.

We next began a 'progressive binning' analysis, in which the lightcurve bins were ordered from lowest to highest TS value. Of the entire set of 75 time bins, 27 showed a TS level consistent with zero for the location of PKS 0637-752 (upper limits in lower panel of Figure 3). Starting from these 27 bins combined, we progressively combine the event files for the lowest bins plus the next lowest bin in TS, at each step optimizing the fit of PKS 0637-752 and the sources within 5° with a binned likelihood. We repeated adding the next-highest bin and getting the maximum likelihood fit until all bins had been added together. Note that this re-combining of the lightcurve in a discontinuous way is appropriate for deriving a limit on the large-scale jet because the IC/CMB emission is predicted to be completely non-variable, and thus there is no risk of any selection effect via variability. The variable core clearly clearly dominates the flux levels determining the ordering, and is disconnected from the jet in any case. At each step we evaluated the TS and flux level in the five canonical *Fermi* energy bands of 0.1-0.3, 0.3-1, 1-3, 3-10 and 10-100 GeV, calculating the 95% upper limit flux value when TS<10 in any given bin. Previous work on 3C 273 has shown that the exact ordering of the bins (whether by using the TS value or the total flux or upper limit value for the bin) does not significantly affect the resulting upper limits (M14).

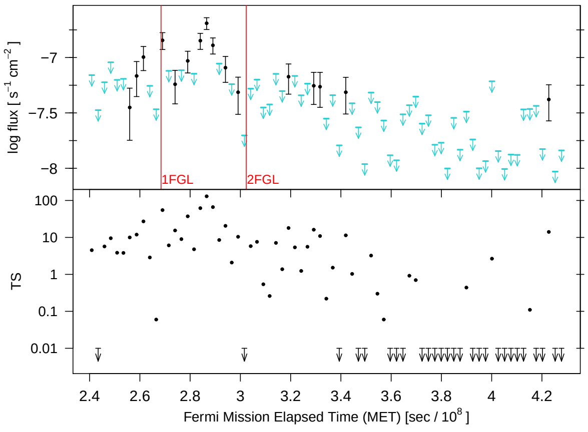

Figure 3: *Upper:* Lightcurve of PKS 0637-752. The total 100 MeV - 100 GeV photon flux for PKS 0637-752 in 10.5-day (total GTI) bins versus the mean Mission Elapsed Time (MET) of the bin. Upper limits are shown where TS<10. The red verticle lines show the end-time for the 1FGL and 2FGL catalogs. *Lower:* The TS value corresponding to the same bin as above.

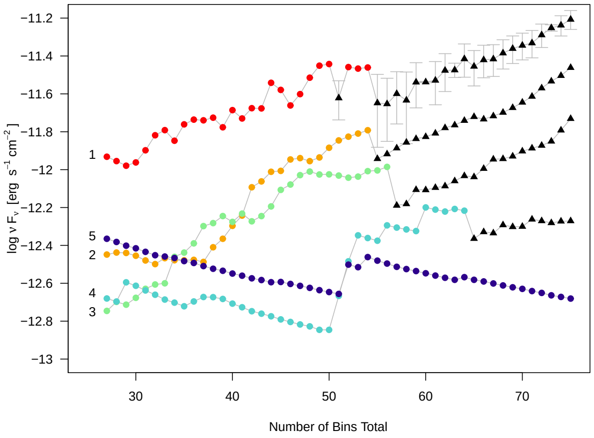

Figure 4: The results of the progressive binning analysis on PKS 0637-752. The upper axis gives the νF_ν flux while lower axis gives the total number of bins combined (where ordering is based on TS value and not time order), starting from the 27 bins with TS<0.01. The points give the upper limits (colored dots) or detected fluxes (TS>10, black triangles) for each of the five *Fermi* energy bands (red, orange, green, cyan, navy from lowest to highest energy). Errors on the detected fluxes are only shown for the lowest-energy bin for clarity but are similar across bins. For the highest-energy bin (10 - 100 GeV) no detection is ever made. The increasing fluxes indicate that the quasar core is being detected in the other bands.

As shown in Figure 4, the highest energy bands gave upper limits which decreased with the increasing exposure as more bins are added, where we have color-coded the upper limits in the 5 energy bands, and black triangles indicate a significant detection in the band. The decrease in upper limits sometimes going faster than $1/\sqrt{t}$ and 'jumpy' behavior is expected in the case of very low backgrounds and low count rates. Note that in the lower-energy bins, where the PKS 0637-752 quasar core dominates due to its soft spectrum, the upper limits reach a minimum rather quickly, and generally increase before becoming detections. It must be noted that the detected Fermi emission in these bands is from the quasar core, not the large-scale jet, based on the soft spectrum, and the fact that the emission level rises as more bins are added (showing that the source is indeed variable and that the bins are ordered by flux level). While the 4th energy band detected points do not rise as quickly as the first three, the flux level is far above the upper limit derived after 50 bins, so cannot be the steady emission of the large-scale jet, which must be below this limit. The highest bin never shows a significant detection of either component.

1.3. *Fermi* Analysis of 3C 273

We re-analyzed the *Fermi* data for 3C 273 using the 6-year dataset to compare with the results from M14 using 4.5 years of data, as the core remained relatively quiescient over the additional time elapsed. We followed the same procedure as outlined above for

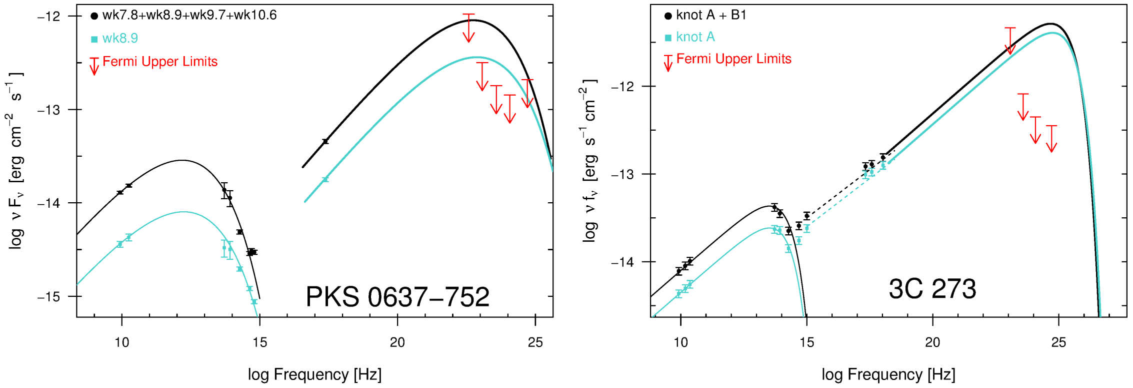

Figure 5: *Left:* The SED for the large-scale jet of PKS 0637-752. Data for the four brightest X-ray detected knots combined is shown as black points. The SED of the X-ray brightest knot, wk8.9, is plotted with blue points. *Right:* The SED for the knots of 3C 273, with black points for knots A and B1 combined, and blue for X-ray brightest knot A only. For both plots, the *Fermi* 95% upper limits are shown in red.

PKS 0637-752, finding six new sources within 7° of the position of 3C 273, listed at right in Table I. The core of 3C 273 was detected with a TS of 17504, with a 100 MeV - 100 GeV photon flux of 3.68×10^{-7} s^{-1} cm^{-2} and $\Gamma_p = 2.67$. A lightcurve was made using bins totaling 10.5 days in GTI time, and ordered according to TS (a total of 88 bins). The progressive-binning was started from the single lowest bin, with the next-highest bin continually added as described above until all bins were added. At each step the flux (or 95% upper limit) was calculated for the five canonincal *Fermi* energy bins.

2. Results: Testing the IC/CMB Model

We show in Figure 5 the radio to X-ray SEDs for the jet of both PKS 0637-752 (left) and 3C 273 (right). For PKS 0637-752 we have taken both the *Chandra* X-ray and Hubble Space Telescope (HST) infrared and optical data (NICMOS, WFPC2 and ACS) from Mehta et al. [2009]. We have also re-derived the *Spitzer* infrared fluxes for the brightest complex of knots (wk7.8, wk8.9, wk9.7, wk10.7), following the same methods reported in Uchiyama et al. [2005]. We have also measured updated radio fluxes based on a re-analysis of archival and new ATCA data at 4.8, 8.4, and 17.8 GHz. For 3C 273, data is taken from Jester et al. [2006, 2005] and Uchiyama et al. [2006] and references therein.

In both figures, we consider two scenarios: the first combines the photometry of the brightest/nearest knots to the core in order to test the IC/CMB prediction (black points and lines). In 3C 273, Jester et al. [2005] have already shown that only knots A and B1 have X-ray indices similar to their radio indices (which is required for IC/CMB), so our "combined knot" scenario includes only these two knots. For PKS 0637-752, we use all the bright X-ray knots just before the turn in the jet (wk7.8, wk8.9, wk9.7, and wk10.6) where one might assume that some deceleration likely takes place. The second scenario assumes that the X-rays from the weaker knots are already *not* from IC/CMB, and so only the photometry of the X-ray brightest knot is plotted (knot A in 3C 273 and wk8.9 in PKS 0637-752, plotted as blue points and lines). The thin solid lines through radio-optical points show a (phenomenological) synchrotron spectrum fitting the data, while the heavy line shows the corresponding IC/CMB curve to match the X-ray flux levels. As shown, for both jets, the 95% upper limits in several bands violate the IC/CMB predictions under either scenario.

We report in the upper part of Table II a summary of the *Fermi* data analysis for PKS 0637-752 and 3C 273. We list the definition of the energy bins in columns 2-5, followed by the deepest 95% upper limit flux level (in νF_ν) reached in our progressive binning for each energy bin in column 6. The corresponding number of bins co-added is given in column 7. In column 8 we list the flux predicted under the IC/CMB at the frequency given in column 5. This flux corresponds to the IC/CMB model prediction for the combination of knots wk7.8, wk8.9, wk9.7, and wk10.7 in PKS 0637-752, and knots A and B1 for 3C 273. In the former case, we do not include the only other X-ray detected not (wk5.7) because it is not consistently detected at other wavelengths. For 3C 273, only knots A and B1 have X-ray spectra consistent with their radio spectra, so the knots further downstream are assumed to be producing X-rays via synchrotron emission. In column 10, we have calculated at what significance level our observations rule out the level of predicted IC/CMB flux given in col-

Table II Results of the Fermi Data Analysis

Source	Band	E_1 (GeV)	E_2 (GeV)	log Freq. (Hz)	95% Limit (erg s^{-1} cm^{-2})	Bins Added	Combined Knots^{a}* $F_{\rm IC/CMB}$ (erg s^{-1} cm^{-2})	% Ruled Out	Single Knot^{b}† $F_{\rm IC/CMB}$ (erg s^{-1} cm^{-2})	% Ruled Out
(1)	(2)	(3)	(4)	(5)	(6)	(7)	(8)	(9)	(10)	(11)
0637-752	1	0.1	0.3	22.6	1.05×10^{-12}	29	9.0×10^{-13}	92.9	3.6×10^{-13}	...
	2	0.3	1	23.1	3.17×10^{-13}	32	8.8×10^{-13}	99.8	3.6×10^{-13}	94.5
	3	1	3	23.6	1.80×10^{-13}	27	7.4×10^{-13}	99.98	3.2×10^{-13}	98.7
	4	3	10	24.1	1.43×10^{-13}	50	5.3×10^{-13}	99.95	2.5×10^{-13}	98.6
	5	10	100	24.7	2.09×10^{-13}	75	2.3×10^{-13}	95.9	1.3×10^{-13}	...
3C 273	1	0.1	0.3	22.6	2.72×10^{-11}	1	2.1×10^{-12}	...	1.6×10^{-12}	...
	2	0.3	1	23.1	4.63×10^{-12}	2	2.8×10^{-12}	...	2.1×10^{-12}	...
	3	1	3	23.6	8.20×10^{-13}	5	3.6×10^{-12}	>99.99	2.8×10^{-12}	>99.99
	4	3	10	24.1	4.46×10^{-13}	31	4.5×10^{-12}	>99.99	3.5×10^{-12}	>99.99
	5	10	100	24.7	3.56×10^{-13}	30	5.2×10^{-12}	>99.99	4.1×10^{-12}	>99.99

umn 9. For the final two columns, we also give the predicted flux under IC/CMB and the significance-level that we can rule it out, but only for the X-ray brightest knot of each jet (wk8.9 and knot A, respectively). As shown, the IC/CMB model is ruled out at a $>$ 99.9% level for PKS 0637-752 and at $>$ 99.99% level for 3C 273.

3. Discussion

These two cases where the IC/CMB origin for the X-rays has been unambiguously ruled out join with that of PKS 1136-135, where high UV polarization has shown that the second component (UV to X-ray) must be synchrotron in origin, since significant polarization is not expected in the IC/CMB scenario [Cara et al. 2013]. we focus the rest of the paper on the implications for jet physics if the X-ray flux in quasar jets is synchrotron emission from a separate, high-energy electron population.

A synchrotron origin for the X-rays is not in conflict with any of the data in hand, and further, relaxes many of the 'uncomfortable' constraints of the IC/CMB model. Very small angles to the line of sight are not required, and the total jet power required is considerably less [Dermer and Atoyan 2004], as the electron energy distribution need not be extended to very low values. The main objection to a second component heretofore has simply been its unexplained nature; Schwartz et al. [2000] notes that there is no reason why a second population of high-energy electrons should be co-spatial with the first. However, this co-occurance of two very different electron populations, if the correct interpretation, is obviously a very important clue to the particle acceleration mechanism in large-scale jets, of which we still know little.

An interesting consequence follows for our accounting of the large-scale-jet contribution to various backgrounds, especially at TeV energies. Jet one-sidedness clearly indicates that the kpc-scale jets are at least mildly relativistic, and thus IC/CMB emission must occur at some level. Due to the very low background in the highest-energy *Fermi* bands, the flux limits reachable by *Fermi*'s sky-scanning mode of operation should allow us to eventually either detect this emission or put very strong limits on the factor of B/δ which characterizes the flow on the kpc scale. The current *Fermi* upper limits already constrain $\delta \lesssim 7.8$ for 3C 273 and $\delta \lesssim 6.5$ PKS 0637-752, under the assumption of equipartition magnetic fields, where we take $B\delta = 1.5\times10^{-5}$ G for PKS 0637-752 from Tavecchio et al. [2000] and $B\delta$=1.0×10^{-4} for 3C 273 from G06. These limits are already low enough to have interesting consequences for our understanding of the total radiative output of AGN jets on the kpc scale.

It is generally assumed that the radiative output of quasar jets is dominated by that occurring at the 'core', the base of the jet which is presumed to be very near the black hole (or $\sim$ parsecs away at most) and is therefore unresolved even in VLBI imaging. Certainly, the observed fluxes are dominated by this part of the jet due to Doppler beaming whenever the jet is pointed fairly along our line-of-sight. This is depicted in Figure 6, where the core points of both jets are shown as gray circles, and the jet photometry as gray triangles (flux scale on right axis). The luminosity scale at left applies to these points only under the incorrect assumption of isotropy. If we correct these values for beaming, we get the real 'angle-integrated' total power output from the core and the jet, plotted as a dark blue dashed line and the gray shaded area, respectively. VLBI observations of superluminal motions place a lower limit on Γ=15 for the cores of both 3C 273 and PKS 0637-752, respectively [Lister et al. 2013, Edwards et al. 2006]. We have applied a correction (multiplying by $1/\delta^2$) assuming δ=15 for the cores of both jets to give the angle-integrated core luminosity (dark blue dashed line). To calculate the angle-integrated luminosity of

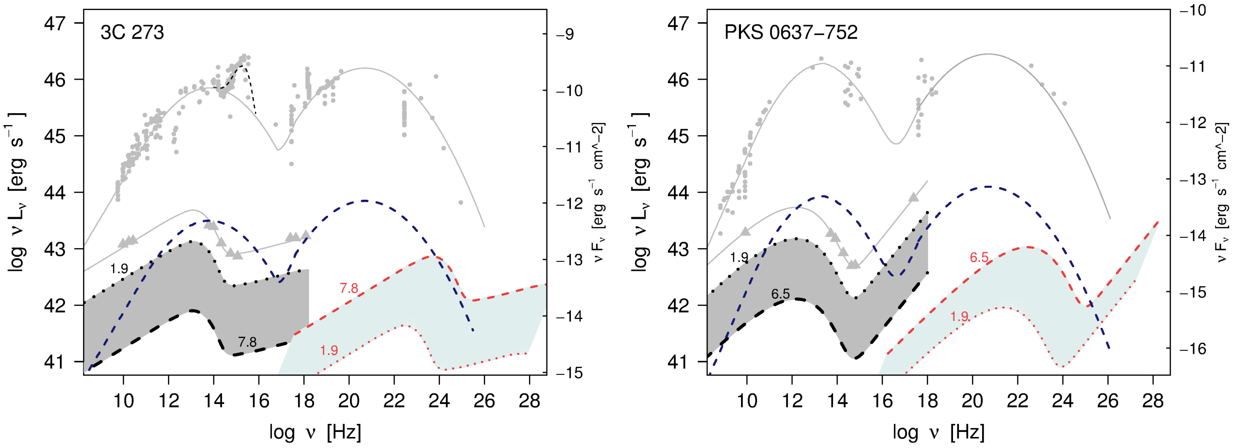

Figure 6: (Note: Figure description below applies to both panels; 3C 273 is shown at left and PKS 0637-752 is shown at right). The Core flux points are shown as gray circles with phenomenological SED fit through the points as a thin gray line (big blue bump shown as black dashed line and not included in the beamed emission fits). In comparison, the core points are shown as gray triangles. The flux scale at right only applies to solid curves in the figure. The impression of the total dominance of the core flux is mainly a product of the beaming difference between the two components, as seen when beaming-corrected (angle-integrated) luminosities are plotted, rather than those assuming isotropy. Blue dashed line is the core fit times $1/\delta^2$ with $\delta = 15$ for both jets. The gray zone is the range of possible beaming-corrected SEDs for the knots given our current constraints on δ for the knots. Finally, the light blue shaded area is the range of IC/CMB emission possible given the same δ constraints. Note that the TeV emission in particular is already constrained to be much higher than is typical for 'TeV blazars' ($\approx 10^{41}$ erg s^{-1}).

the knots, we apply a lower limit value of $\delta = 1.9$ which comes from statistical arguments based on populations [Arshakian and Longair 2004], which gives the dotted-line upper edge to the gray shaded area, while the current δ limits from *Fermi* give the lower dashed-line limit. The true angle-integrated luminosity of the knots is thus somewhere in the gray zone.

It is interesting to note that the knots are apparently *not* insignificant in total output when compared to the core. Definite conclusions will require tighter constraints on the δ factors of both the core and the knots, but it is possible that large-scale jets contribute more than the core in the UV to X-rays, in addition to their general dominance in the radio (which was already well known). Large-scale jets could thus be an important contributor to some astrophysical backgrounds.

A further observation follows from the realization that the X-rays are synchrotron in origin: the electrons producing the synchrotron X-rays will themselves upscatter the CMB to produce a GeV to TeV spectrum. The angle-integrated total power in the IC/CMB component is shown in Figure 6 as a light blue shaded area. Note that the bounds in this case are flipped; the upper δ limit forms the upper edge of the allowed zone. Even in the minimum δ=1.9 case, these jets are already constrained to produce fluxes in excess of 10^{41} erg s^{-1} which is the typical total radiative output for the canonical low-power FR I type 'TeV blazars'. We have not applied an EBL correction to these spectra merely to illustrate the total intrinsic output. However, EBL absorption is very important at TeV energies, and would make direct observation of this TeV component very difficult. Even assuming the most optimistic case of δ=7.8 for 3C 273, at redshift 0.158 the EBL absorption [Finke et al. 2010] is already high enough that it would take at least 100 hours of observations by the future CTA mission to detect the beamed IC/CMB component at TeV energies. Thus it is unlikely that many anomalous X-ray jets will have a synchrotron origin for the X-rays directly confirmed via TeV observations, though if *Fermi* begins detecting the IC/CMB component, an upturn at the highest energies might be visible in a few cases. The remaining best direct observation is via polarization – either in the UV, for those that show the second component emerging there, or with future X-ray polarimiters. Finally, we note that as long as *Fermi* continues to operate, the low background at the highest energies should allow continually improving constraints on the δ factors of large-scale jets.

Acknowledgments

Work supported by Fermi Grant NNX13AO88G.

References

D. A. Schwartz, H. L. Marshall, J. E. J. Lovell, B. G. Piner, S. J. Tingay, M. Birkinshaw, G. Chartas, M. Elvis, E. D. Feigelson, K. K. Ghosh, et al., ApJ **540**, L69 (2000), astro-ph/0005255.

G. Chartas, D. M. Worrall, M. Birkinshaw, M. Cresitello-Dittmar, W. Cui, K. K. Ghosh, D. E. Harris, E. J. Hooper, D. L. Jauncey, D.-W. Kim, et al., ApJ **542**, 655 (2000), astro-ph/0005227.

A. S. Wilson and Y. Yang, ApJ **568**, 133 (2002), astro-ph/0112097.

S. G. Jorstad, A. P. Marscher, M. L. Lister, A. M. Stirling, T. V. Cawthorne, W. K. Gear, J. L. Gómez, J. A. Stevens, P. S. Smith, J. R. Forster, et al., AJ **130**, 1418 (2005), astro-ph/0502501.

M. L. Lister, M. H. Cohen, D. C. Homan, M. Kadler, K. I. Kellermann, Y. Y. Kovalev, E. Ros, T. Savolainen, and J. A. Zensus, AJ **138**, 1874 (2009), 0909.5100.

T. G. Arshakian and M. S. Longair, MNRAS **351**, 727 (2004), astro-ph/0310503.

L. M. Mullin and M. J. Hardcastle, MNRAS **398**, 1989 (2009), 0906.2088.

F. Tavecchio, L. Maraschi, R. M. Sambruna, and C. M. Urry, ApJ **544**, L23 (2000), astro-ph/0007441.

A. Celotti, G. Ghisellini, and M. Chiaberge, MNRAS **321**, L1 (2001), astro-ph/0008021.

R. M. Sambruna, C. M. Urry, F. Tavecchio, L. Maraschi, R. Scarpa, G. Chartas, and T. Muxlow, ApJ **549**, L161 (2001), astro-ph/0101299.

R. M. Sambruna, L. Maraschi, F. Tavecchio, C. M. Urry, C. C. Cheung, G. Chartas, R. Scarpa, and J. K. Gambill, ApJ **571**, 206 (2002), astro-ph/0201412.

A. Siemiginowska, R. K. Smith, T. L. Aldcroft, D. A. Schwartz, F. Paerels, and A. O. Petric, ApJ **598**, L15 (2003), astro-ph/0310241.

R. M. Sambruna, J. K. Gambill, L. Maraschi, F. Tavecchio, R. Cerutti, C. C. Cheung, C. M. Urry, and G. Chartas, ApJ **608**, 698 (2004), astro-ph/0401475.

H. L. Marshall, D. A. Schwartz, J. E. J. Lovell, D. W. Murphy, D. M. Worrall, M. Birkinshaw, J. M. Gelbord, E. S. Perlman, and D. L. Jauncey, ApJS **156**, 13 (2005), astro-ph/0409566.

D. E. Harris and H. Krawczynski, ARA&A **44**, 463 (2006), astro-ph/0607228.

A. Siemiginowska, Ł. Stawarz, C. C. Cheung, D. E. Harris, M. Sikora, T. L. Aldcroft, and J. Bechtold, ApJ **657**, 145 (2007), astro-ph/0611406.

H. L. Marshall, J. M. Gelbord, D. A. Schwartz, D. W. Murphy, J. E. J. Lovell, D. M. Worrall, M. Birkinshaw, E. S. Perlman, L. Godfrey, and D. L. Jauncey, ApJS **193**, 15 (2011), 1101.5822.

P. Kharb, M. L. Lister, H. L. Marshall, and B. S. Hogan, ApJ **748**, 81 (2012), 1201.4178.

L. E. H. Godfrey, G. V. Bicknell, J. E. J. Lovell, D. L. Jauncey, J. Gelbord, D. A. Schwartz, E. S. Perlman, H. L. Marshall, M. Birkinshaw, D. M. Worrall, et al., ApJ **755**, 174 (2012), 1208.0069.

M. J. Hardcastle, MNRAS **366**, 1465 (2006), astro-ph/0511511.

C. D. Dermer and A. Atoyan, ApJ **611**, L9 (2004), astro-ph/0404139.

Y. Uchiyama, C. M. Urry, C. C. Cheung, S. Jester, J. Van Duyne, P. Coppi, R. M. Sambruna, T. Takahashi, F. Tavecchio, and L. Maraschi, ApJ **648**, 910 (2006), astro-ph/0605530.

S. Jester, D. E. Harris, H. L. Marshall, and K. Meisenheimer, ApJ **648**, 900 (2006), astro-ph/0605529.

D. E. Harris, A. E. Mossman, and R. C. Walker, ApJ **615**, 161 (2004), astro-ph/0407354.

J. Kataoka and Ł. Stawarz, ApJ **622**, 797 (2005), astro-ph/0411042.

M. Cara, E. S. Perlman, Y. Uchiyama, C. C. Cheung, P. S. Coppi, M. Georganopoulos, D. M. Worrall, M. Birkinshaw, W. B. Sparks, H. L. Marshall, et al., ApJ **773**, 186 (2013), 1305.2535.

M. Georganopoulos, E. S. Perlman, D. Kazanas, and J. McEnery, ApJ **653**, L5 (2006), astro-ph/0610847.

E. T. Meyer and M. Georganopoulos, ApJ **780**, L27 (2014), 1307.8421.

P. L. Nolan, A. A. Abdo, M. Ackermann, M. Ajello, A. Allafort, E. Antolini, W. B. Atwood, M. Axelsson, L. Baldini, J. Ballet, et al., ApJS **199**, 31 (2012), 1108.1435.

K. T. Mehta, M. Georganopoulos, E. S. Perlman, C. A. Padgett, and G. Chartas, ApJ **690**, 1706 (2009), 0809.1608.

Y. Uchiyama, C. M. Urry, J. Van Duyne, C. C. Cheung, R. M. Sambruna, T. Takahashi, F. Tavecchio, and L. Maraschi, ApJ **631**, L113 (2005), astro-ph/0508569.

S. Jester, H.-J. Röser, K. Meisenheimer, and R. Perley, A&A **431**, 477 (2005), astro-ph/0410520.

M. L. Lister, M. F. Aller, H. D. Aller, D. C. Homan, K. I. Kellermann, Y. Y. Kovalev, A. B. Pushkarev, J. L. Richards, E. Ros, and T. Savolainen, AJ **146**, 120 (2013), 1308.2713.

P. G. Edwards, B. G. Piner, S. J. Tingay, J. E. J. Lovell, J. Kataoka, R. Ojha, and Y. Murata, PASJ **58**, 233 (2006).

J. D. Finke, S. Razzaque, and C. D. Dermer, ApJ **712**, 238 (2010), 0905.1115.

Flaring γ-ray emission from high redshift blazars

M. Orienti, F. D'Ammando, M. Giroletti, D. Dallacasa, T. Venturi
INAF-IRA, via Gobetti 101, 40129 Bologna, Italy
J. Finke
US Naval Research Laboratory, Code 7653, 4555 Overlook Avenue SW, Washington, DC 20375-5352, USA
M. Ajello
Department of Physics and Astronomy, Clemson University, Clemson, SC 29634, USA

High redshift blazars are among the most powerful objects in the Universe. Although they represent a significant fraction of the extragalactic hard X-ray sky, they are not commonly detected in γ-rays. High redshift (z>2) objects represent <10% of the AGN population observed by *Fermi* so far, and γ-ray flaring activity from these sources is even more uncommon. The characterization of the radio-to-γ-ray properties of high redshift blazars represent a powerful tool for the study of both the energetics of such extreme objects and the Extragalactic Background Light. We present results of a multi-band campaign on TXS 0536+145, which is the highest redshift flaring γ-ray blazar detected so far. At the peak of the flare the source reached an apparent isotropic γ-ray luminosity of 6.6×10^{49} erg/s, which is comparable with the luminosity observed from the most powerful blazars. The physical properties derived from the multi-wavelength observations are then compared with those shown by the high redshift population. In addition preliminary results from the high redshift flaring blazar PKS 2149-306 will be discussed.

1. Introduction

The population of high redshift ($z > 2$) blazars represents a small fraction (<10%) of the extragalactic γ-ray sky. They are mainly associated with flat spectrum radio quasars (FSRQ), although a few BL Lacs with $z > 2$ are present in the third catalog of active galactic nuclei detected by the Large Area Telescope (LAT) on board the *Fermi* satellite after the first four years of scientific observations [6]. The number counts drop when higher energies are considered. In the first LAT catalog of γ-ray sources above 10 GeV (1FHL) only seven objects with $z > 2$ are detected [5].

Although the detection of high redshift blazars during a γ-ray flare is even more uncommon, the characterization of the radio-to-γ-ray properties of high redshift blazars represent a powerful tool for the study of both the energetics of such extreme objects and the Extragalactic Background Light (EBL). During γ-ray flaring episodes the spectra of FSRQ sometimes show a moderate hardening [17], allowing us to explore energies that are usually strongly attenuated due to the intrinsic source spectrum.

So far, 10 blazars at $z > 2$ have been detected during γ-ray flaring activity. Among these objects there are TXS 0536+145 at $z = 2.69$, and PKS 2149-306 at $z = 2.34$. TXS 0536+145 was not part of the *Fermi*-LAT first (1FGL) and second source (2FGL) catalogs [1, 14], indicating its low activity state during the first two years of *Fermi*-LAT observations. On 2012 March 22 it underwent a γ-ray flare, becoming the γ-ray flaring object at the highest redshift observed so far [16].

PKS 2149-306 was detected by *Fermi*-LAT in a flaring state on 2013 January 4 [9], with a daily γ-ray flux about 25 times higher than the average source flux reported in the 2FGL catalog [14].

The high activity states observed in both sources triggered multiwavelength monitoring observations aimed at characterizing the variability in the various bands of the electromagnetic spectrum and at determining the spectral energy distribution of these extreme objects.

2. TXS 0536+145

2.1. *Fermi*-LAT data

We analyzed *Fermi*-LAT data collected during the first five years of scientific observations, from 2008 August 4 (MJD 54682) to 2013 August 4 (MJD 56508). We considered an energy range between 0.1 and 100 GeV, and we followed the standard LAT analysis procedures (for more details see [16]).

TXS 0536+145 was not detected during the first two years of observations. The 2σ upper limit estimated over this period is 10^{-8} ph cm^{-2} s^{-1}. During the third and fourth years of observations, the source was detected with a flux of $(4.2 \pm 0.6)\times10^{-8}$ ph cm^{-2} s^{-1} and a photon index $\Gamma = 2.37\pm0.09$. On 2012 March 22 the source was observed during a γ-ray flare, when it reached a flux of $(1.0 \pm 0.3)\times10^{-6}$ ph cm^{-2} s^{-1} and a photon index $\Gamma = 2.05 \pm 0.08$, indicating a hardening of the spectrum. This flux corresponds to an apparent isotropic luminosity of 6.6×10^{49} erg/s. Before this flare, the source was first detected in γ-rays on 2012 January showing an enhancement of its high-energy activity, but without reaching a similar peak flux (Fig. 1).

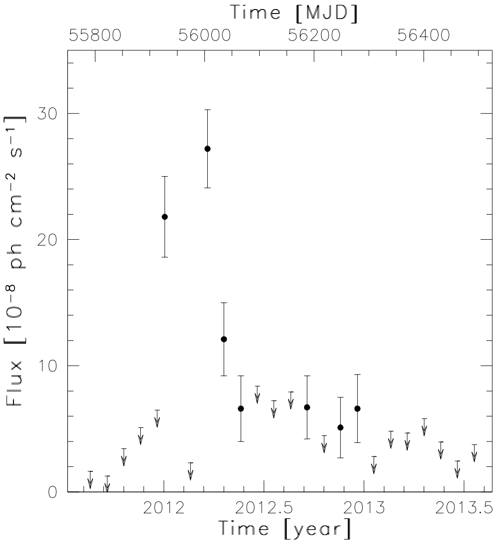

Figure 1: Integrated *Fermi*-LAT light curve (0.1-100 GeV) of TXS 0536+145 between 2011 August 4 and 2013 August 4 with 1-month time bins. Adapted from [16].

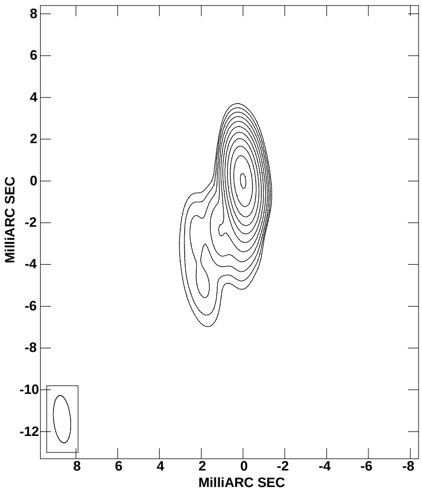

Figure 2: VLBA image at 8.4 GHz of the source TXS 0536+145. The peak flux density is 438.8 mJy/beam, while the first contour is 0.4 mJy/beam and corresponds to three times the off-source noise level measured on the image plane. The contours increase by a factor of 2. The restoring beam is plotted in the bottom-left corner. Adapted from [16].

The analysis of the *Fermi*-LAT data with E > 10 GeV collected between 2011 August and 2013 August could not detect the source at such high energies. We evaluated the 2σ upper limit as 9.3×10^{-11} ph cm^{-2}s^{-1} (assuming $\Gamma = 2.37$).

2.2. Radio properties

Monitoring campaigns of TXS 0536+145 with the Very Long Baseline Array (VLBA) at 8.4, 15, and 24 GHz, and with the European VLBI Network (EVN) at 22 GHz were triggered by the γ-ray flare with the aim of studying changes in the parsec-scale structure and the flux density variability related to the central region of the source. The observations were performed between 2012 April and 2013 October. The source has a core-jet structure (Fig. 2). The radio emission is dominated by the compact bright core component, which accounts for about 90 per cent of the total flux density at 8.4 GHz, and about 95 per cent at 15 and 24 GHz. The jet emerges from the main component with a position angle of about 180°, then at ~ 1.5 mas (i.e. ~ 12 pc) it slightly changes orientation to about 160° and extends to ~ 6 mas (i.e. ~ 48 pc).

The flux density variability is ascribed to the core region, while the jet is not variable. The radio light curves show a flux density increase about 2-3 months after the γ-ray flare, with longer delay occurring at lower frequencies. The spectral index of the core computed between 8.4 and 15 GHz shows a softening of the spectrum from $\alpha \sim -1.0$ just after the flare, to $\alpha \sim 0.1$[1] a few months later (upper panel of Fig. 3). The light curve at 15 GHz shows a possible double hump similar to that observed in γ-ray light curve (bottom panel of Fig. 3).

No new superluminal component was observed after the flare. This may be related to the high redshift of the target. In fact, only superluminal components with a speed higher than 35c would have been picked up during the 16-month monitoring campaign.

2.3. *Swift* data and SED

Triggered by the flaring activity, *Swift* observed TXS 0536+145 a few days after the 2012 March γ-ray flare, and the source was found in a high state in X-rays. The X-ray flux decreases of a factor of two a couple of weeks after the peak. An additional observation was carried out a few months later, when the source was in a similar low activity state. In the past, the source was not detected by the ROSAT all-sky survey. Therefore, this is the first detection of TXS 0535+145 in X-rays.

Due to severe Galactic absorption and the short exposures, the source was not detected by UVOT in

---

[1] The radio spectral index is defined as $S_\nu \propto \nu^{-\alpha}$

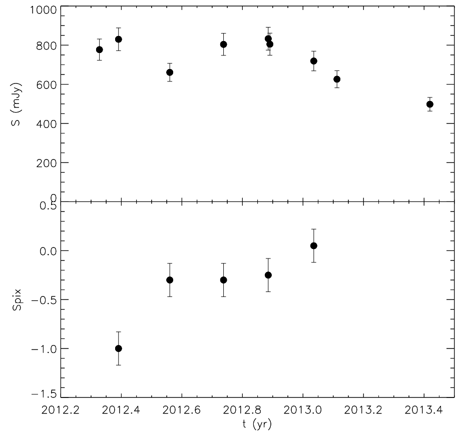

Figure 3: Light curve at 15 GHz (*top*) and the spectral index computed between 8.4 and 15 GHz (*bottom*) for TXS 0536+145. Adapted from [16].

any filter.
The hard X-ray flux of this source turned out to be below the sensitivity of the BAT instrument for such short exposures, and therefore the source was not detected. The source was not present in the *Swift* BAT 70-month hard X-ray catalogue [8].
The spectral energy distribution (SED) of TXS 0536+145 in flaring activity is well fitted by a synchrotron/external Compton model where the seed photons upscattered to high energies may be those from the dusty torus (see e.g., [16]). Due to the rather poor optical coverage, the model parameter are not well constrained.

3. PKS 2149-306

The FSRQ PKS 2149-306 was observed by *Fermi*-LAT during a flaring episode on 2013 January 4 and preliminary results were reported in [9]. This source was part of the 2LAC [4], indicating on average a higher level of γ-ray activity with respect to TXS 0536+145.
We analyzed *Fermi*-LAT data collected during the first six years of scientific observations, from 2008 August 4 (MJD 54682) to 2014 August 4 (MJD 56873). As in the case of TXS 0536+145, we considered an energy range between 0.1 and 100 GeV, and we followed the standard LAT analysis procedures.
The source was clearly detected by *Fermi*-LAT for most of the period with one-month integration time (Fig. 4). A first significant increase of activity was observed in 2011 February. During the strong flaring activity observed in 2013 January, the source reached a daily peak flux of $(3.0\pm0.4)\times10^{-6}$ ph cm^{-2} s^{-1}, and showed a hardening of the spectrum. This value corresponds to an apparent peak luminosity of 1.5×10^{50} erg/s. A dedicated multiwavelength analysis of PKS 2149-306 is ongoing aiming at studying the high-energy SED, also in perspective of the next generation of high-energy telescopes.

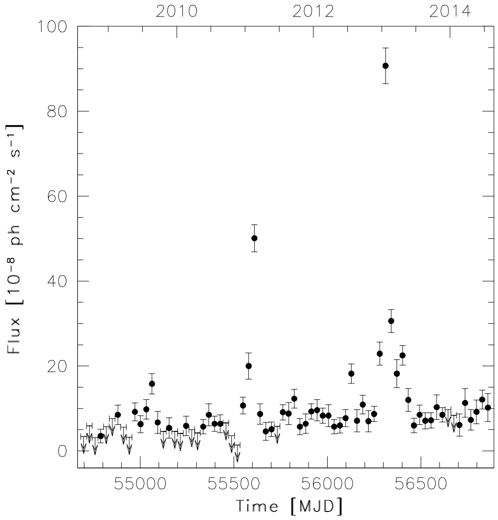

Figure 4: Integrated *Fermi*-LAT light curve (0.1-100 GeV) of PKS 2149-306 between 2011 August 4 and 2013 August 4 with 1-month time bins. Adapted from [10].

4. Discussion and conclusions

High redshift flaring blazars are among the most luminous objects in the Universe. The high redshift FSRQ TXS 0536+145 and PKS 2149-306 underwent a huge γ-ray flare, reaching an apparent isotropic luminosity (0.1-100 GeV) of 6.6×10^{49} erg/s and 1.5×10^{50} erg/s, respectively. Such values are comparable to the luminosity observed in the high-redshift gravitationally lensed blazar PKS 1830-211 detected during a flare ($L_\gamma \sim 3\times10^{49}$ erg/s; [3]), as well as in the brightest flaring blazars, like 3C 454.3 ($L_\gamma \sim 2\times10^{50}$ erg/s; [2]), PKS 1510-089 ($L_\gamma \sim 4\times10^{48}$ erg/s; [15]), and PKS 1622-297 ($L_\gamma \sim 4\times10^{48}$ erg/s; [13]).
We compared the γ-ray properties of TXS 0536+145 and PKS 2149-306 with those shown by the population of high redshift ($z > 2$) γ-ray sources from the 2LAC [4]. The photon index and the luminosity in the low activity state of the targets are in agreement with those of the other high-z objects. During the flaring state both sources showed a hardening of the spectrum. A similar behaviour was observed in the high-z flaring blazar 4C+71.07 [7].
Despite the harder spectrum, no significant emission

above 10 GeV is observed for TXS 0536+145. Although this value is consistent with current EBL models (e.g. [12]), the low statistics do not allow us to attribute the spectral curvature to this effect [16]. The improved sensitivity of the LAT at a few GeV with Pass 8 data will be important for characterizing in more detail the γ-ray spectrum of the high-redshift blazar population.

Acknowledgments

The *Fermi* LAT Collaboration acknowledges generous ongoing support from a number of agencies and institutes that have supported both the development and the operation of the LAT as well as scientific data analysis. These include the National Aeronautics and Space Administration and the Department of Energy in the United States, the Commissariat à l'Energie Atomique and the Centre National de la Recherche Scientifique / Institut National de Physique Nucléaire et de Physique des Particules in France, the Agenzia Spaziale Italiana and the Istituto Nazionale di Fisica Nucleare in Italy, the Ministry of Education, Culture, Sports, Science and Technology (MEXT), High Energy Accelerator Research Organization (KEK) and Japan Aerospace Exploration Agency (JAXA) in Japan, and the K. A. Wallenberg Foundation, the Swedish Research Council and the Swedish National Space Board in Sweden. Additional support for science analysis during the operations phase is gratefully acknowledged from the Istituto Nazionale di Astrofisica in Italy and the Centre National d'Études Spatiales in France. The VLBA is operated by the US National Radio Astronomy Observatory which is a facility of the National Science Foundation operated under a cooperative agreement by Associated Universities, Inc. The European VLBI Network is a joint facility of European, Chinese, South African, and other radio astronomy institutes funded by their national research councils.

References

[1] Abdo, A.A., et al. 2010b, ApJS, 188, 405
[2] Abdo, A.A., et al. 2011, ApJ, 733, 26
[3] Abdo, A.A., et al. 2015, ApJ, 799, 143
[4] Ackermann, M., et al. 2011, ApJ, 743, 171
[5] Ackermann, M., et al. 2013, ApJS, 209, 34
[6] Ackermann, M., et al. 2015, ApJS submitted (arXiv:1501.06054)
[7] Akyuz, A., et al. 2013, A&A, 556, 71
[8] Baumgartner W.H., et al. 2013, ApJS, 207, 19
[9] D'Ammando, F., Orienti, M. 2013, ATel, 4706
[10] D'Ammando, F., et al. 2015, MNRAS, in preparation
[11] Finke, J.D., Dermer C.D., Böttcher, M. 2008, ApJ, 686, 181
[12] Finke, J.D., Razzaque, S., Dermer C.D. 2010, ApJ, 712, 238
[13] Mattox J.R., et al. 1996, ApJ, 461, 396
[14] Nolan, P., et al. 2012, ApJS, 199, 31
[15] Orienti, M., et al. 2013, MNRAS, 428, 2418
[16] Orienti, M., et al. 2014, MNRAS, 444, 3040
[17] Pacciani, L., et al. 2014, ApJ, 790, 45

Fermi-LAT Upper Limit for NGC 4151 and its Implications for Physics of Hot Accretion Flow

R. Wojaczyński, A. Niedźwiecki
Department of Astrophysics, University of Łódź, Pomorska 149/153, 90-236 Łódź, Poland
F.-G. Xie
Key Laboratory for Research in Galaxies and Cosmology, Shanghai Astronomical Observatory, Chinese Academy of Sciences, 80 Nandan Road, Shanghai 200030, China

We present preliminary results of our analysis of the *Fermi*-LAT data from the direction of NGC 4151. We find a new γ-ray source with a statistical significance $\sigma > 5$, shifted by 0.5° from the position of NGC 4151. Apparently, the source was bright only during a 1.5-year period between December 2011 and June 2013 and it strongly contaminated the signal from NGC 4151. Therefore, we neglect this period in our analysis. We find two additional, persistent γ-ray sources with high σ, shifted from NGC 4151 by $\sim 1.5°$ and 5°, whose presence has been recently confirmed in the Third Fermi Catalog. After subtracting the above sources, we still see a weak residual, with $\sigma \lesssim 3$, at the position of NGC 4151. We derive an upper limit (UL) for the γ-ray flux from NGC 4151 and we compare it with predictions of the ADAF model which can explain the X-ray observations of this object. We find that the *Fermi* UL strongly constrains non-thermal acceleration processes in hot flows as well as the values of some crucial parameters. Here we present the comparison with the hot flow models in which heating of electrons is dominated by Coulomb interactions with hot protons. In such a version of the model, the γ-ray UL, combined with the X-ray data, constrains the energy content in the non-thermal component of proton distribution to at most a few per cent, rules out a weak (sub-equipartition) magnetic field and favors a rapid rotation of the supermassive black hole.

1. INTRODUCTION

Low-luminosity AGNs, with the luminosities below $\sim 0.01 L_{\rm Edd}$, are likely to be powered by optically thin, hot accretion flows (a.k.a. ADAFs, see e.g. [12]). The two-temperature structure is a key property of ADAFs, as such flows are supported by the proton pressure. In their innermost parts, the hot protons have energies above the threshold for pion production. As estimated e.g. in [6,8], the decay of pions leads to substantial fluxes of γ-rays, which may be probed in nearby AGNs at the current sensitivity of *Fermi*-LAT surveys. The *Fermi*-LAT data for radio-quiet AGNs were analyzed in [10] (two years of data) and [2] (three years) and the derived upper limits are already quite stringent compared to expectation. In [11]we revisit the issue of searching the signatures of hadronic emission from hot flows and the related implications for hot-flow models. We perform the detailed analysis of nearby, low-luminosity Seyfert galaxies using over 6 years of *Fermi*-LAT data and we compare the results with the model predictions for a complete range of the model parameters. In this contribution we report our preliminary results for one of the best-studied AGNs, NGC 4151.

NGC 4151 is one the X-ray brightest AGNs, with the bolometric $L \sim 0.01 L_{\rm Edd}$, showing no signatures of a relativistically distorted reflection component (constraints on the width of Fe Kα line imply the lack of an optically thick material within at least the innermost $\sim 100 R_{\rm g}$) as well as showing a spectral similarity to black hole binaries in their hard states (also most likely powered by hot flows), see e.g. [4]. All these properties make it a relevant objects for testing the hot flow scenario. Below we use the black hole mass $M = 3.8 \times 10^7 M_\odot$ from the stellar dynamical mass measurement [9].

2. LAT DATA ANALYSIS

We analyzed the data from the direction of NGC 4151, comprising 6.4 years of Fermi-LAT observations carried out between 2008 August 4 and 2015 January 10. Events we selected from a region with the radius of 10° centered on the position of NGC 4151. We performed the unbinned likelihood analysis using the v9r33p0 *Fermi* Science Tools with CALDB instrument response functions. We used the standard templates for the Galactic (`gll_iem_v05_rev1.fits`) and the isotropic (`iso_source_v05_rev1.txt`) backgrounds. In our initial model of the region we took into account only the sources from the Second Fermi Catalog (2FGL) [7], i.e. our model included the same sources as those used in [2]. 2FGL J1209.6+4121 (marked by the red circle in Fig. 1a) is the 2FGL source closest to NGC 4151, with the distance of $\simeq 2°$.

Fig. 1a shows the TS map of the region, built after subtracting the 2FGL sources. The map reveals residual structures indicating the presence of additional point-like sources, marked by the green circles. For each of these objects we use the `gtlike` and `gtfindsrc` tools to find its significance, best-fit position and spectral parameters; the results are given in Table I. Sources S1 (beyond the map in Fig. 1) and S3 have been recently reported in 3FGL [1], with parameters very similar to these estimated in our analysis. S2 is not reported in 3FGL, however, this source is

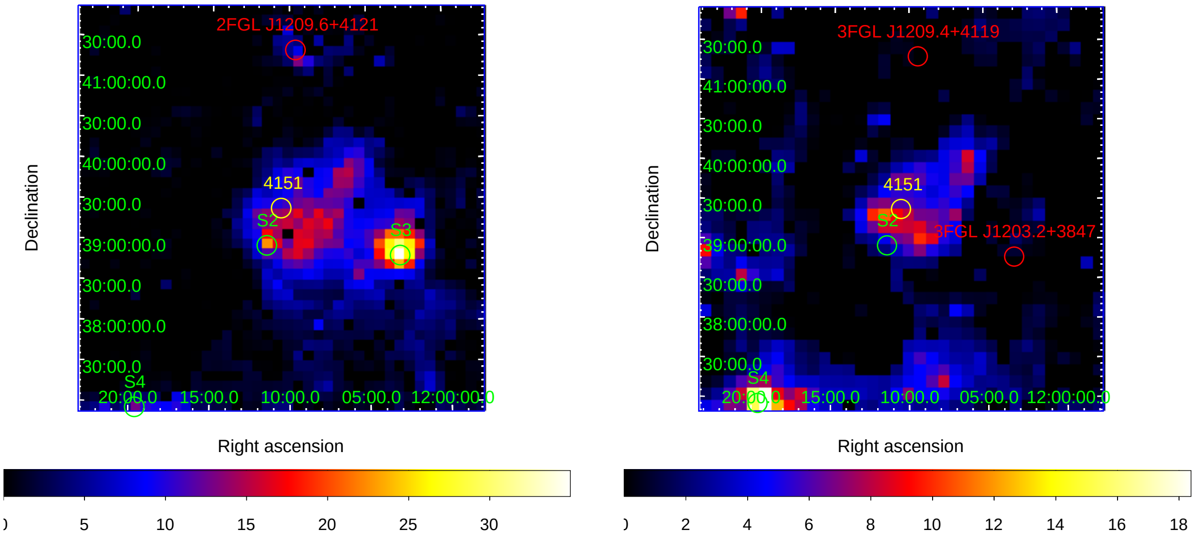

Figure 1: Test-statistic maps of the 5° × 5° region around the position of NGC 4151 (yellow circle) with the pixel size of 0.125° (left) and 0.15° (right). The left map was generated from the data from the total 6.4 years and only the sources from 2FGL were subtracted from this map (the only 2FGL source in this region of the sky is marked by the red circle); the green circles indicate new sources revealed in our analysis. The right map was generated from the data taken before December 2011 and after June 2013 and the sources from 3FGL (red circles) were subtracted from this map.

Table I New sources introduced in the model of the region around NGC 4151, not reported in 2FGL. (1) Source (see Fig. 1), (2) 3FGL name, (3) `gtlike` TS values, (4) and (5) `gtfindsrc` coordinates. Results for S2 were obtained using the data taken between December 2011 and June 2013; for the remaining sources the total data set for 6.4 years was used.

(1)	(2) 3FGL name	(3) TS	(4) RA	(5) DEC
S1	3FGL J1220.2+3434	191	185.06	34.57
S2	not reported	30	182.86	38.95
S3	3FGL J1203.2+3847	32	180.81	38.79
S4	not reported	22	184.90	36.93

critical for the analysis of a signal from NGC 4151, as its distance of $\sim 0.5°$ is comparable (or smaller below ~ 1 GeV) to the LAT point spread function. Therefore, we check properties of this source in more details.

By using `gtsrcprob` we find that the position of S2 is determined mostly by 4 photons with energies between 10 and 20 GeV which arrived from the same direction (within 10 arcmin) between December 2011 and June 2013. At lower energies, neglecting the four events with $E > 10$ GeV, we also see the signature of increased activity of S2 during that period, in the form of an extended residual covering the nominal positions of NGC 4151 and S2.

In the TS map built for the data neglecting the above period (see Fig. 1b) we do not see a strong signal at the S2 position, we therefore conclude that S2 strongly dominated the emission from the region around NGC 4151 only during the 1.5 year out of the total 6.4 considered years. Note that S2 is not reported in 3FGL which includes sources detected with $TS > 25$ using the data taken during the four years up to 2012 July (i.e. covering only $\sim 30\%$ of the time of the increased activity of S2).

For our further analysis we neglect the data taken during the 1.5 year when S2 was bright. We subtract the sources reported in 3FGL and we get the TS map shown Fig. 1b. The map shows a weak residual, which can be fully compensated for by adding the source at the nominal position of NGC 4151 and `gtlike` gives $TS \simeq 8$ for such a source. At its very low statistical significance, it is not possible to assess whether it represents a background fluctuation or an actual emission from the studied object; it may also contain some contribution from emission of S2 in its lower luminosity states.

We then derive the 95% confidence level upper limit (UL) for the integrated photon flux from NGC 4151 neglecting the data between December 2011 and June 2013. The pion decay spectra can be approximated by a simple power-law only in limited energy ranges (see Fig. 2 below), therefore, we assume relevant values of the photon index, Γ, and find the UL in the 0.3–1 GeV range to compare with the π^0-decay spectra for the thermal distribution of protons, and in the 1–10 GeV to compare with the model assuming a power-law distribution of protons. The results are given in

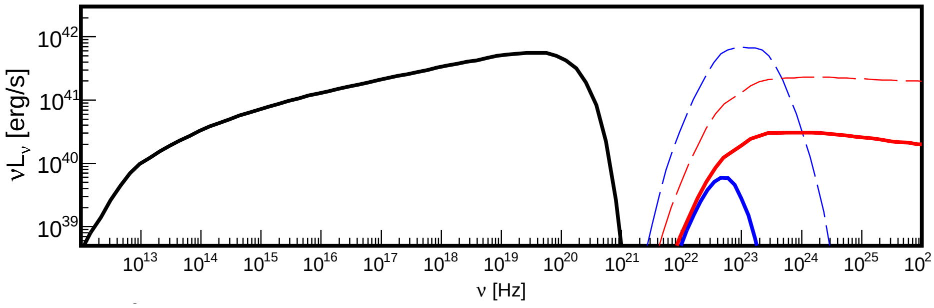

Figure 2: Spectra received by a distant observer from a hot flow around the black hole with $M = 4 \times 10^7 M_\odot$ for $a = 0.95$, $\beta = 9$, $\delta = 10^{-3}$ and $\dot{m} = 0.3$. The black solid line shows the component formed by the cooling of electrons (mostly thermal Comptonization). The blue and red solid lines show the component formed by π^0-decay for thermal and power-law (with $s = 2.1$) distribution of protons, respectively; the thin dashed lines show the corresponding spectra of the hadronic component in the rest frame of the flow (the spectra shown by solid lines are affected by the GR transfer and $\gamma\gamma$ absorption).

Table II 95% C.L. upper limits for the photon flux (3) and γ-ray luminosity (4) for the energy ranges given in column (1) and the assumed value of γ given in column(2).

(1) Energy range [GeV]	(2) Photon index	(3) UL: F [phot/cm^2/s]	(4) UL: L_γ [erg/s]
0.3 - 1	4	6×10^{-10}	6.5×10^{39}
1 - 10	2.1	1.5×10^{-10}	3.1×10^{39}
1 - 10	2.7	1.3×10^{-10}	1.9×10^{39}

Table II.

3. GAMMA-RAY EMISSION FROM HOT FLOWS AND COMPARISON WITH NGC 4151

In [5,6] we present a precise model for emission from hot flows, taking into account the relevant leptonic and hadronic processes, and using (1) a fully general relativistic (GR) description of both the radiative and hydrodynamic processes; (2) an exact, Monte Carlo computation of global Comptonization; (3) seed photons input from nonthermal synchrotron emission of $\pi^{\pm}$-decay electrons; (4) an exact computation of the absorption of γ-ray photons in the radiation field of the flow. The model is parametrized by: the black hole mass, M, the dimensionless accretion rate, $\dot{m} = \dot{M}c^2/L_{\rm Edd}$, the ratio of gas to magnetic pressure, β, the fraction of the dissipated energy which heats directly electrons through MHD processes, δ, and the spin parameter, $a = J/(cR_{\rm g}M)$, where J is the black hole angular momentum and $R_{\rm g} = GM/c^2$. We take into account models with thermal and with power-law distrubutions of protons; in the latter the power-law index, s, is also a free parameter.

Here we focus on models with small δ, i.e. with electrons heated by Coulomb interactions. We briefly summarize properties crucial for our final conclusions; Fig. 2 shows example spectra of radiation produced in a hot flow by thermal Comptonization and by π^0 decay.

(i) The nonthermal synchrotron radiation from $\pi^{\pm}$-decay electrons gives the dominating input of seed photons for Comptonization and it allows to reconcile the hot-flow model with the AGN X-ray data. It also provides an attractive explanation of spectral differences between AGNs and black-hole transients within the same physical model, see [5].

(ii) For bolometric $L \sim (0.001 - 0.01)L_{\rm Edd}$, the size of the γ-ray photosphere (inside which the flow is opaque to γ-rays) equals several $R_{\rm g}$. As a result, for models assuming thermal protons, the γ-ray flux detected by a distant observer is reduced by several orders of magnitude, because the γ-rays are produced mostly inside the photosphere. We note that [8] assessed comparable X-ray and γ-ray fluxes from flows surrounding rapidly rotating black holes. However, they neglected the GR transfer and $\gamma\gamma$ absorption; taking into account these effects we get, for thermal protons, the γ-ray fluxes smaller by ~ 3 (large β) to ~ 5 (small β) orders of magnitude than the X-ray flux.

(iii) In models assuming a thermal distribution of protons, the γ-ray flux is extremely sensitive to the value of β. In flows with smaller β (larger B), a larger fraction of the accretion power is used to build up the magnetic field strength; therefore, the energy heating the particles, and hence the proton temperature, is smaller. As for thermal protons the γ-ray luminosity, L_γ, is extremely sensitive to the proton temperature, the above effect leads to the difference by $2 - 3$ orders of magnitude between L_γ for a strong (in equipartition with gas) and weak magnetic field.

(iv) The proton temperature increases with a and hence the γ-ray emissivities strongly depends on a for thermal protons. However, the largest difference be-

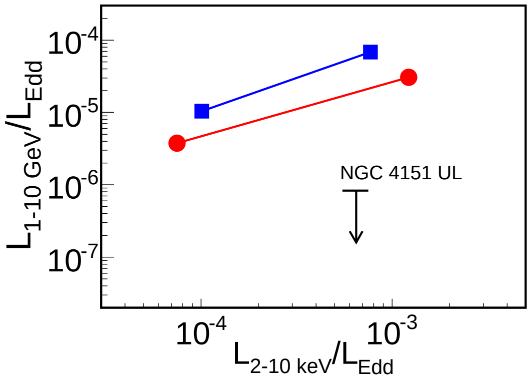

Figure 3: The γ-ray (1–10 GeV) luminosity Eddington ratio as a function of the X-ray (2–10 ken) luminosity Eddington ratio. The squares and circles show the hot flow model predictions for the *nonthermal proton distribution* with $s = 2.1$. The *Fermi* UL was obtained for the assumed $\Gamma = 2.1$ in the 1–10 GeV range (see Table 2) and the average X-ray luminosity was estimated from the *Swift*-BAT data. The red circles are for $a = 0.998$, $\beta = 1$, $\dot{m} = 0.1$ and 0.3; the blue squares are for $a = 0.95$, $\beta = 9$, $\dot{m} = 0.3$ and 0.8.

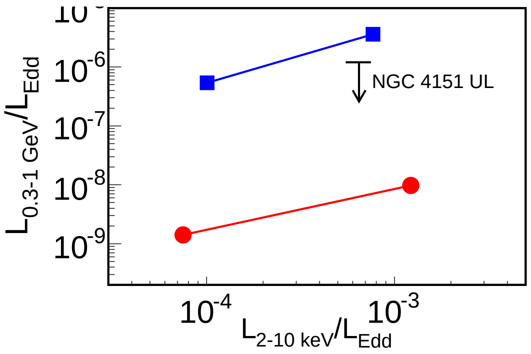

Figure 4: The same as in Fig. 3 but the model points are for the *thermal* distribution of protons and the γ-ray Eddington ratio is determined for the 0.3–1 GeV range; $\Gamma = 4$ was assumed for the *Fermi* UL.

tween the emissivities occurs within the photosphere and, therefore, the dependence of the observed L_γ on a is reduced by $\gamma\gamma$ absorption. On the other hand, a sufficiently strong input of seed photons from the emission of $\pi^{\pm}$-decay electrons requires either a rapid rotation of the black hole or a significant content of nonthermal protons.

Using the publicly available *Swift*-BAT data [3] we find the average X-ray luminosity of NGC 4151 between 2009 and 2014 (we find that it corresponds to the intermediate state as defined in [4]), which then allows us to compare the L_γ predicted by the model with the *Fermi* UL. The results are shown in Figs 3 and 4. For the power-law distribution of protons (Fig. 3) the UL is over an order of magnitude lower than the model prediction, which constrains the energy content in the nonthermal component of the proton distribution to at most a few per cent.

For the thermal distribution of protons (Fig. 4), the *Fermi* UL is sufficiently low to exlude models with large β, which, taking into account the above, rules out any version of the model with a weak magnetic field. For an equipartition value of $\beta \sim 1$ the predicted flux is below the UL value.

Then, the *Fermi* data favor a strongly magnetized plasma with a weak content of nonthermal protons. For such a case, a high spin value is required for a sufficiently strong flux of seed photons from nonthermal emission of pion-decay electrons.

4. SUMMARY

We thoroughly analyzed the γ-ray data from a region around NGC 4151, which led us to identification of new γ-ray sources. After subtracting their contribution, we get a weak residual signal at the position of NGC 4151. At its low statistical significance, $\sigma \lesssim 3$, it is not possible to assess its nature.

Comparison of the derived upper limits with the model predictions allows to constrain several crucial quantities which illustrates the potential of *Fermi* measurements in probing the properties of flows powering AGNs at low luminosities.

Acknowledgments

This research has been supported in part by the Polish NCN grant DEC-2011/03/B/ST9/03459. We made use of data and software provided by the Fermi Science Support Center, managed by the HEASARC at the Goddard Space Flight Center, and Swift/BAT transient monitor results provided by the Swift/BAT team.

References

1. Acero F., et al. 2015, ApJSS, submitted
2. Ackermann M., et al. 2012, ApJ, 747, 104
3. Krimm H. A., et al. 2013, ApJSS 209, 14.
4. Lubiński P., Zdziarski A. A., Walter R., Paltani S., Beckmann V., Soldi S., Ferrigno C., Courvoisier T. J.-L. 2010, MNRAS, 408, 1851
5. Niedźwiecki A., Stępnik A., Xie F.-G. 2015, ApJ, 799, 217
6. Niedźwiecki A., Xie F.-G., Stępnik A. 2013, MNRAS, 432, 1576
7. Nolan P. L., et al. 2012, ApJSS, 199, 31

8. Oka K., Manmoto T. 2003, MNRAS, 340, 543
9. Onken C. A., et al. 2014, ApJ, 791, 37
10. Teng S. H., Mushotzky R. F., Sambruna R. M., Davis D. S., Reynolds C. S. 2011, ApJ, 742, 66
11. Wojaczyński R., et al. 2015, in preparation
12. Yuan F., & Narayan R. 2014, ARAA, 52, 529

A panchromatic view of relativistic jets in γ-ray emitting narrow-line Seyfert 1 galaxies

F. D'Ammando[1,2], M. Orienti[1], J. Finke[3], M. Giroletti[1], J. Larsson[4], on behalf of the *Fermi* Large Area Telescope Collaboration
[1]*INAF - Istituto di Radioastronomia, Via Gobetti 101, I-40129 Bologna, Italy*
[2]*Dip. di Fisica e Astronomia, Universitá di Bologna, Viale Berti Pichat 6/2, I-40127 Bologna, Italy*
[3]*U.S. Naval Research Laboratory, 4555 Overlook Ave. SW, Washington, DC 20375-5352, USA and*
[4]*KTH, Dep. of Physics, and the Oskar Klein Centre, AlbaNova, SE-106 91 Stockholm, Sweden*

Before the launch of the *Fermi* satellite only two classes of Active Galactic Nuclei (AGN) were known to generate relativistic jets and thus to emit up to the γ-ray energy range: blazars and radio galaxies, both hosted in giant elliptical galaxies. The first four years of observations by the Large Area Telescope (LAT) on board *Fermi* confirmed that these two populations represent the most numerous identified sources in the extragalactic γ-ray sky, but the discovery of variable γ-ray emission from 5 radio-loud Narrow-Line Seyfert 1 (NLSy1) galaxies revealed the presence of a possible emerging third class of AGN with relativistic jets. Considering that NLSy1 are thought to be hosted in spiral galaxies, this finding poses intriguing questions about the nature of these objects, the knowledge of the development of relativistic jets, and the evolution of radio-loud AGN. In this context, the study of the radio-loud NLSy1 from radio to γ-rays has received increasing attention. Here we discuss the radio-to-γ-rays properties of the γ-ray emitting NLSy1, also in comparison with the blazar scenario.

1. Introduction

Relativistic jets are the most extreme expression of the power that can be generated by a superluminal black hole (SMBH) in the center of an active galactic nucleus (AGN), with a large fraction of the power emitted in γ-rays. Before the launch of the *Fermi* satellite only two classes of AGN were known to generate these structures and thus to emit up to the γ-ray band: blazars and radio galaxies, both hosted in giant elliptical galaxies [11]. The first 4 years of observation by the Large Area Telescope (LAT) on board *Fermi* confirmed that the extragalactic γ-ray sky is dominated by radio-loud AGN, being mostly blazars and some radio galaxies [4]. However, the discovery by *Fermi*-LAT of variable γ-ray emission from a few radio-loud narrow-line Seyfert 1 (NLSy1) galaxies revealed the presence of a possible third class of AGN with relativistic jets [1].

NLSy1 are a class of AGN identified by [43] and characterized by their optical properties: narrow permitted lines (FWHM (Hβ) < 2000 km s^{-1}), [OIII]/Hβ < 3, and a bump due to Fe II (e.g., [44]). They also exhibit strong X-ray variability, steep X-ray spectra, relatively high luminosity, and substantial soft X-ray excess (e.g., [31]). These characteristics point to systems with smaller masses of the central black hole (10^6–10^8 M$_\odot$) than blazars and radio galaxies, and higher accretion rates (close to or above the Eddington limit). NLSy1 are generally radio-quiet (radio-loudness $R < 10$), with only a small fraction ($< 7\%$; [34]) classified as radio-loud. Objects with high values of radio-loudness ($R > 100$) are even more sparse ($\sim$2.5%), while generally $\sim$15% of quasars are radio-loud. Considering also that NLSy1 are thought to be hosted in spiral galaxies, their detection in γ-rays poses intriguing questions about the nature of these sources, the production of relativistic jets, the mechanisms of high-energy emission, and the cosmological evolution of radio-loud AGN.

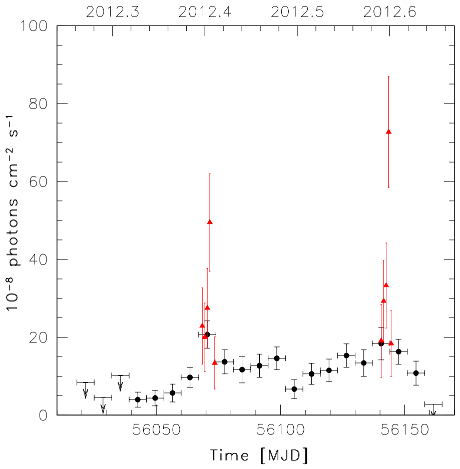

Figure 1: *Fermi*-LAT (E > 100 MeV) light curve of SBS 0846+513 obtained during 2012 April 1 - August 28 with 7-day (black circles) and 1-day (red triangles) time bins. Arrows refer to 2-σ upper limits. Upper limits are computed when TS <10. Adapted from [21].

2. The γ-ray view of NLSy1

Five radio-loud NLSy1 galaxies have been detected at high significance by *Fermi*-LAT so far: 1H 0323+342, SBS 0846+513, PMN J0948+0022, PKS 1502+036, and PKS 2004−447 [1, 4, 16], with a redshift between 0.061 and 0.585. The average apparent

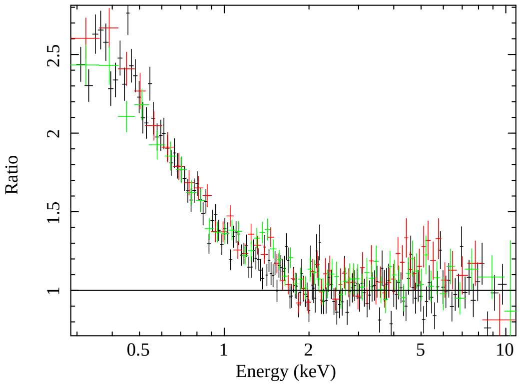

Figure 2: *XMM-Newton* EPIC pn (black), MOS1 (red) and MOS2 (green) data of PMN J0948+0022 shown as a ratio to a power law with $\Gamma = 1.48$. Adapted from [22].

isotropic luminosity of these sources in the 0.1–100 GeV energy band is between 10^{44} erg s^{-1} and 10^{47} erg s^{-1}, a range of values typical of blazars [18]. This may be an indication of a small viewing angle with respect to the jet axis and thus a high beaming factor for the γ-ray emission, similarly to blazars. Several strong γ-ray flares were observed from SBS 0846+513 (Fig. 1) and PMN J0948+0022, reaching a peak apparent isotropic γ-ray luminosity of $\sim 10^{48}$ erg s^{-1}, comparable to that of the bright FSRQ [21, 23, 27]. In particular, SBS 0846+513 and PMN J0948+0022 showed a γ-ray flaring activity combined with a moderate spectral evolution [16, 27], a behaviour that was already observed in bright flat spectrum radio quasars (FSRQ) and low-synchrotron-peaked BL Lacs [2]. Variability and spectral properties of these two NLSy1s in γ-rays indicate a blazar-like behaviour. An intense γ-ray flaring activity was observed by LAT also from 1H 0323+342 [13]. This is another indication that radio-loud NLSy1 are able to host relativistic jets as powerful as those in blazars.

3. X-ray properties

The X-ray spectra of NLSy1 are usually characterized by a steep photon index ($\Gamma_X > 2$, [31]). On the contrary, a relatively hard X-ray spectrum was detected in the *Swift*/XRT observations of SBS 0846+513 [16, 20], PMN J0948+0022 [22, 23, 27, 28], 1H 0323+342 [19], and PKS 1502+036 [17]. This suggests a significant contribution of inverse Compton radiation from a relativistic jet, similar to what is found for FSRQ.

The high quality *XMM-Newton* observation of PMN J0948+0022 performed in 2011 May allowed us to study in detail its X-ray spectrum, as reported in [22]. The spectral modelling of the *XMM-Newton* data of PMN J0948+0022 shows that emission from the jet most likely dominates the spectrum above $\sim$2 keV, while a soft X-ray excess is evident below $\sim$2 keV (Fig. 2). The origin of the soft X-ray excess is still an open issue both in radio-quiet and radio-loud AGN (e.g., [29]). Such a Seyfert component is a typical feature in the X-ray spectra of radio-quiet NLSy1, but it is quite unusual in jet-dominated AGN, even if not unique (e.g., PKS 1510-089; [33]). In the case of PMN J0948+0022, the statistics did not allow us to distinguish between different models for the soft X-ray emission. Models where the soft emission is partly produced by blurred reflection, or Comptonisation of the thermal disc emission, or simply a steep power-law, all provide good fits to the data. A multicolor thermal disc emission also gives a comparable fit, but the temperature is too high (kT = 0.18 keV) and is incompatible with a standard Shakura & Sunyaev accretion disc [22].

4. Radio properties

On pc scale a core-jet structure was observed for SBS 0846+513 [16] (Fig. 3), PKS 2004−447 [41], PKS 1502+036 [17], and PMN J0948+0022 [22, 30], although the jet in the two latter sources is significantly fainter than that observed in the former two sources.

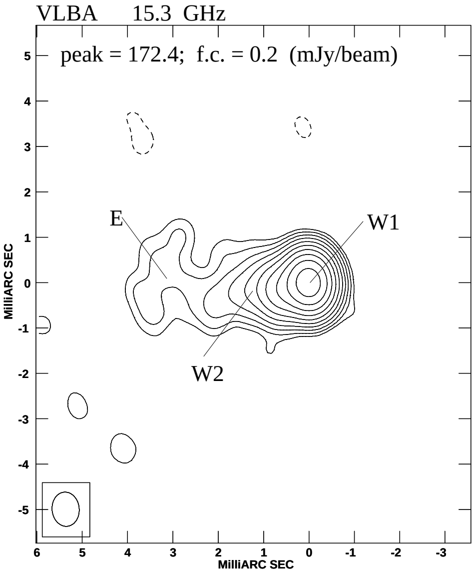

Figure 3: 15.3 GHz VLBA image of SBS 0846+513. On the image we provide the peak flux density, in mJy/beam, and the first contour intensity (f.c., in mJy/beam) that corresponds to three times the noise measured on the image plane. Contour levels increase by a factor of 2. The beam is plotted on the bottom left corner of the image. Component W1 is the core region, W2 is a knot, and E is the jet structure. Adapted from [20].

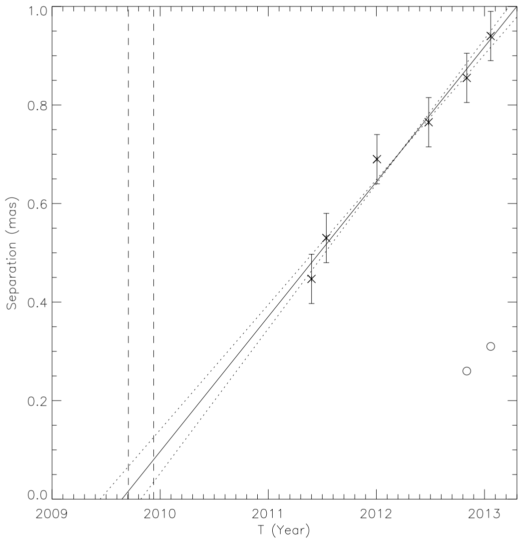

Figure 4: The separation between the core component of SBS 0846+513 and the knot ejected in 2009 as a function of time. The solid line represents the regression fit to the 15 GHz VLBA MOJAVE data, while the dotted lines represent the uncertainties from the fit parameters. Dashed lines indicate the beginning and the peak of the radio flare. Adapted from [21].

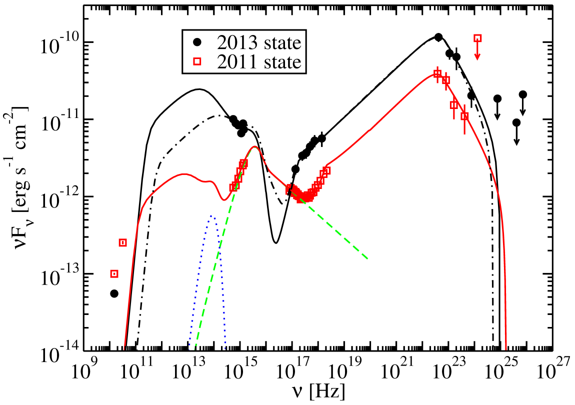

Figure 5: SED and models for the 2013 and 2011 activity states of PMN J0948+0022. The filled circles are the data from the 2013 flaring state, and the open squares are the data from the 2011 intermediate state taken from [22]. The dashed curve indicates the disc and coronal emission, and the dotted line indicates the thermal dust emission. Solid lines represent models consistent with scattering dust torus radiation, while the dashed-dotted curve represents a model consistent with the scattering of BLR radiation. Arrows refer to 2σ upper limits on the source flux. The VERITAS upper limits are corrected for EBL absorption using the model of [26]. Adapted from [23].

The analysis of the 6-epoch data set of SBS 0846+513 collected by the MOJAVE programme during 2011-2013 indicates that a superluminal jet component is moving away from the core with an apparent angular velocity of (0.27 ± 0.02) mas yr^{-1} (Fig. 4), corresponding to $(9.3\pm0.6)c$ [20]. This apparent superluminal velocity indicates the presence of boosting effects for the jet of SBS 0846+513. On the contrary, VLBA observations did not detect apparent superluminal motion at 15 GHz for PKS 1502+036 during 2002−2012, although the radio spectral variability and the one-sided jet-like structure seem to require the presence of boosting effects in a relativistic jet [17].

Strong radio variability was observed at 15 GHz during the monitoring of the OVRO 40-m telescope of PMN J0948+0022 [22, 23], PKS 1502+036 [17], and SBS 0846+513 [16, 20]. An inferred variability brightness temperature of 2.5×10^{13} K, 1.1×10^{14} K, and 3.4×10^{11} K was obtained for PKS 1502+036, SBS 0846+513, and PMN J0948+0022, respectively. These values are larger than the brightness temperature derived for the Compton catastrophe [45], suggesting that the radio emission of the jet is Doppler boosted. On the other hand, a high apparent brightness temperature of 10^{13} K, comparable to that of the γ-ray NLSy1, was observed for TXS 1546+353. However, no γ-ray emission has been detected from this source, so far [42]. Moreover, an intensive monitoring of these γ-ray NLSy1 from 2.6 GHz to 142 GHz with the Effelsberg 100-m and IRAM 30-m telescopes showed, in addition to an intensive variability, spectral evolution across the different bands following evolutionary paths explained by travelling shocks, typical characteristics seen in blazars [8].

5. Multifrequency variability and SED modelling

The first spectral energy distributions (SED) collected for the four NLSy1s detected in the first year of *Fermi* operation showed clear similarities with blazars: a double-humped shape with a first peak in the IR/optical band due to synchrotron emission, a second peak in the MeV/GeV band likely due to inverse Compton emission, and an additional component related to the accretion disc in UV for three of the four sources. The physical parameters of these NLSy1 are blazar-like, and the jet power is in the average range of blazars [1].

For PMN J0948+0022 we compared the broadband SED of the 2013 flaring activity state with that from an intermediate activity state observed in 2011 (Fig. 5). Contrary to what was observed for some FSRQ (e.g., PKS 0537−441; [21]) the SED of the two activity states, modelled as synchrotron emission and as an external Compton scattering of seed photons from a dust torus, could not be modelled by changing only the electron distribution parameters. A higher magnetic field is needed for the high activity

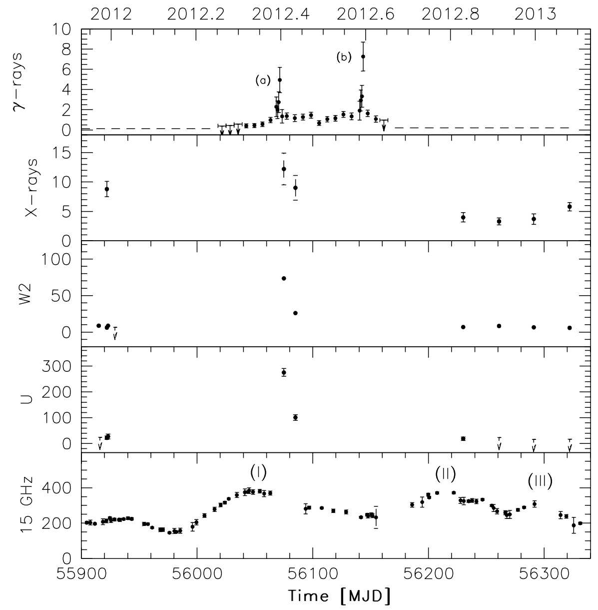

Figure 6: Multifrequency light curve for SBS 0846+513 during 2011 December - 2013 January. The data sets were collected (from top to bottom) by *Fermi*-LAT (γ-rays, 0.1−100 GeV; in units of 10^{-7} ph cm^{-2} s^{-1}), *Swift*-XRT (0.3−10 keV; in units of 10^{-13} erg cm^{-2} s^{-1}), *Swift*-UVOT (w2 and u bands; in units of μJy) and OVRO (15 GHz; in units of mJy). Arrows refer to 3σ upper limits on the source flux densities for the w2 and u bands, and to 2σ upper limits on the source fluxes for the γ-ray light curve. Adapted from [20].

state, consistent with the modelling of different activity states of PKS 0208−512 [14]. We also modelled the 2013 flaring state assuming Compton-scattering of broad line region (BLR) line radiation. The model reproduces the data as well as the scattering of the IR torus photons. However, we note that the BLR scattering model requires magnetic fields which are far from equipartition.

We also compared the SED of SBS 0846+513 during the flaring state in 2012 May with that of a quiescent state. Similar to PMN J0948+0022, the SED of the two different activity states, modelled by an external Compton component of seed photons from a dust torus, could be fitted by changing the electron distribution parameters as well as the magnetic field [20]. A significant shift of the synchrotron peak to higher frequencies was observed during the 2012 May flaring episode, similar to FSRQ (e.g., PKS 1510−089; [15]). Contrary to what is observed in PMN J0948+0022, no significant evidence of thermal emission from the accretion disc has been observed in SBS 0846+513.

A complex connection between the radio and γ-ray emission was observed for SBS 0846+513 and PMN J0948+0022, where γ-ray and radio flares have not a similar behaviour, as discussed in detail in [20, 22, 28].

Optical intraday variability has been reported for PMN J0948+0022 by [32, 35, 38], sometimes associated with a significant increase of the optical polarisation percentage, indicating a relativistic jet as the most likely origin for the optical emission in this object.

At Very High Energy (VHE; E > 100 GeV), VERITAS observations of PMN J0948+0022 were carried out during 2013 January 6–13, after the γ-ray flare observed by *Fermi*-LAT on 2013 January 1. These observations resulted in an upper limit of $F_{>0.2\,\mathrm{TeV}} < 4\times10^{-12}$ ph cm^{-2} s^{-1} [23]. The lack of detection at VHE could be due to different reasons: 1) The distance of the source ($z = 0.5846$) is relatively large and most of the GeV/TeV emission may be absorbed due to pair production from γ-ray photons of the source and the infrared photons from the extragalactic background light (EBL). However, we must note that the most distant FSRQ detected at VHE up to now, 3C 279 [5] is at a comparable distance. 2) The VERITAS observations were carried out a few days after the peak of the γ-ray activity, thus covering only the last part of the MeV/GeV flare. 3) Considering the similarities with FSRQ, a BLR should be present in these NLSy1. The presence of a BLR could produce a spectral break due to pair production, suppressing the flux beyond a few GeV and preventing a VHE detection. However, the detection at VHE of the FSRQ 3C 279, PKS 1510−089 [3, 7], and 4C +21.35 [6] have shown that the spectrum of some FSRQ extends to VHE energies during some flares, indicating that the γ-rays may be produced outside the BLR during those high-activity periods. The same scenario may apply to the γ-ray emitting NLSy1.

6. Radio-loudness, host galaxy, and jet formation

The mechanism at work for producing a relativistic jet is not clear. In particular, the physical parameters that drive the jet formation is still under debate. By considering that NLSy1 are thought to be hosted in spiral galaxies (e.g., [25]) the presence of a relativistic jet in these sources seems to be in contrast to the paradigm that such structures could be produced only in elliptical galaxies (e.g., [37]). The most powerful jets are found in luminous elliptical galaxies with very massive central BH and low accretion rates (e.g., [39, 46]). This was interpreted as an indirect evidence that a high spin is required for the jet production, since at least one major merger seems to be necessary to spin up the SMBH. At the same time, low accretion rates, which are associated with geometrically thick advection dominated accretion flows, may be important in jet formation by creating large-scale poloidal magnetic fields [48].

Therefore one of the most surprising facts related to the discovery of NLSy1 in γ-rays is the development of a relativistic jet in objects with a relatively small BH mass of 10^7-10^8 $M_\odot$. However, it is worth noting that the mass estimation of the BH in these sources may have large uncertainties due to the effect of radiation pressure [36] and the possible disc-like structure of their BLR [24]. [12] modelling the optical/UV data of some radio-loud NLSy1 with a Shakura & Sunyaev disc spectrum have estimated higher BH masses than those reported in the past, for PMN J0948+0022 and PKS 1502+036 comparable to the values estimated for blazars. This may solve the problem of the minimum BH mass predicted in different scenarios of relativistic jet formation and development, but introduces a new problem. How is it possible to have such a large BH mass in a class of AGN usually hosted in spiral galaxies? Only very sparse observations of the host galaxy of radio-loud NLSy1 are available up to now. Among the NLSy1 detected by LAT only for the closest one, 1H 0323+342, the host galaxy was clearly detected, suggesting two possible scenarios: the spiral arms of the host galaxy [52] or the residual of a galaxy merger [9, 49]. Therefore the possibility that the production of relativistic jets in these objects could be due to strong merger activity, unusual in disc/spiral galaxies, cannot be ruled out.

The accretion rate (thus the mass) and the spin of the BH seem to be related to the host galaxy, leading to the hypothesis that relativistic jets can form only in elliptical galaxies [10, 37]. We noted that the BH masses of radio-loud NLSy1 are generally larger than those in the whole sample of NLSy1 ($M_{BH} \approx$(2–10)$\times 10^7$ $M_\odot$; [34, 50]), even if still small if compared to radio-loud quasars. The larger BH masses of radio-loud NLSy1 with respect to radio-quiet NLSy1 may be related to prolonged accretion episodes that can spin-up the BHs. In this context, the small fraction of radio-loud NLSy1 with respect to radio-loud quasars could be an indication that not in all the former the high-accretion regime lasted long enough to spin-up the central BH [47].

Acknowledgments

The *Fermi* LAT Collaboration acknowledges support from a number of agencies and institutes for both the development and the operation of the LAT as well as scientific data analysis. These include NASA and DOE in the United States, CEA/Irfu and IN2P3/CNRS in France, ASI and INFN in Italy, MEXT, KEK, and JAXA in Japan, and the K. A. Wallenberg Foundation, the Swedish Research Council and the National Space Board in Sweden. Additional support from INAF in Italy and CNES in France for science analysis during the operations phase is also gratefully acknowledged.

We thank the *Swift* team for making these observations possible, the duty scientists, and science planners. This research made use of data from MOJAVE database that is maintained by the MOJAVE team (Lister et al. 2009, AJ, 137, 3718). The OVRO 40-m monitoring program is supported in part by NASA grants NNX08AW31G and NNX11A043G, and NSF grants AST-0808050 and AST-1109911. This work is partly based on observations obtained with *XMM-Newton*, an ESA science mission with instrument and contributions directly funded by ESA Member States and the USA (NASA). Part of this work was done with the contribution of the Italian Ministry of Foreign Affair. FD, MO, MG acknowledge financial contribution from grant PRIN-INAF-2011.

References

[1] Abdo, A. A., Ackermann, M., Ajello, M., et al. 2009, ApJ, 707, L142
[2] Abdo, A. A., Ackermann, M., Ajello, M., et al. 2010, ApJ, 710, 1271
[3] Abramowski, A., Acero, F., Aharonian, F., et al. 2013, A&A, 554, A107
[4] Acero, F., Ackermann, M., Ajello, M., et al. 2015, ApJS submitted, arXiv:1501.02003
[5] Albert, J., Aliu, E., Anderhub, H., et al. 2008, Science, 320, 1752
[6] Aleksic, J., Antonelli, L. A., Antoranz, P., et al. 2011, ApJ, 730, L8
[7] Aleksic, J., Ansoldi, S., Antonelli, L. A., et al. 2014, A&A, 569, A46
[8] Angelakis, E., Fuhrmann, L., Marchili, N., et al. 2015, A&A in press, arXiv:1501.02158
[9] Anton, S., Browne, I. W. A., Marcha, M. J. 2008, A&A, 490, 583
[10] Böttcher, M., & Dermer, C. D. 2002, ApJ, 564, 86
[11] Blandford, R. D., & Rees, M. J. 1978, in BL Lac Objects ed. A. M. Wolfe, 328
[12] Calderone, G., Ghisellini, G., Colpi, M., Dotti, M. 2013, MNRAS, 431, 210
[13] Carpenter, B., & Ojha, R. 2013, The Astronomer's Telegram, 5344
[14] Chatterjee, R., Fossati, G., Urry, C. M., et al. 2013, ApJ, 763, L11
[15] D'Ammando, F., Raiteri, C. M., Villata, M., et al. 2011, A&A, 529, 145
[16] D'Ammando, F., Orienti, M., Finke, J., et al. 2012, MNRAS, 426, 317
[17] D'Ammando, F., Orienti, M., Doi, A., et al. 2013, MNRAS, 433, 952
[18] D'Ammando, F., Tosti, G., Orienti, M., Finke, J. 2013, 2012 Fermi Symposium proceedings - eConf C121028
[19] D'Ammando, F., Carpenter, B., Ojha, R. 2013, The Astronomer's Telegram, 5352

[20] D'Ammando, F., Orienti, M., Finke, J., et al. 2013, MNRAS, 436, 191
[21] D'Ammando, F., Antolini, E., Tosti, G., et al. 2013, MNRAS, 431, 2481
[22] D'Ammando, F., Larsson, J., Orienti, M., et al. 2014, MNRAS, 438, 3521
[23] D'Ammando, F., Orienti, M., Finke, J., et al. 2015, MNRAS, 446, 2456
[24] Decarli, R., Dotti, M., Fontana, M., Haardt, F. 2008, MNRAS, 386, L15
[25] Deo, R. P., Crenshaw, D. M., Kraemer, S. B. 2006, AJ, 132, 321
[26] Finke, J., Razzaque, S., Dermer, C. 2010, ApJ, 712, 238
[27] Foschini, L., Ghisellini, G., Kovalev, Y. Y., et al. 2011, MNRAS, 413, 1671
[28] Foschini, L., Angelakis, E., Fuhrmann, L., et al. 2012, A&A, 548, A106
[29] Gierlinksi. M. & Done, C. 2004, MNRAS, 349, L7
[30] Giroletti, M., Paragi, Z., Bignall, H., et al. 2011, A&A, 528, L11
[31] Grupe, D., Komossa, S., Leighly, K. M., Page, K. L. 2010, ApJS, 187, 64
[32] Itoh, R., Tanaka, Y. T., Fukazawa, Y., et al. 2013, ApJ, 775, L26
[33] Kataoka, J., Madejski, G., Sikora, M., et al. 2008, ApJ, 672, 787
[34] Komossa, S., Voges, W., Xu, D., et al. 2006, AJ, 132, 531
[35] Liu, H., Wang, J., Mao, Y., & Wei, J., 2010, ApJ, 715, L113
[36] Marconi, A., Axon, D. J., Maiolino, R., et al. 2008, ApJ, 678, 693
[37] Marscher, A. 2009, in Lecture Notes in Physics 794, ed. T. Belloni, 173
[38] Maune, J. D., Miller, H. R., Eggen, J. R. 2013, ApJ, 762, 124
[39] McLure, M. L., Willott, C. J., Jarvis, M. J., et al. 2004, MNRAS, 351, 347
[40] Nolan, P., Abdo, A. A., Ackermann, M., et al. 2012, ApJS, 199, 31
[41] Orienti, M., D'Ammando, F., Giroletti, M. 2012, 2012 Fermi & Jansky Proceedings - eConf C1111101
[42] Orienti, M., D'Ammando, F., Larsson, J., et al. in preparation
[43] Osterbrock, D. E., & Pogge, R. W. 1985, ApJ, 297, 166
[44] Pogge, R. W. 2000, New Astron. Revs, 44, 381
[45] Readhead, A. C. S. 1994, ApJ, 426, 51
[46] Sikora, M., Stawarz, L., Lasota, J.-P. 2007, ApJ, 658, 815
[47] Sikora, M. 2009, AN, 330, 291
[48] Sikora, M., Begelman, M. C. 2013, ApJ, 764, L24
[49] Leon-Tavares, J., Kotilainen, J., Chavushyan, V., et al. 2014, ApJ, 795, L58
[50] Yuan, W., Zhou, H.-Y., Komossa, S., et al. 2008, ApJ, 685, 801
[51] Zhou, H.-Y., Wang, T.-G., Yuan, W., et al. 2006, ApJS, 166, 128
[52] Zhou, H.-Y., Wang, T.-G., Yuan, W., et al. 2007, ApJ, 658, L13

Suzaku X-Ray Monitoring of Gamma-Ray-Emitting Radio Galaxy, NGC 1275

Ikumi Edahiro, Yasushi Fukazawa, Kenji Kawaguchi, Yasuyuki Tanaka, Ryosuke Itoh, Yuka Kanda, Kensei Shiki
Hiroshima University/Hiroshima High Energy & Optical/Infrared Astrophysics Laboratory, Higashi-Hiroshima, Hiroshima, 739-8526

NGC 1275 is a gamma-ray-emitting radio galaxy at the center of the Perseus cluster. Its multi-wavelength spectrum is similar to that of blazers, and thus a jet-origin of gamma-ray emissions is believed. In the optical and X-ray region, NGC 1275 also shows a bright core, but their origin has not been understood, since a disk emission is not ruled out. In fact, NGC 1275 exhibits optical broad emission lines and a X-ray Fe-K line, which are typical for Seyfert galaxies. In our precious studies of NGC 1275 with Suzaku/XIS, no X-ray time variability was found from 2006 to 2011, regardless of moderate gamma-ray variability observed by it Fermi-LAT [1]. We have continued monitoring observations of NGC 1275 with Suzaku/XIS. In 2013-2014, MeV/GeV gams-ray flux of NGC 1275 gradually increased and reached the maximum at the beginning of 2014. Correlated with this recent gamma-ray activity, we found that X-ray flux also increased, and this is the first evidence of X-ray variability of NGC 1275. Following these results, we discuss the emission component during the time variability, but we cannot decide the origin of X-ray variability correlating with gamma-ray. Therefore, for future observation, it is important to observe NGC 1275 by using Fermi gamma-ray, XMM-Newton, NuStar, ASTRO-H X-ray, CTA TeV gamma-ray and Kanata optical telescope.

1. Introduction

Active Galactic Nucleus(AGN) is one of high energy objects. AGN are thought to be composed of massive black hole, emission-line region around the black hole, absorption of torus, and bidirectional plasma AGN jets. AGN observed in wide wavelength range from radio to gamma-ray and appearance of AGN and the time variation are different for each wavelength. However, detailed structure of AGN and radiation mechanism of AGN jet have not been clear with past various observations. Radio galaxes which is one of types of having AGN are very important to study AGN jet phenoneta.

NGC 1275 as shown in Figure 1 is an elliptical galaxy, locating at the center of the Perseus cluster. A viewing angle of apparent jet is about 30-55 degree [2]. NGC 1275 is known as an AGN and classified as a radio-loud Seyfert galaxy or a radio galaxy. In recent years, Fermi detected GeV gamma-ray emission for the first time and NGC 1275 is the brightest in gamma-ray among radio galaxies [3] [4].

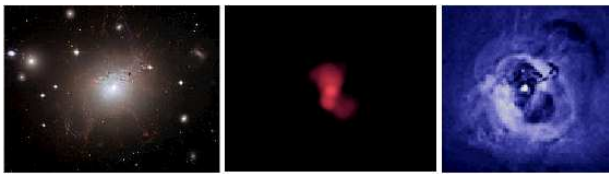

Figure 1: The pictures of NGC 1275. (left) Optical band. There are many galaxies.(middle) Radio band. We can see the structure of AGN jet. (right) X-ray band. At the center of this picture, we can see the nucleus.

NGC 1275 has been observed various wavelength. Fermi observation shows the time variation of GeV gamma-ray flux with several months scale and the gamma-ray flare was also reported [4] [5] [6]. From the above Fermi observations, it is suggested that the gamma-ray emission does not come from Perseus cluster via the cosmic ray interactions. Furthermore, TeV gamma-ray was detected with MAGIC [7] . Recently, from light curve of Fermi gamma-ray and MAGIC KVA optical R-band from 2010 to 2011, variability correlation between GeV gamma-ray and optical R-band was found [8].

Therefore, a radio-loud gamma-ray emitting Seyfert galaxy NGC 1275 is very attracting to study these structure. The SED of NGC 1275 nucleus can be explained by synchrotron self-Compton(SSC) model [3] [1]. The SED of NGC 1275 jet component rely on the radio and gamma-ray band because of optical and X-ray emission from jet has not been clear. So, it is important to search X-ray jet flux that could change SSC model parameters.

In the X-ray band, Einstein detected a point-like source [9]. However, the past observations could not constrain the X-ray spectrum. Recently, XMM-Newton and Chandra observed NGC 1275 and could resolve the nucleus emission spacially. From the results of XMM-Newton observation, a photon index of NGC 1275 is 1.65 and a flux is $1.43 \pm 0.29 \times 10^{-11}$erg/cm^2/s in 0.5-8 keV band [10] and the results of Chandra observation, a photon index is 1.6 ± 0.1 and a flux is 6.1×10^{-12}erg/cm^2/s in 0.5-5 keV band [11]. However, the number of observations are small, simultaneous observations with Fermi are poor, and Chandra data suffer from pile-up for the nucleus because of the hosting Perseus cluster is very bright. From Swift/BAT spectrum of NGC 1275, AGN emission is reported to be marginally detected, but Swift/BAT could not resolve the nucleus spatially. A photon index is $1.7^{+0.3}_{-0.7}$ and a flux is 1×10^{-11}erg/cm^2/s in 15-55 keV band [12].

Therefore, we tried to search nucleus emitting of Perseus cluster by using archival Suzaku/XIS data. Suzaku/XIS has observed the Perseus Cluster every half year with 40ks. From Yamazaki+13[1], they search variability correlation between Suzaku/XIS X-ray and gamma-ray flare, and there seem no correlation between X-ray and gamma-ray from 2008 to 2011.From the results of Suzaku/XIS observation, photon index is 1.6-1.8 and this result is consistent with the XMM-Newton resutls. Recently, from 2013 to 2014, a big GeV gamma-ray flare occurred as shown in bottom of Figure 4 in orange arrow region. So, we tried to extend the analysis of Suzaku/XIS observation data to stury the variability correlation with a big GeV gamma-ray flare. If we find the variability correlation between X-ray and gamma-ray, it is a key to solve the AGN emission mechanism.

2. Analysis of Suzaku/XIS data of NGC 1275

Here is the method of the analysis of Suzaku/XIS data of NGC 1275. Suzaku PSF cannot resolve NGC 1275 nucleus well. So, we extracted the AGN emission by imaging spectroscopy. First, we created images at 2-3, 3-4, 4-5, 5-6, 6-7, 7-8, 8-9, 9-10, 10-12 keV energy band and derived radial count profiles. For example, Figure 2 is X-ray radial profiles and images in 9-10 keV band (left) and 2-3 keV band (right). We can find that the hard X-ray AGN emission is seen at the center region in 9-10 keV band.

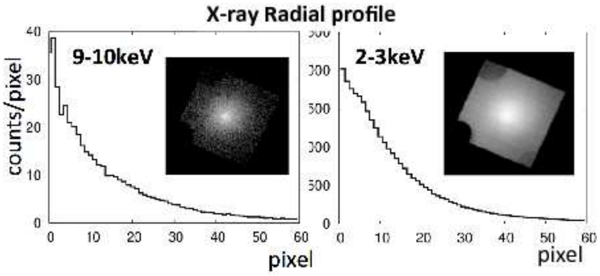

Figure 2: X-ray radial profile and image (left) 9-10 keV band (right) 2-3 keV band

Figure 3 is the ratio of these two radial profile. Hard X-ray is clearly seen at the center region. We fitted this profile with Gaussian and quadratic function as

$$f(x) = \frac{2n}{\sqrt{2\pi}\sigma} exp\left[-\frac{1}{2}\left(\frac{x}{\sigma}\right)^2\right] + d\left[a(x-b)^2 + c\right] \quad . \tag{1}$$

Here, Gaussian express the emission from the AGN at the center region and quadratic function express the emission from Perseus cluster at the outside region. We subtracted the model-cluster component from the data, and obtained the AGN photon counts. We analyzed the data from 2006 to 2014 and derived an X-ray light curve. This method is not usual, and we confirmed whether the results of using this method are good or not by applying the same way to brazar 3C 454.3. From comparing with the results of standard way and above way, we got the consistent results with Chandra, XMM-Newton and Swift/BAT observations results as same as Yamazaki+13 [1].

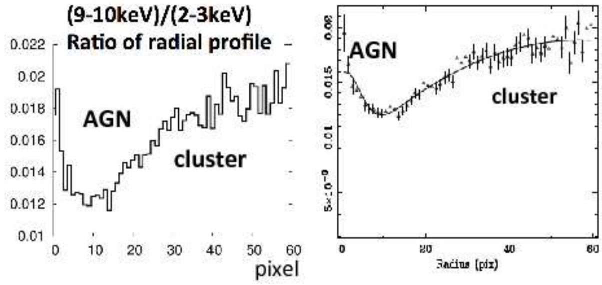

Figure 3: (9-10 keV)/(2-3 keV) ratio of radial profile. (left) At the center region, AGN emission is dominant. (right) By fitting with f(x), we obtained the AGN photon counts.

3. Results and discussion

3.1. Suzaku/XIS X-ray Light Curve of NGC 1275

The top of Figure 4 is Suzaku X-ray light curve from 2006 to 2011. Compared with Suzaku X-ray and Fermi gamma-ray light curve(as shown in bottom of Figure 4), we can see brightening of the nucleus in the X-ray band in 2013-2014 in orange arrow region, correlating with GeV gamma-ray flare. This is the first evidence of X-ray variability of NGC 1275. X-ray spectrum is consistent with the XMM-Newton results. However, it is not clear how the X-ray spectrum varied, because of Suzaku/XIS PSF. In 2010-2011 at the blue arrow region in bottom of Fig. 4, there are no correlation and this result is consistent with Yamazaki+13 [1].

3.2. Disccussion of Origin of X-ray Variability

We consider what is the origin of X-ray variability. Figure 5 is XMM-Newton spectra of NGC 1275 in 2006. From Fig. 5, the spectrum is well described by the simple power-law with a photon index of 1.73 and a Fe-K line of equivalent width of 70 keV. This is similar to that of Seyfert galaxies. Because of weak

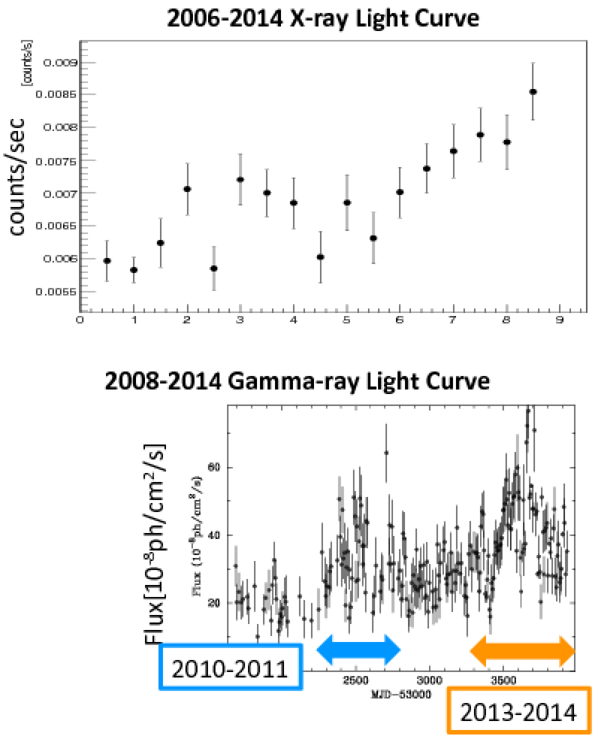

Figure 4: Light curve of NGC 1275 (top) 2006-2014 Suzaku X-ray (bottom) 2008-2014 GeV gamma-ray (archival light curve supplied by GSFC). The bin size of the horizontal axis are collect between top and bottom.

correlation between X-ray and gamma-ray in 2008-2011, disk/corona emission seems to be dominant in the X-ray band.

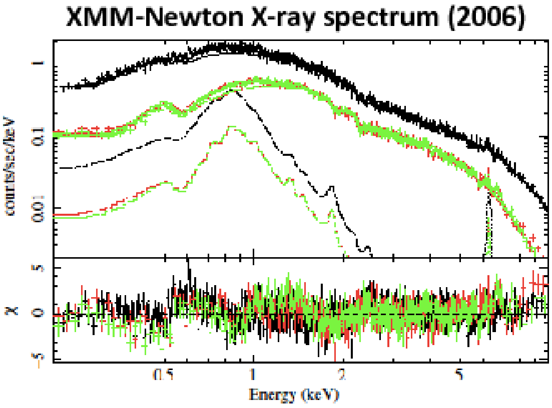

Figure 5: XMM-Newron X-ray Spectrum of 2006.

On the other hand, what is the origin of X-ray variability correlating with gamma-ray? The possible origin is jet emission or disc/corona emission. If disc/corona emission is the origin of X-ray variability correlating with gamma-ray, NGC 1275 would become a rare object from which both disk/corona emission and jet emission from X-ray to gamma-ray band. We can study the disk/jet connection from the X-ray and gamma-ray correlation. Optical lines are reprocess of disk/corona emission, while X-ray traces the disk/corona emission directly.

If jet emision is the origin of X-ray variability correlating with gamma-ray, variable X-ray component would be a low energy tail of inverse Compton. We can trece a precise SED variability from X-ray to gamma-ray to constrain the flare mechanism. In the near future, we can trace the jet flare from X-ray and gamma-ray, with NuStar, ASTRO-H, Fermi, and CTA as shown in Figure 6.

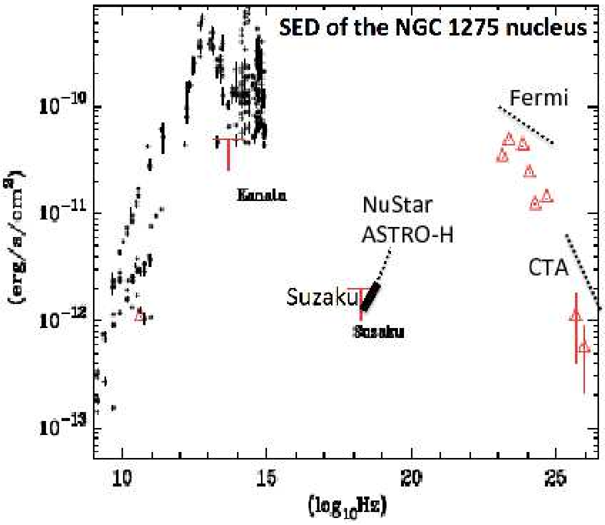

Figure 6: SED of the NGC 1275 nucleus [1] and observation region with each satellites.

We infer that the following X-ray spectral components for NGC 1275, disk/corona, reflection, and jet, as shown in Figure 7 (left). If we could obtain the X-ray spectral variability of harder-when-brighter as shown in Fig. 7 upper right, the variable component is jet inverse compton. If softer-when-brighter as shown in Fig. 7 lower right, the variable component is disk/corrona emission. So, future X-ray observations, for example, XMM-Newton, NuStar, ASTRO-H, are importan. In addition, it is important to observe NGC 1275 by observed optical region.

4. Conclusions

We analyzed Suzaku/XIS observation data of NGC 1275. From 2013 to 2014, brightening of the nucleus in the X-ray band was found, correlating with GeV gamma-ray flare. This is the first evidence of X-ray variability of NGC 1275. However, we cannot find what the variability component is, disc/corrona or jet. For future prospects, in addition to Fermi ob-

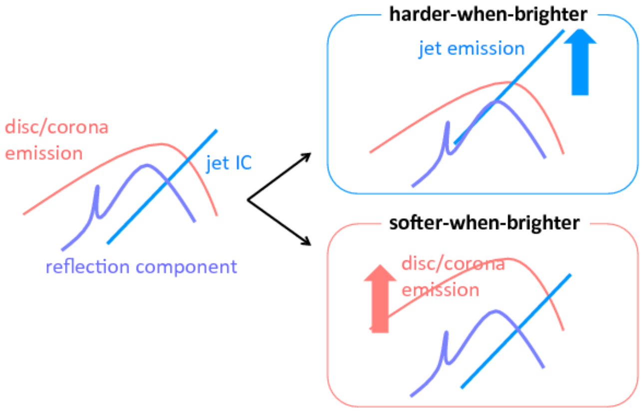

Figure 7: Inference of X-ray components(disc/corrona(red), jet(blue), and reflection(purple)) for NGC 1275 and correlation between variable component and energy band.

servation, it is important to observe NGC 1275 by using XMM-Newton, NuStar, ASTRO-H. CTA TeV gamma-ray observation is also important to understand the gamma-ray flare. We are also continuing to monitor NGC 1275 by Kanata optical telescope. By using simultaneous multi wavelength spectra, we want to find the detail structure of AGN.

References

[1] Yamazaki et al. “X-Ray and Optical Monitoring of a Gamma-Ray-Emitting Radio Galay, NGC 1275” 2013, PASJ 65, 30

[2] R.C.Walker et al.,”Detection of a VLBI counter-jet in NGC 1275: A possible probe pf the parsec-scale accretion region”, 1994, ApJ, 430L, 45W

[3] Abdo. A. A. et al., “Fermi Discovery of gamma-ray Emission from NGC 1275”, 2009, ApJ, 699, 31A

[4] J. Kataoka et al., “gamma-ray Spectral Evolution of NGC 1275 Observd with Fermi Large Area Telescope”, 2010, ApJ, 715, 544K

[5] Donato. D. et al., “Fermi LAT detection of gamma-ray flaring activity from the radio galaxy NGC 1275”, 2010, ATel, 2737, 1D

[6] M. Brown et al., “High-energy gamma-ray properties of the Fanaroff-Riley type I radio galaxy NGC 1275”, 2011, MNRAS, 413, 2785B

[7] Aleksic. J. et al., “MAGIC Gamma-ray Telescope Observation of the Perseus Cluster of Galaxies: Implications for Cosmic Rays, Dark Matter, and NGC 1275”, 2010, ApJ, 710, 634A

[8] J. Aleksic. et al., “Contempotaneous obsercations of the radio galaxy NGC 1275 from radio to very high energy gamma-ray”, 2014, A&A, 564A, 5A

[9] Branduardi-Raymont. G. et al., “Soft X-ray Images of the Central Region of the Perseus Cluster”, 1981, ApJ, 248, 55B

[10] Churazov. E. et al., “XMM-Newton Observation of the Perseus Cluster. I. The Temperature and Surface Brightness Structure”, 2003, ApJ, 590, 225C

[11] Balmaverde. B. et al., “The Chandra view of the 3C/FR I sample of low luminosity radio-galaxies”, 2006, A&A, 451, 35B

[12] Ajello. M. et al., “Galaxy Clusters in the Swift/Burst Alert Telescope Era; Hard X-rays in the Intercluster Medium”, 2009, ApJ, 690, 367A

Study of the X-ray emission mechanism of radio-loud narrow-line Seyfert 1 galaxy

H. Shirakawa and Y. Fukazawa, Y. Tanaka, R. Itoh and K. Kawaguchi
School of Science, Hiroshima University, 1-3-1,
Kagamiyama, Higashi-hiroshima, Hiroshima, Japan 739-8526

1H0323+342 is one of narrow-line radio-loud Seyfert 1 galaxies (RL-NLS1), which is a new class of gamma-ray emitting AGNs. Narrow-line Seyfert 1 galaxies (NLS1) have a small-mass black hole, but its mass accretion rate is almost as high as Eddington limit. Therefore, by observing NLS1s, we can know the evolution of supermassive black holes at the center of galaxies. Some of NLS1s are radio-loud and we call them RL-NLS1. From past observations, multi-wavelength spectrum of RL-NLS1s is similar to that of typical blazars; the synchrotron emission in the lower energy band up to the optical band, and inverse Compton scattering of low energy photons from disk, torus, and broad line region. X-ray band is a transittion region between the synchrotron and inverse Compton, and also there is a possible disk/corona emission. Therefore, we studied the energy-dependence of time variability of the X-ray emission of 1H0323+342, which have been observed by Suzaku in 2009 and 2013, in order to constrain the emission mechanism. We found that the lower energy below 1 keV and the higher energy above 7 keV show a different variability from the middle energy band, indicating at least two emission components in the X-ray band. X-ray spectrum is not a simple power-law, but requires an additional features; a broken power-law plus flat hard component, or a power-law plus a relativistic reflection component. Each spectral component seems to vary independently.

I. NALLOW-LINE RADIO-LOUD SEYFERT 1 GALAXY (RL-NLS1)

Narrow-line Seyfert 1 galaxy (NLS1) is a class of active galactic nuclei (AGN). The width of optical emission lines is narrower than that of Seyfert 1 galaxies, and NLS1s do not exhihit strong X-ray absorption like Seyfert 2 galaxy. In the X-ray spectrum, there is often a large soft-excess. NLS1s are identified by the following three characteristics.

1. FWHM (Hβ) < 2000 kms^{-1} (Goodrich 1989)
2. [OIII] / H$\beta < 3$ (Osterbrock & Pogge 1985)
3. strong permitted Fe II emission lines (Boroson & Green 1992)

NLS1s have a small-mass black hole, but its mass accretion rate is almost as high as Eddington limit (Marconi et al. 2008). We can study the evolution of supermassive black holes at the center of galaxies by observing NLS1s.

A. Nallow-line radio-loud Seyfert 1 galaxy (RL-NLS1)

Most of NLS1s are radio-quiet (R < 10, R : radio loudness, ratio of 5 GHz radio to B-band flux densities) (Kellermann et al. 1989), but 7 % of NLS1s are radio-loud (R > 10) and 2.5 % are very radio-loud (R > 100) (Komossa et al. 2006), and they are called as radio-loud narrow-line Seyfert 1 galaxies (RL-NLS1).

With early Fermi observation, GeV gamma-ray emission has been discovered from PMN J0948+0022, one of RL-NLS1s (Abdo et al. 2009a). After that, GeV gamma-ray emission was found from other three RL-NLS1s (Abdo et al. 2009b), so it is found that RL-NLS1s generally emit GeV gamma-rays. From past observations, the multi-wavelength spectrum of RL-NLS1 is similar to that of typical blazars; the synchrotron emission in the lower energy band up to the optical band and the inverse Compton scatterred X-ray and gamma-ray emission of low energy photons from disk, torus, and broad line region. X-ray band is a transition region between the synchrotron and the inverse Compton, and also there is a possible disk/corona emission.

As described above, X-ray emission mechanism of RL-NLS1s is uncertain. Therefore, we studied the energy-dependence of time variability of the X-ray emission of a RL-NLS1s 1H 0323+342, which have been observed by Suzaku in 2009 and 2013.

II. DATA ANALYSIS

A. Energy-dependence of time variability

Fig.1 is a light curve of 1H 0323+342 observed by Suzaku in 2013. 1H 0323+342 varies with a time scale of several ks, but the soft X-ray band below 1 keV shows a independent behavior from the other bands . Fig.2 shows correlations of count rates between 2–3 keV and other bands. The lower energy below 2 keV and the higher energy above 7 keV show a different variability from the middle energy band, suggesting that there are at least two spectral components in the X-ray band.

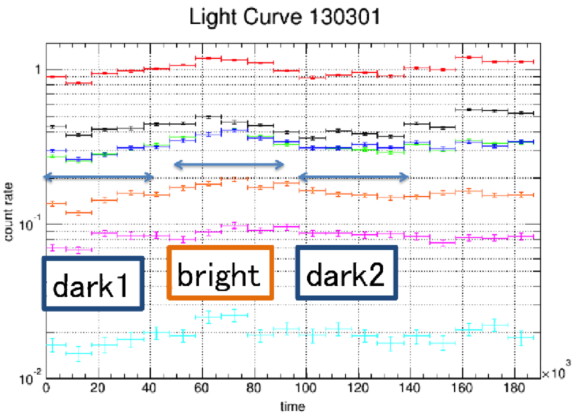

FIG. 1: Suzaku X-ray light curves of 1H 0323+342 in various energy bands. Band1 : 0.5–1 keV (black), band2 : 1–2 keV (red), band3 : 2–3 keV (green), band4 : 3–5 keV (blue), band5 : 5–7 keV (orange), band6 : 7–10 keV (magenta), band7 : Fe-k line region (cyan). Definition of bright and dark period is also shown for spectral analysis.

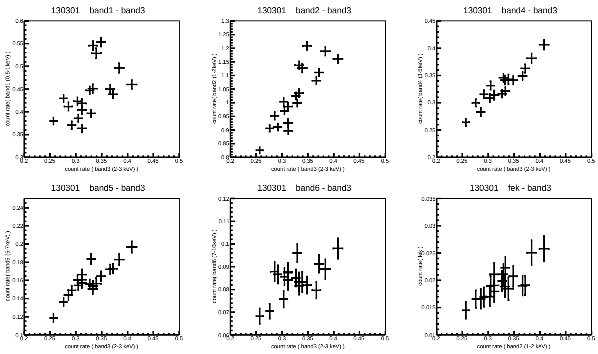

FIG. 2: Correlations of count rates between band3 (2–3 keV) and other energy bands in 2013

B. Spectral fitting

First, we fit the X-ray spectrum of 1H 0323+342 with the absorbed power-law model, but there remain redisuals at the higher and lower energy region ($\chi^2/dof = 1017.26/528$) and thus the spectrum is not a simple power-law shape (Fig. 3).

1. *Jet emission model*

To reduce the redisual in Fig.3, we added a broken power-law model This model of one hard power-law and one broken power-law represents a jet emission of inverse Compton and synchrotron, respectively. As in Fig.4 and Fig.5, X-ray spectra can be fitted with this model for 2009 and 2013 (Table I). The breaking energy becomes around 0.7 keV.

Next, we analyzed the spectra of three periods during the 2013 observation as in Fig.1, defined by brightness in 2013. Only a broken power-law component varied, suggesting a fast variable synchrotron emission if the jet emission model is correct. This behavior is similar to blazars.

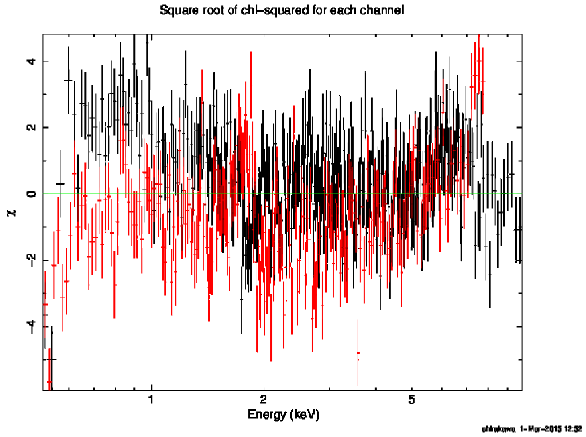

FIG. 3: Redisuals of fitting of the 1H 0323+342 spectra in 2013 with the absorved power-law model.

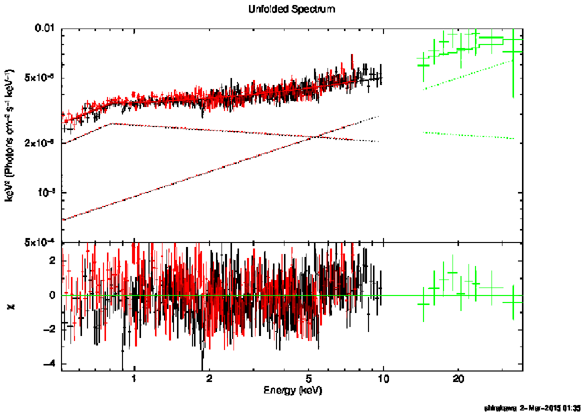

FIG. 4: Fitting the 2009 spectrum with a broken power-law plus a power-law model (jet emission model).

2. *Disk emission model*

When we look at the residual fitted with jet emission model in 2013 (Fig.5) in detail, there is a feature like a broad Fe line around 6 keV. Therefore, we fit the 2013 spectrum with an additional Fe-K line

	photon index 1	breaking energy (keV)	photon index 2	photon index	χ^2/dof
2009	1.3±0.1	0.80±0.03	2.1(fix)	1.5(fix)	602.10/496
2013	0.33±0.36	0.63±0.02	2.1(fix)	1.5(fix)	975.22/536

TABLE I: Fitting parameters of jet emission model in 2009 and 2013

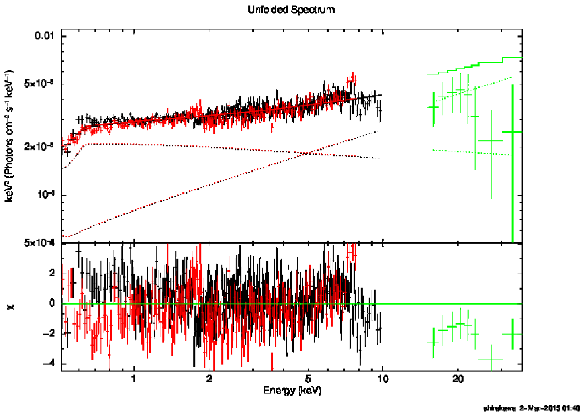

FIG. 5: Fitting the 2013 spectrum with a broken power-law plus a power-law model (jet emission model).

(E = 6.5 keV, width = 0.5 keV), together with the above jet emission model (Fig.6). Fe line intensity is $(1.2\pm0.4)\times10^{-5}$ counts/s/cm^2 (2.7σ statistical significance) and $\chi^2/dof = 908.28/528$; the fit improved.

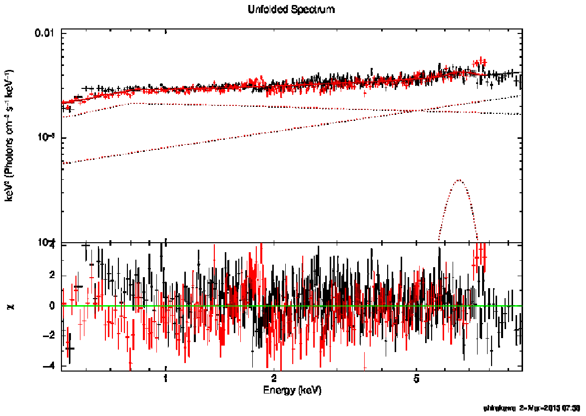

FIG. 6: Fitting with an additional Fe-K line (E=6.5keV, width=0.5keV), together with the above jet emission model.

Then, we try to fit the spectra with a single power-law model plus a relativistic reflection model. The relativistic refelction component represents a reflection of a power-law incident photons by the ionized accretion disk around a rotating black hole. We call this disk emission model. In this case, the spectra are also be fitted (Fig.7 and Fig.8). The broad Fe line feature is represented by the relativistic reflection component. The broken-like feature around 0.7 keV is represented by the Fe-L line complex.

We also try to fit the spectra of two periods defined in fig 1 with disk emission model, as jet emission model. As a result, a "powerlaw" component varied. If disk model is correct, the variability is almost attributed to the disk/corona component and the reflection component is stable. This behavior is similar to other Seyfert galaxies.

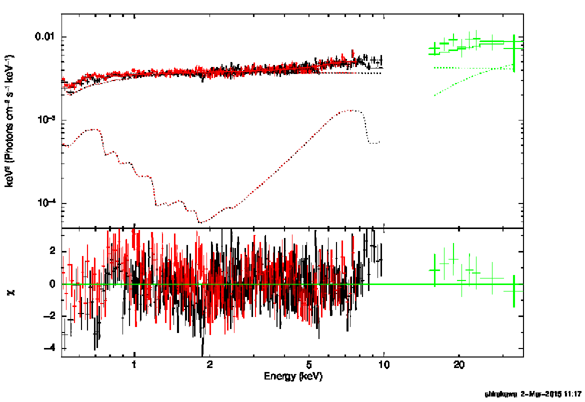

FIG. 7: Fitting the 2009 spectrum with disk emission model. See the text in detail.

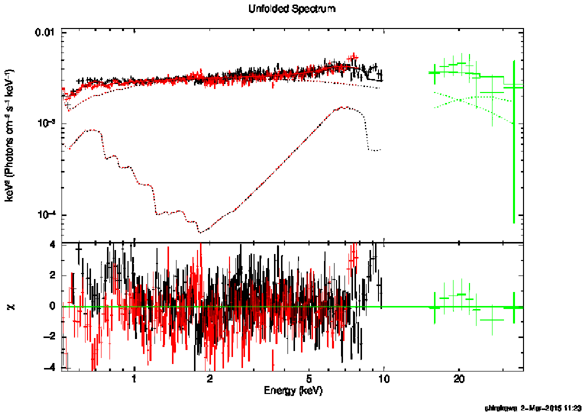

FIG. 8: Fitting the 2013 spectrum with disk emission model. See the text in detail.

III. SAMMARY AND FUTURE WORKS

We suggests that X-ray emission of 1H 0323+342 has at least two emission components, based on energy-dependence of time variability. If the X-ray emission of 1H 0323+342 is dominated by jet emission, a variable component is a synchrotron, and it is similar to other blazers. If the emission is dominated by disk/corona emission, disk/corona emission varies while disk reflection is stable, this is similar to Seyfert galaxies. We cannot distinguish these two models by current data. Therefore an extensive study by ASTRO-H observations with high energy resolution and good sensitivity in wide X-ray band is hopeful.

	cut-off energy(keV)	fold energy (keV)	photon index	a	Inclination (degree)	Fe/solar	Xi	χ^2/dof
2009	0.1(fix)	1000(fix)	2.02±0.02	0.998±0.02	84.3±1.4	4.55±1.00	10.0(fix)	640.69/493
2013	0.1(fix)	20(fix)	1.92±0.017	0.998±0.014	84.6±1.07	5.00±1.25	10.0(fix)	984.40/534

TABLE II: Fitting parameters of disk emission model in 2009 and 2013

[1] Abdo A.A. et al. 2009a ApJ., 699, 976
[2] Abdo A.A. et al. 2009b ApJ., 707, L142
[3] Boroson T.A. & Green R.F. 1992 ApJS 80, 109
[4] Goodrich R.W. 1989 ApJ., 342, 224
[5] Kellermann K.L. et al. 1989 AJ., 98, 1195
[6] Komossa S. et al. 2006 AJ., 132, 531
[7] Marconi A. et al. 2008 ApJ., 678, 693
[8] Osterbrock D.E. & Pogge R.W. 1985 ApJ., 297, 166

Kanata optical and X-ray monitoring of Gamma-ray emitting Narrow-Line Seyfert 1 and Radio galaxies

K. Kawaguchi, Y. Fukazawa, R. Itoh, Y. Kanda, K. Shiki, K. Takaki
Department of Physical Science, Hiroshima University, Higashi-Hiroshima, Hiroshima 739-8526, Japan
Y.T. Tanaka, M. Uemura, H.Akitaya
Hiroshima Astrophysical Science Center, Hiroshima University, Higashi-Hiroshima, Hiroshima 739-8526, Japan

Broadband spectrum of AGN consists of multiple components such as jet emission and accretion disk emission. Temporal correlation study is useful to understand emission components and their physical origins. We have performed optical monitoring using Kanata telescope for 4 radio galaxies and 6 radio-loud Narrow-Line Seyfert 1 (RL-NLSy1): 2 gamma-ray-loud RL-NLSy1s, 1H 0323+342 and PMN J0948+0022, and 4 gamma-ray-quiet RL-NLSy1s. From these results, it is suggested that RL-NLSy1s show a disk-dominant phase and a jet-dominant phase in the optical band, but it is not well correlated with brightness.

1. Introduction

Active Galactic Nucleus (AGNs) emit electromagnetic radiation from radio up to TeV gamma-ray ranges. Spectral Energy Distribution (SED) of blazars is often dominanted by 2 component, synchrotron emission and Inverse Compton from a relativistic jet. However, SED of misaligned radio-loud AGNs is complicated due to disk/corona emission. In addition to the above two components, we can see disk emission from near-infrared to ultraviolet bands and corona emission in X-ray band. Because it is difficult to separate these components, optical emission mechanism is still unclear.

Radio galaxy is radio-loud AGN which has a relative large viewing angle. Thanks to high sensitive observation by Fermi Gamma-Ray Space Telescope/ Large Area Telescope (LAT), correlation study between optical and MeV/GeV gamma-ray bands has become available, but correlation between optical and X-ray bands is still unclear.

Narrow-Line Seyfert 1(NLSy1) is a subclass of Seyfert 1 galaxies. Most of NLSy1 is radio-quiet, but a few objects(7%) are radio-loud. Recently, Fermi-LAT detected MeV/GeV gamma-ray emission from radio-loud NLSy1 (RL-NLSy1) and now RL-NLSy1 is a new class of gamma-ray emitting AGNs. Radio-loud NLSy1 shows fast and strong variability like blazars. The most gamma-ray bright NLSy1 PMN J0948+0022 showed minute-scale optical variability, correlated with polarization degree[4]. This indicates that synchrotron emision from the jet is dominant in the optical band, but other study shows disk emission is also dominant in the optical band[1]. Hence emission mechanism in the optical band in RL-NLSy1 is still unclear.

Table I Target lists

Radio galaxies	
3C 111	3C 120
3C 390.3	NGC 1275
Gamma-ray loud NLSy1s	
PMN J0948+0022	1H 0323+342
Gamma-ray quiet NLSy1s	
FBQS J1629+4007	FBQS J1644+2619
SDSS J1722+5654	SDSS J1450+5919

2. Observation

We have performed optical monitor with the Kanata optical telescope. We use MAXI, Swift-BAT and Fermi-LAT public data for X-ray and gamma-ray monitor.

We selected famous and X-ray bright objects for radio galaxies. For RL-NLSy1, we selected gamma-ray loud objects and a few gamma-ray quiet objects. These gamma-ray quiet objects are reported to have a blazar-like radio structure and high brightness temperature by Komossa et al. (2006)[2] Doi et al. (2011)[6] and Doi et al. (2012)[7]. So if these gamma-ray quiet NLSy1 has a relativistic jet, flares in the optical band are expected.

3. Results

Radio galaxies

Fig 1–4 show the results for radio galaxies. Each figure show optical R-band(top), V-band(second) magnitude by Kanata, 2-20 keV daily X-ray count rate by MAXI (third), and 15-150 keV weekly count rate by Swift-BAT (bottom). The gaps in MAXI light curves are the period when objects are not in FOV of MAXI. There is no Swift-BAT public data for 3C 390.3. We can see a clear flux variability in the optical band for 3C 111 and 3C 120, but no object shows a significant X-ray flux variability.

Gamma-ray loud NLSy1s

Fig 5 and 6 show the light curves of gamma-ray loud NLSy1. Each figure shows optical R-band (top), optical R-band polarization degree (middle), and 0.1-300 GeV gamma-ray (bottom). We can see some flares in optical and gamma-ray bands. Fig 7 and 8 show the correlation between optical flux and gamma-ray flux. We cannot see any clear correlation between these bands.

Fig 9 and 10 show the correlation between flux and polarization degree (PD) in the optical band. In PMN J0948+0022, optical flux and PD are not correlated and maximum PD reaches more than 10%. 1H 0323+342 shows high optical PD when optical flux is high. But optical PD value is low in the whole period (less than 5%).

Gamma-ray quiet NLSy1s

Fig 11–14 shows the results for gamma-ray quiet NLSy1. Each figure show optical R-band light curve (top) and V-band light curve (bottom). Only FBQS J1644+2619 shows daily-scale flux variability around MJD=56560. In this period, optical flux increases about 0.4 mag in 3 days both in R-band and V-band.

4. Discussion

No radio galaxies show a clear correlation between optical and X-ray bands. Probably this is due to low signal-to-noise ratio of X-ray light curves. We need more sensitive monitoring for X-ray study.

For gamma-ray loud NLSy1s, a jet-dominant phase or a disk-dominant phase is inferred to appear in addition to quiet phase. As shown in Fig 15, (1) in quiescence, disk emission seems to be dominant in optical band. (2) Jet-dominant phase is suggested to appear as flares in both optical and gamma-ray with an increase of an optical polarization degree. (3) Disk-dominant phase is indicated to be a quiet phase or an optical flare without polarization increase. Optical polarization and variability time-scale are important information to study emission mechanism in the optical band. Jet emission is polarized and shows a short-term variability. Further dense monitoring observations are needed to conclude the above.

For gamma-ray quiet NLSy1s, only FBQS J1644+2619 shows rapid flux variability. Previous studies in the radio band for FBQS J1644+2619 shows characteristics similar to blazars. Also, this object is listed in the 3rd FGL catalog as a new gamma-ray source. Optical short-term variability supports that this object shows a synchrotron emission in the optical band during the flare, like Fig. 15 (2) jet-dominant phase.

References

[1] Abdo et al.2009, ApJ, 707L.142A

[2] Komossa et al.2006, AJ, 132.531K

[3] Yuan et al.2008, ApJ, 775L.26I

[4] Itoh et al.2013, ApJ, 775L.26I

[5] Itoh et al.2014, PASJ

[6] Doi et al.2011, ApJ, 739.126D

[7] Doi et al.2012, ApJ, 760.41D

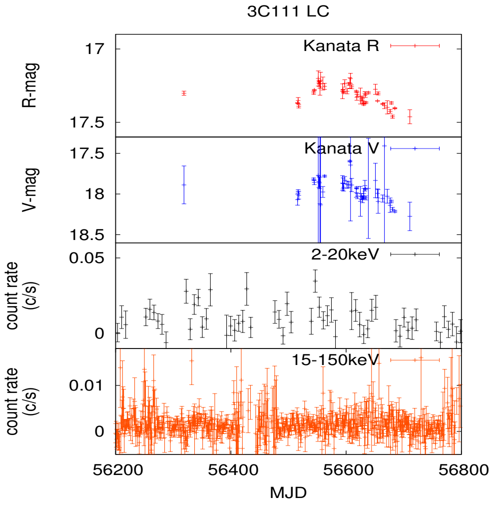

Figure 1: Light curve of a radio galaxy 3C 111

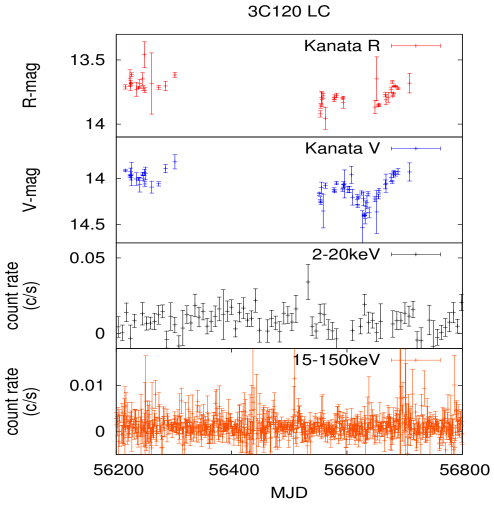

Figure 2: Light curve of a radio galaxy 3C 120

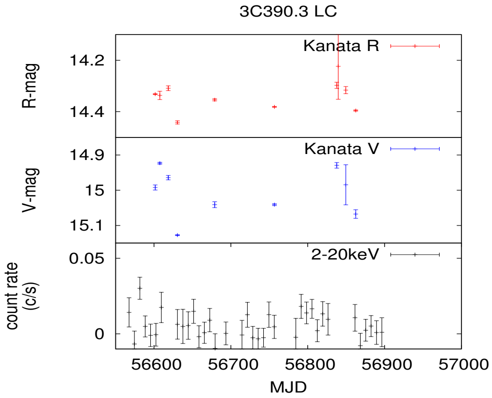

Figure 3: Light curve of a radio galaxy 3C 390.3

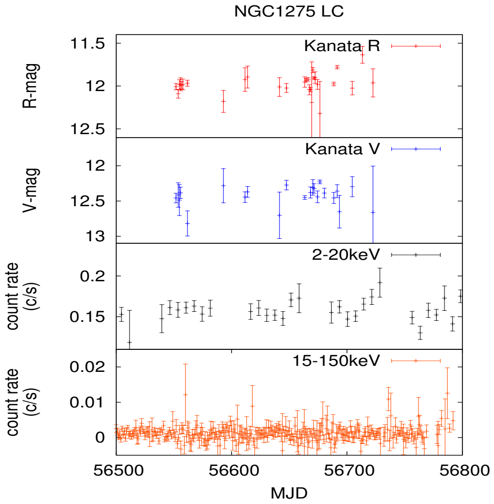

Figure 4: Light curve of a radio galaxy NGC 1275

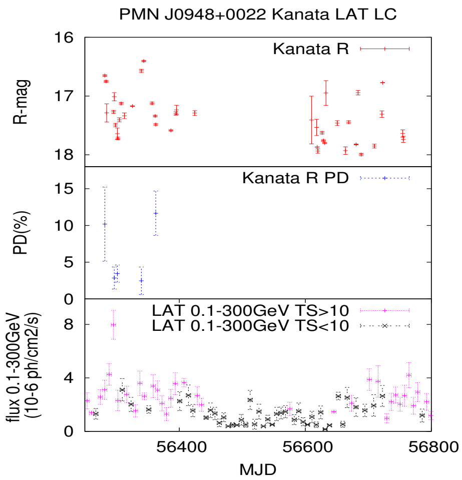

Figure 5: Light curve of a gamma-ray loud NLSy1 PMN J0948+0022

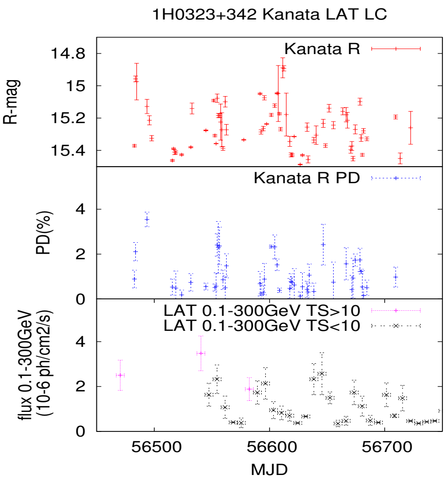

Figure 6: Light curve of a gamma-ray loud NLSy1 1H 0323+342

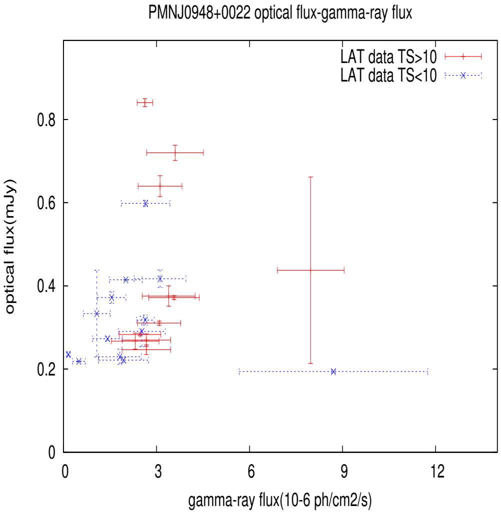

Figure 7: Correlation between optical flux and gamma-ray flux of PMN J0948+0022

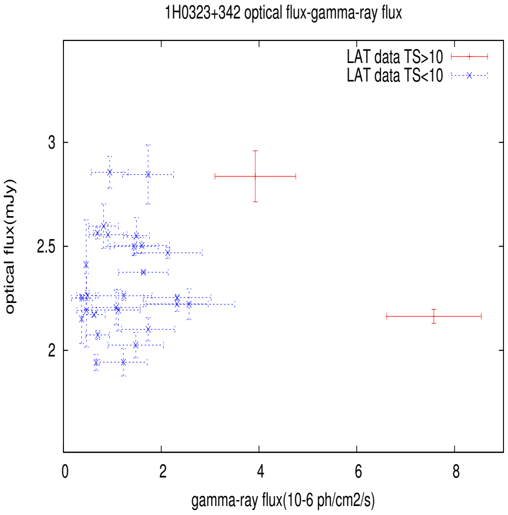

Figure 8: Correlation between optical flux and gamma-ray flux of 1H 0323+342

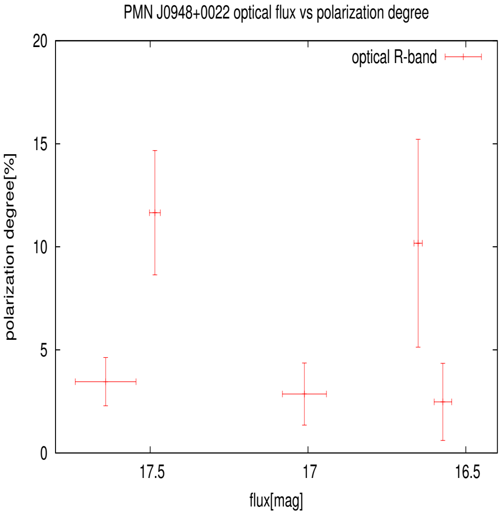

Figure 9: Correlation between optical flux and optical polarization degree of PMN J0948+0022

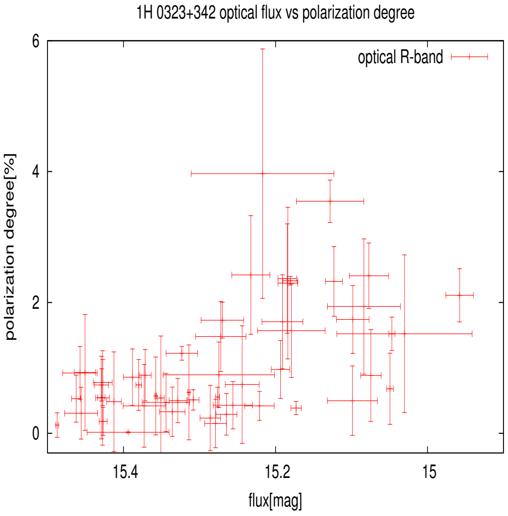

Figure 10: Correlation between optical flux and optical polarization degree of 1H 0323+342

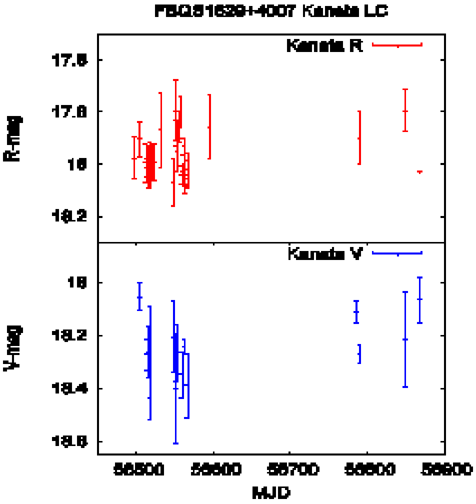

Figure 11: Light curve of a gamma-ray quiet NLSy1 FBQS J1629+4007

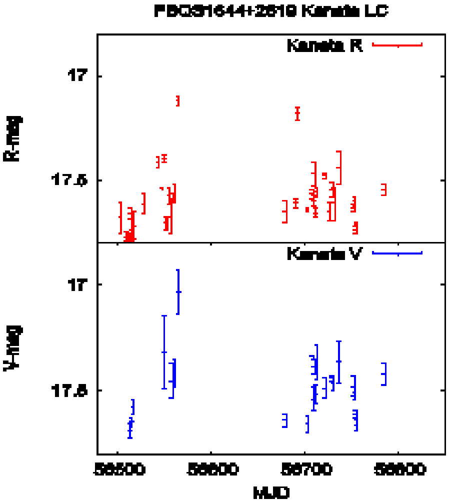

Figure 12: Light curve of a gamma-ray quiet NLSy1 FBQS J1644+2619

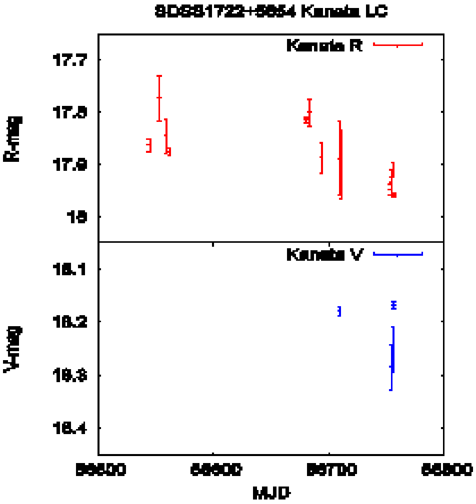

Figure 13: Light curve of a gamma-ray quiet NLSy1 SDSS J1722+5654

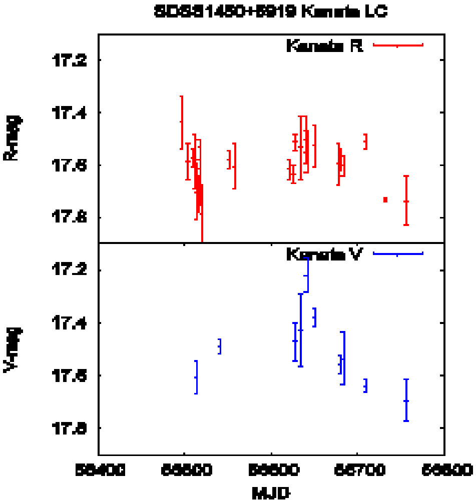

Figure 14: Light curve of a gamma-ray quiet NLSy1 SDSS J1450+5919

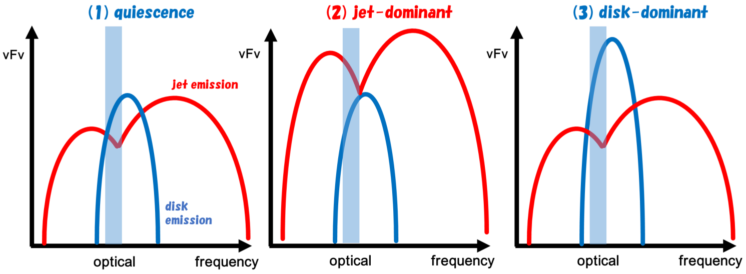

Figure 15: optical emission phases for RL-NLSy1s

Fermi-LAT and Multi-wavelength Monitoring of the Broad Line Radio Galaxy 3C 120

Y. T. Tanaka[1], A. Doi[2], Y. Inoue[2], C. C. Cheung[3], L. Stawarz[2,4], Y. Fukazawa[5], M. A. Gurwell[6],
M. Tahara[7], J. Kataoka[7], and R. Itoh[5], on behalf of the Fermi-LAT collaboration
[1]*Hiroshima Astrophysical Science Center, Hiroshima University, Higashi-Hiroshima, 739-8526, Japan*
[2]*ISAS/JAXA, Sagamihara, Kanagawa, 252-5210, Japan*
[3]*Space Science Division, Naval Research Laboratory, Washington, DC 20375-5352, USA*
[4]*Astronomical Observatory, Jagiellonian University, ul. Orla 171, 30-244 Kraków, Poland*
[5]*Department of Physical Sciences, Hiroshima University,*
Higashi-Hiroshima, Hiroshima 739-8526, Japan
[6]*Harvard-Smithsonian Center for Astrophysics, Cambridge, MA 02138, USA and*
[7]*Research Institute for Science and Engineering, Waseda University, Tokyo 169-8555, Japan*

We present six-year multi-wavelength monitoring result for broad-line radio galaxy 3C 120. The source was sporadically detected by *Fermi*-LAT and after the MeV/GeV γ-ray detection the 43 GHz radio core brightened and a knot ejected from an unresolved core, implying that the radio-gamma phenomena are physically connected. We show that the γ-ray emission region is located at sub-pc distance from the central black hole, and MeV/GeV γ-ray emission mechanism is inverse-Compton scattering of synchrotron photons. We also discuss future perspective revealed by next-generation X-ray satellite *Astro-H*.

I. BROAD LINE RADIO GALAXY 3C 120

3C 120, known as broad-line radio galaxy (BLRG) at $z = 0.033$, is classified as Fanaroff-Riley Class I (FR I) radio galaxy based on the radio morphology. Since the viewing angle of the jet is not as small as blazars (whose jets are directed toward the Earth), both thermal disk and non-thermal jet components are present in the broad band spectrum. In this regard, 3C 120 and also 3C 111 are ideal objects to investigate the disk-jet connection. For example, from long-term Very Long Baseline Array (VLBA) and X-ray monitorings, X-ray dimmings are found to be followed by radio knot ejections [1, 2, 11]. This phenomenon is understood by a scenario that the disk materials suddenly fall onto the central black hole (BH) and then they are ejected as a jet [e.g., 11].

It is reported that three BLRGs, namely 3C 111, 3C 120, and 3C 390.3, showed blue-shifted Fe XXV/XXVI K-shell absorption lines in the *Suzaku* X-ray spectrum [19]. This feature is interpreted as highly ionized gas outflow whose velocity is of the order of 0.1*c*. Since 3C 120 and 3C 111 are also detected by *Fermi*-LAT, these sources are ideal objects to study a physical link between accretion disk, ultra-fast outflow, and jet. Indeed, Tombesi et al. [20, 21] performed detailed study of 3C 111 by using X-ray and VLBA data [see also 3].

Location of jet dissipation region is a long-standing matter of debate. To unveil this problem, multi-wavelength light curve and high spatial resolution VLBA images provide useful information. Here, we show *Fermi* Large Area Telescope monitoring result, together with 230 GHz Sub-Millimeter Array (SMA) and 43 GHz VLBA ones. Based on the light curves and broadband spectrum from radio to MeV/GeV γ rays, we show that jet dissipation took place at sub-pc scale from the central BH and MeV/GeV γ rays would be produced by synchrotron self Compton process, rather than inverse-Compton scattering of external photons from broad line region and dusty torus. Details are described in Tanaka et al. [18].

II. FERMI-LAT AND MULTI-WAVELENGTH OBSERVATIONS

Fig 1 shows the *Fermi*-LAT, 230 GHz SMA, and 43 GHz VLBA light curves. After the *Fermi*-LAT detection, VLBA light curve showed brightening. Closed-up light curves between MJD 56100 and 56500 are displayed in Fig. 2. MeV/GeV γ-ray emission is followed by core brightening and knot ejection.

Fig 3 shows a broadband spectrum from radio to GeV band. Swift/UVOT and XRT data points obtained during the GeV flaring state are also plotted together. Radio, sub-mm, and MeV/GeV fluxes are nicely fitted by one-zone synchrotron-self-Compton modeling (see Section III), while optical-UV and X-ray fluxes are obviously above the jet component and are reasonably represented by accretion-related disk model by Koratkar & Blaes [10].

III. DISCUSSION

We first assume that the MeV/GeV γ-ray enhancement and radio knot ejection event are physically connected. Then, our observation (the γ-ray detection before the core brightening and subsequent knot ejection) indicates that γ-ray emission region is located inside the VLBA core. From long-term X-ray and

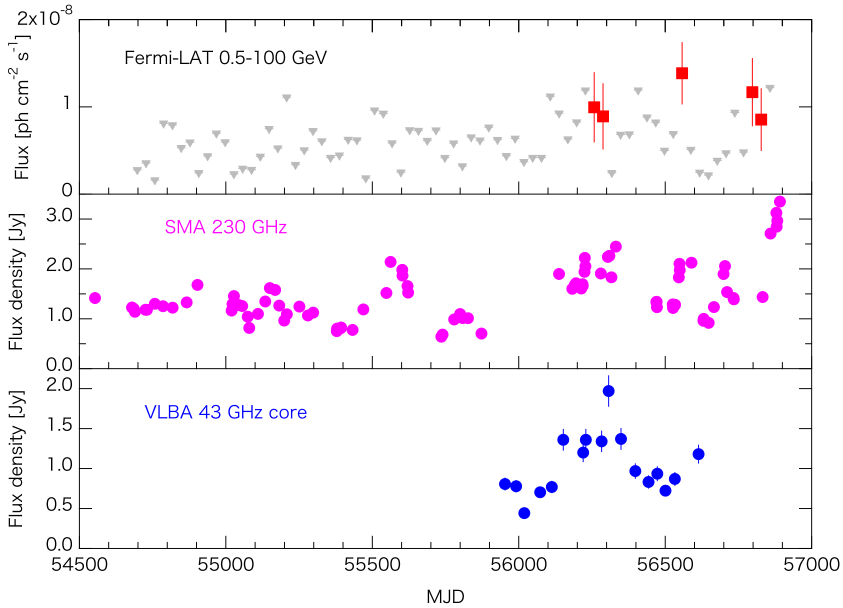

FIG. 1: *Fermi*-LAT (30-day bin), SMA, and VLBA light curves for 3C 120 since 2008 August. Gray triangles in the top panel show 90% confidence level flux upper limits when TS < 9. Zoom-up light curve between MJD 56100 and 56500 are shown in Fig. 2. Taken from Tanaka et al. [18].

VLBA monitoring over six years, [1] derived the distance from the central BH to 43 GHz VLBA core as ∼0.5 pc. Then, we can infer the location of the γ-ray emission region from the time lag (~ 60 and ~ 35 days) and viewing angle of $\sim 20.5^\circ$ as ~ 0.1 and ~ 0.3 pc from the central BH.

MeV/GeV γ rays are thought to be produced by inverse Compton scattering. There are three candidate photons sources; synchrotron photons, photons from broad line region, and hot dusty torus. Since the γ-ray emission region is located far beyond the broad line region of $R_{\rm BLR} = 0.019 - 0.024$ pc, which is derived by reverberation mapping [13], we can safely neglect the contribution of BLR photons as targets. By using reasonable parameter values, we obtain $L_{\rm ERC}/L_{\rm SSC} \approx 0.1$, indicating that synchrotron self Compton is favored [see 18, for details].

To derive the physical quantities, we performed SED modeling. See Tanaka et al. [18] for the derived parameter values, but here we briefly summarize the important points. The ratio of comoving electron and magnetic field density is obtained as $u'_{\rm e}/u'_{\rm B} \sim 0.4$, suggesting almost equipartition. Total radiated power estimated from SED modeling is $L_{\rm rad} \sim 4.9 \times 10^{44}$ erg s^{-1}. Given the observational fact that $L_{\rm jet} \simeq L_{\rm rad}$ for AGN jets [12], we obtain $L_{\rm jet} \approx 5 \times 10^{45}$ erg s^{-1}. On the other hand, total power of accreting plasma $L_{\rm acc}$ is estimated as $L_{\rm acc} \approx 10 L_{\rm disk} = 2 \times 10^{45}$ erg s^{-1}. Hence, we obtain $L_{\rm jet} \simeq L_{\rm acc}$, meaning the jet launch is extremely efficient [e.g. 5, 15, 17].

Finally, we mention a future perspective. Next-generation X-ray satellite *Astro-H* [16] is scheduled to be launched in 2015/2016. Ultra-high-resolution spectroscopy by micro-calorimeter SXS and simultaneous broadband spectral measurement by SXI, HXI, and SGD will provide new information about a physical link between accretion disk, ultra-fast outflow, and jet. In particular, highest sensitivity of SGD at 50–600 keV will enable us to detect the jet component in soft γ-ray band, as was detected by *Suzaku* from Centaurus A core by [4]. Hence, simultaneous *Fermi*-LAT and VLBA observations are also complementary and allow us to precisely derive physical parameters (such as electron distribution and magnetic field) at the emission region by SED modeling.

IV. SUMMARY

We presented six-year multi-wavelength light curve since the launch of *Fermi*-LAT in 2008 August[22]. Under the assumption that MeV/GeV γ-ray flux increase is physically connected by the subsequent VLBA core brightening and knot ejection, we derived the γ-ray emission region is located at ~ 0.1 and ~ 0.3 pc from the central BH. We conclude that synchrotron-self-Compton process is preferred as a γ-ray emission mechanism. Future *Astro-H* observation will provide unique opportunity to study physical relation between accretion disk, ultra-fast outflow and relativistic jet.

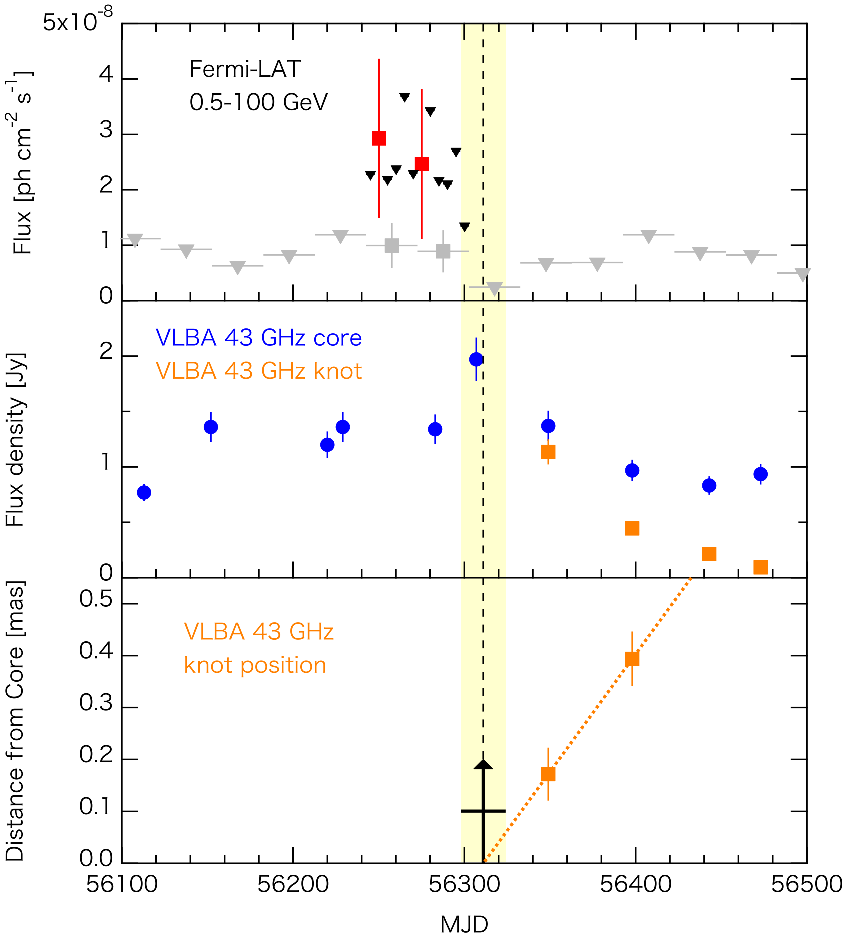

FIG. 2: Enlarged *Fermi*-LAT (5-day bin, top) and VLBA (mid) light curves between MJD 56100 and 56500. Black triangles in the top panel are 90% confidence level flux upper limits when TS < 4. Gray squares and triangles are 30-day-bin flux and upper limits shown in the top panel of Fig. 1. The lower panel represents the relative position of the ejected knot from the central BH. Black arrow indicates the timing when the knot was ejected from the VLBA core. Taken from Tanaka et al. [18].

Acknowledgments

The *Fermi*-LAT Collaboration acknowledges support for LAT development, operation and data analysis from NASA and DOE (United States), CEA/Irfu and IN2P3/CNRS (France), ASI and INFN (Italy), MEXT, KEK, and JAXA (Japan), and the K.A. Wallenberg Foundation, the Swedish Research Council and the National Space Board (Sweden). Science analysis support in the operations phase from INAF (Italy) and CNES (France) is also gratefully acknowledged.

This study makes use of 43 GHz VLBA data from the VLBA-BU Blazar Monitoring Program (VLBA-BU-BLAZAR; http://www.bu.edu/blazars/VLBAproject.html), funded by NASA through the Fermi Guest Investigator Program. The VLBA is an instrument of the National Radio Astronomy Observatory. The National Radio Astronomy Observatory is a facility of the National Science Foundation operated by Associated Universities, Inc.

---

[1] Chatterjee, R., Marscher, A. P., Jorstad, S. G., et al. 2009, *ApJ* , 704, 1689

[2] Chatterjee, R., Marscher, A. P., Jorstad, S. G., et al. 2011, *ApJ* , 734, 43

[3] Coppi, P., Stawarz, L., Done, C., et al. 2014, arXiv:1412.1190

[4] Fukazawa, Y., Hiragi, K., Yamazaki, S., et al. 2011, *ApJ* , 743, 124

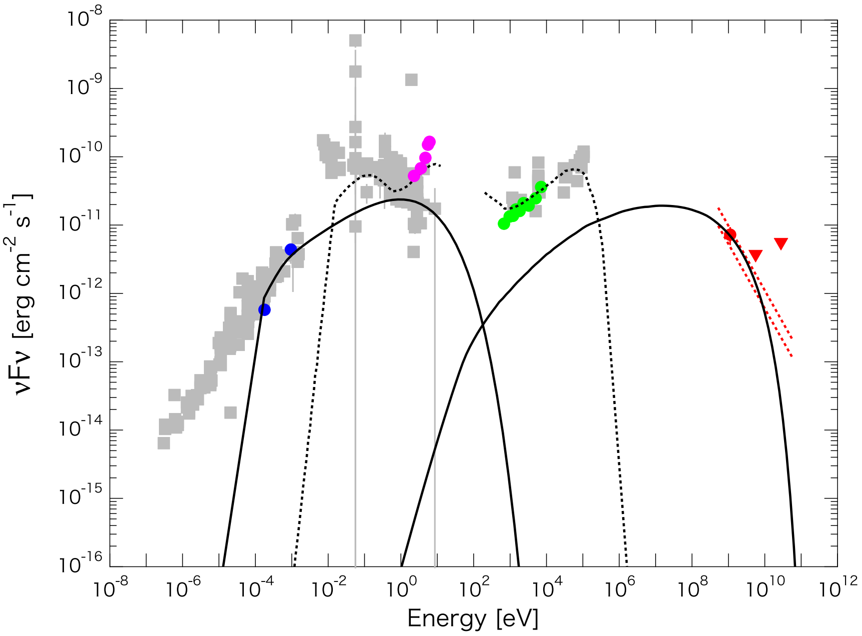

FIG. 3: Broadband spectrum of 3C 120. Shown by gray are historical fluxes taken from NED database. 43 and 230 GHz fluxes measured on MJD 56283 and 56280, respectively, are shown by blue squares. Magenta and green are Swift/UVOT and XRT fluxes observed on MJD 56276. Red squares and triangles are *Fermi*-LAT flux and 95% upper limits, derived from 60-day accumulated data from MJD 56242.7 to 56302.7. Solid line indicates one-zone synchrotron+SSC modeling, while dashed line are accretion-related model. Taken from Tanaka et al. [18].

[5] Ghisellini, G., Tavecchio, F., Maraschi, L., Celotti, A., & Sbarrato, T. 2014, *Nature* , 515, 376

[6] Inoue, Y. 2011, *ApJ* , 733, 66

[7] Jorstad, S. G., Marscher, A. P., Lister, M. L., et al. 2005, *AJ* , 130, 1418

[8] Kataoka, J., Reeves, J. N., Iwasawa, K., et al. 2007, *PASJ* , 59, 279

[9] Kataoka, J., Stawarz, Ł., Takahashi, Y., et al. 2011, *ApJ* , 740, 29

[10] Koratkar, A., & Blaes, O. 1999, *PASP* , 111, 1

[11] Marscher, A. P., Jorstad, S. G., Gómez, J.-L., et al. 2002, *Nature* , 417, 625

[12] Nemmen, R. S., Georganopoulos, M., Guiriec, S., et al. 2012, Science, 338, 1445

[13] Pozo Nuñez, F., Haas, M., Ramolla, M., et al. 2014, *A&A* , 568, AA36

[14] Sahakyan, N., Zargaryan, D., & Baghmanyan, V. 2015, *A&A* , 574, AA88

[15] Saito, S., Stawarz, Ł., Tanaka, Y. T., et al. 2013, *ApJL* , 766, LL11

[16] Takahashi, T., Mitsuda, K., Kelley, R., et al. 2012, *Proc. SPIE* , 8443, 84431Z

[17] Tanaka, Y. T., Stawarz, Ł., Thompson, D. J., et al. 2011, *ApJ* , 733, 19

[18] Tanaka, Y. T., Doi, A., Inoue, Y., et al. 2015, *ApJL* , 799, LL18

[19] Tombesi, F., Sambruna, R. M., Reeves, J. N., et al. 2010, *ApJ* , 719, 700

[20] Tombesi, F., Sambruna, R. M., Reeves, J. N., Reynolds, C. S., & Braito, V. 2011, *MNRAS* , 418, L89

[21] Tombesi, F., Sambruna, R. M., Marscher, A. P., et al. 2012, *MNRAS* , 424, 754

[22] Similar *Fermi*-LAT analysis paper for 3C 120 by Sahakyan et al. [14] was posted on the arXiv during the review process of our original paper Tanaka et al. [18].

Gamma-ray light curve and VLBI polarization connection in Mrk 421

M. Giroletti[a], F. D'Ammando[a,b], M. Orienti[a], D. Paneque[c] on behalf of the *Fermi*-LAT collaboration
R. Lico[a,b], G. Giovannini[a,b], J. L. Gómez[d], S. Jorstad[e], A. Marscher[e]
[a] *INAF Istituto di Radioastronomia, Bologna, 40129, Italy*
[b] *University of Bologna, Department of Physics and Astronomy, Bologna, 40127, Italy*
[c] *Max-Planck-Institut für Physik, Föhringer Ring 6, 80805 München, Germany*
[d] *Instituto de Astrofísica de Andalucia, IAA-CSIC, Apdo. 3004, 18080 Granada, Spain*
[e] *Institute for Astrophysical Research, Boston University, Boston, MA 02215, USA*

We present *Fermi*-LAT and multi-frequency, multi-epoch VLBA data for the TeV blazar Mrk 421. We collected the data during a long and intensive multi-frequency campaign in 2011. We study the gamma-ray light curve, the photon index evolution and their connection to the radio data on sub-parsec scales, including total intensity, polarized flux density, polarization angle, spectral index, and rotation measure both in the core and the jet region. The VLBA data were obtained at 15 and 24 GHz for 12 epochs and at 43 GHz for 23 epochs, thus providing the best temporal and spatial coverage in the radio band ever achieved for a TeV blazar. We provide significant constraints on the jet Doppler factor, the presence of proper motion, the magnetic field configuration, and an intriguing connection between variability in the radio data and the gamma-ray light curve: the total intensity and polarized core emission reach a peak simultaneously to the main gamma-ray peak, followed by a rotation of the polarization angle at low frequency. Opacity-related, long wavelength polarization swings are also detected later in the year, possibly related to secondary peaks in the gamma-ray light curve, setting constraints on the physics of the gamma-ray zone.

1. INTRODUCTION

Multi-wavelength variability studies provide an extraordinary opportunity to break degeneracies between the various blazar emission models [8, 11, 15], which predict flux variations (at a given energy band) with particles of different energies, cooling times, and cross sections for different processes [7]. However, the complexity in resolving the underlying processes occurring in blazars can only be achieved through a well-sampled dedicated monitoring from radio to gamma rays lasting several years. Indeed, some of the latest and most interesting results on blazars come precisely from variability studies from well-sampled coordinated years-long multi-instrument observations [1, 6, 13]. Unluckily, these multi-instrument observations were performed on flat spectrum radio quasars, but not on TeV BL Lac objects [with the exception of BL Lacertae, 12], perhaps owing to the fact that these sources were challenging to observe in radio and gamma rays. The advent of *Fermi*-LAT and the current generation of Cherenkov telescopes (H.E.S.S., MAGIC and VERITAS) permits the accurate and systematic (regardless of the activity level) monitoring of the high energy bump, where a large fraction of the blazar emission is produced. In addition, recent works have shown that TeV blazars can be successfully imaged with the VLBA at up to 43 GHz, revealing the core and the inner jet structure with great accuracy [14]. Therefore, the currently available instrumentation allows to study these sources with an unprecedented level of detail, which has the potential to shed light on the understanding of these complex objects.

In order to address the challenge involved in breaking the degeneracy between models, we have organized the most ambitious multifrequency monitoring to date of the famous TeV BL Lac object Mrk 421, covering sub-mm (SMA), optical/IR (GASP), UV/X-ray (*Swift*, RXTE, MAXI), and gamma rays (*Fermi*-LAT, MAGIC, VERITAS). We summarize here the main results of the multi-frequency, multi-epoch, full polarization VLBA observations and of the gamma-ray *Fermi*-LAT monitoring through 2011 [3, 9, 10].

Throughout this paper, we adopt $H_0 = 70$ km sec^{-1} Mpc^{-1}, $\Omega_M = 0.25$ and $\Omega_\Lambda = 0.75$, in a flat Universe, so that at the redshift of Mrk 421 ($z = 0.031$), 1 mas = 0.59 pc. Spectral and photon indexes α and Γ are defined such that the radio flux density and the gamma-ray photon flux are proportional to $\nu^{-\alpha}$ and $E^{-\Gamma}$, respectively; angles are measured from north through east.

2. OBSERVATIONS

2.1. Radio observations

We observed Mrk 421 with the VLBA for 12 times (once per month) throughout 2011 at 15, 24, and 43 GHz; at the latter frequency, we expanded our dataset with 11 more observations obtained through the VLBA-BU-BLAZAR monitoring program. We carried out a full calibration and analysis describing the evolution with time of total intensity and polarized flux density, and of their combinations such as spectral index and rotation measure. Core and inner jet are spatially resolved and separately analyzed. Spatial resolution is as good as 0.2 pc at 43 GHz and sensitivity just below 1 mJy/beam.

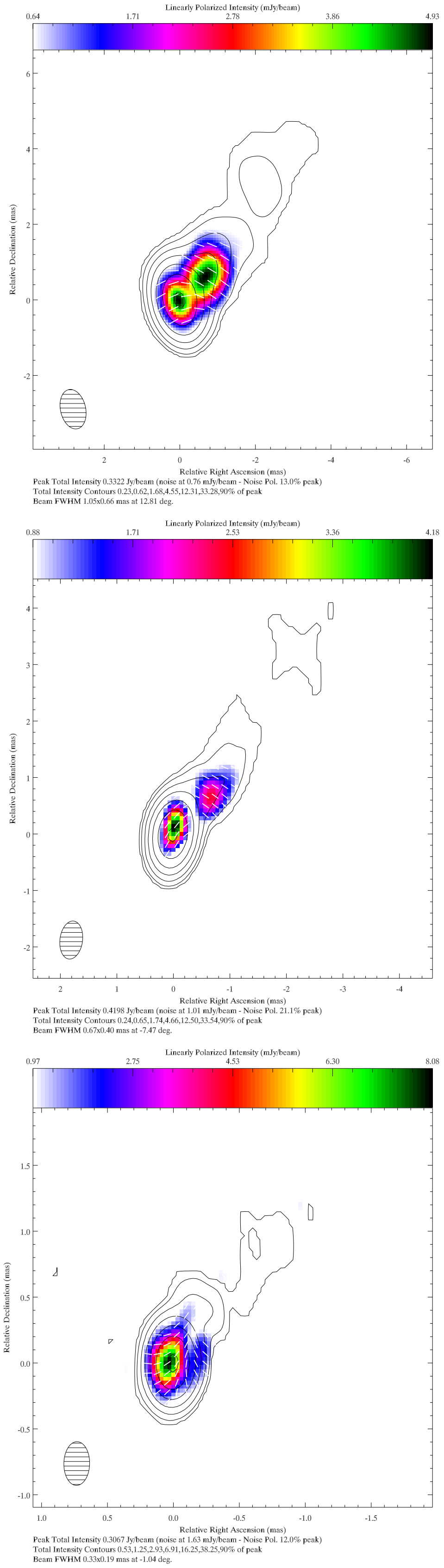

Figure 1: VLBA images of Mrk 421 at 15 GHz (top, 2011 January), 24 GHz (middle, 2011 February), and 43 GHz (bottom, 2011 April).

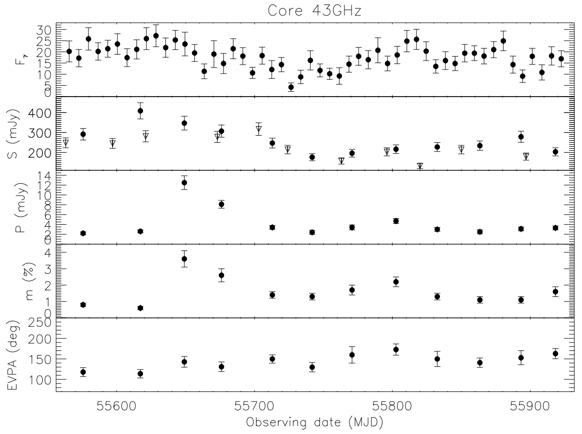

Figure 2: Mrk 421 43 GHz core parameters as a function of time. From top to bottom panel: gamma-ray light curve (0.1 to 100 GeV, in 10^{-8} ph cm^{-2} s^{-1} units, shown for comparison), total intensity flux density, polarized flux density, fractional polarization, EVPA. In the total flux density panel (second panel from top), filled circles indicate data from the main set of observations, empty triangles indicate additional data from the VLBA-BU-BLAZAR monitoring project.

2.2. Gamma-ray observations

We analyzed gamma-ray data from the Large Area Telescope on board *Fermi*, which continuously scans the whole sky in the energy range 100 MeV $< E <$300 GeV. We analyzed the data with the ScienceTools software package version v9r32p5, using instrument response functions P7REP_SOURCE_V15 and following the standard procedures[1]. Mrk 421 is bright enough to be significantly detected in every weekly bin, and we obtained photon flux and photon index for every bin.

3. RESULTS

We present sample images at the three frequencies in total intensity and polarization in Figure 1. In the following subsections, we describe the main results about the radio emission from the core (Sect. 3.1) and jet (Sect. 3.2), and the unresolved gamma-ray source (Sect. 3.3).

3.1. Radio core

The core is the most prominent feature in the radio images. It is bright and compact at all epochs and

---

[1] `http://fermi.gsfc.nasa.gov/ssc/data/analysis/documentation/Cicerone/`

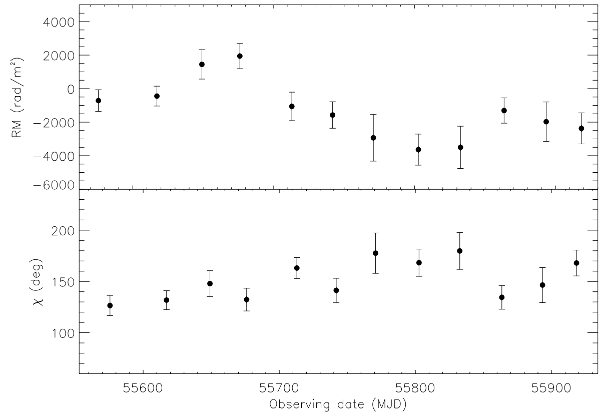

Figure 3: Mrk 421 core rotation measure (top panel) and intrinsic EVPA (bottom panel) as a function of time throughout 2011.

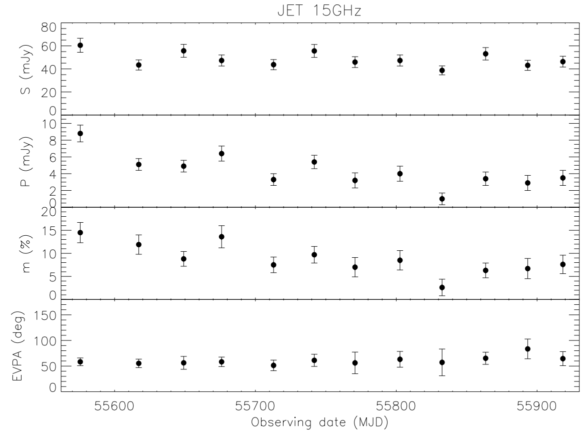

Figure 4: Mrk 421 15 GHz jet parameters as a function of time. From top to bottom panel: total intensity flux density, polarized flux density, fractional polarization, EVPA.

frequencies and it shows variability in total intensity and polarization. We show its light curve and the time evolution of its polarization properties in Figure 2, along with the gamma-ray light curve that is described later on (Sect. 3.3).

The radio core light curve showed a broad peak around 2011 February-March at all frequencies. This peak is particularly prominent at 43 GHz, thanks to the improved sampling offered by the additional 11 observations from the Boston University blazar monitoring project. In particular, the core flux density reached its peak of $S_{43} = 415$ mJy on 2011 March 1 at 43 GHz. The core spectrum is generally flat, with average spectral indexes $\alpha_{15}^{24} = 0.16$ and $\alpha_{24}^{43} = 0.43$. The spectral index shows a flatter when brighter behaviour.

The core polarization properties are also variable: the polarization fraction varies as a function of both frequency (being $\sim 1\%$ at 15 and 24 GHz and $\sim 2\%$ at 43 GHz) and time, with a $(3.6 \pm 0.5)\%$ peak on 2011 March 29. The electric vector position angle (EVPA) χ has some fluctuations, which are more prominent at low than at higher frequency. At 43 GHz, it oscillates slightly with a mean value of 144° and a standard deviation of 17°, being overall well aligned to the jet axis. At 15 GHz, we detect two prominent 90° flips in July and September, most likely due to opacity; even after correcting these values, there is larger variability with a mean of 119° and a standard deviation of 29°.

Epoch by epoch, we performed a χ vs λ^2 fit to determine the rotation measure RM and the intrinsic EVPA χ_0 in the source, under the assumption that the frequency dependence of the observed EVPA's is due to Faraday rotation effect. The evolution of RM and χ_0 is shown in Figure 3. The RM values oscillate between −3000 and 2000 rad m^{-2}.

3.2. Radio jet

The VLBA data clearly detect a one-sided jet at all three frequencies. The jet extends for about 5 mas (3 pc) in PA −35° at 15 GHz and somewhat less as frequency increases. In Figure 4, we show the total intensity and polarized flux density, the fractional polarization, and the EVPA of the jet emission at 15 GHz, from top to bottom.

We do not detect any prominent variation in neither the jet's structure nor its total intensity flux density. In particular, we did not detect any significant superluminal motion of components [3, 10]; as a matter of fact, we do not detect well defined, compact jet components at all. At a reference distance of 1.5 mas from the core, the jet-counterjet brightness ratio is $R > 30$. The spectrum is steeper than in the core.

In polarization, we detect emission from the jet at 15 and 24 GHz, with a fractional polarization value that is much larger than in the core ($\sim 15\%$). However, given the steep spectrum of the jet and its low surface brightness, at 43 GHz the polarized emission is below the noise level. The EVPA in the jet is remarkably stable, with a mean of 61° and a standard deviation of just 9°. Given the jet axis PA of −35°, this means that the EVPA is nearly orthogonal to the direction of the flow, and the magnetic field well aligned with it.

3.3. Gamma-ray source

Mrk 421 is point like at the *Fermi* angular resolution. This is not only true for the angular scales probed by the VLBA observations presented here but also when we consider the total extent of the source as mapped by compact interferometers best suited to

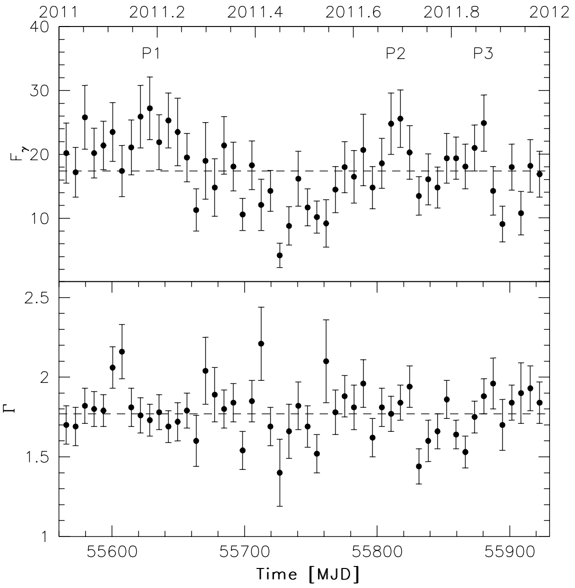

Figure 5: Mrk 421 gamma-ray parameters as a function of time. Top: photon flux; bottom: photon index. The dashed lines indicate the 1-yr mean value.

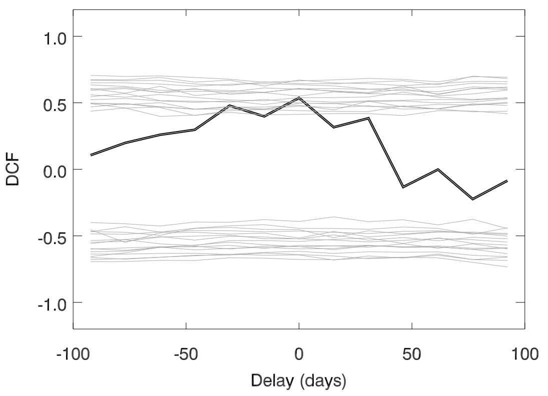

Figure 6: DCF results for Mrk 421, considering gamma-ray *Fermi* data and 43 GHz VLBA data. Black line: observed data; gray curves: 99.7% confidence level threshold obtained from the combination of different PSD slopes.

map a possible large scale diffuse emission [5]. However, the variability time scales observed for the high energy emission and the broadband spectral energy distribution modelling [2] clearly suggest that most of the gamma-ray photons are produced in a compact region of size smaller than the radio core itself.

During 2011, the mean photon flux and the photon index are $F = (17.4 \pm 0.5) \times 10^{-8}$ ph cm^{-2} s^{-1} and $\Gamma = 1.77 \pm 0.02$, respectively. The light curve on weekly time bins shown in Figure 5 (top panel) reveals variability, with three peaks in 2011 March, September, and November. The brightest week is that between 2011 March 5 and 11, (MJD 55 625-55 631), with a gamma-ray flux as large as $(38 \pm 11) \times 10^{-8}$ ph cm^{-2} s^{-1}. The photon index on the other hand is quite stable and we do not find any evidence for spectral variability (see Figure 5, bottom panel).

4. DISCUSSION

The results from the radio observations suggest that the jet is not strongly Doppler boosted already on parsec scale. This stems from the low brightness temperature estimated both from the variability time scales ($T_{\rm B,\,var} \sim 2.1 \times 10^{10}$ K) and the core size and flux density ($T_{\rm B} \sim 10^{11}$ K) [10]. On the contrary, TeV variability on time scales of about 30 minutes [4], and both hadronic (synchrotron proton blazar) or leptonic (one-zone synchrotron self-Compton scenario) fits to the broadband spectral energy distribution require Doppler factors δ in excess of ~ 10, and possibly as large as $\delta = 50$ [2]. This so-called "Doppler factor crisis" characterizes also other TeV blazars; the most natural way to solve this crisis is to localize the radio and the gamma-ray emission zones in different regions; typically, a velocity structure of the jet is assumed, either along or across the jet axis.

In our case, we have the possibility to compare the radio and gamma-ray light curves and to carry out a discrete cross-correlation function (DCF) analysis for the two datasets. In particular, we carried out a DCF analysis over a range of radio-gamma ray delays between -100 and $+100$ days, with a bin of 15 days. We find a peak for the correlation (0.54) is obtained for $\Delta t = 0$ day delay. In order to assess the significance of this peak, we generated 3000 fake light curves with the same mean and standard deviation as the observed light curves but with variable power spectral densities (PSD). We show in Figure 6 the results of our DCF analysis on the real data compared to those obtained for various combinations of the simulated ones. In particular, the peak is significant at the $> 99.7\%$ confidence level for the combinations of light curves with short time scale gamma-ray variability ($\beta_{\gamma-{\rm ray}} < 1.5$) and longer time scale radio variability ($1 < \beta_{\rm r} < 2.5$).

As for the magnetic field configuration in the radio core and jet, we found somewhat discrepant results. The core B-field perpendicular to the jet axis is typical of shocked regions; in the jet, the magnetic field is aligned with the jet axis; possible interpretations of this result include stretching of an initially transverse magnetic field by a layered velocity structure and an helical field with a small pitch angle. Finally, we note that the variability features in the polarized flux light curve indicate also a connection between magnetic field and gamma-ray emission.

Acknowledgments

The *Fermi*-LAT Collaboration acknowledges support for LAT development, operation and data analysis from NASA and DOE (United States), CEA/Irfu and IN2P3/CNRS (France), ASI and INFN (Italy), MEXT, KEK, and JAXA (Japan), and the K.A. Wallenberg Foundation, the Swedish Research Council and the National Space Board (Sweden). Science analysis support in the operations phase from INAF (Italy) and CNES (France) is also gratefully acknowledged.

We acknowledge financial contribution from grant PRIN-INAF-2011. Part of this work was done with the contribution of the Italian Ministry of Foreign Affair. Part of this work was supported by the Marco Polo program of the University of Bologna and the COST Action MP0905 "Black Holes in a Violent Universe". The research at the Instituto de Astrofisica de Andalucia was supported in part by the Spanish Ministry of Economy and Competitiveness grant AYA2010-14844 and by the Regional Government of Andalucía (Spain) grant P09-FQM-4784. The research at Boston University was supported in part by NASA through Fermi grants NNX08AV65G, NNX08AV61G, NNX09AT99G, NNX09AU10G, and NNX11AQ03G, and by US National Science Foundation grant AST-0907893.

References

[1] Abdo, A. A., Ackermann, M., Ajello, M., et al. 2010, Nature, 463, 919

[2] Abdo, A. A., Ackermann, M., Ajello, M., et al. 2011, ApJ, 736, 131

[3] Blasi, M. G., Lico, R., Giroletti, M., et al. 2013, A&A, 559, A75

[4] Gaidos, J. A., Akerlof, C. W., Biller, S., et al. 1996, Nature, 383, 319

[5] Giroletti, M., Giovannini, G., Taylor, G. B., & Falomo, R. 2006, ApJ, 646, 801

[6] Jorstad, S. G., Marscher, A. P., Larionov, V. M., et al. 2010, ApJ, 715, 362

[7] Krawczynski, H., Coppi, P. S., & Aharonian, F. 2002, MNRAS, 336, 721

[8] Krawczynski, H., Sambruna, R., Kohnle, A., et al. 2001, ApJ, 559, 187

[9] Lico, R., Giroletti, M., Orienti, M., et al. 2014, A&A, 571, A54

[10] Lico, R., Giroletti, M., Orienti, M., et al. 2012, A&A, 545, A117

[11] Maraschi, L., Fossati, G., Tavecchio, F., et al. 1999, ApJ, 526, L81

[12] Marscher, A. P., Jorstad, S. G., D'Arcangelo, F. D., et al. 2008, Nature, 452, 966

[13] Marscher, A. P., Jorstad, S. G., Larionov, V. M., et al. 2010, ApJ, 710, L126

[14] Piner, B. G., Pant, N., & Edwards, P. G. 2010, ApJ, 723, 1150

[15] Tavecchio, F., Maraschi, L., & Ghisellini, G. 1998, ApJ, 509, 608

Suzaku and Fermi Observations of Gamma-Ray Bright Radio Galaxies: Origin of the X-ray Emission and Broad-Band Modeling

Y. Fukazawa, S. Tokuda, R. Itoh, Y. Tanaka
Department of Physical Science, Hiroshima University; Hiroshima Astrophysical Science Center, Hiroshima University
J. Finke
U.S. Naval Research Laboratory
L. Stawarz
Institute of Space and Astronautical Science, JAXA; Astronomical Observatory, Jagiellonian University

We performed a systematic X-ray study of eight nearby γ-ray bright radio galaxies with *Suzaku* for understanding the origin of their X-ray emissions. The *Suzaku* spectra for five of those have been presented previously, while the remaining three (M 87, PKS 0625−354, and 3C 78) are presented here for the first time. Based on the Fe-K line strength, X-ray variability, and X-ray power-law photon indices, and using additional information on the [O III] line emission, we argue for a jet origin of the observed X-ray emission in these three sources. We also analyzed five years of *Fermi* Large Area Telescope (LAT) GeV gamma-ray data on PKS 0625−354 and 3C 78 to understand these sources within the blazar picture. We found significant γ-ray variability in the former object. Overall, we note that the *Suzaku* spectra for both PKS 0625−354 and 3C 78 are rather soft, while the LAT spectra are unusually hard when compared with other γ-ray detected low-power (FR I) radio galaxies. We demonstrate that the constructed broad-band spectral energy distributions of PKS 0625−354 and 3C 78 are well described by a one-zone synchrotron/synchrotron self-Compton model. The results of the modeling indicate lower bulk Lorentz factors compared to those typically found in other BL Lac objects, but consistent with the values inferred from modeling other LAT-detected FR I radio galaxies. Interestingly, the modeling also implies very high peak ($\sim 10^{16}$ Hz) synchrotron frequencies in the two analyzed sources, contrary to previously-suggested scenarios for FR I/BL Lac unification. We discuss the implications of our findings in the context of the FR I/BL Lac unification schemes.

1. Introduction

This contribution is based on Fukazawa et al. [2015]. Here, we very briefly describe the digest. *Fermi* Large Area Telescope (LAT) established that radio galaxies are bright gamma-ray emittors [Abdo et al. 2010]. However, inner jet emission has been detected mainly in the radio and GeV gamma-ray band for most object, due to bright stellar and accretion disk components in the optical and X-ray band; Spectral Energy Distribution (SED) of jet emission is often unclear, even for Cen A and NGC 1275. Thus, X-ray detection of jet emission is important for SED modeling.

Suzaku X-ray satellite has observed 8 nearby GeV-emitting radio galaxies listed in Abdo et al. [2010]; some of observations are originally proposed by ourselves. Most of *Suzaku* results has been published, and some of them exhibit a Fe-K line (3C 111, 3C 120, NGC 1275, Cen A) and others do not (NGC 6251, M 87). Here we report *Suzaku* and *Fermi* results on PKS 0625−354 and 3C 78[Fukazawa et al. 2015].

2. X-ray Results

Figure 1 shows *Suzaku* X-ray spectra of PKS 0625−354 and 3C 78. Quality of X-ray spectra are better than ever for both objects. We fitted their spectra by one or two plasma model plus power-law model. The former represents a soft thermal emission associated with host galaxies. The spectra are well fitted by this modeling, and the power-law photon index is 2.25±0.02 and 2.32±0.04 for PKS 0625−354 and 3C 78, respectively. This value is relatively larger for Seyfert galaxies whose X-ray emission is dominated by disk/corona emission. Fe-K line is not detected for both; an upper limit of equivalent width (EW) of Fe-K line is 7 eV and 75 eV for PKS 0625−354 and 3C 78, respectively. X-ray time variation during one *Suzaku* observation is weak or little. We compared X-ray peoperties with those of Seyfert galaxies, together with other GeV-emitting radio galaxies. Fe-K line EWs of PKS 0625−354 , 3C 78, M 87, NGC 6251 are smaller tha those of typical Seyfert galaxies as shown in figure 2. Fe-K line is emitted when the X-ray emission from the central disk/corona region is reflected by the dust torus with a large reflection angle. Therefore, a weak or no Fe-K line indicates that the X-rays are not a disk/corona emission but likely a beamed jet emission. X-ray luminosity of PKS 0625−354 is higher than that of typical Seyfert galaxies with a smilar [O III] luminosity. Combined with studies of other X-ray properties, such as spectral index, variability, X-ray emission of low excitation radio galaxies (LERG), which are considered to have a low mass accretion rate, is likely to be a jet emission.

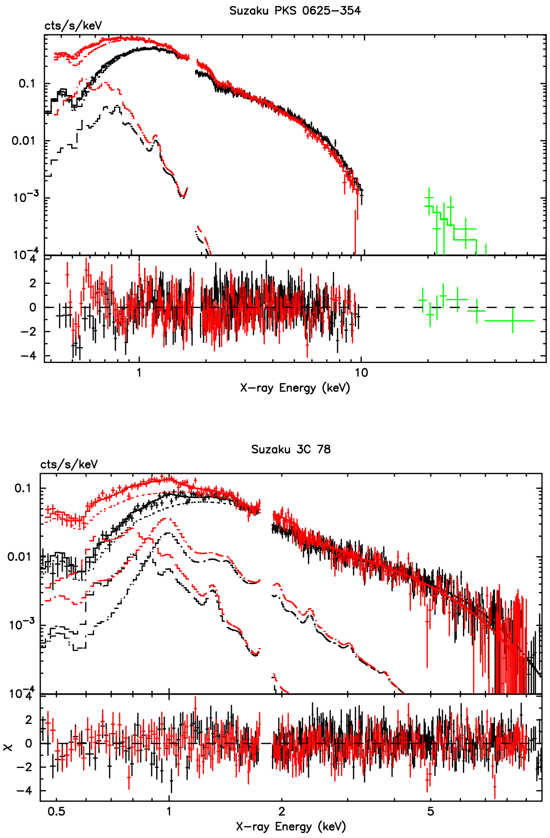

Figure 1: *Suzaku* spectra of PKS 0625−354 and 3C 78. The black, red, and green symbols are XIS-F, XIS-B, and HXD-PIN spectra, respectively. The solid line represents the best-fit total model, while the dashed and dotted lines are the `apec` and power-law model components, respectively. The bottom panels show the residuals in units of σ.

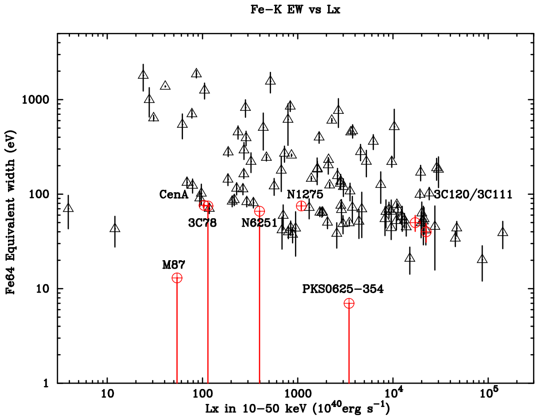

Figure 2: Fe-K line EW plotted against the X-ray luminosity for our sample of radio galaxies (red circles) and Seyfert galaxies (black triangles) analyzed by Fukazawa et al. [2011]. The data points with only the lower error bar represent upper limits.

3. GeV Gamma-ray results and SED

We analyzed *Fermi* LAT 5 years data of PKS 0625−354 and 3C 78. For the analysis, LAT Science Tools version v9r32p5 was utilized with the `P7REP_SOURCE_V15` Instrument Response Functions (IRFs). Both radio galaxies are clearly visible in the 0.2 to 300 GeV LAT counts maps. We extracted the data within a 12×12 deg^2 rectangular region centered on each object. The binned likelihood fitting with the `gtlike` tool was performed. The field background point sources within 14.5° from each source, listed in the LAT 2 year catalog [Nolan et al. 2012], were included. The standard LAT Galactic emission model was used (`gll_iem_v05.fits`) and the isotropic diffuse gamma-ray background and the instrumental residual background were represented as a uniform background (`iso_source_v05.txt`). A likelihood analysis was performed with the energy information binned logarithmically in 30 bins in the 0.2–300 GeV band, and the spatial information binned with 0.15×0.15 deg^2 bin size.

Gev gamma-ray spectra of both galaxies show a flat power-law with a photon index of 1.72±0.06 and 2.01±0.16 for PKS 0625−354 and 3C 78, respectively. Studies of time variability show a flare-like event for PKS 0625−354 and no significant variation for 3C 78. Figure 3 and 4 shows a SED of both galaxies, based on our *Suzaku* and *Fermi* data and other available data. SEDs are well modellded by the one-zone synchrotron self-Compton model from Finke et al. [2008]. Compared with other GeV-emitting radio galaxies whose results were also all done by the same model of Finke et al. [2008], lower bulk Lorentz factors of 2–6 are preferred when compared to those of typical blazars. An unique property of PKS 0625−354 and 3C 78is a higher breaking energy of electron spectrum. This is attributed to higher SED-peaking energies of both galaxies (figure 3, 4). Considering this property, we plot the Synchrotron peak luminosity against the Synchrotron peaking frequency as shown in figure 5, where most of other data of blazars and radio galaxies are taken from Meyer et al. [2011]. For this plot, Meyer et al. [2011] states the high-E peaked objects are only the most aligned jet objects with radiatively inefficient accretion and decelerating weak jet. However, PKS 0625−354 and 3C 78are outliers of this model, and thus they are at odds with the FR-I/BL Lac unification.

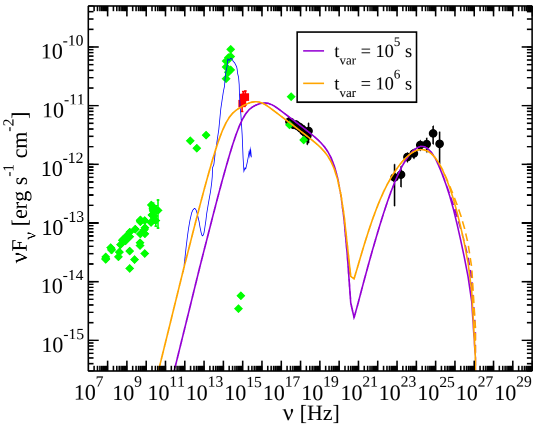

Figure 3: SEDs of PKS 0625−354 . Black circles indicate the *Suzaku* X-ray and *Fermi*-LAT γ-ray data presented in this paper, green diamonds are archival data. The thick curves denote the synchrotron/SSC model fits with two different variability timescales, as given in the legend. The solid curves include $\gamma\gamma$ absorption with the EBL model of **?**, while the dashed curves do not. The thin

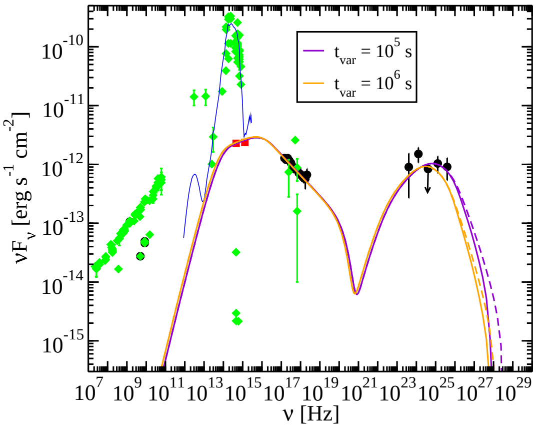

Figure 4: SEDs of 3C 78. Same as figure 3.

it

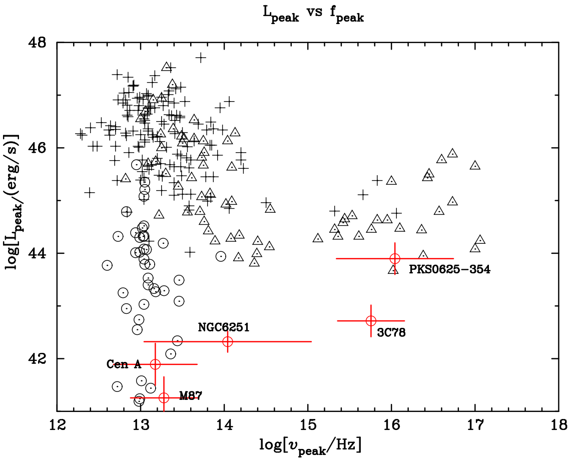

Figure 5: Relation between synchrotron peak frequencies and peak luminosities of PKS 0625−354 and 3C 78, together with other sources from our sample of radio galaxies (red **circles**). For a comparison, radio galaxies, BL Lacs, and FSRQs from Meyer et al. [2011] are also plotted (black circles, triangles, and crosses, respectively).

References

Abdo, A. A., Ackermann, M., Ajello, M., et al. 2010b, Science, 328, 725

Finke, J. D., Dermer, C. D., Böttcher, M. 2008, ApJ, 686, 181

Fukazawa, Y., Hiragi, K., Mizuno, M., et al. 2011a, ApJ, 727, 19

Fukazawa, Y., Finke, J., Stawarz, Ł., et al. 2015, ApJ, 798, 74

Meyer, E. T., Fossati, G., Georganopoulos, M., & Lister, M. L. 2011, ApJ, 740, 98

Nolan, P. L., Abdo, A. A., Ackermann, M., et al. 2012, ApJS, 199, 31

Using Likelihood for Combined Data Set Analysis

B. Anderson
Wallenberg Academy Fellow. Stockholm, Sweden.
J. Chiang
W. W. Hansen Experimental Physics Laboratory, Kavli Institute for Particle Astrophysics and Cosmology, Department of Physics and SLAC National Accelerator Laboratory, Stanford University, Stanford, CA 94305, USA
J. Cohen-Tanugi
Laboratoire Univers et Particules de Montpellier, Université Montpellier 2, CNRS/IN2P3, Montpellier, France
J. Conrad
Department of Physics, Stockholm University, AlbaNova, SE-106 91 Stockholm, Sweden
The Oskar Klein Centre for Cosmoparticle Physics, AlbaNova, SE-106 91 Stockholm, Sweden
Royal Swedish Academy of Sciences Research Fellow, funded by a grant from the K. A. Wallenberg Foundation and
The Royal Swedish Academy of Sciences, Box 50005, SE-104 05 Stockholm, Sweden
A. Drlica-Wagner
Center for Particle Astrophysics, Fermi National Accelerator Laboratory, Batavia, IL 60510, USA
M. Llena Garde and S. Zimmer
Department of Physics, Stockholm University, AlbaNova, SE-106 91 Stockholm, Sweden and
The Oskar Klein Centre for Cosmoparticle Physics, AlbaNova, SE-106 91 Stockholm, Sweden
on behalf of the Fermi LAT Collaboration

The joint likelihood is a simple extension of the standard likelihood formalism that enables the estimation of common parameters across disjoint datasets. Joining the likelihood, rather than the data itself, means nuisance parameters can be dealt with independently. Application of this technique, particularly to Fermi-LAT dwarf spheroidal analyses, has already been met with great success. We present a description of the method's general implementation along with a toy Monte-Carlo study of its properties and limitations.

1. Introduction

Several recent studies [Ackermann et al. 2011, 2012a,b, 2014a,b] by the LAT Collaboration successfully apply the joint likelihood technique, combining constraints for searches ranging from galaxy cluster emission to effects of large extra dimensions. In the following, we introduce the technique from a more generic standpoint and compare/contrast it with other common methods of data combination. We proceed with the aid of a toy Monte-Carlo (MC) to demonstrate the method's properties and explore some interesting behavior.

2. Likelihood analysis, Joint likelihood, and basic data stacking

2.1. Likelihood

The likelihood incorporates information regarding both model and experiment into a function whose maximization provides an estimate of the true parameter values. It can be expressed as

$$\mathcal{L}(\alpha|\mathcal{D}) = P(\mathcal{D}|\alpha), \tag{1}$$

where P is the probability of outcome, $\mathcal{D}$, given the parameter α. Parameters are often separated into those of interest, $\boldsymbol{\mu}$, and nuisance, $\boldsymbol{\theta}$, in order to profile or marginalize the latter.

We will focus on the specific form of $\mathcal{L}$ to be a binned Poisson probability function so that

$$\mathcal{L}(\boldsymbol{\mu}, \boldsymbol{\theta}|\mathcal{D}) = \prod_k \frac{\lambda_k^{n_k} e^{-\lambda_k}}{n_k!}, \tag{2}$$

where the symbols $\lambda(\boldsymbol{\mu}, \boldsymbol{\theta})$ and n represent the predicted and observed counts in a given bin, k. The parameters $(\hat{\boldsymbol{\mu}}, \hat{\boldsymbol{\theta}})$ which yield the greatest value for $\mathcal{L}$ are known as the maximum likelihood estimate (MLE).

When testing a hypothesis, the MLE likelihood must be compared with that of the null hypothesis, i.e. a model lacking the effect(s) of interest, where $\boldsymbol{\mu} \equiv \boldsymbol{\mu}_0$. Typically, we compare the logarithms of the two likelihoods with a measure called the Test Statistic:

$$\mathrm{TS} = -2 \ln \left(\frac{\mathcal{L}(\hat{\boldsymbol{\mu}}_0, \hat{\boldsymbol{\theta}}|\mathcal{D})}{\mathcal{L}(\hat{\boldsymbol{\mu}}, \hat{\boldsymbol{\theta}}|\mathcal{D})} \right). \tag{3}$$

When its distribution is known, the TS can be mapped to a p-value associated with the alternative hypothesis. In most cases, it obeys the asymptotic theorem

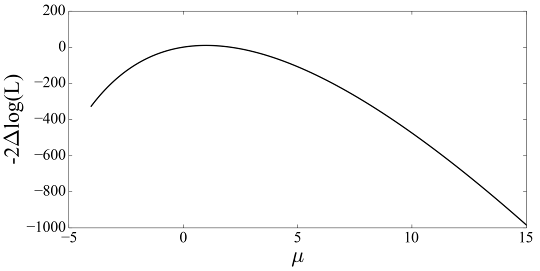

Figure 1: A typical delta log-likelihood profile for a single-parameter source with no signal.

[Chernoff 1954] and follows a $\chi^2/2$ with degrees of freedom equal to the number of free signal parameters (assuming signal is constrained to be positive). There are scenarios (some are mentioned in Section 4 and Ackermann et al. [2014a]) where this does not hold, and one must derive the TS behavior from a set of control data, e.g. with Monte-Carlo.

Once the distributions are known, confidence intervals can be set for parameters by exploring the log-likelihood space surrounding the MLE. Figure 1 illustrates a typical delta log-likelihood profile for a simple system where there is only one free parameter that controls the strength of the new phenomenon. Within the asymptotic regime, confidence limits would be set at levels corresponding to the χ^2 probability density function, e.g. a difference of 2.71 from the maximum indicates 90% one-sided coverage.

2.2. Joint Likelihood

To make use of a joint likelihood, one presumably has N datasets which share some signal parameter(s), $\boldsymbol{\mu}$. The procedure for joining is analogous to the way binned probabilities make up $\mathcal{L}$ — simply take the product of each set's likelihood [Conrad 2015]. Explicitly,

$$\mathcal{L}_{\text{joint}}(\boldsymbol{\mu}, \boldsymbol{\theta}|\boldsymbol{\mathcal{D}}) = \prod_{d=1}^{N} \mathcal{L}(\boldsymbol{\mu}_d, \boldsymbol{\theta}_d|\mathcal{D}_d) \tag{4}$$

This construction is clean in the sense that the data sets remain disjoint. Each could have different backgrounds, exposures, or have even come from different instruments. All these characteristics (nuisance parameters) are accounted for in the individual likelihoods.

2.3. Data stacking

Alternative methods for combining data exist, the most basic of which being to evaluate the likelihood of the data set union. That is, instead of

$$\prod_{d=1}^{N} \mathcal{L}(\boldsymbol{\mu}_d, \boldsymbol{\theta}_d|\mathcal{D}_d), \tag{5}$$

we evaluate the stacked data likelihood:[1]

$$\mathcal{L}(\boldsymbol{\mu}, \boldsymbol{\theta}| \cup \boldsymbol{\mathcal{D}}). \tag{6}$$

Here, data sets are lumped together and then the hypothesis test is performed with respect to a model which is also the sum of individual expectations. Switching to Pearson's χ^2 and keeping the notation from the previous section, a stacked test statistic might look like this:

$$\chi^2_{\text{stack}}(\boldsymbol{\mu}, \boldsymbol{\theta}) = \frac{\sum_k \left[\sum_d n_{d,k} - \sum_d \lambda_{d,k}(\boldsymbol{\mu}, \boldsymbol{\theta})\right]^2}{\sum_{d,k} \lambda_{d,k}(\boldsymbol{\mu}, \boldsymbol{\theta})} \tag{7}$$

As before, parameters are adjusted to optimize (in this case minimize) the χ^2. Significance and confidence intervals are directly interpreted according to the expected probability density function.

Although easily done, it is not difficult to envision problems with such a strategy. Data sets with weak signal-to-noise wash out when combined with those which are larger, though not necessarily more constraining. This method throws away information and is therefore not optimal.

One can do better by combining *residuals*, i.e.

$$\chi^2_{\text{resid}}(\boldsymbol{\mu}, \boldsymbol{\theta}) = \sum_{d,k} \frac{\left[n_{d,k} - \lambda_{d,k}(\boldsymbol{\mu}, \boldsymbol{\theta})\right]^2}{\lambda_{d,k}(\boldsymbol{\mu}, \boldsymbol{\theta})} \tag{8}$$

This is a much more viable alternative to the joint likelihood method. Depending on the situation, however, its implementation can be tricky. For example, suppose that the predicted number of events also depends on some nuisance parameter, ϵ (e.g. time or exposure). Uncertainties on this parameter can be accounted for by adding an additional term to χ^2_{resid} if they can be modeled as Gaussian. If not, there is no obvious way to include them in the data stacking approach, whereas modifying the likelihood is straightforward for any known model of the nuisance parameter uncertainty.

3. Properties

3.1. Toy Model

To illustrate the fundamental properties of the method, we employ a simple toy MC model for com-

---

[1] A common example would be the addition of counts maps.

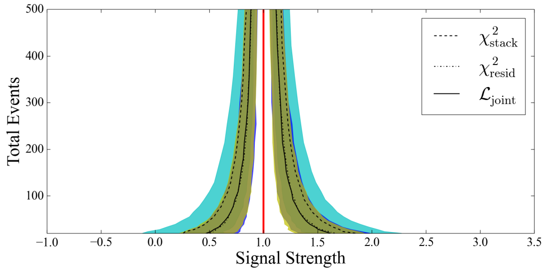

Figure 2: Confidence intervals on the shared signal parameter, μ, derived for two single-bin data sets with signal-to-background ratios of 1:1 and 1:10. For an increasing number of total counts, 1000 MC realizations determine the median intervals for each method of combination. Bands represent the 68% containment among realizations.

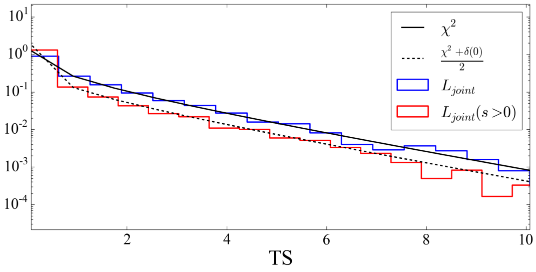

Figure 3: TS distribution of two-set joint likelihood for both unconstrained and positive-only signal fits, along with the corresponding expected asymptotic distributions.

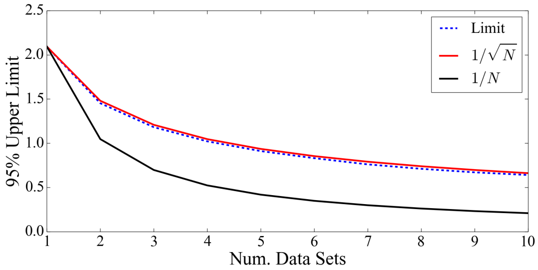

Figure 4: Behavior of toy-model upper limits with the addition of sets. Signal-to-background is 1:10 with 100 total events.

bining constraints: single-bin data sets with Poisson counts generated according to

$$\begin{aligned} \lambda_d(\boldsymbol{\mu},\boldsymbol{\theta}) &= \mu \cdot s_d + b_d \qquad (9)\\ \boldsymbol{\mu} &= \{\mu, s_d\} \\ \boldsymbol{\theta} &= \{b_d\} \end{aligned}$$

Each set may have a different number of total events and has a background determined by the nuisance parameter, b. Signal is determined from an individual, s_d, and common scale factor parameter, μ. The latter is the value we wish to estimate.

3.2. Confidence Interval, Coverage, and Power.

As a starting point, we investigate the combination of two sets with signal-to-background ratios of 1:1 and 1:10. Fig. 2 illustrates how the confidence intervals behave as a function of total events for the χ^2_{stack}, χ^2_{resid}, and $\mathcal{L}_{\mathrm{joint}}$ formulations. In all scenarios, the coverage adheres to the nominal value and the limits improve in approximate proportion to the square root of the set size. As expected, we see that the χ^2 formed from residuals out-performs the simple stack (by yielding a tighter interval), and matches the joint likelihood.

The TS distribution of the two-set joint likelihood is depicted in Fig. 3. Note that the distribution is halved (with the remaining stacked at zero TS) when the signal parameter is constrained to be greater than zero.

3.3. Effects of Additional Data Sets

Increasing the number of data sets comprising the joint likelihood naturally improves the power and tightens the limits, albeit at a rate dependent on their signal-to-noise ratios. As long as the model uncertainties remain consistent, sets can be added indefinitely with no ill effect on the sensitivity. As an example, see Fig. 4, where 95% confidence upper limits are calculated with a cumulative number of toy-model sets. Each set is identical, with signal-to-noise equal to 1:10 with 100 total events. In this regime, limits improve with the square root of the number of sets, N.

In certain situations the joint upper limits can improve even more rapidly. Any time $\ln[\mathcal{L}_{\mathrm{joint}}] \propto \mu$ holds throughout the allowed range of μ, the constraints scale in direct proportion to N. For example, a very low background might give a Poissonian likelihood, resulting in linear log-space behavior. Forming the joint likelihood in log-space consists of adding these profiles together. For the case of a set of linear functions, the limit level is then proportional to the sum of the slopes, i.e.

$$\mu_{\mathrm{UL}} \propto \left(\sum_d \frac{\partial \mathcal{L}_d}{\partial \mu}\Big|_{\mu=0} \right)^{-1}. \qquad (10)$$

The sum can be reduced to N in the case of set of profiles with identical slopes. See Fig. 5 where a low background induces an appreciable effect.

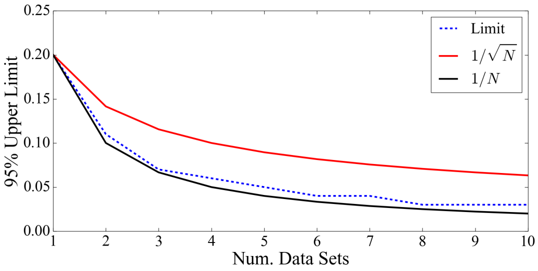

Figure 5: Behavior of upper limits with the addition of data sets, with very low background $[(s, b) = (1,0.1)]$ and the constraint that $s > 0$.

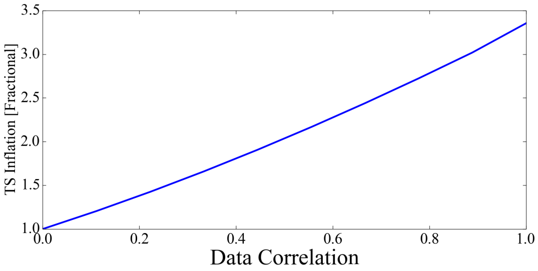

Figure 6: The inflation of TS as two equivalent data sets gradually overlap.

4. Caveats

4.1. Overlapping Data Sets

It is best to avoid overlap between data sets. If they do, then where there is signal, the TS will be erroneously increased by double-counting (Figure 6), approximately in direct proportion to the percentage of overlap [See also appendix of Ackermann et al. [2014b]]. When constructing a TS distribution, the significance derived from low-probability fluctuations will be similarly inflated. See Figure 7, where this is demonstrated using the preceding toy model. The upward skew there indicates that type II errors are more common than usual, effectively lowering the sensitivity of the study.

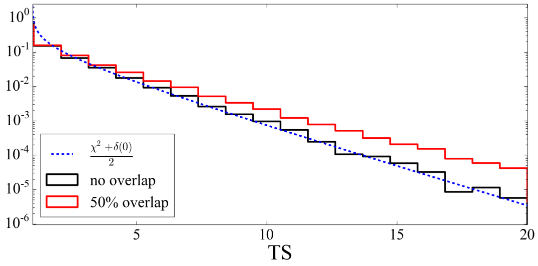

Figure 7: Effect on the null distribution from a 50% overlap correlation between a two-set joint likelihood.

5. Discussion and Conclusions

The technique of joint likelihood, already widely used among Fermi-LAT Collaboration analyses, provides a straightforward and universal tool for combining constraints from astrophysical targets and other disjoint data sets. We demonstrate that it matches the performance of residual stacking, and note that it often requires less effort to implement. We model and describe the method's behavior in two interesting regimes: first for very low background and second for the case of overlapping data sets. The possible applications of the technique have by no means been exhausted and we encourage its continued use. Lastly, we plan to expand on studies of the method's behavior in an upcoming publication.

Acknowledgments

The authors wish to thank JACoW for their guidance in preparing this template.

Work supported by Department of Energy contract DE-AC03-76SF00515.

References

M. Ackermann et al. (Fermi-LAT Collaboration), Phys.Rev. **L107**, 241302 (2011), 1108.3546.

M. Ackermann et al. (Fermi-LAT Collaboration), Science **338**, 1190 (2012a), 1211.1671.

M. Ackermann et al. (Fermi-LAT Collaboration), JCAP **2**, 012 (2012b), 1201.2460.

M. Ackermann et al. (Fermi-LAT Collaboration), Phys.Rev. **D89**, 042001 (2014a), 1310.0828.

M. Ackermann et al. (Fermi-LAT Collaboration), ApJ **787**, 18 (2014b), 1308.5654.

H. Chernoff, Ann. Math. Statist. **25**, 573 (1954), URL `http://www.jstor.org/stable/2236839`.

J. Conrad, Astroparticle Physics **62**, 165 (2015), 1407.6617.

Calorimeter-only analysis of the Fermi Large Area Telescope

M. Takahashi
The University of Tokyo
R. Caputo
University of California Santa Cruz
D. Paneque
Max Planck Institute for Physics, The University of Tokyo
C. Sgrò
INFN Sezione di Pisa
on behalf of the Fermi-LAT collaboration

arXiv:1503.01364v1 [astro-ph.HE] 4 Mar 2015

Above tens of GeV, γ-ray observations with the *Fermi* Large Area Telescope (LAT) can be dominated by statistical uncertainties due to the low flux of sources and the limited acceptance. We are developing a new event class which can improve the acceptance: the "Calorimeter-only (CalOnly)" event class. The LAT has three detectors: the tracker, the calorimeter, and the anti-coincidence detector. While the conventional event classes require information from the tracker, the CalOnly event class is meant to be used when there is no usable tracker information. Although CalOnly events have poor angular resolution and a worse signal/background separation compared to those LAT events with usable tracker information, they can increase the instrument acceptance above few tens of GeV, where the performance of Fermi-LAT is limited by low photon statistics. In these proceedings we explain the concept and report some preliminary characteristics of this novel analysis.

1. Introduction

The *Fermi* Large Area Telescope (*Fermi* LAT) is an instrument on the *Fermi* γ-ray telescope operating from 20 MeV to over 300 GeV. The instrument is a 4×4 array of identical towers, each one consisting of a tracker–converter (TKR), based on Silicon detector layers interleaved with Tungsten foils, where the photons have a high probability of converting to pairs, which are tracked to allow reconstruction of the γ-ray direction and a segmented calorimeter (CAL), made of CsI crystal bars, where the electromagnetic shower is partially absorbed to measure the γ-ray energy. The tracker is covered with an anti-coincidence detector (ACD) to reject the charged-particle background. Further details on the LAT, its performance, and calibration are given by [1] and [2].

Most of the science done with *Fermi* LAT spans photons with energies from 50 MeV to about 10 GeV, where the sensitivity of the instrument is good and the available number of detected photons high. However, there are many sources which emit γ-rays above a few tens of GeV. These energies that are almost accessible by the current generation of Imaging Atmospheric Cherenkov Telescopes (IACTs). Even though the detection area of LAT is small (in comparison to that of IACTs), *Fermi* LAT provides all-sky coverage and a very high duty cycle, which are crucial characteristics for producing γ-ray source catalogs and study source variability in an unbiased way. A prime example is the the first *Fermi* LAT catalog of >10 GeV sources (1FHL) [3], which contains 514 sources, out of which $\sim$100 sources have already been detected at very high energies(>100 GeV, or VHE), and $\sim$200 additional sources have been identified as good candidates to be VHE emitters and be detected with IACTs.

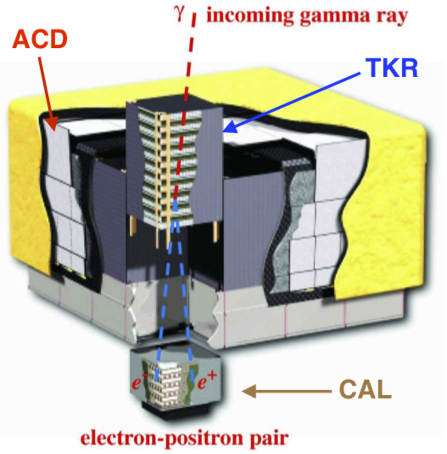

Figure 1: Schematic diagram of the Large Area Telescope. The telescopes dimensions are 1.8m × 1.8m × 0.72m. [1]

The performance of *Fermi* LAT above 10 GeV is excellent. The angular resolution and signal/background separation is best at the highest photon energies, where one only suffers from a slight deterioration of the energy resolution due to the fact that the showers are no longer contained in the calorimeter. However, the steep falling photon flux with energy of most γ-ray sources, together with the relatively small effective area of LAT ($\sim$1m^2), results in a substantial limitation due to the very low number of detected photons (e.g., in the 1FHL, many sources were characterized with only 4–5 photon events over a background signal of 0–1 event). The low statistics from γ-ray sources is going to be an even larger problem for the second *Fermi* high-energy LAT catalog (2FHL, in preparation), which is expected to consist on γ-ray sources detected above 50 GeV (instead of 10 GeV).

In these proceedings we report an analysis which can help increase the photon statistics at few tens of GeV, hence improving the ability to perform science at the highest LAT energies, where the IACTs start operating. The methodology is still being developed. Here we only present the concept and report some preliminary characteristics.

2. The Calorimeter-only (CalOnly) Fermi-LAT analysis

The regular *Fermi* LAT event classes require usable information from the TKR. This is a sensible approach, given that the TKR information is crucial to determine accurately the incoming direction of the γ-ray event. The LAT TKR comprises only $\sim$1.5 radiation lengths (on axis), which means that a large fraction of γ-rays from the astrophysical sources are discarded at the very beginning of the analysis because they do not convert in the TKR, or they convert in the bottom layers and the TKR information is not sufficient for a proper determination of the incoming direction of the γ-ray event. This situation is depicted in Figure 2.

In the standard LAT analysis, the CAL is essentially used for signal/background separation (together with the TKR and ACD) and to determine the energy of the γ-rays and electrons. The LAT has a hodoscopic calorimeter, consisting of 16 towers with 8 layers of 12 crystals each because of three driving reasons. First, shower profiling improves energy reconstruction. Next, shower topology contains valuable information for signal/background separation. Last, it realizes independent event acceptance and reconstruction.

To create a usable event class without using TKR information, one must determine the incoming direction of the γ-rays with sufficient resolution (a few degrees) while keeping a reasonable background rejection ($\sim$0.999).This would increase the number of available high-energy events for performing γ-ray astronomy. The above mentioned (non-standard) LAT analysis, dubbed Calorimeter-only (CalOnly) analysis, is currently being developed by the *Fermi* LAT collaboration, and is aimed to deliver yet another class of events, the CalOnly event class, which may be added to the other photon event classes coming from the regular LAT analysis. For the CalOnly analysis, it fully reconstructs the electromagnetic showers and determine its main axis, which points to the direction of the incoming γ-ray event.

Since the main event trigger for LAT is based on the TKR, those events with no usable TKR information have a low chance of being recorded and transferred to the ground. However, large energy depositions in CAL generate a trigger that is fully independent of TKR, and on-board event selection records events that deposit energy larger than 20 GeV in CAL. Consequently, the CalOnly event class will only be effective above a few tens of GeV.

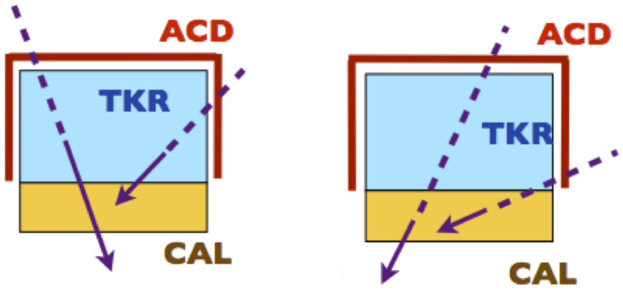

Figure 2: The left panel depicts two events that convert to electron pairs in the TKR (from the broken lines to the solid lines in these figures). These events would be used in the regular *Fermi* LAT analysis. The right panel shows two events without usable TKR information. One is a side-entering event that goes through a small fraction of the TKR. The other one crosses the entire TKR, but converts to an electron pair in the CAL. These two events would be rejected and not be used for regular LAT analysis. These are the type of events which could be recovered with a dedicated analysis that does not require TKR information, the so-called CalOnly events.

2.1. Pass 8

The development of the CalOnly analysis is done in the context of Pass 8, which is the new iteration of the LAT event-level analysis package. Pass 8 was originally designed to address the effect of coincidences with cosmic rays (‘ghost’ events), but quickly evolved in a comprehensive revision of the instrument simulation, the event reconstruction, and the background rejection, with the goal of improving all the aspects of the LAT performance: larger acceptance, better angular and energy resolution, and extension of the energy reach below 100 MeV and in the TeV range.

The details on the Pass 8 analysis chain can be found in [4]. The CAL reconstruction begins with a clustering stage that tries to isolate the genuine γ-ray shower from smaller energy deposition due to ghost events. At this point we can exploit the segmentation of the CAL to identify the energy deposition centroid and the shower axis (via a moment analysis) that, for CalOnly, corresponds to the photon incoming direction. This direction is propagated to the ACD (in addition to the tracks from the tracker) in order to associate energy deposition in the tiles and discriminate charged particle without the TKR direction. This is one of the main improvements introduced with Pass 8 and proved to be very useful even if its separation

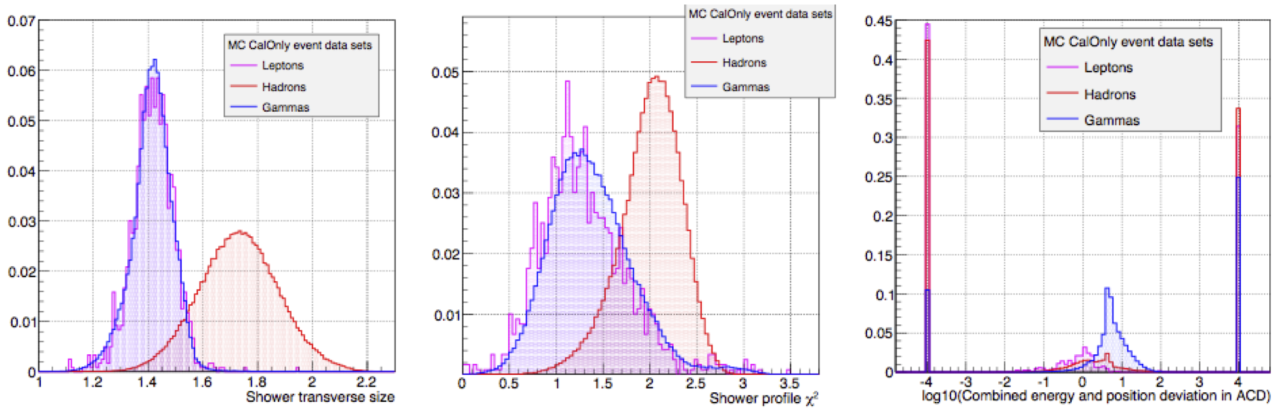

Figure 3: The left, middle and right panels show the logarithm of the CAL first cluster transverse profile RMS, the logarithm of χ^2 of the profile fit computed over a 100mm radius cylinder around the trajectory, and the logarithm of combined energy and position deviation in ACD respectably. The last one needs some more description. It is the number of sigmas less than an expected MIP signal, combined with the number of sigmas the track propagation is away from tile or ribbon most likely to veto the first CAL cluster and the number of sigmas the energy deposited in the ACDs is away from the expected amount. If the value of this combined quantity is zero, then the log10 of this quantity is set to -4. This is more likely to happen to MIPs than for γ-rays. If there are no tracks associated to ACD signals, this quantity is set to +4. Charge particles are likely to have smaller values than the γ-rays.

capability is limited by the angular resolution of the CAL, that is obviously worse than that of the TKR..

Another important improvement in the CAL reconstruction is the energy measurement that, for CalOnly, is based on a full three-dimensional fit of the shower energy deposition. This method needs a precise modeling of the longitudinal and lateral development of showers inside the CAL and a reference axis. The latter, usually taken from the tracker, can be obtained from the aforementioned moment analysis with a small change in performance.

The last step of the Pass 8 development is the high-level analysis that links together all the outputs of the reconstruction and classify events as good γ rays or not. This is the core of the CalOnly development and is described in next section.

2.2. Signal / Background separation

The *Fermi* LAT needs to reject a cosmic-ray background that outnumbers the signal (γ rays) by many orders of magnitude, and hence an efficient signal/background separation (rejecting 10^{3-4} of the background events) is required to be able to perform γ-ray astronomy. The LAT background consists mostly on protons and electrons, but also on alpha particles and heavy nuclei. As the γ-ray energy increases, we have a natural improvement in the signal/background ratio due to the fact that most γ-ray sources have spectra that can be parameterized with power-law indices harder than 2.5 (often even harder than 2.0), while the spectra of the proton background follows a power-law index of ~2.7 and that of the electrons a power-law index of ~3.1.

The rejection of the background cosmic-ray events in the CalOnly analysis is based on the different topology of electromagnetic and hadronic showers, and the ACD signals produced by the charged particles. It is worth noting that, while protons and heavy nuclei can be effectively distinguished from γ rays using only information from the CAL, the electrons/positrons produce electromagnetic showers that are essentially identical to those of the γ rays, and hence the information from the ACD is crucial to be able to reject electrons. The left and middle panels in Figures 3 show the normalized MC distributions of two CAL-related parameters that can effectively distinguish between electromagnetic (*gammas* and leptons) and hadronic showers. In order to be able to reject the leptons, one needs the help of ACD-related parameters, as depicted in the right panel in Figure 3.

In order to maximize the separation of signal and background, instead of making simple cuts in the distributions of CAL and ACD parameters as the ones shown above, we perform the analysis through a multivariate analysis (MVA) that uses a large number of CAL and ACD parameters. For the most effective background rejection, we applied the Boosted Decision Tree (BDT), one of the methods of multi-variate analysis. In this method, we train many classification trees with Monte Carlo (MC) data, for which can identify unambiguously what is signal and what is background. We are using the ROOT-based TMVA package to train the classification tree analysis [5]. We build the trees and then evaluate the gamma-likeness of each event. Next we can cut on the gamma-likeness and get the events classified as signal or background. By selecting events with a very high gamma-likeness,

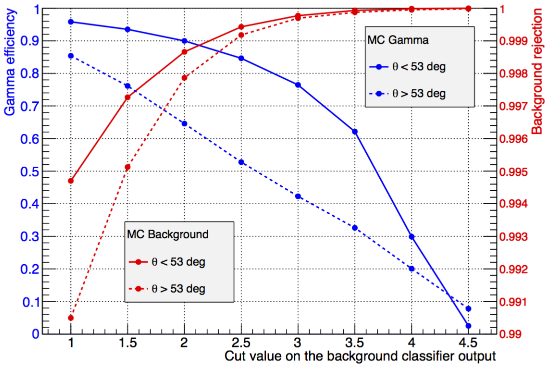

Figure 4: Efficiency of MC γ events (blue) and rejection of MC background events (red) vs. cut value of a classifier output.

one can increase the purity of the selected data set, but at the expense of reducing the number of γ-ray candidates. This is represented in Figure.4. The optimal value to increase the signal/background is typically obtained for a cut value between 2 and 3 (dependent on the energy range and incidence angle of the γ-ray considered).

At the present time we are optimizing the classification tree by modifying the input CAL and ACD parameters (including creating new composite variables), as well as by building the classification trees in different modes. Consequently, the results presented in this proceedings should be considered as preliminary, and likely reporting a lower limit of the actual performance of the CalOnly analysis.

2.3. Quality of the reconstructed events

In this section we address the quality of the reconstructed CalOnly events (after signal/background separation) using dedicated MC simulations of γ-ray events.

Two basic quantities are being evaluated: the angular and the energy resolution. Given that the thickness of the calorimeter increases rapidly with the incidence angle, one expects a different performance for low and high incidence angle γ rays. In this section we define low (high) incidence angle as smaller (larger) than 53 degrees ($\cos(53°) \sim 0.6$) and evaluate the performance for these two cases. And naturally, as it occurs in the regular *Fermi* LAT analysis, the performance can also vary with the energy of the incoming γ ray. Here we define low (high) energy as being in the range ∼30-100 GeV (∼100-300 GeV), and evaluate the performance for these two energy bands.

Figure 5 shows the normalized distributions in the error of the reconstructed directions for low/high energy bands and incidence angles. The angular resolution can be defined as the 68% containment in those distributions (PSF68), which would result in ∼2 degrees for high inclination γ rays, and ∼3–4 degrees for low inclination γ rays (with a relatively small dependence on the energy). The PSF68 for regular LAT photons (i.e. with usable TKR information) at these energies is ∼0.1–0.2 degrees, which is more than one order of magnitude better than for CalOnly photons.

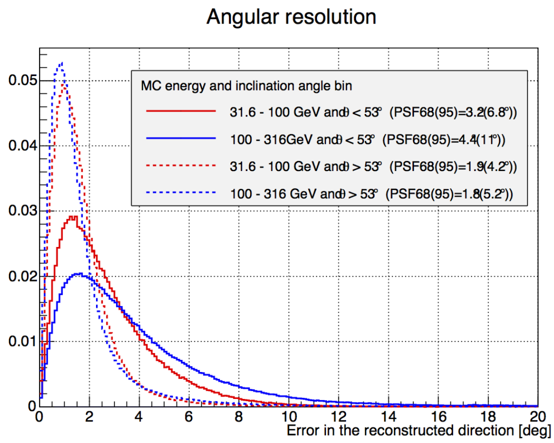

Figure 5: Normalized histograms of the angular distances between reconstructed and MC direction of CalOnly events in 2 inclination angle × 2 energy bins.

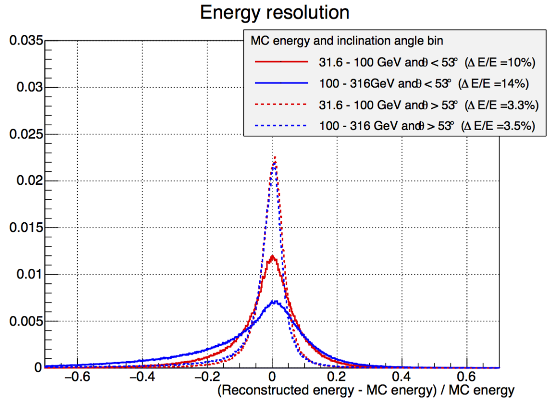

Figure 6: Normalized histograms of the dispersions in the reconstructed energy of MC CalOnly events in 2 inclination angles × 2 energy bins.

Figure 6 shows the normalized distributions in the error of the reconstructed energies for low/high energy bands and incidence angles. The energy resolution can also be defined as the 68% containment on these distributions, and using the largest distance from the peak position to the edge of the 68% containment. The energy resolution is $\sim 3-4\%$ for high inclination and $\sim 10-15\%$ for low inclination γ-rays, with little dependence on the energy of the event. This performance is very close to that of regular LAT photons. The quality of the energy reconstruction is mainly connected to the path length of shower axis (related to the shower containment) and the accuracy of the shower direction reconstruction. While the latter is worse for CalOnly events, this class can benefit from a larger field of view and therefore longer trajectories. It must be noted that both direction and energy resolution can be improved with a dedicated selection of good quality events, at the price of a lower effective area. The best trade off between these conflicting requirements is still to be evaluated.

3. Conclusions

Pass 8 provides an unprecedented framework to develop an analysis that uses events without usable TKR information.

The CalOnly event class, currently under development within the Fermi-LAT collaboration, could be used to increase the acceptance of *Fermi* LAT above few tens of GeV (where the performance is photon statistics limited), by recovering for astronomical studies γ-ray events without usable TKR information. This implies that CalOnly events will have a worse signal/background separation and angular resolution, when compared to the regular LAT events. However, they can have a better energy resolution, if considering the high incidence angle events.

The CalOnly event class may be particularly relevant in the following two scientific topics:

- Search for line-signals potentially coming from Dark Matter annihilation (because of the larger number of events and the excellent energy resolution for the large-incident angle events)
- Study of transient events like GRBs and AGN flares (because of the larger number of events and the valuable increase in the temporal coverage of the source)

Acknowledgments

The *Fermi*-LAT Collaboration acknowledges support for LAT development, operation and data analysis from NASA and DOE (United States), CEA/Irfu and IN2P3/CNRS (France), ASI and INFN (Italy), MEXT, KEK, and JAXA (Japan), and the K.A. Wallenberg Foundation, the Swedish Research Council and the National Space Board (Sweden). Science analysis support in the operations phase from INAF (Italy) and CNES (France) is also gratefully acknowledged.

We would like to thank M. Wood for developing a python module for multi-variate analysis, which was heavily used in this study.

References

[1] W. B. Atwood *et al.* “THE LARGE AREA TELESCOPE ON THE FERMI GAMMA-RAY SPACE TELESCOPE MISSION”, 2009, ApJ 697 1071

[2] M. Ackermann *et al.* “The Fermi Large Area Telescope on Orbit: Event Classification, Instrument Response Functions, and Calibration”, 2012, ApJS, 203, 4

[3] M. Ackermann *et al.* “THE FIRST FERMI-LAT CATALOG OF SOURCES ABOVE 10 GeV”, 2013 ApJS 209 34

[4] W. B. Atwood *et al.* “Pass 8: Toward the Full Realization of the Fermi-LAT Scientific Potential”, 2013, arXiv:1303.3514 [astro-ph.IM].

[5] A. Hoecker *et al.* “TMVA4 Users Guide”, 2013, arXiv:physics/0703039

Fermi Communications and Public Outreach

L. Cominsky, A. Simonnet and the Fermi E/PO team

Sonoma State University, Rohnert Park, CA, 94928 USA

The Sonoma State University (SSU) Education and Public Outreach (E/PO) group participates in the planning and execution of press conferences that feature noteworthy *Fermi* discoveries, as well as supporting social media and outreach websites. We have also created many scientific illustrations for the media, tools for amateur astronomers for use at star parties, and have given numerous public talks about *Fermi* discoveries.

1. PRESS CONFERENCES AND PRESS RELEASES

Beginning with the activities leading up to the launch of *Fermi* on June 11, 2008, there have been many press conferences, media telecons, press releases and news features that showcase the discoveries and news about *Fermi*. Table I summarizes the number of news releases and features issued each year since launch, as well as each year's top stories that were showcased in press briefings or media telecons. Many of the press briefings occurred at scientific conferences including: the American Astronomical Society (AAS) winter and summer meetings, the American Physics Society (APS) April meeting, the AAS High Energy Astrophysics Division (HEAD) meeting, and the American Geophysical Union (AGU) annual meeting. For complete links see `http://fermi.gsfc.nasa.gov/ssc/library/news/`

1.1. Science Magazine Covers

Fermi discoveries in 2009 and 2014 were the subject of cover stories in *Science* magazine. Illustrations by Aurore Simonnet that depicted the discoveries were chosen for cover art. The 2009 publications featured *Fermi* observations of pulsars while the 2014 cover portrayed GRB 130427A, one of the brightest gamma-ray bursts ever seen. This GRB was observed by many experiments on Earth and in space, including *Fermi*. Figure 1 shows the *Science* cover art illustrating GRB 130427A.

1.2. Fermi Pulsar Interactive Explorer

Developed by SSU's Kevin John, this interactive map illustrated the Fermi pulsar discoveries that were highlighted in a media telecon on 3 November 2011. For each pulsar observed by Fermi, the interactive provides the pulse rate, location and a user-friendly description of the pulsar's significant observations. The pulsar videos in this interactive have been viewed more than 145,000 times to date. The pulsar interactive can be viewed at: `http://www.nasa.gov/externalflash/fermipulsar/`

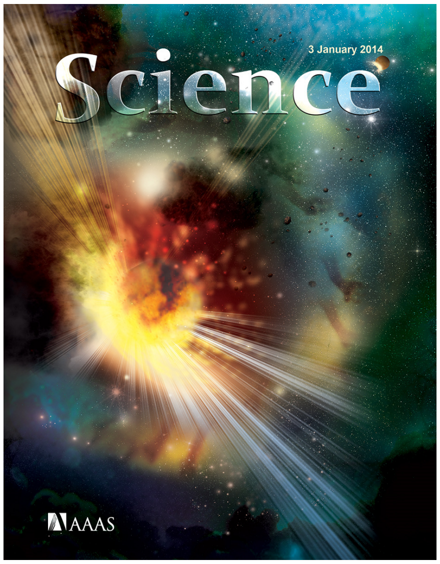

Figure 1: *Science* magazine cover from 3 January 2014 illustrating GRB 130427A, a "shockingly bright" gamma-ray burst

1.3 YouTube and SVS Videos

NASA Goddard's Scientific Visualization Studio (SVS) employs many talented animators and illustrators that help explain *Fermi*'s scientific discoveries to the public. Many press briefings, media telecons, press releases and news features include illustrations and video products that help to explain the extreme Universe that *Fermi* observations are revealing. Since launch, the number of views of *Fermi* videos on the SVS website (`http://svs.gsfc.nasa.gov`) has exceeded 3.4 million. Table II lists *Fermi* SVS videos with more than 100,000 views, along with viewing statistics and the SVS reference numbers.

Beginning in 2011, animated media products that were created to illustrate press releases and briefings have been uploaded to NASA's YouTube channel. Table III lists *Fermi* YouTube videos with more than 50,000 views, along with viewing statistics and the YouTube reference codes.

Table I Media Releases and Briefings

Year	Releases	Media Events
2008	9	Launch Coverage, First Light
2009	13	Pulsars (AAS), Space Time (NASA), Star Factories (Fermi Symposium)
2010	7	Millisecond Pulsars (AAS), SNR (APS), Extragalactic Background (HEAD), Fermi Bubbles (NASA)
2011	9	Anti-matter from Thunderstorms, Non-constant Crab (AAS), Millisecond Pulsar (NASA)
2012	5	High-energy Sky (AAS), Dwarf Galaxies and Dark Matter (APS), Ancient starlight (Fermi Symposium)
2013	8	Black Hole Flares (AAS), Fermi Turns 5 (NASA)
2014	9	Gravitational Lens (AAS), Blazar Batteries (AAS), Thunderstorms (AGU)

Table II Fermi SVS Videos with more than 100,000 views to date

Video	Date	Views	SVS Number
GLASTcast for iTunes	3 Jun 2008	321,408	10250
Einstein's Cosmic Speed Limit	28 Oct 2009	258,721	10510
Terrestrial Gamma-ray Flashes Create Antimatter	10 Jan 2011	169,945	10706
Fermi Discovers Youngest Millisecond Pulsar	3 Nov 2011	160,499	10858
Fermi Sees a Nova	12 Aug 2010	150,080	20184
Fermi Pulsar Interactive Videos	3 Nov 2011	145,118	10861
Fermi Observations of Dwarf Galaxies Provide New Insights on Dark Matter	2 Apr 2012	117,882	10943
Stellar Odd Couple Makes Striking Flares	29 Jun 2011	109,434	10798
Fermi's Latest Gamma-ray Census Highlights Cosmic Mysteries	9 Sep 2011	105,726	10819

2. PUBLIC OUTREACH

From the top of Mt. Tamalpais to seniors in Oakmont to amateur astronomers all across the USA, E/PO lead Lynn Cominsky has given dozens of public lectures about blazing galaxies, monstrous black holes and the extreme Universe as seen by *Fermi*. Other US *Fermi* team members who have given many public talks include LAT Principal Investigator Peter Michelson, Project Scientist Julie McEnery, Deputy Project Scientist David Thompson, and team member Roopesh Ojha.

The "make your own pulsar model" activity is one of *Fermi*'s most popular public engagements, and was originally featured on the back of the *Fermi* lithograph and in the Supernova Educator's Guide, both developed by the SSU E/PO team. This shining model is suitable for kids of all ages, and teaches about pulsars as well as about simple circuit design, using a battery and an LED. It has been showcased at the American Astronomical Society student engagement events for the past three years, as well as at many public open house events, including the SLAC-KIPAC open house, school science fairs, and the North Bay Discovery Days. Figure 2 shows Lucy and Abby Dilbeck demonstrating the pulsar model at a recent SLAC-KIPAC Open House.

Figure 2: Lucy and Abby Dilbeck demonstrate how to make your own model pulsar

2.1. Epo's Chronicles

From 2008 - 2013, the SSU E/PO team produced over 200 weekly "eposodes" of Epo's Chronicles, a web comic that illustrated the adventures of Alkina and her sentient spaceship Epo. Alkina and Epo traveled through the galaxy, learning about space science and searching for their origins. Translated from English into French, Italian and Spanish, these popular comic strips were viewed by thousands each month. During 2012 (the last complete year of the webcomic), over 80,000 unique IP addresses viewed the site. External evaluations of Epo's Chronicles indicated that "Participants particularly liked the "Web 2.0" aspect of the comic, and the use of links to learn more and pursue various topics in a multimedia platform." In addition, the "artwork was highly praised." Figure 3 shows one of the comics related to *Fermi*.

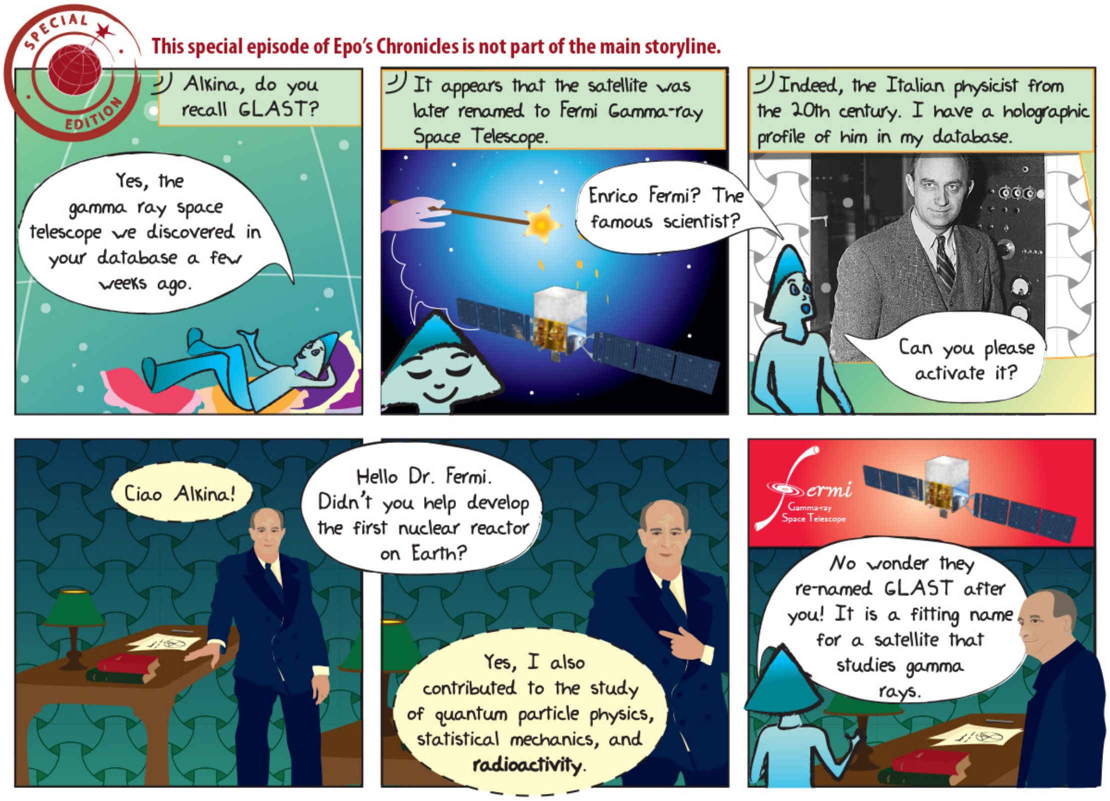

Figure 3: Epo's Chronicles special "eposode" about *Fermi*

2.2. Citizen Science through a *Fermi*-LIGO Collaboration

The collaboration between *Fermi* and the Laser Interferometer Gravitational-wave Observatory's Einstein@Home project was advertised with a postcard-sized handout inviting participants to try to discover a gamma-ray pulsar using *Fermi* data. Several have been discovered by citizen scientists running the Einstein@Home program on their home computers as a screen saver. The postcard is shown in Figure 4.

Figure 4: Einstein@Home postcard inviting the public to search for pulsars in the *Fermi* data

2.3. *Fermi* Skymap Poster

The poster shown in Figure 5 was created in 2012 by Aurore Simonnet for distribution at the *Fermi* Symposium in Rome. Eight major *Fermi* discoveries are called out from the iconic image of the high-energy gamma-ray sky as seen by the Large Area Telescope through 2011. The discoveries that are illustrated include:

- CTA1, the first gamma-ray-only pulsar
- Nova V407 Cygni, the first gamma-ray nova
- Repeated gamma-ray flares from the active galaxy 3C454.3
- Resolved GeV gamma rays from the supernova remnant W44
- Giant gamma-ray lobes emanating from the center of the Milky Way now known as the *Fermi* bubbles
- Resolved extended gamma rays surrounding the active galaxy Centaurus A
- Flaring gamma-ray emission and changing x–ray emission from the Crab nebula, previously thought to be a constant "standard candle"
- GRB 090510A, the distant short gamma-ray burst that was used to set limits on the foaminess of spacetime

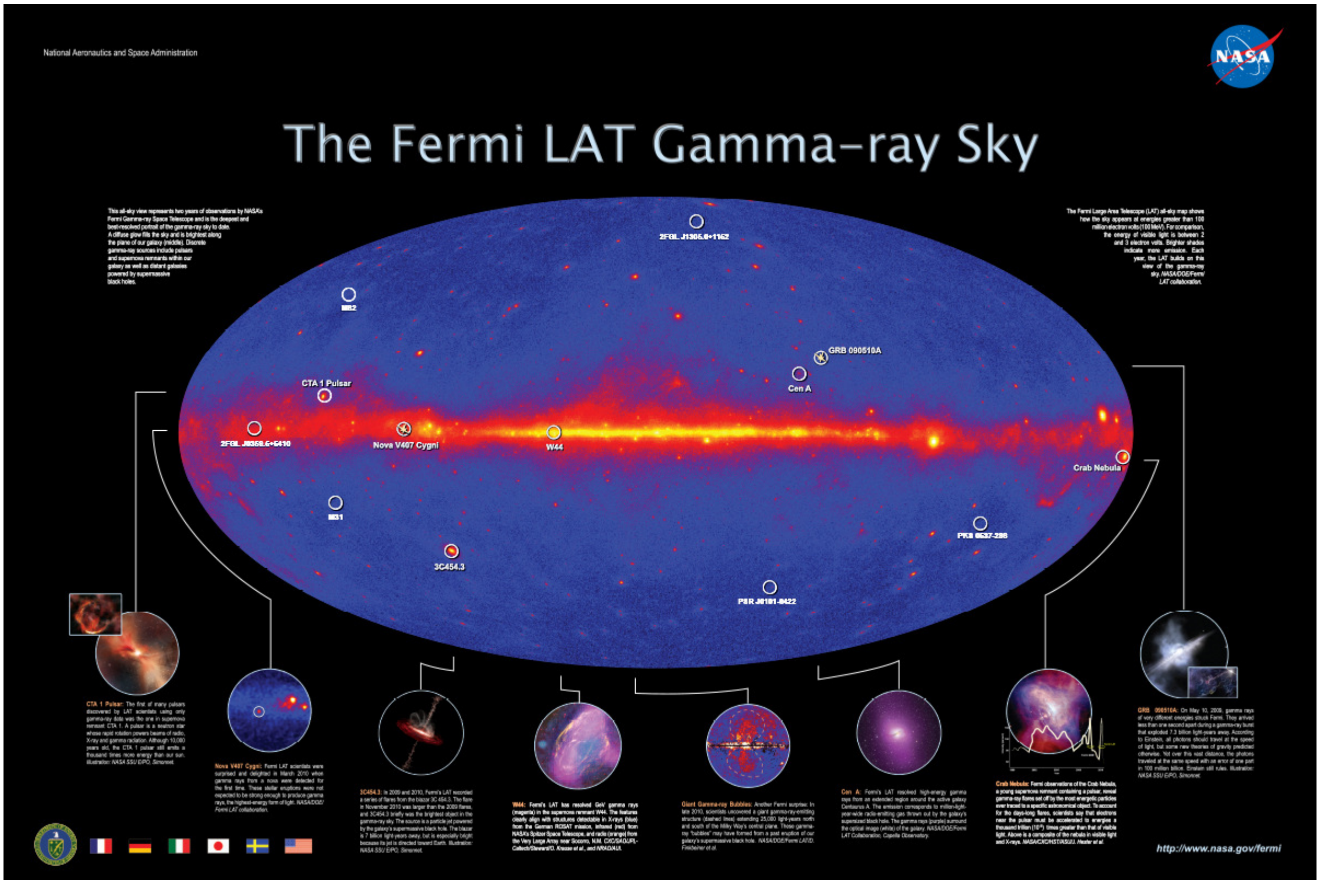

Figure 5: Two-year *Fermi* skymap with highlights printed in 2012

2.4. Amateur Astronomers

Public outreach is often conducted by amateur astronomers through star parties held nation-wide. The *Fermi* E/PO team co-sponsored the SUPERNOVA! toolkit for use by these passionate advocates for astronomy. Since 2008, when the toolkit went into national distribution, it has reached over 138,000 attendees through more than 1300 events. Of these events, 680 events reported including almost 25,000 minorities and over 39,000 women/girls.

2.5. *Fermi* Exhibits

The *Fermi* exhibit booth has undergone many transformations over the years. The most recent booth graphics feature the *Fermi* skymap silhouetted with an image of the satellite as shown in Figure 6. The exhibit booth is often accompanied by the *Fermi* banner stand, which features a blueprint style graphic that illustrates the project logo, the satellite, the flags of the participating countries, and the skymap. The exhibit booth and/or the banner have been used at venues including the AAS winter meetings, the USA Science and Engineering Festival, and the Goddard Jamboree.

The SSU E/PO team has a multi-mission exhibit booth drawn in the style of Epo's Chronicles that includes images of Alkina and other characters from the web comic. This booth has been used extensively at educator and student events, including California Science Teachers Association annual meetings, Expanding Your Horizons, SSU Seawolf Day, and the North Bay Science Festival.

2.6. Social Media

Fermi's presence in the world of social media includes a Facebook page and the Twitter feed @NASAFermi. Since launch, there have been 300 tweets from @NASAFermi, and the feed has over 35,000 followers. The *Fermi* Facebook page has over 30,000 likes and can be found at: `http://www.facebook.com/nasafermi`.

2.7. International Year of Astronomy

The year 2009 was the International Year of Astronomy (IYA). Public outreach events occurred throughout the world, and the *Fermi* E/PO team participated in many of them, including the creation of special illustrated lithographs featuring the objects of the month as explained by Alkina from the Epo's Chronicles webcomic. Over 18,000 of these lithographs were distributed nationwide through amateur astronomy clubs through NASA's Night Sky Network.

Another special creation was an Epo's Chronicles podcast distributed through the 365 Days of Astronomy

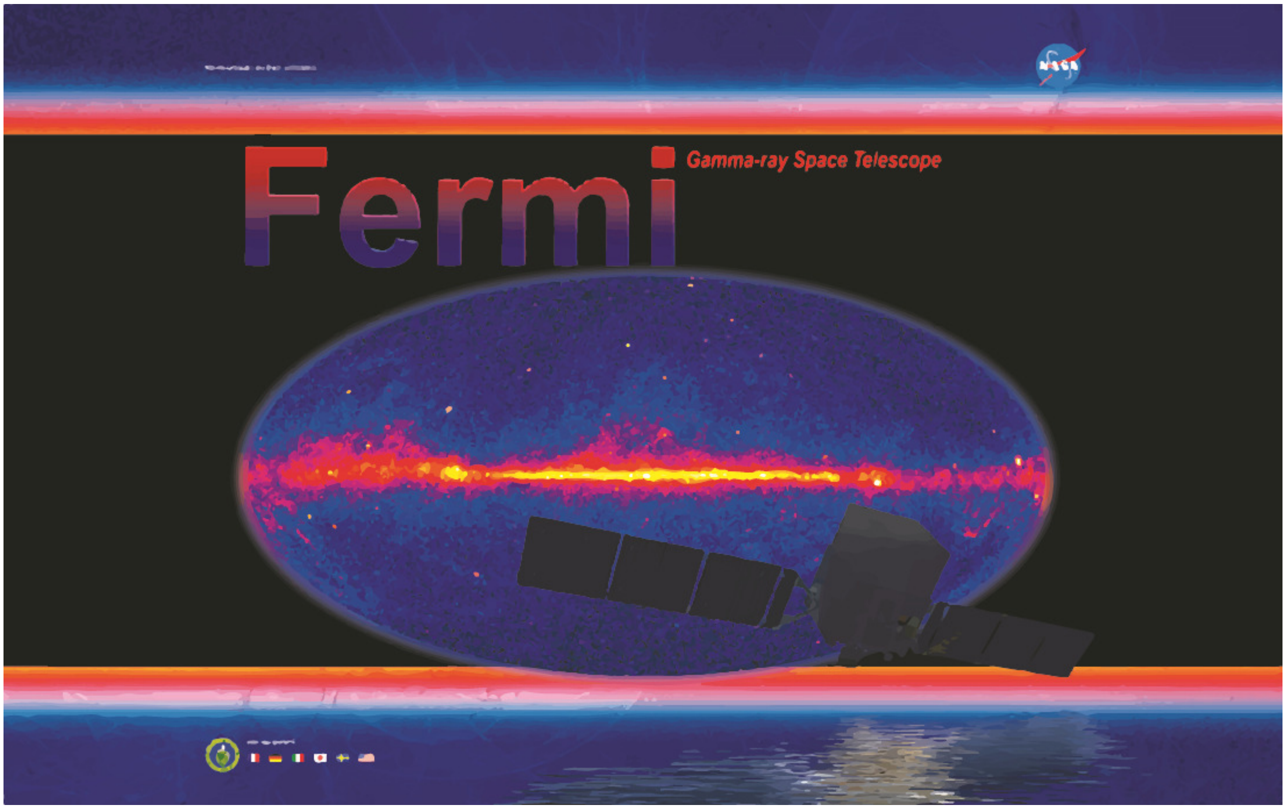

Figure 6: Current *Fermi* exhibit booth graphics

website. This podcast was downloaded over 6000 times following its initial release on 16 September 2009.

SSU E/PO created a traveling exhibit of IYA images that circulated around the San Francisco Bay Area during 2009. This small exhibit was featured at 20 venues, with an estimated viewing by over 100,000 participants. A larger IYA exhibit appeared at the California Academy of Sciences and San Jose Tech Museum, with estimated viewing of 50,000 at each location.

2.8. Black Hole Shows

"Black Holes: The Other Side of Infinity" and the PBS NOVA show "Monster of the Milky Way" were produced in partnership with *Swift*, the National Science Foundation, the Denver Museum of Nature & Science, PBS NOVA and Tom Lucas Productions. Premiering in 2006, the planetarium show has been featured in over 30 venues and has reached millions of people world-wide. Narrated by Liam Neeson, this full-format digital dome show included state-of-the art scientific visualizations of black holes and warped spacetime created by experts at the National Center for Supercomputer Applications at the University of Illinois Urbana-Champaign. The PBS NOVA show was initially seen by over 10 million viewers and has aired many times since then. It is still available for viewing on the PBS website. The black hole shows were initially seed-funded by *Fermi* E/PO and Lynn Cominsky served as a scientific director.

2.9. Printed Materials

Many printed materials were developed by the *Fermi* E/PO team for distribution to the general public. Table IV summarizes the number of these items that were handed out during 2000 - 2013. Prior to the renaming of the mission in late 2008, these products listed the satellite name as GLAST (Gamma-ray Large Area Space Telescope) rather than *Fermi*.

The *Fermi* sticker features a colorful image of the satellite on the front along with text describing the mission on the back. It is shown in Figure 7.

The *Fermi* lithograph features an illustration of the satellite on the front, and an explanation of the overall scientific objectives of the mission on the back. Instructions for the "make your own pulsar" activity are also included.

The *Fermi* fact sheet is a four-page color brochure that describes the science of the mission, as well as providing tables that summarize the instrumental parameters and the mission participants.

The *Fermi* brochure describes in detail the science that *Fermi* does and explains how it does it. The description includes the instruments, background information on gamma-ray astronomy and detection methods. It also describes pre-launch thinking about about active galaxies, gamma-ray bursts, solar flares, gamma-rays from dark matter and other highly energetic sources seen in the Universe.

Figure 7: Official Fermi mission sticker

The *Fermi* paper model provides a short description of the scientific instruments on board the satellite, as well as links to other resources about its instruments. There is also a short description of how *Fermi* detects gamma rays with the Large Area Telescope as well as the Gamma-ray Burst Monitor detectors. The product includes three pages of parts that can be cut out and easily assembled using common household items.

Table IV Printed Materials

Product	Created	Number Distributed
Stickers	2005	45,500
Lithograph	2008	10,000
Fact Sheet	2008	9500
Brochure	2008	15,000
Paper model	2007	8800
Race card game	2005	7350
Black Hole FAQ	2006	32,000

The *Fermi* Race Card game challenges two teams of players to strategically maneuver to be the first to assemble the parts of the satellite and then use it to observe five astronomical objects. As players build their satellites they must overcome hurtles and obstacles thrown at them by their opponents while doing the same in order to slow their opponents down. To win, players must successfully have their operational *Fermi* satellite observe five gamma-ray emitting objects.

The black hole frequently-asked questions (FAQ) brochures answers eight of the most commonly asked questions about black holes, and explains how *Fermi* studies black holes. The FAQ brochures were distributed to attendees at many of the planetaria who experienced “Black Holes: the Other Side of Infinity.”

2.10. Tesla Coil Show

From 2000-2012, *Fermi* E/PO provided funding to support the Tesla Coil show put on by scientists and students from the University of California, Santa Cruz Institute for Particle Physics. These popular shows reached thousands of students annually.

Acknowledgments

The SSU Education and Public Outreach group would like to acknowledge support from NASA NNX07AF53G, NNX12AE34G and NAS5-00147 through Stanford University. We also would like to thank the many talented science writers and animators at NASA Goddard Space Flight Center with whom we have worked during the years including Christopher Wanjek, Robert Naeye, Francis Reddy, Scott Wiessinger, and the staff at Goddard’s Scientific Visualization Studio.

The GAMMA-400 Space Mission

P. Cumani and V. Bonvicini, M. Boezio, F. Longo, E. Mocchiutti, A. Vacchi, N. Zampa
Istituto Nazionale di Fisica Nucleare, Sezione di Trieste and Physics Department of University of Trieste, Trieste, Italy
A.M. Galper, N.P. Topchiev, V.A. Dogiel, Yu.V. Gusakov, S.I. Suchkov
Lebedev Physical Institute, Russian Academy of Sciences, Moscow, Russia
I.V. Arkhangelskaja, A.I. Arkhangelskiy, G.L. Dedenko, V.V. Kadilin, V.A. Kaplin, A.A. Kaplun, M.D. Kheymits, A.A. Leonov, V.A. Loginov, V.V. Mikhailov, P.Yu. Naumov, M.F. Runtso, A.A. Taraskin, E.M. Tyurin, Yu.T. Yurkin, V.G. Zverev
National Research Nuclear University MEPhI, Moscow, Russia
S.G. Bobkov, M.S. Gorbunov, A.V. Popov, O.V. Serdin
Scientific Research Institute for System Analysis, Russian Academy of Sciences, Moscow, Russia
R.L. Aptekar, E.A. Bogomolov, M.V. Ulanov, G.I. Vasilyev
Ioffe Institute, Russian Academy of Sciences, St. Petersburg, Russia
A.L. Men'shenin
Research Institute for Electromechanics, Istra, Moscow region, Russia
V.N. Zarikashvili
Pushkov Institute of Terrestrial Magnetism, Ionosphere, and Radiowave Propagation, Troitsk, Moscow region, Russia
O. Adriani, E. Berti, M. Bongi, S. Bottai, N. Mori, P. Papini, P. Spillantini, A. Tiberio, E. Vannuccini
Istituto Nazionale di Fisica Nucleare, Sezione di Firenze and Physics Department of University of Florence, Firenze, Italy
G. Castellini, S. Ricciarini
Istituto di Fisica Applicata Nello Carrara - CNR and Istituto Nazionale di Fisica Nucleare, Sezione di Firenze, Firenze, Italy
G. Bigongiari, S. Bonechi, P. Maestro, P.S. Marrocchesi
Department of Physical Sciences, Earth and Environment, University of Siena and Istituto Nazionale di Fisica Nucleare, Sezione di Pisa, Italy
P.W. Cattaneo, A. Rappoldi
Istituto Nazionale di Fisica Nucleare, Sezione di Pavia, Pavia, Italy
C. De Donato, P. Picozza, R. Sparvoli
Istituto Nazionale di Fisica Nucleare, Sezione di Roma 2 and Physics Department of University of Rome Tor Vergata, Rome, Italy
M. Tavani
Istituto Nazionale di Astrofisica IASF and Physics Department of University of Rome Tor Vergata, Rome, Italy
L. Bergström
Stockholm University, Department of Physics; and the Oskar Klein Centre, AlbaNova University Center, Stockholm, Sweden
J. Larsson, M. Pearce, F. Ryde
KTH Royal Institute of Technology, Department of Physics; and the Oskar Klein Centre, AlbaNova University Center, Stockholm, Sweden
A.A. Moiseev
CRESST/GSFC and University of Maryland, College Park, Maryland, USA
I.V. Moskalenko
Hansen Experimental Physics Laboratory and Kavli Institute for Particle Astrophysics and Cosmology, Stanford University, Stanford, USA
B.I. Hnatyk
Taras Shevchenko National University of Kyiv, Kyiv, Ukraine
V.E. Korepanov
Lviv Center of Institute of Space Research, Lviv, Ukraine

GAMMA-400 is a new space mission which will be installed on board the Russian space platform Navigator. It is scheduled to be launched at the beginning of the next decade. GAMMA-400 is designed to study simultaneously gamma rays (up to 3 TeV) and cosmic rays (electrons and positrons from 1 GeV to 20 TeV, nuclei up to 10^{15}-10^{16} eV). Being a dual-purpose mission, GAMMA-400 will be able to address some of the most impelling science topics, such as search for signatures of dark matter, cosmic-rays origin and propagation, and the nature of transients. GAMMA-400 will try to solve the unanswered questions on these topics by high-precision measurements of the Galactic and extragalactic gamma-ray sources, Galactic and extragalactic diffuse emission and the spectra of cosmic-ray electrons + positrons and nuclei, thanks to excellent energy and angular resolutions.

1. INTRODUCTION

GAMMA-400 (Galper et al. [2013]) is a Russian space mission, approved by the Russian space agency, with an international contribution. Foreseen to be launched at the beginning of the next decade, the satellite will be positioned on a circular orbit at ∼200000 km. This specific orbit, combined with a pointing mode observational strategy, allows to perform continuous observations of a source without Earth occultation. During its first year of mission, GAMMA-400 is planned to observe the Galactic plane.

Designed as a dual experiment, GAMMA-400 will be able to study gamma rays, from 100 MeV up to several TeV, as well as cosmic rays, electrons up to 20 TeV and protons and nuclei up to the "knee" (10^{15}-10^{16} eV). It will search for possible dark matter signal thanks to an unprecedented energy resolution that will permit to detect features associated to dark matter annihilation or decay in the spectra of sources such as the Galactic Center. GAMMA-400 will also study gamma-ray sources such as active galactic nuclei, supernova remnants, pulsars and gamma-ray bursts (GRBs). The GRB study will be performed using both the main instrumentation, described in the next section, and the Konus-FG detectors. Six Konus-FG will be installed on GAMMA-400 to study GRBs in the 10 keV - 15 MeV energy range with a field-of-view of 2π sr. Four of these detectors will be able to reconstruct the direction of the incoming photons with an accuracy between 0.5° and 3°, while the remaining two will serve as spectrometric detectors.

GAMMA-400 will address the remaining issues regarding cosmic-rays origin, acceleration and propagation by studying the high energy all electron spectrum, with a 2% energy resolution, and the cosmic-ray elemental spectra up to the knee, with high statistics and energy resolution.

Some of the GAMMA-400 performance, and the scientific objectives that will be addressed, are summarized in tab. I.

Performance		Scientific Objectives
Energy Res.	$\sim 1\%\ \gamma$	DM
	$\sim 2\%\ e^{\pm}$	CRs origin
	$\sim 35\%$ p	CRs propagation
Angular Res.	∼0.6° @ 1 GeV	CRs origin
	∼0.02° @ 100 GeV	Transients
	∼0.006° @ 1 TeV	EBL
GF	$> 3\ \mathrm{m^2 sr}$	DM
		CRs origin
		CRs propagation

Table I Summary of the GAMMA-400 performance and scientific topics.

2. GEOMETRY

The GAMMA-400 apparatus, of which a schematic view is presented in fig. 1, will comprise:

- A converter/tracker (C) where the impinging gamma ray creates an electron-positron pair subsequently detected by Silicon layers;
- A calorimeter composed partially by CsI(Tl) slabs and Silicon sensors (CC1, also referred to as pre-shower in the following) and partly by CsI(Tl) cubes (CC2, also referred to as calorimeter in the following);
- An Anticoincidence system covering both the sides and the top of the detector (AC top and lat) to reject the charged particles for gamma-ray observations;
- A Time-of-flight system composed by four layers of scintillating materials (S1 and S2) to discriminate upgoing particles, such as backsplashed particles from the calorimeter, and downgoing particles;
- A charge identification system (LD), to discriminate between the different elements interacting inside the detector;
- A neutron detector (ND) and scintillation detectors (S3 and S4), used to improve the electron/hadron rejection factor.

A comparison between the tracker and calorimeter of *Fermi* and GAMMA-400 is presented in tab. II.

2.1. Tracker

The tracker is divided into four towers. Each tower is composed by ten planes of single-sided Silicon detectors. The first eight planes are interleaved by a 0.1 X_0 of Tungsten, absent in the last two planes, for a total of ∼1 X_0 in the whole tracker. The tungsten, where present, and two Si layers, for the x and y view, are mounted on a honeycomb Al support. A 2 mm gap separates two different trays. Each Si layer is composed by an array of 5×5 tiles each of which has a $9.7\times9.7\ \mathrm{cm}^2$ area. Five tiles are wired-bonded together to form a ∼49 cm long ladder. The sensors are single-sided strip detectors with a strip pitch of 80 μm and a read-out pitch of 240 μm. The read-out of the strips is analog, similar to the one used by AGILE (Tavani et al. [2001]). This read-out system permits to retain the information on the energy released inside the strip, allowing to reach a low error on the hit position (less than 40 μm) as well as using the tracker Si planes as a charge identifier. Thanks to this detector configuration, GAMMA-400 will be able to achieve an angular resolution at low energy comparable to the

		Fermi	GAMMA-400
Tracker	Dimension (cm^2)	~140×140	~97×97
	Radiation Length	12 planes: 0.03 X_0 4 planes: 0.18 X_0 2 planes: no W	8 planes: 0.1 X_0 2 planes: no W
	Pitch (μm)	228	80
	Readout Pitch (μm)	228	240
	Readout	Digital	Analog
Calorimeter	Vertical R.L. (X_0)	8.6	23 (CC1 not included)
	Vertical I.L. (λ_I)	0.4	1.1 (CC1 not included)
	Segmentation	96 Bars × Tower 2.7×2.0×32.6 cm^3	9408 Cubes 3.6×3.6×3.6 cm^3

Table II Comparison between the tracker and calorimeter of *Fermi* (Atwood et al. [2009]) and GAMMA-400

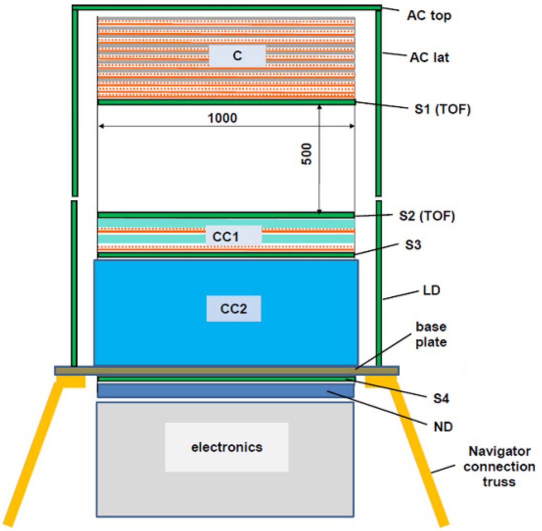

Figure 1: Schematic view of the apparatus. From top to bottom: converter-tracker (C), anticoincidence system (AC top and lat), time-of-flight system (S 1 to 4), calorimeter (CC1 and CC2), charge identification system on the side of the calorimeter (LD) and neutron detector (ND). The dimensions values are in mm.

one of *Fermi* front (Atwood et al. [2009]), as can be noticed at the left of fig. 2, even with a more than doubled tungsten thickness.

2.2. Pre-shower

The pre-shower is composed by two planes of CsI(Tl) slabs interleaved by single-sided Si detectors, two layers for the x and y view. The Si layers are equal in pitch, dimensions and read-out to the Si layers inside the tracker. The total radiation length of the detector is of $\sim 2\ X_0$.
Each CsI(Tl) plane is divided in an array of 20×3 slabs, each with a volume of 33.3×5×2 cm^3. The orientation of the slabs on the first plane is perpendicular to the orientation on the second plane in order to have the separate x and y view.
The 50 cm lever arm between the tracker and the pre-shower, combined with the finely pitched Si in both detectors, allows to reach an optimal angular resolution at high energy, as shown on the left of fig. 2. A direction reconstruction can be also performed using only information from the pre-shower, helping in increasing the total effective area of the instrument.

2.3. Calorimeter

The design of the calorimeter is based on a novel configuration. It is composed by 28×28×12 cubes of CsI(Tl), each with a side of 3.6 cm. This particular segmentation permits to reconstruct the shower created by particles coming not only from above but also from the sides of the detector, greatly increasing the geometrical factor (GF) of the instrument. The planar GF is 10.1 m^{2}sr which, taking into consideration the quality cuts necessary to the reconstruction, corresponds to an effective GF of more than 3 m^{2}sr.
The expected electron/proton rejection factor is of the order of 10^5 with an energy resolution for protons in the 100 GeV-100 TeV energy range, between 30% and 40%.
The energy resolution for gamma rays, using also the tracker, reaches 1% at 10 GeV, as shown at the right of fig. 2.
The possibility of reconstructing the shower of particles coming also from the sides of the detector can be exploited also for gamma-ray observations. Thanks to an angular resolution of the order of some degrees, a more than 2π sr field-of-view and a considerable effective area, the GAMMA-400 calorimeter can indeed be used to provide a trigger for observations of transients from the ground. A prototype of the calorimeter, photograph shown in fig. 3, has already been tested at the CERN SPS (Mori et al. [2013]).

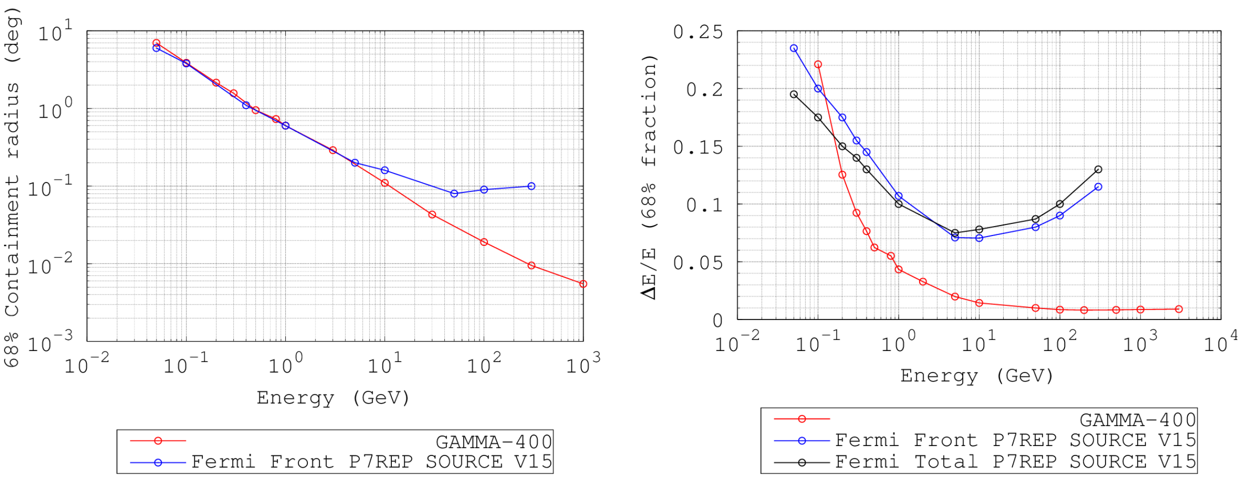

Figure 2: Comparison between the angular (*left*) and energy (*right*) resolutions of *Fermi*-LAT (URL [2013]) and GAMMA-400, using information from both calorimeter and tracker (Galper et al. [2013]).

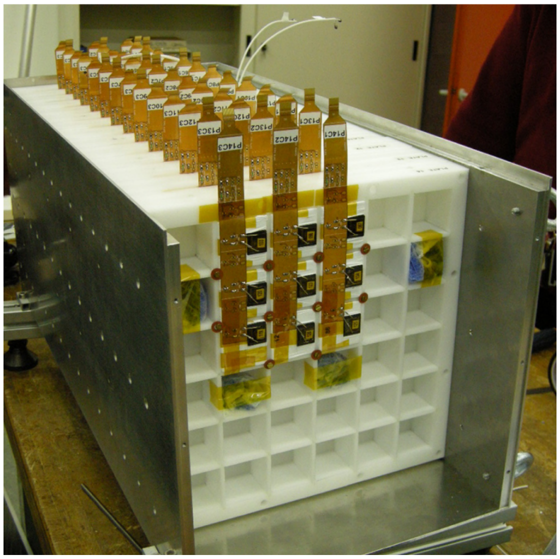

Figure 3: The calorimeter prototype inside the Al frame. The photodiodes, as well as the kapton readout cables, are visible on the first layer (Mori et al. [2013]).

3. CONCLUSIONS

GAMMA-400 is a space mission dedicated to the study of both gamma rays and cosmic rays, electrons, protons and nuclei. Thanks to the configuration of its detectors it will have an unprecedented energy resolution and an optimal angular resolution. GAMMA-400, considering its performance, will use a multi-messenger approach to search for possible dark matter signal as well as to try solving the remaining issues on the cosmic-rays origin, acceleration and propagation mechanisms. The launch of the satellite is currently scheduled for the beginning of the next decade.

References

A. M. Galper, O. Adriani, R. L. Aptekar, I. V. Arkhangelskaja, A. I. Arkhangelskiy, G. A. Avanesov, L. Bergstrom, E. A. Bogomolov, M. Boezio, V. Bonvicini, et al., ArXiv e-prints (2013), 1306.6175.

W. B. Atwood, A. A. Abdo, M. Ackermann, W. Althouse, B. Anderson, M. Axelsson, L. Baldini, J. Ballet, D. L. Band, G. Barbiellini, et al., The Astrophysical Journal **697**, 1071 (2009), 0902.1089.

M. Tavani, G. Barbiellini, A. Argan, N. Auricchio, P. Caraveo, A. Chen, V. Cocco, E. Costa, G. Di Cocco, G. Fedel, et al., in *Gamma 2001: Gamma-Ray Astrophysics* (2001), vol. 587 of *American Institute of Physics Conference Series*, pp. 729–738.

(2013), URL `http://www.slac.stanford.edu/exp/glast/groups/canda/lat_Performance.htm`.

N. Mori, O. Adriani, A. Basti, G. Bigongiari, L. Bonechi, S. Bonechi, M. Bongi, S. Bottai, P. Brogi, R. D'Alessandro, et al., Nuclear Instruments and Methods in Physics Research Section A: Accelerators, Spectrometers, Detectors and Associated Equipment **732**, 311 (2013), ISSN 0168-9002, URL `http://www.sciencedirect.com/science/article/pii/S0168900213007493`.

Study of the Gamma-ray performance of the GAMMA-400 Calorimeter

P. Cumani and V. Bonvicini, M. Boezio, F. Longo, E. Mocchiutti, A. Vacchi, N. Zampa
Istituto Nazionale di Fisica Nucleare, Sezione di Trieste and Physics Department of University of Trieste, Trieste, Italy
A.M. Galper, N.P. Topchiev, V.A. Dogiel, Yu.V. Gusakov, S.I. Suchkov
Lebedev Physical Institute, Russian Academy of Sciences, Moscow, Russia
I.V. Arkhangelskaja, A.I. Arkhangelskiy, G.L. Dedenko, V.V. Kadilin, V.A. Kaplin, A.A. Kaplun, M.D. Kheymits, A.A. Leonov, V.A. Loginov, V.V. Mikhailov, P.Yu. Naumov, M.F. Runtso, A.A. Taraskin, E.M. Tyurin, Yu.T. Yurkin, V.G. Zverev
National Research Nuclear University MEPhI, Moscow, Russia
S.G. Bobkov, M.S. Gorbunov, A.V. Popov, O.V. Serdin
Scientific Research Institute for System Analysis, Russian Academy of Sciences, Moscow, Russia
R.L. Aptekar, E.A. Bogomolov, M.V. Ulanov, G.I. Vasilyev
Ioffe Institute, Russian Academy of Sciences, St. Petersburg, Russia
A.L. Men'shenin
Research Institute for Electromechanics, Istra, Moscow region, Russia
V.N. Zarikashvili
Pushkov Institute of Terrestrial Magnetism, Ionosphere, and Radiowave Propagation, Troitsk, Moscow region, Russia
R. Sarkar
Indian Centre for Space Physics, Kolkata, India
O. Adriani, E. Berti, M. Bongi, S. Bottai, N. Mori, P. Papini, P. Spillantini, A. Tiberio, E. Vannuccini
Istituto Nazionale di Fisica Nucleare, Sezione di Firenze and Physics Department of University of Florence, Firenze, Italy
G. Castellini, S. Ricciarini
Istituto di Fisica Applicata Nello Carrara - CNR and Istituto Nazionale di Fisica Nucleare, Sezione di Firenze, Firenze, Italy
G. Bigongiari, S. Bonechi, P. Maestro, P.S. Marrocchesi
Department of Physical Sciences, Earth and Environment, University of Siena and Istituto Nazionale di Fisica Nucleare, Sezione di Pisa, Italy
P.W. Cattaneo, A. Rappoldi
Istituto Nazionale di Fisica Nucleare, Sezione di Pavia, Pavia, Italy
I. Donnarumma, G. Piano, S. Sabatini, V. Vittorini
Istituto di Astrofisica e Planetologia Spaziali, Rome, Italy
A. Argan
Istituto Nazionale di Astrofisica, Rome, Italy
A. Bulgarelli, V. Fioretti
Istituto di Nazionale di Astrofisica Spaziale e Fisica Cosmica, Bologna, Italy
M. Tavani
Istituto di Astrofisica e Planetologia Spaziali and University of Rome Tor Vergata, Rome, Italy
C. De Donato, P. Picozza, R. Sparvoli, F. Palma
Istituto Nazionale di Fisica Nucleare, Sezione di Roma 2 and Physics Department of University of Rome Tor Vergata, Rome, Italy
M. Tavani
Istituto Nazionale di Astrofisica IASF and Physics Department of University of Rome Tor Vergata, Rome, Italy
L. Bergström
Stockholm University, Department of Physics; and the Oskar Klein Centre, AlbaNova University Center, Stockholm, Sweden
J. Larsson, M. Pearce, F. Ryde
KTH Royal Institute of Technology, Department of Physics; and the Oskar Klein Centre, AlbaNova University Center, Stockholm, Sweden
A.A. Moiseev
CRESST/GSFC and University of Maryland, College Park, Maryland, USA
I.V. Moskalenko
Hansen Experimental Physics Laboratory and Kavli Institute for Particle Astrophysics and Cosmology, Stanford University, Stanford, USA
B.I. Hnatyk
Taras Shevchenko National University of Kyiv, Kyiv, Ukraine
V.E. Korepanov

arXiv:1502.03287v2 [astro-ph.IM] 7 Mar 2015

Lviv Center of Institute of Space Research, Lviv, Ukraine

GAMMA-400 is a new space mission, designed as a dual experiment, capable to study both high energy gamma rays (from ~100 MeV to few TeV) and cosmic rays (electrons up to 20 TeV and nuclei up to $\sim 10^{15}$ eV). The full simulation framework of GAMMA-400 is based on the Geant4 toolkit. The details of the gamma-ray reconstruction pipeline in the pre-shower and calorimeter will be outlined. The performance of GAMMA-400 (PSF, effective area) have been obtained using this framework. The most updated results on them will be shown.

1. INTRODUCTION

GAMMA-400 (Galper et al. [2013]) is a Russian space mission, approved by the Russian space agency, with an international contribution. Foreseen to be launched at the beginning of the next decade, the satellite will be positioned on a circular orbit at ~200000 km. This particular orbit, combined with a pointing mode observational strategy, permits to perform continuous observations of a source without Earth occultation. During its first year of operation, GAMMA-400 is planned to observe the Galactic plane.

Designed as a dual experiment, GAMMA-400 will be able to study gamma rays, from 100 MeV up to several TeV, as well as cosmic rays, electrons up to 20 TeV and protons and nuclei up to the knee (10^{15}-10^{16} eV). It will search for possible dark matter signal thanks to an unprecedented energy resolution that will permit to detect features associated to dark matter annihilation or decay in the spectra of sources such as the Galactic Center. GAMMA-400 will also study gamma-ray sources such as active galactic nuclei, supernova remnants, pulsars and gamma-ray bursts (GRBs).

GAMMA-400 will address the remaining issues regarding cosmic-rays origin, acceleration and propagation by studying the high energy all electron spectrum, with a 2% energy resolution, and the cosmic-ray elemental spectra up to the knee, with high statistics and energy resolution.

A gamma-ray reconstruction pipeline using only the pre-shower or the calorimeter will be presented in the following. The reconstruction pipeline is part of a larger framework based on the Geant4 (Agostinelli et al. [2003]) toolkit. The framework contains tools to create the geometry, simulate the particle interactions inside the apparatus, digitize the output of the simulations and analyze the results as well as an event displayer.

2. GEOMETRY

The GAMMA-400 apparatus, of which a schematic view is presented in fig. 1, will comprise:

- A converter/tracker (C) where a gamma ray interacts with a tungsten layer (8 layers, 0.1 X_0 each) creates an electron-positron pair subsequently detected by single-sided Silicon layers (10 layers);

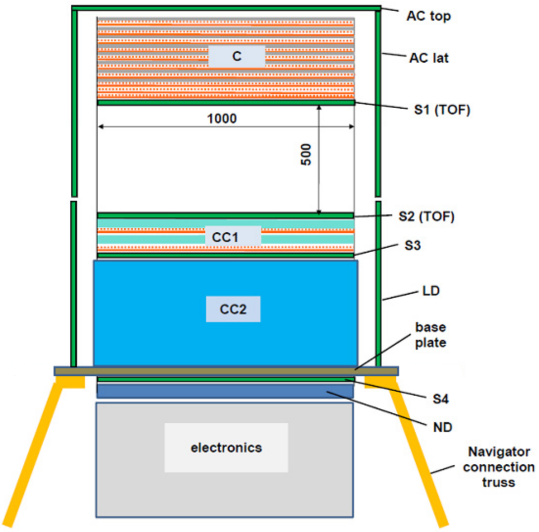

Figure 1: GAMMA-400 physical scheme. The dimensions values are in mm.

- A calorimeter composed partially by two planes of CsI(Tl) slabs and Silicon (CC1, also referred to as pre-shower in the following) and partly by CsI(Tl) cubes (CC2, also referred to as calorimeter in the following), arranged in a 28×28×12 array;

- An Anticoincidence system covering both the sides and the top of the detector (AC top and lat) to reject the charged particles for gamma-ray observations. The possibility to retrieve also timing information from the AC is currently under study;

- A Time-of-flight system composed by four layers of scintillating materials (S1 and S2) to discriminate upgoing particles, such as backsplashed particles from the calorimeter, and downgoing particles;

- A charge identification system (LD), to discriminate between the different elements interacting inside the detector;

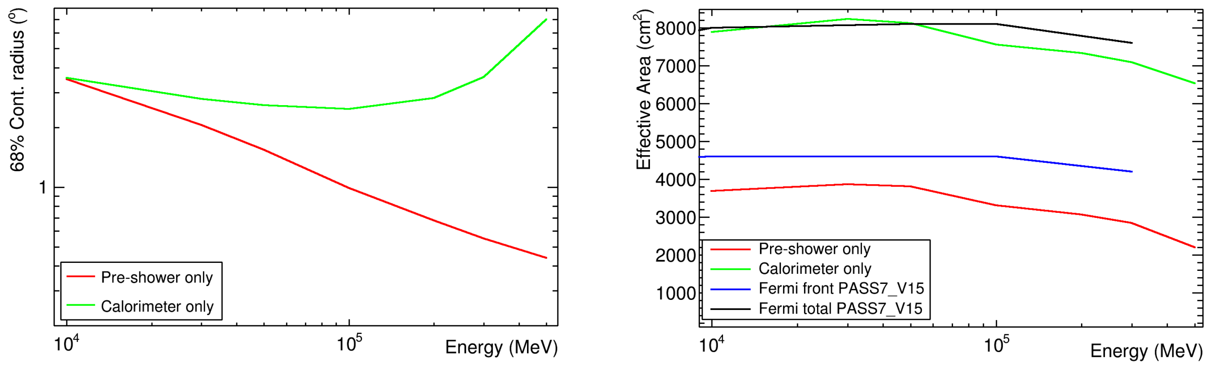

Figure 2: Angular resolution (*left*) and effective area (*right*) of GAMMA-400, using its different detectors. The results on the effective area are compared with the performance of *Fermi*-LAT (URL [2013])

- A neutron detector (ND) and scintillation detectors (S3 and S4), used to improve the electron/hadron rejection factor.

3. DIRECTION RECONSTRUCTION

The reconstruction of the direction of an incoming gamma ray with the GAMMA-400 apparatus can be performed using either the combination of information from the tracker, pre-shower and calorimeter or only one of these detectors. While the results of the reconstruction using also information from the tracker are presented in, e.g., Galper et al. [2014], the reconstruction using only the pre-shower or the calorimeter will be discussed in the following.

3.1. Pre-shower Only Reconstruction

A direction reconstruction can be performed using information from only the pre-shower. The requirement is for both Si planes to be hit. On each plane a median weighted on the energy is computed. The resulting points are fit through a straight line. The method is iterated several times, excluding the hits outside a cylinder centered along the found direction and reducing the cylinder radius at each iteration.

3.2. Calorimeter Only Reconstruction

Thanks to the novel configuration of the calorimeter, it is possible to reconstruct the shower created by particles coming not only from the top but also from the side of the detector as well as their original direction. The direction reconstruction method is similar to the one described in sec. 3.1, but it starts with a rough estimation of the original direction of the incoming particle. This estimation is needed to define the inclination of the planes on which the points to fit are computed. The planes are defined as perpendicular to the direction result of the fit of the three cubes with the highest energy release. Since only a rough estimation is needed, the inclination of the planes is rounded to the nearest $\pi/4$ multiple.
At least three hit planes are necessary for the reconstruction. No requirement on the containment of the shower are applied. Once the planes are found, an average weighted on the energy is performed on each of them to find the barycenter. The barycenters on different planes are fit and the method is iterated by excluding the hit outside a cylinder centered on the found direction and reducing the cylinder radius after each iteration.

3.3. Results

The events that contributes to the calorimeter only and pre-shower only angular resolution and effective area are the events lacking of an overall reconstruction. The overall reconstruction, making use of the tracker, is indeed better and these other events are used to improve the effective area rather than the angular resolution. The sum of the three different effective areas gives an estimation of the total effective area of the instrument.
The angular resolution of the pre-shower improves with the energy because the identification of the hit in the pre-shower is made easier by the higher energy of the pair. Since no requirements on the containment of the shower in the calorimeter are applied, the angular resolution of the calorimeter only reconstruction decreases at high energy.
The different effective area between GAMMA-400 and *Fermi* is due not only to the different reconstruction algorithm but also to the difference in the geometrical area of the two instrument.

4. CONCLUSIONS

GAMMA-400 is a dual experiment dedicated to the study of both gamma rays and cosmic rays, electrons, protons and nuclei. It is possible to reconstruct the direction of the incoming gamma ray using information not only from the tracker, as shown in Galper et al. [2014], but also from only the pre-shower or the calorimeter. The results of these type of reconstruction can be used to increase the total effective area of the instrument, at the expense of the angular resolution. The calorimeter, because of a novel configuration, is capable of reconstruct the direction of particles coming also from its sides, resulting in a more than 2π sr field-of-view. It can then be used to provide a trigger for observations of transients from the ground with telescopes such as the future CTA.

References

A. M. Galper, O. Adriani, R. L. Aptekar, I. V. Arkhangelskaja, A. I. Arkhangelskiy, G. A. Avanesov, L. Bergstrom, E. A. Bogomolov, M. Boezio, V. Bonvicini, et al., ArXiv e-prints (2013), 1306.6175.

S. Agostinelli et al. (GEANT4), Nucl. Instrum. Meth. **A506**, 250 (2003).

(2013), URL `http://www.slac.stanford.edu/exp/glast/groups/canda/lat_Performance.htm`.

A. M. Galper, V. Bonvicini, N. P. Topchiev, O. Adriani, R. L. Aptekar, I. V. Arkhangelskaja, A. I. Arkhangelskiy, L. Bergstrom, E. Berti, G. Bigongiari, et al., ArXiv e-prints (2014), 1412.4239.

Wide-Field MAXI: soft X-ray transient monitor

Makoto Arimoto, Nobuyuki Kawai, Yoichi Yatsu
Tokyo Institute of Technology, 2-12-1 Ookayama, Meguro-ku, Tokyo, 152-8551, Japan
Hiroshi Tomida, Shiro Ueno, Masashi Kimura
Japan Aerospace Exploration Agency, 2-1-1 Sengen, Tsukuba, Ibaraki, 305-8505, Japan
Tatehiro Mihara, Motoko Serino, Mikio Morii
RIKEN, 2-1 Hirosawa, Wako, Saitama, 351-0198, Japan
Hiroshi Tsunemi
Osaka University, 1-1 Machikaneyama, Toyonaka, Osaka, 560-0043, Japan
Atsumasa Yoshida, Takanori Sakamoto
Aoyama Gakuin University, 5-10-1 Fuchinobe, Chuo-ku, Sagamihara, Kanagawa, 252-5258, Japan
Takayoshi Kohmura
Tokyo University of Science, 2641, Yamazaki, Noda, Chiba, 278-8510, Japan
Hitoshi Negoro
Nihon University, 1-8-14 Surugadai, Chiyoda, Tokyo, 101-8308, Japan
Yoshihiro Ueda
Kyoto University, Kitashirakawa-Oiwake-cho, Sakyo-ku, Kyoto, 606-8502, Japan
Yohko Tsuboi
Chuo University, Kasuga 1-13-27, Bunkyo-ku, Tokyo, 112-8551, Japan
Ken Ebisawa
Institute of Space and Astronautical Science (ISAS), 3-1-1 Yoshinodai, Sagamihara, Kanagawa, 229-8510, Japan

Wide-Field MAXI (*WF-MAXI*: Wide-Field Monitor of All-sky X-ray Image) is a proposed mission to detect and localize X-ray transients including electro-magnetic counterparts of gravitational-wave events such as gamma-ray bursts and supernovae etc., which are expected to be directly detected for the first time in late 2010's by the next generation gravitational telescopes such as Advanced LIGO and KAGRA. The most distinguishing characteristics of *WF-MAXI* are a wide energy range from 0.7 keV to 1 MeV and a large field of view (~ 25 % of the entire sky), which are realized by two main instruments: (i) Soft X-ray Large Solid Angle Camera (SLC) which consists of four pairs of crisscross coded aperture cameras using CCDs as one-dimensional fast-readout detectors covering $0.7 - 12$ keV and (ii) Hard X-ray Monitor (HXM) which is a multi-channel array of crystal scintillators coupled with avalanche photo-diodes covering 20 keV $-$ 1 MeV.

1. Scientific goals

Wide-Field MAXI (*WF-MAXI*: Wide-Field Monitor of All-sky X-ray Image) [1] on the ISS is a mission to detect and localize X-ray transients with a large field of view (FoV ~25% of the entire sky) covering a wide energy band from 20 keV to 1MeV, monitoring the entire sky. The characteristic feature is a strong capability of detecting soft X-ray photons (< 10 keV) from X-ray transients with a fine localization accuracy of ~0.1°, with a cadence of 90 min. The transient search below 10 keV with the large FoV has been done with only a few satellites (e.g., HETE-2 [2], MAXI[3]), so there is huge room for discovery space on the high energy astronomy.

The most challenging target object of *WF-MAXI* is X-ray transients including electro-magnetic counterparts of gravitational-wave (GW) events such as gamma-ray bursts (GRBs) and supernovae (e.g., core-collapse SNe) which are expected to be directly detected for the first time in late 2010's by the next generation GW telescopes such as Advanced LIGO, Virgo and KAGRA. However, the localization by the GW telescopes is too coarse (~10°) to associate the detected GW sources with known astronomical objects, and/or measure their distances, and identify their physical origins. Soft X-ray band gives us a promising channel considering the huge energy density at the source, and yet all-sky monitoring with sufficient sensitivity and cadence has never been performed. If a GW event is detected by *WF-MAXI*, its localization will be performed with an positional accuracy of 0.1°. After that, *WF-MAXI* issues its alert to the international astronomical community, which leads to enabling follow-up observations with X-ray, optical and infrared observatories (e.g., ASTRO-H, Subaru, TMT, JWST etc.) to measure its distance and study on its environment and progenitor.

A part of GW events is thought to originate from compact-binary coalescence sources including neutron stars, stellar-mass black holes and intermediate-mass black holes. Although there is a large uncertainty of expected GW event rate [4], we show a summary of expected detection rates of GW events by current X-ray observatories with a large FoV in Table I, assuming that 10 GW events happen in a year. *WF-MAXI* has the highest detectability of GW sources among the current observatories.

Table I Expected detection rates of GW source by current X-ray observatories assuming that 10 GW events happen in a year

Mission	**FoV** [%] ratio to $4\pi str$	**operation ratio** [%]	**expected detection rate of GW events** [events/year]	**soft X-ray sensitivety** (below 10 keV)
Swift/BAT	11	80	0.88	N/A
MAXI	2	40	0.08	○
Integral IBIS	0.2	100	0.02	N/A
WF-MAXI	25	70	**1.67**	○

Not only for GW events but also for energetic members of astrophysical objects, such as neutron star binaries, black hole binaries and active galactic nuclei (AGN), *WF-MAXI* detects the onset of its activities and issues alerts to the astronomical community of the world (e.g., The Astronomer's Telegram). Furthermore, *WF-MAXI* also detects short high-energy transients such as GRBs and tidal disruption events and short soft X-ray transients such as stellar flares, nova ignitions and supernova shock breakouts.

2. Mission instruments

WF-MAXI has two main instruments of Soft X-ray Large Solid Angle Camera (SLC) and Hard X-ray Monitor (HXM) to detect X-ray photon in the wide energy range of 0.7 keV to 1 MeV. Four modules of SLC and HXM are mounted on the payload at different four angles to cover ∼25% of the entire sky as shown in Fig. 1.

SLC and HXM are sensitive for the energy band of 0.7 − 12 keV and 20 keV − 1 MeV, respectively. Both two instruments share the same FoV. SLC plays an important role in localizing X-ray transients with an accuracy of ∼0.1°. Furthermore for HXM it is quite important to observe GRBs with a wide X-ray band: GRBs' spectra are well represented by two powerlaw functions connected smoothly, which is called the Band function [5], and a maximum peak energy $E_{\rm peak}$ in the νF_ν space is one of the fundamental quantities for GRBs. As the $E_{\rm peak}$ ranges from a few keV to a few MeV, HXM plays a crucial role in determining $E_{\rm peak}$ in the energy band from 20 keV to 1MeV. Combined with SLC, even $E_{\rm peak}$ of soft-class GRBs called X-ray flashes can be determined in the range down to a few keV.

2.1. Soft X-ray Large Solid Angle Camera

The primary scientific instrument of WF-MAXI is SLC [6], which has a capability of detecting and localizing various soft X-ray (< 10 keV) transients including possible GW counterparts, GRBs, SN shock breakouts, tidal disruption events, nova ignition, X-ray bursts, AGN flares, and stellar flares. In the energy band numerous characteristic X-ray lines (e.g. Ne, Mg, Si, S, Fe) exist to trace the environment of the progenitor or burst mechanism and these can be resolved by the energy resolution of a CCD instrument. We therefore adopt a CCD as a position sensitive detector. Coded mask is adopted for the localization, as it can achieve a large field of view without much technical difficulty.

Since the imaging field of a CCD camera fixed to the ISS platform moves in the sky at an angular velocity of ∼0.1°/s, we need to read out the image data on a timescale shorter than 1 s (e.g., 0.1 s) to achieve ∼0.1° position accuracy. We therefore use one dimensional image from CCD with a time resolution of 0.1 s for fast readout. We assign X and Y coordinates to a CCD plane where CCDs are vertically-aligned in two directions. Thus, each module of SLC contains two arrays of CCD in X and Y directions, a pair of coded masks, a part of the electronics that drives and reads out CCD's image data, a mechanical cooler and the chassis as shown in Fig. 1. The dimensions of the camera module are 380mm × 250mm × 220mm without the mechanical cooler.

We use 16 CCDs (Hamamatsu) for a SLC with an effective area of 293 $\rm cm^2$ larger than that used in MAXI/SSC [7]. The CCD is a similar model developed for ASTRO-H/SXI [8] with some minor changes that include pixel format, PGA packaging (instead of wire bonding), an addition of fiducial mark used for alignment with the coded mask and a surface processing on the CCD. The surface of the CCD is covered with 150 ∼ 200 nm aluminum to block the optical light from optical sources and scattered lights from bright objects. Both sides are coated with black colorant to prevent the infrared light leaking into the silicon CCD chip. Furthermore, we dispose a thin aluminum-coated polyimide layer at the camera window to block incoming heat and reflected sun light and He II ultraviolet emission from the upper atmosphere.

Cooling 16 CCD chips to 100°C on the ISS payload is a critical task for our mission to assure the CCD performance. As *WF-MAXI* has no attitude control system, the payload will be illuminated by the sun light every orbit (∼90 minutes). There is no place for radi-

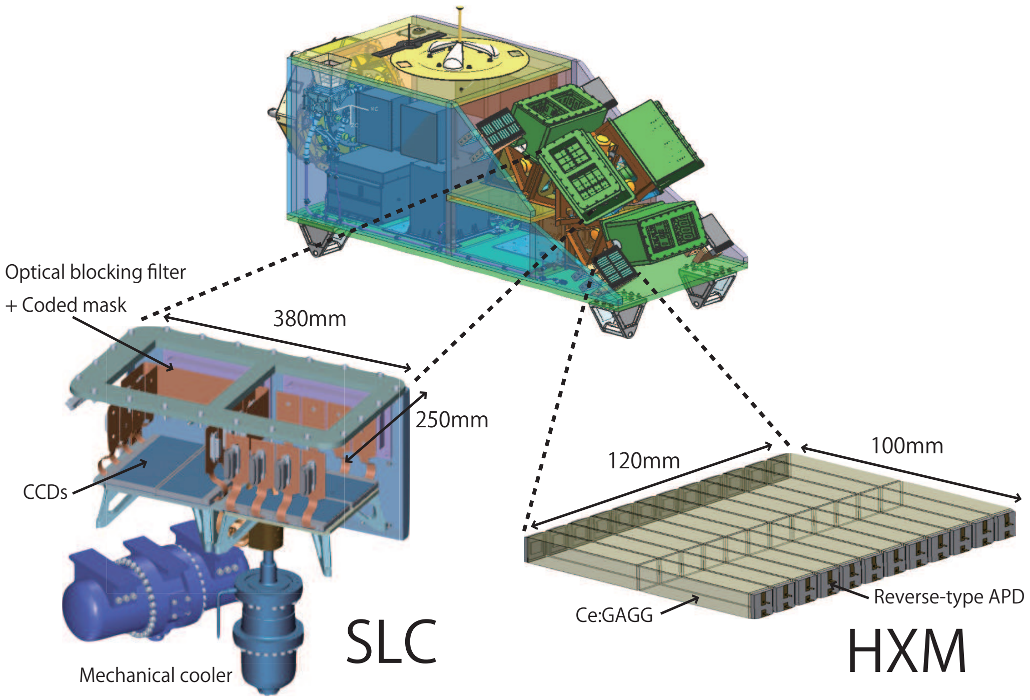

Figure 1: Configuration of the *WF-MAXI* payload. Four modules of SLC and HXM are implemented at different four angles to cover 25 % of the entire sky in the energy band from 0.7 keV to 1 MeV. SLC: Soft X-ray Large Solid Angle Camera, HXM: Hard X-ray Monitor

ators permanently facing the deep space to release the heat. Then development of a thermal model for the SLC module is in progress and verification of its feasibility was almost achieved. We find that the dominant heat paths to the CCD contribute from conductances through flexible cables to the CCD packages, the support legs of the base plate, cold plate to bus interface plate and the radiation from the flexible cables, while the heat production on the CCD itself is small. Taking account these heat paths, the target temperature of the CCD is achievable. However the four mechanical coolers consume a significant amount of power ($>$ 300 W). Further design study of the conductances which attribute to the critical thermal path such as CCD flexible cables (e.g., use of thinner conductive wires) or relaxation of the required temperature by improving the CCD dark current (e.g., surface processing on the CCDs), is underway. Especially, the required heat load for the mechanical cooler is estimated to be 5.2 W and we plan to verify the thermal model with a prototype model by 2015 (Fig. 2).

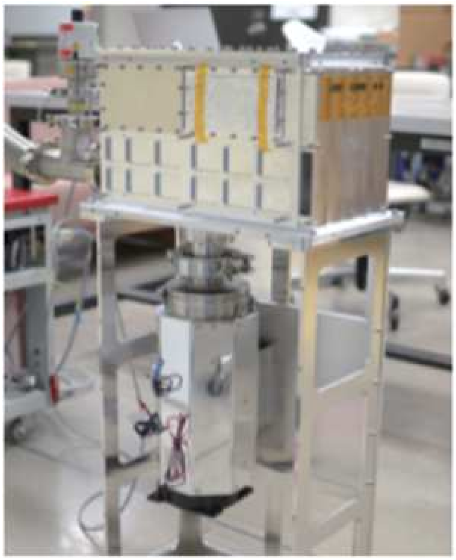

Figure 2: Prototype model of the mechanical cooler for SLC

2.2. Hard X-ray Monitor

As the secondary scientific instrument of *WF-MAXI*, HXM [9] measures the energy spectra and light curves of short transient events in the 20 keV 1 MeV energy range and provides the trigger for GRBs.

HXM consists of a 24-channel array of Ce-doped $Gd_3Al_2Ga_3O_{12}$ (Ce:GAGG) scintillator coupled with avalanche photodiode (APD) covering the hard X-ray band with an effective area of 120 cm^2 (Fig. 1). To obtain a better signal to noise (S/N) ratio and detect higher-energy photons, we select the Ce:GAGG crystal due to its high light yield (46,000 photons/MeV) and density (6.63 g/cm^3), where scintillation light peaks at a wavelength of 520 nm, in well matching with the sensitivity of the silicon photon detector. The lower energy threshold of 20 keV is achievable by operating it at 20 ∼ 0 °C using a passive thermal structure or a thermoelectric cooler.

We adopt flight-proven reverse-type APDs with a pixel size of 5 × 5 mm^2 provided by Hamamatsu Photonics to detect scintillation lights of the Ce:GAGG crystal. The performance of the APD is low-noise and flight-proven to be radiation hardness on CubeSat (*Cute-1.7+APD II* [10]) working in a polar orbit for five years as a radiation particle monitor. Its technology is also adopted for micro-satellite *Tsubame* [11] and ASTRO-H [12]. In addition, as it is well known that the gain of APDs strongly depends on temperature and the bias voltage, in the HXM system the APD gain dependent on temperature is controlled by adjusting the bias voltage.

We developed a new LSI dedicated for an analog amplification of APDs' signal. The new LSI contains 32-channel amplifiers and AD converters with a chip size of 4.8 × 8.4 mm^2 (Fig. 3). Especially, to accomplish the quick development we utilized well-studied 0.35 μm CMOS technology based on Open IP project by Professor Hirokazu Ikeda and accumulated knowledge for a decade. As a detector capacitance of APDs is large (∼100 pF), its capacitive noise is crucial for detection of X-ray photons around the lower energy threshold (∼20 keV). We thus designed the analog circuit to suppress the capacitive noise (e.g., larger transconductance, larger gate area of input FETs and so on). We show the performance of the developed LSI in Table II and one of obtained spectra in Fig 4. Signals from 32 keV and 662 X-rays are clearly detected and its energy resolutions (FWHM) are determined to be 28.0% and 6.9 %, respectively. The detection of 32 keV X-rays shows the low-noise amplifier in the new LSI almost has achieved the lower energy threshold of 20 keV in HXM.

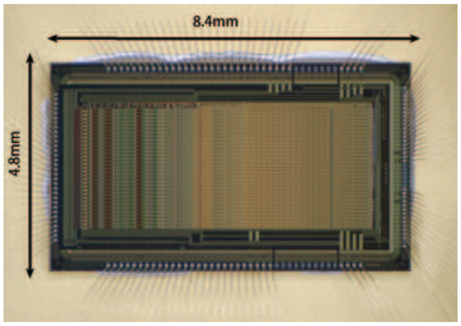

Figure 3: Developed LSI dedicated for processing APD signals (HXM). The LSI contains 32-ch analog amplifiers and AD converters and the design of the noise suppression is implemented.

Table II Specification & performance of the new LSI for HXM

Number of channels	32
Dynamic range	0 – 300 fC
Non linearity	<4%
Peaking time for trigger	0.5 μs
Peaking time for spectroscopy	3 μs
Equivalent Noise Charge	∼2400 e^-
Power supply	±1.65 V
Power consumption	∼100 mW

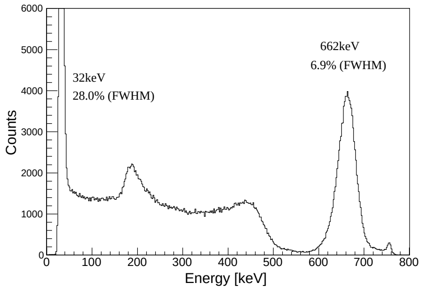

Figure 4: Energy spectrum of ^{137}Cs with the reverse-type APD (S8664-55) coupled to the Ce:GAGG crystal scintillator.

3. Summary

WF-MAXI is a proposed mission of X-ray transient monitor as a payload on the ISS. Its science goal is to detect and localize X-ray transient sources and issue prompt alerts to the astrophysical community all over the world. The X-ray counterpart of the first directly detected GW event is the prime target of the *WF-MAXI* mission. Furthermore, it is the first dedicated transient monitor mission that covers a significant fraction (∼25 %) of the entire sky in the soft X-ray band with a energy resolution of CCD plus the hard X-ray band, which promises to open a new discovery space.

We have been developing two mission instruments of SLC Soft X-ray Large Solid Angle Camera and HXM Hard X-ray Monitor. For SLC, the thermal design of cooling the CCD chips to -100°C, the prototype and its readout electronics are being developed. For HXM, the new LSI dedicated for the readout of signals from APDs was developed and we find that the designed low-noise analog amplifier achieved our goal of the lower energy threshold (20 keV). We will apply the *WF-MAXI* mission or modified mission to Small-size project 2015 funded from JAXA to develop and launch the payload for the beginning of the operation of next generation gravitational-wave observatories.

Acknowledgments

This work is supported by Grant-in-Aid for Scientific Research on Innovative Areas New development in astrophysics through multi-messenger observations of gravitational wave sources, MEXT KAKENHI Grant Number 80195031.

References

[1] Kawai, N., Tomida, H., Yatsu, Y., et al. 2014, SPIE, 9144, 91442P

[2] Ricker, G. R., Atteia, J.-L., Crew, G. B., et al. 2003, Gamma-Ray Burst and Afterglow Astronomy 2001: A Workshop Celebrating the First Year of the HETE Mission, 662, 3

[3] Matsuoka, M., Kawasaki, K., Ueno, S., et al. 2009, PASJ, 61, 999

[4] Abadie, J., Abbott, B. P., Abbott, R., et al. 2010, Classical and Quantum Gravity, 27, 173001

[5] Band, D., Matteson, J., Ford, L., et al. 1993, ApJ, 413, 281

[6] Kimura, M., Tomida, H., Ueno, S., et al. 2014, SPIE, 9144, 914460

[7] Tomida, H., Tsunemi, H., Kimura, M., et al. 2011, PASJ 63, 397

[8] Hayashida, K., Tsunemi, H., Tsuru, T. G., et al. 2014, SPIE, 9144, 914429

[9] Arimoto, M., Yatsu, Y., Kawai, N., et al. 2014, SPIE, 9144, 91445Z

[10] Kataoka, J., Toizumi, T., Nakamori, T., et al. 2010, Journal of Geophysical Research (Space Physics), 115, A05204

[11] Yatsu, Y., Ito, K., Kurita, S., et al. 2014, SPIE, 9144, 91440L

[12] Sato, G., Kokubun, M., Nakazawa, K., et al. 2014, SPIE, 9144, 914427

Pathfinder flight of the Polarized Gamma-ray Observer (PoGOLite) in 2013

Takafumi Kawano, On behalf of the PoGOLite Collaboration
High Energy & Optical/Infrared Astrophysics Laboratory, Hiroshima University, Higashi-Hiroshima, Hiroshima, 739-8526

The Polarized Gamma-ray Observer (PoGOLite) is a balloon-borne instrument that can measure polarization in the energy range 25–240 keV. The instrument adopts an array of well-type "phoswich" detectors in order to suppress backgrounds. Based on the anisotropy of Compton scattering angles resulting from polarized gamma-rays, the polarization of the observed source can be reconstructed. During July 12-26 of 2013, a successful near-circumpolar pathfinder flight was conducted from Esrange, Sweden, to Norilsk, Russia. During this two-week flight, several observations of the Crab were conducted. Here, we present the PoGOLite instrument and summarize the 2013 flight. *tkawano@hep01.hepl.hiroshima-u.ac.jp.*

1. Measuring polarization

Astrophysical phenomena can be observed with electromagnetic radiation by imaging, spectroscopy, timing analysis, and polarimetry. Since X-ray observations began 50 years ago, many observatories have provided data for imaging, spectroscopy, and timing analyses. On the other hand, polarization measurements of X-rays and gamma-rays have been technically difficult and only a few sensitive observations have been performed. Polarized X-rays and gamma-rays are expected to be emitted from a wide variety of astronomical sources, including pulsars, X-ray binary systems, strongly magnetized neutron stars, collimated outflows from active galactic nuclei and gamma-ray bursts. Therefore, polarimetric studies of these sources are expected to provide important new insight into the physics of such highly energetic objects. In particular, it is important to understand the acceleration site and magnetic field structure of pulsars and their surrounding wide nebulae by identifying the emission mechanisms with polarimetry.

2. Target object: the Crab nebula

2.1. Outline

The Crab nebula is a remnant of the historical supernova in 1054 A.D., located around 2 kpc from the Earth. This celestial object is named "Crab nebula" after the characteristic filament structure in optical wavelengths, and it has been studied intensively in all wavelengths from radio to gamma-rays since the early days of astronomy. The Crab consists of a pulsar, a synchrotron nebula and a bright expanding shell of thermal gas. We can also see a highly collimated bipolar outflow (jet), which is aligned to the spin axis of the pulsar, as well as a circumstellar torus visible in X-rays. The high-energy emission is brightest near the center of the nebula.

The Crab pulsar is considered as a neutron star with a radius of 10 km, a mass of 1.4 $M_\odot$, a rotation period P = 33 ms, $\dot{P} = 4.21 \times 10^{-13}$, magnetic field $B \approx 10^{12}$ G, and spin-down luminosity $L_s \approx 5 \times 10^{38}$ erg/s. The strong magnetic field and short rotation period produce a relativistic outflow of electron-positron pairs which is called the pulsar wind. This ultrarelativistic outflow is confined by the thermal ejecta. The inner ring of the nebula, reported to be at a distance of about 3×10^{17} cm from the pulsar, corresponds to a termination shock, created when the pulsar wind interacts with the surrounding synchrotron nebula. It is considered that the pulsar wind and possibly other particles are accelerated to energies as high as $\sim 10^{16}$ eV at the termination shock. High energy charged particles interact with the magnetic field in the nebula ($\sim$a few mG), and emit synchrotron radiation. The X-ray emission becomes softer toward the outer region owing to adiabatic and radiative losses. At the edge of the nebula, there are only low-energy radio-emitting electrons. The spectrum of X-rays and gamma-rays below 1 GeV for the Crab nebula is well described by synchrotron emission, and inverse Compton scattering dominates above 1 GeV [5].

2.2. Previous polarization measurements of the Crab nebula

A. Measurement by OSO-8

The OSO-8 satellite carried an X-ray polarimeter consisting of a panel of mosaic graphite crystals, which were utilized for Bragg reflection [10].

The polarization fraction of the Crab nebula observed by OSO-8 was (19.19 ± 0.97)% with (156.36 ± 1.44)° polarization angle at 2.6 keV, and (19.50 ± 2.77)% polarization fraction with (152.59 ± 4.04)° polarization angle at 5.2 keV, where the errors correspond to 67% confidence contours.

These results are in agreement with optical polarization measurements (FIG. 1) [10].

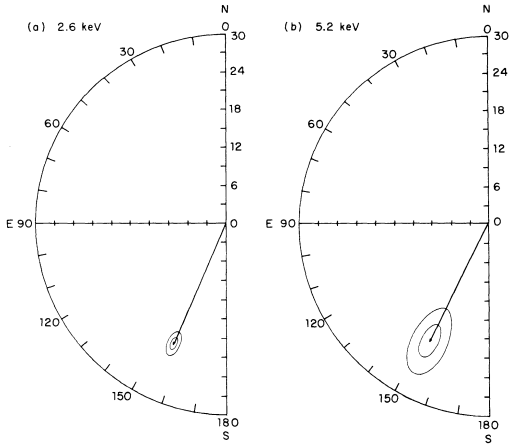

Figure 1: The polarization vectors for the Crab nebula at (a) 2.6 keV and (b) 5.2 keV. Surrounding regions (in order of increasing size) correspond to the 67% and 99% confidence contours [10].

B. Observation by INTEGRAL/SPI

The SPI (spectrometer onboard INTEGRAL; INTErnational Gamma-Ray Astrophysics Laboratory) has a capability for polarization measurements using Compton scattering [6].

A polarization analysis of the Crab nebula was performed with data recorded from February 2003 to April 2006, and only events during the off-pulse fraction of the pulsar cycle were included (FIG. 2 top).

A polarization fraction of (46 ± 10)% was observed, with the polarization angle (123 ± 11)°, which is closely aligned with the pulsar spin axis ((124 ± 0.1)°) (FIG. 2 bottom), but the errors are dominated by systematic effects. The observed alignment of the polarization axis with the jet axis suggests an orthogonal magnetic field configuration towards the jet axis if the soft gamma-ray emission is caused by synchrotron emission. The observed polarization fraction is quite high, but less than the maximum limit for synchrotron radiation, ~75% [3][1].

C. Observation by INTEGRAL/IBIS

The IBIS (imager on INTEGRAL) is also using Compton scattering for polarimetry [4]. Also this instrument has been used to study the polarization of the Crab.

The results are shown with respect to the pulsar phase (FIG. 2 top). For the "off-pulse" phase and "off-pulse and bridge" phase, the polarization fraction is reported to be quite high (>72%), with the polarization angle aligned along the jet axis (FIG. 3). This result suggests that the off-pulse polarized emission recorded above 200 keV can come from a striped wind, jets, and/or equatorial wind near the bright knot. The magnetohydrodynamics models predict that the polarization is strongest at the pulsar, in the knot, and along the jets, and it should be mostly parallel to the rotation axis [4].

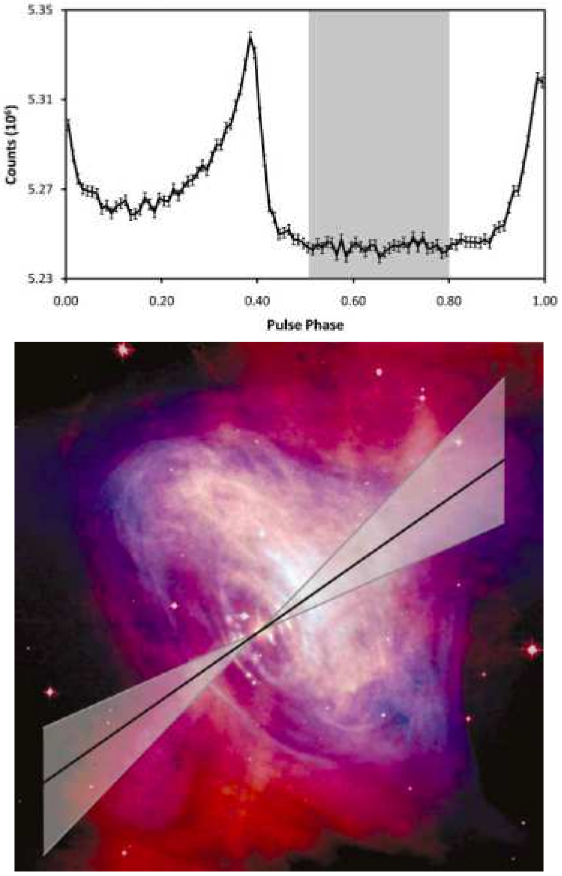

Figure 2: Top: The light curve of the Crab pulsar. There are two pulse phases (0.88<ϕ<0.14 and 0.25<ϕ<0.52), off-pulse phase (0.52<ϕ<0.88), and last phase called as "Bridge" phase (0.14<ϕ<0.25). The data for polarization analysis for INTEGRAL/SPI is selected from within the phase interval from 0.5 to 0.8 of the pulsar period (shaded area) in 100–1000 keV. Bottom: Composite image of the Crab, blue: Chandra X-ray image, red: Hubble Space Telescope optical image, and the gamma-ray polarization vector is superimposed (gray area). The direction of the polarization vector is along the jet axis. [3]

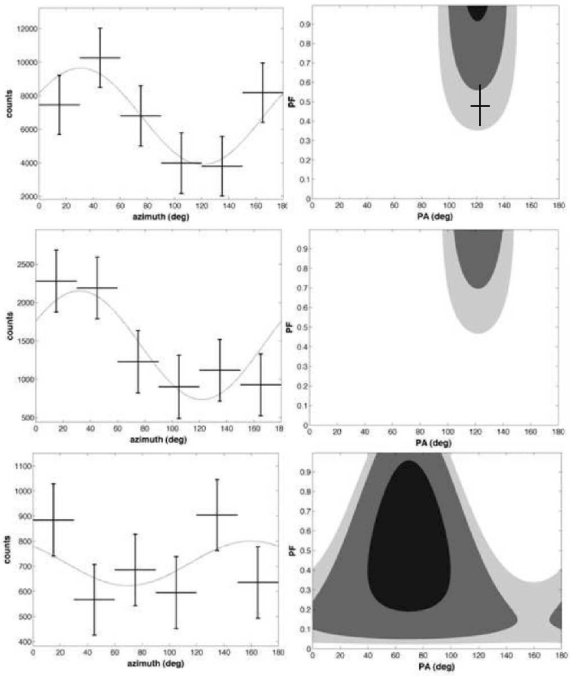

Figure 3: The polarization of the Crab nebula observed by INTEGRAL/IBIS. The polarization angle and polarization fraction are measured for the Crab data between 200–800 keV, in the off-pulse (top), off-pulse and bridge (middle), and two-peak (bottom) phase intervals. The error bars for the profile are at 1σ. The 68%, 95%, and 99% confidence regions are shaded from dark to light gray. The SPI result [3] is indicated in the top figure by a cross [4].

3. The PoGOLite balloon-borne instrument

3.1. Overview

PoGOLite (Polarized Gamma-ray Observer Lightweight version) is a balloon-borne Compton polarimeter (FIG. 4), measuring the polarization of hard X-rays/soft gamma-rays from celestial objects in the energy range 25–240 keV [8]. Polarization in the 25–100 keV energy band has not been observed previously.

Observational targets for PoGOLite include the Crab and Cygnus X-1, and the instrument is able to detect 10% liner polarization from the Crab nebula for 15-hour exposure time with the 99% confidence, in a signal-to-background scenario of 1:1. The detector is optimized for point sources, with a narrow field of view of 2.4° × 2.6°, and the required pointing precision is 0.1°. Since radiation from sources follows an inverse power-law and photons are additionally absorbed in the atmosphere, a high float altitude of the instrument (∼40 km) and sensitivity extending as low as possible are crucial. The collaboration is international, involving institutes and universities from Japan[1], Sweden[2], and the United States[3].

Figure 4: Overview of the PoGOLite payload. The height is ∼4 m and the weight is ∼2 tonnes. A 1.1 million cubic meter helium-filled balloon is used for lifting the payload.

The full-size version of PoGOLite consists of 217 units. It is intended to be able to measure as low as 10% polarization from a 200 mCrab source in a six-hour flight [7]. The 61-unit "Pathfinder" version of PoGOLite has been prepared for launch from Esrange in northen Sweden in 2011, 2012 and 2013. In this paper, we simply refer to the "PoGOLite Pathfinder" as "PoGOLite". On July 6th, 2011 (UTC), the payload was launched for a flight with a foreseen landing in Canada (duration ∼5 days). However, there was a leak of helium from the balloon, and the gondola was returned to ground after ∼5 hours. A second launch was foreseen in July 2012, but had to be cancelled due to unfavorable weather conditions. PoGOLite was successfully launched from Esrange, Sweden, on July 12th at 0818 UT in 2013 (FIG. 5). A circumpolar flight was possible thanks to permission received from Russian authorities. The flight ended on July 26th when the gondola touched down close to the Siberian city of Norilsk (∼3000 km to the East of Moscow) at 0015 UT.

---

[1] Hiroshima University, Tokyo Institute of Technology, Yamagata University, Japan Aerospace Exploration Agency (JAXA).

[2] Royal Institute of Technology (KTH), Stockholm University (SU).

[3] Stanford Linear Accelerator Center (SLAC), Kavli Institute for Particle Astrophysics and Cosmology (KIPAC), University of Hawaii.

Figure 5: The launch of PoGOLite from Esrange on July 12th 2013, 0818 UT. The distance from the top of the balloon to the gondola is ∼300 m.

3.2. Detector configuration

To suppress the high rate of background events at float altitude (∼40 km), we adopted an array of 61 well-type phoswich detector cells (PDCs) surrounded by a segmented BGO (bismuth germanate oxide, $Bi_4Ge_3O_{12}$) anticoincidence shield comprising 30 units. A LiCAF ($LiCAl_6$) neutron-sensitive scintillator [9] is also included (FIG. 6 top). Each PDC consists of three active components: a hollow "slow" plastic scintillator (60 cm), a solid "fast" plastic scintillator (20 cm), and a BGO crystal (4 cm), read out by a photomultiplier tube (from Hamamatsu Photonics, 19 cm) (FIG. 6 bottom). The LiCAF scintillator is made for neutron detection since neutrons are expected to dominate the background. This detector is sandwiched between two BGO elements for rejecting gamma-rays, allowing neutron interactions to be distinguished.

The photomultiplier tube waveforms are sampled at a 37.5 MHz rate and digitized with to 12 bit accuracy.

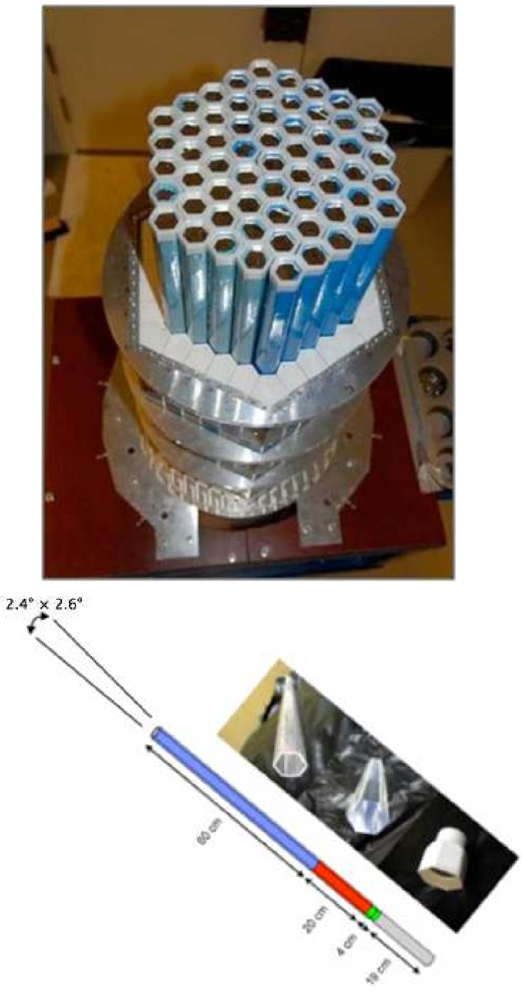

Figure 6: Top: The main detector consists of 61 PDCs and 30 SASs with BGO. Bottom: One of the PDCs, which is consisting of a hollow "slow" plastic scintillator (60 cm), a solid "fast" plastic scintillator (20 cm), a BGO crystal (4 cm) and photomultiplier tube (from Hamamatsu Photonics, 19 cm).

The "fast" scintillator, "slow" scintillator and BGO crystal have different decay times, resulting in different pulse shapes for waveforms originating from these components (FIG. 7). By identifying these differences, we can determine in which component an interaction has taken place, allowing background events to be discarded. The PDC units are hexagonal so they can be tightly packed in a honey-comb structure, while surrounding SAS segments have two different pentagonal shapes to fit closely around detector array (FIG. 8).

3.3. Polarimeter design

An indicator of performance of X-ray and gamma-ray polarimeters, which is called as MDP (Minimum Detectable Polarization; degree distinguishable from

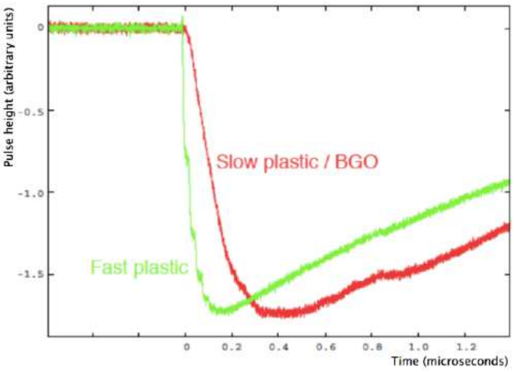

Figure 7: Examples of characteristic waveforms (shown with a negative polarity). The rise time is shorter for a signal from the fast plastic scintillator than for one from the slow scintillator or BGO crystal.

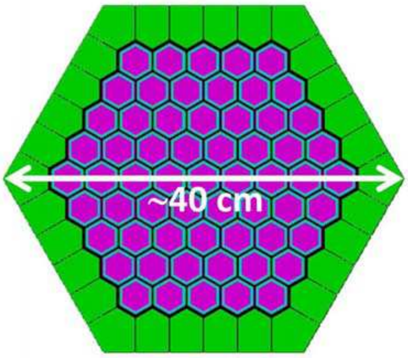

Figure 8: Top view of a 61-unit detector array. The PDCs (purple) are surrounded by a segmented side anti-coincidence shield (green).

statistical fluctuation with 3σ), is written in equation (1).

$$MDP = \frac{4.29}{M \times R_S}\sqrt{\frac{R_S + R_B}{T}} \quad (1)$$

where M is the modulation factor (depends on the instrument geometry and the spectrum of the incident photon flux), R_S is the signal rate, R_B is the background rate and T is the exposure time. This represents the minimum polarization fraction measurable by the instrument for the given confidence level [11]. A large M, a large R_S, a small R_B, and a large T are needed to achieve a low MDP, i.e. good sensitivity to polarization. For a given source, a large R_S corresponds to a large effective area of the instrument.

For PoGOLite, the effective area is $\sim$22 cm^2, with a reasonable modulation factor (M $\sim$26% at 50 keV) [2].

4. Measuring polarization

The PoGOLite instrument is using Compton scattering for polarimetry. The procedure is illustrated below (FIG. 9):

- Polarized gamma-rays undergo Compton scattering in a hexagonal array of plastic scintillators.
- Polarized photons tend to scatter perpendicularly to the polarization direction, following equation (2).
- Observed azimuthal scattering angles are modulated by polarization.

$$\frac{d\sigma}{d\Omega} = \frac{1}{2} r_e^2 \frac{k^2}{k_0^2}\left(\frac{k}{k_0} + \frac{k_0}{k} - 2\ sin^2\theta cos^2\phi\right) \quad (2)$$

where k_0 and k are the momenta of the incident and scattered photon, respectively, r$_e$ is the classical electron radius and θ and ϕ correspond to the polar and azimuthal scattering angles. Angle ϕ is defined relative to the polarization direction of the incident photon, resulting in a polarization-dependence for the scattering process.

Tracking individual photons through coincident detection of Compton scattering and photoelectric absorption allows the azimuthal scattering angles to be reconstructed. Since photons scatter preferentially perpendicular to the polarization direction, the resulting distribution of scattering angles will be anisotropic (modulated) for a polarized flux of photons.

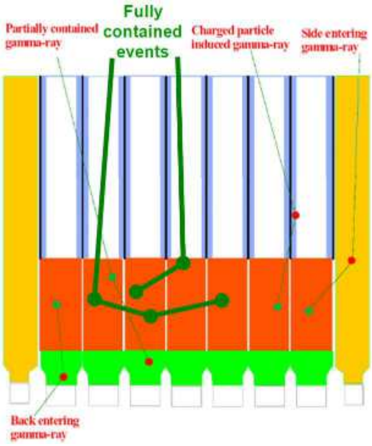

Figure 9: The detection method of polarization. Cross section of the detector, tracking both of scattering and absorption position of X-rays. Some examples of background events have also been indicated.

5. Flight trajectory & Results

As mentioned in section 3.1, during July 12-26 of 2013, a successful near-circumpolar pathfinder flight was conducted from Esrange, Sweden, to Norilsk, Russia (FIG. 10). During the daytime, the balloon has higher altitude because of heating of the helium inside the balloon. Conversely, the balloon has lower altitude during the night, resulting in a diurnal variation of the pressure.

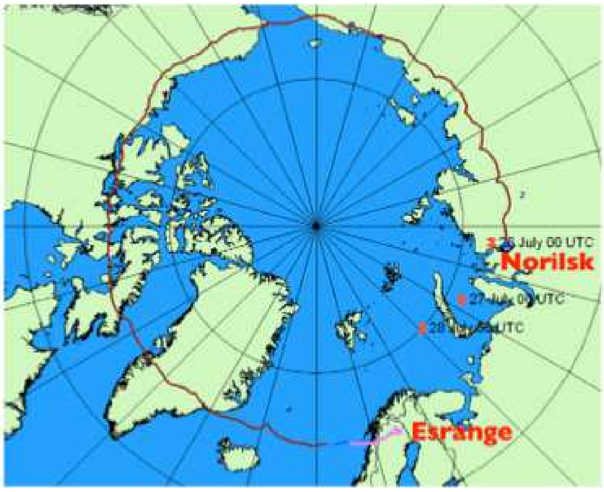

Figure 10: The trajectory of PoGOLite flight in 2013. PoGOLite was launched from Esrange, Sweden at 0818 UT on July 12th in 2013, and landed Norilsk, Russia at 0015 UT on July 26th. Courtesy of SSC Esrange.

The attitude control system performance has been evaluated from Crab measurements, and the observed performance was found to be an order of magnitude better than the design requirement of 0.1°.

We obtained the pulse-folded light curve of the Crab pulsar. The data includes two- and three-hit events in the energy range 20 keV – 110 keV, and we can clearly see the Crab pulsation from the light-curve. This shows that X-ray photons from the Crab pulsar are indeed detected by the polarimeter, confirming that the instrument and attitude control system are working as intended.

6. Summary & Outlook

During July 2013, the PoGOLite Pathfinder made a circumpolar flight (∼13.5 days) from Esrange. This flight was possible thanks to permission from the Russian government and help from Russian colleagues. We have confirmed that the polarimeter detected the Crab pulsation. Crab polarization results are in preparation. We have a plan to improve the polarimeter design based on the experience from the 2013 flight, to reject background more efficiently. Reflight of PoGOLite is proposed for the summer of 2016.

References

[1] Chauvin, M., Roques, J. P., Clark, D. J., & Jourdain, E. 2013, Astrophysical Journal, 769, 137

[2] Chauvin, M., Florén, H.-G., Jackson, M., Kamae, T., Kawano, T., Kiss, M., Kole, M., Mikhalev, V., Moretti, E., Rydström, S., Takahashi, H., Pearce, M., Astroparticle Physics Journal submitted

[3] Dean, A. J., Clark, D. J., Stephen, J. B., et al. 2008, Science, 321, 1183

[4] Forot, M., Laurent, P., Grenier, I. A., Gouiffès, C., & Lebrun, F. 2008, ApJL, 688, L29

[5] Hester, J. J. 2008, ARA&A, 46, 127

[6] Kalemci, E., Boggs, S., Wunderer, C., & Jean, P. 2004, 5th INTEGRAL Workshop on the INTEGRAL Universe, 552, 859

[7] Kamae, T., Andersson, V., Arimoto, M., et al. 2008, Astroparticle Physics, 30, 72

[8] Kiss, M., Royal Institute of Technology Doctoral Thesis, "Pre-flight development of the PoGOLite Pathfinder" (2011), ISBN 978-91-7415-896-0.

[9] Takahashi, H., Chauvin, M., Fukazawa, Y., et al. 2014, SPIE Proceedings, 9144, 91444I

[10] Weisskopf, M. C., Silver, E. H., Kestenbaum, H. L., Long, K. S., & Novick, R. 1978, ApJL, 220, L117

[11] Weisskopf, M. C., Elsner, R. F., & O'Dell, S. L. 2010, SPIE Proceedings, 7732, 77320E

Observations of Gamma-ray Bursts with ASTRO-H and Fermi

M. Ohno[1], T. Kawano[1], M. S. Tashiro[2], H. Ueno[2], D. Yonetoku[3], H. Sameshima[4], T. Takahashi[4], H. Seta[5], R. Mushotzky[6], K. Yamaoka[7], *ASTRO-H* SWG team and *Fermi* LAT/GBM collaborations
[1]*Department of Physical Sciences, Hiroshima University, 1-3-1 Kagamiyama, Higashi-Hiroshima, Hiroshima 739-8526*
[2]*Department of Physics, Saitama University, 255 Shimo-Okubo, Sakura-ku, Saitama-shi, Saitama 338-8570*
[3]*Department of Physics, Kanazawa University, Kadoma-cho, Kanazawa, Ishikawa 920-1192*
[4]*Institute of Space and Astronautical Science Aerospace Exploration Agency (ISAS/JAXA), 3-1-1 Yoshinodai, Sagamihara, Kanagawa 229-8510*
[5]*Department of Physics, Rikkyo University, Nishi-Ikebukuro, Toshimaku, Tokyo 171-8501*
[6]*Department of Astronomy, University of Maryland College Park, MD 20742-2421 and*
[7]*Solar-Terrestrial Environment Laboratory, Nagoya University, Furo-cho, Chikusa-ku, Nagoya 464-8601*

ASTRO-H, the sixth Japanese X-ray observatory, which is scheduled to be launched by the end of Japanese fiscal year 2015 has a capability to observe the prompt emission from Gamma-ray Bursts (GRBs) utilizing BGO active shields for the soft gamma-ray detector (SGD). The effective area of the SGD shield detectors is very large and its data acquisition system is optimized for short transients such as short GRBs. Thus, we expect to perform more detailed time-resolved spectral analysis with a combination of *ASTRO-H* and Fermi LAT/GBM to investigate the gamma-ray emission mechanism of short GRBs. In addition, the environment of the GRB progenitor should be a remarkable objective from the point of view of the chemical evolution of high-z universe. If we can maneuver the spacecraft to the GRBs, we can perform a high-resolution spectroscopy of the X-ray afterglow of GRBs utilizing the onboard micro calorimeter and X-ray CCD camera.

1. Introduction

Gamma-ray Bursts (GRBs) are one of the most energetic explosion in the universe, but there are still many issues to be understood such as gamma-ray emission mechanism of prompt emission, physical composition of jet outflow, and environment of progenitor. GRBs are also known to be originated at cosmological distance and they would be useful to explore the chemical evolution of high-z universe.

ASTRO-H is the sixth X-ray observatory from Japan, which is scheduled to be launched by the end of Japanese fiscal year 2015. Four onboard instruments of *ASTRO-H*, the high-resolution X-ray micro-calorimeter (Soft X-ray Spectrometer: SXS), X-ray CCD camera (Soft X-ray Imager: SXI), Hard X-ray Imager (HXI), and Soft Gamma-ray Detector (SGD) realize wide-band and high-sensitivity observation from 0.3 to 600 keV energy band. The high-resolution spectroscopy by SXS and X-ray observations with enough photon statistics by SXI could be very powerful tool to investigate spectral features and detail of X-ray absorption structure in the afterglow spectrum of GRBs. And also, high-sensitive hard X-ray observation by HXI might observe interesting features from afterglow in hard X-rays. In addition to such afterglow observations by focal plane instruments, *ASTRO-H* is also able to observe the prompt gamma-ray emission utilizing SGD. Therefore, *ASTRO-H* will bring us a comprehensive observation of GRBs from prompt gamma-ray emission to subsequent X-ray afterglow emission. In this paper, we demonstrate a capability of GRB observation by *ASTRO-H*.

2. Prompt emission observation by the SGD shield

Our understanding of gamma-ray emission mechanism of GRBs, especially for short duration GRBs is still poor. One of key observation to solve such problem is time-resolved spectroscopy as was performed for long duration GRBs. However, photon statistics of short GRBs is too low to perform such time-resolved analysis, and therefore, observation of short GRBs with large effective area is important. *ASTRO-H* has capability to observe prompt gamma-ray emission of short GRBs with large effective area and good time-resolution utilizing SGD. The main detector, Compton camera of the SGD is surrounded by large 25 BGOs to reduce background by anti-coincidence technique as shown in Fig 1. Thanks to its large geometrical area and high gamma-ray stopping power of BGO crystal, the effective area of those "shield" detectors retain $\sim$ 800 cm^2 even at 1 MeV. Therefore, the SGD shield detector acts as a powerful all-sky monitor like Suzaku WAM[8]. We have developed the SGD shield detector so that we can observe short transients such as short GRBs or Soft Gamma Repeaters with many advantages compared with Suzaku WAM. Table I shows some specifications of the SGD shield detector as an all-sky monitor comparing with Suzaku WAM. The main advantage of the SGD shield detector is that it can obtain spectral information with very large effective area. We also improved data acquisition timing of GRB data of the SGD shield so that we can transfer GRB data to the spacecraft soon ($\sim$10 min) after trigger and we can set the trigger to be ready for the next GRB. This enable us to improve the efficiency of

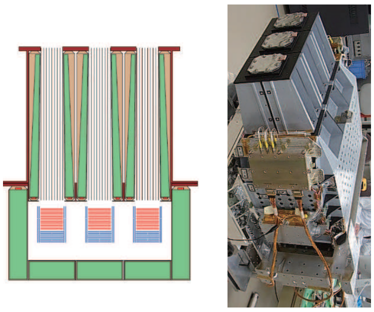

Figure 1: A schematic picture and a real flight model picture of the SGD. The three main detectors are located inside of BGO crystals.

Table I Performance of the SGD shield detector as all-sky monitor comparing with Suzaku-WAM

	SGD shield	Suzaku WAM
Time resolution	16 ms	16 ms
Time coverage	5.376 s (-1.376 to 4.0 s)	64 s (-8 to 56 s)
Spectral channels	32 ch	4 ch
Energy range	150 – 5000 keV	50 – 5000 keV
Effective area (1MeV)	$\sim$ 800 cm^2	$\sim$ 400 cm^2

GRB observation.

Figure 2 shows an example of simulated light curve of bright short GRB with peak flux of about a few times of 10 photons s^{-1} cm^{-2} in 1 second time scale. In this simulation, we consider poisson fluctuation in each time bin of the SGD shield (16 ms) and we assumed simple Band function with low-energy index $\alpha = -0.8$ and high-energy index $\beta = -2.3$. The peak energy $\mathrm{E}_{\mathrm{peak}}$ has changed depending on the flux. Figure 3 shows the time-resolved spectrum extracted with 0.1 s time windows, which are shown by hatched area in the figure 2. We can see that the simulated light curve exhibit fine time structure and extracted time-resolved spectra show clear evolution of $\mathrm{E}_{\mathrm{peak}}$. Therefore, we can expect to have such GRB data with the SGD shield. After launch of *ASTRO-H*, GRB data observed by the SGD shield will be publicly available as well as Suzaku WAM. The GRB observation by the SGD shield can provide complementary dataset to Fermi-GBM. Based on simultaneously detection rate between Suzaku-WAM and Fermi-GBM, about a half of GRBs detected by Fermi-GBM are expected to be also detected by the SGD shield.

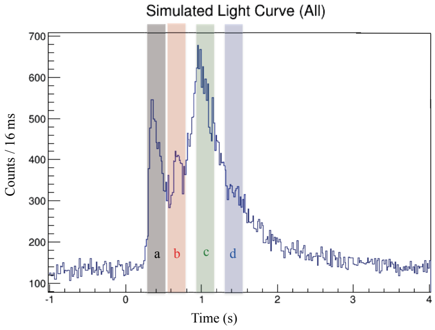

Figure 2: An example of light curve simulation of bright short GRB with photon flux of a few tens of photons s−1 cm^{-2} by the SGD shield. Each hatched region show the time window for the demonstration of time-resolved spectral analysis in the below figure.

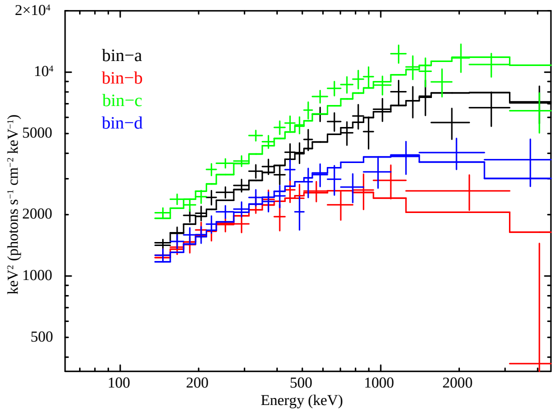

Figure 3: A simulated time resolved spectral analysis using above simulated light curve data.

3. ToO observations of afterglow with SXS and SXI

As for the X-ray afterglow of GRBs, which is widely believed that the X-ray emission is coming from synchrotron emission due to accelerated electrons in the external forward shock. Therefore, most of X-ray spectrum of afterglow show featureless simple power-law shape. However, there are several reports of marginal detection of spectral features such as iron-K emission line, its recombination edge, and several lines due to light metals [2],[3],[5]. Although, they are still controversial probably because of limited statistics and/or spectral resolution, such spectral features would be very important to investigate physical conditions of GRB jet and composition of environment of GRB host, and also they are useful to determine the redshift of GRB by X-ray observation itself. In addition to such spectral features, Behar et al. (2011) and Starling et al. (2013) have pointed out the evidence of excess absorption in soft X-ray energy band using huge sample of Swift X-ray afterglow observation. One possibility of origin for such excess absorption is contribution of absorption by intergalactic medium (IGM). Therefore, detail spectroscopy in soft X-ray band could give important information to investigate the property of IGM in high-z universe. An X-ray observation with high spectral resolution is a key to solve above open questions in GRB afterglow. Those emission line and/or absorption line spectral features can be investigated by unprecedented high energy resolution spectroscopy by *ASTRO-H* SXS, and detail of continuum structure can be determined by SXI. Figure 4 shows a 100 ks *ASTRO-H* simulation with SXS and SXI. Here we assumed GRB 991216 spectrum as the baseline model fro simulation. In this model, 2−10 keV flux is set to be 3×10^{-12} erg cm^{-2} s^{-1}. This GRB has been reported to have iron-K line and its recombination edge[4] and thus we include those spectral features in the simulation. We also added soft X-ray lines reported by Reeves et al. (2003) for GRB 011211, and intergalactic warm absorbers (WHIM) with the temperature of 10^5 K, the column density of N_H of 10^{22} cm^{-2}, and we put those absorption material on redshift of z=0.1. From this simulation, we can see that the iron-K related spectral features can be detected clearly by *ASTRO-H* if they are really exist. In addition, some resonance absorption lines due to WHIM are also detectable with about 4 sigma significance level, thanks to high energy resolution of SXS. Figure 5 shows the same simulation with figure 4 but with shorter exposure of 10 ks and we changed intrinsic line width from 5 eV to 30 eV. We can clearly detect the iron-K line emission if it is intrinsically narrow with σ < 10 eV with short exposure of 10 ks. This indicates that we can investigate the time variability of such iron-K line emission, which is useful to discuss the environment of host galaxy o GRBs.

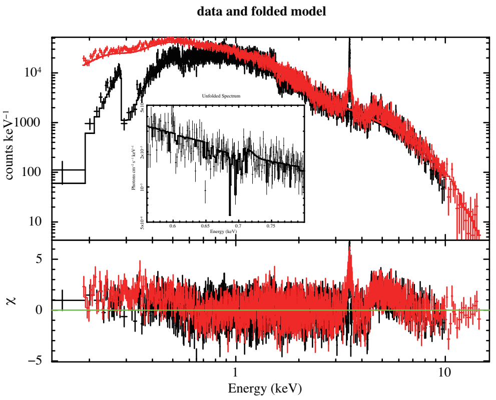

Figure 4: *ASTRO-H* simulation of GRB afterglow spectrum with warm absorber model (see text in detail). The enlarged structure around 0.6-0.8 keV, where the most prominent absorption features can be seen are also shown in the inset. Bottom part shows the residuals from single power-law model with absorption from cold materials.

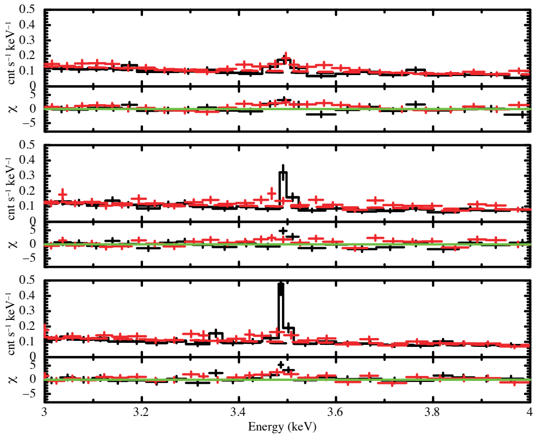

Figure 5: 10 ks simulation of around iron-K emission line. Each panel show the simulation with different intrinsic line width (σ= 30 eV, 10 eV, and 5 eV from top to bottom). Lower part in each panel shows the residual from single power-law model.

4. Expected event rate of ToO observations of GRB afterglow with *ASTRO-H*

As we shown in previous section, *ASTRO-H* has a capability of detection of spectral features from GRB afterglow such as iron-K emission line and resonance absorption lines due to intergalactic warm absorbers. Then, we have to estimate how many number of GRBs we can observe with such interesting spectral features by *ASTRO-H*. For this purpose, we calculated a luminosity function of GRB afterglow based on 572 samples of 6-years Swift-XRT data base which is publicly available in the web page [7]. Figure 6 shows the luminosity functions of GRB afterglow for several times after GRB trigger. From this result, we can see that about 10 GRBs/year are expected which have 10^{-12} erg s^{-1} cm^{-2} flux level, which corresponds to that of we used in the iron-K line simulation in Fig 5, even 30 hours after the trigger. This means that if we can slew the *ASTRO-H* spacecraft within 1-day after the trigger, we could have 10 GRBs/year samples for possible iron-K line search with *ASTRO-H*.

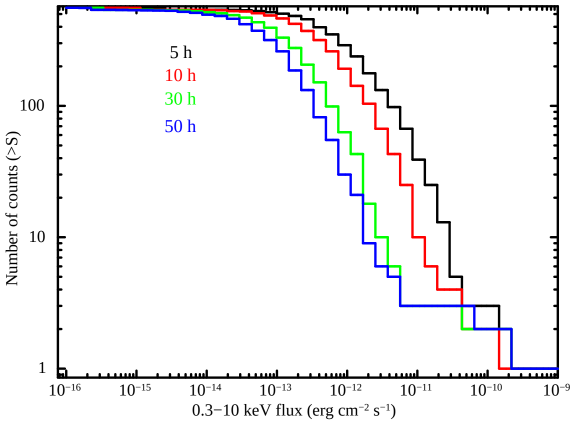

Figure 6: Estimated luminosity functions of GRB afterglow based on 6-yeas Swift-XRT data base. Different colors show the function corresponds to the different observation start time from GRB trigger. (black: 5 hours, red: 10 hours, green: 30 hours, and blue: 50 hours).

5. Summary

In this paper, we demonstrated the capability of GRB observation by *ASTRO-H*. As for the prompt gamma-ray emission, the SGD shield detector will act as powerful GRB monitor with very large effective area. Especially for the short GRBs, time-resolved spectroscopy with good photon statistics can be performed by the SGD shield and such GRB data can be a complimentary data set to Fermi-GBM. About a half of GRBs that are detected by Fermi-GBM are also expected to be observed by the the SGD shield simultaneously. High resolution spectroscopy by *ASTRO-H* SXS and SXI is expected to reveal the existence of spectral features in the GRB afterglow spectrum such as emission lines from iron-K and/or other light metals, and absorption by intergalactic medium. The expected event rate of GRBs which can be used for such search of spectral features is estimated to be ~ 10 GRBs/year, if we can slew the spacecraft within 1-day after the GRB trigger. More details about *ASTRO-H* observation of GRB afterglow can be found in the *ASTRO-H* white paper[1].

References

[1] M. S. Tashiro, et al. "ASTRO-H White Paper - Chemical Evolution in High-z Universe", arXiv:1412.1179, 2014.
[2] Piro, L., et al. "The X-Ray Afterglow of the Gamma-Ray Burst of 1997 May 8:Spectral Variability and Possible Evidence of an Iron Line", ApJ, 514, L73, 1999.
[3] Yoshida, A., et al. , Proc. of “Gamma-ray bursts in the afterglow era’ , (A&AS, 138), 433, 1999.
[4] Piro, L. et al. "Observation of X-ray Lines from a Gamma-Ray Burst (GRB991216): Evidence of Moving Ejecta from the Progenitor", Science, 290, 955, 2000.
[5] Reeves, J. N. et al. "The signature of supernova ejecta in the X-ray afterglow of the -ray burst 011211", Nature, 416, 512, 2002.
[6] Reeves, J. N. et al. "Soft X-ray emission lines in the afterglow spectrum of GRB 011211: A detailed XMM-Newton analysis", A&A, 403, 463, 2003.
[7] Evans, P. A. et al. "Methods and results of an automatic analysis of a complete sample of Swift-XRT observations of GRBs", MNRAS, 397, 1177, 2009
[8] Yamaoka, K, et al. "Design and In-Orbit Performance of the Suzaku Wide-Band All-Sky Monitor", PASJ, 61S, 35, 2009.
[9] Behar, E., Dado, S., Dar, D., Laor, A. "Can the Soft X-Ray Opacity Toward High-redshift Sources Probe the Missing Baryons?", ApJ, 734, 26, 2011.
[10] Starling, R. L. C., et al. "X-ray absorption evolution in gamma-ray bursts: intergalactic medium or evolutionary signature of their host galaxies", MNRAS, 431, 3159, 2013.

Development of a micro-satellite TSUBAME for X-ray polarimetry of GRBs

Shin Kurita, Haruka Ohuchi, Makoto Arimoto, Yoichi Yatsu, Nobuyuki Kawai
Dept. of Physics, Tokyo Institute of Technology, 2-12-1 Ookayama, Meguro-ku, Tokyo, Japan 152-8551
Kei Ohta, Masaya Koga, EuGene Kim, Kyosuke Tawara, Souta Suzuki, Kazuyoshi Miyasato, Takashi Nagasu, Shouta Kawajiri, Masanori Matsushita
Dept. of Mechanical and Aerospace Engineering, Tokyo Institute of Technology, 2-12-1 Ookayama, Meguro-ku, Tokyo, Japan 152-8551
Saburo Matunaga
Dept. of Mechanical and Aerospace Engineering, Tokyo Institute of Technology, 2-12-1 Ookayama, Meguro-ku, Tokyo, Japan 152-8551 and
Dept. of Space Structure and Materials, Institute of Space and Astronautical Science, Japan 252-5210
Nagahisa Moriyama, Shin'ichi Kimura
Dept. of Electrical Engineering, Tokyo University of Science, Japan
and TSUBAME team

arXiv:1503.01975v1 [astro-ph.IM] 6 Mar 2015

TSUBAME is a micro-satellite that the students of Tokyo Institute of Technology took the lead to develop for measuring hard X-ray polarization of Gamma-Ray Bursts(GRBs) in order to reveal the nature of the central engine of GRBs. TSUBAME has two instruments: Wide-field Burst Monitor (WBM) and Hard X-ray Compton Polarimeter (HXCP). We aim to start observing with HXCP in 15 seconds by pointing the spacecraft using Control Moment Gyro.
In August 2014, we assembled TSUBAME and performed an integration test during 2 weeks. On Nov 6 2014, TSUBAME was launched from Russia and it was put into Sun-synchronous orbit at 500 km above the ground. However, serious trouble occurred to the ham radio equipment. Therefore we could not start up the X-ray sensors until Feb 10 2015. In this paper, we report the system of TSUBAME and the progress after the launch.

1. Introduction

Gamma-ray bursts(GRBs) are known as one of the powerful explosions in the universe. However, it is not yet clear how to form the collimated outflow wave and accelerate particles. In recent theoretical models, the magnetic field plays a important role that connects the central engine and the relativistic outflow. The magnetic field might affect the charged particles in the shock front that radiates the X-ray prompt emission. Therefore, the X-ray polarization information of prompt emission can constrain the physical process that generate the relativistic outflow from GRBs.

To reveal the physical process of GRBs, we developed a micro-satellite TSUBAME (Figure.1). The details of TSUBAME's BUS system are summarized in Table.I.

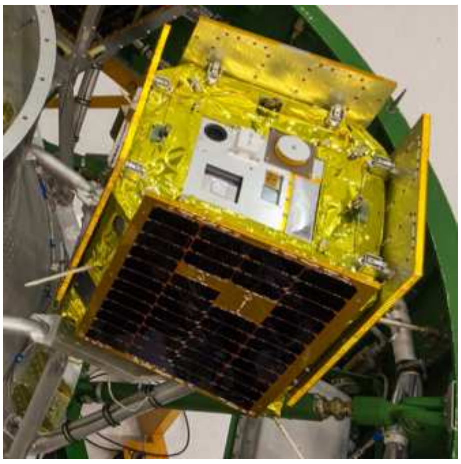

Figure 1: Overview of a micro-satellite TSUBAME.

2. GAMMA-RAY OBSERVATION SYSTEM

2.1. Overview

The micro-satellite TSUBAME has 2 instruments for X-ray polarimetry of GRBs: Wide-field Burst Monitor(WBM) and Hard X-ray Compton Polarimeter(HXCP). The HXCP utilizes the asymmetry of the Compton scattering arising from the polarization of incident photons. The WBM, which consists of five X-ray detectors mounted on the five faces of the satellite, detects GRBs and determines those positions by comparing the count rates in them. To detect GRBs, WBM is always monitoring X-ray from half of the sky. If WBM detects a GRB, this satellite points to the target rapidly using a high-speed attitude control system and starts the observation within 15 s after the detection(Figure.2).

Size	610 x 610 x 540 mm^3	
Mass	48.6 kg	
Orbit	500 km (Sun Synchronous)	
Launch	Nov 6, 2014	
Electrical Power Supply	Cell	InGaP/InGaAs/Ge
	Power	130 W (EOL)
	Battery	360Wh (Li-Polymer)
Command & Data Handling(CDH)	Tx	S-band (BSPK-100 kbps) UHF (CW/GMSK-9600bps AFSK-1200bps)
	Rx	VHF AFSK-1200bps
Attitude Determination and Control Systems (ADCS)	3-axis bias momentum control	
	Actuator	Control Moment Gyro./Magnetic Torquers
	Sensor	Gyro (MEMS/FOG), Sun Sensor, Magnetometer, Star Tracker, GPS

Table I BUS System of TSUBAME.

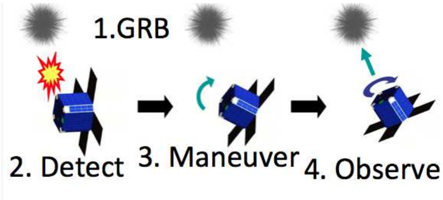

Figure 2: Sequence when a GRB occurs.

2.2. Hard X-ray Compton Polarimeter

To maximize the cross section of the Compton scattering, HXCP employed 8 × 8 ch plastic scintillators connected with the multi-anode photomultipliers(MAPMTs). These scintillators are surrounded by 28 ch CsI scintillators connected with 5 × 5 mm^2 APDs. Incident photons are scattered at plastic scintillators, and absorbed at CsI scintillators. Linearly polarized photons tend to be scattered perpendicular to the polarization plane. HXCP measures the X-ray polarization using this angular dependence.

In order to evaluate and demonstrate the performance of the HXCP, we executed the performance test at a synchrotron beam facility, the Photon Factory of KEK the high energy accelerator research organization, in December 2012. We irradiated 80 % on-axis 90 % polarized synchrotron X-ray. Before calculating the azimuthal scattering angle for every single photon, we filtered the accumulated photon events with three criteria: (1) a lower threshold energy for PMTs, $>$ 2keV, (2) a lower threshold energy for APDs, $>$ 20keV, (3) a geometric constraint on the energy distribution between the recoil electron and the scattered photon. The modulation curve as functions of the azimuthal scattering angle using the screened event data with the above three criteria are shown in Figure.4. We obtained 68 % of the modulation factor. As well, we drew a modulation curve using the photon event date of same X-ray with off-axis, and we obtained over 60 % of the modulation factor(Figure.5).

2.3. Wide-field of Burst Monitor

Wide-field Burst Monitor(WBM) consists of five sintillation gamma-ray counters with APDs and CsI scintillator for real time detection and localization of GRBs. These detectors are mounted on the five faces of TSUBAME.

The time scale of GRBs ranges from milli-second to kilo-seconds. In order to start a pointing observation with the HXCP as soon as possible, WBM must detect any GRBs faster. To detect GRBs, on-board CPU checks the variation of X-ray count rate of WBM every 125 msec. WBM employs 4 trigger systems with different time constants which covers short GRBs and long GRBs. In designing these trigger systems, we refer to the trigger systems of HETE-II(Figure.7). The on-board CPU estimates the background events, $C'_{\rm BG}$, at the time window, $T_{\rm FG}$, from the past background events, $C_{\rm BG}$, at the time window, $T_{\rm BG}$, using the recorded light curves. The net photon events, $C_{\rm Sig}$, can be written as

$$C_{\rm Sig} = C_{\rm FG} - C'_{\rm BG} = C_{\rm FG} - \frac{T_{\rm FG}}{T_{\rm BG}}. \qquad (1)$$

If we assume that the background rate fluctuates statistically, the significance, s, of the $C_{\rm Sig}$ comparing with the background fluctuation is expressed as $s = C_{\rm Sig}/\sqrt{C_{\rm BG}}$. The on-board CPU evaluates s^2 at every 125 ms to check the variability of the light curves for each energy band and detector.

When trigger system detect a GRB, WBM determines the position of GRB by comparing the event rates of these five X-ray detectors with an accurary of 5 degree for a bright GRB with an occurrence rate of

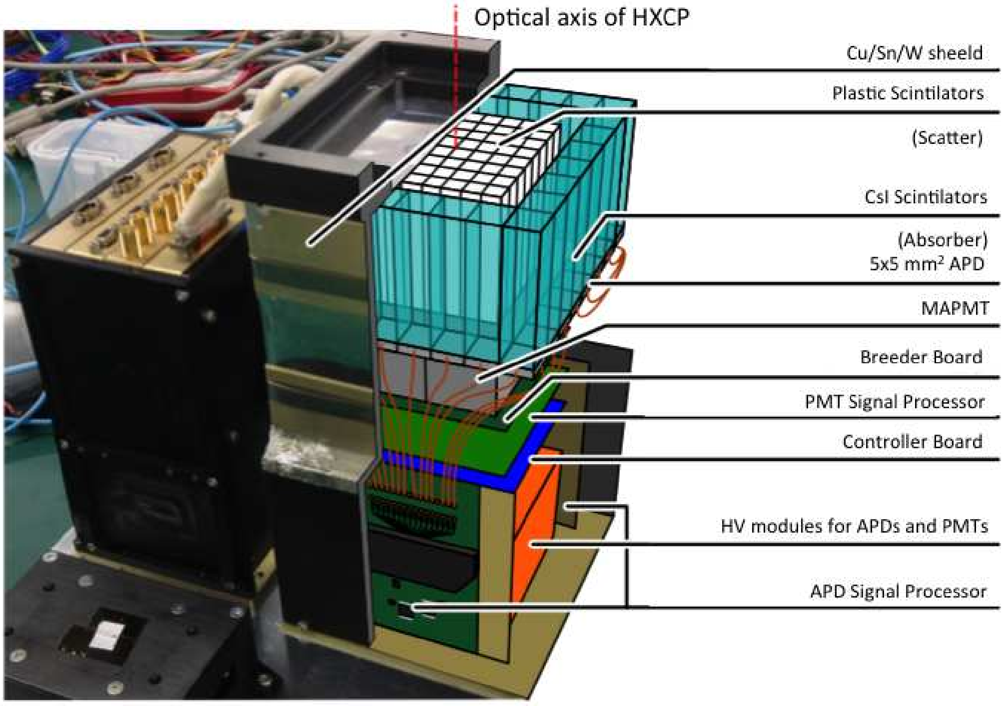

Figure 3: Overview of HXCP and a circuit box.

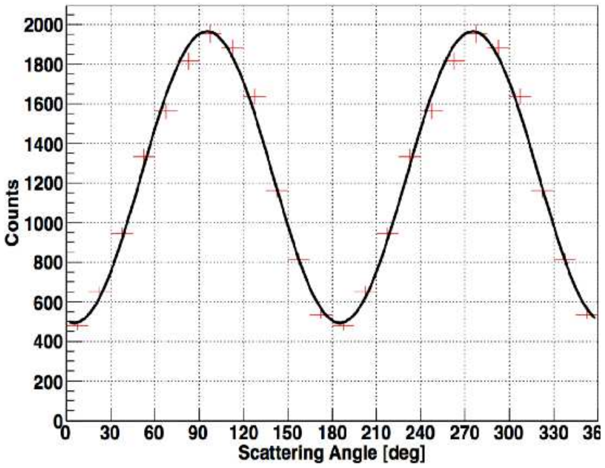

Figure 4: Modulation Curve with 80 % on-axis 90 % synchrotron X-ray. We got 68.5 ± 0.3 % of modulation factor.

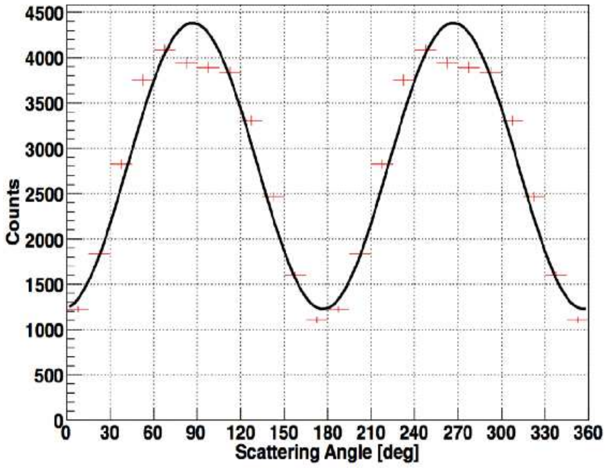

Figure 5: Modulation Curve with 80 % off-axis 90 % synchrotron X-ray. The incident angle is 30 degree. We got 62.6 ± 0.6 % of modulation factor.

10 bursts per year. This method have been employed by the BATSE abroad CGRO and the GBM on the Fermi gamma-ray observatory. However the expected position accuracy is not so good, this accuracy is sufficient for polarimetry using the flight model HXCP with a wide FoV.

After WBM determines the position of GRB, TSUBAME starts high-speed attitude control with Control Moment Gyroscopes pointing to the GRB. Using Control Moment Gyroscopes, TSUBAME can maneuver ten times as fast as Swift.

3. Operation

To protect HXCP from the damages in South Atlantic Anomaly(SAA) and Auroral zone, we will have to drop the high voltage of MAPMTs. TSUBAME

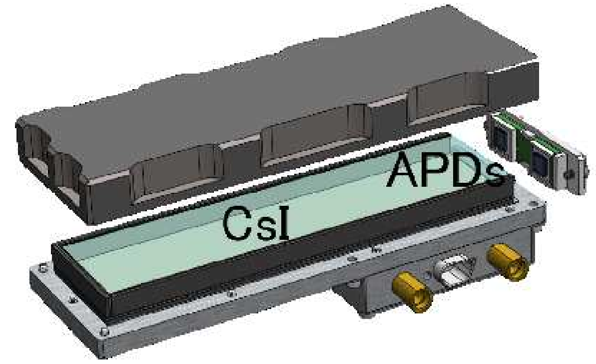

Figure 6: Overview of WBM.

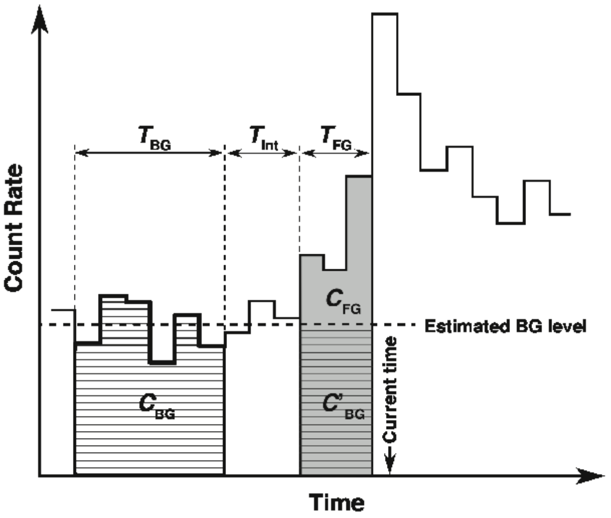

Figure 7: Description of the WBM trigger algorithm.

has three ways to judge whether it is in SAA or not. At first, on-board CPU compares GPS location to the stored SAA map in Figure.8. The shading area describes the prohibited regions in which the particle flux of electrons above 1 MeV exceeds 300 counts s^{-1} cm^{-2} and that of protons above 20 MeV exceeds 0.3 counts s^{-1} cm^{-2}. This map is based on Space Environment Information System and Cute-1.7+APDII data in orbit. Secondly, we set specific GRB trigger patterns as indications of SAA. When TSUBAME enters this area, the count rate of WBM increase slowly than GRBs. Because the trigger system of WBM can detect every increase of count rate depending on parameters, we set 1 trigger for SAA trigger. Finally, we predict the timing from the satellite orbital element and uplink the stored commands via 430MHz band.

However the trigger system detects the variation of count rate of WBM, it can not distinguish GRBs or known blight sources. In order to avoid false triggers caused by a steady bright X-ray sources appearing from the horizon, GRB triggers must be disabled by the stored commands at these predicted timings.

For above reasons, we must uplink over-100 commands for an observation. In order to execute commands at relevant timings, we developed the command generating program. Refering to DP10 which is a graphical command check program used in Suzaku operation, we developed the program, the dp10 of TSUBAME, to display the types and timings of commands at a time axis so as to confirm generated commands by human eyes. Figure.9 is a graphical check sheet generated by the dp10 of TSUBAME.

After observations, we downlink the observation data via S-band. The maximum data size is about 6 MByte and it will take 80 min to downlink.

4. After Launch

In August 2014, we assembled TSUBAME and performed an integration test. We operated TSUBAME continuously during ∼ 2 weeks. We successfully operated all the sequence.

TSUBAME was launched from Russia on Nov 6 2014. After the launch, we succeeded to obtain telemetries at Tokyo Tech ground station. We confirmed that TSUBAME had succeeded to expand the solar cell panels and to point at the Sun, However, serious trouble occurred to the ham radio equipment. Therefore we could not start up the X-ray sensors until Feb 10 2015.

References

[1] Y. Yatsu et al, “Pre-flight performance of a micro-satellite TSUBAME for X-ray polatimetry of gamma-ray bursts”, Proceeding of SPIE, Vol.9144, 2014

[2] T. Tavenner et al, “The Effectiveness of the HETE-2 Triggering Algorithm”, American Institute of Physics Conference Services 662, 2003

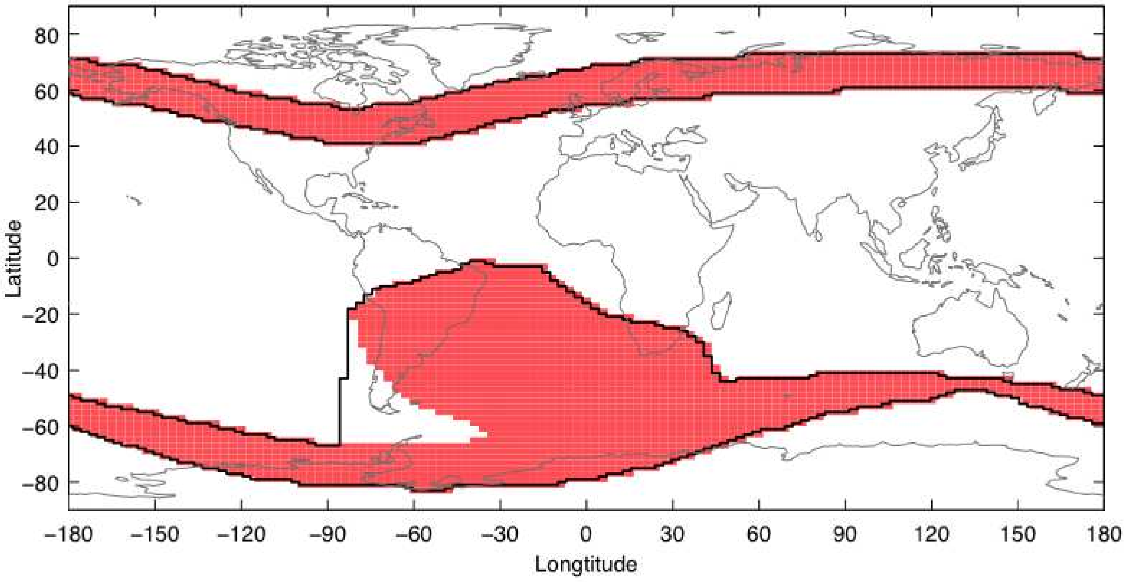

Figure 8: Stored SAA map.

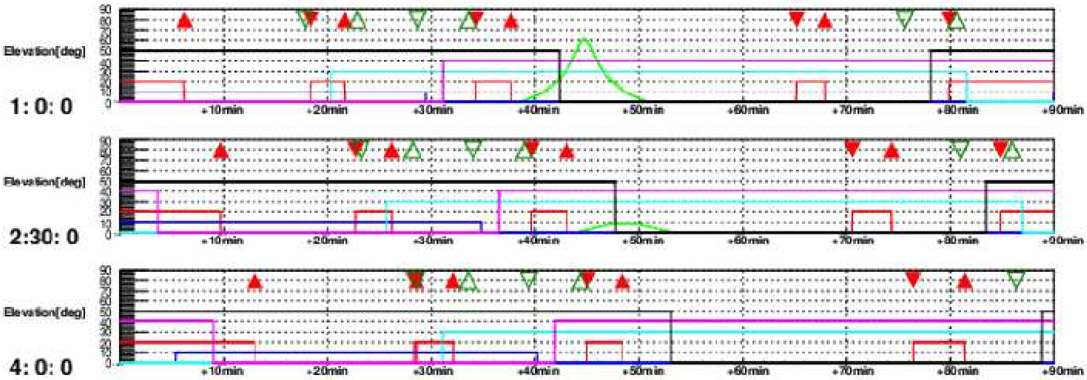

Figure 9: Graphical check sheet generated by the dp10 of TSUBAME. The green line shows the elevation of TSUBAME. The red, blue, magenta, cyan, and black lines shows the flag of SAA, shade, Sco-X1, Cygnus-X1, and Crab respectively. The red triangles show the timings of HV on/off. The green triangles show the timings of WBM trigger enable/disable.